

RECENT ADVANCES IN  
MODELLING AND SIMULATION



# **RECENT ADVANCES IN MODELLING AND SIMULATION**

EDITED BY  
GIUSEPPE PETRONE AND GIULIANO CAMMARATA

***I-Tech***

Published by I-Tech Education and Publishing

I-Tech Education and Publishing  
Vienna  
Austria

Abstracting and non-profit use of the material is permitted with credit to the source. Statements and opinions expressed in the chapters are those of the individual contributors and not necessarily those of the editors or publisher. No responsibility is accepted for the accuracy of information contained in the published articles. Publisher assumes no responsibility liability for any damage or injury to persons or property arising out of the use of any materials, instructions, methods or ideas contained inside. After this work has been published by the I-Tech Education and Publishing, authors have the right to republish it, in whole or part, in any publication of which they are an author or editor, and the make other personal use of the work.

© 2008 I-Tech Education and Publishing  
[www.i-techonline.com](http://www.i-techonline.com)  
Additional copies can be obtained from:  
[publication@ars-journal.com](mailto:publication@ars-journal.com)

First published June 2008  
Printed in Croatia

A catalogue record for this book is available from the Austrian Library.  
Recent Advances in Modelling and Simulation,  
Edited by Giuseppe Petrone and Giuliano Cammarata  
p. cm.  
ISBN 978-3-902613-25-7  
1. Modelling 2. Simulation. I. Petrone. II. Cammarata

## Preface

We live in the Information Age. This term often alludes to the global economy's shift in focus away from the Industrial Age. The relatively recent field of information technology concerns the use of computer-based information systems to convert, store, protect, process, transmit and retrieve information. Technological advances in this field have changed lifestyles all over the world.

Some years ago a well-known book captured one of the essences of the ongoing changes. It discusses similarities and differences between products made of atoms and products made of bits. It was pointed out as it is becoming more and more cheaply and quickly making - or better saying "modelling" - a bits made copy of a product (for instance a letter) and ship it around the world at very low cost. The negative historical connotation of the word "simulation", that referred to the meaning of let appear events different from reality, quickly faded out, giving way to the modern and among all accepted meaning of virtual reproduction of physical systems.

Since 1960's the idea of emulating reality in a computer environment rapidly spread among researchers, being accepted as one of the most powerful tool both for understanding phenomenological aspects of a chosen physics and for predicting functional or operative conditions of technological systems. The main concept standing on the basis of the simulating approach consists in numerically solving a mathematical model that governs a chosen physical system, whose the analytical solution is not known or difficult to reach for a specific application. In spite of many efforts spent in the past for formulating accurate and robust algorithms for solving mathematical models, the effectiveness of that approach strongly depends on computational resources. This explains why we are only since few years attending at the large scale diffusion of the simulating approach in solving both scientific and industrial problems.

The advances in computer hardware have led to new challenges and opportunities for researchers aimed at investigating on complex systems. The actual computational speed and capability, very often related to the opportunity of exploiting parallel distributed memories and processors, allow to carry out simulation of real world problems, characterized by interdependent effects of multiple, coupled and simultaneous physical phenomena, whether they be structural, fluid, acoustic, chemical, electromagnetic or thermal in nature.

This book collects original and innovative research studies concerning modeling and simulation of physical systems in a very wide range of applications, encompassing micro-electro-mechanical systems, measurement instrumentations, catalytic reactors, biomechanical applications, biological and chemical sensors, magnetosensitive materials, silicon photonic devices, electronic devices, optical fibers, electro-microfluidic systems, composite materials, fuel cells, indoor air-conditioning systems, active magnetic levitation systems and more. Some of the most recent numerical techniques, as well as some of the software among the most accurate and sophisticated in treating complex systems, are applied in order to exhaustively contribute in knowledge advances.

Heterogeneous just at first sight, all original contributions collected in this book are strictly jointed by a recursive leitmotiv: recognized as one of the keys for the present and future developing in numerical simulation, the multi-physical based analysis can be credited as the most important modelling tool for the complex systems comprehension.

Editors

**Giuseppe Petrone and Giuliano Cammarata**

---

## Contents

Preface	V
1. Braking Process in Automobiles: Investigation of the Thermoelastic Instability Phenomenon <i>M. Eltoukhy and S. Asfour</i>	001
2. Modeling and Numerical Investigation of Photoacoustic Resonators <i>Bernd Baumann, Bernd Kost, Marcus Wolff and Hinrich Groninga</i>	017
3. Multi-Agent Systems for the Simulation of Land Use Change and Policy Interventions <i>Pepijn Schreinemachers and Thomas Berger</i>	039
4. Pore Scale Simulation of Colloid Deposition <i>M. Ekrem Cakmak, Bin Gao, John L. Nieber, and Tammo S. Steenhuis</i>	055
5. Practical Application of Simulation Technique for the Resonators Using Piezoelectric Ceramics <i>Jeong-Ho Cho, Yong-Hyun Lee, Myung-Pyo Chun and Byung-Ik Kim</i>	067
6. Computation of the Complex Impedance of a Cylindrical Conductor in an Ideal Two-Probe Configuration <i>V. Siva Kumar G. Kelekanjeri and Rosario A. Gerhardt</i>	085
7. Evolutionary Constructive Approach for Studying Dynamic Complex Systems <i>Takashi Hashimoto, Takashi Sato, Masaya Nakatsuka and Masanori Fujimoto</i>	111
8. Transient Runaway in a Fixed-Bed Catalytic Reactor <i>Redhouane Henda</i>	137
9. Carotid Plaque Stresses <i>Samuel Alberg Kock and Jens Vinge Nygaard</i>	147
10. Electromagnetic Flow Metering <i>Jens Krause</i>	165
11. Finite Element Modelling of Micro-cantilevers Used as Chemical Sensors <i>G. Louarn and S. Cuenot</i>	187
12. Analysis of Electrical Phenomena Occurring in Thermally Assisted Mechanical Dewatering Processes (TAMD)-a Preliminary Study <i>Akrama Mahmoud, Aurora Fernandez and Patricia Arlabosse</i>	201

13.	Simulation of Plastic Deformation Processes Through a Navier-Stokes Approach <i>Carlo Mapelli, Cristian Corna and Francesco E. Magni</i>	223
14.	2D Model of a Floating Body Under Nonlinear Waves <i>Luca Martinelli and Piero Ruol</i>	233
15.	Modelling of Magnetosensitive Elastomers <i>Bohdana Marvalova</i>	245
16.	Simulation of Net Structures Hydrodynamic Fields <i>Leonid Meyler</i>	261
17.	Modeling and Simulation of Microscale Flows <i>Auro Ashish Saha and Sushanta K. Mitra</i>	283
18.	Multiphysics Modelling and Simulation in Engineering <i>Alexandru M. Morega and Juan C. Ordonez</i>	317
19.	New Methods to Model and Simulate Both Air Exchange and Particle Contamination of Portable Devices <i>Markus Olin, Lauri Laakso, Jukka Hannula, Timo Galkin, Kyösti Väkeväinen, Kari Hartikainen and Eini Puhakka</i>	341
20.	Recent Advances in Modelling and Simulation of Silicon Photonic Devices <i>Vittorio M. N. Passaro and Francesco De Leonardis</i>	367
21.	Numerical Modelling for Thermal Design of Electronic Equipments <i>Giuseppe Petrone and Giuliano Cammarata</i>	391
22.	Modelling of Long Period Gratings in Photonic Crystal Fibres and Sensors Based on Them <i>Jovana Petrovic</i>	417
23.	A New Methodology for RF MEMS Simulation <i>Peyrou David, Coccetti Fabio, Achkar Hikmat, Pennec Fabienne, Pons Patrick and Plana Robert</i>	433
24.	Active Magnetic Suspension and Bearing <i>Adam Krzysztof Piłat</i>	453
25.	Modeling and Simulation of Piezoelectric Devices <i>Dorina Popovici, Florin Constantinescu, Mihai Maricar, Florea Ioan Hantila, Miruna Nitescu and Alexandru Gheorghe</i>	471
26.	Multiphysical Modeling of DC and AC Electroosmosis in Micro- and Nanosystems <i>Michal Přibyl, Dalimil Šnita and Miloš Marek</i>	501



---

27.	Efficient Simulation of Thermal and Electrical Behaviour of Industrial Cables <i>Hans-Peter Schmidt</i>	523
28.	Finite Element Simulation of Heat Transfer in Ferrofluid <i>Tomasz Streck</i>	533
29.	Computational Modelling of Mass Transport in Large Arteries <i>Nanfeng Sun, Nigel B. Wood and X. Yun Xu</i>	555
30.	Modeling of Surface-bed Reactor for Endothermic and Exothermic Reactions Coupling <i>Salvatore Vaccaro and Paolo Ciambelli</i>	581
31.	Multiscale Heat, Air and Moisture Modelling and Simulation <i>A.W.M. van Schijndel</i>	607
32.	Numerical Simulation of Turbulent Air Flows in Aseptic Clean Rooms <i>Eleonora Bottani, Roberto Rizzo and Giuseppe Vignali</i>	633
33.	Elastic Modulus FEM Modelling of the Layered Woven Composite Material <i>Pavla Vozkova</i>	651
34.	Two-Dimensional PEM Fuel Cells Modeling using COMSOL Multiphysics <i>Zhongying Shi and Xia Wang</i>	677



# Braking Process in Automobiles: Investigation of the Thermoelastic Instability Phenomenon

M. Eltoukhy and S. Asfour

*Department of Industrial Engineering, College of Engineering, University of Miami  
USA*

## 1. Introduction

During the braking action, the kinetic energy produced at the wheel is transformed into heat energy, which doesn't dissipate fast enough into the air stream from the brake to the brake disk; as a result, the thermal conductivity plays a critical role in handling such heat generated.

Thermal judder, which is a result of non-uniform contact cycles between the pad and the disk brake rotor, which is primarily an effect of the localized Thermo-Elastic Instabilities (TEI) at the disk brake rotor surface. Localized TEI act at the friction ring surface generating intermittent hot bands around the rubbing path which may in turn leads to the development of so-called hot spots.

In this chapter a case study regarding a transient analysis of the thermoelastic contact problem for disk brakes with frictional heat generation, performed using the finite element analysis (FEA) method is described in details. The computational results are presented for the distribution of the temperature on the friction surface between the contacting bodies (the disk and the pad).

Also, the influence of the material properties on the thermoelastic behavior, represented by the maximum temperature on the contact surface is compared among different types of brake disk materials found in the literature, such as grey cast iron (grey iron grade 250, high-carbon grade iron, titanium alloyed grey iron, and compact graphite iron (CGI)), Aluminum metal matrix composites (Al-MMC's), namely Al<sub>2</sub>O<sub>3</sub> Al-MMC and SiC Al-MMC (Ceramic brakes).

This comparison was performed in order to improve the conceptual design of the disk brakes. The results obtained from the suggested model are compared with actual measurements obtained from experiments performed by Cueva et al.(2003). The FEA results were in excellent agreement with the actual measurements reported by Cueva et al. for all of the suggested brake disk materials.

A comparison between two different brake disk rotor designs was performed as well in order to study the effect of the perforated brake disks on the maximum temperature, the temperature distribution, and the heat flux produced under the same braking conditions.

### 1.1 Braking process

By pressing the brake pedal the car transmits the force from the driver's foot to the brakes through a fluid then the brakes transmit the force to the tires by friction, as a result the tires transmit that force to the road using friction as well. Figure 1 depicts a simple braking system. One important conclusion can be drawn from the shown figure, that the force applied by the driver is multiplied by a certain factor (about 36) through two mechanisms, first is through the distance from the cylinder to the pivot, and second is the difference in the brake cylinder compared to the pedal cylinder.

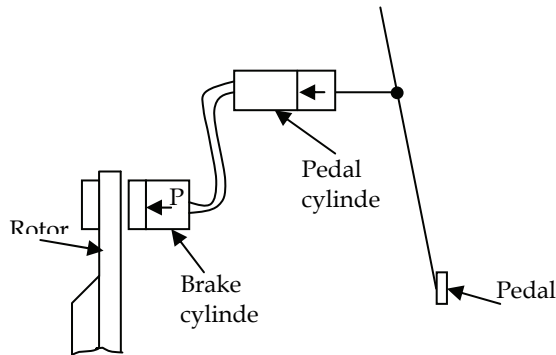


Figure 1. Simple braking system

In this chapter, the main type of brakes that are investigated is the single-piston floating calliper disk brakes. Figure 2 shows the main components of that type of disk brakes, which are; the calliper, the rotor, and the pads.

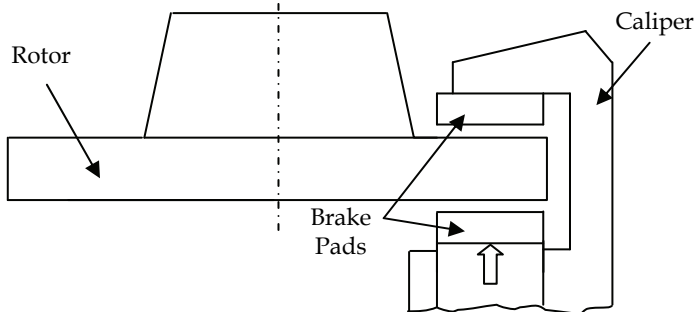


Figure 2. Disk brake components

## 2. Vehicles Dynamics

Load transfer refers to the shifting of weight around a vehicle during acceleration. This includes braking, and deceleration. It is important to differentiate between two terms that are used, in the literature, interchangeably although they are not synonymous; load transfer and weight transfer. The difference between the two terms is that, load transfer is an imaginary shift in the weight due to acceleration while the weight transfer involves the actual movement of the vehicle's centre of gravity relative to the wheel axes. These two

terms are used to describe the redistribution of the total vehicle load among the different tires. The traction at each wheel to accelerate the vehicle in such direction is affected by load transfer; if the load is equally distributed among the tires then more total traction will be available.

The main forces that accelerate a vehicle occur at the tires' contact patches. Since these forces are not directed through the vehicle's CoG, one or more moments are generated whose forces are the tires' grip forces, the other one, which is equal in magnitude but opposed in direction, is the mass inertia located at (CoG). These moments cause variation in the load distributed among the tires.

According to Newton's second law written for the x-direction (see Fig.3.), the braking forces can be written as:

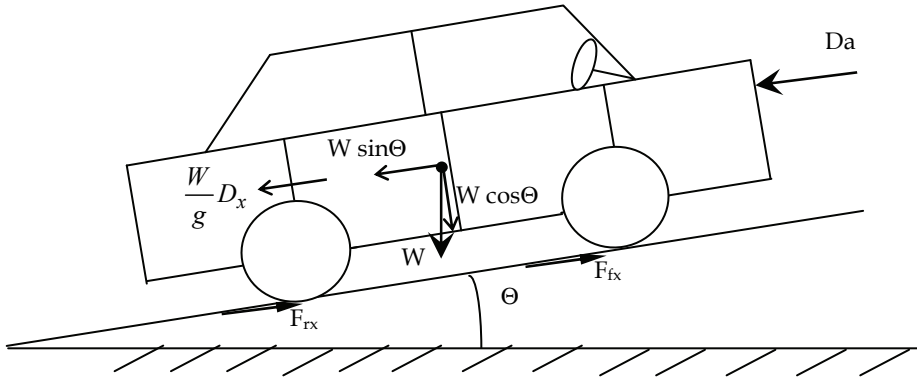


Figure 3. The major forces acting on the vehicle

$$\sum F_x = M.a_x = -\frac{W}{g}D_x = -F_{fx} - F_{rx} - D_a - W \sin \Theta \quad (1)$$

Where:

$F_x$ : Forces in the x-direction

M: Mass

$a_x$ : Acceleration in the x-direction

W: Body weight

g: Gravitational acceleration

$D_x$ : Linear deceleration

$F_{fx}$ : Front braking force

$F_{rx}$ : Rear braking force

$D_a$ : Aerodynamic drag

$\Theta$ : Uphill grade

A number of important terms related to the braking performance are described below; these terms are constant deceleration, rolling resistance, and aerodynamic drag.

#### **Constant deceleration**

Based on the assumption that the forces acting on the vehicle will remain constant during the braking application, and according equation (1), the following can be obtained:

$$D_x = \frac{F_{tx}}{M} = -\frac{dV}{dt} \quad (2)$$

Where:

$F_{tx}$ : The total deceleration forces in the x-direction

V: Velocity

Assume that the vehicle initial velocity is  $V_1$  and the final velocity is  $V_2$ , and the time needed for the velocity to be changed from  $V_1$  to  $V_2$  is  $T$ . By integrating equation (2) the following will be obtained:

$$\int_{V_1}^{V_2} dV = -\frac{F_{tx}}{M} \int_0^T dt \quad (3)$$

$$V_1 - V_2 = \frac{F_{tx}}{M} T \quad (4)$$

In case of complete stop ( $V_2=0$ ), and according to the relationship between distance and velocity, the distance ( $X_s$ ) and time ( $T_s$ ) needed for the vehicle to reach complete stop can be determined as follows;

$$X_s = \frac{V_1^2}{2D_x} \quad (5)$$

$$T_s = \frac{V_1}{D_x} \quad (6)$$

### ***Rolling Resistance***

This resistance helps the brakes stopping the vehicles; a typical value to this type of resistance is  $0.3 \text{ ft/sec}^2$ .

### ***Aerodynamic Drag***

Depends on the dynamic pressure, and its proportional to the speed squared. This type of drag is to be neglected at low speeds.

## **3. Thermo-Elastic Instability (TEI)**

As shown before, the brake pads squeeze against the rotor, thus friction between the pads and the disc slows the vehicle down. The brakes then have to remove the kinetic energy from the vehicle, and in turn it converts it into heat.

Frictional heat generated due to friction as well as the thermoelastic deformation alters the contact pressure distribution between the two contacting surfaces, as a result and above a certain speed (critical speed), hot spots are observed due to the localization of heat generated (Barber, 1969 and Kennedy & Ling, 1974). Hot spots can be a source of frictional vibrations known as hot judder (Zagrodzki, 1990).

Once the brake pads come in contact with the sinusoidal surface during braking severe vibrations are induced. Thermal stresses due to high temperatures may induce a number of unfavorable conditions such as surface cracks and permanent distortions. Frictional heating, thermal deformation and elastic contact in sliding contact systems affect the contact pressure and temperature on the friction surfaces.

Accordingly, TEI imposes design constraints on systems such as automotive brakes and clutches, thus it has been investigated by a number of researchers. The mechanism of TEI in sliding systems involving frictional heating was first explained by Barber (1967), who observed experimentally the resulting hot spots in railway brakes. Kennedy and Ling (1974) were first to obtain numerical simulations of thermomechanical behaviours occurring in aircraft-type multidisk brakes.

Zagrodzki et al.(1990) implemented a transient finite element simulation for the 2-D thermoelastic contact problem of a stationary layer between two sliding layers with frictionally excited thermoelastic instability using the Petrov–Galerkin algorithm. Choi and Lee developed a finite element model for an axisymmetric coupled thermoelastic contact problem simulating a disk brake and investigated the TEI phenomena of disk brakes during the drag braking process.

### **3.1 Thermo-Mechanical Distortion of Disk Rotors**

Due to the non equilibrium thermal expansion of the rotor, increase in the thermal deformation takes place which in turn results in further localization of the friction contact. Thermal deformation contributes to a number of geometrical distortions in the disk rotor, it may lead to warped friction ring (thermal buckling), and also it may result in disk coning (Sterne, 1989). The thermal judder phenomenon may also lead to radial cracking as a result of the high generated compressive hoop stresses and / or plastic flow of the rotor surface.

The pattern of surface temperature variation in the radial direction of the friction ring being seen to be the same for both sides of the friction ring. Lateral / axial, Side-face RunOut of the disc brake rotor has also been shown to make some contribution to the phenomenon of hot spotting and thus to thermal judder (Inoue, 1986). As a result of the high thermal stresses involved, permanent deformations of the rotor geometry may also persist beyond the braking applications where judder phenomena are experienced. Also, the occurrence of hot spots places high thermal load on the rotor material and may lead to phase transformations within the cast iron.

A number of approaches have been suggested to help solving the thermal judder problem, these approaches have in common that they try improving the distribution of the heat generated, some of the solutions suggested includes improving the thermal conductivity and specific heat capacity of the rotor material, and reducing the friction contact arc length.

## **4. Case study**

### **4.1 Problem definition**

During the braking action, the kinetic energy produced at the wheel is transformed into heat energy, which doesn't dissipate fast enough into the air stream from the brake to the brake disk, because of that, one of the disk brake material properties; the thermal conductivity plays a critical role in handling such friction heat generated. Thermal judder occurs as a result of non-uniform contact cycles between the pad and the disk brake rotor, which is primarily an effect of the localized Thermo-Elastic Instabilities at the disk brake rotor surface.

Localized TEI act at the friction ring surface generating intermittent hot bands around the rubbing path which may in turn leads to the development of so-called hot spots (Eggleston, 2000).The mechanism of the TEI phenomena taking place during the braking process has been of interest to many researchers (Lee, 2000; Jang & Khonsari, 2003; Lee & Brooks, 2003; Dufrenoy, 2004; Jacobsson, 2003).

The suggested FEA model simulates the braking action by investigating both the thermal and elastic actions occur during the friction between the two sliding surfaces (the disk brake and the pad). The TEI phenomenon of disk brakes is investigated during repeated brake cycles. Also, the influence of the material properties on thermoelastic behaviours is investigated to facilitate the conceptual design of the disk brake system.

## 4.2 Methodology

In this case study (Based on the work done by Eltoukhy et al., 2006) an assumption has been made that the thermomechanical phenomenon of each disk are in symmetry about the disk's mid-plane. Also, the wear action taking place during the braking process, resulting from the friction between the disk brake and the pad, is assumed to be so small and thus to be neglected in the analysis.

The simulation was divided into two parts: thermal and elastic. During the analysis, the braking parameters are set to certain values based on the values that have been stated in the literature. These parameters include the rotational speed of the disk brake and the cycle of the pressure applied. Figure 4 depicts the change in pressure during the braking process, and the time period of the different phases of, braking, dragging, and release.

As shown in figure 4, it is assumed that the pressure will first increase linearly until it reaches the maximum value  $P_{\max}$  (point A to B) within a period of time depends on the vehicle's dynamics, then the pressure remains constant (point B to C), then it drops to zero (point D).

The governing equation for the transient heat transfer problem is:

$$\rho C \frac{\partial T}{\partial t} + \nabla \cdot (-k \nabla T) = Q - \rho C_p u \cdot \nabla T \quad (8)$$

Where:

$\rho$ : Density	$k$ : Thermal conductivity
$C$ : Heat capacity	$Q$ : Heat source or heat sink
$T$ : Temperature	$C_p$ : Specific heat capacity
$u$ : Velocity field	

While the governing equation for the elastic problem is:

$$\rho \frac{\partial^2 u}{\partial t^2} - \nabla \cdot c \nabla u = K \quad (9)$$

Where, K is the force vector.

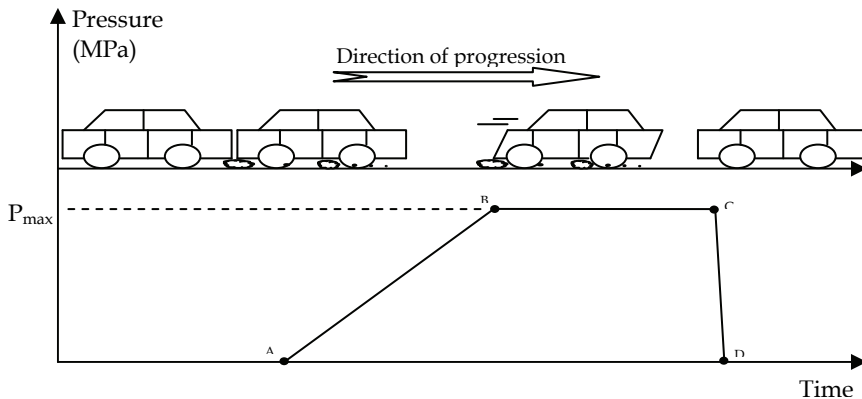


Figure 4. The change in the applied Pressure during the braking process



### Boundary Conditions

Figure 5 shows the boundary conditions assumed during the simulation of the heat transfer problem.

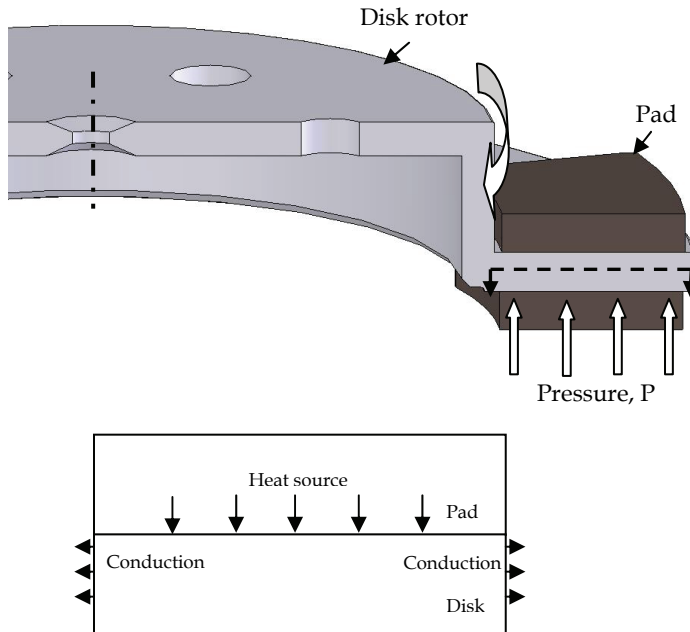


Figure 5. Heat transfer boundary conditions

The boundary conditions stated for the elastic problem are shown in figure 6.

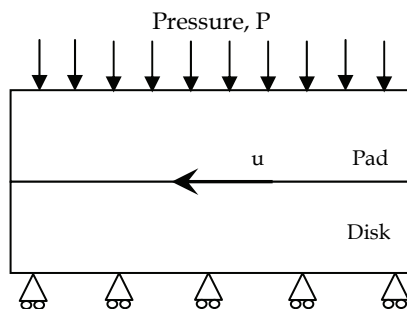


Figure 6. Elastic problem boundary conditions

The objective of this case study is to simulate the thermoelastic phenomenon taking place during the braking process. In addition, a comparison of the thermal behavior of the different brake disk materials found in the literature. Another comparison is performed between two different brake disk designs (perforated and the notched disks), in which the temperature distribution and the heat flux developed under the same operating condition was conducted.

The comparison performed between different types of brake disk rotor materials reported in the literature, was namely between grey cast iron (grey iron grade 250, high-carbon grade iron, titanium alloyed grey iron, and compact graphite iron (CGI)), Aluminum metal matrix composites (Al-MMC's), namely Al<sub>2</sub>O<sub>3</sub> Al-MMC and SiC Al-MMC (Ceramic brakes). The comparison was performed in order to improve the conceptual design of the disk brakes. The results obtained from the model were compared with actual measurements obtained from experiments performed by (Cueva et al., 2003). Also, a comparison of the different brake disk designs was performed in order to study the effect of the perforated brake disks on the maximum temperature, temperature distribution, and the heat flux produced as well, under the same braking conditions.

The elastic problem was simulated in order to investigate the mechanical action taking place at the disk's contact surface during the braking process, the deformation obtained from the elastic problem was relatively small (200  $\mu\text{m}$ ).

### 4.3 Results

The developed finite element analysis model contains a total of 278 elements and 597 degrees of freedom, while the time step used during the numerical computation was 0.01sec. The initial temperature used during the simulation was set as 20 °C.

Figure 7 depicts one of the typical temperature distributions developed using the suggested finite element analysis model. It's shown how the temperature increases further from the centre of the disk rotor to the point of the maximum temperature within the contact area between the disk and the pad, and then it decreases.

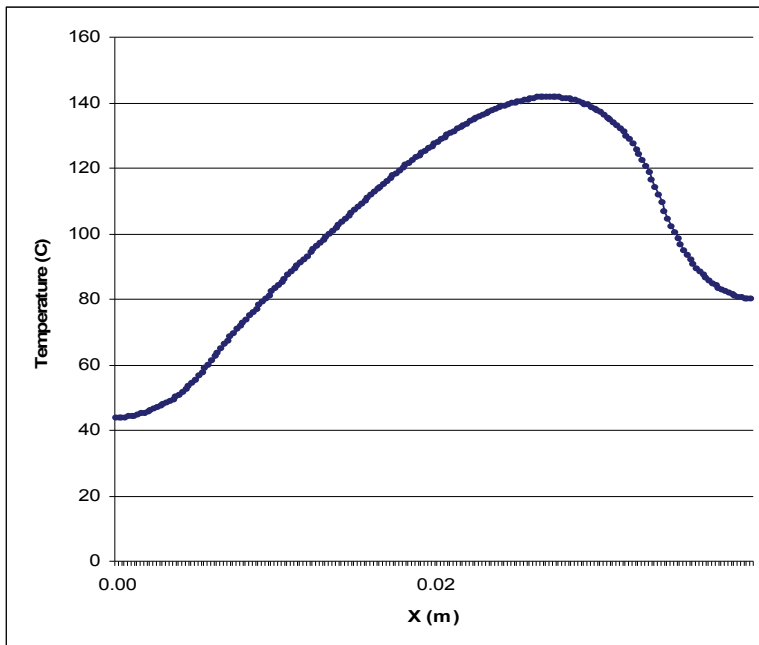


Figure 7. Typical temperature distribution produced during the braking process

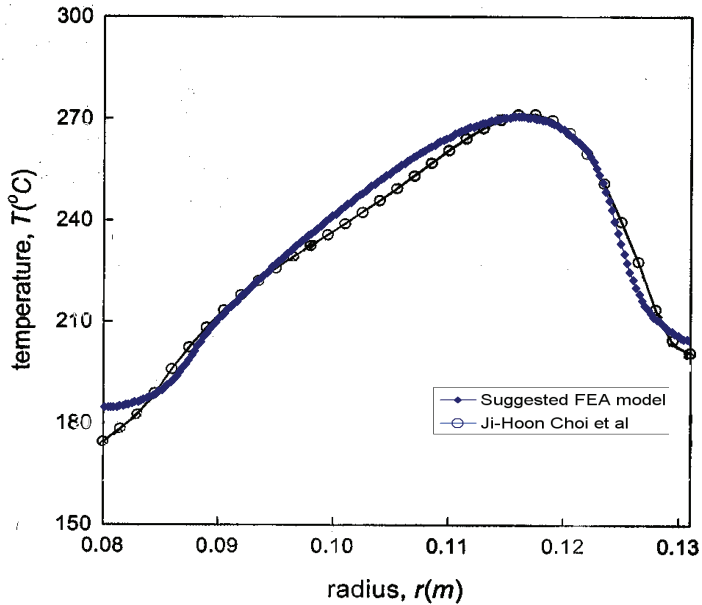


Figure 8. Comparison between the temperature distribution plot obtained by Choi et al. (2004) and the suggested model output

A comparison between the produced temperature distribution using the proposed finite element analysis model and the distribution presented by Choi et al. (2004), under the same operating conditions, is shown in figure 8. A very close fit between the proposed model and the one developed by Choi et al. was obtained.

Figure 9.a presents a 3D plot of the temperature distribution along the contact surface during and after the braking action (time steps 1 to 10 s). While figure 9.b shows the line plot of the temperature distribution at each time step during the same periods of time. As shown in the figure, the temperature produced increases till it reaches its maximum value at the time step 4s, then it decreases after the applied pressure is released.

The temperature distributions during the braking process at 4 different time instants (1,3,4, and 5 seconds) are shown in figure 10 for one of the brake disk materials investigated, namely GI250.

As shown in the figure, at time step 5sec. localization of the heat generated is noticed, which is represented by the dark area on the contact surface, resulted in the development of a hot spot.

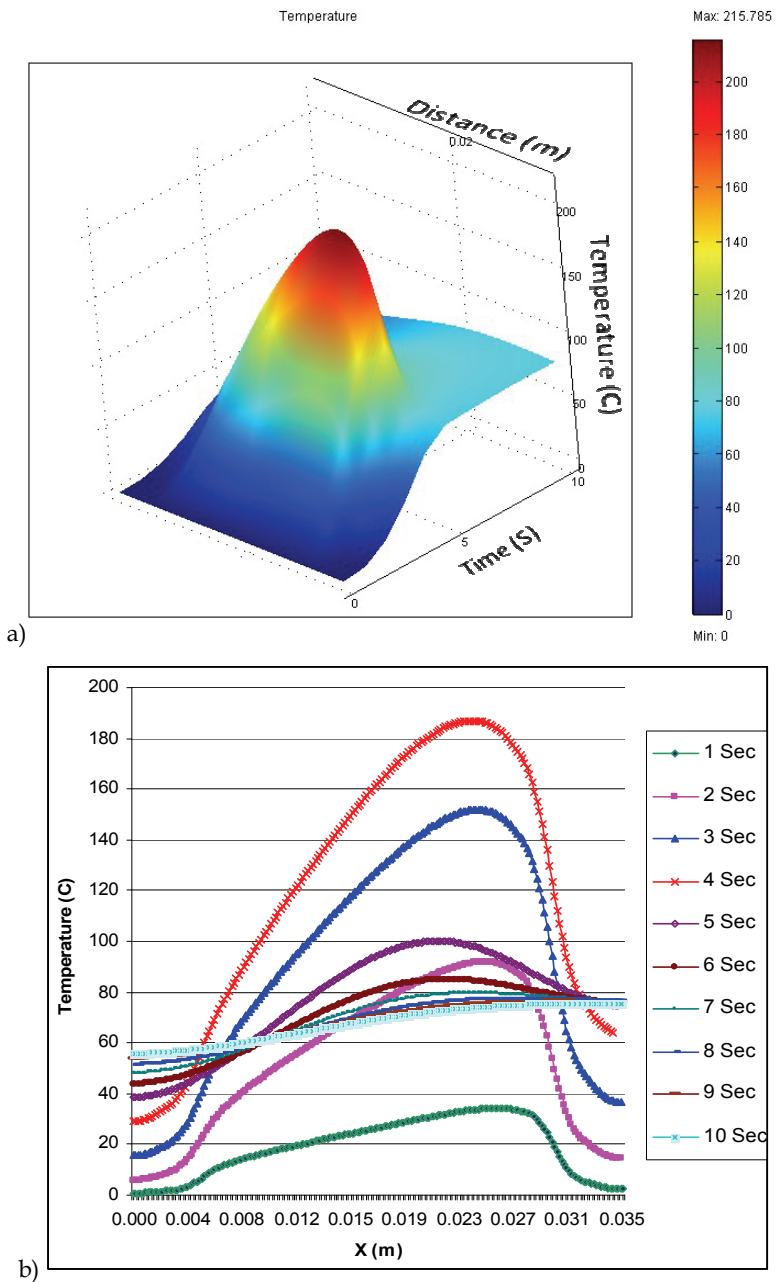


Figure 9. a) 3D temperature distribution during a 10 seconds time period. b) Temperature distribution plot at the different time steps

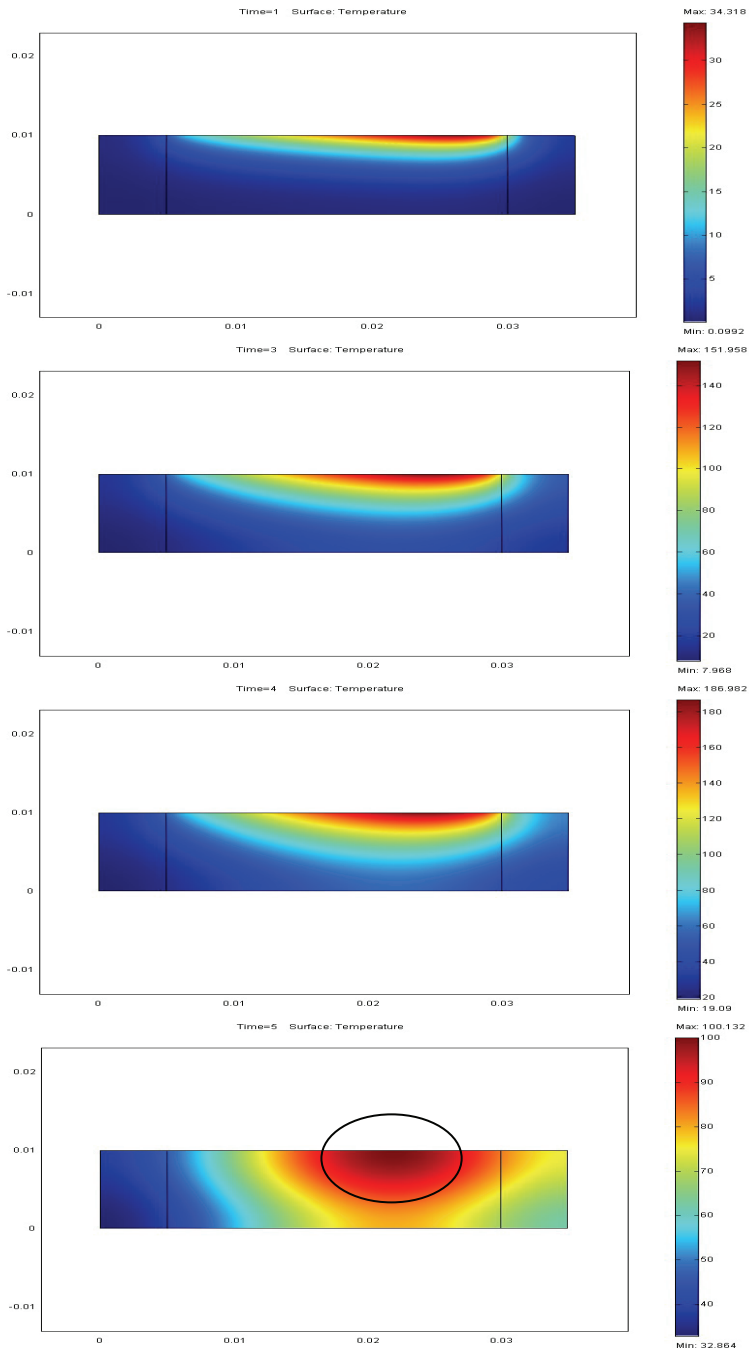


Figure 10. Change of the surface temperature across the disk brake, at time steps, 1, 3, 4, and 5s

A comparison between the temperature distributions produced during the braking process for the suggested different brake disk materials is shown in figure 11, as shown in the figure, the temperature distributions along the contact surface are plotted for the suggested disk materials, figure 11.a shows the temperature produced at an applied pressure of 4 MPa, while figure 11.b shows the temperature distribution produced at a pressure of 2 MPa.

From figures 11.a and b it can be concluded that both the Aluminum Metal Matrix composites and the ceramic brakes give better temperature distribution than the carbon-carbon composites. In other words, the Al-MMC's and the ceramic brakes provided evenly distributed temperature than the carbon-carbon composites, i.e. no localization of heat is expected compared to the carbon-carbon brakes.

In order to validate the proposed model and testing how accurate the model is, the maximum temperature obtained from the proposed model were compared to the actual measurement performed. A comparison was performed between the maximum temperature produced during the braking process using the proposed finite element analysis model and the actual measurements performed by Cueva et al. (2003), which is shown in table 1.

In their study, Cueva et al. measured the actual temperature produced during the braking process for 4 different types of iron, at different values of the applied pressure, as shown in the table a maximum difference of 10% between the calculated and the measured temperature was obtained. That percentage difference was considered as an accepted deviation between the simulated and the actual maximum temperature values produced.

	Actual temperature (°C) at 4MPa	Simulated temperature (°C)	Difference (%)	Actual temperature (°C) at 2MPa	Simulated temperature (°C)	Difference (%)
GI250	200 ±10	190	5	90 ±5	86	4.4
GIHC	210 ±10	189	10	85 ±5	82	3.5
GI250Ti	210 ±10	191	9	95 ±5	94	1
CGI	240 ±10	219	8.75	115 ±5	107	7

Table 1. comparison between the actual temperature measures by Cueva et al. and the simulated values obtained from the suggested finite element analysis model

Also, another comparison between two brake disk designs was conducted, in which the perforated and the notched disks were compared from the point of view of the temperature distribution and the heat flux as well. Figure 12 shows the temperature distributions for the two mentioned designs. Figure 12.a shows both the temperature distribution and the heat flux produced in the perforated disk brakes at time steps 4 and 10 s.

On the other hand, figure 12.b illustrates both the temperature distribution and the heat flux for the notched disk at the same time steps. As shown in Figure 12.a and b, both the perforated and the notched disks provided better results as far as the temperature distribution and the heat flux compared to the solid disk brakes, despite the fact that the maximum temperature produced is the same. It can be also concluded that the perforated disks gives better temperature distribution and heat flux compared to the notched ones.

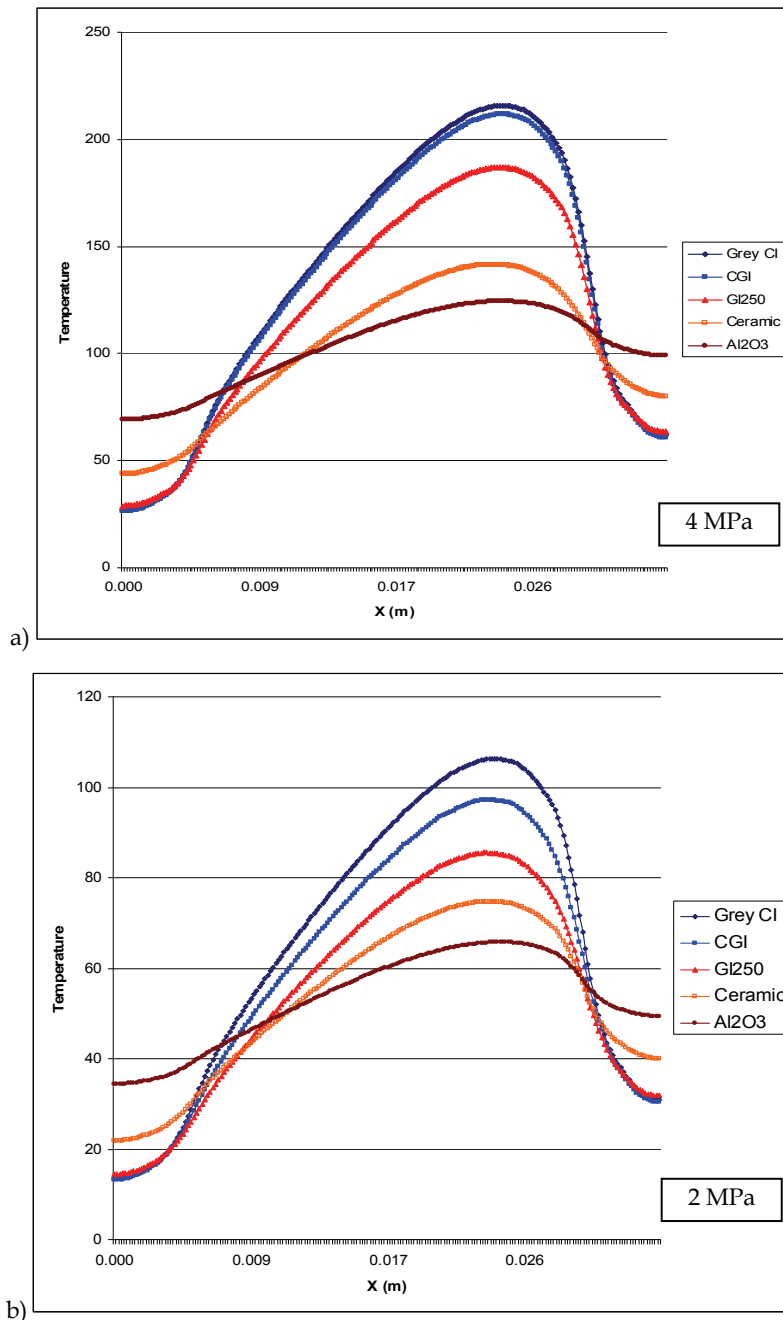


Figure 11. Comparison between the temperature distribution produced in Grey CI, CGI, GI250, Ceramic, and Al<sub>2</sub>O<sub>3</sub> disk brakes at a pressure of a) 4MPa b) 2MPa

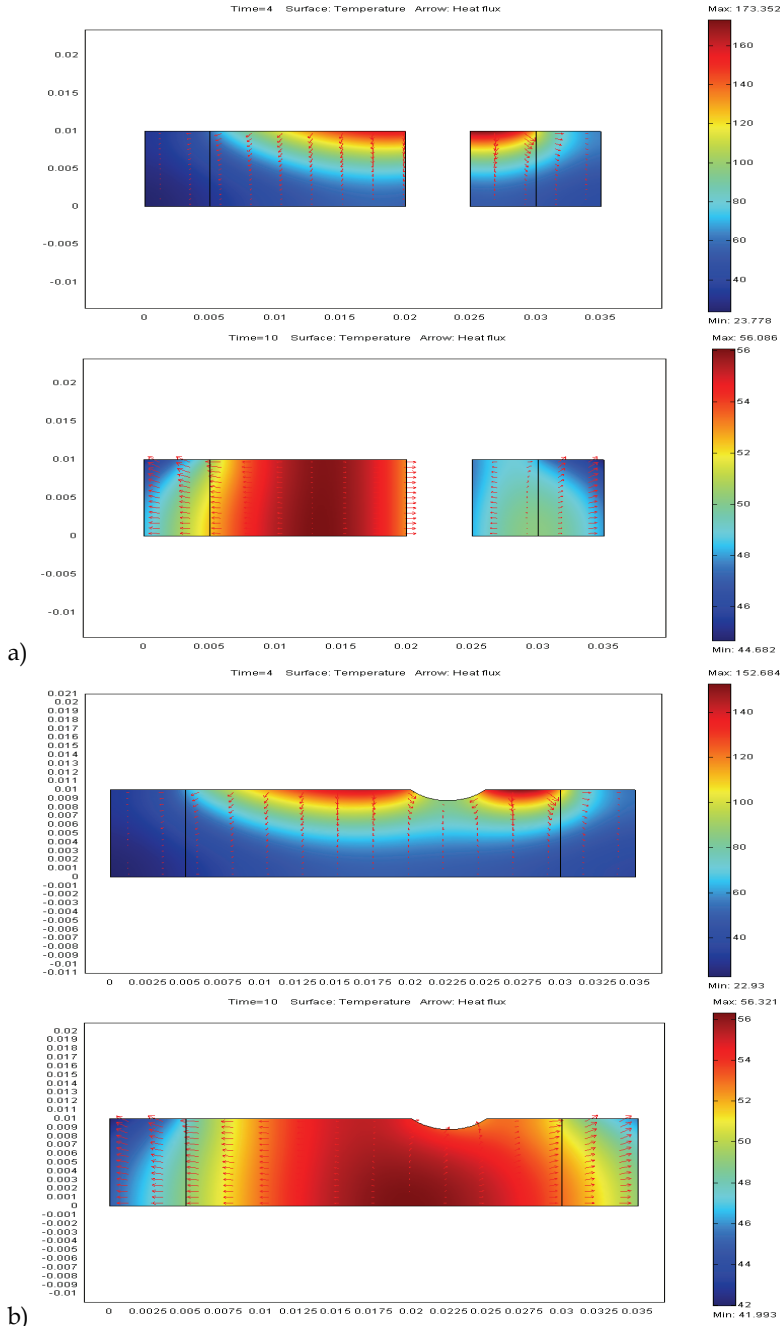


Figure 12. Comparison between the temperature distribution and the heat flux produce in a) the perforated disks b) the notched disks



#### 4.4 Discussion

A finite element analysis model was developed in order to investigate both the thermal and mechanical behaviours taking place between the disk brake and the pad, during the braking process. The developed model was compared with actual measurements performed by Cueva et al. (2003) in order to validate the proposed model, and it showed very close simulated results compared to the actual ones. One of the obtained temperature distributions obtained during the braking action using the proposed model was compared to the one obtained by Choi et al. (2004) and it showed an excellent agreement.

The temperature distributions produced for five different disk's materials (Grey CI, CGI, GI250, Ceramic, and Al<sub>2</sub>O<sub>3</sub>) were compared to each other. Among the investigated materials, the ceramic and Al<sub>2</sub>O<sub>3</sub> disk showed a better thermal behaviour during the braking process, as far as the maximum temperature and the temperature distribution produced, thus eliminating the localization of the produced heat, which means minimizing the probability of having hot spots.

Another comparison was performed between the perforated and the notched disks, in which the two designs were investigated under the same braking conditions. It was found that despite the fact that the maximum temperature produced in both was the same; the perforated disks produced better temperature distribution as well as heat flux as compared to notched disks.

An interesting article by Kevin C. (2006), published at the New York Times, discussed the potential of the ceramics disk brakes and how that type of brakes represents the future of the disk brakes, he also mentioned a number of advantages that it possess, yet taking in to consideration the high cost of such rotor material. One of the advantages that the ceramic disk brake possesses is the outstanding hardness, the ability to maintain its strength and shape at extremely high temperature conditions, and more importantly it's considerably light in weight (almost half the weight of the conventional iron disk brakes).

One of the good reasons to consider the ceramic brakes is that they are light weight which will help reduce the weight of the vehicle which in turn will allow car manufacturers to meet the corporate average fuel economy standard (CAFE), which is now mandatory upon automakers. The importance of reducing the weight of the disk brakes in particular is because that as a vehicle accelerates, its rotating parts require more energy to accelerate than non rotating parts like engine blocks. This is because they gain energy from both their accelerating forward motion and from their increasingly rapid rotation and this gives brake discs a special importance in fuel economy.

#### 5. References

- Abdelahamid, M. K. (1997). Brake judder analysis: Case studies, *SAE, Technical Paper Series*, no. 972027.
- Anderson, E., et al. (1990). Hot spotting in automotive friction systems, *Wear*, v. 135, pp. 319-337.
- Barber, J.R. (1967). The influence of thermal expansion on the friction and wear process, *Wear*, 10, 155-159.
- Barber, J.R. (1969). Thermoelastic instabilities in the sliding of conforming solids, *Proc. R. Soc. A* 312 381-394.
- Barber, R. J. et al. (1985). Implications of thermoelastic instabilities for the design of brakes, *Jnl. Tribology*, v. 107, pp. 206-210.

- Choi, J.H. & Lee, I. (2003). Transient thermoelastic analysis of disk brakes in frictional contact, *Journal of Thermal Stresses*, 26, 223–244.
- Choi, J.H. & Lee, I. (2004). Finite element analysis of transient thermoelastic behaviors in disk brakes, *Wear*, 257, 47–58
- Cueva, G.; Sinatora, A.; Guesser, W.L. & Tschiptschin, A.P. (2003). Wear resistance of cast irons used in brake disk rotors, *Wear*, 255, 1256–1260
- De Vries, A. et al. (1992). The brake judder phenomenon, *SAE Technical Paper Series*, no. 920554.
- Dufrenoy, P. (2004). Two-/three dimensional hybrid model of the thermomechanical behavior of disc brakes, Proceedings of the Institution of Mechanical Engineers, *Journal of Rail and Rapid Transit*, 218, 17–30
- Eggleston, D. (2000). Thermal Judder, *EURAC Technical Bulletin*, 34056
- Eltoukhy, M.; Asfour, S.; Almakky, M. & Huang, C. (2006). Thermoelastic Instability in Disk Brakes: Simulation of the Heat Generation Problem, *Proceedings of the COMSOL Users Conference*, Boston
- Inoue, H. (1986). Analysis of brake judder caused by thermal deformation of brake discs, *SAE Technical Paper Series*, no. 865131.
- Jacobsson, H. (2003). Aspects of Disc Brake Judder, Proceedings of the Institution of Mechanical Engineers, *Journal of Automobile Engineering*, 217, 419–430
- Jang, J.Y. & Khonsari, M.M. (2003). A generalized thermoelastic instability analysis, Proceedings of the royal society, A459, 309–329
- Kennedy, F. E., & Ling, F. F. (1974). Thermoelastic, and Wear Simulation of a High-Energy Sliding Contact Problem, *Journal of Lubrication Technology*, 97, pp. 497–508.
- Kevin, C. (2006). Using Ceramics Brakes Are Light but Cost Is Heavy, *The New York Times journal*, published at: <http://www.nytimes.com/2006/06/18/automobiles/18BRAKES.html?pagewanted=2&r=1>
- Lee, K. (2000). Frictionally excited thermoelastic instability in automotive drum brakes, *ASME Journal of Tribology*, 122, 849–855
- Lee, K. & Brooks, F.W. (2003). Hot Spotting and Judder Phenomena in Aluminum Drum Brakes, *Transactions of the ASME*, 125, 44–51
- Rhee, K., S. et al. (1989). Friction-induced noise and vibration of disc brakes, *Wear*, v. 133, pp. 39–45.
- Sterne, D.D. (1989). Monitoring brake disc distortions using lasers, I.Mech.E. (Institution of Mechanical Engineers) *AUTOTECH '89 Conference*, Seminar paper C399/34.
- Zagrodzki, P. K.; Lam, B.; Al Bahkali, E. & Barber, J.R. (2001). Nonlinear transient behavior of a sliding system with frictionally excited thermoelastic instability, *Journal of Tribology*, 123, 699–708.

# Modeling and Numerical Investigation of Photoacoustic Resonators

Bernd Baumann<sup>1</sup>, Bernd Kost<sup>1</sup>, Marcus Wolff<sup>1,2</sup>  
and Hinrich Groninga<sup>2</sup>

*<sup>1</sup>Hamburg University of Applied Sciences, <sup>2</sup>PAS-Tech GmbH, Hamburg  
Germany*

## 1. Introduction

Photoacoustic spectroscopy is based on the photoacoustic effect, that was discovered in 1880 by A. G. Bell (Bell, 1880). One year later, W. C. Röntgen published a paper on the application of photoacoustic spectroscopy on gas (Röntgen, 1881). Sensors based on the photoacoustic effect are devices which allow the detection of molecules of very low concentration. It is even possible to discriminate different isotopes of one molecule.

In a photoacoustic sensor (PAS) a gas sample contained in the measuring cell is subjected to a laser beam. The wavelength of the laser is tuned to a vibrational or rotational line of the searched molecules. The technique takes advantage of the fact, that absorbed electromagnetic radiation is due to non-radiant transitions partially transferred into thermal energy of the surrounding molecules. This leads to an increase of the pressure in the sample. A modulated emission generates a sound wave. The resulting acoustic wave is detected by a microphone and phase-sensitively measured. A typical set-up for photoacoustic investigation is shown in Figure 1.

To detect low molecule concentrations one enhances the microphone signal by utilizing the acoustic resonances of the measuring chamber. The achievable amplification depends on the shape of the resonator and on the precise coupling of the laser profile and the acoustic modes. Experimental investigations of different PAS set-ups are very time consuming and expensive. Addressing the related questions numerically is much more efficient.

The theoretical treatment of PAS has a long history. Analytical calculations have been performed for cylinder shaped resonators, which play an important role among the variety of measuring chambers. Resonator shapes of higher complexity, however, are not amenable to these methods. Numerical techniques like the finite element method (FEM) represent a suitable tool to investigate such systems.

Generally, the investigation of the excited gas requires the solution of a system of coupled partial differential equations. The FEM allows the treatment of such coupled problems. However, this is rather computer time consuming and, considering the numerous design variants, should be avoided. In literature, methods are discussed, that allow to circumvent the coupled problem. We combine these methods with the FEM and are now able to calculate the photoacoustic signal for arbitrary resonator shapes. This offers the possibility

to compare different photoacoustic cells by numerical means. In this paper we review the applied methods and compare the achieved results with experimental data.

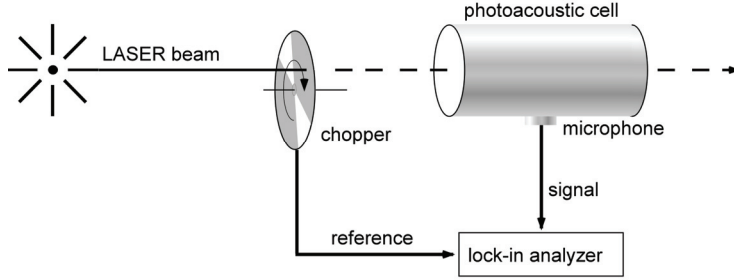


Figure 1. Principle set-up of a photoacoustic sensor used for the investigation of gaseous samples

## 2. Photoacoustic spectroscopy

### 2.1 Absorption of the radiation field

If a sample is irradiated with resonant light, a small fraction of the molecules is excited from the ground state  $E_1$  into an energetic higher level  $E_2$  by absorption of photons of the energy

$$h\nu = E_2 - E_1. \quad (1)$$

Here,  $\nu$  is the frequency of the radiation and  $h$  is Planck's constant. The intensity  $I_{\text{abs}}$  absorbed in the sample can be derived from Lambert-Beer's law

$$I_{\text{abs}} = I_0(1 - e^{-\alpha L}), \quad (2)$$

where  $I_0$  is the input intensity and  $L$  the cell length. This applies for linear absorption, i. e. no saturation or multi-photon absorption (Haken & Wolf, 1993).

The absorption coefficient  $\alpha$  of the transition  $E_1$  to  $E_2$  is defined by

$$\alpha = \sigma(N_1 - N_2). \quad (3)$$

$N_1$  and  $N_2$  are the population densities of the ground state  $E_1$  and excited state  $E_2$ , respectively, and  $\sigma$  is the absorption cross-section of the transition. If the upper level  $E_2$  is not thermally populated,  $N_1$  is approximately the total population density  $N$

$$N_1 \approx N \quad (4)$$

and the absorption coefficient  $\alpha$  becomes

$$\alpha = \sigma N. \quad (5)$$

The change of the population density  $N_2$  of the higher level  $E_2$  is derived from the number of molecules that are excited from  $E_1$  to  $E_2$ , minus the number of those, that relax from  $E_2$  to  $E_1$ . Collisional excitation is negligible, as long as  $h\nu \gg k_B T$ , with Boltzmann's constant  $k_B$  and the gas temperature  $T$  (Zharov & Letokhov, 1986). This condition is fulfilled at room temperature in the near and mid infrared spectrum (vibrational transition). Only the excitation by absorption of  $h\nu$  as well as the relaxation through fluorescence and collision

have to be considered. With the excitation rate  $R$  and the time constant  $\tau$  of relaxation, the rate equation is as follows

$$\frac{dN_2}{dt} = NR - N_2\tau^{-1}. \quad (6)$$

The relaxation rate  $\tau^{-1}$  can be expressed as the sum over the reciprocal time constant  $\tau_n^{-1}$  for non-radiant relaxation and the reciprocal time constant  $\tau_r^{-1}$  for radiant relaxation

$$\tau^{-1} = \tau_n^{-1} + \tau_r^{-1}. \quad (7)$$

For the infrared region it applies that  $\tau_r \gg \tau_n$ . Therefore, we can use the simplification

$$\tau^{-1} \approx \tau_n^{-1}. \quad (8)$$

The excitation rate  $R$  of the molecules in the ground state equals

$$R = \Psi\sigma \quad (9)$$

where the irradiated photon flux  $\Psi$  is, for a harmonically modulated source, given by the real part of

$$\Psi = \Psi_0(1 + e^{i\omega t}). \quad (10)$$

For the generation of a photoacoustic signal, only the time dependent term with the modulation frequency  $\omega$  is relevant. Using Equation (9) and (10) in Equation (6) leads to the solution of the rate equation

$$N_2 = \frac{N\Psi_0\sigma\tau}{\sqrt{1 + (\omega\tau)^2}} e^{i(\omega t - \phi)}. \quad (11)$$

For the phase shift  $\phi$  between the population density  $N_2$  of the higher level and the photon flux applies (Zharov & Letokhov, 1986)

$$\phi = \arctan(\omega\tau). \quad (12)$$

## 2.2 Production of heat

The heat production by non-radiant relaxation is given by the number of molecules in the higher level multiplied with the rate of non-radiant relaxation  $\tau_n^{-1}$  and the average energy per molecule  $h\nu$

$$H = N_2 h\nu \tau_n^{-1}. \quad (13)$$

Using Equation (11) in Equation (13) together with the simplification Equation (8) results in

$$H = H_0 e^{i(\omega t - \phi)} \quad (14)$$

with the phase shift  $\phi$  from Equation (12) and the amplitude

$$H_0 = \frac{N\sigma I_0}{\sqrt{1 + (\omega\tau)^2}}. \quad (15)$$

The amplitude  $I_0$  of the radiation intensity is described by

$$I_0 = \Psi_0 h\nu. \quad (16)$$

For low modulation frequencies with  $\omega \ll 10^6 \text{ s}^{-1}$  it follows that  $\omega\tau \ll 1$  and Equation (15) can be simplified to

$$H_0 = N\sigma I_0, \quad (17)$$

with the phase shift  $\phi$  being practically zero, according to Equation (12). With the time dependent and position dependent radiation intensity  $I(\vec{r}, t)$  as well as Equation (5) and the simplification Equation (4), the heat production in the gas can be derived to

$$H(\vec{r}, t) = \alpha I(\vec{r}, t). \quad (18)$$

Equation (18) applies as long as the modulation frequency is not higher than the kHz-range, i. e.  $\omega \ll \tau^{-1}$ , and saturation effects are negligible, i. e.  $R \ll \tau^{-1}$ . It is assumed that the absorbed energy is completely transferred into heat via inelastic collisions.

### 2.3 Cell geometry and resonance

A specialty of the PAS, compared to other spectroscopic techniques, is taking advantage of acoustic resonances of the sample cell. Constructive interference of the sound waves leads to the formation of a standing wave in the sample cell, that allows for a signal boost and hence for an immense enhancement of the sensitivity. The prevalent geometry of sample cells is cylindrical, however, a large variety of other cell shapes has been investigated (Miklós et al., 2001). In (Wolff et al., 2005) the so called T cell has been introduced (see Figure 2 and Table 1). The advantage of the T cell compared to the cylinder cell is that this design allows independent optimization of the key parameters affecting sound generation and signal enhancement.

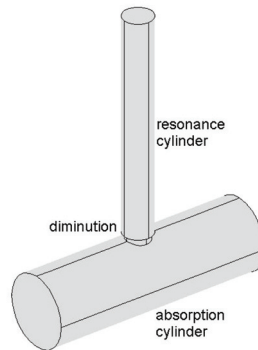


Figure 2. T cell. For technical reasons there is a diminution at the connection of absorption and resonance cylinder

Absorption Cylinder	Diameter	$D_A = 26 \text{ mm}$
	Length	$L_A = 82 \text{ mm}$
Resonance Cylinder	Diameter	$D_R = 11 \text{ mm}$
	Length	$L_R = 10 - 140 \text{ mm}$
Diminution	Diameter	$D_D = 8.9 \text{ mm}$
	Length	$L_D = 2 \text{ mm}$

Table 1. Dimensions of the photoacoustic T cell. The length of the resonance cylinder is adjustable

### 3. Theoretical treatment of the sound field

#### 3.1 Balance equations

For the calculation of the pressure distribution inside a cavity and at resonance, it is required to include loss. Therefore, the lossless wave equation is not an appropriate description of the fluid dynamics. Since it is well known, that loss in the PA resonator appears mainly at its walls, the inclusion of a loss term in the wave equation is also not a proper approach for the problem at hand. Balance equations, however, represent an adequate starting point. In this case, the continuity equation (mass balance)

$$\frac{D\rho}{Dt} + \rho \vec{\nabla} \cdot \vec{u} = 0, \quad (19)$$

( $D/Dt$  substantive derivative,  $\rho$  density,  $\vec{u}$  velocity), the Navier-Stokes equation (momentum balance)

$$\rho \frac{D\vec{u}}{Dt} = -\vec{\nabla} p + \eta \vec{\nabla}^2 \vec{u} + \left(\frac{1}{3}\eta + \mu\right) \vec{\nabla} (\vec{\nabla} \cdot \vec{u}) \quad (20)$$

( $p$  pressure,  $\eta$  coefficient of viscosity,  $\mu$  expansion coefficient of viscosity) and the equation that expresses the energy balance (1. law of thermodynamics) are required. In the present context the 1. law is most useful in the form (Temkin, 1981)

$$\rho c_p \frac{DT}{Dt} - \beta T \frac{Dp}{Dt} = \vec{\nabla} \cdot (\kappa \vec{\nabla} T) + \left(\mu - \frac{2}{3}\eta\right) (e_{ii})^2 + 2\eta e_{ij} e_{ij} \quad (21)$$

( $c_p$  specific heat at constant pressure,  $T$  absolute temperature,  $\beta$  coefficient of thermal expansion,  $\kappa$  coefficient of heat conduction,  $e_{ij} := \frac{1}{2} \left( \frac{\partial u_i}{\partial x_j} + \frac{\partial u_j}{\partial x_i} \right)$  rate of strain tensor). These partial differential equations have to be supplemented by an equation of state (equilibrium conditions are assumed to be approximately appropriate except for very high frequencies), i. e.

$$p = p(\rho, T). \quad (22)$$

This results in six equations for the six field quantities  $\vec{u}$ ,  $T$ ,  $\rho$  and  $p$ .

A first step towards the solution of these equations is linearization. All field quantities except  $\vec{u}$  are split into a large static and a small varying (acoustic) part:

$$T(\vec{r}, t) = T_0 + \tilde{T}(\vec{r}, t), \quad (23)$$

$$p(\vec{r}, t) = p_0 + \tilde{p}(\vec{r}, t), \quad (24)$$

$$\rho(\vec{r}, t) = \rho_0 + \tilde{\rho}(\vec{r}, t). \quad (25)$$

$\vec{u}$  is assumed to be small. Insertion into the differential equations and dropping all terms, that are proportional to small quantities, leads to the linearized counterparts of the balance and state equations. When combined, the following two equations can be derived (Morse & Ingard, 1981):

$$\vec{\nabla}^2 \tilde{p} = \frac{\gamma}{c^2} \left( \frac{\partial^2}{\partial t^2} - l_\eta c \frac{\partial}{\partial t} \vec{\nabla}^2 \right) (\tilde{p} - \alpha_V \tilde{T}) \quad (\text{modified wave equation}) \quad (26)$$

and

$$l_\kappa c \vec{\nabla}^2 \tilde{T} = \frac{\partial}{\partial t} \left( \tilde{T} - \frac{\gamma - 1}{\alpha_V \gamma} \tilde{p} \right) \quad (\text{modified heat equation}). \quad (27)$$

$\gamma$  denotes, as usual, the ratio of the specific heat at constant pressure  $c_p$  to the specific heat at constant volume  $c_v$  and  $\alpha_V = \left( \frac{\partial p}{\partial T} \right)_V$ .  $c$  refers to the speed of sound. The characteristic lengths  $l_\eta$  and  $l_\kappa$  are defined in Section 3.3. The quantity of greatest interest  $\tilde{p}$  decouples from all field quantities but from  $\tilde{T}$ .

### 3.2 Reduction to an uncoupled problem

In order to avoid the coupled system (Equations (26) and (27)) different possibilities of simplification are possible:

1. Disregard heat conduction ( $\kappa = l_\kappa = 0$ ). In this case, temperature and acoustic pressure are proportional to each other ( $\tilde{T} = (\gamma - 1)\tilde{p}/(\alpha_V \gamma)$ ) and  $\gamma(\tilde{p} - \alpha_V \tilde{T})$  equals  $\tilde{p}$ , which implies

$$\vec{\nabla}^2 \tilde{p} = \frac{1}{c^2} \left( \frac{\partial^2}{\partial t^2} - l_\eta c \frac{\partial}{\partial t} \vec{\nabla}^2 \right) \tilde{p}. \quad (28)$$

The problem decouples and the resulting wave equation includes a dissipative term.

2. Maintaining heat conduction and assuming  $l_\kappa \approx l_\eta$  leads to the following modified wave equation

$$\vec{\nabla}^2 \tilde{p} = \frac{1}{c^2} \left( \frac{\partial^2}{\partial t^2} - \gamma l c \frac{\partial}{\partial t} \vec{\nabla}^2 \right) \tilde{p} \quad (29)$$

where  $l$  is the mean value of  $l_\kappa$  and  $l_\eta$  (Hess, 1989).

The mathematical structure of the two differential equations is identical. Performing a Fourier Transformation, we obtain

$$\vec{\nabla}^2 p(\vec{r}, \omega) + \frac{k^2}{1 - i\Lambda k} p(\vec{r}, \omega) = 0 \quad (30)$$

where  $\Lambda = l_\eta$  in the first case and  $\Lambda = \gamma l$  in the second case.  $p(\vec{r}, \omega)$  is the Fourier transform of the acoustic pressure  $\tilde{p}(\vec{r}, t)$  and  $k = \frac{\omega}{c}$  is the wave number. In the case of photoacoustic cells, the sound waves are a result of the interaction of the laser beam and the molecules. Therefore, the differential equations above have to be supplemented by a source term which accounts for the sound generation.

Instead of attempting to solve the differential Equation (30) we discuss a further solution procedure that has been widely used in the theoretical treatment of photoacoustic cells of cylinder shape (Kreuzer, 1977). Combined with the finite element method it can be applied to cells of arbitrary geometry. Starting point is the loss free Helmholtz equation which describes the generation and propagation of sound waves:

$$\vec{\nabla}^2 p(\vec{r}, \omega) + k^2 p(\vec{r}, \omega) = i\omega \frac{\gamma - 1}{c^2} \mathcal{H}(\vec{r}, \omega). \quad (31)$$

$\mathcal{H}(\vec{r}, \omega)$  is the Fourier transform of the power density  $H(\vec{r}, t)$ . Assuming that the absorbing transition of the molecules is not saturated and that the modulation frequency of the light



source is considerably smaller than the relaxation rate of the molecular transition, the relation  $\mathcal{H}(\vec{r}, \omega) = \alpha \mathcal{I}(\vec{r}, \omega)$  applies, where  $\mathcal{I}(\vec{r}, \omega)$  is the Fourier transformed intensity of the electromagnetic field and  $\alpha$  is the absorption coefficient (see Section 2.1 and 2.2). It is assumed that the walls of the photoacoustic cell are sound hard which is adequately described by the boundary condition

$$\frac{\partial p}{\partial n} = 0, \quad (32)$$

i. e., the normal derivative of the pressure is zero at the boundary.

It is well known that the solution of the inhomogeneous wave equation can be expressed as a superposition of the acoustical modes of the photoacoustic cell:

$$p(\vec{r}, \omega) = \sum_j A_j(\omega) p_j(\vec{r}). \quad (33)$$

The modes  $p_j(\vec{r})$  and the according eigenfrequencies  $\omega_j = ck_j$  are obtained by solving the homogeneous Helmholtz Equation

$$\vec{\nabla}^2 p(\vec{r}) + k^2 p(\vec{r}) = 0 \quad (34)$$

under consideration of the boundary condition (32). Equation (33) requires the modes to be normalized according to

$$\int_{V_C} p_i^* \cdot p_j \, dV = V_C \delta_{ij} \quad (35)$$

where  $V_C$  denotes the volume of the photoacoustic cell and  $p_i^*$  is the conjugate complex of  $p_i$ . The amplitudes  $A_j(\omega)$  of the photoacoustic signal are determined from

$$A_j(\omega) = i \frac{A_j \omega}{\omega^2 - \omega_j^2} \quad (36)$$

with the excitation amplitude

$$A_j = \frac{\alpha(\gamma - 1)}{V_C} \int_{V_C} p_j^* \cdot \mathcal{I} \, dV. \quad (37)$$

The inhomogeneous Helmholtz Equation (31) does not contain terms that account for loss. Therefore, loss effects are included via the introduction of quality factors  $Q_j$  in the amplitude Formula (36):

$$A_j(\omega) \rightarrow A_j(\omega) = i \frac{A_j \omega}{\omega^2 - \omega_j^2 + i\omega\omega_j/Q_j}. \quad (38)$$

There is a whole collection of loss mechanisms, each contributing to the quality factor. The combined effect of all loss mechanisms is calculated from

$$\frac{1}{Q_j} = \sum_i \frac{1}{Q_j^i}. \quad (39)$$

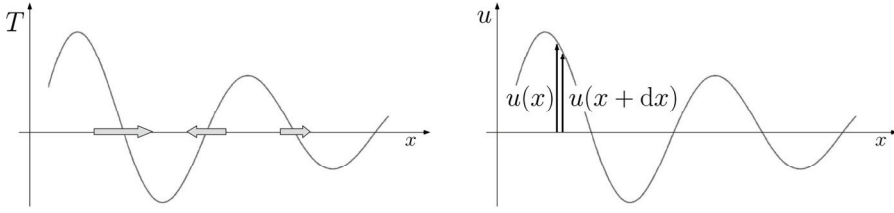


Figure 3. Sound waves are accompanied by temperature waves. Heat flows from regions of elevated temperature to regions of lower temperature (left). Due to the different fluid velocity of neighboring fluid layers, viscosity results in shear stress and, therefore, in loss (right)

### 3.3 Volume and surface loss

The wave equation for sound waves is derived under the assumption that the fluid behaves adiabatically, i. e. thermal conductivity of the fluid is negligible. Then, no heat is exchanged between neighboring pressure maxima and minima. If on the other hand this heat exchange cannot be neglected, the energy density fluctuations will die out and the sound wave dissipates (Figure 3, left). A second loss mechanism is due to viscosity. Neighboring layers of the fluid move at different velocities when the sound wave travels through the resonator (Figure 3, right). This generates shear stress and therefore, viscous friction. The characteristic lengths of these loss mechanisms can be estimated by

$$l_{\eta} = \frac{4}{3} \frac{\eta}{\rho c} \quad \text{and} \quad l_{\kappa} = \frac{\kappa}{\rho c_p c}. \quad (40)$$

These lengths are very small for many fluids of practical interest, which means that a substantial attenuation occurs only after the wave has traveled over large distances. Stokes-Kirchhoff loss due to viscosity and thermal conduction in the gas volume is described by

$$\frac{1}{Q_j^v} = \frac{\omega_j}{c} (l_{\eta} + (\gamma - 1)l_{\kappa}). \quad (41)$$

The dominant loss effects happen at the wall of the photoacoustic cell. They are due to heat conduction and viscosity as well. Typical cells are manufactured out of metal which has a high coefficient of thermal conductivity compared to the fluids. Therefore, temperature waves occur far away from the cell wall whereas the wall itself constitutes a region of isothermal behaviour. This results in a heat exchange as is indicated in Figure 4 (left). The transition from the adiabatic to the isothermal behaviour takes place in a boundary layer of thickness

$$d_{\kappa} = \sqrt{\frac{2\kappa}{c_p \rho \omega}}. \quad (42)$$

Thermal conductivity surface loss results in

$$\frac{1}{Q_j^{s_{\kappa}}} = \frac{1}{2} (\gamma - 1) \frac{d_{\kappa}}{V_C} \int_{S_C} |p_j|^2 dS. \quad (43)$$

If viscosity is taken into account, one has a "no slip" condition at the wall, whereas the fluid moves due to the wave propagation in the interior of the container. Again, neighboring layers of the fluid have different velocities which results in viscous friction (Figure 4, right). The thickness of Prandtl's boundary layer is

$$d_\eta = \sqrt{\frac{2\eta}{\rho\omega}} \quad (44)$$

and the corresponding quality factor

$$\frac{1}{Q_j^{s_\eta}} = \frac{1}{2} \left( \frac{c}{\omega_j} \right)^2 \frac{d_\eta}{V_C} \int_{S_C} |\vec{\nabla}_t p_j|^2 dS. \quad (45)$$

$\vec{\nabla}_t p_j$  is the component of the pressure gradient tangential to the cell wall. There exist further loss mechanisms which are not discussed in this article (Kreuzer, 1977; Morse & Ingard, 1981).

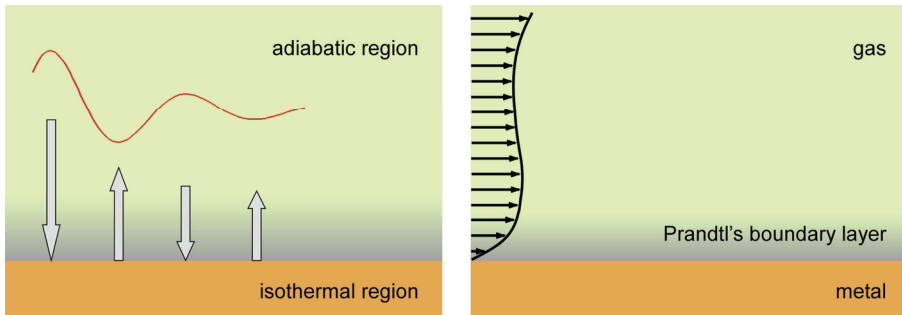


Figure 4. Boundary loss of temperature wave due to heat conduction (left) and velocity profile in the vicinity of Prandtl's boundary layer (right)

density	$\rho = 2.376 \text{ kg/m}^3$
sound velocity	$c = 211 \text{ m/s}$
viscosity	$\eta = 7.6 \cdot 10^{-6} \text{ Pa s}$
coefficient of heat conduction	$\kappa = 1.62 \cdot 10^{-2} \text{ W/m K}$
specific heat capacity at constant volume	$c_V = 1.598 \cdot 10^3 \text{ J/kgK}$
specific heat capacity at constant pressure	$c_P = 1.735 \cdot 10^3 \text{ J/kgK}$

Table 2. Gas parameters of *n*-butane under atmospheric conditions ( $T = 300 \text{ K}$ ,  $p = 1013 \text{ hPa}$ ) (VDI-Wärmeatlas, 2002)

## 4. Results of numerical investigations

### 4.1 Resonator modes

In this chapter results of finite element calculations performed with the FE tool COMSOL Multiphysics (see [www.comsol.org](http://www.comsol.org)) are reviewed. In addition, these results are compared to corresponding experiments. The FE calculations are based on the quality factor approach

described in Section 3.2. Since in this approach the acoustic pressure field inside the measuring chamber of the PA sensor is expressed as a sum over eigenmodes, a first and important step consists in the determination of the modes. Cylinder cells represent a perfect testing ground for the numerical analysis, because in this case the eigenfrequencies can be calculated analytically. Excellent agreement of analytical and numerical results has been found (Baumann et al., 2006). This confirms the reliability of the FE model used for the calculation of the modes of the T cell, where no analytical results are available. The physical parameters of *n*-butane used for the experiments and the simulations described in this article can be found in Table 2.

In the following, we present results for T cells with different lengths  $L_R$  of the resonance cylinder (see Table 3 and Figures 5 and 6).

$L_R = 320$  mm: All three lowest eigenmodes (1-3) are basically eigenmodes of the resonance cylinder (one end open, one end closed), see Figure 5. This interpretation is confirmed by Table 3 and the observation that the acoustical pressure in the absorption cylinder is approximately zero (Figure 5, left). Only for the lowest eigenmode, a minor deviation from zero is observed. This and the deviation between finite element frequency and  $\frac{c}{4L_{R'}}$ , the frequency of the half-open pipe, indicates, that the ground state (lowest eigenmode) is not a pure cylinder mode. The ground mode has been observed experimentally and the deviation between measured frequency and finite element result is small.

$L_R = 160$  mm: The two lowest eigenmodes (1-2) are longitudinal modes of the resonance cylinder whereas the third mode is associated with the first longitudinal mode of the absorption cylinder (two closed ends). Because this mode shows a node at the opening of the resonance cylinder, it does not excite an oscillation in the resonance cylinder. Again, this interpretation is supported by Table 3 and the agreement between numerical result and measurement is excellent.

$L_R = 80$  mm: The interpretation of the spectrum is essentially the same as in the case of the  $L_R = 160$  mm-T cell. Merely the order of the eigenmodes has changed: The first longitudinal mode of the absorption cylinder is now the second mode of the T cell. The agreement with the measured frequency is good.

$L_R = 40$  mm: The ground state represents the first longitudinal mode of the resonance cylinder. The second mode is the first longitudinal mode of the absorption cylinder (see Figure 6). The length of the resonance cylinder now almost equals the length of the absorption cylinder. Therefore, the third mode shows an interesting characteristic: The second longitudinal mode of the absorption cylinder is excited. This mode shows an antinode at the opening of the resonance cylinder. Therefore, a  $\lambda/2$ -wave is excited in the resonance cylinder. That is, both the  $\lambda$ -wave of the absorption cylinder and the  $\lambda/2$ -wave in the half-open resonance cylinder are present. The latter would not be possible in the case of a single halfopen cylinder. The mode is depicted in Figure 7. Agreement with the measured frequency is good.

$L_R = 20$  mm: Now, the first longitudinal mode of the absorption cylinder constitutes the ground state of the T cell. This mode cannot be detected experimentally due to the node at the opening of the resonance cylinder. The experiment detected the remnants of the resonance cylinder's first longitudinal mode. The length of the resonance cylinder has now become similar to the diameter of resonance and absorption cylinder. Therefore, the formula of the half-open cylinder is not

applicable anymore. Figure 7 shows that the third mode cannot be disentangled into two cylinder modes.

$L_R = 10$  mm: The ground state is again the first longitudinal mode of the absorption cylinder.

The two higher modes cannot be brought into connection with cylinder modes.

Both of these modes are detected experimentally.

For large lengths of the resonance cylinder one observes essentially modes, which are compatible with the well known formulae for the vibration of gas columns whereas for short resonance cylinders, this is no longer true. These observations are consistent with expectations and, therefore, we have a coherent picture of the T cell's spectrum.

$L_R$ [mm]	FEM		Resonance Cyl.			Absorption Cyl.			Experiment	
	Mode	$f$ [Hz]	$f$ [Hz]	Dev. [%]	Type	$f$ [Hz]	Dev. [%]	Type	$f$ [Hz]	Dev. [%]
320	1	197.9	165.6	-16.3	$\lambda/4$				203	2.6
	2	497.9	496.9	-0.2	$3\lambda/4$					
	3	813.7	828.1	1.8	$5\lambda/4$					
160	1	354.0	331.3	-6.4	$\lambda/4$				356	0.6
	2	953.2	993.8	4.3	$3\lambda/4$	1292.7	-0.2	$\lambda/2$		
	3	1295.2								
80	1	636.5	662.5	4.1	$\lambda/4$				629	-1.2
	2	1295.2				1292.7	-0.2	$\lambda/2$		
	3	1788.4	1987.5	11.1	$3\lambda/4$					
40	1	1114.6	1325.0	18.9	$\lambda/4$				1092	-2.0
	2	1295.2				1292.7	-0.2	$\lambda/2$		
	3	2583.2	2650.0	2.6	$\lambda/2$	2585.4	0.1	$\lambda$		
20	1	1295.2				1292.7	-0.2	$\lambda/2$	1722	-5.6
	2	1824.2								
	3	2684.3								
10	1	1295.2				1292.7	-0.2	$\lambda/2$	2392 3003	-1.3 -3.9
	2	2424.0								
	3	3124.0								

Table 3. Eigenfrequencies of the T cell for different lengths  $L_R$  of resonance cylinder. The frequencies for resonance and absorption cylinder are calculated using the formula for gas columns. End corrections have not been included. The experimental frequencies are measured with an accuracy of about 1%. Due to the chosen frequency ranges not all of the numerically found eigenmodes have been measured

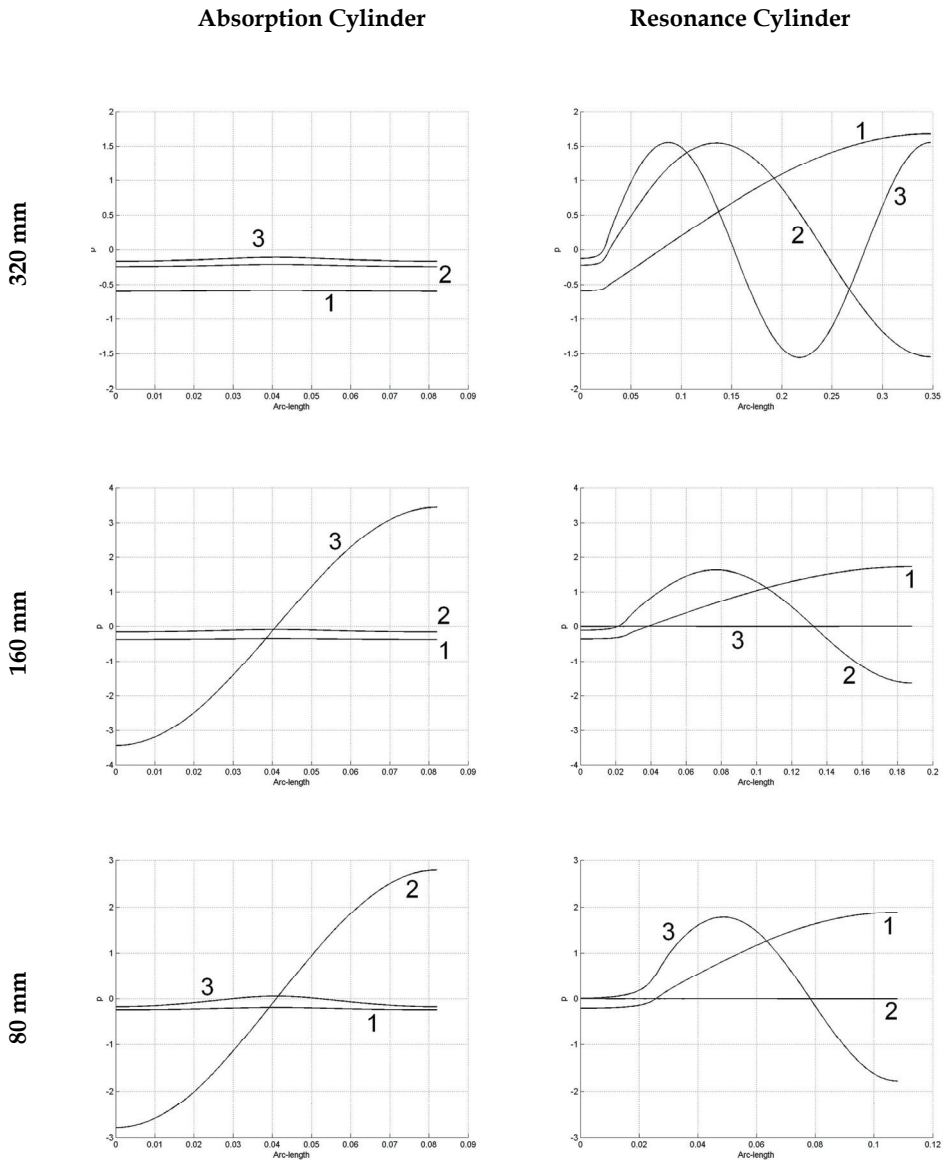


Figure 5. Pressure distribution of the three lowest nontrivial eigenmodes (1, 2, 3) of the T cell along the symmetry axis of the absorption cylinder and the resonance cylinder for  $L_R = 320$  mm,  $L_R = 160$  mm and  $L_R = 80$  mm. The actual length of the abscissa in the figures on the right-hand side is  $D_A + L_D + L_R$  (see Table 1). The absolute values of the pressure is of no significance

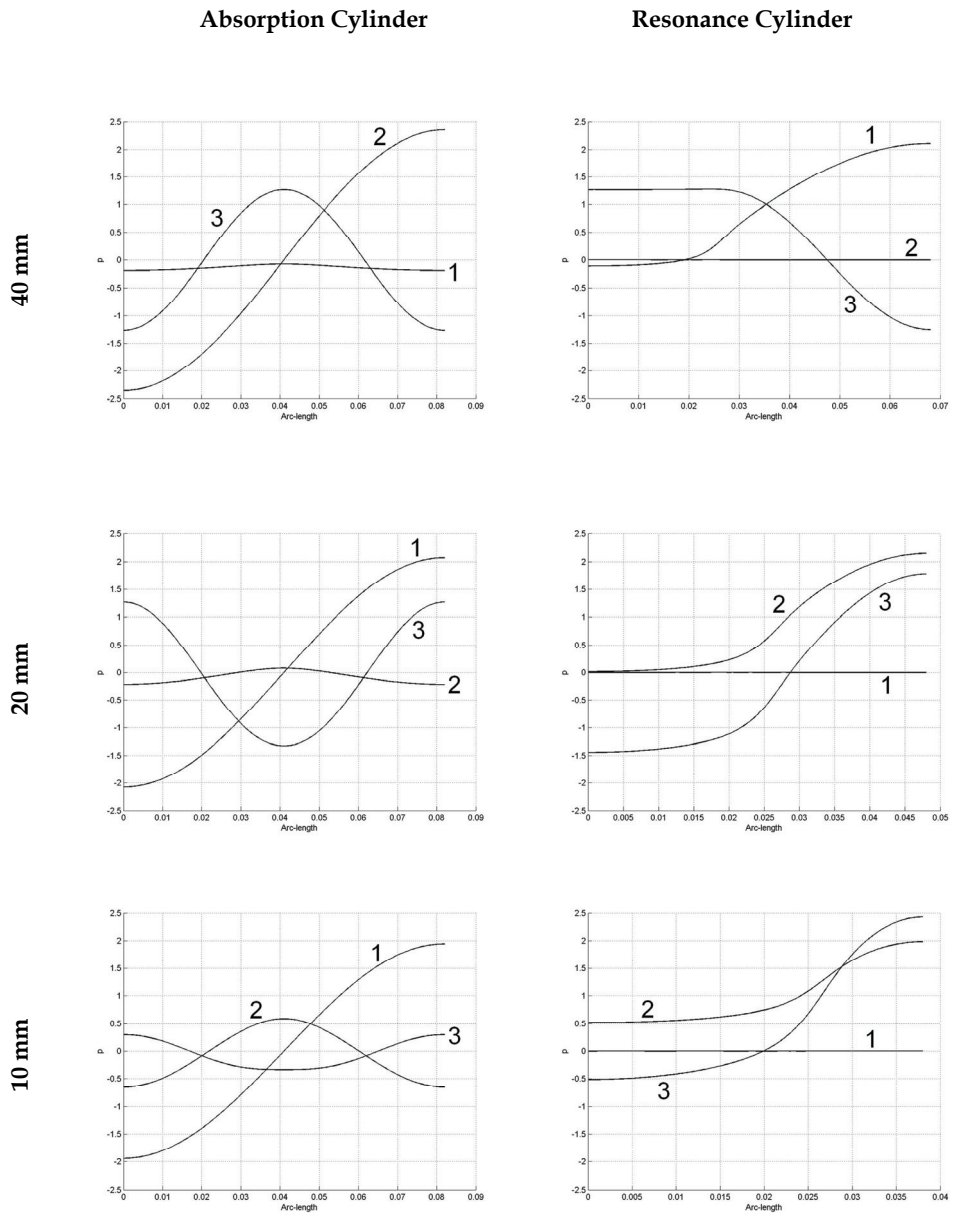


Figure 6. Pressure distribution of the three lowest eigenmodes of the T cell for  $L_R = 40$  mm,  $L_R = 20$  mm and  $L_R = 10$  mm. For details consult the caption of Figure 5

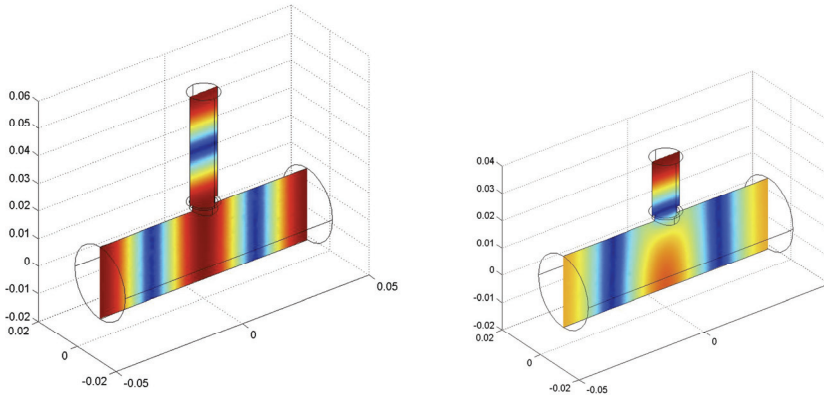


Figure 7. Third mode of  $L_R = 40$  mm T cell (left) and of  $L_R = 20$  mm T cell (right). Depicted is  $|p|$ . For a proper interpretation consult Figure 6

#### 4.2 Quality factors and amplitudes

To calculate quality factors for PA resonators requires the evaluation of the surface integrals (43) and (45). If one even wants to calculate PA signals, in addition the volume integral (37) has to be calculated. Fortunately, for pure modes of low order of cylinder cells the surface integrals can be calculated analytically. Therefore, cylinder cells again have been used as a test case. Very good agreement of numerical results and exact formula has been observed (Baumann et al., 2007).

We performed the calculations of the quality factors for T cells of various lengths of the resonance cylinder filled with *n*-butane and compared the results to measurement. For the numerical modeling of sound waves the characteristic FE size is required to be smaller than  $h = 0.2c/f$ , where  $c$  is the speed of sound and  $f$  the frequency of the sound wave. In our case the largest frequency of relevance is 3500 Hz. When calculating amplitudes, not only the sound waves but also the heat generating laser beam has to be resolved in the finite element mesh. Here, element sizes of  $h = 0.05c/f$  result in a satisfactory numerical accuracy. Modes of order higher than eight have no considerable contribution to the simulation. Therefore, we truncated the sum (33) after the 8th term.

We have extracted resonance frequencies, quality factors and amplitudes by fitting Lorentzian profiles

$$A(f) = i \frac{A_j f}{f^2 - f_j^2 + i f f_j / Q_j} \quad (46)$$

to the experimental data. The quality factor is related to the half width (FWHM) of the resonance by  $\Delta f_j = f_j / Q_j$ . Two sets of data, together with the fit functions are exemplarily depicted in Figure 8.

In Figure 9, values of the quality factors for resonance cylinders of length 1 cm to 14 cm are depicted. The obvious parallelism of the two curves demonstrates the suitability of the model for the description of sound propagation in photoacoustic measuring cells. For very short resonance cylinders only a deviation of the parallelism is observable. The fact, that experimental values are consistently smaller than FE values, is understandable because the



FE simulation does not include all effects that contribute to loss of the photoacoustic signal. For example, the microphone and its surrounding are not modeled in detail. The sharp edges and non-sound hard parts are not considered. Also, we did not model the gas inlet and gas outlet of the cell, which also add sharp edges. There might be impurities in the gas, that we do not have control of. Also, non negligible coupling of the sound wave with the gas container might occur. These and other origins of loss are not included in the FE model. Therefore, we expect higher loss, i. e. smaller quality factors, in the experiment than in the simulation. This is exactly what we observe.

Furthermore, the amplitudes according to Equation (37) have been calculated. In order to evaluate the volume integral, we use the following description of the radiation intensity of the laser beam:

$$\mathcal{I}(\vec{r}) = \mathcal{I}_0 \exp\left(-2\left(\frac{r_{\perp}}{w}\right)^2\right). \quad (47)$$

We assume that the  $z$ -axis coincides with the symmetry axis of the absorption cylinder and  $r_{\perp} = \sqrt{x^2 + y^2}$  is the distance perpendicular to this axis (see Figure 10).  $w$  is the beam radius estimated to be 2 mm. The analytical calculation of the amplitudes according to Equation (37) with the Gaussian laser beam profile (47) is not even possible for the simple case of cylinder cells and numerical methods are necessary.

Since we compare our FE results to the phase-sensitively amplified photoacoustic signals of T cells, absolute pressure values are not relevant. Therefore, the value of the product  $\alpha l_0$  can be used to rescale the numerical data. We performed a least square fit to adjust the parameter  $\alpha l_0$ . Results are displayed in Figure 11. Numerical results and experimental results are in very good accordance.

Once modes, quality factors and amplitudes are known, the PA signal can be calculated. Experimental and FE signals for a large variety of T cells are depicted in Figure 12. The good agreement is obvious. The experimental resonance amplitudes at low frequencies are smaller than the FE amplitudes. This could be attributed to the frequency characteristic of the microphone used for the measurements (Baumann et al., 2007).

### 4.3 Laser beam location for a T cell

The sensitivity of a photoacoustic sensor depends on a variety of influences. Possible system variables of a photoacoustic cell could be e. g. geometrical dimensions, shape parameters, the location of the laser beam, the location of the resonance cylinder and the number and locations of microphones.

In the following investigations as a measure of the signal strength of the photoacoustic cell the absolute value of the pressure field  $p$  at the microphone position will be used, i. e. the signal  $F := \max_{f \in \mathcal{F}} \{|p|\}$ , where  $\mathcal{F}$  is the considered frequency range, can be calculated by a finite element analysis as described in Section 3. For the investigations described in this and in the following section the previously mentioned diminution has not been taken into account.

Depending on how the laser beam is crossing the photoacoustic cell, different eigenmodes can be excited. The task is to find the beam position which leads to the strongest signal.

The laser beam is assumed to be parallel to the  $z$ -axis (i. e. the axis of the absorption cylinder). For the investigation of the influence of the laser beam position the cross-sectional area has been covered by a regular grid  $(x_i, y_i)$  of evaluation points (see Figure 10 for the

coordinate system of a T cell). The grid points have to fulfill the inequality  $x^2 + y^2 - r_L^2 \leq 0$  where  $r_L = \frac{D_A}{2} - w$  is a given limit for the radius. This constraint has been imposed to ensure a proper energy input into the system.

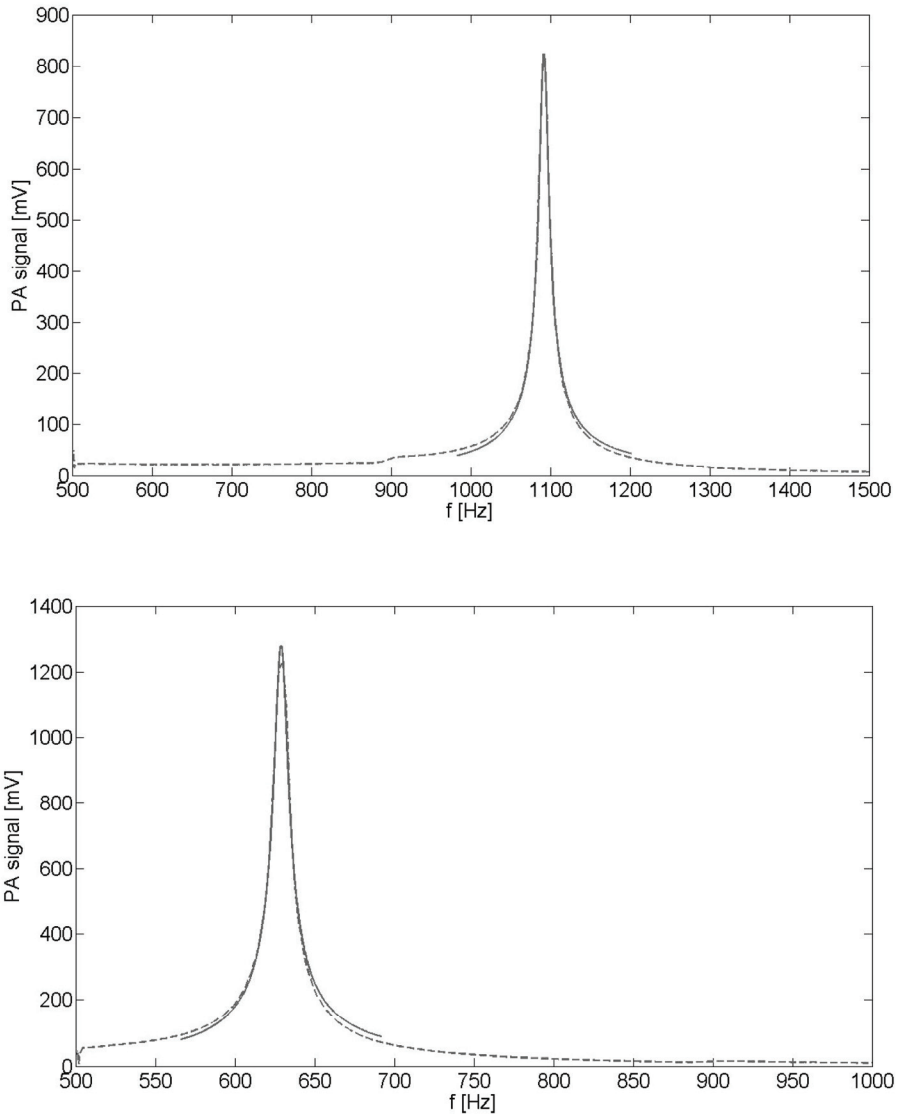


Figure 8. Experimental response function (dashed line) and corresponding fit (solid line) for the  $L_R = 4$  cm (upper) and  $L_R = 8$  cm (lower) T cell

In Figure 13 the signal strength function  $F(x, y)$  is depicted for different lengths of the resonance cylinder. For  $L_R = 1$  cm and  $L_R = 2$  cm the signal function is not concave. In Figure 14 the distribution of the dominant mode over the cross-sectional area of the absorption cylinder is shown. The open and filled circles represent different frequency values. It can be seen that the decrease of the signal strength function and its non-concavity is due to a frequency switch.

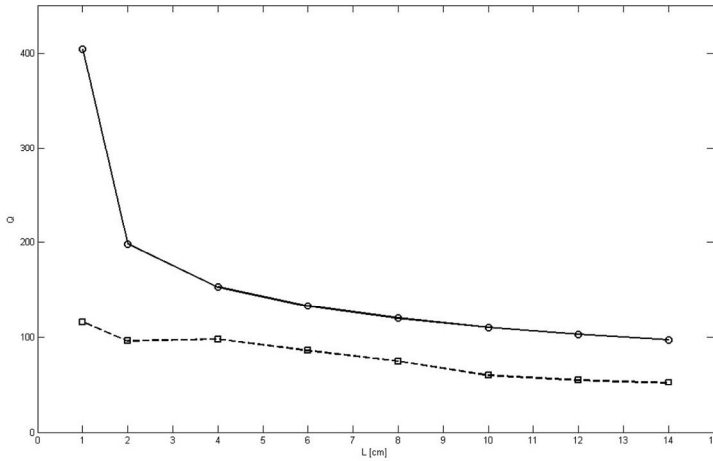


Figure 9. Q-factors of T cell as a function of resonance cylinder length. The upper (solid) curve represents the numerical Q-factors, where the lower (dashed) curve shows the experimental values

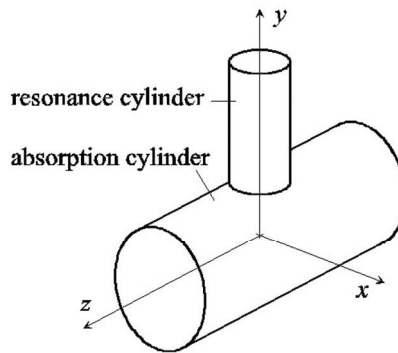


Figure 10. Coordinate system of T cell. In the following the use of "top", "bottom", "horizontal" etc. refers to this system

The strongest influence of the laser beam position occurs for  $L_R = 1$  cm. For larger resonance cylinder lengths the function  $F$  tends to be uniform. In all cases the maximum value  $F_{max}$  on the response surfaces can be located at the position  $(0, y_{min})$  which suggests that a laser beam going through the lower part of the absorption cylinder results in the best signal.

In Figure 15 the extremal values,  $F_{max}$  and  $F_{min}$ , of the response function and the value  $F_{ori}$  for the coordinate system origin have been depicted for different resonance cylinder length.

The difference  $F_{\max} - F_{\min}$  can be interpreted as a measure for the influence of the laser position on the signal strength. Considering this difference the tendency of the function to become uniform with larger resonance cylinder lengths is clearly visible. For  $L_R > 6$  cm  $F_{\text{ori}} \approx F_{\max}$  and this indicates that a laser beam going through the central position  $(0, 0)$  could be sufficient to obtain approximately the maximal response value.

The most important information of Figure 15 is the fact that a strong signal strength can be achieved with a small resonance cylinder length in the range of  $L_R = 1$  cm. The maximum for a resonance cylinder length of 1 cm is approximately the same as for  $L_R = 16$  cm (not shown in the figure). This offers the opportunity to build small and compact T cell sensors. But in this context it has to be taken into account that the sharp peak in the graph displays the sensitivity against length variations.

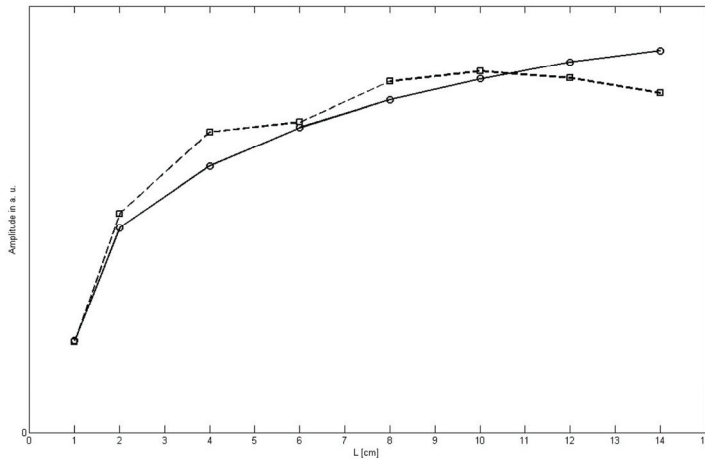


Figure 11. Photoacoustic signal amplitudes of T cell as a function of resonance cylinder length. The solid curve represents the numerical amplitudes, where the dashed curve shows the experimental values. The numerical values have been fitted to the data by a one-parameter least square fit for the scale factor

#### 4.4 Resonance cylinder location

For the investigation in this section the laser beam has been held fixed, going in  $z$ -direction through the center of the absorption cylinder.

Starting from a T cell configuration with a resonance cylinder on top of the absorption cylinder the resonance cylinder has been shifted step by step in the negative  $y$ -direction. The shift has been performed in such a way that the total length  $L_R$  of the resonance cylinder has been split up in two parts located at the top and at the bottom of the absorption cylinder. A shift value of  $y_s = L_R/2$  refers to the symmetrical situation, i. e., the so called X cell, and  $y_s = L_R$  is a T cell with resonance cylinder at the bottom of the absorption cylinder. The microphone is mounted on top of the upper part of the two resonance cylinders; in case of  $y_s = L_R$  that means on the surface of the absorption cylinder (it is worth mentioning, that this design is not equivalent to the original T cell design). The results of these investigations can be seen in Figure 16 (left). For all inspected parameter values  $L_R$  the T cell with resonance cylinder on top of the absorption cylinder ( $y_s = 0$ ) gives the strongest signal.

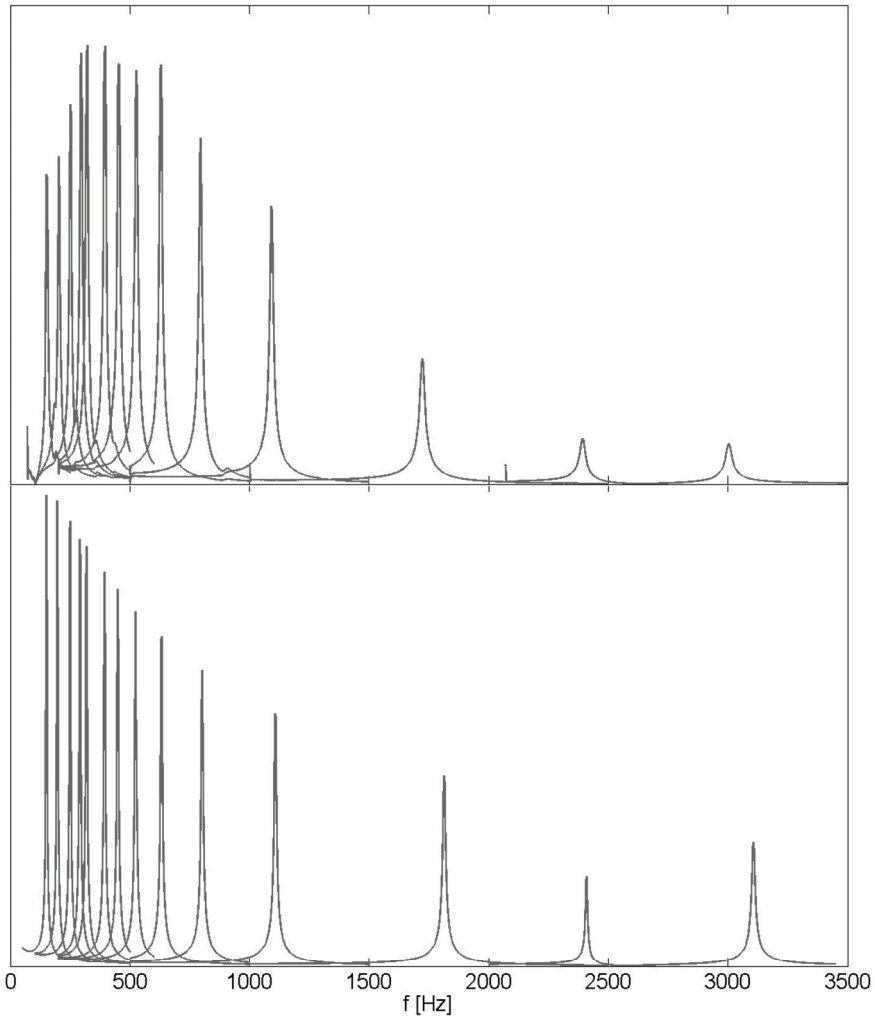


Figure 12. Experimental (upper) vs. finite element (lower) response function for various T cells. From right to left the peaks correspond to the  $L_R = 1, 1, 2, 4, 6, 8, 10, 12, 14, 18, 20, 24, 32, 44$  cm T cell

A closer examination of Figure 16 (left) leads to a suggestion with respect to the design of the photoacoustic sensor. If two microphones will be used, one located at the top of the upper, the second at the bottom of the lower resonance cylinder part, the two signals could be combined. A possible difference of phase could be compensated electronically so that the in-phase signals are considered only. Figure 16 (right) shows an estimation of this effect. The signal strength function values  $F(s)$  of Figure 16 (left), where  $s = y_s / L_R$  is the normalized shift, are processed according to  $F(s) + F(1 - s)$  to simulate the presence of two microphones.

The positions of the maxima in Figure 16 (right) show that the strongest signal can be achieved with asymmetrical cell types.

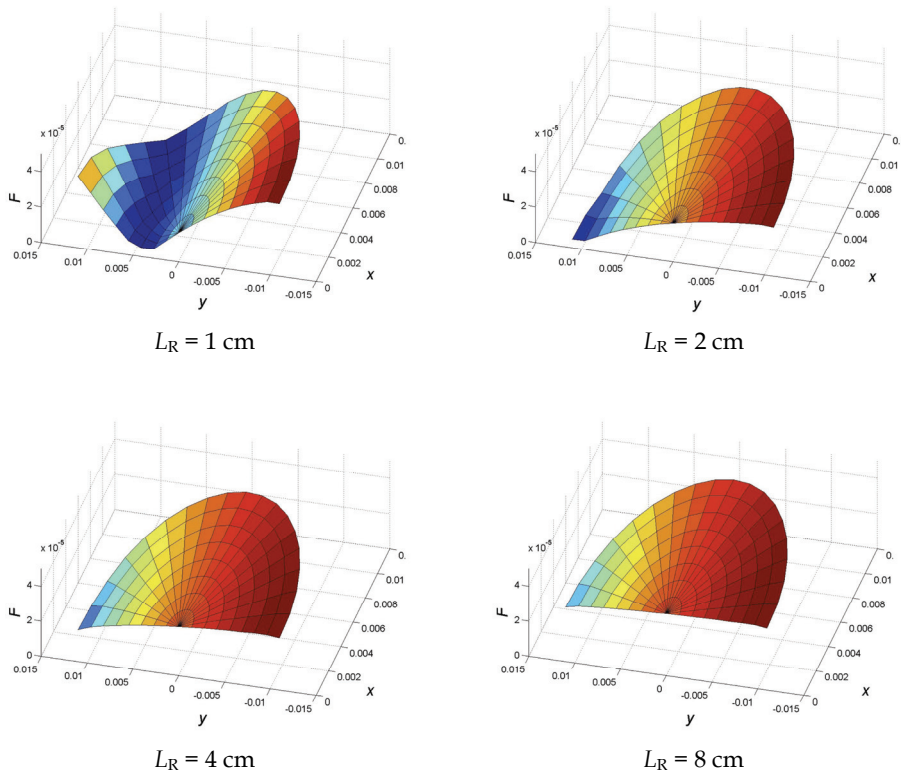


Figure 13. Signal strength function of T cells with different resonance cylinder length  $L_R$  for the laser beam position problem

## 5. Conclusion

We have performed the complete modeling of photoacoustic signal generation and detection using the finite element method. The model allows the calculation of photoacoustic response functions for any given cell geometry. Experimental and numerical results were found to be in good agreement.

Furthermore the influence of certain design parameters on the signal has been investigated numerically. With respect to T cells the exploration shows that the laser position may have a strong effect depending on the length of the resonance cylinder. For short resonance cylinders strong signals can be achieved provided the laser beam is no longer centrally aligned. Additionally, it could be shown, that it might be useful to build asymmetrical photoacoustic cells with two microphones at the ends of the resonance cylinders.

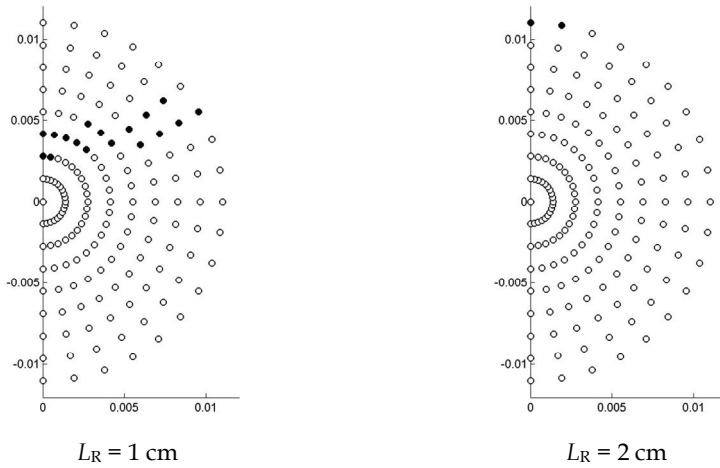


Figure 14. Distribution of dominating mode over the cross-sectional area of the absorption cylinder for the laser beam position problem for T cells with different resonance cylinder length  $L_R$ . The open and filled circles represent different frequency values for each length  $L_R$

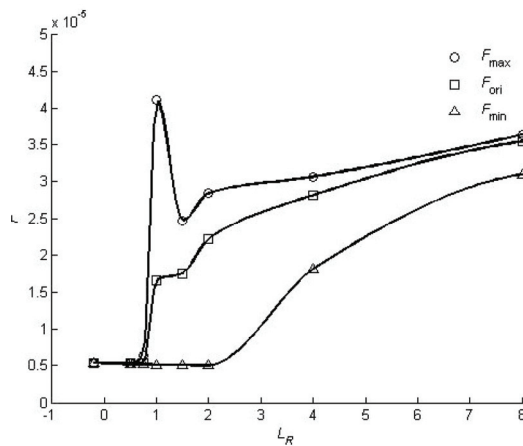


Figure 15. Comparison of extreme values of the signal strength function for a T cell with different resonance cylinder length  $L_R$

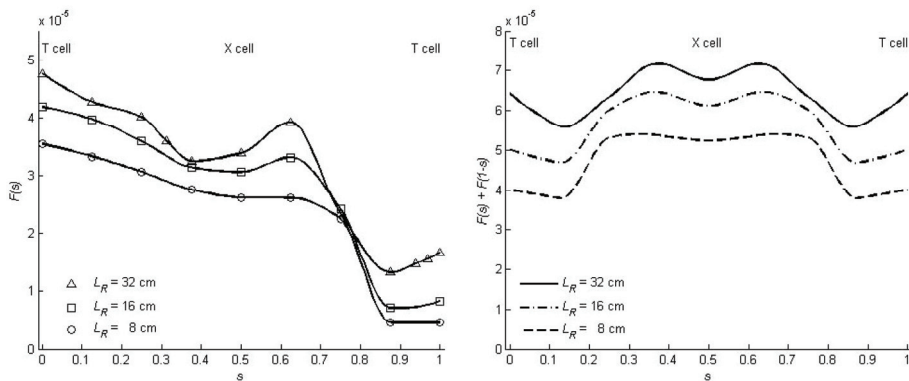


Figure 16. Signal strength function values for unconventional cell shapes between T cell and X cell (left). Simulated signal of two combined microphones on top (right). The abscissa is  $s = y/L_R$ .  $s = 0$  refers to a T cell with a resonance cylinder on top,  $s = 1$  to a cell with a single resonance cylinder at the bottom of the absorption cylinder

## 6. References

- Baumann, B., Kost, B., Groninga, H. G. & Wolff, M. (2006) Eigenmode analysis of photoacoustic sensors via finite element method, *Review of Scientific Instruments*, 77, 044901.
- Baumann, B., Wolff, M., Kost, B. & Groninga, H. G. (2007) Finite Element Calculation of Photoacoustic Signals, *Applied Optics*, Vol. 46, No. 7, 1120-1125.
- Bell, A. G. (1880) On the Production and Reproduction of Sound by Light, *Am. J. Science* 20, 305-309.
- Haken, H. & Wolf, H. C. (1993) *Molecular Physics and Quantum Chemistry*, Springer-Verlag, Berlin.
- Hess, ed. (1989) *Photoacoustic, Photothermal and Photochemical Processes in Gases*, Springer-Verlag, Berlin.
- Kreuzer, L. B. (1977) The Physics of Signal Generation and Detection, in: Pao, Y.-H., ed., *Optoacoustic Spectroscopy and Detection*, Academic Press, New York, 1-25.
- Miklós, A., Hess, P. & Bozóki, Z. (2001) Application of acoustic resonators in photoacoustic trace gas analysis and metrology, *Rev. Sci. Instr.*, Vol. 2, No. 4, 1937-1955.
- Morse, P. M. & Ingard, K. U. (1968) *Theoretical Acoustics*, McGraw-Hill, New York.
- Röntgen, W. C. (1881) Versuche über die Absorption von Strahlen durch Gase; nach einer neuen Methode ausgeführt, *XX. Bericht der Oberhessischen Gesellschaft für Natur- und Heilkunde*, 52-58.
- Temkin, S. (1981) *Elements of Acoustics*, JohnWiley & Sons, New York.
- VDI-Wärmeatlas (2002) 9. Auflage, Springer Verlag, Berlin.
- Wolff, M., Groninga, H. G., Baumann, B., Kost, B. & Harde, H. (2005) Resonance Investigations using PAS and FEM, *Acta Acustica*, Vol. 91, Suppl. 1, 99.
- Zharov, V. P. & Letokhov, V. S. (1986) *Laser Optoacoustic Spectroscopy*, Springer Ser. Opt. Sci. 37, Springer Verlag, Berlin.



# Multi-Agent Systems for the Simulation of Land Use Change and Policy Interventions

Pepijn Schreinemachers and Thomas Berger  
*Universität Hohenheim  
Germany*

## 1. Introduction

Multi-Agent Systems (MAS) are increasingly used as simulation tools to disentangle and explore the complex relationships between environmental change, human actions, and policy interventions. The strength of these models lies in their ability to combine spatial modelling techniques, such as cellular automata or geographical information systems (GIS), with biophysical and socioeconomic models at a fine resolution (Parker et al. 2003). MAS are flexible in their representation of human decisions concerning natural resources and therefore appeal to scholars from diverse backgrounds, such as sociology, geography, and economics.

The behaviour of individual actors can be modelled one-to-one with computational agents which allows for direct observation and interpretation of simulation results. Large part of their fascination—especially to scholars who are otherwise sceptical of any attempt to quantify and model human behaviour—rests on this intuitive and potentially interactive feature. Scholars have combined MAS with role-playing games in which a group of resource users, typically farmers using some common-pool resource, specify the decision rules of computational agents and study how these rules affect people's well-being and their natural resources (Bousquet et al. 2001; Becu et al. 2003; D'Aquino et al. 2003).

In this chapter we reflect on the use of multi-agent models for the ex-ante assessment of policy interventions on land use dynamics with emphasis on developing country agriculture. Field experiments can be costly and time-consuming or might be infeasible when it involves social experimentation; for example, assessing the impact of new policies in the area of water privatization, a control group might have to be deprived of public services. Simulation models can be useful under such circumstances. For instance, plant breeders and agronomists can use simulation models to study the effect of water shortages on crop yields instead of measuring it in the field.

Understanding the dynamics of coupled human-environmental systems is, however, more complicated than non-coupled systems due to nonlinearities and emergent behaviour. Scientific disciplines usually focus on isolated aspects of the system, such as hydrology, crops, or farm households but even if knowledge on all parts of the system were available, these pieces of knowledge could not simply be aggregated to predict the overall system behaviour. MAS can be one approach to combine various disciplinary models; by allowing

interactions between components as well as between elements within each component such model can reproduce nonlinear patterns and emergent behaviour.

At Hohenheim University, we have developed a software package called MP-MAS for empirical applications to study sites in Thailand, Uganda, Chile and Ghana (Berger 2001; Berger et al. 2006; Berger et al. 2007b; Schreinemachers et al. 2007). MP-MAS distinguishes itself clearly from most other agent-based land use models in its use of a constrained optimisation routine, based on mathematical programming (MP), for simulating agent decision-making. Section 2 discusses options for representing human behaviour in MAS and explains the rationale for choosing MP as the core decision-making routine of agents. Section 3 describes the implementation of MP-MAS and its various features. Section 4 outlines how we parameterise our software with empirical data and section 5 explains the procedures for model validation. Section 6 presents results from a case study in Uganda and section 7 concludes.

## 2. Modelling human behaviour with computational agents

Agent-based models of land use and land cover change couple a cellular component that represents a landscape with an agent-based component that represents human decision-making (Parker et al. 2002). MAS have been applied in a wide range of settings, for overviews see Janssen (2002) and Parker et al. (2003), yet have in common that model agents are autonomous decision-makers who interact and communicate and make decisions that can alter the environment. Most MAS applications have been implemented with software packages such as Cormas, NetLogo, RePast, and Swarm (Railsback et al. 2006). The philosophy of agent-based modelling has always been to replicate the complexity of human behaviour with relatively simple rules of action and interaction. In the following we discuss options for implementing the decision making of agents in MAS applied to land use simulation.

### 2.1 Agent behaviour based on heuristics

Agent decision-making in most land-use MAS has been represented as behavioural heuristics, also called condition-action rules, stimulus-response rules, or if-then rules. One simple example would be a rule that agents must grow maize to meet their subsistence needs, but if subsistence needs are met then agents grow coffee on the remaining plots. The use of heuristics can be justified from the concept of bounded rationality, which refers to the limited cognitive capabilities of humans in making decisions. Herbert Simon described bounded rationality as a search process guided by rational principles, what he called *satisficing*—a word created by blending *satisfying* with *sufficing* (Gigerenzer and Goldstein 1996). Satisficing is a decision-process that goes on until an aspiration level is reached (Selten 2001). This process not only holds for the decision to grow maize but also for the selection of maize varieties. Before planting, the farmer does not endlessly shop around to find the optimum variety for his soils (with the optimum being some weighted calculation of all relevant criteria: yield, maturity, disease resistance, tolerance, fodder quality, etc.). Instead he is much more likely to go to the usual farm shop and buy the same seed as last year or, if perhaps not so satisfied with last year's crop, to try a different variety recommended by a peer or the shopkeeper.

Behavioural heuristics have been implemented in most land-use MAS with fairly simple decision trees. For instance, Jager et al. (2000) in a theoretical application used six decision nodes, Becu et al. (2003) in an empirical application to Thailand used 13 nodes, and Castella et al. (2005) used 24 nodes with these last two applications also employing continuous feedback loops. The use of decision trees, and heuristics in general, is intuitive as agent behaviour is straightforward to follow from the tree's structure. Because they are transparent, they are easy to validate by farmers or experts. Constructing a decision tree is, however, not straightforward. The researcher needs to identify not only the most important decisions, but also in the correct sequence and appropriate values at which the tree branches (e.g. saturation levels). Decision trees can be parameterised using sociological research methods (Huigen 2004), data-mining techniques applied to survey data (Ekasingh et al. 2005), participatory modelling and role-playing games (Barreteau et al. 2001; Becu et al. 2003), laboratory experiments (Deadman 1999), group discussions (Castella et al. 2005), or expert opinion.

## 2.2 Agent behaviour based on optimisation

Several studies justified the use of heuristics on the grounds that the economic model of utility maximisation is unrealistic or that empirical evidence has shown that people use simple heuristics to make decisions (Parker et al. 2003). Optimising agents would be cognitive supermen able to process large amounts of information on all feasible alternatives and always select the best one. For this ability, optimising behaviour is frequently criticised (and occasionally ridiculed) as unrealistic and not describing the way real people think (e.g. Todd & Gigerenzer 2000).

Agricultural economists will agree that farm households in developing countries do not perform complex algebra to make optimal decisions. Applied models of farm household decision-making in developing countries are also much different from textbook examples of pure profit maximisation and regularly include risk and uncertainty, limited information, and non-profit goals. Yet the assumption of optimal decision-making clears the way to focus on the hypothesised sources of inefficiency: lack of physical infrastructure, failing institutions, market imperfections, and limited information flows, all of which have clear policy relevance. This points us to a key difference between the heuristics and optimisation approach in that the latter seeks to identify inefficiencies not in the limited cognitive capacity of the human mind but in structural factors external to the decision-maker, which may be addressed through policy intervention.

In land-use simulation, optimising agents have been implemented in MAS using a variety of optimisation techniques. For instance, Balmann (1997), Berger (2001), and Happe (2006) used mathematical programming while Manson (2005) used genetic programming to optimise agent land-use decisions. Neural networks could also be used to optimise land-use decisions but we are unaware of any such empirical application. Different from the heuristic approach, MP requires the explicit specification of an objective function. In applications to farm households in developing countries, objectives of agents usually include cash income, food, and leisure time, which can be either specified in monetary units or in terms of utility. It is noted that heuristic approaches commonly use the same objectives (Deadman et al. 2004).

## 2.3 Synthesis

As argued above, MAS have traditionally been multi-disciplinary approaches in which a large variety of theories and methods co-exist. This also holds for the representation of agent

decision-making in these models. There is no superior decision-model as the choice of decision model depends as much on the research question as on the taste and scientific background of the researcher. Table 1 synthesises the main points of discussion.

	Criterion	Heuristic agents	Optimising agents
1	Focus	Decision process as much as decision outcomes	Decision outcomes
2	Sources of inefficiency	Internal: the limited cognitive capacity of the mind	External: imperfect markets, physical infrastructure, etc.
3	Strengths	<p>Simulating broad categories of land use (e.g. pasture, fallow, crops)</p> <p>Inclusion of multiple stakeholders, each with their own heuristics</p> <p>Validation through stakeholder interaction</p>	<p>Representing heterogeneity through detailed crop and input choices</p> <p>Can capture economic trade-offs</p> <p>Flexible as agents are object-oriented (rather than decision-oriented)</p> <p>Providing quantitative policy support</p>
4	Data needs	High for well-designed and detailed heuristics	High for well-designed and detailed optimisation models
5	Calibration	Relatively quick and easy	Time consuming, especially for detailed models
6	Data source	Laboratory experiments, role-playing games, expert opinion	Surveys, crop-yield experiments, expert opinion

Table 1. Comparison of approaches

The heuristic approach works especially well in abstract and experimental applications or in empirical applications where the objective is not to quantify change but, for instance, to support collective decision-making processes (e.g. D'Aquino et al. 2003). In group discussions it is much easier to present a decision tree than to explain an MP model. If the objective is to quantitatively support policy intervention and to get detailed knowledge about the agricultural land-use systems then an MP model including detailed production and consumption functions is perhaps the more suitable method.

One advantage of MAS is the flexibility to combine and integrate different decision models. The use of one type of agent decision-making does certainly not exclude the use of other types as some heuristic models can easily be formulated in terms of an MP model and vice versa (Schreinemachers and Berger 2006). When using an optimisation approach, heuristics can additionally be used to capture many other aspects of household decision-making. These heuristics can either be directly included in the MP model or implemented in the source code. In Schreinemachers and Berger (2006) we defined four categories of heuristics:

- *Behavioural heuristics directly related to production and consumption decisions of farm households:* For instance, crop rotation requirements or the observation that vegetables are only grown close to the farmstead. These rules should be included as constraints in the MP model as they constrain production decisions.
- *Behavioural heuristics indirectly related to production and consumption decisions:* For instance, Berger (2001) in a MP-based application to Chile included a rule that if the income of an agent is below the opportunity cost of labour then the agent migrates out

of the region. Such rules should be implemented outside the MP in the MAS source code because they do not constrain production decisions but are an evaluation of decision outcomes.

- *Behavioural heuristics of agent interaction*: For instance, the communication of information among agents. These rules should be implemented outside the MP as they go beyond the decisions of an individual agent.
- *Behavioural heuristics related to exceptional circumstances*: For instance, how to re-allocate the land if an agent's last household member deceases, and what to do if the household agent does not produce enough food and income to sustain itself? In the case where no household members are left, the rule should be implemented outside the MP as the agent ceases to exist. Yet, when the agent does not immediately cease to exist, as is the case when income is not enough for subsistence, the rule is best handled inside the MP.

### 3. Description of MP-MAS

#### 3.1 Component-based architecture

The modelling approach we developed for land use simulation is called MP-MAS, which stands for mathematical programming based MAS. It builds on previous work by Berger (2001); a freeware version and manual are available for download at <http://www.uni-hohenheim.de/mas/software>. MP-MAS has a component-based architecture with its source code written in C++. Depending on the needs of a particular application, existing components can be included or excluded while new components can be developed and plugged into the model. Input data for each component are organized in separate Microsoft Excel workbooks, which are converted into plain text ASCII files at the start of the model run. The following sections are largely based on Schreinemachers et al. (2007) and describe the application of MP-MAS to a case study in Uganda, in which we simulated the introduction of new maize varieties and policy programs to address soil degradation and rural poverty. For an application of MP-MAS to water management we refer to Berger et al. (2007a).

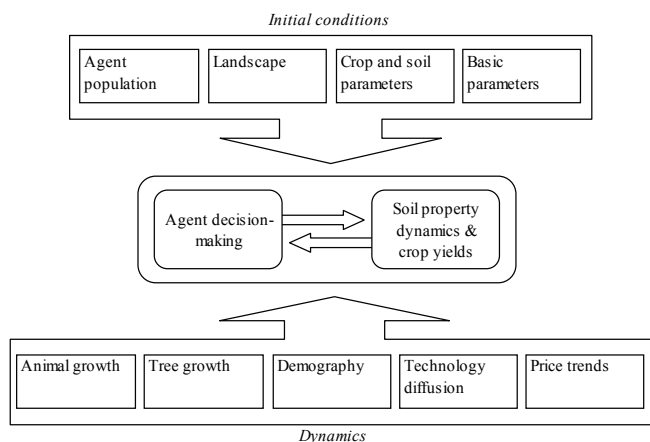


Figure 1. Components of the MP-MAS as applied to Uganda

Figure 1 shows the model design with each box representing a separate component. Three groups of components can be distinguished. At the nucleus of the model is the bio-economic component that simulates the decision-making process, crop yields, and soil fertility changes. A group of four components define the initial conditions for each agent, such as the location of plots, the fertility of the soil, the composition of the households, and parameter values that initiate the model. Another group of five components define the dynamics, including animal and tree growth, technology diffusion, demography, and price changes.

### 3.2 The agent-based decision model

The agent component consists of an economic model, which uses recursive MP models to simulate the decision-making of real-world farm households. It builds on a long tradition of whole farm programming models in agricultural economics (Hazell and Norton 1986; Dillon and Hardaker 1993). Any MP model has three parts. The first part is an explicit specification of all possible decisions related to agriculture (also called activities or decision variables); these include growing crops, raising livestock, and selling, consuming, and purchasing agricultural products. The second part is a utility function that specifies how much each activity contributes to the attainment of the decision-makers' objectives; in the model here these objectives include household net cash income – i.e., the farm cash surplus plus other household receipts, household consumption of food produced on the farm, and the expected future farm cash surplus and home consumption from investments. The third part is a set of equations that link the decision variables and constrain them to only feasible solutions; for instance, they ensure that an agent does not cultivate more land than it actually has available.

Agent decision-making is simulated by a computerised search for a combination of activities that yield the greatest objective value while not violating any constraints. The non-linear response of crop yields to different combinations of inputs was captured using a piecewise linear segmentation. The model includes 11 crops and 7 intercrop combinations; each crop was segmented into various activities by specifying different combinations of land quality, management, and fertilizers. The full matrix has 2350 activities and 556 constraints. For more details about the model equations and parameters the reader is referred to Schreinemachers (2006).

Two novelties about the MP model are worth mentioning. First, the consumption part includes a detailed budgeting system that allocates the income from farm and non-farm activities to savings, non-food expenditures (using a modified Working-Leser model), and eight categories of food products (using a Linear Approximation of the Almost Ideal Demand System (LA/AIDS)). By converting the expenditures on each food category into energy units, it gives an estimate of (consumption) poverty. A second innovation is a three stage decision model that separates the decisions to invest, to produce, and to consume while capturing the interdependencies between each stage; this is described in Schreinemachers & Berger (2006).

Figure 2 conceptualizes the annual sequence of farm household decision-making as three horizontally ordered rectangles (this sequence is repeated for all agents over the simulation horizon, here: 15 years). An MP model is solved for each agent at each stage. Investment and production decisions are based on expected yields and expected prices. The biophysical model, simulating crop yields, intersects the decision sequence after input decisions have been made in the production stage. Expected yields and expected prices are then replaced

by simulated actual yields and actual prices after which the obtained income is allocated to consumption and savings in the consumption stage. This figure also shows the interdisciplinary nature of the MAS model, as impact indicators (nutrient stocks and food consumption) are incorporated into the model's kernel where they interact through the crop yield equation.

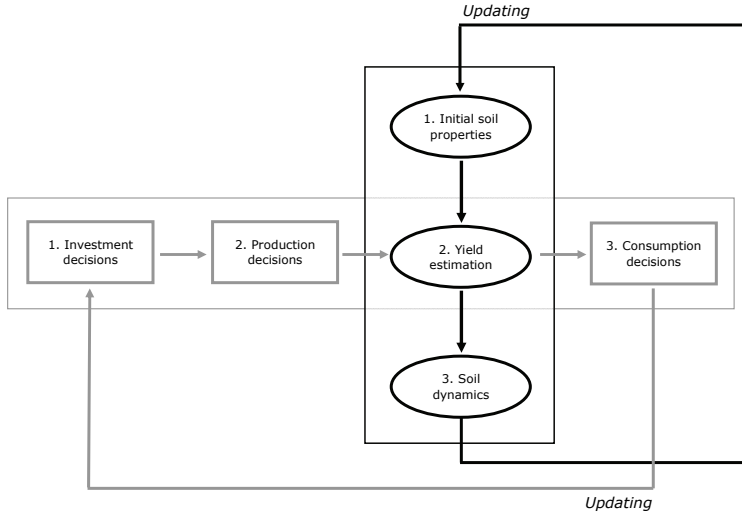


Figure 2. Dynamics and interaction of soil processes and farm decision-making

### 3.3 Soil fertility dynamics and crop yield

Following the vertically ordered ovals in Figure 2, crop-soil processes are modelled as a continuous sequence of three stages:

- The computation of yield limiting factors based on soil properties (at the start of the period) and applied levels of variable inputs (fertilizer and labour).
- The computation of crop and residue yields.
- The updating of soil properties based on the harvested amounts of crop yields and residues and natural processes such as erosion, deposition, leaching, and decomposition.

These three phases were modelled using an extended version of the Tropical Soil Productivity Calculator TSPC (Aune and Lal 1995, 1997; Aune and Massawe 1998). The TSPC was specifically designed for tropical soils and includes nitrogen, phosphorus, potassium, soil organic carbon, and acidity (pH) as determinants of crop yield. Following Figure 2, initial soil properties together with farm management decisions determine crop yields. The TSPC simulates crop yields based on empirical crop yield functions that resemble a Mitscherlich-type of crop yield response as factors are assumed complementary and yields plateau if a factor is in limited supply. This non-linear crop yield equation computes the yield of crop  $i$  at plot  $k$  and at time  $t$  as:

$$Y_{ikt} = p_i * F_{LABikt} * F_{NAVikt} * F_{PAVikt} * F_{KAVikt} * F_{SOCikt} * F_{pHikt} * h_{ij} * g_i \quad (1)$$

with  $Y_{ikt}$  denoting yield (kg/ha/season) and  $p_i$  the yield potential of crop  $i$ , the subsequent six variables are reduction factors for management ( $F_{LAB}$ ), available nitrogen in the soil ( $F_{NAV}$ ), available phosphorus ( $F_{PAV}$ ), available potassium ( $F_{KAV}$ ), soil organic carbon ( $F_{SOC}$ ), and acidity ( $F_{pH}$ ). The factor  $h_{ij}$  adjusts the yield of crop  $i$  if intercropped with a crop  $j$ . Finally,  $g_j$  is an adjustment factor that fits the equation to an observed level of yield. All reduction factors were specified as logarithmic functions while soil organic carbon was taken as a quadratic function. Factors were scaled from 0 to 1; the closer to zero, the stronger it constrains yields and the lower the efficiency of all other factors. Factors with a value of one do not limit crop yield. The crop reduction factors can be obtained by analysing fertilizer experiments and corresponding soil data.

### 3.4 Agent interactions

Various types of agent interactions can be captured in MP-MAS, ranging from exchange of water and land rights on local markets, upstream and downstream use of irrigation water, to diffusion of innovations. In the present application, technology diffusion was implemented as a behavioural heuristic of agent interaction and based on individual network-thresholds as described in Berger (2001). An individual network threshold is the proportion of peers in a network who must have adopted before the individual will consider adoption. An agent with a low threshold value is risk-taking, while an agent with a threshold value closer to unity is risk-averse as it needs much information before it will consider adopting. The advantage of using this approach is that network-thresholds can be estimated from empirical data.

The diffusion of innovations can then be simulated as a two stage procedure as shown in Figure 3. In the first stage, the agent compares the adoption level in the network with its own threshold; if the first exceeds the second then the innovation becomes accessible to the agent and enters the MP model, which by solving simulates the adoption decision. The innovation is adopted if it is selected among the decision variables, which increases the aggregate adoption level in the network, making the innovation accessible for agents with higher threshold values in the following periods of the simulation.

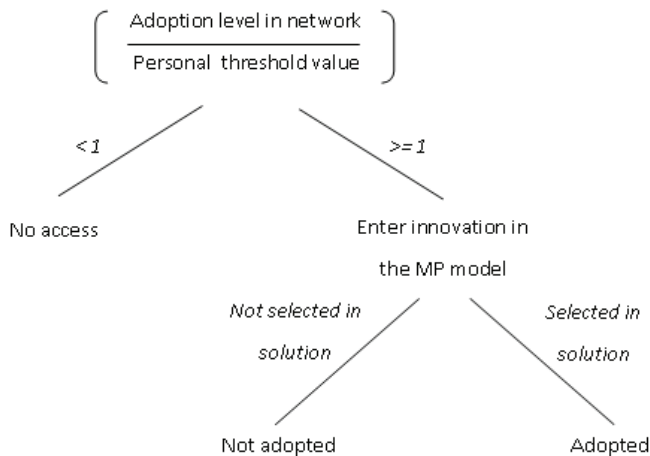


Figure 3. Decision tree for technology adoption



## 4. Empirical parameterization

When generating empirically based MAS, every computational agent must represent a single real-world farm household. Our method for this was previously described in Berger and Schreinemachers (2006) and this section is largely based on this.

To increase the quality and detail of empirical data, random samples are typically preferred to population censuses or censuses of agriculture (Carletto 1999). In the Uganda study, data were collected for about 17 percent of the 520 farm households in the study area by means of a random sample survey. The challenge was to extrapolate the sample population to parameterise the remaining 83 percent of the agents that have no corresponding farm household in the survey. The most obvious strategy would be to multiply every farm households in the sample by a factor six. Average values in such agent population would exactly equal those of the sample survey. This copy-and-paste procedure, however, is unsatisfactory for the several reasons:

First, it reduces the variability in the population. A sampling fraction of 17 percent gives six identical agents, or clones, in the agent population. This might affect the simulated system dynamics, as these agents are likely to behave analogously. It becomes difficult then to interpret, for instance, a structural break in simulation outcomes: is the structural break endogenous, caused by agents breaking with their path dependency, or is the break simply a computational artefact resulting from the fact that many agents are the same? This setback becomes the more serious the smaller the sampling fraction is, because a higher share of the agents is identical.

Second, the random sample contains a sampling error of unknown magnitude, which is also multiplied in the procedure. When using the copy-and-paste procedure, only a single agent population can be created, while for sensitivity analyses a multitude of alternative agent populations is needed. For these reasons, the procedure for generating agent populations is automated using a Monte Carlo approach, to generate a whole collection of possible agent populations.

### 4.1 Monte Carlo approach

Monte Carlo studies are generally used to test the properties of estimates based on small samples. It is thus well suited to this study, where data about a relatively small sample of farm households is available but the interest goes into the properties of an entire population. The first stage in a Monte Carlo study is modelling the data generating process, and the second stage is the creation of artificial sets of data.

The methodology applied here is based on empirical cumulative distribution functions. Figure 4 illustrates such a function for the distribution of goats over farm households. The figure shows that 35 percent of the farm households in the sample have no goats; the following 8 percent has one goat, etc. This function can be used to randomly distribute goats over agents, as well as all other resources in an agent population. For this, a random integer between 0 and 100 is drawn for each agent and the number of goats is then read from the y-axis. Repeating this procedure many times recreates the depicted empirical distribution function. By varying the random seed number, the procedure yields a different agent population each time.

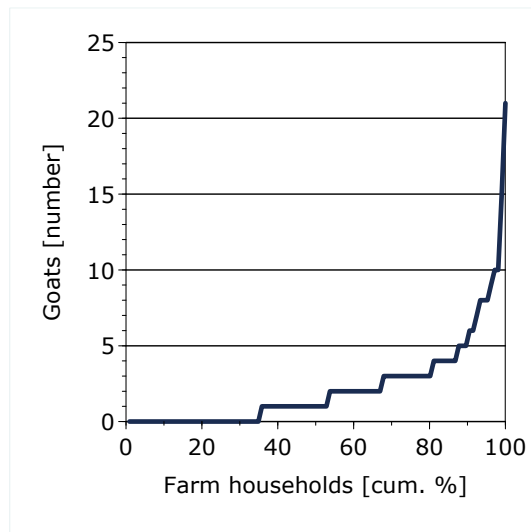


Figure 4. Empirical cumulative distribution of goats over all households in the sample

This straightforward procedure can allocate all resources to the agents; but each resource will then be allocated independently, excluding the event of possible correlations between different resources. In reality resource endowments typically correlate; for example, larger households have more livestock and more land. To include these correlations in the agent populations, first the resource that most strongly correlates with all other resources is identified and used to divide the survey population into a number of clusters. Empirical cumulative distribution functions are then calculated for each cluster of sample observations.

In the Uganda study, the sample was divided into clusters defined by household size because this was the variable most strongly correlated with all other variables. Cluster analysis can also be used for this purpose if several variables show strong correlations, but clusters produced this way are more difficult to interpret, especially when many variables are used. Nine clusters were chosen, as this number captures most of the different household sizes and allocates at least five observations to each cluster. Each agent was then allocated quantities of up to 80 different resources in the Monte Carlo procedure. These resources included 68 different categories of household members (34 age groups of two sexes), 4 livestock types (she-goats, billy goats, cows and young bulls), area under coffee plantation, female head of household, liquidity, ratio of equity and debt capital, plus innovativeness. Agents were generated sequentially, that is, agent No.1 first draws 80 random numbers in 80 different cumulative distribution functions before agent No. 2 does the same.

As most resources only come in discrete units, a piecewise linear segmentation was used to implement the distribution functions. Five segments were chosen as this captured most resource levels; more segments would be needed if the number of resource levels per cluster is larger than five or if many resources have continuous distribution functions.

## 4.2 Checks for statistical consistency

In order to get both statistically consistent and realistic agents, the generated agent populations were submitted to three tests at various levels of aggregation:

- *Checks for inconsistencies at the population level:* The average resource endowments of the agent population have to lie within the confidence intervals of each estimated sample mean. If not, the agent population generated from this seed value is rejected, and the agent random assignment is repeated with a new seed.
- *Checks for inconsistencies at the cluster level:* The generated average resource endowments have to lie within the confidence interval of the estimated sample mean, and the correlation matrix of the agent population has to reflect the correlation matrix of the sample population. Otherwise the agent population is rejected.
- *Checks for inconsistencies at the agent-level:* An agent with 20 household members is very unlikely to have only one plot of land. Yet, because of the randomness of the resource allocation, unrealistic settings can occur in the agent population. By defining a lower and/or upper bound for some critical combinations, this problem can be overcome. If a resource combination lies outside such bound the generated agent is rejected, and the random assignment of this particular resource combination is repeated. Two sets of bounds are included. The first set defines minimum land requirements for livestock and the second set defines demographic rules to ensure realistic family compositions.

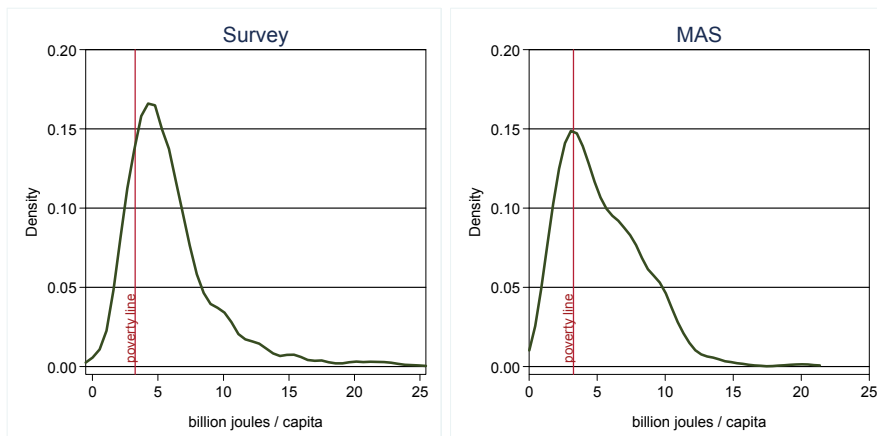
The Monte Carlo approach outlined here works well if correlations among agent characteristics are not too tight. If individual agents, clusters of agents or entire agent populations are continuously being rejected on one of the above three criteria, then the cluster-specific distribution functions have to be fine-tuned. By skewing the distribution functions towards otherwise under-represented combinations of agent characteristics—as was necessary in on-going research in Chile—the random assignment may then still yield statistically consistent agent populations.

## 5. Model Validation

McCarl & Apland (1986) separated model validation into ‘validation by construct’ and ‘validation by results’. The first type of validation we have sought to tackle by building the MAS model on well-established theories in economics and agro-ecology and by including model components, such as production functions and expenditure models, which are little disputed. The validation of the results was accomplished in three steps. First, econometrically estimated functions were validated using standard statistical methods (signs of the parameters, significance, and predictive power of the model). Second, separate components (expenditure model, production functions, crop-soil model, agent populations) were validated by comparing observed values with predicted values. Third, the MP-MAS model – combining all the separate components – was validated by comparing observed values with predicted values from running the baseline scenario.

This baseline scenario was defined as the simulation run that reflects the present situation and the present sources of change. The baseline assumes that current trends in demography, soil processes, and the diffusion of innovations will continue and that there are no new external interventions. This third step in the validation procedure was performed for the main indicators in the model: soil nutrient balances, crop production, and poverty levels. We here give an example for the validation of poverty levels while the reader is referred to Schreinemachers et al. (2007) for more details.

Poverty levels were validated by comparing the distribution of food energy consumption between the survey population and the agent population, using a kernel density function as shown in Figure 5. The vertical line in the figure indicates the poverty line, which was defined as the minimum food energy intake of an average male adult (3.259 billion Joules per annum). The kernel estimates were not fully comparable because the survey estimate of food energy consumption was based on a much larger area of Uganda. Yet, the figure shows the similarity between both distribution functions; both have a positive skew as a small share of the households reaches high per capita food energy intakes. The share of households in poverty is somewhat greater in the MAS than in reality as indicated by a larger area under the curve left of the poverty line.



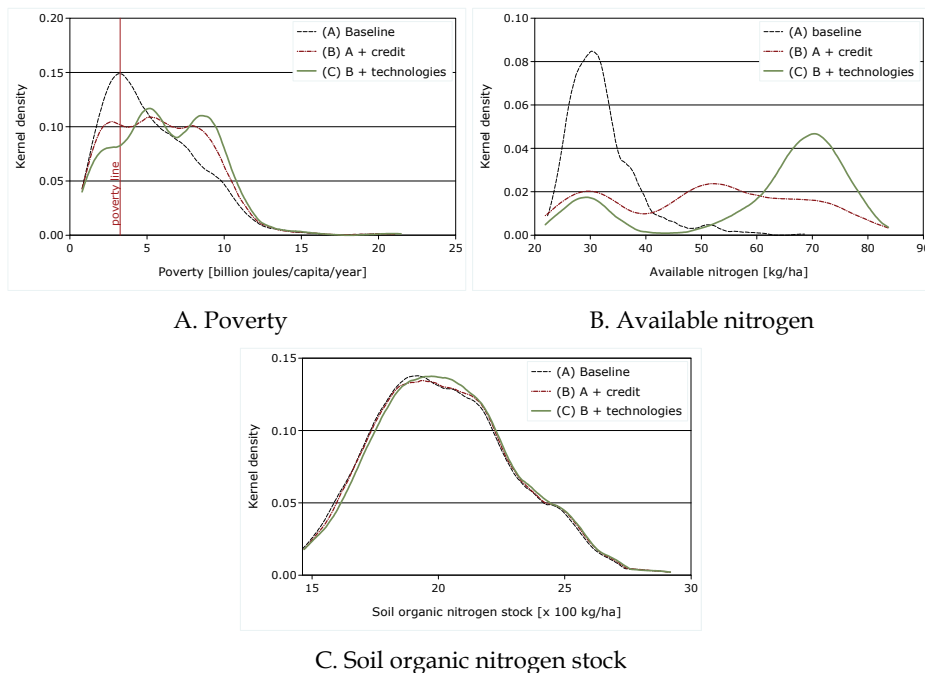
Notes: In male adult equivalents. Epanechnikov kernel used. The survey estimate is based on the farm households in southeast Uganda as recorded by the 1999-2000 UNHS.

Figure 5. Validation per capita food energy consumption

## 6. Simulating the impact of improved maize and mineral fertilizer

In the following, we present results of simulation experiments from a case study in Uganda, previously published in Schreinemachers et al. (2007). The study is about soil fertility decline in Uganda, which is a problem in many countries of sub-Saharan Africa. High population pressure and rapid population growth put pressure on the capacity of the land to supply food in sufficient amounts. The Ugandan government has therefore prioritized the introduction of improved maize varieties and mineral fertilizers. The model was used to analyze the potential impact of improved access to short-term credit and technologies. The baseline scenario, which assumes the continuation of current dynamics, was compared with two alternative scenarios. In the first policy scenario, a new credit program for technology innovation was introduced. The credit could only be used for purchasing two types of innovations: seeds of two improved maize varieties and two types of mineral fertilizers. In the baseline scenario the access to these technologies is constrained by the network diffusion model. In the second scenario this constraint was relieved and agents were given full access to these technologies and short-term credit so as to analyze the maximum effect that this policy program could have.

Figure 6 shows the simulation results for these scenarios in terms of three indicators: poverty (measured in per capita food energy consumption), the total stock of nitrogen in the soil, and the amount of available nitrogen for plants. The results are shown as kernel density graphs, which are suitable to show the distributional effects of the three scenarios. For this, the values for each indicator were averaged per agent over all time periods.



Note: Simulation for 520 agents in three scenarios averaged over 15 years. Epanechnikov kernel used. Figure 6. Simulated effect of credit and technologies on poverty (A), available nitrogen (B), and the stock of soil organic nitrogen (C)

Diagram (A) compares the average 15-year well-being of agents between the three scenarios. In the baseline scenario, 28.9 percent of the agents fell below the poverty line, which was defined as the level of consumption where food supply equals the physical food demand. Access to credit and innovations reduced poverty, as indicated by the shift of agents across the vertical poverty line. The incidence of poverty in this scenario was 24.4 percent, which corresponds to a 15.3 percent reduction in poverty. Results of the third scenario show that the incidence of poverty would be further reduced to 19.8 percent by improving the access to technologies in addition to credit, as 31.3 percent of the agents moved across the poverty line as compared to the baseline scenario. It is, however, noted that the present model does not expose the agents to the vagaries of pests, weather, and prices, which could reduce the simulated positive impact of mineral fertilizers, improved varieties, and short-term credit.

In terms of the sustainability of the agro-ecosystem, the results are mixed. The increased use of mineral fertilizers adds much to the amount of available nitrogen to the crops (Diagram B), thereby increasing crop yields and the well-being of agents. Yet, it does not improve the

stock of nitrogen in the soil (Diagram C) and hence does not guarantee long-term ecological sustainability.

## 7. Conclusion

This chapter showed how MAS models can capture the complexities of human-environment systems. Two alternative designs of agent decision-making algorithms were discussed: heuristics and optimisation. On the basis of an empirical study on soil fertility decline in Uganda, it showed that both the designs can be combined. The empirical application furthermore illustrated the calibration and validation of the agent-based simulation models and their use as tools to explore the impact of alternative policy interventions on land use and socio-economic dynamics.

## 8. Acknowledgement

The authors gratefully acknowledge the financial support of the Robert Bosch Foundation. The research in Uganda was conducted under scientific agreements between the Center for Development Research (University of Bonn), the Institute for Regional Studies (Seoul National University), Noragric (Norwegian University of Life Sciences), and the International Food Policy Institute (IFPRI). We thank our colleagues Soojin Park, Hosangh Rhew, and Jens B. Aune for their inputs.

## 9. References

- Aune, J.B., and Lal, R. 1995. The Tropical Soil Productivity Calculator—A Model for Assessing Effects of Soil Management on Productivity. In *Soil management. Experimental basis for sustainability and environmental quality*, eds. R. Lal and B. A. Stewart. London: Lewis Publishers.
- Aune, J.B. and Lal, R. 1997. Agricultural productivity in the tropics and critical limits of properties of oxisols, ultisols and alfisols. *Tropical Agriculture* 74:96-103.
- Aune, J.B., and Massawe, A. 1998. Effects on Soil Management on Economic Return and Indicators of Soil Degradation in Tanzania: a Modelling Approach. *Advances in GeoEcology* 31:37-43.
- Balmann, A. 1997. Farm-based Modelling of Regional Structural Change: A Cellular Automata Approach. *European Review of Agricultural Economics* 24:85-108.
- Barreteau, O., Bousquet, F., and Attonaty, J.M. 2001. Role-playing games for opening the black box of multi-agent systems: method and lessons of its application to Senegal River Valley irrigated systems. *Journal of Artificial Societies and Social Simulation* 4 (2). Available from <http://www.soc.surrey.ac.uk/JASSS/4/2/5.html>.
- Becu, N., Perez, P., Walker, B., Barreteau, O., and Page, C.L. 2003. Agent-based simulation of a small catchment water management in northern Thailand. Description of the Catchscape model. *Ecological Modelling* 170:319-331.
- Berger, T. 2001. Agent-based models applied to agriculture: a simulation tool for technology diffusion, resource use changes and policy analysis. *Agricultural Economics* 25 (2/3):245-260.

- Berger, T., Birner, R., Díaz, J., McCarthy, N., and Wittmer, H. 2007a. Capturing the Complexity of Water Uses and Water Users within a Multi-Agent Framework. *Water Resources Management* 21 (1):129-148
- Berger, T., and Schreinemachers, P. 2006. Creating agents and landscapes for multiagent systems from random samples. *Ecology and Society* 11 (2):Art.19. Available from <http://www.ecologyandsociety.org/vol11/iss2/>.
- Berger, T., Schreinemachers, P., and Arnold, T. *Mathematical programming-based multi-agent systems to simulate sustainable resource use in agriculture and forestry. A software manual 2007b* Available from <http://www.uni-hohenheim.de/mas/software>.
- Berger, T., Schreinemachers, P., and Woelcke, J. 2006. Multi-agent simulation for the targeting of development policies in less-favored areas. *Agricultural Systems* 88:28-43.
- Bousquet, F., Lifran, R., Tidball, M., Thoyer, S., and M., A. 2001. Agent-based modelling, game theory and natural resource management issues. *Journal of Artificial Societies and Social Simulation* 4 (2). Available from <http://www.soc.surrey.ac.uk/JASSS/4/2/0.html>.
- Carletto, C. 1999. *Constructing samples for characterising household food security and for monitoring and evaluating food security interventions: theoretical concerns and practical guidelines*. Washington, D.C., USA.: International Food Policy Research Institute.
- Castella, J.C., Trung, T.N., and Boissau, S. 2005. Participatory simulation of land-use changes in the northern mountains of Vietnam: the combined use of an agent-based model, a role-playing game, and a geographic information system. *Ecology and Society & Natural Resources* 10 (1):27. Available from [www.ecologyandsociety.org/vol10/iss1/art27/](http://www.ecologyandsociety.org/vol10/iss1/art27/).
- D'Aquino, P., Le Page, C., Bousquet, F., and Bah, A. 2003. Using self-designed role-playing games and a multi-agent system to empower a local decision-making process for land use management: the selfcormas experiment in Senegal. *Journal of Artificial Societies and Social Simulation* 6 (3). Available from <http://jasss.soc.surrey.ac.uk/6/3/5.html>.
- Deadman, P., Robinson, D.T., Moran, E., and Brondizio, E. 2004. Colonist household decisionmaking and land-use change in the Amazon rainforest: an agent-based simulation. *Environment and Planning B: Planning and Design* 31 (5):693-709.
- Deadman, P.J. 1999. Modelling individual behaviour and group performance in an intelligent agent-based simulation of the tragedy of the commons. *Journal of Environmental Management* 56:159-172.
- Dillon, J.L., and Hardaker, J.B. 1993. *Farm management research for small farmer development*. Vol. 6. Rome: Food and Agriculture Organization of the United Nations.
- Ekasingh, B., Ngamsomsuke, K., Letcher, R.A., and Spate, J. 2005. A data mining approach to simulating farmers' crop choices for integrated water resources management. *Journal of Environmental Management* 77:315-325.
- Gigerenzer, G., and Goldstein, D.G. 1996. Reasoning the fast and frugal way: models of bounded rationality. *Psychological Review* 103:650-669.
- Happe, K., Kellermann, K., and Balmann, A. 2006. Agent-based analysis of agricultural policies: an Illustration of the Agricultural Policy Simulator AgriPoliS, its adaptation and behavior. *Ecology and Society* 11 (1):49.

- Hazell, P., and Norton, R. 1986. *Mathematical programming for economic analysis in agriculture*. New York: Macmillan.
- Huigen, M.G.A. 2004. First principles of the MameLuke multi-actor modelling framework for land use change, illustrated with a Philippine case study. *Journal of Environmental Management* 72 (1-2):5-21.
- Jager, W., Janssen, M.A., De Vries, H.J.M., De Greef, J., and Vlek, C.A.J. 2000. Behaviour in commons dilemmas: homo economicus and homo psychologicus in an ecological-economic model. *Ecological Economics* 35:357-379.
- Janssen, M.A., ed. 2002. *Complexity and ecosystem management: The theory and practice of multi-agent systems*. Cheltenham, U.K. and Northampton, Mass.: Edward Elgar Publishers.
- Manson, S.M. 2005. Agent-based modeling and genetic programming for modeling land change in the Southern Yucatan Peninsular Region of Mexico. *Agriculture, Ecosystems and Environment* 111 (1):47-62.
- McCarl, B.A., and Apland, J. 1986. Validation of linear programming models. *Southern Journal of Agricultural Economics* December:155-164.
- Parker, D.C., Berger, T., and Manson, S.M. 2002. Agent-Based Models of Land-Use/Land-Cover Change: Report and Review of an International Workshop. In *LUCC Focus 1, Publication 6*. Bloomington: LUCC Focus 1 Office, Indiana University.
- Parker, D.C., Manson, S.M., Janssen, M.A., Hoffmann, M.J., and Deadman, P. 2003. Multi-agent systems for the simulation of land-use and land-cover change: a review. *Annals of the Association of American Geographers* 93 (2):314-337.
- Railsback, S., Lytinen, S., and Jackson, S. 2006. Agent-based simulation platforms: review and development recommendations. *Simulation* 82 (9):609-623.
- Schreinemachers, P. 2006. *The (Ir)relevance of the crop yield gap to food security in developing countries. With an application of multi-agent modeling to farming systems in Uganda*. Göttingen. Cuvillier Verlag. Available online at: [http://hss.ulb.uni-bonn.de/diss\\_online/landw\\_fak/2006/schreinemachers\\_pepijn/](http://hss.ulb.uni-bonn.de/diss_online/landw_fak/2006/schreinemachers_pepijn/).
- Schreinemachers, P., and Berger, T. 2006. Land-use decisions in developing countries and their representation in multi-agent systems. *Journal of Land Use Science* 1 (1):29-44.
- Schreinemachers, P., Berger, T., and Aune, J.B. 2007. Simulating soil fertility and poverty dynamics in Uganda: A bio-economic multi-agent systems approach. *Ecological Economics* 64 (2):387-401. Available from <http://www.sciencedirect.com/science/article/B6VDY-4PP23GB-1/2/90199a01713e7f2373072dec5fbfbddb>.
- Selten, R. 2001. What is bounded rationality? In *Bounded Rationality, The Adaptive Toolbox*, ed. G. G. a. R. Selten, 13-36. Cambridge, MA: The MIT Press.



# Pore Scale Simulation of Colloid Deposition

M. Ekrem Cakmak<sup>1,2</sup>, Bin Gao<sup>3</sup>, John L. Nieber<sup>4</sup>, and Tammo S. Steenhuis<sup>1</sup>

<sup>1</sup>*Cornell University Ithaca, NY USA*; <sup>2</sup>*Cukurova University, Adana, University of Florida, Gainesville, FL, USA*; <sup>4</sup>*University of Minnesota, St. Paul, MN*  
<sup>1,3,4</sup>*USA*, <sup>2</sup>*Turkey*

## 1. Introduction

Mobile subsurface colloids have received considerable attention because the migration of colloids and colloid-contaminant complexes through the solid matrix substantially increase the risk of groundwater pollution. Typically defined as suspended particulate matter with diameter less than 10 $\mu$ m, colloids include both organic and inorganic materials such as microorganisms, humic substances, clay minerals and metal oxides. Accurate prediction of the fate of colloids is important to predict colloid facilitated transport of pollutants, and the transport of biocolloids such as viruses and bacteria.

In colloid transport studies colloid deposition, that is, the capture of colloids by grain surfaces, is considered as the primary mechanism controlling the transport of colloids in groundwater (Ryan & Elimelech; 1996). The role of electrostatic and hydrodynamic forces in controlling colloid deposition behavior of colloids has been afforded detailed investigation in the field of colloid science to gain more understanding about colloid-surface interaction processes. The study of deposition rates of colloids onto model collectors has provided substantial information on the electrostatic and hydrodynamic forces involved in the transport of colloids (Elimelech et al., 1995; Tien & Ramarao, 2007). Most of these studies have focused on colloid transport under saturated conditions (Yao et al., 1971; Rajagopalan & Tien, 1976; Ryan & Elimelech, 1996; Keller & Auset, 2007). However, there is not much information available on colloid behavior under unsaturated conditions due to the complexity of the conditions involved (DeNovio et al., 2004; Keller & Sirivithayapakorn, 2004; Auset & Keller; 2004; Crist et al., 2005; Zevi et al., 2005; Keller & Auset, 2007).

Most of the experimental and modeling studies on colloid transport under unsaturated conditions have focused primarily on colloid concentration in drainage water with very little emphasis on the precise mechanisms retaining the colloids in the pores (Corapcioglu & Choi, 1996; Lenhart & Saiers, 2002; DeNovio et al., 2004).

Generally, the approaches used to simulate colloid transport can be classified into two types, Lagrangian or Eulerian. The Lagrangian approach focuses on the movement of distinct particles and tracks particle position in a moving fluid (Rajagopalan & Tien, 1976; Ryan and Elimelech, 1996). In contrast, the Eulerian approach considers the concentration distribution of particles in a porous media (Yao et al., 1971; Tufenkji & Elimelech, 2004). The Eulerian approach has advantages over the Lagrangian approach, in that it does not require high computational performance, and it is easy to incorporate Brownian motion (Ryan and Elimelech, 1996; Nelson & Ginn, 2005).

The deposition of colloids in porous media has been investigated by several researchers to improve existing methods by incorporating the forces such as hydrodynamic and attractive forces into the governing equations (Yao et al., 1971; Rajagopalan & Tien, 1976; Tufenkji & Elimelech, 2004). For instance, Yao et al. (1971) developed colloid filtration theory as a method for predicting colloid deposition in saturated porous media. A limitation of these studies is that the colloid transport and deposition simulations have been performed only for saturated media consisting of clean and spherical solid grains (collectors). These limitations led us to find a method to simulate colloid transport under unsaturated conditions where the air phase comes into play in addition to solid grains and moving water. This may be partly accomplished by modifying existing methods developed for saturated conditions.

The main difficulty in more complex calculations is that the simulation methods are cumbersome, usually slow and cannot capture the complex pore geometries that exist in nature. That is why an effective, reliable, user-friendly and easy to be modified simulation software is very important and needed in the modeling and simulation studies.

The objective for this chapter is to illustrate a test of the suitability of a finite element based computational modeling and simulation software package named COMSOL Multiphysics® v33.a (COMSOL, Inc., Burlington, MA, USA), for simulating colloid deposition on solid grains and air bubbles for conditions where Brownian motion dominates.

In the first part of the chapter we compare the COMSOL finite element solution with the analytical solutions of Yao et al. (1971), Rajagopalan & Tien (1976), and Tufenkji & Elimelech (2004) of classical filtration theory for one grain of a porous media. The second part involves the simulation of colloid deposition onto an inert air bubble.

## 2. Colloid Filtration Theory

In colloid filtration theory, the deposition efficiency of a porous medium is represented by the deposition efficiency of a unit collector, i.e. an isolated solid grain (Yao et al., 1971; Ryan & Elimelech, 1996; Tufenkji & Elimelech, 2004). It is assumed that the porous medium is represented by an assemblage of perfect spherical solid grains (collectors). According to the theory, the transport of suspended colloids in the pore fluid to the vicinity of a stationary collector (i.e. a solid grain) is typically governed by three mechanisms: interception, gravitational settling, and Brownian diffusion. Interception takes place when the particles moving along the trajectories of flow streamlines come into contact with the collector due to the collector's finite size. Gravitational settling occurs when colloid particles have densities greater than the fluid density. These particles can then collide with a collector. The Brownian motion mechanism leads to diffusive migration of particles within a fluid and becomes significant for particles smaller than 1  $\mu\text{m}$ .

The transport of colloids is usually simulated by solving the convection-diffusion equation using a velocity field for the pore space between grains simulated with the Navier-Stokes equation for creeping flow conditions. The deposition of colloids from the fluid occurs by transfer of the colloids from the moving pore fluid onto the grain surface by the three aforementioned mechanisms. It is assumed that colloids do not accumulate on the grain surface, but that colloids 'disappear' once they are intercepted by the grain. The rate of overall particle deposition is found by integrating the particle flux over the collector surface. Within filtration theory it is also common to assume no colloid-colloid interaction, and that colloids do not affect the fluid flow.

The deposition of colloids onto a single grain has been simulated by Yao et al. (1971), Rajagopalan & Tien (1976) and Tufenkji & Elimelech (2004). Yao et al. (1971) developed an equation to find the deposition efficiency of a unit collector by analytically solving the convection-diffusion equation based on the additivity assumption that allows the addition of the analytical solutions of each deposition mechanisms (interception, gravitational settling, and Brownian diffusion) independently (Nelson & Ginn, 2005). They assumed that the collector existed in an infinite fluid stream with no interaction from surrounding collectors. For the same problem, Rajagopalan and Tien (1976) used the Lagrangian approach, (i.e., particle trajectory analysis) with boundary conditions for the flow field similar to Happel (1958). These boundary conditions took into account the neighboring collectors as if the single (simulated) grain was located in a real porous media. Finally, Tufenkji and Elimelech (2004) developed a closed-form solution for calculating colloid deposition efficiency of a solid grain by combining the approaches of Yao et al. (1971) and Rajagopalan & Tien (1976).

### 3. Simulation Methodology

Since in addition to gravity effects, Brownian movement of colloids is of particular interest in the work presented here, the Eulerian colloid filtration theory originally developed by Yao et al. (1971) is chosen in our simulations. In this manuscript, the deposition of colloids on a single collector is simulated for the same boundary conditions as Rajagopalan and Tien (1976). To find the velocity field the Navier-Stokes equations are solved with the finite element method. The resulting velocity field is then used in the solution to the convection-diffusion equation, with diffusion being due to Brownian motion of colloids and with gravitational settling included. In the next sections, the Navier-Stokes equation and the convection-diffusion equations are discussed both in general, and specifically how they are used in our simulations.

#### 3.1 Navier-Stokes Equation

The Navier-Stokes equations are employed to represent steady state creeping incompressible flow conditions, i.e.

$$-\frac{\partial p}{\partial i} + \mu \cdot \nabla^2 v_i + \rho_w g_i = 0 \quad i = x, y, z \quad (1)$$

$$\nabla \cdot \underline{v} = 0 \quad (2)$$

where  $p$  is the pressure (Pa),  $\mu$  is the dynamic viscosity of the water (Pa.s),  $v_x, v_y, v_z$  are the vector components for the velocity ( $\underline{v} = v_x \vec{i} + v_y \vec{j} + v_z \vec{k}$ ) of the water (m/s),  $\rho_w$  is the density of the water (kg/m<sup>3</sup>), and  $g_x, g_y, g_z$  are the vector components for the gravitational acceleration (9.81 m/s<sup>2</sup>). Equation (1) is valid for Reynolds number much less than one. The Reynolds number is defined as

$$R_e = \frac{vd\rho_w}{\mu} \quad (3)$$

where  $d$  is the diameter of the collector (m).

In a porous medium, fluid flow around a spherical collector is affected by the presence of other collectors around it. Therefore, a proper flow model for porous media is needed to reflect the disturbance of the flow field around the individual collectors. Among the various theoretical models Happel's fluid shell model is the most commonly used model (Elimelech, 1994; Tien & Ramarao, 2007). Though the effect of neighboring collectors on fluid flow around the isolated unit collector is neglected in the original colloid filtration theory (Yao et al., 1971), it is considered in this chapter by adopting Happel's model.

In Happel's model, the porous medium is constructed of identical spherical collectors, each of which is in a fluid shell (Fig. 1). In order to maintain the overall porosity of the porous medium for a single collector, the thickness of the shell,  $b$ , is defined as

$$b = d(1 - \epsilon)^{-1/3} \quad (4)$$

where  $\epsilon$  is the porosity of the porous medium.

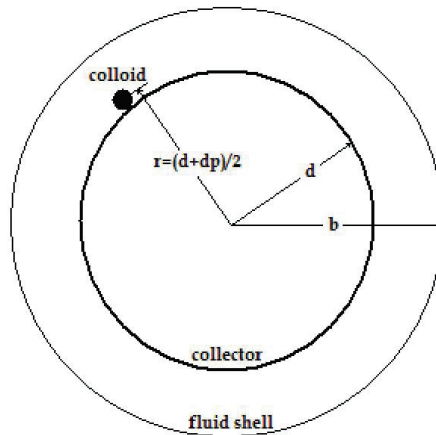


Figure 1. Schematic representation of a unit collector, and Happel's fluid shell

The boundary conditions used in our simulations in the solution of the Navier-Stokes equations can be summarized as follows. The surface of the fluid shell is specified as a symmetry boundary to take the effect of neighboring collectors on fluid flow into account. The symmetry boundary means that the velocity of the water normal to the boundary is zero at that boundary, and that the tangential component of the viscous force vanishes. A no-slip boundary condition is specified at the surface of the solid grain where the water velocity equals zero (Spielman, 1977; Tien & Ramarao, 2007). Later we will consider the simulations for flow around a single air bubble, and for that case the surface of the bubble is specified to be a slip boundary (Nguyen & Jameson, 2005; Shew & Pinton, 2006).

### 3.2 Convection-Diffusion Equation

Once the velocity field is determined, the distribution of colloids within the pore space of a porous medium can be found by solving the convection-diffusion equation for steady state conditions (Yao et al., 1971). The convection-diffusion equation is given by

$$[\underline{v} \cdot \nabla C] - [D \cdot \nabla^2 C] - \sum_i \left[ \left(1 - \frac{\rho_w}{\rho_p}\right) \frac{mg_i}{3\pi\mu d_p} \frac{\partial C}{\partial x_i} \right] = 0 \quad (5)$$

where  $C$  is the concentration of the colloids (number of colloids/m<sup>3</sup>),  $D$  is the diffusion coefficient of the colloids calculated by Einstein's equation (Equation 9) (m<sup>2</sup>/s),  $\rho_p$  is the density of an individual colloid (kg/m<sup>3</sup>),  $m$  is the mass of the colloids (kg), and  $d_p$  is the diameter of the colloids (m). The terms in the equation represent (left to right) the colloid transport processes of convection, diffusion, and gravitational settling.

When colloids make contact with a collector surface it is assumed that they disappear into the collector by specifying the collector surface as being a perfect sink. This means that all colloids arriving at the collector surface are irreversibly captured. The condition for a perfect sink can be achieved by setting the concentration in the vicinity of the collector surface to zero, i.e.,

$$C = 0 \text{ at } r = (d+d_p)/2 \quad (6)$$

where  $r$  represents the radius of an imaginary spherical surface displaced slightly outward from the surface of the collector (m) (Fig. 3.1).

At an infinite distance from the collector center the colloid concentration is assumed to be equal to the free stream concentration,  $C_0$  (Yao et al., 1971; Elimelech, 1994).

$$C = C_0 \text{ at } r = \infty \quad (7)$$

In previous analyses that used Happel's model for the flow velocity field, the above boundary condition is specified at the surface of the fluid shell, i.e.,

$$C = C_0 \text{ at } r = b \quad (8)$$

The diffusion coefficient in the convection-diffusion equation is calculated by Einstein's equation

$$D = kT/3\pi\mu d_p \quad (9)$$

where  $k$  is the Boltzmann's constant (1.3806503 10<sup>-23</sup> J/K), and  $T$  is the absolute temperature (Kelvin).

### 3.3 Deposition (Collision) Efficiency

Solution of equations (1), (2) and (5) subject to the corresponding boundary conditions will yield the mass of particles entering the shell, the concentration of particles within the spherical shell, and the mass of particles leaving the shell. Also, the flux of particles passing into the ideal sink will also be determined from that solution. The solution can then be used to determine the particle deposition efficiency,  $\eta$ , which is calculated as

$$\eta = \frac{I}{v_0 C_0 \frac{\pi d_p^2}{4}} \quad (10)$$

where  $I$  is the total particle deposition rate onto a collector, obtained by integrating the particle flux over the surface of the collector,  $v_0$  is the free stream (initial) water velocity (m/s) (Yao et al., 1971; Tufenkji & Elimelech, 2004). This integration can be done readily with COMSOL.

### 3.4 Numerical Solution

A finite element based computational modeling and simulation software package, COMSOL Multiphysics® (COMSOL, Inc., Burlington, MA, USA), is chosen for simulating colloid deposition in this study due to its features that seemed to meet the above needs. This software is fast and reliable, allows creation of complex geometries, and the influences of boundary conditions can be assessed easily.

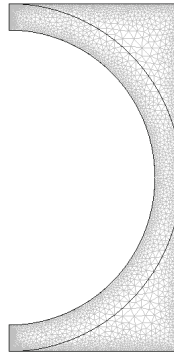


Figure 2. The mesh system used in this study

The simulations are performed, as in earlier studies (Yao et al., 1971; Rajagopalan & Tien, 1976; Tufenkji & Elimelech, 2004), in an axisymmetric domain that provides three-dimensional results from two-dimensional simulations (Nelson et al., 2007).

Triangular elements are used in the mesh system (Fig. 2). The number of elements in the mesh system used in the simulations is determined by trial and error. The number of elements is increased until the results do not vary substantially. By default COMSOL generates mesh systems automatically. In our case with a sub-domain that has a high aspect ratio due to the boundary condition specified by Equation 6, better results were obtained when the mesh system was created in part by manual specification of mesh generation parameters.

Once the mesh system was established the simulations were performed with colloid diameters varying from 0.05 to 2  $\mu\text{m}$ , and a constant collector diameter of 0.6 mm as described in more detail in the next section.

## 4. Simulations: Setup and Results

### 4.1 Colloid Deposition on a Grain Collector

In this section, the colloid deposition efficiency of a spherical solid grain (collector) is simulated numerically using COMSOL. The results are compared with three previous studies (Yao et al., 1971; Rajagopalan & Tien, 1976; Tufenkji & Elimelech, 2004).

The boundary conditions for the solution of the Navier-Stokes equation are summarized in Table 1 and shown graphically in Fig. 3. Flow direction and gravity are both opposite to the direction of the y-axis. The convection-diffusion equation is solved with the same boundary conditions as in Yao et al. (1971) except that, the colloid concentration at the fluid shell surface is set to be equal to the initial concentration (Equation 8), while Yao et al. (1971) assumed the concentration to be equal to the initial concentration at an infinite distance from the collector surface (Equation 7).

Boundary	Condition
Inlet	$v_0 = 9 \times 10^{-6} \text{ m/s}$
Collector Surface	No-slip ( $v = 0 \text{ m/s}$ )
Outlet	Pressure (0 Pa)
Sides, Fluid Shell	Symmetry

Table 1. The boundary conditions used to solve the Navier-Stokes equation for a solid grain

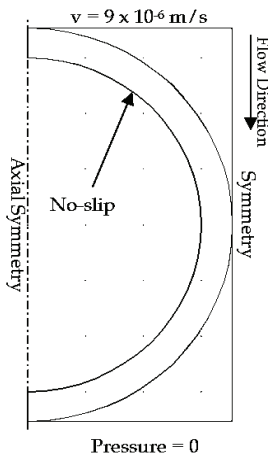


Figure 3. The boundary conditions for the Navier-Stokes Equation (solid grain)

In order to compare our results with the previous studies, the parameter values used in the simulations were adopted from the study of Tufenkji & Elimelech (2004) (Table 2). Simulations were performed for colloids with diameters of 0.05, 0.10, 0.50, 0.75, 1, 1.5, and 2  $\mu\text{m}$  and a grain diameter of 0.6 mm. The most time-consuming step in our simulations was the trial and error generation of the mesh. Once the optimum mesh system was found, each simulation took an average of 37 seconds.

Variable		Value
$d$	Collector diameter	0.6 mm
$v_0$	Initial water velocity	$9 \times 10^{-6} \text{ m/s}$
$T$	Temperature	288 K
$k$	Boltzmann constant	$1.3806503 \times 10^{-23} \text{ J/K}$
$\varepsilon$	Porosity	0.39
$\rho_w$	Density of water	1000 kg/m <sup>3</sup>
$\rho_p$	Density of colloids	1050 kg/m <sup>3</sup>
$\mu$	Dynamic viscosity of water	0.001 Pa.s

Table 2. Variables used in the simulations (Tufenkji & Elimelech, 2004).

The simulation results are given in Fig. 4 together with the results of the three other studies (Yao et al., 1971; Rajagopalan & Tien, 1976; Tufenkji & Elimelech, 2004). Similar to the other studies, colloid deposition efficiency is the greatest for the 0.05  $\mu\text{m}$  colloids than decreases with larger colloids diameter. When colloid diameters are on the order of 1  $\mu\text{m}$  colloid deposition increases again (Fig. 4).

The integration of the particle flux on the zero concentration boundary (Equation 6) reveals that the diffusion as well plays an important role in the increased collection efficiency because the ratio of the colloid efficiencies is not the same for the different colloid diameters.

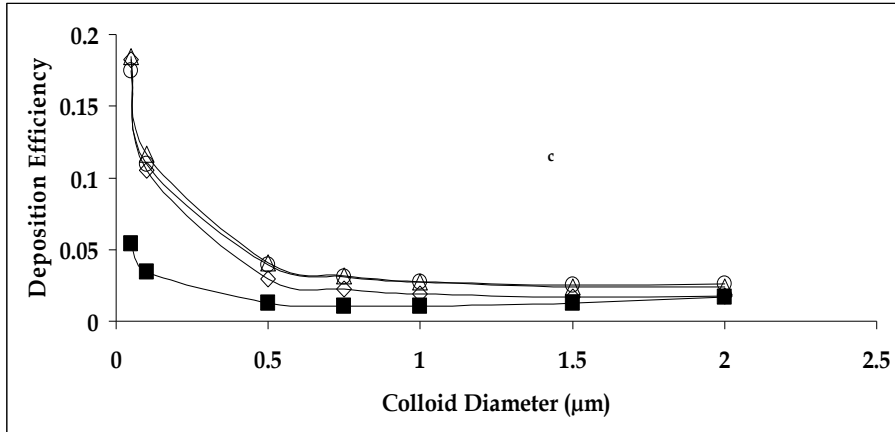


Figure 4. Deposition efficiency of a single collector vs. colloid size (diameter) (△) Rajagopalan & Tien, 1976 (◇) Tufenkji & Elimelech, 2004 (■) Yao et al., 1971 (○) Result of the current analysis

A comparison of our simulated deposition efficiency with those of the other three studies is presented in Fig. 4. It is observed that our results agree very well with the Rajagopalan & Tien (1976) results. The worst comparison is with the result of Yao et al. (1971), while an intermediate agreement is achieved with the results of Tufenkji & Elimelech (2004). One reason why our results are so different from the results of Yao et al. (1971) is that they did not incorporate the boundary effect of neighboring collectors into their solution. Another possible reason for the difference is that the efficiency calculations made by Yao et al. (1971) were based on the additivity assumption. While this assumption simplifies the solution, it could be problematic as noted by Nelson & Ginn (2005). We do not yet know why our solution results disagree with those of Tufenkji and Elimelech (2004).

#### 4.2 Colloid Deposition on an Air Bubble Collector

In this simulation of colloid deposition efficiency, the only change made was replacing the grain with an air bubble of the same size. For the numerical simulation this means that the no slip boundary becomes a slip boundary condition at the collector surface while the remaining parameter values and grid remain the same (Table 3 and Fig. 5). The slip boundary has been used before for rising air bubbles in fluids by Nguyen & Jameson (2005) and Shew & Pinton (2006).

Boundary	Condition
Inlet	$v_0 = 9 \times 10^{-6}$ m/s
Collector Surface	Slip ( $v \neq 0$ m/s)
Outlet	Pressure (0 Pa)
Sides, Fluid Shell	Symmetry

Table 3. The boundary conditions used to solve the Navier-Stokes equation for air bubble



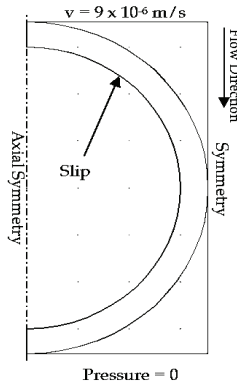


Figure 5. The boundary conditions for the Navier-Stokes Equation (air bubble)

The results of the simulation with the air bubble collector are compared to those for the solid particle in Fig. 6. It is observed that the deposition efficiency of the air bubble is approximately twice that of the solid grain. The effects of the no-slip and slip boundaries on the water flow velocities are illustrated in Fig. 7. The water velocity around the air bubble is greater than the water velocity around the solid grain because under laminar flow conditions, the water (and thus the colloid velocity) approaches zero near the grain surface.

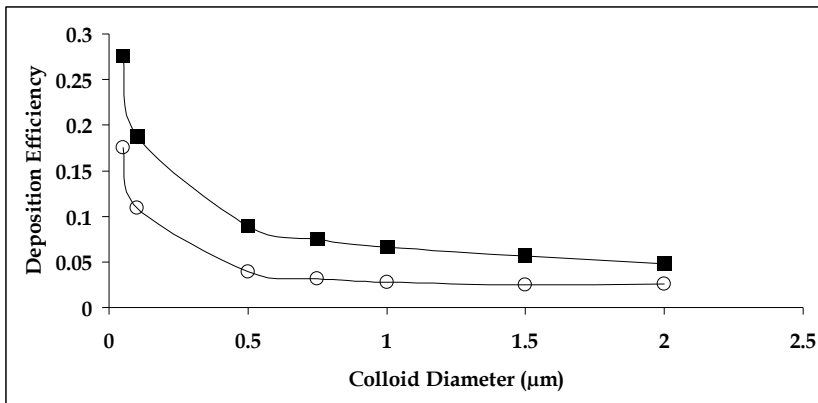


Figure 6. Deposition efficiency of the collectors vs. colloid size (diameter) (■) Air Bubble (○) Solid Grain

The differences between the two cases are due to the relative fraction of colloids that come into the vicinity of the diffusion boundary. Regions of high velocity will transport a larger fraction of colloids in contrast to regions of low velocity. For the case of the bubble, the slip boundary results in high water velocity near the diffusion boundary and therefore a relatively high fraction of colloids will be transported in the vicinity of that boundary, resulting in higher concentration gradients at the diffusion boundary. For the case of the solid particle, the no-slip boundary results in a lower velocity near the diffusion boundary and therefore a relatively lower fraction of colloids will be transported in the vicinity of the diffusion boundary, resulting in lower concentration gradients at that boundary. That the

difference between the two cases decreases as the particle size increases can be explained by fact that as the colloid diffusion decreases (with increasing diameter) the differences in transport across the diffusion boundary will also decrease. As the diffusion becomes vanishingly small, the colloid concentrations at the diffusion boundary will be identical for the two cases, exactly equal to the initial concentration,  $C_0$ .

While various surface forces (capillary, DLVO, electrostatic, etc.) were not considered in our analysis, the differences in flow velocity near the collector surface between the solid collector and the air bubble are expected to have significant influence on the predicted efficiency of colloid deposition when such forces are incorporated into the governing transport equations (Wan & Tokunaga, 2002; Zevi et al., 2005; Elimelech et al., 1995; Tien & Ramarao, 2007).

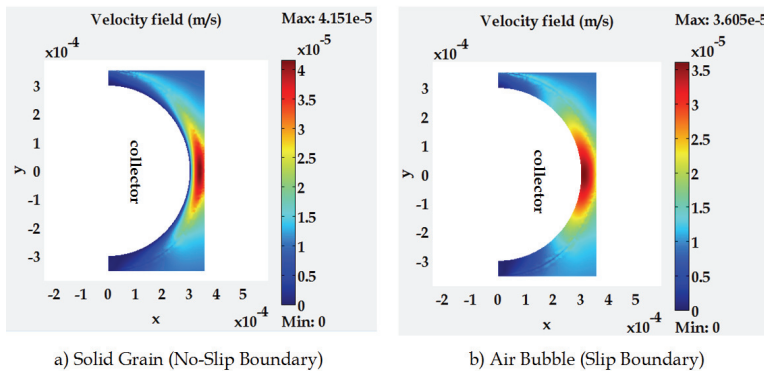


Figure 7. Velocity fields around the collectors

## 5. Conclusions

The re-examination of the colloid filtration theory revealed that it is crucial to consider the effect of surrounding solid grains on the flow field in order to gain more realistic results.

The application of the colloid filtration theory on the air bubble showed that more colloids collided with the air bubble than with the solid grain due to high pore water velocity around its surface. The pore water velocity and the disturbances in the flow field have a substantial effect on the deposition and transport paths of the colloids. Nevertheless, in order to thoroughly examine the effect of pore water velocity on the dominant deposition mechanism, the simulations should be done with various initial water velocities. To better model an unsaturated porous medium, simulations with assemblages of collectors need to be performed.

## 6. Future Work

Our simulations of the colloid deposition in unsaturated porous media need to be extended to take domains composed of assemblages of collectors into account. We are interested to study the variables/parameters that will affect the colloid deposition.

It is planned to construct a model porous medium consisting of solid grains and air bubbles in two dimensions and three dimensions. This is expected to provide more insight into the colloid deposition for unsaturated conditions. This is partially done and sample simulations are shown in Fig. 8.

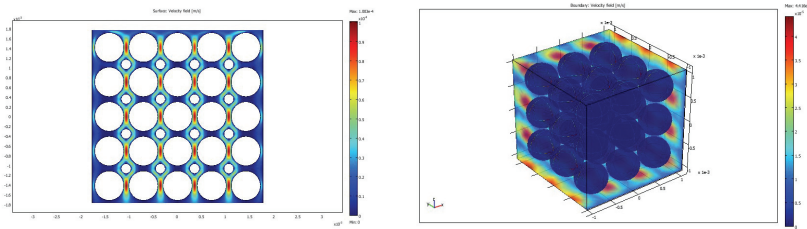


Figure 8. Future simulations to be performed for 2-D and 3-D domains

## 7. Nomenclature

- $C$ : Concentration of the colloids (number of colloids /  $\text{m}^3$ )  
 $C_0$ : Initial (free stream) concentration of colloids (number of colloids /  $\text{m}^3$ )  
 $b$ : Thickness of Happel's fluid shell (m)  
 $d$ : Diameter of a unit collector (i.e. air bubble or solid grain) (m)  
 $d_p$ : Diameter of colloids (m)  
 $D$ : Diffusion coefficient ( $\text{m}^2/\text{s}$ )  
 $g_i$ : Components of gravitational acceleration ( $g_x, g_y, g_z$ ) ( $9.81 \text{ m/s}^2$ ) in the  $x, y$  and  $z$  coordinate directions  
 $I$ : Total colloid deposition rate onto a collector  
 $k$ : Boltzmann's constant (J/K)  
 $m$ : Mass of the colloids (kg)  
 $p$ : Pressure (Pa)  
 $r$ : The radius of an imaginary spherical surface displaced slightly outward from the surface of the collector (m)  
 $R_c$ : Reynolds number  
 $T$ : Absolute temperature (Kelvin)  
 $\underline{v} = v_x \vec{i} + v_y \vec{j} + v_z \vec{k}$ : Resultant velocity (m/s), with  $v_x, v_y$  and  $v_z$  being velocity components in the  $x, y$  and  $z$  coordinate directions, respectively  
 $v_0$ : Free stream (initial) water velocity (m/s)  
 $\varepsilon$ : Porosity of porous medium  
 $\mu$ : Dynamic viscosity of water (Pa.s)  
 $\rho_w$ : Density of water ( $\text{kg}/\text{m}^3$ )  
 $\rho_p$ : Density of an individual colloid ( $\text{kg}/\text{m}^3$ )  
 $\eta$ : The particle deposition efficiency

## 7. References

- Auset, M. & Keller, A. A. (2004). Pore-scale processes that control dispersion of biocolloids in saturated porous media. *Water Resour Res*, 40, 3, (Mar 2004) W03503, ISSN: 0043-1397.  
 Corapcioglu, M. Y. & Choi, H. (1996). Modeling colloid transport in unsaturated porous media and validation with laboratory column data. *Water Resour Res*, 32, 12, (Dec 1996) 3437- 3449, ISSN: 0043-1397.  
 Crist, J. T.; Zevi, Y.; McCarthy, J. F.; Throop, J. A. & Steenhuis, T. S. (2005). Transport and retention mechanisms of colloids in partially saturated porous media. *Vadose Zone J*, 4, 1, (Feb 2005) 184- 195, ISSN: 1539-1663.

- DeNovio, N. M.; Saiers, J. E. & Ryan, J. N. (2004). Colloid movement in unsaturated porous media: Recent advances and future directions. *Vadose Zone J*, 3, 2, (May 2004) 338–351, ISSN: 1539-1663.
- Elimelech, M. (1994). Particle deposition on ideal collectors from dilute flowing suspensions: mathematical formulation, numerical solution, and simulations. *Sep Technol*, 4, 4, (Oct 1994) 186-212, ISSN: 0956-9618.
- Elimelech, M.; Gregory, J.; Jia, X. & Williams, R. A. (1995). *Particle deposition and aggregation: measurement, modelling, and simulation*, Butterworth-Heinemann, ISBN:075067024X, Oxford, England.
- Happel, J. (1958). Viscous flow in multiparticle systems: slow motion of fluids relative to beds of spherical particles. *AIChE J*, 4, 2, 197–201, ISSN: 0001-1541.
- Keller, A. A. & Auset, M. (2007). A review of visualization techniques of biocolloid transport processes at the pore scale under saturated and unsaturated conditions. *Advances in Water Resour*, 30, 6-7, (Jun-Jul 2007) 1392-1407, ISSN: 0309-1708.
- Keller, A. A. & Sirivithayapakorn, S. (2004). Transport of colloids in unsaturated porous media: Explaining large-scale behavior based on pore scale mechanisms. *Water Resour Res*, 40, 12, (Dec 2004) W12403, ISSN: 0043-1397.
- Lenhart, J. J. & Saiers, J. E. (2002). Transport of silica colloids through unsaturated porous media: Experimental results and model comparisons. *Environ Sci Technol*, 36, 4, (Feb 2002) 769-777, ISSN: 0013-936X.
- Nelson, K. E.; Massoudieh, A. & Ginn, T. R. (2007). *E. coli* fate and transport in the Happel sphere-in-cell model. *Advances in Water Resour*, 30, 6-7, (Jun-Jul 2007) 1492-1504, ISSN: 0309-1708.
- Nelson, K. E.; Massoudieh, A. & Ginn, T. R. (2007). *E. coli* fate and transport in the Happel sphere-in-cell model. *Advances in Water Resour*, 30, 6-7, (Jun-Jul 2007) 1492-1504, ISSN: 0309-1708.
- Nguyen, A. V. & Jameson, G. J. (2005). Sliding of fine particles on the slip surface of rising gas bubbles: Resistance of liquid shear flows. *International Journal of Multiphase Flow*, 31, 4, (Apr 2005) 492-513, ISSN: 0301-9322.
- Rajagopalan, R. & Tien, C. (1976). Trajectory analysis of deep-bed filtration with the sphere-in-cell porous media model. *AIChE J*, 22, 3, (May 1976) 523–533, ISSN: 0001-1541.
- Ryan, J. N. & Elimelech, M. (1996). Colloid mobilization and transport in groundwater. *Colloid Surf A*, 107, (Feb 1996) 1–56, ISSN: 0927-7757.
- Shew, W. L. & Pinton, J. F. (2006). Viscoelastic effects on the dynamics of a rising bubble. *J Stat Mech*, (Jan 2006) P01009, ISSN: 1742-5468.
- Spielman, L. A. (1977). Particle capture from low-speed laminar flows. *Annual Review Of Fluid Mechanics*, 9, 297-319, ISSN: 0066-4189.
- Tien, C. & Ramarao, B. V. (2007). *Granular filtration of aerosols and hydrosols*, Butterworth-Heinemann, ISBN:9781856174589, Great Britain.
- Tufenkji, N. & Elimelech, M. (2004). Correlation equation for predicting single collector efficiency in physicochemical filtration in saturated porous media. *Environ Sci Technol*, 38, 2, (Jan 2004) 529–536, ISSN: 0013-936X.
- Yao, K. M.; Habibi, M. T. & O'Melia, C. R. (1971). Water and waste water filtration: concepts and applications. *Environ Sci Technol*, 5, 11, (Nov 1971), 1105–1112, ISSN: 0013-936X.
- Zevi, Y.; Dathe, A., McCarthy, J. F.; Richards, B. K. & Steenhuis, T. S. (2005). Distribution of colloid particles onto interfaces in partially saturated sand. *Environ Sci Technol*, 39, 18, (Sep 2005) 7055–7064, ISSN: 0013-936X.

# Practical Application of Simulation Technique for the Resonators Using Piezoelectric Ceramics

Jeong-Ho Cho, Yong-Hyun Lee, Myung-Pyo Chun and Byung-Ik Kim  
*Korea Institute of Ceramic Engineering & Technology  
Korea*

## 1. Introduction

In this couple of decades, applications of piezoelectrics to resonators, sensors and actuators have been dramatically accelerated, in addition to the discovery of new materials and devices. Some of the highlights include electrostrictive materials for positioners, ferroelectric single crystals with very high electromechanical couplings for medical transducers, thin/thick films for Micro-Electro-Mechanical Systems starting from a sophisticated chemical technology, and multilayer type actuators fabricated by cofiring technique. All will provide a remarkable industrial impact in the 21<sup>st</sup> century.

Piezoelectric materials exhibit electromechanical coupling, which is useful for the design of devices for oscillating, sensing and actuation. The coupling is exhibited in the fact that piezoelectric materials produce an electrical displacement when a mechanical stress is applied and can produce mechanical strain under the application of an electric field. Due to the fact that the mechanical-to-electrical coupling was discovered first, this property is termed the direct effect, while the electrical-to-mechanical coupling is termed the converse piezoelectric effect.

The representative converse piezoelectric effect-applied example is a ceramic resonator. Frequency sources are a key component of much of today's electronics. Frequency sources are used as sensor, clocks and filters, and the ability to control the accuracy and stability of these devices is vital to their performance characteristics and ability to bring forth advancements in technology. Ceramic resonators stand between quartz crystals and LC/RC oscillators in regard to accuracy. They offer low cost and high reliability timing devices with improved start-up time to quartz crystals. The oscillation of ceramic resonators is dependent upon mechanical resonance associated with their piezoelectric crystal structure. The ceramic resonator oscillates in thickness-shear vibration mode for fundamental frequencies (typical less or equal than 8MHz) and thickness-longitudinal vibration mode for third-overtone mode (above 8MHz to 50MHz). Ceramic resonators have superior resonant impedance than quartz crystal, which offer much better start-up time. They have low cost because of high mass production rate, small size, no need for adjustment.

Recently, narrow frequency tolerance characteristics of piezoelectric ceramic resonators have been required for fabricating highly accurate electronic devices. Because of this trend, a low electromechanical coupling coefficient and a high mechanical quality factor have been

required in piezoelectric materials. Widely used piezoelectric materials such as lead zirconate titanate (PZT) type materials have electromechanical coupling coefficient of over 30% for the fundamental thickness extensional and thickness shear vibration modes. The third harmonic thickness extensional vibration mode has also been used for resonator applications and their electromechanical coupling coefficients are low; however spurious vibration from the fundamental mode resonance is inevitable in this type of resonator. Spurious modes occurrence is one of the significant problems for various applications because those spurious vibrations worked as the cause of occurring the malfunction of devices. Therefore, it is an important issue to implement the configuration which spurious vibration doesn't affect the fundamental vibration as designing the resonator.

## 2. Basic Theory of Piezoelectricity

To simulate the piezoelectric properties, it is important to evaluate the material constants of piezoelectric ceramics exactly. The piezoelectric effect can be seen as a transfer of electrical to mechanical energy and vice-versa. It is observed in many crystalline materials. The direct piezoelectric effect consists of an electric polarization in a fixed direction when the piezoelectric crystal is deformed. The polarization is proportional to the deformation and causes an electric potential difference over the crystal. The inverse piezoelectric effect, on the other hand, constitutes the opposite of the direct effect. This means that an applied electric field induces a deformation of the crystal. The piezoelectric effects are written as the set of linear equations. The expressions for the piezoelectric effect can be combined into one matrix expression by writing the relationship between strain ( $S$ , m/m) and electric displacement ( $D$ , C/m<sup>2</sup>) as a function of applied stress ( $T$ , N/m<sup>2</sup>) and applied field ( $E$ , V/m):

$$\begin{Bmatrix} S \\ D \end{Bmatrix} = \begin{bmatrix} s & d \\ d & \epsilon \end{bmatrix} \begin{Bmatrix} T \\ E \end{Bmatrix} \quad (1)$$

Where  $s$  is the mechanical compliance (m<sup>2</sup>/N),  $d$  is the piezoelectric strain coefficient (C/N), and  $\epsilon$  is the dielectric permittivity (F/m).

It can be inverted to write the expressions with stress and field as the dependent variables and strain electric displacement as the independent variables.

$$\begin{Bmatrix} T \\ E \end{Bmatrix} = \frac{1}{s\epsilon - d^2} \begin{bmatrix} \epsilon & -d \\ -d & s \end{bmatrix} \begin{Bmatrix} S \\ D \end{Bmatrix} \quad (2)$$

It is possible to generalize this result to the case of an arbitrary volume of piezoelectric materials. Consider a cube of piezoelectric material, although there is no assumptions regarding the direction in which the electric field is applied or the directions in which the material is producing stress or strain. It is used as the common convention that the 3 direction is aligned along the poling axis of the material (Figure 1).

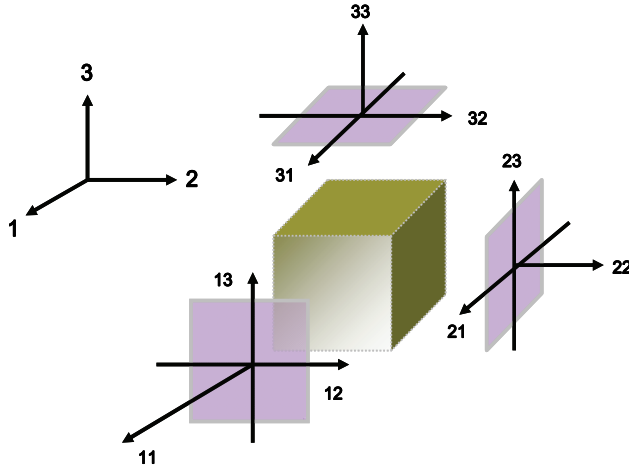


Figure 1. Piezoelectric cube indicating the coordinate axes of the 3D analysis

For a linear elastic material, the electric field and the electric displacement are expressed in terms of the vectors:

$$\mathbf{E} = \begin{pmatrix} E_1 \\ E_2 \\ E_3 \end{pmatrix} \quad (3)$$

$$\mathbf{D} = \begin{pmatrix} D_1 \\ D_2 \\ D_3 \end{pmatrix} \quad (4)$$

Similarly, the stress and the strain can be expressed in terms of the vectors. The components of stress and strain that are normal to the surface of the cube are denoted  $T_{11}(T_1)$ ,  $T_{22}(T_2)$ ,  $T_{33}(T_3)$  and  $S_{11}(S_1)$ ,  $S_{22}(S_2)$ ,  $S_{33}(S_3)$ , respectively. There are six shear components,  $T_{12}(T_6)$ ,  $T_{13}(T_5)$ ,  $T_{23}(T_4)$ ,  $T_{21}(T_6)$ ,  $T_{32}(T_4)$ ,  $T_{31}(T_5)$  and  $S_{12}(S_6)$ ,  $S_{13}(S_5)$ ,  $S_{23}(S_4)$ ,  $S_{21}(S_6)$ ,  $S_{32}(S_4)$ ,  $S_{31}(S_5)$ . The parentheses are the compact notation for piezoelectric constitutive equations. With the compact notation form, the full constitutive relationships are represented by equations (5) and (6).

$$\begin{bmatrix} S_1 \\ S_2 \\ S_3 \\ S_4 \\ S_5 \\ S_6 \end{bmatrix} = \begin{bmatrix} s_{11} & s_{12} & s_{13} & s_{14} & s_{15} & s_{16} \\ s_{21} & s_{22} & s_{23} & s_{24} & s_{25} & s_{26} \\ s_{31} & s_{32} & s_{33} & s_{34} & s_{35} & s_{36} \\ s_{41} & s_{42} & s_{43} & s_{44} & s_{45} & s_{46} \\ s_{51} & s_{52} & s_{53} & s_{54} & s_{55} & s_{56} \\ s_{61} & s_{62} & s_{63} & s_{64} & s_{65} & s_{66} \end{bmatrix} \begin{bmatrix} T_1 \\ T_2 \\ T_3 \\ T_4 \\ T_5 \\ T_6 \end{bmatrix} + \begin{bmatrix} d_{11} & d_{12} & d_{13} \\ d_{21} & d_{22} & d_{23} \\ d_{31} & d_{32} & d_{33} \\ d_{41} & d_{42} & d_{43} \\ d_{51} & d_{52} & d_{53} \\ d_{61} & d_{62} & d_{63} \end{bmatrix} \begin{bmatrix} E_1 \\ E_2 \\ E_3 \end{bmatrix} \quad (5)$$

$$\begin{bmatrix} D_1 \\ D_2 \\ D_3 \end{bmatrix} = \begin{bmatrix} d_{11} & d_{12} & d_{13} & d_{14} & d_{15} & d_{16} \\ d_{21} & d_{22} & d_{23} & d_{24} & d_{25} & d_{26} \\ d_{31} & d_{32} & d_{33} & d_{34} & d_{35} & d_{36} \end{bmatrix} \begin{bmatrix} T_1 \\ T_2 \\ T_3 \\ T_4 \\ T_5 \\ T_6 \end{bmatrix} + \begin{bmatrix} \epsilon_{11} & \epsilon_{12} & \epsilon_{13} \\ \epsilon_{21} & \epsilon_{22} & \epsilon_{23} \\ \epsilon_{31} & \epsilon_{32} & \epsilon_{33} \end{bmatrix} \begin{bmatrix} E_1 \\ E_2 \\ E_3 \end{bmatrix} \quad (6)$$

As shown on equation (5) and (6), the elastic compliance matrix (s), the piezoelectric strain coefficient (d), and the dielectric permittivity ( $\epsilon$ ) have a different value depending on the crystal structure or symmetry of material. For example, in the equation (7), (8) and (9) it indicates respectively the elastic stiffness constant (c) to tetragonal, rhombohedral, and orthorhombic symmetry. The inverse matrix of the elastic compliance matrix (s) is the elastic stiffness constant (c).

$$\begin{bmatrix} c_{11} & c_{12} & c_{13} & 0 & 0 & 0 \\ c_{12} & c_{11} & c_{13} & 0 & 0 & 0 \\ c_{13} & c_{13} & c_{33} & 0 & 0 & 0 \\ 0 & 0 & 0 & c_{44} & 0 & 0 \\ 0 & 0 & 0 & 0 & c_{44} & 0 \\ 0 & 0 & 0 & 0 & 0 & c_{66} \end{bmatrix} \quad (7)$$

$$\begin{bmatrix} c_{11} & c_{12} & c_{13} & c_{14} & 0 & 0 \\ c_{12} & c_{11} & c_{13} & -c_{14} & 0 & 0 \\ c_{13} & c_{13} & c_{33} & 0 & 0 & 0 \\ c_{14} & -c_{14} & 0 & c_{44} & 0 & 0 \\ 0 & 0 & 0 & 0 & c_{44} & c_{14} \\ 0 & 0 & 0 & 0 & c_{14} & (c_{11} - c_{12}) / 2 \end{bmatrix} \quad (8)$$

$$\begin{bmatrix} c_{11} & c_{12} & c_{13} & 0 & 0 & 0 \\ c_{12} & c_{22} & c_{23} & 0 & 0 & 0 \\ c_{13} & c_{23} & c_{33} & 0 & 0 & 0 \\ 0 & 0 & 0 & c_{44} & 0 & 0 \\ 0 & 0 & 0 & 0 & c_{55} & 0 \\ 0 & 0 & 0 & 0 & 0 & c_{66} \end{bmatrix} \quad (9)$$

Most materials that has good piezoelectric properties in room temperature like BaTiO<sub>3</sub> and PbTiO<sub>3</sub> have a tetragonal symmetry of space group P4mm, however, Pb(Zr,Ti)O<sub>3</sub>-based



material mainly used in commercial products uses a morphotropic phase boundary composition where a tetragonal phase and a rhombohedral phase coexist. Another piezoelectric materials such as  $\text{NaNbO}_3$ ,  $\text{KNbO}_3$ ,  $\text{PbZrO}_3$ , and etc. show orthorhombic symmetry at room temperature. Therefore, to make an accurate simulation for devices using piezoelectric material, exact information on the space group of the crystal structure and the elastic stiffness constant or the elastic compliance constant is necessary.

### 3. Modelling

The resonant frequency of the ceramic resonator is directly influenced by the vibration mode in accordance with the configuration of ceramic. According to the trend of the recent electronic parts, the utilized-oscillation frequency of resonator is getting to a high frequency. The ceramic resonator which is mainly used in the MHz band mostly uses thickness shear vibration or thickness trapped vibration. Thickness shear vibration is used in the frequency range of 2 MHz ~ 8 MHz and the above frequency range uses thickness trapped vibration. The 2<sup>nd</sup> or 3<sup>rd</sup> overtone vibration is mostly used in the case of thickness trapped vibration rather than the 1<sup>st</sup> fundamental vibration. In the Fig. 2, it shows configuration, vibration direction and dipole array direction of the thickness shear vibration and thickness trapped vibration.

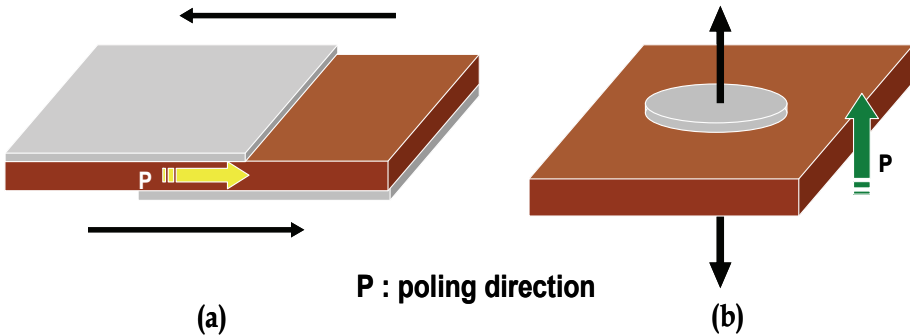


Figure 2. Configuration and vibration direction of thickness shear vibration and thickness trapped vibration (a) thickness shear mode; (b) thickness trapped mode

Commercial ceramic resonators over 8MHz have used mainly  $(\text{Pb},\text{La})\text{TiO}_3$ (PLT). However, manufacturers have been trying to apply layer structure compounds to resonator, these products are distributed to market recently.

The lattice of  $\text{PbTiO}_3$  exhibits a strong tetragonal distortion at 20°C. The lattice constant of a-axis ( $a$ ) increases smoothly as a result of heating, while the lattice of c-axis ( $c$ ) and  $c/a$  decrease. At 490-500°C the lattice constants  $c$  and  $a$  change sharply and the lattice becomes cubic.

PLT has a perovskite structure which the part of Pb is substituted by La and it shows a similar behavior to  $\text{PbTiO}_3$ . Layer-structure compounds such as  $\text{SrBi}_2\text{Nb}_2\text{O}_9$  are good alternatives to PLT. Its great anisotropy is one of the characteristics and over 60 kinds of compounds have been reported so far. Newnham et al. reported that the spontaneous polarization of layer structure compound is almost parallel in the plane of a, b axis and located 2-dimensionally. Because these materials specifically have great anisotropy and their

poisson's ratio is less than 0.25, they show different characteristics of frequency dependence from the material based on  $\text{Pb}(\text{Zr,Ti})\text{O}_3$ . As explained above, PLT has tetragonal structure with  $P4mm$  of space group at room temperature. The layer structure compounds have  $Fmm2$  of orthorhombic symmetry at room temperature, although it has tetragonal symmetry of  $I4/mmm$  below a curie temperature. Therefore, the elastic stiffness constant matrix of equation 7 and 8 should be used respectively. However, because a very complicated process is needed to find all constants, layer structure compounds are also assumed as a tetragonal symmetry to simplify the simulation. In this case, the piezoelectric strain coefficient is formed like following equation.

$$d = \begin{bmatrix} 0 & 0 & 0 & 0 & d_{15} & 0 \\ 0 & 0 & 0 & d_{15} & 0 & 0 \\ d_{13} & d_{13} & d_{33} & 0 & 0 & 0 \end{bmatrix} \quad (10)$$

The elastic compliance constants and the piezoelectric strain coefficients can be found referring IEEE standard or Japan's EMAS. And in case of that EMAS was referred, they can be found by measuring electric properties with a material sample manufactured like shown in table 3. The configuration, dimension, and the representative constants of the standard material found here is shown in table 3.

Although several kinds of software can be used in a simulation of ceramic resonator, we used COMSOL Multiphysics. COMSOL Multiphysics is a good interactive environment for modeling and solving scientific and engineering problems based on partial differential equations. Thanks to the built-in physics modes it is possible to build models by defining the relevant physical quantities – such as material properties, loads, and constraints – rather than by defining the equations.

Fig. 3 is the comparison of the simulation result of disk shape sample with the actually measured result, using COMSOL Multiphysics. In Fig. 3, (a) represents the dimension of disk sample and (b) represents measured frequency dependence of impedance. (c) represents the impedance waveform by simulation. It conformed to the measured result even though there was little shift of resonant frequency.

## 4. Resonator and Vibration Mode

### 4.1 Thickness shear vibration (TS mode vibration)

The thickness shear vibration occurs when poling direction and voltage direction are perpendicular. This vibration mode is mostly used in 2 ~ 8 MHz band because it is less influenced by a spurious vibration when used as a resonator. Boundary condition is set to make displacement to be 0 on both sides of resonator. Poling is along the length direction, while voltage was supplied on both top and bottom sides setting poling direction and voltage direction perpendicular to make the thickness shear mode occur. The structure of resonator using thickness shear mode is shown in Fig. 4. It is 2 mm long and 0.15 mm thick.

Fig. 5 and 6 show general deformed shape in thickness shear mode and displacement distribution within the material in the same condition. In case of thickness shear vibration, most displacements are concentrated in the part where the electrode is present, and the maximum displacement occurs at the end of the electrode.

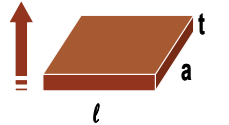
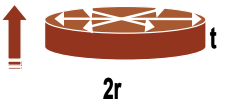
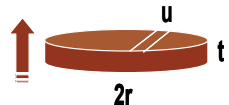
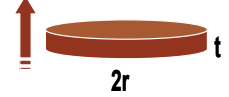
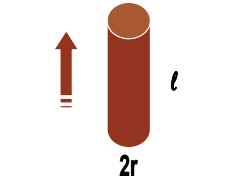

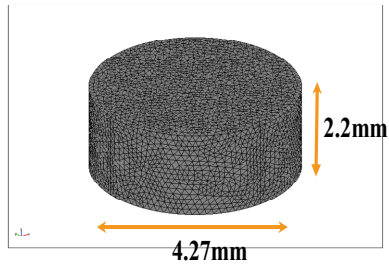
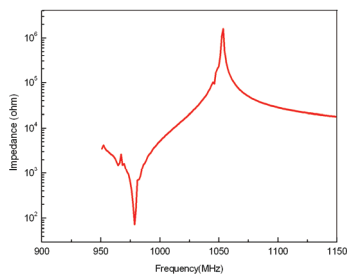
Vibrating mode		Dimension	Constant		Unit
lengthwise vibration		a = 3mm l = 12mm t = 1mm	$\epsilon_{33}^T$	155	-
			$s_{11}^E$	7.52	$10^{-12}$
radius vibration		r = 7.5mm t = 1mm	$d_{31}$	-4.38	$10^{-12}$
		r = 7.5mm t = 0.5mm u = 1mm	$s_{12}^E$	-1.51	$10^{-12}$
			$\sigma$	0.201	-
thickness vibration		r = 5mm t = 1mm	$s_{13}^E$	-1.08	$10^{-12}$
longitudinal vibration		r = 3mm l = 15mm	$s_{33}^E$	7.98	$10^{-12}$
			$d_{33}$	53	$10^{-12}$
thickness shear vibration		a = 2.5mm l = 10mm t = 0.25mm	$\epsilon_{11}^T$	220	-
			$s_{44}^E$	16.3	$10^{-12}$
			$d_{15}$	55	$10^{-12}$

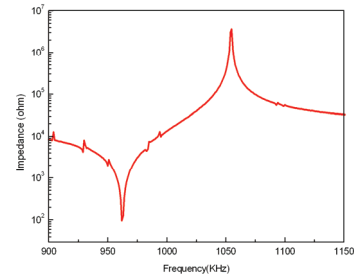
Table 1. Dimension of the sample recommended by EMAS and typical material properties of PLT



(a)

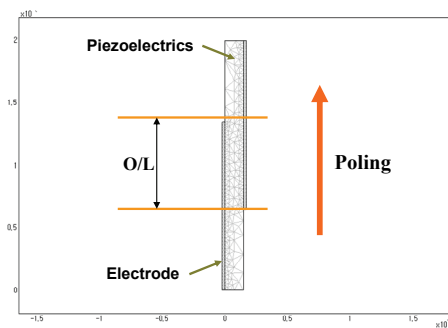


(b)

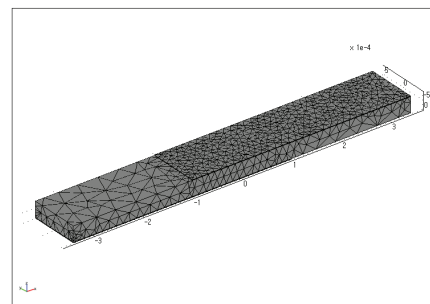


(c)

Figure 3. (a) Sample configuration; (b) Measured-impedance response; (c) Simulation result

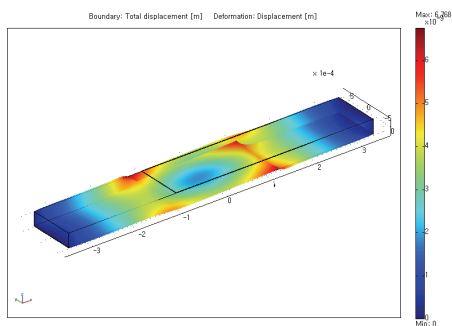


(a)

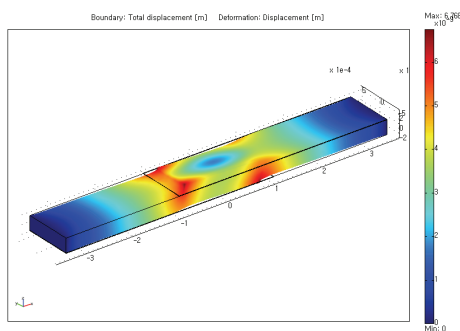


(b)

Figure 4. Simulation model for resonator using thickness shear vibration



(a)



(b)

Figure 5. Vibration configuration of thickness shear mode

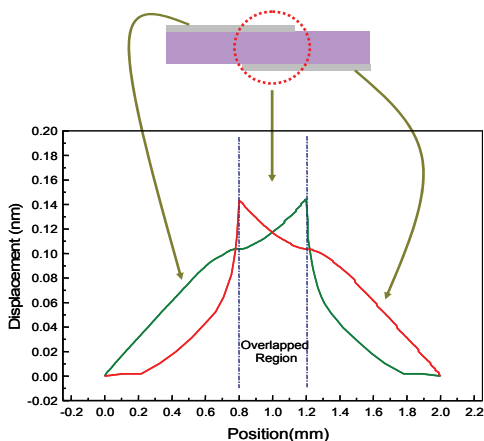


Figure 6. Displacement distribution in the thickness shear mode

The overlapped length (O/L) where top and bottom electrodes are overlapped has decisive effect on resonator property. Fig. 7 is showing frequency dependence of impedance according to the overlapping length (O/L). If O/L is small, the spurious vibration was is big

as the thickness shear vibration, and when  $O/L$  is not optimum, thickness shear vibration and other vibration is seen overlapped in the resonant frequency area.

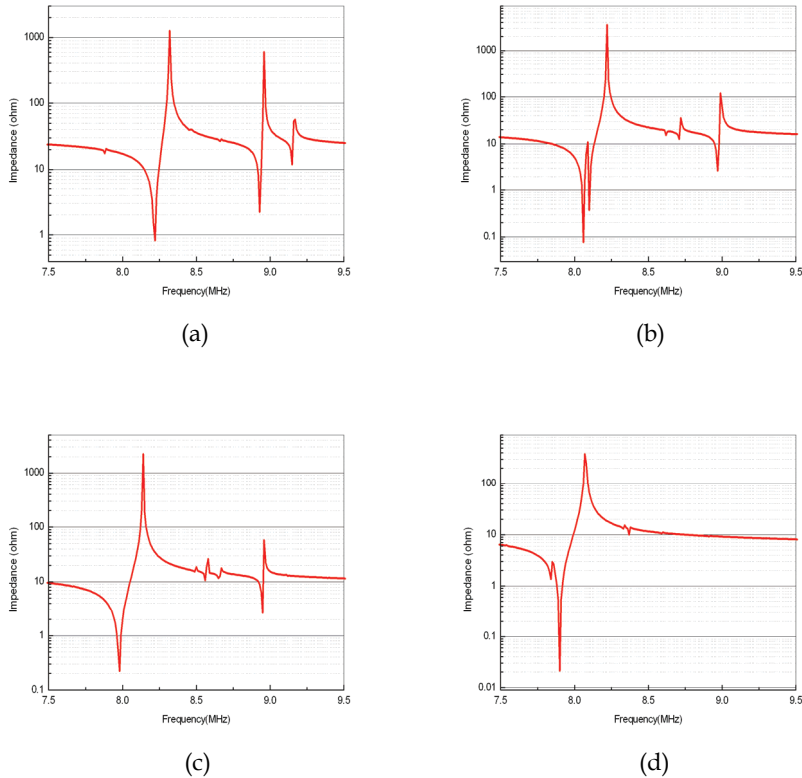


Figure 7. Frequency dependence of impedance (a)  $O/L = 0.2$  mm; (b)  $O/L = 0.4$  mm; (c)  $O/L = 0.6$  mm; (d)  $O/L = 0.8$  mm

#### 4.2.2 Thickness Extensional Vibration (TE2 mode vibration)

Recently the use of the TE2-mode vibration has been studied to minimize the resonator and elevate its functional features, in addition it was reported that the TE2-mode could promote the temperature feature and give a higher  $Q_m$ .

Fig. 8 shows the basic model for the simulation of TE2 mode and it is 1.5 mm wide, 0.5 mm long. The height was set based on 0.2 mm. Two sheets of ceramic were layered in TE2 resonator, the internal electrode is located between 2 sheets. Fixed point is set to make displacement 0 at the end of the resonator in length direction. Poling is in thickness direction. Round electrodes were attached to both top and bottom sides of resonator to supply the voltage here. Poling direction and voltage direction were set to be same in order to make the thickness extending mode occur. Generally, both sides of outside electrode are to be same pole, and the opposite pole is to be connected in the internal electrode to operate.

Fig. 8(c) shows poling direction and voltage direction. A vibration shape of TE2 mode occurring in this condition is shown in Fig. 9.

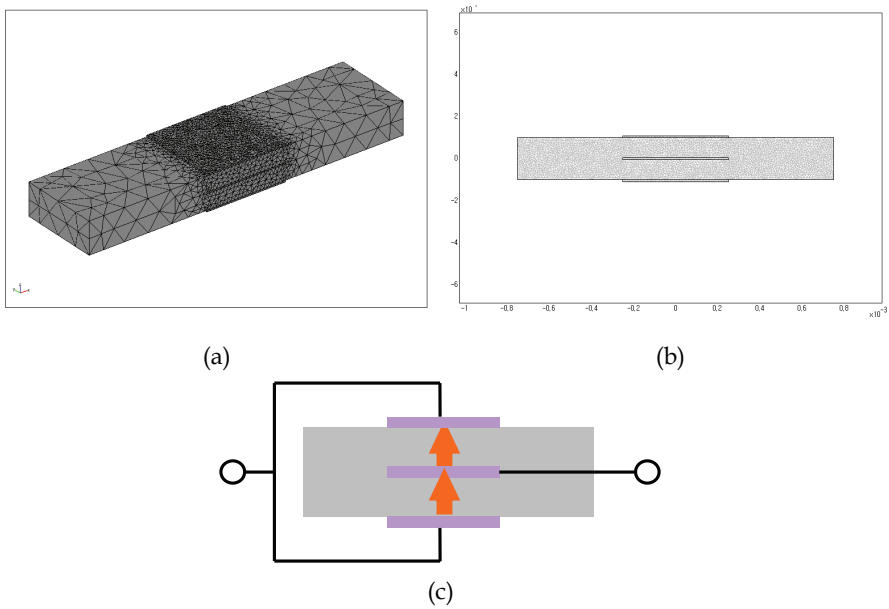


Figure 8. Simulation model for resonator using TE2 mode vibration

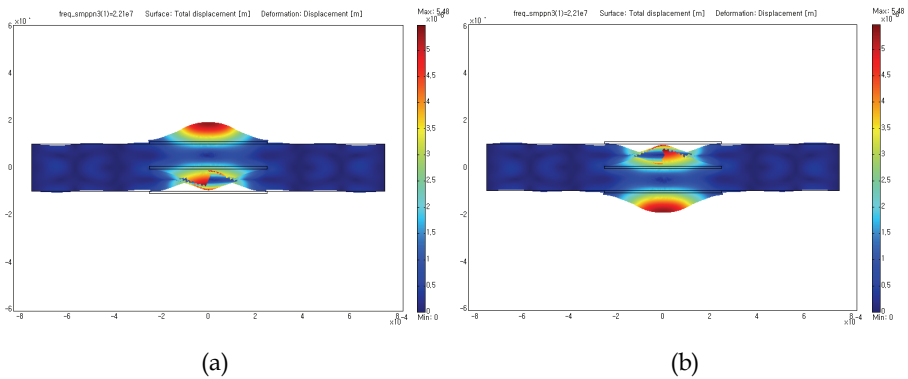


Figure 9. Vibration shape of TE2 mode vibration

In case of a resonator using TE2 mode, the electrode diameter has the most effect on impedance. The simulation result of the frequency dependence of displacement in piezoelectric ceramics with the electrode diameter is shown in Fig. 10. When electrode diameter becomes smaller, the amplitude of spurious vibration becomes very high to influence on TE2 mode vibration. On the other hand, when electrode diameter becomes larger, the resonant frequencies of TE2 mode vibration and a spurious vibration become closer. In case of that the electrode is 0.6 mm, it is expected that two vibrations become very

close to lead an interaction. Therefore, to keep main vibration out of the influence of spurious vibration, the optimum dimension of electrode should be formed.

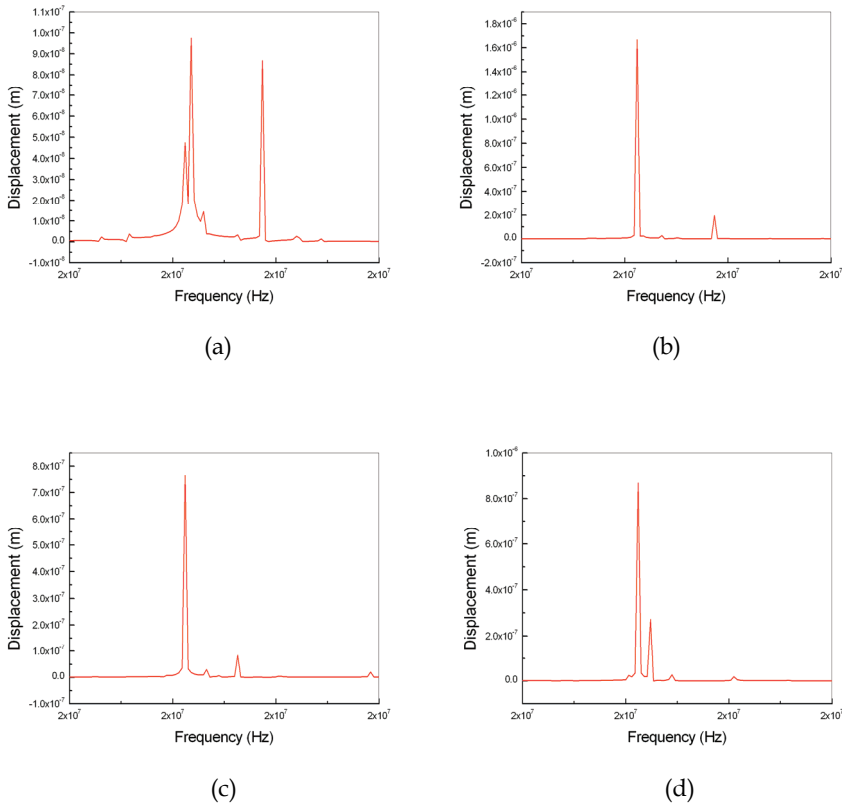


Figure 10. Frequency displacement of resonator using TE2 mode (a) electrode diameter = 0.3 mm; (b) electrode diameter = 0.4 mm; (c) electrode diameter = 0.5 mm; (d) electrode diameter = 0.6 mm

Fig. 11 shows the displacement distribution of the resonator when a TE2 mode vibration occurs. The rectangular part in this figure represents the area of the electrode. We can see that most displacements occurred concentratedly in the electrode.

#### 4.3.3 Thickness Extensional Vibration (TE3 mode vibration)

This is because ceramic resonators that exhibit the energy trapping phenomenon of the TE3 mode vibration have better temperature characteristics and higher  $Q_m$  than those of the fundamental thickness vibration. However, resonators that use the TE3 mode vibration exhibit spurious responses of the TE1 mode vibration, the 5th-harmonic thickness extensional vibration etc.



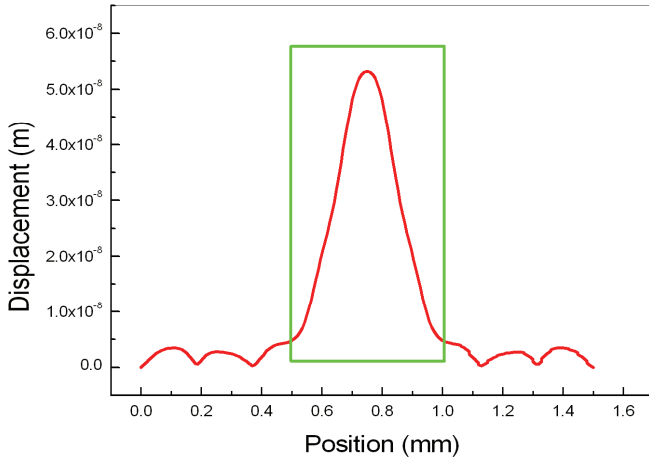
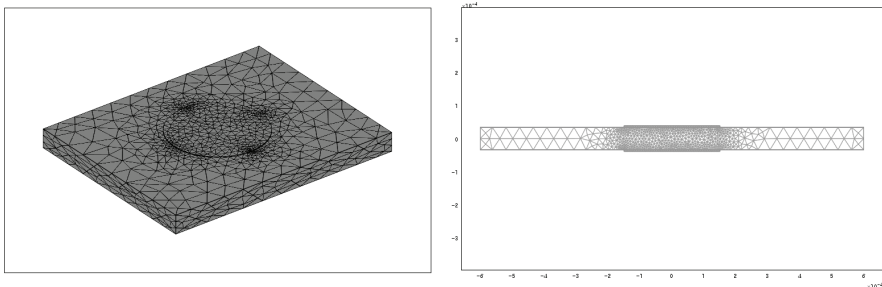


Figure 11. Distribution of inside displacement of resonator using TE2 mode vibration

There is the basic model of TE3 mode resonator in Fig. 12. It is 1.2 mm wide and 1.0 mm long. The height is set based on 0.068 mm. In case of the fixed point, boundary condition was set to have 0 displacement at the end of the resonator's 4 exterior faces. Poling is in thickness direction. Round electrodes were attached to both top and bottom sides of resonator to supply the voltage here. Poling direction and voltage direction were set to be same in order to make the TE3 mode vibration occur. Fig. 13 and Fig. 14 show typical deformation and the displacement distribution of deformation. As shown in the figure, it is expected that other spurious vibration can affect more likely, because the displacement occurs at the whole resonator.



(a)

(b)

Figure 12. Simulation model for resonator using TE3 mode vibration

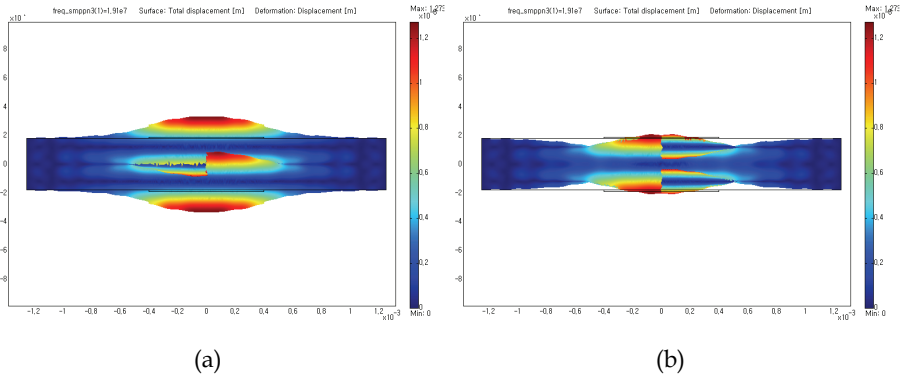


Figure 13. Vibration shape of TE3 mode vibration

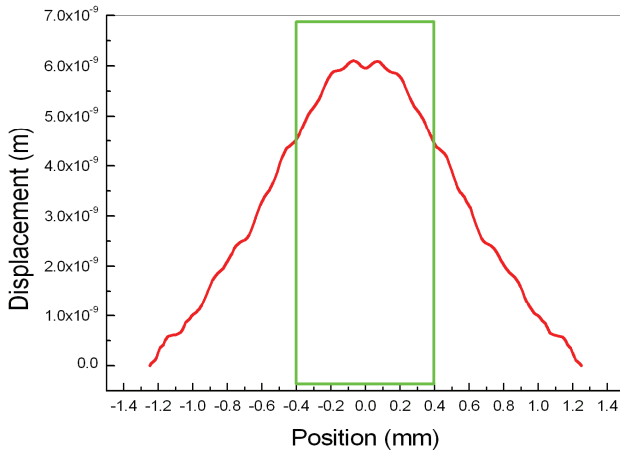


Figure 14. Distribution of inside displacement of resonator using TE3 mode vibration

TE3 mode resonator requires more precise control in manufacturing because it is more likely affected by spurious vibration compared to resonators using thickness shear vibration or TE2 vibration. The most influential variable on impedance waveform in TE3 mode resonator is of course the ratio of a electrode diameter and a resonator thickness. The influence of the ratio can be found by observing the influence of electrode diameter maintaining constant thickness of resonator. It is found that when electrode diameter becomes larger, the resonant frequency of a fundamental vibration and a spurious vibration become closer, and the amplitude of spurious vibration becomes also bigger. When the diameter of electrode is larger than 0.25 mm, the resonant frequency of spurious vibration and the anti-resonant frequency becomes very close to lead a break in the waveform of anti-resonant impedance of the fundamental vibration. Then anti-resonant impedance of the spurious vibration became higher than that of the fundamental vibration. On the other hand, when the diameter of electrode becomes less than 0.15, it was found that although the influence of the spurious

vibration occurring on high frequency becomes insignificant, other vibrations have influence near the resonant frequency. This reflects the possibility of the assumption that the spurious vibration of high frequency range moved close to the resonant frequency as the electrode diameter decreases, or the possibility of influence from other vibration. However, the certain cause has not been found yet. The thickness of the resonator is fixed to certain dimension corresponding to the frequency when the desired frequency is determined. Therefore, the optimal configuration can be designed by carefully controlling the ratio of the electrode diameter and the resonator thickness.

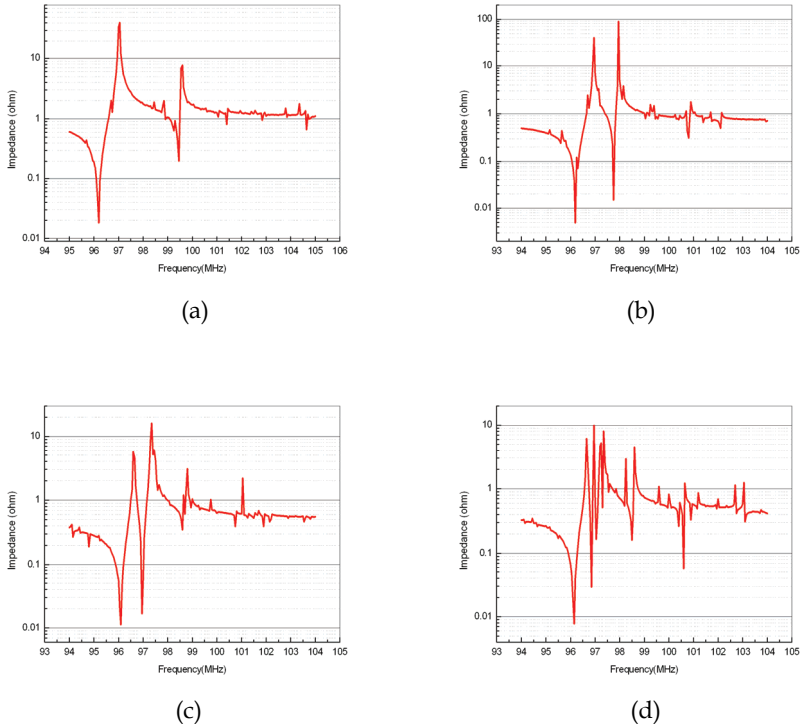


Figure 15. Impedance by the frequency of resonator using TE3 mode. (a) electrode diameter = 0.15 mm; (b) electrode diameter = 0.25 mm; (c) electrode diameter = 0.35 mm; (d) electrode diameter = 0.4 mm

In TE3 mode resonator, spurious vibration is always accompanied on slightly higher frequency along with the 3<sup>rd</sup> overtone vibration. Therefore, through the simulation study, we can find out the cause of spurious vibration and which variable affect on spurious vibration. Fig. 16 shows the form of the 3<sup>rd</sup> thickness vibration and of the following spurious vibration. Various examples of the influence of the strength and location of the spurious vibration on the impedance of 3<sup>rd</sup> vibration are shown. These are waveforms of impedance which is found in actual commercial products.

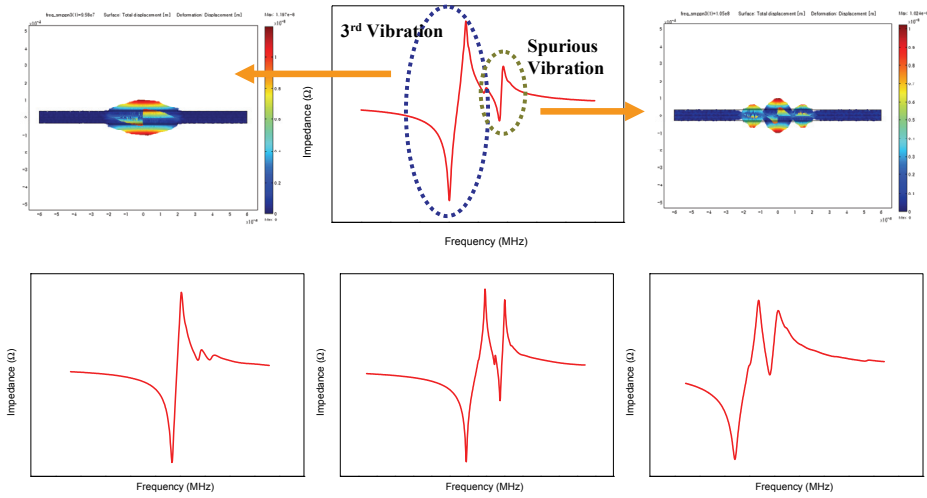


Figure 16. The effect of the interaction of TE3 mode vibration and spurious vibration on the impedance configuration

Therefore, the most important factor in designing a TE3 mode resonator shape is to make the spurious vibration, shown in the Fig. 16, occur as far as possible from the 3<sup>rd</sup> overtone vibration, or to design a shape that can minimize the amplitude.

Fig. 17(a) and (b) show the resonant frequency of the 3<sup>rd</sup> overtone vibration and the spurious vibration with the resonator thickness and the electrode diameter respectively. In case of the 3<sup>rd</sup> overtone vibration, the frequency constant was 1421, and the frequency constant of the spurious vibration was expected to be 1409. Also, we found out that while the resonant frequency of the 3<sup>rd</sup> vibration just slightly decreased as the diameter of electrode increased, the resonant frequency of the spurious vibration rapidly decreased. That is, we could expect that the 3<sup>rd</sup> vibration would be less influenced by the spurious vibration as the resonant frequency of the 3<sup>rd</sup> vibration and that of the spurious vibration become distant.

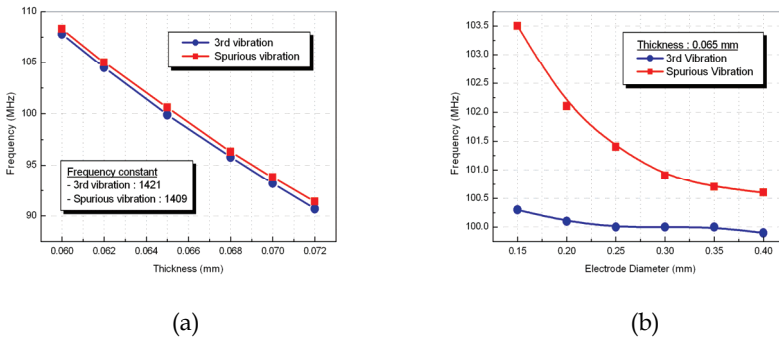


Figure 17. The effect of resonator thickness and electrode diameter on resonant frequency

## 5. Conclusion & Discussion

The ceramic manufacturing process is so complicated and process-dependent, that achieving reproducibility is very hard in many cases. Especially, ceramic resonator is smaller than other piezoelectric ceramics applications and more precise process control is needed. Therefore, understanding configuration design and tendency through simulation is very useful to avoid unnecessary effort. In recent trend, as piezoelectric ceramics is used in the various actuators and sensors, the use of simulation in this field is also increasing. Some of actuator, sensor or acoustic applications may have a complicated shape depending on the purposes, however, basic simulation process was regarded as same as resonator. Therefore, the accuracy of simulation depends on the accuracy of the knowledge on the material constants of piezoelectrics.

## 6. References

- A. Ando, T. Kittaka, T. Okada, Y. Sakabe and K. Wakino, Energy Trapping Characteristics of the Second Harmonic Thickness Extensional Vibration in a Two-Layered Monolithic Piezoelectric Plate, *Ferroelectrics*, Vol. 112, 1990, pp. 141-153.
- A. Ando, T. Sawada, H. Ogawa, M. Kimura and Y. Sakabe, Fine-Tolerance Resonator Application of Bismuth-Layer-Structured Ferroelectric Ceramics, *Jpn J. Appl. Phys.*, Vol. 41, (2002) 7057-7061.
- A. Ando, M. Kimura and Y. Kakabe, Piezoelectric Resonance Characteristics of  $\text{SrBi}_2\text{Nb}_2\text{O}_9$ -based Ceramics, *Jpn J. Appl. Phys.*, Vol. 42, (2003) 150-156.
- T. Azuma, J. Yamazaki, M. Inoue and K. Miyabe, Investigation of Spurious Mode in Piezoelectric Ceramic Resonators using Optical Fiber Interferometric Sensing, *Journal of the Korean Physical Society*, Vol. 32, February 1998, pp. S1294-S1297.
- S. E. Cummins and L. E. Cross, Electrical and Optical Properties of Ferroelectric  $\text{Bi}_4\text{Ti}_3\text{O}_{12}$  Single Crystals, *J. Appl. Phys.*, 39 (1968) 2268.
- H. Fan, L. Zhang, X. Yao, Relaxation Characteristics of Strontium Barium Niobate Ferroelectric Ceramics, *J. Mater. Sci.*, 33 (1998) 895-900.
- A. Fouskova and L. E. Cross, Dielectric Properties of Bismuth Titanate, *J. Appl. Phys.*, 41 (1970) 2834.
- C. Fujioka, R. Aoyagi, H. Takeda, S. Okamura and T. Shiosaki, Effect of non-stoichiometry on ferroelectricity and piezoelectricity in strontium bismuth tantalite ceramics, *Journal of the European Ceramic Society*, 25 (2005) 2723-2726.
- C. Galassi. (2000), *Piezoelectric Materials: Advances in Science, Technology and Applications*, pp. 14-17, Kluwer Academic Publishers, 0-7923-6212-8, Dordrecht.
- H. Kaida and J. Inoue, Strip-Type Resonators Using-Second-Harmonic Thickness-Extensional Vibration, *Jpn. J. Appl. Phys.*, Vol. 40, 2001, pp. 3680-3682.
- D. J. Kim, J. H. Lee and D. K. Kim. (2001). *An Introduction to the Mechanical Properties of Ceramics*, pp.48-49, Scitechmedia, Inc., 89-88397-78-9, Seoul. (Korean)
- M. Kimura, T. Sawada, A. Ando and U. Sakabe, Energy Trapping Characteristics of Bismuth Layer Structured Compound  $\text{CaBi}_4\text{Ti}_4\text{O}_{15}$ , *Jpn J. Appl. Phys.*, Vol. 38, (1999) 5557-5560.
- C. K. Lee, J. K. Moon and S. D. Lee, Dielectric Properties of ferroelectric  $\text{Sr}_{0.5}\text{Ba}_{0.5}\text{Nb}_2\text{O}_6$  cermaics, *J. Basic Sciences*, Vol.17 (2003) 45-52.

- D. J. Leo. (2007), *Smart Material Systems*, pp.122, John Wiley & Sons, Inc., 978-0-471-68477-0, Hoboken, New Jersey.
- T. Mitsui and S. Nomura. (1981). *Ferroelectrics and Related Substances*, Springer-Verlag, 0-387-09880-1, Berlin-Heidelberg.
- R. R. Neurgaonkar, W. F. Hall, J. R. Oliver, W. W. Ho and W. K. Copy, Tungsten Bronze  $Sr_{1-x}Ba_xNb_2O_6$  – A Case History of Versatility, *Ferroelectrics*, Vol. 87, 1988, pp. 167-179.
- R. E. Newnham, R. W. Wolfe and J. F. Drrian, Structural Basis of Ferroelectricity in the Bismuth Titanate Family, *Mater. Res. Bull.*, 6, 1029 (1971).
- H. Ogawa, M. Kimura, A. Ando and Y. Sakabe, Temperature Dependence of Piezoelectric Properties of Grain-Oriented  $CaBi_4Ti_4O_{15}$  Ceramics, *Jpn J. Appl. Phys.*, Vol. 40, (2001) 5715-5718.
- G. A. Smolenskii, V. A. Bokov, V. A. Isupov, N. N. Krainik, R. E. Pasynkov, and A. I. Sokolov. (1984). *Ferroelectrics and Related Materials*, Gordon and Breach Science Publishers, 2-88124-107-7, New York.
- M. G. Stachiotti, C. O. Rodriguez, C. Ambrosch-Draxl and N. E. Christensen, Electronic structure and ferroelectricity in  $SrBi_2Ta_2O_9$ , *Phys. Rev. B*, 61 (2000) 14434-14439.
- E. C. Subbarao, A Family of Ferroelectric Bismuth Compounds, *J. Phys. Chem. Solid*, Vol. 23, (1962) 655.
- Y. Yamashita, S. Sakano, and Isamu Toba, TE Harmonic Overtone Mode Energy-Trapped Ceramic Filter with Narrow Frequency Tolerance, *Jpn J. Appl. Phys.*, Vol. 36, (1997) 6096-6102.

# Computation of the Complex Impedance of a Cylindrical Conductor in an Ideal Two-Probe Configuration

V. Siva Kumar G. Kelekanjeri and Rosario A. Gerhardt  
*Georgia Institute of Technology*  
USA

## 1. Introduction

Impedance spectroscopy is an alternating current technique that can be used to probe materials or devices at length scales ranging from the atomic to macroscopic dimensions. Since its first application to solid state materials (Bauerle 1969), it has been used to characterize the electrical response of ionic electrolytes, ferroelectrics, intrinsic conducting polymers, ceramic and polymer matrix composites and biomaterials to name a few (Gerhardt 2005). The technique is based on probing the sample using an ac signal over a wide range of frequencies and studying the polarization phenomena associated with the electrical response. It is ideally suited for studying specimens where there is good electrical contrast at interfaces, either because of different constituent materials or because of space charge formation or dissipation. Impedance spectroscopy has recently been applied to nickel-base superalloys (Zou, Makram et al. 2002; Kelekanjeri<sup>a</sup> and Gerhardt 2006). These metallic alloys contain heterogeneities ranging in size from nanometers to micrometers and the measured impedance response shows interesting dependencies. As a first approximation, for the computations presented in this chapter, the heterogeneous material medium is regarded as a continuum with a uniform conductivity on a macro scale. This treatment is justified because the size of the microstructural heterogeneities is extremely small in relation to the measurement contact area. The problem dealt with here pertains to the specific case wherein circular electrodes are placed on opposite sides of a cylindrical specimen.

There are a few cases in the literature, where closed-form solutions in the frequency domain are available for problems similar to the current one. For example, Ney (Costache and Ney 1988; Ney 1991) derived a closed-form solution for the electric field distribution in a solid non-perfectly conducting flat ground plane as a result of electromagnetic interference. The derivation accounted for constriction effect as a result of confinement of current lines near the contact points and skin-effect due to finite conductivity of the ground plane. Bowler (Bowler<sup>a</sup> 2004) presented closed-form analytical expressions for the electric field distribution in a conducting half-space region due to alternating current injected at the surface. The analytical formulation was conducted in terms of a single, transverse magnetic potential in cylindrical coordinates and the solution was obtained by the use of the Hankel transform. In another publication, Bowler presented closed-form analytical expressions for the electric

field inside and outside a metal plate due to alternating current injected at the surface (Bowler<sup>b</sup> 2004). Current was injected and extracted via two separate wires, which were oriented normal to the surface of the plate. The problem was treated in two separate cylindrical co-ordinate systems where each wire was considered as the symmetry axis for the respective system (Bowler<sup>b</sup> 2004).

The derivation presented here addresses the specific problem of obtaining the electric field distribution inside a cylindrical metallic specimen due to current injection and extraction via oppositely placed electrode contacts (Kelekanjeri and Gerhardt 2007). Therefore, the problem while similar to the literature references cited above, corresponds to a distinctly different situation. This chapter also contains a description of the analytical treatment needed for computing the complex impedance response under the same conditions. All formulations are supported by independent finite-element (FE) validation using FEMLAB 3.1 (now COMSOL Multiphysics).

## 2. Problem description

A two-probe impedance measurement relies on the application of an ac signal across a specimen placed in between the source and the sink electrodes. The problem dealt with here considers the case where the electrodes are placed on the circular faces of the specimen and share the same axis of symmetry (see Fig. 1(a)). The measurement in essence can be treated as current injection into the specimen at the source electrode and current extraction at the sink electrode. In the actual measurement; however, the current is measured upon the application of a voltage.

An analytical formulation of this problem is developed by using Maxwell's equations for conductors (Hallen 1962; Cottingham and Greenwood 1991) and closed form analytical expressions for the resultant electric field distribution are derived in terms of Bessel series (www.mathworld.com; Gray and Mathews 1952; Abramowitz and Stegun 1964; Kreyszig 1994; Weber and Arfken 2004). The electric field distributions are then converted to the relevant impedance parameters. Additionally, finite element solutions for the electric field distributions and the impedance parameters are also presented in order to validate the derived analytical solutions. The Electromagnetics Module of FEMLAB package (COMSOL AB<sup>a</sup> 2004) is used to layout the finite element model. The finite element problem is formulated as a time-harmonic quasistatic application in the Meridional Currents/Potentials mode in terms of magnetic and electric potentials. The electric fields are ultimately obtained in terms of derivatives of magnetic and electric potentials. The solution obtained for the fields is subsequently used in computing an impedance spectrum of the specimen for the prescribed measurement configuration.

More specifically, the problem can be treated as the injection of an alternating current  $I_0 \exp(-j\omega t)$  of angular frequency  $\omega$  into a cylindrical metallic disk specimen, via a source electrode and extraction by means of a sink electrode (Kelekanjeri and Gerhardt 2007). The electrodes are modeled as perfect infinitesimally thick contacts of radius  $r_c$  contacting the specimen of radius  $r_o$  ( $r_o \gg r_c$ ) and thickness  $t_o$  ( $t_o < r_o$ ) as shown in Fig. 1(a). The contact electrodes and the specimen are both axi-symmetric. The injected current at the source electrode, is assumed to be along the  $z$  direction. Due to a discrepancy between the size of the electrode contact and the specimen radius, there will be radial spreading of current flow lines within the specimen as shown in Fig. 1(b). This phenomenon, referred to as striction



effect or constriction (Costache and Ney 1988; Ney 1991), is where convergence or divergence of current flow lines occurs. A second effect is that of current flow confined to the surface of a conductor at high frequencies, an effect generally known as the skin-effect (Casimir and Ubbink 1967; Giacoletto 1996). As a consequence of the above two electrodynamic effects, there will be electric fields along both axial ( $z$ ) and radial ( $r$ ) directions ( $E_z$  and  $E_r$ ) within the specimen, but, there will be no electric field in the tangential ( $\phi$ ) direction. The modeling measurement configuration ( $r$ - $z$  plane), illustrating the skin and the constriction effects, is shown in Fig. 1(b). Since symmetry also exists about the  $z$  axis, the modeling space can further be condensed to one half of the  $r$ - $z$  plane from  $r=0$  to  $r=r_o$ .

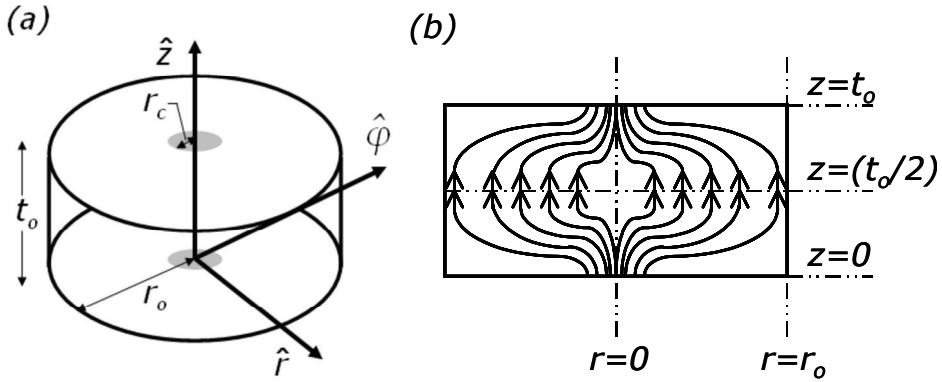


Figure 1. (a) Schematic illustrating the measurement geometry comprising of the specimen with coaxially placed electrodes (shown in gray shade) in a cylindrical co-ordinate system. The illustration in (b) shows the current flow contour incorporating both skin and constriction effects inside the specimen ( $r$ - $z$  cross-section). The extent of radial spreading is enhanced with increasing frequency.

### 3. Analytical approach

#### 3.1 Formulation and generic solution

The analytical solution for the electric field distribution (of angular frequency  $\omega$ ) inside the specimen (of uniform conductivity- $\sigma$  and magnetic permeability- $\mu$ ) is obtained by solving the following second order partial differential equation (PDE) (Ney 1991; Giacoletto 1996):

$$\nabla^2 \bar{E} = \mu\sigma \left( \frac{\partial \bar{E}}{\partial t} \right) = j\omega\mu\sigma \bar{E} \quad (1)$$

Two independent partial differential equations in  $E_z$  and  $E_r$  may be written upon expanding the vector Laplacian (www.mathworld.com) using cylindrical co-ordinates as follows:

$$\frac{\partial^2 E_r}{\partial r^2} + \frac{\partial^2 E_r}{\partial z^2} + \frac{1}{r} \frac{\partial E_r}{\partial r} - \frac{E_r}{r^2} = j\omega\mu\sigma E_r \quad (2)$$

$$\frac{\partial^2 E_z}{\partial r^2} + \frac{\partial^2 E_z}{\partial z^2} + \frac{1}{r} \frac{\partial E_z}{\partial r} = j\omega\mu\sigma E_z \quad (3)$$

The general solutions for  $E_r(r, z)$  and  $E_z(r, z)$  for above PDE's may be expressed as follows:

$$E_r(r, z) = (C'_5 e^{-\xi_1 z} + C'_6 e^{\xi_1 z}) J_1(\lambda_1 r) \quad (4)$$

$$E_z(r, z) = (C'_7 e^{-\xi_2 z} + C'_8 e^{\xi_2 z}) J_0(\lambda_2 r) \quad (5)$$

where  $C'_l$  ( $l = 5, 6, 7$  and  $8$ ) are the modified coefficients resulting from grouping the radial and axial solutions together.

### 3.2 Boundary conditions

The electric field distribution within the specimen is determined completely upon knowledge of the constants in the electric field expressions in equations (4) and (5). Examining the boundary conditions governing the two-probe impedance measurement problem is necessary to obtain the constants (Kelekanjeri and Gerhardt 2007):

a. Source and sink conditions:

$$(E_z)_{z=0, t_0} = \frac{I_0}{\pi r_c^2 \sigma} \quad (0 \leq r \leq r_c) \quad (6)$$

$$= 0 \quad (r_c < r \leq r_o)$$

$$\left( \frac{\partial E_z}{\partial r} \right)_{z=0, t_0} = -\frac{I_0}{\pi r_c^2 \sigma} \delta(r_c - r) \quad (7)$$

b. Limiting normal current on curved boundary:

$$(E_r)_{r=r_o} = 0, \quad \forall z \quad (8)$$

c. Conservation of current ( $I_0$ ) via Ampere's law (Hallen 1962; Cottingham and Greenwood 1991):

$$\oint_c H_\varphi(r)_{r=r_o} r_o d\varphi = I_0 \quad (9)$$

where  $H_\varphi$  is the magnetic field in the azimuthal ( $\varphi$ ) direction, expressed in terms of the electric field components ( $E_r$  and  $E_z$ ) as follows: (Hallen 1962; Cottingham and Greenwood 1991; Kelekanjeri and Gerhardt 2007):

$$H_\varphi(r, z) = \frac{1}{j\omega\mu} \left( \frac{\partial E_z}{\partial r} - \frac{\partial E_r}{\partial z} \right) \quad (10)$$

### 3.3 Determination of unique solution for electric field distribution

Applying the limiting current boundary condition imposed on  $E_r(r, z)$ , listed in equation (8), we obtain  $J_1(\lambda_1 r)|_{r=r_0} = 0$  for a non-trivial solution. This equation has infinite roots (Kreyszig 1994; Weber and Arfken 2004), given by-  $\lambda_{1i} = \frac{\beta_{1i}}{r_0}$  ( $i = 1, 2, 3, \dots$ ), where  $\beta_{1i}$  is a root of  $J_1(x)$ . Therefore, using the principle of superposition  $E_r(r, z)$  may be rewritten as:

$$E_r(r, z) = \sum_m \left( C'_{5m} e^{-\xi_{1m} z} + C'_{6m} e^{\xi_{1m} z} \right) J_1(\lambda_{1m} r) \quad (11)$$

Next, the total current condition given by Ampere's law in equation (9) yields:

$$2\pi r_0 H_\phi(r, z)|_{r=r_0} = I_0 \quad (12)$$

Substituting for  $H_\phi(r, z)$  from equation (10), we have:

$$\left( \frac{\partial E_z}{\partial r} \right)_{(r_0, z)} = \frac{j\omega\mu}{2\pi r_0} I_0 \quad (13)$$

Since, the right hand side (RHS) term in the above equation is a constant,  $E_z(r, z)$  must contain at least one term that is just a function of  $r$  and independent of  $z$ . Therefore, the expression for  $E_z(r, z)$  may be modified as:

$$E_z(r, z) = f(r) + \left( C'_7 e^{-\xi_2 z} + C'_8 e^{\xi_2 z} \right) J_0(\lambda_2 r) \quad (14)$$

Substituting this new expression for  $E_z(r, z)$  in equation (13), it is seen that only  $f(r)$  contributes to total current and therefore  $\left( \frac{\partial J_0(\lambda_2 r)}{\partial r} \right) = 0$ . A non-trivial solution to this

condition (see Appendix) is given by  $\lambda_{2m} = \frac{\beta_{1m}}{r_0}$  ( $m = 1, 2, 3, \dots$ ), where  $\beta_{1m}$  is a root of  $J_1(x)$ .

Thus the set of  $\lambda_i$ 's and  $\xi_i$ 's in the electric field expressions for  $E_r(r, z)$  and  $E_z(r, z)$  are determined as  $\lambda_{1m} = \lambda_{2m} = \frac{\beta_{1m}}{r_0}$  and  $\xi_{1m}^2 = \xi_{2m}^2 = \gamma^2 + \lambda_{1m}^2$ . Applying the principle of superposition, the expression for  $E_z(r, z)$  becomes:

$$E_z(r, z) = f(r) + \sum_m \left( C'_{7m} e^{-\xi_{1m} z} + C'_{8m} e^{\xi_{1m} z} \right) J_0(\lambda_{1m} r) \quad (15)$$

#### 3.3.1 Problem symmetry

The pre-exponential coefficients -  $C'_i$ 's that are left to be determined for a unique solution of the electric fields-  $E_r(r, z)$  and  $E_z(r, z)$  may be reduced in number by exploiting the symmetry of the problem. As mentioned previously, the problem geometry is both rotationally symmetric and axi-symmetric (about  $z$  axis). In addition, there is symmetry

about  $z = \left(\frac{t_0}{2}\right)$  because the source and sink electrodes are placed on opposite circular faces of the specimen and centered about the  $z$  axis. A schematic illustrating the symmetric current flow contour incorporating constriction and skin effects is shown in Fig. 1(b). It is evident from the illustration that  $E_z(r, z)$  is symmetric about  $z = \left(\frac{t_0}{2}\right)$ , whereas,  $E_r(r, z)$  is anti-symmetric. Thus, we can write the following conditions:

$$E_r(r, z) = -E_r(r, t_0 - z) \quad (16)$$

$$E_z(r, z) = E_z(r, t_0 - z) \quad (17)$$

Using these conditions, the electric field expressions  $E_r(r, z)$  and  $E_z(r, z)$  may be modified by eliminating the constants-  $C'_{6m}$  and  $C'_{8m}$  as follows:

$$E_r(r, z) = \sum_m C'_{5m} \left( e^{-\xi_{1m}z} - e^{-\xi_{1m}(t_0-z)} \right) J_1(\lambda_{1m}r) \quad (18)$$

$$E_z(r, z) = f(r) + \sum_m C'_{7m} \left( e^{-\xi_{1m}z} + e^{-\xi_{1m}(t_0-z)} \right) J_0(\lambda_{1m}r) \quad (19)$$

### 3.3.2 Validation of 1-D skin-effect solution for $f(r)$

Consider the case of alternating current ( $I_0 \exp(-j\omega t)$ ) flow through an infinitely long thin cylindrical wire along the  $z$  direction. In this case, the electric field distribution is governed only by skin-effect, which is given as (Giacoletto 1996):

$$E_z(r) = a J_0(\kappa r) \quad (20)$$

where  $a = \frac{\kappa I_0}{2\pi\sigma r_0 J_1(\kappa r_0)}$  and  $\kappa^2 = -j\omega\mu\sigma = -\gamma^2$ .

Let us assume this solution for  $f(r)$  in the expression for  $E_z(r, z)$  in equation (19). This assumption will be justified in the following by testing for the total current condition listed in equation (13). By virtue of this assumption, the expression for  $E_z(r, z)$  now becomes:

$$E_z(r, z) = a J_0(\kappa r) + \sum_m C'_{7m} \left( e^{-\xi_{1m}z} + e^{-\xi_{1m}(t_0-z)} \right) J_0(\lambda_{1m}r) \quad (21)$$

Substituting this expression for  $E_z(r, z)$  in equation (13) (see Appendix for derivative of  $J_0(x)$ ),

$$\left( \frac{\partial E_z}{\partial r} \right)_{(r_0, z)} = -\kappa a J_1(\kappa r_0) + \sum_m C'_{7m} \left( e^{-\xi_{1m}z} + e^{-\xi_{1m}(t_0-z)} \right) \left( -\lambda_{1m} J_1(\lambda_{1m} r_0) \right) = \frac{-\kappa^2 I_0}{2\pi\sigma r_0} = \frac{j\omega\mu}{2\pi r_0} I_0 \quad (22)$$

The summation term vanishes as  $J_1(\lambda_{1m} r_0) = J_1(\beta_{1m}) = 0$ . The result is identical to the RHS of equation (13). Therefore, the starting assumption for  $f(r)$  is justified and the modified solution for  $E_z(r, z)$  given in equation (21) stands correct. The first term in the expression

for  $E_z(r, z)$  accounts for the skin-effect and the summation signifies the contribution from current constriction at the contacts.

The pre-exponential coefficient  $C'_{7m}$  may be determined by evaluating the integral

$\int_0^{r_0} \left( \frac{\partial E_z}{\partial r} \right)_{z=0} J_1(\lambda_{1p} r) r dr$  using the source condition (equation (7)) and alternately using the

expression for  $E_z(r, z)$  in equation (21). The final answer is listed below:

$$C'_{7m} = \frac{\left\{ \frac{I_0 J_1(\lambda_{1p} r_c)}{\pi r_c \sigma} \right\} - \left\{ \frac{\kappa a r_0}{(\kappa^2 - \lambda_{1p}^2)} \left[ \kappa J_2(\kappa r_0) J_1(\lambda_{1p} r_0) - \lambda_{1p} J_1(\kappa r_0) J_2(\lambda_{1p} r_0) \right] \right\}}{\left\{ \frac{\lambda_{1p} r_0^2 [J_2(\beta_{1p})]^2 (1 + e^{-\xi_{1p} t_0})}{2} \right\}} \quad (23)$$

The second coefficient  $C'_{5m}$  appearing in the expression for  $E_r(r, z)$  may be determined by making use of Faraday's law (Cottingham and Greenwood 1991) as follows:

$$\nabla \times \bar{H} = \sigma \bar{E} \Rightarrow - \left( \frac{\partial H_\phi}{\partial z} \right) \hat{r} + \left( \frac{\partial H_\phi}{\partial r} \right) \hat{z} = \sigma E_r \hat{r} + \sigma E_z \hat{z} \quad (24)$$

By substituting for  $H_\phi$  from equation (10) and then comparing the  $r$  component on both sides of the equation, we have:

$$\left( \frac{\partial^2 E_z}{\partial z \partial r} - \frac{\partial^2 E_r}{\partial z^2} \right) = -j\omega\mu\sigma E_r \quad (25)$$

The coefficient  $C'_{5m}$  may be solved for by substituting the expressions for  $E_r(r, z)$  and  $E_z(r, z)$  in the above equation. The final answer is given as follows:

$$C'_{5m} = \frac{C'_{7m} \lambda_{1m} \xi_{1m}}{\xi_{1m}^2 - j\omega\mu\sigma} \quad (26)$$

This completes the determination of the electric field distribution (described by equations (18) and (21)) inside a cylindrical disk shaped conductor for a two-probe impedance measurement.

### 3.3.3 Semi-infinite solution

Consider the case when the cylinder is infinitely long in the thickness ( $z$ ) direction. The electric field distribution in this case can be obtained as a corollary to the derivation presented thus far. All the boundary conditions listed earlier are equally valid here. Therefore, the approach for obtaining the final solution is similar to the one presented for the disk problem. However, the only major difference between the solutions is that, terms involving  $e^{+\xi_i z}$  are excluded from  $z$ -solutions for the present case. This essentially means

that the probability of a wave rebounding from the opposite boundary is negligible, which is a good approximation for large values of  $t_0$ .

The expressions for the axial and radial electric fields can then be written as follows (Kelekanjeri and Gerhardt 2007):

$$E_r(r, z) = \sum_m C'_{8m} e^{-\xi_{1m} z} J_1(\lambda_{1m} r) \quad (27)$$

$$E_z(r, z) = a J_0(\kappa r) + \sum_m C'_{9m} e^{-\xi_{1m} z} J_0(\lambda_{1m} r) \quad (28)$$

The coefficients  $C'_{8m}$  and  $C'_{9m}$  may be solved for in a similar manner as shown for the disk solution. The above expressions are only valid from  $z = 0$  to  $\left(\frac{t_0}{2}\right)$ ; the solution for the other half of the cylinder is readily obtained by using the symmetry conditions listed in equations (16) and (17). Therefore, this problem will hereafter be referred to as the 'semi-infinite' case.

#### 4. Finite element approach

The closed-form analytical expressions for the electric field distribution presented in the previous section were validated independently using a finite element solution obtained using the Electromagnetics Module of FEMLAB package (COMSOL AB<sup>a</sup> 2004). Modeling was conducted in the Meridional Currents/Potentials mode, which ensured rotational symmetry as well as symmetry about the  $z$  axis. The latter enforces that the radial current density and the gradient in the axial current density are both zero on the  $z$  axis, i.e.

$$J_r|_{r=0} = 0 \text{ and } \left(\frac{\partial J_z}{\partial r}\right)|_{r=0} = 0 \text{ (COMSOL AB}^a \text{ 2004). The finite element model was formulated}$$

as a time-harmonic quasistatic problem in terms of magnetic ( $\bar{A}$ ) and electric ( $V$ ) potentials. The modeling geometry consists of one-half of  $r$ - $z$  cross-section of the specimen (boundary 1 shows axial symmetry), which has been divided into sub-domains I and II as shown in Fig. 2. Boundaries-2 and 3 correspond to the source and sink electrode contacts respectively, where a constant current density is specified. The electric and magnetic fields are forced to be continuous across the vertical boundary (boundary-4) at  $r = r_c$ . Electric and magnetic insulation is specified at boundaries-5, 6 and 7. A Direct UMFPACK linear stationary solver (COMSOL AB<sup>b</sup> 2004) was used for obtaining the solution of the dependent variables, viz. the vector magnetic potential ( $\bar{A}$ ) and the electric potential ( $V$ ), for the following PDE (COMSOL AB<sup>a</sup> 2004):

$$\left(j\omega\sigma - \omega^2 \epsilon_0 \epsilon_r\right) \bar{A} + \nabla \times \left(\frac{\nabla \times \bar{A}}{\mu_0 \mu_r}\right) - \sigma \nabla \times (\nabla \times \bar{A}) + (\sigma + j\omega \epsilon_0 \epsilon_r) \nabla V - \bar{J}^e = 0 \quad (29)$$

In the above equation,  $\epsilon_0$  and  $\epsilon_r$  refer to the absolute and relative permittivity and  $\mu_0$  and  $\mu_r$  refer to the absolute and relative magnetic permeability respectively. Subsequently, the electric and magnetic fields are obtained as:

$$\bar{E} = -\nabla V - \frac{\partial \bar{A}}{\partial t} \text{ and} \tag{30}$$

$$\bar{B} = \nabla \times \bar{A} \tag{31}$$

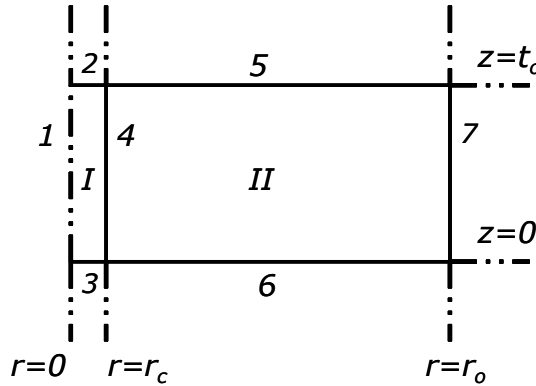


Figure 2. Illustration of the problem geometry ( $r$ - $z$  cross-section) detailing the various sub-domains and boundaries as modeled in FEMLAB. Sub-domains I and II are parts of the complete specimen and are differentiated in order to indicate the electrode contacts on boundaries ( $z=0$  and  $z=t_o$ ) of sub-domain I. Sub-domain boundaries are numbered using Arabic numerals

## 5. Simulation results and discussion

In the first part of this section, a comparison between the electric field profiles ( $E_z$  and  $E_r$ ) obtained via analytical and finite element simulations is presented. The two electrodynamic effects pertinent here, viz. the constriction and skin effects are discussed in detail based on the electric field profiles. Subsequently, the effects of varying one or more geometric parameters on the electric field profiles are studied systematically. Finally, the concept of a limiting thickness  $t_{o,lim}$  is discussed, which is useful in ascertaining the applicability of the disk and semi-infinite analytical solutions for a given geometric configuration.

### 5.1 Electric field profiles

The following set of material properties and geometric parameters is used for computing the electric field profiles:  $\sigma = 8.34 \times 10^5$  S/m,  $\mu_r = 1.004$ ,  $r_o = 5$ mm,  $r_c = 0.5$ mm and  $t_o = 2$ mm. An amplitude of  $I_o = 50$ mA is assumed for the alternating current. A total of 53288 elements and 3126 boundary elements corresponding to a simulation space of  $5 \times 2$ sq.mm were used for finite element simulations. Figure 3 shows a comparison between the analytical and FEMLAB solutions as cross-section plots of the axial ( $E_z$ ) and radial ( $E_r$ ) electric field profiles at  $z = \frac{t_o}{6}$  and a frequency of 1 MHz (Kelekanjeri<sup>b</sup> and Gerhardt 2006). It is clear from these plots that the analytical and FEMLAB solutions are in excellent agreement with

each other. Figure 4 shows surface plots of the axial field ( $E_z$ ) at frequencies of 0.1 MHz ((a) & (c)) and 1 MHz, ((b) & (d)) obtained from the FEMLAB solution. The scale has been adjusted to emphasize the constriction behavior in 4(a) & 4(b) and the skin-effect behavior in 4(c) & 4(d). The symmetry of the field distribution about  $z = \frac{t_0}{2}$  is clear from all the surface plots. It is seen from Figs. 4(a) and 4(b) that the field is concentrated near the electrode contacts, which is due to the constriction effect. The constriction effect in essence signifies the extent of radial spreading of the current. That this is the case, may be seen from Fig. 3(b), where the radial field  $E_r(r, z)$  is a maximum at  $r = r_c$ , where the contacts terminate. Further away from the electrode contacts, the field decays rapidly along both  $z$  and  $r$  directions, as seen from the surface plots. The decay in  $E_z$  along the radial direction from  $r = 0$  to  $r = r_o$ , may also be seen in the cross-section plot in Fig. 3(a), as the initial drop-off. This is due to progressive attenuation of the signal as it propagates within the medium. Increasing the frequency has the effect of enhancing the rate of field decay in the constriction region, as seen from the surface plots 4(a) and 4(b). The surface plots in Figs. 4(c) and 4(d) emphasize the skin-effect behavior at large values of  $r$  by using an altered scale. The surface plot in Fig. 4(d) clearly demonstrates that after the constriction drop-off, the field starts to rise near the end regions of the disk. This late rise in the field, as  $r$  approaches  $r_o$ , is also seen in the plot of  $E_z$  vs.  $r$  in Fig. 3(a). This behavior is due to the skin-effect, which forces the current to propagate closer to the surface, resulting in higher fields near the surface (Casimir and Ubbink 1967; Giacoletto 1996). The extent of rise is greater, the higher the frequency, as shown by the surface plots 4(c) and 4(d) at frequencies of 0.1 and 1MHz respectively. Thus at high frequencies, both the constriction and skin effects in combination determine the overall field distribution, whereas, constriction is the only dominant effect at low frequencies.

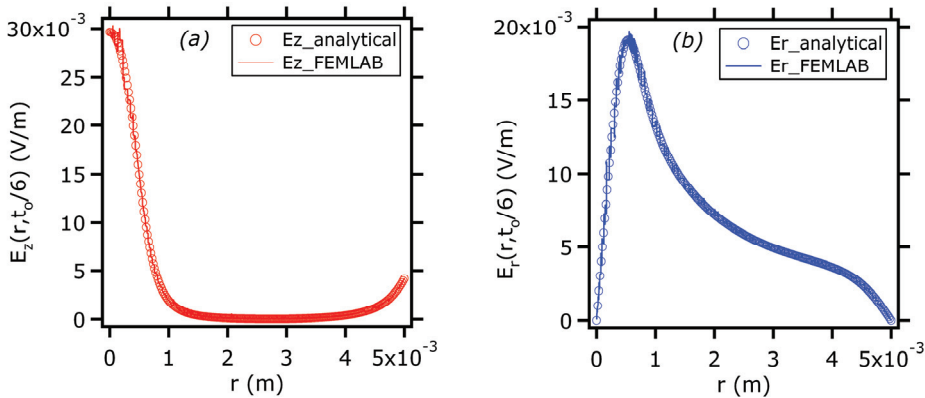


Figure 3. Plots of  $E_z(r, z)|_{z=t_0/6}$  and  $E_r(r, z)|_{z=t_0/6}$  versus  $r$  at 1 MHz, showing the good match between the analytical and FEMLAB solutions. The profiles correspond to the following measurement geometry:  $r_o=5\text{mm}$ ,  $r_c=0.5\text{mm}$  and  $t_0=2\text{mm}$



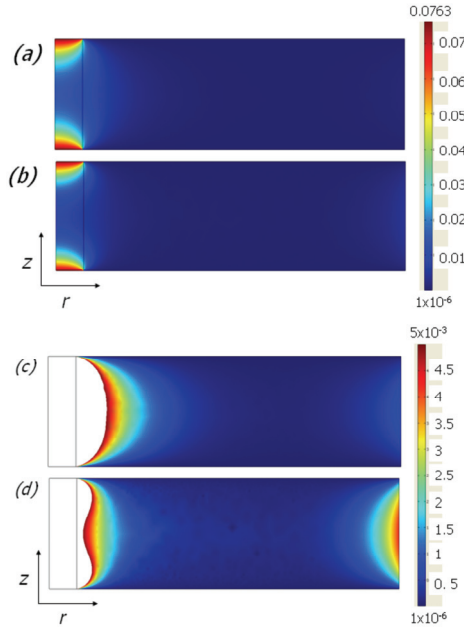


Figure 4. Surface plots of axial electric field in (V/m) emphasizing constriction behavior in (a) and (b) at frequencies of 0.1 MHz and 1 MHz respectively and skin-effect in (c) and (d) at the same two frequencies

### 5.2 Geometric effects on electrodynamic phenomena

Simulation studies on the effect of different geometrical parameters on the two important electrodynamic phenomena pertinent to this problem viz. the skin-effect and constriction are presented next. For these studies, the material parameters ( $\sigma, \mu$ ) and the total injected current ( $I_0$ ) are left unchanged from earlier values.

Simulations for studying the skin-effect behavior (at large  $r$ ) were conducted by a systematic variation of  $r_0$  and  $t_0$  at three different values of the electrode contact radius  $r_c$ . The field

on the boundary, viz.  $E_z(r, z) \Big|_{(r_0, \frac{t_0}{2})}$ , was chosen as the representative parameter for studying the skin-effect behavior. This is because, the constriction effect is minimal at the center of the disk ( $z = \frac{t_0}{2}$ ), whereas, the skin-effect is a maximum on the boundary ( $r = r_0$ ).

Therefore, the field parameter  $E_z(r, z) \Big|_{(r_0, \frac{t_0}{2})}$  will hereafter be referred to as the skin-effect field.

Figure 5 (a) shows the skin-effect field at 1MHz plotted versus  $t_0$  by systematically varying  $r_0$  keeping  $r_c$  constant and vice-versa. It is evident from the plots that the skin-effect field is

primarily influenced by  $r_o$  (Kelekanjeri<sup>b</sup> and Gerhardt 2006) and remains invariant with changes in the electrode contact radius  $r_c$ . Next, the skin-effect field goes through a maximum (at  $t_o = t_{o,cri}$ ) before ultimately reaching a steady value. These inferences may be understood by examining the expression for the skin-effect field, which is given as:

$$E_z(r_o, \frac{t_o}{2}) = a J_o(\kappa r_o) + \sum_m 2C'_{7m} e^{-\frac{\xi_{1m} t_o}{2}} J_o(\lambda_{1m} r_o) \quad (32)$$

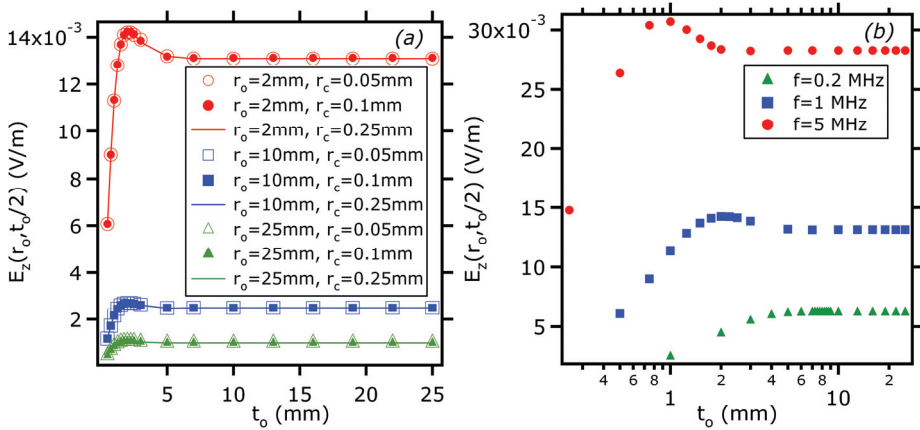


Figure 5. Plots of the skin-effect field vs. the specimen thickness  $t_o$  upon a systematic variation of (a) specimen radius  $r_o$  and electrode contact radius  $r_c$  at a frequency of 1 MHz and (b) frequency of the current by fixing  $r_c = 0.1\text{mm}$  and  $r_o = 2\text{mm}$

In general, both terms in this expression are complex quantities. The first term actually describes the skin-effect, which for the most part is dependent on  $a$ . Therefore, the magnitude of this term scales inversely with  $r_o$ , which is evident from the expression for  $a$  given earlier (see section 3.3.2). The magnitude of the second term that arises due to the constriction effect is mostly influenced by  $t_o$ . The contribution from the constriction term is significant only for small values of  $t_o$ . Therefore, the magnitude of the skin effect field is governed by both terms at small values of  $t_o$ . The maximum occurs when the phase difference between the two complex phasors is minimal. At large  $t_o$ , the contribution from the summation term becomes increasingly less significant, which is the reason for the asymptotic behavior. Physically, this implies that as the specimen thickness increases progressively, the constriction effect decays progressively to a point where it is no longer significant and the situation becomes identical to 1D skin-effect (Kelekanjeri<sup>b</sup> and Gerhardt 2006).

From the plot in Fig. 5(a), it is also noted that the value of  $t_{o,cri}$  (corresponding to the maximum field) remains almost invariant for all combinations of  $r_o$  and  $r_c$  investigated. However, the position of the maximum ( $t_{o,cri}$ ) was found to shift to larger values of  $t_o$

upon decreasing the frequency, with a simultaneous drop in the skin-effect field as shown in Fig. 5(b) (Kelekanjeri<sup>b</sup> and Gerhardt 2006). The scaling of the field with frequency is because the parameter  $a$  is proportional to the square-root of the angular frequency. Additionally the contribution from the second term also scales with frequency and therefore the maximum is displaced further along the  $t_o$  axis upon lowering the frequency. A good analogy to this situation is that of 1D skin-effect, where the field spreads more into the conductor from the surface as the frequency decreases. In essence, frequency behaves like a kinetic parameter in controlling the dispersion of the electric field (Kelekanjeri<sup>b</sup> and Gerhardt 2006).

Next, the results from simulations on constriction behavior are discussed. The magnitude of

the field parameter  $E_z(r, z) \Big|_{(r_c, \frac{t_o}{6})}$  was chosen as the representative parameter for studying

the constriction behavior (Kelekanjeri and Gerhardt 2007). The constriction effect from the previous discussion is clearly the largest at  $r = r_c$ , while the choice of the  $z$  co-ordinate was arbitrary. This field parameter will be referred to as the constriction field, hereon. It is intuitive that  $r_c$  should have a major impact on the constriction field, as it is in turn dependent on the impressed field, which is dictated by  $r_c$ . Therefore, the effect of systematically varying  $r_o$  and  $t_o$  on the constriction field was investigated at a fixed value of  $r_c = 0.1\text{mm}$ . Figure 6(a) shows the constriction field computed at 1MHz, plotted as a function of  $t_o$  for three different values of  $r_o$ . It is clear from the plot that for a given  $r_o$ , a monotonic decrease in the constriction field is noted before ultimately reaching an asymptote. Additionally, the asymptote is noted to occur at a higher value of  $t_o$  as  $r_o$  increased. This may be understood by looking at the following expression for the

constriction field  $E_z(r, z) \Big|_{(r_c, \frac{t_o}{6})}$  :

$$E_z(r_c, \frac{t_o}{6}) = aJ_0(\kappa r_c) + \sum_m C_m \left( e^{-\frac{\xi_{1m} t_o}{6}} + e^{-\frac{5\xi_{1m} t_o}{6}} \right) J_0(\lambda_{1m} r_c) \quad (33)$$

The contribution from the summation term decays exponentially with increasing  $t_o$ . Therefore, at small values of  $t_o$ , the magnitude of the constriction field is entirely determined by the summation term and is independent of  $r_o$ . For large values of  $t_o$ , the summation term becomes negligible and therefore the constriction field is only dependent on  $r_o$ , which explains the eventual asymptotic behavior in terms of  $t_o$ . In the intermediate regime, contributions from both terms are comparable and the extent of this regime is dependent on the parameter  $a$ , which scales inversely with  $r_o$ . Therefore, a specimen with a larger radius has an extended intermediate regime and also a smaller asymptotic constriction field, directly attributable to the contribution from the first term. The physical significance of this is that the constriction behavior equilibrates at a much smaller thickness in a specimen of smaller radius as compared to a larger one. The reason is because the field

spreads out over a larger distance in a specimen of larger radius and consequently equilibrates at a lower asymptote (Kelekanjeri and Gerhardt 2007).

Figure 6(b) shows the constriction behavior upon varying the frequency at fixed values of

$r_o = 5\text{mm}$  and  $r_c = 0.1\text{mm}$ . The general trend of  $E_z(r, z) \Big|_{(r_c, \frac{t_o}{6})}$  vs.  $t_o$  described in the previous

paragraph is also valid at all the three different frequencies investigated here. The most important effect noted upon varying the frequency is that the saturation field decreased drastically with increasing frequency, as is evident from Fig. 6(b). Additionally, the onset of saturation occurred at progressively smaller values of  $t_o$  with increasing frequency. Both these effects pertinent to the constriction region again bear testimony to the fact that frequency behaves like a kinetic parameter in determining the equilibrium field distribution, similar to that seen in Fig. 5(b) for the skin-effect field.

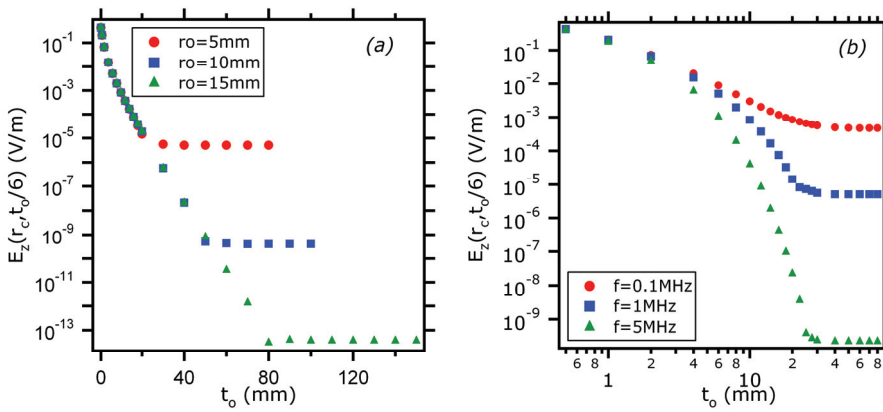


Figure 6. Plots showing the constriction field  $E_z(r, z) \Big|_{(r_c, \frac{t_o}{6})}$  versus  $t_o$  with systematic variation in (a) specimen radius-  $r_o$  at a frequency of 1MHz and (b) frequency at  $r_o = 5\text{mm}$ . The electrode contact radius  $r_c$  is fixed at 0.1mm for these simulations

### 5.3 Limiting Thickness Analysis

The concept of a limiting thickness  $t_{o,lim}$ , is proposed so as to investigate the applicability of the disk and semi-infinite closed-form analytical solutions to a given geometric configuration. The limiting thickness is defined as the smallest disk thickness for which a limiting field profile  $E_{z,lim} \Big|_{z=\frac{t_{o,lim}}{2}}$ , is reached at the center of the disk (Kelekanjeri and Gerhardt 2007). This means that a disk with thickness larger than  $t_{o,lim}$ , (say  $t_1 > t_{o,lim}$ ) will

yield the same profile  $E_{z,lim} \Big|_{z=\frac{t_{o,lim}}{2}}$ , for all values of  $z$  between  $\left(\frac{t_{o,lim}}{2}\right)$  and  $\left(\frac{t_1}{2}\right)$ . It is

intuitive that both the limiting thickness and the limiting field profile should be frequency dependent, because the constriction effect varies with frequency as explained previously.

An optimization routine was developed for determining  $t_{o,lim}$  and  $E_{z,lim}\Big|_{z=\frac{t_{o,lim}}{2}}$ , which is

described in the following. The electric field at the center of the specimen  $E_z(r, z)\Big|_{(0, \frac{t_o}{2})}$  (for

any arbitrary  $t_o$ ), hereafter referred to as the center field, was chosen as the optimization

parameter. This is because the electric field at  $\left(0, \frac{t_o}{2}\right)$  was observed to be the last to

equilibrate in the electric field profile at the center of the disk. The center field is given by the following expression (Kelekanjeri and Gerhardt 2007):

$$E_z\left(0, \frac{t_o}{2}\right) = a + \sum_m 2C'_m e^{-\frac{\xi_m t_o}{2}} \quad (34)$$

The routine begins by initializing upper and lower bounds for  $t_o$ , such that  $t_{o,upper} \gg t_{o,lower}$ . The center fields corresponding to thickness values of  $t_{o,lower}$ ,  $t_{o,upper}$  and

$t_{o,middle} = \left(\frac{t_{o,lower} + t_{o,upper}}{2}\right)$  were then determined as  $E_{z,lower}$ ,  $E_{z,upper}$  and

$E_{z,middle}$  respectively. Next, the correct thickness interval ( $[t_{o,lower}, t_{o,middle}]$  or  $[t_{o,middle}, t_{o,upper}]$ ) for determination of  $t_{o,lim}$  was identified by examining the relative

differences between the corresponding center fields *i.e.*  $|E_{z,upper} - E_{z,middle}|$  and

$|E_{z,middle} - E_{z,lower}|$ . The interval corresponding to the smallest difference in the fields was the

obvious choice. The upper and lower bounds were updated after choosing the new interval.

This procedure was repeated until convergence was achieved simultaneously in both the center field and the thickness, which uniquely determined the limiting thickness  $t_{o,lim}$  and

the associated limiting field profile  $E_{z,lim}\Big|_{z=\frac{t_{o,lim}}{2}}$ , for a given geometric configuration and a

frequency. The results of computations of the limiting thickness  $t_{o,lim}$  and the limiting

center field  $E_{z,lim}\Big|_{(0, \frac{t_{o,lim}}{2})}$  are listed in Table 1 for multiple frequencies. These calculations

were performed for the same set of material parameters and for values of  $r_c$  and  $r_o$  of 0.5mm and 5mm respectively. It is clear from the table that the limiting thickness as well as the limiting center field, increase progressively to an asymptotic quantity with decreasing frequency.

The limiting thickness parameter thus determined was then used as a reference for comparing the disk and the semi-infinite analytical solutions with the FEMLAB solution.

The FEMLAB solution proved to be indispensable in verifying the computation of  $t_{o,lim}$ .

Figure 7 shows the limiting electric field profile ( $E_{z,lim}|_{z=\frac{t_o,lim}{2}}$  at 1 MHz) computed from the disk and the semi-infinite analytical solutions and also the FEMLAB solution for the following cases:  $t_o \ll t_{o,lim}$ ,  $t_o \cong t_{o,lim}$  and  $t_o > t_{o,lim}$ . The cross-section at the center of the disk ( $z = \frac{t_o}{2}$ ) was chosen because, the discrepancies if present, were always a maximum here. In the case where  $t_o \ll t_{o,lim}$ , a clear mismatch is noted between the profiles yielded by the disk and the semi-infinite analytical solutions. As  $t_o$  increased, the mismatch decreased progressively and the solutions yielded a perfect match at  $t_{o,lim}$  and the match remained intact for  $t_o > t_{o,lim}$ .

Frequency (Hz)	$t_{o,lim}$ (mm)	$E_{z,lim} _{(0, \frac{t_{o,lim}}{2})}$ (V/m)
$10^6$	15.4	$5.08 \times 10^{-6}$
$5 \times 10^5$	16.9	$4.36 \times 10^{-5}$
$2 \times 10^5$	19.8	$2.36 \times 10^{-4}$
$10^5$	22.8	$4.70 \times 10^{-4}$
$5 \times 10^4$	22.8	$6.53 \times 10^{-4}$
$2 \times 10^4$	22.8	$7.44 \times 10^{-4}$
$10^4$	22.8	$7.60 \times 10^{-4}$
$10^3$	22.8	$7.65 \times 10^{-4}$
$5 \times 10^2$	22.8	$7.65 \times 10^{-4}$

Table 1. Limiting thicknesses and limiting center fields at several frequencies via optimization of the disk solution for chosen values of  $r_o = 5\text{mm}$  and  $r_c = 0.5\text{mm}$

The total number of elements used in the FEMLAB models for the cases-  $t_o \ll t_{o,lim}$ ,  $t_o \cong t_{o,lim}$  and  $t_o > t_{o,lim}$  were 20824, 67880 and 72017 respectively. The maximum mesh size ( $\Delta_{max}$ ) on the vertical boundaries of the geometry (spanning a length of  $t_o$ ) was adjusted so as to improve the match with the analytical solution(s). A constant value of  $\Delta_{max}$  could not be used for all three cases because of memory handling constraints associated with the solver. A nearly identical profile to that of the analytical disk solution was obtained using the FEMLAB solution for  $t_o < t_{o,lim}$ . In cases where  $t_o \geq t_{o,lim}$ , the FEMLAB solution deviated marginally from the two analytical solutions, which showed a perfect match. The match could be better provided the memory constraints of the solver upon lowering  $\Delta_{max}$  could be met. However, for practical purposes, the analytical disk solution and the FEMLAB

solution are in agreement with each other for all values of  $t_o$ , while, the semi-infinite analytical solution is clearly a rough approximation for  $t_o \ll t_{o,lim}$ .

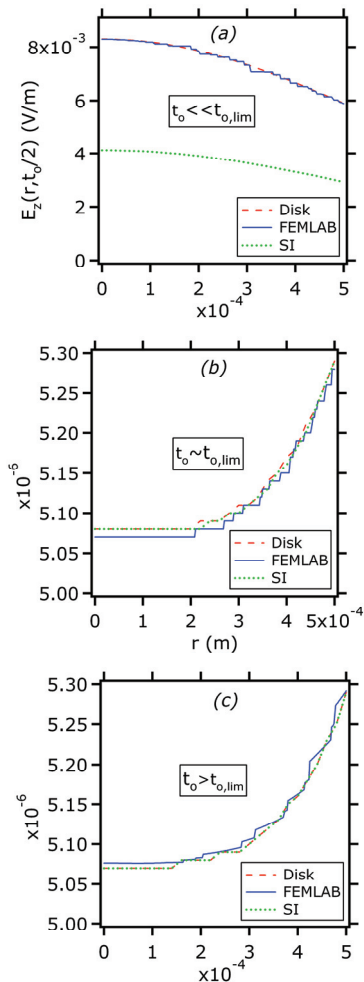


Figure 7. Plots showing the axial field at 1MHz as a function of  $r$  to show the relative match between the semi-infinite, disk analytical solutions and the FEMLAB solution for the following cases - (a)  $t_o \ll t_{o,lim}$ , (b)  $t_o \cong t_{o,lim}$  and (c)  $t_o \geq t_{o,lim}$

## 6. Computation of Specimen Impedance

In this section, a procedure for computing the complex impedance of the specimen in the shape of a cylindrical disk is described based on the expressions for the electric field distribution that were presented in section 3. As before, computation of impedance from the analytical model was validated using the FEMLAB model at a number of frequencies. The

following material properties and geometric parameters were used for computing the specimen impedance:  $\sigma=8.34 \times 10^5 \text{ S/m}$ ,  $\mu_r=1.004$ ,  $r_o=6.35\text{mm}$ ,  $r_c=0.5\text{mm}$  and  $t_o=2\text{mm}$ . The complex impedance ( $Z$ ) of a specimen for an alternating current flow situation consists of real ( $Z'$ ) and imaginary ( $Z''$ ) components, viz. a resistance ( $R$ ) and a reactance ( $X$ ).

$$Z = Z' + jZ'' = R + jX \quad (35)$$

In the case of a metallic specimen, the reactance is primarily due to the contribution from the internal inductance ( $L_i$ ) of the specimen. While the resistance is related directly to energy loss due to ohmic heating, the inductance describes the ability of a conductor to store magnetic energy (Hallen 1962). The expression for the complex impedance by incorporating the inductance is written as follows:

$$Z = R + j\omega L_i \quad (36)$$

The computation of  $R$  and  $L_i$  of a metallic cylindrical disk specimen using the analytical electric field expressions was conducted via energy methods (Kelekanjeri 2007). The resistance and the inductance are obtained by calculating the Joule heat-loss and the total internal magnetic energy respectively, the expressions for which, are listed as follows (Hallen 1962):

$$R = \frac{1}{I_{rms}^2} \int_V \sigma \bar{E} \cdot \bar{E}_c dV \quad \text{and} \quad (37)$$

$$L_i = \frac{1}{I_{rms}^2} \int_V \bar{B} \cdot \bar{H}_c dV = \frac{1}{I_{rms}^2} \int_V \mu \bar{H} \cdot \bar{H}_c dV \quad (38)$$

In the above expressions  $\bar{E}$  and  $\bar{H}$  are the total complex electric and magnetic fields respectively, while the subscript  $c$  denotes the complex conjugate. The total magnetization- $\bar{B}$  is related to the magnetic field  $\bar{H}$  by the magnetic permeability  $\mu$ . The root mean square value of the current of amplitude  $I_o$  is given by  $I_{rms} = \frac{I_o}{\sqrt{2}}$ . The total electric field  $\bar{E}$  and the magnetic field  $\bar{H}$  are given in terms of the electric field components  $E_r$  and  $E_z$  as follows:

$$\bar{E} = E_r \hat{r} + E_z \hat{z} \quad \text{and} \quad (39)$$

$$\bar{H} = \frac{1}{j\omega\mu} \left( \frac{\partial E_z}{\partial r} - \frac{\partial E_r}{\partial z} \right) \quad (40)$$

The analytical expressions for  $E_r$  and  $E_z$  are given in section 3. The reader is referred to the Appendix for further details on evaluation of the volume integrals.

In the case of the FEMLAB model, the overall Joule heat loss and the magnetic energy are obtained by integration of the time average resistive heating per unit volume ( $Q_{av}$ ) and the



magnetic energy density ( $W_{mag}$ ) over the specimen volume respectively. The expressions for the time average quantities, viz. the Joule heat loss per unit volume and the magnetic energy density are given as follows (COMSOL AB<sup>a</sup> 2004):

$$Q_{av} = \frac{1}{2} \text{Re}(\overline{J \cdot E_c}) \quad \text{and} \quad (41)$$

$$W_{mag} = \frac{1}{4} \text{Re}(\overline{H \cdot B_c}) \quad (42)$$

The resistance  $R$  and the inductance  $L_i$  are subsequently obtained by dividing out the time average quantities by  $I_{rms}^2$ .

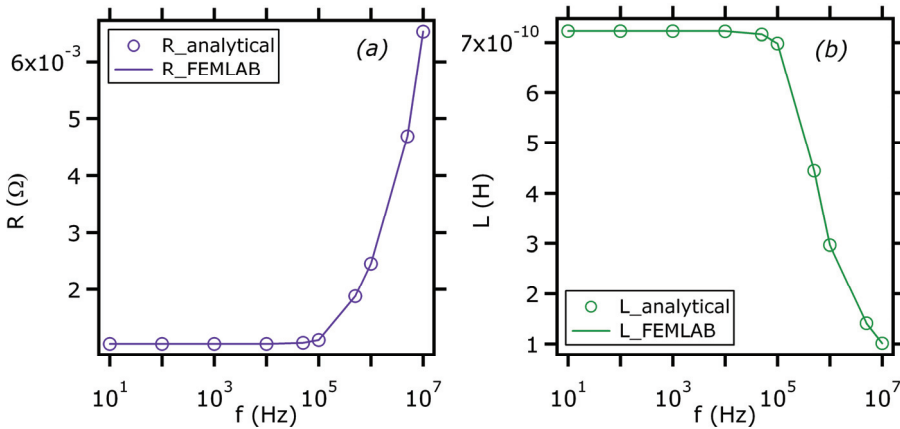


Figure 8. Plots of the frequency dependent resistance (a) and inductance (b) computed from both analytical (open symbols) and finite element models (solid line)

Plots of  $R$  and  $L_i$  as a function of the frequency are shown in Figs. 8(a) and 8(b) respectively. The perfect match between the quantities computed via the closed-form analytical solution and the finite element FEMLAB solution is evident from both plots. The resistance behavior as a function of frequency may be understood by examining the cross-section plots of  $E_z(r, z)$  and  $E_r(r, z)$  in Fig. 3 and the surface plots of  $E_z(r, z)$  in Fig. 4. It is clear from Fig. 3(a) that the axial field  $E_z(r, z)$  drops quickly to zero past the constriction region and reappears at larger values of  $r$  (near the surface). The rise in  $E_z(r, z)$  near the surface (see Fig. 3(a)) is non-existent for frequencies below 10kHz. The radial field  $E_r(r, z)$  (see Fig. 3(b)) on the other hand remains finite beyond the constriction region and is extended to large values of  $r$  with increase in the frequency. The extent of rise in  $E_z(r, z)$  near the surface and the radial spreading in terms of  $E_r(r, z)$  past the constriction region are both enhanced with increase in frequency. The variation in the field profiles for frequencies below 10kHz is negligible. This redistribution in the axial and radial fields with frequency has the effect of decreasing the Joule loss contribution from  $E_z(r, z)$  and increasing that from  $E_r(r, z)$

(Kelekanjeri 2007). The overall Joule heat loss however, increases drastically with frequency (10kHz and above) as the predominant effect is that of  $E_r(r, z)$ . Consequently, the resistance  $R$  remains relatively constant for frequencies up to 10kHz and increases progressively upon further increase in the frequency.

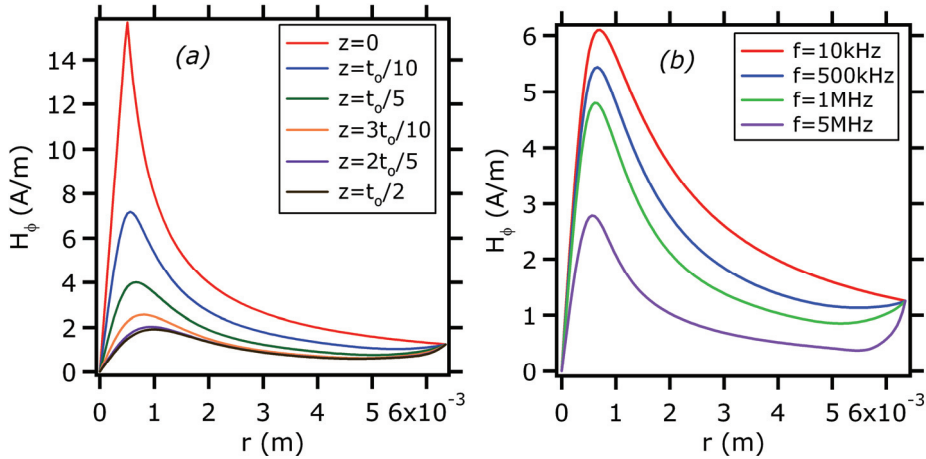


Figure 9. Plots of the magnetic field  $H_\phi(r, z)$  vs.  $r$  with varying (a)  $z$  cross-section from the surface to the center of the specimen at a frequency of 1MHz and (b) frequency at  $z = \frac{t_o}{6}$ .

The geometry was fixed at  $r_o = 6.35$ mm,  $r_c = 0.5$ mm and  $t_o = 2$ mm

The inductance behavior as a function of the frequency is dependent on the distribution of the magnetic field inside the specimen (Hallen 1962). Figure 9(a) shows plots of the magnetic field  $H_\phi$  versus  $r$  at different  $z$  cross-sections starting from the boundary at ( $z=0$ )

to the center of the disk ( $z = \frac{t_o}{2}$ ). It is evident from the plots that  $H_\phi$  is a maximum at  $r = r_c$ , (where the constriction effect is maximum) and reaches a constant value on the curved boundary ( $r = r_o$ ). Additionally, the weakening of the magnetic field  $H_\phi$  may be

noted near the constriction region as  $z$  increases from 0 to  $\frac{t_o}{2}$ . This gradual weakening of the magnetic field is aggravated with increasing frequency, as may be seen from Fig. 9(b), which shows plots of  $H_\phi|_{z=\frac{t_o}{6}}$  at frequencies ranging from 10 kHz to 5 MHz. The lesser

penetration of the magnetic field results in a lower overall magnetic energy for the specimen and consequently a lower internal inductance with a rise in the frequency (Hallen 1962). The reactance  $X$  on the other hand is a product of the internal inductance and the angular frequency (see equation (36)) and therefore increases with increasing frequency (Hallen 1962).

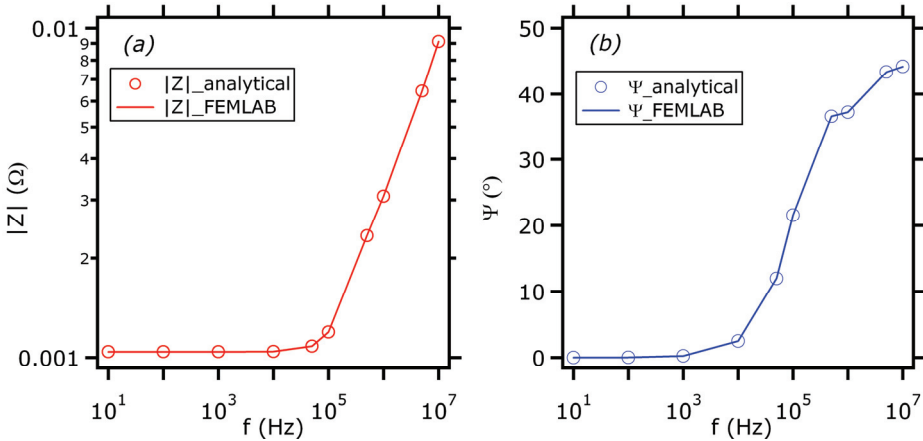


Figure 10. Plots of the complex impedance magnitude-(a) and the phase angle-(b) versus frequency showing a comparison between the analytical (open symbols) and finite element models (solid line)

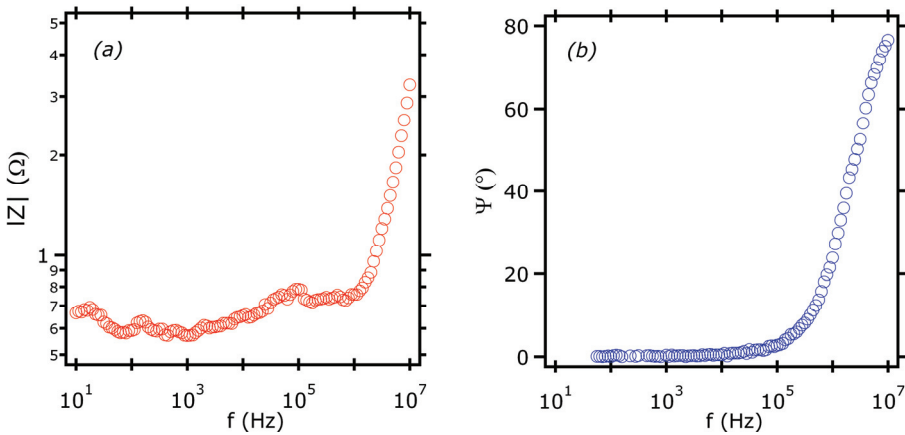


Figure 11. Plot of the complex impedance magnitude-(a) and phase angle-(b) vs. frequency from an actual two-probe impedance measurement of a superalloy specimen of dimensions-  $r_o=6.35\text{mm}$ ,  $t_o=2\text{mm}$  and conductivity  $\sigma=8.34 \times 10^5 \text{ S/m}$ . The electrode contact radius  $r_c$  was  $0.5\text{mm}$

The magnitude of the overall impedance ( $|Z|=\sqrt{R^2+X^2}$ ) and the phase angle ( $\psi = \tan^{-1} \frac{X}{R}$ ) are shown as a function of the frequency in Fig. 10(a) and 10(b), for the closed-form analytical and the finite-element solutions respectively. The excellent match between the two solutions is again obvious. It is seen that the phase angle increases dramatically in the frequency range from 10kHz to 1MHz followed by a near saturation type behavior. The impedance only increases slightly from 10kHz to 100kHz, followed by a steep rise. It is interesting to note that both the resistance and reactance increase nearly at the same rate at

the highest frequencies, indicated by the saturation in  $\psi \sim 45^\circ$ . The latter observation is analogous to 1-D skin-effect situation, where both components of the complex impedance increase as square root of the angular frequency at high frequencies (Gosselin, et al., 1982). It should be mentioned that the specimen impedance computed here is a function of the electrode contact radius ( $r_c$ ). This is because the electric and magnetic field distribution inside the specimen is governed by the constriction effect, which in turn is affected by variations in  $r_c$ . There is however another important factor which affects the measured two-probe impedance response viz., the contact resistance between the electrode and the specimen. The present model does not account for the contact resistance effect on the overall impedance and therefore, caters to an ideal situation only.

The measured two-probe impedance and the corresponding phase angle response from a specimen with dimensions and electrical conductivity similar to that used for impedance calculations are shown in Fig. 11. It is clear that the measured impedance (Fig. 11(a)) is orders of magnitude off from the computed impedance (Fig. 10(a)); however the overall increasing trend in impedance with frequency is almost identical in shape. The measured phase angle (Fig. 11(b)) also shows a similar trend as the computed one; however, the actual magnitude of the frequency dependent phase angle is different from the computed response. The reasons for the discrepancies between the measured and computed responses are discussed below. As mentioned previously, the electrode-specimen contact resistance is one factor responsible for the rather high value of the measured impedance and is prevalent at all frequencies. Secondly, the flow of alternating current generates a time-varying magnetic field, as a consequence of Faraday's law. This magnetic field is responsible for an induced voltage besides that from the specimen, if any loops are present in the circuitry (Kelekanjeri 2007). While the contact resistance offsets the specimen impedance (at all frequencies), the induced voltage from the magnetic field primarily affects the reactance at high frequencies (10 kHz and beyond). The reactance increases nearly exponentially for frequencies above 100 kHz, owing to induced voltage from the circuitry and consequently obscures the measurement of actual impedance associated with the specimen. This is also the reason for the relatively higher values of the measured phase angle at the highest frequencies. The fluctuations in impedance noted up to 1MHz could be due to inadequate compensation of residual impedance arising from the circuitry. The problems mentioned heretofore for two-probe impedance measurements of a conducting specimen are not major concerns in the case of semiconducting or dielectric specimens due to the inherently large impedance of the specimen itself.

## 7. Future Work

The applicability of the present model of an ideal two-probe impedance measurement, treated as a current injection/extraction problem, is demonstrated for a fairly good conductor, in this case a nickel-base superalloy. However, the scope of this model may be extended to good semiconductors and polymer-conducting filler composites with fairly high conductivities, keeping in mind the assumptions made in the model. The validity will be ensured only when the conduction current density is still dominant over the displacement current density by orders of magnitude. As the next step, the model could be extended to address impedance measurements of more insulating materials by accounting for the displacement current term. In this case, the inherent dependence of conductivity and dielectric constant on the frequency will add more complexity into the model. This could also play a role in the case of the

conductor-filled polymer specimens, mentioned above. Another important problem in today's nanoscale research is the quantitative determination of localized electrical properties of a microstructure using scanning probe microscopy (SPM) based electrical techniques. Nanoimpedance microscopy is an SPM-based AC technique in which, a local probe tip serves as a replacement to one of the bulk electrodes for measuring the local impedance of the region of interest (Kalinin and Gruverman 2007). In this case, however, the measured response is dominated by the region that is directly underneath the probe tip, the size of which, is determined directly by the tip-radius. In addition, the contact force applied by the tip, determined by the force constant of the tip, also affects the measured response. This type of localized measurement could also be treated as a current injection/extraction problem similar to the current one. However, the spatial variations in conductivity, the surrounding medium, the relative size of the feature vs. tip-radius, the nature of the contact between the tip and the sample are all important factors that should be included in the model.

## 8. Summary

Closed-form analytical expressions for the electric field distribution inside a cylindrical disk conductor are presented for the problem of a two-probe impedance measurement, treated as a current injection/extraction problem. The specimen was treated as a homogeneous material medium with uniform electrical and magnetic properties. A finite element solution obtained using a commercially available finite element package, FEMLAB 3.1, was used for independent validation of the closed-form expressions. Analytical expressions for the case of an infinitely long cylinder are also given as a corollary to the disk problem.

The expressions for the axial and radial electric fields consist of terms that account for both the skin effect and the constriction effect. The skin effect term becomes important at high frequencies ( $10^4$  Hz to  $10^6$  Hz) near the end regions of the disk (large  $r$ ), while the constriction term is dominant in regions near the electrode contacts (small  $r$ ) at all frequencies.

The effects of varying the measurement geometry viz. the electrode contact radius  $r_c$ , the disk radius  $r_o$ , and the disk thickness  $t_o$ , were investigated systematically. The skin effect behavior at high frequencies was found to be dependent only on the specimen dimensions ( $r_o$  and  $t_o$ ) and was independent of the electrode contact radius  $r_c$  ( $r_c \ll r_o$ ). The skin effect field reached a maximum in  $t_o$ , before eventually reaching an asymptote with increasing  $t_o$ . The dominant effect on the constriction was that of  $r_c$ . In addition, the specimen geometry also impacted the constriction behavior; the dependency on  $r_o$  was only ruled out for small values of  $t_o$ .

The concept of a limiting thickness and a limiting field profile was proposed in order to assess the range of applicability of the disk and semi-infinite analytical solutions for a given specimen geometry. Simulations indicated that the disk analytical solution and the FEMLAB solution matched with each other for all values of  $t_o$ . The semi-infinite analytical solution also matched well with the other solutions when  $t_o \geq t_{o,lim}$ . However, when  $t_o \ll t_{o,lim}$ , the semi-infinite solution was only a rough approximation to the actual solution yielded by the disk solution.

The real and imaginary parts of the complex impedance for an ideal two-probe impedance measurement were computed using the closed-form analytical and finite-element solutions via energy-based methods. The frequency dependent specimen resistance was found to be a

constant up to ~100kHz and increased monotonically with further rise in the frequency. The internal inductance on the other hand showed a monotonic decrease after 100kHz. These effects were explained as due to the increase in the overall Joule heat-loss and a decrease in the magnetic energy storage with rise in the frequency. The measured impedance response differed by orders of magnitude from the computed impedance due to factors such as the specimen-electrode contact resistance and the induced voltage from the measurement circuitry.

## 9. Acknowledgements

Research funding for this work was provided by the US Department of Energy under grant DE-FG 02-03-ER 46035. The authors would also like to acknowledge Dr. S. P. Gurrum for helpful discussions pertaining to analytical derivation and finite element models. Figures 1(a) and (b), 2, 6(a) and 7 and Table 1 are reprinted with permission from Journal of Applied Physics 101, 0449041 Copyright American Institute of Physics (2007)

## 10. Appendix

### I. Sifting property of the delta function

$$\int f(x)\delta(x_0 - x)dx = f(x_0)$$

### II. Derivative of Bessel functions

$$[x^{-\nu}J_{\nu}(x)]' = -x^{\nu}J_{\nu+1}(x)$$

### III. Orthogonality property of Bessel functions

For a given  $\nu$ , the Bessel functions  $J_{\nu}(\lambda_{1\nu}x)$ ,  $J_{\nu}(\lambda_{2\nu}x)$ ,  $J_{\nu}(\lambda_{3\nu}x)$ ,...with  $\lambda_{m\nu} = \frac{\beta_{m\nu}}{R}$  ( $m = 1,2,3,\dots$ ) form an orthogonal basis in the interval  $0 \leq x \leq R$  with respect to the weight function  $p(x) = x$ . This property is expressed as:

$$\begin{aligned} \int_0^R x J_{\nu}(\lambda_{m\nu}x) J_{\nu}(\lambda_{n\nu}x) dx &= 0 \quad (m \neq n) \\ &= \frac{R^2}{2} J_{\nu+1}^2(\lambda_{m\nu}R) \quad (m = n) \end{aligned}$$

### IV. Indefinite integral of product of Bessel functions

$$\begin{aligned} &\int_z \left\{ (k^2 - l^2)t - \frac{(\mu^2 - \nu^2)}{t} \right\} J_{\mu}(kt) J_{\nu}(lt) dt \\ &= z \left\{ k J_{\mu+1}(kz) J_{\nu}(lz) - l J_{\mu}(kz) J_{\nu+1}(lz) \right\} - (\mu - \nu) J_{\mu}(kz) J_{\nu}(lz) \end{aligned}$$

### V. Complex identities

If  $u$  and  $v$  are any two complex numbers, then the following identities hold true for operations on their complex conjugates  $\bar{u}$  and  $\bar{v}$ .

a. (a)  $\overline{(u \pm v)} = \bar{u} \pm \bar{v}$

- b. (b)  $\overline{uv} = \overline{u} \overline{v}$   
 c. (c)  $\overline{J_\mu(u)} = J_\mu(\overline{u})$ , where  $J_\mu(x)$  is a Bessel function in  $x$  of order  $\mu$ .

## 11. References

- Abramowitz, M. & Stegun, I. A. (1964) eds. *Online Version of Handbook of Mathematical Functions*, U. S. Government Printing Office, Washington
- Bauerle, J. E. (1969) Study of solid electrolyte polarization by a complex admittance method. *Journal of the Physics and Chemistry of Solids*, 30, (Dec. 1969) (2657-70), ISSN: 0022-3697.
- Bowler<sup>a</sup>, N. a. (2004). Analytical solution for the electric field in a half space conductor due to alternating current injected at the surface. *Journal of Applied Physics*, 95, 1, (1<sup>st</sup> January, 2004) (344-348), DOI: 10.1063/1.1630700
- Bowler<sup>b</sup>, N. a. (2004). Electric field due to alternating current injected at the surface of a metal plate. *Journal of Applied Physics*, 96, 8, (15<sup>th</sup> October, 2004) (4607-4613), DOI: 10.1063/1.1793332
- Casimir, H. B. G. & Ubbink, J. (1967). The skin effect, I. Introduction; the current distribution for various configurations. *Philips Technical Review*, 28, 9, (271-283),
- COMSOL AB<sup>a</sup> (2004). *User's Guide to Electromagnetics Module, FEMLAB 3.1* COMSOL AB, Stockholm, Sweden
- COMSOL AB<sup>b</sup> (2004). *FEMLAB 3.1 User's Guide*, COMSOL AB, Stockholm, Sweden
- Costache, G. I. & Ney, M. M. (1988). A time domain approach for determining ground impedance on printed circuit boards. *2<sup>nd</sup> Symposium on Antenna Technology and Applied Electromagnetics*, pp. 1-6, ISBN: 0969256310, Winnipeg, Canada, August 10-12, 1988
- Cottingham, W. N. & Greenwood, D. A. (1991). *Electricity and Magnetism* Cambridge University Press, ISBN: 0-521-36803-0, New York
- Gerhardt, R. A. (2005). Impedance Spectroscopy and Mobility Spectra, In: *Encyclopedia of Condensed Matter Physics* eds. Bassani, G., Liedl, G. & Wyder, P., (350-363), Elsevier Press, ISBN-13: 978-0-12-227610-1, New York, NY, USA
- Giacoletto, L. J. (1996). Frequency- and Time-Domain Analysis of Skin Effects. *IEEE Transactions on Magnetics*, 32, 1, (220-229), Publisher Item Identifier: S 0018-9464(96)00089-1
- Gosselin, J. R., Rochon, P. & Gauthier, N. (1982). Study of eddy currents in a cylindrical wire: an undergraduate laboratory experiment. *American Journal of Physics*, 50, 5, (May 1982) (440-443)
- Gray, A. & Mathews, G. B. (1952). *A Treatise on Bessel Functions and Their Applications to Physics*, Macmillan and Co., Limited, 2<sup>nd</sup> edition edited by Gray, A. and MacRobert, T. M., London
- Hallen, E. G. (1962). *Electromagnetic Theory, Translated from the Swedish ed. by Runar Gasstrom*, Wiley & Sons Inc., New York
- Kalinin, S. & Gruverman, A. (2007). *Scanning probe microscopy: Electrical and electromechanical phenomena at the nanoscale*, Springer, 1<sup>st</sup>, ISBN: 978-0-387-28667-9, New York, NY, USA

- Kelekanjeri<sup>a</sup>. V. S. K. G. & Gerhardt, R. A. (2006). Characterization of microstructural fluctuations in Waspaloy exposed to 760°C for times up to 2500 h. *Electrochimica Acta*, 51, (1873-1880), DOI:10.1016/j.electacta.2005.02.099
- Kelekanjeri<sup>b</sup>. V. S. K. G. & Gerhardt, R. A. (2006). Finite-element Validation of Electric Field Distribution inside a Cylindrical Conductor for an Ideal Two-Probe Impedance Measurement. *COMSOL 2006 Users Conference*, pp. 117-123, 0-9766792-2-1, Boston, MA, USA, October 22<sup>nd</sup>-24<sup>th</sup>, COMSOL Inc., USA
- Kelekanjeri, V. S. K. G. & Gerhardt, R. A. (2007). Electric field distribution within a metallic cylindrical specimen for the case of an ideal two-probe impedance measurement. *Journal of Applied Physics*, 101, (0449041-04490410), DOI: 10.1063/1.2405734
- Kelekanjeri, V. S. K. G. (2007). *Non-destructive Electrical Characterization of Controlled Waspaloy Microstructures*, Ph.D. Dissertation, Materials Science and Engineering, Georgia Institute of Technology, Atlanta
- Kreyszig, E. (1994). *Advanced Engineering Mathematics* Wiley Eastern Limited, 5<sup>th</sup>, ISBN: 81-224-0016-7, New Delhi, India
- Ney, M. M. (1991). Striction and Skin Effects on the Internal Impedance Value of Flat Conductors. *IEEE Transactions on Electromagnetic Compatibility*, 33, 4, (321-327), IEEE Log Number 9102196
- Weber, H. J. & Arfken, G. B. (2004). *Essential Mathematical Methods for Physicists* Elsevier, ISBN: 81-8147-616-6, New Delhi
- [www.mathworld.com](http://www.mathworld.com)
- Zou, X., Makram, T. & Gerhardt, R. A. (2002). Detection of compositional fluctuations in high temperature exposed Waspaloy. *Electrically Based Microstructural Characterization III. Materials Research Society Symposium*, pp. 301-306, 1 55899 635 4, Boston, MA, USA, Materials Research Society



# Evolutionary Constructive Approach for Studying Dynamic Complex Systems

Takashi Hashimoto, Takashi Sato, Masaya Nakatsuka and  
Masanori Fujimoto

*School of Knowledge Science, Japan Advanced Institute of Science and Technology (JAIST)  
Japan*

## 1. Introduction

In this chapter, we introduce a scientific methodology called “evolutionary constructive approach”. This approach is suitable for studying dynamic features of complex systems. At first, we identify two types of simulation methodologies, realistic and constructive. The latter is especially needed to clarify complex systems, since the complex systems have distinct characteristics from objects of conventional scientific studies. We characterize such characteristics as “undecomposabilities”. We show three example simulation studies using the evolutionary constructive approach. They are about 1) dynamic change of social structures, 2) language change and displacement, and 3) dynamics of communication.

These days, computer simulations have been getting popular in science and engineering. For example, the Earth Simulator developed in Japan has been producing interesting results for meteorology and environmental science (Sato, 2004). Multi-agent simulations, or agent-based simulations, are an enterprise of new method in social science (Conte et al., 1997; Gilbert & Troitzsch, 2005).

The simulation techniques are expected to contribute for understanding and prediction of the future of our world. But our world is not so easy to comprehend and to deal with. We have reached good understanding of some parts of the world, when simple sub-parts can be extracted as systems. Complex systems in which extracting simple sub-parts or breaking down into simple systems are very hard have been still remaining untractable for us. If we try to use modeling and simulation for understanding such complex systems, we should establish the way of thinking, the methodologies and the approach to model the complex world.

The purpose of this chapter is to discuss if constructive approach, especially, evolutionary constructive approach, can contribute to understand the complex world. The constructive approach is a scientific methodology in which an objective system is to be understood by constructing the system and operating it. In evolutionary constructive approach, evolutionary operations, not only genetic evolution but also lifetime development, individual learning and social learning, are incorporated to construct models.

This chapter organizes as follows. In section 2, we describe some seminal constructive studies not limited to works using computer simulations. In section 3, we explain how complex systems are characterized as a preparation to discuss if the constructive approach is

suitable for studying complex systems. The important concept to view complex systems is “undecomposability”. In section 4, we explain evolutionary constructive approach in detail. Section 5 is devoted to show examples of simulation studies taking the evolutionary constructive approach. We summarize this chapter with discussion about the future direction of the evolutionary constructive studies in section 6.

## 2. Two Types of Simulation Methodologies: Realistic and Constructive

We can identify two types of methodologies in simulation studies, one is realistic simulations and the other is constructive simulations. The former tries to make operational copies of actual phenomena as possible as realistic in order to predict what occur in the target phenomena. The latter constructs rather simplified non-realistic models in order to extract essential features and to understand underlying mechanisms and logics of the objective phenomena.

A typical example of the realistic simulation is “the Earth Simulator” (Sato, 2004). In the Earth Simulator, the Navier-Stokes equation, the fundamental equation for fluid dynamics, is calculated with approximation such as finite element method but as possible as accurate using parallel computers. In order to realize the high accuracy, the surface of the earth is divided into square areas as possible as small. Therefore, massive computational power is required. One of the main purposes of the Earth Simulator is to predict the state of the atmosphere of the Earth. An outcome of such effort is depicted in Figure 1(left). This is not a satellite image but the simulation result of a typhoon approached Japan in August, 2003.

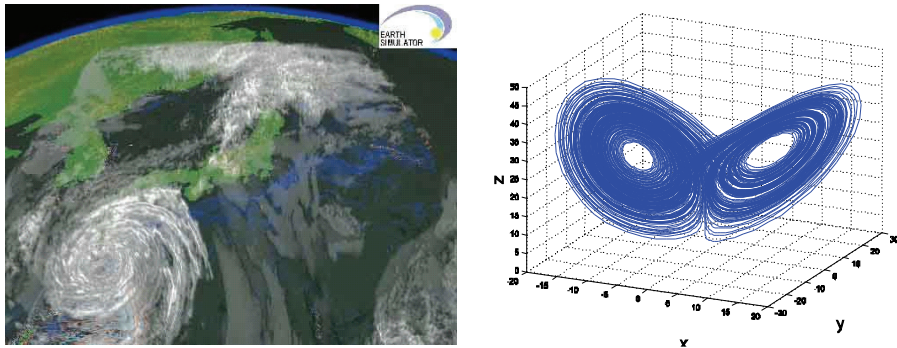


Figure 1. Simulation results from the earth simulator (left) and the Lorenz attractor (right). Both are derived from the same equation but with the completely different methodologies. The former is cited from the Home Page of Multiscale Simulation Research Group, The Earth Simulator Center (<http://www.es.jamstec.go.jp/esc/research/Mssg/index.ja.html>)

On the other hand, the Navier-Stokes equation is often calculated using different approximation called modal decomposition. Lorenz was one of such meteorologists. He extracted five modes of the equation and calculated using a computer in 1950's. After some period of calculation, he restarted the numerical simulation starting from the printed results. After a while, he found that the result was not the same as the first calculation. He could find neither any bug of the computer program nor any glitch in the computer. What he found was the sensitivity to initial conditions. The initial condition of the first and second calculations was slightly different, since the printed result was truncated at some digits. In

some nonlinear systems, such as fluid dynamics, very small difference can be grown into the system size. Lorenz (1963) called the phenomenon “deterministic nonperiodic flow”, which was named *chaos* later (Li & Yoak, 1975).

Lorenz (1963) studied a more simplified system having the sensitivity to initial condition with three dimensional differential equations, now called Lorenz system. Figure 1(right) is a trajectory of the numerical simulation of the system. This geometrical structure is called the Lorenz attractor. He clarified such unstable and complex dynamics is induced by stretching and folding in the phase space.

This study can be thought of as a constructive simulation. Lorenz constructed a more simplified and more non-realistic model than the Earth Simulator and extracted the essential features in the dynamics of atmosphere. Although, using the Lorenz model, we cannot forecast weather at all, the underlying mechanisms, stretching and folding, of complex dynamics of climate was understood and logics of the objective phenomena why weather forecast is fundamentally impossible was comprehended.

The other classical examples of constructive studies are von Neumann’s self-reproducing automata (von Neumann, 1963) and Turing pattern (Turing, 1952).

Taking notice of the self-reproduction as one of the essential features of life, von Neumann (1963) propounded the question, “whether a machine can reproduce itself”, and considered by what kind of logic the self-reproduction would be possible. By constructing an abstract machine, composed of three parts: a universal constructor, a blueprint and a copier of the blueprint, that actually carried out self-reproduction, he proved that self-reproduction is possible for machines.

On the way of construction he found two important logics in self-reproduction. One is that the self-reproducing machine should have a static description of the machine, since the system has to observe itself in order to reproduce itself but the action of observation inevitably affects both the object and the subject of observation. This is a self-referential problem. This problem can be resolved by preparing a blueprint that is stable for observation. The second point is that the content of the blueprint is used twice in the different manners, interpreted and uninterpreted. When the blueprint is used at the first time, the universal constructor should appropriately interpret the information content that is the way to construct the machine. At the second time, the copier reads the blueprint literally and copies all the letters on the blueprint accurately. What is interesting is that these two points were proved to be realized in living organisms. Especially, the structure of the machine and the two distinct manners of information utilization are critical to make the machine evolvable. von Neumann did not perform simulation of the machine, since the computational power was not enough to calculate his self-reproducing machine at his time.

Turing was also interested in life. Having spatial patterns, most of them are static and some dynamic, is one of the essential features of living organism. Turing (1952) proposed a simple reaction diffusion system for morphogenesis, partial differential equations with two variables. In this system, he supposed an interaction between two imaginary chemical substances, called morphogens. He proved that a particular character of the morphogens and particular manner of interaction realized various stable patterns from spatially uniform state. We can produce such various patterns as stripes and dots in numerical simulations by adjusting parameters of the system. This system is not a model abstracted from precise observation of real concrete phenomena, but Turing constructed the system from the bottom-up by introducing imaginary substances. While chemical substances precisely

corresponding to the morphogens have not been found, we can understand the logic and the sufficient conditions for the emergence of nonuniform spatial patterns from uniform initial conditions.

A recent (nonclassical) development of the constructive simulation is Kaneko's coupled chaotic maps (Kaneko, 1986, 1990). He tried to understand high dimensional chaos, but no handy model existed. There are many good models in low dimensional chaos such as the logistic map, Hénon map, Lorenz system, Rössler system (Alligood et al., 1996). Thus, his idea to make a high dimensional system was to connect many low dimensional chaotic maps. Basically, there are two types of coupled chaotic systems. One is a coupled map lattice which consists of chaotic maps with a local coupling (Kaneko, 1986),

$$x_{n+1}(i) = (1-\epsilon)f(x_n(i)) + (\epsilon/2)\{f(x_n(i-1)) + f(x_n(i+1))\}, \quad (1)$$

where  $n$  is the index for time and  $i$  for space, and  $x$  is the value of the state, that is,  $x_n(i)$  represents the state of the  $i$ th map at the  $n$ th time step. Each element receives the influence of adjacent elements. The strength of the influence is controlled by a parameter  $\epsilon$ . The function  $f(x)$  is a chaotic map, e.g. the logistic map  $f(x)=1-ax^2$ , where  $a$  is a nonlinear parameter. The other type is called globally coupled maps, which is a system of chaotic maps with a mean field coupling (Kaneko, 1990),

$$x_{n+1}(i) = (1-\epsilon)f(x_n(i)) + (\epsilon/N)\sum_j f(x_n(j)), \quad (2)$$

where  $N$  is the number of maps. The average of all elements affects each element. Thus the larger value of the coupling constant,  $\epsilon$ , makes the system uniform, and the large value of nonlinearity,  $a$ , makes the system disordered. In computer simulations of the systems, we can find fruitful complex dynamic phenomena, such as spatio-temporal chaos, dynamic clustering, pattern dynamics and chaotic itinerancy, by adjusting the parameters.

The chaotic itinerancy is a remarkably dynamic motion, in which a trajectory chaotically transits among varieties of low dimensional ordered states through high dimensional unordered states; or transits among low dimensional dynamical states including fixed points, periodic and chaotic motions through high dimensional chaotic motions (Kaneko & Tsuda, 2003). We depict an example of chaotic itinerancy observed in globally coupled maps in Figure 2. This graph shows dynamics of effective dimensionality, that is the degree of freedoms, of a system of globally coupled maps with 10 logistic maps. The system has 10 dimensionalities at most, since it consists of 10 one-dimensional maps. The maps continue to synchronize with other maps and to desynchronize. When all elements synchronize, that is thought of as a state with complete order, the effective dimension is 1. When they desynchronize at all, that is an unordered state, the effective dimension is 10. A state with mid dimensionality is a partially ordered state. Figure 2 demonstrates that the effective dimensionality changes with time. The system moves between full ordered state, the effective dimension is 1, and full disordered state, the effective dimension is 10, with chaotic fluctuations. This change does not cease forever.

The coupled map lattice and the globally coupled maps are not models in its rigorous sense, since they do not represent any concrete phenomena. They are realizations of pure abstract concept of high dimensional chaos. In other words, an object of study is created by the coupled chaotic system. While the coupled chaotic system is an abstract mathematical

object, it is utilized to study actual concrete phenomena of life, especially diversification of the cells (Kaneko, 2006).

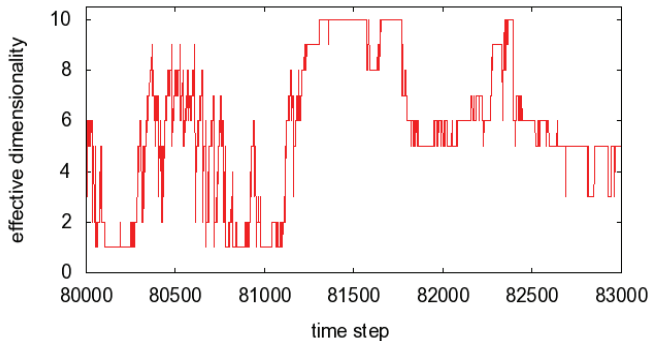


Figure 2. Example of chaotic itinerancy in a system of globally coupled chaotic maps. The effective dimensionality of the system fluctuates with time

### 3. Characteristics of Complex Systems

Above mentioned constructive studies are concerned with complex phenomena, such as chaos and life, in which dynamics and interactions play important roles. This fact is not by a mere chance. Constructive approach is suitable for studying complex dynamical systems. Before explaining the (evolutionary) constructive approach, we discuss the characteristics of complex systems.

Complex systems are not the same as complicated systems. A system composed of mere vast amount of elements or having mere entangled relations may be identified as complicated but not as complex. We claim that complex systems are characterized by three *undecomposabilities* (Hashimoto, 2007). Conventional scientific methodology has made premise three types of decompositions. They are decompositions or separations between operators and operands, between parts and whole, and between observations and observed objects. Most objects of complex systems studies refuse some or all of such decompositions. Conventional descriptions are likely to divide an objective system into states and fixed functions governing the behavior of the states, or into a black box having certain functions and inputs to/outputs from the black box. Suppose that there is an unidentified machine with several buttons and we are going to know how it works. We may try to give the machine some inputs, for example, pushing the buttons, and then wait responses to the inputs. Here, we presuppose that the machine has some states and some functions that are evoked by pushing the buttons. The functions are operators acting on the states and the state changes are brought by the operators. If we can describe good correspondences between the inputs and the outputs, we will feel that we are approaching understand of the objective machine. The objective system is made to resolve into operators, what act on something, and operands, on what the operators act, and the operators are supposed not to change by the operation.

This decomposition is not necessarily obvious for systems with self-referential and self-modification features. In such systems, the movement of the system may act on the system (self-reference) and change the system itself (self-modification). Namely, the systems can

work both as an operator, acting on the system, and an operand, the object of the action, at the same time. This characteristic is called the undecomposability between operators and operands. This undecomposability brings the systems "rule dynamics", i.e., rules describing the dynamics of the systems have dynamics.

Biological evolution has this characteristic. Biological evolution is defined as changes of the gene frequencies in a group of organisms with respect to their environment for adapting to a fitness landscape. In classical view of neo-Darwinian evolution, the organisms unilaterally changes to fit to the environment. The environment selects organisms which can survive in the environment (natural selection). In this view, the environment is an operator and the organisms are operands. But actually, the organisms are not so passive but often modify their environment actively. The environmental change brought by the organisms persists for several generations, and thus the environmental change affect the natural selection. The process to modify the environment or to make a new environment to live is called niche construction (Odling-Smee et al., 2003). In the view of niche construction, biological organisms are both operators and operands. The evolutionary dynamics must be understood from such dynamic viewpoint.

Complex dynamical systems such as language and social institutions are other examples with the undecomposability between operators and operands. Language can be thought of as a system for making and understanding utterances. Any language continues to change with our use of the language. A dead language which no one uses is not subject to change. Social institutions are habits in the ways of thought common to social members. The institutions seem to regulate behavior of the social members. But the institutions are seldom static. Once a social institution established, it is not continue forever. Most of people conform to the institution, the change of the institution occurs often from within the society. Namely, social institutions change with the behavior of the social members, that is regulated by the social institutions. This is a representative of the rule dynamics.

In reductionism, temporal and spatial levels of an object of study are restricted, and it is often said that the whole is the sum of all parts. More macro level than the focusing level is often thought of as closely analogous to static. More micro level than the focusing one is likely to be approximated as random. However, if a small change arisen in one of parts of the objective system is expanded and spread to the whole system, the decomposition of levels and the reduction into partial systems become impossible. It is commonly conceded in many literatures that complex systems do not accept such decomposition. Chaotic systems have this undecomposability. The behavior of the system sharply depends on initial conditions. A small change in the initial conditions or in the state of a partial system may make the state of the system completely different, as described in the previous section.

When a small fluctuation is expanded into the system level, another conventional decomposition between observation and an object of the observation is collapse. Since any observation inevitably perturbs the object, the influence of the observation may become apparent in such system. If a system composed of an observer and an observed object has the undecomposability between operator and operand, that is, the observer is the operator and the object is the operand, the undecomposability between observer and observed object is also induced. In social systems, it is recognized that observation and description, or investigation and its publication, may affect the behavior of the objective social systems. Thus, a methodological problem has been pursued in social science. Several methods different from natural science are devised in social science, such as participatory

observation, ethnomethodology, and action research. The difficulty comes from the fact that biological organisms have subjective agency. They may react differently to the same situation. Therefore, reproducible observations become difficult for biological and social systems.

#### 4. Evolutionary Constructive Approach

A new scientific approach is required so as to progress understanding of dynamic complex system which have the undecomposabilities described above. Here we introduce “evolutionary constructive approach” (Kaneko & Tsuda, 1998; Kaneko & Ikegami, 2000; Hashimoto, 2002; Asada & Kuniyoshi, 2006). It is a methodology in which we try to understand an object through *constructing and operating* the object.

We make a model, often mathematical or computational, of an object and implement the model using some media. This is construction. In making a model and constructing a system, individual concrete phenomenon of the object is not necessarily modeled realistically. As exemplified in section 2, the logic, not materialistic details, to realize the target phenomena is focused on. The systems constructed should consist of elements and factors which are considered to be essential to the objective system. As for the media of construction and operation, we use hardware, such as robots, software, such as computer programs, and wetware, such as biochemical molecules.

In trying to construct a complex object, we may be perplexed by a paradox:

In order to construct something, a blueprint is required. In order to draw the blueprint, the object must be analyzed and understood well. This is a deadlock situation.

Therefore, constructive understanding is impossible for an object which is difficult for analysis and description.

However, in evolutionary systems like life, cognitive system, language, economic and social systems, which have their own intrinsic dynamics, the final complex state is not needed to be designed for construction. Instead, as illustrated in Figure 3, we design a simpler state which has the possibility to attain the final state as a result of change, or which is thought of as the origin of the object; and incorporate mechanisms of change, such as genetic evolution, individual learning, social learning, development or diversification. We call this methodology “the evolutionary constructive approach”. This approach releases us from the paradox that what is too complex to understand cannot be constructed. This approach has another merit. We can observe the changing processes in which initial states arrive at the target state through the process of complexification and structuralization. The mechanisms of change are usually not easy to implement in hardware construction and are not easy to control in wetware construction. Therefore, software construction may be suitable for this approach at the present.

We operate the system constructed. For software construction, computer simulations are performed extensively by testing the varieties of the settings, parameters, initial conditions and algorithms of change. We investigate which setups result in what kind of consequences and observe processes to complexify and structuralize. Through the operation and analysis, we try to clarify what occurs inevitably, in what kind of logic the objective phenomenon occurs, what the sufficient conditions for the objective phenomenon are.

We may observe changing processes or final states that differ from those seen in the actual world, depending on the setups. In this case, knowledge about the “could-be” state of the target phenomenon is obtained. In order to establish the theory of evolution, it is necessary

to attain integrative comprehension including evolutionary paths which possibly might exist. Therefore, recognizing the “could-be” states is important. Experiments of the evolutionary paths in various setups can be repeatedly conducted usually. Besides, many variables of the system are measurable. Therefore, we can treat phenomena of which empirical observation is difficult and objects with historical dependency or a one-time-only nature. Accordingly, the evolutionary constructive approach is an effective method for the comprehension of origin and evolution.

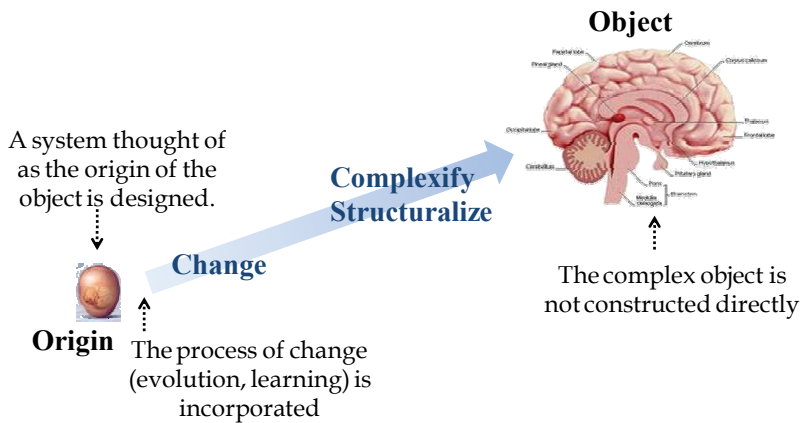


Figure 3. Evolutionary constructive approach

Another effective aspect of the constructive approach is the specification of the details of ideas. When we make a model which can be operated actually in simulations or in robotic systems, we must make every fine features clear and detailed. In the process of specification, we need to formalize the important concept, to determine the relationships among subparts of the model and the idea. We sometimes find a missing link in the logic to form the target phenomena which was overlooked before actual modeling. We may also find such a missing link during operating the model by observing unexpected results. In particular, in cases where multiple causalities and logics work simultaneously, which is usual in complex dynamical systems, we are not good at following such multiple flows of causalities and logics without mathematical or computational thinking tools. In some research areas, researchers often rely on verbal theorizing, even based on empirical evidence. When the objective system is so complex that the verbal theorizing may easily lead us astray, the constructive approach can be used to corroborate or to suspect the reasoning.

The constructive approach concerns to engineering. We construct systems using some media with technologies, often high technologies. In contrast to engineering, the constructive approach may be considered as a scientific methodology, since the purpose of constructive studies is mainly to understand some objects. In engineering, something designed based on conceptualization – be it experiential or theoretical – is constructed and utilized for the world. Therefore, engineering has the directionality “from the concept to the world”, namely, we realize in the world what is conceptualized. On the other hand, science has the directionality “from the world to the concept”, namely, we conceptualize and understand the world. In constructive studies, the methodologies of these two directionalities,



engineering, “concept  $\rightarrow$  world”, and science, “world  $\rightarrow$  concept”, are connected as “concept  $\rightarrow$  world  $\rightarrow$  concept”.

The constructive approach is basically a hypothetico-deductive method. At the first “concept” stage, we have a working hypothesis based on knowledge so far about the objectives. A system is constructed based on the idea that “certain phenomena and process should occur according to existing knowledge and a working hypothesis”. If the process and the phenomena currently assumed are actually realized as results of the operation of the system, it means that the hypothesis was verified in part. Here, the deductive stage is executed through the operation of system constructed. We modify the hypothesis and reconstruct the system, when the assumed consequence is not obtained.

When assumed consequence is realized, we should analyze thoroughly which settings or which part of hypothesis bring the consequence. This analysis may give us a new insight about the core of the problem and the important part of the hypothesis. If we intend to understand further fundamental mechanism of the target phenomena or to study the origin of the objective system, we try to construct a new system in which the setting that brings the assumed consequence in the previous construction is not incorporated as a model. Such setting forms a new object and we search for a hypothesis that realizes the setting as a consequence of evolution in operating the new system.

A nontrivial consequence which was not considered initially may be observed as the result of the operation. This is an *emergence* for a researcher. It is necessary to ask why such a consequence comes out and what kind of significance it has in the target phenomenon, and to clarify the mechanism in which the nontrivial consequence occurs. Accordingly, the emergence must not be left as it is. We have to advance our understanding so that the emergence is resolved as reasonable. By this activity, a new light is shed on the object, generation of a new hypothesis is brought about, and further comprehension progresses. Therefore, the constructive approach plays the role of hypothetical generation and is a tool of thought as well as hypothetical verification.

The new object and new hypothesis leads us the second “concept” stage, and the process of construction and operation continues as “concept  $\rightarrow$  world  $\rightarrow$  concept  $\rightarrow$  world  $\rightarrow$  ...”. In evolutionary constructive approach, new features are added to a system constructed at the later constructions. The accumulative addition of new features is also considered as a kind of evolutionary process.

We should notice that, in the constructive approach, while finding sufficient conditions may be possible, a necessary condition cannot be acquired. Even if the target state can be attained starting from a certain setting and condition, there may always be a possibility that the setting and the condition are not indispensable to attain the state, because other settings and conditions may bring about the target state. It will, however, be possible to narrow sufficient conditions by repeating experiments with various setups and elaborating models. Moreover, it is also impossible to answer the question concerning origins straightforwardly by this approach, i.e., “when” an event occurred in the actual world. The constructive approach can contribute to find essential logic, that is, the “how” question, while the “when” question must be clarified by empirical evidences. One possible course to approach the “when” question in constructive studies is to clarify strict conditions for the event to occur and to propose reasonable hypotheses, about the conditions for the event to come into being, which should be provable with empirical evidence.

## 5. Examples of Evolutionary Constructive Simulations

In this section three example studies taking the evolutionary constructive approach are introduced. The examples are concerned with institutional change and language dynamics. As we saw in section 3, they are typical objects of complex systems study. Concretely, we describe the simulations about 1) Endogenous dynamics of macro social structure, 2) Meaning change and displacement in evolution of language, and 3) Dynamics of communication.

### 5.1 Endogenous Dynamics of Macro Structure

We apply the evolutionary constructive approach to dynamic social phenomena (Sato, 2005; Sato & Hashimoto, 2007). The target phenomenon of the study introduced in this subsection is the endogenous changes of social structures/institutions. We ask how the dynamics of macro structures in a society, such as institutions, occurs endogenously. Social structures and social institutions are often considered as equilibria, especially in neo-classical economics. If a society is really in an equilibrium and is not given an exogenous shock, no change occurs in the society. In actual fact, however, we often experience changes in the social structures and institutions. We think that not all of the changes are induced by external sources.

The key ideas for the endogenous social dynamics are the internal dynamics of individuals and the micro-macro loop. The internal dynamics is autonomous change of the individual's internal states. We think social individuals have internal states and the states change dynamically, especially in humans, even without any change in the outside of the individuals. The internal dynamics can explain the diversity and the consistency of human behavior. Individuals can act differently under the same environmental state, if they have various internal states. If the states change dynamically, not random, the behavior may have some causal relationships. The micro-macro loop is a mutual relationship of dependences or influences between micro and macro levels in a society (Shiozawa, 1999). The micro-macro loop should be discriminated from micro-macro couplings. There are many macro variables in a society which are decided by actions of the social members, for example, the stock prices, GDP, the average income, and so on. Some of them are just the sum or the average of all members' variables and affect the actions of social members. We regard such interactions between the micro and macro *variables* as the micro-macro coupling. On the other hand, the micro-macro loop is structural relationships between micro and macro *structures*.

#### 5.1.1 Modeling of Agent and Social Interaction

The agent with internal dynamics is modeled by a kind of neural network with recursive connections. The architecture of the neural network, drawn in Figure 4, is equipped with two recurrent connections. One is between a hidden layer and a context layer, which is introduced by Simple Recurrent Network (Elman, 1990). The other is between output and input layers. The system's own past output affects its behavior through the latter connection. We call this architecture Simple Recurrent Network with Self-Influential Connection (SRN-SIC). The hidden layer represents the internal state. In addition to the external stimuli, the network changes its output based on the internal state and its own past output, which forms the internal dynamics. This type of neural network can learn a time

series by adjusting the synaptic weights according to teacher signals. We use the back propagation algorithm for the learning.

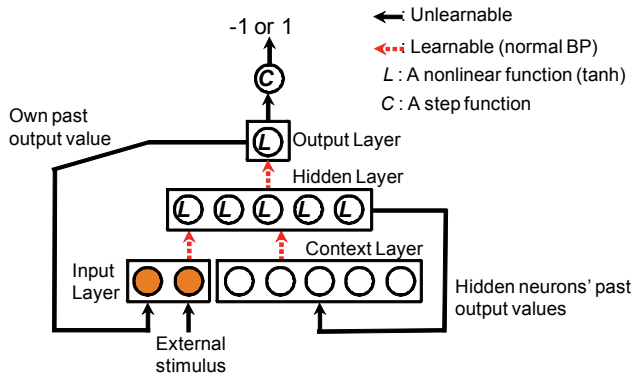


Figure 4. Simple Recurrent Network with Self-Influential Connection (SRN-SIC): Each circle is a neuron. A group of the neurons, a layer, is surrounded by a square. A neuron is added after the output in order to make the outputs from the network rounded to the choices of the minority game. The synaptic weights of the recursive connections are fixed at 1.0

In this study, the social interactions among the agents is modeled by the minority game (Challet & Zhang, 1997) in which players selecting a minority choice from two alternative choices, say -1 and 1, win. This game is the model of a competitive situation for limited resources, which is common in a society, such as market, mating, competition for water and food source, and so on.

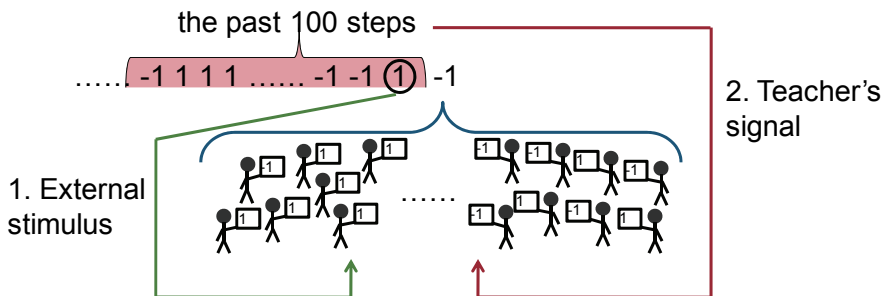


Figure 5. The micro-macro coupling in our system

The micro-macro coupling is explained in Figure 5. The winner of game, that is, the minority side, is the macro variable of the system. This is decided from the choices of all players, which are the micro variables. This is the coupling from micro to macro. We prepare two couplings from macro to micro. One is that the last minority side is given to the agents as an external stimulus. The other is that a past time series of the minority side is given to all agents as a teacher's signal to learn. We consider dynamical patterns in the time series of minority side as the macro structure and the neural network structure shaped through the learning as the micro structure, which represents the behavioral rule of each agent.

### 5.1.2 Simulation Results

The computer simulation of this system was done with the following parameter settings:

- The number of agents: 101
- Learning: every 10,000 games
- Teacher's signal: 100 past steps
- Learning rate, momentum coefficient, nonlinearity of neurons: 0.01, 0.8, 0.8
- Initial learnable synaptic weights: uniform random value between -0.5 and 0.5
- Initial input to the input and context layer neurons: 0.0

This system shows the variety of dynamic patterns at the macro level, both in the minority side and in the number of the winners (Figure 6). Among others, the most interesting pattern is Figure 6(d). In this pattern, both the minority side and the number of winners change aperiodically.

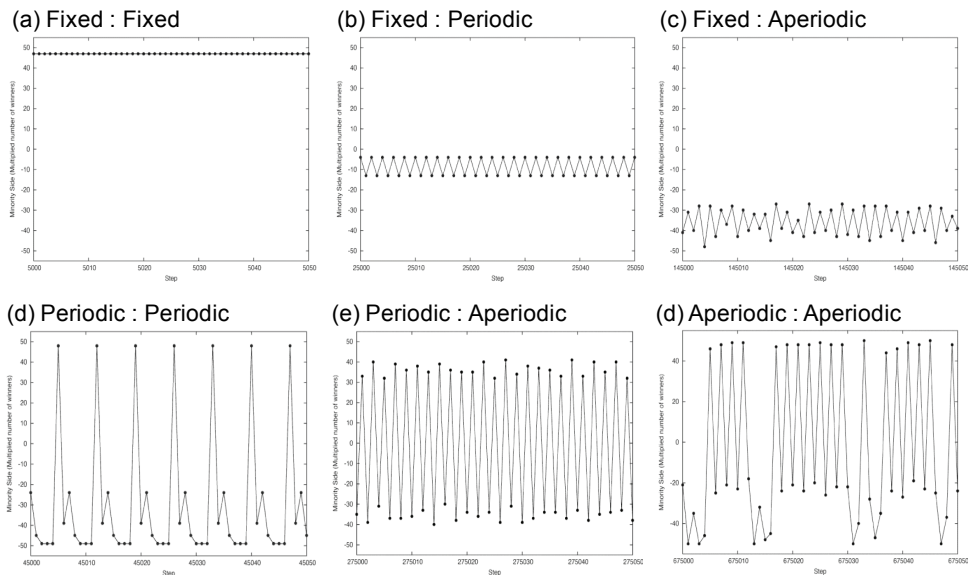


Figure 6. The dynamic patterns at the macro level: The X axis is the steps, the Y axis is the minority side (-1 or 1) times the number of winners. The label above each graph means that the first one is the dynamical state of the minority side and the second that of the number of winners

We closely analyzed this aperiodic pattern. The long term dynamics of the minority side is shown in Figure 7 which is the dynamics of the weighted moving average of the minority side in 20 steps. The  $i$ th past step is weighted by  $2^{-i}$ , namely, the older information is more lightly weighted. As we see, the state chaotically change among various ordered dynamical patterns, fixed at 1.0 or -1.0 and periodic cycles with different periods, through aperiodic motions. It is a similar dynamics to chaotic itinerancy (Kaneko & Tsuda, 2003), a spontaneous transition among attractors, which is introduced in section 2. Note that this dynamics occurs in between learning (within 10,000 steps). Therefore no change takes place in the structures of neural networks and no external disturbance exists. We have confirmed that this dynamics does not cease how long the calculation continues without learning.

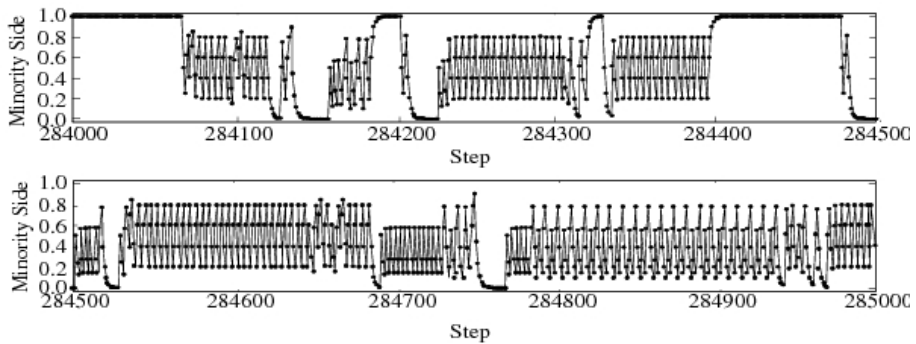


Figure 7. Itinerant dynamics of the minority side: The Y axis is weighted moving average of the minority side

We found that the agent had chaotic internal dynamics under the macro itinerant dynamics. An instance of the internal dynamics of an agent is exemplified in Figure 8 which shows the state change of two hidden and output neurons. This resembles a strange attractor. We measured the correlation dimension and the lyapunov exponent (Figure 9). This measurement proved that the agent structure has low dimensional chaos with weak nonlinearity (the correlation dimension is 0.92, the lyapunov exponent is around 0.02). We also found that when the macro dynamics shows the itinerant dynamics, the micro level is occupied by the agents with aperiodic, maybe chaotic, motions (Table 1).

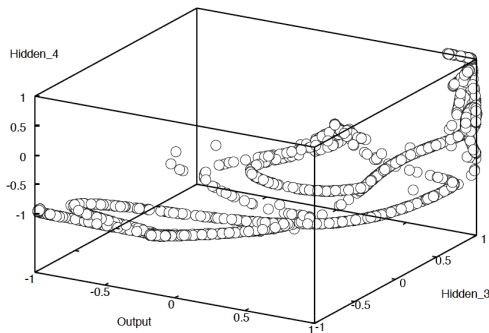


Figure 8. The internal dynamics of an agent when the macro level shows itinerant dynamics: The X and Z axes are the state of some hidden neurons. The Y axis is the state of the output neuron (before rounding)

### 5.1.3 Discussion: Itinerant Dynamics and Rule Dynamics

The itinerant dynamics (Figure 7), i.e., the continuous transitions among ordered patterns, at the macro level is interpreted as the perpetual changes of social structures, since the fact that the system with many individuals (very high dimension) is in a low dimensional dynamical state implies that the system has some sort of order, that is, structuralized. This dynamics is a kind of rule dynamics. The agents behave with certain order, namely, they seem to share a kind of rules to govern their behavior. These rules undergo changes by their behavior. An important point is that the agents' internal structures do not undergo any change, for no

learning takes place in that period. The agents acquire the internal structure that is able to induce the macro changes. This is confirmed by the fact that most agents have chaotic internal dynamics (Figure 9). Chaotic dynamics can expand small fluctuations into the whole system scale. As we discussed in section 3, this situation causes the undecomposability between parts and whole. Since there are many agents with chaotic internal dynamics in the case of itinerant macro dynamics (Table 1), a small fluctuation of one agent transmits to the other agents with expansion and finally the whole structure is modified.

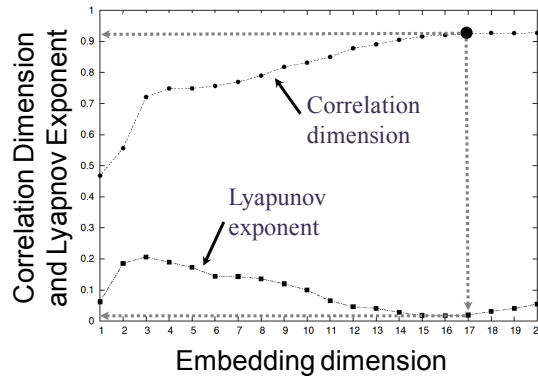


Figure 9. The correlation dimension and the lyapunov exponent of the internal dynamics of an agent depicted in Figure 8

Macro Level		Micro Level		
Minority Side	# of Winners	Fixed	Periodic	Aperiodic
Fixed	Fixed	101	0	0
Fixed	Periodic	84	17	0
Fixed	Aperiodic	50	46	5
Periodic	Periodic	63	38	0
Periodic	Aperiodic	20	77	4
Itinerant	Itinerant	8	6	87

Table 1. The number of agents having three types of internal dynamics, fixed, periodic and aperiodic in the various macro dynamical patterns

The competitive interaction implemented in the minority game also plays important role for the rule dynamics. When there is a rule at the macro level, the agents try to play the winner’s move by following the rule. But more than half agents go to the “winner’s side”, the side is no more winner. Thus, the macro rule collapses. Since the macro rule is not a mere operator for the micro behavior, we can find the undecomposability between operator and operand. We have confirmed that the itinerant dynamics is not observed under the cooperative interaction, the majority game (Sato, 2005).

The micro-macro loop is considered to be established in our system. The ordered dynamical pattern at the macro level, which implies the macro structure, is composed of the dynamical patterns in the internal structures of the agents, which are the micro structures. The agents acquire the micro structure through learning of the macro dynamics. We have also

confirmed that the removal of the micro-macro loop eliminated the itinerant dynamics (Sato, 2005).

We can conclude that endogenous dynamics of macro structure is likely to be induced by the chaotic internal dynamics, the competitive social interaction and the micro-macro loop.

### 5.2 Cognitive Modeling for Language Evolution and Displacement

The second topic is the dynamics of language. Humans have cognitive ability not only to acquire and use symbols but also to create them. One characteristic of the human symbol system is displacement. Displacement is to refer something detached from “now, here and I”. Namely, it is to be away, in space, in time and in subject, from the place where the body and the mind exist. It is said that the displacement is one of the critical natures that discriminate human communication system from other animals’ communication systems. Other important features of the human communication system, such as symbolism and syntax, are found in animals’ communication systems, for example, of verbet monkey (Cheney & Seyfarth, 1985) and birdsong (Okanoya, 2002). Messages of animal communication are practically about situations that a sender or a receiver confront, especially about biologically fundamental affairs such as survival, danger and reproduction. Considering about displacement is an important issue in the emergence and the evolution of human symbol system, and also of human language. Further, it is straightforwardly understandable that the displacement brings creativity.

The emergence and evolution of the symbol system can be divided into four stages as described in Figure 10. The first stage is articulation, in which object to be referred is singled out as an entity. The second is the stage of labelling or symbolization, in which a sign is assigned to the entity. The sign becomes a symbol. Symbol grounding is concerned with this stage. Next stage is to manipulate the entity referred virtually through manipulating the symbol. Artificial intelligence had aimed at realizing this stage. The last stage is to release static connection between signs and entities, and to make signs represent or to create new entities and new meanings. This stage can be called as symbol expansion or meaning creation.

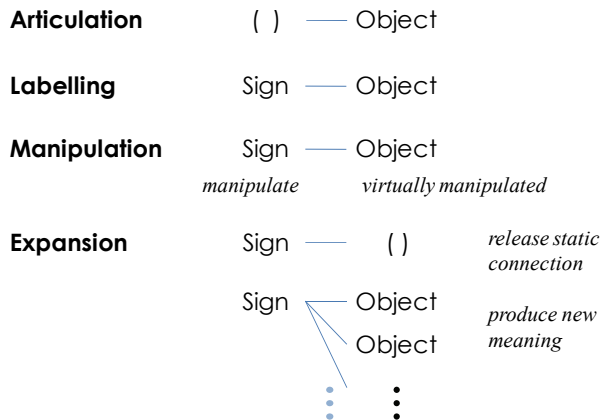


Figure 10. Four stages in the evolution of symbol system

The displacement is related to this forth stage. In this subsection, we study the symbol expansion and the meaning creation by considering a kind of language change processes called grammaticalization with the evolutionary constructive approach.

### 5.2.1 Grammaticalization

Grammaticalization is a type of meaning change in which content words obtain functional meanings (Heine, 2005). The content words represent some contents like nouns, verbs and adjectives. The functional words play some grammatical roles like auxiliary verbs, prepositions and conjunctions. A representative example of grammaticalization is “be going to” in English, in which a content word “go” acquired a functional meaning of future tense. In the process of grammaticalization, meanings of a word often changes from concrete meaning related to a part of body or bodily experiences to an abstract concept such as space or time, and then further abstracted to represent grammatical function. This change is usually unidirectional from content to functional and from concrete to abstract. This unidirectionality is a remarkable feature of grammaticalization. The unidirectionality of grammaticalization progresses from representing concrete experiences to expanding symbol relations into abstract entities. This coincides with the fourth evolutionary stage of the symbol system illustrated in Figure 10. Another important feature of grammaticalization is universality. Similar changes are found in many different languages (Heine & Kuteva, 2002a). The universality and the unidirectionality imply the universal tendency of human cognition.

Grammaticalization is interesting from the viewpoint of language evolution (Heine & Kuteva, 2002b; Hurford, 2003; Newmeyer, 2006). Language evolution is a long term changing process of complexification and structuralization of human languages from an initial language which is expected to be simpler than the present. The fact that grammaticalization is unidirectional and universal brings an insight that the initial language may be composed of only content words (nouns and verbs) and have complexified through the processes of grammaticalization (Hurford, 2003).

Further, considering what cognitive structure causes the unidirectional language changes from concrete to abstract will yield knowledge about the origin of language. The origin of language is a biological evolutionary process in which human cognitive abilities related to language emerged and evolved. In order to clarify such evolutionary process, the evolutionary constructive approach is effective, since the process must be complex and empirical evidences are rare. Constructing and operating models of language change and language evolution are to search for structures, settings and conditions for general properties of human language to be possible (Hashimoto & Nakatsuka, 2006).

### 5.2.2 Cognitive Modeling of Grammaticalization

We explain the modeling of grammaticalization. The description is limited to the important part because of the space limit. The details should be referred to (Nakatsuka, 2006; Hashimoto & Nakatsuka, 2007).

We focus on reanalysis and analogy which Hopper & Traugott (2003) point out as the necessarily processes for grammaticalization. Reanalysis is internal structural change of sentences, which is not apparent at the level of forms. Analogy is to generalize grammatical rules and to apply a rule to forms in which the rule is not applied formerly. We think of



them as cognitive abilities of language users and equip agent with the following three abilities:

- Reanalysis : ability to articulate sentences based on contextual information and existing knowledge
- Cognitive analogy : ability to find similarities among situations and among forms
- Linguistic analogy : ability to apply linguistic rules extensively in its own knowledge

We adopt the iterated learning model (Kirby, 2002) as the interaction between agents, which is illustrated schematically in Figure 11. Suppose two agents, a speaker and a learner, look at various situations. The learner attempting to acquire language receives utterances which describe the situations from the speaker who already has linguistic knowledge. The linguistic knowledge is composed of rules to correspond situations or part of situations (meaning) to utterances or part of utterances (forms), category/⟨meaning⟩ → form. The learner structuralizes its own linguistic knowledge in order to produce appropriate utterances for situations. After a while of learning, the learner becomes to a new speaker and a new learner is introduced. They compose the next generation. The new speaker gives the new learner language inputs based on its knowledge acquired at the learning process. It is a characteristic of the iterated learning model that linguistic knowledge is transmitted and structuralized through generations.

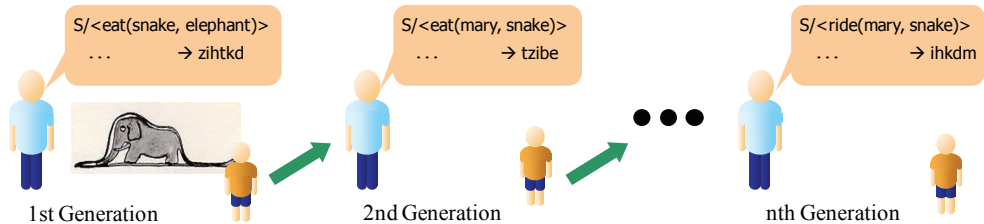


Figure 11. A schematic view of iterated learning model

In this learning process, the learner performs three learning operations, called chunk, merge and replace, to generalize linguistic knowledge. These operations have the following correspondences to the abilities of the agent (Hashimoto & Nakatsuka, 2006): Reanalysis is realized mainly by chunk. Cognitive analogy is premised in all three operations. Linguistic analogy is realized mainly by replace.

We further introduce two designs of meaning space: pragmatic extension and cooccurrence. The former is to make use of a form representing a meaning in order to describe another meaning. The latter is that a meaning often appears with another particular meaning.

### 5.2.3 Simulation Results

The simulations were done under the following setting:

- Meanings: 5 verbs, 5 nouns, 3 tense meanings, ⟨past⟩, ⟨present⟩ and ⟨future⟩
- Pragmatic extension: the speakers can make use of forms for ⟨run⟩ and ⟨walk⟩ to describe the meaning ⟨go⟩
- Cooccurrence: two meanings ⟨go⟩ and ⟨future⟩ have high probability to appear in the same situations
- The number of utterances in one generation: 50
- Initial knowledge: both a speaker and a learner do not have any rules.

The frequencies of application of the three learning operations, chunk, merge and replace, change with generations as Figure 12 (left). The frequency of replace operation is much larger than the other two. This operation works effectively for promoting the descriptive power of linguistic knowledge. We made an experiment in which the learners cannot use replace operation. In this case, the application frequency was not compensated by remaining two operations as seen in Figure 12 (right) and the total frequency decreases than the case with replace. The descriptive power does not grow so much. The important finding is that meaning change, that is, a form representing a meaning at some generation becomes to represent another meaning at later generations, is rarely observed.

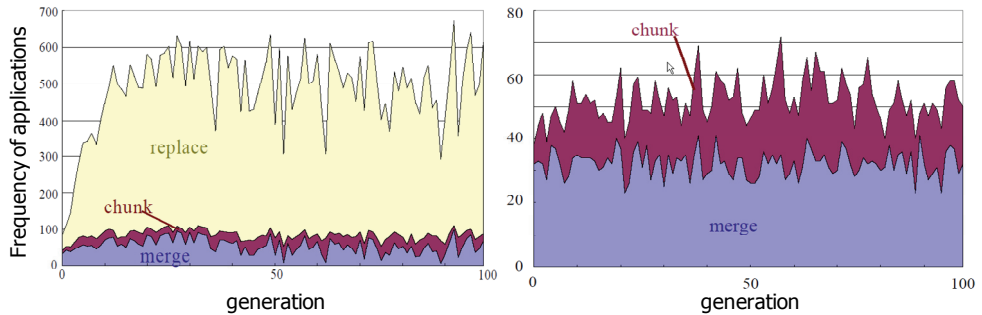


Figure 12. The application frequency of three learning operations with replace (left) and without replace (right)

There are four conditions about introducing the two designs of meaning space. We counted the frequency of meaning change for all four conditions. Figure 13 shows the total frequency of meaning changes. The results of significance testing are written above the bars. The solid and dashed lines mean the difference between two values is significant or not, respectively. It is found from this result that setting the pragmatic extension significantly heightens the meaning change. We then counted the frequency of meaning change concerning grammaticalization, that is, from <go> to functional meanings, <past>, <present> and <future> (Figure 14). In this case, introducing the cooccurrence makes the frequency from <go> to <future> twice than the other changes. From these results, we found that the pragmatic extension promotes the meaning change and the occurrence brings the unidirectionality.

#### 5.2.4 Discussion: Significance of Replace Operation

We showed that the replace operation is indispensable for meaning change. In order to consider what is the significance of replace operation, we explain this operation. The replace is defined as follows: When a meaning and a form in a rule are included in another rule, the latter is replaced with a new rule having a variable where the former is substituted. For example, suppose an agent has two rules,

$$N / \langle \text{john} \rangle \rightarrow \text{ot},$$

$$S / \langle \text{read}(\text{john}, \text{book}) \rangle \rightarrow \text{swote},$$

where N represents a category of the meaning <john> belonging to and S represents a sentence. Since both rules have <john> in the left hand side and "ot" in the right hand side, the replace operation can be applied. The latter one is replaced by a new rule

$$S / \langle \text{read}(x, \text{book}) \rangle \rightarrow \text{sw } N / x e ,$$

where  $x$  is a variable.

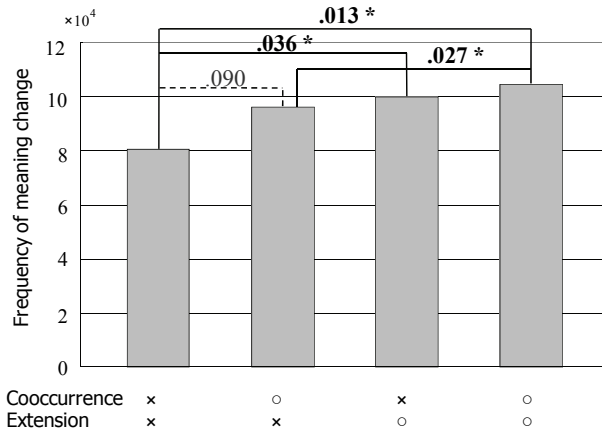


Figure 13. The total frequency of meaning change for four conditions about cooccurrence and pragmatic extension

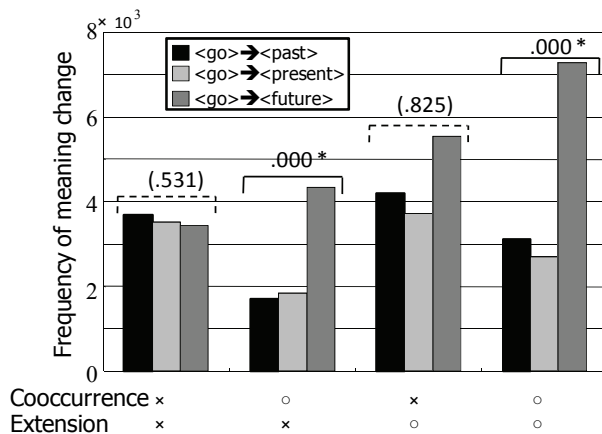


Figure 14. The frequency of meaning change from <go> to functional meaning for four conditions about cooccurrence and pragmatic extension

Note that any rule in the category N can be substituted in the variable. If the agent has other rules in the category N, say  $N / \langle \text{elephant} \rangle \rightarrow \text{ir}$ , the agent can produce an utterance corresponding to a situation  $\langle \text{read}(\text{elephant}, \text{book}) \rangle$  using the rule set after the replace operation. The rule before the replace operation is acquired through an experience to watch a situation “John reads a book” and to hear an utterance “swote”. But extensive application of the new rule acquired by the replace operation makes new utterances about situations that were not in the agent’s experience.

This feature to produce sentences about situations detached from direct experiences is thought of as corresponding to displacement. The replace operation realizes the linguistic analogy. It is

suggested that the linguistic analogy in which a linguistic rule acquired is applied extensively to other rules is important for meaning change. We can consider that the significance of the linguistic analogy is caused by learning operation bringing the displacement.

### 5.3 Dynamics of Communication

Communication is a dynamic process. A symbol used in communication is composed of three terms: form, reference and interpretation (Peirce, 1935). The interpretation is physically unknowable different from the other two terms. Further, people often have different ways of interpretation and the ways are unknowable by other people. Despite of the unknowability, we communicate with each other. We are engaged in communication under a tacit supposition that the counterpart of the communication must have the same interpretation. Since the difference between interpretations actually remains, however, inconsistency and misunderstanding inevitably become unconcealed and the communication sometimes fails. We try to communicate again by modifying our interpretation under a supposition that this modification should be valid. Namely, communication has the dynamics of success and failure in mutual understandings. In this section, we try to model such dynamic feature of communication (Fujimoto & Hashimoto, 2008).

#### 5.3.1 Modeling Communication Dynamics Based on Language Game

As we have mentioned, communication has the following features:

- Inconsistency of interpretation occurs on the way of communication and we retry communication through modification of interpretation.
- Even if a way of interpretation once leads to successful communication, the success with the same way of interpretation in following communication is not guaranteed.
- Success and failure of mutual understanding continues forever.

We hypothesize that ambiguity and context play important roles for maintaining the dynamics of success and failure in communication.

Our modeling is based on Steels' Language Game (Steels, 1996; Steels & Kaplan, 2002). The Language Game is a model of language evolution, in which an establishing process of the common vocabulary is represented. The basic procedure of the Language Game is the following:

1. Some of objects, discriminated by IDs, are decided (randomly) as an object-set.
2. A speaker selects one topical object from the object-set and utters a name of the topical object according to its own lexicon.
3. A hearer answers an object according to its own lexicon.
4. If the answer is correct, the communication is success. If not correct, the speaker teaches the hearer the selected object and the hearer updates its lexicon by recording the correspondence between the name and the object's ID.

A cycle from the stage 2 to 4 is called one step.

Repeating this procedure, the agents who cannot communicate with each other at first come to be mutual understanding finally. That is a process from failure to success of communication. But after a while they succeed always, if there is no change in the objects or in the communicating members. Namely, the dynamics of communication fades away.

We introduce two features concerning our assumption into the Language Game. One is a mechanism to maintain the ambiguity of symbols, the other is a disambiguation mechanism

of the polysemous symbols by utilizing contextual information. We construct two new games. In one game, called game A, hereafter, the following two settings are added:

- Each object has multiple features in addition to ID. The speaker gives particular names to all features and ID. The hearer accepts all utterances as names of the objects' IDs. This device is for ambiguity.
- The hearer reconfigures its lexicon sometimes. In the reconfiguration process, the hearer finds a feature that is common to all objects having the same name and makes the name and the common feature correspond. This process represents a kind of induction to disambiguate polysemous names.

The other one, game B, has the following setup:

- All objects are discriminated only by IDs (no features).
- The number of symbols is restricted. This promotes ambiguity.
- Each object-set has particular objects that appear with high probability. This setting is called "situation". The speaker names each object associated to the situations. Situation changes sometimes but the hearer cannot notice the change of situation.

### 5.3.2 Simulation Results

The computer simulation of the game A was done with the following parameter settings:

- The number of objects: 50
- Features: 3 features and 3 values for each feature; Form {circle, triangle, square}, Color {red, green, blue}, Size {large, middle, small}
- The number of names: 60
- Lexicon reconfiguration: Every 100 steps or 200 steps (different simulation runs)
- Initial lexicon: Both the speaker and hearer do not have any name.

Name	ID	Form	Color	Size	Name	ID or Feature
34	23	Square	Blue	Large	34	Square
34	41	Square	Green	Small	1	Small
34	11	Square	Green	Middle	9	34
15	50	Circle	Blue	Middle	13	Circle
33	50	Circle	Blue	Middle	24	24
1	32	Circle	Green	Small	5	Red
1	2	Triangle	Red	Small	39	14
1	8	Triangle	Red	Small	32	1
					17	7

Table 2. Parts of the hearer's lexicon before (left) and after (right) several times of the reconfigurations in the game A with 100 step interval of reconfiguration

Table 2 (left) shows a part of hearer's lexicon at the 199th steps in the game A with 100 step interval of reconfiguration. This timing is just before reconfiguration. There are some ambiguous symbols, shaded in the table. Namely, the names correspond to plural objects (IDs). The ambiguity was lost through reconfigurations. The right table depicts a part of the hearer's lexicon at the 900th step. Each name makes one-to-one correspondence to an ID or a feature. The communication became full success, the same as Steels's Language Game (Steels, 1996), with the lost of ambiguity as shown in Figure 15. The reconfiguration by induction is so strong in this small lexicon that all ambiguity resolved. No dynamics of communication was found in this game.

Next, we describe the simulation results of the game B. The setting of game B is as follows:

- The number of objects: 30
- The number of symbols (names): 10
- Four of five objects are peculiar to a situation.
- The number of situations: 5
- The situation changes every 5 steps. New situation is randomly selected from 5 situations.

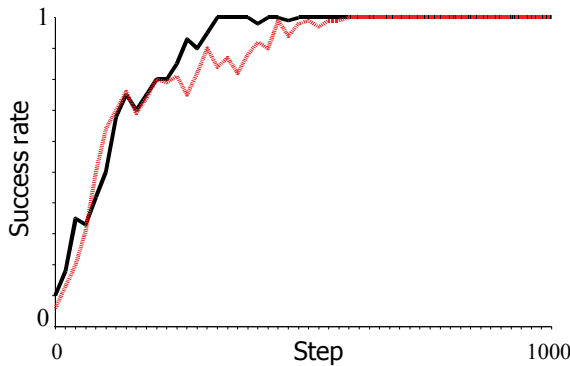


Figure 15. The change of the success rate of communication in game A with 100 step intervals of reconfiguration (solid) and 200 step intervals (broken)

Table 3 is parts of lexicons of the speaker and the hearer at the 200th step. All names in this table are ambiguous, i.e., one name corresponds to plural objects. The success rate of communication changes with steps as shown by the solid line in Figure 16. It grows roughly until around the 100th step (25th situation), but stays around 0.5 with fluctuations after the 100th step. Even after acquiring all names, communication between the agents may fail since the hearer does not know when situation changes. This dynamics does not disappear how long the communication continues.

<i>Speaker</i>			<i>Hearer</i>		
Name	Obj.	Sit.	Name	Obj.	Sit.
2	3	1	2	3	1
	2	3		2	3
	3	3		18	4
4	5	3		5	3
	7	5	7	5	
7	6	2	5	1	2
	6	5		4	3
9	14	4		23	1
	2	2		27	3
	11	2		9	2
			11	2	

Table 3. Parts of the lexicons of the speaker (left) and the hearer (right) at the 200th steps

We compare the success/failure between at the beginning and the end of each situation (Figure 17). The bottom graph is apparently dense. This means that the hearer identifies the situation through communication and can decide the meanings of ambiguous names utilizing the information of situation.

The ambiguity sometimes brings “superficial” success of communication. The hearer succeeds communication at the beginning of new situation but fails at the next step in the same situation. Namely, the hearer does not understand the situation at that time. But thanks to the ambiguity of symbols, the agents happen to succeed the communication.

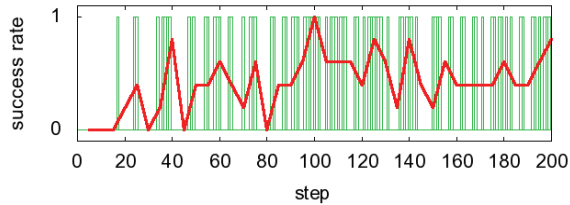


Figure 16. The success rate of communication averaged per each situation (5 steps) (line) and the success/failure of communication at each step (bars). 1 and 0 mean success and failure, respectively

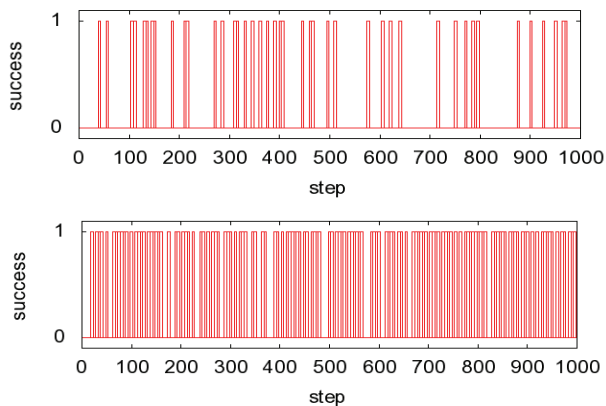


Figure 17. The success and failure at the beginning (top) and the end (bottom) of each situation

### 5.3.3 Discussion: Role of Ambiguity and Context

We are engaged in communication with indefiniteness and mutual understanding. These two antithetical features make our communication dynamic. In our simulation, we introduce ambiguity and context into Language Game. The indefiniteness is realized by the ambiguity of symbols and the change of the context. But if inductive reasoning is too strong, the ambiguity is disambiguated completely and the indefiniteness may fade away. The mutual understanding is attained by utilizing the contextual information. We found that the ambiguity also works to yield “superficial” communicative success.

We have realized the dynamics of communication by ambiguity and context in our model (game B). Thus, our hypothesis is verified to some extent. The critical point, however, to induce the dynamics of communication is the change of context. If the context does not change, the agents may attain the full success. The change of the context is implemented by hand in our present model. The context change should be endogenous in order truly to

realize the dynamics of communication. This means that rule dynamics should be introduced to our model. The context plays as a rule in communication. The progress of communication in a context leads to the change of the context in natural language conversation. This study can be thought of as revealing the crucial importance of the rule dynamics in communication.

## 6. Conclusion: Towards Embedding Subjectivity in Objective System

In this chapter, we have discussed the evolutionary constructive approach as a methodology to study dynamic complex systems. In the evolutionary constructive study, we construct an objective system including some mechanism of change, and we operate the system. The constructive studies introduced in the previous section are concerned with intrinsic dynamics in social and linguistic systems the endogenous changes of social structures; the displacement causing language change and creativity; and continuing the success and failure of communication. From the viewpoint of complex systems explained in section 3, these themes are associated with rule dynamics, in which the operation of a system induces the change of the system's governing rules, and therefore associated with the undecomposability between operator and operand. The example studies represent that the evolutionary constructive approach has suitability for treating such dynamic complex systems.

Since we often treat the biological, cognitive, linguistic and social issues in constructive studies, the models are usually agent-based and consist of cognitive individuals. The individuals are equipped with internal structure, internal dynamics and mechanisms to change their internal states and internal structures. The individuals change their internal structures according to interactions with the circumstances and other individuals. The individuals develop their own ways to behave in their world, which is a basis of subjectivity and autonomy. We study the whole system consisting of such individuals objectively. Using evolutionary constructive approach, we may be able to embed systems having subjectivity and autonomy or systems having the ability to develop subjectivity and autonomy in a system that is an object of scientific investigation. Conventional scientific methodology is not good at dealing with subjectivity, since scientific research becomes possible by finding an objective entity in which subjective feature is stripped off. But treating subjectivity scientifically is unavoidable, if we are going to deepen our insight about complex systems as we described in section 3. We should develop further the evolutionary constructive approach in order to make such embedding possible.

## 7. References

- Alligood, K. T., Sauer, T. & Yorke J. A. (1996), *Chaos: An Introduction to Dynamical Systems*, Springer, ISBN: 978-0387946771, Berlin
- Asada, M. & Kuniyoshi, Y. (2006), Synthetic study of intelligence (in Japanese), In: *Robot Intelligence*, Asada, M. & Kuniyoshi, Y., pp. 14-26, Iwanami Shoten, ISBN: 978-4000112444, Tokyo
- Challet, D. & Zhang, Y.-C. (1997), Emergence of cooperation and organization in an evolutionary game, *Physica A*, Vol. 246, No. 3-4, 407-418, ISSN: 0378-4371
- Cheney, D. L. & Seyfarth, R. M. (1985), Vervet monkey alarm calls: manipulation through shared information?, *Behaviour*, Vol. 94, No.1-2, 150-166, ISSN: 0005-7959



- Conte, R., Hegselmann, R. & Terna, P. (Eds.) (1997), *Simulating Social Phenomena*, Springer, ISBN: 978-3540633297, Berlin
- Elman, J. L. (1990), Finding structure in time, *Cognitive Science*, Vol. 14, No. 2, 179-211, ISSN: 0364-0213
- Fujimoto, M. & Hashimoto, T. (2008), Constructive study on dynamics of communication: The role of ambiguity and context, *The Proceedings of International Conference of Cognitive Science 2008*, Seoul, Korea, July, 2008 (To appear)
- Gilbert, N. & Troitzsch, K. G. (2005), *Simulation for the Social Scientist* (2<sup>nd</sup> edition), Open University Press, ISBN: 978-0335216000, Berkshire
- Hashimoto, T. (2002), The constructive approach (in Japanese), In: *Knowledge Science*, Sugiyama, K. Nagata, A. & Shimojima, A. (Eds.), pp.132 - 135, Kinokuniya Shoten, ISBN: 978-4314101530, Tokyo
- Hashimoto, T. (2007), Three types of undecomposabilities in complex systems, *Proceedings of European Conference on Complex Systems (ECCS2007)* (CD-ROM), Dresden, Germany, October, 2007
- Hashimoto, T. & Nakatsuka, M. (2006), Reconsidering Kirby's compositionality model - towards modelling grammaticalization In: *The evolution of language*, Cangelosi, A., Smith, A. D. M. & Smith, K. (Eds.), pp. 415-416, World Scientific, ISBN: 978-9812566560, Singapore
- Hashimoto, T. & Nakatsuka, M. (2007), Constructive modeling of grammaticalization: from the viewpoint of evolutionary linguistics (in Japanese), In: *The Proceedings of the Japanese Cognitive Linguistics Association*, Vol. 7, 33-43
- Heine, B. (2005), Grammaticalization. In: *Encyclopedia of Linguistics volume 1*, Strazny, P. (Ed.), 402-404, Fitzroy Dearborn, ISBN: 978-1579583910, Chicago
- Heine, B. & Kuteva, T. (2002a), *World Lexicon of Grammaticalization*, Cambridge University Press, ISBN: 978-0521005975, Cambridge
- Heine, B. & Kuteva, T. (2002b), On the evolution of grammatical forms. In: *The Transition to Language*. Wray, A. (Ed.), pp. 376-397, Oxford University Press, ISBN: 978-0199250660, Oxford
- Hopper, P. J. & Traugott, E. C. (2003), *Grammaticalization* (2<sup>nd</sup> edition), Cambridge University Press, ISBN: 978-0521804219, Cambridge
- Hurford, J. R. (2003), The language mosaic and its evolution, In: *Language evolution*, Christiansen, M. H. & Kirby, S. (Eds.), pp. 38-57, Oxford University Press, ISBN: 978-0199244836, Oxford
- Kaneko, K. (1986), *Collapse of Tori and Genesis of Chaos in Dissipative Systems*, World Scientific, ISBN: 978-9971978617, Singapore
- Kaneko, K. (1990), Clustering, coding, switching, hierarchical ordering, and control in network of chaotic elements, *Physica D*, Vol. 41, No.2, 137-172, ISSN: 0167-2789
- Kaneko, K. (2006), *Life: An Introduction to Complex Systems Biology*, Springer, ISBN: 978-3540326663, Berlin
- Kaneko, K. & Ikegami, T. (1998), *The Evolutionary Scenario of Complex Systems* (in Japanese), Asakura Shoten, ISBN: 978-4254105155, Tokyo
- Kaneko, K. & Tsuda, I. (2000), *Complex Systems: Chaos and Beyond - A Constructive Approach with Applications in Life Sciences*, Springer, ISBN: 978-3540672029, Berlin
- Kaneko, K. & Tsuda, I. (2006), Chaotic itinerancy, *Chaos*, Vol. 13, No. 3, 926-936, ISSN: 1054-1500

- Kirby, S. (2002), Learning bottlenecks and the evolution of recursive syntax, In: *Linguistic Evolution through Language Acquisition: Formal and Computational Models*, Briscoe, T. (Ed.), pp. 173-203, Cambridge University Press, ISBN: 978-0521662994, Cambridge
- Li, T.-Y. & Yorke, J. A. (1975), Period three implies chaos, *The American Mathematical Monthly*, Vol. 82, No. 10, 985-992, ISSN: 0002-9890
- Lorenz, E. N. (1993). *The Essence of Chaos*, University of Washington Press, ISBN: 978-0295975146, Washington
- Lorenz, E. N. (1963), Deterministic nonperiodic flow, *Journal of the Atmospheric Sciences*, Vol. 20, 130-141, ISSN: 0022-4928
- Nakatsuka, M. (2006), *Modeling of Grammaticalization Based on Reanalysis and Analogy* (in Japanese), Master Thesis of School of Knowledge Science, Japan Advanced Institute of Science and Technology, 2005 academic year.
- Newmeyer, F. J. (2006), What can grammaticalization tell us about the origin of language? In: *The evolution of language*, Cangelosi, A., Smith, A. D. M. & Smith, K. (Eds.), pp. 434-435, World Scientific, ISBN: 978-9812566560, Singapore
- Okanoya, K. (2002), Sexual display as a syntactical vehicle: the evolution of syntax in birdsong and human language through sexual selection, In: *The Transition to Language*. Wray, A. (Ed.), pp. 46-63, Oxford University Press, ISBN: 978-0199250660, Oxford
- Odling-Smee, F. J., Laland, K. N. & Feldman, M. W. (2003), *Niche Construction: The Neglected Process in Evolution*, Princeton University Press, ISBN: 978-0691044378, Princeton
- Peirce, C. S. (1935). *Collected Papers of Charles Sanders Peirce*, Vol. 2, Harvard University Press, ISBN: 978-0674138001, Harvard, MA
- Sato, T. (2004), The earth simulator: roles and impacts, *Parallel Computing*, Vol. 30, No. 12, 1279-1286, ISSN: 0167-8191
- Sato, T. (2005), *Dynamic Social Simulation with Multi-Agents Having Internal Dynamics* (in Japanese), Doctoral Thesis of School of Knowledge Science, Japan Advanced Institute of Science and Technology, 2004 academic year.
- Sato, T. & Hashimoto, T. (2007), Dynamic social simulation with multi-agents having internal dynamics, *New Frontiers in Artificial Intelligence: Joint Proceeding of the 17th and 18th Annual Conferences of the Japanese Society for Artificial Intelligence*, A. Sakurai (Ed.), pp. 237-251, Springer, ISBN: 978-3540354703, Berlin
- Shiozawa, Y. (1999), On the micro-macro loop (in Japanese), *Keizai Ronsou (Kyoto Daigaku) (Proceedings of Economic Papers of Kyoto University)*, Vol. 164, No.5, 1-67
- Steels, L. (1996), Emergent adaptive lexicons, In: *From Animals to Animats 4*, Maes, P., Mataric, M. J., Meyer, J.-A., Pollack, J. & Wilson, S. W., (Eds.), pp.562-567, ISBN: 978-0262631785, The MIT Press, Cambridge, MA
- Steels, L. & Kaplan, F. (2002), Bootstrapping grounded word semantics, In: *Linguistic Evolution through Language Acquisition: Formal and Computational Models*, Briscoe, T. (Ed.), pp. 53-74, Cambridge University Press, ISBN: 978-0521662994, Cambridge
- Turing, A. M., (1952), The chemical basis of morphogenesis, *Philosophical Transactions of the Royal Society B (London)*, Vol. 237, No. 641, 37-72, ISSN: 0962-8436
- von Neumann, J. (1966), *Theory of Self-Reproducing Automata*, Burks, A. W., (Ed.), University of Illinois Press, ISBN: 978-0598377982, Urbana

# Transient Runaway in a Fixed-Bed Catalytic Reactor

Redhouane Henda

*School of Engineering, Laurentian University, Sudbury, Ontario  
Canada*

## 1. Introduction

Fixed-bed tubular reactors have important commercial applications in the chemical and allied process industries. A typical reactor consists of a cylindrical tube filled with solid catalyst particles and is mounted in a vertical upright position. After the reacting fluid has entered the reactor, it moves along the packed bed and reacts on the catalyst particles to produce the desired products. While fixed-bed reactors, relatively to other types of catalytic reactors, are flexible, efficient, low-cost, and require low maintenance, their most serious disadvantage is poor heat transfer with attendant poor temperature control (e.g., see Bartholemew and Farrauto, 2006).

When a highly exothermic reaction is carried out in a packed bed reactor some problems associated with the operation of the reactor may arise. In this case, if the reaction generates heat faster than it can escape the reactor, viz., through reactor walls, the temperature of the fixed bed increases. The reaction and heat generation rates then increase, which causes a further rise in the reactor temperature. This can result in thermal runaway, with the temperature increasing ever more rapidly until the reactants have been finally exhausted. Runaway, or parametric sensitivity, describes a situation in which a small change in an operating variable such as feed temperature, concentration, or flow rate induces a large change in the temperature profile of the reactor. Further, a number of runaways occur due to scale-up, inadequate procedures and training, raw material quality control, maintenance, etc (Etchells, 1997; Barton and Rogers, 1997). Runaway can promote undesired side reactions, catalyst deactivation, productivity loss, and deterioration of product selectivity. Because of the risk associated with thermal runaway, many industrial reactors are operated under overly suboptimal conditions. It should be noted that near-runaway operation is potentially advantageous to catalytic processes as it may result in optimum reactor operation, especially if energy savings can be attained. For these reasons, understanding thermal runaway is of significant industrial importance.

The concept of thermal runaway was first introduced to chemical reactor analysis in late 1950s (Bilous and Amundson, 1956). There have been many studies in the literature on the derivation of runaway criteria, e.g., in tubular and fixed-bed reactors with a single reaction (van Welsenaere and Froment 1970; McGreavy and Adderley, 1973; Morbidelli and Varma 1982, 1988; Bashir et al. 1992), in reactors with multiple reactions (Hosten and Froment, 1986; Henning and Perez, 1986; Morbidelli and Varma, 1989; van Woezik and Westerterp, 2000,

2002), with the effect of coolant temperature (Henning and Perez, 1986; Hosten and Froment, 1986; Hagan et al. 1988; Bauman et al., 1990). All of this research has focused on developing steady-state criteria for thermal runaway. Specifically, these studies have identified regions in which small changes in the reactor operating conditions lead to large steady-state changes in the reactor temperature. Because this research has been performed on steady-state systems, the results indicate only process conditions under which the system is prone to thermal runaway. Once the system parameters reach values indicating runaway, however, the parametric sensitivity results provide no indication of when thermal runaway occurs. Recently only, correlations for time to runaway for a continuous stirred tank reactor have been developed (Slaback and Riggs, 2004). In order to derive the correlations analytically, a first-order, exothermic reaction has been considered and the reactant has been assumed to be in excess to eliminate the material balance equation.

The focus of this chapter is on the investigation of the thermal behavior of a two-dimensional fixed-bed tubular reactor, and the development of a dynamic criterion indicating the onset of thermal runaway. The ability to predict the tendency towards thermal runaway over time is of valuable importance, and can help in correcting operating conditions in order to suppress runaway before it has occurred. This chapter is organized as follows: a detailed description of the reactor model is given in section 2. In section 3, the model is solved using brute force and simulation results for two inlet temperatures are discussed. In the fourth section, runaway conditions are qualitatively elucidated and the transient criterion is developed.

## 2. Reactor Model

A dynamic model is used in this study to develop a criterion pointing to the onset of runaway in a two-dimensional tubular (of radius  $R_i$ ) catalytic reactor (see Figure 1). The catalyst particles have a diameter  $d_p$ . The reaction system considered in this study consists of a single, irreversible, exothermic reaction. As an example, carbon monoxide conversion over copper chromite ( $\text{CO} + \frac{1}{2} \text{O}_2 \rightarrow \text{CO}_2$ ,  $\Delta H_r = -23.8 \text{ kJ/mol}$ ) is considered, the reaction rate of which is given by (Dekker et al., 1992; Mardanova et al., 1996; Koning and Westerterp, 1999).

$$\mathfrak{R}(C_s, T_s) = \frac{k_r b_{\text{CO}} p_{\text{CO}}}{1 + b_{\text{CO}} p_{\text{CO}} + b_{\text{O}_2} p_{\text{O}_2}} \quad (1)$$

where  $p_i$  ( $i = \text{CO}, \text{O}_2$ ) is the partial pressure of  $i$ , and

$$k_r = k_r^o e^{-E_a/R_g T}, \quad b_i = b_i^o e^{\Delta H_i^{ads}/R_g T} \quad (2)$$

The dimensionless reaction rate is defined by

$$R(C_s, T_s) = \frac{\mathfrak{R}(C_s, T_s)}{\mathfrak{R}(C_s, T_s)|_{in}} \quad (3)$$

where the denominator term is the reaction rate at inlet conditions.

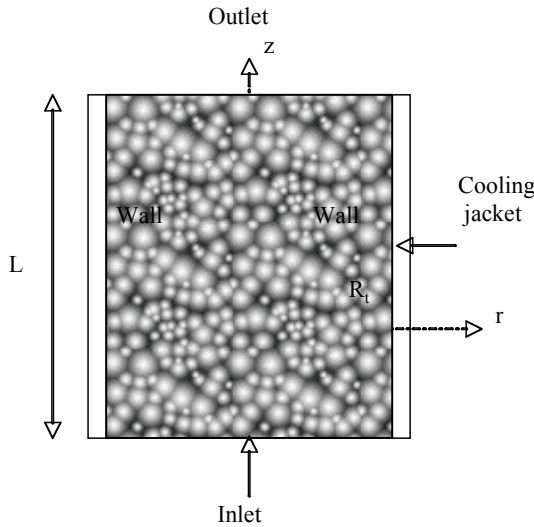


Figure 1. Schematics of the fixed bed

The porosity profile,  $\psi(r)$ , over a cross-section of the bed is given by (Vortmeyer and Schuster, 1983)

$$\psi(r) = \psi_{\infty} [1 + C \exp(-N[1-r])] \tag{4}$$

where  $N = 2R_i/dp$ . The parameter  $C = 0.5$ , corresponding to a value of the porosity at the wall of 0.6 (Giese et al, 1998) and a value of the porosity at the core of the bed,  $\psi_{\infty}$ , of 0.4. The radial, superficial velocity distribution has been obtained by the same authors via the solution of a modified Birkman equation (Birkman, 1947) with the porosity profile given above (equation 4). The following equation has been proposed

$$\frac{u(r)}{u_0} = K [1 - (1-A[1-r]) \exp(B[1-r])] \tag{5}$$

where expressions for  $K$ ,  $A$ , and  $B$  are given elsewhere (see Vortmeyer and Schuster, 1983; Borkink and Westerterp, 1994). The porosity and velocity distributions are shown in Figure 2, where the wall effect can be clearly discerned.

The transient material and energy balance equations are expressed using a pseudo-heterogeneous formulation as follows.

Material balance:

Fluid phase:

$$\psi a \frac{\partial C_f}{\partial t} = \frac{1}{Pe_{m,a}} \frac{\partial^2 C_f}{\partial z^2} + \frac{1}{Pe_{m,r}} \frac{1}{r} \frac{\partial}{\partial r} \left( r \frac{\partial C_f}{\partial r} \right) - \frac{\partial C_f}{\partial z} + St_m (C_s - C_f) \tag{6}$$

Solid Phase:

$$(1-\psi) a \frac{dC_s}{dt} = -(1-\psi) Da R(C_s, T_s) - St_m (C_s - C_f) \tag{7}$$

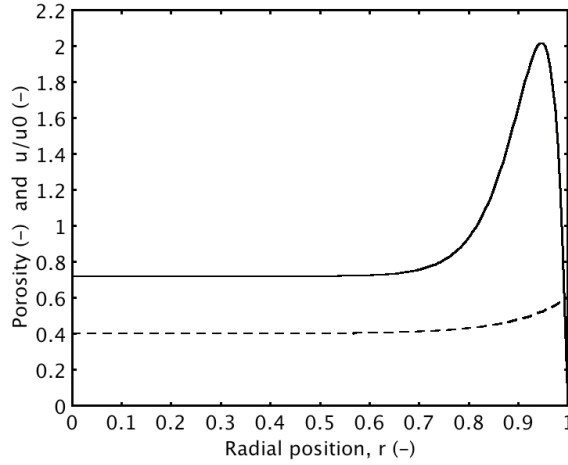


Figure 2. Velocity (—) and porosity (---) profiles across the fixed-bed reactor

Energy balance:

Fluid phase:

$$\psi a \frac{\partial T_f}{\partial t} = \frac{1}{Pe_{h,a}} \left( \frac{\partial^2 T_f}{\partial z^2} \right) + \frac{1}{Pe_{h,r}} \frac{1}{r} \frac{\partial}{\partial r} \left( r \frac{\partial T_f}{\partial r} \right) - \frac{\partial T_f}{\partial z} + St_h (T_s - T_f) \quad (8)$$

Solid Phase:

$$\frac{(1-\psi)\rho_s c_{p,s}}{\rho_f c_{p,f}} a \frac{dT_s}{dt} = (1-\psi) Da R(C_s, T_s) - St_h (T_s - T_f) \quad (9)$$

where  $C_f$  and  $C_s$  are the dimensionless concentrations of carbon monoxide in the fluid and solid phases, respectively, and  $T_f$  and  $T_s$  are the dimensionless temperatures of the fluid and solid phases, respectively. The independent variables are the dimensionless time,  $t$ , and dimensionless radial,  $r$ , and axial,  $z$ , coordinates. The variables and parameters of the model are defined as

$$\begin{aligned} r &= \frac{r^*}{R_t}, \quad z = \frac{z^*}{R_t}, \quad t = \frac{t^*}{t_o}, \quad C_f = \frac{C_f^*}{C_{in}^*}, \quad C_s = \frac{C_s^*}{C_{in}^*}, \quad T_f = \frac{T_f^* - T_{in}^*}{\Delta T_{ad}^*}, \quad T_s = \frac{T_s^* - T_{in}^*}{\Delta T_{ad}^*}, \quad a = \frac{R_t}{t_o u}, \\ \Delta T_{ad}^* &= \frac{|\Delta H_r| C_{in}^*}{\rho_f c_{p,f}}, \quad Bi = \frac{h_w R_t}{k_{r,eff}}, \quad Pe_{m,a} = \frac{u R_t}{D_{a,eff}}, \quad Pe_{m,r} = \frac{u R_t}{D_{r,eff}}, \quad Pe_{h,a} = \frac{u \rho_f c_{p,f} R_t}{k_{a,eff}}, \\ Pe_{h,r} &= \frac{u \rho_f c_{p,f} R_t}{k_{r,eff}}, \quad St_m = \frac{a_p h_m R_t}{u}, \quad St_h = \frac{a_p h_p R_t}{u \rho_f c_{p,f}}, \quad Da = \frac{\rho_s R_t}{u C_{in}^*} \mathfrak{R}(C_s, T_s)|_{in} \end{aligned} \quad (10)$$

where the asterisk denotes variables with absolute values, and subscript *in* denotes inlet conditions. Parameter  $\Delta T^*_{ad}$  is the adiabatic rise, i.e., the highest possible temperature rise in the reactor under adiabatic operation and full conversion of the reactant. In equation 10,  $k_{a,eff}$  ( $k_{r,eff}$ ) is the effective axial (radial) thermal conductivity,  $D_{a,eff}$  ( $D_{r,eff}$ ) is the effective axial (radial) mass diffusivity,  $\rho_f$  ( $\rho_s$ ) is the fluid (solid) density,  $c_{p,f}$  ( $c_{p,s}$ ) is the fluid (solid) heat capacity,  $h_p$  ( $h_m$ ) is the inter-phase heat (mass) transfer coefficient,  $h_w$  is the wall heat transfer coefficient, and  $a_p$  is the specific area of the solid. The dimensionless numbers appearing in the second and third rows of equation 10 are defined in the usual way.

Equations 1-10 are solved subject to the following initial and boundary conditions:

IC:

$$t = 0, C_f = C_s = 0, T_f = T_s = 0. \tag{11}$$

BCs:

$$\begin{aligned} z = 0, \forall r, -\frac{\partial C_f}{\partial z} &= -Pe_{m,a}(C_f - C_{in}), -\frac{\partial T_f}{\partial z} = -Pe_{h,a}(T_f - T_{in}) \\ z = L/R_t, \forall r, -\frac{\partial C_f}{\partial z} &= 0, -\frac{\partial T_f}{\partial z} = 0 \\ r = 0, \forall z, -\frac{\partial C_f}{\partial r} &= 0, -\frac{\partial T_f}{\partial r} = 0 \\ r = 1, \forall z, -\frac{\partial C_f}{\partial r} &= 0, -\frac{\partial T_f}{\partial r} = Bi(T_f - T_w) \end{aligned}$$

The material and energy balance equations 6-10, along with equations 1-5 and initial/boundary conditions 11, have been solved using a finite-element scheme under various process parameters and operating conditions. The latter and other process parameters are given in Table 1.

L	1 m	$\rho_f$	31.1 mol/m <sup>3</sup>	$\Delta H^*_{co}$	30.60 kJ/mol
$R_t$	0.02655 m	$c_{p,f}$	29.45 J/mol/K	$b^o_{o_2}$	3.08 10 <sup>-5</sup> Pa <sup>-1</sup>
$C^*_{in}$	0.75 mol/m <sup>3</sup>	$c_{p,s}$	149.32 J/mol/K	$\Delta H^*_{o_2}$	24.44 kJ/mol
$u_o$	0.1 m/s	$k^o_r$	39.7 kmol/kg/s	$b^o_{co}$	6.81 10 <sup>-8</sup> Pa <sup>-1</sup>
$T^*_{in}$	335 K, 380 K	$\Delta H_r$	-23.8 kJ/mol	$\Delta H^*_{co}$	30.60 kJ/mol
$T^*_w$	335 K, 380 K	$E_a$	57.29 kJ/mol	Bi	0.24
$\rho_s$	10.6 kmol/m <sup>3</sup>	$b^o_{co}$	6.81 10 <sup>-8</sup> Pa <sup>-1</sup>	Re	683

Table 1. Process parameters and conditions used in the simulations

Materials properties and effective transport parameters have been estimated using a number of widely known correlations (see Agnew and Potter, 1970; Bauer and Schlunder, 1978; Poling et al., 2000; Elsari and Hughes, 2002; Incropera and DeWitt, 2002; Klemme and van Miltenburg, 2002).

### 3. Simulation

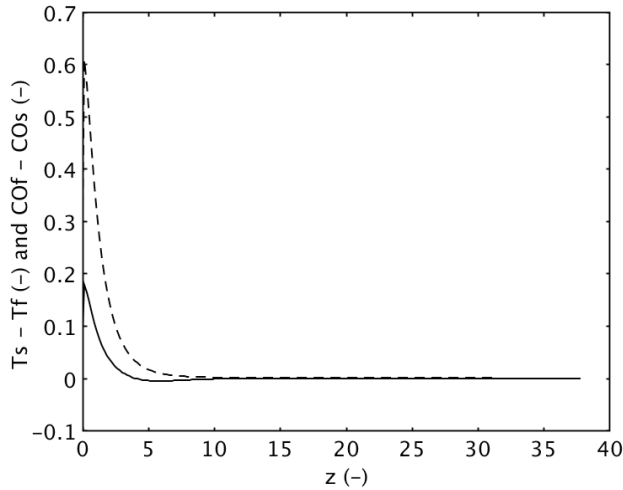


Figure 3: Inter-phase temperature (—) and concentration (---) differences along the bed centerline and at  $t = 1$

Typical process conditions and parameters along with phase properties and kinetic data are listed in Table 1. For all simulation runs, the value of the temperature of the reactor wall,  $T_w^*$ , coincides with the value of the initial reactor temperature as well as the value of the reactor inlet temperature,  $T_{in}^*$ . The Reynolds number corresponds to the value of the velocity at the reactor core, i.e.,  $u(r) = u_0$ . The simulation results have been obtained at two values of  $T_{in}^* = T_w^*$ , starting from 380 K at fixed inlet concentration,  $C_{in}^*$ , and velocity profile. The other value of the temperature has been identified so as to have the reactor under runaway conditions by keeping all other parameters constant.

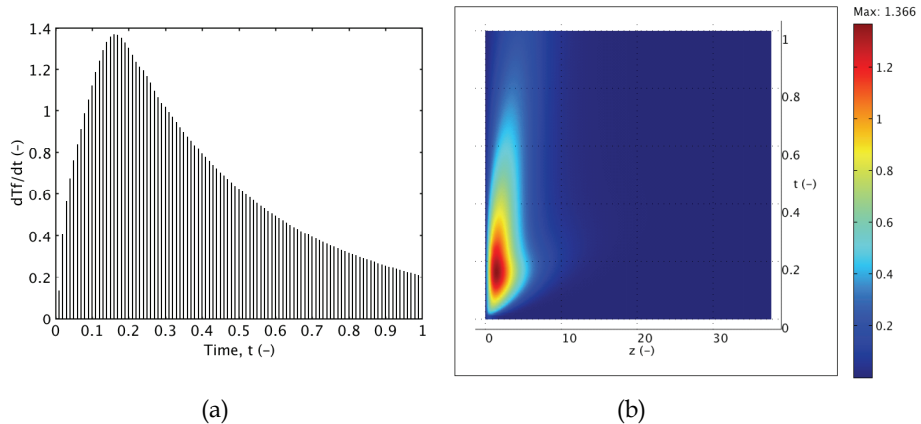


Figure 4. Time derivative of fluid temperature versus time along the bed centerline (a), and versus time and axial direction (b)



### 3.1 Inlet temperature = 380 K

Figure 3 depicts the difference in temperature and concentration between the solid and fluid phases. As it can be noticed from the figure, the model is clearly two dimensional with the largest inter-phase temperature and concentration differences just downstream the fixed-bed inlet. In this region of the bed, the temperature reaches a maximum value (referred to as a hot spot) as shown in Figure 4, where the inter-phase temperature difference reaches  $\sim 40$  K in absolute value. The time dependence of the derivative of the fluid temperature,  $dT_f/dz$ , throughout the reactor and along the bed centerline ( $r = 0$ ) is illustrated in Figure 4 (a). In this figure, each vertical line represents the entire axial direction envelope. The time derivative of the fluid temperature increases to reach a maximum value then decreases over time. Figure 4 (b) is a surface map of the derivative of the fluid temperature as a function of the axial position and time. As time goes by, the change in the fluid temperature increases to reach a maximum value corresponding to time  $t \cong 0.2$  (see Figure 4, b), followed with a monotonous decrease with time thereafter.

### 3.2 Inlet temperature = 335 K

In this case, the inlet temperature of the fluid has been decreased from 380 K until it has reached the value of 335 K at which runaway occurs (this is elucidated in the next section). The change in the fluid temperature as a function of time along the reactor centerline is shown in Figure 5 (a). The temperature derivative increases with time initially then it relatively levels off before it increases over time again. Over the entire time interval, this increase is monotonous though. The surface map of the time derivative as a function of time and along the bed centerline is depicted in Figure 5 (b). This figure illustrates the appreciable increase in the time derivative of the fluid temperature towards large values of time downstream the fixed-bed inlet.

## 4. Runaway Criterion

The runaway condition has been defined in various ways in the classical parametric sensitivity literature (Chambré, 1956; Barkleew, 1959). In both studies the use of isoclines in the determination of the runaway criterion was introduced. This approach provides a graphical method for determining runaway conditions in a reactor. Several other studies have used modifications of this approach, defining the runaway condition by locating maxima in some parameter of the reaction system. All of this work, however, was performed using a steady-state analysis of the system. Of special relevance to the present work is the criterion whereby thermal runaway occurs in steady-state tubular reactors when the second derivative of the temperature is larger than zero, i.e., runaway is identified by the presence of an inflection point in the temperature profile ahead of the hot spot locus (developed by Bashir et al., 1992).

In the present work, a particular characteristic of the dimensionless temperature profile is advanced to define runaway for the transient system under investigation. Using the inflection point criterion above, we have noticed that the latter coincides with a special trend in the variation of the time derivative of the fixed-bed temperature. For both cases of the previous section, Figure 6 depicts the fluid temperature and the corresponding space second derivative,  $dT_f^2/dz^2$ , along the centerline of the fixed-bed reactor. From Figure 6 (a), corresponding to  $T_m^* = T_w^* = 380$  K, there is no indication of reactor runaway as the second

derivative approaches the zero line from the negative side but does not cross it before the hot spot locus. At  $T_{in}^* = T_w^* = 355$  K on Figure 6 (b), however, the second derivative breaks through the zero line before the hot spot locus and takes on positive values: runaway occurs. This result has been compared to a few variations of the temperature of the bed, and found to coincide with a trend whereby the first time derivative of the temperature increases monotonously over time throughout the reactor (see Figure 5). In other terms, for runaway to occur  $dT_f^2/dt^2$  must be positive over the entire time interval. This finding holds for other runaway conditions as we have changed the value of the inlet concentration for  $T_{in}^* = T_w^* = 355$  K.

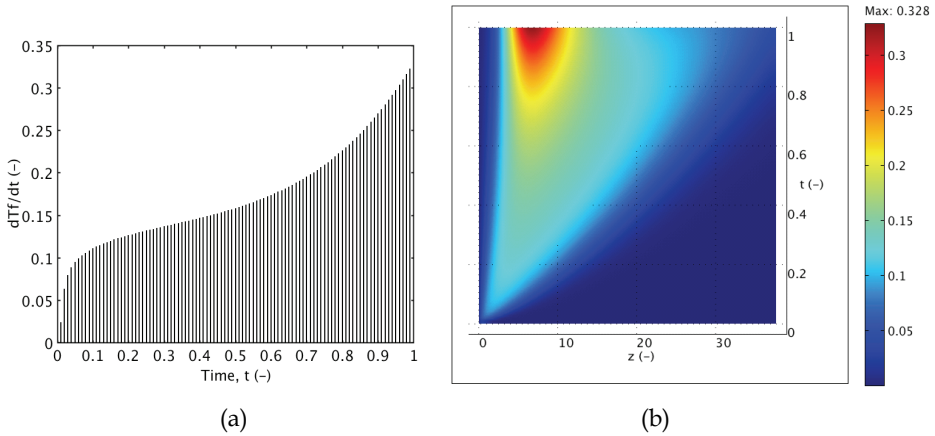


Figure 5. Time derivative of fluid temperature versus time along the bed centerline (a), and versus time and axial direction (b)

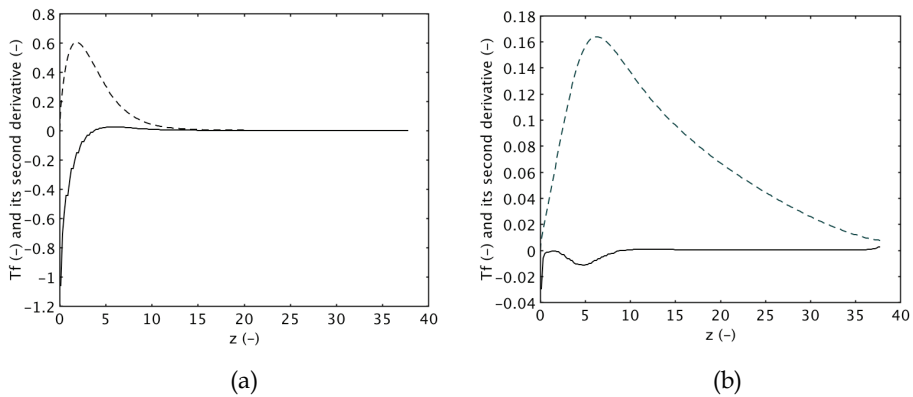


Figure 6. Fluid temperature (—) and its space second derivative (---) versus axial direction along the centerline at  $t = 1$  for  $T_{in}^* = T_w^* = 380$  K (a) and 335 K (b)

## 5. Conclusions

In this chapter we have discussed the thermal behavior of a fixed-bed tubular reactor with an exothermic chemical reaction. The work performed in the present study has focused on developing a transient criterion for thermal runaway. A criterion for the onset of thermal runaway has been advanced whereby the second time derivative of the bed temperature must be positive over the entire time interval. The proposed criterion, although qualitative in nature, is simple and can potentially be used to preclude the occurrence of runaway in fixed-bed tubular reactors. For practical purposes, a quantitative expression of the transient criterion needs to be developed in the future.

## 6. Acknowledgments

The author wishes to thank the Canadian Natural Sciences and Engineering Research Council (NSERC) for the partial financial support of this work.

## 7. References

- Agnew, J. B. & Potter, O.E. (1970). Heat transfer properties of packed tubes of small diameter. *Trans. Inst. Chem. Eng.*, Vol. 48, p. 15.
- Barkeley, C. H. (1959). Stability of Chemical Reactors. *Chem. Eng. Prog. Symp. Ser.*, Vol. 55, pp. 37-46.
- Bartholomew, C. H. & Farrauto, R. J. (2006). *Fundamentals of Industrial Catalytic Processes*. 2<sup>nd</sup> ed., Wiley, Hoboken, N.J.
- Barton, J. A. & Rogers, R. L. (1997). *Chemical Reaction Hazards*, 2<sup>nd</sup> ed., Institution of Chemical Engineers, Rugby, UK.
- Bashir, S., Chovan, T., Masri, B.J., Mukherjee, A., Pant, A., Sen, S. & Vijarayaghavan, P. & J. Berty (1992). Thermal Runaway Limit of Tubular Reactors, Defined at the Inflection Point of the Temperature Profile. *Ind. Eng. Chem. Res.*, Vol. 31, pp. 2164-2171.
- Bauer, R. & Schlunder, E.U. (1978). Effective radial thermal conductivity of packings in gas flow. Part I. Convective transport coefficient. *Int. Chem. Eng.*, Vol. 18, pp. 189-204.
- Bauman, E., Varma, A., Lorusso, J., Dente, M. & Morbidelli, M. (1990). Parametric Sensitivity in Tubular Reactors with Co-Current External Cooling. *Chem. Eng. Sci.*, Vol. 45, No. 5, pp. 1301-1307.
- Bilous, O. & Amundson, N. R. (1956). Chemical Reactor Stability. *AIChE J.*, pp. 117-126.
- Borkink J. G. H. & Westerterp, K. R. (1994). Significance of the Radial Porosity Profile for the Description of Heat Transport in Wall-Cooled Packed Beds. *Chem. Eng. Sci.*, Vol. 49, No. 6, pp. 863-876.
- Chambré, P. L. (1956). On the Characteristics of a Non-Isothermal Chemical Reactor. *Chem. Eng. Sci.*, Vol. 5, pp. 209-216.
- Dekker, N.J.J., Hoorn, J.A.A., Stegenga, S., Kapteijn, F. & Moulijn, J.A. (1992). Kinetics of the CO Oxidation by O<sub>2</sub> and N<sub>2</sub>O over Cu-Cr/Al<sub>2</sub>O<sub>3</sub>. *AIChE J.*, Vol. 38, pp. 385-396.
- Elsari, M. & Hughes, R. (2002). Axial Effective Thermal Conductivities of Packed Beds. *Appl. Therm. Eng.*, Vol. 22, pp. 1969-1980.
- Etchells, J.C. (1997). Why Reactions Run Away. *Organic Process Research & Development*, Vol. 1, pp. 435-437.

- Giese, M., Rottschäfer, K. & Vortmeyer, D. (1998). Measured and Modeled Superficial Flow Profiles in Packed Beds with Liquid Flow. *AIChE J.*, Vol. 44, No. 2, pp. 484-490.
- Henning, G. P. & Perez, G. A. (1986). Parametric Sensitivity in Fixed-Bed Catalytic Reactors. *Chem. Eng. Sci.*, Vol. 41, No. 1, pp. 83-88.
- Hosten, L. H. & Froment, G. F. (1986). Parametric Sensitivity in Co-currently Cooled Tubular Reactors. *Chem. Eng. Sci.*, Vol. 41, No. 4, pp. 1073-1080.
- Incropera, F.P. & DeWitt, D.P. (2002). *Fundamentals of Heat and Mass Transfer*. 5th ed., Wiley, New York, N.Y.
- Klemme, S. & van Miltenburg, J.C. (2002). Thermodynamic Properties of Nickel Chromite ( $\text{NiCr}_2\text{O}_4$ ) Based on Adiabatic Calorimetry at Low Temperatures. *Phys. Chem. Minerals*, Vol. 29, pp. 663-667.
- Koning, G.W. & Westerterp, K.R. (1999). Modeling of Heat Transfer in Wall-Cooled Tubular Reactors. *Chem. Eng. Sci.*, Vol. 54, pp. 2527-2533.
- Mardanov, N.M., Akhverdiev, R.B., Talyschinskii, R.M., Medzhidov, A.A., Ali-zade, F.M. & Rizaev, R.G. (1996). Oxidation of Carbon Monoxide on  $\text{Cu-Cr-Mn}/\gamma\text{-Al}_2\text{O}_3$  Catalysts from Various Sources. *Kinet. Catal.*, Vol. 37, pp. 84-89.
- McGreavy, C. & Adderley, C. I. (1973). Generalized Criteria for Parametric Sensitivity and Temperature Runaway in Catalytic Reactors. *Chem. Eng. Sci.*, Vol. 28, pp. 577-584.
- Morbideilli, M. & Varma, A. A. (1982). Parametric Sensitivity and Runaway in Tubular Reactors. *AIChE J.*, Vol. 28, No. 5, pp. 705-713.
- Morbideilli, M. & Varma, A. A. (1988). Generalized Criterion for Parametric Sensitivity: Application to Thermal Explosion Theory. *Chem. Eng. Sci.*, Vol. 43, No. 1, pp. 91-102.
- Morbideilli, M. & Varma, A. A. (1989). Generalized Criterion for Parametric Sensitivity: Application to a Pseudohomogeneous Tubular Reactor with Consecutive or Parallel Reactions. *Chem. Eng. Sci.*, Vol. 44, No. 8, pp. 1675-1696.
- Poling, B.E., Prausnitz, J.M. & O'Connell, J.P. (2000). *The Properties of Gases and Liquids*. 5th ed., McGraw-Hill, New York, N.Y.
- Slaback, D. D. & Riggs, J. B. (2004). Time to Runaway in a Continuous Stirred Tank Reactor. *Ind. Eng. Chem. Res.*, Vol. 43, pp. 3723-3730.
- van Woezik, B. A. A. & Westerterp, K. R. (2000). The Nitric Oxidation of 2-Octanol. A Model Reaction for Multiple Heterogeneous Liquid-Liquid Reactions. *Chem. Eng. Process.*, Vol. 39, pp. 521-537.
- van Woezik, B. A. A. & Westerterp, K. R. (2002). Runaway Behaviour and Thermally Safe Operation of Multiple Liquid-Liquid Reactions in the Semibatch Reactor. The Nitric Acid Oxidation of 2-Octanol. *Chem. Eng. Process.*, Vol. 41, pp. 59-77.
- Welsenaere, R. J. & Froment, G. F. (1970). Parametric Sensitivity and Runaway in Fixed Bed Catalytic Reactors. *Chem. Eng. Sci.*, Vol. 25, pp. 1503-1516.

# Carotid Plaque Stresses

Samuel Alberg Kock<sup>1</sup> and Jens Vinge Nygaard<sup>2</sup>

<sup>1</sup>Aarhus University Hospital Skejby, <sup>2</sup>Aarhus University: iNANO  
Denmark

## 1. Introduction

Cardiovascular atherosclerotic disease is the leading cause of death and severe disability worldwide (Rosamond et al., 2007; WHO and CDC, 2004; Yusuf et al., 2001). Carotid atherosclerotic plaques are a major cause of cerebrovascular thromboembolic events including transitory ischemic attacks and strokes (Virmani et al., 2006; Redgrave et al., 2006; Nighoghossian et al., 2005; Carr et al., 1996).

### 1.1 Current Carotid Risk Assessment

In current clinical practice, selection for surgical removal of the carotid plaque (carotid endarterectomy) is determined by the degree of luminal narrowing known as the degree of stenosis (Rothwell et al., 2003a). The operation has been determined beneficial in patients with symptomatic, severe stenosis in two large, randomized trials; the North American Symptomatic Carotid Endarterectomy Trial (NASCET, 1991) and the European Carotid Surgery Trial (ECST, 1998). To determine the degree of stenosis, NASCET and ECST used measurements based on x-ray digital subtraction angiographies. Today, Doppler ultrasound is used in clinical practice for determination of the degree of stenosis (Nederkoorn et al., 2003; Titi et al., 2007). This technique does not rely on direct measurements of the degree of stenosis but uses determination of maximum peak systolic and end diastolic blood flow velocities as well as the spectral composition of these velocities to assess the degree of stenosis. The ultrasound Doppler techniques, though in universal clinical use, are problematic due to problems with the insonation angle affecting the Doppler equation (Tola and Yurdakul, 2006; Claudon et al., 2001), inter- and intra-observer variations (Mead et al., 2000; Lui et al., 2005), and interpretation in the presence of complex geometries (Clevert et al., 2006; Clevert et al., 2007).

Preventive treatment of patients with carotid plaques but no symptoms (asymptomatic patients) would be preferable but is controversial, since trials have shown only marginal effect of treatment from current risk stratification, and total mortality after five years is unchanged in treated vs. untreated groups (Halliday et al., 2004; Redgrave et al., 2006). To prevent a single stroke, the number needed to treat for symptomatic patients is seven (Rothwell et al., 2003a) rising to forty for asymptomatic patients (Halliday et al., 2004).

Using the current risk assessment algorithm, the majority of patients operated are thus needlessly exposed to peri-operative risks. Further, atherosclerotic plaques tend to grow outwards initially, which may result in normal luminal size belying substantial plaque volumes, a process known as arterial remodeling (Glagov et al., 1987; Glagov et al., 1988;

Pasterkamp and Smits, 2002) making risk assessment based on the degree of stenosis problematic. In addition, most ruptured plaques are less than 50% stenosed, the current limit at which carotid endarterectomy is offered (Casscells et al., 2003; Falk et al., 1995). Thus, the decision of whether or not to operate is based on scientifically problematic methodologies. A great need therefore exists for improved methods of selecting patients with carotid atherosclerosis who may benefit from operation.

### **1.2 Vulnerable Plaque Features**

Histological examinations have determined the hallmarks of plaques at risk of rupture (vulnerable plaques) to be large lipid-rich, necrotic cores covered with thin fibrous caps (Virmani et al., 2006; Gronholdt et al., 1998; Falk, 2006; Naghavi et al., 2003; Casscells et al., 2003; Virmani et al., 2000; Stary et al., 1995). Many studies have shown that inflammation and the subsequent immune response contribute to atherosclerosis. Further, blood pressure is known to influence the incidence of strokes (Kario et al., 2003; Staessen et al., 1997; Dart and Kingwell, 2001; Rothwell et al., 2003b).

### **1.3 Plaque Imaging**

Through the advent of high-resolution in-vivo imaging techniques such as intravascular ultrasound (Sipahi et al., 2007; Imoto et al., 2005), optical coherence tomography (Huang et al., 1991; Yabushita et al., 2002), and magnetic resonance imaging (MRI) (Yuan and Kerwin, 2004), detailed morphologic and structural characterization of atherosclerotic plaques has been enabled. In particular, MRI has proven a valuable modality for imaging carotid plaques with the capability of non-invasively imaging necrotic cores (Yuan et al., 1997; Yuan et al., 2001), fibrous caps (Hatsukami et al., 2000; Yuan et al., 2002; Mitsumori et al., 2003), and presence of intraplaque hemorrhage (Chu et al., 2004). Indeed, the characterization of atherosclerotic lesions using MRI approaches histological definitions (Cai et al., 2002). Recently, semi-automated tissue segmentation has been enabled (Liu et al., 2006). Furthermore, MRI has the ability to measure blood velocities through phase-contrast imaging (Firmin et al., 1990; McDonnell, III et al., 1994) and deformations using cine MR imaging (Draney et al., 2002; Metafratzi et al., 2002).

### **1.4 Computational Simulations of Plaque Stresses**

Since plaque rupture by definition represents a structural failure of the protective fibrous cap, it seems reasonable to assume that plaque morphology as well as biomechanical properties of the atherosclerotic lesion may influence the plaque vulnerability. To estimate stress levels in the fibrous cap, fluid structure interaction analysis has emerged as a tool combining blood flow simulation through computational fluid dynamics combined with finite element analysis of the corresponding stress levels in the surrounding tissues. Thus, a number of studies have been performed investigating intraplaque stresses as a potential risk marker of vulnerable plaques (Li et al., 2006a; Imoto et al., 2005; Kaazempur-Mofrad et al., 2004; Chau et al., 2004; Steinman, 2002; Huang et al., 2001; Li et al., 2006b; Tang et al., 2004; Zhao et al., 2002). Indeed, in vitro studies of coronary arteries have shown markedly elevated fibrous cap stresses in ruptured coronary lesions compared to stable lesions (Cheng et al., 1993) and a recent publication found carotid fibrous cap stress levels in symptomatic patients to be nearly twice those of asymptomatic patients (Li et al., 2007).

In principle, 3D simulations of fibrous cap stresses would be preferable since they inherently provide more information than 2D sections. However, the computational demands for performing 3D fluid structure interaction simulations are great requiring substantial solution times. Thus, simulations in 2D cross-sections corresponding to either histological data (Cheng et al., 1993) or MRI scans (Li et al., 2006a) have been suggested. Though the use of cross-sectional data matches the orientation of the available morphologic data, this approach precludes fluid structure interaction analysis and necessitate assumptions regarding the longitudinal blood pressure distribution used to load the blood/vessel wall interface. We have recently developed a novel semi-automated method of creating longitudinal 2D models from transverse MRI scans allowing simulations of longitudinal stress distributions including the effects of fluid structure interactions and determination of correct blood pressure distribution enabling predictions of plaque rupture risk and examinations of correlations between local stress variation and morphology.

To investigate the clinical usefulness of the method, we performed fluid-structure interaction simulations of an idealized carotid artery based on the geometry of a symptomatic patient. We investigated the impact of different known markers of plaque vulnerability, i.e. propensity for rupture, namely degrees of luminal stenosis, fibrous cap thicknesses, lipid core sizes, and lipid core positions to determine their effect on plaque stress levels and risk of plaque rupture.

## 2. Morphology Generation

A variety of imaging modalities have been employed for generating morphology suitable for computational fluid dynamics simulations including magnetic resonance imaging (Li et al., 2006a; Tang et al., 2004), intravascular ultrasound (Wentzel et al., 2003; Ramaswamy et al., 2006), computed tomography (Jin et al., 2004), and optical coherence tomography (Chau et al., 2004). In particular, magnetic resonance imaging has gained widespread usage as the method-of-choice for producing computational fluid dynamic models given the modality's excellent soft tissue contrast and inherent capability of obtaining velocity images alongside the morphological imagery. In addition, dynamic deformational images may be obtained allowing for evaluations of the computational simulations with regards to induced deformations. In the present work, magnetic resonance imaging was used to scan a male patient (age 69) with a 70% stenosed carotid artery, awaiting surgery for carotid atherosclerosis who gave informed written consent before participation. The protocol was approved by the local ethics committee.

### 2.1 Plaque Morphology

The critical plaque components to be identified include lipid-rich necrotic cores, fibrous caps, and intraplaque hemorrhages. Histological studies have demonstrated that plaque tissue components often exist in a mixture state, especially in advanced lesions. Thus lipid-rich necrotic cores largely consist of cholesterol esters, free cholesterols, and triglycerides, which all contribute differently to the MRI signal based on their physical states (Yuan et al., 2001; Small and Shipley, 1974). In addition, signal features of intraplaque hemorrhage may change depending on the evolution stage (Chu et al., 2004). A single contrast weighting is thus insufficient for characterizing plaque tissues. Therefore, noninvasive visualizations of

carotid plaque morphology mainly rely on multispectral (or multicontrast) weighted MRI techniques to characterize atherosclerotic lesions.

A well-validated MRI multicontrast protocol has been developed for the noninvasive detection and characterization of atherosclerotic plaques in carotid arteries employing T1-weighted (T1W), T2-Weighted (T2W), Proton Density Weighted (PDW), and Time Of Flight (TOF) scans (fig. 1) (Yarnykh and Yuan, 2003; Yuan and Kerwin, 2004; Cai et al., 2002).

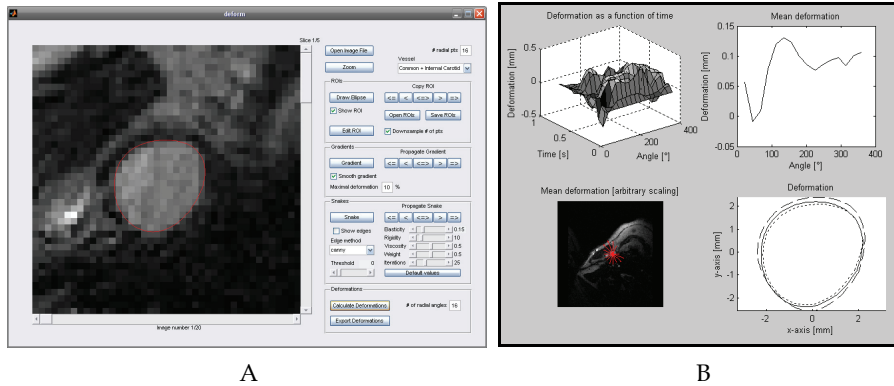


Figure 1. Custom Matlab toolbox for measuring time-resolved deformation. A: Cross-sectional B-TFE MRI scan with contour of CCA outlined in red. B: Top left: Deformation as a function of time and radial angle. Top right: mean deformation as a function of radial angle. Bottom left: Mean radial deformation overlaid the MRI scan. Bottom right: Mean (solid line), maximal (dashed line), and minimal (dotted line) deformation

Though current state of the art MRI protocols for carotid plaque imaging have an accuracy proven to approach histological AHA classifications of plaque morphology (Cai et al., 2002), current spatial resolution of the employed sequences is only  $0.6 \times 0.6 \times 2$  mm. The critical fibrous cap thickness is typically thought to be below 0.25 mm in the carotid artery, and below 0.1 mm in the coronaries (Bassiouny et al., 1997; Li et al., 2006b; Imoto et al., 2005). Increasing spatial resolution of MRI scans to enable visualization of very thin fibrous caps of 0.25 mm or below in thickness could thus prove of importance. Moving towards scanners with higher field strengths (Yarnykh et al., 2006) or switching from 2D to 3D acquisitions (Koktzoglou and Li, 2007) may facilitate this.

Presently, complete morphological imaging of the carotids requires scans with a total duration of approximately 45 minutes. Though shortened scan times would be desirable in terms of clinical feasibility, signal-to-noise ratios will thereby be negatively impacted. The conflicting demands of time requirements and signal-to-noise ratio must be considered, and compromises reached. The increased signal-to-noise ratio of scanners with higher field strengths and 3D acquisitions may also be used for shorter scan durations instead of increased resolution.

The carotid arteries are superficial structures whose length is greater than their distance from the surface, a configuration well suited for the use of phased-array coils consisting of several adjacent small surface coils from which data are collected simultaneously (Hayes et al., 1996; Botnar et al., 2001; Roemer et al., 1990). Such coils have been reported to increase signal-to-noise ratio by 37% and would be preferable for carotid imaging (Yuan and Kerwin, 2004).



## 2.2 Velocity Measurements

Phase-contrast MRI scans may be used to measure time-resolved blood velocities in the internal (ICA), external (ECA), and common (CCA) carotid arteries over a cardiac cycle. The accuracy of phase-contrast MRI is generally considered high, even in unsteady flows as present in patients with severe degrees of stenosis (Frayne et al., 1995).

The measured velocities were applied at the ICA and ECA as parabolic flow profiles. Previous studies have shown non-parabolic velocity profiles in the carotid arteries affecting the WSS distributions (Perktold and Rappitsch, 1995). However, since stress levels are mainly the result of pressure distributions rather than effects of blood flow adjacent to the vessel walls, these are thought to be less affected thereby.

## 2.3 Vessel Deformation

Vessel deformation can be monitored using a cine MRI Balanced True Field Echo sequence (B-TFE). A custom Matlab toolbox (fig. 1) was constructed allowing semi-automatically measurements of deformations as a function of time and radial position. An initial circle surrounding the carotid vessel was drawn, the center of mass found, and a polar image constructed of the carotid vessel. Using thresholding, the vessel outline was detected and transformed back to a Cartesian space. Snakes were used to generate smooth outlines surrounding the vessel (Yuan et al., 1999).

The measured deformations can be used for tuning material parameters of the tissue surrounding the carotids to ensure deformations in the computational simulations matches the in-vivo measurements.

## 2.4 Segmentation

As previously stated, atherosclerotic tissues may exhibit heterogeneous signal levels necessitating the use of multicontrast protocols. Table displays the appearance of typical plaque features on the different contrast weightings. Given this heterogeneity, reproducibility of the segmentations might have been expected to be low. However, the opposite holds true, studies have shown excellent reproducibility of MRI-based segmentations of carotid plaque morphological features.(Yuan et al., 1998; Shinnar et al., 1999) Further, all the scans presented in I, II, and III were validated by an experienced reviewer at the Vascular Imaging Lab at the University of Washington, USA. Recently, an approach utilizing computational morphology enhanced probability maps was described allowing for fully automated segmentation of carotid plaque morphology.(Liu et al., 2006)

Plaque Component	MR Contrast Weighting			
	TOF	T1W	PDW	T2W
Recent intraplaque hemorrhage	+	+/-0	-/0	-/0
lipid-rich necrotic cores	0	+	-/0	-/0
Intimal calcifications	-	-	-	-

Table 1. Magnetic resonance imaging criteria used to identify plaque tissue components (Yuan et al., 2001). The intensities listed are relative to the adjacent sternocleidomastoid muscle

## 2.5 Computational Model Generation

The segmented data describing the spatial distribution of plaque components in each MRI slice were exported as a collection of spline curves. These were imported into Matlab® R2006b (The MathWorks Inc., Natick, MA, USA) and converted to 2D grayscale images (fig. 2). From the 2D images, a region-of-interest was selected and collected into a single 3D matrix describing the spatial distribution of segmented tissue within the scanned volume. The dataset was resampled using linear interpolation to obtain an isotropic voxel size of  $0.3125 \times 0.3125 \times 0.3125 \text{ mm}^3$  followed by Gaussian smoothing.

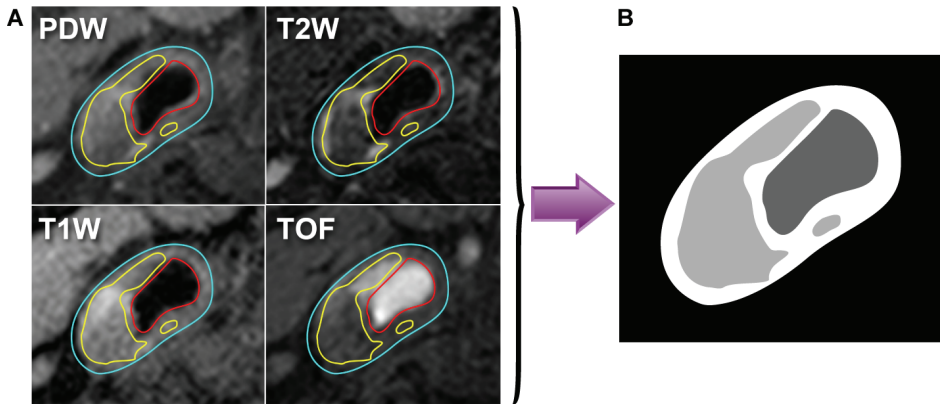


Figure 2. (A) Four MRI weightings were performed in order to enable segmentation into blood, vessel wall, and lipid-rich necrotic core. PDW=Proton Density Weighted image, T2W=T2 Weighted image, T1W=T1 Weighted image, TOF=Time Of Flight scan. (B) Grey-scale images were constructed from the segmented MRI images and used for constructing logical images of the plaque morphological distribution. Visible features include blood stream (red), vessel wall (purple), and lipid-rich necrotic cores (yellow)

From the isotropic dataset, isosurfaces surrounding each component were created (fig. 3A). To create a longitudinal 2D model, the 3D isosurface model was sectioned along skeletonization points by a Non-Uniform Rational B-Spline (NURBS) (Piegl and Tiller, 1997) surface (fig. 3A), yielding a final 2D model to be analyzed (fig. 3B). To minimize boundary effects the model was extended linearly 5 cm up- and downstream, corresponding to approximately five times the CCA diameter.

The close proximity of blood lumen and lipid-rich necrotic cores, with fibrous cap thicknesses of 0.25 mm or below may cause problems with overlapping isosurfaces in some patients, necessitating manual adjustment of interpolation and smoothing parameters. Further, due to the slice thicknesses of 2 mm employed in the MRI scans, the flow divider was seldom depicted and the resulting longitudinal model had a distinct flattened profile at this location. Thus manual adjustment of the area surrounding the flow divider from longitudinal MRI scans was needed.

Initially, the patient was scanned using the aforementioned magnetic resonance protocol which was used to generate an initial model using the described methodology. In order to suppress local effects of uneven vessel wall borders, a simplified longitudinal model was created using the previously generated curves as guidelines. A cosine function was used to

generate the walls surrounding the plaque, initially calculated horizontally before being rotated using the plaque angle ( $-65.5^\circ$ ).

$$f(x) = \left( \frac{S * MS}{100} - mS \right) * \left( \frac{1}{2} + \frac{1}{2} * \left( \cos \left( \frac{2\pi}{l} * x - \pi \right) \right) \right) \quad (1)$$

where  $f$  = horizontal plaque height,  $S$  = degree of stenosis in percent,  $MS$  = amplitude at 100% degree of stenosis,  $mS$  = amplitude at 0% degree of stenosis (negative), and  $l$  = length of stenosis. User-selected amplitudes ( $S$ ) were applied to simulate models with 95%, 90%, 80%, and 70% degrees of stenosis, measured using the NASCET standard (Rothwell et al., 2003a). Lipid pools were generated as ellipsoids with varying sizes (6x3 mm, 4x2 mm, and 2x1 mm) inside the plaque area at specified locations to generate models with proximal/distal lipid core position and decreasing fibrous cap thicknesses (0.5, 0.2, 0.1, and 0.05 mm).

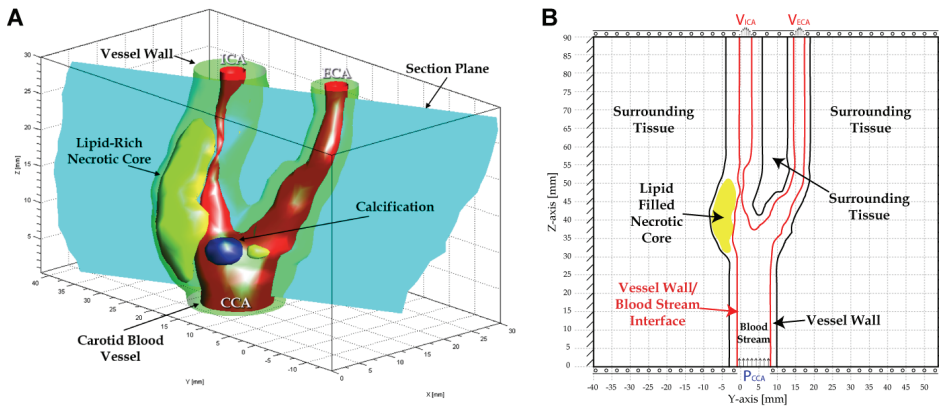


Figure 3. (A) A 3D skeletonization was performed on the blood-stream and a NURBS surface constructed intersecting the center of the blood stream throughout the model. (B) Intersections between NURBS surface and the iso-surfaces delineating the plaque tissues were used to derive a longitudinal 2D model which was embedded in a slab of surrounding tissue. External boundary conditions are also presented, rollers at top and bottom with fixed boundaries at either side. ICA = Internal Carotid Artery, ECA = External Carotid Artery, CCA = Common Carotid Artery,  $V_{ICA}$  = Velocity at ICA,  $V_{ECA}$  = Velocity at ECA,  $P_{CCA}$  = Pressure at CCA

## 2.6 Boundary Specifications

Blood flow was simulated as Navier-Stokes flow and treated as an incompressible, homogeneous, Newtonian, viscous fluid with a density of  $1050 \text{ kg/m}^3$  and dynamic viscosity of  $0.0035 \text{ Pa}\cdot\text{s}$ . The two outflows were specified as parabolic velocity outlets using the phase-contrast MRI measured mean blood flow velocities of the patient at the internal and external carotids (fig. 3B). A no-slip boundary condition was applied along the blood-stream/vessel wall interface, and an Arbitrary Lagrangian-Eulerian (ALE) formulation was used to couple the fluid forces to the structural deformation and vice versa along the vessel wall/blood-stream interface. Reynold's number in the normal healthy carotid is insufficient

to warrant turbulence modeling, however flow fields in carotid phantoms with large degrees of stenosis are more accurately depicted using  $\kappa\text{-}\omega$  models than both laminar flow and  $\kappa\text{-}\epsilon$  turbulence models (Banks and Bressloff, 2007). If blood flow is modeled as being turbulent, recent research suggests that the  $\kappa\text{-}\omega$  model is superior with regard to flow field depiction (Banks and Bressloff, 2007), thus this model was chosen.

A carotid pulse pressure profile was measured noninvasively using the applanation tonometry technique (Chen et al., 1996; Zhao et al., 2002) with a high-fidelity external pressure transducer (SPT-301, Millar Instruments Inc., Texas, USA) applied to the skin above the common carotid artery. The pulse pressure profile was scaled using the systolic and diastolic blood pressures of the patient and applied as the inlet boundary condition at the common carotid inlet.

The model was embedded in a rectangle of surrounding tissue the width of which was determined from cross-sectional MRI scans. Left and right boundaries were fully constrained and top and bottom boundaries (excluding the fluid boundaries) constrained in the Z-direction. The boundary between the top surrounding tissue block and vessel wall was also fully constrained (fig. 3B).

Using MRI phase contrast scans, fluid velocities were measured at both outlets in the patient with 70% degree of stenosis. To account for the change in velocities caused by the varying degree of stenosis, the internal carotid artery was modeled as a Venturi tube:

$$Q = C \cdot \sqrt{\frac{1}{1 - (D_2/D_1)^4}} \cdot \frac{\pi \cdot D_2^2}{4} \cdot \sqrt{\frac{2 \cdot \Delta p}{\rho}} \quad (2)$$

where  $Q$  = volumetric flow rate,  $C$  = coefficient of discharge (0.77),  $D_1$  = diameter of normal internal carotid artery (after the stenosis),  $D_2$  = diameter of internal carotid artery at maximal point of constriction,  $\Delta p$  = pressure difference, and  $\rho$  = mass density of blood (1050 kg/m<sup>3</sup>).

Initial conditions were specified using the diameters and flow measured in the patient to estimate the pressure difference. Subsequently, the  $D_2$  diameter was changed to that of the individual degrees of stenosis, and the resulting flows ( $Q$ ) were used to calculate the velocities in the internal carotid artery in each of the models. To preserve common carotid flow rate, the loss in internal carotid flow was assigned to the external carotid. Laminar, parabolic velocity profiles were assigned at both outlets using the calculated velocities. The systolic blood pressure of the patient was prescribed at the inlet (160 mmHg  $\approx$  21.300 Pa). The blood was initialized using the inlet blood pressure and mean external outlet velocity. Although a simplification, blood was simulated as a Newtonian fluid with a constant viscosity. Due to the content of formed elements within the bloodstream shear thinning occurs in vivo and the viscosity is not constant. However, recent research (Lee and Steinman, 2007) suggests that the use of Newtonian models for simulations of blood flow are reasonable in the carotid artery.

## 2.7 Material Properties

Tissues were simulated as isotropic homogenous entities. To account for the non-linear stress/strain dependency of human tissues, a computationally efficient Neo-Hookean hyper-elastic model was used to specify the material properties of the tissues using the following strain energy function ( $W$ ):

$$W = \frac{\mu}{2} \cdot (\bar{I}_1 - 3) + \frac{K}{2} \cdot (J - 1)^2 \quad (3)$$

where  $\mu$  designate the initial shear modulus and  $\bar{I}_1$  is the first deviatoric strain invariant,  $J$  is the ratio of the deformed elastic volume over the undeformed volume, and  $K$  is the bulk modulus calculated as follows:

$$K = \frac{2 \cdot (C_1 + C_2)}{1 - 2 \cdot \nu} \quad (4)$$

where  $C_1$  and  $C_2$  are the material constants in the Mooney-Rivlin hyper-elastic model (the Neo-Hookean model can be considered a subset of the Mooney-Rivlin model with  $C_1 = 0$  and  $C_2 = \mu / 2$ ),  $\nu$  represents Poisson's ratio, assigned to be 0.495 to mimic the almost incompressible human tissues. The initial bulk modulus  $K$  was thus set to 100 times that of the initial shear modulus. The initial shear modulus  $\mu$  was set to 6 MPa for the vessel wall (COMSOL AB, 2005). Lipid was treated as an isotropic material with Young's modulus set to 1/100<sup>th</sup> that of the equivalent Young's modulus of the vessel wall (Young's modulus = 1E5 Pa, Poisson's ratio = 0.45) (Tang et al., 2004). The initial shear modulus of the surrounding tissue was adjusted until the deformation near the common carotid inlet matched that measured by MRI B-TFE scans as measured by the change in vessel diameter between diastole and systole.

The Neo-Hookean model is considered to be valid for the moderate deformations present in atherosclerotic plaques and was validated with a geometry similar to a previously described model (Li et al., 2006b). Other researchers have used linear orthotropic models (Imoto et al., 2005), modified Mooney-Rivlin models (Chau et al., 2004; Tang et al., 2004), and Ogden hyperelastic models (Li et al., 2007; Versluis et al., 2006; Antheunis et al., 2006). Since different hyperelastic models and material specifications may substantially affect resulting stress levels, comparison of stress levels between different models should be interpreted with caution.

To simplify the present finite element analysis, the materials were assumed to be isotropic, incompressible, and uniform solids. By assuming that plaques, lipids, and normal arterial walls could each be characterized by a single set of structural variables, spatial and interspecimen variations within a particular component were not considered (Holzapfel et al., 2004). However, these assumptions have been widely accepted as allowable for the assessment of biomechanical properties of atherosclerotic lesions (Loree et al., 1992; Cheng et al., 1993; Imoto et al., 2005).

### 2.8 Solving the FSI model

The coupled fluid-structure interaction simulations were performed using COMSOL, a commercially available finite element solver (COMSOL 3.4, COMSOL Inc, Stockholm, Sweden). Streamline diffusion was applied to artificially stabilize the solution.

## 3. Results

Two examples of velocity fields, first principal stress distributions, and velocity streamlines are presented in fig. 4. A 90% degree of stenosis model with a proximal 6x3 mm lipid core and minimal fibrous cap thickness of 0.2 mm yielded maximal principal stresses of 674.4 kPa occurring at the area of minimal fibrous cap thickness (fig. 4A, red arrowhead). Immediately

adjacent to the area with maximal first principal stresses equal to tensile stresses, was a pressure zone with negative first principal stresses of  $-101.4$  kPa (fig. 4A, white arrowhead). A second model with 80% degree of stenosis, a distal  $4 \times 2$  mm lipid core, and minimal fibrous cap thickness of  $0.2$  mm is presented in fig. 4B. The velocities in the internal carotid artery were higher in this model due to the Venturi calculations, generating a large zone of recirculating blood above the plaque (fig. 4B, yellow asterisk). Again, maximal (fig. 4B, red arrowhead) and minimal (fig. 4B, white arrowhead) first principal stresses were found to be adjacent and located at the area of minimal fibrous cap width, with a magnitude of  $429.1/-89.5$  kPa, respectively.

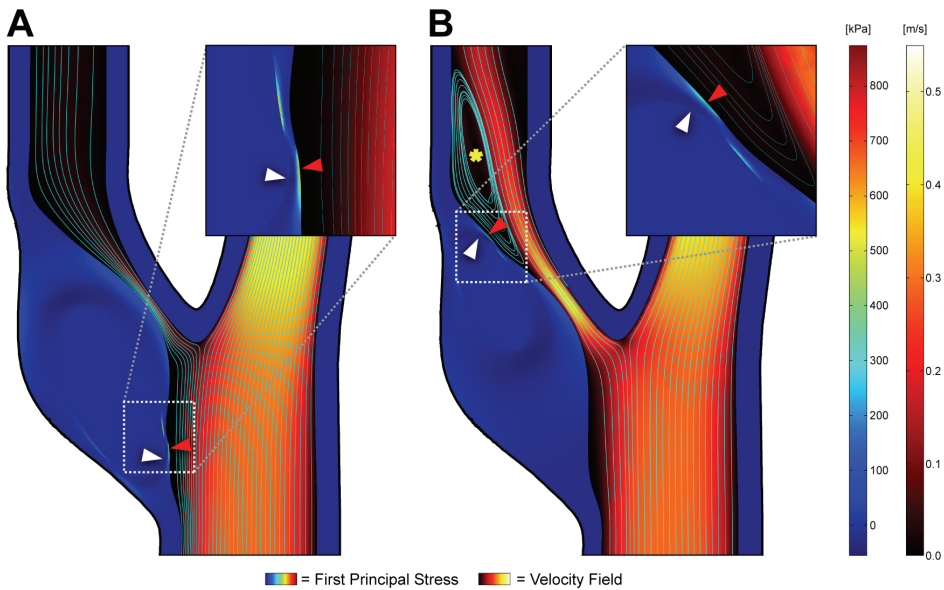


Figure 4. Examples of the results generated from the simulations. Arrowheads mark the location of maximal/ minimal first principal stresses, red/ white respectively. Insets depicts areas of maximal/ minimal stress levels. (A) Carotid with 90% stenosis, proximal  $6 \times 3$  mm lipid pool, and minimal fibrous cap width of  $0.2$  mm. (B) Carotid with 80% stenosis, distal  $4 \times 2$  mm lipid pool, and minimal fibrous cap width of  $0.2$  mm. A large zone of recirculating blood was present above the plaque (yellow asterisk)

The combined effects of degrees of stenosis, fibrous cap thicknesses, lipid core size, and lipid core location on peak principal stress levels are depicted in fig. 5. Stresses are seen to increase with decreasing fibrous cap thickness, and increasing degrees of stenosis. However, the degree of stenosis mainly affects peak principal stresses in models with fibrous caps below  $0.2$  mm in width. This is evident by the observation that the variation in peak principal stresses increases as the fibrous cap width decreases. Lipid core sizes have a marked influence on peak principal stress levels. Peak principal stress in a model with 95% degree of stenosis, a proximal lipid core, and fibrous cap thickness of  $0.1$  mm varied from  $1861.2$  kPa with a  $6 \times 3$  mm lipid core to  $445.6$  kPa with a  $2 \times 1$  mm lipid core.

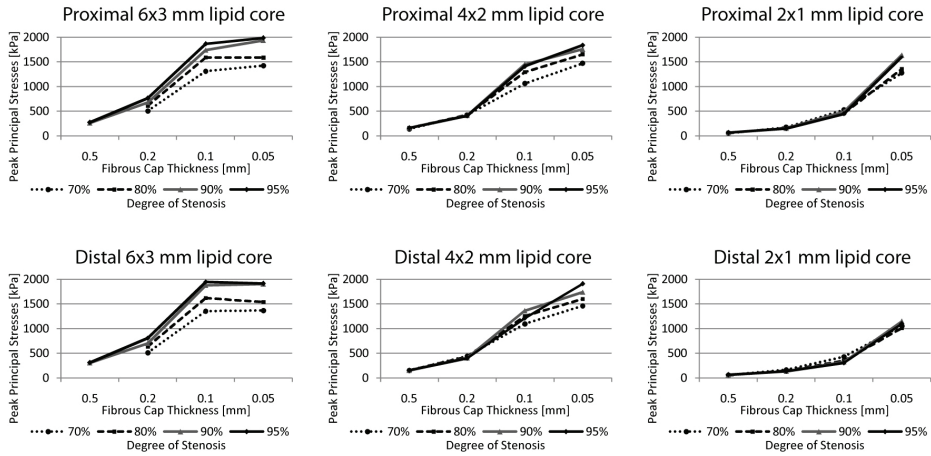


Figure 5. Effects of fibrous cap thickness, degree of stenosis, lipid core size, and lipid core position on peak principal stress levels

The longitudinal position of the lipid core did not affect peak principal stress levels in this model, as shown in fig. 5. Also evident in fig. 5 are the effects of decreasing lipid core sizes producing substantial reductions in median peak principal stress levels.

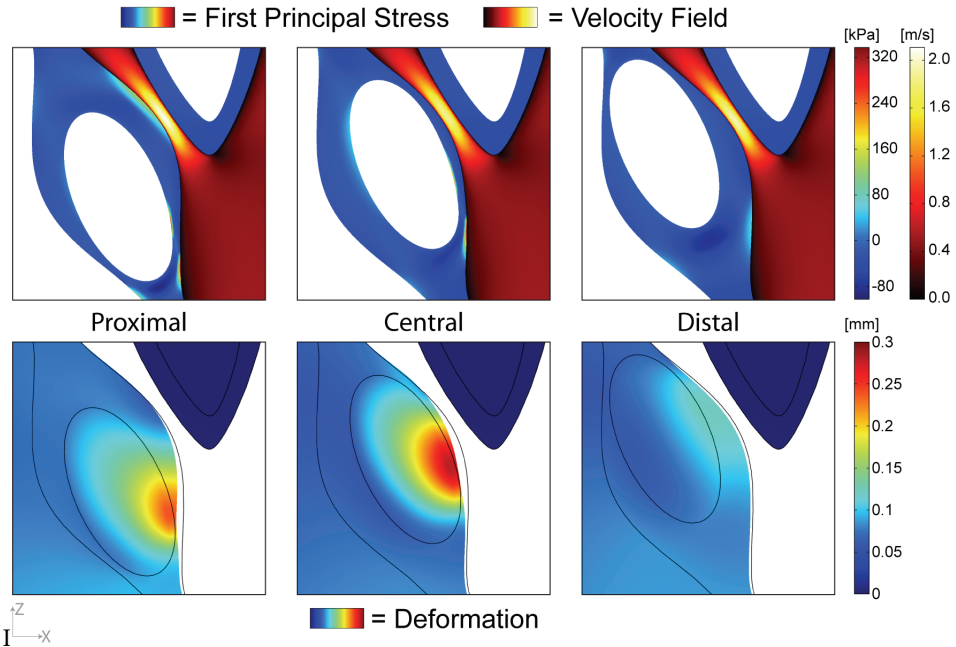


Figure 6. Principal stress levels and deformations as a function of lipid core position in a model with 90% degree of stenosis, 0.5 mm fibrous cap thickness, and 6x3 mm lipid core size

In another model with a 90% degree of stenosis employing the original flow values measured in the patient with a 70% degree of stenosis instead of using the Venturi calculations, lipid core position was seen to influence peak principal stress levels substantially, as presented in fig. 6. Using this model, peak principal stresses were 323.4 kPa, 335.0 kPa, and 64.6 kPa in the proximal, central, and distal lipid core simulation, respectively.

#### 4. Discussion

Currently, carotid risk assessment is based on measuring the degree of stenosis to determine if carotid endarterectomy should be offered symptomatic patients (NASCET, 1991; ECST, 1991; Rothwell et al., 2003a). However, there is growing evidence that morphological composition rather than degree of luminal stenosis may be the deciding factor in determining plaque vulnerability (Virmani et al., 2006; Gronholdt et al., 1998; Falk, 1992). In particular, large lipid cores with thin fibrous caps have been determined to be the hallmark of unstable plaques at high risk of rupture. Through the advent of high-resolution MR imaging combined with computational analysis, in-vivo estimations of mechanical stresses in the fibrous cap have been enabled (Li et al., 2007; Tang et al., 2004; Zhao et al., 2002).

In a recent study by Li et al. (Li et al., 2006b), the effect of stenosis severity and fibrous cap thickness on resulting mechanical stress levels was investigated. This study showed that plaques with a degree of stenosis at 70% or above all gave rise to high fibrous cap stress levels regardless of fibrous cap width. Plaques with lower degrees of stenosis also reached high stress levels depending on the thickness of the fibrous cap. However, to simplify the computational analysis a straight tube without bifurcation was used and the plaque was modeled as a large homogeneous lipid core covered by a fibrous cap of varying thickness.

In our study, we used an idealized bifurcation model based on geometry obtained from a patient awaiting carotid endarterectomy. Ellipsoidally shaped lipid cores were used to create heterogeneous plaques with varying position of the lipid cores allowing for examinations of the effects of lipid core size and position in addition to the effects of the degree of stenosis and fibrous cap width. To account for the effect of increasing degrees of stenosis on fluid flows, the internal carotid artery was modeled as a Venturi tube, and the velocities adjusted accordingly.

The findings of Li et al. (Li et al., 2006b) were confirmed; increasing degrees of stenosis and decreasing fibrous cap thicknesses were found to affect peak principal stress levels severely (fig. 5). Though decreases in fibrous cap width was by far the most influential parameter on fibrous cap stress levels it cannot stand alone. Lipid core sizes also impacted mechanical stress levels significantly (fig. 5) and a comprehensive approach towards fibrous cap mechanical stress estimations is deemed important.

In an angiographic study of plaque ulceration, Lovett (Lovett and Rothwell, 2003) determined ulcerations to be asymmetrically distributed longitudinally with the majority occurring upstream to the plaque rather than downstream. To investigate if this phenomenon could be attributed to mechanical stress levels, symmetrical simulations were performed with lipid cores placed proximally and distally inside the plaque. However, no significant differences were found between models with proximal cores vs. distal cores, indeed the stress levels were virtually identical except for very small lipid cores (fig. 5). This effect may be due to the modeling of the internal carotid artery as a Venturi tube keeping the pressure difference across the stenosis constant. Thus a second round of simulations was performed using the original flow values measured in the patient with a 70% degree of



stenosis instead of adjusting these using the Venturi calculations. These revealed vast increases in stress levels if the fibrous cap was thinnest on the proximal side of the plaque, compared with the distal side. These results thus agree with the findings of Lovett (Lovett and Rothwell, 2003), and principal stress levels may be the cause of the asymmetrical longitudinal distribution of plaque rupture with the majority occurring proximally to the plaque.

Previous studies have used principal stress levels in excess of 300 kPa to be predictive of plaques at high risk of rupture (Cheng et al., 1993; Li et al., 2006b; Li et al., 2007). However, the choice of material model and parameters may substantially affect simulated stress levels (Li et al., 2006a). Care should thus be taken comparing absolute stress levels across different simulations employing different material models, and the choice of an absolute level at which the plaques are considered to be at risk of rupture may be problematic.

Currently, state-of-the-art MRI scans employ typical in plane spatial resolutions of 0.5 – 0.6 mm (Yuan and Kerwin, 2004; Crowe et al., 2005). Stress levels increased dramatically with decreasing fibrous cap widths, particularly below 0.2 mm. Increasing spatial resolution to enable visualization of very thin fibrous caps could thus prove of vital importance. Moving towards scanners with higher field strengths (Yarnykh et al., 2006) or switching from 2D to 3D acquisitions (Koktzoglou and Li, 2007) may facilitate this.

## 5. Conclusion

The new technique of obtaining longitudinal 2D computational models of the carotid artery was systematically investigated using idealized carotid bifurcation geometry with variables thought to be linked to risk of carotid plaque rupture; degree of stenosis, fibrous cap thickness, and lipid core size, all of which affected stress levels severely. Numerous histopathological studies have indicated lipid pool size and fibrous cap thickness to be key determinants of plaque vulnerability. Principal stresses may be of additional merit, since this parameter combines effects of fibrous cap thickness, lipid pool size, degree of stenosis, and blood pressure into a single comprehensive risk assessment marker. With the advent of fast computational techniques for obtaining in-vivo stress levels, assessing risk of plaque rupture using peak principal stress levels is enabled which may lead to improved reliability of carotid risk assessment in the future.

## 6. References

- Versluis, A., Bank, A.J., Douglas, W.H., 2006. Fatigue and plaque rupture in myocardial infarction. *Journal of Biomechanics* 39, 339-347
- Antheunis, V Alan, JB William, HD, (2006). Fatigue and plaque rupture in myocardial infarction. pp. 339-347.
- Banks, J. Bressloff, N.W., 2007. Turbulence modeling in three-dimensional stenosed arterial bifurcations. *Journal of Biomechanical Engineering* 129, 40-50.
- Bassiouny, H.S. Sakaguchi, Y. et al., 1997. Juxtalumenal location of plaque necrosis and neoformation in symptomatic carotid stenosis. *J.Vasc.Surg.* 26, 585-594.
- Botnar, R.M. Stuber, M. et al., 2001. Magnetic resonance coronary lumen and vessel wall imaging. *Rays* 26, 291-303.
- Cai, J.M. Hatsukami, T.S. et al., 2002. Classification of human carotid atherosclerotic lesions with in vivo multicontrast magnetic resonance imaging. *Circulation* 106, 1368-1373.

- Carr, S. Farb, A. et al., 1996. Atherosclerotic plaque rupture in symptomatic carotid artery stenosis, , . *Journal of Vascular Surgery* 23, 755-766.
- Casscells, W. Naghavi, M. et al., 2003. Vulnerable atherosclerotic plaque: a multifocal disease. *Circulation* 107, 2072-2075.
- Chau, A.H. Chan, R.C. et al., 2004. Mechanical analysis of atherosclerotic plaques based on optical coherence tomography. *Ann.Biomed.Eng* 32, 1494-1503.
- Chen, C.H. Ting, C.T. et al., 1996. Validation of Carotid Artery Tonometry as a Means of Estimating Augmentation Index of Ascending Aortic Pressure. *Hypertension* 27, 168-175.
- Cheng, G.C. Loree, H.M. et al., 1993. Distribution of circumferential stress in ruptured and stable atherosclerotic lesions. A structural analysis with histopathological correlation. *Circulation* 87, 1179-1187.
- Chu, B. Kampschulte, A. et al., 2004. Hemorrhage in the atherosclerotic carotid plaque: a high-resolution MRI study. *Stroke* 35, 1079-1084.
- Claudon, M. Winninger, D. et al., 2001. Power Doppler US: Evaluation of the Morphology of Stenoses with a Flow Phantom. *Radiology* 218, 109-117.
- Clevert, D.A. Johnson, T. et al., 2007. Color Doppler, power Doppler and B-flow ultrasound in the assessment of ICA stenosis: Comparison with 64-MD-CT angiography. *European Radiology* 17, 2149-2159.
- Clevert, D.A. Johnson, T. et al., 2006. High-grade stenoses of the internal carotid artery: Comparison of high-resolution contrast enhanced 3D MRA, duplex sonography and power Doppler imaging. *European Journal of Radiology* 60, 379-386.
- COMSOL AB, (2005). Comsol Multiphysics: Structural Mechanics Module. COMSOL AB, Stockholm, Sweden.
- Crowe, L.A. Keegan, J. et al., 2005. 3D volume-selective turbo spin echo for carotid artery wall imaging with navigator detection of swallowing. *J Magn Reson.Imaging* 22, 583-588.
- Dart, A.M. Kingwell, B.A., 2001. Pulse pressure--a review of mechanisms and clinical relevance. *Journal of the American College of Cardiology* 37, 975-984.
- Draney, M.T. Herfkens, R.J. et al., 2002. Quantification of vessel wall cyclic strain using cine phase contrast magnetic resonance imaging. *Ann.Biomed.Eng* 30, 1033-1045.
- ECST, 1991. MRC European Carotid Surgery Trial: interim results for symptomatic patients with severe (70-99%) or with mild (0-29%) carotid stenosis. *European Carotid Surgery Trialists' Collaborative Group. Lancet* 337, 1235-1243.
- ECST, 1998. Randomised trial of endarterectomy for recently symptomatic carotid stenosis: final results of the MRC European Carotid Surgery Trial (ECST). *Lancet* 351, 1379-1387.
- Falk, E., 2006. Pathogenesis of atherosclerosis. *Journal of the American College of Cardiology* 47, C7-12.
- Falk, E., 1992. Why do plaques rupture? *Circulation* 86, III30-III42.
- Falk, E. Shah, P.K. et al., 1995. Coronary Plaque Disruption. *Circulation* 92, 657-671.
- Firmin, D.N. Nayler, G.L. et al., 1990. The application of phase shifts in NMR for flow measurement. *Magn Reson.Med.* 14, 230-241.
- Frayne, R. Steinman, D.A. et al., 1995. Accuracy of MR phase contrast velocity measurements for unsteady flow. *J Magn Reson.Imaging* 5, 428-431.

- Glagov, S. Weisenberg, E. et al., 1987. Compensatory enlargement of human atherosclerotic coronary arteries. *New England Journal of Medicine* 316, 1371-1375.
- Glagov, S. Zarins, C. et al., 1988. Hemodynamics and atherosclerosis. Insights and perspectives gained from studies of human arteries. *Arch Pathol Lab Med* 112, 1018-1031.
- Gronholdt, M.L. Dalager-Pedersen, S. et al., 1998. Coronary atherosclerosis: determinants of plaque rupture. *Eur.Heart J.* 19 Suppl C, C24-C29.
- Halliday, A. Mansfield, A. et al., 2004. Prevention of disabling and fatal strokes by successful carotid endarterectomy in patients without recent neurological symptoms: randomised controlled trial. *Lancet* 363, 1491-1502.
- Hatsukami, T.S. Ross, R. et al., 2000. Visualization of fibrous cap thickness and rupture in human atherosclerotic carotid plaque in vivo with high-resolution magnetic resonance imaging. *Circulation* 102, 959-964.
- Hayes, C.E. Mathis, C.M. et al., 1996. Surface coil phased arrays for high-resolution imaging of the carotid arteries. *J.Magn Reson.Imaging* 6, 109-112.
- Holzapfel, G.A. Sommer, G. et al., 2004. Anisotropic mechanical properties of tissue components in human atherosclerotic plaques. *J Biomech Eng* 126, 657-665.
- Huang, D. Swanson, E.A. et al., 1991. Optical coherence tomography. *Science* 254, 1178-1181.
- Huang, H. Virmani, R. et al., 2001. The Impact of Calcification on the Biomechanical Stability of Atherosclerotic Plaques. *Circulation* 103, 1051-1056.
- Imoto, K. Hiro, T. et al., 2005. Longitudinal Structural Determinants of Atherosclerotic Plaque Vulnerability: A Computational Analysis of Stress Distribution Using Vessel Models and Three-Dimensional Intravascular Ultrasound Imaging. *Journal of the American College of Cardiology* j.
- Jin, S. Yang, Y. et al., 2004. Flow patterns and wall shear stress distributions at atherosclerotic-prone sites in a human left coronary artery—an exploration using combined methods of CT and computational fluid dynamics. *Conf.Proc.IEEE Eng Med Biol Soc.* 5, 3789-3791.
- Kaazempur-Mofrad, M.R. Isasi, A.G. et al., 2004. Characterization of the atherosclerotic carotid bifurcation using MRI, finite element modeling, and histology. *Ann Biomed Eng* 32, 932-946.
- Kario, K. Pickering, T.G. et al., 2003. Morning Surge in Blood Pressure as a Predictor of Silent and Clinical Cerebrovascular Disease in Elderly Hypertensives: A Prospective Study. *Circulation* 107, 1401-1406.
- Koktzoglou, I. Li, D., 2007. Submillimeter isotropic resolution carotid wall MRI with swallowing compensation: imaging results and semiautomated wall morphometry. *J Magn Reson.Imaging* 25, 815-823.
- Lee, S.W. Steinman, D.A., 2007. On the relative importance of rheology for image-based CFD models of the carotid bifurcation. *J.Biomech.Eng* 129, 273-278.
- Li, Z.Y. Howarth, S. et al., 2006a. Stress analysis of carotid plaque rupture based on in vivo high resolution MRI. *Journal of Biomechanics* 39, 2611-2622.
- Li, Z.Y. Howarth, S.P.S. et al., 2006b. How Critical Is Fibrous Cap Thickness to Carotid Plaque Stability?: A Flow-Plaque Interaction Model. *Stroke* 37, 1195-1199.
- Li, Z.Y. Howarth, S.P.S. et al., 2007. Structural analysis and magnetic resonance imaging predict plaque vulnerability: A study comparing symptomatic and asymptomatic individuals. *Journal of Vascular Surgery* 45, 768-775.

- Liu, F. Xu, D. et al., 2006. Automated in vivo segmentation of carotid plaque MRI with Morphology-Enhanced probability maps. *Magnetic Resonance in Medicine* 55, 659-668.
- Loree, H.M. Kamm, R.D. et al., 1992. Effects of fibrous cap thickness on peak circumferential stress in model atherosclerotic vessels. *Circulation Research* 71, 850-858.
- Lovett, J.K. Rothwell, P.M., 2003. Site of carotid plaque ulceration in relation to direction of blood flow: An angiographic and pathological study. *Cerebrovascular Diseases* 16, 369-375.
- Lui, E.Y.L. Steinman, A.H. et al., 2005. Human factors as a source of error in peak Doppler velocity measurement. *Journal of Vascular Surgery* 42, 972.
- McDonnell, C.H., III Herfkens, R.J. et al., 1994. Magnetic resonance imaging and measurement of blood flow. *West J Med.* 160, 237-242.
- Mead, G.E. Lewis, S.C. et al., 2000. Variability in Doppler ultrasound influences referral of patients for carotid surgery. *European Journal of Ultrasound* 12, 137-143.
- Metafratzi, Z.M. Efremidis, S.C. et al., 2002. The clinical significance of aortic compliance and its assessment with magnetic resonance imaging. *Journal of Cardiovascular Magnetic Resonance* 4, 481-491.
- Mitsumori, L.M. Hatsukami, T.S. et al., 2003. In vivo accuracy of multisequence MR imaging for identifying unstable fibrous caps in advanced human carotid plaques. *J.Magn Reson.Imaging* 17, 410-420.
- Naghavi, M. Libby, P. et al., 2003. From Vulnerable Plaque to Vulnerable Patient: A Call for New Definitions and Risk Assessment Strategies: Part I. *Circulation* 108, 1664-1672.
- NASCET, 1991. Beneficial effect of carotid endarterectomy in symptomatic patients with high-grade carotid stenosis. North American Symptomatic Carotid Endarterectomy Trial Collaborators. *New England Journal of Medicine* 325, 445-453.
- Nederkoorn, P.J. van der, G.Y. et al., 2003. Duplex ultrasound and magnetic resonance angiography compared with digital subtraction angiography in carotid artery stenosis: a systematic review. *Stroke* 34, 1324-1332.
- Nighoghossian, N. Derex, L. et al., 2005. The Vulnerable Carotid Artery Plaque: Current Imaging Methods and New Perspectives. *Stroke* 36, 2764-2772.
- Pasterkamp, G. Smits, P.C., 2002. Imaging of atherosclerosis. Remodelling of coronary arteries. *J.Cardiovasc.Risk* 9, 229-235.
- Perktold, K. Rappitsch, G., 1995. Computer simulation of local blood flow and vessel mechanics in a compliant carotid artery bifurcation model. *J.Biomech.* 28, 845-856.
- Piegl, L., Tiller, W., (1997). The NURBS Book. Springer-Verlag, New York, NY.
- Ramaswamy, S.D. Vigmostad, S.C. et al., 2006. Comparison of left anterior descending coronary artery hemodynamics before and after angioplasty. *J Biomech Eng* 128, 40-48.
- Redgrave, J.N.E. Lovett, J.K. et al., 2006. Histological Assessment of 526 Symptomatic Carotid Plaques in Relation to the Nature and Timing of Ischemic Symptoms: The Oxford Plaque Study. *Circulation* 113, 2320-2328.
- Roemer, P.B. Edelstein, W.A. et al., 1990. The NMR phased array. *Magn Reson.Med.* 16, 192-225.
- Rosamond, W. Flegal, K. et al., 2007. Heart Disease and Stroke Statistics--2007 Update: A Report From the American Heart Association Statistics Committee and Stroke Statistics Subcommittee. *Circulation* 115, e69-171.

- Rothwell, P.M. Eliasziw, M. et al., 2003a. Analysis of pooled data from the randomised controlled trials of endarterectomy for symptomatic carotid stenosis. *Lancet* 361, 107-116.
- Rothwell, P.M. Howard, S.C. et al., 2003b. Relationship Between Blood Pressure and Stroke Risk in Patients With Symptomatic Carotid Occlusive Disease. *Stroke* 34, 2583-2590.
- Shinnar, M. Fallon, J.T. et al., 1999. The diagnostic accuracy of ex vivo MRI for human atherosclerotic plaque characterization. *Arteriosclerosis, Thrombosis, and Vascular Biology* 19, 2756-2761.
- Sipahi, I. Tuzcu, E.M. et al., 2007. Does the extent and direction of arterial remodeling predict subsequent progression of coronary atherosclerosis? A serial intravascular ultrasound study. *Heart hrt*.
- Small, D.M. Shipley, G.G., 1974. Physical-chemical basis of lipid deposition in atherosclerosis. *Science* 185, 222-229.
- Staessen, J.A. Fagard, R. et al., 1997. Randomised double-blind comparison of placebo and active treatment for older patients with isolated systolic hypertension. *The Lancet* 350, 757-764.
- Stary, H.C. Chandler, A.B. et al., 1995. A Definition of Advanced Types of Atherosclerotic Lesions and a Histological Classification of Atherosclerosis : A Report From the Committee on Vascular Lesions of the Council on Arteriosclerosis, American Heart Association. *Arteriosclerosis, Thrombosis, and Vascular Biology* 15, 1512-1531.
- Steinman, D.A., 2002. Image-based computational fluid dynamics modeling in realistic arterial geometries. *Ann.Biomed.Eng* 30, 483-497.
- Tang, D. Yang, C. et al., 2004. 3D MRI-based multicomponent FSI models for atherosclerotic plaques. *Annals of Biomedical Engineering* 32, 947-960.
- Titi, M. George, C. et al., 2007. Comparison of carotid Doppler ultrasound and computerised tomographic angiography in the evaluation of carotid artery stenosis. *Surgeon*. 5, 132-136.
- Tola, M. Yurdakul, M., 2006. Effect of Doppler Angle in Diagnosis of Internal Carotid Artery Stenosis. *Journal of Ultrasound in Medicine* 25, 1187-1192.
- Virmani, R. Kolodgie, F.D. et al., 2000. Lessons from sudden coronary death: a comprehensive morphological classification scheme for atherosclerotic lesions. *Arterioscler.Thromb.Vasc.Biol*. 20, 1262-1275.
- Virmani, R. Ladich, E.R. et al., 2006. Histopathology of carotid atherosclerotic disease. *Neurosurgery* 59, S219-S227.
- Wentzel, J.J. Gijzen, F.J.H. et al., 2003. Shear stress, vascular remodeling and neointimal formation. *Journal of Biomechanics* 36, 681-688.
- WHO and CDC, (2004). *The Atlas of Heart Disease and Stroke*.
- Yabushita, H. Bouma, B.E. et al., 2002. Characterization of Human Atherosclerosis by Optical Coherence Tomography. *Circulation* 106, 1640-1645.
- Yarnykh, V.L. Terashima, M. et al., 2006. Multicontrast black-blood MRI of carotid arteries: comparison between 1.5 and 3 tesla magnetic field strengths. *Journal of Magnetic Resonance Imaging* 23, 691-698.
- Yarnykh, V. L., Yuan, C., (2003). High-Resolution Multi-Contrast MRI of the Carotid Artery Wall for Evaluation of Atherosclerotic Plaques. *Current Protocols in Magnetic Resonance Imaging*. John Wiley & Sons.

- Yuan, C. Beach, K.W. et al., 1998. Measurement of atherosclerotic carotid plaque size in vivo using high resolution magnetic resonance imaging. *Circulation* 98, 2666-2671.
- Yuan, C. Kerwin, W.S., 2004. MRI of atherosclerosis. *Journal of Magnetic Resonance Imaging* 19, 710-719.
- Yuan, C. Lin, E. et al., 1999. Closed contour edge detection of blood vessel lumen and outer wall boundaries in black-blood MR images. *Magn Reson. Imaging* 17, 257-266.
- Yuan, C. Mitsumori, L.M. et al., 2001. In vivo accuracy of multispectral magnetic resonance imaging for identifying lipid-rich necrotic cores and intraplaque hemorrhage in advanced human carotid plaques. *Circulation* 104, 2051-2056.
- Yuan, C. Petty, C. et al., 1997. In vitro and in situ magnetic resonance imaging signal features of atherosclerotic plaque-associated lipids. *Arterioscler. Thromb. Vasc. Biol.* 17, 1496-1503.
- Yuan, C. Zhang, S.X. et al., 2002. Identification of fibrous cap rupture with magnetic resonance imaging is highly associated with recent transient ischemic attack or stroke. *Circulation* 105, 181-185.
- Yusuf, S. Reddy, S. et al., 2001. Global Burden of Cardiovascular Diseases: Part I: General Considerations, the Epidemiologic Transition, Risk Factors, and Impact of Urbanization. *Circulation* 104, 2746-2753.
- Zhao, S.Z. Ariff, B. et al., 2002. Inter-individual variations in wall shear stress and mechanical stress distributions at the carotid artery bifurcation of healthy humans. *Journal of Biomechanics* 35, 1367-1377.

# Electromagnetic Flow Metering

Jens Krause  
*FuE Zentrum FH Kiel GmbH, Kiel  
Germany*

## 1. Introduction

Numerical simulations have become an integral part of new sensor design and they are essential to understand the physical principles of completely new sensors. In this chapter we want to demonstrate that, when using modern software tools, relevant results are in reach even for small development departments.

The electromagnetic flow meter, that measures the volume flow rate of conducting liquids passing through pipes, is a very practical example for a sensor that is used in real applications, but that has still potential for improvement and optimisation by numerical simulations. The goal of this chapter is to show, in three concrete cases, different levels of modelling.

The chapter will introduce the concepts of electromagnetic flow metering and the physical phenomena needed for numerical modelling. The main goal is to show that physical principles can be studied with detail and that, nevertheless, calculations are relevant to practical applications.

We demonstrate the ideas in three detailed cases.

1. Until now, commercially available devices require a minimum conductivity of water, i.e., a minimum concentration of ions. Using numerical methods one can study the low concentration limit of the electromagnetic flow meter. The central idea is to apply a drift-diffusion model to the system of electric charges present in the fluid.
2. For standard devices several physical phenomena are encountered: fluid dynamics, magnetostatics, and electrostatics. We demonstrate the efficient use of multiphysics solvers for the geometric optimisation of a sensor. The geometric shape is optimised much easier numerically than it can be done in experiments.
3. A completely new sensor principle can be verified using numerical simulation for turbulent flows. By studying the amplitude of fluctuations we find a new way of measuring the mean flow, which is in accordance with experiments.

The numerical scheme for these calculations is based on finite methods: in many cases the very flexible finite element method can be employed. It can solve a wide range of physical problems and a large class of geometries. Standard software packages are available for all equations needed for flow sensor design. On the other hand the finite difference method requires regular grids but can, due to its inherent speed, solve large problems like the turbulent direct numerical simulation, where space and time must be resolved in a fine discretisation.

## 2. Magnetic-inductive flow meter

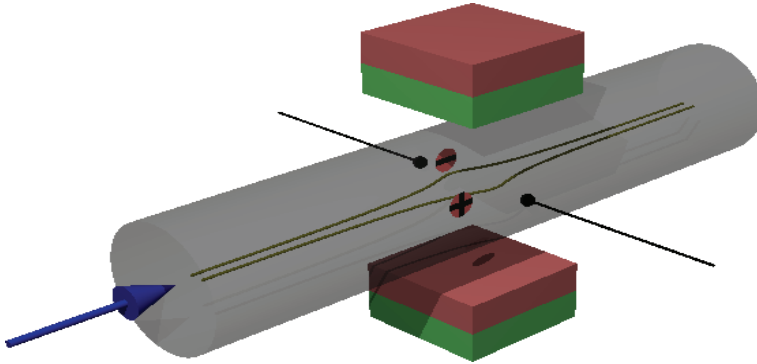


Figure 1. Principle of the electromagnetic flow meter. Ions are displaced by an outer magnetic field and a electric voltage can be measured at galvanic contacts (black circles)

The basic idea of the electromagnetic (or magnetic-inductive, MI) flow meter for measuring fluid flow in pipes shall be explained with the help of fig. 1. An external magnetic field perpendicularly penetrates the tube carrying fluid flow. If the fluid contains mobile electric charges these are displaced (with respect to the fluid) due to the Lorentz-force. The accumulated charges form a space charge density and an electric field is induced which prevents further charge separation. The electric potential can be sensed using galvanic or capacitive coupling. In ideal cases the measured voltage is proportional to the flow rate in the tube.

The idea of this method is old, if one considers Michael Faraday's famous experiment at the river Thames as a starting point. Later, in 1930, Williams reported the first experimental proof (Williams 1930) and today the MI-flow meter has become a commercial product used in many applications in industry: process, food, waste water, etc. The theory is mature and text books have been published that are entirely (Schommartz 1974) or in parts (Fiedler 1992) devoted to the subject.

The sensors are mainly employed for water as liquid, although the use for other electrically conducting fluids is feasible. Standard devices avoid permanent magnets because of spurious electrochemical voltages at the sensing contacts. Even with electrodes made of noble metals, chemical reactions are present in water at galvanic contacts and lead to time-varying electric potentials, that are larger than the actual MI-signal. By using alternating or pulsed magnetic fields these variations can be filtered. Capacitive coupling suffers from the difficulty to measure small charges when the inner resistance of the pick-up circuit is finite.

But the price for time varying magnetic fields is high energy consumption. Up to 99% of the total energy is spent on the generation of the magnetic field, which is prohibitive for battery driven devices. Using modern electronic devices with ultra-high-ohmic amplifiers, static measurements have become feasible and a recent patent (Stange 2002) describes a method to bypass spurious voltages. Therefore some aspects in the field of electromagnetic flow metering have to be rethought and can be studied using numerical simulations.

The Finite-Element method has become a versatile tool in solving partial differential equations (PDEs) in many scientific and engineering disciplines. Many text books describe the method in different aspects and we only want to cite one of the most influential by



Zienkiewicz (Zienkiewicz & Taylor 1989) first published on structural mechanics. Since then the method has been applied to other engineering fields and due to the increased computer power became available to developers for daily use.

For MI-sensors the literature using FE-simulation is sparse but many applications in industry are on optimising the coils generating the magnetic field. Here we focus on the study of fundamental physical understanding and geometric optimisation. Many publications on electromagnetic flow meters use the concept of a *weight function* to analyse the design. This concept will be mentioned briefly because it is widely used but it is restricted to the high concentration limit (that we want to study in detail) and to galvanic contacts concentrated in points.

### 3. Mathematical models

The different physical effects and their equations are discussed in the following with their relevance to the electromagnetic flow meter.

#### 3.1 Fluid dynamics (Navier-Stokes equations)

The equations for fluid flow are derived from the basic physical principles of conservation of mass, of momentum, and of energy applied to continuum mechanics. Many text books on this subject, e.g., Spurk & Aksel (2006), are available and only basic properties are stated here without proofs.

Fluid flow is usually described by the Eulerian view, that represents the velocity of the fluid as vector field  $\mathbf{u}$  at a fixed point in space. Two additional scalar fields are needed in general: the pressure  $p$  and the mass density  $\rho$ . In an incompressible fluid the system reduces to  $\mathbf{u}$  and  $p$  and the incompressibility condition replaces the conservation of mass:

$$\nabla \cdot \mathbf{u} = 0. \quad (1)$$

The conservation of momentum leads to

$$\rho \dot{\mathbf{u}} + \rho(\mathbf{u} \cdot \nabla) \mathbf{u} = -\nabla p + \mu \Delta \mathbf{u}. \quad (2)$$

The left hand side represents the change of momentum in time at a fixed point in space. The right hand side denotes that the contributing forces are the pressure gradient as the driving force of the flow and the dissipative friction term. In the viscous model friction is caused by a velocity gradient and the proportionality constant  $\mu$  is called viscosity. These equations are known as the incompressible Navier-Stokes (NS) equations. The boundary condition at physical walls is that the flow velocity is zero. Other mathematical boundary conditions are applied to inlets, outlets, and symmetry planes. The system of equation (1) and (2) is closed: it comprises four equations for four unknowns.

#### 3.2 Magnetic inductive effect

The basic principle is that electric charges (like ions from dissolved salts) in the fluid are displaced due the Lorentz-force in response to an external magnetic field that is orthogonal to the fluid flow. The charge separation leads to an electric field  $\mathbf{E}$  perpendicular both to the flow and the magnetic field. The electric potential  $\phi$  can be sensed with galvanic contacts or with capacitive sensors.

In a conducting medium the electric current density  $\mathbf{j}$  in presence of an electromagnetic fields is

$$\mathbf{j} = \sigma(\mathbf{E} + \mathbf{u} \times \mathbf{B}) \quad (3)$$

where  $\sigma$  is the specific conductivity. In an equilibrium state the current density is divergence free because of charge conservation and it follows that

$$\Delta \varphi = \nabla \cdot (\mathbf{u} \times \mathbf{B}). \quad (4)$$

This equation has been cited in the literature (Shommartz 1974; Fiedler 1992) and is called here the *high concentration limit* and we discuss the validity of this model later. Here and in later models it is assumed that  $\mathbf{B}$  is the external magnetic field only. The flowing medium itself drives electric currents which induce magnetic fields that are in the case of electrolytes too weak to have an influence. Two types of currents can be distinguished: The first one is generated by the charge density that is convected by the fluid, whereas the second one is the current as expressed in eq. (3).

The *weight function* approach applies Green's theorem to equation (4) and is often used to examine MI-flow meters. The Green's function that corresponds to the Laplace operator reads

$$G(\mathbf{x}, \mathbf{x}') = \frac{1}{4\pi|\mathbf{x} - \mathbf{x}'|} \quad (5)$$

and can be employed to express solutions of (4) as an integral. If two galvanic contacts are concentrated in points the voltage

$$\begin{aligned} V_{ab} &= \varphi(a) - \varphi(b) \\ &= -\int [\nabla_x G(a, \mathbf{x}) - \nabla_x G(b, \mathbf{x})] \cdot (\mathbf{u} \times \mathbf{B}) d^3x \end{aligned} \quad (6)$$

is measured. The expression in square brackets is called the weight function  $\mathbf{W}(a, b, \mathbf{x})$  (Shercliff 1954; Fiedler 1992). The integral can be transformed to

$$V_{ab} = \int \mathbf{u} \cdot (\mathbf{W} \times \mathbf{B}) d^3x. \quad (7)$$

In this form the integral formulation is helpful to design the magnetic field, e.g., to guarantee the property that the voltage is independent of flow profile. This approach is, however, limited to a simple governing equation and to pointlike galvanic contacts. Since more general problems must be solved we adopt the more flexible Finite-Element-Method.

### 3.3 Electrostatics and Magnetostatics

Maxwell's equations are only applied to the static field case only. In the macroscopic form, i.e., using material properties like permittivity, permeability, and magnetisation, the following equations are valid for the electric field:

$$\begin{aligned} \nabla \cdot (\varepsilon_0 \varepsilon_r \mathbf{E}) &= \rho \\ \mathbf{E} &= -\nabla \varphi \end{aligned} \quad (8)$$

where  $\mathbf{E}$  is the electric field,  $\varphi$  the potential,  $\epsilon_0$  the permittivity of the vacuum and  $\epsilon_r$  the relative permittivity of the material in question.

The relations for the fields  $\mathbf{H}$  (magnetic field),  $\mathbf{B}$  (magnetic induction), and  $\mathbf{M}$  (magnetisation) are

$$\begin{aligned}\nabla \cdot \mathbf{B} &= 0 \\ \nabla \times \mathbf{H} &= 0 \\ \mathbf{B} &= \begin{cases} \mu_0 \mu_r \mathbf{H} \\ \mu_0 (\mathbf{H} + \mathbf{M}) \end{cases}\end{aligned}\quad (9)$$

The first material relationship is used for the usual linear response to a magnetic field, whilst the second is used as an approximation for permanent magnets with a given fixed magnetisation.

As mentioned above the magnetic fields produced by the currents in the medium are weak and these currents are altogether neglected as sources of the magnetic field. Since the curl of the magnetic field is zero under these circumstances a scalar magnetic potential with

$$\mathbf{H} = -\nabla\theta \quad (10)$$

is introduced and used later for solving magnetostatic equations.

### 3.4 Drift-Diffusion

The evolution of the concentration  $c$  of an ion species in a medium is often described in electrochemistry (Hamann & Vielstich 2004) using the drift-diffusion approach. The effective current is generated in two ways: first, a driving force  $\mathbf{F}$  on the individual particle and second the thermal diffusion. Applying Einstein's law we can write for each species

$$\mathbf{j} = \mu(c\mathbf{F} - k_B T \nabla c) \quad (11)$$

where  $\mu$  is the mobility,  $k_B$  Boltzmann's constant and  $T$  the absolute temperature. We want to apply this model to diluted salts in water. For higher concentrations the linear mobility model is not valid, but here study only low concentration effects (Atkins 1988). The force  $\mathbf{F}$  is due to an electrostatic field and to a magnetic induction

$$\mathbf{F} = q(\mathbf{E} + \mathbf{u} \times \mathbf{B}). \quad (12)$$

We only consider the Lorentz-force caused by the medium flow  $\mathbf{u}$ , the additional velocity induced by the movement of ions with respect to the water is small and neglected in our model. The conservation of particle number is written as

$$\dot{c} + \nabla \cdot \mathbf{j} = G, \quad (13)$$

where the dot signifies the derivative with respect to time and  $G$  the particle generation rate. The boundary conditions are generally of the homogeneous Neumann-type for wall boundaries that the particles cannot penetrate. Often the total number of particles is fixed and an integral constraint in the form

$$\int c \, d^3x = N \quad (14)$$

is added to the equations. When multiple species are present the equations (11,12,13) have to be formulated for each type separately.

#### 4. Finite-Element-Method

The finite element method is an established technique in academia and industry to approximately solve partial differential equations and applies to boundary value problems. Many authors (Zienkiewicz & Taylor 1989; Ciarlet 1978) have discussed the method in detail and for many applications.

One way of formulating boundary value problem, which is useful for many physical applications, is based on generalised sources and fluxes. For a degree of freedom  $u$ , the flux  $\mathbf{J}$  and the source term  $S$  depend on  $u$  and its derivatives. The boundary value problem sets conditions on the inner of a domain  $\Omega$  and on the boundary such that

$$\begin{aligned} \nabla \cdot \mathbf{J} &= S \quad \text{in } \Omega & (15) \\ u &= f \quad \text{in } \Gamma_D \subseteq \partial\Omega \\ \mathbf{n} \cdot \mathbf{J} &= g \quad \text{in } \Gamma_N = \partial\Omega / \Gamma_D. \end{aligned}$$

These equations imply the conservation of a quantity in the domain, Dirichlet condition (prescribed value  $f$ ) on one part of the boundary, and Neumann condition (prescribed normal flux  $g$ ) on the remaining boundary. In the case of a vectorial physical property or a multiphysics problem, several unknowns  $u_i$  have to be taken into account. For each unknown there is one set of equations in the form (15). If the generalised fluxes and sources depend mutually on each other the system is coupled.

The Finite-Element (FE) method approximates the solution by polynomial functions defined on elements (e.g. triangles or tetrahedrons), i.e., a continuous problem is projected on a discrete problem that can be solved on computers. A finite number of elements forms a conformal mesh of the domain thus leading to a finite number of degrees of freedom. Using the method of weighted residuals (Zienkiewicz & Taylor 1989) a discrete system with the same number of equations can be deduced from eq. (15). This system of equations is in general nonlinear and Newton's method is employed to find solutions. The resulting linear equations are sparse so that memory efficient methods for solving are available.

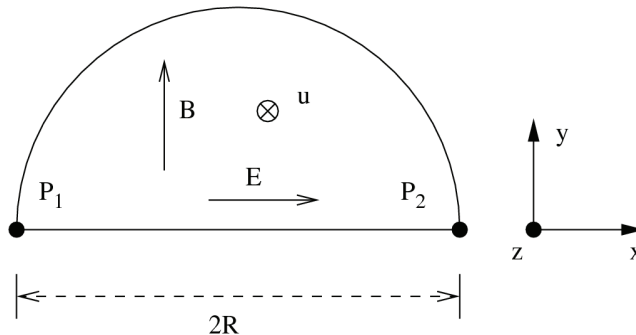


Figure 2. Sketch of evaluation model: a semicircle with radius  $R$

The FE-technique has evolved in many engineering disciplines into software optimised for the needs of particular problems. Recently multiphysics simulations have come into focus that couples different models into one solution process. The results shown in this chapter were achieved with Comsol Multiphysics (Comsol 2005), a program that easily allows to integrate different physical phenomena and also to add further equations to the model in a mathematical form.

## 5. Minimum concentration

For an MI-device to work the fluid must contain mobile electric charges. Here we want to discuss the minimum requirements for water with dissolved salts. Since a certain concentration of ions also means that water conducts electrically, usually a minimum conductivity is required by the manufacturer and values are of the order of 5  $\mu\text{S}/\text{cm}$ . Actually AC measurements depend on conductivity for a second reason because during measurement a current flows in the medium. When using a high impedance measurement in a static field one can assume that no current flows in the medium and only the built-up of a space charge is the limiting factor for a minimum concentration. Three sources of charge have to be considered in water:

- ions from dissolved salts,
- $\text{H}^+$  and  $\text{OH}^-$  ions generated by the autoprotonation reaction of water, and
- water molecules themselves, which constitute electric dipoles and can be oriented in a field to form a net polarisation charge.

It is informative to study these effects separately.

### 5.1 The model

The influence of the mentioned charge sources is studied on a very simple example of an infinite long circular tube with laminar flow in a homogeneous magnetic field. With radius  $R$  and maximum flow velocity  $u_0$  the profile has the form

$$\mathbf{u} = \frac{u_0}{R^2} (R^2 - x^2 - y^2) \mathbf{e}_z, \quad (16)$$

where the axis of the tube is oriented along the  $z$ -axis. If we assume further that the magnetic induction of strength  $B_0$  is along the  $y$ -axis, the high concentration limit (eq. (4)) can be solved analytically and reads

$$\varphi = B_0 \frac{u_0}{4} R^2 x (3R^2 - x^2 - y^2). \quad (17)$$

The voltage measured in an experiment corresponds to the potential difference between two points. It reaches its maximum for two points diametrically opposed in  $x$ -direction. Its value is simply

$$V_{\text{high}} = B_0 u_0 R, \quad (18)$$

which we call the high concentration value further on. Taking the values  $B_0=0.1 \text{ T}$ ,  $u_0=0.1 \text{ m/s}$ , and  $R=1 \text{ mm}$  we get  $V_{\text{high}}=50 \mu\text{V}$ .

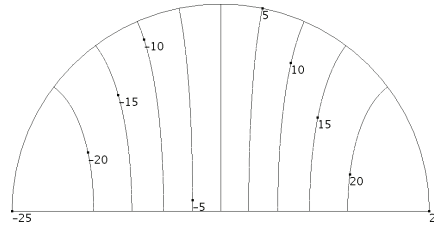


Figure 3. Equipotential lines in the high concentration limit. The grounded reference is in the centre. Values given in  $\mu\text{V}$

Since the problem is constant along  $z$  a 2-D problem results. Furthermore it is symmetric and a semicircle contains all information. Figure 2 shows the relevant coordinate settings. For the high concentration solution (eq.(17)) we show the potential over the cross section as contour lines in Fig. 3.

### 5.2 Ions

First, we study salts that are completely dissolved, so that the generation rate in equation (13) vanishes. For each species labelled  $i$  with charge  $q_i$  equations (11,12,13) are valid separately. The model equations are in the static case:

$$\begin{aligned} \nabla \cdot (c_i q_i (-\nabla \varphi + \mathbf{u} \times \mathbf{B}) - k_b T \nabla c_i) &= 0 \quad i = 1 \dots n \\ -\nabla \cdot (\epsilon_0 \epsilon_r \nabla \varphi) &= \sum q_i c_i. \end{aligned} \tag{19}$$

The magnetic induction and temperature are assumed to be homogeneous. For  $n$  different types of ions the system is represented by  $n+1$  degrees of freedom and as many equations. The first equations state essentially conservation of the particle numbers. Note that in the static case the particle mobilities do not appear in the equations. The assumption here is that the system relaxes to the equilibrium fast enough.

Since ions species with the same charge lead to identical equations we treat the concentration variables  $c_i$  in equation (19) as the accumulation of all ions having the same charge. Our model example is simplified in another respect, because only anions and cations with elementary charge are included and hence only two concentration variables  $c_+$  and  $c_-$  remain (where  $q_0$  denote the elementary charge):

$$\begin{aligned} \nabla \cdot [c_+ q_0 (-\nabla \varphi + \mathbf{u} \times \mathbf{B}) - k_B T \nabla c_+] &= 0 \\ \nabla \cdot [-c_- q_0 (-\nabla \varphi + \mathbf{u} \times \mathbf{B}) - k_B T \nabla c_-] &= 0 \\ -\nabla \cdot \epsilon_0 \epsilon_r \nabla \varphi &= q_0 (c_+ - c_-). \end{aligned} \tag{20}$$

The model can be extended to ions with higher order charge ions with no difficulties. The solution for this system of equations is depicted in fig. 4 (solid line) as a plot of the voltage across the diameter in dependence on the salt concentration. We state that above a concentration of  $10^{14} \text{ 1/m}^3$  the high concentration limit is attained. This is as we will see later five orders of magnitude above the concentration of the  $\text{H}^+$  and  $\text{OH}^-$  ions in pure water.

### 5.3 Dipoles

The water molecule features an electric dipole moment and for this reason is oriented in an electric field. In a nonhomogeneous electric field this leads to a net polarisation. The

susceptibility of a material  $\epsilon_0(\epsilon_r-1)$  measures its ability to create such a polarisation charge. It can be shown from thermodynamics (Feynman et al. 1966) that

$$\rho_{\text{pol}} = -\nabla \cdot \epsilon_0 (\epsilon_r - 1) \mathbf{E}. \tag{21}$$

Usually this polarisation charge does not show up explicitly in the equations because it is automatically included in the macroscopic Maxwell equations in the form of the relative permittivity. When a magnetic induction is present and the medium moves, equation (21) has to be extended to

$$\rho_{\text{pol}} = -\nabla \cdot \epsilon_0 (\epsilon_r - 1) (\mathbf{E} + \mathbf{u} \times \mathbf{B}), \tag{22}$$

which is discussed by Simonyi (1979) in more detail and derived by Engl (1960) for the electromagnetic flow meter. This gives rise to an augmented form of Poisson's equation:

$$-\nabla \cdot \epsilon_0 \epsilon_r \nabla \phi = \rho_{\text{mac}} - \nabla \cdot \epsilon_0 (\epsilon_r - 1) (\mathbf{E} + \mathbf{u} \times \mathbf{B}). \tag{23}$$

At first let us note that in the case when the liquid contains no other mobile charges, equation (23) is equivalent to equation (4) with the potential being reduced by a factor of  $(\epsilon_r - 1)/\epsilon_0$ . In water, which has a relative permittivity of 80, this means that the MI-voltage reaches  $79/80 \approx 99\%$  of the high concentration value, even when there are no dissolved ions at all.

For demonstration purposes we repeat the calculations from subsection 5.2 for a liquid with polarisation effects that has  $\epsilon_r=3$ , which is easier to discriminate in fig. 4 (where it is shown as dashed line) than water. The transition to the high concentration limit is at the same concentration value but at lower concentrations the MI-effect is never zero.

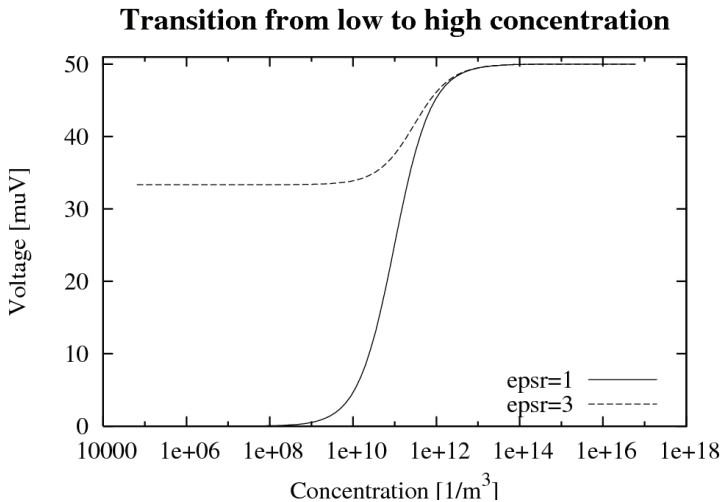


Figure 4. Transition for a solution with monovalent ions in a hypothetical liquid with no polarisation ( $\epsilon_r=1$ ) and with polarisation effects ( $\epsilon_r=3$ )

### 5.4 Autoprotonation

Even pure water contains ions which are  $H^+$  and  $OH^-$  and originate from the autoprotonation reaction of water



In this context we do not want to discuss the nature of these ions and in which embodiment they are dissolved in water, but we treat all quantities (concentration, mobility, ...) as effective quantities for a positive and a negative charge respectively. In fact these effective properties are measured in experiments; for the effective mobility Atkins (1988) reports the values

$$\begin{aligned} \mu_{H^+} &= 2.26 \cdot 10^{12} \text{ m}^2 / \text{Js} \\ \mu_{OH^-} &= 1.29 \cdot 10^{12} \text{ m}^2 / \text{Js} \end{aligned} \quad (25)$$

Two aspects have to be taken into account. First, the generation rates (see eq.(13)) are equal for the two ion species because they are created or destroyed in pairs. Second, in a chemical equilibrium the mass action law states that the product of the two concentrations is constant

$$c_{H^+} c_{OH^-} = K^2 \quad (26)$$

with  $K = 10^{-7} \text{ mol/l} = 6.06 \cdot 10^{19} \text{ 1/m}^3$ . The value  $K$  is the concentration of the ions in pure water or at pH=7. As a consequence of mass action only one concentration variable is independent. A convenient parametrisation is the choice

$$\begin{aligned} c_{H^+} &= K e^{\Psi} \\ c_{OH^-} &= K e^{-\Psi} \end{aligned} \quad (27)$$

The new degree of freedom  $\Psi$  is related to the pH-value in chemistry. When applying the drift-diffusion model (equations (11) and (13)) to the concentration variables for a nonpolarisable medium we get the system of equations

$$\begin{aligned} \mu_{H^+} \nabla \cdot [c_{H^+} q_0 (\mathbf{E} + \mathbf{u} \times \mathbf{B}) - k_B T \nabla c_{H^+}] &= G \\ \mu_{OH^-} \nabla \cdot [-c_{OH^-} q_0 (\mathbf{E} + \mathbf{u} \times \mathbf{B}) - k_B T \nabla c_{OH^-}] &= G \\ -\nabla \cdot \varepsilon_0 \varepsilon_r \nabla \varphi &= q_0 (c_{H^+} - c_{OH^-}) \end{aligned} \quad (28)$$

After elimination of the generation rate and using the  $\Psi$  variable, the following equations remain

$$\begin{aligned} \nabla \cdot (\mu_{H^+} e^{\Psi} + \mu_{OH^-} e^{-\Psi}) \left( \mathbf{E} + \mathbf{u} \times \mathbf{B} - \frac{k_B T}{q_0} \nabla \Psi \right) &= 0 \\ \nabla \cdot \varepsilon_0 \mathbf{E} &= q_0 K (e^{\Psi} - e^{-\Psi}) \end{aligned} \quad (29)$$

Only the ratio of the mobilities exerts influence in this equation. We want to approximate these equations further. For small values of  $\Psi$  the exponential functions can be expanded in lowest order, giving



$$\begin{aligned}\nabla \cdot (\mu_{H^+} + \mu_{OH^-})(\mathbf{E} + \mathbf{u} \times \mathbf{B}) &= 0 \\ \nabla \cdot \epsilon_0 \mathbf{E} &= 2q_0 K \Psi\end{aligned}\quad (30)$$

We see that this approximation results in the high concentration limit (first equation), which can be solved analytically for the model problem (see eq. (17)). The second equation can also be solved analytically:

$$\Psi = \frac{u_0 B_0 \epsilon_0}{R^2 q_0 K} = 3.67 \cdot 10^{-8} \frac{1}{m} x \quad (31)$$

Hence for the sizes in question (centimetre range) the approximation is justified and, hence, the use of the high concentration limit.

### 5.5 Consequences

The main result of the study of water including the effects of dissolved salts, polarisation of the water molecule, and autoprotonation shows that dissolved salts are not needed for the built-up of a magnetic inductive potential. The electric and chemical properties of water alone produce sufficient charge density for the (previously known) high concentration limit. This can already be seen in the fact that the transition found in subsection 0 occurs at a concentration below  $10^{14} \text{ 1/m}^3$  which is five orders of magnitude below the concentration of  $H^+$  and  $OH^-$  in pure water. Adding up the different effects (salt ions, polarisation, autoprotonation) justifies the use of the high concentration limit for water in all cases.

One important constraint has to be mentioned here concerning technical implementations. In currently available devices an AC magnetic field is used and during measurement an electric current is flowing in the medium, thus requiring a conductive medium. This must be considered an additional reason for the need for a minimum conductivity (and minimum salt concentration at the same time). In a static measurement with high-ohmic amplifiers no current flows in the medium and the minimum concentration is no longer needed.

Another interesting consequence derives from the polarisation effect that is not only present in water but also in other liquids like oil or petrol. These liquids are not conducting under normal circumstances. Therefore the electromagnetic flow meter can be used in an even wider range of applications as previously known.

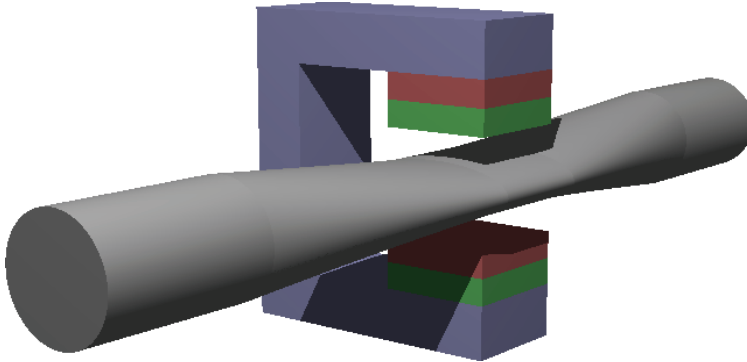


Figure 5. Model for geometry optimisation

## 6. Geometric shape optimisation

The design of a complete electromagnetic flow meter requires the solution of a coupled system. The results of section 5 justify the application of the high concentration limit and the model comprises equations of magnetostatics (eq. (9)), fluid dynamics (eq.(1,2)), and the magnetic-inductive effect (eq. (4)). We apply this system of equations to an optimisation problem. The main idea is as follows: the sensor region usually has a circular cross section but can also have other shapes, for instance an ellipse. The geometry influences the flow and in consequence the electric output of the sensor. Also the magnetic system changes because the magnet poles can be placed closer to each other. Figure 5 shows the model as it was used in the calculations. In the sensitive region the cross section is quenched to an elliptic shape with a smooth transition to circular pipes that are attached to the sensor. The poles of the magnet are placed close to the pipe and a return yoke is included for efficient utilisation of the magnetic field. The electric connections are not shown in this figure but in the calculations capacitive coupling is used. These contacts must be large for an efficient electric coupling and span an angle of  $150^\circ$ .

The shape of the cross section is parametrised such that the ellipse has the half axes  $(R\beta(1-a), R/(1-a))$ , where the parameter  $a$  applies to the shape of the ellipse,  $\beta$  changes the size, and  $R$  is the equivalent radius of a circular tube. The parameter  $a$  is chosen such that at the value zero the circle is recovered as the cross section. The area of the cross section is  $\pi\beta R^2$ . The goal of the optimisation is highest sensitivity and two constraints must be met:

- The pressure drop shall be the same as for a straight tube.
- The sensor is nonlinear but should not deviate from the ideal linear case too much.

### 6.1 Model size

Naturally the results of such an optimisation depend on the material parameters, geometric sizes and flow conditions. So numeric results should be taken as an example and the main objective of this section is the methodology. The application field in the numeric case is water at room temperature in tubes with 1 cm diameter in a flow range of 0-4 m/s medium flow velocity. A target velocity is fixed at 1 m/s, for which the pressure drop is adjusted, so that the flow meter is neutral in the pipe circuit. For other velocities the flow meter is operational but the pressure drop differs. The values mentioned must be considered as one example: the methodology can be employed to other cases in the same way. The relevant properties of water are

- density:  $1000 \text{ kg/m}^3$
- viscosity:  $8.54 \cdot 10^{-4} \text{ Pa s}$
- relative dielectric constant: 80.

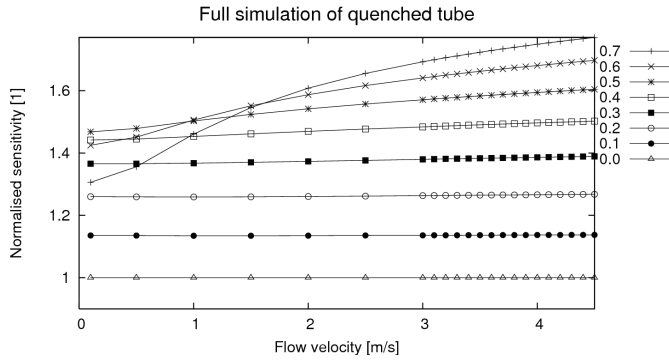


Figure 6. Sensitivity of quenched flow meter for different  $\alpha$ -values

**6.2 Pressure drop**

The first constraint is equivalent to the demand that the flow meter should have no disturbing effect on the flow circuit. In fact if the tube is quenched the flow resistance of the tube increases. Therefore enlarging the area (via parameter  $\beta$ ) neutralises the effect. In order to find the compensation, NS equations are solved for various parameters. For each given parameter value  $\alpha$  the corresponding  $\beta$ -value can be found such that the pressure drop equals that of a straight tube. It is instructive to convert this dependence into polynomial form

$$\beta(\alpha) = 1 + 0.922\alpha^2 + 0.698\alpha^4 + 1.618\alpha^6 \tag{32}$$

This compensation function depends on the velocity; in this case the target velocity is 1 m/s.

**6.3 Magnetostatics**

The calculation of the magnetic field follows the approach of a scalar magnetic potential as outlined in subsection 3.3. For the permanent magnet we assume a constant magnetisation and the ferromagnetic material of the return yoke is simulated by a very large relative permeability.

**6.4 Simulations**

Using this pressure compensated system we perform the three simulation steps (magnetostatics, fluid dynamics, and electrostatics) needed to establish the magnetic-inductive response. Figure 6 shows the sensitivity  $S = V/u_0$  for different deformation parameters. For values  $\alpha > 0.5$  we judge that the nonlinearity is unacceptably large. This depends in fact on the envisaged application.

In the next step we compare the sensitivity for different values of the deformation parameter at the target velocity  $u_M$ . We get the result displayed in fig. 7. The optimal configuration, if higher nonlinear behaviour can be tolerated, is at  $\alpha = 0.55$ , but keeping the previously outlined limit the optimal shape is with  $\alpha = 0.5$ . The improvement in the magnetic-inductive effect compared to the standard configuration is between 45% and 50%.

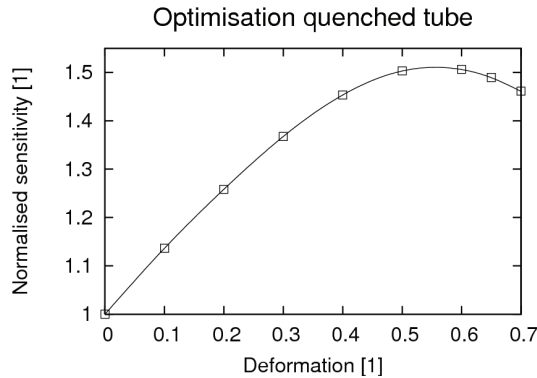


Figure 7. Sensitivity at 1 m/s with optimum at  $\alpha=0.55$

### 6.5 Methodology and efficient calculations

Since for an optimisation problem many single computations of the model are needed an efficient methodology is important. The design of a flow sensor supported by FE-simulations is done in the following steps. We start with a given standard configuration, like having a circular cross section, the operating range in terms of a velocity interval and the main operating velocity  $u_M$ .

1. A parametrised CAD-model of the flow sensor is created with a deformation parameter  $\alpha$  such that for  $\alpha=0$  the standard configuration is met. A second parameter  $\beta$  is used to scale the area. The inlet and outlet tubes with circular cross section and appropriate connection to pipes are included. The parametrised CAD model also adjusts the magnet's position to the deformed sensor device.
2. In a first set of FE-simulation at the velocity  $u_M$  the NS equations are solved for ranges of the parameters  $\alpha$  and  $\beta$ . The goal is to find the function  $\beta(\alpha)$  that adjusts the area of the cross section, so that the pressure drop at each value of  $\alpha$  is that of the standard configuration.
3. For each parameter value  $\alpha$  the magnetic field is computed by solving the magnetostatic equation for the adjusted positions of the magnet.
4. The NS equations are solved for the entire velocity range in the compensated model and the resulting magnetic inductive potential is computed.
5. The results are first analysed for linearity. That means for each value  $\alpha$  the magnetic-inductive response (the voltage  $V$  at the capacitive contacts) is examined. Depending on the needs of the applications an upper bound for the allowed  $\alpha$ -values is established.
6. Comparing the sensitivity  $S=V/u_0$  at  $u_M$  for all  $\alpha$  gives the optimal parameter value.

### 6.6 Geometric symmetry

The different physical models have their own symmetries and an efficient simulation employs these symmetries in the way that the domain is restricted and the solution is mirrored. This technique reduces the number of degrees of freedom and in consequence the time and memory requirement for a single simulation considerably. Figure 8 shows the minimal model with a tube that is oriented in  $z$ -axis. The flow field has a fourfold symmetry

and the NS equations are only solved in a quarter. The full solution result can be constructed by mirroring at the planes  $x=0$  and  $y=0$ . Next, the magnetic subsystem also has a fourfold symmetry but along the  $x$ -axis and the solution is mirrored at  $z=0$  and  $y=0$ . Because the right hand side of the MI-equation is determined from the flow field and magnetic field, the electrostatic model has a twofold symmetry with mirror plane  $y=0$ .

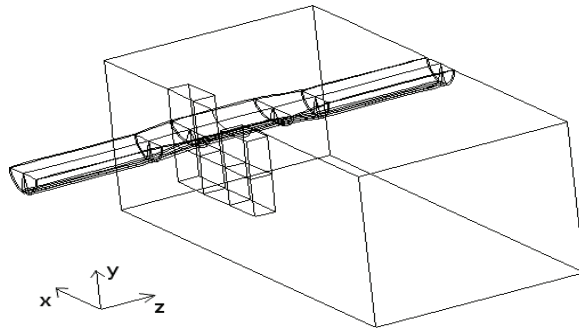


Figure 8. Geometric model for simulation

## 6.7 Conclusions

A novel and simple improvement in the configuration of the magnetic inductive sensor allows an increase of the measured voltage, and therefore the sensitivity, of about 50%. In the new configuration the cross section of the measuring unit is not circular any more but, in the present example, elliptical. This increase in sensitivity can be explained by two effects:

- The fluid flow has a different pattern, which induces a larger space charge density and in consequence a higher voltage.
- Due to the deformation of the tube the magnet pole faces can be placed closer to each other and the magnetic field is exploited more efficiently.

The potential use of the increase in the MI effect is that sensors can be built smaller or with higher sensitivity. The main drawback is that, compared with a straight tube, the MI response is not linear any longer. The design method, however, gives full control over the limits of the nonlinearity. Also the nonlinear behaviour is such that the response is even larger than one would expect with a linear sensor. That means that even stronger signals can be achieved if nonlinear behaviour can be tolerated.

## 7. Turbulent fluctuations

Turbulence is a phenomenon in fluid dynamics of great attention in research and application. It corresponds to solutions of the (nonlinear) NS-equation that are unsteady and exhibit chaotic behaviour. In contrast, laminar flow is represented by stable solutions of the stationary NS equations. Stability in this respect means that small perturbations to the flow are damped and disappear with time. The flow can be characterised by the dimensionless Reynolds number

$$\text{Re} = \frac{\rho u_0 L}{\mu}, \quad (33)$$

where  $u_0$  and  $L$  are characteristic velocity and length scale values, respectively.

The NS equations can be transformed into a nondimensional form and the Reynolds-number remains as the only parameter (Spurk & Aksel 2006):

$$\dot{\mathbf{u}} + (\mathbf{u} \cdot \nabla) \mathbf{u} = -\nabla p + \frac{1}{\text{Re}} \Delta \mathbf{u}. \quad (34)$$

This form of the NS equations has the advantage to demonstrate that different fluids obey the same laws parametrised by the Reynolds-number. The necessary transformations are:

$$\begin{aligned} \mathbf{u} &\rightarrow u_0 \mathbf{u} \\ x &\rightarrow Lx \\ p &\rightarrow Lu_0^2 p \\ t &\rightarrow \frac{L}{u_0} t \end{aligned} \quad (35)$$

Laminar flow is characterised by Reynolds-numbers smaller than 2000-3000. At higher Reynolds-numbers the inertia term exceeds friction in influence and small perturbations are amplified. In a fully developed flow the field quantities fluctuate in a chaotic form. In many practical applications only mean values are of interest, which is reflected in CFD by models for the mean flow velocity (Reynolds-average Navier Stokes, RANS). One popular model for high Reynolds-numbers is the *ke*-model which adds two auxiliary properties (turbulent kinetic energy and dissipation rate) to the equation system. The literature on this subject is rich, e.g., see Eggels (1994), Launder et al. (1975).

The consequence of turbulence for the magnetic-inductive flow meter is that the fluctuations of the flow lead to fluctuations in the potential and in the measured voltage. When the average voltage is evaluated, the *ke*-model replaces the NS equations in the modelling and the electric potential and field are understood as average quantities. In the following we want to examine the fluctuations themselves and aim to find the amplitude of these voltage fluctuations and for this reason the *ke*-model cannot be applied. The goal is to examine the strength of these amplitudes and to establish the dependence of the amplitude from the volume flow in the tube. These results turn out to be convincing that the amplitude of the voltage fluctuations can be used as a measure for the volume flow.

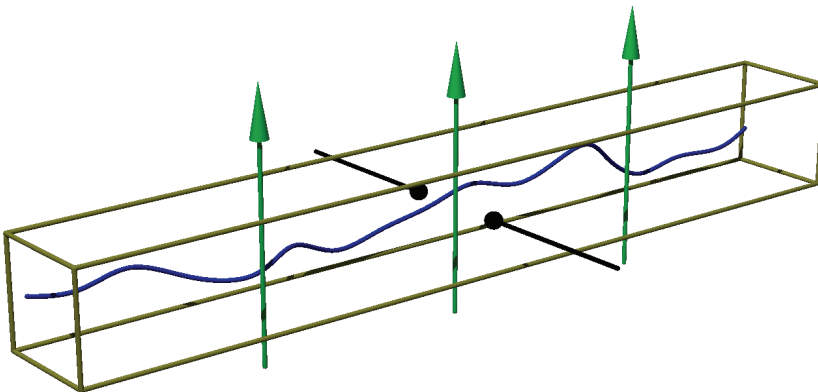


Figure 9. Model for LE-simulations: a tube with square cross section and a homogeneous magnetic field. Blue line indicates a possible turbulent flow line

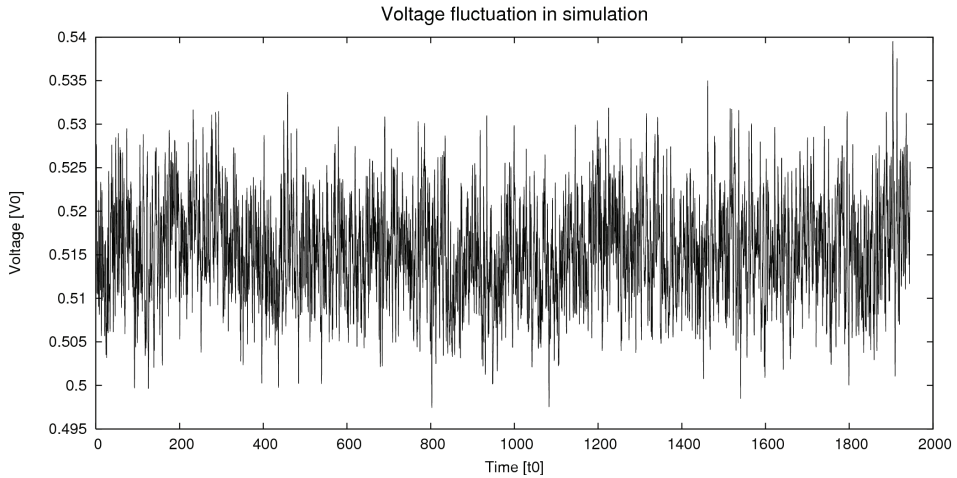


Figure 10. Voltage fluctuation of MI flow meter in large eddy simulations at  $Re=14000$ . The amplitude is about 5% of the mean value and therefore large enough to be measured

For realistic simulation of turbulent phenomena including fluctuations small time and space scales have to be resolved. Here the FE-method demands too many computer resources and the Finite-Difference (FD) method is preferred. Since the FD method calls for a regular grid only simple geometries can be treated.

Whereas the so called *direct numerical simulation* use the plain NS equations, the large-eddy simulations only treat large scale turbulences and suppress small eddies, so the resource requirements are less severe.

To test the influence of turbulence on the electromagnetic flow meter we describe FD simulations that calculate the amplitude of a MI signal in a straight tube with square cross section (fig. 9). The model has a homogeneous magnetic field (green arrows) and pointlike galvanic electrodes (black lines). The blue line shows the stream line of one fluid particle.

### 7.1 Large-eddy (LE) simulation

We employ the large-eddy model in the way it is described in the reference by Eggels (1994). The governing equations follow from the NS equations by applying a spatial filter operator. This filter averages the fluctuating velocity components in a small environment around a point and has the effect to suppress small eddies (called sub-grid scale) and preserve larger ones (grid scale).

The governing equations for the LE-model are essentially the the NS-equation for the filtered unknowns  $\mathbf{u}$  and  $p$ . In dimensionless form they read:

$$\begin{aligned} \dot{\mathbf{u}} + (\mathbf{u} \cdot \nabla) \mathbf{u} &= -\nabla p - \nabla P + \frac{1}{Re} \Delta \mathbf{u} - \nabla \tau \\ \nabla \cdot \mathbf{u} &= 0. \end{aligned} \quad (36)$$

An additional quantity, the LE-stress tensor  $\tau$ , must be introduced to model the subgrid eddies. All detailed information about these eddies is lost in the averaging process but heuristic models can be formulated to account for their influence on the main flow and this

influence is expressed in the stress tensor  $\tau$ . Here the pressure gradient is split in two parts: on one side the gradient of  $P$ , which is constant in space for a straight tube and drives the flow through the tube. On the other side the unknown part  $p$  ensures incompressibility. In the Smagorinsky model the LE-strain is found from the strain tensor (Denev et al. 2003)

$$S = (\nabla \otimes \mathbf{u}) + (\nabla \otimes \mathbf{u})^t \quad (37)$$

assuming that the stress has the form

$$\tau = -l_{mix}^2 \sqrt{2\text{trace}(S^2)} S \quad (38)$$

i.e., the LE-stress has the anisotropy of the strain and the effective LE-viscosity is proportional to the magnitude of the strain. The mixing length  $l_{mix}$  is related to the average grid size

$$l_{grid} = \sqrt{\delta x^2 + \delta y^2 + \delta z^2} \quad (39)$$

by  $l_{mix} = c_s l_{grid}$ , where  $c_s$  is Smagorinsky's constant. Its value is open to debate but values in the range 0.1...0.2 are usually chosen. In this work  $c_s = 0.16$ .

As boundary conditions homogeneous Dirichlet *no-slip* conditions are applied on the walls of the tube for all velocity components and Neumann conditions for the pressure  $p$ . In axial direction the model in principle requires an infinitely long tube. Considering the fact that in streamline direction the fluctuations at two points are not correlated any more if the distance is large enough, one can apply periodic boundary conditions to a tube of finite length. This can be regarded as a feedback loop of the outlet to the inlet. If the length of the tube is larger than the correlation length no artefacts are introduced by this procedure. Eggels (1994) reported that a length of at least five times the diameter of the tube is sufficient. In the present results the length is eight times the edge length of the cross section. Usually LE simulations are performed at constant pressure gradient, which implies a fluctuating mean flow because the resistance of the tube depends on the turbulent activity, which is fluctuating by nature. We force a constant mean flow (which is important for flow-metering) by allowing the pressure gradient to vary in time and evaluate the integral

$$\partial_x P|\Omega| = \int \left( \frac{1}{\text{Re}} \Delta u_x - (\nabla \cdot \tau)_x \right) dx^3 \quad (40)$$

at every time step. The integral follows from eq. (36) by integrating the stream-wise component over the tube volume  $\Omega$  and applying boundary conditions. The other components of the pressure gradient are zero. In reference Denev et al. (2003) the flow velocity is corrected after each time step to ensure constant global mass flow rate.

The magnetic inductive potential is solved at each time step using equation (4) in a post-processing step. Similar LE-simulation were reported by Boersma & Nieuwstadt (1999) but only for one Reynolds-number. Since the dependence on flow rate is our main interest we repeated calculations on a  $265 \times 65 \times 65$  grid for a pipe of length 8 over a unit square cross section with sufficient accuracy.

As a typical example we show the magnetic inductive voltage fluctuation of a simulation at  $\text{Re} = 14000$  in fig. 10. The amplitude of the fluctuation is about 15% of the mean value. This, in our belief, is high enough to be measured reliably in experiments.



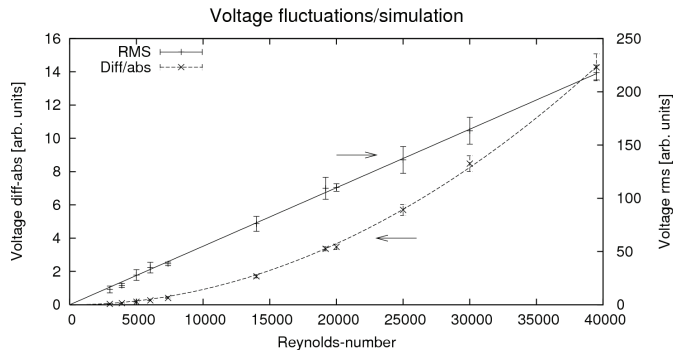


Figure 11. Amplitude of voltage fluctuations of an electromagnetic flow meter in dependence on Reynolds-number in the simulation. The analysis as root-mean-square shows linear behaviour, where the amplitude of the differentiated signal has quadratic dependence

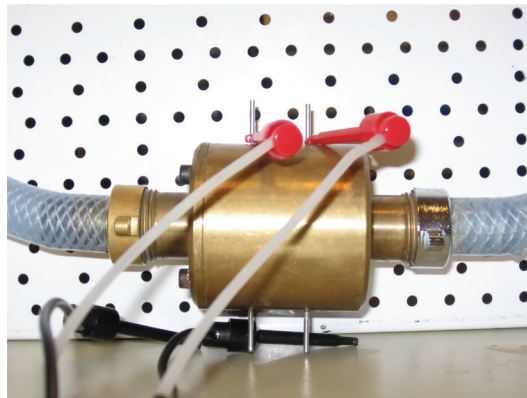


Figure 12. Experimental set-up for the measurement of the turbulent flow meter

Further analysis of the experimental data has been undertaken in two ways:

- as statistical root-mean-square of the voltage and
- as the average of the modulus of the time-differentiated signal.

The averaging is done for packages of sampling points together with the calculation of error intervals. The results are shown in fig. 11 with a maximum Reynolds-number of 40,000, which corresponds to a mean flow velocity of 3.8 m/s for water at room temperature and a tube with 1 cm edge length. We observe that the root-mean-square linearly depends on the Reynolds-number while the amplitude of time-differentiated is a quadratic function of the Reynolds-number and hence of the mean flow velocity. The consequence of the monotonous dependence of the noise on the flow rate suggests that the amplitude can be employed to measure the mean flow. Since the error of the time-differentiated signal is small, the type of evaluation is preferred.

At low flow rates when the flow is laminar this type of flow sensor cannot be used. In the present parametrisation where  $u_0$  is the mean flow velocity and  $L$  the edge length of the cross section the flow is laminar below a Reynolds number of 3000.

## 7.2 Experimental verification

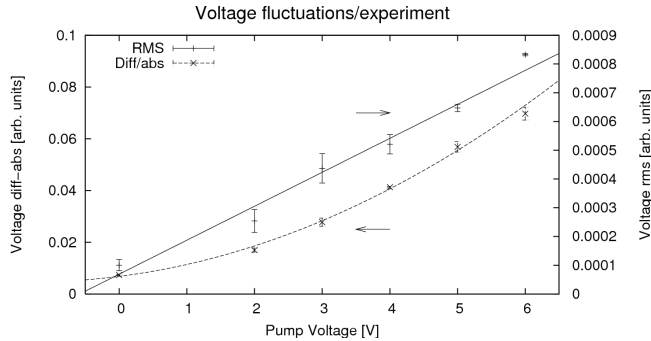


Figure 13. Amplitude of voltage fluctuations of an electromagnetic flow meter in dependence on the pump voltage (proportional to the mean flow velocity) in the experiment. Simulation and experiments agree in the functional dependence of the amplitudes

Briefly we want to show that the LE-simulation that we have presented can be verified in experiments. The measurements were performed with the simple set-up shown in fig. 12 using tap water at room temperature. The water circuit is constructed with plastic tubes with inner radius of 13 mm and a voltage driven pump. In the actual sensitive region the cross section is narrower (75 mm<sup>2</sup>) and the magnetic induction from permanent magnets is at maximum 0.5 T. Using this small set-up the results in fig. 13 are measured. The analysis is done in the same two techniques as for the simulations. The dependence on the mean flow rate is the same that was found in the calculations.

Measuring the amplitude of these fluctuations is hampered by other noise sources coming from the electric circuit, electrochemical double layers, and radiation. Some of these noise sources are flow independent and explain the noise amplitude at zero flow. Of the flow dependent noise the agreement between simulation and experiment suggests that indeed the turbulence explains a major part of the noise.

## 7.3 Optimal placing of contacts

The optimal placement of the two contacts in a conventional MI-flow meter is such that the contacts are arranged perpendicularly to the magnetic field. The voltage reaches its maximum in this configuration. For a flow meter working on the turbulent paradigm the optimal position differs as can be deduced from fig. 14. It shows in a colour scale (blue to red) the amplitude of the fluctuations (in the root-mean-square measure). The reference contact is fixed at one the standard positions, i.e., at the centre of the blue spot. All points of the surface are sampled to measure in the simulation the noise amplitude relative to the reference point and the result plotted in the figure. It turns out that the fluctuation is strongest if the second contact is placed in the axis of the magnetic field, i.e., at an angle of 90° degrees with the reference. In this respect the LE-simulation foresees future experiments and helps to optimise a new flow meter principle.

## 7.4 Conclusion

A new measurement principle relying on the turbulent nature of liquid flow in a pipe is verified with numerical simulations. In fact, fluctuations in the flow lead to fluctuations in

the pick-up voltage and the amplitude of the these fluctuations depends monotonously on the mean flow and can therefore be used as measure for the mean flow. The functional dependence of the signal is the same for experiments and simulations. The simulation also shows that the strength of the signal is high enough to be measured. This fact strongly supports the view point that the flow dependent fluctuations in the experiment are explained by the turbulent activity.

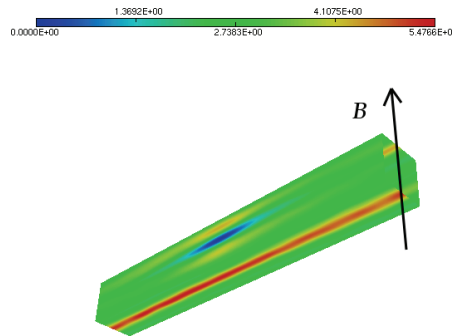


Figure 14. Turbulent flowmeter: distribution of amplitude of fluctuations on the surface. The reference point is in the centre of the blue spot, the optimal position of the second contact in the area

## 8. Summary

Numerical simulations are used in sensor design in an advance fashion. We have shown for the electromagnetic flow meter that basic physical and electrochemical phenomena can be modelled such that engineers can make forecasts about new generation devices.

The first concrete result, that we demonstrated, concerns the minimum concentration of dissolved salt ions needed for a magnetic inductive flow meter to work. Until now industrial applications required a minimum conductivity. Using basic models for all possible mobile charges (ions from dissolved salts, autoprotonation of water, and polarisation effects) we can show that even in pure water and other polarisable liquids the MI-effect is strong enough to be measured. The possible impact on technology is enormous: the application range of electromagnetic flow meters is wider than it was believed before. The trade-off is that high-ohmic electronic circuits must be implemented because no electric current can flow in the medium. But modern electronic devices offer this possibility.

Second, we can use the Finite-Element technique for geometric shape optimisation. Naturally, optimisation using actual prototypes can be tedious and computations allow shorter design cycles. On the other side the simulation of the MI flow meter demands software that easily and effectively handles multiphysics problems like for instance Comsol Multiphysics does. In the detailed example we improve the sensitivity of an electromagnetic by 50% solely by changing the cross section of the measuring tube.

The third and final result treats turbulent flows and requires direct numerical simulations or large-eddy simulations. These techniques used to be reserved to supercomputers but with small server becoming faster smaller departments can investigate turbulences on small time and length scales. This leads to the following new principle for flow metering. Turbulent flow is intrinsically unsteady and flow quantities fluctuate. These fluctuations lead to fluctuations in

the voltage measured by an MI device. We investigate the amplitude of the fluctuations as a function of the Reynolds-number, i.e., the flow rate. We find a monotonous dependence, that is sufficiently confirmed in experiments, and propose to use this amplitude to measure the flow rate. The simulations are also used to optimise the placement of the pick-up electrodes with the astonishing outcome that the electrodes are best placed at an angle of  $90^\circ$ .

We note that these results can be obtained using advanced software tools and moderate computer resources. These simulations based on fundamental physical properties are in reach of every engineering department.

## 9. References

- Atkins P. W. (1988), *Physikalische Chemie*, VCH, Weinheim
- Boersma B.J. & Nieuwstadt F.T.M. (1999). On the Electric Potential Induced by a Homogeneous Magnetic Field in a Turbulent Pipe Flow. *Flow, Turbulence and Combustion* Vol. 62, 29-51. ISSN 1386-6184
- Ciarlet P.G. (1978) *The Finite Element Method for Elliptic Problems*, North-Holland, Amsterdam.
- Comsol AB (2005). *Comsol Multiphysics Modelling Guide*; Version Sep. 2005, Stockholm
- Denev J.; Frank Th. & Pachler K. (2003). Large Eddy Simulation of Turbulent Square Channel Flow Using a PC-Cluster Architecture, In: *4th Intl. Conf. on Large-Scale Scientific Computations*, 363-370.
- Eggels J. G. M. (1994). *Direct and Large Eddy Simulation of Turbulent Flow in a Cylindrical Pipe Geometry*, Ph.D. thesis Technische Universiteit Delft, Delft.
- Eggels J.G.M.; Unger F.; Weiss M.H.; Westerweel J.; Adrian R.J.; Friedrich R. & Nieuwstadt F.T.M. (1994). Fully developed turbulent pipe flow: A comparison between direct numerical simulation and experiment. *Journal of Fluid Mechanics*, Vol. 268, 175-209.
- Eggels J.G.M.; Westerweel J.; Nieuwstadt F.T.M. & Adrian R.J. (1993). Direct numerical simulation of turbulent pipe flow. *Applied Scientific Research*. Vol. 51, 319-324.
- Engl W. (1960). Relativistische Theorie des induktiven Durchflussmessers, *Archiv für Elektrotechnik*, Vol. 46, 173-189
- Fiedler O. (1992). *Strömungs- und Durchflußmeßtechnik*, R. Oldenbourg, München
- Feynman R. P., Leighton R. B, Sands M. (1966). *The Feynman Lectures on Physics*, Vol. 2, Addison-Wesley
- Hamann C. H. & Vielstich W. (2005). *Elektrochemie*, 4th edition, Wiley-VCH
- Launder B. E.; Reece G. J. and Rodi W. (1975). Progress in the Development of a Reynolds-Stress Turbulent Closure. *Journal of Fluid Mechanics*, Vol. 68, No. 3, 537-566.
- Schommartz G. (1974) *Induktive Störungsmessung*, VEB Verlag Technik, Berlin
- Simonyi K. (1979). *Theoretische Elektrotechnik*, VEB Deutscher Verlag der Wissenschaften, Berlin
- Shercliff J. A. (1954), Relation between the velocity profile and the sensitivity of electromagnetic flowmeters. *Journal of Applied Physics*. Vol. 25, 817-818
- Stange G. (2002) *Verfahren zur Messung eines ein Messrohr durchströmenden Mediums*, German Patent
- Spurk J. H. & Aksel N. (2006) *Strömungslehre: Einführung in die Theorie der Strömungen*, 6th edition, Springer
- Williams E. J. (1930). The induction of electromotive forces in a moving liquid by a magnetic field, and its application to an investigation of the flow of liquids. *Proceedings of the Physical Society* Vol. 42, 466-478
- Zienkiewicz O. C. & Taylor R. L. (1989). *The finite element method*, 4th edition, McGraw-Hill, London

# Finite Element Modelling of Micro-cantilevers Used as Chemical Sensors

G. Louarn and S. Cuenot

*Institut des Matériaux Jean Rouxel, University of Nantes  
France*

## 1. Introduction

During the last twenty years, the spectacular advances in micro-mechanical systems, and more generally in micro-electro-mechanical systems (MEMS), have enabled the emergence of an innovative family of biological and chemical sensors. The functionality of such sensors involved the transduction of a mechanical energy, which comes from the deformations of the micro-machined components. Among the different geometrical shapes of these components, clamped-free beams also called cantilevers represent the simplest MEMS. Although cantilevers play a role of basic building block for complex MEMS devices, they are nowadays widely used as force sensor probes in atomic force microscopy (AFM).

The recent developments of AFM have enabled the mass-fabrication of micrometer-sized cantilevers with various geometrical shapes and different materials (silicon, silicon nitride...) (). Indeed, beam cantilevers but also V-shaped cantilevers are commercially available with different dimensions. Recently, this variety of AFM cantilevers is become the base of a novel class of highly sensitive sensors operating essentially for chemical and biological detections (Raiteri et al., 2001 ; Sepaniak et al., 2002 ; Moulin et al., 2003 ; Lavrik et al., 2004). These micro-cantilevers, which can be extremely versatile sensors, present many advantages such as a relatively low cost of production and a reduced size of the active area (typically  $10^{-6}$  cm<sup>2</sup>). The detection principle of such sensors is based on the measurement of the cantilever deflection change or of the resonance frequency change of the cantilever (figure 1). These changes are induced by the adsorption of chemical species on the functionalized surface of a micro-cantilever (Chen et al., 1995 ; Betts et al., 2000).

Such adsorption may come from the interactions between specific molecules present in analyte and the sensitive coating of the cantilever. The measurement of the resonance frequency shift offers the interesting advantage to be relatively insensitive to interference from external factors such as thermal drift. Therefore, this method seems particularly well-suited for use in various environments such as gaseous or vacuum ones, and to measure the cantilever response upon exposure to optical radiation and to chemical vapours. Several applications of these AFM micro-cantilevers as sensors were developed during the ten last years (Lange et al., 2002 ; Baselt et al., 2003). According to the realized coating, the chemically modified surfaces of cantilevers can be used to produce transducers that are activated for specific analytes. For instance, cantilevers coated with a thin gold film become ideal sensors to achieve ultrasensitive detection of mercury vapour (Thundat et al., 1995a). A

metallic coating allows the calorimetric detection of chemical reactions with picojoule sensitivity (Gimzewski et al., 1994), while a gelatine coating is sensitive to the changes in relative humidity (Wachter & Thundat et al., 1995). Others detection can also be achieved such as pH-variation (Ji et al., 2001 ; Bashir et al., 2002) or optical radiation by coating the cantilevers with ultraviolet cross-linking polymers (Thundat, 1995b).

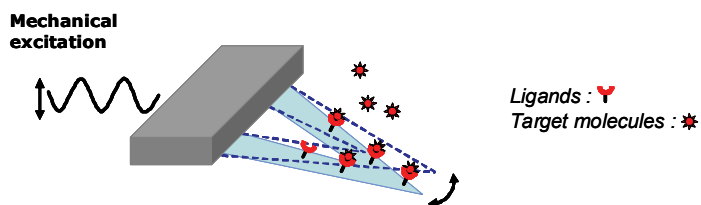


Figure 1. Cantilever deflection change induced by the adsorption of chemical species on the functionalized surface

In order to predict the sensitivity of these versatile sensors, it is crucial to precisely calculate the resonance frequencies of these micro-cantilevers (Dufour et al., 2003 ; Lochan et al., 2005). The resonance frequencies can be only calculated analytically for cantilevers with simple geometries like straight beams. In the other cases, for multilayer structures or more complex shapes, where the cross-section is not constant along the cantilever length (case of "V-shaped" micro-cantilevers), the resonance frequencies can not be analytically calculated. Among the different approaches allowing to calculate them, the finite element modelling (FEM) seems to be a particularly interesting approach. In this chapter, FEM is applied to "V-shaped" silicon micro-cantilevers for predicting their resonance frequencies and the sensitivity of these cantilevers employed as chemical sensors.

First, in order to validate the accuracy of the FEM approach, we carried out a comparison between analytical, experimental and FEM-computed values of the resonance frequencies for homogenous rectangular shaped micro-cantilevers. Then, we performed a modelling of silicon beams coated with a thin metallic layer. To precisely calculate the resonance frequencies of these multilayer-cantilevers, the influence of the mesh parameters on the calculated frequencies was strongly investigated.

Second, the sensitivity of different "V-shaped" silicon cantilevers was estimated, as a function of their geometrical dimensions and of their mechanical parameters (Young modulus, density). The resonance frequencies of uncoated cantilevers were calculated and compared with the values experimentally determined. Then, a similar approach could be employed to predict the sensitivities of such cantilevers recovered with a sensitive layer.

This chapter clearly shows that the use of finite element modelling allows the computation of the resonance frequencies of micro-sized cantilevers having a complex shape. Moreover, in the case of applications as sensors based on the resonance frequency measurement, this approach offers the ability to predict the sensitivity of multilayer-cantilevers. In this way, by simple calculation, the shape and the geometrical dimensions of these cantilevers can be optimized for obtaining the best sensitivities and detection limits.

## 2. Natural frequencies and normal modes of vibration

When a linear mechanical system undergoes free vibrations, i.e. without being subjected to any external periodic load, its behaviour is characterized by its so-called "eigen modes". An

eigen mode is a global synchronous type of motion where the various degrees of freedom exhibit all the same time behaviour (with different amplitudes), viz. harmonic motion at a frequency which is characteristic of the mode. An  $n$  degrees of freedom system has  $n$  eigen modes, hence  $n$  characteristic eigen frequencies, also called “natural” frequencies.

When the system undergoes forced harmonic vibration, its behaviour is characterized by the frequency response relating the amplitude (and phase) of the steady-state harmonic response to that of the excitation. The main feature of this response is a series of peaks appearing at forcing frequencies close to the natural frequencies. These large response amplitudes (theoretically infinite if no damping is present) relate to the so-called “resonant” behaviour of the system – generally to be avoided in practice in most engineering application.

When the system is undamped, the (infinite) resonance peaks appear at forcing frequencies, which are identical to the natural frequencies of the system. From a physical point of view, since the system is excited at a frequency at which it would tend to freely oscillate, its vibration amplitude increases steadily, tending towards infinity.

In the case of a damped system, there are various definitions of the related “resonance” frequencies. One of these is the forcing frequency (close to a natural frequency) at which the maximum of a peak is reached. However, at a forcing frequency equal to a natural frequency, the phase shift between the response and the excitation is always an odd multiple of  $90^\circ$ , and this is generally chosen as the most reliable and accurate definition of resonance.

We see therefore that “natural” and “resonance” frequencies are two names for the same notion, albeit related to two different situations (“free” and “forced” vibrations). In the following, we shall use the term “natural” frequencies when analyzing free vibrations, and “resonance” frequencies when dealing with forced vibrations.

### 3. Experimental procedure

Nowadays, the atomic force microscopy (AFM) is widely used to characterize the surface of all kinds of materials, conductive as well as insulating samples. Although the most innovative advent of the AFM is its ability to measure locally different physical properties, the AFM offers real tri-dimensional images of the sample surface (Cuenot, et al., 2003).

The sample is fixed onto a piezoelectric ceramic, which has the property to expand or to contract when a voltage is applied. By scanning across the surface with an AFM tip, topographical information can be easily obtained from atomic-scale imaging to micron-sized images. In contact mode, topographic images can be achieved by two ways. First, by measuring directly the vertical deflection of the cantilever, which indicates the local sample height, when the AFM tip scans the sample. To measure this vertical deflection, a laser beam focused on the gold coating of the cantilever backside is reflected onto a photo-detector consisting of two side-by-side photodiodes. The difference between the signals coming from the up-and-down photodiodes reflects the vertical deflection of the cantilever (figure 2).

Second, topographic images can also be obtained by recording the vertical displacement of the piezoelectric ceramic when a constant force is applied by the tip on the sample surface. Indeed, the feedback loop existing between the ceramic and the photodiodes allows to keep the same cantilever deflection (i.e. a constant value of tension read from the photodiodes) by varying the voltage applied to the ceramic and hence adjusts the height of the sample.

In this chapter, the resonance frequencies of different cantilevers were measured. To measure them, a piezoelectric bimorph (located under the cantilever) is used to induce the

cantilever oscillations. By monitoring the cantilever deflection signal as a function of the frequency sweep of the bimorph, it is possible to completely characterize the resonance spectrum of cantilever.

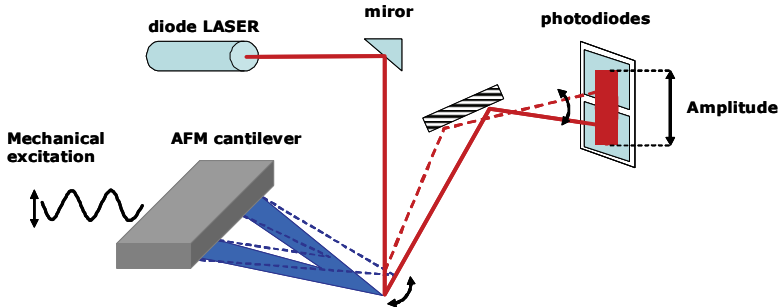


Figure 2. Principle of detection of the AFM

#### 4. Natural frequencies of free rectangular cantilevers

The fundamental vibration mode of a cantilever, i.e. the one with the lowest resonance frequency, always corresponds to a flexural vibration mode. The natural frequencies related to this vibration mode will be computed in the following sections.

##### 4.1 Analytical calculation

For many practical applications, the natural frequencies of uniform beam can be determined with sufficient accuracy by an analytical approach (Stokey, 1988). The classical approach is based on the use of the relation which relates the curvature of the beam to the bending moment at each section of the beam :

$$M = EI\chi = EI \frac{\partial^2 y}{\partial x^2} \quad (1)$$

This equation is based upon the assumptions that the material is homogeneous, isotropic and obeys Hooke's law. The beam must be straight with a uniform cross section. In order to neglect the shear deflection, the lateral displacement in direction of the  $y$  axis,  $y(x,t)$ , has to be small and the beam has to be long compared to cross sectional dimensions.

$E$  is the modulus of elasticity in tension and compression (Young's modulus), and  $I$  is the area moment of inertia.

The equation of motion for lateral vibration is found by considering the force action on the element which is formed by passing two parallel planes A and B through the beam normal to the longitudinal axis (figure 3). The vertical elastic shear force acting on section A and B are  $V$  and  $V' = V + (\partial V / \partial x)dx$  respectively (figure 3). The sum of the vertical forces acting on the element must equal the product of the mass of the element and the acceleration ( $\partial^2 y / \partial t^2$ ) in the lateral direction:

$$\frac{\partial V}{\partial x} + \rho S \frac{\partial^2 y}{\partial t^2} = 0 \quad (2)$$



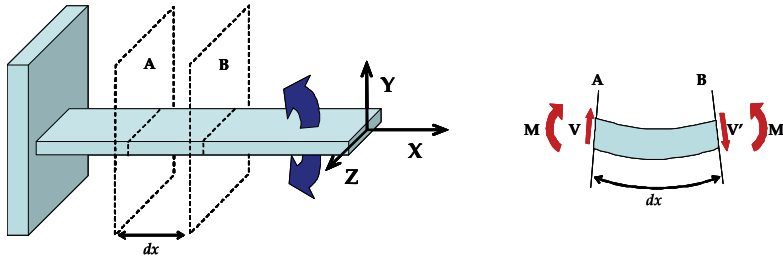


Figure 3. clamped-free beam executing lateral vibration, (B) element of beam showing shear force and bending moments

In this element, the equilibrium of the moment drives to  $V = \partial M / \partial x$ . Other differentials of higher order can be neglected. Then, from eq. 1 and 2, the basic equation for the lateral vibration of beams is given :

$$\frac{\partial^2}{\partial x^2} \left( EI \frac{\partial^2 y}{\partial x^2} \right) + \rho S \frac{\partial^2 y}{\partial t^2} = 0 \quad (3)$$

The solution of this equation if  $EI$  is constant, is of the form  $y = A(x) \times [\cos(\omega_n t + \varphi)]$  in which  $A$  is a function of  $x$  only. Substituting  $\beta^4 = \rho S \omega^2 / EI$  and dividing eq (3) by  $\cos(\omega_n t + \varphi)$  :

$$\frac{d^4 A(x)}{dx^4} = \beta^4 A(x) \quad (4)$$

The following function represents the solution of the eq. (4). The constants  $A, B, C, D$  are found from the boundary conditions.

$$A(x) = A \operatorname{ch} \beta x + B \operatorname{sh} \beta x + C \cos \beta x + D \sin \beta x \quad (5)$$

In applying the end conditions in the case of a rectangular beam, clamped at one extremity and free at the other, we have to solve the following equation:

$$1 + \operatorname{ch} \beta \ell \cos \beta \ell = 0 \quad (6)$$

With  $\ell$  the length of the beam. The solutions of that transcendental equation can be estimated from a numerical approach. As an example, with the Newton' method implemented with Matlab2007, we are able to found  $\lambda_n = \beta_n \ell$  :

$$\lambda_1 = 1.8751 ; \lambda_2 = 4.6941 ; \lambda_3 = 7.8547 ; \lambda_4 = 10.9955 ; \lambda_n \approx (2n-1) \frac{\pi}{2} \rightarrow \forall n > 4$$

The corresponding undamped natural frequency-angular are found by substituting the length of the beam to find each  $\beta$  and then :

$$\omega_n = \beta_n^2 \sqrt{\frac{EI}{\rho S}} \quad (7)$$

In the case of rectangular cantilever (one end clamped and the other one free), formula (8) gives the natural frequencies corresponding to the normal flexural modes of vibration of the beam (figure 4).

$$f_n = \alpha_n \frac{e}{\ell^2} \sqrt{\frac{E}{\rho}} \quad (8)$$

with  $\alpha_n = \frac{1}{4\pi\sqrt{3}} \lambda_n^2$  and  $e$  the thickness of the beam.

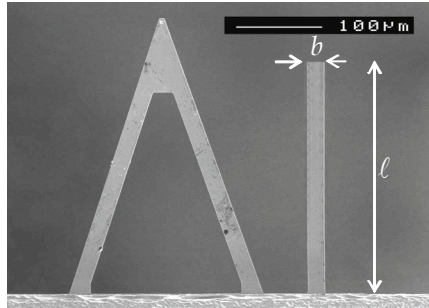


Figure 4. Description of the main geometrical parameters used in the computation

#### 4.2 Simulation with finite element method

The purpose of this analysis is to find the transient response from an harmonic load with an excitation frequency in the range 10-1000 KHz. These frequency values are typically in the range of the resonance frequencies obtained by the analytical and experimental approaches. Finite element modelling (FEM) is particularly well-suited to numerically solve the mechanical equations.

Adaptive meshing and re-meshing is used to tackle the problem of differing length scales. The 3D model makes use of an extruded triangular mesh. High-resolution solutions with minimum computation requirements are tracked. The mesh results in around 250 elements and 6000 degrees of freedom. The numerical model was defined, solved and analyzed in MATLAB using the script functions of COMSOL multiphysics (v3.4 with MEMS module) in conjunction with other in-house functions.

The FEM method was applied to two models. The first one was the three dimensional geometry (FEM 3D). The second one is a 2D Plate model where the thickness of the planar structure is less than one tenth of its width. The forces are applied in the direction normal to the plate; the main deformation takes place in the out-of-plane direction. In thin plate theory, the transverse shear deformation is neglected.

The default element type is quadratic Lagrange elements. They use second-order polynomials, which is often a good trade off between memory usage and accuracy.

In table 1, we have reported the natural frequencies obtained on a rectangular micro-cantilever. We have compared the results calculated with the formula (8), and those simulated by FEM (for the 2D Plate model and for the 3D model). As expected, a very good agreement is obtained between the three different approaches.

n	Mode	Analytic (KHz)	Plate model	FEM 3D
1	Long <sub>x</sub> 1	16.4	16.5	16.5
2	Long <sub>x</sub> 2	103,0	103.5	103.6
3	Long <sub>x</sub> 3	288.5	289.9	290.1
4	Long <sub>y</sub> 1	---	---	298.5
5	Torsional vib.	---	531.9	531.2
6	Long <sub>x</sub> 4	565.3	568.6	568.8
7	Long <sub>x</sub> 5	934.5	940.9	941.2

Table 1. Assignment of the first seven natural modes for a rectangular cantilever ( $\ell = 170 \mu\text{m}$ ,  $b = 10 \mu\text{m}$ , thickness  $e = 0,550 \mu\text{m}$ , Young's modulus: 143 GPa)

Figure 5 shows the deflection of the beam for the modes 2 and 3.

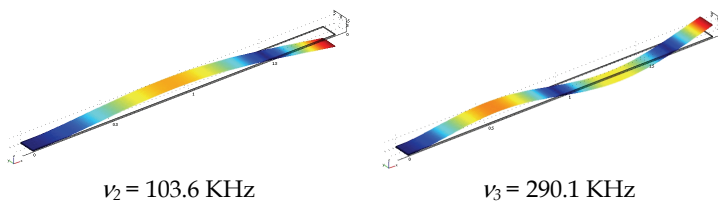


Figure 5. Deformation shapes and corresponding frequencies for two natural vibration modes:  $n=2$  and  $3$  (3D model). The boundaries display the total displacement; the black edges indicate the non-deformed beam geometry; and the white edges delineate the deformed geometry

#### 4.3 Experimental and modelling results on a rectangular beam

By using the classical detection system of an atomic force microscope, we have measured the natural frequencies of a micro-cantilever, which is generally used in intermittent contact mode. A typical spectrum is presented in figure 6. We have also reported on the graph the simulated results (blue line). For the simulation, the thickness of the beam is constituted of 430 nm of silicon and a thin film of gold (70 nm). In order to precisely mesh the structure, we have twice extruded the 2D geometry.

A good agreement is observed between experimental and calculated frequencies. However, it is interesting to note that only one parameter was adjusted in this simulation: the thickness of the thin film of gold. Indeed, an accurate knowledge of this parameter is very difficult to obtain experimentally.

This first part concerning the rectangular cantilevers is very important because it shows the ability of the COMSOL software to precisely calculate the frequencies of very thin films. Moreover, this fact is confirmed by comparing the classical analytical solutions with experimental measurements on bi-layers beams.

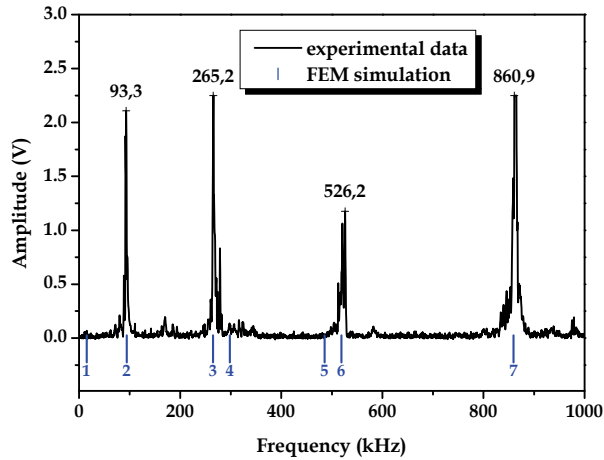


Figure 6. Experimental spectrum measured on a rectangular beam with the AFM set-up (Veeco Inst.). Underneath, we reported the FEM 3D simulated frequencies (blue line) (thickness 520 nm,  $E = 143$  GPa, density = 4,800 kg/m<sup>3</sup>, mesh: de 1,024 extruded square elements)

### 5. Natural frequencies of “V-shaped” micro-cantilevers

In the case of “V” shaped cantilevers, no exact solution (analytic resolution) is known. As an alternative approach, FEM method is particularly useful to calculate the fundamental natural frequencies. In figure 7, we present two SEM images of two commercial AFM cantilevers. The left image correspond to the STS E type and the right to the STS F type.

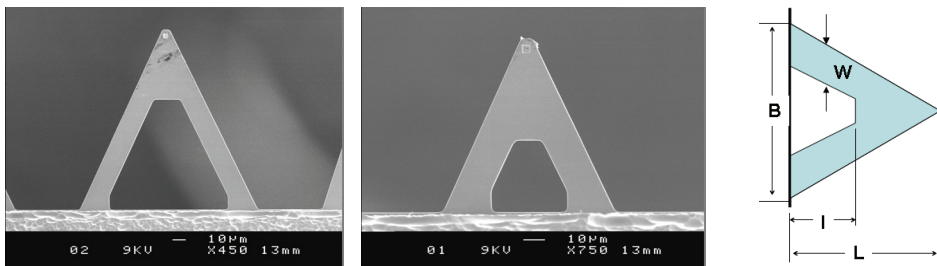


Figure 7. Examples of commercial AFM-cantilevers and definition of the main geometrical parameters used in FEM simulation.

The main geometrical parameters have been measured using SEM microscope. These parameters are defined in figure 7 and numerical values are reported in table 2. In the same way, experimental and calculated frequencies are reported in table 2.

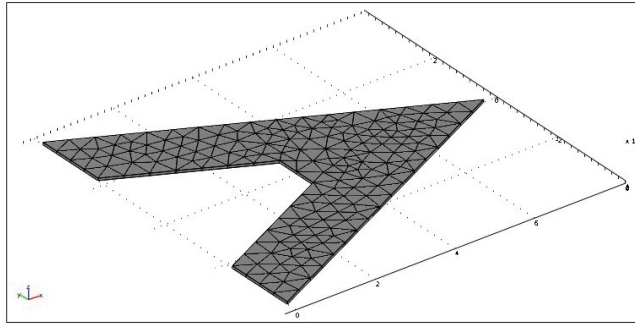


Figure 8. The 3D mesh produced by extruding a 2D triangular mesh, of very thin “V” shaped cantilever (STS F type)

A particular attention has been devoted to mesh the geometry of our cantilevers. Indeed, it is well-known that very thin structures are very difficult to simulate by FEM. Thank to the mesh module of COMSOL Multiphysics, it is possible to extrude the meshes with a very thin thickness (figure 8).

As an example, the computed deformations of the first six fundamental modes of the STS F type cantilever is presented in figure 9.

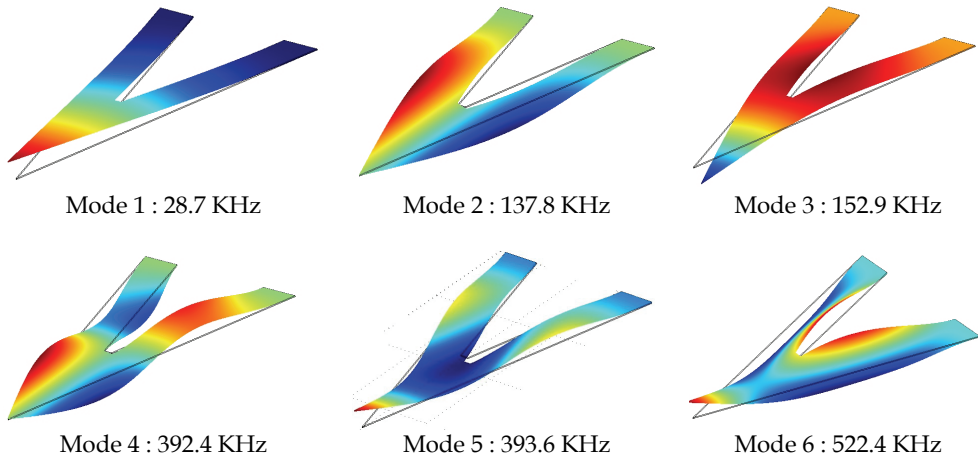


Figure 9. Deformed shapes corresponding to the first six vibration modes of the “V-shaped” cantilever. (STS F type cantilever). Underneath, FEM calculated frequencies are reported

A comparison between the natural frequencies measurements and the simulated frequencies is showed in figure 10. We have to point out that the amplitude of the first vibration mode is often very low with our experimental set-up. This amplitude is proportional to the slope of the free end of the beam but almost independent of the lateral deflection. In the simulations, the thickness of the micro-cantilever was the only adjusted parameter.

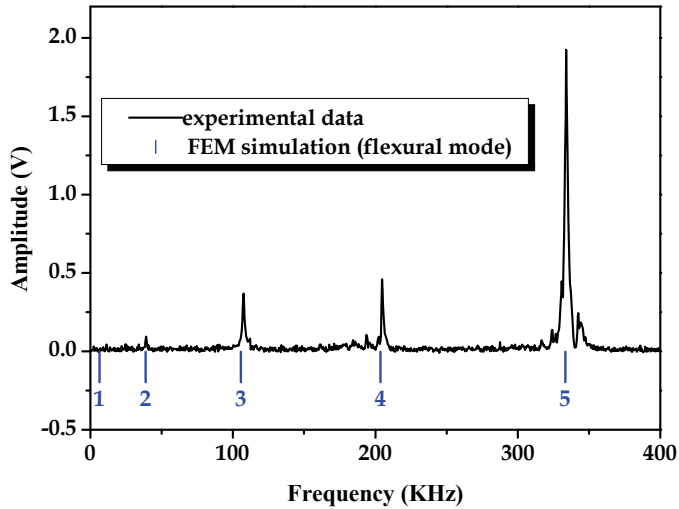


Figure 10. Experimental spectrum measured on a “V-shaped” micro-cantilever (STS C type). Underneath, the first five FEM calculated frequencies are reported

Cantilever type	L ( $\mu\text{m}$ )	l ( $\mu\text{m}$ )	w ( $\mu\text{m}$ )	B ( $\mu\text{m}$ )	Thickness (nm)	Mode n	Experimental frequency (KHz)	Simulated frequency (KHz)	Relative error (%)
STS C	323	235	21	227	680	1	-	6.41	- %
						2	39.1	38.8	0.7 %
						3	107.5	105.6	1.7 %
						4	204.6	203.6	0.4 %
						5	334.0	333.3	0.2 %
STS D	225	133	21	158	700	2	88.7	87.7	1.1 %
						3	233.2	234.4	0.5 %
STS E	128	78	18	140	560	2	193.4	194.7	0.8 %
						3	505.5	503.0	0.5 %

Table 2. Measured and simulated resonance frequencies of different “V-shaped” cantilevers (Young modulus: 143 GPa, density = 4800 kg/m<sup>3</sup>)

## 6. Natural frequencies of “V-shaped” coated cantilevers

These cantilevers can be easily coated with organic or inorganic layers, which offer interesting anchoring points for further functionalizations. For example, thin films of N,N'-diphenyl-1,4-phenylenediamine (B3) (purchased from Aldrich) were deposited on the backside of the cantilever by vacuum thermal evaporation (De Santana et al., 2006). Figure

11 presents the experimental frequency shifts of a cantilever coated with different thicknesses of B3, and the same cantilever in its uncoated state.

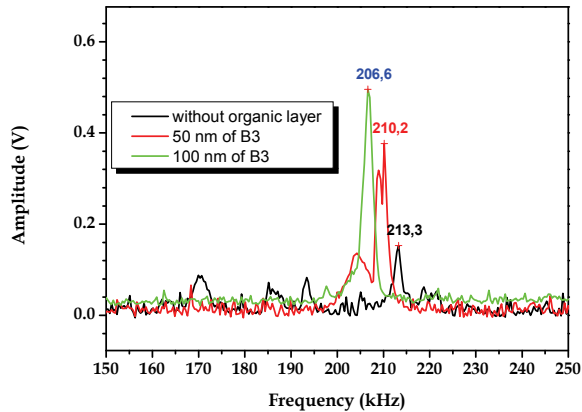


Figure 11. Resonance spectra of uncoated and organic layer - coated cantilever

By using an home-made arrangement of plasma reactors, the surface of “V-shaped” cantilevers was coated with a thin layer of platinum. Prior to the metallization, these reactors were employed to remove dust particles. Then, by plasma sputtering without breaking the vacuum, a thin layer of platinum (between 5 and 20 nm) was deposited (Chaigneau et al., 2007).

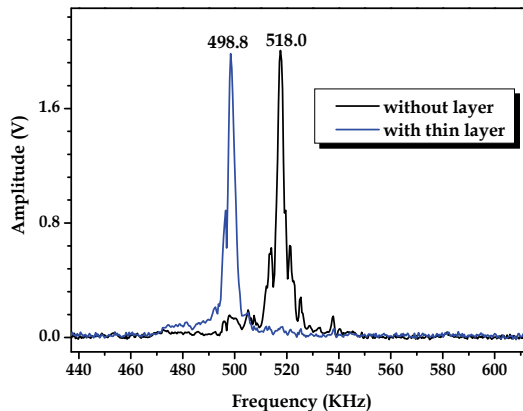


Figure 12. Resonance spectra of uncoated and platinum-coated micro-cantilever

A thin solid film of 10 nm of platinum was deposited onto a STS C type micro-cantilever. In figure 12, a significant frequency shift is observed for the coated cantilever (498.8 KHz) with respect to the frequency of the uncoated cantilever (518.0 KHz).

By taking into account the mass density and the deposited volume, a crude calculation indicates a mass change varying between 1.3 pg (platinum thickness of 5 nm) to 5.5 pg (20 nm thick).

Then, the finite element modelling can be used to evaluate the sensitivity of the used cantilever depending on the deposited thickness.

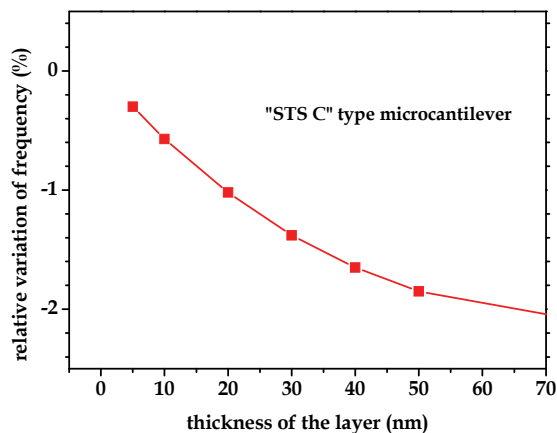


Figure 13. Relative variation of the resonance frequency as a function of the layer thickness of deposited platinum

As an example, figure 13 shows the simulated values of the frequency shift as a function of the deposited layer thickness (which can be easily converted into added mass). The slope of this curve gives us the sensitivity of the modified cantilever. In future, such simulations could be used to predict the sensitivity for different cantilevers with various geometrical dimensions, as well as for different deposited layer thicknesses.

## 7. Conclusion and prospects

The AFM cantilevers offer interesting prospects as biological and chemical sensors with very high sensitivity. To allow the adsorption of chemical species on the functionalized surface of cantilevers, these cantilevers are previously coated with a thin film of gold or silver. The sensitivity of such sensors could be predicted from the modelling of these cantilevers. As the principle of detection is generally based on the measurement of the resonance frequency shift, it seems crucial to calculate the resonance frequencies of cantilevers. For complicated shapes of cantilevers, like V-shaped cantilevers, these resonance frequencies can only be obtained by using a finite element modelling.

In this way, this chapter presents some results concerning the use of FEM to estimate the resonance frequencies of rectangular and V-shaped cantilevers. First of all, this approach was applied to rectangular micro-cantilevers to compare the analytical, experimental and FEM-computed values of the resonance frequencies. As expected, the frequencies determined by FEM approach were very close to those obtained experimentally or analytically. Then, the FEM method was employed to evaluate the frequencies of V-shaped



cantilevers, which can not be analytically calculated. By adapting the mesh parameters, a good agreement was obtained between the FEM-values and the experimental frequencies. In prospects, the same approach could be employed to predict the sensitivities of such cantilevers recovered with a sensitive layer. Moreover, an interesting use of finite element modelling would be to optimize the shape and the geometrical dimensions of these cantilevers for obtaining the best sensitivities and detection limits.

## 8. Acknowledgments

S.C. and G.L. acknowledge the "Agence Nationale de la Recherche" for financial support in the frame of "ANR06-Jeunes Chercheurs-n°24" program. The authors would like to thank M. Collet for fruitful discussions.

## 9. References

- Baselt, D. R.; Fruhberger, B.; Klaassen, E.; Cemalovic, S.; Britton C.L.; Patel, S. V.; Mlsna, T. E.; McCorkle, D. & Warmack, B. (2003). Design and performance of a microcantilever-based hydrogen sensor. *Sensors and Actuators B*, 88, 120-131
- Bashir, R.; Hilt, J. Z.; Elibol, O.; Gupta, A. & Peppas, N.A. (2002). Micromechanical cantilever as an ultrasensitive pH microsensor *Appl. Phys. Lett.*, 81, 3091-3093
- Betts, T. A.; Tipple, C. A.; Sepaniak, M. J. & Datskos, P. G. (2000). Selectivity of chemical sensors based on micro-cantilevers coated with thin polymer films, *Analytica Chimica Acta*, 422, 89 -99
- Chaigneau, M.; Minea, M. & Louarn, G. (2007). Comparative study of different process-steps for the near-field optical probes manufacturing. *Ultramicroscopy* 107 1042-1047
- Chen, G. Y.; Thundat, T., Wachter, E. A. & Warmack, R. J. (1995). Adsorption-induced surface stress and its effects on resonance frequency of microcantilevers *J. Appl. Phys.* 77(8), 3618-3622
- Cuenot, S.; Fretigny, C.; Demoustier-Champagne, S. & Nysten B. (2003). Measurement of elastic modulus of nanotubes by resonant contact atomic force microscopy *J. Appl. Phys.* 93, 5650 (2003).
- De Santana, H.; Quillard, S.; Fayad, E. & Louarn, G. (2006). In situ UV-VIS and Raman spectroscopic Studies of the electrochemical behavior of N,N'-Diphenyl-1,4-Phenylenediamine. *Synthetic Metals* 156 81-85
- Dufour, I. & Fadel, L. (2003). Resonant microcantilever type chemical sensors: Analytical modelling in view of optimization. *Sensors and Actuators B*, 91, 353-361
- Gimzewski, J. K.; Gerber, C., Meyer, E. & Schlittler, R. R. (1994). Observation of a chemical reaction using a micromechanical sensor *Chem. Phys. Let.* 217, 589-594
- Ji, H- F.; Hansen, K. M.; Hu, Z. & Thundat, T. (2001). Detection of pH variation using modified microcantilever sensors *Sensors and Actuators B* 72, 233-238
- Lange, D.; Hagleitner, C.; Hierlemann, A.; Brand, O. & Baltes, H. (2002). Complementary metal oxide semiconductor cantilever arrays on a single chip: Mass-sensitive detection of volatile organic compounds. *Analytical Chemistry*, 74, 3084 -3095
- Lavrik N.; Sepaniak M. & Datskos P. (2004). Cantilever transducers as a platform for chemical and biological sensors. *Rev. Sci. Instrum.*, 75, 2229-2253

- Lochon, F.; Dufour, I. & Rebière, D. (2005). An alternative solution to improve sensitivity of resonant microcantilever chemical sensors: Comparison between using high-order modes and reducing dimensions. *Sensors and Actuators B*, 108, 979-985
- Moulin, A. M.; O'Shea, S. J. & Welland, M.E. (2000). Microcantilever-based biosensors *Ultramicroscopy* 82, 23-31
- Raiteri, R.; Grattarola, M.; Butt, H. -J. & Skládal, P. (2001). Micromechanical cantilever-based biosensors. *Sensors and Actuators B*, 79, 115-126
- Sepaniak, M.; Datskos, P.; Lavrik, N. & Tipple, C. (2002). Microcantilever transducers: A new approach in sensor technology. *Analytical Chemistry*, 74, 568 -575
- Stokey W. F. (1988). Vibration of systems having distributed mass and elasticity, In: *Shock and vibration Handbook*, Cyril M. Harris (Ed.), chapter 7, McGraw Hill book Company, ISBN 0-07-026801-0, New-York, USA
- Thundat, T.; Wachter, E. A.; Sharp, S.L. & Warmack, R. J. (1995a). Detection of mercury vapor using resonating microcantilevers. *Appl. Phys. Lett.*, 66, 1695-1697
- Thundat, T.; Sharp, S. L.; Fisher, W. G.; Warmack, R. J. & Wachter E. A. (1995b). Micromechanical radiation dosimeter *Appl. Phys. Lett.* 66, 1563-1565
- Wachter, E. A. & Thundat, T. (1995). Micromechanical sensors for chemical and physical measurements. *Rev. Sci. Instrum.*, 66, 3662-3667

# Analysis of Electrical Phenomena Occurring in Thermally Assisted Mechanical Dewatering Processes (TAMD)-a Preliminary Study

Akrama Mahmoud<sup>1</sup>, Aurora Fernandez<sup>1</sup> and Patricia Arlabosse<sup>2</sup>

<sup>1</sup> UMR5504, UMR792 *Ingenierie des Systemes Biologiques et des Precedes*, Toulouse

<sup>2</sup> RAPSODEE CENTRE (UMR CNRS 2392), *Ecole des Mines d'Albi-Carmaux*  
France

## 1. Introduction

The design, modelling and simulation of solid-liquid separation processes remain a challenging area due to difficulties in quantifying distribution of the phases in the filter cake, and in acquiring reliable experimental data for model development. Usually, overall mechanical dewatering parameters, such as filtrate volume, average volume fraction of solids, or cake thicknesses are measured. A more fundamental approach is to determine the internal structure of filter cakes, i.e., the profile of the solid volume fraction, in order to investigate the role of the material behaviour during compression steps. In most cases, profiles of solid volume fraction have been investigated using electrical resistance meters (Shirato & Aragaki, 1972; Chase & Willis, 1991). During the measurements, iron pins are positioned at the wall of the filter cell, disturbing the liquid flow and cake formation. Some investigators studied profiles of solid volume fraction in filtration cakes with X-rays (Bierck et al., 1988; Tiller et al., 1990) or nuclear magnetic resonance (NMR) (Horsfield et al., 1989). In our knowledge, the investigation of the solid distribution in a filter cake by electrical tomography technique has not been reported before. This contribution describes preliminary studies for the application of electrical resistance tomography (ERT) for the determination of local volume fractions of solids in a filter cake during the thermally assisted mechanical dewatering process (TAMD) (Fernandez et al., 2005). ERT is a non intrusive and non-destructive technique, which does not influence cake. Moreover, electrical resistance tomography (ERT) belongs to real-time, low-cost, easy to implement and fast techniques which exploit differences in the electrical properties of solids and liquids.

Electrical resistance tomography basically consists in reconstruction of the conductivity distribution from electrical data which characterize the electrical response of a medium. The electrical current flow in a saturated packed bed submitted to an electrical field is depending on the solid and liquid phases, namely the dispersed and the continuous phases, which have different properties. Several theories have been proposed for the transport of electrical current in mixtures (Helfferich, 1962). However, most of the theories are based on the assumptions of either a regular lattice-type arrangement or a completely random distribution of the components that are not well adapted for filtration cakes. Electrical conductivity of saturated packed bed varies with the mobility and affinity of ions with

which solid particles are in contact (Helfferich, 1962). For very low specific conductivity of the liquid phase, the specific conductivity of the packed bed is enhanced by the presence of solid particles. In contrast, when liquid phase conductivity is high, their contribution to electrical transport becomes more significant. This is especially useful in ERT applications where concentration of electrolyte plays a significant role. Nevertheless, the electrical features of solid particles have been little investigated, in spite of the appreciable ohmic drops measured in packed beds.

The present chapter concerns the investigation of the electrical behaviour of a packed-bed, with particular emphasis on bed conductivity determination. For this, different packed-beds have been constituted using potassium chloride solutions, as liquid phase, and model materials, with different particle size distribution, as solid phase. The electrical conductivities of the packed-beds were determined, using a model for the conductivity of two-phase media, by measurement of the bed impedance in a lab cell with two facing Pt sheets. Then the primary potential distribution and current density (field analysis) in a TAMD dedicated cell were carried out in a two-dimensional domain using Femlab™ software. Current density field deduced from the potential field led to second estimation of the electrical bed conductivity. The measured bed conductivities were compared to the numerical predictions and the consistency of these techniques is discussed. After this introductory section, section 2 gives a brief overview of the electrical tomography technique. Section 3 devotes to the introduction of different strategies for data collection and section 4 concerns with the primary sensors (electrodes) of a typical ERT system. Section 5 discusses mathematics for describing electrical fields in ERT, and numerical methods used to approximate the solution. After that, a study of the theoretical relationship between packed-bed conductivity and solid content is carried out in section 6, and the proposed plug flow model is described. The experimental procedures and some experimental results are presented and discussed in sections 7 and 8. Section 9 describes the numerical approach to tomography-forward problem with an emphasis on modelling and computation used to predict current density fields using Femlab Multiphysics®. Finally, conclusions are given in section 10.

## 2. A historical overview

Tomography methods are mainly employed for obtaining estimated images of a cross section of an object. X-ray tomography was the first to be developed (in 1960s) and its use is now routine not only in medicine but in some industrial applications as well (internal inspection of mechanical components and flaw detection in materials, for example). Since then a number of new tomography methods aimed at industrial processes have emerged, collectively known as process tomography (Williams & Beck 1995).

The main goal of process tomography methods, which started to develop in the mid 1980s, is to produce an image of the phase or component distribution in an industrial process using only external sensors and without causing any perturbation to it. In other words, process tomography provides a way of '*looking*' inside the process, from the outside and with no need for physical intrusion or alteration, in a radically new global approach to gathering structural information on the process, unlike the traditional methods based on local sampling. Examples of suitable processes are those occurring in mixing or stirring vessels, fluidized bed reactors, separator tanks, or a pipeline carrying multiphase flow. There is a whole range of principles and techniques that can be exploited in process tomography,

including electrical methods based on impedance measurement, ultrasound, magnetic resonance, optical methods and those based on ionizing radiation (X- and gamma-rays). Generally speaking, ionizing radiation methods produce images with the highest definition, but are relatively slow to achieve. On the other hand, electrical methods yield lower resolution images but are much faster, robust and relatively inexpensive. In particular with regard to electrical impedance tomography, or electrical tomography for short, there has been a very noticeable progress in the last few years. This type of tomography has three main modalities: electrical capacitance tomography (ECT), electromagnetic tomography (EMT) and electrical resistance tomography (ERT), as shown in Table 1. Each of these techniques has its advantages, disadvantages and limitations. The choice of a particular technique is usually dictated by many, very often contradictory, factors. These include: physical properties of the constituents of multiphase flow, the desired spatial and temporal resolution of imaging, cost of the equipment, its physical dimensions, human resources needed to operate it, and potential hazards to the personnel involved (e.g. radiation).

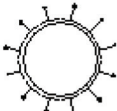
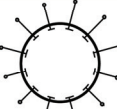

Method	Typical arrangement	Measure values	Typical material properties	Typical material
ECT	 Capacitive plates	Capacitance C	Permittivity $\epsilon_r: 10^0 - 10^2$  Conductivity $\kappa: < 10^{-1} \text{ S/m}$ (low)	Oil, deionised water, non metallic powders, polymers burning gasses
ERT (EIT)	 Electrode array	Resistance (Impedance) R/Z	Conductivity $\kappa: 10^{-1} - 10^7 \text{ S/m}$ (wide) Permittivity $\epsilon_r: 10^0 - 10^2$	Water/saline, biological tissue, rock/geological materials, semi-conductors
EMT	 Coil array	Self/mutual Inductance L/M	Conductivity $\kappa: 10^2 - 10^7 \text{ S/m}$ (high) Permeability $\mu_r: 10^0 - 10^4$	Metals, some minerals, magnetic materials and ionised water

Table 1. Comparison of electrical tomography techniques: principles and applications

In electrical capacitance tomography or ECT (Beck et al., 1997; Gamio, 1997; Plaskowski et al., 1995), normally used with mixtures where the continuous phase is non-conducting, the sensor employed is made of a circular array of electrodes distributed around the cross-section to be examined, and the capacitance between all the different electrode-pair combinations is measured. With the help of a computer and a suitable image reconstruction algorithm, this information is used to create a map showing the variation of the dielectric constant (or relative permittivity ( $\epsilon_r$ )) inside the sensor area, thus providing an indication of the physical distribution of the various components of the mixture. In this particular case,

the electrodes can be located on the outside of a non-conducting pipe, in order to simplify sensor construction and avoid direct contact with the process fluids. A second external grounded metallic pipe serves as an electric screen and to provide mechanical resistance. In principle, ECT has important applications in multiphase flow measurement, particularly gas-oil two-phase flow, which often occurs in many oil wells. Additionally, ECT has potential applications to imaging, monitoring and controlling numerous industrial multiphase processes. However, so far the main limiting factor to the practical application of ECT has been the lack of fidelity or accuracy of the images obtained using the available image reconstruction methods (Yang & Peng, 2003).

On the other hand, more sophisticated methods, based on iterative local optimization techniques, generally require one or more regularization parameters whose optimal value depends precisely on the (unknown) image to be reconstructed. The regularization employed has the effect of smoothing the image contours, making it more diffuse. Thus, better and more accurate image reconstruction methods are still being developed in the context of this application.

Electromagnetic tomography (EMT), based on the measurement of complex mutual inductance, is relatively new and is so far unexploited for process tomography applications. This form of EMT could more accurately be termed '*mutual inductance tomography*' and can extract data on permeability ( $\mu$ ) and conductivity ( $\kappa$ ) distributions. EMT can be selected for processes involving mixtures of ferromagnetic and/or conductive materials. It may be applied in following or concentration measurements of ferrite labelled particles in transport and separation processes, foreign-body detection and location for inspection equipment such as used in the food processing, textile and pharmaceutical industries, crack or fault detection, and possibly imaging water concentration where the water phase is significantly ionized to ensure a high conductivity (Al-Zeibak & Saunders, 1993).

In electrical resistance tomography (ERT), the basic aim is to reconstruct the distribution of electrical conductivity ( $\kappa$ ) within an object from measurements of voltage around the periphery of a vessel. Potential applications for ERT technique are where the continuous phase is electrically conducting while the dispersed phase could be conducting or insulating. Such conditions are typically found in minerals processing applications, medical field, petrochemical field, pressure filtration, mixing, transport and separation processes (Slater et al., 2002; William & beck, 1995; Brown, 2000; Wang et al., 1999; Bond et al., 1999). Of the three techniques mentioned above, ERT is, in certain cases, the easiest to implement and the most attractive method for real-time imaging due to the availability of multi-plane measurement systems and the scalability of ERT sensors. They are also small, which makes the equipment more mobile. The low spatial resolution is well counter-balanced by high temporal resolution.

In this work, it was decided to investigate the use of electrical resistance tomography (ERT) as a means of measuring the volume fraction of solids in a thermally assisted mechanical dewatering process (TAMD). Thermally assisted mechanical dewatering (TAMD) is a new process for energy-efficient liquid/solid separation which enhances conventional-device efficiency. The main idea of this process is to supply a flow of heat in mechanical dewatering processes to favour the reduction of the liquid content. An electrical tomography system will be used to image the electrical conductivity of the filtration cake. Since the conductivity of the cake depends on the product nature and composition, but also on the temperature and specific conductivity of the solid fraction, a digital treatment of the

electric signals will allow a calculation of the volume fraction of solids profile inside the filtration cake. This non-intrusive measurement method will contribute largely to the understanding of the physical mechanisms involved in thermal dewatering.

### 3. Electrical measurement strategies

In electrical tomography technique, electrodes are distributed on the internal wall of the cell, a current is injected between a source/sink electrode pair and the corresponding differences of potential are recorded between the other pairs. The procedure is repeated for other source/sink pairs to reconstruct the spatial distribution of the conductivity of the internal medium. There are four main strategies of data collection: adjacent, opposite, diagonal and conducting boundary (Dickin & Wang, 1996). For brevity, in the following the most common methods to configure electrodes in ERT were described.

#### 3.1 Adjacent strategy

Brown & Segar (1987) suggested a method whereby the current is applied through two neighbouring electrodes and the voltage is measured successively from all other adjacent electrode pairs. Current is then applied through the next pair of electrodes and the voltage measurements repeated. The procedure is repeated until all the independent measurements have been made. Figure 1a illustrates the application of this method for a cylindrical volume conductor with  $N$  equally spaced electrodes. The adjacent measurement yields  $N^2$  measurements. However, of these, only  $(N(N-1)/2)$  are independent. Furthermore, to avoid electrode/electrolyte contact resistance problems, the voltage is not measured at a current-injecting electrode and therefore the total number of independent measurements is reduced to  $(N(N-3)/2)$ . The adjacent strategy has a non-uniform current distribution since most of the current density travels near the peripheral electrodes. Therefore, the current density at the centre of the vessel is relatively low which makes the strategy very sensitive to measurement error and noise (Hua et al., 1993).

#### 3.2 Opposite strategy

The opposite strategy, as the name suggests and as shown in Figure 1b, applies current through diametrically opposed electrodes. The electrode adjacent to the current-injecting electrode is used as the voltage reference. Thus, for a particular pair of current-injecting electrodes, the voltages are measured with respect to the reference at all the electrodes except the current-injecting ones. The next set data is obtained by switching the current to the next pair of opposite electrodes in the clockwise direction and the voltage reference electrode is changed accordingly. The whole procedure is repeated until all independent measurements have been made. Compared with adjacent strategy, the opposite strategy is less sensitive to conductivity changes at the boundary since most of the current flows through the central part of the region. Hua et al. (1993) noted that the opposite strategy yields a relatively good distinguishability due to the even distribution of currents. The number of independent measurements is given by  $N(3N-1)/8$  (Breckon & Podcock, 1988). Consequently, the image resolution will be decreased down to 23% compared to the adjacent strategy for the same number of electrodes (Breckon & Podcock, 1985). Although the adjacent strategy results in slightly more independent measurements, the opposite strategy results in better quality measurements. This is due to the fact that the current is

more uniformly distributed in the opposite strategy and, therefore, less sensitive to noise (Dickin & Wang, 1996).

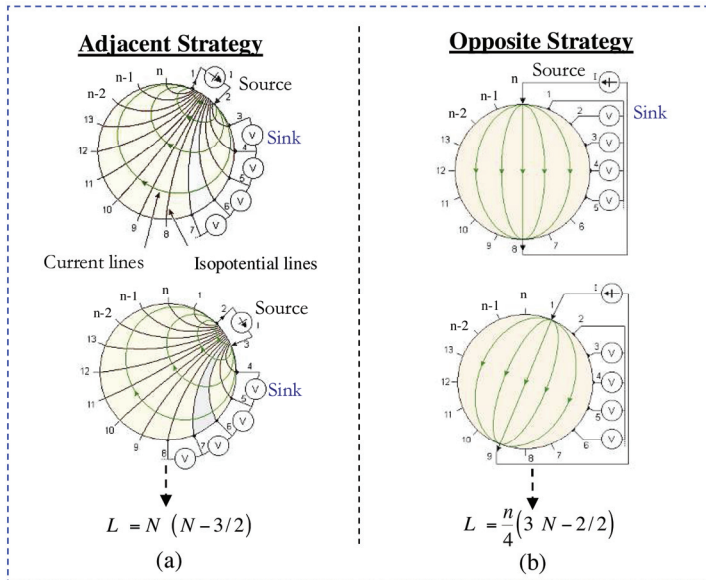


Figure 1. (a) The adjacent measurement strategy illustrated for a cylindrical volume conductor and  $N$  equally spaced electrodes, (b) The opposite measurement strategy

#### 4. Sensors of ERT

Several recommendations for the design of ERT sensors are available in the literature (pyakowski et al., 1999; Dickin & Wang, 1996; Wang et al., 1995; Hua et al., 1993). A number of important factors must be considered. The electrodes must be in direct contact with the process fluid to be analyzed. While being invasive, electrodes should be as non-intrusive as possible. The electrodes must be more conductive than the process fluid in order to obtain reliable measurements. For the majority of process application, the electrodes are metallic, e.g. stainless steel, silver, gold, platinum, silver palladium or any suitable material exhibiting similar properties. The material of construction should be selected by considering the following factors (Dickin & Wang, 1996): cost, ease of fabrication and installation, good electrical conductivity, and resistance to abrasion and corrosion. Other factors can be added such as compatibility with the vessel construction material, thermal expansion properties, safety, reliability and robustness. Positioning of the electrodes is important, because the reconstruction algorithm employed in data analysis uses assumptions regarding the relative location of the electrodes. Electrodes are commonly located at equidistant positions around the periphery of the vessel to map electrical conductivity variations across a plane or planes of interest. The size of the electrodes is also an important factor. Ideally, current-injecting electrodes should have a large surface area to ensure that an even current density is generated, while the voltage measuring electrodes should have a small surface area, ideally a needle point, in order to avoid averaging across several equipotentials (Dickin & Wang,



1996). The optimal electrode size is dependent on a number of parameters, including the background conductivity. Despite these alternative recommendations, primarily for reasons of simplicity, identically sized electrodes are generally used for both current injection and voltage measurement. When choosing the number of electrodes  $N$ , it must be noted that the time taken to acquire data and reconstruct the image is a function of  $N$ , whereas the spatial resolution is proportional to  $\sqrt{L}$ , where  $L$  is the number of independent measurements. Finally, a primary consideration when building the sensors into vessel is the length of the signal-carrying cable between the electrode and the current injection/voltage measurement circuitry. Therefore, the electrodes are connected to the data-acquisition system by short lengths of co-axial cable to reduce the effect of the extraneous environmental noise and interference.

### 5. Governing equations

The main idea of the ERT is rather simple. With a known conductivity distribution,  $\kappa_b$ , and injection current pattern,  $I_0$ , as shown in Figure 2, the resultant voltage distribution,  $V$ , at the boundary of the system as well as at its interior can be determined uniquely by the Laplace equation:

$$\nabla \cdot (\kappa_b \cdot \nabla V) = 0 \quad \text{in } \Omega \tag{1}$$

where  $\Omega$  is the domain of the interest and  $\partial\Omega$  its boundary. The boundary conditions are as follows:

$$V = V_0 \quad \text{on } \partial\Omega \tag{2}$$

$$\kappa_b \cdot \frac{\partial V}{\partial n} = I_0 \quad \text{on } \partial\Omega \tag{3}$$

on the assumption that there is no current source inside the system. Here  $n$  is the unit normal vector.

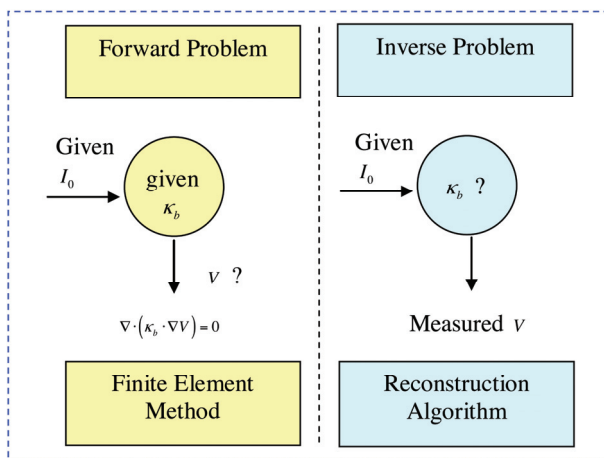


Figure 2. ERT forward and inverse problems

Hence, the basic idea of the ERT technique is to determine (or '*reconstruct*') the unknown conductivity distribution in the system with voltage data measured only at the boundary of the system using a proper image reconstruction algorithm.

Resolution of the Laplace Equation (1) to obtain the voltage distribution under the known conductivity distribution is usually called '*Forward Problem*'. The problem to determine the unknown conductivity distribution-the major task of the ERT-is known as a very hard '*Inverse Problem*' due to its nonlinearity and ill-conditioning phenomena (Cho et al., 1999).

Therefore, it is almost essential (i) to develop an accurate ERT measuring technique for the practical implementation of the ERT and (ii) to develop a fast and reliable ERT inverse problem solver. Along with the hardware improvements, several algorithms have been proposed to reconstruct the unknown conductivity by processing the measured data.

## 6. Flow parameter calculation using ERT

With conductivity data from ERT, the local volume fraction of solids,  $\varepsilon_s$ , can be determined by applying the Maxwell equation (Maxwell, 1981; Lucas et al., 1999; George et al., 2000):

$$\varepsilon_s = \frac{\kappa_b - \kappa}{2\beta\kappa + \beta\kappa_b} \quad (4)$$

where  $\kappa$  is the conductivity of the continuous phase,  $\kappa_b$  is the local bed conductivity,  $\varepsilon_s$  is the volume fraction of the dispersed phase of conductivity  $\kappa$ , and  $\beta$  is given by

$$\beta = \frac{\bar{\kappa} - \kappa}{\kappa + 2\kappa} = \frac{\alpha - 1}{\alpha + 1}; \quad \alpha = \frac{\bar{\kappa}}{\kappa} \quad (5)$$

Electrical conductivity of saturated packed beds is complex because of the presence of two conducting phases, namely the dispersed,  $\kappa$ , and the continuous phases,  $\kappa$ . According to Maxwell, the validity of Equation (4) is limited to small volume fractions. However, various researches found that Equation (4) produced good agreement with experimental data over a wide range of void fractions (Neal & Nader, 1973; Turner, 1976). If the dispersed phase is assumed to be a non-conductive material, the Equation 4 can be simplified as follows:

$$\varepsilon_s = \frac{1 - K}{1 + 0.5 K} \quad (6)$$

where K is the relative conductivity ( $K = \frac{\kappa_b}{\kappa}$ ). The conductivity of the continuous phase,  $\kappa$ , can be found easily with a widely available commercial conductivity meter, while the local bed conductivity is determined from the pixel conductivity of ERT image. If Maxwell's equation is expanded as a Taylor series, the solids assumed to be non-conductive and only two terms are considered, the following equation results:

$$K = (1 - \varepsilon_s)^x \quad (7)$$

where the value of the exponent  $x$  is 1.5, as originally determined by Bruggeman (1935). Rayleigh (1892) attempted to calculate the conductivity of regular arrays of spheres under conditions when their interactions could not be neglected. The result of Rayleigh's treatment, after correcting a numerical error in the original paper, is

$$K = 1 + \frac{3 \beta \varepsilon_s}{1 - \beta \varepsilon_s - 0.525 \left( \frac{\alpha - 1}{\alpha + 4/3} \right) \beta \varepsilon_s^{10/3}} \tag{8}$$

which applies in strictness only when the spheres are arranged in cubic order, and, further, when  $\varepsilon_s$  is moderate.

Other theoretical solutions to take into account the effect of the presence of solids on the electrical flux field exist, such as the obtained by Merdith & Tobias (1960) for oil-in-water emulsions:

$$K = \frac{\left( \frac{2 + \alpha}{1 - \alpha} \right) - 2 \varepsilon_s + 0.409 \left( \frac{6 + 3\alpha}{4 + 3\alpha} \right) \varepsilon_s^{7/3} - 2.133 \left( \frac{3 - 2\alpha}{4 + 3\alpha} \right) \varepsilon_s^{10/3}}{\left( \frac{2 + \alpha}{1 - \alpha} \right) + \varepsilon_s + 0.409 \left( \frac{6 + 3\alpha}{4 + 3\alpha} \right) \varepsilon_s^{7/3} - 0.906 \left( \frac{3 - 2\alpha}{4 + 3\alpha} \right) \varepsilon_s^{10/3}} \tag{9}$$

For non-conducting solids, the Equation (9) can be simplified as following:

$$K = \left( \frac{8(2 - \varepsilon_s)(1 - \varepsilon_s)}{(4 + \varepsilon_s)(4 - \varepsilon_s)} \right) \tag{10}$$

Concerning Merdith's works, they have little advantage over the use of Equation (7) with an empirically determined value for the exponent  $x$ .

The relative conductivity with respect to volume fraction of solids has been plotted in Figure 3, for non-conducting solids, together with theoretical solutions by Maxwell, Rayleigh, Bruggeman and Merdith, respectively.

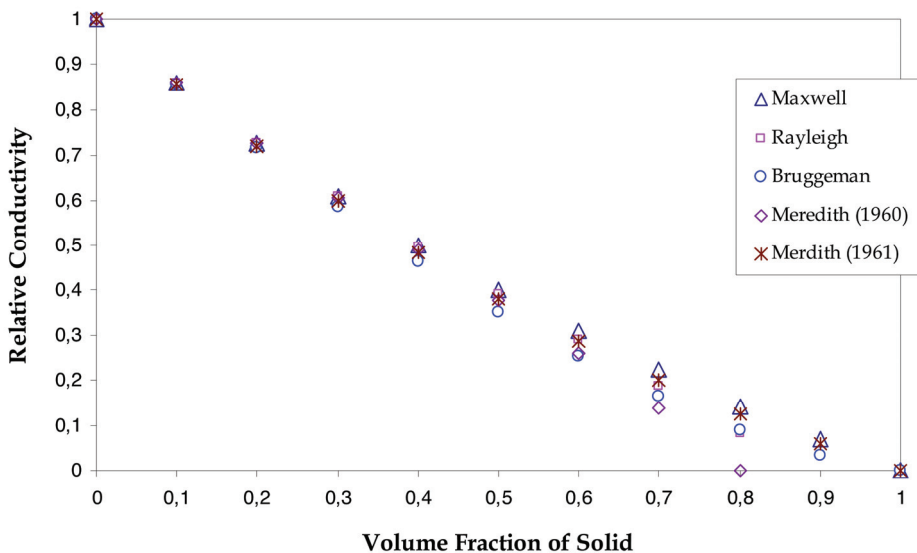


Figure 3. Relative conductivity versus volume fraction of solid

In contrast to the case of a saturated packed beds of solid inert particles (as in the present study), the geometrical, electrical and chemical properties of particles are sensitive to the chemical composition of the liquid, continuous phase, as adsorption equilibrium prevails. First attempts in modelling often involved regular lattice arrangements, as that suggested by Baron (Helfferich, 1962) who considered a statistical cage model. However, most approaches were not valid for solid particles in contact with one another. A more realistic model was developed decades ago (Wyllie et al., 1955; Mahmoud et al., 2006). It relies upon the 'porous-plug' model described below. The electrical current is considered to pass through three different paths within the bed: (i) through alternating layers of particles and interstitial solution, (ii) through particles in contact with each another, and in the channel of the liquid phase (iii). In most cases, process (i) predominates, however contribution of (ii) is significant for low-conducting liquids. If the conductivity of the liquid is considerably higher than that of the particles, the third mechanism becomes the most important. The principle can be depicted in terms of electrical resistances in parallel, as shown in Figure 4, each of them corresponding to one conduction process.

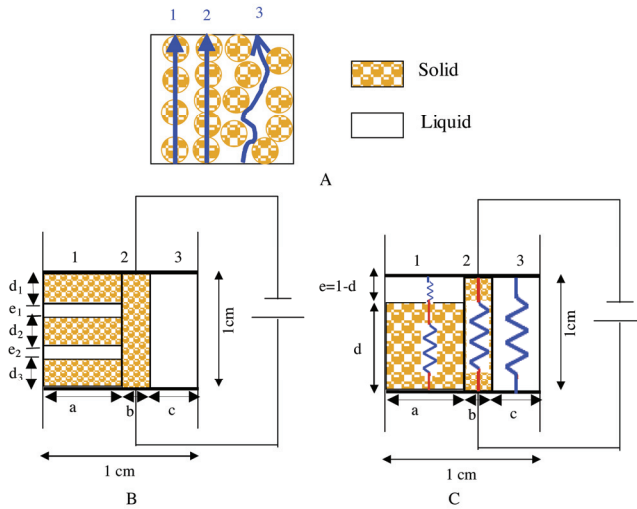


Figure 4. The 'porous-plug' model. A: schematic representation of the three paths for the current. B, simplified model consisting in three conductance elements in parallel. C, extension of the model

From the electrical circuit, the bed conductivity,  $\kappa_b$ , may be written as is the sum of contributions  $\kappa_1$ ,  $\kappa_2$ , and  $\kappa_3$ , of the three conductance elements:

$$\kappa_b = \kappa_1 + \kappa_2 + \kappa_3 = \frac{a\kappa \bar{\kappa}}{d\kappa + e\bar{\kappa}} + b\bar{\kappa} + c\kappa \tag{11}$$

where the parameters  $a$ ,  $b$  and  $c$  are the fractional cross-section equivalents of the three elements:

$$a + b + c = 1 \tag{12}$$

The  $(d\kappa + e\bar{\kappa})$  term in Equation (11) expresses the contribution of the liquid, with weight  $d$ , and of the solid, weight  $e$  in the first conduction process. Parameters  $d$  and  $e$  obey the relation:

$$d + e = 1 \quad (13)$$

For a porous medium, the parameters of the model must be estimated to predict the electrochemical properties of the dispersed phase.

## 7. Experimental set-up and ERT system

### 7.1 Experimental set-up

At laboratory scale, the TAMD device, schematically represented in Figure 5, consists of a filtration/compression cell inserted in a CARVER® hydraulic press (not represented in Fig. 5), which has a maximum pressing capacity of 148 bars. The compressive piston (external diameter  $\Phi$  150 mm) is made of copper and is heated by three thermal resistances, which can supply up to 350 W each. A Teflon™ cylindrical vessel, ensuring both electric and thermal insulation, with a stainless steel external jacket, which ensures the mechanical resistance of the unit, is intended to receive the product to be treated. A microfibers glass filter (Whatman®) deposited on a Teflon™ grid is used as filter media. The filtration/compression cell is specifically instrumented:

- Three thermocouples inserted into the copper piston. The heat flux transferred from the piston to the product can be estimated by solving the inverse conduction problem in the piston wall, knowing the copper temperature at various positions from the front side of the piston.
- Thermocouples arranged at various heights on the cell wall measure the product temperatures at the cake periphery;
- A movement sensor gives the thickness of the cake as a function of time;
- Scale measure the mass of solvent separated.

### 7.2 ERT system

The TAMD device is connected to a typical electrical resistance tomography ERT system. It is composed of several elements linked together:

- Sensing electrode array: cylindrical electrodes were designed with a size of 20 x 2 mm and were regularly distributed on the periphery of the cell, following literature recommendation (see Section 4). Copper was selected as the material of construction of the electrodes. Given the complexity of the electrode construction, only 5 planes of sensors were implemented. Each plane consisted of 4 copper electrodes located equidistantly around the cell, as shown in Figure 5;
- Current/voltage generator: for an ERT current/voltage generator, the amplitude stability and high output resistance are the most important aspect of the design (Blad et al., 1994). In this study an EX354D generator was used. It injects current at a range of 0-4 A and measures voltage in the range of 0-35 V;
- Multiplexer: in order to acquire data, it is necessary to connect elements from the electrode array to the measuring instrument in a specified sequence. Multiplexing strategies are generally a compromise between hardware complexity and flexibility in the measuring sequences. The multiplexers used in an ERT system must exhibit a

number of properties: such as low on-resistance, fast switching speed, low inter-switch cross talk, low cost, high reliability and low power consumption. However, because acquisition time is the critical factor in TAMD-process, the relatively low switching speeds of the reeds (typically tens of milliseconds) combined with their cost and reliability preclude their use. Consequently, Agilent 34970A 16-channel multiplexers were selected. They have the following properties: 50  $\Omega$  on-resistance, 600 ms on-off transition time and 30 mA continuous switched current,

- Data acquisition system (DAS), a variety of injection strategies can be used to carry out electrical conductivity measurement and export data to a reconstruction algorithm. The enhanced data acquisition system working in an opposite measurement strategy (see Section 3.2). As the name implies, current,  $I$ , is injected through diametrically opposing electrodes. The resulting potential differences,  $V$ , are measured on adjacent electrodes that are not used for current injection. Other specifications of the DAS are: current range 0-25 mA; frequency 9600 Hz; voltage range 0-5 V; frame speed could be increased up to 1000 ms. The measurement time is governed by the number of electrodes, the measurement strategy, current injection pattern, frequency of applied current, target accuracy for concentration measurements. This measurement time must be chosen according to whether steady or transient states are to be observed. Usually, when the time of measurement is required to be small, the time between two measurements must also be small; hence, the quantity of data to be reconstructed increases.

Here the switching time of the relays is 100 ms, 450 ms for permutations in a plane and 1000 ms for passage from one plane to another. Therefore, the total time needed to acquire five planes frame data is 5200 ms.

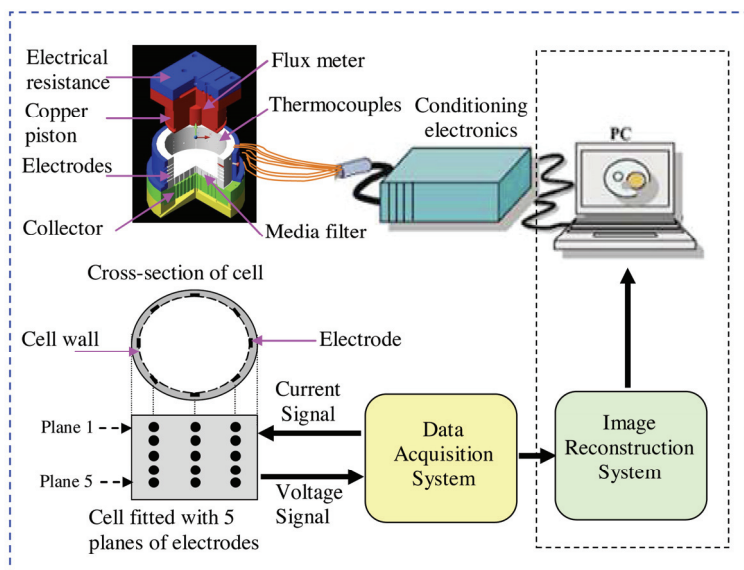


Figure 5. Schematic diagram of the measurement principle of ERT system

### 7.3 Materials used

Five models of synthetic mineral and organic aqueous suspensions with particle sizes ranging from 11 to 60  $\mu\text{m}$  were used for this study: (talc, kaolin, cellulose105, cellulose101, and microcrystalline cellulose (MMC)). The particle size distribution of these materials was determined using laser diffraction spectrometry (Malvern Master Sizer MS20). Then saturated synthetic suspensions of each material type were made up with a conducting continuous phase, such as diluted potassium chloride solutions.

## 8. Measurement of the electrical conductivity in laboratory cell

### 8.1 Experimental set-up

Conductivity measurements were carried out in a cubic lab cell 2 cm in dimensions. Flat platinum electrodes were fixed at two opposite inner walls of the cell. The electrodes were connected to an Autolab PGSTAT 20 potentiostat with a sine function generator. The cell was first filled with the liquid phase using a polyethylene syringe and the electrochemical impedance was measured at zero cell voltage. The voltage amplitude was 5 mV and the frequency of the signal varied from 30 kHz to 30 Hz, with ten points per decade. The amount of liquid introduced was determined accurately, taking into account the meniscus of the G/L interface, corresponding to an excess of liquid. The error involved in filling the cell was estimated at approx. 2% in the 8 cm<sup>3</sup> cell volume. After measurement of the liquid conductivity, the solid was introduced in the cell, and the bed was compacted by vibrating the cell; the excess liquid was removed using a syringe. Compact beds were obtained after the top shiny surface of the liquid over the packed bed disappeared and was replaced by the granular, irregular surface of the packed bed, uncovered by the liquid. Impedance spectra were then recorded. The formerly used solution was thereafter diluted with pure water by 20-30% and the solids were rinsed in the obtained liquid. The experimental procedure of successive measurements with the liquid, then with particles bed, was repeated. Solutions were progressively diluted until their conductivity was of the order of 10<sup>-4</sup> S cm<sup>-1</sup>.

The intercept of the impedance spectrum recorded at rest potential with the real axis led to the ohmic resistance,  $R$ , and the conductivity of the medium,  $K$ , was deduced using the relation:

$$\kappa = \frac{1}{R} \frac{l}{S} \quad (14)$$

where  $l$  is the electrode gap (2 cm), and  $S$  the electrode area (2x2 cm<sup>2</sup>). Nevertheless after calibration, the  $l/S$  ratio was taken at 0.52 cm<sup>-1</sup>.

Besides, former experiments conducted with packed beds of inert materials with conducting solutions allowed estimation of parameter  $c$  (see Section 6). Numerous measurements conducted with the softest model materials led to  $c=0.33$ . This value agrees well with the value obtained by Martin et al. from modelling of heat transfer in packed beds (Raghavan & Martin, 1995), with a liquid void fraction of 40%. Then, for these model materials, only two independent parameters had to be determined amongst the series a - e.

### 8.2 Experimental results

Figure 6 shows the conductivity of the different packed beds versus the conductivity of the interstitial solution. The variation depends on the concentration of electrolyte solution and

the material grade, as expected. At zero liquid phase conductivity, the current takes its way exclusively through particles which are in contact with on another (the second conductance element (ii)). Even when particle contribution to bed conductivity is very small (because of the small contact area of the particles), the bed conductivity at these conditions can not be equal to zero. The bed conductivity in dilute solutions increases rapidly and is far below than that of the liquid: ions are mainly transferred by the liquid phase. The difference between  $\kappa_b$  and  $\kappa$  decreases for higher concentrations of electrolyte, as shown in Figure 6, and the contribution of the liquid phase in the ion transport becomes more significant. At the 'equiconductance' point ( $\kappa_b = \kappa = \kappa_c$ ), the bed conductivity is equal to the solution conductivity. This point represents also the conductivity of the corresponding model material.

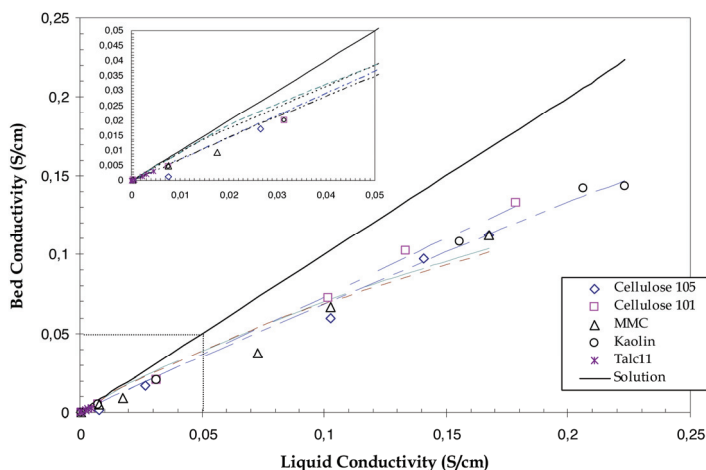


Figure 6. Variation of the bed conductivity with the solution conductivity. Dotted lines are for theoretical results

### 8.3 Modelling of conductivities by the porous-plug model

Fitting of the experimental curves to the model gave access to the values of the parameters involved in the 'porous-plug' model. Agreement between experimental data and theoretical variations was generally good, as shown in Figure 6. The 'equiconductance' point, as explained in the previously paragraphs, represents the conductivity of the corresponding model material bed and the values obtained are given in Table 2. This Table shows good agreement between the theoretical predictions of  $\kappa$  and the experimental values. Figure 7 schematically illustrates the ion flux within the backed beds, both horizontally and vertically, following the electrical circuit shown in Figure 4. In Figure 7, the current flows in the vertical direction. Gray-filled blocks represent the solid phase contribution whereas white blocks correspond to the solution phase. From the left, they illustrate transport through both the solution in contact to the solid phase, the solid phase, and the solution phase, respectively. For all model materials, the current is mainly transported through the alternating layers of particles and solution. Therefore, the model materials used in this study are less conductive than the solution to be treated, as expected. Although the 'porous-plug'



model illustrates the pattern of the ionic flux, the conductivity of the backed bed is an important operating variable for the sake of maximum ion flux.

The conductivity parameters were used to predict the conductivity of model material beds impregnated with a 1 M potassium chloride solutions. Conductivity of the solution was  $0.112 \text{ S cm}^{-1}$ .

Material	Diameter ( $\mu\text{m}$ )	Theoretical electrical conductivity $10^5 \text{ (S/cm)}$	Experimental electrical conductivity $10^5 \text{ (S/cm)}$
Cellulose 105	20	0.72	0.77
Cellulose 101	60	5.65	6.05
Microcrystalline cellulose (MMC)	40	0.62	0.68
Kaolin	6	2.10	2.17
Talc	11	0.47	0.45

Table 2. Experimental and theoretical conductivities of the solid particles

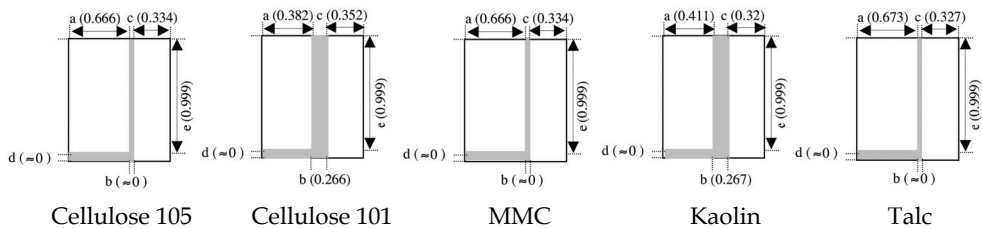


Figure 7. Representation of the ratio between the solid and solution phases; grey blocks are solid phases and white blocks are solution phases. Current flows vertically in the representation

### 9. Estimation of the bed conductivity from TAMD cell

As indicated before, bed conductivity will be a function of product nature, liquid composition, temperature and specific conductivity of the solid fraction in the cell. Ideally, the full three-dimensional problem would be solved; even when, this problem is complex. Due to the experimental limitations and computational facilities, in this work, only the calculation from the primary distribution of potential and current density was made with the following assumptions:

- 2-D analysis has been carried out;
- liquid void fraction was fixed at 40%;
- initial stage was first considered (at  $t = 0$ );
- at room temperature;

- uniform composition of the conductivity;
- absence of concentration gradients.

Fortunately, the conductivity of the suspension varies slowly in the axial direction, which allows significant simplifications to the forward problem.

At low frequency electrical current, the material in the imaging area follows Ohm's law Equation (1). Boundary conditions are modelled as follows:

$$V_{anode} = V_{cell}, V_{cathode} = 0 \quad (15)$$

$$\kappa_b \cdot \frac{\partial V}{\partial n} = 0 \quad \text{on the inert walls} \quad (16)$$

where  $V$  is the electrical potential,  $n$  is the unit normal vector and  $V_{cell}$  is the electrical potential considered for the primary distribution. This problem can be solved analytically only for a few configurations.

The geometry of our system requires a numerical method. Different numerical methods can be used in complex geometries such as the finite difference method (FDM), boundary element method (BEM), and finite element method (FEM).

### 9.1 Iterative calculation of the bed conductivity

In the present study, the Conductive Media DC application mode from Femlab™ software was used to determine the electrical potential field in TAMD cell (see Figure 8). The forward problem is computed on a FEM grid consisting of 12512 triangular elements as shown in Figure 8a.

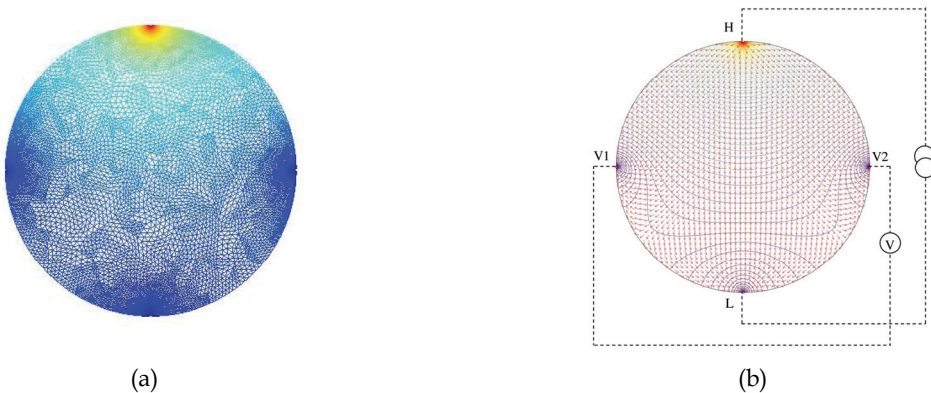


Figure 8. (a) Finite element grid used for the forward problem. The grid consists of 12512 triangular elements, (b) Talc's distribution of the potential and current lines. ( $V_{cell} = 1.7 \text{ V}$ ,  $I = 0.0017 \text{ A}$ )

For an applied current,  $I$ , injected through opposing electrodes (H and L) and an electrical potential,  $V_{cell}$ , the current density field is deduced from the electrical potential field using a postulated value for the bed conductivity,  $\kappa_b^{est}$ . Integration of the current along the cathode ( $V = 0$ ) yields close estimates for the cell current value,  $I_{est}$ . A new estimation for the bed

conductivity can then be obtained from the estimated and applied currents,  $I_{est}$  and  $I$  respectively:

$$\kappa_b^{new} = \kappa_b^{est} \frac{I}{I_{est}} \quad (17)$$

Satisfactory convergence is usually obtained after a few iterations, yielding the bed conductivity for the current-voltage couple considered.

### 9.2 Porous-plug model application for bed conductivity

The bed conductivity was calculated using Equation (11), and taking into account both the actual conductivity of the solid and the local variations of  $\kappa$ , as explained below. Beds are assumed to be of uniform composition. With respect to the liquid phase, the packed bed was modelled as a porous-plug flow reactor, with negligible dispersion. The porous-plug flow was approximated by cascade of  $n$  beds of uniform composition, with height  $\Delta x$ , so that  $l_b = n\Delta x$  high of bed. The overall bed was modelled as a circuit of  $n$  electrical resistances in parallel, because of the cross-flow configuration of the system. Therefore:

$$\frac{1}{R_b} = \sum \frac{1}{R_{x,\Delta x}} = \sum \kappa_b(x) \frac{w\Delta x}{d_b} \approx \int_0^{l_b} \kappa_b(x) \frac{w}{d_b} \partial x \quad (18)$$

where  $d_b$  is the width of the bed and  $w$  is the depth of the cell.

The average bed conductivity,  $\kappa_{b,av}$  was defined from overall bed resistances,  $R_b$

$$R_b = \frac{1}{\kappa_{b,av}} \frac{d_b}{wl_b} \quad (19)$$

Leading to:

$$\kappa_{b,av} = \frac{1}{l_b} \int_0^{l_b} \kappa_b(x) \partial x \quad (20)$$

It can be observed that the axial variation of the bed conductivity was not accounted for the calculations of primary distributions, which allow the average conductivity to be estimated.

### 9.3 Comparison of the two approaches

The bed conductivity values determined by both methods are reported in Table 3. Data calculated from the value of the electrical potential and subsequent treatment through calculations of the primary distribution of potential/current density, are in good agreement with the experimental value estimated using porous-plug model.

As a matter of fact, electrochemical cells in which the electrolyte is of uniform composition can be characterized by secondary or primary current distribution, depending on whether or not electrode kinetic effects are significant, respectively. Therefore, the present work concerned with the primary current does not take into account the electrode polarization.

More rigorous calculation to overcome this inherent problem could have been made by

- Considering the secondary potential distribution in the cell. When slow electrode kinetics are taken into account, the electrolytic solution near the electrodes is no longer an equipotential surface, and the result of the calculations is the so-called secondary current distribution. This point requires more thorough investigation;
- Modelling was carried out with a volume fraction of the solid,  $\varepsilon_s$ , fixed at 60%. For a more complete analysis, a sensitivity study of the bed conductivity to the volume fraction of solids must be performed. Then modelling may be done using Equation (4) for a volume fraction of solid varying from 54 to 66%, which corresponds to  $\pm 10\%$  of parameter variations, as usually used. As an example, the influence of these variations on the bed conductivity is shown in Figure 9 for talc suspensions. The computed bed conductivity decreases to 0.029 S cm<sup>-1</sup> for a differential of + 10% from the face value, and increases to 0.041 S cm<sup>-1</sup> for a - 10% variation. The response of the model is linear for a variation of  $\pm 10\%$  of this parameter around the face value. The sensitivity coefficient of the bed conductivity  $\kappa_b$  to the parameter  $\varepsilon_s$  will be written as follows:

$$S\kappa_b = \frac{\partial \kappa_b(\varepsilon_s)}{\partial \varepsilon_s} \quad (21)$$

The reduced sensitivity coefficient of the bed conductivity  $S\kappa_b'$  to a parameter  $\varepsilon_s$  is computed by finite difference as:

$$S\kappa_b' = \varepsilon_s \frac{\kappa_b(\varepsilon_s + \delta\varepsilon_s) - \kappa_b(\varepsilon_s - \delta\varepsilon_s)}{2\delta\varepsilon_s} \quad (22)$$

The use of reduced coefficients, which have the dimension of bed conductivity, allows a direct comparison of the parameters influences. A negative (respectively a positive) value of  $S\kappa_b'$  means that an increase of the volume fraction of solid results in a decrease (respectively an increase) of the bed conductivity.

Material	Numerical electrical conductivity of bed (S/cm)	Experimental electrical conductivity of bed (S/cm)
Cellulose 105	0.056	0.061
Cellulose 101	0.088	0.097
Microcrystalline cellulose (MMC)	0.061	0.067
Kaolin	0.052	0.059
Talc	0.035	0.039

Table 3. Experimental and numerical of the bed conductivity obtained with a liquid void fraction of 40%. ( $V_{cell} = 1.7$  V,  $I = 0.0017$  A)

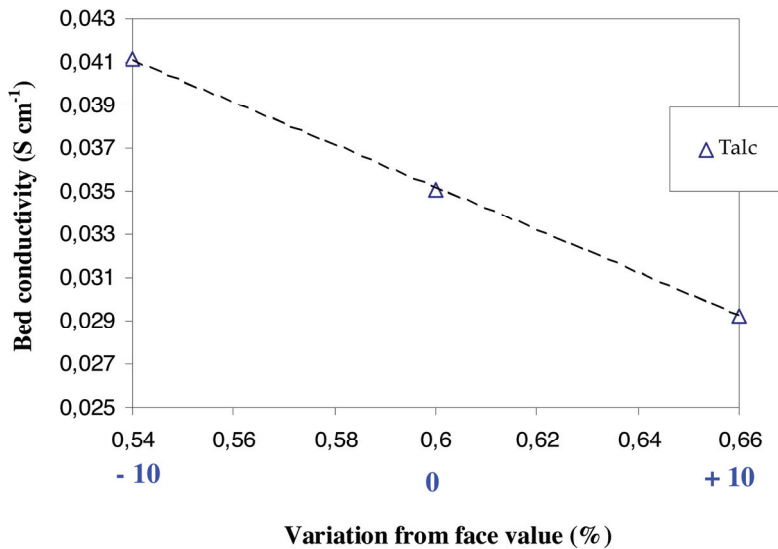


Figure 9. Variation of bed conductivity with the volume fraction of solid variations for talc suspensions and for a face value fixed at 60%

### 10. Conclusion

Electrical resistance tomography is a technique able to identify solid/liquid distribution in packed beds by identification of the bed conductivity and its subsequent modelling as a function of electrical properties of each phase. It can be performed via an array of equispaced electrodes inserted into the periphery of a process cell to map non-intrusively the spatial distribution of electrical current within. The methods of analyzing measured data of ERT system were presented and applied to estimate volume fraction of solids.

The ohmic drop in conducting beds was determined using two techniques. Electrical conductivity of model material in electrolyte solutions was shown to obey the two-phase plug flow model developed decades ago by Wyllie et al. (1954). In particular, for ERT, the solution and the solid-liquid interaction terms prevail, leading to bed conductivity smaller than the electrolyte solution conductivity. Parameters of the model were determined for model material beds, allowing first estimation of the electrical conductivity of the packed beds. Using the voltage of the cell, primary distribution of potential led to a second estimation of the bed conductivity, which was plotted versus the liquid conductivity. Agreement with application of Wyllie's model was good. Future work will focus on the application of the porous-plug flow model to three-dimensional geometry since the link by Wyllie model promise for extending the analysis to more complicated geometries. Furthermore, variations in electrical conductivity need to be link to variations in temperature since it is well known that an increase in temperature leads to a decrease in electrical conductivity.

## 11. References

- Al-Zeibak, S. & Saunders, N. H. (1993). A Feasibility study of in vivo electromagnetic imaging. *Phys. Med. Bio/.*, Vol. 38, No. 1,151-160, ISSN 1361-6560
- Beck, M. S.; Byars, M.; Dyakowski, T.; Waterfall, R.; He, R.; Wang, S. M. & Yang, W. Q. (1997). Principles and industrial applications of electrical capacitance tomography. *Measurement & Control*, Vol. 30,197-200, ISSN 0020-2940
- Blad, B.; Johnnesson, J.; Bachman, B. & Lindsrom, K. (1994). Waveform generator for electrical impedance tomography using linear interpolation with multiplying D/A converters. *Journal of Medical Engineering & Technology*, Vol. 18, No. 5,173-178, ISSN 7776358
- Bond, J.; Cullivanu, J. C; Climpson, N.; Faulkes, I.; Jia, X.; Knstuch, J. A.; Paylon, D.; Wang, M.; Wang, S. J.; West, R. M. & Williams, R. (1999). Industrial Monitoring of Hydrocyclone Operation Using Electrical Resistance Tomography. *Mineral Engineering*, Vol. 12, No. 10,1245-1252, ISNN 0892-6875
- Breckon, W. R. & Picdcok, M. K. (1985). Mathematical aspects of BIT imaging. *Clin. Phys. Physiol. Meas.*, Vol. 8, No. 4, 77-84, ISSN 0143-0815
- Breckon, W. R. & Picdcok, M. K. (1988). Some mathematical aspects of EFT mathematic and computer science in medical imaging, M. A. Viergever and A. E. Todd-Pokropk (Berlin: Springer), PP 351-362
- Brown, B.H.; Seagar, A.D. & Barber, D. C. (1987). Electrical impedance imaging. *IEE Proceedings, Part A: Physical Science, Measurement and Instrumentation, Management and Educati*, Vol. 134, No. 2,201-210, ISNN 0143-702X
- Brown, B. (2001). Medical impedance tomography and process impedance tomography: A brief review. *Measurement Science and Technology*, Vol. 12, No. 8, 991-996, ISSN 0957-0233
- Bruggeman, D.A.G. (1935). Berechnung verschiedener ohysikalischer Konstanten von heterogenen Substanzen. I. Dielectrizitatkonstanten und Leitfähigkeiten der Mischkörper aus isotropen Substanzen. *Ann. Physik Leipzig*, Vol. 24, 636-679, ISSN 0003-3804
- Cho, K.-H.; Kim, S. & Lee, Y.-J. (1999). A fast BIT image reconstruction method for the two-phase flow visualization. *Int. Comm. Heat Mass Transfer*, Vol. 5, No. 26, 637-646, ISSN 0735-1933
- Dickin, F. & Wabg, M. (1996). Electrical resistance tomography for process applications. *Measurement Sciences and Technology*, Vol. 7, No. 3,247-260, ISSN 0957-0233
- Dyakowski, T.; Miko, M.; Vlaev, D.; Mann, R.; Follows, G. W.; Boxman, A. & Wilson, M. P. W. (2000). Imaging nylon polymerisation by applying electrical tomography. *Chemical Engineering Journal*, Vol. 77, No. 1,105-109, ISSN 1385-8947
- Fernandez, A.; Arlabosse, P. & Descoins, N. (2005). Thermally assisted mechanical dewatering: state of the art and new developments. *Chem. Eng. Transactions*, Vol. 7, 737-742, ISBN 88-900775-8-1
- Gamio J. C. (1997). A High-sensitivity Flexible-excitation Electrical Capacitance Tomography System. *PhD Thesis*, University of Manchester Institute of Science and Technology, UK.

- George, D. L.; Torczynski, J. R.; Shollenbeger, K. A.; Cfhen, T. J. & Ceceio, S. L. (2000). Validation of electrical-impedance tomography for measurements of material distribution in tow-phase flows. *International journal of Multiphase Flow*, Vol. 26, No. 4,549-581, ISSN 0301-9322
- Hua, P.; Woo, E. J.; Webster, J. G. & Tompkins, W. J. (1987). Effect of the measurement method on noise handling and image quality of EFT imaging. *Proceedings of the 9<sup>th</sup> annual conference of the IEEE engineering in medicine and biology society*, pp. 1429-1430, Institute of electrical and electronics engineers; Piscataway, N.J. : Order from IEEE Service Center,, New York
- Lucas, G. P.; Cory, J.; Waterfall, R.; Loh, W. W. & Dickin, F. J. (1999). Measurement of the solids volume fraction and velocity distribution in solid-liquid flows using dual-plane electrical resistance tomography. *Flow Meas. Instrum.*, Vol. 10, No. 4, 249-258, ISSN 0955-5986
- Mahmoud, A.; Muhr, L.; Grevillot, G.; Valentin, G. & Lopicque, F. (2006). Ohmic drops in the ion-exchange bed of cationic electrodeionization cells. *Journal of Applied Electrochemistry*, Vol. 3, No. 36,277-285, ISSN 0021-891X
- Maxwell, J.C. (1981). *A Treatise on Electricity and Magnetism*. Clarendon Press, ISBN 0-486-60636-8, Oxford.
- Meredith, R. E., & Tobias, C. W. (1960). Resistance to potential flow through a cubical array of spheres, *Journal of applied Physics*, Vol. 31, No. 7,1270-1273, ISSN 0021-8979
- Neal, G. H. & Nader, W. K. (1974). Prediction of transport process within porous media: diffusion flow processes within an homogeneous swarm of spherical particles, *AIChE Journal*, Vol. 20, No. 3,530-538, ISSN 1547-5905
- Plaskowski, A.; Beck, M. S.; Thorn, R. & Dyakowski, T. (1995). *Imaging Industrial Flows: Applications of Electrical Process Tomography*. Institute of Physics Publishing, ISBN 9780750302968, UK.
- Raghavan, V.R. & Martin, H. (1995). Modelling of two-phase thermal conductivity. *Chemical Engineering and Processing*, Vol. 34,439-446, ISSN 0255-2701
- Rayleigh, L. (1892). On the Influence of Obstacles arranged in Rectangular Order upon the Properties of a Medium. The London, Edinburgh and Dublin Philosophical Magazine and journal of Science, 5th series, Vol. 34,481-502
- Slater, L.; Binley, A.; Versteeg, G.; Cassiani, R.; Birken, R. & Sandberg, S. (2002). A 3D ERT study of solute transport in a large experimental tank. *Journal of Applied Geophysics* Vol. 49, No. 4,211-229, ISSN 0926-9851
- Spiegler, K. S.; Yoest, R. L. & Wyllie, M. R. J. (1956). Electrical potentials across porous plugs and membranes. Ion-exchange resin-solution systems. *Discuss. Faraday Soc.*, Vol. 21,174-185, ISSN 1754-7679
- Turner, J. C. R. (1976). Two-phase conductivity: the electrical conductance of liquid-fluidized beds of spheres. *Chemical Engineering Science*, Vol. 31, No. 6, 487-492, ISSN 0009-2509
- Wang, M.; Dickin, F. J. & Williams, R. A. (1995). The grouped-node technique as means of handling large electrode surfaces in electrical impedance tomography. *Physiological measurement*, Vol. 16, A219-A226, ISSN 0967-3334
- Wang, M.; Donvard, A.; Vlaey, D. & Mann, R. (2000). Measurements of gas-liquid mixing in stirred vessel using electrical resistance tomography (ERT). *Chemical Engineering Journal*, Vol. 77, No. 1, 93-98, ISSN 1385-8947

- Williams, R. A.; Beck, M. S. (1995). *Process Tomography: Principles, Techniques and Applications*, Butterworth-Heinemann, ISBN 0750607440
- Wyllie, M.R.J. & Southwick, P.P. (1954). An experimental investigation of the S.P. and resistivity phenomena in shaly sand. *J. Petroleum Technol.* Vol. 6, 44-57, ISSN 0368-2722
- Wyllie, M.R. J., Sauer, M.C., Southwick, P. F. and Spiegler, K. S (1955). Electrical Conductance of Porous Plugs, Ion Exchange Resin-solution Systems. *Ind. and Eng. Chem.*, Vol. 47,2187, ISSN 0019-7866
- Yang, W. Q. & Peng, L. (2003). Image reconstruction algorithms for electrical capacitance tomography. *Measurement Science and Technology*, Vol. 14, No. 1, R1-R13, ISSN 0957-0233



# Simulation of Plastic Deformation Processes Through a Navier-Stokes Approach

Carlo Mapelli, Cristian Corna and Francesco E. Magni

*Dipartimento di Meccanica - Politecnico di Milano, via La Masa 34, 20156 Milan  
Italy*

## 1. Introduction

The main issue for fulfilling a correct and reliable simulation of a plastic deformation process is the identification of strain, strain rate and stress fields. The definition of these aspects can also permit to state the heat developed by the plastic deformation, which is a ruling factor for the micro-structural evolution of the formed materials. On the other hand, in a lot of plastic deformation technologies, the only physical condition certainly known is the velocity assumed by the material on some boundaries (i.e. inlet and outlet velocity of the material during rolling, extrusion, wiredrawing etc.).

The use of Navier-Stokes' equations can appear unusual in the study of the mechanical behaviour of solid materials, but this is due to the fact that the plastic deformation phenomena are usually treated starting from the dynamic point of view and rarely starting from a kinematic point of view. On the other hand, the plastic deformation is related to the slip on some activated lattice systems, where the resolved shear stress becomes greater than the critical one needed for permitting the slip to take place; the slip velocities are related to the deformation and to its rate (through a time integration). The activation of some systems by the application of a stress field causes the transmission of the forces to the adjacent systems, which can assume a particular movement velocity. The transmission of the motion among the sliding systems is ruled by the viscosity of the transmitting mean (i.e. the bulk plastically deformed material). Actually, on the basis of its physical definition, the viscosity points out the relation between an applied shear stress and the gradient of the velocities transmitted among the layers parallel to the direction of the applied shear stress. So, when a velocity is imposed on a mass of plastically deformed metal, it can be transmitted to the adjacent regions as a function of the particular viscosity of the worked material, in a way mainly dependent on the temperature. Thus the velocity field, which characterizes the plastic deformation of the metal, can be calculated starting from the imposition of the correct kinematic boundary conditions. When the velocities are imposed on the boundary, the viscosity of the metal rules their transmission to the inner volumes of the metals. It is impressive and worth noting the analogy between the well known velocity profile of a liquid flowing on a plane and the morphology of the plastic flow deformation line observed in the immediately sub-surface layers of a metal which underwent a wear process featured by the plastic deformation. The difference in the movement entities between the liquid and the solid case is due to the different order of magnitude of the viscosity interesting the liquid phase and the solid one.

The transmission of the boundary velocities within the material volume can be fully described through the imposition of the correct viscosity and by solving the Navier-Stokes' equations. In this approach, the flow stress becomes important in the determination of the correct viscosity, because it depends on the temperature, which is influenced on its turn by the enthalpy developed by the plastic deformation. This enthalpy is a function of the flow stress of the material during the evolution of the plastic deformation, as will be shown later. The Navier-Stokes' equations have to be coupled with a recrystallization model, which allows the computation of the flow stress which is needed for the determination of a reliable viscosity, fundamental for the followed approach. In the implemented simulation model, an iterative strategy is adopted for coupling the flow analysis of plastic deformation with the thermal analysis. Strain and temperature distribution of the materials mutually affect each other, because the flow stress is temperature-dependent and the plastic work produces the heat which is dissipated by some of the applied deformation works. The stress field is computed by the constitutive equation which relates stresses, temperatures, strains and strain rates. The approach described in this work was first applied to the description of rolling and extrusion and was carefully validated through the comparison with experimental results.

## 2. Theoretical background

A flow model based on the Navier-Stokes' equations is applied to simulate the plastic deformation. Provided a function describing the viscosity of the extruded materials, the applied approach permits to obtain the material velocity field during the hot extrusion on the basis of easily measurable boundary conditions: the die geometry, the piston velocity and the velocity of the extruded material at the die exit. The stress field is computed by the constitutive equation which relates stresses, temperature, strain and strain rate (Tseng & Wang, 1995) (Prasad & Sashidara, 1997). In this study a hyperbolic sinusoidal function was adopted and its parameters were defined by systematic experimental tests. A model based on the Fourier equation in stationary conditions was used for describing the thermal evolution featuring the extruded material. The hot material was assimilated to a material featured by a specific viscosity and in the case of this study the viscosity was set to  $5 \cdot 10^4 \text{ Pa s}$ ; this value was provided by the experimental evidences related to the observation of the plastic flow-stream lines by means of macrographic techniques (Chenot & Wagoner, 1997) (Dixit et al., 1995) (Chin & Steif, 1995). On the basis of these assumptions, the material behaviour was studied by the Navier-Stokes' equations. The use of this method permitted to calculate the velocity field in the material, starting from a little number of experimental data, easily taken from industrial production. In the case of hot extrusion the study can be developed on the basis of the knowledge about the three dimensional geometry of the die, the initial billet temperature (when it enters the press), the initial and final velocities of the material when it enters and goes out the die. Thus the experimental data needed to perform the simulation were constituted by a group of few elements which can be easily determined. The temperature at the entry into the press can be measured by several optical pyrometers. Provided the advancing velocity of the press, the velocity at the exit of the die can be approximated on the basis of the mass conservation rule. The realized model, set the viscosity of the extruded material and starting from the formerly measured data, calculates the velocity field without the need of difficult hypothesis about the friction, because a no-slip condition was imposed on the boundary; the effect of the velocity gradient caused by

friction was included in the study through the viscosity. Then, the velocity field has three components:  $u$  in  $x$ -direction,  $v$  in  $y$ -direction and  $w$  in  $z$ -direction. As previously described, the material must respect three fundamental principles:

1. the mass conservation;
2. the momentum conservation;
3. the energy conservation.

The flow in the die was regarded as steady, three-dimensional and laminar and it was supposed that the density of the metal remained the same during the whole process, whereas the viscosity was considered temperature-dependent and followed an exponential law that was obtained by experimental measurements performed on the materials under analysis. The energy problem was solved separately because the density was supposed temperature-independent, so the final fundamental system of equations results:

$$\left\{ \begin{array}{l} \frac{\partial(\rho u)}{\partial x} + \frac{\partial(\rho v)}{\partial y} + \frac{\partial(\rho w)}{\partial z} = 0 \\ \frac{\partial}{\partial x}(\rho u u - \mu \frac{\partial u}{\partial x}) + \frac{\partial}{\partial y}(\rho v u - \mu \frac{\partial u}{\partial y}) + \frac{\partial}{\partial z}(\rho w u - \mu \frac{\partial u}{\partial z}) = -\frac{\partial p}{\partial x} \\ \frac{\partial}{\partial x}(\rho u v - \mu \frac{\partial v}{\partial x}) + \frac{\partial}{\partial y}(\rho v v - \mu \frac{\partial v}{\partial y}) + \frac{\partial}{\partial z}(\rho w v - \mu \frac{\partial v}{\partial z}) = -\frac{\partial p}{\partial y} - \rho g \\ \frac{\partial}{\partial x}(\rho u w - \mu \frac{\partial w}{\partial x}) + \frac{\partial}{\partial y}(\rho v w - \mu \frac{\partial w}{\partial y}) + \frac{\partial}{\partial z}(\rho w w - \mu \frac{\partial w}{\partial z}) = -\frac{\partial p}{\partial z} \end{array} \right. \quad (1)$$

The velocities on the boundary were imposed on the basis of experimental data. On the first section  $w$  was set to be equal to the advancing velocity of the press while on the last section the speed assumed the value measured at the exit of the die. On the boundary side of each section  $u$ ,  $v$  and  $w$  values were set to zero, imposing a no-slip condition. An iterative procedure was applied until the convergence was reached.

The determination of the velocity field allowed the strain rate  $\dot{\epsilon}_{ij}$  evaluation (Patankar, 1980).

$$\dot{\epsilon} = \frac{1}{2} \left( \frac{\partial v_i}{\partial x_j} + \frac{\partial v_j}{\partial x_i} \right) \quad (2)$$

(where  $x_i$  and  $x_j$  are two directions in the space and  $v_i$  and  $v_j$  are two components of the velocity) from which the effective strain rate  $\dot{\epsilon}$  was calculated:

$$\dot{\epsilon} = \sqrt{\frac{2}{3} \left[ (\dot{\epsilon}_{xx}^2 + \dot{\epsilon}_{yy}^2 + \dot{\epsilon}_{zz}^2) + 2(\dot{\epsilon}_{xy}^2 + \dot{\epsilon}_{yz}^2 + \dot{\epsilon}_{xz}^2) \right]} \quad (3)$$

The components of the effective stress  $\sigma$  (necessary for a correct thermal analysis) have been identified through:

$$\sigma_{ii} = 2\eta \left( \frac{\partial v_i}{\partial x_i} \right) + p \quad (4)$$

$$\sigma_{ij} = \eta \left( \frac{\partial v_i}{\partial x_j} + \frac{\partial v_j}{\partial x_i} \right) \quad (5)$$

but in another approach they can be estimated using a hyperbolic sine constitutive equation suitable for high temperatures:

$$\dot{\epsilon} = A [\sinh(\alpha\sigma)]^n \exp(-Q/RT) \quad (6)$$

where A depends on  $\epsilon$  in a polynomial way. For each studied material, the values of parameters  $\alpha$ , Q and n and the expression of A were determined by averaging the results of different tensile tests.

The material during the process is subjected to three different heat transfer mechanisms: conduction, convection and radiation but conduction is the main heat transfer process in the die. The Fourier equation was expressed taking into account velocities and a source term linked to the plastic deformation of the material (Patankar, 1980)(Mapelli & Venturini, 2004)(Li et al., 2002):

$$q = \beta \cdot \frac{1}{2} \sigma_{ijk} \cdot \dot{\epsilon}_{ijk} \quad (7)$$

The parameter  $\beta$  represents the fraction of plastic deformation power dissipated as heat and has been set to 0.9. The strain rate distribution and the heat power generated by deformation are those obtained by the module previously described. The correct computation of this term was fundamental for the correct comprehension of the microstructural phenomena occurring in the extruded alloy. On the other hand, the thermal situation of the material within the die is related to the balance between the heat development and the heat transmission through the die during the motion of the plate against the billet. Thus, a correct approach needs the performing of a time-variant simulation including the geometry variations in the extrusion system and the related movement of the die, which produces the deformation and the related heat development.

### 3. Significant Application Trials

#### 3.1 Hot Extrusion of Metal Alloys

A three dimensional space was studied considering three Cartesian coordinates: z-axis was in the extrusion direction; x-axis was the horizontal direction perpendicular to z-axis while y-axis was the vertical direction perpendicular to z-axis. Actually the studied geometry (Figure 1, Figure 2) does not permit the simplification through the 2D-axisymmetric simulation, because this could be reliable only in the presence of one central hole of extrusion.

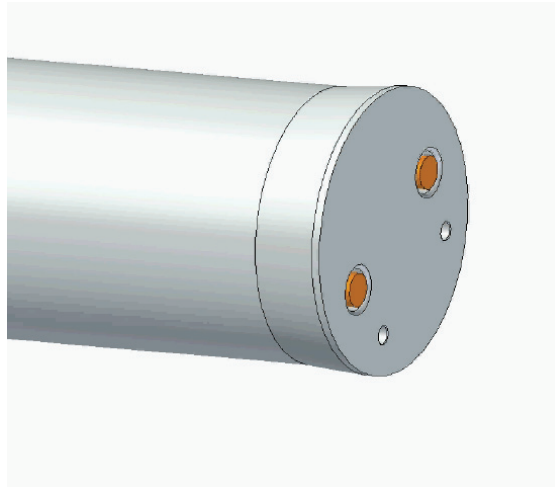


Figure 1. The studied geometry typical of an inverse extrusion

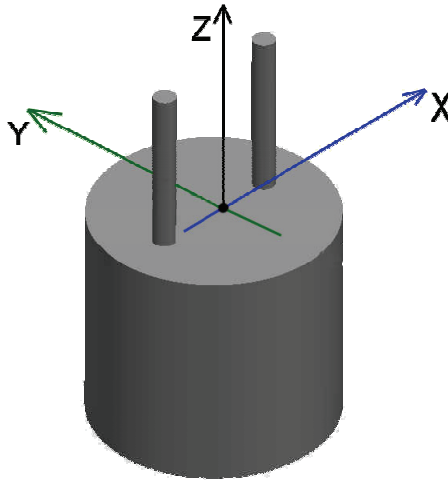


Figure 2. The studied geometry typical of an inverse extrusion and the applied reference system

The simulations were performed setting two different initial thermal conditions (650°C and 750°C) of the brass CW617N. The die movement against the billet (0.15 m/s) was imposed using a module which modifies the geometry of the mesh following the time-variant displacement of the die. Even in this transient condition the model remained very stable, but this was probably due to the fact that working in presence of the high viscosity, typical of the solid material, prevents any turbulent phenomena. The condition of  $p=0$  was imposed on the two exit sections, for leading the material towards the correct position of the die play. The velocity field within the die appears to be extremely plausible (Figure 3, Figure 4, Figure 5).

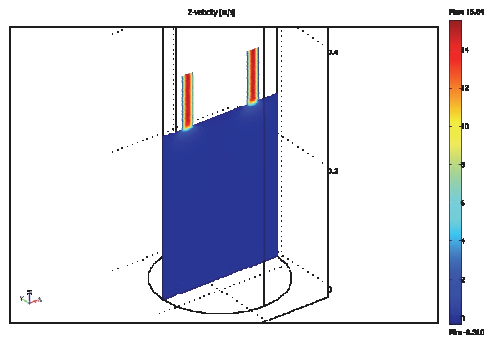


Figure 3. The vertical component of the velocity field developed during the inverse extrusion of the brass billet ,visualized along a plane including the extrusion die

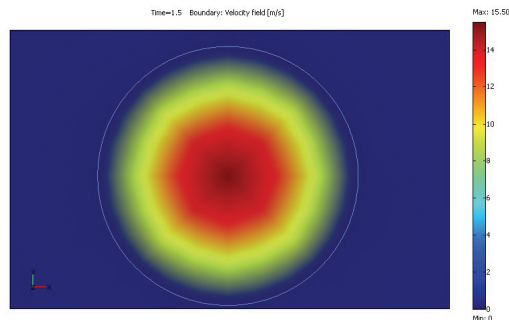


Figure 4. The values assumed by the vertical component of the velocity field developed within the extrusion die during the deformation of the brass billet

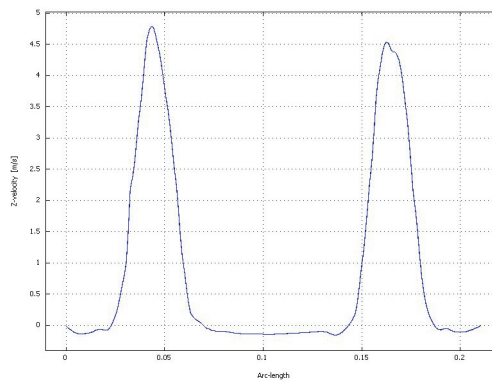


Figure 5. Trend of the vertical component of the velocity field just under the extrusion die holes

The associated stress field is reliable and its computation allowed to perform a correct identification of the thermal source and of the thermal state realized within the extruded brass (Figure 6, Figure 7, Figure 8, Figure 9).

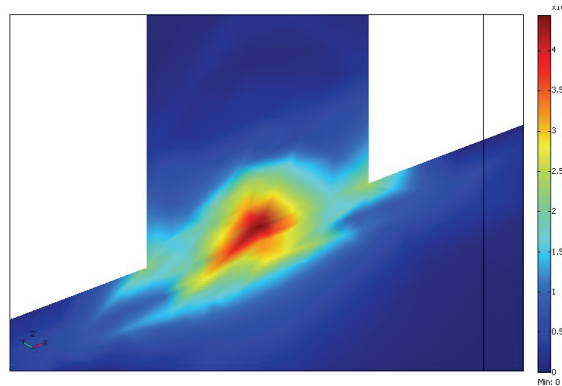


Figure 6. Stress field developed in one hole of the extrusion die

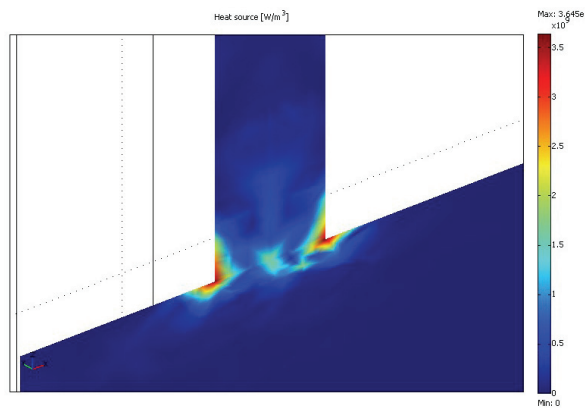


Figure 7. Heat power developed in one hole of the extrusion die

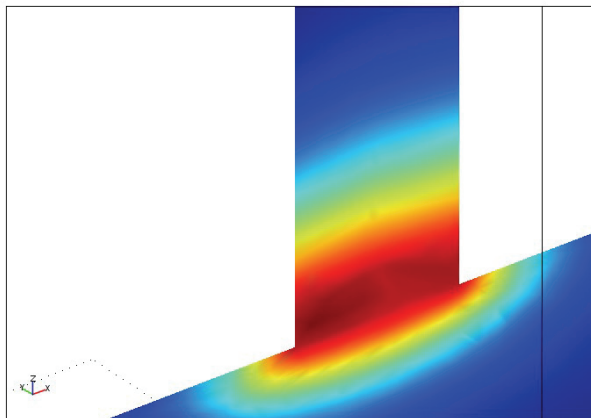


Figure 8. Qualitative image of the thermal state developed in one hole of the extrusion die

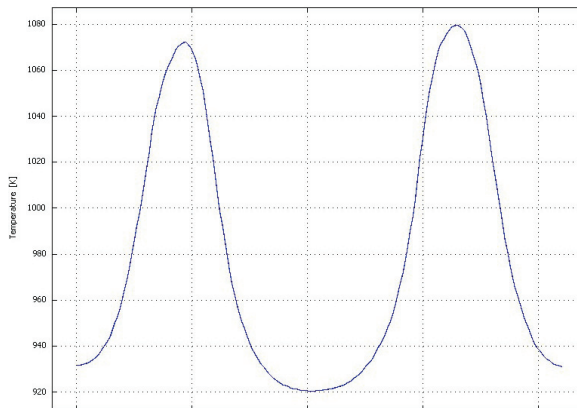


Figure 9. Profile of the temperature developed in the holes of the extrusion die

The validation was performed through the comparison between the hardness experimental data and the computed temperature value (Figure 10). The higher is the imposed thermal state, the lower is the measured final hardness and this is completely consistent with the well known effect of the induced thermal state on the softening phenomena affecting the extruded material.

The effect of temperature trend revealed along the section of the extruded material was also pointed out.

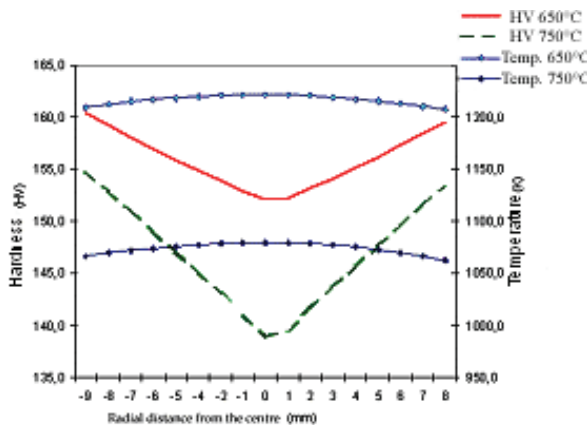


Figure 10. Comparison between the measured hardness profile in the extruded products and the temperature developed in the extrusion die

### 3.2 Steel Rolling

The rolling of metal alloys represents another example of the application of a Navier-Stokes approach for a reliable description of the plastic deformation process on the basis of boundary conditions which can be defined with a good certainty level.

In this case the boundary conditions to be defined are:

- the inlet velocity of the metal alloy between the strand rollers;



- the outlet velocity;
- the working rollers peripheric velocity.

Once the inlet velocity of the forwarding material is known, the outlet velocity can be easily stated through the mass conservation. For instance, in the case of a rectangular section:

$$v_{\text{out}} = \frac{v_{\text{in}} h_{\text{in}}}{h_{\text{out}}} \quad (8)$$

while the velocity of the surface in contact with the working rollers can be stated equal to the roller one. This statement is not precisely correct, because it is well known that the peripheral velocity of the rollers is equal to the one of the rolled products only at the neutral point or in the so called neutral area. This inconsistency can be rapidly overlapped drawing a thin layer of metal over the rolled products and imposing on this side the velocity of the rollers, so on the basis of the imposed viscosity and of the inlet and outlet velocities the system computes the correct velocity profile on the surface of the rolled material.

The computed field of stress, strain and strain rate is completely consistent with the one turned out through other approaches (Figure 11).

Moreover, the advantage of the shown approach consists in the fact that this allows a rapid and reliable simulation of some innovative rolling techniques, like the asymmetric simulation, in which the velocity of the upper and lower rollers are different. In this case the approach based on the Navier-Stokes formulation is suitable without any problem avoiding the imposition of strange and unusual condition on the friction interesting the contact among the rollers and the material going to be thinned. The comparison between the shear stress profile in a traditional rolling operation and the asymmetric one along the middle line between the entry and the exit sections can be clearly pointed out through a very simple change of the peripheral imposed velocity (Figure 12). Thus, also in this innovative and unusual situation, the developed approach seems to show its good performance.

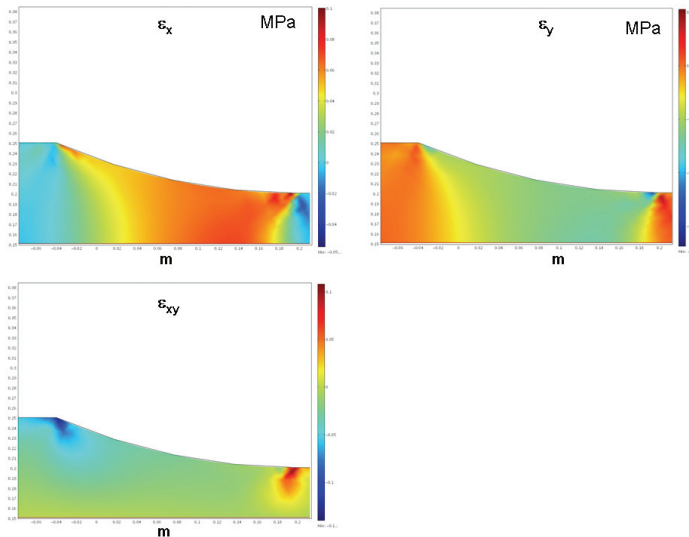


Figure 11. Example of deformation patterns computed for a rolling operation

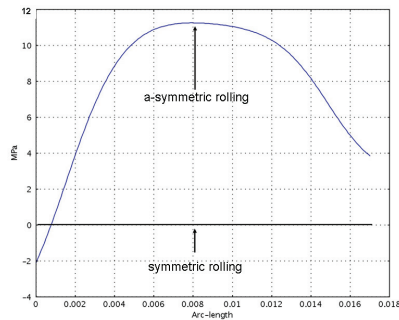


Figure 12. Comparison of the shear stresses revealed at the middle of the thickness of rolled steel in a-symmetric and symmetric rolling conditions

#### 4. Conclusions

The use of the Incompressible Navier-Stokes equations for defining the velocity and the stress fields and the heat power source within the die appears to be an efficient method, also because the high viscosity of the solid material to be deformed avoids the treatment of the turbulent behaviour. The other advantage is represented by the few and easily measurable variables that must be taken into account in order to perform the simulations.

The future development can be focused on the application of the shown approach to more complex geometrical situation.

#### 5. References

- Chenot J.L., Wagoner, R.H. (1997). *Fundamentals of metal forming*, pp.369-371, John Wiley & Sons, ISBN-9780471570042, United Kingdom.
- Chin, R.K.; Steif, P.S. (1995). A computational study of strain inhomogeneity in wire-drawing, *Int.J.Mach.Tools Manufact.*, 35, 8, 1995, pp. 1087-1098, ISSN 0890-6955.
- Dixit, P.M.; Lal, G.K.; Venkata Reddy, N.(1995). Die design for axisymmetric extrusion, *Journal of Materials Processing Technology*, 55, 1995, pp.331-339, ISSN 0924-0136.
- Li, L.X.; Rao, K.P.; Lou, Y.; Peng, D.S. (2002), A study on hot extrusion of Ti-6Al-4V using simulations and experiments, *International Journal of Mechanical Sciences*, 44, 12, 2002, pp. 2415 -2425, ISSN 0020-7403.
- Mapelli, C.; Venturini, R. (2004). Flow, thermal and microstructural analysis during the cast rolling of steel in In-line Strip Production process, *Steel Research Int.*, 75, 4, 2004, pp. 257-266, ISSN 1611-3683.
- Patankar, S.V. (1980). *Numerical heat transfer and fluid flow*, pp1-197, McGraw-Hill, ISBN 0070487405.
- Prasad, Y.V.R.K; Sasidhara, S. (1997). *Hot working guide: a compendium of processing maps*, pp.1-23, ASM international, ISBN-100871705982, Materials Park - Ohio (USA).
- Tseng, A.A.; Wang, S.R. (1995). Macro- and micro-modeling of hot rolling of steel coupled by micro-constitutive relation, *Material & Design*, 16, p. 315-336, ISSN 0261-3069.

# 2D Model of a Floating Body Under Nonlinear Waves

Luca Martinelli<sup>1</sup> and Piero Ruol<sup>2</sup>

<sup>1</sup>University of Bologna, DISTART, <sup>2</sup>University of Padova, IMAGE  
Italy

## 1. Introduction

This study is motivated by the need of optimising generic floating wave energy converters based on the oscillating water column (OWC), principle in the framework of a new FP7 project (CORES) involving DISTART. Similarly IMAGE, that deals since long with floating breakwaters, is planning to further investigate this kind of device. The key aspect of our interest is the OWC dynamic, which affects the efficiency of the energy conversion.

The dynamic response of a floating body is a typical two-way interaction problem: the body dynamics is determined by the wave pressure and the body movements essentially influence the wave and velocity field.

The OWC under exam is moored with piles, so that some of the degrees of freedom of the system are restrained by the anchoring device: only heave and, to some extent, roll, is possible. This simplification of the problem, that in origin has 6 degrees of freedom, allows for the set up of an easier model, which is also appropriate for didactic purposes.

This problem has been solved for instance in connection to floating breakwaters (see McCartney, 1985 for a description of this kind of structure) in a simplified form. Usually waves are assumed to propagate in an inviscid irrotational flow and behave as if having an infinitesimal height, whereas the floating body is assumed as rigid. After being extensively studied in the decade 75-85, mainly in connection with floating breakwater performance, the floating body simulation is now the subject of several new papers (according to the Sirius database, starting in 1965, 50% of journal papers regarding floating breakwater dynamics are written after 2001).

The Authors compared experiments (Ruol and Martinelli, 2007) to simulations based on such simple hypotheses and found significant differences, almost 10%, which are too high for the purpose of optimising OWC devices. It seemed that wave non-linearities were the main cause of such dissimilarities and the need for a further investigation was established.

Aim of this note is to evaluate the floating body dynamics under non-linear waves in 2DV (2 Dimensions, Vertical) conditions. A novel and simple model is set up that considers the exchange of forces between the (rigid) body and a fluid, actually sea water, described by equations able to account for all (wave) non-linearities.

The Navier Stokes (NS) equations are solved in a moving grid through a finite element discretisation by means of the Comsol Multiphysics engine. The modeled equations are

described in detail and are given directly in weak form. Turbulence is not accounted for, since, as we will see, it is an inessential complication for the problems under analysis. The model is described assuming that the reader is familiar with the basics of the finite element method (Hughes, 1987), fluid mechanics (see for instance Kudu and Cohen, 2002), and the related numerical methods (Fletcher, 1988).

## 2. State of the art

Gravity waves are due to the periodic transformation between kinetic and potential energy and therefore they can only propagate in a domain with a free surface.

The treatment of free surface flows is complicated by the feature that the domain of interest has an unknown boundary.

In case of an ideal fluid, the flow is most likely irrotational and the problem is extremely simplified.

Rotational flows are rather complicated to simulate. Difficulties are, on the one hand, common to computations of flows without a free surface as, for instance, the presence of large Reynolds numbers. On the other hand, additional problems exist such as those associated to the presence of beakers, of a free surface that is not univocally related to the horizontal co-ordinate (overturning waves), existence of singularities at the intersection between body and free surface (water tend to penetrate into the body), presence of waves that may overtop the structure, free-surface turbulence, wet and dry conditions. Unfortunately, simulations of the floating body dynamics can potentially arise all these difficulties simultaneously.

### 2.1 Irrotational flow conditions

The easiest possible way to simulate the free surface flow is to follow the Airy theory and apply the linearised dynamic and kinetic boundary conditions on the undeformed configuration, in absence of viscous dissipation (Dean & Dalrymple, 1991). The flow field is evaluated by the radiation diffraction theory in which the velocity potentials are expressed as linear summation of incident, radiated and diffracted waves. Fugazza and Natale (1988) presented a comparison between experiments and a linear model based on this method accounting for energy losses.

In other cases, the boundary conditions are described on the deformed configuration, preserving all non-linearities. Note that the fluid may still be assumed irrotational and incompressible, so that the domain equation is linear, since the presence of 2 coupled non-linear dynamic and kinematic boundary conditions on the free surface introduce the main sources of non-linearities.

The governing equations can be found in Mei (1989).

The solution of the linearised equations is only valid in case of regular waves. The response to random waves is still sometime assessed, ignoring the significant non-linear interactions between frequency components, by combining the structure response to a number of single frequencies.

It is not clear if non-linear interactions can result in a major effect, but it appears that a correct approach for the simulation of the floating body dynamics under random wave conditions should account for non-linearities.

Numerical solutions are based on finite difference, finite element or boundary element methods. The first two methods tackle the field equation directly. The third is based on an integral equation formulation.

Finite difference schemes are not particularly suited in principle, since the free surface boundary does not easily intersect the mesh at grid points that are regularly spaced. In theory several approaches can overcome this inconvenience, like the use of refined grids at the surface, markers (Chan & Hirt, 1974), finite volume method or transformation of variables.

In practice the finite element method can cope much more easily with arbitrary boundary geometry, such as that of a free surface that is described by a moving grid.

The boundary element method appears less intuitive compared to the previous ones. Nevertheless, it has the advantage that the space dimension of the problem is reduced by one. Green functions typically satisfy either the linearised free surface and radiation condition or merely the infinite fluid source condition. The solution to the fully nonlinear potential flow is obtained by applying iteratively the more accurate Green function (the former of the two cited ones) starting from initial state and then tracking the free surface boundary in time.

Analytical solutions of the linearised inviscid flow problem around floating bodies are also available for simple geometries (Drimer et al, 1992), obtained by a partition of the domain in homogeneous sub-regions, where the velocity potential can be expressed in simple forms, and by matching the solutions found for each sub-region.

## 2.2 Rotational flow conditions

In the previous paragraph, we have seen that methods that solve the inviscid flow problem by spatially discretizing the whole domain appear quite inefficient, since they handle a lot of useless data in the interior of the domain, compared to the methods based on the Green function: this depends from the fact that the domain equation is linear.

The rotational case must be handled by the Navier Stokes equations, which, due to the convective terms, are nonlinear. Therefore in this case a volume discretization is required.

In the context of free-surface flows, the numerical methods can be classified into fixed grid, moving grid approaches, meshfree and particle methods.

The famous Marker and Cell or the Volume of Fluid methods are examples of the fixed grid method.

The moving grid approach appears more suited since it can fit the free surface, thus reaching greater accuracy for a given mesh size. One efficient way to move the grid is to prescribe the velocity of the vertices to be exactly the unknown fluid velocity. Alternatively, one may transform the vertical coordinate into a different one, that is the algebraic sum of water depth and wave elevation and re-write the conservation laws in terms of this new coordinate. Or even combine both approaches (Zhou and Stansby, 1998).

Meshfree and particle methods appear also promising (Monaghan, 1994) in case of very large deformations, although still computationally too expensive.

Note that even if several possible approaches to handle the NS equations in presence of a free surface exist, it is a challenging task to actually solve a real problem.

### 3. The adopted model

The vertical body movement is described by a mass-spring equation. The vertical force is derived by integration of the hydrodynamic stress applied to the floating body at each time step. The forces applied by the fluid are modelled by means of the NS equations in a standard Arbitrary Lagrangian Eulerian (ALE) reference system.

The ALE method is a numerical scheme according to which the vertices of the grid may be considered in motion with the fluid (Lagrangian, free of the nasty convective terms), fixed (Eulerian), or move with any arbitrarily assigned law. In practice there is a relation between the domain at time  $t'$  and a reference domain and the conservation laws are written for a reference system moving at the grid speed.

The biggest problem arising from the combination of the a rotational domain equation and the ALE method is that the element tend to become too distort, or even to invert the area (one vertex of the triangle crosses the line connecting the other two) with loss of physical meaning. When waves are propagating, it is a clever idea to limit the grid movements along the vertical direction only, so that the grid can not rotate. For a general situation with a floating body that moves horizontally and rotates, the grid must be allowed to move horizontally at least in proximity of the body itself. This possibility is not contemplated by our example, but we worked with this specific problem: in order to avoid that the grid follows the vortexes and becomes too distorted, it was found quite effective to use elements of lower order for the spatial interpolation of the Laplace equation necessary to describe the grid movements than elements describing velocities. This method worked at least for small movements.

#### 3.1 The body geometry

In order to compare the results with experiments, the dimensions of the floating body under exam is in the same scale of the laboratory model. The structure cross section is rectangular: 0.4 m wide, 0.3 m high, 0.16 m of draught. Mass is 64 kg/m. The buoyancy force can be associated to a vertical spring  $K_v = \rho g \cdot 0.4m = 4 \text{ kN/m}^2$ . Natural period is 1.15 s according to the irrotational flow model (added mass of 61 kg/m).

The body floats in the center of a flume as wide as the structure, 12 m long, with depth held constant and equal to 0.5 m. Actually, the numerical wave flume is quite shorter than in laboratory (33 m), in order to reduce the computational effort.

#### 3.2 The domain equations

The reference system has co-ordinates  $X$  and  $Y$ , whereas the grid points have co-ordinates  $x$  and  $y$ , which are function of the independent variables  $X$ ,  $Y$ , and  $t$ . Fig. 1 shows an example of grid movements.

In the volume  $V$ , which is the water in the wave flume, the following equations must hold:

$$\int_V \left( \frac{\partial^2 x}{\partial X \partial t} \frac{\partial \tilde{x}}{\partial X} + \frac{\partial^2 x}{\partial Y \partial t} \frac{\partial \tilde{x}}{\partial Y} \right) dV + \int_{\partial V} = 0 \quad (1)$$

$$\int_V \left( \frac{\partial^2 y}{\partial X \partial t} \frac{\partial \tilde{y}}{\partial X} + \frac{\partial^2 y}{\partial Y \partial t} \frac{\partial \tilde{y}}{\partial Y} \right) dV + \int_{\partial V} = 0 \quad (2)$$

where the second integral refer to the boundary conditions and is null in presence of zero flux and the tilde refer to the trial functions used to interpolate the variables.

The fluid is described in the  $x$ - $y$  coordinate system by the NS-equations with density  $\rho=1000$  kg/m<sup>3</sup> and kinematic viscosity  $\nu=10^{-6}$  m<sup>2</sup>/s. The domain equation for the grid movement is the Laplacian operator.

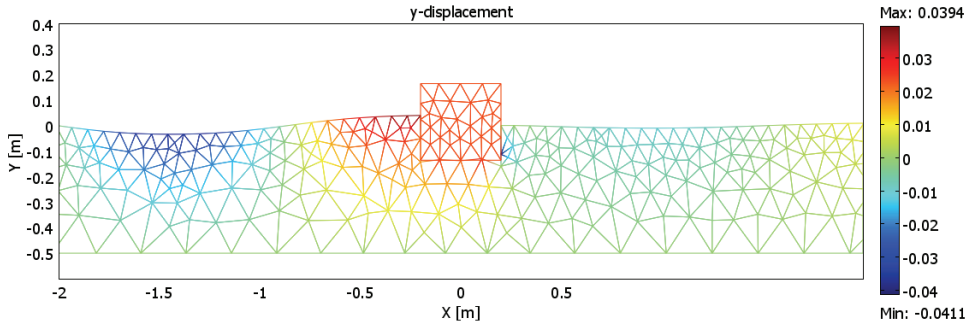


Figure 1. Position of the mesh at  $t=9.7$  s, i.e. when the wave is maximum in front of the floating body. Displacement along the vertical position is emphasized by the color scale

The NS equations are given below in weak form, where only the integrand of the volume integral is given, for simplicity of notation:

$$\left( \frac{\partial u}{\partial x} + \frac{\partial v}{\partial y} \right) \tilde{p} = 0 \quad (3)$$

$$\rho \frac{\partial u}{\partial t} \tilde{u} + \rho \left( u \frac{\partial u}{\partial y} + v \frac{\partial u}{\partial x} \right) \tilde{u} = \left( -2v \frac{\partial u}{\partial x} + p \right) \frac{\partial \tilde{u}}{\partial x} - v \left( \frac{\partial u}{\partial y} + \frac{\partial v}{\partial x} \right) \frac{\partial \tilde{u}}{\partial y} + S_x \quad (4)$$

$$\rho \frac{\partial v}{\partial t} \tilde{v} + \rho \left( u \frac{\partial v}{\partial y} + v \frac{\partial v}{\partial x} \right) \tilde{v} = \left( -2v \frac{\partial v}{\partial y} + p \right) \frac{\partial \tilde{v}}{\partial y} - v \left( \frac{\partial u}{\partial y} + \frac{\partial v}{\partial x} \right) \frac{\partial \tilde{v}}{\partial x} - \rho g \tilde{v} + S_y \quad (5)$$

where  $u$  and  $v$  are horizontal and vertical velocity,  $p$  is pressure,  $S_x$  and  $S_y$  are stability terms, discussed in the following, which do not exist in the NS-equations.

### 3.3 The wave generation problem and the adopted numerical scheme

A regular wave is generated with period 1.1 s and 1.3 s. The wave is generated by a sinusoidal source of mass (this technique is often used in VOF methods) placed 2.5 m away from the floating body. Generation area is 0.1 m by 0.3 m, and distant 0.1 m from the bottom and from the initial still free surface. This method is very efficient since waves reflected by the floating body can pass the generation area without interfering with it.

The reason for generating a regular wave is that comparison with tests and linear model is easier.

The area that generates waves has non-zero divergence. Fig. 2 shows the divergence of the velocity during a randomly chosen instant. It can be noticed that the divergence is almost null in the domain and far from zero in the generation area. In the generation area, eq. 3 is indeed substituted by:

$$\left( F(t) + \frac{\partial u}{\partial x} + \frac{\partial v}{\partial y} \right) \tilde{p} = 0 \quad (6)$$

where  $F(t)$  is the source function with, that assures a wave of height  $H$  (in our case 0.04 m):

$$F(t) = Ka(t) \frac{L}{TD} H \cos\left(\frac{2\pi}{T}t\right) \quad (7)$$

where  $T$  and  $L$  are the wave period (1.1 s and 1.3 s) and length ( $\approx 1.7$  and 2.3 m as found by the dispersion relation with depth of 0.5 m);  $D$  is the height of the generation area (0.3 m);  $K$  is a calibrating constant that assures that the generated wave is actually the desired one,  $a(t)$  is a regular ramp function that is zero at the beginning of the simulation and 1 after the instant  $t_r$  ( $t_r$  is taken numerically equal to  $T$ ) and defined as:

$$a(t) = \begin{cases} 1 & \text{for } (t > t_r) \\ 3\left(\frac{t}{t_r}\right)^2 - 2\left(\frac{t}{t_r}\right)^3 & \text{for } (t \leq t_r) \end{cases} \quad (8)$$

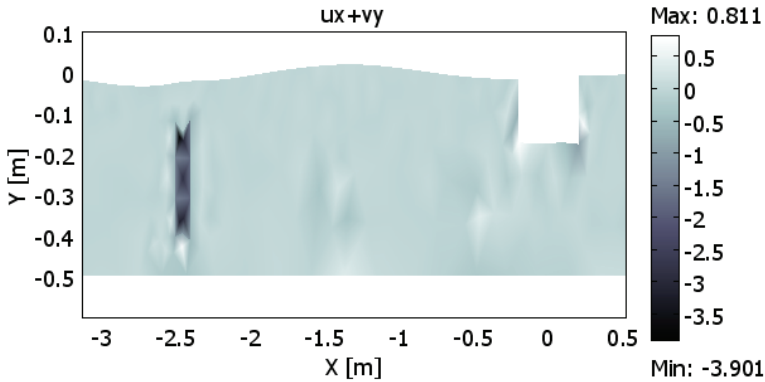


Figure 2. Divergence of the velocity in gray scale.  $t=9.25$

### 3.4 Stabilisation

It is known that if a convective diffusion equation, like Eqs. (4) or (5), is directly discretised, the cell Reynolds number must be lower than 2 in order to avoid instabilities. This constraint would require a mesh size which is not feasible for an engineering approach and numerical schemes must be adopted.

Unfortunately, the most efficient numerical schemes assume implicitly that the field is divergence-free. Both the least square Galerkin and the Petrov-Galerkin pressure stabilisation techniques, would require some significant modifications in order to match with Eq. 6.

For simplicity the isotropic diffusion equation was used, with tuning parameter 0.5, since this technique only affects the diffusive terms in the momentum balance Eqs. (4) and (5). In



short, it adds an artificial diffusion equal to the absolute value of the momentum flux multiplied by  $0.5 h$ , where  $h$  is the size of the mesh element:

$$S_x = -0.5h\sqrt{(\rho u)^2 + (\rho v)^2} + \varepsilon \left( \frac{\partial u}{\partial x} \frac{\partial \tilde{u}}{\partial x} + \frac{\partial u}{\partial y} \frac{\partial \tilde{u}}{\partial y} \right) \tag{9}$$

$$S_y = -0.5h\sqrt{(\rho u)^2 + (\rho v)^2} + \varepsilon \left( \frac{\partial v}{\partial x} \frac{\partial \tilde{v}}{\partial x} + \frac{\partial v}{\partial y} \frac{\partial \tilde{v}}{\partial y} \right) \tag{10}$$

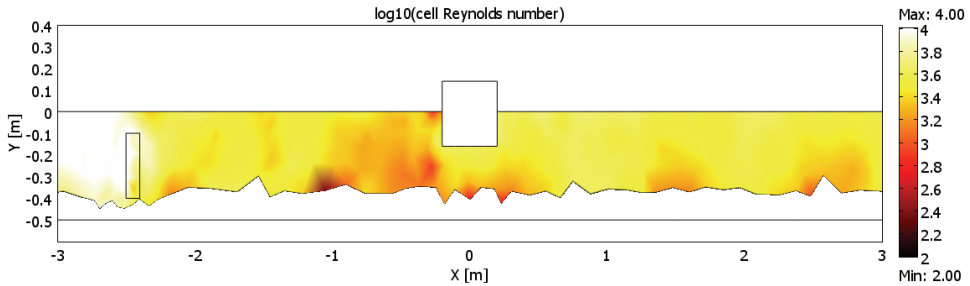


Figure 3. Cell Reynolds number, i.e.  $hu/\nu$ . In order to appreciate its horizontal spatial variation, the logarithm in the range between 2 and 4 is plotted in color scale. At the bottom, velocities are small and the cell Reynolds number is of order 1, and it is not plotted. In the sponge layer i.e. for  $X < -4$  and  $X > 4$ , low cell Reynolds numbers are found due to the increase of viscosity

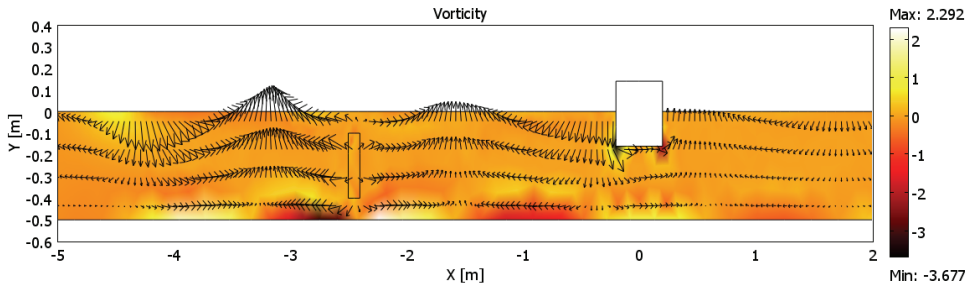


Figure 4. Vorticity in color scale (whose unit measure is in  $s^{-1}$ ) and velocity field through arrows (horizontal and vertical components  $u$  and  $v$  in scale with  $X$  and  $Y$  axis, i.e. a vertical arrow 0.1 m long denotes a vertical velocity of 0.1 m/s)

Of course we accept a significant loss of accuracy due to the introduction of a great artificial viscosity where needed. We have two reasons for doing it: a) we already have the inviscid result and b) by refining the mesh, the artificial viscosity is proportionally reduced and we can appreciate its effects. The effects of mesh refinement will be discussed in Section 5. The simulated cell Reynolds number is presented in Fig. 3. It shows that quite some artificial viscosity was added. Effect of the artificial viscosity is anyway small, as we can see

from the spatial distribution of the vorticity, given in Fig. 4, that is small except at the bottom and at the body corners.

A requirement for stability is also that that higher-order basis functions must be used for the velocities than for the pressure. This condition is known as the Babuska-Brezzi condition. We then used Lagrange quadratic for velocities, Lagrange linear for pressure and grid displacements.

### 3.5 The sponge layers

At the 2 ends of the basin, two sponge layers, 2 m long, are described by means of a gradually increasing viscosity  $\nu_S$ :

$$\nu_S = \nu + 250'000 \nu (X - X_0)^2 \quad (11)$$

where  $X_0$  is the co-ordinate denoting the beginning of the sponge layer.

### 3.6 The rigid body

The vertical oscillations are described by a dynamic equation for the vertical body movements  $\xi$ :

$$F_v - Mg - M\ddot{\xi} = 0 \quad (12)$$

with trivial initial conditions on position and null velocity. Here  $F_v$  is the integral of the vertical force applied at the bottom of the floating body. At each time step,  $F_v$  is evaluated, and Eq. (12) is advanced in time to find the new vertical elevation of the floating body.

## 4. Boundary Conditions

Boundary conditions must be supplied to both set of domain equations: a) the moving mesh (ALE), where typically the vertical and/or the horizontal grid velocity may be constrained, and b) the NS-Equation, where the constraint may interest the horizontal or vertical fluid velocity or the pressure.

A delicate issue is the definition of the boundary condition between water and a wall, when it is not known a priori whether the wall is in dry or in wet conditions. Let us suppose for simplicity that the wall is the vertical side of the container and that it extends from the bottom to a level which is much higher than the free surface (no overtopping is possible). We will also neglect the effect of friction at the wall and consider slip conditions. In this case, we suggest to:

- a. mesh the wall of the container. The wall is now a rectangle, whose width is taken conveniently large. Of the two vertical faces of the wall, one is in contact with water, say the front face, the other is not in contact with water, and is the rear face;
- b. at the rear, top and bottom faces of the wall apply null horizontal and vertical grid velocity;
- c. at the part of the front face that is initially wet, apply null horizontal grid velocity and a vertical grid velocity equal to the velocity of the fluid;
- d. at the part of the front face that is initially dry, constrain only the horizontal grid velocity to be zero.

Should the wall be oblique, the procedure would remain the same but the horizontal direction becomes the direction normal to the wall, and the vertical direction the parallel one.

Where the boundary is certainly wet, like at the bottom, there is no need to model the container and the boundary conditions are those of point (c) above.

At the free surface, grid vertical velocity is constrained to be that of the fluid, with no constraint on the horizontal component. For the fluid, the natural condition is applied (zero flux).

Contact between fluid and floating body. Again, the body is meshed and it is schematised as if it were a little higher than in reality, to avoid possible overtopping and to allow for a greater mobility of the mesh. The parts which can be either wet or dry are constrained exactly as described above, regardless of the body velocity; the parts of the body that are always dry (top) are constrained by setting a vertical grid velocity equal to the value found from Eq. 12, and horizontal grid velocity equal to zero; the parts of the body that are always wet (the bottom) are only are constrained by setting a vertical grid velocity equal to the value found from Eq. 12.

## 5. Results

The target applied wave height is 0.04 m. Fig. 5 and 6 show the surface elevation in presence and in absence of the floating body. The former figure gives therefore the incident wave, which is decreasing along the flume in an unrealistic way, due to the great artificial viscosity. The actual generated wave becomes the target one in  $X=0$ , i.e. where the floating body is placed. The latter figure gives the wave field perturbed by the presence of the body. It can be easily observed that there is a strong reflection in front of the structure, and that the transmission is low.

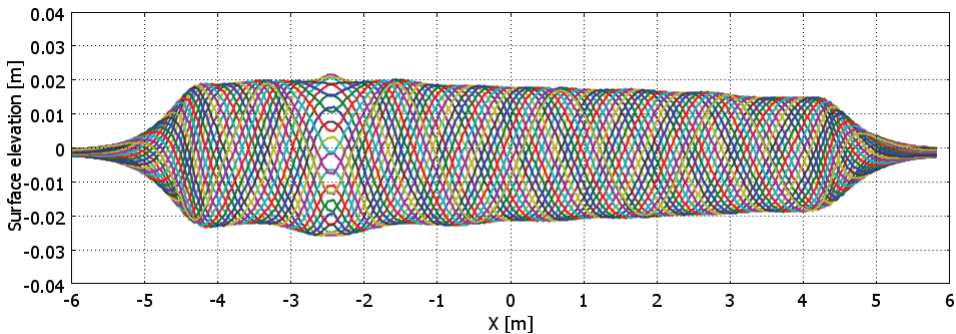


Figure 5. Surface elevation in absence of floating body along the flume. Each line gives the elevation at different instants, spanning a wave cycle (1.3 s) with interval (0.05 s)

In order to verify the validity of the result, the first operation to be done is to refine the mesh. Therefore triangles with horizontal and vertical dimension 3 times smaller were generated and tested. Fig. 7 shows the cell Reynolds number in this case, which is still very high. Anyway, the result of interest is the amplitude of the oscillations of the floating body,  $\xi_{\max}$ .

Fig. 8 gives the computed vertical oscillation  $\xi(t)$  for the two meshes. It is seen that the differences due to an increase of the degrees of freedom of 9 times are small. They both point out a maximum height of the oscillation of 0.045 m.

In the literature, the ratio between  $\xi_{max}$  and  $H$  is termed Response Amplitude Operator (RAO). The RAO for our case is of  $0.045 \text{ m} / 0.04 \text{ m} = 1.1$ , and is relative to a wave period of 1.3 s, for a structure with natural period of 1.15. The computation with a period of 1.1 s, not shown here, gives a RAO of approximately 1.3.

In general, when the wave period is similar to the natural period of oscillation, the body oscillations are much overestimated by the inviscid model. What is the behaviour of our non-linear model?

Tests were carried out by Ruol and Martinelli (2007) with a floating body of geometry similar to the one analysed here, subject to regular and irregular waves, under different kind of mooring system. Results in terms of RAO are presented in non-dimensional form. One of the tests is indeed suitable for a comparison. In that case, the RAO for  $T/T_n=1.15$ , where  $T_n$  is the natural period of the vertical oscillations, was just above 1.0.

Fig. 9 compares the result of a classical linear inviscid model, the results presented here and the experimental result. It can be seen that the non-linear simulation appears much closer to the experiments.

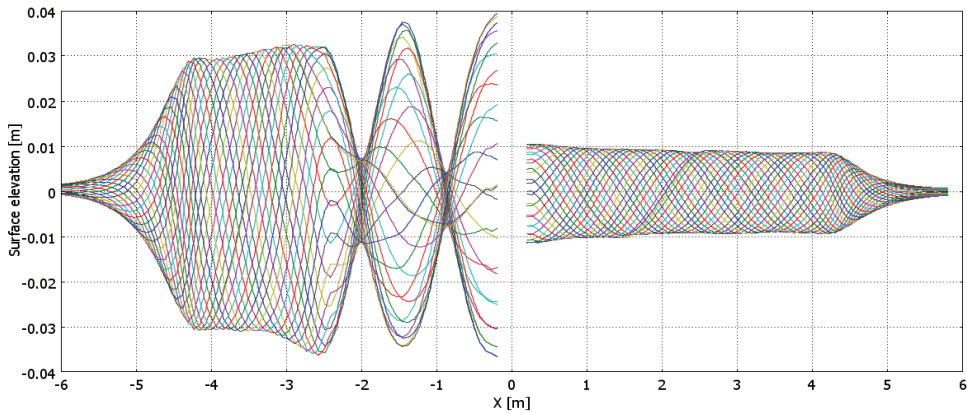


Figure 6. Surface elevation along the flume. Each line gives the elevation at different instants, spanning a wave cycle (1.3 s) with interval (0.05 s). The floating body is placed in  $X=0$ , where the surface elevation is absent

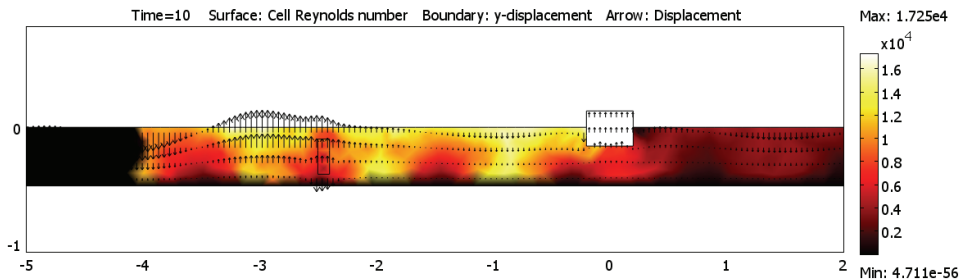


Figure 7. Cell Reynolds number for the refined mesh, and vertical displacements (arrows)

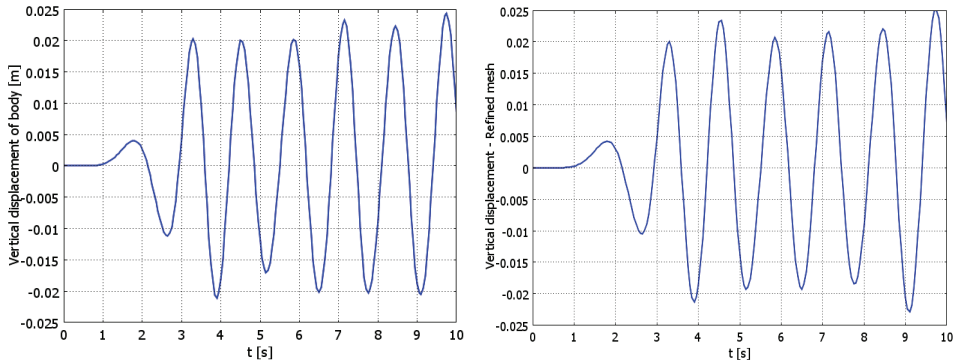


Figure 8. Vertical movements of the floating body along the flume. Left: usual mesh. Right: mesh refined 3 times horizontally and vertically

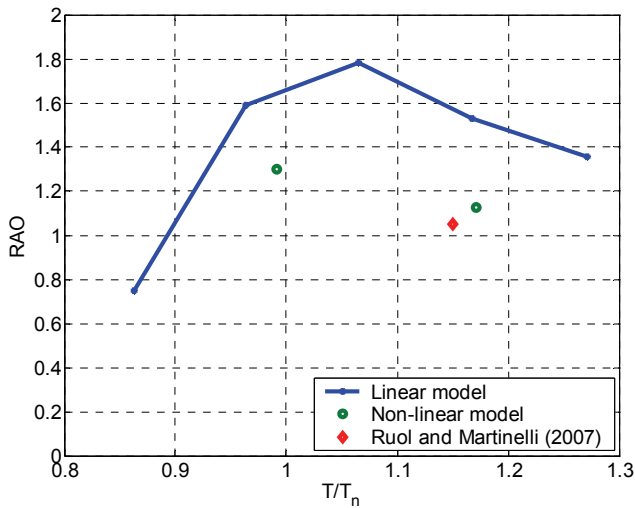


Figure 9. Computed RAOs with the non-linear model presented here and comparisons

### 6. Conclusions

A model describing the dynamics of a floating body by solving the NS-equations in a moving grid framework with free surface is presented.

The model has several interesting features, like the peculiar way of describing: a) the grid movements; b) the slip boundary conditions in presence of a wet and dry interface; c) the generation of waves and, to some extents, the sponge layers.

The investigated feature is the ratio between the oscillation of the floating body and the wave oscillation, which is usually quite overestimated by viscousless models when the load frequency is close to the floating body eigenfrequency. A simulation of this condition with the non-linear model reproduced much more closely the experimental results described in

Ruol and Martinelli (2007) than the corresponding simulation carried out with a classical model based on linear waves and irrotational flow.

## 7. Acknowledgements

The support of DISTART and the fruitful collaboration with its maritime research group, is gratefully acknowledged.

## 8. References

- Chan R.K.C. and Hirt, C.W. (1974). Two dimensional calculations of the motion of floating bodies. *10th Symp. naval Hydrodyn.*, Cambridge, Mas., 667-682.
- Dean R.G., Dalrymple R.A. (1991). Water wave mechanics for engineers and scientists. The Advanced Series on Ocean Engineering. *World scientific*, Vol. 2.
- Drimer N., Agnon Y. and Stiassnie M. (1992). A simplified analytical model for a floating breakwater in water of finite depth. *Applied Ocean Research*, 14, 33-41.
- Fletcher, C.A.J. (1988). Computational techniques for fluid dynamics, *I-Fundamental and general techniques and II-Special techniques for different flow categories*, New York, Springer-Verlag.
- Fugazza, M and Natale L. (1988). Energy losses and floating breakwater response. *Journal of Waterway Port, Coastal and Ocean Eng.*, 114(2), 191-205.
- Hauke G. and Hughes, T.J.R. (1998). A comparative study of different sets of variables for solving compressible and incompressible flows, *Computer Methods in Applied Mechanics and Engineering*, 153, 1-44.
- Hughes, T.J.R. (1987). The finite element method, *Linear static and dynamic finite element analysis*, Englewood Cliffs, Prentice-Hall.
- McCartney B. (1985). Floating Breakwater Design. *Journal of Waterway Port, Coastal and Ocean Eng.* 111(2), 304-318.
- Monaghan, L. (1994). Simulating free surface flows with SPH. *Journal of Computational Physics*, 110, 399- 406.
- Mei C.C. (1989). The applied dynamics of ocean surface waves. The Advanced Series on Ocean Engineering. *World scientific*, Vol. 1.
- Kundu K. and Cohen M. (2002). *Fluid mechanics*, New York, Academic Press.
- Ruol P. and Martinelli L. (2007). Wave flume investigation on different mooring systems for floating breakwaters. *Coastal Structures 07*, Venice, Italy, in print.
- Zhou J. G. and P. K. Stansby (1998). An arbitrary Lagrangian-Eulerian s (ALES) model with non-hydrostatic pressure for shallow water flows. *Computer Methods in Applied Mechanics and Engineering*, 178 (1-2), 199-214.

# Modelling of Magnetosensitive Elastomers

Bohdana Marvalova  
*Technical University of Liberec*  
*Czech Republic*

## 1. Introduction

Magnetorheological elastomers (MREs), also referred to as magnetosensitive (MS) elastomers, are smart materials composed of micron-sized ferrous particles dispersed in a polymer matrix. Commonly, magnetic fields are applied to the polymer composite during cross-linking so that chainlike columnar particle structures can be formed and fixed in the matrix after curing. The unique characteristic of MRE is that its shear modulus can be continuously controlled by the external magnetic field (Gong et al., 2005). Shearing of the cured composite in the presence of the magnetic field causes particle displacement from their low energy state, thereby requiring additional work. This work rises monotonically with applied magnetic field, thus resulting in a field dependent shear modulus. It has been reported (Jolly and all., 1996) that the maximum increase in the shear modulus due to the MR effect is about 50–60% of the zero-field modulus, depending on the matrix elastomer. For hard elastomers like natural rubber the relative increase has typically been 30–40%. The field-induced modulus increase is substantial even at kilohertz mechanical frequencies (Ginder et al., 2002). Such properties make MREs promising in many applications in automotive industry as variable stiffness suspension systems and active damping components (Carlson & Jolly, 2000, Lerner & Cunefare, 2007, Kalio et al., 2007, Deng & Gong, 2007).

To provide basic guidelines for designing and optimization of MR devices it is necessary to simulate the static and dynamic behaviour of magnetosensitive materials submitted simultaneously to the action of the mechanical loading and magnetic field. Modern design practices in the rubber industry are largely based on finite element simulations and the accuracy of these analyses relies on the ability of the used constitutive model to predict the mechanical response of the MS material.

Nowadays the so-called magnetoelastic coupling is widely used for simulations of the reciprocal effect between the magnetic and the elastic field. In particular, the linear elastic behaviour is usually considered along with the linear or non linear magnetic properties. Most of the simulations are based on very simple linear magnetoelastic models defined by using the magnetic forces as loads. In these weak-coupling models the magnetic equations and the mechanical equations are solved separately. More accurate linear elastic models, based on the strong coupling, solve simultaneously the governing equations of the problem (Belahcen, 2004, Hasebe et al., 2007, Zhou & Wang, 2006a,b).

However, elastomers exhibit strongly nonlinear elastic behaviour and undergo large deformations. The truthful magnetoelastic models of MS elastomers should incorporate the

nonlinear response at finite strains in order to enable the simulation of basic features and important aspects of the experimentally observed behaviour. The mathematical theory of nonlinear elasticity, the application of this theory to the solution of boundary-value problems and the analysis of the mechanical properties of solid materials capable of large elastic deformations are available in the books by Ogden (1984) and Holzapfel (2000).

A rigorous phenomenological theory of magnetoelastic interaction in elastic solids based on finite strain theory and the classical theory of ferromagnetism was developed by Brown (1966). His concepts of magnetic force and stress were used by Pao and Yeh (1973) who deduced the nonlinear field equations, boundary conditions and constitutive equations for soft ferromagnetic elastic materials and applied them to the magnetoelastic buckling of a plate. The comprehensive review of the basic principles, theories and equations in mechanics and electromagnetism can be found in the paper of Pao (1978) where the corresponding constitutive equations for solids and boundary conditions are discussed as well. Modern consistent electromagnetic theory is presented in the recent book by Kovetz (2000) where the complete set of laws of electromagnetism, mechanics and thermodynamics is treated.

While the theory of magnetoelasticity is well-known and advanced, the theoretical basis of most current research in the field of MS elastomers is very recent. The full system of equations suitable for deformable MS solids in an electro-magnetic field was first considered by Brigadnov and Dorfmann (2003, 2004) who suggested a simple energy function for isotropic MS elastomers and derived the basic system of constitutive relations. The strain tensor and the magnetic induction vector are chosen as the basic variables. They presented also a numerical simulation of the simple shear of an incompressible MS elastomer between two infinite parallel plates subjected to a magnetic field perpendicular to shear direction.

In the recent series of papers of Dorfmann and Ogden (2003-2005) a theory of nonlinear magnetoelasticity for MS elastomers was developed and applied to a number of simple boundary-value problems. Other recent related theoretical works are those by Steigmann (2004, 2007) and Kankanala and Triantafyllidis (2004, 2007). Important guidelines for the experimentalists and for people involved in numerical simulations of MS elastomer response can be found in further papers of Dorfmann et al. (2005) and Bustamante et al. (2006). In the recent paper of Ottenio et al. (2008) the linearized equations governing incremental effects in a magnetoelastic solid subject to finite deformation in the presence of a magnetic field are derived and the tensors of magnetoelastic moduli are defined. These equations are then used to examine the problem of surface stability of a homogeneously pre-strained half-space.

Mentioned papers also contain solutions to representative boundary-value problems for which exact solutions can be found. For the most part such solutions are idealized in the sense that they apply only to bodies of infinite extent in one or more directions so that edge effects are not present. The first numerical simulation of a boundary-value problem involving finite geometry is reported by Bustamante et al. (2007). In their paper the problem of a circular cylindrical tube of finite length that is deformed and then subjected to an axial magnetic field is examined. The magnetic field vector is chosen as the independent magnetic variable in the constitutive law and the resulting boundary-value problem is solved using a finite-difference method.

The purpose of the present paper is to outline a possibility of the magnetoelastic problem implementation in the finite element code Comsol Multiphysics which is suitable for the simulation of coupled-field problems.



We adopt the formulation of Dorfmann and Ogden (2004) as the starting point. The relevant magnetic and mechanical balance equations and boundary conditions are summarized in Sect. 2.

Then, in Sect. 3, the general constitutive equations for magnetoelastic interactions are summarized following Dorfmann and Ogden (2005) for both compressible and incompressible magnetoelastic materials and then specialized for specific application to incompressible, isotropic magnetoelastic materials.

In Sect. 4, we present the simulation of the simple shear of a rectangular block of finite size subjected to a magnetic field, which, in the far field, is uniform and perpendicular to the shear direction. The constitutive equations are based on a modified free-energy function that depends, in addition to the deformation gradient, on the magnetic flux density vector as the independent magnetic variable.

## 2. Governing equations

In this section the equations for nonlinear magnetoelastic deformations, as developed by Dorfmann and Ogden (2003-2005), are summarized. We suppose that a body made of MS elastomer deforms under the common action of mechanical loading and magnetic field. The deformation is characterized by the deformation gradient tensor  $\mathbf{F}$  and the strain tensors  $\mathbf{C}$  or  $\mathbf{b}$ . We describe the magnetic field by the magnetic flux density vector  $\mathbf{B}$ , the magnetic field vector  $\mathbf{H}$  and the magnetization vector  $\mathbf{M}$ .

### 2.1 Basic kinematics of finite deformations

We consider a continuum body with fixed reference configuration  $\mathcal{B}_0$  and reference time  $t=0$ . Then an assumed motion  $\chi$  maps the reference configuration  $\mathcal{B}_0$  to the current configuration  $\mathcal{B}$  at time  $t$ . Hence a point  $\mathbf{X} \in \mathcal{B}_0$  transforms to a point  $\mathbf{x} \in \mathcal{B}$ , where  $\mathbf{X}$  and  $\mathbf{x}$  (with material and spatial coordinates  $X_1, X_2, X_3$  and  $x_1, x_2, x_3$ ) characterize positions of a particle in the reference and current configurations. The deformation gradient tensor  $\mathbf{F}$  and its determinant  $J$  are

$$\mathbf{F} = \text{Grad} \chi, \quad F_{ia} = \frac{\partial x_i}{\partial X_a}, \quad J = \det \mathbf{F} > 0, \quad (1)$$

where Grad is the gradient operation with respect to  $\mathbf{X}$  and the Jacobian of the deformation gradient  $J$  is the volume ratio. If we consider a geometric setting relative to the reference configuration (Lagrangian description) it is appropriate to introduce a strain measure in terms of material coordinates which is the symmetric and positive definite right Cauchy-Green tensor  $\mathbf{C} = \mathbf{F}^T \mathbf{F}$ . The strain measure in terms of spatial coordinates (Eulerian description) is the symmetric and positive definite left Cauchy-Green tensor  $\mathbf{b} = \mathbf{F} \mathbf{F}^T$ .

### 2.2 Basic equations of magnetostatics

When a magnetizable elastic solid is placed in the magnetic field, magnetic moments are induced in the body. The magnetic moment per unit volume of the deformed body is called the magnetization and it is denoted by  $\mathbf{M}$  with units [A/m]. Inside the deformed body, the

magnetic induction vector is  $\mathbf{B}$  with units [T] or [Wb/m<sup>2</sup>]. The induced magnetization is related to  $\mathbf{B}$  by the relation

$$\mathbf{B} = \mu_0(\mathbf{H} + \mathbf{M}), \tag{2}$$

where  $\mathbf{H}$  is the magnetic intensity vector and  $\mu_0=4\pi \cdot 10^{-7}$  [H/m] is the permeability of vacuum. In a vacuum  $\mathbf{M}=\mathbf{0}$  and  $\mathbf{B}=\mu_0\mathbf{H}$ . In a ponderable body, two of these three quantities are related by a constitutive law which depends on the properties of the solid under investigation. For example, once  $\mathbf{M}$  is given in terms of  $\mathbf{B}$  by an appropriate constitutive law Eq. (2) determines  $\mathbf{H}$ .

The  $\mathbf{B}$  field satisfies Gauss' law for magnetism and is solenoidal. The field  $\mathbf{H}$  is governed by Ampère's law. If we suppose the quasistatic deformation, the stationary magnetic field and non-conducting MS elastomeric material, we may omit the induced current effects and the static magnetic field equations thus can be written in the global form

$$\int_{\partial\mathcal{B}} \mathbf{B} \cdot \mathbf{n} ds = 0, \quad \oint_{\mathcal{C}} \mathbf{H} \cdot d\mathbf{x} = 0. \tag{3}$$

After application of the divergence theorem to Eq. (3)<sub>1</sub> and Stokes' theorem to (3)<sub>2</sub> we can deduce the local form

$$\text{div}\mathbf{B} = 0, \quad \text{curl}\mathbf{H} = \mathbf{0}, \tag{4}$$

where div and curl relate to the spatial coordinates. Across a boundary surface of deformed body  $\partial\mathcal{B}$  the boundary conditions for  $\mathbf{B}$  and  $\mathbf{H}$  are

$$\mathbf{n} \cdot [\mathbf{B}^+ - \mathbf{B}^-] = 0, \quad \mathbf{n} \times [\mathbf{H}^+ - \mathbf{H}^-] = \mathbf{0}, \tag{5}$$

where the square brackets indicate a discontinuity across the surface and  $\mathbf{n}$  is the unit normal to the surface, which, at the material boundary, is taken as the outward pointing normal, thus the (-) subscript indicates interior of the body while (+) subscript is used to indicate the surrounding space.

The fields  $\mathbf{B}$  and  $\mathbf{H}$  may be pulled back from  $\mathcal{B}$  to  $\mathcal{B}_0$  to their Lagrangian forms, denoted  $\mathbf{B}_l$  and  $\mathbf{H}_l$  respectively. By using Nanson formula (Ogden, 1984) and relation  $d\mathbf{x}=\mathbf{F}d\mathbf{X}$  in (3) we receive the pull-back of the field variables

$$\mathbf{B}_l = \mathbf{J}\mathbf{F}^{-1}\mathbf{B}, \quad \mathbf{H}_l = \mathbf{F}^T\mathbf{H}. \tag{6}$$

In terms of these quantities the analogues of (4) in Lagrangian coordinates become

$$\text{Div}\mathbf{B}_l = 0, \quad \text{Curl}\mathbf{H}_l = \mathbf{0}. \tag{7}$$

Since  $\mathbf{H}$  and  $\mathbf{M}$  occur as a sum in (2), it is appropriate to define, similarly to (6)<sub>2</sub>, a Lagrangian form of  $\mathbf{M}$ , denoted  $\mathbf{M}_l$ , by  $\mathbf{M}_l = \mathbf{F}^T\mathbf{M}$ . The Lagrangian counterpart of (2) reads

$$\mathbf{J}^{-1}\mathbf{C}\mathbf{B}_l = \mu_0 (\mathbf{H}_l + \mathbf{M}_l), \tag{8}$$

where  $\mathbf{C}$  is the right Cauchy-Green deformation tensor. The boundary conditions (5) can also be expressed in Lagrangian form, namely

$$\mathbf{N} \cdot [\mathbf{B}_l^+ - \mathbf{J}\mathbf{F}^{-1}\mathbf{B}^-] = 0, \quad \mathbf{N} \times [\mathbf{H}_l^+ - \mathbf{F}^T\mathbf{H}^-] = \mathbf{0}, \tag{9}$$

where  $\mathbf{N}$  is the outward unit normal to the surface  $\partial\mathcal{B}_0$  in the reference configuration. Under certain circumstances it can be helpful to formulate the problem in term of the magnetic vector potential  $\mathbf{A}$  that is given by the equality  $\mathbf{B}=\text{curl}\mathbf{A}$  (Perez-Apparicio, 2004) or in term of a scalar magnetic potential function  $\mathbf{H}=-\text{grad}\phi$  (Bustamante, 2007) with appropriate boundary conditions. Such option ensures that the expression (41) or (42) will be fulfilled identically.

## 2.2 Basic equations of mechanics

From the mass balance we have the following relation between the mass density  $\rho_0$  in the material configuration  $\mathcal{B}_0$  and the mass density  $\rho$  in the spatial configuration  $\mathcal{B}$

$$\rho = J^{-1}\rho_0. \quad (10)$$

Cauchy's equations of motion of elastostatics resulting from the basic balance principles of mechanics such as the momentum balance principle and the angular momentum balance principle and Cauchy's stress theorem (Holzapfel, 2000) are

$$\text{div}\boldsymbol{\sigma} + \rho\mathbf{f} = \rho\dot{\mathbf{v}}, \quad \boldsymbol{\sigma} = \boldsymbol{\sigma}^T, \quad \mathbf{t} = \boldsymbol{\sigma} \cdot \mathbf{n}, \quad (11)$$

where  $\boldsymbol{\sigma}$  is the symmetric Cauchy's stress tensor,  $\mathbf{f}$  is the body force per unit mass and  $\mathbf{t}$  represents the Cauchy's traction vector (force per unit surface area).

For the case of continuum magnetoelasticity there are several different ways of defining stresses, tractions and body forces. The influence of the magnetic field on the deforming continuum may be incorporated either through magnetic force per unit volume  $\mathbf{f}_m$

$$\text{div}\boldsymbol{\sigma} + \rho\mathbf{f} + \mathbf{f}_m = \mathbf{0}, \quad (12)$$

or through the total Cauchy stress measure  $\boldsymbol{\tau}$  which is symmetric and includes both mechanical and electromagnetic contributions (Kovetz, 2000)

$$\text{div}\boldsymbol{\tau} + \rho\mathbf{f} = \mathbf{0}. \quad (13)$$

The expressions for the magnetic force and for the total stress tensor depend on the type of the particular constitutive model. Summary of possible forms of constitutive equations, body forces and traction conditions can be found in Kankanala & Triantafyllidis (2004) and in Dorfmann et al. (2005).

At the external boundary of the body the boundary condition for the total stress tensor is

$$\boldsymbol{\tau} \cdot \mathbf{n} = \mathbf{t}, \quad (14)$$

where the traction vector  $\mathbf{t}$  includes applied mechanical tractions and the contribution of Maxwell stress in the surrounding. The Maxwell stress in the absence of material is

$$\boldsymbol{\tau} = \mu_0^{-1} \left[ \mathbf{B} \otimes \mathbf{B} - \frac{1}{2}(\mathbf{B} \cdot \mathbf{B})\mathbf{I} \right], \quad (15)$$

where  $\mathbf{I}$  is the unit second order tensor and  $\otimes$  signifies the tensor product.

### 3. Constitutive equations

Constitutive models for nondissipative MS elastic materials are based on modified free-energy function  $\Omega$  per unit volume (Dorfmann & Ogden, 2004, Bustamante et al., 2006) which depends on a deformation measure in addition to a magnetic field variable. This modified free-energy function incorporates the magnetic energy contribution.

If the deformation gradient tensor  $\mathbf{F}$  and the magnetic induction  $\mathbf{B}_I$  are selected as the basic variables, the free-energy function reads  $\Omega = \Omega(\mathbf{F}, \mathbf{B}_I)$ . The total nominal stress tensor  $\mathbf{T}$  and the magnetic field vector  $\mathbf{H}_I$  in the Lagrangian configuration, the total stress tensor  $\boldsymbol{\tau}$  and the magnetic field  $\mathbf{H}$  in the current configuration are by sequel

$$\mathbf{T} = \frac{\partial \Omega}{\partial \mathbf{F}}, \quad \mathbf{H}_I = \frac{\partial \Omega}{\partial \mathbf{B}_I}, \quad \boldsymbol{\tau} = \mathbf{J}^{-1} \mathbf{F} \frac{\partial \Omega}{\partial \mathbf{F}}, \quad \mathbf{H} = \mathbf{F}^{-T} \frac{\partial \Omega}{\partial \mathbf{B}_I}. \quad (16)$$

Note that nominal stress tensor  $\mathbf{T}$  corresponds to the transpose of first Piola-Kirchhoff stress tensor. Analogical relations in which the independent variable is the magnetic field  $\mathbf{H}_I$  or the magnetization  $\mathbf{M}_I$  are presented by Bustamante et al. (2006).

For a volume preserving (isochoric) deformation we have  $\mathbf{J} = 0$ . It is the internal constraint for so called incompressible material which is a common idealization for rubberlike materials. The constitutive relations for stress in such materials include the Lagrange multiplier  $p$  as in

$$\mathbf{T} = \frac{\partial \Omega}{\partial \mathbf{F}} - p \mathbf{F}^{-1}, \quad \boldsymbol{\tau} = \mathbf{F} \frac{\partial \Omega}{\partial \mathbf{F}} - p \mathbf{I}. \quad (17)$$

In order to be objective, the free-energy function is the scalar function of the invariants of an objective strain measure such is the right (or left) Cauchy-Green strain tensor  $\mathbf{C}$  (or  $\mathbf{b}$ ) and its first three invariants. The magnetic field induces a preferred direction in the initially isotropic MS material. The constitutive expressions are similar to those of a transversely isotropic material and depend on the additional invariants involving the vector  $\mathbf{B}_I$

$$\begin{aligned} I_1 &= \text{tr}(\mathbf{C}), \quad I_2 = \frac{1}{2} \left[ (\text{tr}(\mathbf{C}))^2 - \text{tr}(\mathbf{C}^2) \right], \quad I_3 = \det \mathbf{C}, \\ I_4 &= |\mathbf{B}_I|^2, \quad I_5 = (\mathbf{C} \mathbf{B}_I) \cdot \mathbf{B}_I, \quad I_6 = (\mathbf{C}^2 \mathbf{B}_I) \cdot \mathbf{B}_I. \end{aligned} \quad (18)$$

The explicit forms of the total stress tensor  $\boldsymbol{\tau}$  and the magnetic field vector  $\mathbf{H}$  obtained from Eqs (6, 15-17) are

$$\begin{aligned} \boldsymbol{\tau} &= 2\Omega_1 \mathbf{b} + 2\Omega_2 (I_1 \mathbf{b} - \mathbf{b}^2) - p \mathbf{I} + 2\Omega_3 \mathbf{B} \otimes \mathbf{B} + 2\Omega_6 (\mathbf{B} \otimes \mathbf{b} \mathbf{B} + \mathbf{b} \mathbf{B} \otimes \mathbf{B}), \\ \mathbf{H} &= 2(\Omega_4 \mathbf{b}^{-1} \mathbf{B} + \Omega_5 \mathbf{B} + \Omega_6 \mathbf{b} \mathbf{B}), \\ \Omega_i &= \frac{\partial \Omega}{\partial I_i}, \quad \mathbf{b} = \mathbf{F} \mathbf{F}^T. \end{aligned} \quad (19)$$

The constitutive theory developed by Dorfmann, Ogden and coworkers captures the basic features of the MS elastomer magnetoelasticity and constitutes comprehensive guidelines for experimentalists in the design of tests and loading conditions necessary for practical evaluations of the material response. The relatively simple formulation of the constitutive equations is suitable for the implementation into the finite element code.

#### 4. Modelling of magnetoelastic coupling in COMSOL Multiphysics

COMSOL Multiphysics is the interactive software for modelling and solving scientific and engineering problems based on partial differential equations (PDEs). This environment runs finite element analysis together with adaptive meshing and error control using a variety of numerical solvers. COMSOL Multiphysics converts all application mode and PDE mode equation formulations and systems to the weak form before solving them with the finite element method.

The software includes many built-in application modes which can be combined into a single multiphysics model capable of simultaneous solving of the coupled physical problem. The application modes consist of predefined templates and user interfaces already set up with equations and variables for specific areas of physics.

The application mode interfaces consist of dialog boxes for the physics in subdomains and on boundaries, edges, and points along with PDEs. The equation system view provides the possibility to modify the underlying PDEs in the case where a predefined application mode does not exactly match the application. The predefined constitutive relations can be easily modified or replaced as well.

We focused our FE simulation on the simple structure and loading as the highly nonlinear character of the coupled problem impedes so far the modelling of complicated boundary value problems. We present the FE solution of a simple quasistatic boundary value problem representing a feasible experimental set-up as well. We chose a block of MS elastomer in plain strain subjected to the simple shear and to the action of the magnetic field which, due to the chosen magnetic far-field boundary conditions, is homogeneous and perpendicular to the shear direction. We simplify the problem to two-dimensional due to the calculation time requirement however the extend to three dimensions is straightforward.

##### 4.1 Implementation

We use the Structural Mechanics Module in combination with Magnetostatics Application Mode which allow the magnetic field and strain coupling in both directions. With regard to large displacements we adopt Moving Mesh Application Mode for the calculation of magnetic field.

We utilize the free-energy function  $\Omega = \Omega(\mathbf{F}, \mathbf{B}_i)$  which is the combination of Mooney-Rivlin free-energy function for hyperelastic materials implemented in Comsol and two additional terms involving the invariant  $I_4$  and  $I_5$  mentioned in (18)

$$\Omega(\mathbf{F}, \mathbf{B}_i) = \frac{1}{2} \kappa (J - 1)^2 + C_{10} (\bar{I}_1 - 3) + C_{01} (\bar{I}_2 - 3) + \mu_0^{-1} (\alpha I_4 + \beta I_5), \quad (20)$$

where  $\bar{I}_1$  and  $\bar{I}_2$  are the modified invariants (18) and the coefficients  $\alpha$  and  $\beta$  are dimensionless material parameters characterizing the magnetoelastic coupling. Similar function was proposed by Ottenio et al. (2008). From the Eqs (19) we see that the constant  $\alpha$  contained in  $\Omega_4$  does not affect the stress but provides the coupling between the magnetic properties of material and the deformation. On the other hand the stress is influenced by means of the parameter  $\beta$  contained in  $\Omega_5$ . The positive value of  $\beta$  produces the stiffening of material in the direction of magnetic field i.e. a larger stress is required to achieve the given deformation. The parameter  $\beta$  simultaneously furnish the linear term in the constitutive relation (19<sub>2</sub>) of the magnetic field  $\mathbf{H}$ .

Instead of the common approach, using the conjugate pairs second Piola-Kirchhoff stress and Green-Lagrange strain, Comsol uses the first Piola-Kirchhoff stress  $\mathbf{P}$  and its conjugate strain measure the displacement gradient,  $\text{Grad}\mathbf{u}$ . The first Piola-Kirchhoff stress  $\mathbf{P}$  is then calculated as

$$\mathbf{P} = \frac{\partial \Omega}{\partial \text{Grad}\mathbf{u}} \tag{21}$$

and the variation of the corresponding part of the internal energy is

$$\delta W_{\text{int}_e} = \int_{B_0} \mathbf{P} : \text{Grad}\delta\mathbf{u} dV. \tag{22}$$

The Magnetostatics Application Mode uses the magnetic vector potential  $\mathbf{A}$  defined by the relation  $\mathbf{B}=\text{curl}\mathbf{A}$  together with the Coulomb gauge transformation defined by  $\text{div}\mathbf{A}=0$ . The variation of the magnetic part of the internal energy is

$$\delta W_{\text{int}_{mg}} = \int_B \mathbf{H} \cdot \delta \text{curl}\mathbf{A} dv. \tag{23}$$

As we use the moving mesh for the magnetostatics and the magnetic variables are in the spatial configuration, the coupled part of the stress  $2\Omega_5\mathbf{B} \otimes \mathbf{B}$  must be pulled-back into material coordinates as well as the Maxwell stress (14) used for determination of the traction vector at boundaries where the displacements are not prescribed.

**4.2 Example-Simple shear**

In two recent papers (Brigadnov & Dorfmann, 2003; Dorfmann & Brigadnov, 2004) the closed-form solution of the problem of unidirectional shear of an incompressible MS elastomer between two infinite parallel plates subjected to a magnetic field perpendicular to shear direction was presented. We reconsider here this problem but for a finite geometry where the magnetic field is no longer homogeneous. The problem is considered as two-dimensional restricted to x-z plane as illustrated in Fig.1.

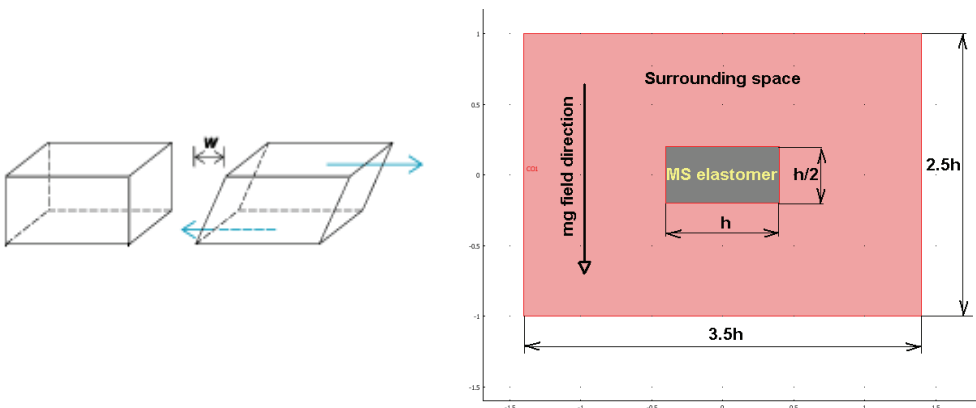


Figure 1. Block of MS elastomer in simple shear and its surrounding in Comsol geometry

The model consists of two parts – of a MS block in plain strain and of the surrounding representing the free space.

The lower face of the MS block is fixed and the upper face is subjected to the prescribed displacement in the x-direction. The lateral faces of the MS elastomeric block are free to move.

The magnetic field in the surrounding depends on the vector potential  $\mathbf{A}$  prescribed to be the linear function of x-coordinate at the external boundaries. The direction of the resulting magnetic field in the surrounding space is then parallel with the y-axis. At the internal boundaries the conditions (5) for  $\mathbf{B}$  and  $\mathbf{H}$  are prescribed.

The moving mesh is used for the calculation of the magnetic field values. The mesh movement inside the internal subdomain and at its boundaries is determined by the displacements of the deformed block. The deformation of the mesh is smoothed in the surrounding domain toward the external boundaries where the mesh is fixed.

The loading proceeds in three stages:

- the upper face of the block is displaced gradually up to the final x-distance  $w=h/8$ , in this stage the magnetic field is inactive
- the block displacement  $w$  is constant and the magnetic field start to act gradually from 0 to its final value
- the magnetic field is constant and the upper face of the block returns gradually to its starting position

The numerical values of the parameters used in the free energy function are  $C_{10}=0.2$  MPa,  $C_{01}=0.2$  MPa,  $\kappa=104$  MPa,  $\alpha=0.5$ ,  $\beta=0.5$ .

### 4.3 Results of the simulation

The shear stress increases with the magnetic field intensity and rearranges simultaneously namely at free boundaries in consequence of the applied traction vector due to Maxwell stress at the surrounding as shown at Fig. 2 and 3.

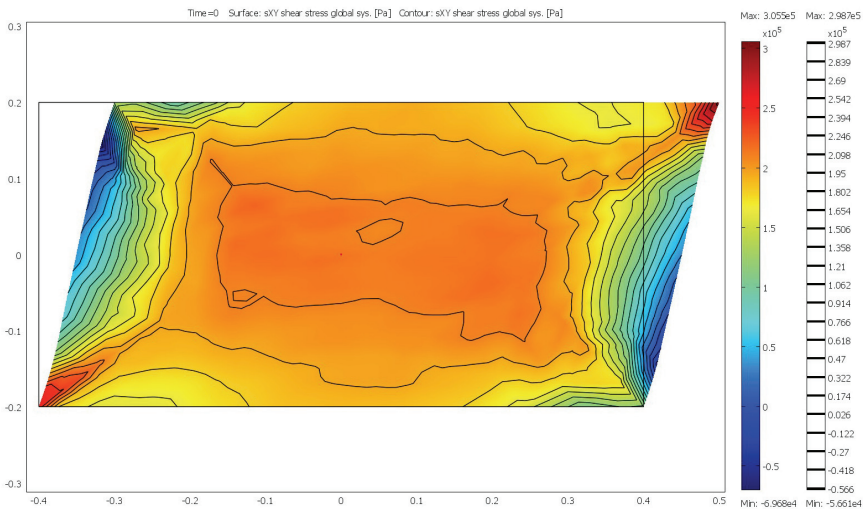


Figure 2. Shear stress  $\sigma_{xy}$  in the deformed block without the magnetic field

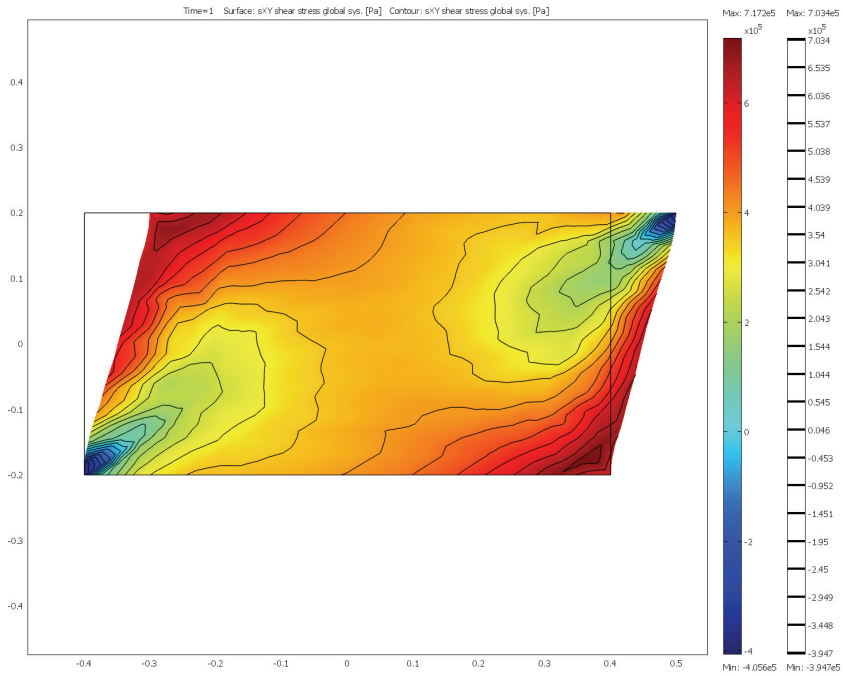


Figure 3. Shear stress  $\sigma_{xy}$  in the deformed block with the magnetic field action

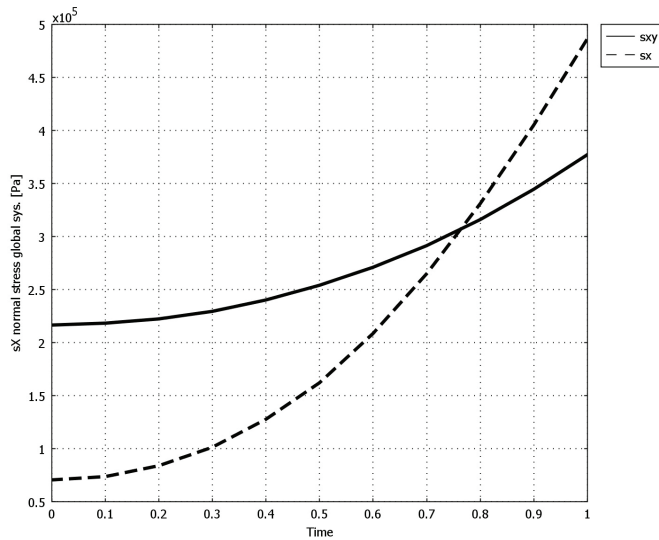


Figure 4. Variation of the shear stress  $\sigma_{xy}$  (solid line) and of normal stress  $\sigma_x$  (dashed) in the center of the block - constant deformation of the block, growing intensity of the magnetic field



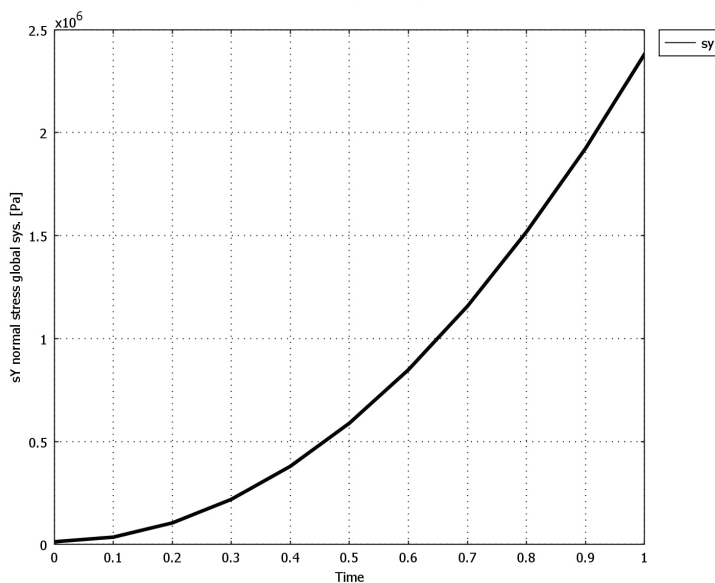


Figure 5. Rise of the normal stress  $\sigma_y$  in the center of the block - constant deformation of the block, growing intensity of the magnetic field

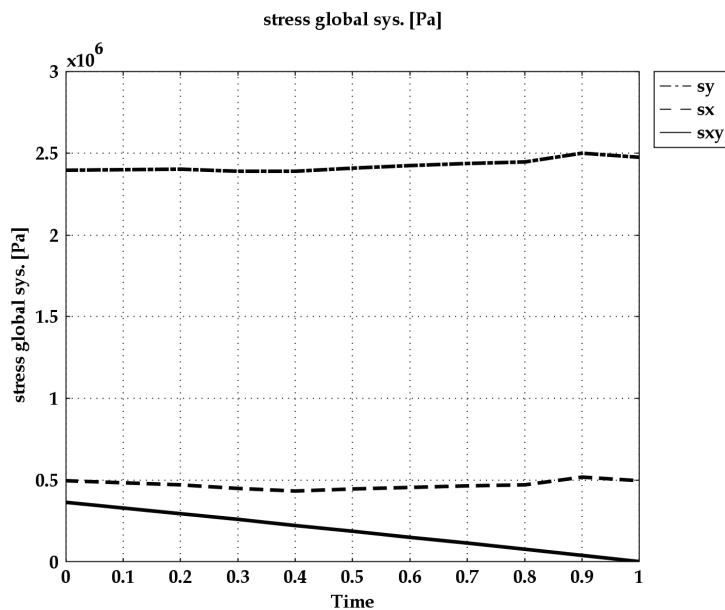


Figure 6. Variation of the stresses in the center of the block - constant intensity of the magnetic field, decreasing deformation of the block

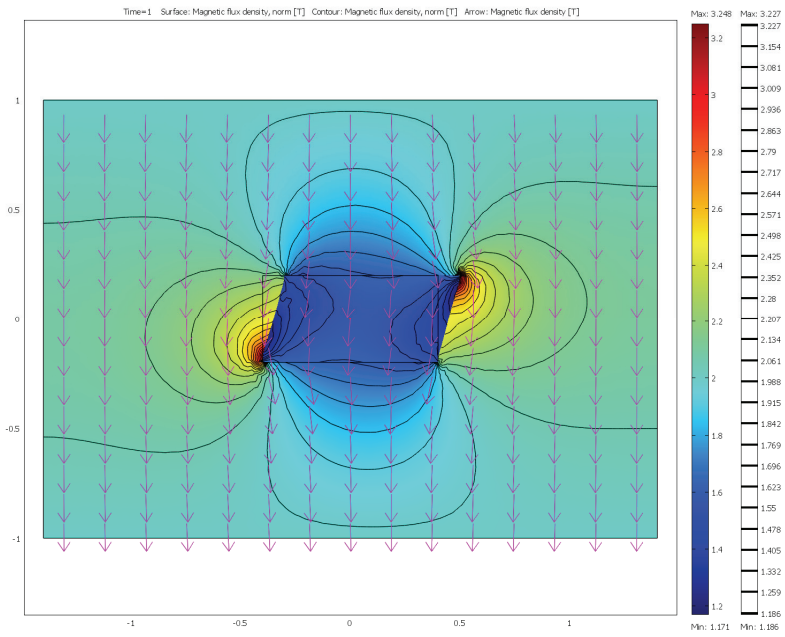


Figure 7. Norm of density of magnetic flux  $B$  - deformed block

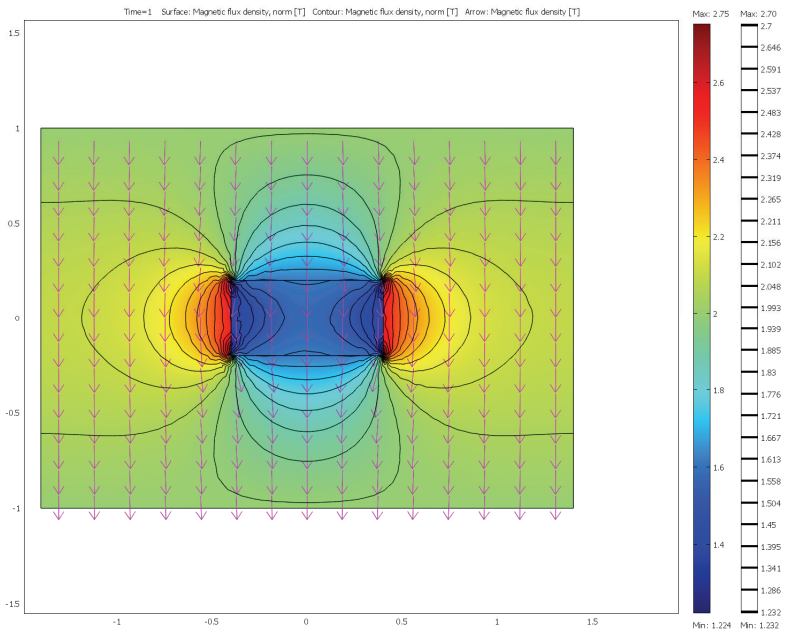


Figure 8. Norm of density of magnetic flux  $B$  - undeformed block

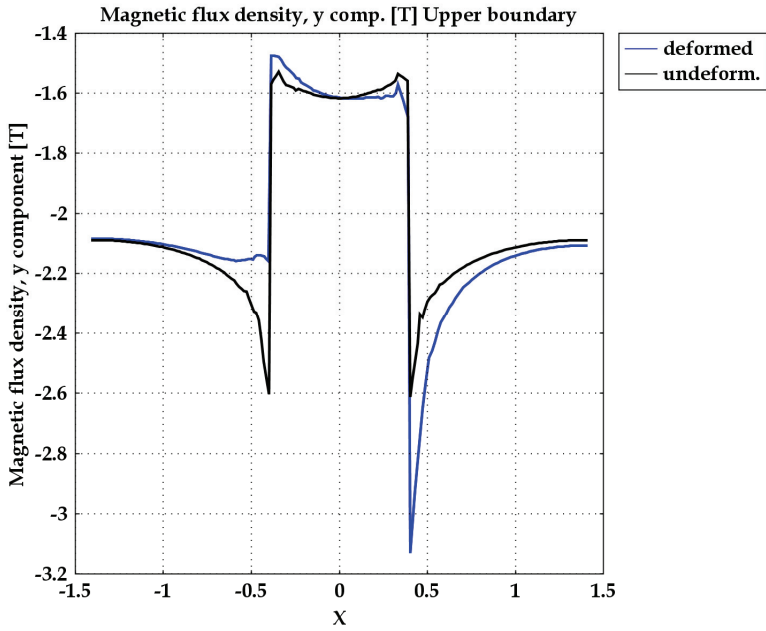


Figure 9. Magnetic flux density component  $B_x$  near the upper boundary level of the block

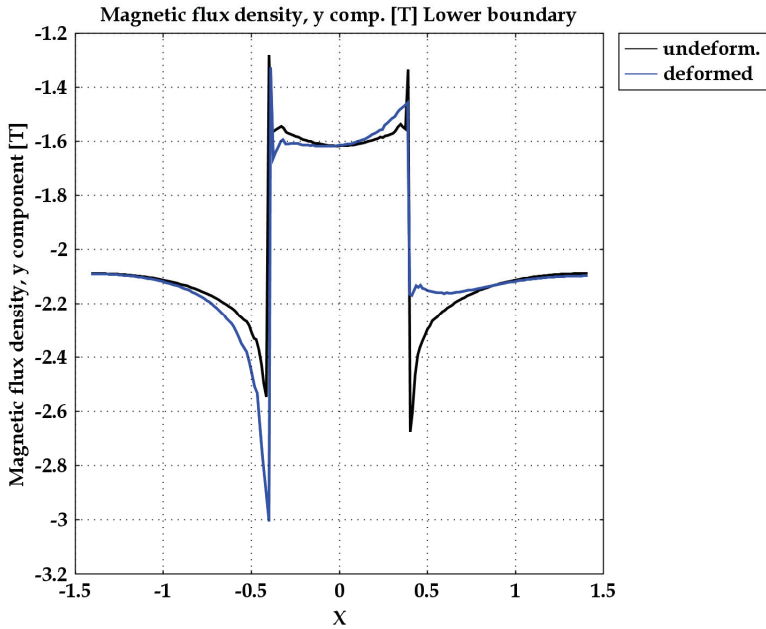


Figure 10. Magnetic flux density component  $B_x$  near the lower boundary level of the block

At the second stage of the loading, when the displacement of the upper boundary of the block is held constant and the magnetic field is switched on, the stress components start to grow cf. Fig. 4. Not only the shear stress increase with the increasing stiffness caused by the magnetic field, the component of stress  $\sigma_y$  spring up and grows also due to the magnetostriction, see Fig. 5. During the third stage of loading, when the magnetic field holds its maximum value and the block returns to its initial position, the component  $\sigma_y$  remains almost constant and even grows slightly in the final phase when the block becomes straight as can be seen at Fig. 6. The change of the norm of the magnetic flux density is obvious from the Figs 7. and 8. and from the graphs at Figs 9. and 10. where the component  $B_y$  near the block boundaries is displayed. We can conclude that the results of the simulation are in the qualitative accordance with the reality.

## 5. Conclusion

We present an illustrative simulation of a simple nonlinear boundary value problem of magnetoelastic interaction at finite strains. The finite element software used proved a flexibility and ability of an easy implementation of fairly complicated coupled problem. Our FE simulation involved not only the edge effects due to the finite geometry of the body but also the influence of the large displacement of the boundaries. The free energy function that we have used is of a very simple form and represents only a first approach towards a valuable constitutive model. Appropriate experiments which are in preparation will allow the elaboration of the constitutive relations. The constitutive model should involve also the anisotropy of MS elastomers cured in the presence of the magnetic field and the complex dissipative behaviour of the material.

In the thirties the renowned imaginative Czech artist Josef Sima painted a series of enigmatic pictures entitled "Mlno" (Czech archaic term for electromagnetism). Possibly, only artists can contemplate deep mysteries of this abstract science.

## 6. Acknowledgement

We gratefully acknowledge the support of the Ministry of Education of the Czech Republic through the Contract Code MSM 4674788501.

## 7. References

- Albanese-Lerner, A.M. & Cunefare, A.K. (2007). Performance of MRE-based vibration absorbers. *J. Intell. Mater. Syst. Struct.*, 0, 5, ISSN 1045-389X, To appear.
- Brigadnov, I.A. & Dorfmann, A. (2003). Mathematical modelling of magneto-sensitive elastomers. *Int. J. of Solids Struct.*, 40, 4659–4674, ISSN 0020-7683
- Brown, W.F. (1966). *Magnetoelastic Interactions*. Springer, Berlin
- Belahcen A. (2004). *Magnetoelasticity, Magnetic Forces and Magnetostriction in Electrical Machines*, PhD Thesis, Helsinki University of Technology.
- Bustamante, R.; Dorfmann, A. & Ogden, R.W. (2006). Universal relations in isotropic nonlinear magnetoelasticity. *Quart. J. Mech. Appl. Math.* 59, 3, 435-450, ISSN 0033-5614
- Bustamante, R.; Dorfmann, A. & Ogden, R.W. (2007). A nonlinear magnetoelastic tube under extension and inflation in an axial magnetic field: numerical solution. *J. Eng. Math.*, 59, 139-153, ISSN 0022-0833

- Carlson, J.D. & Jolly, M.R. (2000). MR fluid, foam and elastomer devices. *Mechatronics*, 10, 555-569, ISSN 0957-4158
- Deng, H.X. & Gong, X.L. (2007). Adaptive tuned vibration absorber based on magnetorheological elastomer. *J. Intell. Mater. Syst. Struct.*, 18, 1205-1210, ISSN 1045-389X
- Dorfmann, A. & Brigadnov, I.A. (2004). Constitutive modelling of magneto-sensitive Cauchy-elastic solids. *Comput. Mater. Sci.*, 29, 270-282, ISSN 0927-0256
- Dorfmann, A. & Ogden, R.J. (2003). Magnetoelastic modelling of elastomers. *Eur. J. Mech. A/ Solids*, 22, 497-507, ISSN 0997-7538
- Dorfmann, A. & Ogden, R.W. (2004). Nonlinear magnetoelastic deformations of elastomers. *Acta Mechanica*, 167, 1-2, 13-28, Published online Dec. 2003, ISSN 0001-5970
- Dorfmann, A. & Ogden, R.W. (2005). Some problems in nonlinear magnetoelasticity, *Z. angew. Math. Phys. (ZAMP)*, 56, 718-745, ISSN 0044-2275
- Dorfmann A.; Ogden, R.W. & Saccomandi, G. (2004). Universal relations for non-linear magnetoelastic solids. *Int. J. Non-Lin. Mech.*, 39, 1699-1708, ISSN 0020-7462
- Dorfmann A.; Ogden, R.W. & Saccomandi, G. (2005). The effect of rotation on the nonlinear magnetoelastic response of a circular cylindrical tube. *Int. J. of Solids Struct.*, 42, 3700-3715, ISSN 0020-7683
- Ginder, J.M.; Clark, S.M.; Schlotter, W.F. & Nichols, M.E. (2002). Magnetostrictive phenomena in magnetorheological elastomers. *Int. J. Mod. Phys. B*, 16, 17 & 18, 2412-2418, ISSN 0217-9792
- Gong, X.L.; Zhang, X.Z. & Zhang, P.Q. (2005). Fabrication and characterization of isotropic magnetorheological elastomers. *Polymer Testing*, 24, 5, 669-676, ISSN 0142-9418
- Hasebe, N.; Wang, X. F. & Nakanishi, H. (2007). On magnetoelastic problems of a plane with an arbitrarily shaped hole under stress and displacement boundary conditions. *Quart. J. Mech. Appl. Math.*, 60, 4, 423-442, ISSN 0033-5614
- Holzappel, G.A. (2000). *Nonlinear Solid Mechanics: A Continuum Approach for Engineering*, Wiley, ISBN 0471823198, Chichester
- Jolly, M.R.; Carlson, J.D.; Munzo, B.C. & Bullions, T.A. (1996). The magnetoviscoelastic response of elastomer composites consisting of ferrous particles embedded in a polymer matrix. *J. Intell. Mater. Syst. Struct.*, 7, 613-622, ISSN 1045-389X
- Kallio, M.; Lindroos, T.; Aalto, S.; Järvinen, E.; Kärnä, T. & Meinander, T. (2007). Dynamic compression testing of a tunable spring element consisting of a magnetorheological elastomer. *Smart Mat. Struct.*, 16, 506-514, ISSN 0964-1726
- Kankanala, S. V. & Triantafyllidis, N. (2004). On finitely strained magnetorheological elastomers. *J. Mech.Phys. Solids*, 52, 2869-2908, ISSN 0022-5096
- Kankanala, S. V. & Triantafyllidis, N. (2008). Magnetoelastic buckling of a rectangular block in plane strain. *J. Mech.Phys.Solids*, 56, 4, 1147-1169, ISSN 0022-5096
- Kovetz, A. (2000). *Electromagnetic Theory*. Oxford University Press, ISBN 0198506031, Oxford
- Ogden, R.W. (1984). *Non-Linear Elastic Deformations*. Ellis Horwood Ltd, ISBN 0853122733, Chichester
- Ottenio, M., Destrade, M. & Ogden, R.W. (2008). Incremental magnetoelastic deformations, with application to surface instability, *J. Elast.*, 90, 1, 19-42, ISSN 0374-3535
- Pao, Y.H. & Yeh, C.S. (1973). A linear theory for soft ferromagnetic elastic solids. *Int. J. Engng Sci.*, 11, 415-436, ISSN 0020-7225

- Pao, Y.H. (1978). Electromagnetic forces in deformable continua. In: *Mechanics Today 4*, Nemat-Nasser, S., (Ed.), 209–305, Pergamon Press, Oxford,
- Sima, J. (1933). *Mlno*. Galerie Tea-Art, Prague, <http://www.tea-art.cz/galerie/sima/sima.htm>
- Steigmann, D.J. (2004). Equilibrium theory for magnetic elastomers and magnetoelastic membranes. *Int. J. Non-Linear Mech.*, 39, 1193–1216, ISSN 0020-7462
- Steigmann, D.J. (2007). On the Formulation of Balance Laws for Electromagnetic Continua, *Math. Mech.Solids*, 0, 10, ISSN 1081-2865, To appear.
- Zhou, G.Y. & Wang, Q. (2006a). Use of magnetorheological elastomer in an adaptive sandwich beam with conductive skins. Part I: Magnetoelastic loads in conductive skins. *Int. J. Solids Struct.*, 43, 5386–5402, ISSN 0020-7683
- Zhou, G.Y. & Wang, Q. (2006b). Use of magnetorheological elastomer in an adaptive sandwich beam with conductive skins. Part II: Dynamic properties. *Int. J. Solids Struct.*, 43, 5403–5420, ISSN 0020-7683

# Simulation of Net Structures Hydrodynamic Fields

Leonid Meyler  
*The Baltic State Fishing Fleet Academy  
Russia*

## 1. Introduction

Important problems in industrial fishery are catchability and selectivity of fishing gears. These characteristics depend on various parameters of gears that usually have a highly hydroelastic net structure without a predefined shape. The shape forms in motion or under flow action. Curved net structures are usually highly three-dimensional. The study of the net structure volume deformation is complex, requiring treatment of structural properties like flexibility, discontinuity, anisotropy and uneven surface shapes. Hydrodynamics of fishing net structures, in particular, a fishing trawl and its rear part – cod-end, attracts an attention of scientists for a long time. Fig. 1 shows a trawl system scheme.

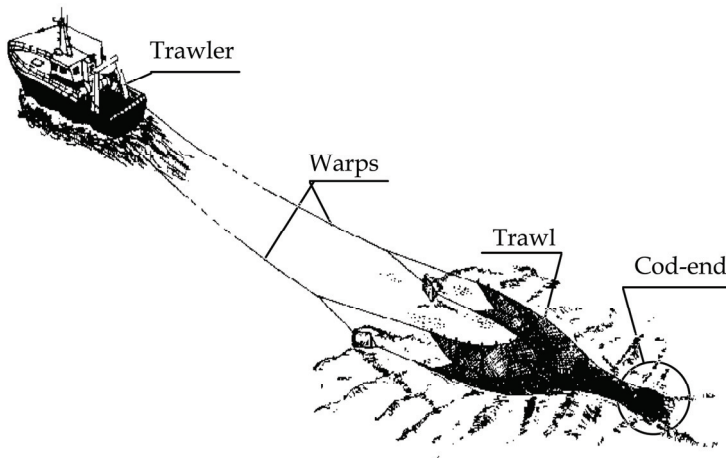


Figure 1. Scheme of a fishing trawl system

The dynamic interaction between a net structure, a fishing vessel, rigging, warps and other trawl elements connected together are complex. An importance of flow velocities and pressures estimation both around and in trawl consists in an exclusive dependence of the forces acting on each part of the trawl system. The knowledge of these forces allows to define the shape, drag and behavior of the structure during a trawling process, tension and loads in its twines and ropes. As well, flow velocities and pressures in the cod-end, have a

very significant influence on the fish motion process. The quantity and quality of the catch collected in the cod-end depends on fish behavior. Besides influencing of the cod-end design on flow velocities/pressures it causes a net "meshing" with fish that in its turn influences hydrodynamics of the cod-end and consequently on its catchability and selectivity. From the point of view of modern fishing engineering (Paschen et al., 2001) the key to understand these characteristics is to complete consideration of fish, fishing gear and fluid as a whole. Therefore velocity and pressure distribution ahead of and in the fishing gear have to be predicted on a basis of experimental investigations and numerical simulations.

## 2. A brief review of previous studies

This article does not pursue the objective to give a general review of such works. Nevertheless, it is possible to mention some of them. The earliest publications described experimental methods of testing net cylinders, cones, models of trawls and real trawls. Results have been presented usually as graphic dependences of flow velocities or pressures on net structures characteristics and empirical expressions describing these dependences.

Cones as a main part of a trawl design were studied more often. Such investigations have been carried out using special experimental plants. For example, a flume tank was used (Higo, 1964) for velocities measurements around net cones with a thermister current meter and experimental data and empirical dependences of flow velocities on cones characteristics were presented. A research of different trawl models (Stengel & Fischer, 1964) conducted in a wind tunnel allowed to evaluate pressures distribution in front of and into the models. A Pitot tube used for these experiments. A wind tunnel also was used as the experimental plant for tests (Rehme & Scheel, 1988) of a big size net cone made of different size netting. Nondimensional velocities as a function of cross coordinates were resulted. A net cone made of metal wire was studied (Scharping, 1974) in a wind tunnel in order to measure pressures at the different longitudinal sections both in and outside the model. Cones towed by a vessel in order to investigate velocities influence at the net "mouth" on velocities inside the net and to get the correspondent dependence (Higo et al, 1974). Experiments (Imai, 1974) carried out in a circular tank permitted to study velocities distribution inside trawl models made of thin and thick net webbing.

The big contribution to the problem studying has been brought by Z. Ziembo (Ziembo, 1974; 1987 a, b; 1988; 1989; 1993). The author carried out many experimental researches and suggested mathematical models to describe a process "water flows in trawls". These articles describe methods of investigations, results and comparison between theoretical and experimental approaches. In particular, trawl models having different mesh sizes have been towed by a catamaran equipped with special facility for direct observations and measurements. Velocity and pressure distributions around the models have been compared both to a simplified mathematical model based on considering of ideal, incompressible non-viscous liquid and to mathematical model for real water. Another experiment devoted to study of kinetics of water flow through trawl models and real trawl. Solving this problem has a great importance since it gives possibility to design trawls with best shape parameters adapted to fish reactions on the net structure. Calculations of water flow velocity through the cod-end under the assumption that the flow is uniform and equal on its entire surface were made (Moderhak, 1993) for different ratios of codend length to its diameter, mesh bar length to mesh bar diameter, and for various mesh opening coefficients. The results obtained were analyzed with regard to the impact of flow velocity on hydrodynamic forces



opening the cod-end. A simplified mathematical model was used for flow velocities normal to a cod-end calculation. An idea of a new set-up of meshes in the codend, changing the effect of operation of longitudinal forces (hydromechanical drag forces) was presented.

Hydromechanics of towed trawl models was investigated (Gabriuk & Chernetsov, 1985) by special designed catamaran. Some of researchers (Kroeger, 1984; Ziembo, 1989) investigated towed full-scale trawls in order to evaluate dependences of longitudinal flow velocities along the different design trawls using propeller type flow meters. Others (Miziurkin & Kostiukov, 1982; Kostiukov & Shevchenko, 1983) studied fish behavior and hydrodynamic fields by means of special detectors put inside real trawls. Data registration made from an underwater manned vehicle.

Serial experimental researches on net cones and cylinders, trawl models, cod-end models with imitation of a catch have been carried out in one of the world largest flume tanks, which is located in Kaliningrad, Russia. Fig. 2 shows its scheme. Many publications followed these experiments. A trawl cod-end model was tested (Baev & Belov, 1987) for the velocity field determination. As a result of trawl cod-ends investigations (Korotkov & Meyler, 2000; 2001), an improved design of the cod-end was proposed and realized for industrial trawlers.

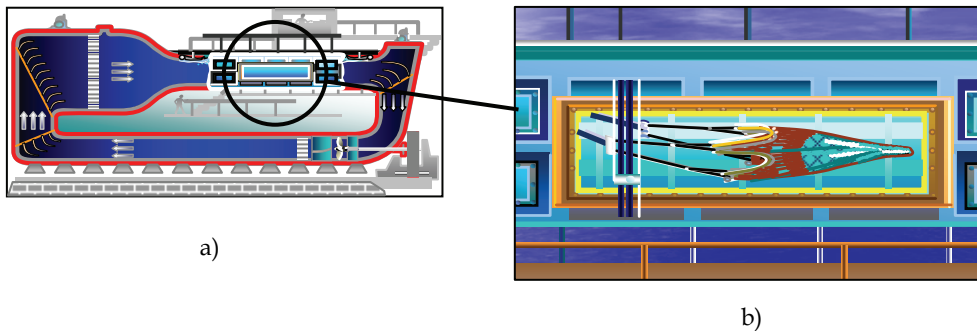


Figure 2. View of the flume tank (a) and the working part (b)

Flow velocities have been measured in experiments (Belov, 1987, 2002) both inside and outside of net construction. An example of longitudinal flow velocities experimental data is shown in Fig. 3. Special attention is paid to the theoretical and experimental methods for the design of fishing gears and investigations on cod-end selectivity in the framework of the international workshops "Methods for the Development and Evaluation of Maritime Technologies - DEMaT". Measurements of the flow by using the Scanmar speed sensor were carried out (Thiele, 1997) inside and outside of a selectivity cod-end. The results show that the velocity of the flow inside the cod-end is strongly influenced by the mesh size and the cover. Systematic model experiments on net cones were carried out (Paschen & Winkel, 1999) in order to obtain the necessary quantitative relation between the known design of the net shape and the corresponding flow and pressure distributions in the environment as well as inside the net structure.

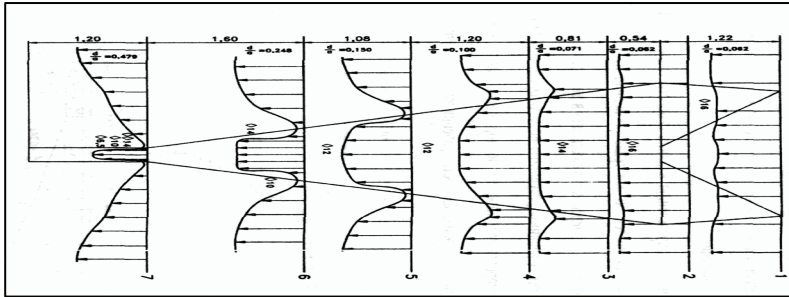


Figure 3. Flow speed distribution in/around a trawl model

The suggested methodology is suitable to carry out basic analysis of net-fluid interactions. Among the received experimental results, the geometrical angle of attack of the net cone is of crucial importance for the velocity and pressure distributions already in front and within the reticulate structure. In addition, the paper gives an approach to approximate calculation of pressure increase in a towed conical net using assumption that meshes themselves and the caught fish cause a blockage effect and drag. This influence is of primary importance for static pressure and velocity inside the cone. Authors notice that the structure fluid interactions with trawls and their elements are very complex due to the high flexibility of net constructions and mathematical modeling of this interactions become more and more important in connection with the efforts to increase the selectivity of trawls. Considering methods and limits for wind tunnel tests (Winkel & Paschen, 2001) an importance of the analysis of temporally variable flows inside or around fishing nets was emphasized. It gives a better understanding of fish behaviour and net selectivity. Flow velocities was measured (Enerhaug, 2005) in conical shaped models with high net solidity. Experiments have been carried out in a flume tank in order to verify theoretical approaches for modeling, predicting and interpreting the flow in fine-meshed pelagic trawls. An experimental approach for the analysis of the flow distribution in a brailer-codend (Fuwa et al., 2007) was studied in a flume tank. Flow speed inside the codend was measured using the current meter.

According to a three-dimensional numerical model of the fluid flow (Fredheim & Faltinsen, 2001), that takes into consideration the influence of the structure on the flow, the net is divided into a set of cylindrical and spherical elements to represent the twines and knots respectively. Each of these different elements is modeled as a set of source distribution and single point sources. This model allows to describe the disturbance of the fluid flow due to the presence of the net and to determine the influence from the net on the flow.

The study (Benoit & Marichal, 1996) took place in a global improvement project of trawl selectivity, which means its capacity to let young fish escape through the meshes. The authors used Navier-Stokes equations for calculation of velocities in the cod-end. They undertake necessity to know water velocity in the trawl to be able to calculate mesh geometry. Indeed, mesh geometry depends on hydrodynamic forces due to flow. The cod-end is supposed to be homogeneous and permeable surface, because equations mentioned above cannot describe flow around each twine of cod-end. Specific equations were used to compute tangential and normal components at the net's surface.

In spite of the significant experimental and theoretical material on the problem which has been collected since sixties of the last century, recent publications devoted to increasing of reliability of flow parameters in net structures and simulation methods development

testifies that the problem remains actual at present time. Interesting researches (O'Neill, 2003, Priour & Herrmann, 2005) are devoted to factors influencing the cod-end shape under a flow and with caught fish.

As it was said in the above mentioned study (Paschen et al., 2001), the predictability of the flow field inside and outside a net structure is necessary in order to simulate the connection between net structure, fluid and fish. Authors underline that even if highly efficient Computational Fluid Dynamics (CFD) methods are applied, the problem seems to be rather complex. A study (Enerhaug et al., 2003) gives experimental tests description of the flow velocity field around a solid cone and a reticulate one in the flume tank. Then experimental data were compared with numerical calculations. The flow depends on the cone solidity value. Authors used FEMLAB CFD software for the two-dimensional simulation where the reticulate cones were idealized by a number of slender parallel cylinders, authors made a conclusion that such approach only meant to illustrate the overall physical principles. However, such simulations give the basis for further research because the real net structure has a dynamic moving, equipped with rigging elements, etc. Anyway, if results of experiments and calculations will have a rather good convergence, this method can be used for hydrodynamic field characteristics prediction. Due to the fact that netting can be approximated by very large number of small cylinders connected in knots, an approach (Patursson et al., 2007) to simulate the net as a thin volume of porous media was presented. Fig. 4 shows a scheme of the suggested method.

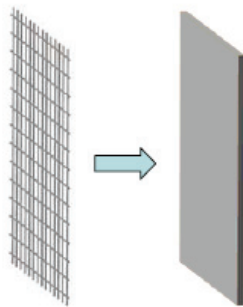


Figure 4. The net conversion to a thin volume of porous media

Predicted drag- and lift coefficient of the net panel and the velocity reduction behind the net panel was calculated by the model available in FLUENT CFD software. These data were compared against values measured during experiments in a flume tank. The modeled results have a good agreement with measured values.

### 3. CFD software description

As it was mentioned above, more and more researches have now numerical character when the various software products based on the equations of mathematical physics decision are used. Methods of computer modelling give unique technologies of physical fields studies. It is possible to use ready programs and to model various combinations of the interconnected physical fields. Thus the engineer, the designer or the researcher does not have necessity to create programs for the decision of the problems. One of the applications is hydrodynamics of various bodies. For example, it can be a combination of velocity or pressure fields inside

and around net structures. Certainly, at such statement it is important to be sure that the software is based on a mathematical model adequate to the real physical process. Thus, reliability of numerical calculation has to be supported by comparison with experimental data that will allow to evaluate the so-called «scale effect». Development of mathematical models and the software are based on CFD methods. CFD is a modern component of market CAE (Computer Aided Engineering). CFD is based on FEM (the Finite Element Method) or FEA (the Finite Element Analysis). This article has no purpose of making a thorough survey of similar software products, but some of them will be mentioned as an opportunity for the concrete applied problem decision - a numerical estimation of a net structures hydrodynamic field.

The ANSYS software (<http://www.ansys.com>) is the program of the finite-element analysis. ANSYS gives a possibility to apply computing methods of hydrodynamics for parameters of a liquid or gas flow definition. The solved problems can be stationary or non-stationary and the flow can include up to six components disconnected among themselves. The hydrodynamic analysis is used for definition of such parameters of the liquid as a pressure difference, a velocities distribution, a flow direction, lift and drag forces, influence of heating and cooling. Velocity components, values of pressure and temperature are defined on the basis of laws of mass preservation, quantity of motion and energy. For turbulent motion modelling there is an opportunity to use the description of the phenomenon by means of the continuity and impulse equations.

Another CFD package FLOW-3D (<http://www.flow3d.com>) is capable to model the big variety of problems of liquid flows. They can be flows with a free surface, and the limited and internal flows. It is expressed in the simplified approach to generation of a finite-element grid that affects an accuracy increase, reduction of a memory size, simplification of a numerical approximation. This is the program of visualization, which is simple to use when displaying of results of modelling, creating animation and pictures for presentations and reports.

The software package FLUENT (<http://www.fluent.com>) is also the CFD program for a wide range of flows modelling: incompressible (low subsonic), compressed (transonic) and even super compressed (super-hypersonic). The program gives a set of the physical models allowing to predict parameters of laminar and turbulent liquid or gas flows with the big accuracy.

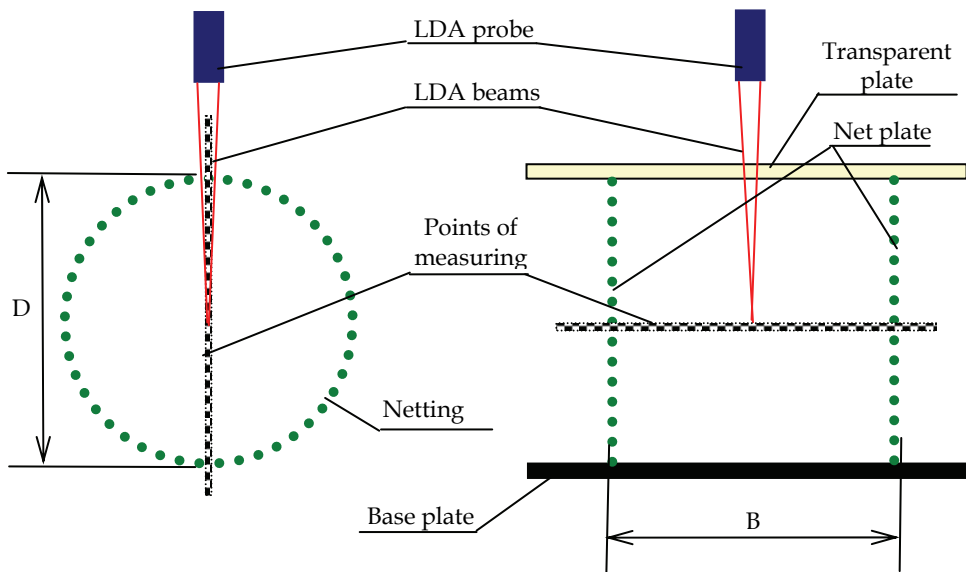
However modelling in these software packages is extremely labour-intensive process and takes a lot of time, which is necessary for definition of finite-element grid geometry and parameters according to the set model.

The program FEMLAB (<http://www.comsol.com>) is a package for solving of the equations modelling investigated system eliminates these problems. The FEMLAB software is the powerful interactive package for the modelling, enabling to solve all kinds of the scientific and technical problems based on Partial Differential Equations (PDE). The interface basing on the Java language has many advantages. Users can create model without programs writing. A library built in the program includes more than 200 completely solved and documentary firmware models, often meeting for solving waves distribution problems, for an analysis of internal combustion engines work, electromechanical systems, etc. After an automatic call of the built in model, users can change names of variables, to set factors and even to change a kind of the equations. The last feature is extremely difficult to realize in other packages. When the model chooses, for example, heating transfer, acoustics,

hydrodynamics, diffusion, electromagnetism, the theory of elasticity or others, the program automatically sets the corresponding equations. As well, it is possible to enter the necessary equations independently. Moreover, users can combine and mutually connect any kinds of the phenomena, creating a multiphysical model.

The program FEMLAB is developed so that modelling of physical fields and connections between them can be carried out simply. There is an opportunity to solve the given system of PDE or to use specialized physical applied modes. These physical modes consist of the predetermined patterns and the interfaces of the user already installed with the equations and variables for specific areas of physics. Further, it is possible to create multiphysical model combining any number of these applied modes in the uniform applied description. It is possible in the FEMLAB system to expand easily usual models for one type of the physical phenomena in multiphysical models that solve the connected phenomena of physics, and make it simultaneously. Access to this opportunity does not demand a profound knowledge of mathematics or the numerical analysis that is very important for the engineer or the designer solving applied problems. Considering the described advantages of FEMLAB software and its latest version named as COMSOL Multiphysics the estimation of a net structure hydrodynamic field has been made.

#### 4. Experiments on schematized net structures



a) cross section of a net cylinder  
Figure 5. Transformation from net structure to SNS

Researchers encountered problems in experiments to measure velocities everywhere inside a net structure because of a difficulty to penetrate with a log through meshes due to their small size especially in cod-end. Therefore, a method of flow velocities studies on

schematized net structures (SNS) was proposed (Meyler, 1995). Taking into account that such constructions as the trawl cod-end has an axisymmetric shape, distributions of flow parameters (velocities and pressures) inside and around the structure have the axisymmetric character as well. Assuming these circumstances, flow velocities were studied by means of the Laser Doppler Anemometer (LDA) on a construction consisting of two vertical net plates attached to two horizontal solid plates the upper of which is made of a transparent material. A view of “transformation” from a real net structure cross section to SNS cross section is shown in Fig. 5. Fig. 6 shows a scheme of a SNS test in the flume tank. It was assumed also that velocities distributions into limits of a very thin measured layer at the diametric section of a net cone or a net cylinder and into such layer at the central symmetric section of the SNS are identical. Net plates of the SNS was made of the same netting and the distance  $B$  between two plates was equal to the diameter  $D$  of the net cylinder or cone. Results of experiments on different SNS simulating net cylinders, cones and their combinations have shown (Meyler, 2000, 2005) a good convergence with measurements on real net structures.

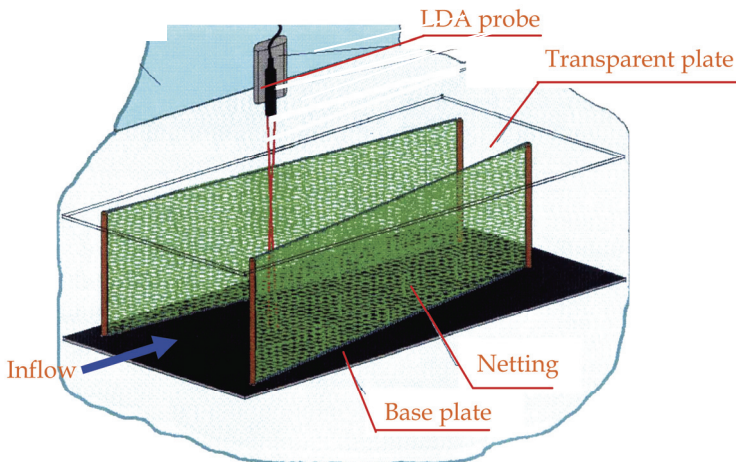


Figure 6. Scheme of the flume tank SNS “a cone” test

## 5. Preliminary estimation of FEMLAB (COMSOL Multiphysics) applicability

Naturally, considering the above described advantages of the given software package a question arises: whether it is possible to use it for counting a net structure hydrodynamic field? Preliminary evaluation of this method for a numerical estimation of a net structures hydrodynamic field was made (Meyler, 2006, 2007) on net cones and cylinders because they are the main elements of various real fishing gears. Taking into consideration assumptions accepted for SNS, cross sections of twines located at the thin layer were replaced with composition of circular cross sections. This composition simulates a longitudinal section of specified net structures: a cone, a cylinder and their combination. The flow around these sections is assumed to be equivalent to the flow around twines. Thus, the two-dimensional parallel-plane flow of an incompressible liquid around a system of the circular cylinder

cross sections located perpendicularly to the flow direction was considered. It is known, that the incompressible liquid flow is described by Navier-Stokes equations consisting of the momentum (balance) equation at performance of the mass preservation law and an incompressibility condition:

$$\begin{cases} \rho \frac{\partial \mathbf{u}}{\partial t} - \rho(\mathbf{u} \cdot \nabla) \mathbf{u} = -\text{grad } p + \text{div}(\eta \cdot (\nabla \otimes \mathbf{u} + \text{grad } \mathbf{u})) + \mathbf{F} \\ \text{div } \mathbf{u} = 0 \end{cases} \quad (1)$$

$$\mathbf{u} = \mathbf{i}_x \cdot u + \mathbf{i}_y \cdot v; \quad \nabla = \mathbf{i}_x \frac{\partial}{\partial x} + \mathbf{i}_y \frac{\partial}{\partial y};$$

where:  $\rho$  - liquid density ( $\text{ML}^{-3}$ );  $\mathbf{u}$  - vectorial velocities field ( $\text{LT}^{-1}$ );  $\mathbf{i}_x, \mathbf{i}_y$  - axes unit vectors;  $p$  - pressure ( $\text{ML}^{-1}\text{T}^{-2}$ );  $\eta$  - dynamic viscosity ( $\text{ML}^{-1}\text{T}^{-1}$ );  $\mathbf{F}$  - field of vectorial force ( $\text{ML}^{-2}\text{T}^{-2}$ );  $\nabla$  - vectorial differential operator.

The COMSOL Multiphysics software uses these equations for the decision of flow dynamics problems. The schemes of each "net" constructions model are shown in Fig. 7. These schemes appear in the Graphic User Interface (GUI) of the COMSOL Multiphysics. The models had the same characteristics as those in experiments. Cross sections of the netting twine were presented in GUI as so called "solid" round bodies placed in that order to get longitudinal sections of a "net" cylinder, a "net" cone, and their combinations. It is possible to change a model "permeability" varying with the distance between "solid" bodies.

Characteristics of models were the following:

- Diameter of a circular cross section was equal to a diameter of a real twine  $d = 2.5 \cdot 10^{-3} \text{ m}$ ;
- Distances between these sections were equal to a mesh size of a real netting  $a = 25 \cdot 10^{-2} \text{ m}$ ;
- Length of models  $L = 1.4 \text{ m}$ ;
- Inflow model diameter  $D = 0.3 \text{ m}$ .

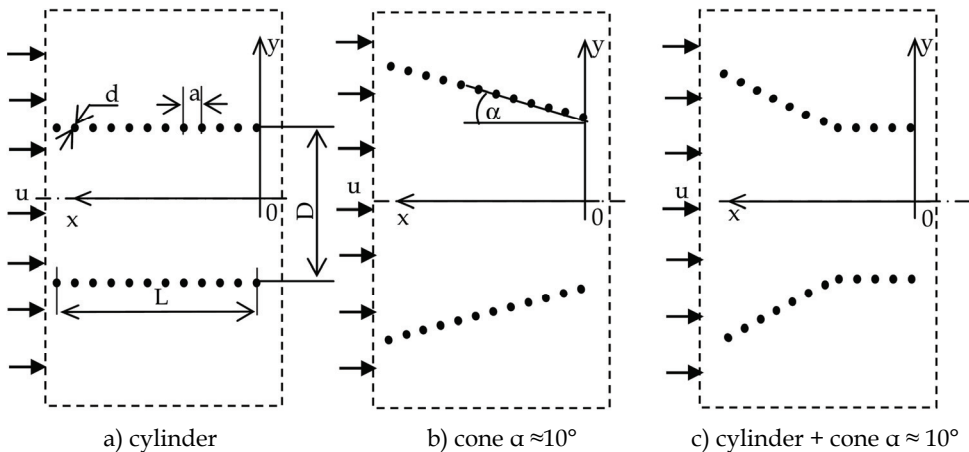


Figure 7. Scheme of the net models

To calculate a hydrodynamic field in/around these objects basing on Navier-Stokes's equations the field of the flow velocity, i.e. the "N-S" subdomain was created in GUI. Fig. 7 shows this subdomain as a dotted rectangular. The left margin of the subdomain is considered as the flow inlet and the right margin as the flow outlet. Values of the water density  $\rho$  and the water dynamic viscosity  $\eta$  as well initial inlet longitudinal  $u_0$  and transversal  $v_0$  flow velocities and initial hydrostatic pressure  $p_0$  are pre-assigned for this subdomain.

The subdomain boundary settings i.e. boundary conditions at the "N-S" subdomain were the following:

- an inlet margin - initial velocities of a water flow, expressed as "inflow/outflow", for the model were equal to real inlet velocities  $u=u_0=1.0$  m/s,  $v_0=0$ ;
- an outlet margin - an outgoing flow expressed as "outflow/pressure";
- at top/down margins - a free flow expressed as "neutral";
- at each "solid" body - a non-leaking body contour expressed as "no slip".

As the analysis has shown, these borders are necessary to place on significant distances from the model, so that "flow" borders do not influence a field of velocities around the model. As it was mentioned, a big advantage of the software is the automatic mode of a finite-element grids generation under the set boundary conditions of the flow. Fig. 8 shows the fragment of a grid near to a "twine". It is possible to see that boundary conditions "no slip" form the tighter grid.

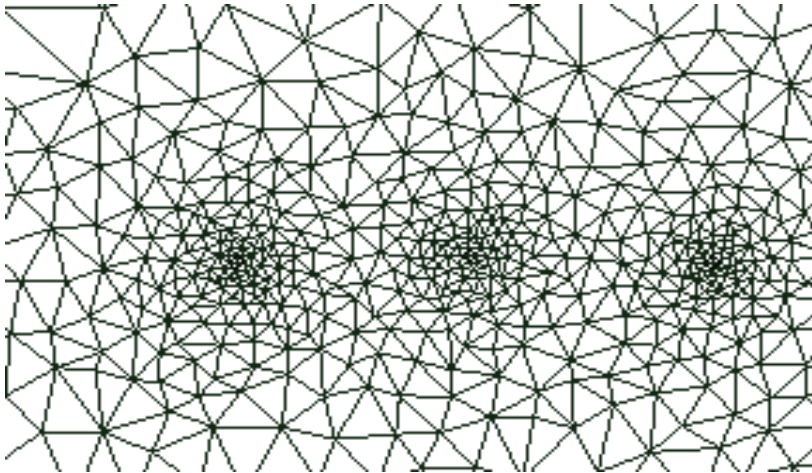


Figure 8. Fragment of a finite-element grid

Fig. 9 shows the calculated velocities distribution for the model - "a close net cylinder", i.e. there is a "net wall" at the outlet. Fig. 10 demonstrates comparison between calculated dependences of the relative longitudinal velocity (solid lines) and experimental data (symbols of the same color), received in research of SNS from the relative longitudinal  $x/L$  and transversal  $\bar{y} = 2 \cdot y/D$  coordinates. Comparison of calculated and experimental data testifies to their insignificant divergence.



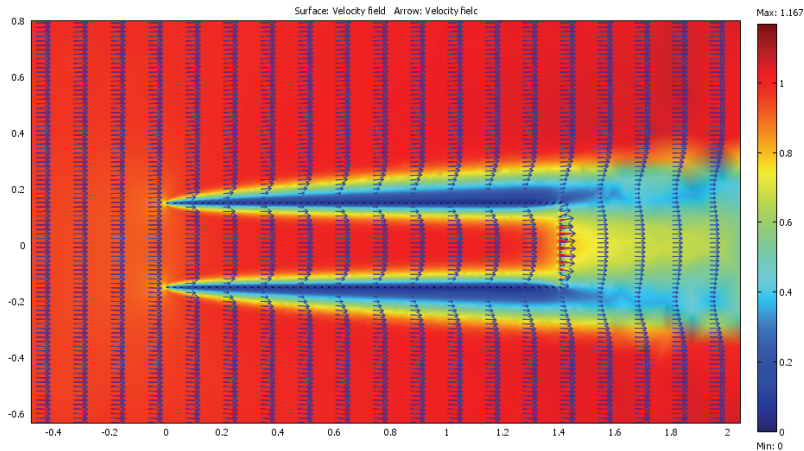


Figure 9. Velocity distributions around a "close net cylinder"

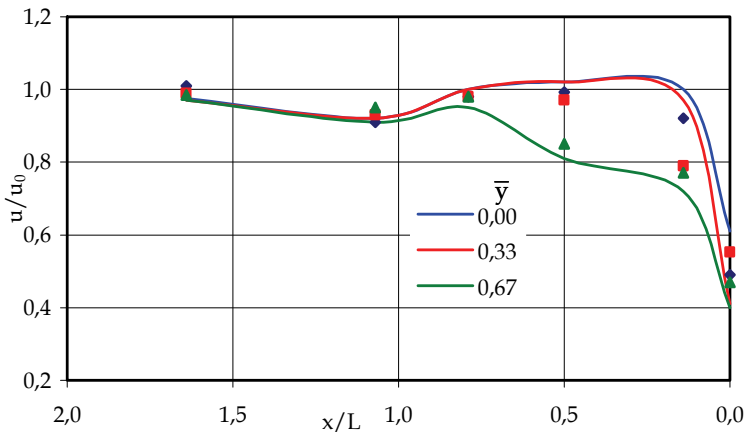


Figure 10. Calculated and measured data comparison for a "close cylinder"

Experimental and calculated data have satisfactory convergence for other variants of models. Velocity distributions for some of them are shown on Fig. 11. These figures give a possibility to estimate both values of flow velocities and features of the flow. It is possible to assume that calculating and summarizing parameters of hydrodynamic fields for similar "net" elements allow estimating such field for a trawl in total. Results of the calculated and experimental data comparison allow to make a conclusion about an opportunity to use the COMSOL Multiphysics software for estimation of net structures hydrodynamic fields.

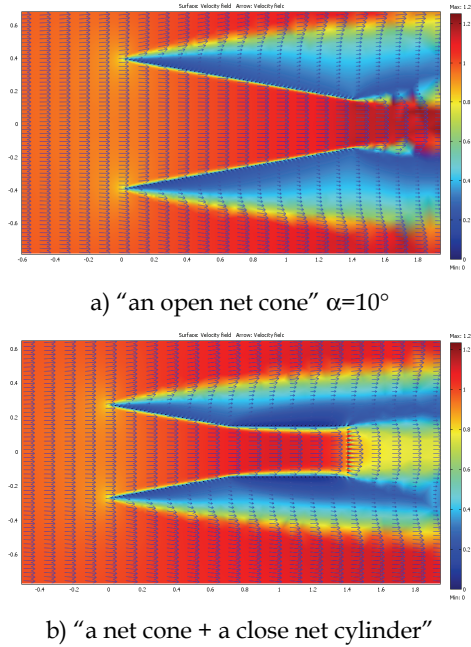


Figure 11. Flow velocities distribution for "net" models

Fig. 12 illustrates the flow into rear net cylindrical part of the cod-end with "a catch" simulation. The fish simulation was created with "solid" bodies given as cylindrical cross sections. It is seen that "the catch" gives a backwater flow and, so called, "locking" effect. It permits to have a possibility for a fish escape from the trawl or make "meshing" of the cod-end that is to block meshes of the net.

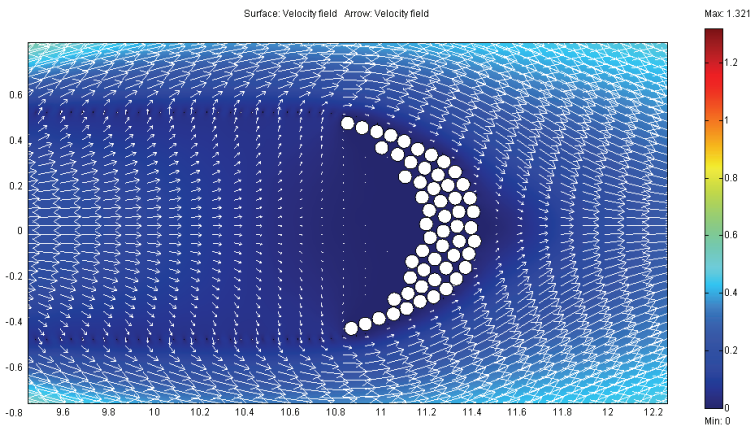


Figure 12. Speed distribution with a "catch" imitation in a cod-end

## 6. A permeable surface concept

However, such kind of simulations faces some difficulties. First, it is complex big sizes “net” models drawing in GUI because of many “solid” bodies, especially when permeability of netting is necessary to change. Secondly, too long time of calculations. Sometimes a PC operative memory had not enough capacity. Therefore, this approach can be sufficient for simple models simulating. In this connection works conducted for description of an ideal or viscous liquid flows around of permeable or perforated bodies, surfaces, envelopes and parachute’s canopies are of interest. Use of these theoretical researches results for fishing net structures depends on effects which are on a permeable surface, in particular on permeability coefficient values which are obvious more for netting, than for a parachute canopies fabric. In addition, the account of viscosity and formation of a vortical structure behind a permeable surface is obviously important. These theoretical researches are based on the known physical laws described by the known mathematical equations and correlations that give the possibility to use them for fishing gears application. The problem of a flow through a permeable surface has been solved as an application to the theory of a parachute (Rakhmatullin, 1950). It was accepted an assumption about a uniform distribution of velocities and pressures at a small area of the permeable surface and that a normal component of a flow velocity and a pressure difference are connected with square-law function. A tangential component of a flow velocity can have a break. It means that on the uniform permeable surface velocities and pressures can have breaks. Because the uniform permeable surface is not a liquid surface, a liquid particle receives some impact flowing through this surface. Fig. 13 shows the scheme of the flow through a permeable surface.

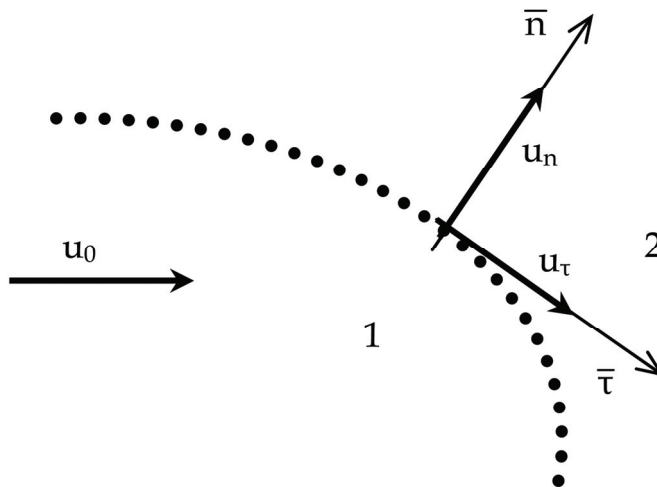


Figure 13. Scheme of a flow through the permeable surface

A flow through a permeable surface is defined with laws:

Mass conservation:

$$\rho_1 \cdot u_{1n} = \rho_2 \cdot u_{2n} \quad (2)$$

Impulse conservation:

$$\begin{aligned}\rho_1 \cdot \mathbf{u}_{1n} \cdot (\mathbf{u}_{2n} - \mathbf{u}_{1n}) &= p_1 - p_2 - R_n, \\ \rho_1 \cdot \mathbf{u}_{1n} \cdot (\mathbf{u}_{2\tau} - \mathbf{u}_{1\tau}) &= -R_\tau,\end{aligned}\quad (3)$$

Energy conservation:

$$\rho_1 \cdot \mathbf{u}_{1n} \cdot \left( \frac{u_2^2}{2} - \frac{u_1^2}{2} \right) = p_1 \cdot \mathbf{u}_{1n} - p_2 \cdot \mathbf{u}_{2n} - \bar{R} \cdot \frac{\bar{u}_1 + \bar{u}_2}{2}, \quad (4)$$

where:  $\rho_1, \rho_2$  - water densities;  $u_{1n}, u_{2n}$  - velocity projections on the normal;  $u_1, u_2$  - velocity modules;  $p_1, p_2$  - pressures;  $R_n, R_\tau$  - normal and tangential components of a flow force acting on a permeable surface unit;  $\bar{R}$  - the resulting vector of  $R_n, R_\tau$ .

Areas "1" and "2" in Fig. 13 and indexes in equations (2 - 4) define flow parameters in front of the permeable surface and behind it. This model needs in evaluation of the permeable surface different details (twines and knots of the net) impact on the water flow. It presents difficulties because of the multiple diffraction and interference of a flow disturbance around twines. Interaction between an incident flow and the permeable surface depends on meshes distribution, their number and inclination to the velocity vector. It is possible to take assumption that the flow around a net surface has some features:

- a shape conservation, i.e. the net structure has factually unchangeable shape under the flow impact;
- a net structure shape creation, i.e. the structure «chooses» itself such shape under the flow that a pressure difference on its surface has a constant value;
- a net structure has a definite permeability that is a main factor of a flow stability around the net structure.

Boundary conditions are defined taking into consideration real features of the water flow through the net surface:

for the fixed permeable surface (for example, a set long line or a seine):

$$\text{on the surface } \frac{\partial \varphi}{\partial n} = u_i; \quad \text{in infinity } \frac{\partial \varphi}{\partial x} = u_0, \quad \frac{\partial \varphi}{\partial y} = \frac{\partial \varphi}{\partial z} = 0.$$

for a moving permeable surface (for example, a trawl or a cod-end):

$$\text{on the surface } \frac{\partial \varphi}{\partial x} = -u_0 \cdot \cos(\mathbf{u} \wedge \mathbf{n}) + u_i; \quad \text{in infinity } \frac{\partial \varphi}{\partial x} = \frac{\partial \varphi}{\partial y} = \frac{\partial \varphi}{\partial z} = 0.$$

where:  $\varphi$  - a velocities potential.

## 7. Use COMSOL Multiphysics for hydrodynamic fields around permeable net structure models calculation

In order to have a possibility to vary easier netting permeability for calculations of hydrodynamic fields of various "net" structures the COMSOL Multiphysics software functions give an opportunity to combine solving of different physical fields. In particular,

parameters of flows through permeable surfaces or bodies can be defined on the basis of Brinkman's equations. These equations describe flow in porous (permeable) media where momentum transport by shear stresses in the fluid is of importance and can be applied when modeling combinations of porous media and free flow. The flow field is determined by the solution of the momentum balance equations in combination with the continuity equation:

$$\begin{aligned} \rho \frac{\partial \mathbf{u}}{\partial t} - \nabla \cdot \eta [\nabla \mathbf{u} + (\nabla \mathbf{u})^T] - \left( \frac{\eta}{k} \mathbf{u} + \nabla p - \mathbf{F} \right) &= 0 \\ \nabla \cdot \mathbf{u} &= 0 \end{aligned} \quad (5)$$

where:  $k$  - permeability of the porous structure ( $L^2$ ), other denotations are the same as in (1). The Brinkman equations account for momentum transport through viscous effects and through pressure gradients in porous media. It was suggested that the porous media is a permeable surface of netting for a fishing gear. Therefore, it is necessary to define a value of the permeability for simulated net structure model using this approach. Naturally, as the first stage of this approach using the model of the "close net cylinder" having the same dimensions as for the corresponding SNS was studied.

Fig. 14a shows this "net" structure model drawn in GUI with real dimensions. The thickness of the contour is equal to the SNS twine diameter. The "N-S" subdomain has a grey color and the "Br" subdomain is in red one. Thus, in this case, two subdomains are necessary to be used for flow velocities and pressures calculation. The "N-S" subdomain describes a flow field in/around the model basing on Navier-Stokes's equations. The contour is the "Br" subdomain that describes flow through the permeable netting contour basing on Brinkman's equations. For these subdomains values of water density  $\rho$  ( $\text{kg}/\text{m}^3$ ) and water dynamic viscosity  $\eta$  ( $\text{kg}/\text{m}\cdot\text{s}$ ) are given. The contour permeability  $k_{\text{mod}}$  has to be given for the "Br" subdomain. The real value of net structure permeability:

$$k_{\text{real}} = F_{\text{real}} - F_{\text{tw}}, \quad (6)$$

where  $F_{\text{real}}$  - the net structure common lateral area;  $F_{\text{tw}}$  - the common twine shaded area. The ratio  $F_{\text{tw}}/F_{\text{real}}$  is assumed to be the same both for the real net structure and for the model. Taking into account that the common model contour area  $F_{\text{mod}} = L \cdot t$ , the value of the model contour permeability:

$$k_{\text{mod}} = L \cdot t \cdot (1 - F_{\text{tw}}/F_{\text{real}}), \quad (7)$$

where  $L$  - the common model contour length;  $t$  - the model contour thickness.

To calculate flow velocities in/around the "net" model  $u_{\text{ns}}, v_{\text{ns}}$ , boundary conditions at the "N-S" subdomain are the following:

- an inlet margin - "inflow/outflow",
- an outlet margin - "inflow/outflow",
- top/down margins - "neutral";

Initial flow velocities at the “N-S” subdomain inlet margin:  $u = u_0$ ;  $v = v_0$ . Flow velocities at the “Br” subdomain inlet/outlet margins, i.e. at the contour’s inside/outside borders, are  $u = u_{ns}$  and  $u = u_{br}$  accordingly.

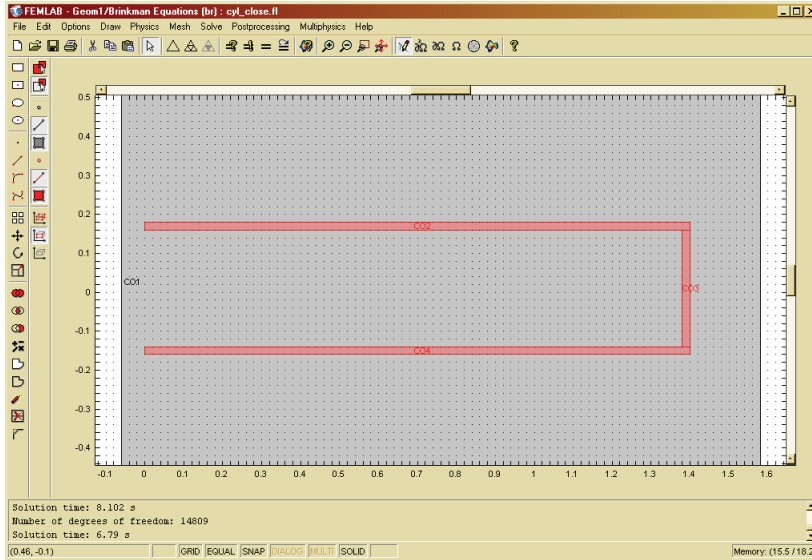


Figure 14. Net permeable model “a close cylinder” in GUI

Fig. 15 illustrates the flow distribution in/around this model. A comparison with the flow distribution in Fig. 9 shows rather similar views. Some difference is observed in the velocity dependence character.

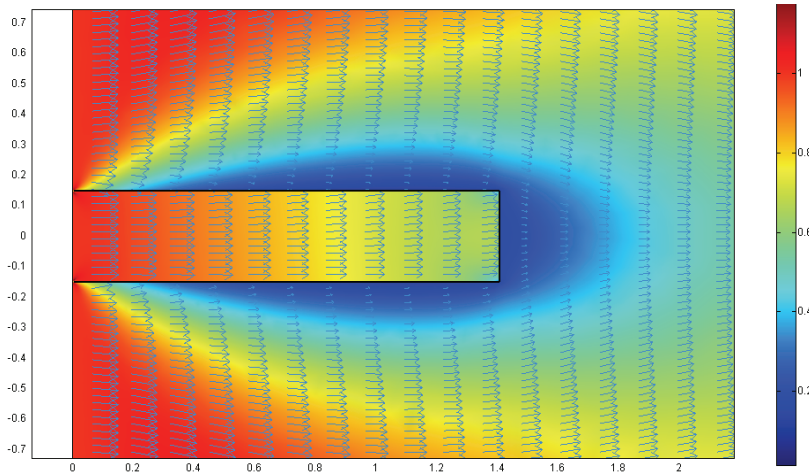


Figure 15. Flow velocities distribution for “a close cylinder” model

Obviously, the correct definition of the permeability value corresponding to real netting conditions can give a possibility to reduce so called “scale effect” and to simulate net structures. It is important that this approach allow changing values of permeability along the model if it is created in GUI as a multicomponent assembly. Fig. 16 shows the velocities field for the model “open net cone  $\alpha=10^\circ$ ”. It is possible to compare it to Fig. 11a.

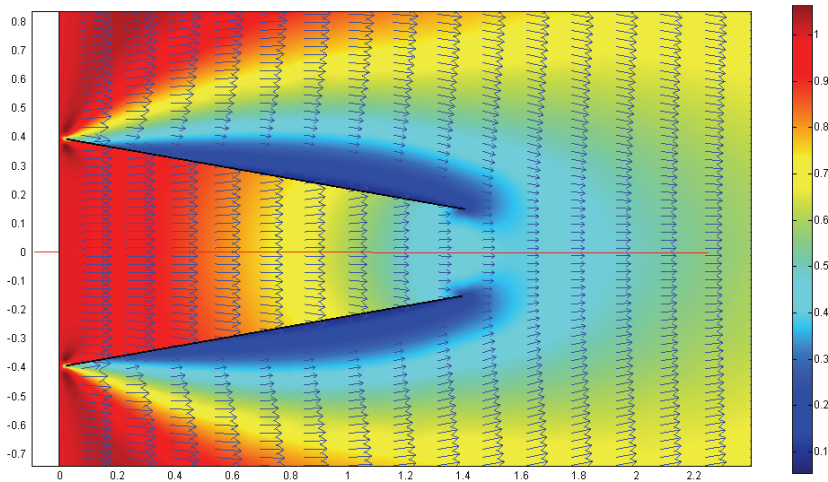


Figure 16. Flow velocities distribution for “an open net cone  $\alpha=10^\circ$ ” model

To calculate a pressure field in/around the “net” model, which are  $p_{ns}$  values boundary conditions at the “N-S” subdomain are the following:

- inlet margin – “normal flow/pressure”,
- outlet margin – “outflow/pressure”,
- top/down margins – “neutral”;

An initial pressure at the “N-S” subdomain inlet margin:  $p=p_0$ . The value of  $p_0$  is equal to the atmospheric and hydrostatic pressures sum for the real net structure. Pressures at the “Br” subdomain inlet/outlet margins, i.e. at the contour’s inside/outside borders, are  $p=p_{ns}$  and  $p=p_{br}$  accordingly.

As an example of real net structure model the contour of a cod-end model tested in the flume tank is shown in Fig. 17. When the model was tested its inlet margin, so called “mouth”, was equipped with a rigid ring in order to keep a shape under flow.

Using all mentioned parameters of “N-S” and “Br” subdomains and calculating a value of permeability for the cod-end model the flow velocities distribution was defined and presented in Fig. 18. It is possible to see that colours change from red to deep blue, i.e. value of velocities decreases to the rear part of the model. Fig. 19. shows effect filling the cod-end with a “catch”. The “catch” simulates by the “solid body” placed into the contour and having a shape similar to real catch. The distribution of the velocities is changed. The velocity decrease is stronger in the rear part of the model and just in front of the “catch” velocities are equal to zero.

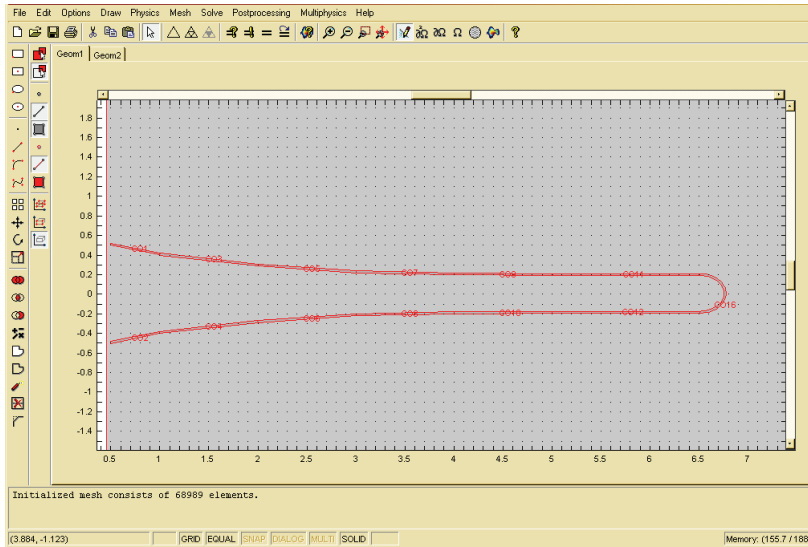


Figure 17. Net permeable model “a cod-end” in GUI

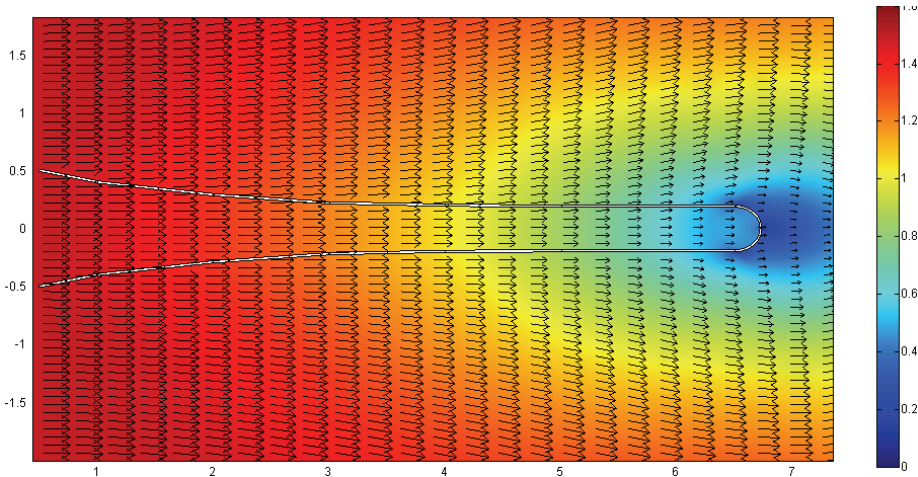


Figure 18. Flow velocities distribution for “a cod-end” model

As it was mentioned in the survey, in reality the cod-end with caught fish has another shape due to its mechanical characteristics. An approximate shape and velocities distribution is shown in Fig. 20. Here it was an artificial drawing of the cod-end shape, but it is necessary to find a solution to predict fishing gears shape under the flow and with a catch taking into account mechanical features of netting.



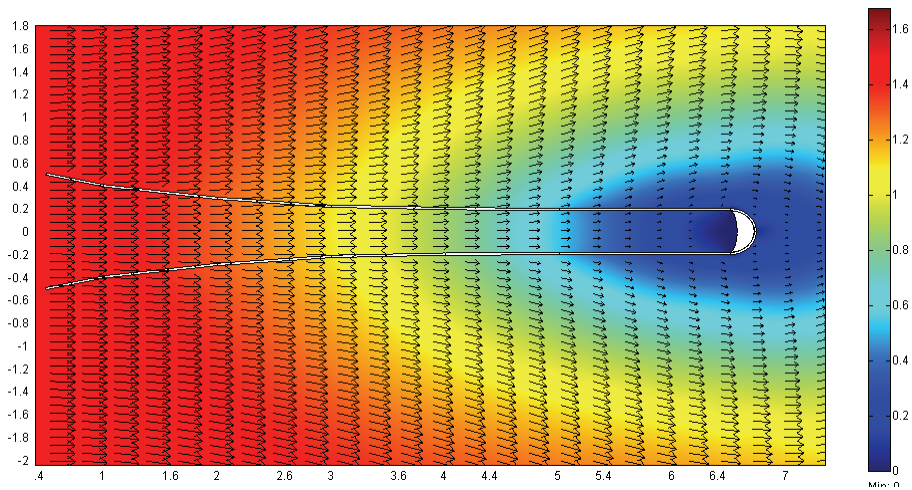


Figure 19. Flow velocities distribution for “a cod-end with “catch” model

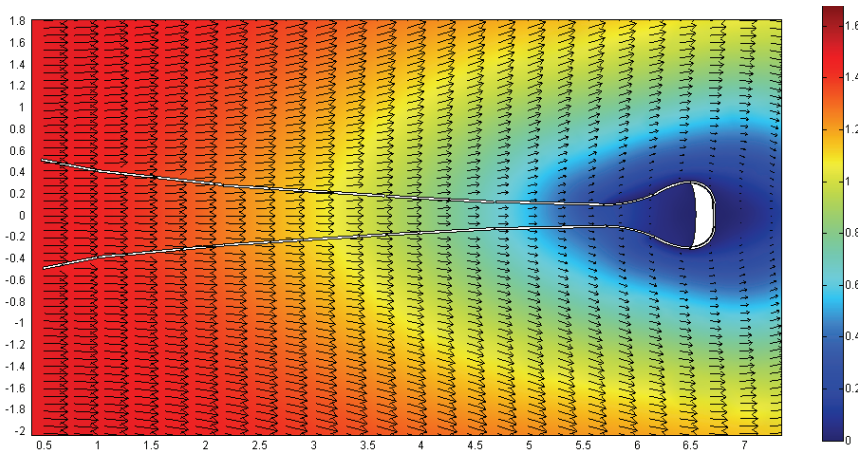


Figure 20. Flow velocities distribution for “a cod-end with “catch” model

## 8. Conclusion

The presented work considers two approaches to use a CFD method for modelling the hydrodynamic field of fishing gear net structures. These approaches are based on the COMSOL Multiphysics software use allowing to model physical fields of various bodies flow of a flow. For an estimation of applicability of the software results of experimental researches on schematized net structures (SNS) carried out in the flume tank have been used.

The SNS contour is represented as combinations of circular cross-sections in the first modelling approach. Such contour is used as the calculated object simulating twines cross-sections. Calculation of flow velocities around "solid" bodies located so that to present a net structure section made basing on Navier-Stokes equations. Comparison of a calculated

dependence of longitudinal flow velocities to the measured velocities values has shown rather satisfactory convergence of data. However, the application of the given approach faces long time for solving when the contour consists of a significant number of the simulating bodies.

The second approach uses a multiphysical statement of a problem in the software. A "net" contour represents a "permeable surface" simulation of the net structure model. A flow through the permeable surface is described by the Brinkman equations. Two subdomains are set for calculation of the structure of multiphysical hydrodynamic field:

1. The Navier-Stokes's subdomain,
2. The Brinkman's subdomain.

It is necessary to set a liquid density, its dynamic viscosity and an initial pressure for the first subdomain. For the second one it is necessary to set the permeability of the contour surface as well. Solution time using the second approach is much less than in the first one. For example, "a closed cylinder" model calculation took about 1 hour in the first case and several minutes in the second case. It is possible to see in Figs 9 and 15 the velocities field picture differs for these two approaches. A reason can be connected with correct given value of net structure permeability that depends on the flow influence on the net structure.

It is necessary to notice, that the second approach enables changes of a net contour permeability if it consists of several elements. This circumstance can be used, for example, in case of imitation of net surfaces blocking up with a catch or for calculation net structures consisting of net panels having various mesh sizes, for example for a fishing trawl.

The systematized comparison of calculated and experimental data for more reliable estimation of applicability of both methods is necessary.

In addition, researches of applicability of the method are necessary to carry out with the purpose of revealing of influence of a hydrodynamic field on the net structure shape.

## 9. References

- Baev, L. & Belov, V. (1987). Determination of a trawl cod-end model velocity field. *Rybnoe khozyaistvo*, № 1, 1987. pp. 47–48 (in Russian);
- Belov, V. (1987). Water flow in a trawl. In *proceedings of the all-Union scientific-technical workshop on hydrodynamics and fishing gears designing*, Kaliningrad, 1987, pp. 110-115 (in Russian);
- Belov, V. (2002). Water flows in trawls. *Rybnoe khozyaistvo*, № 1, 2002, pp. 51–52 (in Russian);
- Gabriuk, V. & Chernetsov, V. (1985). A raft-catamaran for hydromechanics of a trawl and its rigging investigations. *Rybnoe khozyaistvo*, № 5, 1985, pp. 65–66 (in Russian);
- Enerhaug, B.; Gjørund, S.H. & Hansen, K. (2001). Experimental, numerical and analytical studies of flow through reticulate and solid cones, *Proceedings of the 5-th international workshop "Methods for the development and evaluation of maritime technologies (DEMaT '01)"*, pp. 43–59, Rostock, November, 2001;
- Enerhaug, B. (2005). Flow through fine-meshed pelagic trawl. *Proceedings of the 7-th international workshop "Methods for the development and evaluation of maritime technologies (DEMaT '05)"*, pp. 153–163, Busan, November, 2005;
- Fredheim, A. & Faltinsen, O.M. (2001). A numerical model for the fluid structure interaction of a three-dimensional net structure, *Proceedings of the 5-th international workshop "Methods for the development and evaluation of maritime technologies (DEMaT '01)"*, pp. 61–82, Rostock, November, 2001;

- Fuwa, S., Fujita, S., Kumasawa, T. & Hirayama, M. (2007). Flow distribution in a brailer codend, *Proceedings of the 8-th international workshop "Methods for the development and evaluation of maritime technologies (DEMaT'07)"*, pp. 11–21, Rostock, October, 2007;
- Higo, N. (1964). Studies on the drag net - I; An increase of the current velocity inside the net, *Memoirs of the faculty of fisheries, Kagoshima University*, vol. 13, 1964, pp. 78-92;
- Higo N., Tokunaga Y. & Fuwa S. (1974). Studies on the drag net - III; Current velocity reduction at the inside of the net, *Memoirs of the faculty of fisheries, Kagoshima University*, vol. 23, 1974, pp. 29-34;
- Imai T. (1974). Distribution of flow-speed inside the net and performance of the net-shape, *Memoirs of the faculty of fisheries, Kagoshima University*, vol. 23, 1974, pp.45-55;
- Korotkov, V. & Meyler, L. (2000). An improved trawl cod-end design. *Rybnoe khozyaistvo*, № 4, 2000, p. 46, (in Russian);
- Korotkov, V. & Meyler L. (2001). Hydrodynamic investigations, designing and marine tests of a trawl codend with the improved conditions of a catch concentration, *Proceedings of the 5-th international workshop "Methods for the development and evaluation of maritime technologies (DEMaT '01)"*, pp. 175–187, Rostock, November, 2001;
- Kostiukov, V. & Shevchenko, A. (1983). A study of a trawls net shells hydrodynamic field. *Rybnoe khozyaistvo*, № 9, 1983, pp. 63-64 (in Russian);
- Kroeger, M. (1984). Some results of flow measurements on a full-scale pelagic trawl, *ICES-CM-1984/B: 27, Council Meeting Collected papers*. pp. 11-19, Copenhagen, 1984;
- Meyler, L. (1995). Flow speed investigation on schematized net constructions, *Report № 94/71, IFREMER, France, 1995*, 95 p.
- Meyler, L. (2000). A velocity field in a schematized net structure, *Proceedings of the international scientific-technical conference "The 70-th anniversary of the Kaliningrad State Technical University"*, Vol.2, pp. 346-347, Kaliningrad, 2000, (in Russian);
- Meyler, L. (2005). Schematized net structures for fishing gears velocity fields studying. *Rybnoe khozyaistvo*, № 4, 2005, pp. 63–64, (in Russian);
- Meyler, L. (2006). Estimation of flow speed and pressure distribution in a fishing trawl cod-end, *Comsol Users Conference, User Presentations and Proceedings CD, Prague, 2006*;
- Meyler, L. (2007). Use of COMSOL Multiphysics for a hydrodynamic field of net fishing gears calculation. *Rybnoe khozyaistvo*, № 2, 2007, pp. 105–107, (in Russian);
- Miziurkin, M. & Kostiukov, V. (1982). About hydrodynamics of a trawl. *Rybnoe khozyaistvo*, № 6, 1982, pp. 66–67, (in Russian);
- Moderhak, W. (1993). Some problems of water flow through trawl codend. *ICES Council Meeting, Fish Capture Committee, (Collected papers) L, ICES-CM-1993/B:11, Copenhagen, 1993*, 6 p.
- O'Neill, F.G. (2003). A theoretical study of the factors which influence the measurement of fishing netting mesh size. *Ocean Engineering*, № 30, 2003, pp. 2053-2063;
- Paschen, M. & Winkel, H-J. (1999). Flow investigations of net cones, *Proceedings of the 4-th international workshop "Methods for the development and evaluation of maritime technologies (DEMaT '99)"*, pp. 197–216, Rostock, November, 1999;
- Paschen, M., Köpnick, W. & Winkel, H-J. (2001). Flow investigations of net cones, *Proceedings of the 5-th international workshop "Methods for the development and evaluation of maritime technologies (DEMaT '01)"*, pp. 189–205, Rostock, November, 2001;

- Priour, D. & Herrmann, B. (2005). Catch shape in cod-end, *Proceedings of the 7-th international workshop "Methods for the development and evaluation of maritime technologies (DEMaT '05)"*, pp. 41-57, Busan, November, 2005;
- Rakhmatullin, X. (1950). Flow around a permeable body. *Bulletin of the Moscow State University. Series of physic-mathematical and natural sciences*, Moscow, № 3, 1950, pp. 41 - 55 (in Russian);
- Rehme & Scheel, (1988). Experimental investigations to flow through trawl net cones. *Seewirtschaft*, Berlin, Vol. 20, № 1, 1988, pp. 39-42 (in German);
- Scharping, K.-D. Contribution for flow investigations in a fishing net, *Fischerei-Forschung*, № 12, 1974, pp. 57-63 (in German);
- Stengel, H. & Fischer H.-J. (1964). Results of trawl model flow studies in a wind tunnel. *Fischerei-Forschung*, № 2, 1964, pp. 57-100 (in German);
- Thiele, W. (1997). Flow measurements in a trawl, *Proceedings of the 3-rd international workshop "Methods for the development and evaluation of maritime technologies (DEMaT '97)"*, pp. 19-31, Rostock, November, 1997;
- Patursson, Ø., Swift, M. R., Tsukrov, I., Baldwin, K. & Simonsen, K. (2007). Modeling Flow Through and Around a Net Panel Using Computational Fluid Dynamics, *OCEANS'06 MTS/IEEE - Boston*, Boston, Massachusetts, USA, September 2006;
- Vincent, B. & Marichal, D. (1996). Computation of the flow field in the cod-end, *ICES FTFB Working Group Meeting*, 1518, April, Woods Hole;
- Winkel, H.-J. & Paschen, M. (2001). Wind tunnel tests for fishing gear development – methods and limits, *Proceedings of the 5-th international workshop "Methods for the development and evaluation of maritime technologies (DEMaT '01)"*, pp. 29-41, Rostock, November, 2001;
- Ziembo, Z. (1974). Distribution of speed of water flowing through a trawl, *Prace Morskiego Instytutu Rybackego*, Vol. 17, Ser. B, 1974, pp. 7-17;
- Ziembo, Z. (1987, a). Correlations among velocities of water flow through the trawl, *Biuletyn Morskiego Instytutu Rybackego*, Vol. 18, № 5-6, 1987, pp. 14-20;
- Ziembo, Z. (1987, b). Flow of water in trawls, *Scottish Fisheries Research*, SFRT, 66, 1987, Aberdeen;
- Ziembo, Z. (1988). Mean velocity of bound vortex flowing around mesh bars of trawl nets, *Biuletyn Morskiego Instytutu Rybackego*, Vol. 19, № 1-2, 1988, pp. 62-71;
- Ziembo, Z. (1989). Factors affecting longitudinal velocity of water flow inside the trawl, *Biuletyn Morskiego Instytutu Rybackego*, Vol. 20, № 3-4, 1989, pp. 55-59;
- Ziembo, Z. (1993). Turbulent mixing of water flow within trawl walls and method of calculating component force of reaction, parallel to direction of motion, *Biuletyn Morskiego Instytutu Rybackego*, № 130, 1993, pp. 61-73

# Modeling and Simulation of Microscale Flows

Auro Ashish Saha and Sushanta K. Mitra<sup>1</sup>

*Department of Mechanical Engineering, Indian Institute of Technology Bombay, Mumbai  
India*

## Abstract

Modeling and simulation are very powerful tools and have become an integral part in the design and development of engineering systems. In the microscale domain, modeling and simulation have been applied in the development of microfluidic devices. Microdevices developed for sample mixing, sample dispersion, drug discovery, biochemical analysis and micropower systems have become possible only due to the impetus and insight gained from the simulation studies of fundamental microfluidic problems. Microfluidic device modeling comprises of dealing with interplay of multiphysics phenomena such as fluid flow, structure, surface and interfaces, etc. As the surface area to volume ratio increases with the decrease of the system feature size of microdevices, some physical phenomena which are insignificant in the macro domain become prominent in the micro domain. Some of the tried and tested macroscale theory and experimental results no longer show similar trends in the microscale. Hence dealing with simultaneously widely differing physics becomes too complicated in the microscale which include microfluidics, microtransport, microthermal, micromechanics, microelectronics and optics with biochemical thermodynamics and reaction kinetics. In this article, the use of numerical modeling and simulation techniques for flow in microchannels applied to microfluidic devices are presented encompassing all the relevant physics at the microscale by the state of the art multiphysics simulation tools such as CFD-ACE+, COMSOL, Fluent to name a few. Numerical simulation of electroosmotic effect on pressure-driven flows in the serpentine channel of a microfuel cell with variable zeta potential on the side walls is investigated and reported. The Poisson-Boltzmann and Navier-Stokes equations are solved numerically to investigate the electroosmotic driven flow phenomena. It is observed that vortices are developed at the straight portion of the microchannel due to the electroosmosis. Flow control in the serpentine microchannel by regulating the zeta potential at the bend has also been demonstrated. Capillary driven flow in a microchannel with alternate hydrophilic-hydrophobic patterns on the bottom wall is investigated for bioreactor applications. The transient flow is modeled by coupling the incompressible Navier-Stokes equation with the interface evolution equation using volume of fluid (VOF) methodology. Higher order surface reconstruction method is adopted for interface tracking. Flow instability increases as the fluid traverses alternately between the hydrophilic and hydrophobic regions. Such flow phenomena in the microchannel indicate that flow control is possible by patterning the channel walls for applications related to

---

<sup>1</sup> Corresponding Author; Email: skmitra@iitb.ac.in

microfluidic devices. The simulation of dynamic interaction between an elastic membrane structure and fluid in a two-dimensional microchannel is also reported here. The viscous and pressure forces imposed by the fluid flow cause the deformation of elastic membrane which significantly affects the flow field. This involves formulating a coupled fluid structure interaction (FSI) model for the demonstrated case. The solution schemes used for this analysis are based on Lagrangian formulations for the structural parts and Arbitrary Lagrangian Eulerian (ALE) formulations for the fluid regions.

**Keywords:** Modeling, microchannel, transport, simulation, electroosmotic flow, free surface flow, fluid structure interaction

## Nomenclature

$Bo$	Bond number
$Ca$	Capillary number
$C_0$	Ionic concentration in bulk solution
$D_h$	Hydraulic diameter of channel cross section
$d$	Diameter of circular top
$E$	Electric field intensity, elasticity of structure
$F$	Faraday's constant, liquid volume fraction
$F_s$	Volumetric force representing the surface tension
$H_c$	Channel depth
$h$	Local cell dimension
$L$	Half length of section of straight segment of channel, channel length
$l$	Height of structure
$n$	Normal vector
$\hat{n}$	Unit vector normal to the surface
$\hat{n}_w$	Unit vector normal to the wall
$P$	Pressure
$p$	Pressure
$Re$	Reynolds number
$R_c$	Radius of curvature of channel axis at U-bend
$R_u$	Universal gas constant
$t$	Time
$\hat{t}_w$	Unit vector tangent to the wall
$U$	Characteristic velocity
$u$	Velocity component in x-direction
$u_{in}$	Inlet velocity
$V$	Velocity vector
$V_{inlet}$	Velocity of fluid at inlet
$v$	Velocity component in y-direction, interface velocity
$W$	Channel height
$W_c$	Channel width
$w$	Velocity component in z-direction, width of base structure
$z_e$	Valance number of univalent fluid
$z_{+/-}$	Valance number of the positive/negative ions in the fluid

**Greek symbols**

$\epsilon$	Permittivity of fluid
$\lambda$	Debye length
$\mu$	Viscosity of fluid
$\phi$	Applied potential
$\psi$	Potential due to electrical double layer
$\zeta_w$	Zeta potential or wall potential
$\rho$	Density of fluid
$\rho_E$	Charge density
$\sigma$	Surface tension of fluid
$\theta$	Contact angle
$\eta$	Viscosity of fluid
$\kappa$	Curvature of the surface

**Subscripts**

$c$	Channel
$in$	Inlet
$s$	Surface tension
$w$	Wall

**1. Introduction**

Microfluidics refers to devices and methods for controlling and manipulating fluid flows with length scales less than a millimeter. Microfluidic flows are readily manipulated using many kinds of external fields (pressure, electric, magnetic, capillary, etc.). Microfluidic systems have revolutionized by automation of chemistry and biology, by enabling possibility of numerous experiments performed rapidly and in parallel, while consuming little reagent. A large surface-to-volume ratio is a common characteristic for microfluidics architecture so that, relative importance of surface to volume forces increases. A large surface-to-volume ratio results in the dominance of the viscous effect over the momentum effect. Microfluidic flow is usually a low Reynolds number flow. Fluid/surface interactions become more significant as the dimensions shrinks resulting in a very large surface-tension-driven pressure difference. Flow control is essential in many of the microfluidic systems targeted for use in biochemistry analysis, drug delivery, and sequencing or synthesis of nucleic acids, among others. Such systems use microchannels to promote efficient mixing without the use of any external means. These devices typically rely upon the balance of surface tension and fluid pressure forces to perform their function.

The use of numerical simulation and computational techniques applied to the design and development of microfluidic devices is reviewed here. The transport of pressure-driven, electroosmotic, capillary-driven and flows with fluid structure interaction in microchannels are presented. As microfluidic devices become increasingly complex, it is difficult to perform reliable experiments and hence one needs to rely on numerical tools for optimal fluidic and transport designs. There are a variety of commercially available numerical softwares that have been successfully used in modeling microfluidic devices (eg., COMSOL, CFD-ACE+, Fluent and Coventor). These tools offer multiphysics capabilities which

facilitate the coupling and simultaneous solution of different fundamental equations governing the physics of a given problem.

## 2. Electrokinetic Flows in Microchannels

Electroosmosis is the motion of fluid caused by externally applied electric potential. In practice, most surfaces contain a residual negative charge. When such charged surface comes in contact with ionizing fluid, the ions having polarity opposite to the surface charge are attracted towards the surface. These ions accumulate near the surface, forming an *electric double layer (EDL)*. In this layer ion concentration changes from a maximum value (zeta potential,  $\zeta_w$ ) near the wall to a neutral state in the fluid core. The thickness of this layer is characterized by Debye length,  $\lambda$ , which is defined as the distance from the solid surface to which the charge drops to  $e^{-1}$  (37%) of its maximum value. The typical range of zeta potential and Debye length is 20 – 150 mV and  $10^{-9}$  –  $10^{-6}$  m, respectively (Brant et al., 2005; Liechty et al., 2005). When electric potential is applied across a capillary, the ions in the EDL move under the influence of the electric field. This ion movement causes bulk fluid motion due to the momentum transfer from EDL to the fluid core.

The convective transport in micro domain is of great importance as it applies to various application such as Micro Electro Mechanical Systems (MEMS) devices, micro-heat exchangers, micro-fuel cells, etc. (Rawool et al., 2006). In fuel cells, the typical fuel such as hydrogen for Proton Exchange Membrane (PEM) or methanol for Direct Methanol Fuel Cell (DMFC), flows through the serpentine flow field present in the bi-polar plates of the cell. Due to the electric potential generated in the micro-fuel cell, a potential gradient is developed in the bi-polar plate, the direction of which is perpendicular to the flow direction. The presence of an aqueous solution in the flow field such as methanol in case of DMFC, results in electroosmosis driven flow, which is of interest for micro-fuel cell applications.

There have been a few studies reported in the field of electroosmosis driven flow in micro DMFC. Karimi and Li (2005) have modeled the electroosmotic flow in the fuel cell membrane including the electrokinetic effect. They have modeled the membrane pore to determine the electroosmotic flow through the membrane for different geometrical and operating conditions. They have reported a nonlinear increase in electroosmotic flow with increase in pore size and found that the electroosmotic drag coefficient increases linearly with pore size.

Several researchers have investigated the effect of varying zeta potential on electroosmotic flow (EOF) in microchannels (Fu et al., 2003; Herr et al., 2000; Chen et al., 2006; Lee et al., 2005; Zhang et al., 2006). Such EOF are in the direction of the pressure driven flow. The characteristics of EOF in a microchannel depend upon the nature of the zeta potential, i.e., whether it is uniform or nonuniform. Fu et al. (2003) used Nernst-Planck equation along with a Navier-Stokes solution to model the EOF that occurs when a step change in zeta potential is applied. The results indicate that a step change in zeta potential causes a significant variation in the velocity profile and also in the pressure distribution.

Microscale debris and manufacturing irregularities during fabrication of microchannels, and adsorption of organics during analysis of microchannels produce nonuniform zeta potential distributions along the channel walls. Herr et al. (2000) have shown the influence of zeta potential on the velocity profile and sample dispersion rate for electroosmotic flow in cylindrical capillaries with nonuniform zeta potential distribution. Similarly, Chen et al.



(2006) investigated numerically the effects of step change in zeta potential in a cylindrical microchannel on electroosmotic flow. It is observed that the variable zeta potential along the flow direction generated regions of positive and negative pressure gradients in the flow field. Lee et al. (2005) studied electroosmotic flow in a cylindrical microchannel with non-uniform zeta potential distribution. They showed formation of distorted electroosmotic velocity profiles and flow circulation resulting from the axial variation of the zeta potential. However, these studies are related to straight microchannels only.

Zhang et al. (2006) studied the two dimensional flow pattern in microchannels with large aspect ratios with heterogeneous zeta potentials, and discuss the formation of secondary EOF's generated by wavelike zeta potential. Their results show that the heterogeneous zeta potentials could generate complex flow patterns and enhance mixing. However, their study may not be representative for microchannels with nearly square cross section.

Souders et al. (2003) have studied combined electroosmotic and pressure driven flows in a three dimensional microchannel with walls covered by charged bands. Under the influence of electroosmotic flow only, it is found that there is a significant amount of fluid folding and stretching. By adding pressure gradient against electroosmotic flow, they showed an increase in the fluid particle residence time. The helical flow structure is also observed for this combined electroosmotic and pressure driven flow.

Fuel feed into the micro fuel cell is an important process affecting its power density and often there is a need to minimize power loss accounting from fuel delivery. Buie et al. (2006) presented a novel design and performance of a planar silicon electroosmotic pump (EO) for methanol fuel delivery in DMFC. Though the EO pump could not deliver enough pressure head for fuel delivery, nevertheless it was interesting to note that the micro DMFC has shown to have improved polarization and power density characteristics with the EO pump. The study in particular emphasizes the performance enhancement due the combined mechanism of electroosmotic phenomena and diffusion for fuel delivery.

Rawool and Mitra (2006) studied the transport of methanol in micro-fuel cell under the applied potential which is perpendicular to the direction of the flow with the side walls of the channels subjected to a constant zeta potential. As observed in the existing literature (Herr et al., 2000; Chen et al., 2006) the zeta potential tend to change along the flow field as the fuel gets consumed in the chemical reaction occurring at the catalyst layer, adjoining the flow channels. The heterogeneous zeta potentials in microchannels can also be achieved through chemical modifications, coupled capillaries and integrated systems (Zhang et al., 2006). Hence, Saha et al. (2007) performed numerical studies to understand the flow behavior in the microchannel of the fuel cell under variable zeta potential conditions.

## 2.1 Governing Equations

The force acting on ions is accommodated as a body force in Navier-Stokes equation, which reads as

$$\rho(V \cdot \nabla)V = -\nabla P + \mu \nabla^2 V + \rho_E E \quad (1)$$

where  $\rho_E$  is the charge density and  $E$  is the electric field. For steady flow with constant properties, the continuity equation can be written as

$$\nabla \cdot V = 0 \quad (2)$$

The electric field  $E$  in Eqn. (1) has two contributions. One is the field due to applied potential ( $\phi$ ) for which governing equation is

$$\nabla^2 \phi = 0 \tag{3}$$

The second contribution is the field due to EDL which is governed by the equation

$$\nabla^2 \psi = -\frac{\rho_E}{\epsilon} \tag{4}$$

The charge density is given by

$$\rho_E = FC_0 z_- e^{(z_- F\psi/R_u T)} - FC_0 z_+ e^{(z_+ F\psi/R_u T)} \tag{5}$$

which, for a symmetric electrolyte of valance number  $z_c$  becomes

$$\rho_E = 2FC_0 \sinh\left(\frac{z_c F\psi}{R_u T}\right) \tag{6}$$

where  $\psi$  is the potential due to electrical double layer,  $F$  is Faraday's constant,  $R_u$  is universal gas constant. The Poisson-Boltzmann and Navier-Stokes equations are solved numerically to investigate the electroosmotic driven flow phenomena for prescribed operating conditions.

### 2.2 Numerical Simulation

#### Physical Problem

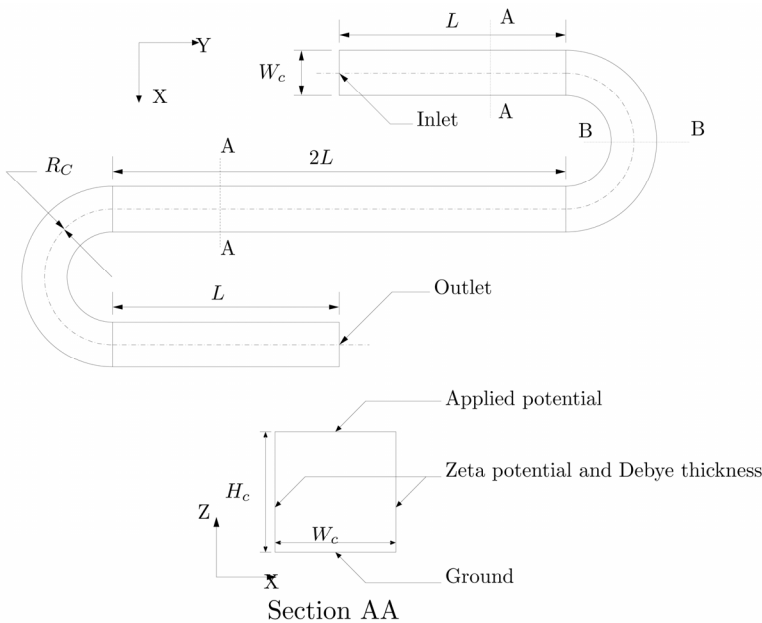


Figure 1. Geometry of serpentine channel

In Fig. 1 schematic of the serpentine microchannel model is shown. The channel considered here is a three dimensional serpentine channel. The cross sectional area of the channel is  $100 \mu m \times 100 \mu m$ . The model consists of a single 'S' shaped segment of the serpentine channel. It has three straight lengths connected by two semicircular arcs. In Fig. 1 length  $L = 300 \mu m$  and the radius of curvature at bend is  $R_c = 200 \mu m$ .

**Boundary Conditions**

For fluid flow, a constant velocity corresponding to a given Reynolds number is specified at the channel inlet. At outlet, a constant pressure (atmospheric) is specified. No slip boundary condition is imposed on all the remaining walls. Following is the mathematical representation of the above conditions:

$$\left. \begin{aligned} u &= 0 \\ v &= Const. \\ w &= 0 \end{aligned} \right\} \text{ for } \left\{ \begin{aligned} 0 &< x < 100 \mu m \\ y &= 0 \\ 0 &< z < 100 \mu m \end{aligned} \right.$$

$$P = 0 \quad \text{for } \left\{ \begin{aligned} 4R_c \mu m &< x < 4R_c + 100 \mu m \\ y &= 0 \mu m \\ 0 &< z < 100 \mu m \end{aligned} \right.$$

$$\left. \begin{aligned} u &= 0 \\ v &= 0 \\ w &= 0 \end{aligned} \right\} \text{ for all other boundaries}$$

For electric field, a fixed potential is specified at top and bottom walls of the channel, as shown in Fig. 1, which can be expressed as,

$$\phi = 0 \text{ Volt for } \left\{ \begin{aligned} z &= 0 \\ \text{for all } x \text{ and } y \end{aligned} \right.$$

$$\phi = 0.1 \text{ Volt for } \left\{ \begin{aligned} z &= 100 \mu m \\ \text{for all } x \text{ and } y \end{aligned} \right.$$

A zeta potential and Debye length are specified on the side walls of the channel as shown in Fig. 1. The Debye length is kept constant at  $1 \times 10^{-7} m$ . The zeta potential is varied linearly on both walls, to investigate the effect of zeta potential profile on the electroosmotic flow. The variable zeta potential condition can be expressed mathematically in the following manner:

$$\zeta_w = -0.01 - \frac{(0.09 - 0.01)}{(100 \times 10^{-6})} ZV \quad \text{for } 0 < z < 100 \mu m \quad \} \text{ On the left and right wall}$$

**Numerical Technique**

The channel geometry is created and meshed using CFD-GEOM modeler. Structured grid is used for simulations. A grid independence study is carried out by successively refining the grid, increasing the number of elements in the domain. The grid is made extra fine in the near wall region where maximum gradients occur. For a grid having 260431 elements, the solution is found to be grid independent. Hence this mesh size was used in all the cases.

CFD software CFD-ACE+ is used for the simulations. Upwind scheme is used in the CGS+Pre solver (ESI CFD Inc., 2006) for velocity and electric field while AMG solver is used for pressure correction. Parametric solver is used to solve for values of inlet velocity corresponding to a range of Reynolds number. A Reynolds number of 0.001 is used in the simulations. Here, Reynolds number is defined as

$$Re = \frac{\rho V_{inlet} D_h}{\mu}$$

where  $D_h$  is the hydraulic diameter of the channel, defined as

$$D_h = \frac{4(W_c \times H_c)}{2(W_c + H_c)}$$

Here  $W_c$  is the width of the channel and  $H_c$  is the depth of the channel as shown in Fig. 1. The effect of zeta potential profile on the velocity profile in the channel is studied. The physical and dielectric properties of methanol at 25° C used for simulations are provided in Table 1.

Physical property	Value	Dielectric property	Value
Density ( $kg/m^3$ )	785	Electric conductivity (1/ohm-m)	$4.4 \times 10^{-4}$
Viscosity ( $Pa. s$ )	$5.6 \times 10^{-4}$	Relative permittivity	33.62

Table 1. Properties of methanol

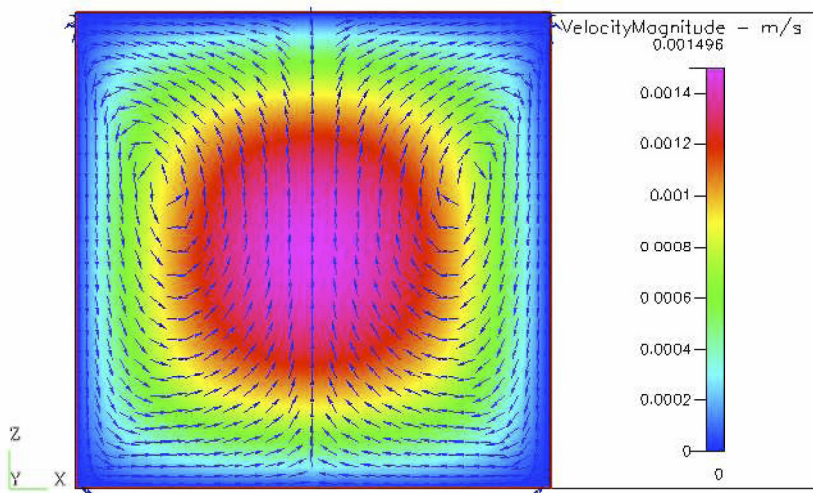


Figure 2. Flow pattern in the channel cross section at 150  $\mu m$  from channel inlet (section AA in Fig. 1)

**Results and Discussion**

The velocity vectors in the straight portion of the microchannel, at a distance of 150  $\mu m$  from the channel inlet, is shown in Fig. 2. The color indicates the velocity magnitude  $\sqrt{u^2 + v^2 + w^2}$  while the vectors indicate direction of  $\sqrt{u^2 + w^2}$ . It can be

seen that due to electroosmotic driving force, a secondary vortex pair has been generated in the flow cross section such that the fluid near the side walls moves towards the bottom plate. The fluid again rises in the central portion of the channel to maintain the continuity. Thus two distinct vortices are formed due to electroosmosis. These kind of vortices are absent in case of flow without electroosmosis. This modified flow profile gives rise to additional pressure drop in case of flow with electroosmosis (Rawool & Mitra, 2006). The centers of both the secondary vortices are shifted towards the top wall due to gradual change in the electroosmotic driven force on the fluid as the zeta potential is linearly varied for each wall. This results in shifting of the secondary vortex by a smaller distance. The streamline plot is shown in Fig. 3 which depicts the formation of vortices and the effect of variable zeta potential is clearly seen.

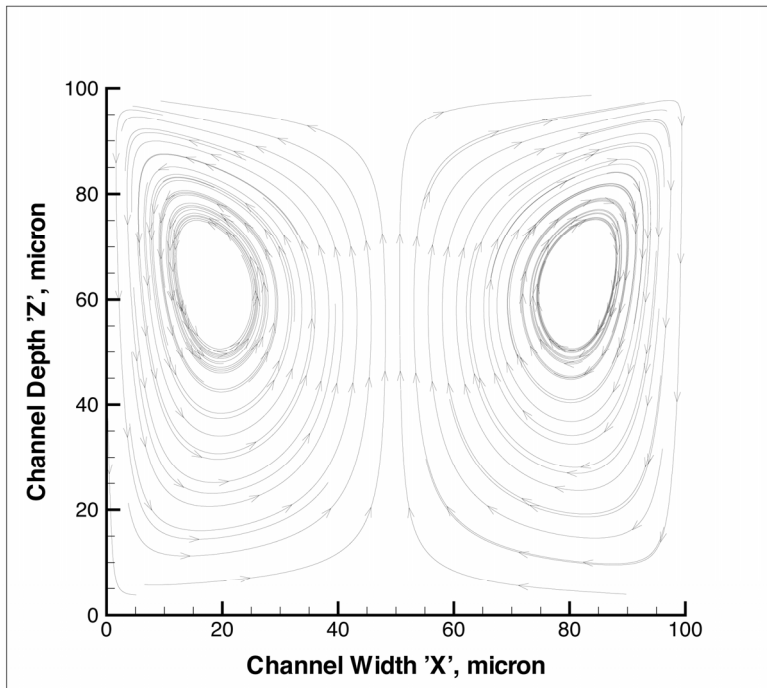


Figure 3. Streamline plot in the channel cross section at  $150\ \mu\text{m}$  from channel inlet (section AA in Fig. 1)

The flow behavior at the semi-circular bend for section BB in Fig. 1 has also been studied for four different cases. Figure 4 shows the streamline plots at the bend for pressure driven flow and the applied zeta potential of  $-0.1\ \text{mV}$ ,  $-1\ \text{mV}$  and  $-50\ \text{mV}$ , respectively. Fig. 4a shows the formation of vortices purely due to the pressure-driven flow with no contribution from the electroosmotic effect. As the applied zeta potential is increased at the semi-circular bend (section BB in Fig. 1), the electroosmotic forces cause the vortices to shift in a clockwise direction as shown in Fig. 4d. The observed shift of secondary vortices in a clockwise direction with an increase in the applied zeta potential presents an excellent opportunity for obtaining flow control in the serpentine microchannel by regulating the zeta potential at the

bend. Formation of additional vortices at the top left and bottom right corners has also been observed when the applied zeta potential is  $-0.1$  mV, as shown in Fig. 4b.

Figure 5 shows the  $z$  component of velocity along the channel width at  $z = 50 \mu\text{m}$  for the cross section BB. It is observed here that for a pressure-driven flow only, the  $z$  component velocity is zero as the secondary vortices appear at the center line and results in a zero velocity at the central core. It is found that the  $z$  component reaches a maximum at a small distance from the wall when zeta potential of  $-0.1$  mV,  $-1$  mV and  $-50$  mV is applied on the side walls. The maximum velocity is reached for the  $-50$  mV of applied zeta potential and decreases in magnitude as the applied zeta potential is reduced. The velocity component then drops to zero and again reaches a maximum value in opposite direction at the center of the channel. Hence, it can be concluded that the  $z$  component velocity influences the formation of vortices in the semi-circular bend at the cross section BB and results in the shifting of the vortices in the clockwise direction.

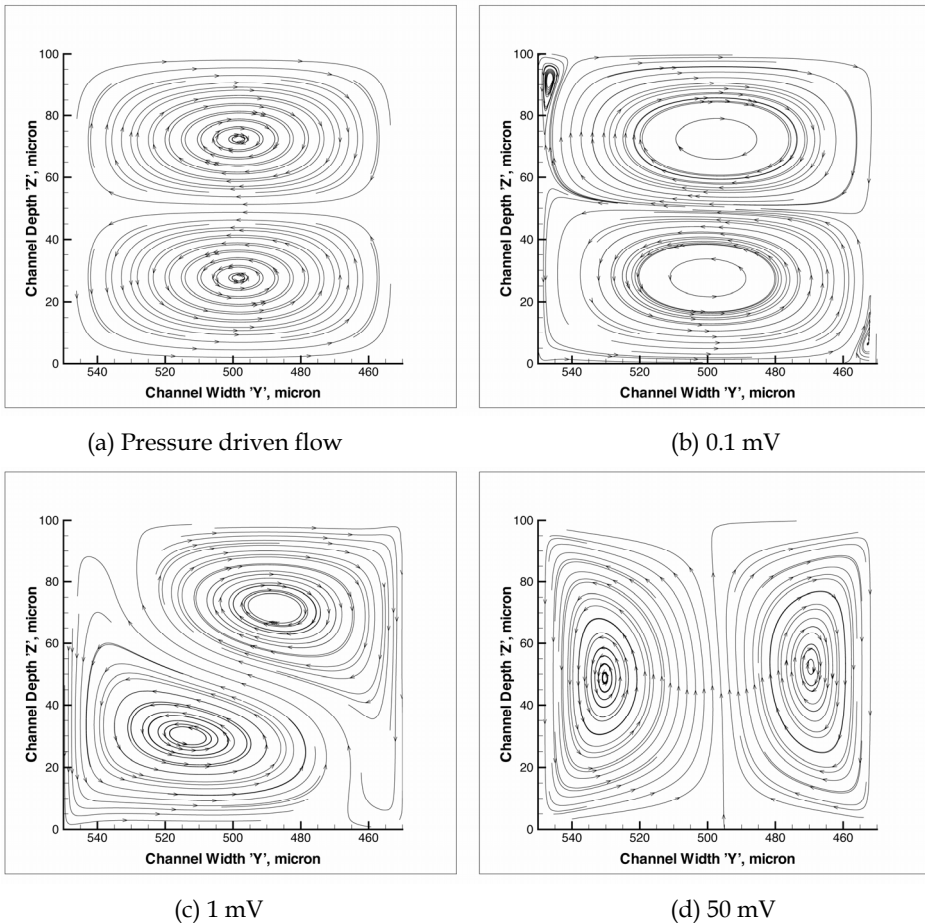


Figure 4. Streamline plots in the channel cross section at the bend (section BB in Fig. 1) for different zeta potential values

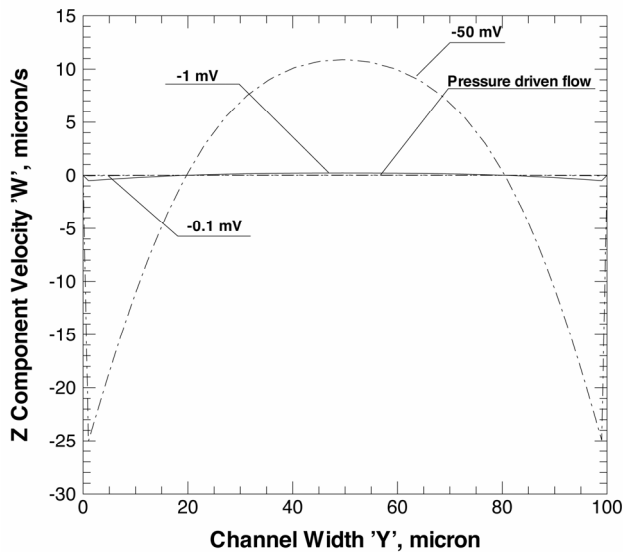


Figure 5. Variation of  $z$  component of velocity at  $z = 50 \mu\text{m}$  along the channel width at section BB

### 3. Free Surface Flows in Microchannels

An interface between a gas and liquid is often referred to as a free surface. There are large differences in the densities of the gas and liquid at the interface. The only influence of the gas is the pressure it exerts on the liquid surface and hence the gas-liquid surface is not constrained, but free.

There are three essential features needed to properly model free surfaces: (1) A scheme is needed to describe the shape and location of a surface, (2) An algorithm is required to evolve the shape and location with time, and (3) Free-surface boundary conditions must be applied at the surface. The free surface problem has been formulated by using Lagrangian and Eulerian representation of continuum motion. In Lagrangian algorithms the nodes move with continuum, in Eulerian algorithms the nodes stay in place while the continuum moves through the stationary mesh or through Eulerian coordinate system. Non-Lagrangian algorithms deal with convection (advection) effect. The Lagrangian Grid Methods follow the Lagrangian formulation. The principal limitation of Lagrangian methods is that they cannot track surfaces that break apart or intersect. Arbitrary-Lagrangian-Eulerian (ALE) method exploit the merits of both Lagrangian and Eulerian formulation. Where as, Surface Height Method, Marker-and-Cell (MAC) Method, Surface Marker Method, Volume-of-Fluid (VOF) Method are purely based on Eulerian formulations. In Lagrangian or ALE-approaches, the free-surface always falls on the boundary of the computational domain. Hence, such methods do not pose any additional difficulty in applying complex boundary conditions. However these methods suffer the deficiency of requiring frequent remeshing. The choice of Lagrangian/ALE-method as opposed to VOF-variants, is based mainly on the type of problem and degree of precision to which the resulting free-surface is to be determined

(Sujatha et al., 2006). VOF technique tracks the fraction of each phase in every computational cell to extract the interface shape. The most successful of the various free surface methods is the VOF technique because of its simplicity and robustness.

Manipulating gas and liquid flows within networks of microchannels is crucial in the design and fabrication of microfluidic devices. As the surface area to volume ratio increases, fluid/surface interactions become more significant with smaller fluidic channels (Madou, 2002). Research on patterned surfaces revealed interesting phenomena that can be exploited to control liquid motions in microfluidic devices. Hydrophobic and hydrophilic regions inside microchannels can be patterned through surface modification. However, fabrication of such patterned surfaces with selective surface characteristics is highly challenging task (Deval et al., 2004).

There have been a few studies reported for flow in patterned microchannels. Zhao et al. (2001) used surface directed liquid flow to create pressure sensitive switches inside channel networks. Self assembled monolayer chemistry is used in combination with multi-stream laminar flow and photolithography to pattern surface inside the microchannel networks. Kim et al. (2002) carried out experimental and numerical investigation for microchannel transient filling process with surface tension. A linear relationship between the dimensionless pressure and capillary number is observed. Their experimental observations indicate that flow blockage in the narrowest width channel is enabled by the surface tension and not by viscous effect.

Yang et al. (2004) discuss the method to characterize the surface energy inside a microchannel by monitoring the marching velocity of capillary meniscus. They formulated one-dimensional mathematical model and performed experimental validation of liquid filling in a capillary. Parylene and silicon nitride microchannels, which are fabricated using surface micromachining technology, are used for experimentation. The study indicates the influence of surface tension driven flow for fluid delivery in microfluidic systems.

Salamon et al. (2005) used finite element based numerical method to study a three-dimensional flow of Newtonian fluid in a 80  $\mu\text{m}$  high microchannel with superhydrophobic lower and upper walls. They have shown a 40% flow enhancement over the smooth non-patterned surface and a apparent slip length of 5.4  $\mu\text{m}$ . Byun et al. (2005) performed numerical visualization to investigate the effect of surface wettability in microchannel on the flow characteristics. The importance of hydrophobic and hydrophilic characteristics on a surface for the handling and control of liquid in the micro-systems are emphasised. The study shows the occurrence of flow instability in the flow path when the meniscus crosses hydrophilic/hydrophobic interface. Dalton et al. (2006) discuss issues in implementing superhydrophobic surfaces by nanostructured posts in a microchannel. The understanding and elimination of contact line movement effects on drag reduction is illustrated. Yang and Przekwas (1998) developed the computational methodology to model surface tension effects of multi fluid flow in ACE+MEMS CAD software. They present systematic validations against analytical solution for typical flows in MEMS devices. The unsteady motion of the free surface governed by the Hamilton-Jacobi evolution equation is solved on Eulerian grid using the Volume of Fluid (VOF) technique. Hirt and Nichols (1981) describe the concept of VOF method for treating complicated free boundary configurations. For simulation related to free surface flows, the water/air interface is characterized by surface tension and sharp changes in viscosity and density (Kothe et al., 1996). Among several general multiphase



models currently in use, the VOF model is the only multiphase model that enables identification of the interface clearly (Yian & Lawal, 2006).

Huang et al. (2006) have studied theoretically and numerically the capillary filling flows inside patterned surface microchannels. Two different patterned microchannel configurations - inner walls patterned with unequal contact angles; each inner wall divided into two equal segments having different contact angles have been considered for carrying out two-dimensional and three-dimensional simulations. Equivalent contact angle model based on surface energy method has been proposed for estimating capillary flows inside the patterned surface microchannels and they validated the model with traditional capillary rise theories.

A new method has been developed to modify the hydrophobic and hydrophilic nature of silicon surfaces by the use of 5-(4-Hydroxyphenyl)-10, 15, 20-tetra (p-tolyl) porphyrin self assembled monolayer (SAM) (Nayak et al., 2007; Mitra & Saha, 2008). The bare SiO<sub>2</sub> substrate exhibited a contact angle of 33 ± 2° showing hydrophilic nature of the surface. In the case of Hydroxy-phenyl porphyrin SAM, the contact angle is found to increase up to 75 ± 3°, indicating a hydrophobic nature of the surface due to the formation of SAM on the SiO<sub>2</sub> surface.

Saha and Mitra (2007, 2008) presented numerical study on the surface dominated flow behavior in a channel with unsymmetrical distribution of surface characteristics with respect to channel axis. A three-dimensional (3D) numerical simulation of flow in patterned microchannels with alternate hydrophilic and hydrophobic surfaces at the bottom wall is considered. Hydrophilic surface induces the acute static contact angle while hydrophobic surface results in the obtuse static contact angle. Passive capillary driven flow phenomena in the microchannel is considered in their study. Capillary driven flows are purely governed by the forces associated with surface tension (Probstein, 1994) and offer positive flow enhancement effect.

### 3.1 Governing Equations

#### VOF Model

The simulations of the capillary flows in the patterned-surface microchannels are performed using a VOF method. In this method, a volume fraction transport equation is employed in addition to the continuity and momentum equations. Two phases (gas-liquid) are treated as a homogeneous gas-liquid mixture. The flow is considered to be laminar, non-gravity, incompressible, Newtonian and isothermal with velocity field  $V$  and governed by the Navier-Stokes and continuity equations, as provided here:

$$\nabla \cdot V = 0 \quad (7)$$

$$\frac{\partial \rho V}{\partial t} + \nabla \cdot (\rho V V) = -\nabla P + \nabla \cdot (\mu (\nabla V + \nabla^T V)) + F_s \quad (8)$$

where  $V$  is the velocity of the mixture,  $P$  the pressure,  $t$  the time,  $F_s$  the volumetric force at the interface resulting from surface tension, and  $\rho$ ,  $\mu$  are the density and viscosity, respectively. In this equation the accumulation and convective momentum terms in every control volume (cell) balance the pressure force, shear force, and additional surface tension force  $F_s$ . Surface tension arises as a result of attractive forces between molecules in a fluid and it is represented as force acting only at the surface, which is required to maintain equilibrium in such instances.

The numerical simulation of free surface flows composed of two immiscible fluids involves two coupled tasks namely resolving the flow field and updating the position of the interface. This involves the application of SIMPLE algorithm (Patankar, 1980) and extending it to include the VOF methodology (Hirt & Nichols, 1981; Kothe et al., 1996). VOF method allows for the simulation of a mixture of two incompressible and immiscible fluids including surface tension effects. The VOF model includes the effects of surface tension along the interface between each pair of phases. The model can be augmented by the additional specification of the contact angles between the phases and the walls. The fluids under consideration are DI water as liquid and air as gas. The tracking of the interfaces between the phases is accomplished by the solution of a continuity equation for the volume fraction of any of the phases. The fields for all variables and properties are shared by the phases and represent volume-averaged values, as long as the volume fraction of each of the phases is known at each location. Thus the variables and properties in any given cell either represent one or a mixture of the phases, depending upon the volume fraction values. The distribution of the liquid phase is described by using a single scalar field variable,  $F$ , which defines the fraction of the liquid volume. Here,  $F = 1$  represents liquid,  $F = 0$  represents gas and  $0 < F < 1$  represents the liquid/gas interface. The volume fraction distribution can be determined by solving the passive transport equation, given as:

$$\frac{\partial F}{\partial t} + V \cdot \nabla F = 0 \quad (9)$$

where,

$$F = \frac{\text{cell volume occupied by liquid}}{\text{total volume of the control cell}} \quad (10)$$

The mixture's physical properties are derived from that of the two phases through the volume fraction function. In particular, the average value of any volume-specific quantity,  $\rho$  in a computational cell can be computed from the value of  $F$  in accordance with:

$$\rho = F\rho_2 + (1-F)\rho_1 \quad (11)$$

where the subscripts 1 and 2 represent the gas phase and the liquid phase, respectively. For an intensive quantity,  $\mu$ , the effect of density can be included as given below:

$$\mu = (F\rho_2\mu_2 + (1-F)\rho_1\mu_1) / (\rho_1 + \rho_2) / 2 \quad (12)$$

The surface tension model follows the continuum surface force (CSF) model proposed by Brackbill et al. (1992). The surface tension is specified as a source term  $F_s$  in Eq. 8 according to the CSF model:

$$F_s = \frac{\rho\sigma\kappa\nabla F}{(\rho_1 + \rho_2) / 2} \quad (13)$$

The surface tension is taken to be constant along the surface and only the forces normal to the interface are considered. According to the CSF model, the surface curvature  $\kappa$  is computed from local gradients in the surface normal to the interface, which is given as:

$$\kappa = \frac{1}{|n|} \left( \left( \frac{n}{|n|} \cdot \nabla \right) |n| - \nabla \cdot n \right) \quad (14)$$

where  $n = \nabla F$  is the normal vector. Wall adhesion is included in the model through the contact angle:

$$\hat{n} = \hat{n}_w \cos \theta + \hat{t}_w \sin \theta \quad (15)$$

where  $n$  is the unit vector normal to the surface,  $\hat{n} = \frac{n}{|n|}$ ,  $\hat{n}_w$  and  $\hat{t}_w$  represents the unit vector normal and tangent to the wall, respectively. The interface needs to be constructed based on the computed value of the volume fraction with the application of interpolation schemes for the identification of the interface. An upwind scheme with the piecewise linear interface construction (PLIC) method, is adopted for surface reconstruction (Kothe et al., 1996). In the PLIC scheme, the liquid-gas interface is assumed to be linear and can take any orientation within the cell. The reconstructed interface is represented by line segments in a two-dimensional flow and by an arbitrary polygonal face for three-dimensional flows. The reconstruction is required at every time step to include the necessary back-coupling of surface forces to the momentum equations as well as flux calculations. Equations (7) – (15) are solved iteratively to obtain the liquid volume fraction and the velocity field solution under appropriate initial and boundary conditions.

For the channel height of 100  $\mu\text{m}$  selected in this study, the Bond number (Bo),  $\rho g H^2 / \sigma$ , and Capillary number (Ca),  $\mu U / \sigma$ , are much less than unity. Hence, the effects of gravity and dynamic contact-angle are not taken into account in the present study.

The solution of the passive transport equation in conjunction with the standard conservation equations in CFD-ACE+ requires three related actions: (1) Compute mixture properties, (2) Reconstruct the fluid-fluid interface in each cell, and (3) Determine the contribution of the secondary fluid flux to the equations for conservation of mass, momentum, energy and volume fraction. The classification of the VOF method as a volume-tracking method follows directly from the use of the single scalar variable  $F$  to describe the liquid distribution and to solve for the liquid volume evolution. One consequence of the purely-volumetric representation of the phase distributions is that there is no unique definition of the interface between the two phases. As such, if the location of the interface is required for any modeling, computational, or visualization purpose, then it must be dynamically reconstructed from the  $F$  distribution. In CFD-ACE+, surface reconstruction is a prerequisite for determining the flux of fluid two from one cell to the next and for determining surface curvatures when the surface tension model is activated. In the PLIC scheme (Fig. 6), the liquid-gas interface is assumed to be planar and allowed to take any orientation within the cell, and will therefore generally have the shape of an arbitrary polygonal face. The facet in a cell is fully defined by specifying: (i) the spatial orientation of the infinite plane that contains the facet; and, (ii) the location of a point within the cell through which the infinite plane passes. The orientation is specified by specifying the outward-pointing unit normal of the infinite plane, and the sense of the normal is here arbitrarily chosen so that it points out of the liquid phase and into the gas phase. The unit normal of the plane is determined by assuming that it is parallel to the gradient vector of  $F$ . The gradient of  $F$  is determined from the local distribution of  $F$  in a set of cells which includes the target cell and all its immediate

neighbors. The location of the anchor point is determined by finding the infinite cutting plane perpendicular to the unit normal of the infinite plane that truncates the correct liquid volume from the cell, in that it satisfies the condition:

$$V_{cut} = F.V_c \tag{16}$$

where  $V_{cut}$  is the volume of the cell truncated by the cutting plane,  $V_c$  is the volume of the whole cell, and  $F$  is as defined above. In the PLIC scheme, each cell has a unique surface normal that can be used to compute the surface curvature from cell to cell. This calculates and adds surface tension forces for the free surfaces.

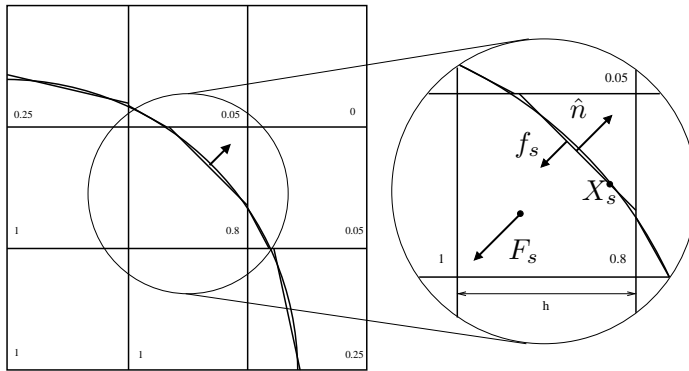


Figure 6. PLIC reconstruction scheme

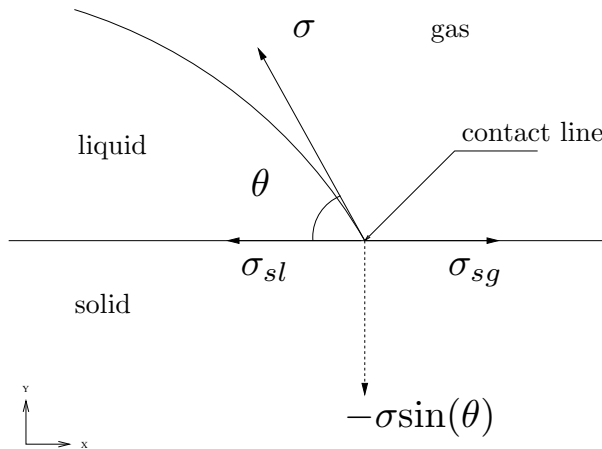


Figure 7. Contact angle

**Lucas-Washburn Model**

Analytical solution for the propagation of a liquid in a channel is derived in the following sections. The analytical solution is based on the Navier-Stokes equation for incompressible, quasi-steady, laminar, Newtonian 2D horizontal flow,

$$-\frac{\partial P}{\partial x} = -\mu \frac{\partial^2 u}{\partial y^2} \tag{17}$$

where  $P$  is the pressure in the fluid at  $x$ ,  $\mu$ , is the viscosity of the fluid,  $u$  is the velocity of the fluid. For a fully developed capillary driven flow, the analysis on the balance of viscous force, surface tension force, and gravitational force yields the classical Lucas-Washburn equation on the penetration length,  $L$ , evolution with time,  $t$  (Washburn, 1921).

For static wetting of a liquid between two surfaces, the minimization of surface area of a liquid may result in a curved interface. The general Young's-Laplace equation describes the relation for the pressure difference across the interface as (Fig. 7):

$$\Delta P = \sigma \left( \frac{1}{R_1} + \frac{1}{R_2} \right) \tag{18}$$

where  $\Delta P$  is the pressure difference,  $\sigma$  is the liquid surface tension, and  $R_1$  and  $R_2$  are the radius of curvature of the interface in directions perpendicular and parallel to the liquid stream. For a two-dimensional channel  $R_2 = \infty$ .

Therefore,

$$\Delta P = \sigma \frac{1}{R} \tag{19}$$

From Fig. 8,

$$R = \frac{h}{2\cos\theta} \tag{20}$$

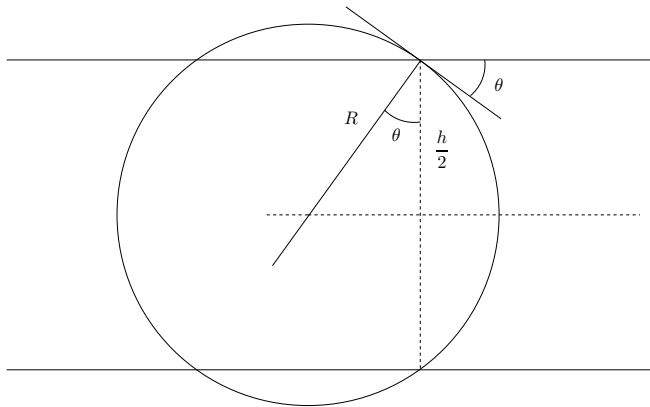


Figure 8. Meniscus in channel

For steady 2D Poiseuille flow,

$$u_{avg} = \frac{1}{12\mu} \frac{\Delta P}{L} h^2 \tag{21}$$

Also,

$$u_{avg} = \frac{dL}{dt} \quad (22)$$

Thus,

$$L = \left( \frac{ht\sigma\cos\theta}{3\mu} \right)^{\frac{1}{2}} \quad (23)$$

It shows that the flow time is inversely proportional to the surface tension, separation distance, and the cosine of the wetting angle, and directly proportional to the viscosity and the square of the flow distance.

### Reduced Order Model

Consider a microchannel, height of which is  $h$ , initially is filled with liquid (density  $\rho$ , dynamic viscous coefficient  $\mu$ ) length of  $L_0$ . The contact property between the liquid and channel wall is defined by surface tension coefficient  $\sigma$  and contact angle  $\theta$ . An overhead pressure is  $\Delta P$ . For a passive capillary filling process,  $\Delta P=0$ . The surface tension force and the pressure overhead drive the liquid free surface in the microchannel.

At time  $t$ , the liquid length is denoted  $L$ , and average velocity is denoted  $u$ . The velocity profile is assumed two-dimensional Poiseuille. The momentum of the liquid column may be written as  $\rho hLu$ . The momentum conversation may be expressed as momentum change is balanced by the sum of the surface tension force, pressure overhead and wall viscous force.

$$\frac{d}{dt}(\rho hLu) = 2\sigma\cos\theta + \Delta Ph - \frac{12\mu L}{h}u \quad (24)$$

The term denoting the momentum change is often omitted, with quasi-steady state assumption (Zeng, 2007). Considering in microfluidics that (1) the Reynolds number is always very small; and (2) the surface tension force is always dominant; this quasi-steady state assumption is valid except for the initial starting stage that is highly transient. In the reduced order model a transient solution is derived accounting for all terms in the equation above. Noting  $u = dL/dt$ , the equation above can be re-written as

$$\frac{d^2}{dt^2}L^2 + B\frac{d}{dt}L^2 = A \quad (25)$$

where,

$$A = \frac{4\sigma\cos\theta + 2\Delta Ph}{\rho h}, B = \frac{12\mu}{\rho h^2} \quad (26)$$

Considering initially the liquid holds column length of  $L_0$  and with zero velocity, the transient solution of the capillary filling problem is given below:

$$L = \left( \frac{A}{B^2} \exp(-Bt) + \frac{At}{B} + \left( L_0^2 - \frac{A}{B^2} \right) \right)^{\frac{1}{2}} \quad (27)$$

$$u = \frac{A(1 - \exp(-Bt))}{2BL} \tag{28}$$

where  $t$  is the time of the filling process,  $L$  is the position of free surface front,  $u$  is the average filling speed.

### 3.2 Numerical Simulation

#### Physical Problem

In Fig. 9 geometry of the microchannel model is shown. The channel considered here is a three-dimensional straight channel. The cross sectional area of the channel is  $100 \mu\text{m} \times 100 \mu\text{m}$ . The model consists of a single straight segment of  $1000 \mu\text{m}$  in length. Alternate patterns of hydrophilic and hydrophobic surface arrangement is shown on the bottom wall of the channel geometry, to account for the surface tension effect on the flow.

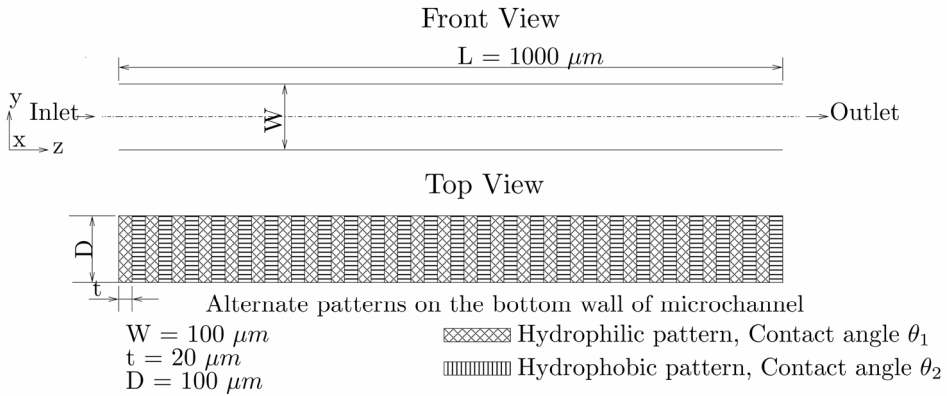


Figure 9. Geometry of microchannel

#### Initial and Boundary Conditions

Initially, at time  $t = 0$ , the liquid meniscus position in the channel is set as  $1 \mu\text{m}$ . No slip boundary condition is imposed on all the walls and the boundary conditions for the surface affinity is described by the contact angle. The contact angle  $\theta_1 = 30^\circ$ ,  $\theta_2 = 120^\circ$  is specified on the bottom walls of the channel as shown in Fig. 9. A contact angle of  $0^\circ$  is specified on all the other walls as it is considered to be fully wet. Passive capillary filling process is considered by specifying a constant pressure (atmospheric) at channel inlet and outlet. A liquid volume fraction (LiqVOF) value of unity and zero is specified at channel inlet and outlet for all the cases.

#### Numerical Technique

The channel geometry is created and meshed using CFD-GEOM modeler (ESI CFD Inc., 2007). Structured grid is used for simulations. Structured grid having having 100000 ( $20 \times 20 \times 250$ ) cells is used for the three-dimensional simulations. CFD software CFD-ACE+ based on finite volume method is used for the time dependent simulations. Flow and free surface (VOF) modules of CFD-ACE+ are used for analysis. Second-order PLIC surface reconstruction method with surface tension effect is specified for VOF with explicit time integration scheme. Explicit option is selected as it exhibits greater stability and better

convergence, but slightly lower accuracy as compared to the implicit scheme. However, for an accurate resolution of the interface and prediction of the interface shape and its location, this is the preferred option. Euler (1st order) scheme is applied for time accuracy. A target Courant-Friedrich's-Lewy ( $CFL = |v| \delta t/h$ ) number of 0.1 is applied for numerical stability of the simulation. This would allow the interface to cross 10 % of the width of a grid cell during each time step in a VOF computation. Upwind scheme is used for spatial differencing. Semi-implicit method for pressure-linked equations consistent (SIMPLEC) algorithm is adopted for pressure-velocity coupling and pressure correction. The conjugate gradient squared plus preconditioning (CGS+Pre) solver (ESI CFD Inc., 2007) for velocity while algebraic multigrid (AMG) solver is used for pressure correction. Initial time step of 1.0E-07 s is selected and the VOF module is allowed to automatically adjust the time step size based on the CFL number and interface velocity. An automatic time step option automatically ensures stability in the CFD-ACE+ solver. Each case is given 100 iterations per time step with a convergence criteria of 0.0001 to control the iterative solution process. The solver quits the iterative procedure when the maximum relative difference between the computed values of variables in two successive iterations is smaller than the specified convergence criteria. The physical properties used for simulations are provided in Table 2.

Physical property	Water	Air
Density ( $kg/m^3$ )	1000	1.1614
Viscosity ( $Pa.s$ )	$1.0 \times 10^{-3}$	$1.846 \times 10^{-5}$
Surface Tension ( $N/m$ )	$75 \times 10^{-3}$	-

Table 2. Properties used in simulation

### Results and Discussion

The snapshot image of the meniscus front is shown in Figs. 10. It shows clearly the meniscus profile obtained on all the walls due to the surface tension effect. It is also observed that the meniscus is symmetric about the y-z coordinate plane and unsymmetrical about x-z coordinate plane passing through the channel axis.

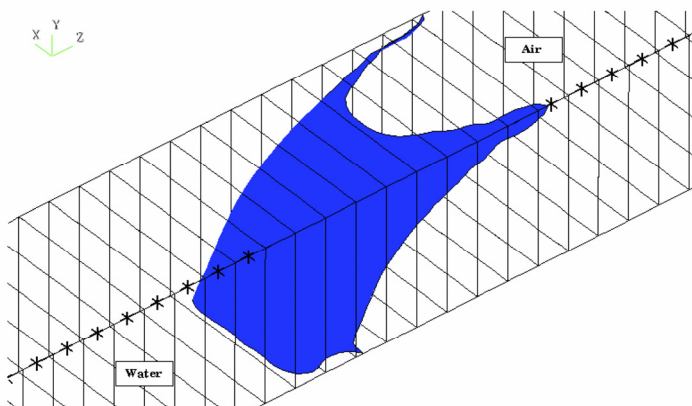


Figure 10. The three-dimensional snapshot image of meniscus front ( $\theta_1 = 30^\circ$ ,  $\theta_2 = 120^\circ$ )



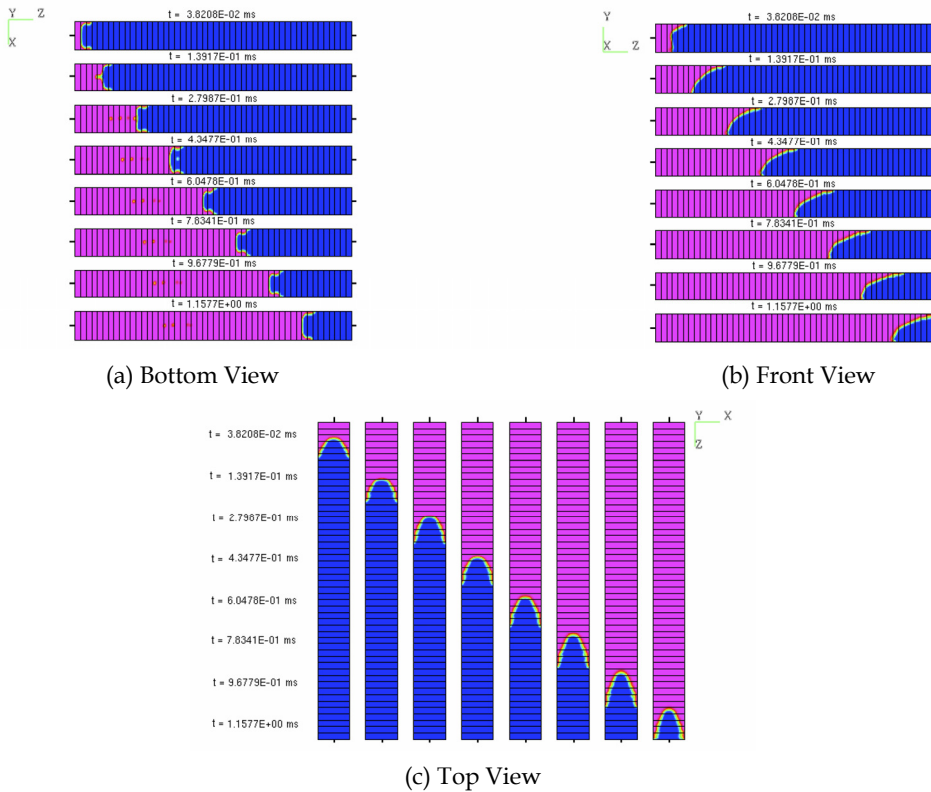


Figure 11. The snapshot image of the time evolution of meniscus front ( $\theta_1 = 30^\circ$ ,  $\theta_2 = 120^\circ$ )

The snapshot image of the time evolution of meniscus front on all the walls in the microchannel is shown in Fig. 11. The pink background indicates the liquid volume fraction (LiqVOF=1) as the fluid advances in the microchannel while blue background indicates air (LiqVOF=0). As the meniscus is symmetric about the y-z coordinate plane passing through the channel axis, the front view of the meniscus is only shown in the figure. It is observed that due to the alternate  $\theta_1 = 30^\circ$ ,  $\theta_2 = 120^\circ$  contact angle specified on the bottom wall the meniscus shape is not symmetric about the x-z coordinate plane passing through the channel axis. The unsymmetrical distribution of surface characteristics with respect to channel axis results in the stretching of the meniscus. This is due to pronounced retarding flow effect on the bottom wall and stretching of the meniscus on the top wall. As the fluid at the bottom wall traverses alternately from hydrophilic region to hydrophobic region, the curvature of the meniscus changes very sharply and large velocity gradients are observed at the wall. This gives rise to high flow instability in the microchannel. It is therefore possible to manipulate fluid flow by controlling, the size of the patterned surface (Saha & Mitra, 2008). Such phenomena will find applications for performing biological reactions in microfluidic devices using the capillary flow. All biological reactions need sufficient incubation time to complete the reaction. It is believed that sufficient incubation time necessary for reaction to proceed will be inherently available in the patterned microchannel.

The biological fluid will come in contact with surface, which will alternately assist and retard its flow. The region where the flow is retarded can be used for the reaction zone.

### Grid Dependency and Validation

Validation of the numerical results with analytical solution has been carried out for non-patterned two-dimensional microchannel 100  $\mu\text{m}$  height and 2000  $\mu\text{m}$  length with contact angle  $\theta = 0^\circ$  for DI water and ethanol. The time evolution of meniscus displacement is considered as the parameter for validating the numerical results. Figure 12 shows the comparison of meniscus displacement obtained numerically with the analytical solution based on a reduced-order model (Zeng, 2007) for DI water and ethanol. Good agreement between numerical and analytical results is observed for DI water and the results deviate by about 5% for ethanol. It is to be noted that, in general, the meniscus displacement in a capillary follows the Lucas-Washburn equation which predicts that the distance travelled by the meniscus to be proportional to  $\sqrt{t}$ . The Lucas-Washburn equation is an asymptotic model for large times and is derived based on the balance of capillary and friction forces when the influence of other forces during the initial transients become insignificant (Stange et al., 2003). This quasi-steady state assumption is valid except for the initial starting stage which is highly transient. The validation studies reported in literature (Yang et al., 2004; Yang & Przekwas, 1998; Huang et al., 2006) are observed for very large time scale ( $t \sim \text{sec}$ ). However, the time scale considered for the present study are in the range of milli seconds ( $t \sim \text{ms}$ ). Therefore, the plots in Fig. 12 do not necessarily obey the Lucas-Washburn equation, but a reduced-order model (Zeng, 2007) which accounts for the inertia is found to be a better choice for the representation of the meniscus displacement under the given conditions. Hence, deviation between the predicted numerical results and the Lucas-Washburn model can be justified and it is also observed that the inertia effects are more prominent for DI water than compared to ethanol.

When performing the VOF free surface simulations, the generation and the choice of grid are generally of great importance. It takes an enormous amount of time to perform any VOF simulation and the simulation time increases with the grid refinement. The simulation time for  $10 \times 200$  grid is typically around 45 minutes on a 2.4 GHz AMD 64 Opteron processor running Linux with an access to 4 GB RAM. It is to be noted that with the increase in the grid resolution in every direction by a factor of 2, the calculation time in a two-dimensional grid increases by a factor of 8. Also, the time step under such condition needs to be decreased by a factor of 2 in order to fulfill the CFL stability criteria.

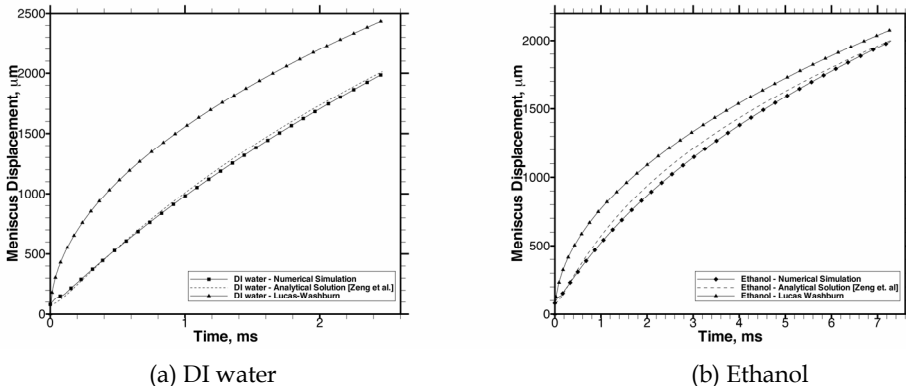


Figure 12. Validation of numerical model with analytical solution (Zeng, 2007)

Figure 13 shows the comparison of coarse and fine grid CFD-ACE+ results for three-dimensional microchannel. It is observed that by increasing the grid resolution, a sharp interface profile of the meniscus is obtained, where as this also has a corresponding influence in under predicting the meniscus displacement. As the VOF method is based on geometric back projection (ESI CFD Inc., 2007) to calculate fluxes, so the solution depends on the grid size. This is contrary to what one would expect, the accuracy obtained from the present VOF code deteriorates with the increase in the grid resolution (Raessi et al., 2007). With the inclusion of surface tension in the VOF model, a balance has to be made between the fine grid and the local accuracy, as finer grid size results in higher spurious velocities. However, it may be noted that, grid refinement affects the dynamics of capillary flows only slightly, allowing coarse grids to be a good basis for qualitative and quick simulations (Trutschel & Schellenberger, 1998).

To compare result of the present VOF algorithm with other available commercial codes, we have run similar test cases with Fluent 6.3.21 which also has a VOF module. However, limited comparison of various VOF codes are available in open literature, which is mainly due to simulation dependence on quality of code and undocumented features of algorithms (Bourago, 2002). Figure 14 shows the comparison of CFD-ACE+ and Fluent results for different grid sizes for two-dimensional microchannel. It is again observed that, both the codes under predict the meniscus displacement with decrease in mesh size.

Figure 15 shows the comparison of CFD-ACE+ and Fluent results with analytical solution for a two-dimensional microchannel ( $40 \mu\text{m} \times 7000 \mu\text{m}$ ) with black ink as working fluid with contact angle  $\theta = 36^\circ$ . The results obtained with both CFD-ACE+ and Fluent show excellent agreement and provide confidence on the current model formulation. It is observed that CFD-ACE+ predicts higher meniscus displacement than compared to Fluent with increasing time. The minor differences observed in the results are primarily due to different solver settings used during the simulation. The cpu time for coarser grids in CFD-ACE+ is lower compared to Fluent, whereas when the grid size is refined, the CFD-ACE+ simulations get extremely slower compared with Fluent simulations. To reduce the cpu time, both the commercial codes offer alternative time step selection, viz., automatic time step (CFD-ACE+) and non-iterative time advancement (Fluent). Considerable amount of time saving is obtained when such features are employed in simulation.

It is also observed that when large number of grid cells are used near the wall, in particular the small ones, compared to the rest of the domain, it results in an unstable solution. This is due to the fact that, grids with high aspect ratios affect the accuracy of the surface-reconstruction algorithm. Moreover, it should be noted that, it is difficult to accurately approximate the long time evolution of moving interfaces with VOF algorithm (Li et al., 2007; Erickson, 2005). This tends to limit the ability of these methods to track capillary driven flows over long distances. To ascertain the accuracy of the method, VOF simulations for a microchannel with very high length to width ratio is also conducted. Figure 16 shows the comparison of meniscus displacement predicted by VOF method for a microchannel  $100 \mu\text{m} \times 10000 \mu\text{m}$  with DI water as working fluid (contact angle  $\theta = 0^\circ$ ) with analytical solution. The meniscus displacement results indicate a 10 % deviation with analytical solution when time is increased asymptotically by both CFD-ACE+ and Fluent. However, as the solution domain considered in the present study are for short time scales, the predicted results are fairly accurate and acceptable.

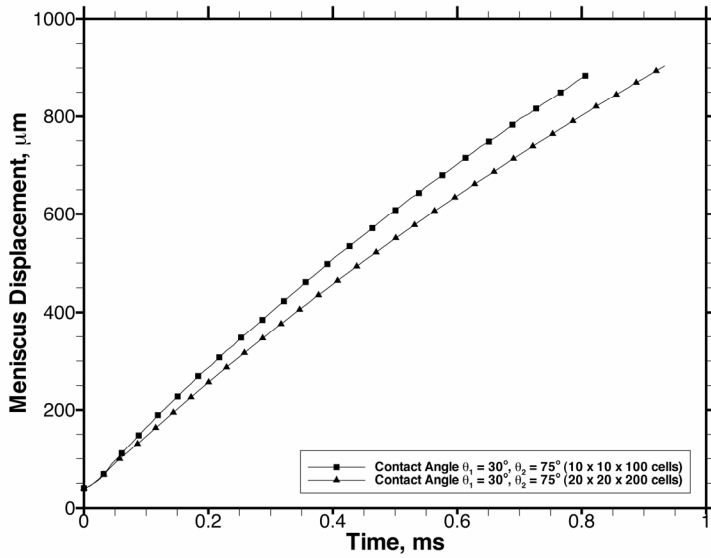


Figure 13. Comparison of coarse and fine grid CFD-ACE+ results (3D)

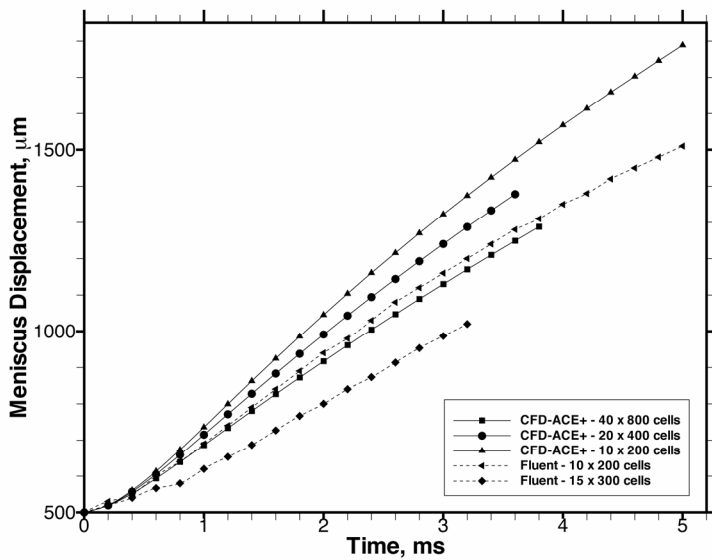


Figure 14. Comparison of coarse and fine grid CFD-ACE+ and Fluent results (2D)

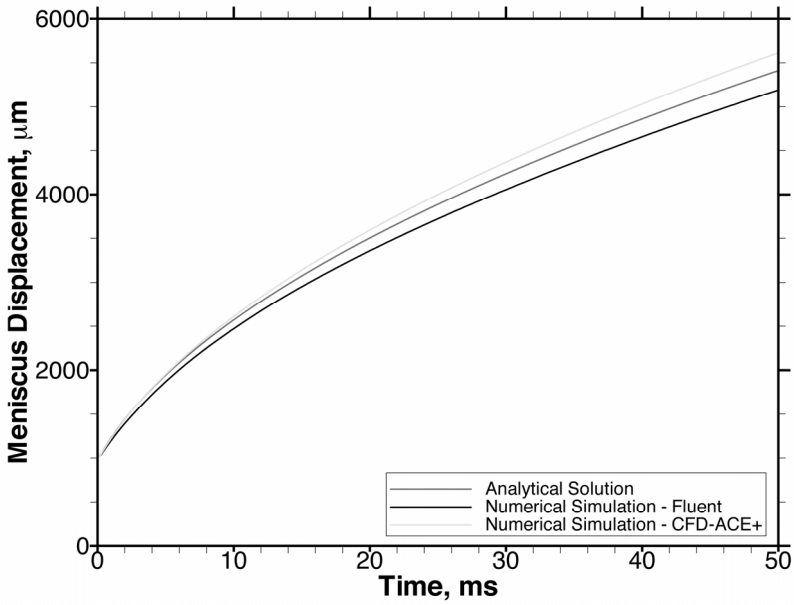


Figure 15. Comparison of CFD-ACE+ and Fluent results with analytical solution (2D)

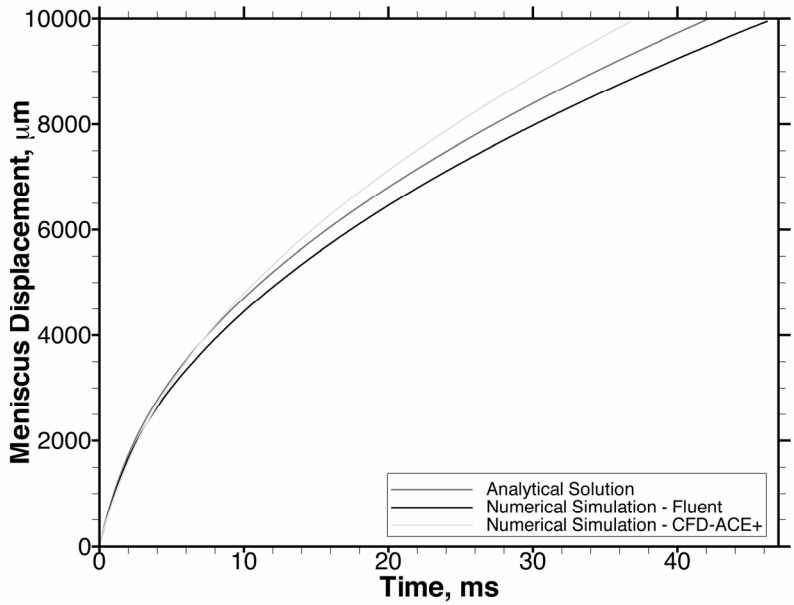


Figure 16. Comparison of CFD-ACE+ and Fluent results with analytical solution for very long microchannel (2D)

## 4. Fluid Structure Interaction

The dynamic interaction between an elastic structure and a fluid has been the subject of intensive investigations in recent years (Dargush & Banerjee, 1990; Fan & Tijsseling, 1992; Fujita, 1990; Lui & Lou, 1990). Since analytical solutions are available only for very simple problems, numerical approaches, which can be formulated in time or frequency domain, have to be employed. Vonestorff and Antes (1991) investigated the coupled fluid-structure systems subjected to dynamic loads using the finite element and boundary element methods. Similar method is used by Olson and Bathe (1985) to analyze fluid-structure interaction. Many researchers have attempted to derive variational principles for different classes of the fluid-structure interaction problems. Pinsky and Abboud (1989) proposed two mixed variational principles for transient and harmonic analyses of non-conservative coupled exterior fluid-structure interaction systems. Kock and Olson (1991) presented a finite element formulation directly derived from a variational indicator based on Hamilton's principle. Zeng and MacCamy (1992) developed an energy-based symmetric coupled finite element and boundary integral method which is valid for all frequencies. Seybert et al. (1993) employed Ritz vectors and eigenvectors along with a combination of finite element and boundary element methods to reduce the problem size. Several finite element studies have considered the gravity and free surface effects along with the fluid structure interaction. Wilson and Khalvati (1983) incorporated the gravity and the free surface effects in a displacement-based method with rotational constraints. They demonstrated results for both static and dynamic floating body problem. Their method necessitates the use of a reduced integration scheme to prevent element locking.

Moondra et al. (2006) numerically studied the flow through a microchannel with an elastic membrane and discuss the effects of various parameters - such as elasticity of the membrane, viscosity of the liquid, and the geometry of the elastic membrane on the displacement of the tip of the membrane and its maximum shear stress.

### 4.1 Governing Equations

Commercial software, COMSOL, is used to analyze the fluid-structure interaction as it provides a strong coupling between the dynamics of fluids and the dynamics of structures. At each computational step, the fluid flow field and the structure evolve as a coupled system. The interaction forces are immediately accounted for and their resultant motions enforced in each step.

Here, the flow field is solved in a continuously deforming geometry using the arbitrary Lagrangian-Eulerian (ALE) technique. The fluid flows in the channel from left to right. An obstacle, however, forces it into the narrower path in the upper portion of the channel, and a force resulting from the viscous drag and fluid pressure is imposed at the walls. Because the structure is made of deformable material, it bends under the applied load. Consequently, the fluid flow also follows a new path, and solving the flow in the original geometry can generate incorrect results. The ALE method handles the dynamics of the deforming geometry and the moving boundaries with a virtual moving grid. It computes new mesh coordinates on the channel area based on the movement of the boundaries of the structure. It reformulates the Navier-Stokes equations that solve the flow. The structural-mechanics portion of the model does not require the use of ALE, and it solves in a fixed coordinate system as usual. However, the strains computed are to be used for the computation of the deformed coordinates with ALE.

Following are the governing equations, which are solved using ALE technique:

$$\rho \frac{\partial V}{\partial t} - \nabla \cdot ((-p)I + \eta(\nabla V + (\nabla V)^T)) + \rho((V - V_m) \cdot \nabla)V = F \tag{29}$$

$$\nabla \cdot V = 0 \tag{30}$$

where  $\rho$  is the fluid's density,  $V = (u, v)$  is the velocity field of the flow,  $V_m = (u_m, v_m)$  is the coordinate system velocity,  $p$  is the fluid pressure,  $I$  is the unit diagonal matrix, and  $F = (f_x, f_y)$  is the volume force affecting the fluid.

### 4.2 Numerical Simulation

#### Physical Problem

A two-dimensional microchannel is considered here with different geometries, as shown in Figs. 17 and 18. The width of the channel is  $100 \mu m$  and length is  $300 \mu m$ . A vertical structure is located  $100 \mu m$  away from the channel inlet. The fluid in the channel has the property of water with a density of  $1000 \text{ kg/m}^3$  and dynamic viscosity of  $0.001 \text{ Pa}\cdot\text{s}$  (unless otherwise stated). The vertical structure is a flexible material with a density of  $7850 \text{ kg/m}^3$  and Youngs modulus of  $20 \text{ kPa}$  (unless otherwise stated).

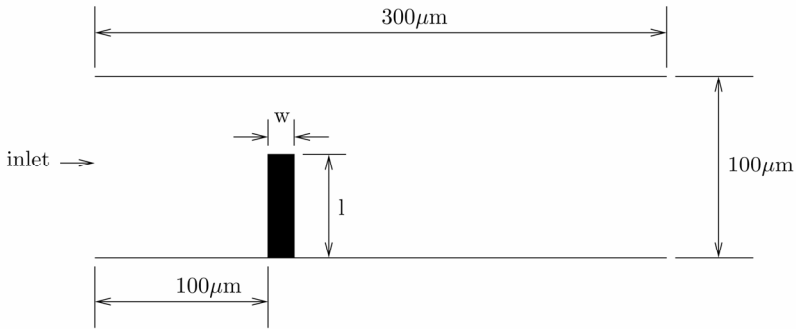


Figure 17. Schematic diagram of the microchannel with elastic structure of height  $l$  and width  $w$  (Case 1)

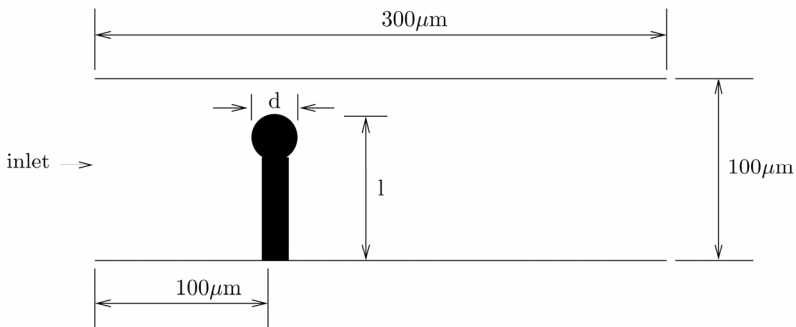


Figure 18. Schematic diagram of the microchannel with elastic structure of height  $l$  and a semicircular top of diameter  $d$  (Case 2)

### Initial and Boundary Conditions

At the entrance the flow is fully developed with a parabolic velocity profile, but the flow amplitude changes with time. At first it increases rapidly, reaching its peak value at 0.215 s; thereafter the flow gradually decreases to its steady-state value of 5 cm/s. The centerline velocity  $u_{in}$  in the x-direction with the steady-state amplitude  $U$  is given as,

$$u_{in} = \frac{Ut^2}{\sqrt{(0.04-t^2)^2 + (0.1t)^2}} \quad (31)$$

It is assumed, there is no effect of gravitation or other volume forces affecting the fluid, so  $F = 0$ . Pressure is specified at the channel outlet, the condition is  $p = 0$ . For all other boundaries, no-slip condition is imposed. However, on boundaries where the fluid forces the structure to deform, the no-slip condition means that the fluid moves with the velocity of the adjacent fluid-structure boundary.

### Numerical Technique

The structural-mechanics part of the model is solved with reference to the fixed coordinates using a plane stress analysis. The deformation of the structure resulting from the fluid can be large. Therefore, to improve the accuracy of the computation of deformations, strain values are given by Green strains. The bottom of the structure is fixed with the channel and hence its movement is restricted in all directions. All other boundaries can move freely, and there is an applied load on these boundaries. The applied load consists of the viscous drag and the pressure of the surrounding fluid.

### Results and Discussion

Figures 19 and 20 show the streamline plot for the two cases considered here. It is observed that the structure with a round tip is deformed further and it results in vortex formation at the tip.

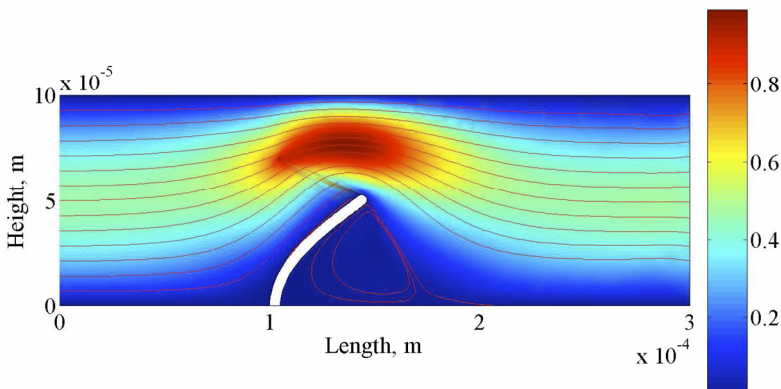


Figure 19. Streamlines for  $1/w = 14$ . Color indicates velocity magnitude. (Case 1)



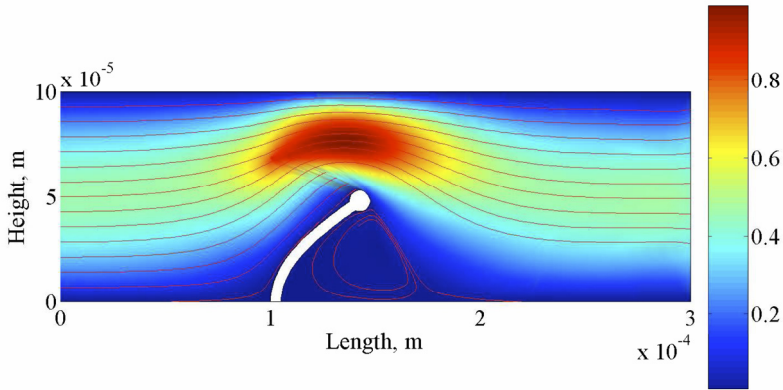


Figure 20. Streamlines for  $1/d = 7$ . Color indicates velocity magnitude. (Case 2)

The variation in the tip deformation is shown in Fig. 21 for different  $1/w$  ratios and in Fig. 22 for different  $1/d$  ratios. It is observed that for all cases the tip deformation increases rapidly for a few initial seconds and then it becomes constant for all subsequent times. The displacement maxima is observed to be slightly higher for the round tip structure.

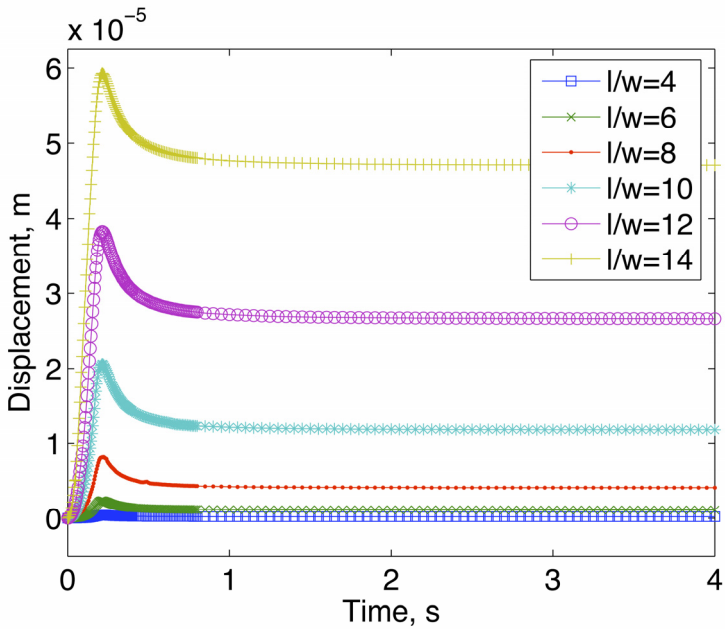


Figure 21. Transient response of tip displacement for various  $1/w$  ratios (Case 1)

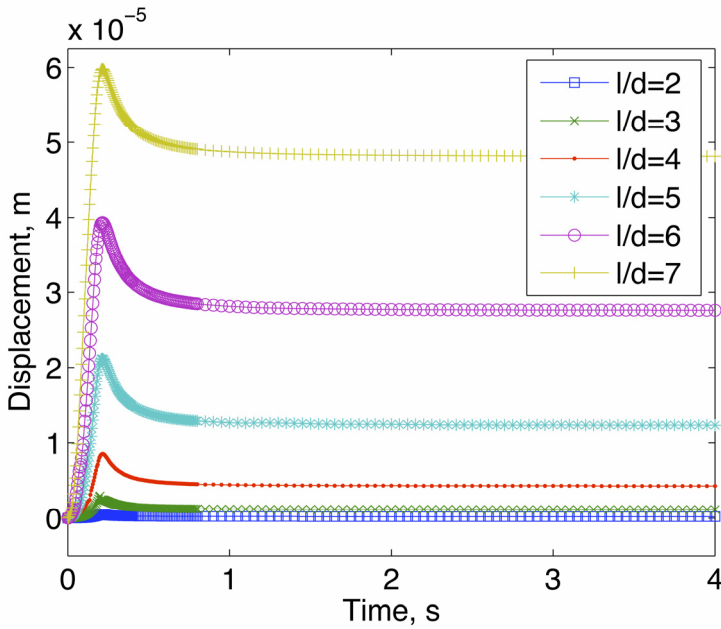


Figure 22. Transient response of tip displacement for various  $1/d$  ratios (Case 2)

It is also observed that, the maximum shear stress increases non-linearly with  $1/w$  and  $1/d$  ratio for Cases 1 and 2. However, for the round tip structure the magnitude of maximum shear stress is higher than the flat tip. This has direct impact in the design of the structural membrane embedded in the microchannel.

## 5. Summary

Microfluidic simulation of flows in microchannels was presented in this chapter. Electroosmotic driven flows in three-dimensional serpentine microchannel was investigated with non-uniform zeta potential. Free surface flows in patterned microchannel having alternate hydrophilic/hydrophobic on the bottom wall was discussed for a three-dimensional microchannel. Flow through a two-dimensional microchannel with an embedded elastic structure was studied

- It is observed that vortices are developed at the straight portion of the microchannel due to electroosmosis for the channel side walls subjected to variable zeta potential. The core of the vortices shifts when variable zeta potentials are applied at both the side walls of the channel. Flow control in the serpentine microchannel by regulating the zeta potential at the bend has also been demonstrated. Formation of additional vortices at the top left and bottom right corners of the serpentine microchannel has been observed at the semi-circular bend for very low values of applied zeta potential.
- The unsymmetrical distribution of surface characteristics with respect to channel axis results in the stretching of the meniscus in patterned microchannel with alternate layers of hydrophilic and hydrophobic surfaces at the bottom wall. Non-symmetric meniscus

profiles are obtained by changing the contact angles of the hydrophilic and hydrophobic surfaces. Flow instability is found to be increased in the microchannel as the fluid at the bottom wall traversed alternately from hydrophilic region to hydrophobic region. The capillary flow phenomena in the microchannel indicate that flow control is possible by surface patterning the channel walls for applications in microfluidic devices.

- A parametric study for different geometries is conducted to study the effect of elasticity of the structure and viscosity of the fluid on the maximum shear stress developed in the structure and the maximum displacement of the tip of the structure. It is observed that stress is more for taller structures. The maximum shear stress in the structure are not affected to a large extent by the change in elasticity of the structure but increase with increasing viscosity of the medium.

## 6. Acknowledgment

The support of Suman Mashruwala Advanced MicroEngineering Laboratory, IIT Bombay is highly appreciated.

## 7. References

- Bourago, N. G. (2002). A survey on Contact Algorithms. *Proceedings of Workshop Grid Generation: Theory and Applications*, Edited by S.A. Ivanenko & V.A. Garanzha, Computing Centre of RAS, Moscow, pp. 42-59. 18
- Brackbill, J. U.; Kothe, D. B. & Zemach, C. (1992). A continuum method for modeling surface tension. *J. Comput. Phys.*, 100, pp. 335-354.
- Brant, J. A.; Johnson, K. M. & Childress, A. E. (2005). Examining the electrochemical properties of a nanofiltration membrane with atomic force microscopy. *Journal of Membrane Science*, 2, pp. 286-294.
- Buie, C. R.; Banin, Y.; Chuyang, T.; Santiago, J. G.; Prinz, F. B. & Pruitt, B. L. 2006. A microfabricated direct methanol fuel cell with integrated electroosmotic pump. *19th IEEE International Conference on Micro Electro Mechanical Systems*, Istanbul, pp. 938–941.
- Byun, D.; Budiono, Yang, J. EL; Lee, C. & Lim, K. W. (2005). Numerical visualization of flow instability in microchannel considering surface wettability. *2nd International Conference on Fuzzy Systems and Knowledge Discovery*, Changsha, LNAI 3613, pp. 1113-1116.
- Chen, X.; Lam, Y. C.; Chen, X. Y.; Chai, J. C. & Yang, C. (2006). Numerical simulation of electroosmotic flow with step change in zeta potential. <https://dspace.mit.edu/bitstream/1721.1/7457/1/IMST018.pdf>, accessed on 21-08-2006.
- Dalton, T.; Eason, C.; Enright, R.; Hodes, M.; Kolodner, P. & Krupenkin, T. (2006). Challenges in using nano textured surfaces to reduce pressure drop through microchannels. *7th International Conference on Thermal, Mechanical and Multiphysics Simulation and Experiments in Micro-Electronics and Micro-Systems*, Milano, pp. 1–3.
- Dargush, G. & Banerjee, P. (1990). Development of an integrated bem for hot fluid-structure interaction. *Journal of Engineering for Gas Turbines and Power-Transactions of the ASME*, 112-2, pp. 243-250.

- Deval, J.; Umali, T. A.; Lan, E. H.; Dunn, B. & Ho, C. M. (2004). Reconfigurable hydrophobic/hydrophilic surfaces in microelectromechanical systems (MEMS). *J. Micromech. Microeng.*, 14, pp. 91-95.
- Erickson, D. (2005). Towards numerical prototyping of labs-on-chip: modeling for integrated microfluidic devices. *Microfluidics and Nanofluidics*, 1, pp. 301-318. 19
- CFD-ACE+ V2006 software manuals. ESI CFD Inc., 2006.
- CFD-ACE+ V2007.2 software manuals. ESI CFD Inc., 2007.
- Fan, D. & Tijsseling, A. (1992). Fluid structure interaction with cavitation in transient pipe flows. *Journal of Fluids Engineering-Transactions of the ASMS*, 114-2, pp. 268-274.
- Fu, L. M.; Lin, J. Y. & Yang, R. J. (2003). Analysis of electroosmotic flow with step change in zeta potential. *Journal of Colloid and Interface Science*, 258, pp. 266-275.
- Fujita, K. (1990). Flow-induced vibration and fluid structure interaction in nuclear power plant components. *Journal of Wind Engineering and Industrial Aerodynamics*, 33-1-2, pp. 405-418.
- Herr, A. E.; Molho, J. I.; Santiago, J. G.; Mungal, M. G. & Kenny, T. W. (2000). Electroosmotic capillary flow with nonuniform zeta potential. *Analytical Chemistry*, 72, pp. 1053-1057.
- Hirt, C. W. & Nichols, B. D. (1981). Volume of fluid (VOF) method for the dynamics of free boundaries. *Journal of Computational Physics*, 39, pp. 201-225.
- Huang, W.; Liu, Q. & Li, Y. (2006). Capillary filling flows inside patterned-surface microchannels. *Chem. Eng. Technol.*, 26, pp. 716-723.
- Karimi, G. & Li, X. (2005). Electroosmotic flow through polymer electrolyte membranes in PEM fuel cells. *Journal of Power Sources*, 140, pp. 1-11.
- Kim, D. S.; Lee, K. C.; Kwon, T. H. & Lee, S. S. (2002). Microchannel filling flow considering surface tension effect. *J. Micromech. Microeng.* 12, pp. 236-246.
- Kock, E. & Olson, L. (1991). Fluid structure interaction analysis by the finite element method - a variational approach. *International Journal for Numerical Methods in Engineering*, 31-3, pp. 463-491.
- Kothe, D. B.; Rider, W. J.; Mosso, S. J. & Brock, J. S. (1996). Volume tracking of interfaces having surface tension in two and three Dimensions. *AIAA Paper*, 96-0859, pp. 1-18.
- Lee, J. S. H.; Ren, C. L. & Li, D. (2005). Effects of surface heterogeneity on flow circulation in electroosmotic flow in microchannels. *Analytica Chimica Acta*, 530, pp. 273-282.
- Li, S.; Lowengrub, J. S. & Leo, P. H. (2007). A rescaling scheme with application to the long-time simulation of viscous fingering in a Hele-Shaw cell. *Journal of Computational Physics*, 225, pp. 554-567.
- Liechty, B.; Webb, B. W. & Maynes, R. D. (2005). Convective heat transfer characteristics of electro-osmotically generated flow in microtubes at high wall potential. *International Journal of Heat and Mass Transfer*, 48, pp. 2360-2371.
- Lui, A. & Lou, J. (1990). Dynamic coupling of a liquid-tank system under transient excitations. *Journal of Ocean Engineering*, 17-3, pp. 263-277.
- Mitra, S. K. & Saha, A. A. (2008). Methods for surface modification. Encyclopedia of Microfluidics and Nanofluidics, Springer- Verlag Heidelberg, Germany.
- Madou, M. (2002). Fundamentals of Microfabrication. CRC Press, New York.

- Moondra, S.; Upadhyay, A. & Mitra, S. K. (2006). Investigation of fluid structure interaction of an elastic membrane in a microchannel. [http://comsol.cntech.com.cn/conf2006/papers/Fluid-Structure\\_Interactions/Mitra/Mitra.pdf](http://comsol.cntech.com.cn/conf2006/papers/Fluid-Structure_Interactions/Mitra/Mitra.pdf), accessed on 29-12-2007.
- Nayak, K.; Kulkarni, P. D.; Deepu, A.; Sitaraman, V. R.; Punidha, S.; Saha, A. A.; Ravikanth, M.; Mitra, S. K.; Mukherji, S. & Rao, V. R. (2007). Patterned microfluidic channels using self-assembled hydroxy-phenyl porphyrin monolayer. *7th IEEE International Conference on Nanotechnology*, Hong Kong, Paper No. 404, pp. 1-5.
- Olson, L. & Bathe, K. (1985). An infinite element for analysis of transient fluid-structure interaction. *Journal of Engineering with Computers*, 2, pp. 319-329.
- Patankar, S. (1980). *Numerical Heat Transfer and Fluid Flow*. Hemisphere Publishing Corp., New York.
- Pinsky, P. & Abboud, N. (1989). Two mixed variational principles for exterior fluid structure interaction problems. *Journal of Computers and Structures*, 33-3, pp. 621 – 635.
- Probstein, R. (1994). *Physicochemical Hydrodynamics*. Wiley, New York.
- Raessi, M.; Mostaghimi, J. & Bussmann, M. (2007). Advecting normal vectors: A new method for calculating interface normals and curvatures when modeling two phase flows. *Journal of Computational Physics*, 226, pp. 774-797.
- Rawool, A. S.; Mitra, S. K. & Kandlikar, S. G. (2006). Numerical simulation of flow through microchannels with designed roughness. *Microfluidics and Nanofluidics*, 2, pp. 215-221.
- Rawool, A. S. & Mitra, S. K. (2006). Numerical simulation of electroosmotic effect in serpentine channels. *Microfluidics and Nanofluidics*, 2, pp. 261-269.
- Saha, A. A.; Mitra, S. K. & Li, X. (2007). Electroosmotic effect on flows in a serpentine microchannel with varying zeta potential. *Journal of Power Sources*, 164, pp. 985-991.
- Saha, A. A. & Mitra, S. K. (2007). Investigation of three-dimensional flow in microchannels with patterned surfaces. *5th International Conference on Nanochannels, Microchannels and Minichannels*, Puebla, Mexico, Paper No. 30052, pp. 1-8.
- Saha, A. A. & Mitra, S. K. (2008). Investigation of capillary flow in microchannels with alternate hydrophilic-hydrophobic bottom wall. *Langmuir*, under review.
- Salamon, T.; Lee, W.; Krupenkin, M.; Hodes, M. & Kolodner, P. (2005). Numerical simulation of fluid flow in microchannels with superhydrophobic walls. *International Mechanical Engineering Conference and Exposition*, Orlando, Florida, Paper No. 82641, pp. 1-11.
- Seybert, A. F.; Wu, T. & Li, W. (1993). A coupled FEM/BEM for fluid-structure interaction using ritz vectors and eigenvectors. *Journal of Vibration and Acoustics-Transactions of the ASME*, 115-2, pp. 152-158.
- Souders, D.; Khan, I.; Yao, G. F.; Incognito, A. & Corrado, M. (2003). A numerical model for simulation of combined electroosmotic and pressure driven flow in microdevices. *7th International Symposium on Fluid Control, Measurement and Visualization*, Perronte, pp. 1 – 7.
- Stange, M.; Dreyer, M. E. & Rath, H. J. (2003). Capillary driven flow in circular cylindrical tubes. *Physics of Fluids*, 15, pp. 2587-2601.
- Sujatha, K. S.; Matallah, H.; Banaai, M. J. & Webster, M. F. (2006). Computational predictions for viscoelastic filament stretching flows: ALE methods and free-surface techniques (CM and VOF). *Journal of Non-Newtonian Fluid Mechanics*, 1137, pp. 81-102.

- Trutschel, R. & Schellenberger, U. (1998). Dynamic simulation of free surfaces in capillaries with the finite element method. *International Journal for Numerical Methods in Fluids*, 26, pp. 485-495.
- Vonestorff, O. & Antes, H. (1991). On FEM-BEM coupling for fluid structure interaction analyses in the time domain. *International Journal for Numerical Methods in Engineering*, 31-6, pp. 1151–1168.
- Washburn, E. W. (1921). The dynamics of capillary flow. *Phys. Rev.*, 17, pp. 273-299.
- Wilson, E. & Khalvati, M. (1983). Finite elements for the dynamic analysis of fluid-solid systems. *International Journal of Numerical Methods in Engineering*, 19, pp. 1657–1668.
- Yang, L. J.; Yao, T. J. & Tai, Y. C. (2004). The marching velocity of the capillary meniscus in a microchannel. *J. Micromech. Microeng.*, 14, pp. 220-225.
- Yang, H. Q. & Przekwas, A. J. (1998). Computational modeling of microfluid devices with free surface liquid handling. *1st International Conference on Modeling and Simulation of Microsystems*, San Juan, Puerto Rico, pp. 498-505.
- Yian, D. & Lawal, A. (2006). Numerical study on gas and liquid slugs for Taylor flow in a T-junction microchannel. *Chemical Engineering Science*, 61, pp. 7609-7625.
- Zeng, J. (2007). On modeling of capillary filling. [http://www.coventor.com/pdfs/on\\_modeling\\_of\\_capillary\\_filling.pdf](http://www.coventor.com/pdfs/on_modeling_of_capillary_filling.pdf), accessed on 15-03-2007.
- Zeng, X. J. B. & MacCamy, R. (1992). Stable variational coupling method for fluid-structure interaction in semi-infinite media. *Journal of Vibration and Acoustics-Transactions of the ASME*, 114-3, pp. 387–396.
- Zhang, J.; He, G. & Liu, F. (2006). Electroosmotic flow and mixing in heterogeneous microchannels. *Physical Review E*, 73, 050301.
- Zhao, B.; Jeffrey, M. S. & Beebe, D. J. (2001). Surface-directed liquid flow inside microchannels. *Science*, 291, pp. 1023-1026.

# Multiphysics Modelling and Simulation in Engineering

Alexandru M. Morega<sup>1</sup> and Juan C. Ordonez<sup>2</sup>

<sup>1</sup>POLITEHNICA University of Bucharest, <sup>2</sup>Florida State University

<sup>1</sup>Romania, <sup>2</sup>USA

## 1. Introduction

As more and more complex and sophisticated hardware and software tools are available, complex problems described by consistent mathematical models are successfully approached by numerical simulation: modelling and simulation are present at almost each level in education, research, and production. Numerical “experiments” have predictive value, and complement physical experiments. They are unique in providing valuable insights in *Gedankenexperiment*-class (thought experiment) investigations.

This chapter presents numerical simulation results related to a structural optimization problem that arises in systems with gradients and fluxes. Although the discussion concerns the optimal electrical design of photovoltaic systems, it may be extended to a larger class of applications in electrical and mechanical engineering: diffusion and conduction problems.

The first concern in simulation is the proper formulation of the physical model of the system under investigation that should lead to consistent mathematical models, or *well-posed* problems (in Hadamard sense) (Morega, 1998). When available, analytic solutions – even for simplified mathematical models – may outline useful insights into the physics of the processes, and may also help deciding the numerical approach to the solution to more realistic models for the systems under investigation. Homemade and third party simulation tools are equally useful as long as they are available and provide for accurate solutions.

Recent technological progresses brought into attention the *Spherical PhotoVoltaic Cells* (SPVC), known for their capability of capturing light three-dimensionally not only from direct sunlight but also as diffuse light scattered by the clouds or reflected by the buildings. This chapter reports the structural optimization of several types of spherical photovoltaic cells (SPVC) by applying the constructal principle to the minimization of their electrical series resistance. A numerically assisted step-by-step construction of optimal, minimum series resistance SPVC ensembles, from the smallest cell (called *elemental*) to the largest assembly that relies on the minimization of the maximum voltage drop subject to volume (material) constraints is presented. In this completely deterministic approach the SPVC ensembles shapes and structures are the outcome of the optimization of a volume to point access problem imposed as a design request.

Specific to the constructal theory, the optimal shape (geometry) and structure of both natural and engineered systems are morphed out of their functionality and resources, and of the constraints to which they are subject.

## 2. Shape and structure out of a multiphysics principle

The development of the *constructal principle* (Bejan, 2000) relies on the analysis of natural dynamic systems with fluxes and gradients (*e.g.*, temperature, pressure, electric potential, chemical potential, etc.) that, internally, are outside thermodynamic equilibrium. A second important aspect is that the variety of geometrical natural forms, which we may recognize and which are found in both animate and inanimate worlds, is not that vast: *natural systems may have the same geometric shape without being identical*. For instance, two bronchial trees are never identical. Basically, when these systems are presented by a single image out of the endless diversity of natural flow forms we have the ability to recognize and classify them as *tree*, *round* and *slice*. If one single principle explains all these forms then it may act everywhere, and it becomes a law that ties different areas such as physics and biology or, better said, two different modes of reasoning, two different points of view.

The constructal principle is used in this work to produce architectures (shapes, structures) based on the optimization of the systems under investigation – purpose, function – rather than by conjectural assumptions.

### 2.1 Functional objective and constraints

Spatial and temporal structures observed in Nature are the results of global optimization subject to local and global constraints: a finite-size heterogeneous system undergoes changes in shape and structure such as to provide for an as easy as possible access, or low impedance paths, of its internal fluxes. Optimization principles such as minimum travel time, minimum flow resistance, minimum power consumption are invoked and used, and it is remarkable that these deterministic principles are independent, and do not follow up, do not result, from other, known laws.

Engineering design starts by a clear understanding of the *objective*: the system mission, its purpose, function and performance. The design's objective implies also *optimization*, because the engineered system is expected to perform the best *possible*. Possible means that there are *local* and *global* constraints (limitations) that the system may have.

Examples of some very common *global* constraints are the system mass and volume; the heat generated within the occupied volume, *e.g.*, by an electronic ensemble, is another global constraint when the electronic components have to fit within an imposed volume.

The *local* constraints are more subtle, but equally important. For instance, in a system with internal heat generation (*e.g.*, a cable that carries electric current, electronic devices, etc.) the maximum temperature is not to exceed a certain safe limit. From this perspective, the number and localization of the hot spots is not important. The local constraints may then be gathered in an *objective function* defined at the system level. The geometry is the unknown. The external shape and the internal structure emerge then by recurrent, iterative design.

In the constructal theory, the deterministic evolution occurs in time, from principle (engineering) to Nature. The history of science and technology abounds in examples where the sense is the opposite *i.e.*, from Nature to engineering – this method is recognized today as *Biomimetics*, and it continues to be a valuable instrument in engineering design. Compared to Biomimetics, constructal theory acts in the opposite sense: the engineering generates a purely theoretic point of view, from which Nature may be better understood, *i.e.* more simply. And this is consistent with Poincaré's conclusion: "C'est là la simplicité cachée, celle qu'il faut découvrir" (Poincaré, 1902).



**2.2 Fermat’s principle; constructal principle**

Fermat’s principle, used only in optics (Lemmons, 1997), postulates that light, which propagates between two points (A,B) located in different optical media, must choose the path that minimizes the travel time. It follows then that the angle of refraction,  $\sin\beta_i/\sin\beta_r = v_{i,r}$ , is an optimization result, where  $v_{i,r}$  is the refraction index relative to the two media. Fermat’s principle covers the much older principle of the shortest path postulated by Heron of Alexandria: *light propagates following a straight path and the incident angle at a mirroring interface is equal to the reflection angle.*

By contrast to the point-to-point “flow” law of Fermat and Heron, the constructal law refers to finite size systems with internal flow generation, from the volume (an infinite number of points) to a sink (M) located on the boundary.

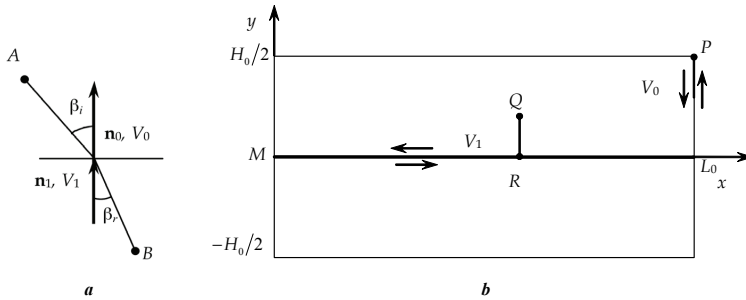


Figure1. Fermat’s (a), and constructal (b) optimal access principles

In Figure 1 the volume is represented by a rectangle of area  $A_0 = H_0L_0$ , called *elemental system*. The size of  $A_0$  is fixed, but the aspect ratio  $H_0/L_0$  may vary. The system is made of two media, where motion may occur at two speeds,  $V_0 \ll V_1$ . The amount of high-speed material ( $V_1$ ) is small and fixed - much smaller than the rest of volume occupied by the low-speed material, ( $V_0$ ), with internal generation (e.g., heat, current, etc.).

The objective of the elemental cell finite-size system optimization consists of maximizing the volume-to-point access between all points of  $A_0$  and M. The geometric shape and the internal structure of  $A_0$  (i.e., the distribution of high speed material throughout the low-speed material) are then natural results. The global constraints are the fixed size of the system and the amount of high permeability material to be distributed within the system. On the other hand, some of the internal points will always have easier access to M than other points. The longest trip to M is associated to the most distant point in  $A_0$  (point P in Fig. 1), which is then the most solicited point - it is the analogous to the point of highest mechanical stress in a mechanical structure or the hottest spot in a thermal structure. The design may be improved by changing the external aspect ratio, to produce more uniform access to the volume from M.

The constructal optimization works similarly to Fermat’s principle that anticipates the geometric shape of the light beam. Unlike Fermat’s principle where the trajectory is broken at the interface between the two semi-infinite media, in the volume-to-point access problem the bent (e.g., R) is found on the central axis of  $A_0$ , and this is the result of an optimization principle. The volume-to-point construct is then a bundle of an infinite number of flow paths that verifies Fermat’s principle.

At this point we may introduce the fundamental constructal problem: “Given a finite size

*volume with internal heat generation and of low conductivity, which is cooled by a small-size sink placed on the boundary, distribute a fixed amount of high conductivity material within the volume such that the hotspot temperature is minimum"* (Bejan, 2000). In other words, find the shape and structure that minimize the system's thermal resistance.

For instance, electronic structures (packages) are subject to thermal objectives and constraints. The global constraint is the finite volume where the system must fit. The thermal design objective consists of installing as many components as possible, hence an as high as possible heat generation rate,  $q$  (electrical structures generate heat). The maximum temperature in the systems may not exceed a specified limit,  $T_{max}$  - this is the local constraint. The optimal design is then superior if  $q$  is large, *i.e.* the global thermal conductance  $q/(T_{max}-T_0)$  is high -  $T_0$  is the initial temperature of the environment that absorbs the heat.

### 3. Photovoltaic cells optimization – a design problem

The interest on PhotoVoltaic Cells (PVC) has increased recently due to the energy crisis and the advance of the alternative energies. Solar cell power generation systems installed in 2000 has reached 711 MW worldwide, and in the future it is expected to grow (Kyosemi, 2006). As over 90% of the nowadays PVCs use polysilicon as a raw material, the recent shortages of high-grade silicon will significantly impact on the growth of the PV industry.

PVCs are semiconductor devices, made of two sandwiched layers of intrinsic semiconductors of  $p$  and  $n$ -type that convert light directly into electricity. The photons absorbed by the PVC wafer generate electric charges (electrons and holes) that are drained across the  $p$ - $n$  junction in opposite directions by the action of an electric field produced by the photovoltaic effect. This segregation generates a voltage across the junction that may conduct a current in an external load (CPE-UNSW, 2004), (EMSOLAR, 2004).

Partial reflection of the incident light, the incomplete absorption and utilization of the photons energy, the partial recombination of electrical charge carriers and the leakage across the junction (Burgers & Eikelboom, 1997), (Green, 1986), (Horzel & De Clerq, 1995), (Verbeek & Metz, 1996), (STARFIRE, 2002) are main factors that reduce the PVC efficiency. The power loss occurs in the bulk of the base material,  $R_p$  (Fig. 2a), in the narrow top-surface layer, at the interface between the cell and the electrical terminals of the PVC.

The cell series resistance,  $R_s$  (Fig. 2a), met by the lateral current in the cell's top layer is responsible for the flattening of the current-voltage characteristic (Fig. 2b) and for the corresponding PVC output power loss. It may be reduced by using a highly conductive material for the top layer (or window), by increasing its thickness, by good galvanic contacts and by optimized geometry for the contact electrode grid (STARFIRE, 2004), (EMSOLAR, 2004).

The front collector - a finger-like metallic contact connected to a busbar system - is to reduce  $R_s$ . Unfortunately, this structure prevents the incident radiation to reach the cell: large electrical contacts may minimize  $R_s$ , but they would cover the cell and block too much of the light. An optimal design is then a compromise between an as low as possible  $R_s$  (closely spaced, highly conductive grid with good adhesion and low  $R_s$ ) and an as high as possible light transmission (fine, widely spaced fingers). Currently, the acceptable loss from the contact shading is 10% in commercial cells (EMSOLAR, 2004), (STARFIRE, 2002, 2004).

The series resistance optimisation consists of minimising the *sum* of the collector shadow and resistance (Joule) losses and, despite the many physical processes within the PVC

(Altermatt et al., 1977) it may be conducted separately (Radike et al., 2002). Instead of the double diode description of the PVC, we used the *maximum power point* (MPP) (Fig. 2,c) approach (Burgers & Eikelboom, 1997), which allows for the PVC to be optimised for either a specific or a mix of irradiation levels, such as it occurs under normal working conditions. In addition, the optimal design of the collector has to comply with criteria such the aesthetic appearance, and several collector patterns derived from the flat-surface *H*-type PVC were proposed (Radike et al., 2002).

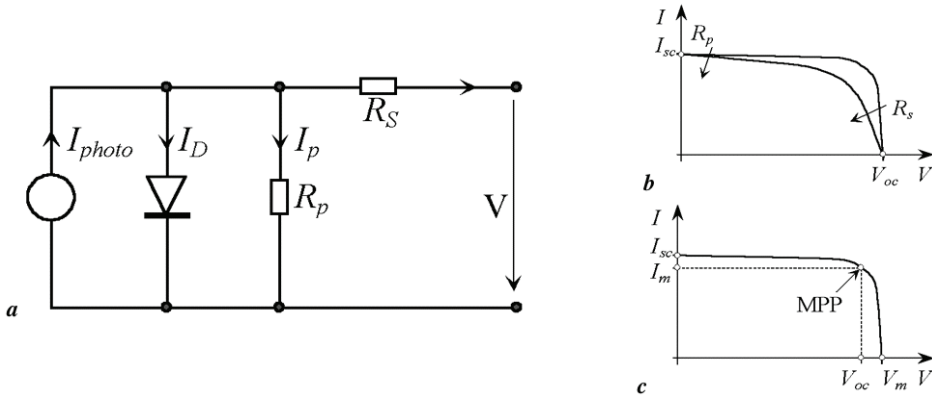


Figure 2. An equivalent circuit for a hetero-junction PVC: (a) Equivalent scheme; (b) The effect of  $R_p$  and  $R_s$ ; (c) Maximum power point, MPP [13]

As seen in the previous subsection, constructal theory is based on the thought that architecture comes from a principle of maximization of flow access for both animate and inanimate flow systems. The theory provides a framework to design and analyze finite-size, constraint systems. We apply this strategy to connect an area with PV current generation to a terminal, with the objective of draining the generated current throughout a minimum resistance path.

The basic volume-to-point access problem has an equivalent electrokinetic formulation (Morega & Bejan, 2005), (Morega et al., 2006a, 2006b): *given a finite size volume in which electrical current is generated at every point, which is connected by a small patch (terminal) located on its boundary, and a finite amount of high (electrical) conductivity material, find the optimal distribution of high conductivity material in a given volume so that the peak voltage is minimized.*

**3.1 The mathematical model in the PVC series resistance optimization**

We assume that the PVC operates under DC conditions hence the associated electric field is potential. For the *n*-layer of the PVC the current flow in the emitter and metallic collector is essentially 2D. By Ohm’s law, the total current density is

$$\mathbf{J} = \sigma_{0,p} (\mathbf{E} + \mathbf{E}_i) = -\sigma_{0,p} \nabla V + \sigma_{0,p} \mathbf{E}_i = -\sigma_{0,p} \nabla V + \mathbf{J}_i. \tag{1}$$

Here,  $\mathbf{J}_i$  is the photovoltaic current density (assumed uniform),  $\sigma_{0,p}$  are the electrical conductivities of the collector and emitter, respectively (assumed linear, homogeneous and isotropic). The partial differential equations that give the electrical field are obtained by setting to zero the divergence of the total current density

$$\frac{\partial^2 V}{\partial X^2} + \frac{\partial^2 V}{\partial Y^2} + \frac{1}{\sigma_0} w''' = 0, \text{ emitter} \tag{2}$$

$$\frac{\partial^2 V}{\partial X^2} + \frac{\partial^2 V}{\partial Y^2} = 0, \text{ collector} \tag{3}$$

Here,  $w''' = \text{div } \mathbf{J}_i$ , and  $\mathbf{J}_i$  are known quantities.. Except for the output port through which the current exits the cell (set at ground potential, a Dirichlet condition), the boundary is assumed electrically insulated (a Neumann homogeneous condition).

This electrokinetic problem is equivalent to the conduction heat transfer problem, with the correspondence  $T \leftrightarrow V$ ,  $q''' \leftrightarrow w'''$ ,  $k_0 \leftrightarrow \sigma_0$ ,  $k_p \leftrightarrow \sigma_p$  ( $k_p, k_0$  are the thermal conductivities of the collector and emitter, respectively). The electrically insulated boundary is equivalent to adiabatic boundaries (Bejan, 1997b), (Ordonez et al., 2003).

Next, we present the constructal growth for the flat surface PVC, from the elemental cell to higher order ensembles. Numerical simulations are validated against analytic solutions, and then used in more realistic circumstances.

### 3.2 Flat-surface PVC optimization – an analytic solution

#### (a) The elemental system

Figure 3 shows the PV smallest system, called elemental system. We consider a rectangular PV cell and its metallic collector (finger), situated on the long symmetry axis. Except for the port at the origin, the boundary is electrically insulated.

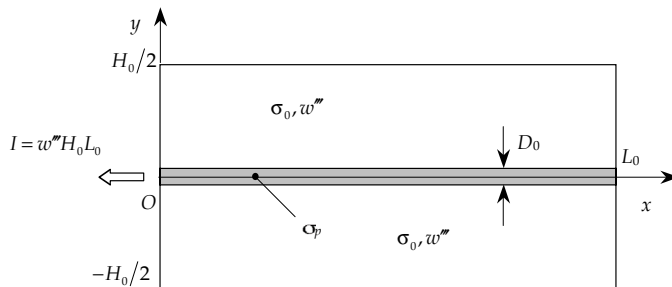


Figure 3. The elemental system with internal PV current generation, and its metallic collector

The cell area  $A_0 = H_0L_0$  and the area of the metallic grid,  $A_p$ , are kept constant throughout the optimization. However,  $H_0$  and  $L_0$  may vary and, as  $H_0 \ll L_0$ , it follows that the current in the emitter flows mainly in  $y$  direction, to be then collected by the  $\sigma_p$  finger at  $y=0$  and drained in  $x$  direction - this assumption is discarded in the numerical model.

The closed form solution to the problem of the current flow in the PVC emitter - eq. (4),

$$\frac{\partial V}{\partial y} \Big|_{y=H_0/2} = 0, \quad V(x,0) = V_0(x) \quad - \text{ is } V(x,y) = \frac{w'''}{2\sigma_0(H_0y - y^2)} + V_0(x,y).$$

solution to the problem of the current flow in the PVC collector -  $\sigma_p D_0 d^2V/dx^2 + w'''H_0 = 0$ ,

$$V_0|_{x=0} = V(0,0), \quad \left. \frac{dV_0}{dx} \right|_{x=L_0} = 0 \quad \text{is} \quad V(x,y) - V(0,0) = \frac{w''}{2\sigma_0} (H_0 y - y^2) + \frac{w'' H_0}{\sigma_p D_0} \left( L_0 x - \frac{x^2}{2} \right) \quad (\text{Morega \& Bejan, 2005}).$$

Using these results, it may be inferred that the maximum voltage drop on the elemental cell,  $\Delta V_0$ , has a minimum with respect to the cell shape  $(H_0/L_0)$

$$\frac{\Delta V_{0,min}}{w'' H_0 L_0 / \sigma_0} = \frac{1}{2} \left( \frac{\sigma_0 H_0}{\sigma_p D_0} \right)^{1/2}, \quad \left( \frac{H_0}{L_0} \right)_{opt} = 2 \left( \frac{\sigma_0 H_0}{\sigma_p D_0} \right)^{1/2}. \quad (4)$$

This conclusion is consistent with the assumption that the elemental system is slender, suggesting that  $\sigma_p / \sigma_0 \gg H_0 / D_0 \gg 1$ .

Two additional properties of this *geometric optimization* are remarkable (Bejan, 1997b):

1. *The principle of equipartition*: the voltage drop in the emitter equals the voltage drop along the finger, *i.e.*,  $\Delta V_{0,min}$  is divided in half by the bend ( $x = L_0, y = 0$ ).
2. At the elemental level, the voltage drop,  $\Delta V_{0,min} = w'' H_0^2 / (4\sigma_0)$ , decreases as  $H_0^2$ . This motivates the effort to manufacture the smallest possible elemental system.

**(b) The first order ensemble**

Figure 4 shows the first order ensemble, where the  $D_0$  fingers are connected to the  $D_1$  current path, called *busbar*. The boundary is insulated, except for the terminal of size  $D_1$  at the origin, where the collected current leaves the structure. The new optimization problem is to find how many elemental volumes to assemble, or the optimal shape  $H_1 \times L_1$ , such that the maximum value of the voltage drop in the assembly from a point to the origin is minimal.

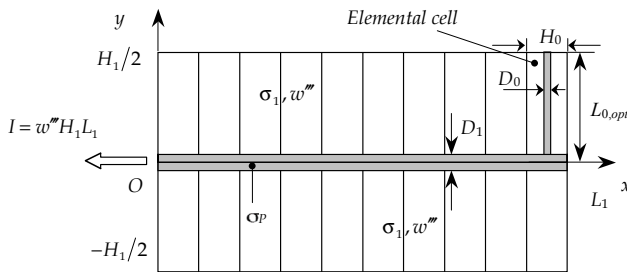


Figure 4. The first construct made of optimized elemental systems

In a volume-average sense, the ensemble behaves as the  $\sigma_0$  region, except that its effective conductivity is  $\sigma_1 = \sigma_p D_0 / H_0$ .

A similar analysis may be conducted to calculate the voltage drop on the first order ensemble,  $\Delta V_1$ . Its maximum has a minimum,  $\Delta V_{1,min} = w'' H_0^2 / 4\sigma_0$ , registered between the farthest corner  $(L_1, H_1/2)$  and the exit port at the origin,  $(0,0)$ .

The resistance of the ensemble is then minimized by using the principle of equipartition, with the constraint  $\phi_1 = A_{p,1} / (H_1 L_{1,opt})$ , where  $A_{p,1} = D_1 L_{1,opt} + n_{1,opt} D_0 L_{0,opt}$  is the area of

high conductivity material ( $\phi_1$  is sometimes called *porosity*) (Morega & Bejan, 2005), yielding  $\Delta V_{a_1, min} = (3/8)w^m H_0^2 / \sigma_0$ . Apparently, the busbar has to be wider than the fingers, and  $(D_1/D_0)_{opt} = [(D_0\sigma_p)/H_0\sigma_0]^{1/2} \gg 1$ .

An important result of this analysis is the *scalability* of the construct: the voltage drop on the optimized ensemble is *almost equal* to the optimized voltage drop on the elemental system.

A *twice* optimized, first order ensemble - with respect to the  $H_1 \times L_1$  shape *and* to the allocation of high conductivity material - is then obtained for the optimal number of fingers  $n_{1,opt} = [(\sigma_p/\sigma_0)(D_0/H_0)]^{1/2} \gg 1$  and for the busbar length  $L_{1,opt} = (1/2)(H_0D_0\sigma_p/\sigma_0)^{1/2}$ .

Remarkably, the optimal shape of this ensemble is a constant,  $(H_1/L_1)_{opt} = 2$ , independent of the type of conducting materials ( $\sigma_p/\sigma_0$ ) and of the proportion in which ( $\phi_1$ ) they are built into the ensemble. Consequently, *the optimal shape  $H_1 \times L_1$  is such that a square of side  $L_1$  forms on either side of the  $D_1$  busbar (x axis)*. By using  $H_1 = 2L_{0,opt}$ , it yields  $(L_1/L_0)_{opt} = 1$ .

**(c) Second and higher order ensembles**

The best *second order ensemble* (Fig. 5a) is made of two optimized first order ensembles patched such that  $H_2 = H_1 = 2L_{1,opt} = 2L_2$ . The  $D_1$  wide strip is the  $D_1$  wide busbar in Fig. 4.

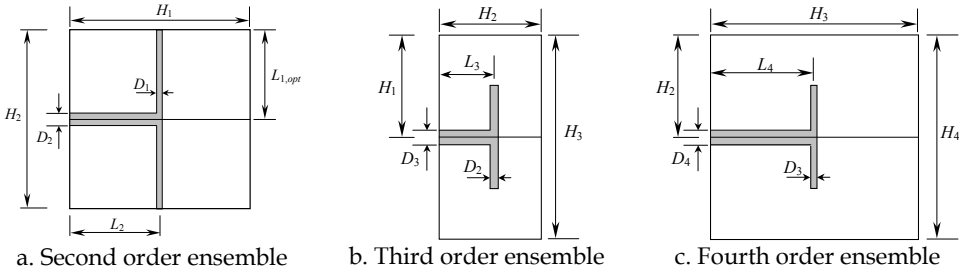


Figure 5. Second to fourth order ensembles: made of two optimized lower order constructs. The best *third order assembly* (Fig. 5b) may be obtained by a double optimisation (geometric shape *and* busbar width) of a system made of optimised second order ensembles. Figure 5c shows the fourth order ensemble made of two third order ensembles

Apparently, in the process of optimization the finger width doubles from one ensemble to the next, higher order one, outlining the following relations, where  $i$  is the ensemble order (Morega & Bejan, 2005)

$$D_{i,opt} = \frac{2^i}{3^{1/2}} D_0 \left( \frac{D_0 \sigma_p}{H_0 \sigma_0} \right)^{1/2} \quad \text{for } i \geq 2, \tag{5}$$

$$L_i = 2^{\frac{i}{2}-m} \left( H_0 D_0 \frac{\sigma_p}{\sigma_0} \right)^{1/2}, \quad i \geq 3, \quad m = \begin{cases} 2, & i \text{ even} \\ 5/2, & i \text{ odd} \end{cases} \tag{6}$$

$$H_i = 2^{2^p} H_0 \left( \frac{D_0 \sigma_p}{H_0 \sigma_0} \right)^{1/2}, \quad i \geq 2, \quad p = \begin{cases} 1, & i \text{ even} \\ 1/2, & i \text{ odd} \end{cases} \quad (7)$$

$$\phi_i = \phi_{i-1} + \frac{2^{(i-2r)/2}}{3^{1/2}} \frac{D_0}{H_0}, \quad i \geq 3, \quad r = \begin{cases} 0, & i \text{ even} \\ 1/2, & i \text{ odd} \end{cases} \quad (8)$$

$$\Delta V_{a_i, min} = \frac{3}{16} \frac{\phi_i}{D_0/H_0} \frac{w'' H_0^2}{\sigma_0}. \quad (9)$$

Figure 6a shows the optimised fourth order ensemble with its constituent parts, including the elemental cells (the strips). The number of such striations is *not* a constant, and it depends on  $2(\sigma_0 H_0 / \sigma_p D_0)^{1/2}$ . Another important feature is that the width of the optimised busbar increases with the ensemble order. Figure 7 shows the high order end of the optimised construction sequence.

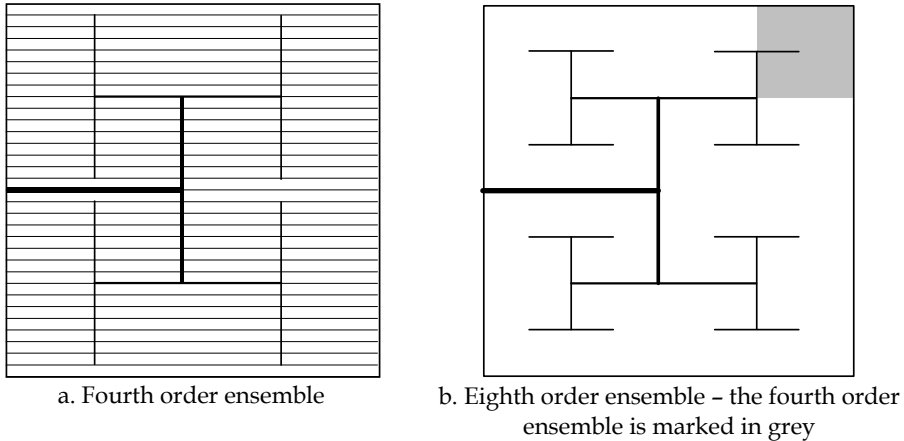


Figure 7. Optimized networks of higher-order ensembles - designs based on analytic solutions

### 3.3 H-type PVC optimization – numerical simulation solution

The analytical work may be accompanied by numerical simulation. First, eqs. (2), (3) are non-dimensionalized

$$\Delta v + 1 = 0, \text{ emitter} \quad (10)$$

$$\Delta v = 0, \text{ collector} \quad (11)$$

by dividing the coordinates with the length scale,  $\sqrt{H_0 L_0}$ , the current source with  $w'' = \text{div } \mathbf{J}_i$ , and the electrical conductivities of the emitter and collector with  $\sigma_0$ . It follows

then that the voltage scale is  $V_0 = w^* H_0 L_0 / \sigma_0$ . In the optimization process of the 2D flat-surface PV ensembles the laplacian [eqs. (10), (11)] is defined as  $\Delta v = \partial^2 v / \partial x^2 + \partial^2 v / \partial y^2$ .

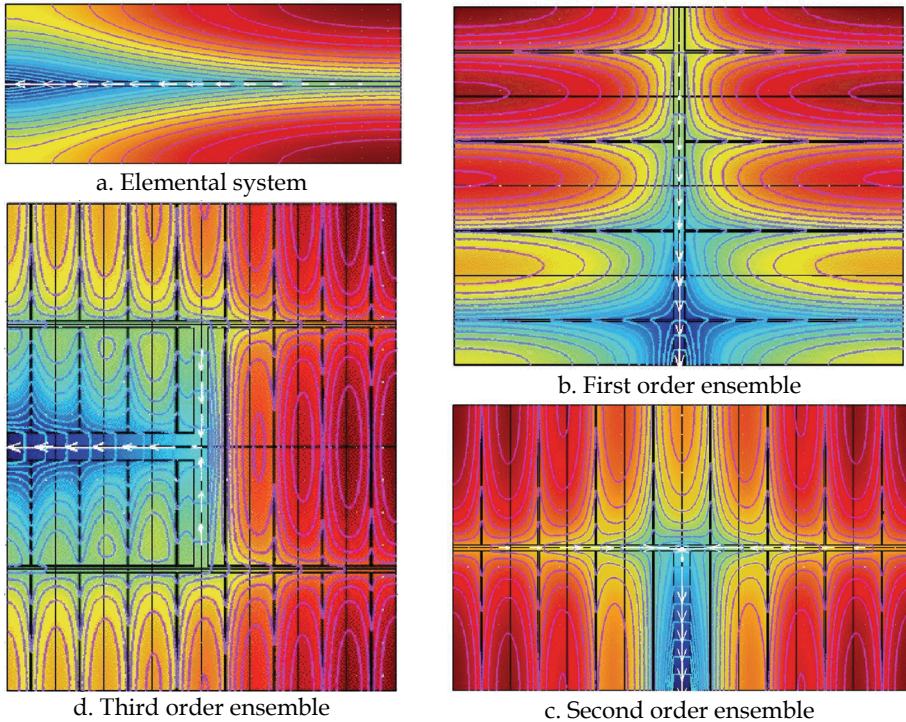


Figure 8. Optimized networks of higher-order ensembles - numerical simulations

To check the first five steps of the procedure we used a finite element software (Comsol, 2004-2008) that implements Galerkin-Lagrange technique. The meshes we used were unstructured, Delaunay-type. Figure 8 displays the typical steps that follow the constructal optimization sequence, conducted for an elemental cell with  $d_0 = 0.005, h_0 = 0.1, l_0 = 0.5$ , and  $\sigma_p / \sigma_0 = 1000$ .

#### 4. Spherical photovoltaic ensembles – structural optimization

A variety of *flat surface* PVCs, materials and manufacturing methods have been developed (CPS-UNSW, 2006). However, the incident sunlight to a solar cell varies according to the position of the sun, weather conditions, the objects around that reflect sunlight, and flat light reception surface cells (Fig. 9,a) cannot sufficiently meet these diverse conditions. Recently, novel Spherical PhotoVoltaic Cell (SPVC) technologies were developed (Fig. 9b,c) that capture sunlight three-dimensionally, not only as direct sunlight but also as light diffused by clouds, and as light reflected from buildings (Kyosemi, 2006), (Fujipream & Clean Venture, 2006), (SSP, 2006).



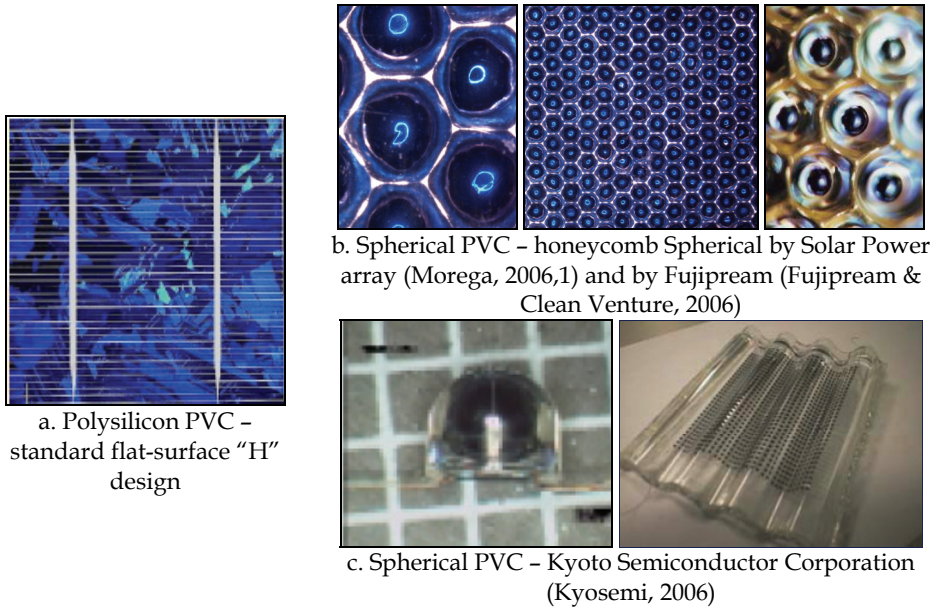


Figure 9. Flat-surface and SPVC ensembles

In contrast to flat-surface cells, Spherical Sunlight Reception Surfaces (SSRS) can receive light in all directions thus increasing their power generation capacity. They minimize the output fluctuations even under direct sunlight, and even when the angle of the reflected incident light changes. Practically non-directive, SSRS can increase their output power by improving the efficiency of light utilization, as there are fewer restrictions on their mounting. The SPVC consists of a single spherical *p-n* junction (Fig. 10).

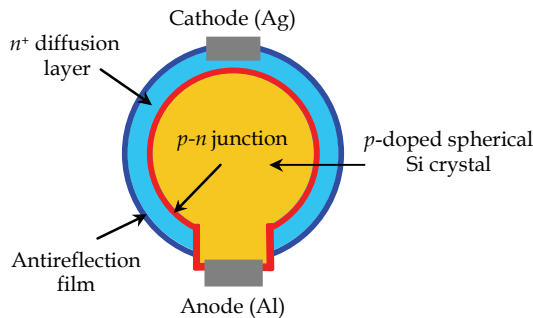


Figure 10. A spherical solar cell captures light in all directions - after (Kyosemi, 2006)

This technology uses less costly silicon, and gives more flexibility and ease of integration in different applications. The process starts with low cost silicon, which is the raw material used in the sphere fabrication process. The silicon is first purified and then formed into tiny spherical beads of proper size (Kyosemi, 2006). The diameter of a SPVC should be small in order to increase the proportion of the light reception surface area of the semiconductor crystal to its volume so as to raise the efficiency of the material (Morega et al., 2006a, 2006b).

Notably, the cells are spherical and thus excellent in mechanical strength. The mounting may be white resin reflection plate, with its surface covered with transparent resin.

Although very small (0.2–2mm), the SPVC maximum open voltage is the same as that of a larger flat junction type cell. SPV modules are produced in a variety of power needs ranging from an extremely small to a large power source – e.g., through connection of cells in series and parallel with fine copper wire (Kyosemi, 2006).

#### 4.1 Structural optimization of SPV ensembles by numerical simulation

The previous section reported the flat-surface PVC ensembles optimization. Unlike that case, here the design goal is to find either the particular pattern of the SPVCs distribution on a high conductivity material foil or a wireframe network that would connect the PV beads such that  $R_s$  is minimized. In both cases we consider the DC regime of the electric field.

The mathematical model (10), (11) with appropriate boundary conditions was solved numerically, by FEM technique (Comsol, 2004-2008), for the two different types of SPV modules: the *honeycomb* and the *interconnected (wired)* ensembles. First, the non-dimensional electrical field ( $v$ ) is solved for. We used solvers that utilize the symmetry of the algebraic system generated by this linear problem. Then, two quantities are sought: the maximum voltage drop on the cell/ensemble (the maximum potential,  $v_{max}$ ) and the series resistance,  $R_s$ , defined here as the ratio of  $v_{max}$  through the total current produced by the cell/ensemble. *The time-arrow of the design goes from the elemental system to higher order ensembles, following the constructal technique*

#### 4.2 Honeycomb arrayed SPVC ensembles – a first model

The honeycomb (SSP, 2006) ensembles fabrication process involves bonding the tiny silicon spheres between sheets of thin and flexible substrates (usually aluminium) – Fig. 9b. The front foil acts as the cathode and determines the spacing of the spheres (Fig. 11), while the back foil acts as the anode to the core of the spheres (Morega et al., 2006a).

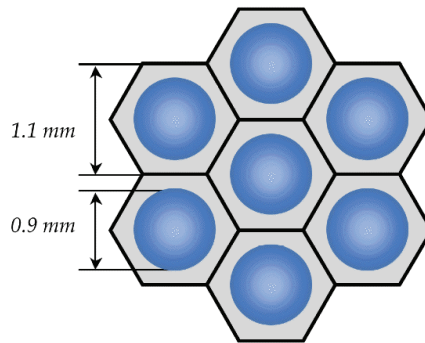


Figure 11. Honeycomb SPVC array

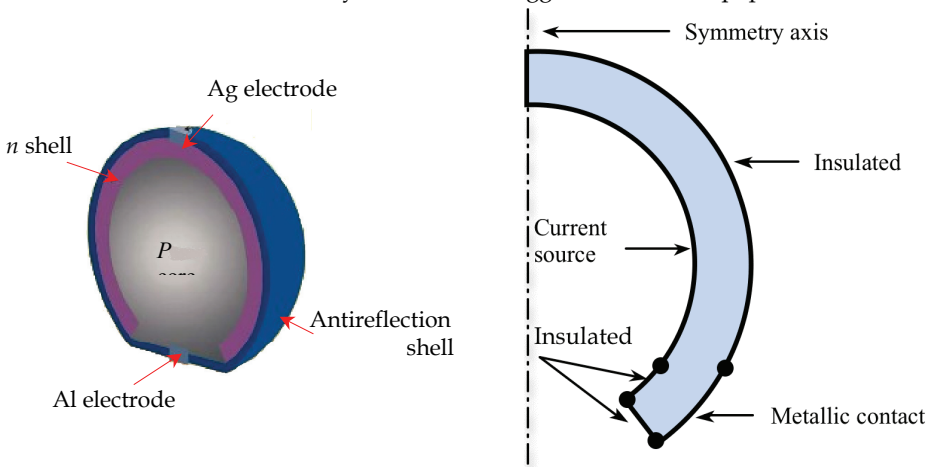
The optimization problem of the honeycomb packaging differs from the fundamental flat-surface PV problem in the sense that the (current) sources are spread throughout a very good conducting material, which embeds the PV beads and cannot be distributed in a spanning tree structure. Further more, the ensemble edges act as paths of high conductive material, draining part of the current generated by the SPV cells closer to the boundary.

Another difficulty related to this design – if modelled at the SPVC level – is the staggered arrangement itself. It appears more convenient – and within satisfactorily accuracy limits – to rely on average, equivalent 2D SPVC models. The first concern is then to define an equivalent elemental cell that consistently represents the actual SPVC (Fig. 5).

**(a) Simplified 2D models for the spherical solar cell**

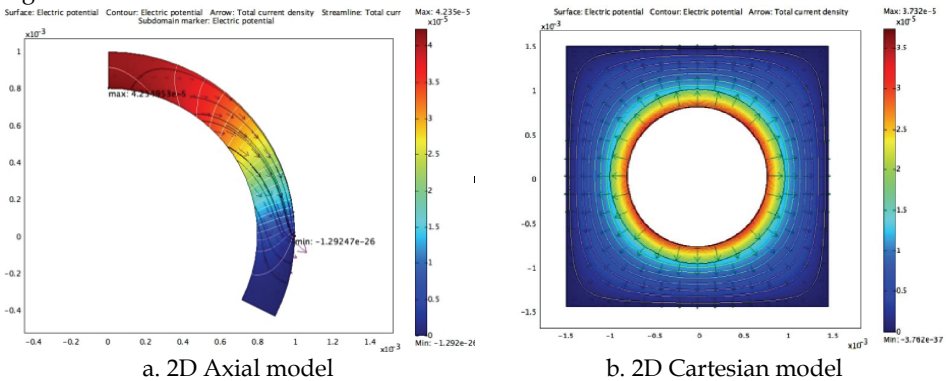
First, a simplified 2D axial-symmetric model may be used to evaluate the current distribution through the  $n$ -layer of the SPV bead – Fig. 12b. The following boundary conditions may be used to close the Laplace problem for the electrical potential:

- On the inner surface of the shell (the  $p$ - $n$  interface) a non-homogeneous Neumann condition defines the photovoltaic current source.
- The outer surface of the bead is electrically insulated.
- The contact between the bead and the aluminum foil collector is set at  $V = 0$ , because the excellent electrical conductivity of aluminum suggests an almost equipotential contact.



a. The spherical SPVC – after (Kyosemi, 2006)      b. A simplified 2D axial-symmetric model  
Figure 12. The SPCV bead – an equivalent 2D axial model and the BCs in the DC problem

This 2D axial model gives an estimate of the series resistance of the  $n$ -layer, which is part of the global series resistance of the SPVC.



a. 2D Axial model      b. 2D Cartesian model  
Figure 13. The 2D equivalent models of a spherical solar cell – electric field spectra

Figure 13a shows the electrical field (voltage surface color map and equipotential contour lines), and the electric current flow (arrows and streamlines) within the shell, obtained by numerical simulation.

The next step is to “flatten” the 2D axial model, *i.e.* to recast it into a 2D Cartesian model that comprises also the collector (aluminum) “territory” of the bead: the  $n$  shell is projected onto a circular crown that has the same series resistance as the actual spherical layer; the inner rim of the crown produces the same amount of current as the inner boundary of the spherical  $n$ -shell. The actual size of the aluminum patch that embeds the bead may make the object of another optimization problem. Figure 13b depicts the voltage (surface color map and contour lines) and the current flow (arrows and streamlines) when the external boundary is set to ground. Of course, symmetry may be used to simplify the problem, but the numerical effort to solve this linear problem for the entire domain is not significant.

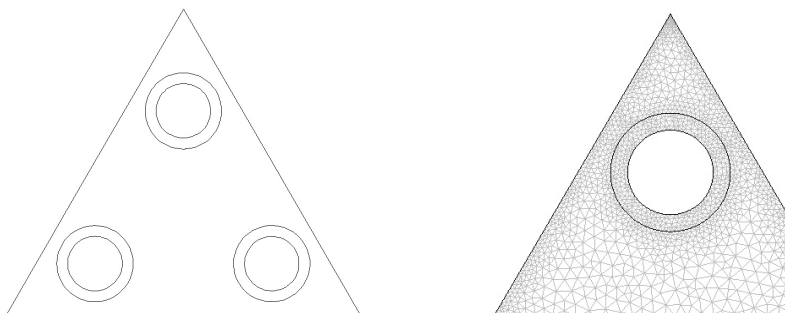
The 2D Cartesian model is further used to define the elemental cell of the structural optimization sequence. The elemental cell may contain a number of SP beads, and it is the smallest entity, the construct or “brick” that is optimized for minimum series resistance: *its shape and structure are essential to the shape and structure of higher order constructs in the optimization sequence.*

#### (b) The elemental system

The first elemental cell design we propose (Fig. 14a) is a simple system that, by constructal growth, may evolve into a staggered honeycomb SPVC ensemble (Fig. 11). It is assumed that the photovoltaic current leaves the cell through the vertices, and that the edges are electrically insulated. The only degree of freedom here is the relative position of the beads along the principal axes of the triangular surface, between vertices and the mass center.

The ratio between the peak-voltage, wherever it occurs, and the total current produced by the SPV beads, defines the series resistance of the cell,  $R_s$ . Its inverse, the series conductance, is a quality factor ( $QF$ ), a design quantity. As  $R_s$  depends on the relative position of the beads, we carried out numerical experiments to find the layout that leads to its minimum.

Figure 14b shows the mesh produced by the adaptive algorithm used to solve the conduction problem. The circular interior boundaries are current source, and the vertices are patched with tiny metallic electrodes: they are the current ports to the structure.



a. The elemental system

b. The FEM mesh for elemental system – detail

Figure 14. The computational domain in the honeycomb SPV ensemble optimization

By symmetry grounds, the *optimal* elemental system should have the same type of symmetry. Figure 15 shows the voltage (surface map and contour lines), the current density (arrows), for three layouts, including the optimal design with highest  $QF$  (minimum, maximum voltage).

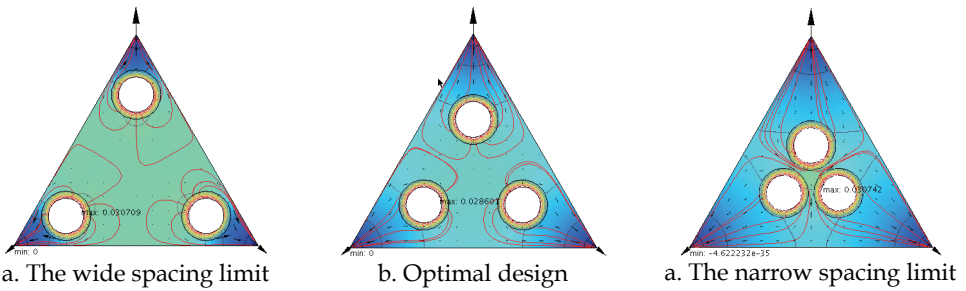


Figure 15. The electric field in the structural optimization of the elemental system

**(c) Higher order ensembles**

Next, the optimal elemental system is used to build higher order ensembles. The first construct is obtained by mirroring the elemental cell with respect to its edges (Fig. 16a).

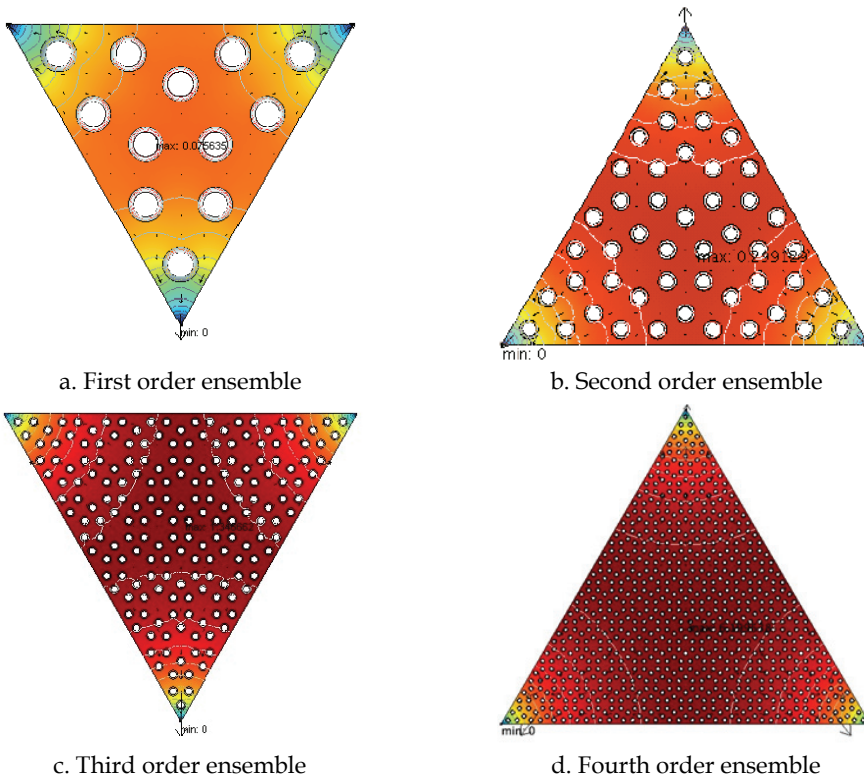


Figure 16. The first four higher order SPVC ensembles – voltage and electric current

As this simple replication does not guarantee an optimum first order construct, numerical experiments (Negoias & Morega, 2005) were needed to validate the optimality of this design:  $QF$  was evaluated for different positions of the SPV beads along the principal lines of the first construct. There are countless layouts that might be considered, however we

used the symmetry of this design to reduce the computational domain to 1/6 of its actual size, and the SPV beads were displaced such as to preserve symmetry. The analysis confirmed the layout obtained by mirroring the elemental cell, and the reason is that the aluminum foil has a very good electrical conductivity as compared to the cells.

The mirroring technique may be pursued to generate ensembles of higher and higher order, thus propagating the triangular symmetry (Fig. 16b-d). Apparently, the inner regions are working at almost uniform voltage, and the vertices regions, acting as electrical terminals, are areas of higher voltage gradients.

Remarkably, all constructs exhibit almost the same series resistance, which is a feature of constructal structures (Morega & Bejan, 2005), (Bejan, 2000).

### 4.3 Honeycomb arrayed SPVC ensembles – a second model

To exemplify the influence that the elemental system has in the shape of the higher order ensembles generated by the constructal growth technique, in this subsection we report a different approach to the honeycomb SPV ensembles optimal design.

Here, we assume that by technological reasons (optimum spacing between spheres) there are no degrees of freedom in changing the size of the honeycomb (Fig. 11) – *e.g.*, (SPP, 2006). We skip the optimization sequence for the elemental system that may make the object of a distinct investigation. In this sense, our approach is *quasi*-constructal.

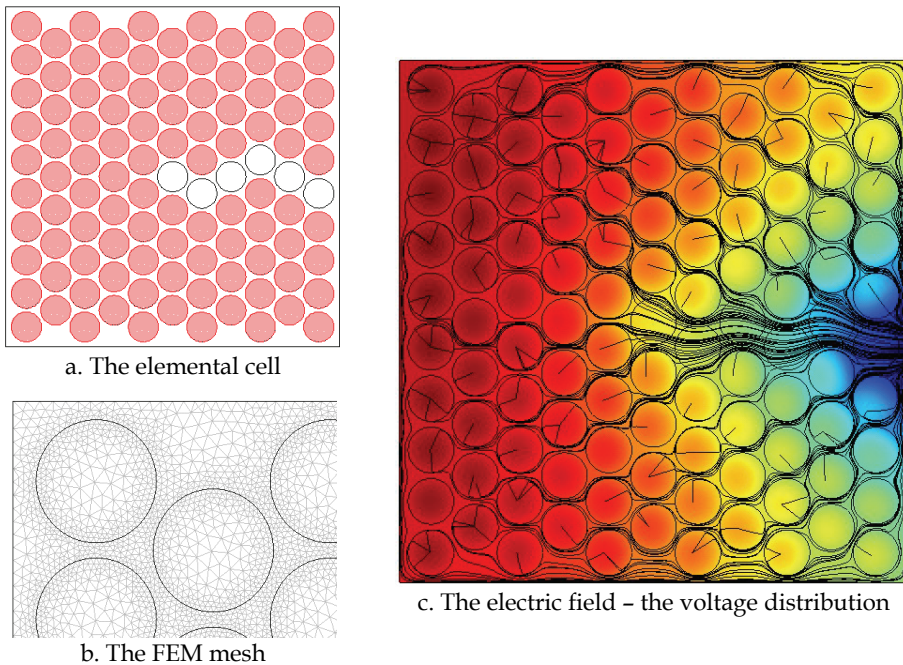


Figure 17. The honeycomb SPVC elemental system

Figure 17 shows the computational domain for the elemental system for the proposed packaging. The optimization was carried out by numerical simulation, and the mathematical model is made of eqs. (10) and (11) with appropriate boundary conditions.

The coloured disks in Fig. 17a represent the SVPCs, and the white background is the aluminium cathode. The port is seen at the boundary on the right. The white disks add to the high conductivity path to the exit port. Figure 17c shows the electric field by voltage surface map and contours. The hardest working point (of the highest voltage) is farthest from the exit port (the upper and lower vertices on the left edge of the elemental cell).

Higher order ensembles are produced starting from the elemental system. Figure 18 shows the computational domains for the 1<sup>st</sup>, 2<sup>nd</sup>, 3<sup>rd</sup>, 4<sup>th</sup> order ensembles. Note that each new ensemble results by combining two, lower level optimized ensembles; in this process either one column or a row (depending on odd-even the order of the ensemble) is lost by partially overlapping the two constituent lower-level ensembles in order to preserve symmetry with an odd number of columns/rows. Also, the high conductivity path obtained by removing SPVCs preserves the same thickness in each ensemble. As seen from Fig. 18, depending on the ensemble order, the path that connects the high conductivity tree to the port on the boundary may be a either a straight or a saw-teeth-like strip.

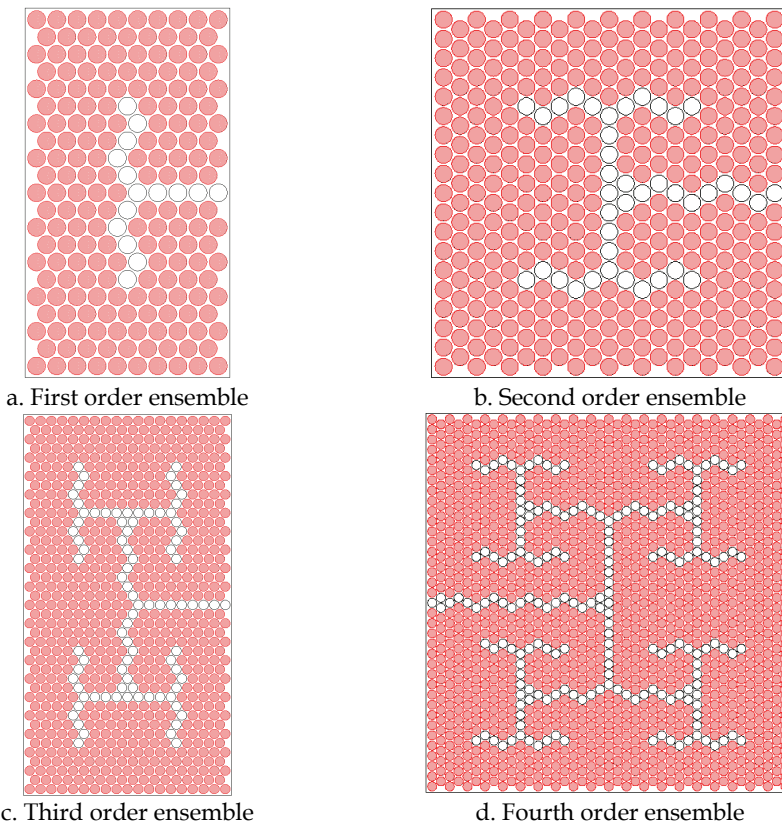
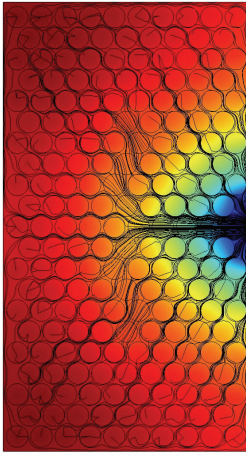


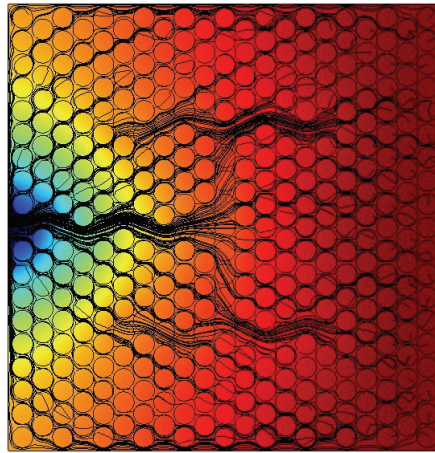
Figure 18. Constructural ensembles – computational domains

Figure 19 shows the voltage distribution on the first four higher order ensembles. As the order of the ensemble increases, the tree-like structure of the highly conductive material emerges: *The tree is the flow architecture that provides the easiest (fastest, most direct) flow access*

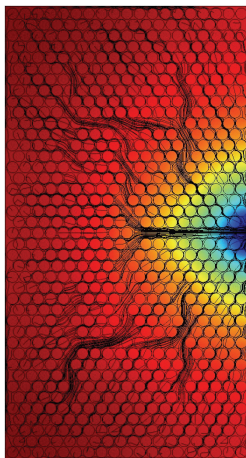
between one point (source, or sink) and infinity of points (curve, area, or volume). Among other practical applications of tree-shaped flow architectures note the cooling of electronics (Bejan, 1997), (Ledezma et al., 1998), reconfigurable power networks (Morega & Ordonez, 2007), (Morega et al., 2006c, 2008) and the flows through porous media (Ordonez et al., 2003), (Azoumah, 2004).



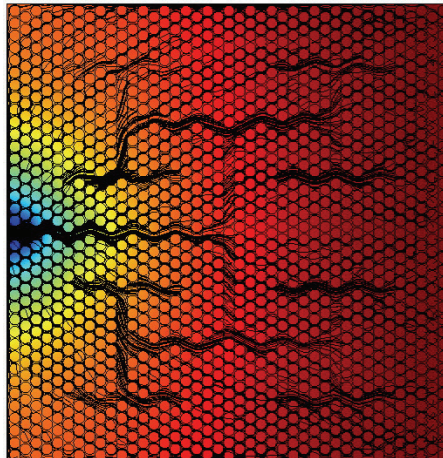
a. First order ensemble



b. Second order ensemble



c. Third order ensemble



d. Fourth order ensemble

Figure 19. Higher order constructal ensembles – electric field

At this point it is instructive to investigate the surface grey map in Fig. 20: the current flow in the second order ensemble. It outlines clearly the cathode foil and the high conductive tree that conveys the current to the exit port on the boundary.



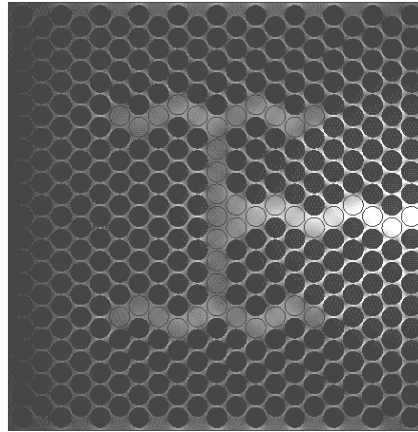


Figure 20. The cathode foil and the high conductive path evidenced by the current density spectrum in the second order ensemble

The non-dimensional maximum voltage and the series resistance obtained by numerical simulation, for different conductivities ratio,  $\sigma_p/\sigma_0$  are given in Fig. 21a,b respectively.

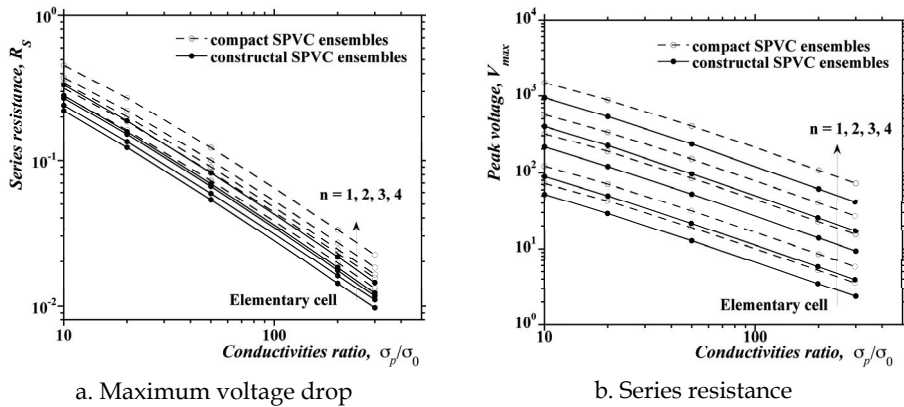


Figure 21. The maximum voltage and the series resistance for the first four ensembles for the honeycomb SPV modules (non-dimensional quantities)

As expected, the higher conductivity ratio, the lower the voltage drop on the module, hence the lower the losses by series resistance. The optimized ensembles (continuous curves) have consistently lower series resistances than their unstructured counterparts (dashed curves). An important result exhibited by the optimized ensembles is that  $R_s$  does not vary with the ensemble order: this is an important feature of constructal structures and it evidences their *scalability* (Bejan, 2000). The fact that the proposed structural growth - from the elemental system to higher order ensembles - is scalable confirms - *a posteriori* - the constructal nature of the design that we adopted, imposed by the technological constraints that come with the assumed honeycomb pattern and the spherical packaging.

#### 4.4 Wired spherical photovoltaic cells

A different technology (Kyosemy, 2006) utilizes larger-size SPV cells that are provided with two, top and bottom electrical contacts, which allow connecting the cells in ensembles through thin wires - in parallel or series - to deliver higher current and voltage. As for the honeycomb module, the spacing between cells, or the "domain of existence" for a SPVC, is not a degree of freedom in the optimization process, and it is assumed imposed by technological grounds: the spheres should not shadow each other, nor should they be too loosely packed since the module has to be compact.

The optimization process starts by assuming an elemental system made of a pair of interconnected SPVCs (Fig. 22a). As the SPVCs are embedded in an electrically insulating mass, the elemental system is reduced to a pair of the SPVCs and the interconnecting wires. All sides are insulated, except for the port where the current leaves the structure. Here too, the structural, quasi-constructural design and its optimization were carried out by numerical simulation. The mathematical model for the kinetic, DC electric field is made of eqs. (10), (11) and appropriate boundary conditions (Morega et al., 2006a).

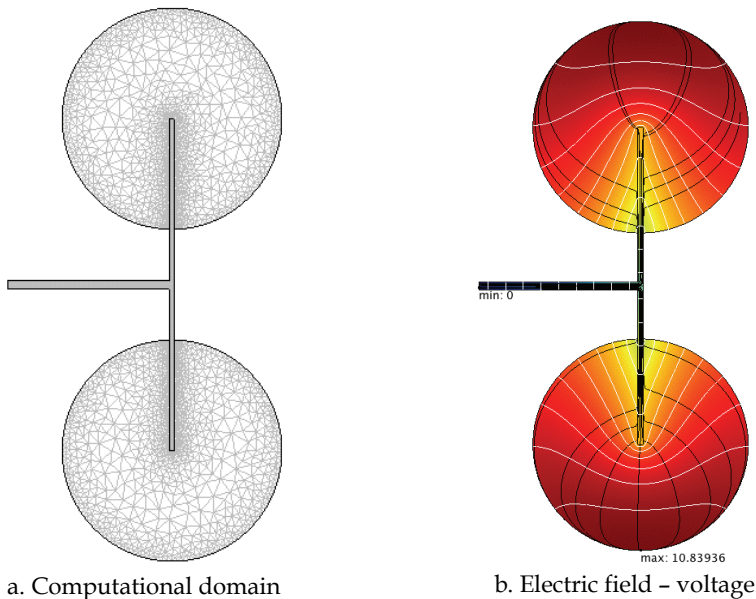


Figure 22. The elemental system for the wired SPVC made of pair of cells

Figure 22b shows the voltage distribution (surface color map and contour lines), and the current density path through streamlines for the elemental system.

The constructural growth follows by first merging two mirroring elemental cells. Then, two first-order ensembles are joined into a second order ensemble, and so on. Figure 23 displays the electric field through the voltage and current density spectra for the first three higher order ensembles.

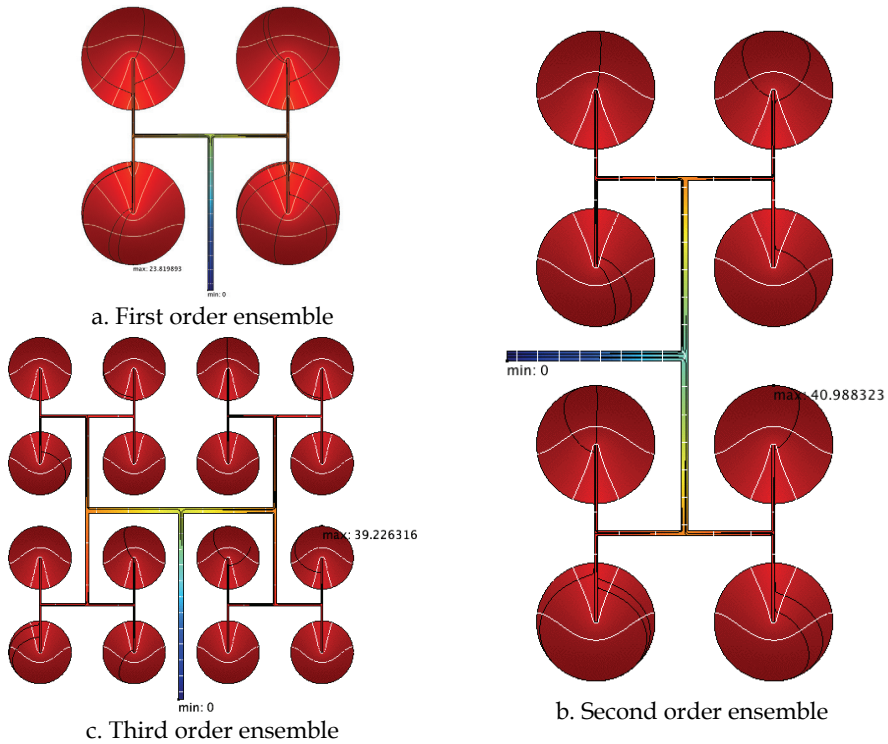


Figure 23. The electric field distribution for several higher order ensembles of wired SPVCs. The simulation results are synthetically presented through the maximum voltage (Fig. 24).

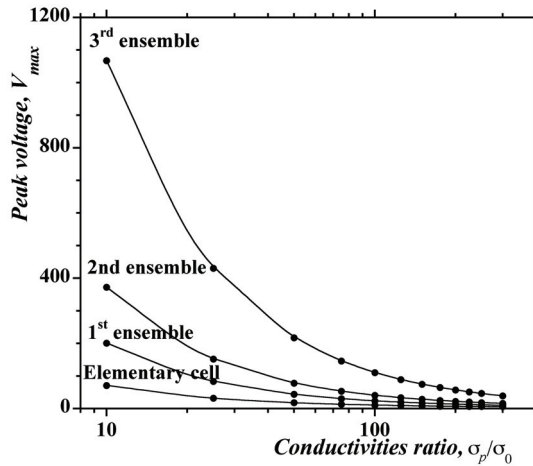


Figure 24. The maximum voltage drop for wired SPV ensembles (non-dimensional quantities)

Apparently,  $V_{max}$  decreases as the conductivity of the high conductivity material increases.

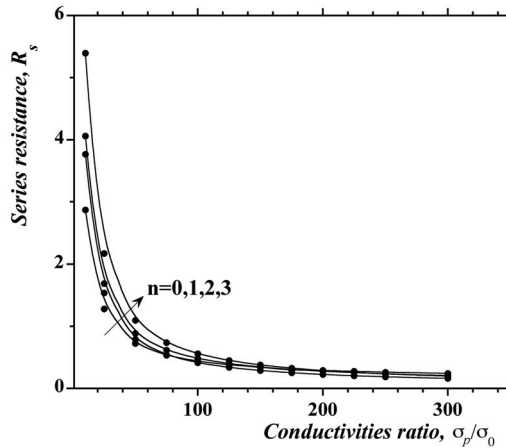


Figure 25. The series resistance for wired SPV ensembles (non-dimensional quantities)

Figure 25 shows the series resistance for the elementary cell ( $n = 0$ ) and the first three higher order ensembles ( $n = 1, 2, 3$ ) as functions of the conductivities ratio,  $\sigma_p/\sigma_0$ .

Clearly, the maximum voltage drops as the conductivity of the high conductivity material increases, which means that the overall voltage drop due to the series resistance is also a decaying function of  $\sigma_p/\sigma_0$ .

As for the honeycomb SPVC ensembles, these results suggest that for higher conductivities ratios all ensembles exhibit almost the same series resistance: a feature consistent with the constructal optimization process.

## 5. Conclusions

In the structural optimization conducted through analytic and numerical simulation the following conclusions were drawn:

- The *constructal principle* is *deterministic*, based on the outlining physical laws in the system under investigation. The optimal series resistance,  $R_s$ , of the PV ensembles are constructed starting from an elemental system, *in a time arrow from small to large*. This technique differs fundamentally from *non-deterministic* (i.e., postulated) designs, e.g., in a top-down sequence from higher order to lower order ensembles.
- The structural optimization used to design each building block and ensemble provides for the minimization of the PV series resistance, or optimal electrical current *access*. *The optimized ensemble exhibits the easiest access of its internal current*.
- The result of the PV  $R_s$  optimization is a structure where the total current is driven to the exterior (terminal) by the smallest voltage drop. This results also in the smallest power loss by the series resistance of the PV system.
- The starting point in the design is the optimization of the elemental system by utilizing the underlying physical laws (here, Maxwell).
- Beginning with the second order flat-surface PV ensemble, one particular rule emerges: *each new ensemble is made of two, lower order, optimized ensembles of the immediately lower level of detail*.
- Although not optimal in a strict mathematical sense, the PV ensembles of order higher than two are *the best blocks that fit together*.

- The optimization based on the analytic solution is valid when the conductivities ratio  $\sigma_p/\sigma_0 \gg 1$ , and when the porosity  $\phi_i \ll 1$ .
- Constructal minimization of  $R_S$  leads to a design that is not only optimal: it has also a *naturally* attractive appeal, where the collector fingers are seen to evolve *naturally* into busbars. Therefore, depending on the shape of the elemental system (rectangular geometry in our analysis), the optimized structures produced by this design may cope with aesthetic criteria requested by architectural and design goals with which PV ensembles have to comply.
- Numerical simulation and the commonly available hardware resources have reached the level where they complement the design tools in engineering.

## 6. Acknowledgments

A.M. Morega acknowledges the “National University Research Council” for financial support through the grant 32/358/2005-2007. J.C. Ordonez acknowledges support from the Office of Naval Research (ONR).

## 7. References

- Altermatt, P.P.; Heiser, G.; Kiesewetter, T.; McIntosh, K.R.; Honsberg, Ch.B.; Wenham, S.R. & Green, M.A. (1977). Establishing an accurate numerical model for the 2D-simulation of buried contact cells. In *the 26<sup>th</sup> IEEE Photovoltaic Specialist Conference*, Anaheim, CA, 29 September – 3 October.
- ATS - Automation Tooling Systems, Inc. (2006). Solar, Industry Note #PV1-0303.01, [www.atsautomation.com](http://www.atsautomation.com)
- Azoumah, Y.; Mazet N. & Neveu, P. (2004). Constructal network for heat and mass transfer in a solid-gas reactive porous medium, *Int. J. Heat and Mass Transfer*, 47, pp. 2961-2970.
- Bejan, A. (1997). The constructal law of structure formation in natural systems with internal flows. In: *Proc. of the ASME, Advanced Energy Systems Division, ASME*, Vol. 37, pp. 257-264.
- Bejan, A. (1997). Constructal theory network of conducting paths for cooling a heat generating volume. *Int. J. Heat Mass Transf.*, Vol. 40, 4, pp. 799-816.
- Bejan, A. (1993). *Heat Transfer*, New York: Wiley.
- Bejan, A. (2000). *Shape and Structure, from Engineering to Nature*, United Kingdom: Cambridge U. Press, Cambridge.
- Burgers, A.R. & Eikelboom, J.A. (1997). Optimizing metalization patterns for yearly yield. *26<sup>th</sup> PVSC*, Sept. 30 – Oct. 3, Anaheim, CA, USA, pp. 219-222.
- Comsol, AB., COMSOL v. 3.0-3.4. (2004-2008). [www.comsol.com](http://www.comsol.com)
- CPS-UNSW, Australia: Centre for Photovoltaic Engineering U. of New South Wales *Solar cells*. (2006) [www.pv.unsw.edu.au](http://www.pv.unsw.edu.au)
- EMSOLAR - Institut für Elektrische Energietechnik, (2007). <http://emsolar.ee.tu-berlin.de/~ilse/solar>
- Green, M. (1986). Operating Principles, Tech. & Systems Applications, In: *Solar Cells*, Australia: U. South Wales.
- Horzel, J. & De Clerq, K. (1995). Advantages of a new metallization structure for the front side of solar cells. *13<sup>th</sup> EC Photovoltaic Solar Energy Conference*, Nice, France. pp. 1368-71.

- Fujipream & Clean Venture, 21, (2006).  
[http://techon.nikkeibp.co.jp/english/NEWS\\_EN/20051209/111508](http://techon.nikkeibp.co.jp/english/NEWS_EN/20051209/111508)
- Viaud, M. (2004). Photovoltaic solar electricity. Part of global strategy, key lecture, *AIE Conference*, Brussels, 23 Sept.
- Kyosemi - Kyoto Semiconductor Corp., (2006). [www.kyosemi.co.jp/index\\_e.html](http://www.kyosemi.co.jp/index_e.html)
- Ledezma, G.A.; Bejan, A. & Errera, M.R. (1997). Constructal tree networks for heat transfer. *J. Appl. Phys.* 82, pp. 89-100.
- Lemmons, D.S., (1997). *Perfect form*, Princeton Univ. Press, Princeton, NJ.
- Morega, A.M., (1998). *Numerical modeling of boundary value problems in engineering* (in Romanian, MatrixRom, ISBN 973-9390-05-6.
- Morega, A.M. & Bejan, A., (2005). A Constructal Approach to the Optimal Design of Photovoltaic Cells, *Int. Journal of Green Energy*, 2, 3, pp. 233-242.
- Morega, A.M.; Ordonez, J.C.; Negoias, A.P. & Hovsapien R. (2006). Spherical photovoltaic cells - A constructal approach to their optimization, *OPTIM 2006*, May 22-24, Brasov, Romania.
- Morega, A.M.; Ordonez, J.C.; Negoias, P.A.; Morega, M. & Hovsapien, R. (2006). Optimal electrical design of spherical photovoltaic cells, *COMSOL Conference*, Congress Center of the Czech Technical University, Prague, October 26.
- Morega, A.M. & Ordonez, J.C. (2006). Constructal Design of Concurrent Power Distribution Networks, *COMSOL Conference*, Boston, October 20-21, Hyatt Regency, Cambridge, Boston, MA, USA.
- Morega, A.M.; Ordonez, J.C. & Morega, M. (2008). A constructal approach to power distribution networks design, *International Conference on Renewable Energy and Power Quality*, ICREPQ'08, 12-14 March, Santander, Spain.
- Negoias, A.P., Morega, A.M., (2005). Constructal Optimization of Spherical Photovoltaic Cells, *Mathematical Modeling of Environmental and Life Sciences Problems, 3<sup>rd</sup> Workshop*, 7-10 September, Constanta, Romania.
- Ordonez, J.C.; Bejan, A. & Cherry, R.S. (2003). Designed Porous Media: Optimally Nonuniform Flow Structures Connecting One Point With One or More Points. *International Journal of Thermal Sciences*, Vol. 42, pp. 857-870.
- Poincaré, H. (1902). *Science and hypothesis* (in English), London and Newcastle-on-Cyne (1905): The Walter Scott publishing Co.
- Radike, M.; Summhammer, J.; Breymesser, A. & Schlosser, V., (2002). Optimization of artistic contact patterns on multicrystalline silicon solar cells, *2<sup>nd</sup> Photovoltaic Solar Energy Conference*. Vienna, Austria [www.ati.ac.at/~summweb](http://www.ati.ac.at/~summweb).
- Travers, D.; Watt, M.; MacGill, I.; Kaye, J.; Kunzi, S. & Spooner, T. (2001). Evaluation tool for building integrated photovoltaic systems. Australia: Photovoltaics Special Research Center, School of Electrical Engineering, Univ. of New South Wales, Sydney, NSW.
- Treble, F.C. Ed. (1991). *Generating electricity from the sun*. (Ifac Symposia Series), Pergamon Press, ISBN13 9780080409368, Oxford, UK.
- SSP - Spherical Solar Power (2006), [www.sspsolar.com](http://www.sspsolar.com)
- Verbeek, M. & Metz, A. (1996). Mechanically grooved high-efficiency Si solar cells with self-aligned metallization. *25<sup>th</sup> IEEE Photovoltaic Specialists Conference*, Washington DC, USA, pp. 521-524.
- STARFIRE, *Photovoltaics Technical Information Guide*, Sc. Ed., Solar energy research institute, [http://starfire.ne.uiuc.edu/ne201/course/topics/solar\\_thermal/](http://starfire.ne.uiuc.edu/ne201/course/topics/solar_thermal/)

# New Methods to Model and Simulate Both Air Exchange and Particle Contamination of Portable Devices

Markus Olin<sup>1</sup>, Lauri Laakso<sup>2</sup>, Jukka Hannula<sup>3</sup>, Timo Galkin<sup>4</sup>,  
Kyösti Väkeväinen<sup>5</sup>, Kari Hartikainen<sup>6</sup> and Eini Puhakka<sup>1</sup>

<sup>1</sup> VTT Technical Research Centre of Finland,

<sup>2</sup> University of Helsinki, Department of Physical Sciences, <sup>3</sup> Nokia Corporation

<sup>4</sup> Nokia Siemens Networks, <sup>5</sup> Metso Automation, <sup>6</sup> Ambertec Ltd  
Finland

## 1. Introduction

Developed countries have made great efforts to improve air quality through adopting clean air plans, which have included measures such as demanding emission and air quality regulations, continuous air quality monitoring in urban/industrial centres and use of cleaner fuels such as natural gas. Meanwhile, in developing countries there is a clear phenomenon of migration from the countryside to the city, which has brought with it greater emissions into the atmosphere, mainly produced by biofuels used in cooking and heating and increasing traffic (Scholorling, 2000; Laakso et al., 2006) with the additional difficulty that in these countries the tendency is to have a stock of old, badly maintained vehicles. These factors have produced far-reaching changes in air quality in urban contexts, especially in the 1990s, when the majority of clean air plans were tightened up (Baldasano et al., 2003).

At the same time, markets for mobile devices have grown strongly in areas with high particle and pollutant concentrations (e.g., Asia, Africa and South America). Exposure to a high amount of fine particles, and the resulting contamination and corrosion, is a potential future reliability risk. To avoid this risk, one must understand the basic physics of particle drifting and, in addition, know the chemical and physical properties of the atmospheric aerosol particles. This includes the mapping and investigation of atmospheric measurements.

Telecommunication equipment is exposed to various kinds of stresses in the course of its life (Roberge et al., 2002; Hannula 2001; Ojala & Väkeväinen 2001; Väkeväinen et al., 2001). The stresses can be divided into mechanical, chemical, thermal, electrical and radiation stresses. The transport of potentially harmful chemical substances, partly or totally bound to fine particles, takes place via molecular diffusion and advection by air flow. Both direct measurements and simulation of flow velocities in electronic devices are complicated tasks, because of the detailed and heterogeneous structure of these devices. In addition to complex

structure, the effect of heat-producing components has to be taken into account since they may alter both the flow velocity and the structure of the device.

The main objectives of the study were to understand the basic chemistry and physics of

- fine particles, air pollution penetration and
- drifting of coarse particles (dust/sand)

into mobile device electronics (e.g., speakers, RF shields and metal display structures, which are the most sensitive to air pollution). Special attention was directed to so-called accumulation-range particles (80 to 1000 nm in diameter) because they are assumed to penetrate constructions such as mobile phones easily and their mass and reactive surface area is relatively large when compared to smaller particles.

Based on this information, the key aims were:

1. Understanding of particle drifts in miniature structures as phenomena.
2. Estimated particle size and number/mass distributions in various use environments.
3. A report concerning particle drifting and deposition in selected mobile devices, including estimation of good and possibly bad material and structural solutions.
4. A verified estimation model for particle drifting in miniature structures capable of estimating dependency on structural differences and particle sizes.
5. Establishment of the link between test conditions and real usage conditions, by using simulation methods.

Our approach has included several steps (see Fig. 1):

1. Development of a model for transport in air both inside and outside the equipment.
2. Development of a model for contamination processes – most often small particles in our cases.
3. Combining and simplification of this knowledge to create a contamination model able to predict phone contamination in a real user environment throughout the phone's service life.

Each step includes several smaller tasks (see Fig. 1). For example, study of air exchange was carried out in separate steps. First, gas flows in the mobile phone were investigated via the helium-based leakage method (its first application to electronic devices), and we observed that the results had no real meaning without extensive modelling. Next, these results were fitted by analytical models, incapable of any predictive calculations, to approximate diffusivity and permeability inside the phone. After that, a much more complicated numerical model was developed. A commercial tool, FEMLAB®, was applied to both apply realistic geometric structures and link several physical phenomena: transport of mass, heat and momentum. Finally, the numerical model was modified for cases where temperature differences (due to the heat-producing components) drive the gas transport. These four steps enabled calculation of air exchange coefficient values for a specific mobile phone model, for a typical use situation: phone on and vertically oriented.

The deposition of harmful aerosol particles in a mobile phone was approached with a similar multi-step approach: Deposition of different-sized particles was estimated via a combination of analytical and numerical approaches. For this, a coupled particle convection/diffusion and flow velocity model was developed to estimate deposition coefficients. First, equations for the flow velocity calculations and aerosol particle transport were formed. Second, the equations were implemented in FEMLAB® with Chemical Engineering Module. Finally, the model was applied in calculating important parameter values needed in the simplified contamination model.



Data from these two steps, gas exchange and deposition, could then be combined with experimental field data, phone user characteristics and an indoor air model modified to be suitable for the conditions inside a phone.

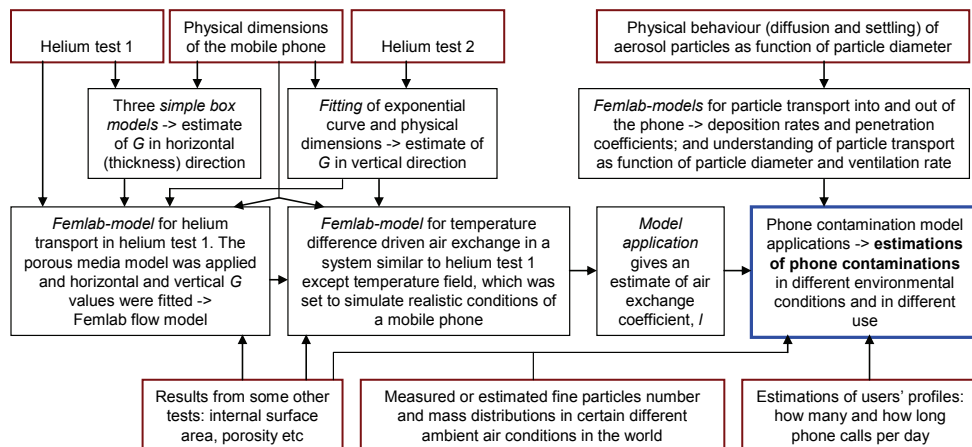


Figure 1. A schematic picture of the models and input parameters used in this study

## 2. Aerosol particles as a contaminating substance

Contamination of mobile devices may be caused by chemical compounds either in gas phase or bound to particles; water, either vapour or aqueous, is a very important contaminant and is discussed separately below.

### 2.1 Effect of chemical composition

Contamination caused by chemical compounds is one of the stresses detected in the structures of small electronic devices. The transport of chemical compounds is caused by molecular diffusion and advection by air flow. Chemical contamination is a very complex and unwanted phenomenon, which causes deposition formation on the surfaces of devices. Despite measurements, control and simulation of flow velocities in electronic devices, the problem of contamination still remains among the unsolved problems. Contamination leads to reduced functionality of the devices, increased power demand and a shortened life. Further, small devices have to be designed so that the effect of contamination is minimised, because the small structures of devices cannot be cleaned mechanically or chemically.

The contamination rate, the chemical composition and the physical properties of material deposited on the device surfaces depend on, e.g., outside and indoor air, air flows inside the devices, ambient operation temperatures and the construction materials of the devices. The contamination by chemical compounds is based on the deposition formation by crystallisation and surface reactions. Surface reactions are very harmful, because in a very short time they can change the surface properties (structural and electrostatic) of devices. Therefore, it is important to know the chemical compounds causing the contamination and possible reactions inside the devices. After that, the attachment of depositions can be controlled by choosing the materials for construction such that the interactions between device surfaces and depositions are as weak as possible.

**2.2 Fine particles and their deposition mechanisms inside an electronic device**

Particles of different sizes come from different sources (see Fig. 2) (Seinfeld & Pandis, 1998). Nucleation-mode particles result from gas-to-particle conversion of different chemical compounds, like sulphuric acid and ammonia. Some nucleation-mode particles are also emitted directly from gasoline engines (Harris & Maricq, 2001). Aitken-mode particles are directly emitted from traffic exhaust, mainly diesel engines. They also result from condensational growth of nucleation-mode particles. Accumulation-mode particles originate from industrial combustion and re-suspension from roadbeds. Some particles also originate from natural sources like sea spraying and cloud processing of particles and vapours. The more polluted the air is, the more accumulation particles there are.

One-micron particles may come from natural sources, re-suspension and combustion, whereas particles of between 1 and 10 microns are mainly mechanically generated; dust, re-suspension, results of industrial processes and sea salt. In developing countries, the main sources are direct emissions from traffic, domestic coal- and biomass-burning and industry.

When an electronic device is used, it is exposed to aerosol particle pollution. Pollution can be transported into the phone by four different mechanisms:

- Convection. Several components heat up during operation. The temperature differences induce convection air flows that can transport aerosol particles into the phone.
- Thermal expansion. Another, possibly important transport mechanism is the thermal expansion of the gas inside the device. If, e.g., the temperature of the gas changes from 25 °C to 85 °C, the volume of the gas changes about 20%. When the air cools down, its volume decreases and new air is imported to the device.
- Mechanically drifting powder material.
- Coarse material (lint, sand and metal particles from keys and the like) is also transported from pocket or bag to the device.

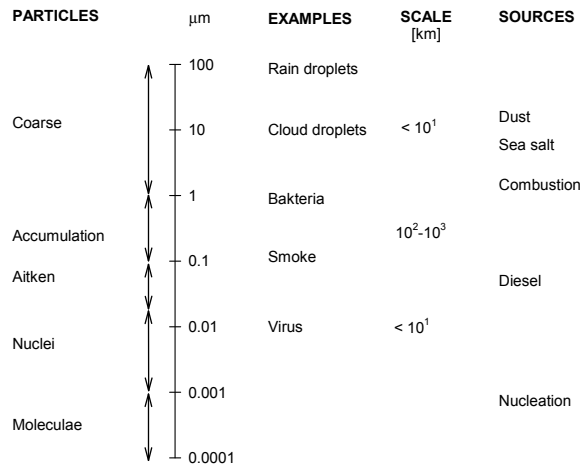


Figure 2. Size scales of aerosol particles. Scale does mean a representative regional transport distance of different particle sizes. It is a combination of typical wind speed and loss mechanisms. For example, nucleation-mode particles coagulate with bigger particles, while coarse particles are deposited rapidly by gravitation. Typical sources and examples of particle types are also shown

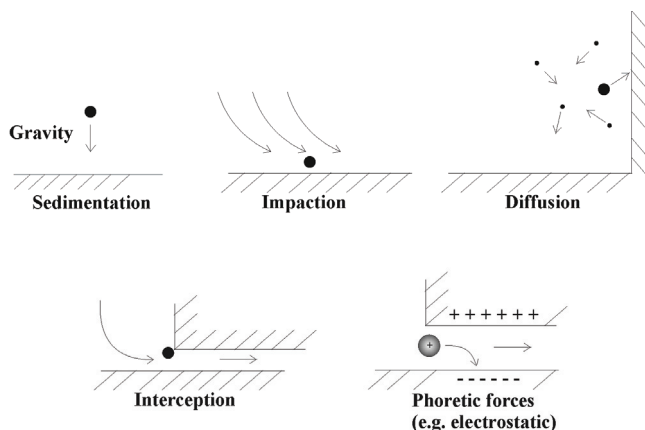


Figure 3. Aerosol particle deposition mechanisms

Once in the device, aerosol particles may be deposited on the internal surfaces of the device. Depending on the aerosol particle size, different mechanisms deposit them in devices. A key aerodynamic property in deposition is the aerodynamic size. For airborne particles, aerodynamic size depends on the particle's shape and density. The aerodynamic size differs from the actual size and accounts for the aerodynamic behaviour of an aerosol. Of all sizes, the accumulation-mode range (0.1–1  $\mu\text{m}$ ) penetrates most efficiently through any filter or construction. This is because smaller particles are filtered due to Brownian diffusion, whereas bigger ones are affected by gravitational settling.

The most important deposition mechanisms of airborne particles in electronic devices are sedimentation, impaction, Brownian diffusion, interception and thermophoresis and electrophoresis. These mechanisms are summarised in Fig. 3 and discussed below.

- *Sedimentation*. Sedimentation represents deposition caused by gravity. The chance of particle deposition in the device by sedimentation increases as the particle size, particle density and amount of time (residence time) spent in the airway increase. Deposition by sedimentation is important for particles with an aerodynamic diameter greater than 0.5  $\mu\text{m}$ .
- *Impaction*. When the aerodynamic diameter is larger than 1  $\mu\text{m}$ , particles can be deposited on external device surfaces. The chance of impaction increases as the air velocity, particle size and particle density increase.
- *Brownian Diffusion*. For particles with an aerodynamic diameter less than 1  $\mu\text{m}$ , Brownian diffusion is a major means of deposition in airways where the bulk flow is very low or absent. Deposition by Brownian diffusion is especially important for particles with aerodynamic diameters less than 0.2  $\mu\text{m}$ . Deposition by Brownian diffusion is unimportant for relatively large particles.
- *Interception*. Particle deposition in the air tract can occur when the edge of the particle contacts the airway wall. For elongated particles (e.g., fibres), interception is an important respiratory-tract deposition mechanism. The chance of particle interception increases as the airway diameter becomes smaller.
- *Thermophoretic and electrophoretic forces*. Aerosol particles are often electrically charged. When they are, they can exhibit greater regional deposition than would be expected

from their size, shape and density. The same applies also for strong temperature gradients, which drives particles from warm to cold places.

According to current knowledge, there can be several possibly harmful (for mobile electronic devices) properties of aerosol particles:

- Contamination. Contamination has adverse effects on conductivity. It also makes screens dirty and may damage connectors.
- Contamination combined with chemical effects like corrosion. In this case also relative humidity (RH) and temperature ( $T$ ) are important. In addition to aerosol particles, air flows transfer water vapour and other gases to the phone. Small aerosol particles are often acidic on account of, e.g., sulphuric compounds. Even if the relative humidity is low, some chemical compounds are hygroscopic and may attract water vapour. If air temperature decreases, vapours condense on the internal surfaces because the saturation vapour pressure is a strong function of temperature. If, for example, the temperature of the phone decreases from 30 °C to 24 °C at a relative humidity of 70%, condensation takes place.
- The possible effect of aerosol particles on harmful gas compound (e.g.,  $\text{SO}_2$ ) deposition. If the surface is covered with aerosol particles, its area can increase greatly, which increases the deposition of gaseous pollutants.

### 2.3 Effect of water vapour

Water is present in everyday life in many forms, and a cubic metre of typical indoor air contains 5–20 grams of it, depending on temperature and relative humidity. This air-bound humidity is easily transported wherever the air itself goes. If the temperature is dropping, the water stored in air may precipitate and attach to surface structures; in combination with chemical compounds (possibly in particle form), this water may be very corrosive or otherwise harmful. Our studies have focused mainly on particulate matter, but they are closely linked to water studies via estimation of air exchange between the device and its environment, and the polluting potential of particle-bound chemicals.

## 3. Laboratory studies of particle exposure

In an aim to understand the processes of contamination by particles, the following experimental studies were carried out:

1. Three sets of copper samples were prepared and exposed to ammonium sulphate aerosol particles. The idea was to find a laboratory method to investigate aerosol particle penetration into the phone.
2. The copper samples were investigated by measuring their electrical conductance and using two ion beam methods to determine the surface impurity concentrations.

### 3.1 Exposure of samples by ammonium sulphate

A polydisperse ammonium sulphate aerosol was generated from an aqueous solution with an atomiser. Droplets from a sprayer were mixed with dry air to solidify the particles. The diluted dry aerosol size distribution was measured using a DMPS where aerosol passed through a charger (bipolar Am-241 neutraliser) and the size distribution of the particles was measured with a differential mobility analyser (DMA) and a condensation particle counter (CPC). The size measurements were done by scanning the voltage of the DMA. The mean

particle size in the experiments was about 50 nm, and the total number concentration was on the order of  $50,000 \text{ cm}^{-3}$ .

The exposures of the copper samples were done in a container (10 cm in diameter and 4 cm high) through which the aerosol was led. The exposure times were 1 day and 4 days for the two pilot samples (case A). A second set of exposures (case B) was done for 4 days and 8 days. For both periods, 2 copper and 2 carbon plates were exposed. Copper plates were investigated with the ERDA method and carbon plates with the RBS method (see section 4.2). In the third experiment set (case C) the samples were prepared by evaporating a 100 nm copper layer on top of a silicon wafer in order to obtain a clean and smooth surface for exposure to ammonium sulphate particles.

### 3.2 Ion beam analysis

Two different ion beam methods were used for the analysis of the atomic concentrations of different elements on the surfaces of the exposed samples. In both of these methods, the concentration values are based on the detection of the products from scattering reactions between accelerated primary ions and target atoms in the samples under study. The scattering reactions are caused by Coulomb interaction, which is well understood, thus enabling us to obtain accurate results without the use of standard samples.

In the Rutherford backscattering spectrometry (RBS) measurements, 2-MeV He ions were used as incident ions. The RBS method gives accurate and reliable concentration values for impurity atoms, which have higher mass than the main constituents of the sample. This is why carbon backings were used in the RBS measurements. The results indicated clearly the existence of sulphur on the sample surfaces, but no distinct correlation was seen between the exposure time and the sulphur concentration. This may be connected to the observation of large amounts of other impurities in the samples.

In elastic recoil detection (ERD) measurements, 20-MeV iodine ions were used as incident ions. A time-of-flight - energy detector was used to detect simultaneously the energy and the velocity of the recoiled target atoms at an angle of  $40^\circ$  relative to the incident beam direction. This made it possible to separate different masses of each recoil atom species, and thus to determine at the same time concentrations of all different elements in the samples, from hydrogen up to the heaviest existing atoms. Exposed copper plates and copper films on silicon wafers were analysed with the ERD method.

The results from copper plates indicated the existence of sulphur, among many other impurities, on the sample surfaces, but no clear correlation was seen between the exposure time and the sulphur concentration. This was mainly because of the large amounts of other impurities on the samples; even on the reference samples, which were not exposed to ammonium sulphate particles.

The results from evaporated copper films indicated clear correlation between the aerosol exposure time and impurity concentrations. A large difference between the two samples with longest exposition times can be explained by the position non-homogeneity in the exposition, which was optically visible on the sample surfaces. A surprising result was the relatively large amount of chlorine on the sample surfaces. The sources of chlorine impurities are currently unknown.

#### 4. Air-exchange experiments and modelling

It is difficult to model directly and productively the air flow inside electronic devices without any experimental data. Therefore, we carried out some helium experiments before starting the model development work. The helium method is based simply on use of this inert, small-sized and rather easily analysed noble gas as a tracer in air flow measurements (see, e.g., Hartikainen et al., 1994).

##### 4.1 Helium experiments

In the first part of the experimental study, the phone was placed inside a metal chamber. The helium injection capillary was connected to the right corner of the bottom of the phone, the nitrogen input was connected to the bottom left corner of the metal chamber and the helium exhauster in the upper right corner of the metal chamber (see Fig. 4). First, pure helium was injected inside the phone over 20 seconds, and then the injection capillary was closed. The mixed gas ( $N_2 + He$ ) flux was measured, and the time constant of total gas flow was calculated from the measured break-through curve (see Fig. 5). The calculated time constant of the total gas flow was 411 seconds.

In the second part of the study, the phone was sealed with elastic gas-tight material (see Fig. 6). Only the selected measuring point was unsealed. The measurement protocol was as follows: 1. Helium was injected inside the phone from point 1 and the overproduction flowed out from point 2. After the phone was filled, both the entry (point 1) and the exit (point 2) channels were closed (see Fig. 6) for 60 seconds. Then the out-flowing gas for the chosen measuring point was measured by helium exhauster. The typical break-through curve is shown in Fig. 7. Local gas flow values were measured from 15 different points (see Table 1).

Results are given as relative gas flow values for every measurement point and as the total time constant. The relative gas flow values were calculated by dividing the measured maximum values (average value of 1.6 to 1.8 minutes) by the maximum value at a reference point.

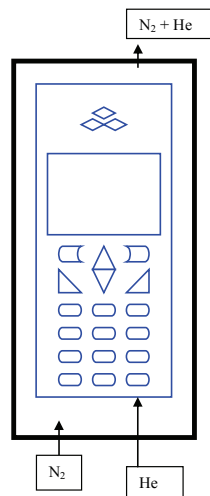


Figure 4. The experimental set-up for the total gas flow through the cover

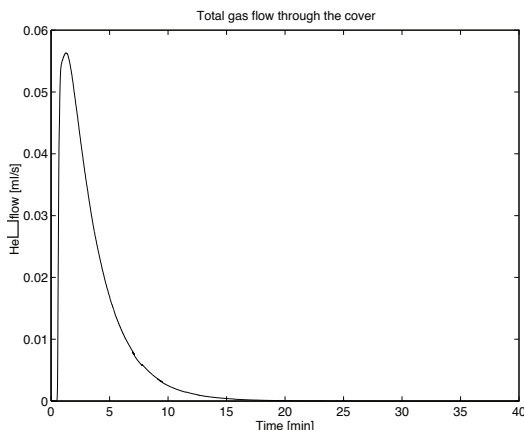


Figure 5. The total gas flow break-through curve

### 4.2 Analytical helium models

In total, four models (three analytical models and one numerical model, He-fit – see Table 2) were developed to utilise the helium test data from the first experimental set-up. The second helium experiment was fitted by a simple exponential function.

The measured total and void volumes, 70 and 28 ml, respectively, give a porosity value of 0.4. With the macroscopically measured internal surface area,  $38,000 \pm 10,000 \text{ mm}^2$ , the ratio to void volume gives about  $1.4 \pm 0.4 \text{ mm}$  for mean free distance between internal surfaces.

The simple analytical models consist of two reservoirs, denoted reservoir 1 (free volume of the measurement chamber) and reservoir 2 coupled only to reservoir 1 (internal volume of the mobile phone), the volumes of which are  $V_1$  and  $V_2$ , respectively (see Fig. 8). There was constant air flow into and out of reservoir 1. The mean velocity at the outlet was  $v_{out}$  and the surface area  $S_{out}$ . Between the reservoirs the studied compound is assumed to have an exchange velocity of  $v_{int}$ , which is assumed to flow by a surface area of  $S_{int}$ . Initially the concentrations in reservoirs 1 and 2 were zero and  $c_0$ , respectively.

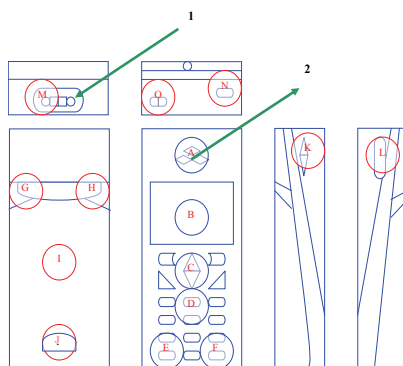


Figure 6. The experimental set-up for the local gas flow through the cover

Measuring point	Relative gas flow value
A	13,700
B	1
C	9,100
D	5,100
E	12,500
F	8,400
G	9,100
H	7,500
I	1
J	8,900
K	11,700
L	8,600
M	10,800
N	10,100
O	73,100

Table 1. The relative gas flow value at point B was equivalent to that at reference point I

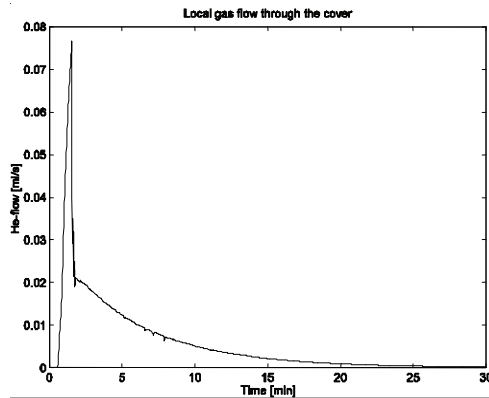


Figure 7. Typical break-through curve for measuring spot H

Name	Description
S1a	Basic analytical model for test case 1
S1b	Well-mixed analytical model for test case 1
S1c	Model S1a without re-flow into mobile phone
S2	Basic analytical model for test case 2
Nfit	Numerical model for test case 1
Nflow	Numerical model for mobile phone flow simulation

Table 2. List of models



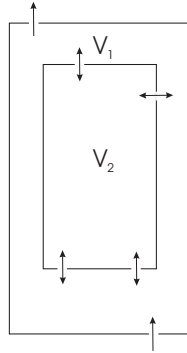


Figure 8. A schematic picture of reservoir volumes used in analytical models

The internal exchange velocity may follow from both molecular diffusion and gas flow, and we assume that the diffusion flux density is a product of diffusivity  $D_0$  (of helium in this case,  $6.8 \cdot 10^{-5} \text{ m}^2/\text{s}$ ) and gradient of concentration,  $c$ . A further simplification is that the gradient is approximated by the ratio of mean concentration to characteristic length scale  $L$ . The internal structure of a mobile phone is quite complicated, causing lengthening of the diffusion path, which is taken account of by correcting the diffusivity via geometric factor  $G$  (van Brakel & Heertjes, 1974). According to these assumptions, the diffusion flux density (see, e.g., Hinds, 1999),  $J$ , may be written as

$$J = -D \frac{dc}{dx} \cong -GD_0 \frac{c}{L} \tag{1}$$

where  $D = GD_0$ . If we approximate the mobile phone as a porous medium, the internal surface area,  $S_{\text{int}}$ , is simply total external surface area  $S$  multiplied by the porosity,  $\phi$ . Therefore, the diffusion flux,  $q$ , is given as

$$q = S_{\text{int}} J \cong -S_{\text{int}} v_{\text{int}} c \tag{2}$$

where  $v_{\text{int}} = GD_0/L$ .

The characteristic length may be approximated from the dimensions of the mobile phone to be about 20–50 mm. Geometric factor  $G$  is then a fitting parameter and describes the internal structure of the mobile phone.

First, we developed a model (S1a) for helium test 1 by applying the internal exchange velocity. We can write the following system of linear differential equations for mass balances of the studied compound in both reservoirs:

$$\begin{cases} V_1 \frac{dc_1}{dt} = -v_{\text{out}} S_{\text{out}} c_1 + v_{\text{int}} S_{\text{int}} (c_2 - c_1) \\ V_2 \frac{dc_2}{dt} = -v_{\text{int}} S_{\text{int}} (c_2 - c_1) \end{cases} \tag{3}$$

The solution with correct initial value is

$$\begin{cases} c_1 = c_0 \frac{\lambda_{int}}{\omega} e^{-\frac{1}{2}(\kappa\lambda_{int} + \lambda_{int} + \lambda_{out})t} \sinh \omega t \\ c_2 = c_0 \left[ \cosh \omega t + \frac{\kappa\lambda_{int} - \lambda_{int} - \lambda_{out}}{2\omega} \sinh \omega t \right] e^{-\frac{1}{2}(\kappa\lambda_{int} + \lambda_{int} + \lambda_{out})t} \end{cases} \quad (4)$$

where

$$\begin{cases} \lambda_{out} = \frac{v_{out} S_{out}}{V_1} \\ \lambda_{int} = \frac{v_{int} S_{int}}{V_1} = \frac{GD_0 S \phi}{L V_1} \\ \kappa = \frac{V_1}{V_2} \\ \omega^2 = \frac{1}{4} (\kappa\lambda_{int} - \lambda_{int} - \lambda_{out})^2 + \kappa\lambda_{int}^2 \end{cases} \quad (5)$$

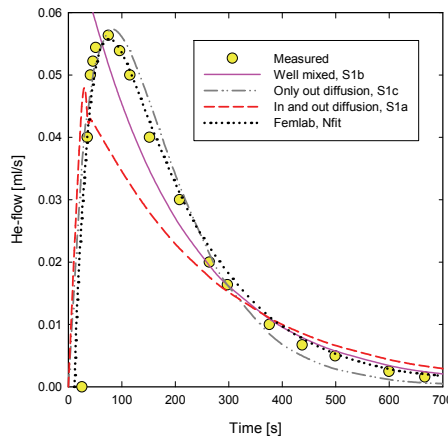


Figure 9. Results of the fittings of the three different analytical models, along with the results of the fitting of the numerical model

Two extreme cases are worth examination: well-mixed (S1b) and a system without return flux into the mobile phone (S1c). The solution for S1b is simply exponential, and S1c has solution

$$\begin{cases} c_1(t) = c_0 \frac{\lambda_{int}}{\lambda_{out} - \kappa\lambda_{int}} (e^{-\kappa\lambda_{int}t} - e^{-\kappa\lambda_{out}t}) \\ c_2(t) = c_0 e^{-\kappa\lambda_{int}t} \end{cases} \quad (6)$$

After fitting the models to one of the experimental data sets, we observed that the simple well-mixed gave the best fit for long times, and the model with internal flux not depending

on the external concentration was best at the beginning. All of the model fittings described below are shown in Fig. 9. For internal exchange  $\lambda_{\text{int}}$  we obtained the best fit with  $a$  value of  $0.0156 \text{ s}^{-1}$ . It is possible to estimate  $G$  from Eq. 10 ( $\varphi = 0.3$ ), which gives  $G = 0.03$ . Finally, the helium diffusivity in this structure will be  $2 \cdot 10^{-6} \text{ m}^2/\text{s}$ .

At the start of the second helium test measurement, there was a peak value (see Fig. 9), but after that the flux decreased clearly exponentially and the fitting gave the value  $0.0029 \text{ s}^{-1}$  for coefficient  $\lambda_{\text{int}}$ .

### 4.3 Numerical helium models

In addition to analytical models, a phenomena-based (diffusion, fluid flow and thermal conduction) model was developed both for prediction of air-exchange values for this work and to be extended and applied in other systems. The complexity of this model makes only numerical solutions available. FEMLAB® (Comsol AB, 2004a), a commercial interactive environment for modelling and solving problems on the basis of partial differential equations, was chosen as the numerical tool. For particular classes of problems, special modules providing a more comfortable working environment are available. In this work, the Chemical Engineering Module (Comsol AB, 2004b) was applied.

A Navier-Stokes model and Brinkman equation were used to calculate two-dimensional velocity ( $v_x, v_y$ ) and pressure fields  $P$  outside and inside the mobile phone, respectively.

The Brinkman equation is an extension of the well-known Darcy's law. It is possible to add a force field to Navier-Stokes equations, enabling, for example, modelling of free convection, when the temperature field is given. Conduction-convection was used to calculate temperature in two dimensions.

To model in more detail the transport of helium out of the phone, we developed a numerical model as explained below. The model geometry is shown in Fig. 10. The mobile phone was assumed to be an anisotropic porous system with porosity  $\varphi = 0.3$ . The transport was assumed to occur by diffusion and convection both in the external volume and inside the mobile phone. The air density,  $\rho$ , was assumed to be  $1.2 \text{ kg/m}^3$ , and dynamic viscosity was equal to  $\eta = 1.8 \cdot 10^{-5} \text{ Pa s}$ . The permeability,  $\kappa_B$ , needed in the Brinkman equation was fixed at  $1.2 \cdot 10^{-5} \text{ m}^2$ , which is near the value calculated for flow between flat surfaces with a distance of  $1.4 \text{ mm}$ . The total number of elements was varied from 3,000 to 8,000. Time-dependent simulations were extended from 0 to 1,000 seconds, with logarithmic output times.

The best fit to the experimental data was obtained with  $G = 0.007$  in the horizontal direction, and, as assumed, ten times higher in the vertical direction. The modelled out-flow curve is also shown in Fig. 9. The fitted  $G$  values were then applied in gas flow modelling calculations with the same geometry. The simulated state of the system 7, 52, 139 and 373 seconds after the injection of helium was stopped is shown in Fig. 11.

To estimate the ventilation coefficient (the ratio of the exchanged air volume per unit time to the volume of the system) inside the mobile phone, the same geometry as in diffusion transport calculations was applied. The Brinkman equation in the applied tool is isotropic, and therefore the  $G$  value was chosen to be the same for both directions.

Finally, we modified the numerical model for cases where temperature differences (due to the heat-producing components) drive the gas transport. This last model was then applied to estimate ventilation coefficients, which may be used in models estimating the long-term contamination of electronic devices. The temperature of the in-flowing gas was set to  $25 \text{ }^\circ\text{C}$ ,

the system walls were maintained at a temperature 10 degrees higher and the outer temperature of the battery was kept at 45 °C. These temperature differences caused an inflow of 1 ml/s. Of the total flow into the measuring system, less than 10% was transported via the mobile phone. The simulated velocity fields inside and outside the mobile phone, and temperature both inside and outside, are shown in Fig. 12. From these calculations it can be deduced that a suitable estimate for ventilation coefficient varies from 3 to 10 h<sup>-1</sup>.

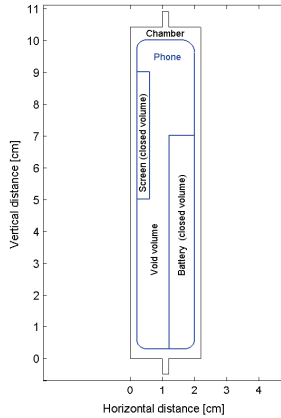


Figure 10. The model geometry for helium and ventilation coefficient calculation is depicted in the figure. Some parts (display and battery) were excluded from the mobile phone – the exclusions were mainly based on results from the second helium experiment

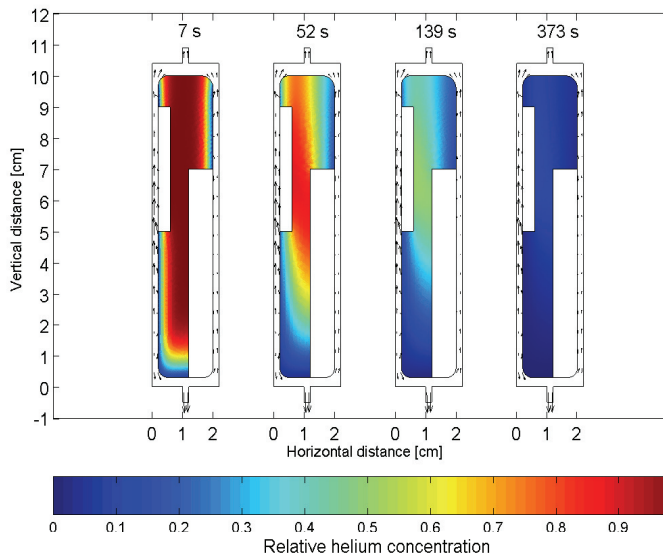


Figure 11. Simulated helium concentration 7, 52, 139 and 373 seconds after the beginning of the test. The colour map shows the relative helium concentration inside the phone, and the arrows describe the total flux density of helium outside the phone

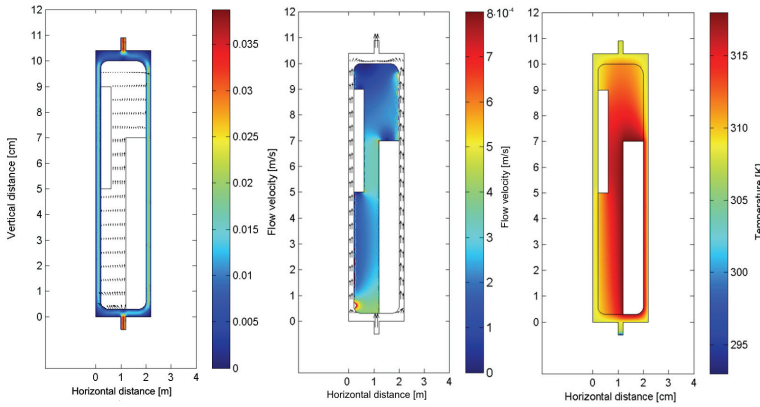


Figure 12. Simulation of flow velocity and temperature inside and outside the phone. The left pane’s arrows indicate the velocity inside the phone and the colour-map that outside. In the middle pane, arrows are applied for outside and colours for internal flow velocity. The colour-map (right) shows the temperature distribution both in- and outside the phone

### 5. Particle penetration models

In this study, we estimated the deposition of harmful aerosol particles in a mobile phone with a multi-step approach, which proceeded from a study of air flows inside a mobile phone (Olin et al., 2006). Next, we generalised an indoor air model to be applied as a contamination model for mobile phones. This model needed some parameter values for both air flow and particle deposition efficiency inside a mobile phone. To have, at least approximate, values of these parameters, we developed a numerical particle transport model, which is described here. The basics and actual application of our contamination model are reviewed only in brief here.

#### 5.1 Governing equations

We developed a coupled particle convection, diffusion and flow velocity model to estimate deposition coefficients of particles of different sizes.

First, we designed a model geometry (see Fig. 13) aimed at describing the inner volume of either end of the mobile phone. The scale of our model may be compared to the matchstick in the same figure. Second, we formed equations for the flow velocity calculations and aerosol particle transport. We applied the Navier-Stokes equations in 2D for flow velocities:

$$\begin{aligned}
 \frac{\partial v_x}{\partial t} + v_x \frac{\partial v_x}{\partial x} + v_y \frac{\partial v_x}{\partial y} &= -\frac{1}{\rho} \frac{\partial P}{\partial x} + \frac{\mu}{\rho} \left[ \frac{\partial^2 v_x}{\partial x^2} + \frac{\partial^2 v_x}{\partial y^2} \right] \\
 \frac{\partial v_y}{\partial t} + v_x \frac{\partial v_y}{\partial x} + v_y \frac{\partial v_y}{\partial y} &= -\frac{1}{\rho} \frac{\partial P}{\partial y} + \frac{\mu}{\rho} \left[ \frac{\partial^2 v_y}{\partial x^2} + \frac{\partial^2 v_y}{\partial y^2} \right]
 \end{aligned}
 \tag{7}$$

and

$$\frac{\partial v_x}{\partial x_x} + \frac{\partial v_y}{\partial x_y} = 0 \quad (8)$$

The transport of the particles was modelled via the following diffusion-convection equation:

$$\frac{\partial c}{\partial t} + v_x \frac{\partial c}{\partial x} + [v_y - v_{TS}(d_p)] \frac{\partial c}{\partial y} = L(d_p) \left[ \frac{\partial^2 c}{\partial x^2} + \frac{\partial^2 c}{\partial y^2} \right] \quad (9)$$

Diffusion coefficients,  $L$ , and terminal settling velocities,  $v_{TS}$ , vary quite a lot as a function of particle size (see Table 3). It is important to note that very small particles have high diffusivity while big particles have high terminal velocity, and medium size particles neither diffuse nor drop down clearly in the time scales studied.

## 5.2 Model implementation

We implemented the governing equations of our particle transport model in the commercial numerical partial differential equation solver FEMLAB<sup>®</sup> 3.0 together with Chemical Engineering Module (Comsol, 2004a; Comsol, 2004b). The flow velocity (see Fig. 15) was caused by the pressure difference between narrow inlets and outlets (1.0 mm), mainly to create an upward velocity component to compete with the terminal settling velocity.

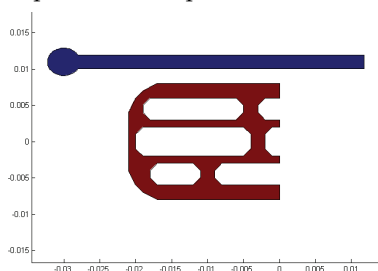


Figure 13. The model geometry applied in our particle transport model and a matchstick (the unit on the axis is the metre)

Diameter (nm)	$L$ ( $\mu\text{m}^2/\text{s}$ )	$v_{TS}$ ( $\mu\text{m}/\text{s}$ )	$\langle x(1 \text{ s}) \rangle$ diff. ( $\mu\text{m}$ )	$\langle x(100 \text{ s}) \rangle$ diff. ( $\mu\text{m}$ )	$100 \text{ s} \times v_{TS}$ ( $\mu\text{m}$ )
10	54,000	0.07	330	3,300	7
30	5,800	0.2	110	1,100	20
100	690	0.88	37	370	88
300	130	4.4	16	160	440
1,000	27	35	7.4	74	3,500
3,000	7.8	270	4.0	40	27,000

Table 3. Diffusion coefficients and terminal settling velocities for some particle diameters (Hinds, 1999). Particles are assumed to be spherical and their density  $1,000 \text{ kg}/\text{m}^3$ . In addition, the mean distances from diffusion in 1 and 100 seconds is calculated; for comparison, distance travelled by terminal settling in 100 seconds is given also. Particles with a diameter of 100–300 nm are neither diffusing nor settling in this time

The mesh was made denser at all surfaces to enable the calculation of particle diffusion flux to them (see Fig. 14). Particles were assumed to have zero concentration at all solid surfaces, which creates sharp gradients. All told, 20,576 mesh elements, of which 2,000 were surface elements, were created for most calculations, giving about 200,000 degrees of freedom. In some cases (e.g., with large particles, when gravitational settling was dominating), more elements were needed, but with the applied computer (0.5 GB memory) this was not possible.

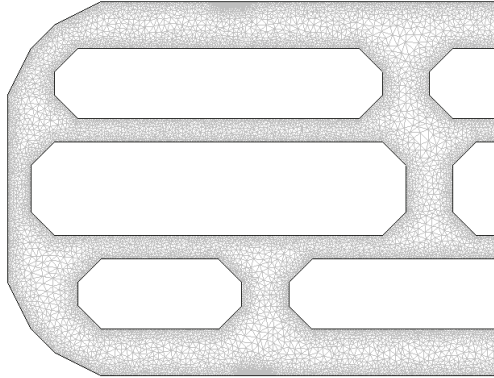


Figure 14. The applied mesh

**5.3 Model applications**

We applied the model in calculation of important parameter values needed in the simplified contamination model. In total, seven different cases (from pure diffusion to maximum inlet flow velocity of 3.0 mm/s) were calculated for particle diameters 30, 100, 300, 1,000 and 3,000 nanometres (particle density 1,000 kg/m<sup>3</sup>). The applied pressure differences, inlet velocities and corresponding ventilation coefficients in our simplified contamination model are shown in Table 4.

All told, 34 test-case calculations were made to include all flow velocity cases and all studied particle diameters. In nine test cases, our model did not converge well. The test cases are named by particle diameter in nanometres and by the flow velocity code, and all test-case names start with 'D'; for example, D100\_AA represents the 100-nanometre particles in case AA. In figures 17 and 18, relative concentration inside the system studied is shown for 12 selected test cases.

Case	$\Delta P$ ( $\mu\text{Pa}$ )	$v$ (mm/s)	$l$ ( $\text{h}^{-1}$ )
0	0	0 *	
AAA	9,2	0.01	0.23
AA	27,6	0.03	0.69
A	92	0.1	2.3
B	276	0.3	6.9
C	920	1.0	23
D	2 760	3.0	69

\* Diffusion only

Table 4. Case numbers, pressure difference  $\Delta P$ , inlet velocity  $v$  and ventilation coefficient  $l$

In the present work, we were mainly interested in the calculated values of deposition rates,  $a$ , which are tabulated in Table 5 and shown in Fig. 16. There was a clear minimum in  $a$  values for particle sizes at around 100 to 300 nm, which means that particles of that size are neither diffused on surfaces nor settled by gravitation on horizontal surfaces. These effects or the lack of them can be seen readily in relative concentration (figures 17 and 18).

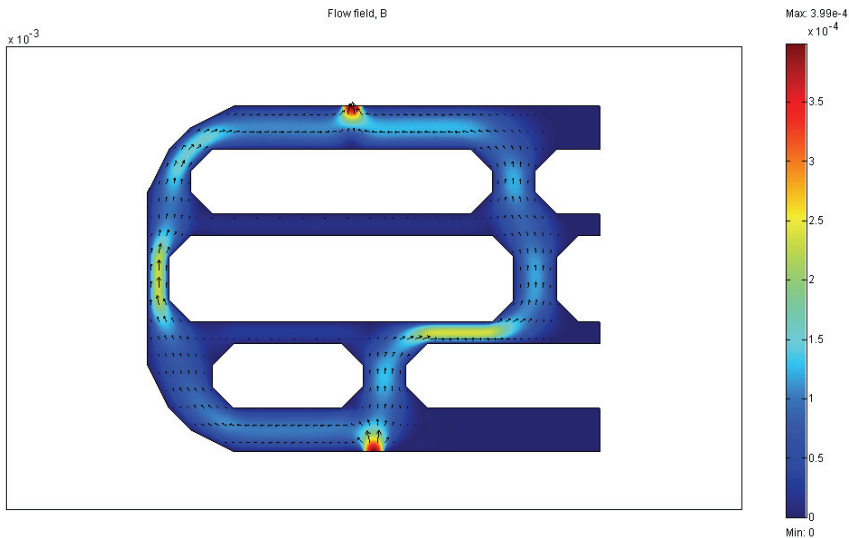


Figure 15. The calculated velocity field for case B. All other cases were similar, except, of course, that the velocity scale varied. The geometry was intentionally created such that both routes from inlet to outlet are in use

$d_p$ (nm)	0	AAA	AA	A	B	C	D
10	645	628	583	474	299	368	412
30	70	52	40	39	44	52	84
100	15	4.7	5.3	5.9	9.0	19	39
300	55	9.2	7.2	6.8	7.3	14	35
1,000	nr	nr	nr	63	54	49	75
3,000	nr	Nr	nr	nr	nr	363	409

Table 5. Calculated deposition rate  $a$  (in  $h^{-1}$ ) for test cases as a function of particle diameter (nr = the model didn't converge)



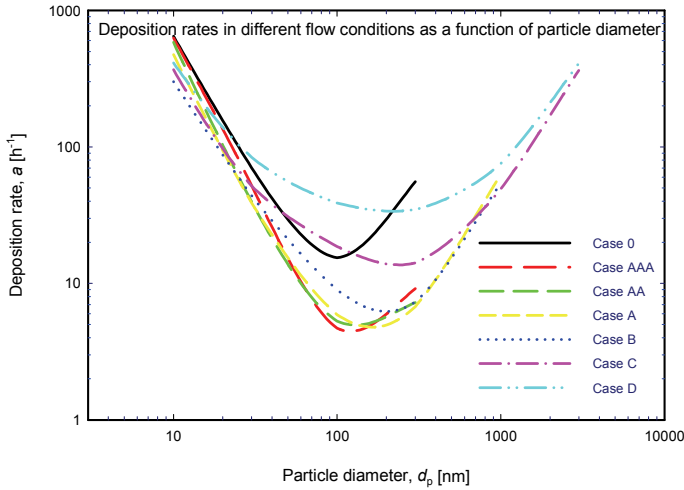


Figure 16. Deposition rate as a function of particle diameter in different cases. There is a clear minimum, which is lowest in the cases with lowest flow velocity

**5.4 Simplified contamination model for particle accumulation estimates**

In order to calculate long-term contamination of mobile electronic devices, we modified our indoor model (Raunemaa et al., 1989) to create a phone contamination model to suit these new conditions. Below, the contamination model is briefly reviewed.

Deposition is characterised by a set of equations (see, e.g., Raunemaa et al., 1989):

$$\frac{dI(d_p)}{dt} = l \cdot s \cdot (d_p) \cdot O(d_p) - [l + a(d_p)]I(d_p) + r(d_p) \cdot B(d_p) + Q(d_p) + D(d_p) \tag{10}$$

$$\frac{dB(d_p)}{dt} = \frac{V}{A} [a(d_p) \cdot I(d_p) - r(d_p) \cdot B(d_p)] \tag{11}$$

$$\frac{dO(d_p)}{dt} = f(t, d_p) \tag{12}$$

A very important part of this modelling approach is the estimation of necessary parameters: air-exchange coefficient *l*, penetration coefficient *s* and deposition rate *a*. We were not able to deduce them from some earlier studies. Therefore, the main application of our particle transport model was to find values for these parameters, in mobile phone applications. Source term *Q* includes many different phenomena, which are beyond the scope of this presentation.

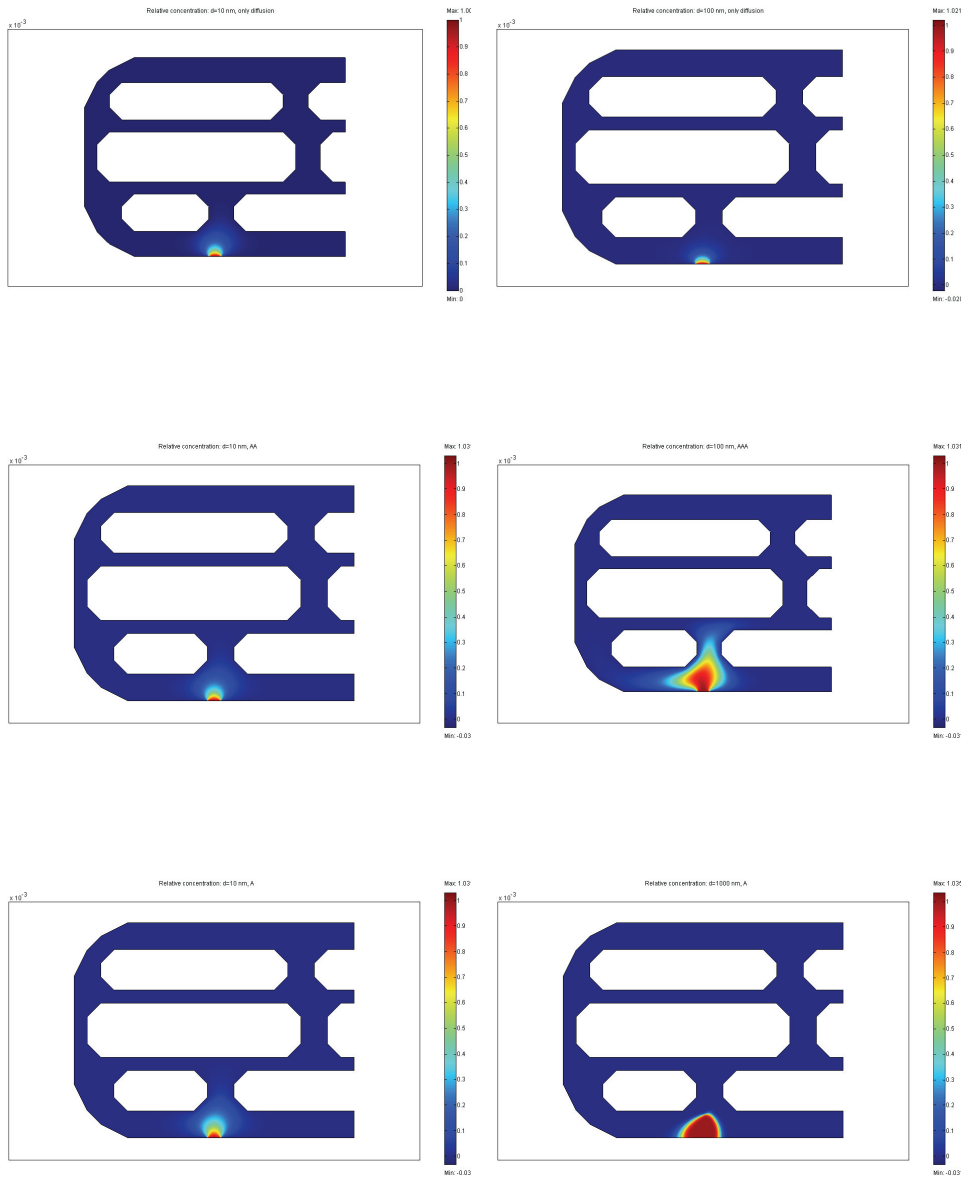


Figure 17. Test cases D10\_0, D10\_AA, D10\_A, D100\_0, D100\_AAA and D1000\_A. In these cases either diffusion or gravitational settling limits the particles' penetration into the system

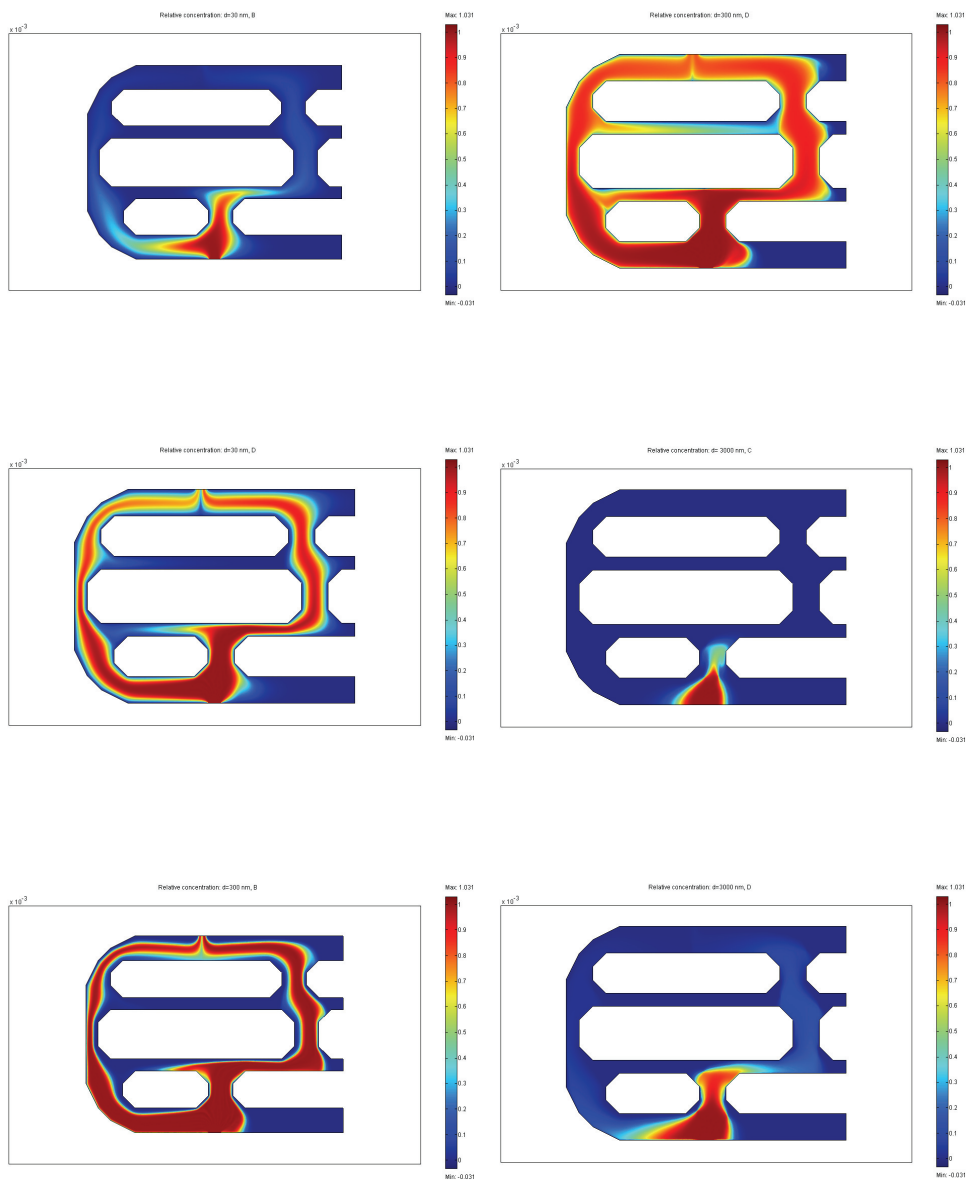


Figure 18. Test cases D30\_B, D30\_D, D300\_B, D300\_D, D3000\_C and D3000\_D (from top to bottom). In these test cases, the particles may even go via the whole system. This is especially clear for particles of size class 300 nm

Diffusion is given by Fick's first law:

$$D(d_p) = L(d_p) \frac{O(d_p) - I(d_p) A_r}{dx} \frac{A_r}{V} \quad (13)$$

If the following assumptions are made:

$r(d_p) = 0$  No re-emission (i.e., particles stay on surface once deposited)

$Q(d_p) = 0$  No sources inside the phone

$f(t, d_p) = 0$  Annual average concentration is used

$I(0, d_p) = 0$  Initial indoor concentration of zero

$B(0, d_p) = 0$  Initial accumulated material of zero

one gets for the indoor concentration

$$I(d_p) = \frac{v_1}{v_2} (1 - e^{-v_2 t}) \quad (14)$$

and for surface deposition

$$B(d_p) = \frac{v_1 v_3}{v_2} \left[ t - \frac{1}{v_2} (1 - e^{-v_2 t}) \right] \quad (15)$$

where

$$v_1 = \left[ l s(d_p) + \frac{L(d_p) A_r}{dx \cdot V} \right] O(d_p), \quad (16)$$

$$v_2 = l + a(d_p) + \frac{L(d_p) A_r}{dx \cdot V} \quad (17)$$

and

$$v_3 = \frac{a(d_p) V}{A} \quad (18)$$

#### 5.4 Application of simplified contamination model

Based on helium and laboratory measurements, and FEMLAB® results, a rough model was created. It was used for two different environments, New Delhi and Helsinki (Laakso et al., 2006). All calculations were done for two characteristic user types: a basic user and a heavy user. The results show for seven years of use that in New Delhi approximately 30% of the inner surfaces of the phone can be covered by aerosol particles in the case of a heavy user. For a basic user, the coverage was less than 5%. In Helsinki, the corresponding figures were about 4% and less than 1%. It was also found that the accumulation-mode particles were responsible for most of the coverage, on account of their large surface, relatively high concentrations and capability to penetrate the phone deeply. However, it should be kept in

mind that the coverage inside the phone is not uniform. It depends a great deal on the flow fields and apertures. When the different use situations were compared, it was found that most of the contamination came about in the case of a heavy user from the call, whereas in the case of the basic user the contamination was due to residual air remaining in the phone after the call.

## 6. Conclusions and discussion

Our first problem was how to study the air exchange of a small electronic device. The helium method was one option among others, and results from these studies are collected in this article. The helium experiments were completed successfully, even though the method was being applied for only the first time with electronic devices. When the experiments started, it was not very clear which strengths and weaknesses the method has. The first observation was that the results had no real meaning without extensive modelling, which enables conclusions to be drawn from experimental results.

During the modelling work it was observed that it is important to include all three basic transport phenomena (mass, heat and momentum) and their couplings (via transport parameters) in the model calculations. A few degrees of temperature difference may cause observable gas velocities, which often transport gases more rapidly than diffusion. Therefore, the application of some computational tool enabling the estimation of these effects even in complicated geometrical structures is highly recommendable.

On the basis of these steps, we were able to calculate air-exchange coefficient values for a specific mobile phone model – the mobile in use, in vertical orientation and in warm conditions. The uncertainties are high, and small variations in the conditions (heat source and temperature field) and assumed structure (the gas-permeability of the cover and internal parts) of the mobile phone increase the variation to 0.5–50 1/h. The uncertainties may be rendered smaller via application of a more detailed geometric model and knowledge of heat sources inside the mobile phone. Results from this study can be used in developing requirements, corresponding test cases and design guides for electronic devices.

Our second problem was to calculate aerosol particle deposition rates for a portable electronic device. The result was that very small and big particles do not easily penetrate the structure deeply, because of diffusion on surfaces and gravitational settling, respectively. Medium-sized particles (of a diameter between 50 and 500 nm), by contrast, penetrate the inner structures and may even pass through the whole apparatus. In the figures, relative particle concentrations for 100- and 1,000-nm particle diameters in the same flow conditions are shown.

In future, it will be desirable to control the contamination of electrical and electronic devices even better than is done today. Because direct experimental measurements in electronic devices are complicated as a result of the detailed and heterogeneous structure of the devices, the role of different modelling and simulation methods becomes more significant. Various molecular modelling techniques have been widely used to estimate chemical reactions among single atoms or small molecules, properties of solid materials and adsorption behaviour of small molecules on solid surfaces (Leach, 2001). We have applied molecular modelling techniques in contamination studies of heat-transfer surfaces (Puhakka et al., 2007). The main advance in molecular modelling was found in defining reaction pathways that may not be defined from process measurements and fouling resistance curves.

In particular, *ab initio* methods are very convenient, because no experimental parameters are needed. There are two main categories: the Hartree-Fock methods and density functional methods (Leach, 2001). The effectiveness of molecular techniques becomes more important when new construction materials like chemical and physical vapour deposition (CVD and PVD) coatings for microelectronics are designed and experimental measurements are not available. Solid techniques make it possible to perform estimations of coating properties in prevention of contamination by means of modelling techniques.

Our main conclusion is that numerical calculations of the particle transport inside electronic devices yield very valuable information about the processes, and, simultaneously, they offer a way to approximate certain important parameters in more practical contamination models. We recommend further modelling with different and perhaps a three-dimensional geometry. The model is applicable to all kinds of small apparatus. Results from this study can be used in developing requirements, corresponding test cases and design guides for electronic devices.

## 7. Nomenclature

### Definitions

Nucleation mode	particles having diameter between 0 and 30 nm
Aitken mode	particles having diameter between 30 and 80 nm
Accumulation mode	particles having diameter between 80 and 1,000 nm
RBS	Rutherford backscattering spectrometry
ERDA	Elastic Recoil Detection Analysis

### Helium and phone

$c$	concentration [ $\text{kg m}^{-3}$ ]
$D$	diffusivity [ $\text{m}^2 \text{s}^{-1}$ ]
$d, d_p$	particle diameter [nm, $\mu\text{m}$ , m]
$G$	geometric factor, which corrects the diffusivity to take account of the longer diffusion path and the form of pores
$J$	flux density [ $\text{kg s}^{-1} \text{m}^{-2}$ ]
$l$	air exchange coefficient [ $\text{h}^{-1}$ ]
$L$	characteristic length scale [m]
$q$	flux [ $\text{kg s}^{-1}$ ]
$S$	surface area [ $\text{m}^2$ ]
$v$	velocity [ $\text{m s}^{-1}$ ]
$V$	volume [ $\text{m}^3$ ]
$v_{\text{TS}}$	gravitational settling velocity for particles [ $\text{m s}^{-1}$ ]
$\kappa$	ratio of volumes
$\lambda$	exchange coefficients [ $\text{h}^{-1}$ or $\text{s}^{-1}$ ]
$\varphi$	porosity, fraction of void space in porous system

### Phone contamination

$A$	internal area of the phone [ $\text{cm}^2$ ]
$a(d_p)$	deposition rate [ $\text{h}^{-1}$ ]
$A_r$	area of the chinks [ $\text{cm}^2$ ]
$B(d_p)$	surface accumulation [ $\text{cm}^{-2}$ ]
$D(d_p)$	diffusion in -transport
$dx$	diffusion distance [cm]

$f(t, d_p)$	outdoor concentration change [ $\text{cm}^{-3} \text{h}^{-1}$ ]
$I(d_p)$	indoor concentration [ $\text{cm}^{-3}$ ]
$l$	air exchange rate [ $\text{h}^{-1}$ ]
$L(d_p)$	particle diffusion coefficient [ $\text{cm}^2 \text{h}^{-1}$ ]
$O(d_p)$	outdoor concentration [ $\text{cm}^{-3}$ ]
$P$	pressure [Pa]
$Q(d_p)$	the indoor source rate [ $\text{cm}^{-3} \text{h}^{-1}$ ]
$r(d_p)$	re-emission rate [ $\text{cm}^{-1} \text{h}^{-1}$ ]
$s(d_p)$	penetration coefficient []
$V$	void volume of the phone [ $\text{cm}^3$ ]
$\mu$	dynamic viscosity [Pa s]
$\rho$	density [ $\text{kg m}^{-3}$ ]

## 8. References

- Baldasano, J.M.; Valera, E. & Jimenez, P. (2003). Air quality data from large cities. *Air Quality Data from Large Cities*, Vol. 307, 141-165
- Comsol AB (2004b). *FEMLAB Chemical Engineering Module User's Guide, Version 3.0*
- Comsol AB (2004a). *FEMLAB User's Guide and Introduction, Version 3.0*
- Hannula, J. (2001). Statistical approach for determination of usage environments, Master's Thesis, University of Helsinki, Helsinki
- Harris, S.J. & Maricq, M.M. (2001). Signature size distributions for diesel and gasoline engine exhaust particulate matter. *Journal of Aerosol Science*, Vol. 32, 749-776
- Hartikainen, K.; Väättäinen, K.; Hautojärvi, A. & Timonen, J. (1994). Further development and studies of gas methods in matrix diffusion. *MRS*, Vol. 333, 821-826
- Hinds, W.C. (1999). *Aerosol Technology*, Wiley, New York
- Laakso, L.; Olin, M.; Hämeri, K.; Kulmala, M.; Hannula, J.; Galkin, T. & Väkeväinen, K. (2004). Deposition of aerosol particles in portable electronic devices, Nokia-internal report
- Laakso, L.; Koponen, I.K.; Mönkkönen, P.; Kulmala, M.; Kerminen, V.-M.; Wehner, B.; Wiedensohler, A.; Wu, Z. & Hu, M. (2006). Aerosol particles in the developing world: A comparison between New Delhi in India and Beijing in China. *Water, Air and Soil Pollution*, 1-16, DOI 10.1007/s11270-005-9018-5
- Leach, A.R. (2001). *Molecular Modelling: Principles and Applications*, 2nd ed., Pearson Education Limited, Essex
- Ojala K. & Väkeväinen K. (2001). Data logger device for usage environment of mobile phones, IEST 47th Annual Technical Meeting, Phoenix
- Olin M.; Laakso L.; Hannula J.; Galkin T.; Väkeväinen K. & Hartikainen K. (2006). Experimental and theoretical studies on air exchange of portable devices, Comsol Conference Copenhagen
- Puhakka, E.; Riihimäki, M. & Keiski, R.L. (2007). Molecular modeling approach on fouling of the plate heat exchanger: Titanium hydroxyls, silanols, and sulphates on  $\text{TiO}_2$  surfaces. *Heat Transfer Engineering*, Vol. 28, No. 3, 248-254
- Raunemaa, T.; Kulmala, M.; Saari, H.; Olin, M. & Kulmala, M.H. (1989). Indoor air aerosol model: Transport indoors and deposition of fine and coarse particles. *Aerosol Science and Technology*, Vol. 11, 11-25

- Roberge, P.R.; Klassen, R.D. & Haberecht, P.W. (2002). Atmospheric corrosivity modeling - a review. *Materials & Design*, Vol. 23, 321-330
- Scholorling, M. (2000). At Sixth International Conference on Urban Transport and the Environment for the 21st Century, Cambridge, 26-28 July
- Seinfeld, J.H. & Pandis, S.N. (1998). *Atmospheric Chemistry and Physics: From Air Pollution to Climate Change*, Wiley, New York
- van Brakel, J. & Heertjes, P.M. (1974). Analysis of diffusion in macroporous media in terms of a porosity, a tortuosity and a constrictivity factor. *International Journal of Heat Mass Transfer*, Vol. 17, 1093-1103
- Väkeväinen K.; Hannula, J. & Ojala, K. (2001). Determination of usage environment of mobile phones, IEST 47th Annual Technical Meeting, Phoenix



# Recent Advances in Modelling and Simulation of Silicon Photonic Devices

Vittorio M. N. Passaro and Francesco De Leonardis  
*Photonics Research Group, Dipartimento di Elettrotecnica ed Elettronica,  
Politecnico di Bari  
Italy*

## 1. Introduction

Nowadays, the interest for a large number of topics in Photonics research field is very high and of increasing importance (Reed, 2004), (Reed & Knights, 2004). A very important Silicon technology Company as Intel Corp. is developing many research programs in Photonics, with the aim to use silicon as a fundamental technological platform for all the photonic functions in any telecommunications system link (including generation, modulation, filtering, wavelength conversion, switching, amplification and detection of light). In fact, silicon low cost, vast existing microelectronics infrastructure and its technology allowing large integration of electronic and photonic devices, make Silicon-on-Insulator (SOI) technological platform a very attractive prospective for Photonics. Silicon photonics most promising applications are in the fields of optical interconnects, low-cost telecommunications and optical sensors. Optical interconnects have been demonstrated as very important because they permit to achieve a significant bandwidth increase in a variety of application areas including rack-to-rack, board-to-board, chip-to-chip and intrachip applications. SOI optical interconnects may permit to overcome the bandwidth limitations due to frequency-dependent losses imposed by copper interconnects.

Actually, employment of electronic and optical micro- and nano-sensors in a great number of application fields such as medicine, microbiology, particle physics, automotive, environmental safety and defence is receiving an increasing interest. Sensor and actuator monolithic integration in micro-electro-mechanical systems (MEMSs), nano-electro-mechanical systems (NEMs) and micro-opto-electro-mechanical systems (MOEMSs) has been achieved in a great number of sensing devices. Photonic sensors have attracted a great attention because of their immunity to electromagnetic interference, good compactness and robustness and high compatibility with fibre networks, but also because they usually exhibit shorter response time and higher sensitivities with respect to MEMS/MOEMS devices. Different integrated optical chemical and biochemical sensors have been proposed adopting prevalently CMOS-compatible technological platforms.

Thus, the tasks of modelling and simulation of photonic devices and systems is becoming as more and more significant. However, a large number of modelling techniques for Photonics is not yet well standardized and many aspects of simulation tasks are still open. In general, different well known modelling techniques include beam propagation methods (BPM),

finite difference time domain (FDTD), as well as coupled mode theory (CMT), transfer matrix methods (TMM), Floquet-Bloch theory (FBT) for periodic structures (Passaro, 2000) and method of lines (MoL) (Scarmozzino et al., 2000). Powerful commercial CAD tools are often used in literature, as those produced by Silvaco Corp., Apollo Photonics Inc., Optiwave Systems Inc., RSoft Design Group.

In this frame, the Photonics Research Group of Politecnico di Bari (URL: <http://dee.poliba.it/photonicsgroup>) is very active and internationally recognized for modelling and simulation of photonic devices and systems. Along many years, it has developed a number of home-made modelling techniques and numerical approaches to design and simulate various devices, including grating-assisted directional couplers, optical modulators, thermo-optic devices, photonic sensors, nonlinear devices and so on.

In this chapter we review recently developed simulation methods for sub-micrometer innovative SOI guiding structures and photonic devices. Techniques based on full-vectorial finite element method (FV-FEM) for modal and sensitivity analysis of silicon slot waveguides will be described in detail, showing as these guiding structures can be made extremely sensitive to sensing medium refractive index shift. Some properties of an innovative novel photonic structure, the hollow waveguide, will be also given. Multiphysics modelling techniques enabling to contextually simulate many physical phenomena taking place within a device have been demonstrated as very useful in a wide spectrum of silicon photonic device modelling. We will also describe how, in a unique simulation environment, it is possible to simulate either optical and electronic phenomena that takes place in SOI photonic modulators or thermal and optical effects characterizing the performance of silicon thermo-optic devices. Finally, some aspects of modelling of nonlinear photonic devices in SOI will be also considered, with emphasis on generation of optical solitons.

## 2. Numerical results

### 2.1 Silicon waveguides

Recently, SOI sub-micrometer wire waveguides (Yamada et al., 2006) have been demonstrated very attractive for integrated optical sensors, because they exhibit a sensitivity significantly larger than in other guiding structures based on silicon oxinitride (SiON), or polymeric materials or silica.

When two Si-wires are very close to each other, it is possible to realize another important SOI nanometer guiding structure, usually known as SOI slot waveguide (Xu et al., 2004)]. A great variety of optical devices has been recently proposed or fabricated by using slot waveguides, including microring resonators, optical modulators, electrically pumped light emitting devices, directional couplers, all-optical logic gates and beam splitters. Moreover, a full-vectorial finite element method (FV-FEM) modal investigation devoted to study the influence of slot waveguide geometrical parameters on optical power fraction confined in the low-index gap region has been also carried out (Muellner & Heinberger, 2006), (Dell'Olio & Passaro, 2007). In this section, some results of SOI slot waveguides are briefly reviewed as obtained by a commercial CAD tool, FEM by COMSOL Multiphysics.

Conventional SOI slot waveguide (whose structure is shown in Fig. 1(a)) has a typical modal behaviour, assuming as cover medium air, silicon oxide or an aqueous solution (cover medium refractive index  $n_c$  equal to 1, 1.444 or 1.33 at wavelength 1550 nm, respectively). In FEM mesh generation for effective index and modal profile calculation, triangular vector-elements have been used and maximum element size fixed as equal to 2.5 nm in the gap

region, 3 nm in the Si wires region, 10 nm in the portion of calculation domain outside both gap region and Si wires region and included in a large rectangle 1  $\mu\text{m}$  wide and 0.45  $\mu\text{m}$  high centred in the centre of the gap region, and 100 nm in the remaining domain portion having a total area of 8  $\mu\text{m}^2$  (4 $\mu\text{m}$   $\times$  2  $\mu\text{m}$ ). In total, about 100,000 mesh elements have been always used. Changing the boundary condition from a perfect electric conductor to a perfect magnetic conductor is demonstrated to have a negligible influence on the simulation results. Adopting these mesh parameters, the slot waveguide fabricated by (Xu et al., 2004) has been simulated. Calculated effective indices (1.757767 for quasi-TM mode and 1.611924 for quasi-TE at the operating wavelength of 1545 nm) are very similar with those experimentally measured, the relative change being lower than 1 %.

Slot guiding structure supports both a quasi-TE mode, highly confined in the gap region as in Fig. 1(b), and a quasi-TM mode too, as in Fig. 1(c). Moreover, slot waveguide fabrication implies silicon deep etching that, in principle, can produce non vertical sidewalls, as depicted in Fig. 1(d). Waveguide modal profiles, either for quasi-TE or quasi-TM modes, are significantly influenced by this kind of fabrication tolerance, as it can be seen in Fig. 1(d) and Fig. 1(e), respectively. Thus, non vertical sidewall effect on conventional SOI slot waveguide modal properties has been also investigated by FV-FEM.

Assuming silicon wires with height  $h = 250$  nm, width  $w = 180$  nm and gap region width  $g = 100$  nm, the effective index change as induced by non vertical sidewalls with respect to vertical case, has been calculated. Tilting angle  $\theta$  as sketched in Fig. 1 (d) with respect to vertical direction has been varied in the range from  $3^\circ$  to  $9^\circ$ , and quasi-TE and quasi-TM modes have been calculated (see Fig. 2). A linear dependence of effective index change on the tilting angle  $\theta$  has been observed for both polarizations. Non vertical sidewalls influence on effective index is stronger for quasi-TE than for quasi-TM mode, because the relevant electric field squared module has its maxima along the vertical interfaces between silicon wires and gap region for quasi-TE mode, while the maxima are outside the gap region for quasi-TM mode. An increase of cover medium refractive index (from air to silicon oxide) will produce a decrease of  $\theta$  influence on effective index, as it is shown in Fig. 2.

Considering  $\theta = 8^\circ$ ,  $g = 100$  nm and  $h = 250$  nm, the effective index change induced by non vertical sidewalls has been investigated as a function of  $w$  for quasi-TE and quasi-TM modes (Fig. 3). If the cover medium is silicon oxide or an aqueous solution, this change monotonically decreases with increasing the silicon wire width. When cover medium is air, the dependence of effective index shift on  $w$  exhibits a maximum for  $w = 180$  nm (maximum values are 20.5 % and 6.15% for quasi-TE and quasi-TM mode, respectively).

The confinement factors in the cover medium  $\Gamma_C$  and in the gap region  $\Gamma_G$  for quasi-TE and quasi-TM modes propagating in slot waveguide can be defined as:

$$\Gamma_C = \frac{\iint_C |\mathbf{E}(x, y)|^2 dx dy}{\iint_{-\infty}^{\infty} |\mathbf{E}(x, y)|^2 dx dy} \quad \Gamma_G = \frac{\iint_G |\mathbf{E}(x, y)|^2 dx dy}{\iint_{-\infty}^{\infty} |\mathbf{E}(x, y)|^2 dx dy} \quad (1)$$

where  $\mathbf{E}(x, y)$  is the electric field vector and  $C$  and  $G$  indicate cover medium and gap region, respectively, being the gap region a part of cover medium region, as shown in Fig. 1 (a).

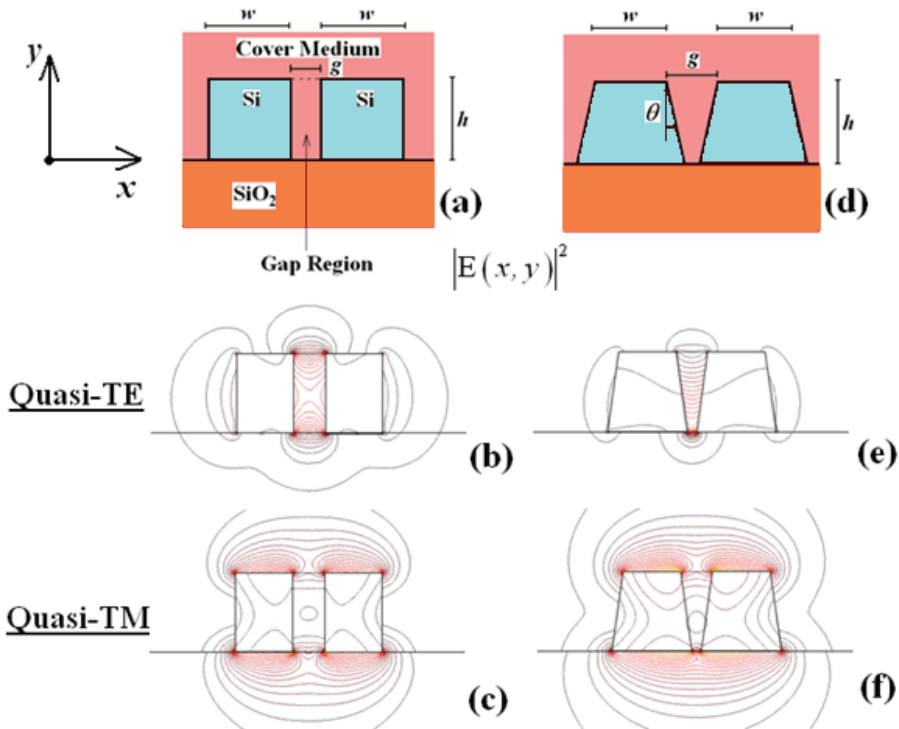


Figure 1. (a) Conventional SOI slot waveguide structure with vertical sidewalls ( $\theta=0^\circ$ ). (b-c) Relevant electric field squared module for quasi-TE and quasi-TM optical modes. (d) SOI slot waveguide with non vertical sidewalls ( $\theta=8^\circ$ ). (e-f) Relevant electric field squared module for quasi-TE and quasi-TM optical modes. For these graphs, an aqueous solution ( $n_c=1.33$ ) is assumed as cover medium ( $h=250$  nm,  $w=180$  nm,  $g=100$  nm)

Dependence of confinement factors  $\Gamma_C$  and  $\Gamma_G$  on  $w$  can be investigated for  $g=100$  nm and  $h=250$  nm. Effect of non vertical sidewalls ( $\theta=8^\circ$ ) on these factors has been also considered. The confinement factors are larger for quasi-TE than for quasi-TM mode. For quasi-TE mode, non vertical sidewalls produce a decrease in  $\Gamma_C$  and an increase in  $\Gamma_G$ . For quasi-TM mode, non vertical sidewalls produce a decrease of both confinement factors.

For both polarizations, when the cover medium is an aqueous solution or silicon oxide,  $\Gamma_C$  monotonically decreases when  $w$  increases, while  $\Gamma_G$  exhibits a maximum when the cover medium is air. Confinement factor  $\Gamma_G$  has a maximum in quite all considered cases (only when we consider silicon oxide, non vertical sidewalls and quasi-TM mode,  $\Gamma_G$  dependence on  $w$  is monotone). These results are very important for design of optimal slot waveguides for sensing purposes.

Another important CMOS-compatible technology involves the use of hollow optical waveguides (Harrington, 2000). Calculations of effective indices and field distributions are again carried out by FV-FEM with 10,000 mesh elements. In Fig. 4 the electric field x-component of fundamental mode is sketched for a  $4 \times 4 \mu\text{m}^2$  squared core structure, having six periods of silicon/silicon nitride all around (effective index 1.438571 in figure). The plot

shows as the mode confinement occurs in the center low index region (silicon oxide in this case), if a grating at resonance wavelength is fabricated all around. The grating can have a variable number of periods, each one being formed in this case by one layer of silicon and one layer of silicon nitride. The thickness of each layer must be designed in order to meet the Bragg condition for that wavelength (i.e.  $\lambda = 1.55\mu\text{m}$ ), thus silicon layers are  $\sim 110$  nm thick, and silicon nitride layers are  $\sim 194$  nm thick. Table 1 summarizes the effective indices for structures with different number of periods. We can note that, starting from at least three periods (three silicon layers), the field confinement is good and losses are expected to be as moderate.

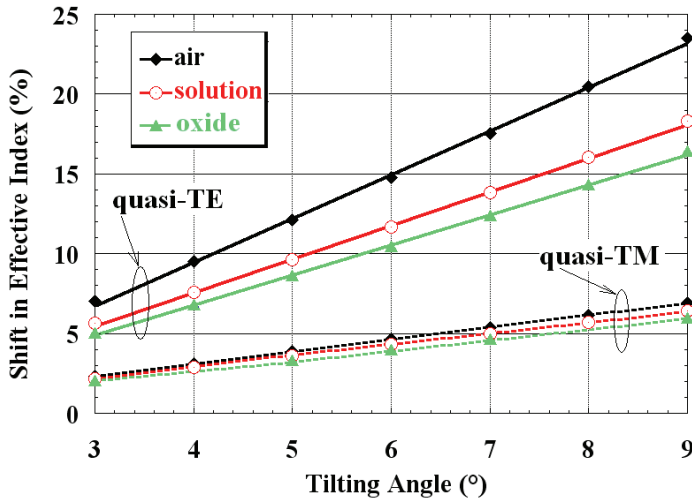


Figure 2. Percentage shift of quasi-TE and quasi-TM mode effective indices, with respect to vertical case, versus  $\theta$  ( $h = 250$  nm,  $w = 180$  nm,  $g = 100$  nm), for various cover materials

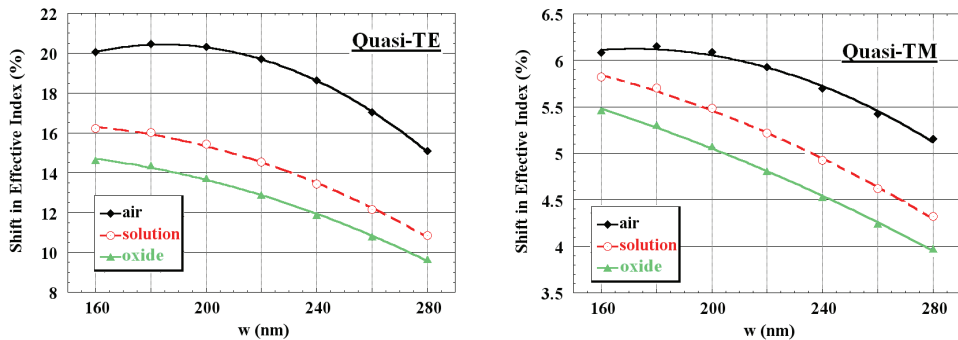


Figure 3. Percentage shift of quasi-TE and quasi-TM mode effective indices (with respect to vertical case) versus  $w$ , as induced by non vertical sidewalls in slot waveguides ( $h = 250$  nm,  $g = 100$  nm,  $\theta = 8^\circ$ )

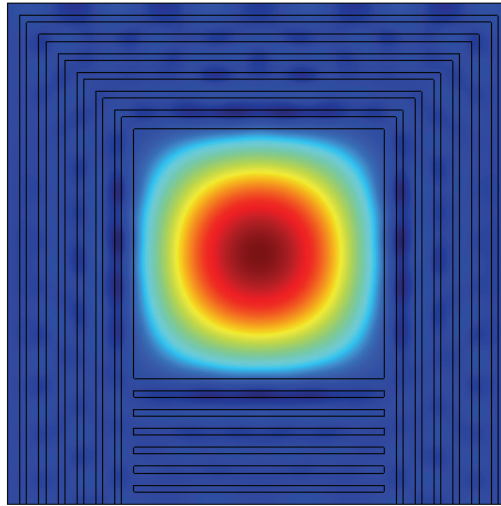


Figure 4. Electric field x-component plot for field confinement in hollow waveguide

Structure	Effective index $n_{\text{eff}}$ x-component	Effective index $n_{\text{eff}}$ y-component
6 periods	1.438571	1.438567
5 periods	1.438581	1.438596
4 periods	1.438636	1.438654
3 periods	1.439916	1.438956
2 periods	1.440526	1.440403
1 period	1.437340	1.437340

Table 1. Effective indices (squared core) versus number of periods for both polarizations

## 2.2 Thermo-optic devices

Recently, there has been also a great interest in the development of optical waveguide modulators, switches, ring resonators, filters, couplers using silicon-on-insulator (SOI) technology (Passaro, 2006). SOI-based optical devices are characterized by small optical losses over telecommunication wavelengths and have the potential for integration with SOI-based CMOS electronics, reduced parasitics, absence of latch-up and enabling high-speed operation at low power.

One significant technological issue is associated with the ability to perform optical modulation. An attractive way to modulate the refractive index in SOI rib waveguides is the thermo-optic effect, allowing low transmission loss, low cost, high stability, low power consumption and very large scale of integration. Apart from the well known optical characteristics, silicon also possesses good thermal features, with its high thermo-optical coefficient and thermal conductivity. Both static and dynamic thermo-optical analysis of small rib waveguides can be carried out by FV-FEM. In this section, we briefly review the

fully integrated thermo-optic simulation where both thermal and optical investigations, without approximations on the refractive index distribution and consequently on effective indices of structure modes, can be carried out. Typically, the two analysis are developed in literature in two different simulation environments, so requiring some methods to export the refractive index distribution and introducing approximations.

Thermo-optic effect in SOI rib waveguides can be appropriately simulated by considering an aluminum heater laying on the top of the structure. The finite element method has been used to solve both thermal and wave propagation problems in rib optical waveguides, at the wavelength of 1.55 $\mu\text{m}$ . The thermal problem is solved and the obtained temperature distribution is used to evaluate the refractive index change in the heated regions, caused by the thermo-optic effect. This distribution of refractive index is then used to solve the optical problem. The analysis of waveguides is carried out in the x-y plane, perpendicular to the light propagation direction z. The mathematical equation for heat transfer by conduction is the heat equation:

$$\rho C \frac{\partial T}{\partial t} + \nabla \cdot (-k \nabla T) = Q \quad (2)$$

where  $T$  is the temperature (K),  $Q$  is a heat source or heat sink ( $\text{W}/\text{m}^3$ ),  $\rho$  is the density ( $\text{kg}/\text{m}^3$ ),  $C$  is the heat capacity ( $\text{J}/\text{kg}\cdot\text{K}$ ) and  $k$  is the thermal conductivity ( $\text{W}/\text{m}\cdot\text{K}$ ) of the medium. These three thermo-physical properties determine the thermal diffusivity  $a$  ( $\text{m}^2/\text{s}$ ), which gives information on how rapidly a temperature variation at the medium surface propagates through the medium itself. If the thermal conductivity is isotropic, equation (2) becomes:

$$\rho C_p \frac{\partial T}{\partial t} - k \nabla^2 T = Q \quad (3)$$

In a stationary problem, the temperature does not change with time and the first term of the equation disappears. If there is not heat production or consumption in the medium,  $Q$  sets to zero. To solve a particular heat conduction problem and find the temperature distribution inside a medium, it is necessary to specify the medium geometry and thermo-physical properties, the distribution of possible sources and the initial and boundary conditions. These conditions are essentially of two types: Dirichlet, where temperature is imposed on the medium surface as  $T = T_0$ , or Neumann, where the heat flux  $q$  on a boundary is  $-\mathbf{n} \cdot \mathbf{q} = q_0$  and  $\mathbf{n}$  stands for the surface normal. The heat flux is defined by the Fourier law as  $\mathbf{q} = -k \nabla T$ , where the negative sign is justified by the opposite directions of heat flux and temperature gradient. Moreover, light propagation is described by the optical wave equation:

$$\nabla^2 E_t + \nabla \left( \frac{\nabla n^2(x,y) \times E_t}{n^2(x,y)} \right) + \left( \frac{2\pi}{\lambda} \right)^2 n^2(x,y) E_t = \left( \frac{2\pi}{\lambda} \right)^2 n_{eff} E_t \quad (4)$$

derived from Maxwell's equations, where  $E_t$  is the transverse electric field,  $\lambda$  is the wavelength,  $n(x,y)$  is the refractive index distribution and  $n_{eff}$  is the effective index (wave

equation eigenvalue).

It is well known as SOI waveguides typically have a silicon core (refractive index  $n \sim 3.5$ ) surrounded by cladding layers of air or silica, with refractive indices between 1 and 2. Hence, the very high index contrast between waveguide core and cladding allows good confinement of optical modes and reduction of device dimensions. A typical SOI rib waveguide is sketched in Fig. 5, with an aluminum heater on the top, having a width  $W$ . The buried oxide (BOX) layer is required to achieve thermal isolation of the waveguide from the substrate, because the thermal conductivity in  $\text{SiO}_2$  is about 100 times smaller than in silicon. The distance  $H$  between the heater and the top of the rib must be thick enough to insulate the waveguide core from the metallic electrode. For all the analyzed structures we have set this distance to  $0.1\mu\text{m}$ , being the buried oxide thickness of  $1\mu\text{m}$ .

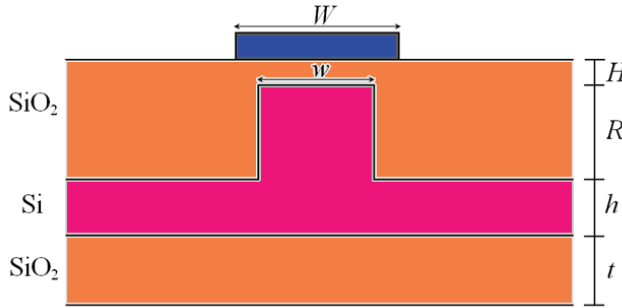


Figure 5. General view of SOI rib waveguide with the heater on the top

We have considered the absence of any thermal generation terms and a scalar conductivity for both static and dynamic analysis. Table 2 collects the thermo-physical values used in the simulations for the materials involved in the waveguide. As initial condition, a constant temperature  $T_0$  has been set at each point of the structure. The boundary conditions are:

$$T = T_0 \text{ on the top and bottom boundary}$$

$$T = T_{heater} \text{ on heater surfaces}$$

$$\mathbf{n} \cdot (k \nabla T) = 0 \text{ on lateral surfaces}$$

$$\mathbf{n} \cdot (k_1 \nabla T_1 - k_2 \nabla T_2) = 0 \text{ on internal boundaries}$$

where  $T_{heater}$  becomes a temperature step in the dynamic analysis, and a constant value in the static analysis. In both cases, the maximum heater temperature change is assumed as  $70^\circ\text{C}$ . The 2D temperature distribution obtained in the thermal investigation has been used to evaluate the new refractive indices of the waveguide, as a result of the thermo-optic effect in silicon ( $n'_{Si} = 3.477 + 1.86 \times 10^{-4} \Delta T$ ) and in silica ( $n'_{SiO_2} = 1.477 + 10^{-5} \Delta T$ ), at the wavelength  $1.55\mu\text{m}$ .  $\Delta T$  is the temperature change caused by heating and the bulk thermo-optic coefficients of silicon and silica are used. The refractive index distribution is taken to solve the eigenvalue optical problem and evaluate the field distributions and the effective indices of the structure modes.

By means of the static analysis, performed at various temperatures of the heater, the dependence of the effective indices on temperature can be derived as an *effective* thermo-optic coefficient,  $\partial n_{eff} / \partial T$ . This procedure is significantly different from that commonly



followed in literature, where only the bulk thermo-optic coefficient is usually considered. Of course, this effective thermo-optic coefficient depends on waveguide materials (refractive index, density, heat capacity, thermal conductivity), geometry, temperature gradient in each layer, heater material and width.

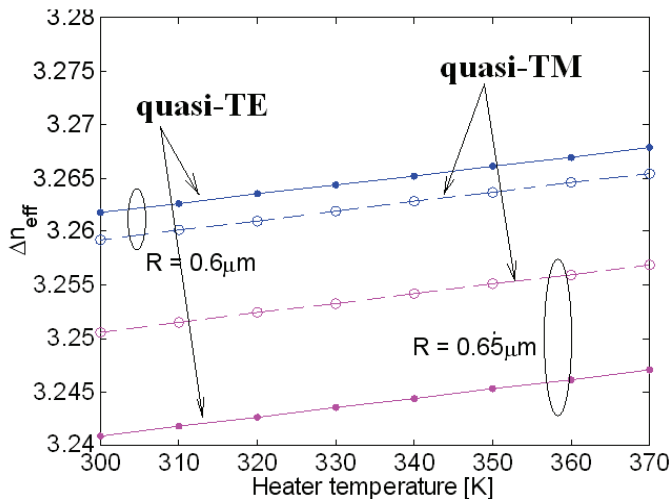
Material	$k$ W/m·K	$P$ kg/m <sup>3</sup>	$C$ J/kg·K
silicon	163	2330	703
silica	1.38	2203	703
aluminum	160	2700	900
Air (@ 30°C)	0.026	1.166	1005

**Table 2.** Thermo-physical constants used in simulations

If a guided-wave optical device employs the thermo-optic effect for switching, filtering or tuning functions, its characteristics and properties will depend on this effective thermo-optic coefficient, that can be seen as a property of the whole guided-wave structure. For example, in a Mach-Zehnder thermo-optic switch, the phase shift is written as:

$$\Delta\varphi = \frac{2\pi}{\lambda} \Delta n_{\text{eff}} L_h = \frac{2\pi}{\lambda} L_h \frac{\partial n_{\text{eff}}}{\partial T} \Delta T \quad (5)$$

where  $L_h$  is the heater length. In the results, rib waveguides with sizes  $h + R = 1\mu\text{m}$ ,  $w = 0.6\mu\text{m}$ ,  $R = 0.6\mu\text{m}$ , and  $W = 0.6\mu\text{m}$  have been considered. Then, etch depth  $R$  and  $h$  (keeping the sum  $h+R$  as constant), waveguide width  $w$  and heater width  $W$  have been changed, and derived their influence on the effective index. Fig. 6 shows the linear dependence of effective index change over heater temperature for both polarizations (quasi-TE and quasi-TM), for waveguides with different etch depth  $R$ .



**Figure 6.** Effective index change versus heater temperature

By means of the dynamic analysis, the time dependence of effective index can be found, so estimating the thermo-optic response time of the analyzed structures. The time constant  $\tau$  of the thermo-optic effect for each considered structure has been evaluated and fitted by an exponential law, as sketched in Fig. 7. The time constant gets better in structures where the effective thermo-optic coefficient is improved too. Furthermore, the time constant and the thermo-optic coefficient are always improved when considering quasi TM mode instead of quasi-TE, because in that case the field maximum is placed in a more heated region. Time constants ranging from 0.93  $\mu\text{s}$  to 0.85  $\mu\text{s}$  have been determined with changing the rib etch depth from 0.6 to 0.7  $\mu\text{m}$ .

Thus, by means of this fully integrated multiphysics analysis, we have avoided the approximation of constant thermo-optic coefficients in the waveguide layers, as usually assumed in literature. This is especially important in the core of the waveguide, where the field intensity is maximum.

Furthermore, our rigorous approach is crucial, especially for operating with waveguides where the guiding layer is constituted of materials with low thermal diffusivity. The importance of the diffusivity can be highlighted in the study of a waveguide where silica is placed over the heater instead air. Both static and dynamic behaviors get better, because the diffusivity of silica is approximately two orders of magnitude lower than for air. Thus, the thermal power could be better confined in the guiding layer.

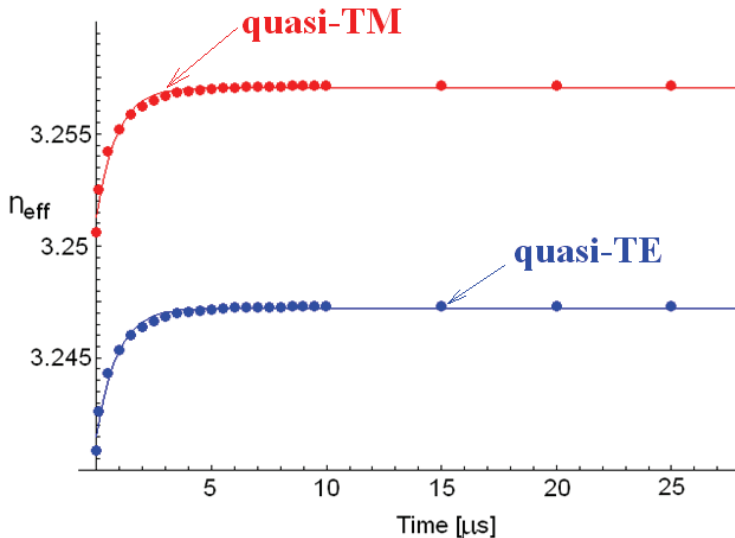


Figure 7. Time response for quasi-TE and quasi-TM modes

### 2.3 Silicon modulators

One of the most important requirements of any integrated optical technology is the ability to perform optical modulation, which permits to encode a bit stream onto the optical carrier provided by the laser source. Light can be modulated using different physical effects, depending on the material used to fabricate modulators. For high-speed modulation, electro-optic effect is commonly employed.

Unfortunately, unstrained silicon does not exhibit this physical effect, thus the plasma dispersion effect is commonly used to solve the problem of optical modulation. It is based on inducing an electrical change of silicon refractive index by varying electron and hole distributions within the material. The free-carrier concentration in silicon electro-optic devices can be varied by charge carrier injection, accumulation or depletion. In literature p-i-n, p-n (see Fig. 8a) and metal-oxide-semiconductor (MOS) (see Fig. 8b) structures have been adopted to this purpose.

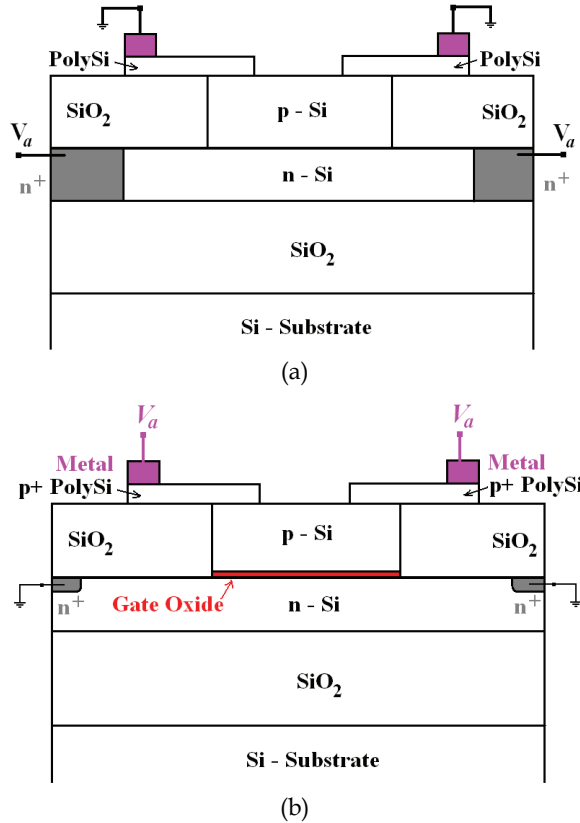


Figure 8. Typical structures for silicon modulators: (a) p-n; (b) MOS

To study this kind of devices, two different models are usually developed. The first allows to investigate the modulator electrical behaviour, whereas the second simulates the device from an optical point of view, taking into account the electrically induced silicon refractive index change (Barrios & Lipson, 2004). Usually, these two models are developed in literature by all authors in two different simulation environments, the former purely electrical and the latter purely optical, giving some consequent problems and inaccuracies in using the electrical simulation results in the environment where optical simulation is performed. In this section, the fully integrated FEM-based optoelectronic model of a SOI optical modulator is briefly reviewed, assuming a typical MOS structure, as in Fig. 9.

Assuming to ground n-type silicon layer, a free carrier thin layer is accumulated on both sides of gate oxide, when a positive voltage  $V_a$ , larger than the MOS flat band voltage, is applied to the device. According with plasma-optic effect, this voltage-induced free carrier accumulation locally changes the silicon refractive index. This operating principle allows high modulation speeds to be achieved, because no slow phenomena are involved in the accumulation process. The electrically induced localized change of silicon refractive index affects the effective index of optical mode propagating within modulator and, finally, the phase of optical signal passing through it. The phase shift can be converted as an amplitude modulation using the typical Mach-Zehnder interferometer architecture.

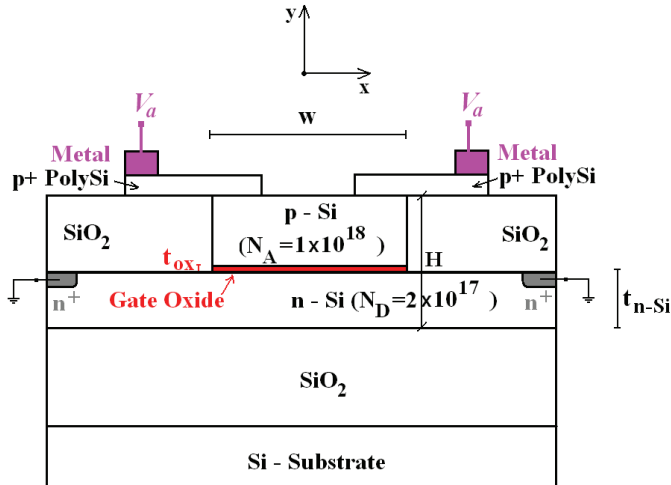


Figure 9. Simulated SOI modulator cross section (dopant concentrations in cm-3)

In our modeling we have assumed device sizes and simulation parameters as summarized in Table 3. Electron and hole distribution dependence on applied voltage ( $V_a$ ) has been investigated using 2D static drift-diffusion model, solved by FEM.

Parameter	Symbol	Value
p-Si region width	$w$	1600 nm
modulator total height	$H$	1550 nm
n-Si region thickness	$t_{n-Si}$	900 nm
gate oxide thickness	$t_{ox}$	10.5 nm
operating wavelength	$\lambda$	1550 nm

Table 3. Modulator sizes and simulation parameters

This model consists of three coupled partial differential equations (PDEs) in the form:

$$\epsilon_0 \epsilon_r (\nabla \Psi) = q(N_e - N_h - C) \quad (6)$$

$$\nabla \cdot (\mu_p v_T \nabla N_h + \mu_p N_h \nabla \Psi) = R_{SRH} \quad (7)$$

$$\nabla \cdot (\mu_n v_T \nabla N_e - \mu_n N_e \nabla \Psi) = R_{SRH} \quad (8)$$

where  $R_{SRH}$  is the Shockley-Hall-Read recombination rate:

$$R_{SRH} = \frac{N_e N_h - N_i^2}{\tau_p (N_e + N_i) + \tau_n (N_h + N_i)} \quad (9)$$

and  $\epsilon_0$  is the vacuum permittivity,  $\epsilon_r$  is the relative permittivity,  $q$  is the elementary charge,  $N_e$  is the electron distribution,  $N_h$  is the hole distribution,  $N_i$  is the silicon free-carrier intrinsic concentration,  $C$  is the doping profile,  $\mu_n$  is the electron mobility,  $\mu_p$  is the hole mobility,  $v_T$  is the thermal voltage,  $\psi$  is the electro-static potential,  $\tau_n$  is the electron lifetime in silicon and  $\tau_p$  is the hole lifetime in silicon.

For boundaries in contact with air, normal components of electric displacement and current density vectors are imposed to be equal to zero. At boundaries in contact with a metal, neutrality condition and action mass law have been applied. Then, hole and electron concentrations and electro-static potential have been imposed as:

$$\Psi = V_a + \frac{kT}{q} \ln \left[ \frac{1}{N_i} \left( \frac{C}{2} + \sqrt{\left(\frac{C}{2}\right)^2 + N_i^2} \right) \right] \quad (10)$$

$$N_e = \frac{C}{2} + \sqrt{\left(\frac{C}{2}\right)^2 + N_i^2} \quad (11)$$

$$N_h = -\frac{C}{2} + \sqrt{\left(\frac{C}{2}\right)^2 + N_i^2} \quad (12)$$

where  $k$  is the Boltzmann constant and  $T = 300$  K is the operating absolute temperature. By solving the coupled equations (10), (11) and (12) with given boundary conditions, both electro-static potential and free carrier distribution can be calculated in modulator cross section for any value of applied voltage,  $V_a$ . In Fig. 10, electro-static potential  $\psi(x,y)$  for  $V_a=2$  V is shown. Free electron distribution along the center of modulator cross section is shown in Fig. 11 for  $V_a$  varying in the range from 0 to 3 V. From simulations, flat band voltage has been estimated as equal to 1.45 V.

Starting from 2D free carrier distribution, silicon refractive index change  $\Delta n_{Si}$  as due to the applied voltage is calculated at each point of modulator cross section. Refractive index shift is related to free carrier distribution by well known Soref's relation at wavelength of 1550 nm (Soref & Bennett, 1987):

$$\Delta n_{Si} = -8.8 \times 10^{-22} \Delta N_e - 8.5 \times 10^{-18} [\Delta N_h]^{0.8} \quad (13)$$

where  $\Delta N_e$  is the electron concentration change and  $\Delta N_h$  is the hole concentration change (both in  $\text{cm}^{-3}$ ). Using this approach, refractive index distribution  $n(x,y)$  is found for any  $V_a$  value. In Fig. 12 refractive index distribution is sketched along the center of modulator cross section, for  $V_a$  ranging from 0 to 3 V.

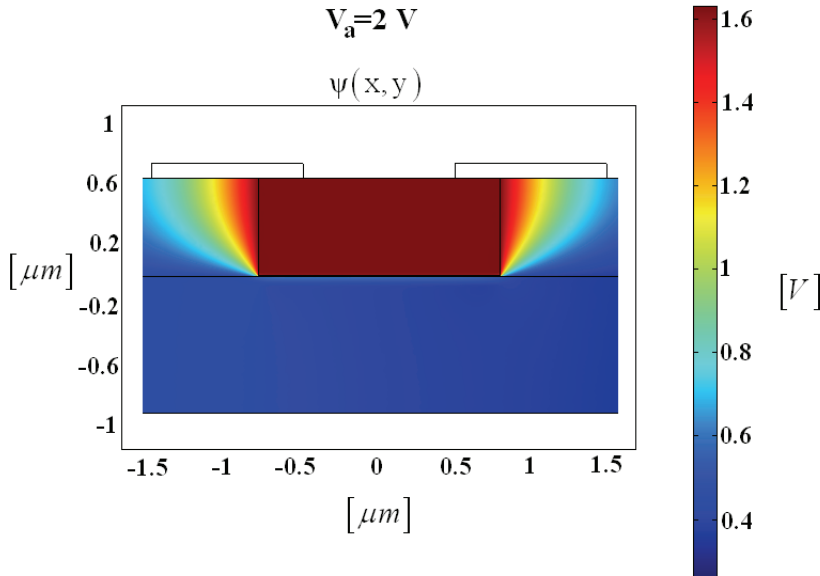


Figure 10. Electro-static potential for  $V_a = 2$  V

From knowledge of function  $n(x,y,V_a)$ , optical mode field distributions propagating within the device and their effective indices  $n_{eff}$  can be calculated as eigen-functions and eigenvalues of the optical wave equation (4). As an example, quasi-TE and quasi-TM mode electromagnetic field distributions have been calculated by FV-FEM and sketched in Fig. 13 and 14, respectively, for  $V_a = 2$  V. Significant difference in quasi-TE and quasi-TM mode profiles are evident. Quasi-TE is more confined in the waveguide as compared to quasi-TM.

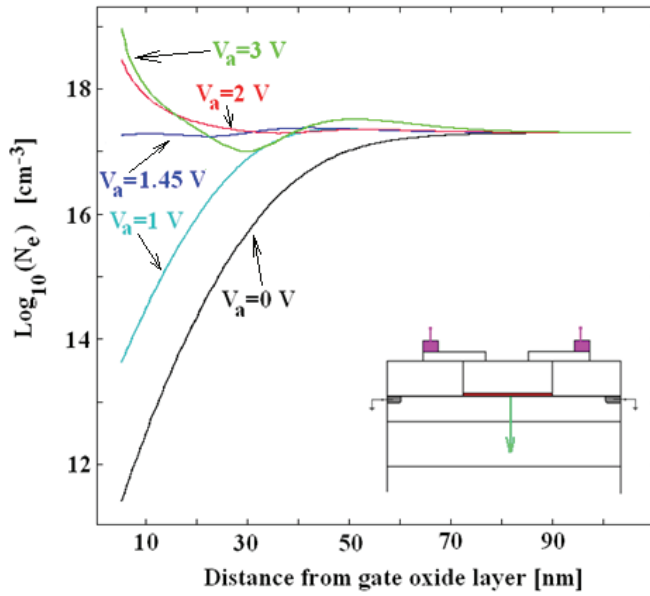


Figure 11. Electron distribution along the center of modulator cross section for  $V_a$  ranging from 0 V to 3 V

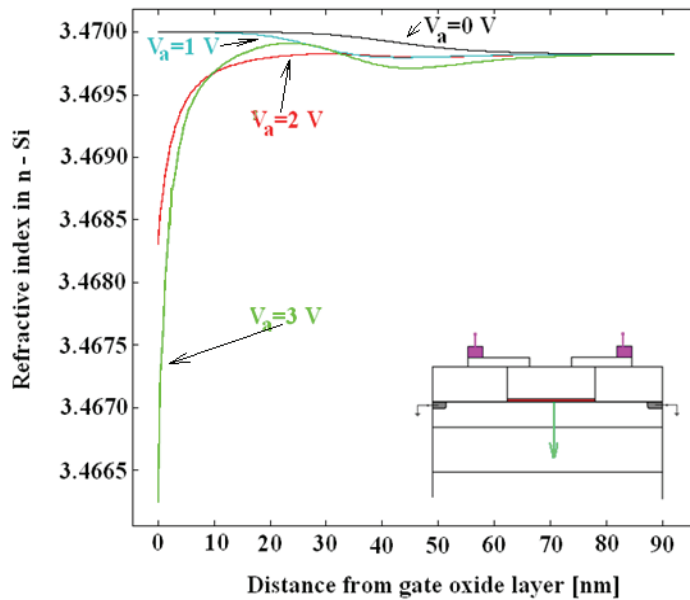


Figure 12. Refractive index distribution along the center of modulator cross section in n-doped silicon, for  $V_a$  ranging from 0 V to 3 V

This difference is due to the continuity condition of electric field  $x$  component,  $E_x$ , and discontinuity of electric field  $y$  component,  $E_y$ , across the interface between silicon and gate oxide. For quasi-TE mode,  $E_y$  is the minor electric field component, whereas for quasi-TM mode  $E_y$  is the major electric field component, then  $E_y$  discontinuity practically produces effects only on quasi-TM polarized light. Therefore, the MOS capacitor based phase-shifter performance is strongly dependent on the incoming light polarization.

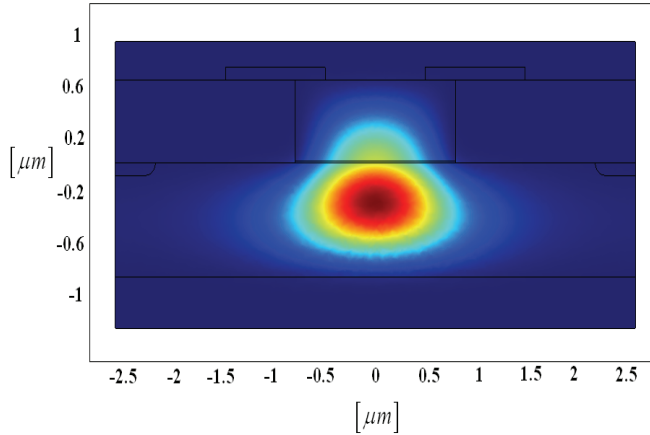


Figure 13. Quasi-TE mode electromagnetic field distribution for  $V_a = 2$  V

Phase shift induced in the optical signal propagating within the modulator and its dependence on applied voltage  $V_a$  have been investigated either for quasi-TE or quasi-TM mode, assuming a modulator length  $L = 8$  mm (see Fig. 15). As expected, phase shift induced by an applied voltage change is significantly lower for quasi-TM polarized light (about 66% for  $L = 8$  mm) than for quasi-TE. Through this calculation, a  $V_\pi L$  product has been estimated as 3.4 V cm for quasi-TE and 10.2 V cm for quasi-TM polarized light.

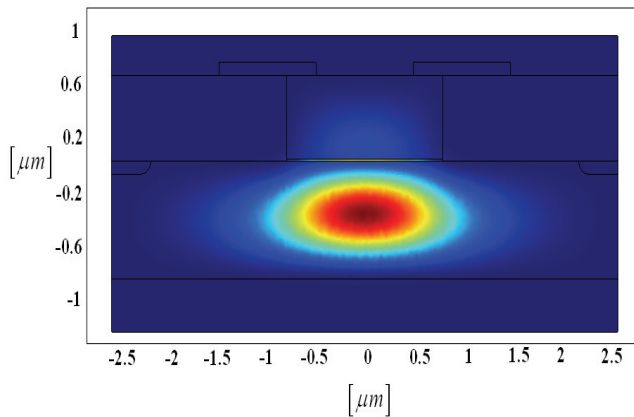


Figure 14. Quasi-TM mode electromagnetic field distribution for  $V_a = 2$  V



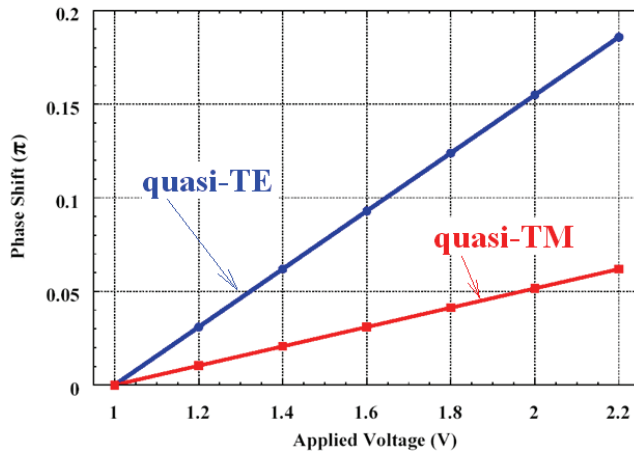


Figure 15. Phase shift induced in TE and TM-polarized light as a function of applied voltage

#### 2.4. Nonlinear silicon photonic devices

Nowadays, there is a very strong interest in literature in investigating and developing silicon photonic devices for nonlinear applications. A number of significant devices have been presented and demonstrated, including Raman amplifiers and lasers (De Leonardi & Passaro, 2007). As a transmission medium, silicon has much higher nonlinear effects than the commonly used silicon dioxide, in particular the Raman effect. The crucial importance of both experimental and theoretical investigations on nonlinear effects in SOI waveguides has been recently demonstrated by a review paper (Lin et al., 2007).

To investigate all nonlinear effects involved in the propagation of ultrafast pulses in SOI rib waveguides, a very generalized modelling is often required (Passaro & De Leonardi, 2006). In fact, a large number of effects is to be taken into account, including two photon absorption (TPA), Free Carrier Absorption (FCA) where the free carriers are generated by TPA of the propagating pulse, plasma dispersion, Self-Phase-Modulation (SPM) as induced by the Kerr nonlinearity, Group-Velocity Dispersion (GVD), third-order dispersion (TOD), self steeping, intra-pulse Raman scattering, mode polarization effects. In this section, some modelling aspects on the formation and propagation of optical solitons in sub-picosecond regime in SOI optical waveguides are investigated, showing the role of a FEM-based approach.

When sub-picosecond optical pulses propagate inside a waveguide, both dispersive and nonlinear effects largely influence their shapes and spectra. Then, the equation system must also take into account a number of higher order nonlinear effects induced by the delayed Raman response. Thus, the nonlinear response function is influenced and, then, SPM effect. In addition, the introduction of this delayed response allows to extend the investigation for pulse time widths well below 1 ps, ranging from 10 to 1000 fs. The nonlinear response function  $R(t)$  can be written as:

$$R(t) = (1 - f_R)\delta(t) + f_R h_R(t) \quad (14)$$

where  $\delta(t)$  indicates the Dirac delta function and  $f_R$  represents the fractional contribution of the delayed Raman response to nonlinear polarization  $P_{NL}$ . Thus,  $R(t)$  includes both electronic and vibrational (Raman) contributions. In addition, the Raman response function  $h_R(t)$  is responsible for the Raman gain spectrum. Its functional form can be deduced from the Raman gain spectrum,  $g_R(\Delta\omega)$ , known to exhibit a Lorentzian shape. Fraction  $f_R$  is estimated from the numerical value of the Raman gain peak and normalization condition  $\int h_R(t)dt = 1$ . Assuming a gain peak value of 20 cm/GW (typical for silicon at  $\lambda = 1550\text{nm}$ ), it results  $f_R = 0.043$ , well smaller than in silica fibers, i.e. 0.18. In the following analysis, we assume a typical SOI waveguide as sketched in Fig. 4, having rib total height  $h+R$ , slab height  $h$ , rib width  $w$  and air cover (without heater). In a single-mode SOI waveguide, two propagating modes are typically confined, one quasi-TE (dominant horizontal  $x$ -component of electric field) and one quasi-TM (dominant vertical  $y$ -component). Under the assumption of translational invariance along the propagation direction ( $z$ ), the electric field in the single-mode SOI waveguide can be given in the form of variable separation,  $E(x, y, z, t) = C \cdot F(x, y)A(z, t)e^{j\beta_0 z}$ , where  $\beta_0$  is the propagation constant,  $F(x, y)$  is the optical mode distribution in the waveguide cross section  $x-y$  (solutions of Helmholtz wave equation), and  $C$  is a normalization constant,  $C = \left( \int \int_{-\infty}^{+\infty} |F(x, y)|^2 dx dy \right)^{-1/2}$ . Thus, the total electric field inside the SOI waveguide can be written without any leak of generality as:

$$\mathbf{E}(x, y, z, t) = \hat{\mathbf{e}} \left[ CA(z, t)F(x, y)e^{j(\beta_0 z - \omega t)} \right] \quad (15)$$

with the following meaning for the unit vector:  $\hat{\mathbf{e}} = \hat{\mathbf{x}}$  for quasi-TE, or  $\hat{\mathbf{e}} = \hat{\mathbf{y}}$  for quasi-TM mode, respectively. In Eq. (15),  $\omega$  is the angular frequency of optical pulse injected into the SOI waveguide. Then, after some manipulations and assuming the nonlinear contributions to  $\mathbf{P}_{NL}$  as a small perturbation of refractive index, we obtain the following differential equation for the propagating pulse:

$$\begin{aligned} & \frac{\partial A(z, t)}{\partial z} + \beta_1 \frac{\partial A(z, t)}{\partial t} + j \frac{1}{2} \beta_2 \frac{\partial^2 A(z, t)}{\partial t^2} - \frac{1}{6} \beta_3 \frac{\partial^3 A(z, t)}{\partial t^3} = \\ & = - \frac{(\alpha^{(prop)} + \alpha^{(FC4)})}{2} A(z, t) - 0.5 \beta^{(TPA)} f |A(z, t)|^2 A(z, t) + \\ & + j \frac{2\pi}{\lambda} \Delta n A(z, t) + j\gamma \left( 1 + \frac{j}{\omega} \frac{\partial}{\partial t} \right) \left[ A(z, t) \cdot \int_{-\infty}^{+\infty} R(t') |A(z, t-t')|^2 dt' \right] \end{aligned} \quad (16)$$

which describes the time-space evolution of both quasi-TE or quasi-TM pulses. The coefficients  $\beta_1$ ,  $\beta_2$ ,  $\beta_3$  indicate the group velocity, GVD and TOD coefficients, respectively.

Moreover, the term proportional to  $\gamma = n_2 \omega f / c$  coefficient represents the SPM effect (due to Kerr nonlinearity), being  $c$  the light velocity and  $n_2$  the nonlinear refractive index, while the term proportional to time derivative takes into account the self-steeping effect and the intrapulse Raman scattering. Moreover,  $f^{-1} = A_{eff}$  represents the effective area of the optical mode for pulse injected into the SOI waveguide (calculated by FEM). Through coefficient  $\beta^{(TPA)}$ , the model includes the TPA effect as induced by the pulse propagation. Further, the total loss coefficient has been written as the summation of two contributions:  $\alpha^{(prop)}$ , the propagation loss coefficient in the rib waveguide, depending on the material absorption and fabrication process, and  $\alpha^{(FCA)}$  the contribution due to FCA, as induced by the change of the free carriers generated mainly by TPA of the pulse. Finally, the term  $\Delta n$  represents the change of effective index due to the plasma dispersion effect as induced by the free carriers, whose dynamics being governed by the following rate equation:

$$\frac{dN_c}{dt} = -\frac{N_c}{\tau_{eff}} + \frac{\beta^{(TPA)}}{2\hbar\omega} \left( |A(z,t)|^2 f \right)^2 \quad (17)$$

where  $\tau_{eff}$  is the relevant effective recombination lifetime for free carriers. The mathematical complexity of our model can be reduced without any leak of accuracy if we assume input pulse FWHM widths  $T_{FWHM} \gg 10$  fs. In this case, the following approximated Taylor-series expansion holds:

$$|A_i(z, t-t')|^2 \cong |A(z,t)|^2 - t' \frac{\partial |A(z,t)|^2}{\partial t} \quad (18)$$

The previous relationship leads to avoid the integral term in Eq. (16). Then, by substituting Eq. (18) in (16), it becomes:

$$\begin{aligned} & \frac{\partial A(z,t)}{\partial z} + \beta_1 \frac{\partial A(z,t)}{\partial t} + j \frac{1}{2} \beta_2 \frac{\partial^2 A(z,t)}{\partial t^2} - \frac{1}{6} \beta_3 \frac{\partial^3 A(z,t)}{\partial t^3} = \\ & = -\frac{(\alpha^{(prop)} + \alpha^{(FCA)})}{2} A(z,t) - 0.5 \beta^{(TPA)} f |A(z,t)|^2 A(z,t) + \\ & + j \frac{2\pi}{\lambda} \Delta n A(z,t) + j \gamma \left( |A(z,t)|^2 A(z,t) + \frac{i}{\omega} \frac{\partial |A(z,t)|^2}{\partial t} A(z,t) - T_R A(z,t) \frac{\partial |A(z,t)|^2}{\partial t} \right) \end{aligned} \quad (19)$$

where  $T_R = f_R \frac{d\tilde{h}_R}{d(\Delta\omega)} \Big|_{\Delta\omega=0}$  governs the intrapulse Raman scattering. In the previous relationship,  $\tilde{h}_R(\Delta\omega)$  represents the Fourier transform of the Raman response  $h_R(t)$ , which is directly related to the complex Raman gain through the Raman susceptibility. Assumption (18) allows to convert the equation system (16)-(17) in a partial differential equation system in the space-time domain (without using any integral term), solved by the

collocation method as a fast and accurate solution approach (Deb & Sharma, 1993). Hereinafter, normalized variables are used for numerical purposes,  $U_i(z, t) = A_i(z, t) / \sqrt{P_0}$  and  $\tau = (t - \beta_1 z) / T_0$ , where  $P_0$  is the Gaussian pulse peak power and  $T_0$  is related to pulse FWHM width by  $T_0 = T_{FWHM} / 1.665$ . Moreover, we will use normalized parameters to simplify the physical discussion, i.e. dispersion  $L_D = T_0^2 / |\beta_2|$ , and nonlinear lengths  $L_{NL} = 1 / \gamma P_0$ . To numerically solve the coupled equation system (17)-(19), the collocation method has been used by developing the unknown functions ( $A, N_c$ ) as a linear combination of  $M$  orthogonal functions  $\phi_m(\tau)$  through  $M$  weight functions  $c_m(z)$ . The algebraic details are presented in our previous work (Passaro & De Leonardis, 2006).

To test the mathematical model and the numerical method used to solve the equation system, we have compared our results with some numerical and experimental results presented in literature for propagation of sub-picosecond pulses in SOI. To the best of our knowledge, the first study involving ultrafast pulses in SOI waveguide has demonstrated the formation of solitons (Zhang et al., 2007). Thus, our general model has been applied to compare our results with that work. The SOI waveguide has rib total height  $R+h = 400$  nm, rib width  $w = 860$  nm and slab height  $h = 100$  nm. Since the optical soliton can be obtained only in the anomalous GVD region, it is crucial to design the SOI waveguide to realise negative values of GVD coefficient. In this sense, our first comparison has involved the evaluation of the GVD coefficient spectrum for that waveguide. Simulations have been performed using the FV-FEM approach with about 60,000 elements mesh, and material dispersion considered by means of Sellmeier relationships. The following Table 4 shows the very good agreement with results in literature (Zhang et al., 2007).

Moreover, the model has been used to investigate the time-space evolution of ultrafast optical pulses. According with (Zhang et al., 2007), the quasi-TM ultrafast pulse is launched at  $\lambda = 1.484$   $\mu\text{m}$  with a Gaussian shape and FWHM width  $T_{FWHM} = 116$  fs. The waveguide length is  $L = 5$  mm, larger than both nonlinear and dispersion lengths. As a result, the interplay between SPM and GVD causes the pulses to evolve into a soliton. Fig. 16 shows the simulated shape of the output pulse by assuming  $\beta^{(TPA)} = 0.45$  cm/GW,  $n_2 = 6 \times 10^{-5}$  cm<sup>2</sup>/GW and  $\alpha_i^{(prop)} = 5$  dB/cm. In addition, the waveguide proposed has an anomalous GVD of -2.15 ps<sup>2</sup>/m for quasi-TM modes, as shown in Fig. 16.

Wavelength	$\beta_2$ (ps <sup>2</sup> /m) literature	$\beta_2$ (ps <sup>2</sup> /m) this work
$\lambda = 1249$ nm	0.81	0.83
$\lambda = 1350$ nm	-0.95	-0.92
$\lambda = 1484$ nm	-2.15	-2.10

Table 4. GVD coefficients for quasi-TM mode

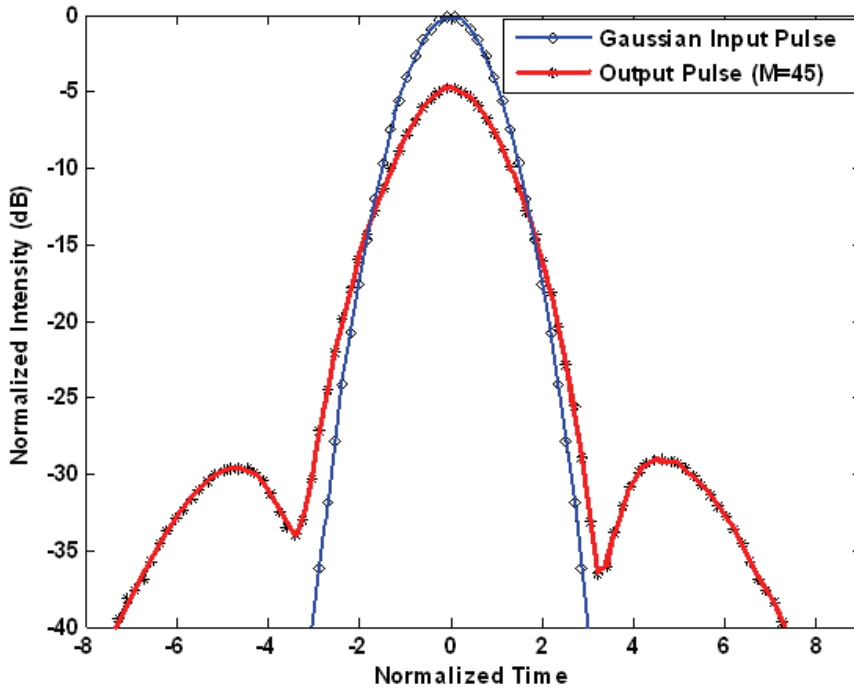


Figure 16. Normalized intensity versus normalized time for input and output pulses

According with data in literature, the input peak power has been selected to realise the condition  $(L_D/L_{NL})^{1/2} \approx 1.35$ . In the plot, the curve with diamond markers designates the input Gaussian pulse, while the curve with asterisk markers indicates the output pulse calculated with  $M = 45$  collocation points. Then, a very good agreement with experimental results is demonstrated. The accuracy improves by increasing  $M$ , but this improvement is not significant for  $M > 45$ . Thus,  $35 \leq M \leq 45$  represents the best trade-off between accuracy and calculation time. Moreover, by comparing the main lobes of input and output pulses, we see as the output pulse can be fitted by a *sech*-like pulse, confirming that the interplay between the SPM and GVD effects has caused the formation of the fundamental soliton.

In many applications, it is critical to find the design rules for any SOI rib waveguide to simultaneously meet single-mode and birefringence free conditions, or to achieve single-mode and zero GVD dispersion. Although the high refractive index contrast between the waveguide cladding and core makes easier the light confinement in submicron-scale structures, it also makes the control of waveguide birefringence extremely challenging. The research in birefringence control is driven primarily by the requirement of polarization insensitivity in interferometer devices such as arrayed waveguide gratings, ring resonators and all-optical devices, such as ultrafast switches and all-optical gates. It is well known that the waveguide core geometry influences not only the modal birefringence, but also other critical parameters, as the effective carrier recombination

lifetime  $\tau_{eff}$ , GVD and TOD coefficients. Free carrier diffusion usually needs to be considered in addition to the recombination lifetime. In fact, if diffusion carriers move out of the modal area, this results in an effective lifetime shorter than the recombination lifetime in SOI structures. Usually a small cross section is necessary to obtain a low value for the carrier lifetime. However, it is known that the FCA induced by the TPA produces negligible effects for short pulses ( $< 1\text{ps}$ ). Thus, the goal of waveguide design in sub-picosecond regime usually consists of the best trade-off between GVD and TOD effects. A submicron structure with  $R+h = 500\text{ nm}$  and  $r = h/(R+h) = 0.2$  has been investigated for different values of rib width  $w$  and wavelength. A parametric plot of GVD coefficient spectrum for various  $w$  and both polarizations is sketched in Fig. 17 as achieved by FV-FEM.

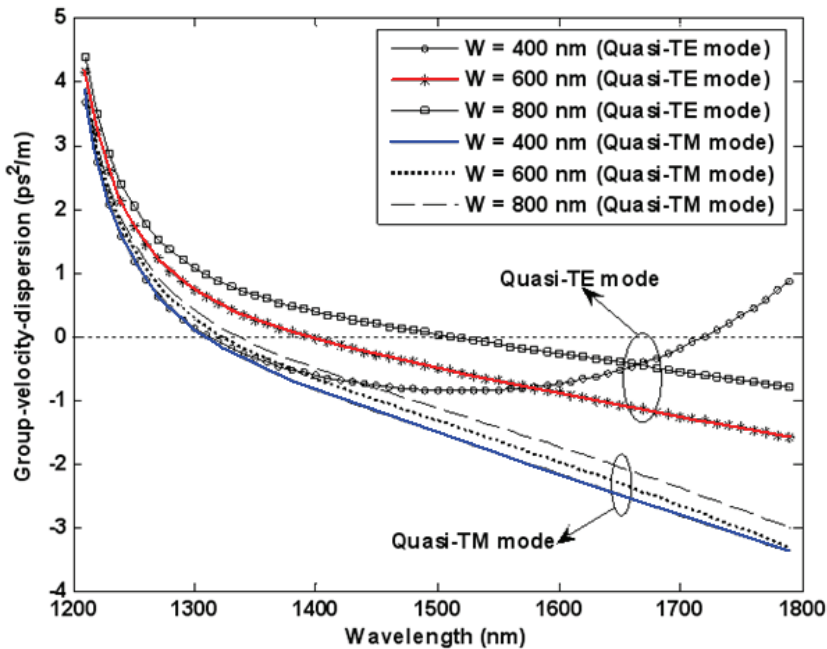


Figure 17. Group-velocity dispersion spectrum for different rib widths and both polarizations

Several features of this figure are noteworthy. In terms of values and shapes, quasi-TM modes show a smaller sensitivity than quasi-TE modes to rib width changes. In addition, for both polarizations it is possible to find the normal and anomalous dispersion regions. It is clear that  $\beta_2$  spectrum shows a particular shape for quasi-TE polarization and  $w = 400\text{ nm}$ . This behaviour is explained considering that quasi-TM polarization is here the fundamental mode (approaching zero birefringence condition with increasing wavelength), differently from the other cases where the fundamental mode is quasi-TE. The plot in Fig. 18 shows the TOD coefficient spectrum for different values of rib width and both polarizations.

The plots indicate that, in the wavelength range 1200-1800 nm, quasi-TM modes have a  $\beta_3$  larger than zero for each value of rib width. Same conclusions can be derived for quasi-TE modes except from the case  $w = 400$  nm, where condition  $\beta_3 = 0$  is satisfied at  $\lambda = 1521.2$  nm.

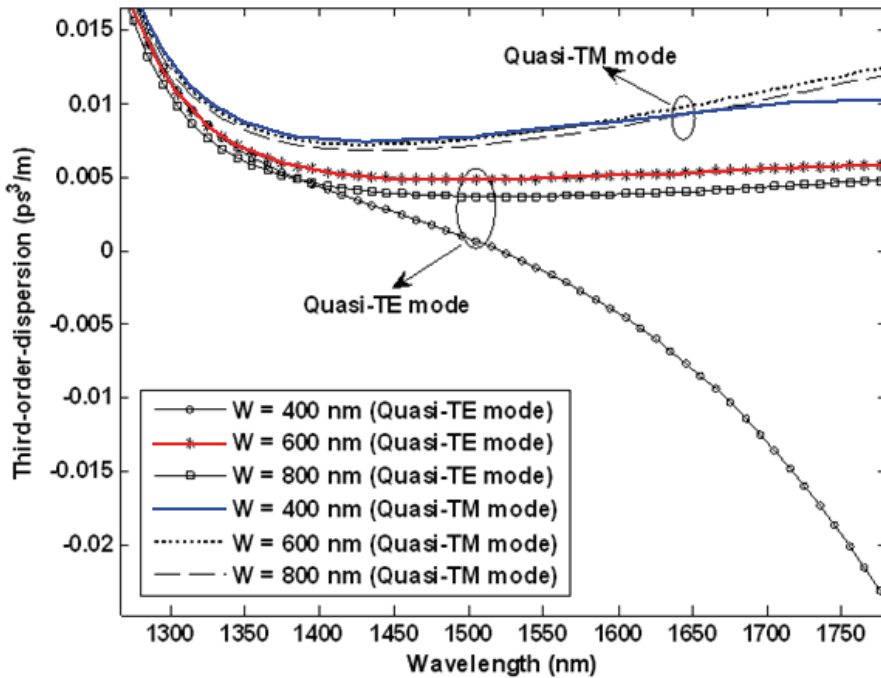


Figure 18. Third-order dispersion spectrum for different rib widths and both polarizations

### 3. Conclusion

This chapter briefly summarizes some important examples of modelling of photonic devices based on silicon technology. The potential, properties and advantages of finite element method-based modelling approaches are clearly presented and emphasized. Significant investigated devices include novel kinds of silicon optical waveguides (slot, hollow), thermo-optic modulated devices, plasma dispersion modulated devices (MOS modulators), as well as non linear silicon devices for generating optical solitons in SOI rib waveguides.

### 4. Acknowledgments

This work has been partially supported by Italian Ministry for University and Research under Interlink project, n. I104C01CDM. The authors wish to thank F. Dell'Olio and F. Magno for their valuable support.

## 5. References

- Barrios, C. A. & Lipson, M. (2004). Modeling and analysis of high-speed electro-optic modulation in high confinement silicon waveguides using metal-oxide-semiconductor configuration. *Journal of Applied Physics*, Vol. 96, No. 11, 6008-6015, ISSN 0021-8979.
- Deb, S. & Sharma, A. (1993). Nonlinear pulse propagation through optical fibers: an efficient numerical method. *Optical Engineering*, Vol. 32, No. 4, 695-699, ISSN 0091-3286.
- De Leonardis, F. & Passaro, V. M. N. (2007). Modeling of Raman amplification in silicon-on-insulator optical microcavities, *New Journal of Physics*, Vol. 9, No. 2, 1-24, ISSN 1367-2630.
- Dell'Olio, F. & Passaro, V. M. N. (2007). Optical sensing by optimized silicon slot waveguides. *Optics Express*, Vol. 15, No. 8, 4977-4993, ISSN 1094-4087.
- Harrington, J. A. (2000). A Review of IR Transmitting, Hollow Waveguides. *Fiber and Integrated Optics*, Vol. 19, No. 3, 211-217, ISSN 0146-8030.
- Lin, Q.; Painter, O. J. et al. (2007). Nonlinear optical phenomena in silicon waveguides: modeling and applications. *Optics Express*, Vol. 15, No. 25, 16604-16644, ISSN 1094-4087.
- Muellner, P. & Hainberger, R. (2006). Structural Optimization of Silicon-on-Insulator slot Waveguides. *IEEE Photonics Technology Letters*, Vol. 18, No. 24, 2557-2559, ISSN 1041-1135.
- Passaro, V. M. N. (2000). Optimal Design of Grating-Assisted Directional Couplers. *Journal of Lightwave Technology*, Vol. 18, No. 7, 973-984, ISSN 0733-8724.
- Passaro, V. M. N. (2006). *Silicon Photonics*, Research Signpost Publ., ISBN 81-308-0077-2, Kerala (India).
- Passaro, V. M. N. & De Leonardis, F. (2006). Space-Time Modeling of Raman Pulses in Silicon-on-Insulator Optical Waveguides. *Journal of Lightwave Technology*, Vol. 24, No. 7, 2920-2931, ISSN 0733-8724.
- Reed, G. T. (2004). The optical age of silicon. *Nature*, Vol. 427, No. 6975, 595-596, ISSN 0028-0836.
- Reed, G. T. & Knights, A.P. (2004). *Silicon Photonics: an introduction*, John Wiley and Sons, ISBN 0-470-87034-6, Chichester (UK).
- Scarmozzino, R.; Gopinath, A. et al. (2000). Numerical Techniques for Modeling Guided-Wave Photonic Devices. *IEEE Journal of Selected Topics in Quantum Electronics*, Vol. 6, No. 1, 150-162, ISSN 1077-260X.
- Soref, R. A. & Bennett, B. R. (1987). Electrooptical Effects in Silicon. *IEEE Journal of Quantum Electronics*, Vol. QE-23, No. 1, 123-129, ISSN 0018-9197.
- Yamada, H.; Chu, T. et al. (2006). Si Photonic Wire Waveguide Devices. *IEEE Journal of Selected Topics in Quantum Electronics*, Vol. 12, No. 6, 1371-1379, ISSN 1077-260X.
- Xu, Q.; Almeida, V. R. et al. (2004). Experimental demonstration of guiding and confining light in nanometer-size low refractive-index material. *Optics Letters*, Vol. 29, No. 14, 1626-1628, ISSN 0146-9592.
- Zhang, J.; Lin, Q. et al. (2007). Optical solitons in silicon waveguides. *Optics Express*, Vol. 15, No. 12, 7682-7688, ISSN 1094-4087.



# Numerical Modelling for Thermal Design of Electronic Equipments

Giuseppe Petrone and Giuliano Cammarata

*Department of Industrial and Mechanical Engineering, University of Catania  
Italy*

## 1. Introduction

During the last decades, reproducing physics of systems by computer simulation has aroused great interest both in academic community and industrial world. Disposing of a virtual model, able to simulate the real behaviour of a system, represents a really powerful tool both for understanding phenomenological aspects of a chosen physics and for predicting functional or operative conditions of a technological system. Because of this, large efforts are continuously spent in developing computational codes for specific applications and in building up simulating models in a very wide range of technological domains. Despite of its unquestionable advantages, experimental approach in studying systems often results expensive and hardly flexible. Instead, developing of reliable software, combined with increasing in hardware capability, are more and more encouraging researchers to adopt the simulating approach also in solving complex systems. This opportunity obviously promises wide gaps of optimisation in manufacturing also, with consequent growth in effectiveness and in economic benefit.

Focalising attention on electronic equipments, it is commonly recognized that careful thermal design represents an unavoidable step in pre-production phase (Harvest et al., 2007), in order to ensure reliability and performance of those components during their functioning (Hanreich et al., 2000). Electronic devices produce a very important rate of specific heat (related to their small dimensions) as a by-product of their normal operation. Exceeding in maximum safe operating temperature specified by the manufacturer means a strong reduction of semiconductors efficiency and functional life (Bailey et al., 2002). Among the high power components, Random Access Memory modules are one of the more sensitive thermal subsystem of an assembled computer (Petrone et al., 2007). Cooling of those devices is always performed by mechanical ventilation systems, that assure a forced convection mechanism in order to dissipate thermal energy. However, the forced air flow is often disturbed by many factors. Cables, drive bays and brackets can determinate bypass over the memory components, forcing the subsystem to operate in mixed or natural convection conditions (El Alami et al., 2005). Therefore, natural convection represents a critical heat transfer mechanism assuring cooling if designed operational conditions, for any reason, partially or totally fall down (Bhowmik & Tou, 2005). Otherwise, the passive character of cooling by natural convection makes it very attractive for possible application in electronic devices (da Silva et al., 2005). From a theoretical point of view, cooling of

electronic packages has furthermore created emphasis on understanding the basic convective fluid flow over discrete heat sources (Bae & Hyun, 2004; Dogan et al., 2006), which have different characteristics from the traditionally studied convection from a heated whole wall. This chapter deals with a numerical analysis on natural and mixed convection heat transfer for Dual In-line Memory Modules, both horizontally and vertically disposed. The physical system is firstly introduced, then implementation and validation of the applied numerical model is discussed and finally the main obtained results are illustrated.

## 2. The physical system

The actually most used Random Access Memories in Personal Computers are the Dual-Inline-Memory-Modules (DIMM). They are made of 4-16 chip of synchrony dynamical memory with random access (SDRAM), type DDR (Double Data Rate) or DDR2. Chips are characterized by very small dimensions and they are mounted on a Printed Circuit Board (PCB). The PCB disposes of a certain number of PIN both on its top and bottom face. An example of a DIMM is reported in Figure 1.

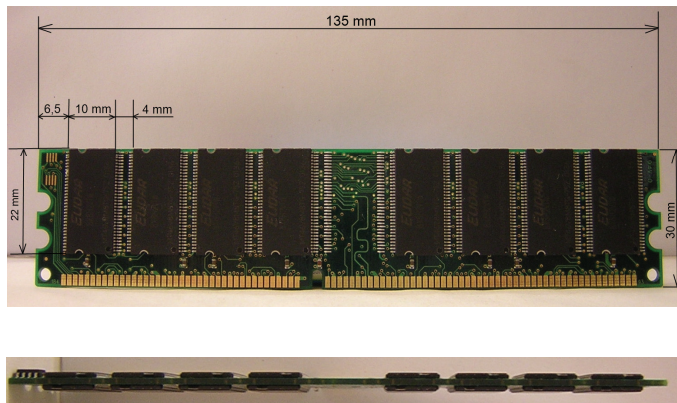


Figure 1. Bottom and backside views of a Dual In-line Memory Module

These components are object of the Joint Electron Device Engineering Council (JEDEC) standards. According to JEDEC specifications, the mean parameter indicating thermal performance of DIMM is the total thermal resistance  $\theta_{TOT}$  between miniaturized integrated circuit and surrounding environment. This represents the sum of sequential thermal resistances, such as junction-package resistance, package-heat sink resistance (if a heat sink is present), heat sink-ambient resistance (Figure 2). By knowing  $\theta_{TOT}$  value, it is possible, for a chosen ambient temperature  $T_{AMB}$  and for a standard active power of 1 [W], analytically evaluating the junction temperature  $T_{JUNCTION}$  of the chip. In order to guarantee the reliability of the memory modules, it is strictly necessary that chip does not overcome, during its functioning, the maximum temperature recommended in the technical documentations of constructors. These values are commonly comprised in the range 80-110 [°C]. Considering a generic vertically disposed mainboard (tower configuration for a PC case), DIMM modules are arranged in horizontal disposition, as showed in the top portion of Figure 3. The PCB, where chips are arranged, is perpendicularly connected to the vertical mainboard by specific sockets with lateral guides.

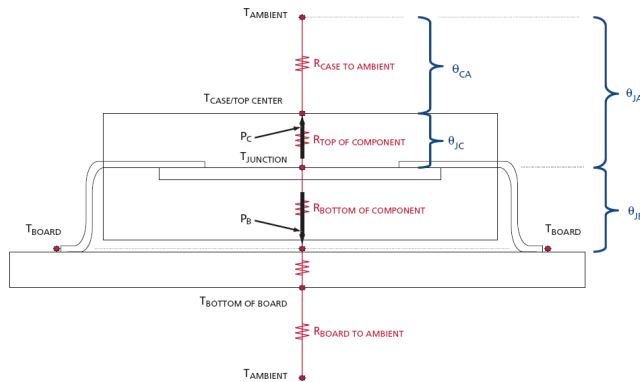


Figure 2. Scheme of a cross section of a chip mounted on a circuit board: primary thermal resistances

For predictive estimation of operative temperature of DIMM, leading constructors recommend computational modelling in spite of analytical determination of temperature by JEDEC indications. In fact analytical determination of  $T_{JUNCTION}$  could be not exhaustive because of the lack of consideration of several significant factors, first of all the proximity of other heat sources.

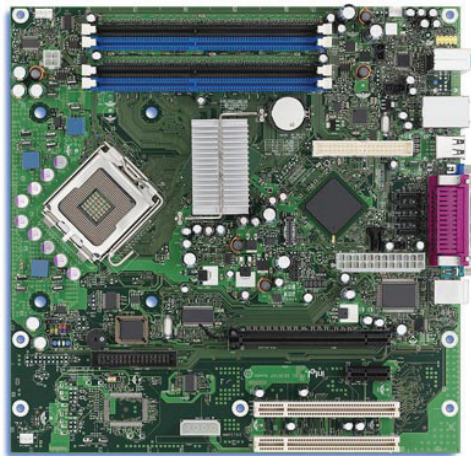


Figure 3. Electronic components arranged on a mainboard of a tower configuration PC

### 3. The numerical model

#### 3.1 Continuous governing equations

The considered physical system is outlined by parallel boards (Printed Circuit Board) surrounded by air and arranging on multiple heat sources (Chip), see Figure 4.

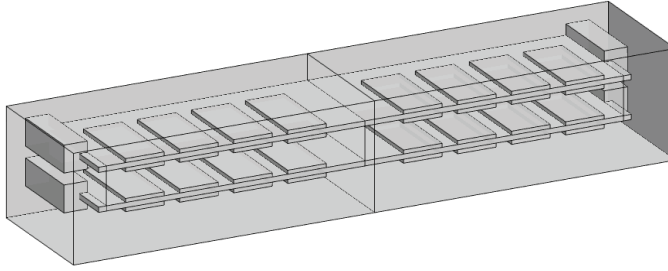


Figure 4. Geometry of two overlapped 16-chip memory modules horizontally arranged

In natural convection, fluid is propelled by the buoyancy force, generated by a non-uniform density distribution due to local temperature gradients. In our problem, heating of fluid is related to the presence of heat sources (chips in operative conditions) plunged in the air volume. The multi-physical problem is mathematically governed by conservation laws, the Navier-Stokes equations, characterizing flow of an incompressible fluid, and the energy equation, defining the equilibrium between heat fluxes (conductive one and convective one) and heat sources. The governing partial differential equations are reported in following:

$$\left\{ \begin{array}{l} \rho \frac{\partial \vec{U}}{\partial t} + \vec{\nabla} \cdot (\rho \vec{U} \times \vec{U}) = -\vec{\nabla} p + \vec{\nabla}^2 (\eta \vec{U}) + (\rho_0 - \rho) \vec{g} \\ \frac{\partial \rho}{\partial t} + \vec{\nabla} \cdot (\rho \vec{U}) = 0 \\ \rho C_p \frac{\partial T}{\partial t} + \vec{\nabla} \cdot (\rho C_p \vec{U} T) = q + \vec{\nabla}^2 (kT) \end{array} \right. \quad (1)$$

The energy equation is to be solved in fluid as well as in solid sub-domains of system, by considering appropriate values for thermal conductivity ( $k_c = 163 [Wm^{-1}K^{-1}]$ ,  $k_p = 0.3 [Wm^{-1}K^{-1}]$ ). Only in chip sub-domains the heat source term is different from zero and its value is  $q = Q_d / (n_c \Omega_c)$ . Adopted properties and conditions for fluid in this study are reported in Table 1.

Parameter	Unit
$M = 0.0288$	$[kg \text{ mol}^{-1}]$
$R = 8.134$	$[J \text{ mole}^{-1} \text{ kg}^{-1}]$
$p_a = 101325$	$[Pa]$
$\rho \equiv p_0 M / (RT)$	$[kg \text{ m}^{-3}]$
$\eta \equiv 6,0 \cdot 10^{-6} + 4,0 \cdot 10^{-8} T$	$[Pa \text{ s}]$
$k \equiv \exp(-3,723 + 0,865 \log T)$	$[W \text{ m}^{-1} \text{ K}^{-1}]$
$C_p = 1100$	$[J \text{ kg}^{-1} \text{ K}^{-1}]$

Table 1. Dynamical and thermal properties of air

Because of the particular technological interest of this kind of study, it seemed favourable solving conservation equations in their original dimensional form. This item allows to focus attention on the specific electronic device considered and make results directly exploitable by operators in this sector. Otherwise, classical non dimensional groups are also used in post-processing of results. The Reynolds number, defined as  $Re \equiv \rho U D_n / \eta$ , is evaluated basing on the hydraulic diameter of the inlet section for air flow (lateral or bottom face according to vertical or horizontal arrangement), while the characteristic linear dimension adopted for Rayleigh number evaluation ( $Ra \equiv g h^3 \Delta \rho / (\eta \alpha)$ ) is the distance  $h$  between the overlapped circuit boards.

### 3.2 Solving procedure

Continuous conservation equations (1) are discretized by Finite Element Method (FEM) on no-structured computational meshes, made of tetrahedral elements. The totality of simulations presented in this study have been carried-out by applying the software Comsol Multiphysics®. Discrete equations are solved with boundary conditions defined below:

Fluid-dynamical conditions:

- No-slip conditions on interfaces between fluid and solid elements;
- Constant pressure values on horizontal boundaries of the fluid domain (inlet velocity for mixed convection models);
- Symmetry conditions on lateral end-section of the fluid domain (simplified models only);

Thermal conditions:

- Adiabatic condition for external walls of circuit boards and socket;
- Convective heat flux for top and lateral boundaries of the fluid domain;
- Imposed temperature for the bottom boundary of the fluid domain;

Time-integration of equations (1) has been only performed in order to compare numerical results with experiments (validation of the numerical model), to compare results of transient analysis with steady solution of conservation equations (validation of the steady approach in solving governing equations), to investigate on transient fluid-dynamics during heating of fluid at initial rest conditions. The temporal integration lies on a backward Euler method and the solver is an implicit time-stepping scheme solving a nonlinear system of equations at each time step (Brenan et al., 1989). In order to simplify the presentation of the adopted algorithm for steady solution of equations (1), let now indicate as  $\bar{S} \equiv (\bar{U}, T)^t$  a generic solution of Navier-Stokes and energy equations, and let consider the following assumptions for grouping transport, diffusion, buoyancy and pressure terms (Petrone et al., 2004):

$$[\mathcal{T}(\bar{U})](\bar{S}) = - \begin{pmatrix} \bar{\nabla} \cdot (\rho \bar{U} \times \bar{U}) \\ \bar{\nabla} \cdot (\rho C_p \bar{U} T) \end{pmatrix}$$

$$\mathcal{D}(\bar{S}) = \begin{pmatrix} \bar{\nabla}^2 (\eta \bar{U}) \\ \bar{\nabla}^2 (k T) \end{pmatrix}$$

$$\mathcal{B}(\bar{S}) = \begin{pmatrix} (\rho_0 - \rho)\bar{g} \\ 0 \end{pmatrix}$$

$$[\mathcal{P}(\bar{U})](\bar{S}) = -\begin{pmatrix} \bar{V}p \\ 0 \end{pmatrix}$$

If  $\bar{S}_0 \equiv (\bar{U}_0, T_0)'$  is a steady solution of equations (1) then it verifies the following expression:

$$[\mathcal{T}(\bar{U}_0) + \mathcal{D} + \mathcal{B} + \mathcal{P}(\bar{U}_0)](\bar{S}_0) = \bar{0} \tag{2}$$

An iterative approximation of steady state  $\bar{S}_0$  by  $\bar{S}^{(k+1)}$  is performed by applying a modified Newton-Raphson method (Deuffhard, 1974), where a damping factor  $0 < \lambda \leq 1$  is introduced in computing of perturbation, as in following:

$$\begin{cases} J_{\mathcal{T}(\bar{U})+\mathcal{D}+\mathcal{B}+\mathcal{P}(\bar{U})}[\bar{S}^{(k)}](\bar{\delta S}^{(k+1)}) = \\ -[\mathcal{T}(\bar{U}^{(k)}) + \mathcal{D} + \mathcal{B} + \mathcal{P}(\bar{U}^{(k)})](\bar{S}^{(k)}) \\ \bar{S}^{(k+1)} = \bar{S}^{(k)} + \lambda \bar{\delta S}^{(k)} \end{cases} \tag{3}$$

where the Jacobian operator  $J_{\mathcal{T}(\bar{U})+\mathcal{D}+\mathcal{B}+\mathcal{P}(\bar{U})}$ , expressed in  $\bar{S}^{(k)}$  and applied to perturbation  $\bar{\delta S}^{(k+1)}$ , consists in difference between perturbed and not perturbed conservation equations linearized close to the  $\bar{S}^{(k)}$  state.

Once  $\bar{S}^{(k+1)}$  evaluated, the relative error  $E^{(k+1)}$  is computed :

$$J_{\mathcal{T}(\bar{U})+\mathcal{D}+\mathcal{B}+\mathcal{P}(\bar{U})}(\bar{S}^{(k)})E^{(k+1)} = -[\mathcal{T}(\bar{U}^{(k+1)}) + \mathcal{D} + \mathcal{B} + \mathcal{P}(\bar{U}^{(k+1)})](\bar{S}^{(k+1)}) \tag{4}$$

If  $E^{(k+1)} > E^{(k)}$  then the code reduces the damping factor  $\lambda$  and computes  $\bar{S}^{(k+1)}$  again. This algorithm repeats the damping-factor reduction until the relative error is less than in the previous iteration or until the damping factor underflows the imposed minimum value. When it has taken a successful step  $\bar{S}^{(k+1)}$ , the algorithm proceeds with the next Newton iteration. A value of  $\lambda = 1$  results in classical Newton's method, which converges at second order if the initial guess is sufficiently close to the solution. The iterative procedure ends when:

$$\mathcal{E} = \left( \frac{1}{N} \sum_{i=1}^N \left( \frac{|E_i^{(k+1)}|}{|S_i^{(k+1)}|} \right)^2 \right)^{1/2} < \mathcal{E}_0$$

where  $N$  is the number of degrees of freedom for the system and  $\mathcal{E}_0$ , fixed at value  $10^{-6}$  in this study, is an arbitrary small number. Algebraic systems coming from differential operators

discretisation are solved by using a direct unsymmetrical multi-frontal method, particularly indicated in order to solve sparse matrix by LU decomposition. Computations have been carried-out on a 64 bit workstation of 16 GB of RAM.

### 3.3 Computational grid studying

Influence of computational grid has been preliminary studied in order to assure mesh-independent results. The numerical approach in solving continuous equations consists in fact in researching an approximate solution of the exact one. The effectiveness of this approximation primary depends by the degree of spatial discretisation for differential operators. In Table 2 we report a summary of the mesh studying obtained for the horizontal configuration of the DIMM. Relative gaps of maximum of temperature and velocity values over all the domains with respect to reference ones (evaluated for the finest tested grid) indicate that a mesh made of 24611 nodes (139857 degrees of freedom, d. o. f.) can be adopted assuring very small sensitivity of results with spatial discretisation. Saturation of error with increasing in mesh refinement is otherwise well testified by Figure 5, where maximum of velocity is reported as function of the number of elements of the computational grid. Further increasing in mesh refinement does not correspond to substantial benefit in precision justifying much more higher computational time.

Elements	Increasing (%)	d. o. f.	$T_{\max}$ [°C]	Relative gap (%)	$U_{\max}$ [m/s]	Relative gap (%)
7052	-	38791	85.61	2.60	0.159	13.14
9871	40.0	55108	86.24	1.87	0.153	9.08
14128	43.1	79140	87.13	0.86	0.147	4.85
24611	74.2	139857	87.74	0.17	0.142	1.34
39536	60.6	225600	87.89	-	0.140	-

Table 2. Maximum values of temperature and velocity as function of the number of mesh elements and relative degrees of freedom. Relative gap with respect to reference values (values obtained for the finest grid) are also reported

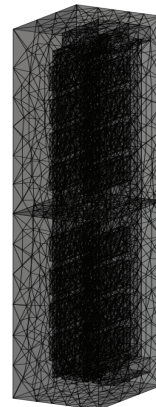
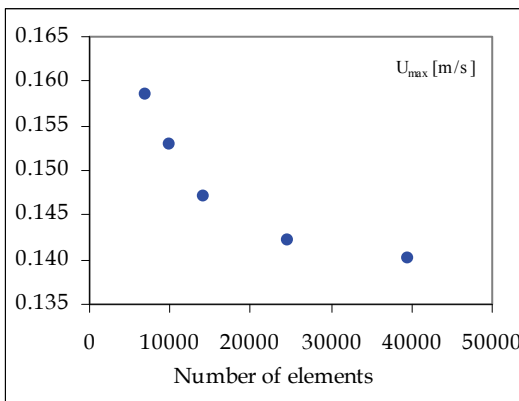


Figure 5. Maximum velocity values reported as function of the elements number for the computational grid (left side) and example of computational grid (right side)

#### 4. Validation of the numerical model

One of the great problem related to the numerical approach in solving the governing equations of a physical system concerns reliability of the adopted simulating model and consequently reliability of the results carried-out by applying the chosen scheme (Towashiraporn, 2004). For that reason it is always advisable firstly testing its reliability. One suitable way to proceed consists in comparing results carried-out by applying the proposed scheme with data concerning similar systems proposed by other researchers and at disposal in scientific literature. Otherwise, sometime this way to proceed could be not possible because we do not dispose of all information needed for exactly replying physical systems studied by other researchers or we are approaching a new problem whose no results are present in literature. The second way to operate (probably better than the previous one) consists, when possible, in setting-up an experimental apparatus reproducing a test section of the physical system we are interested to investigate. By conducting test experiments on this set-up, some data become available to be compared with those obtained by using the numerical model to solve the same configuration of the system. This procedure assures the opportunity of disposing of all technical information needed to reproduce by a virtual model the real system we are studying. Once the numerical model validated by comparison with experimental data, it can be applied to investigate some other configurations (arrangement of components, geometrical dimensions, load conditions, boundary conditions, influence of specific parameters), exploiting all the facilities offered by disposing of a reliable virtual model simulating a real system.

##### 4.1 Comparison with literature results

An example of the first above discussed procedure to validate the numerical model is discussed in this subparagraph. Results of simulation for vertical channels with multiple heat sources plunged in air, have been compared with those experimentally obtained in literature (Ortega, 2002). In Figure 6 we report geometry, thermal and fluid-dynamical fields obtained by numerical models built in conformity with respect to the system analysed in the reference.

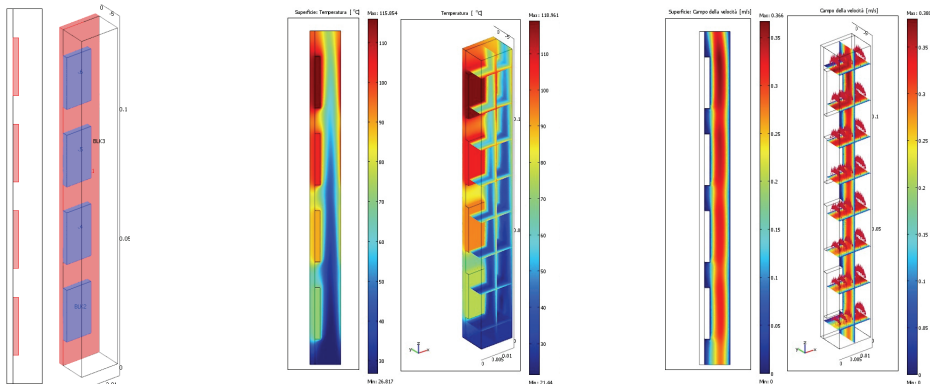


Figure 6. Geometry, thermal fields and velocity fields of the numerical model built for validation with experimental results previously published (Ortega, 2002)



In Figure 7 thermal transmittance  $K_{O_i}$  between the  $i$ -heat source surface (4 surfaces for the presented model) and inlet section for fluid, obtained both for 2D and 3D numerical models, are compared with experimental results of the reference. The compared thermal transmittance is defined as:

$$K_{O_i} = \frac{\frac{1}{\Sigma_1} \int q_i d\Sigma_1}{\frac{1}{\Sigma_2} \int T_{s,i} d\Sigma_2 - T_{f,0}}$$

where  $\Sigma_1$  and  $\Sigma_2$  are the total and vertical surface of the heat sources respectively,  $q_i$  is the specific thermal flux and  $T_{f,0}$  and  $T_{s,i}$  are the inlet temperature for fluid and the  $i$ -vertical surface mean temperature respectively.

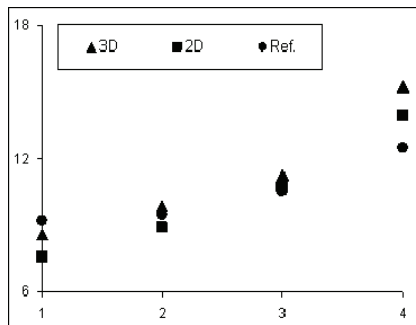


Figure 7. Comparison of thermal transmittance [W/(m<sup>2</sup>K)] for vertical channels in natural convection conditions between present 2D (square) and 3D (triangle) numerical results and those reported in the reference (circle)

From Figure 7 a good agreement between present results and those published in the reference is evident. Remarkable small gaps between present results with respect to reference could be due to thin difference in geometrical dimension of systems.

#### 4.2 Comparison with experiments

During this study an experimental set-up was also used in order to validate reliability of the adopted numerical procedure for solving thermal and fluid-dynamical fields of the studied system. The experimental technique chosen to produce comparing data for numerical results lies on a thermo-graphic investigation on surfaces thermal distribution of Dual In-line Memory Modules during operative conditions. The experimental apparatus mainly consists in a test PC where two 16-chip memory modules (DDR - 512 MB - 266 MHz) were arranged on, an infrared camera (ThermaCAM Flir SC 3000) for detection of surface thermal fields and a laptop PC used for acquisition (Figure 8). In order to reproduce the most critical heat transfer condition of functioning for the electronic devices, some black panels were employed in order to shield the memory modules by the forced air-flow produced by ventilators. The black box built around the investigated devices also resulted helpful for thermo-graphical acquisition. In fact other hot electronic components mounted on the mainboard were hindered by the black panels, allowing to set temperature range of

the acquisition system with thermal values characteristic of the memory modules we were interested to record. During experimental running specific applications were launched on the test PC in order to load memories by a known electrical power (0.3-0.4 [W]).

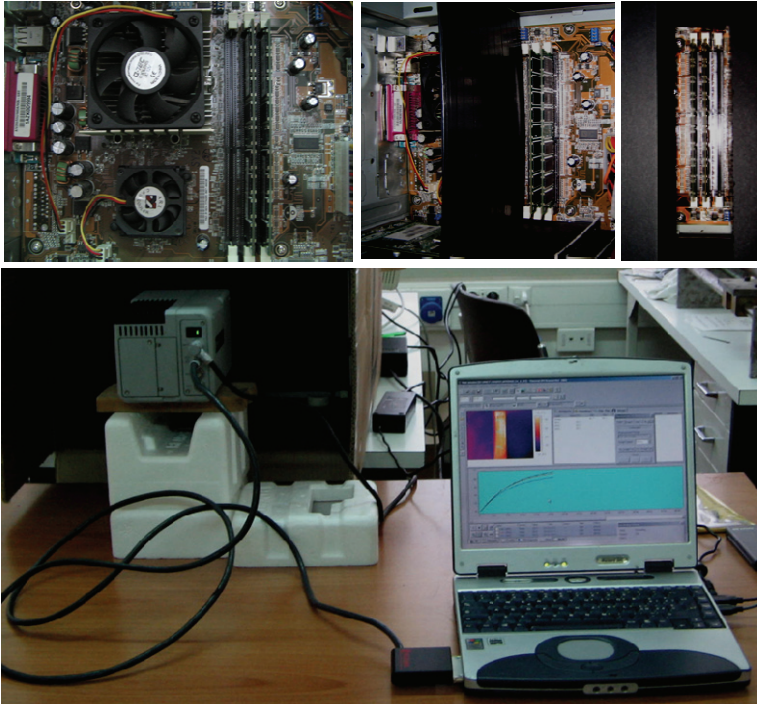


Figure 8. Experimental set-up for thermo-graphic acquisition of thermal levels on DIMM surfaces during functioning under controlled load conditions

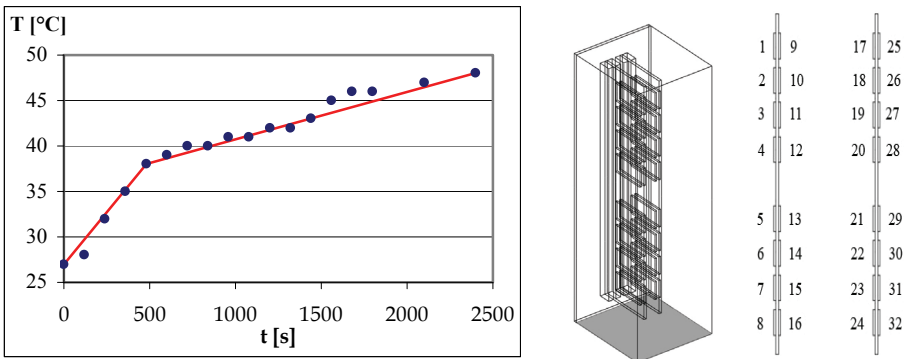


Figure 9. Time-evolution of air temperature experimentally detected at the bottom end of the DIMM (blue dots) and linear functions (red lines) used for implementing the bottom face boundary condition of the numerical model (grey surface). Adopted numeration of the Integrated Circuit for the studies devices (right side of the figure)

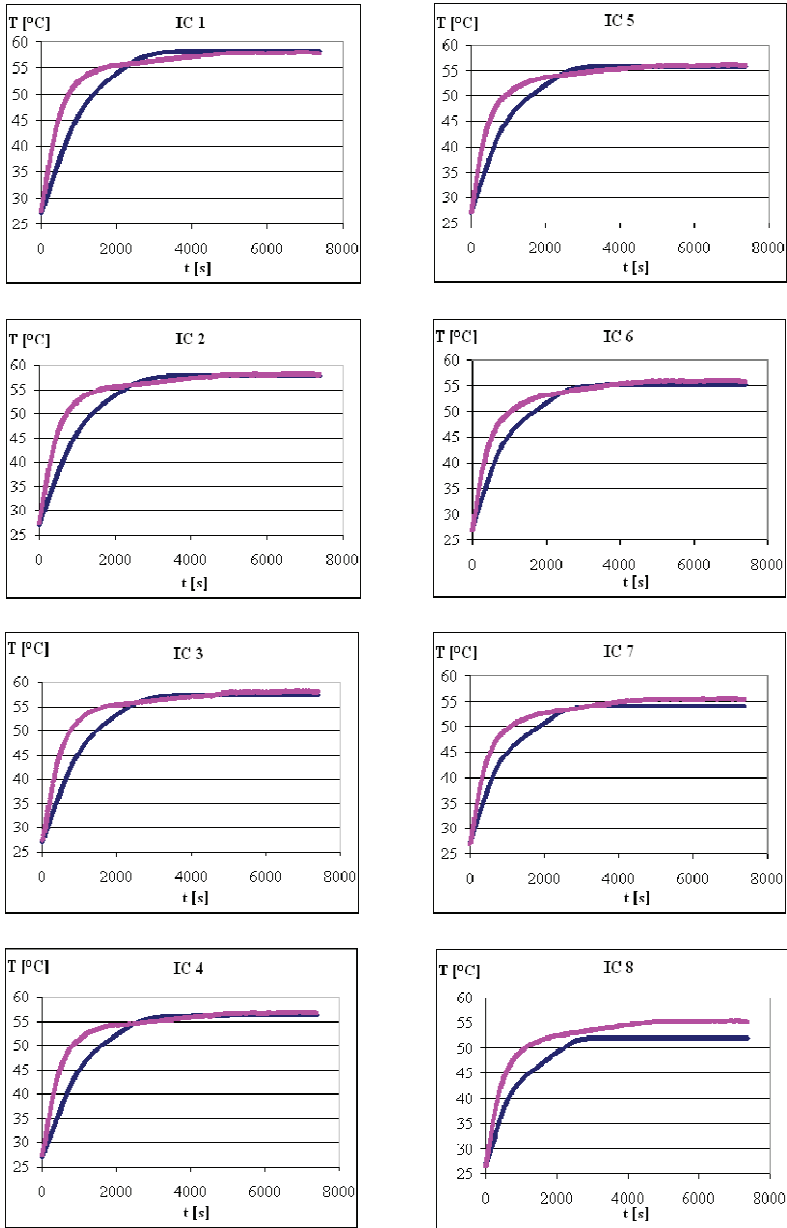


Figure 10. Time evolution of temperature values detected on experimental (pink line) and numerical (blue line) frontal surfaces of the chip (IC 1-8 according to numeration of Figure 9)

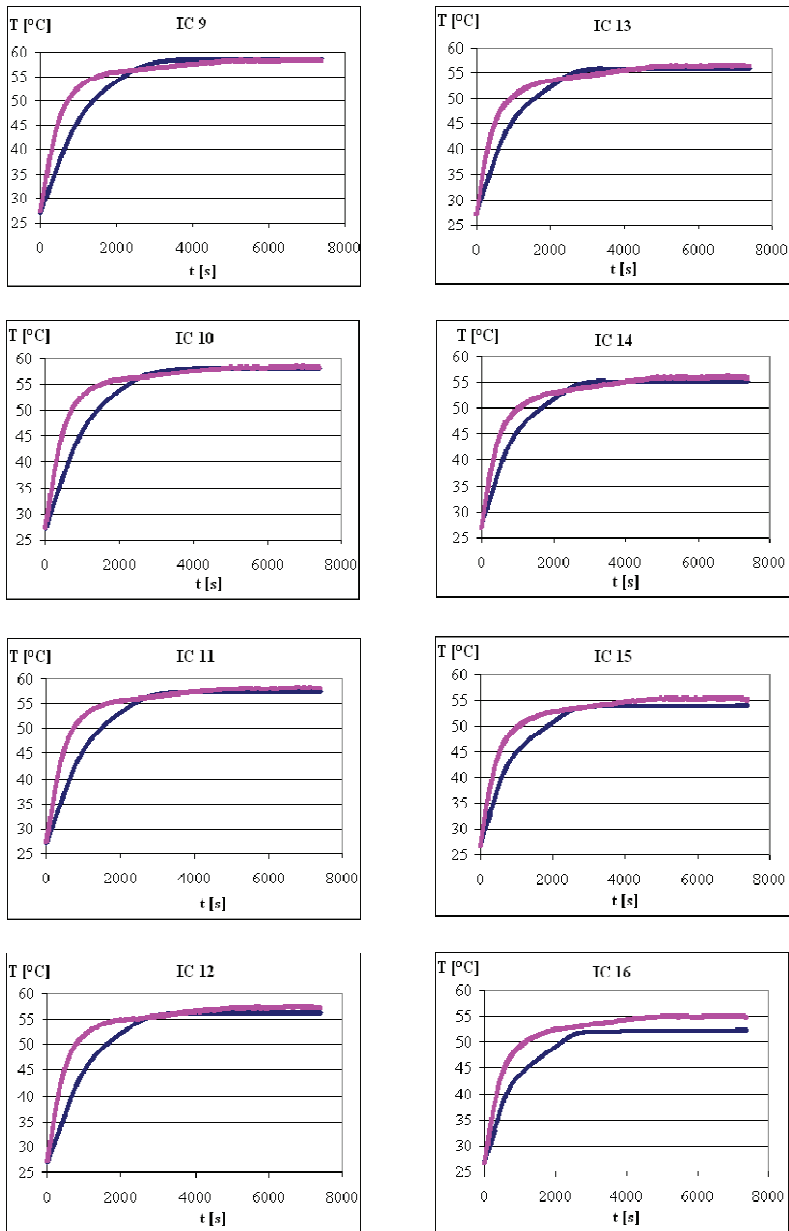


Figure 11. Time evolution of temperature values detected on experimental (pink line) and numerical (blue line) frontal surfaces of the chip (IC 9-16 according to numeration of Figure 9)

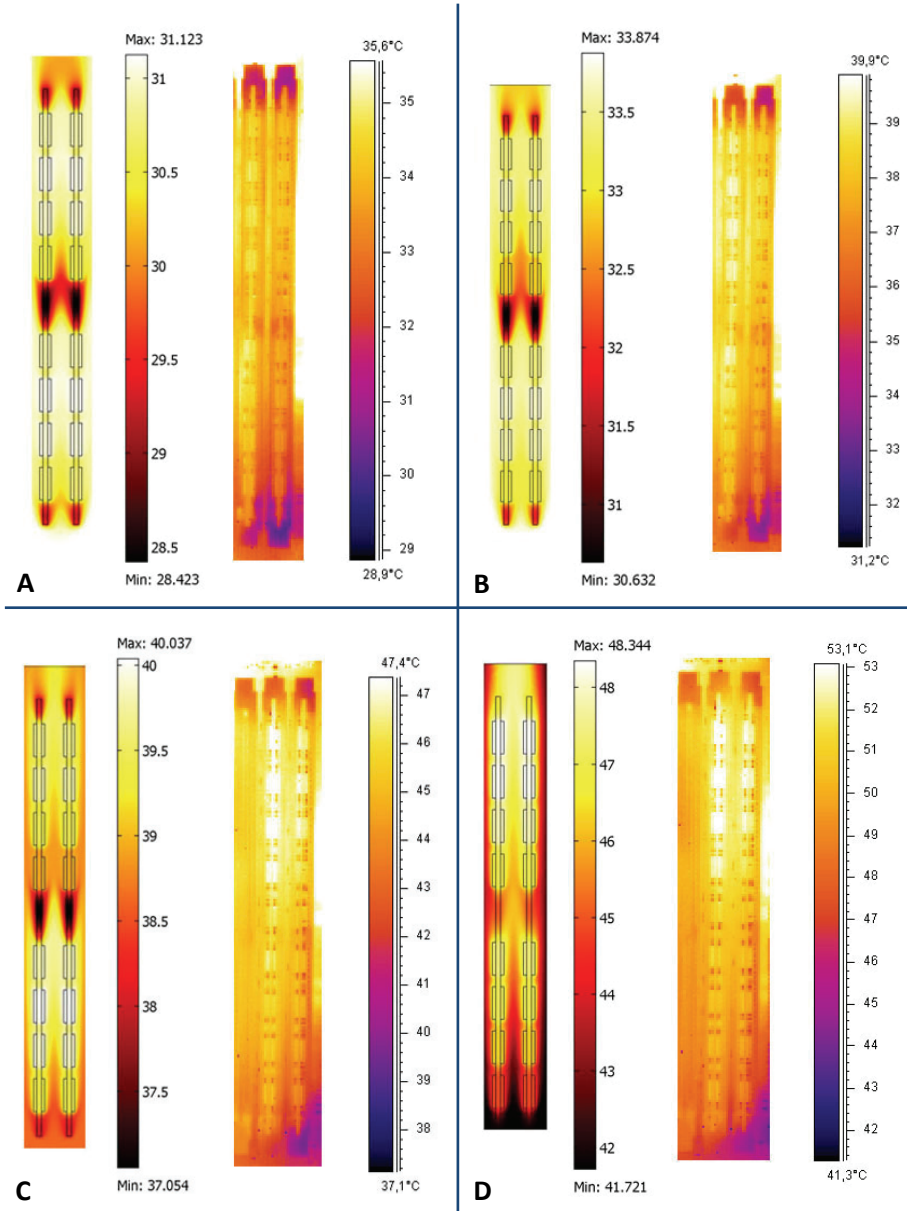


Figure 12. Comparison between numerical and experimental thermal distribution at time steps  $t=180$  (A),  $t=300$  (B),  $t=600$  (C),  $t=1200$  (D)

The experimental acquisitions were recorded each 5 seconds, both for vertical and horizontal arrangement of the case, during a transient time of 3-4 hours. Exceeded this time a stationary thermal behaviour was reached by the dissipating components. Once the test

section built-up under the laboratory facility, numerical models were implemented exactly corresponding to geometrical dimensions and applied thermal load of the test section. Then numerical simulations were carried-out both in transient and in steady conditions for comparing results with the experimental ones. In running transient simulations, the imposed temperature value at the bottom boundary of the air volume surrounding the memory modules ( $T_{AMB}$ ) was assigned as a time-dependent function, approximating, by two linear functions, the temporal evolution of temperature, experimentally detected by a thermometer arranged at the bottom of the slots of the test set-up (Figure 9), in the time-range 0-2400 [s]. Then it was considered constant. Numerical results were then compared with experimental data obtained by the infrared thermo-graphical investigation. In Figure 10 and Figure 11 time evolution of the mean temperature values detected on 16 experimental and numerical frontal surfaces of the chip arranged on one of the two memory modules are reported. From comparison a very good agreement in transient evolution is clearly observable. Special attention was paid to investigate on comparison between experimental and numerical thermal fields in the time range during which the wider difference was pointed-out. In Figure 12 we report thermal fields obtained by experimental (on the right side) and numerical (on the left side) analysis at time steps  $t=180$  (A),  $t=300$  (B),  $t=600$  (C),  $t=1200$  (D). It is to notice that pictures presented in Figure 12 underline the most unfavourable detected conditions in comparing results coming from experimental and numerical investigation. The experimental thermal values are generally higher than the numerical ones during the initial portion of the transitory. This item could be explained by considering that during PC starting-up several other electronic components, very close arranged to memory modules, dissipate an high rate of thermal energy. This heating contribution is not considered in the numerical model, so that it underestimates thermal level of the memory modules during the first range of the transitory. Otherwise, Figure 13 shows distribution of the mean temperature computed on each chip frontal surface once achieved a thermal steady state.

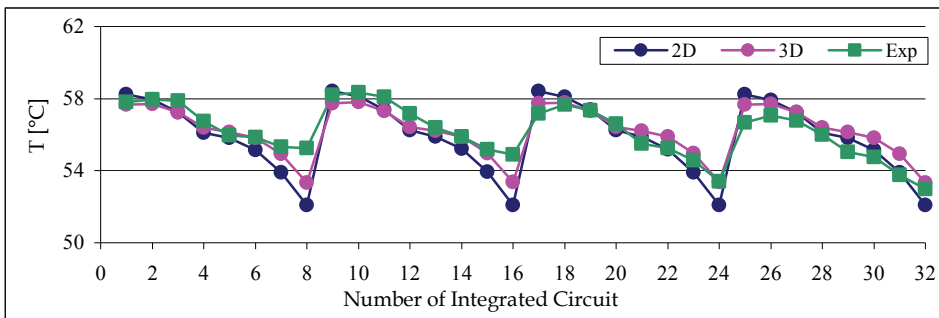


Figure 13. Comparison between steady mean temperature on each chip surface detected by experiments (green square) and computed by 2D (blue dots) and 3D (pink dots) models

Comparison between experimental and numerical results highlights a very good agreement. The best correspondence is obtained for the vertical disposition of the case and, as attended, for the three-dimensional model of the physical system (maximum relative gap with respect to experimental results less than 3.5%).

## 5. Horizontally arranged DIMM

In this section the main results obtained by the numerical modelling of the memory modules horizontally arranged are presented.

### 5.1 Transient fluid-dynamics during DIMM heating

Results obtained by approximating the physical system by its transversal section are presented in following. In Figure 14 (A-D) we report thermal and fluid-dynamical fields for 4 time steps of a transient analysis performed in a temporal range of 0.1 [s].

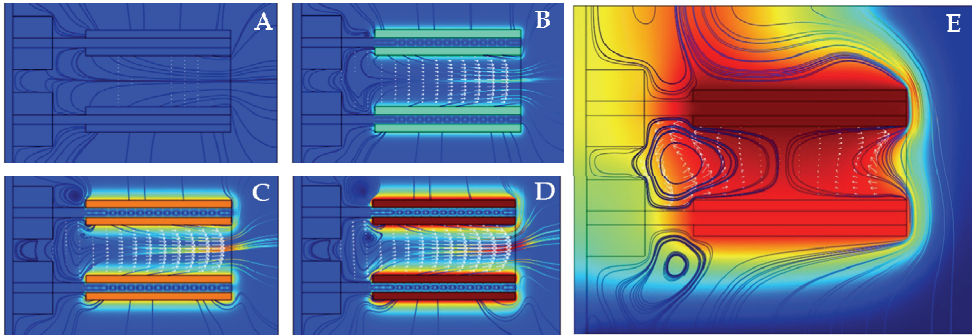


Figure 14. Transient temperature fields, streamlines of flow and velocity vectors for  $t \in \{0$  (A); 0.03 (B); 0.07 (C); 0.1 (D) [s] and for achieved stationary conditions

System is initialized with rest conditions for fluid,  $T_{AMB}=30$  [°C] ( $t=0$  [s]) and a power  $Q_D=1$  [W] globally supplied to the heat sources. The motion transient time for the system has been detected to be very short. Fluid, semi-confined by the overlapped solid layers, is quickly propelled by chips heating and forced to flow outside the semi-confined region ( $t=0.03$  [s]). Velocity field assumes a pseudo-parabolic profile, reaching its maximum in correspondence of the middle region between overlapped boards ( $t=0.07$  [s]). At the same time, a convective fluid structure begins to form close to the upper circuit board and backside socket. Then, this structure assumes a defined shape while a second dissipative re-circulating cell appears in the semi-confined region of fluid ( $t=0.1$  [s]). At steady conditions (Figure 14E) this “internal” re-circulating cell increases, extending over a half about of the semi-confined cavity. Its rotational motion induces arising of a further dissipative “half-roll”, standing close to the geometrical end of the solid boards and chips. Generation of counter-rotating convective cells is induced by the onset of thermo-convective instability, certainly amplified both by adherence conditions at boundaries and geometrical singularity in the cavity shape. Externally, the flow pattern is worthy influenced by flowing-up air, that sensibly modify the shape of the convective transient roll observed in the left top portion of the considered domain. On the other hand, in the left bottom volume of air, a dissipative flow structure is clearly observable. Temperature field is strongly dependent on fluid flow. The maximum detected value of velocity is about 0.095 [m/s]. Chips arranged on the top circuit board are obviously hotter than those placed on the bottom one. Maximum detected temperature is about 54 [°C] for the discussed simulation.

## 5.2 Transient and steady approach in solving governing equations

The most part of results presented in this study comes from solution of conservation equations in their steady formulation. The choice of solving system in steady condition arises from the idea of considering the technological devices in their thermal most unfavourable operative conditions, that consist in constant electrical load of alimentation equal to the maximum value indicated by technical documentation of their constructors. In order to validate the steady approach for solution, a comparison has been preliminary made between results obtained for 2D approximation both by transient and stationary analysis. Figure 15 shows thermal fields and streamlines of flow, on a transversal section of the memory modules, evaluated by transient (left side) and steady (right side) solution of equations (1), respectively.

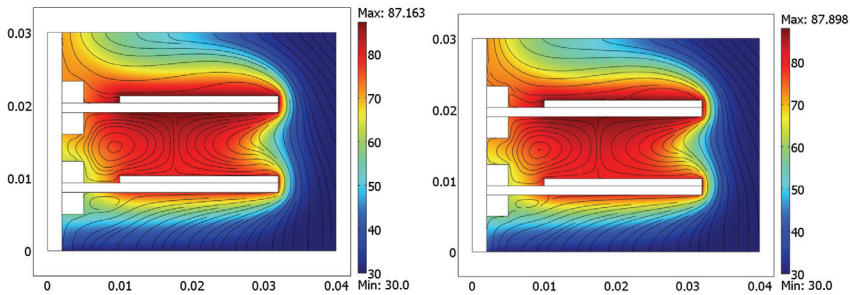


Figure 15. Comparison between transient (left) and steady (right) thermal-dynamical fields

Topology of flow is quite identical for both cases: a primary motion field made of fluid flowing from the bottom boundary of the domain to the upper section turning around the solid domains, and a secondary motion field characterized by the occurrence of a longitudinal convective roll developing in the semi-confined enclosure between the horizontal circuit boards. Drawn thermal levels also show good agreement each other, with a relative discrepancy for the maximum detected temperature of 0.84 %.

## 5.3 Influence of spacing between thermal sources

Three-dimensional simulations have been carried-out for different models approximating the considered DIMM. At first we studied portions of the electronic device, delimited by transversal surfaces considered as symmetry/slipping plans. Models containing 1 and 2 chips arranged on each top surface of the overlapped PCB were firstly studied. The aim of this investigation consists in studying the influence of spacing between thermal sources. From results it appears that small increasing in chip's spacing highly influences flow pattern of the convective roll detected in the semi-confined region between the overlapped boards. Figure 16 shows comparison between one portion of two overlapped memory modules solved imposing different lateral spacing between thermal sources. It is to notice as the thermo-convective roll does not stand confined in the backside of the semi-confined cavity when spacing is increased. Otherwise, it extends over lateral regions adjacent to the chip, improving convective transfer in dissipating thermal energy.



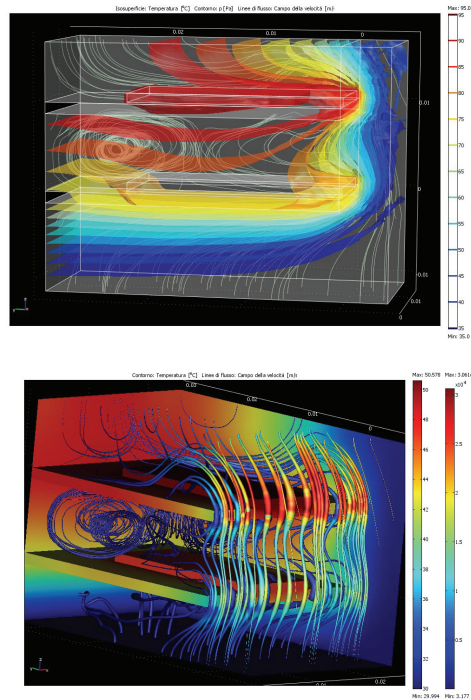


Figure 16. Streamlines of flow and thermal levels for one portion of overlapped memories arranging one chip on top surfaces: influence of chip spacing on convective heat transfer

#### 5.4 Analysis of thermal and fluid-dynamical behaviour during operative conditions

From 3D simulations the motion field of fluid for complete overlapped DIMM appears more complex. As reported in Figure 17, where normalized velocity vectors are plotted in longitudinal and transversal sections, the mean flow exhibits a pronounced chimney effect in correspondence of the central upper chips. The internal flow maintains the longitudinal convective roll flow pattern highlighted by 2D analysis, but developing of thermoconvective instability is seen more articulated. In fact the re-circulation structure is not limited to the backside of the semi-confined cavity, but it also extends around the lateral bounds of the air volume comprised by the overlapped circuit boards. Extension of convective eddy over the lateral portions of volume, close to the lateral guides on the left side, and in correspondence of the half-cross section on the right side, is illustrated in Figure 18. The convective structure assumes a helicoidally developing: fluid particles rotating around the longitudinal roll axis straightly shift along the axis direction. Transport direction mainly follows the way from the lateral guides to the transversal half-cross section of the geometry, where the convective eddy results more intensely developed. From a thermal point of view, the elucidated flow pattern involves the following comments: the maximum value of temperature is detected in correspondence of the third chip standing on

the upper circuit board, as illustrated in Figure 18 where thermal distribution on solid interfaces is plotted.

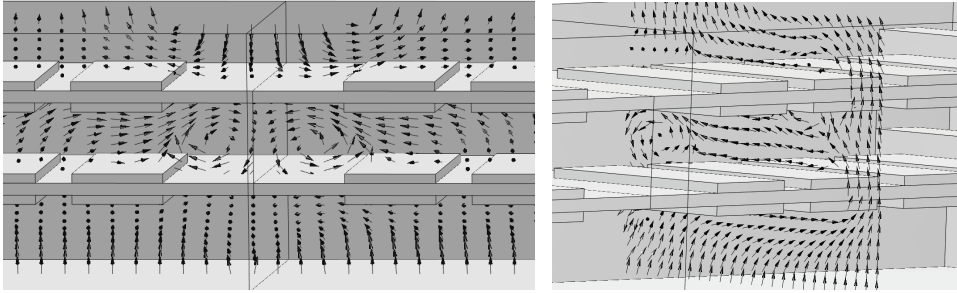


Figure 17. Velocity vectors in longitudinal and transversal sections

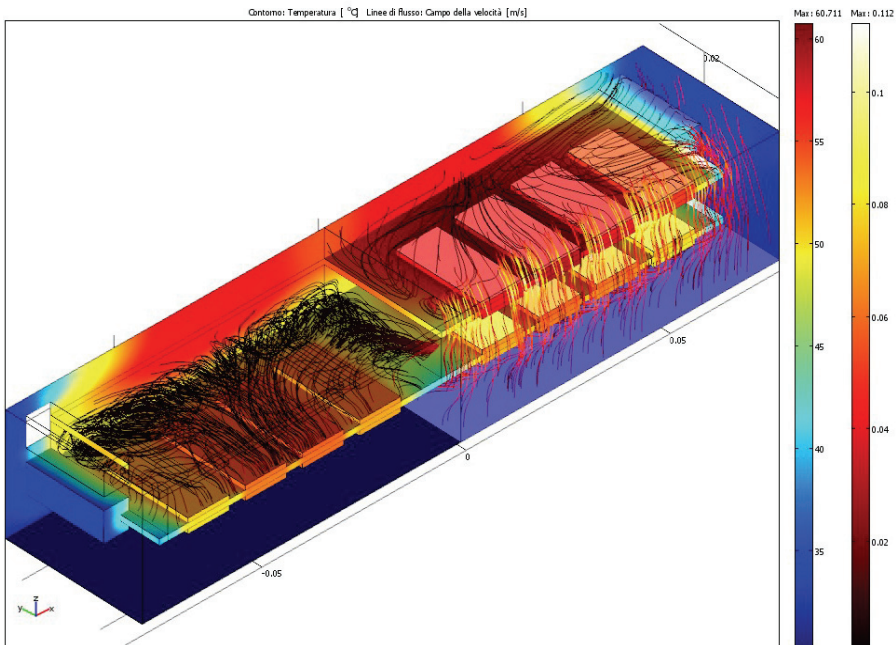


Figure 18. Temperature distribution and streamlines of flow for a double 16-chips model of DIMM obtained for  $T_{AMB}=30$  [°C] and  $Q_D=0.5$  [W] (one PCB is suppressed in plotting)

Convective thermal flux reaches its maximum value close to the right top portion of the fluid volume. As a matter of fact, thermal energy produced inside the semi-confined control volume is worthily dissipated by the discussed dynamical roll, that transports and “ejects” it upward, very close to the middle region of the fluid domain. The illustrated thermal fields well agree with the range of operative temperature indicated by leading DIMM constructors. In fact, in absence of forced airflow, and depending on the benchmark memory stress software applied, a temperature range of 75-95 °C is experimentally measured. Parametric simulations as function of  $Q_D$  and  $T_{AMB}$  have been carried out for the complete

double DIMM model. From the obtained results a sixth order polynomial fitting law is proposed in order to correlate the maximum detected temperature with the supplied power to the DIMM and the ambient temperature. The proposed correlation equation is reported below:

$$T_{\max} = -19,5 \cdot Q_D^6 + 99,3 \cdot Q_D^5 - 204 \cdot Q_D^4 + 216,9 \cdot Q_D^3 - 132 \cdot Q_D^2 + 93,78 \cdot Q_D + T_{\text{AMB}} \quad (5)$$

Simulated maximum temperature values ( $T_{\text{sim}}$ ) are compared with those obtained by applying the above fitting law ( $T_{\text{fit}}$ ) in Table 3.

Reported values for  $T_{\text{AMB}}$  {30; 35; 40} [°C] are listed as function of  $Q_D$  (0.1; 1.2 [0.1]) [W]. Relative gaps between simulated and analytically evaluated temperature are also reported in Table 3. As readable, the maximum gap for the studied  $Q_D$  range of variation is 0.61 %.

$Q_D$ [W]	$T_{\text{AMB}} = 40$ [°C]			$T_{\text{AMB}} = 35$ [°C]			$T_{\text{AMB}} = 30$ [°C]		
	$T_{\text{sim}}$ [°C]	$T_{\text{fit}}$ [°C]	gap %	$T_{\text{sim}}$ [°C]	$T_{\text{fit}}$ [°C]	gap %	$T_{\text{sim}}$ [°C]	$T_{\text{fit}}$ [°C]	gap %
0.1	48.45	48.25	0.40	43.43	43.25	0.40	38.41	38.25	0.41
0.2	54.94	54.91	0.06	49.89	49.91	0.03	44.84	44.91	0.15
0.3	60.77	60.67	0.16	55.69	55.67	0.03	50.60	50.67	0.15
0.4	66.19	65.96	0.35	61.07	60.96	0.18	55.94	55.96	0.04
0.5	71.33	71.01	0.45	66.17	66.01	0.24	61.00	61.01	0.01
0.6	76.24	75.89	0.46	71.04	70.89	0.21	65.84	65.89	0.09
0.7	80.98	80.65	0.41	75.75	75.65	0.13	70.50	70.65	0.21
0.8	85.58	85.27	0.36	80.31	80.27	0.05	75.02	75.27	0.33
0.9	90.05	89.74	0.35	84.74	84.74	0.01	79.42	79.74	0.40
1.0	94.42	94.05	0.39	89.07	89.05	0.02	83.71	84.05	0.40
1.1	98.70	98.22	0.48	93.31	93.22	0.09	87.91	88.22	0.35
1.2	102.89	102.26	0.61	97.46	97.26	0.21	92.04	92.26	0.24

Table 3. Simulated and analytical maximum temperature values on DIMM and their relative gaps as function of ambient temperature and thermal load

### 5.5 Simplifying hypotheses in model implementation

As known, 3D numerical models involve in very expensive computations, both for hardware and time needed for obtaining reliable results. Therefore, the goal of this study also was spending attention in analyzing hypotheses able to simplify the numerical model, maintaining the same standard of result reliability with respect to accuracy assured by more detailed schemes. Simplification of physical system allows to drastically reduce degrees of freedom of the numerical model, so that memory space and computational time can be saved. The first tested hypothesis concerning simplification of the numerical model consists in outlining complete DIMM by one transversal half portion only. In Figure 19 thermal distribution and streamlines of flow for a model are plotted. It represents a half of a twin DIMM of 8 top-arranged chips.

Lateral guides supporting PCB are observable in the left part of the simulated geometry, as well as the socket in its backside. The right transversal section surface represents the considered symmetry/slipping section of the system. Thermal and dynamical fields presented in Figure 19 are obtained for a supplied power  $Q_D=1$  [W] and for  $T_{\text{AMB}}=30$  [°C]. Results carried-out by exploiting symmetry conditions seem to be consistent: the range of

the simulated operative temperatures, and the maximum detected value ( $T \approx 86$  [°C]), well fit with those suggested by the leading constructors of this kind of devices. The second simplifying adopted strategy consists in retaining that the sub-domain simulating the sockets (in the backside of the system) could be suppressed without causing sensible variation in temperature distribution and velocity fields. Following this idea, a simplified model, see Figure 20, giving, for the same level of mesh refinement, a lower number of d.o.f. has been tested in order to replace the above discussed one. In Table 4 a brief comparison between socket and no-socket model is proposed by reporting maximum values of velocity, temperature, Reynolds number and Rayleigh number obtained for both representations. From a global point of view, thermal behaviour of system seems to be not very affected by model simplification, while dynamics appears more sensitive. Suppression in fluid domain of the small sized enclosure due by sockets representation does not modify internal thermo-convective flow pattern. In fact, the secondary flow, assuring heat evacuation in the semi-confined region of the system, does not show any relevant modification with respect to the complete model.

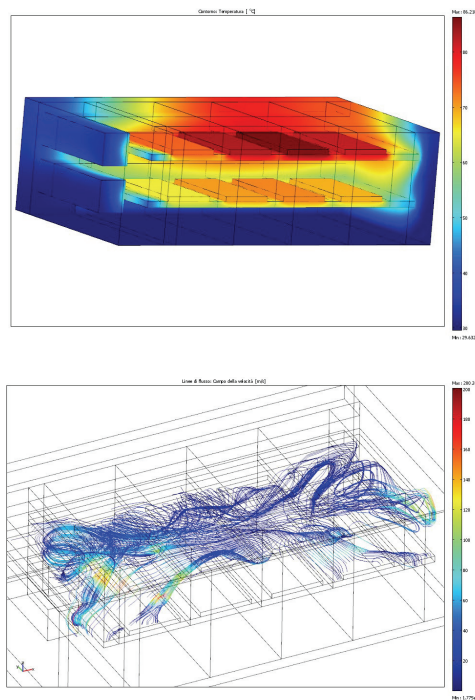


Figure 19. Thermal distribution and streamlines of flow for 8-chip overlapped memories represented by one symmetrical half of their geometry

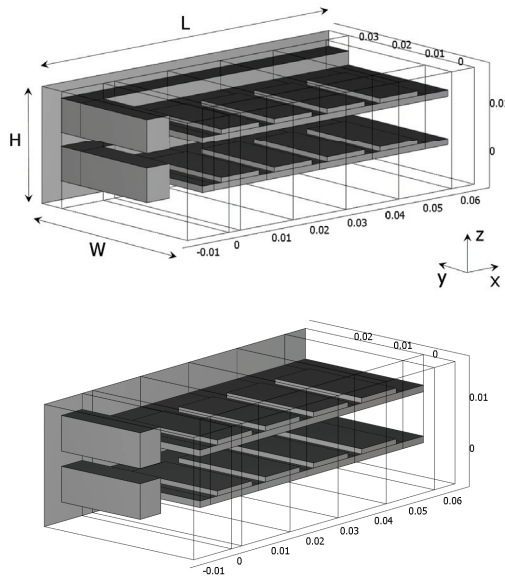


Figure 20. Geometrical model of twin overlapped 8-chip memories outlined with (left side) and without (right side) socket in their backside

	Socket	No-Socket	Relative gap (%)
$U_{max}$	0.142	0.154	8.31
$T_{max}$	87.7	87.9	0.18
$Re_{max}$	423	455	7.41
$Ra_{max}$	2205	2210	0.22

Table 4. Comparison between socket and no-socket models

### 6. Vertically arranged DIMM

Some results concerning memory modules vertically arranged have been yet discussed in the section related to the numerical models validation. From Figure 21 it can be deduced as fluid-dynamical fields for vertical disposition result less complex than those highlighted for the horizontal configuration. Fluid is propelled by buoyancy force to flow up without encountering obstacles in its path. Heat is vertically transported and for that reason the integrated circuits arranged in the top portion of the modules manifest higher thermal levels. From results analysis it globally appears that vertical disposition is preferable from a thermal point of view with respect to the horizontal one. For a fixed value of imposed thermal load, the vertical configuration assures lower thermal levels on the package. However, the interest in studying this configuration was motivated to investigate on convective heat transfer not only in natural convection condition, but also in mixed convection condition. Models considering imposed air flow rate coming from the bottom surface of the outlined air volume have been built and convective heat transfer coefficient

have been computed for several values of fixed velocity for air. The non-dimensional parameter chosen in order to quantify the convective heat transfer rate is the local Nusselt number evaluated on chip top surfaces, defined as:

$$Nu = \frac{1}{H_c \cdot L_c} \int_{z_1}^{z_2} \int_{y_1}^{y_2} \frac{\partial T}{\partial x} dy dz$$

$$(T_c - T_{AMB}) / L$$

The range of fixed values for velocity inlet flow (0.1÷0.2 [m/s]) has been limited to maximum velocity values characteristics of fluid-dynamical motion fields observed in natural convection condition. This procedure allows to reproduce physical systems where natural and forced convection effects in heat transfer could be considered comparable. In Table 5 natural and mixed convection configuration are compared from a thermal point of view. The relative gap, concerning the main temperature evaluated on each chip surface of one memory module (IC 1-16, see Fig. 9) and the computed local Nusselt number, between natural and mixed convection conditions are listed. Relative gaps are evaluated both for minimum ( $v=0.1$  [m/s]) and maximum ( $v=0.2$  [m/s]) velocity values chosen for the inlet forced flow. From analysis of results it appears that benefit of forced flow mainly concerns IC arranged at the bottom position and on external surfaces of the PCB. It is to notice as decreasing in thermal levels on IC surfaces is comprised in the thin range 1-6%, while increasing in heat transfer coefficient results very fluctuant and, depending on IC position, achieves values up to 300%. This item can be explained: the IC standing on the top positions are in natural convection subject to air flow at the higher velocity, while IC standing on the bottom position are plunged in fluid almost at rest conditions. In mixed convection configuration air flow is quantitatively distributed homogeneously, so that the best advantage in heat transfer coefficient is related to those IC arranged in the most unfavourable position when any forced flow is imposed.

## 7. Conclusion

This chapter highlights the opportunity to exploit a numerical approach in order to simulate thermal and fluid-dynamical behaviour of electronic devices. The goal mainly consists in disposing of a predictive and flexible tool for characterising those equipments during several functioning conditions avoiding expensive experimentations. On the other hand, the chapter also underlines the unquestionable importance of a validation step for the numerical model, strictly needed in order to assure effectiveness and reliability of the results carried-out. As applications of the proposed approach, Dual Inline Memory Module dissipation is studied both for horizontal and vertical arrangement and for natural and mixed convection heat transfer mechanism. Detected temperature values are globally in accordance with data reported in technical sheets of the leading constructors of the studied technological devices. Numerical results are mainly carried-out as function of operational parameters, such as ambient temperature and power supplied to the memory modules. Several models are presented, that also resume the adopted strategy in order to optimise them, testing simplifying hypotheses as: opportunity of considering geometrical symmetries, possibility of suppressing in models structural elements not significantly modifying thermal and fluid-dynamical behaviour of the system, reliability of 2D results

with respect to 3D ones. The onset of a thermo-convective instability is highlighted in horizontal configuration. It manifests in arising of complex three-dimensional flow patterns, principally consisting in a dissipative roll that helicoidally develops close to the lateral and backside boundaries of the considered fluid domain. That convective structure seems to significantly contribute in heat dissipation of system, transporting and ejecting thermal energy in correspondence of the frontal opened section of the semi-confined geometry. Concerning thermal efficiency, the vertical configuration is found to be preferable with respect to the horizontal one. Instead, from a theoretical point of view the horizontal disposition results much more interesting to be studied. Non-dimensional parameters, such as Rayleigh, Reynolds and local Nusselt number, are computed in order to quantify the flow regime and the heat transfer coefficients. In order to produce exploitable results of applied interest, a polynomial fitting law, correlating the maximum detectable temperature for the system with the ambient temperature and the supplied thermal load, is proposed.

IC	$\frac{T_{nat} - T_{v=0.1}}{T_{nat}} \%$	$\frac{T_{nat} - T_{v=0.2}}{T_{nat}} \%$	$\frac{Nu_{v=0.1} - Nu_{nat}}{Nu_{nat}} \%$	$\frac{Nu_{v=0.2} - Nu_{nat}}{Nu_{nat}} \%$
1	1.59	3.25	12.52	32.32
2	1.68	3.34	13.52	35.54
3	1.75	3.59	15.59	39.81
4	1.83	3.89	20.48	48.80
5	2.53	5.27	25.79	47.04
6	3.20	5.81	26.76	47.38
7	3.89	5.86	30.20	54.42
8	4.02	5.30	50.81	85.19
9	1.58	3.23	17.42	34.74
10	1.67	3.38	26.84	53.77
11	1.73	3.56	34.96	70.68
12	1.81	3.86	45.88	115.72
13	2.52	5.24	80.97	228.95
14	3.24	5.93	101.31	291.41
15	3.99	6.06	192.06	311.35
16	4.11	5.46	197.02	327.19

Table 5. Relative gaps in temperature and local Nusselt number between natural and mixed convection conditions

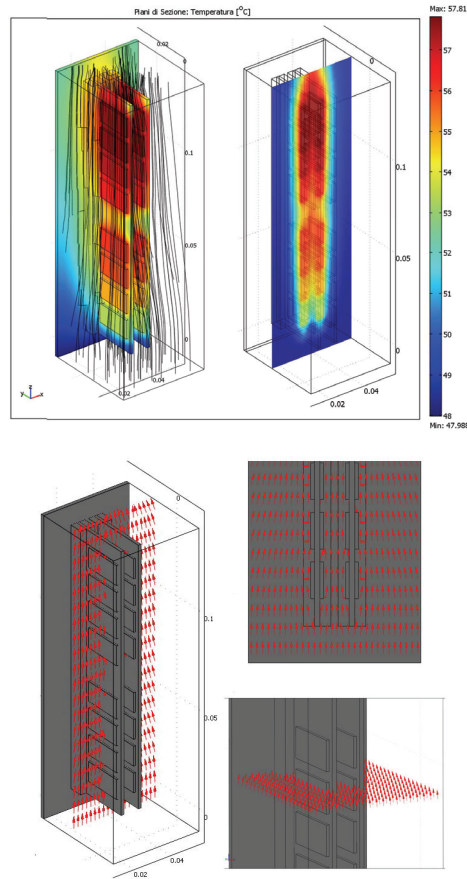


Figure 21. Thermal distribution at fluid-solid interfaces, streamlines of flow and temperature field on a longitudinal section (left side). Velocity vectors in longitudinal and transversal sections of the air volume surrounding the electronic devices (right side)

## 8. Nomenclature

$C_p$	isobaric specific heat	[J/(kg K)]
$D_h$	hydraulic diameter	[m]
$g$	gravity acceleration	[m/s <sup>2</sup> ]
$H$	height of air volume	[m]
$h$	distance between circuit boards	[m]
$k$	thermal conductivity	[W/(m K)]
$L$	length of air volume	[m]
$M$	molecular mass of air	[kg/mole]



$Nu$	Nusselt number, $Nu = \frac{1}{H_c \cdot L_c} \int_{z_1}^{z_2} \int_{y_1}^{y_2} \frac{\partial T}{\partial x} dy dz / (T_c - T_{AMB}) / L$	
$n$	number of integrated circuits	
$p$	pressure	[Pa]
$Q$	thermal flux	[W]
$q$	specific thermal flux	[W/m <sup>3</sup> ]
$R$	Gas constant	[J/(kg mole)]
$Ra$	Rayleigh number, $gh^3 \Delta \rho / \eta \alpha$	
$Re$	Reynolds number, $\rho U D_h / \eta$	
$T$	temperature	[K]
$t$	time	[s]
$\vec{U}$	velocity vector, $(u, v, w)^t$	
$U$	norm of velocity, $(u^2 + v^2 + w^2)^{1/2}$	[m/s]
$W$	width of air volume	[m]
Greek symbols		
$\alpha$	thermal diffusivity	[m <sup>2</sup> /s]
$\eta$	dynamic viscosity	[Pa s]
$\rho$	density	[kg/m <sup>3</sup> ]
$\Omega$	volume	[m <sup>3</sup> ]
Subscripts		
AMB	ambient	
C	Chip	
D	Dual Inline Memory Modules	
P	Printed Circuit Board	

## 9. References

- Bae, H.J.; Hyun & J.M. (2004). Time-dependent buoyant convection in an enclosure with discrete heat sources. *International Journal of Thermal Sciences*, Vol. 43, page numbers (3-11), ISSN 1290-0729
- Bailey, C.; Lu H. & Wheeler D. (2002). Computational modeling techniques for reliability of electronic components on printed circuit boards. *Applied Numerical Mathematics*, Vol. 40, page numbers (101-117), ISSN 0168-9274
- Bhowmik, H. & Tou, K.W. (2005). Experimental study of transient natural convection heat transfer from simulated electronic chips. *Experimental Thermal and Fluid Science*, Vol. 29, page numbers (485-492), ISSN 0894-1777
- Brenan, K.E.; Campbell, S.L. & Petzold, L.R. (1989). *Numerical Solution of Initial-Value Problems in Differential-Algebraic Equations*, Elsevier, ISBN 0898713536, New York
- da Silva, A.K.; Lorenzini, G. & Bejan A. (2005). Distribution of heat sources in vertical open channels with natural convection, *International Journal of Heat and Mass Transfer*, Vol. 48, page numbers (1462-1469), ISSN 0017-9310

- Deuffhard, P. (1974). A modified Newton method for the solution of ill-conditioned systems of nonlinear equations with application to multiple shooting, *Numerical Mathematics*, Vol. 22, page numbers (289-315), ISSN 0168-9274
- Dogan, G.; Sivrioglu, M. & Baskaya, S. (2006). Investigation of mixed convection heat transfer in a horizontal channel with discrete heat sources at the top and at the bottom, *International Journal of Heat and Mass Transfer*, Vol. 49, page numbers (2652-2662), ISSN 0017-9310
- El Alami, M.; Najam, M.; Semma, E.; Oubarra, A. & Penot, F. (2005). Electronic components cooling by natural convection in horizontal channel with slots, *Energy Conversion and Management*, Vol. 46, page numbers (2762-2772), ISSN 0196-8904
- Hanreich, G.; Nicolics, J. & Musiejovsky, L. (2000). High resolution thermal simulation of electronic components, *Microelectronics Reliability*, Vol. 40, pp. 2069-2076,
- Harvest, J.; Fleischer, A.S. & Weinstein R.D. (2007) Modeling of thermal effects of heat generating devices in close proximity on vertically oriented printed circuit boards for thermal management applications, *International Journal of Thermal Sciences*, Vol. 46, page numbers (253-261), ISSN 0226-2714
- Ortega, A. (1996) Conjugate heat transfer in forced air cooling, In: *Air cooling technology for electronic equipment*, Sung-Jin Kim & Sang-woo Lee, pp. 103-172, CRC Press, ISBN 0849394473
- Petrone, G.; Chénier, E. & Lauriat, G. (2004). Stability of free convection in air-filled horizontal annuli: influence of the radius ratio, *International Journal of Heat and Mass Transfer*, Vol. 47, page numbers (3889-3907), ISSN 0017-9310
- Petrone, G.; Sorge, G. & Cammarata G. (2007). Thermal dissipation of DIMM in Tower-BTX configuration, *International Journal of Multiphysics*, Vol. 1, page numbers (231-244), ISSN 1750-9548
- Towashiraporn, P.; Subbarayan, G.; McIlvanie, B.; Hunter, B.C.; Love, D. & Sullivan B. (2004). The effect of model building on the accuracy of fatigue life predictions in electronic packages, *Microelectronics Reliability*, Vol. 44, pp. 115-127

# Modelling of Long Period Gratings in Photonic Crystal Fibres and Sensors Based on Them

Jovana Petrovic  
*University of Oxford<sup>1</sup>*  
*United Kingdom*

## 1. Introduction

Optical fibres are a true representative of the remarkable advancements and speed of adoption and commercialisation of technology in recent decades. Propelled by the invention of the laser in 1960, these tiny waveguides quickly spread from the scientific laboratories into the everyday life: Internet, medical diagnostics, sensors in food, transport, oil and other industries, decoration. Application of fibres relies on possibility of controlling the propagation of light through them which has initiated invention of a range of accessories and fibre-based devices. This chapter is dedicated to a widely exploited group of fibre devices called long period gratings.

In general, grating is a periodic change in the refractive index profile along the fibre. Depending on their periods gratings are divided into: fibre Bragg gratings (FBGs) with periods comparable to the wavelength of the guided light and long period gratings (LPGs) with periods ranging from several tens to several hundreds of microns. The former reflect narrow bandwidths and are therefore used as band rejection filters in transmission or retro reflectors. LPGs were first designed (Vengsarkar et al., 1996) to mend the problem of back reflection in FBGs that appears to be detrimental in some applications, e.g. gain equalizers, (Vengsarkar et al., 1996). Due to the dependence of their spectral bands on external parameters both types of gratings are now widely used in sensing technology. In addition to inherited advantages of fibre sensors such as simplicity of interrogation schemes, compactness, multiplexing capability and non-obtrusive interaction with living tissues, gratings exhibit very high sensitivity and localisation of the parameter change, which makes them suitable for biomedical diagnostics, remote sensing in oil, food and pharmaceutical industry and radioactive environments, as well as build-in sensors in transportation.

Advanced laser processing techniques along with mechanical and chemical methods allow for fabrication of LPGs in practically any fibre regardless of its index profile and material composition, Fig. 1a)-c). Therefore, it is not surprising that the major novelty in fibre industry – the photonic crystal fibre (PCF) (Knight et al., 1996; Russell, 2003), was quickly embraced as a new medium for grating fabrication. Different guiding principle of PCFs

---

<sup>1</sup> Results reported in this chapter are part of the author's PhD thesis produced at the Photonics Research Group at Aston University, UK

introduced new features to LPGs, which opened up new possibilities for sensing applications. For example, the LPG reported in (Dobb *et al.*, 2004) can solve the problem of cross-sensitivity to temperature. Namely, in most grating sensors variations in temperature contribute to the signal in the same way as the changes in other parameters, hence various compensation schemes have to be employed which increases the complexity and cost of the sensor. LPGs fabricated by Dobb *et al.* in endlessly single mode (ESM) PCF by an electric arc are not sensitive to temperature, while they are sensitive to strain, bending and refractive index and therefore represent a simple solution to this problem. It should be noted that the more complex sensors have been reported in which the sensitivity of an LPG to a few parameters has been used for their simultaneous sensing. LPGs in PCFs have also found applications in microfluidics devices. For more information on LPG sensors see (James & Tatam, 2003).

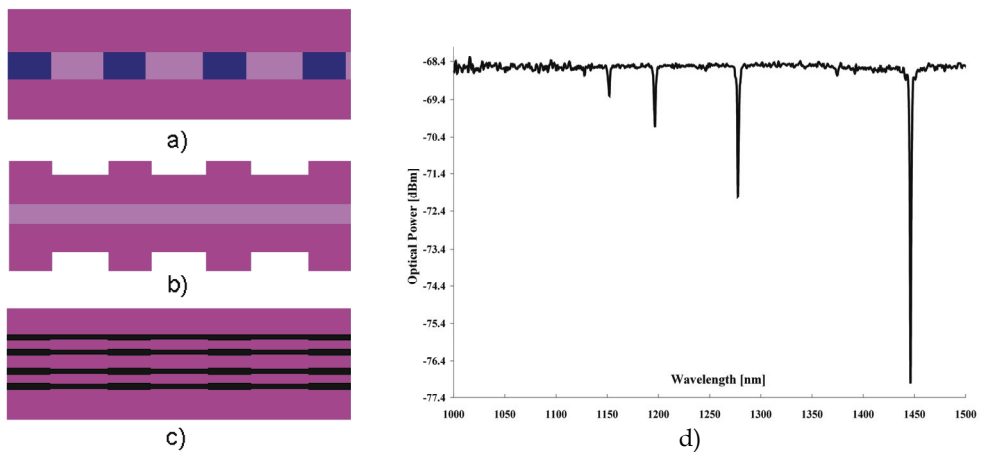


Figure 1. Schematic examples of long period gratings: a) in the core, b) corrugated cladding, c) in PCF. d) Example of grating transmission spectrum (produced by T. Allsop)

In order to fully understand and exploit the potential of LPGs in PCFs the theoretical study and practical models are needed. Naturally, the consideration is based on previous independent extensive studies of LPGs (Erdogan, 1997 a); Kashyap, 1999; Othonos & Kalli, 1999) and PCFs (Birks, 1997; Russel, 2003), to name just a few. The coupled-mode theory (CMT) of fibre gratings (Erdogan, 1997 a) has been the most widely applied model of LPGs, largely due to the relatively simple physical picture based on the phase matching condition. Due to the complex geometry of PCF, accurate simulations of the mode profiles of PCFs require numerical methods, while analytical methods imply calculation of the effective refractive index of the photonic crystal (Park *et al.*, 2006). Various numerical methods have been successfully applied: plain wave expansion method (Ferrando *et al.*, 1999), beam propagation method (Eggleton *et al.*, 2000), full-vectorial finite difference method (Zhu *et al.*, 2002), finite element method (Uranus & Hoekstra, 2004). In this chapter a method based on conjuncture of CMT and finite elements that allows for analysis of spectra and sensitivity of LPGs in PCFs of various geometries is presented.

Section 2 introduces the physical model of LPG and its numerical implementation, and is followed by a detailed example of the application of the model to the temperature

insensitive LPG in Section 3. The analysis of the grating spectrum and resonant modes is further used to calculate grating sensitivity to temperature and strain. The final subsection is dedicated to the application of the model to reverse engineering of the grating index profile. Applications and practical limitations of the model are discussed in Section 4. Finally, Section 5 summarises results and suggests directions for future work.

## 2. Numerical Model

### 2.1 The Physics of Long Period Gratings

Periodic perturbation of the index profile of the fibre that defines fibre grating acts as a resonant scatterer on the incoming core mode. In consequence, the core mode periodically couples to other co- and counter-propagating fibre modes. The former is characteristic of the long period grating and the latter of the fibre Bragg grating, the difference stemming from a large difference in periods of these gratings. The vector sum of the propagation vector of the core mode and the reciprocal grating vector defines the propagation vector of the resonant mode. If the grating period is long enough its vector is shorter than the propagation vector of the core mode, and the coupled modes are copropagating. The opposite is the case for the short period grating (FBG). Both cases are shown in Fig. 2. These are the most commonly used scenarios; for the full description see (Erdogan, 1997 a).

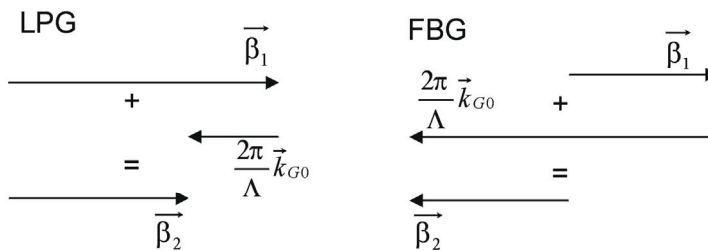


Figure 2. Phase matching in long period grating (left) and fibre Bragg grating (right)

Cladding modes excited by an LPG are irradiated at the interface between cladding and surrounding medium, which causes the losses observed as attenuation bands in the spectrum, Fig. 1d). Resonant wavelengths are determined by the grating period and the order of the cladding mode. Coupling strength of the grating depends on overlap of the electric fields of the core and resonant cladding modes across the grating and the grating refractive index. It determines the magnitude of attenuation bands, the so called 'grating strength'.

### 2.2 Mathematical Model of the Long Period Grating

Given that it consists of a small change in the index profile of the fibre, an LPGs can be successfully treated by the perturbation theory, the adaptation of which to resonant systems is known as the coupled mode theory (CMT). It assumes that each mode excited by the grating can be represented as a linear combination of the eigenmodes of the unperturbed

fibre. The wavelength at which the coupling to a specific cladding mode occurs is given by the phase matching condition

$$\lambda = (n_{co}^{eff} - n_{cl}^{eff})\Lambda_B = \delta n^{eff} \Lambda \quad (1)$$

where  $n_{co}^{eff}$  and  $n_{cl}^{eff}$  are the effective mode indices of the core and cladding modes respectively,  $\Lambda$  is the beat length and  $\lambda$  is the resonant wavelength. This condition allows for the representation of the excited mode by one eigenmode of the fibre, thereby reducing the problem to the system of two coupled mode equations

$$\frac{dA_{co}(z)}{dz} = i\kappa_{co-co}A_{co}(z) + i\frac{s}{2}\kappa_{co-cl}A_{cl}(z)e^{-i2\delta z} \quad (2)$$

$$\frac{dA_{cl}(z)}{dz} = i\kappa_{cl-co}A_{co}(z)e^{i2\delta z} + i\frac{s}{2}\kappa_{cl-cl}A_{cl}(z) \quad (3)$$

where  $A_{co}$  and  $A_{cl}$  are the slowly varying amplitudes of the core and cladding modes,  $\kappa_{co-co}$ ,  $\kappa_{cl-cl}$  and  $\kappa_{co-cl} = \kappa_{cl-co}^*$  are the coupling coefficients,  $s$  is the grating modulation depth and  $\delta = \pi\left(\frac{n_{co}^{eff} - n_{cl}^{eff}}{\lambda} - \frac{1}{\Lambda}\right)$  is the detuning from the resonant wavelength. The coupling is determined by the transverse fields of the resonant modes  $\mathbf{E}(\mathbf{r})$  and the average index of the grating  $\Delta n(\mathbf{r})$

$$\kappa_{ij} = \frac{\omega\epsilon_0 n}{4} \int \Delta n(\mathbf{r})\mathbf{E}_i(\mathbf{r})\mathbf{E}_j^*(\mathbf{r})d\mathbf{r} \quad (4)$$

Here, the electric fields of the modes are normalised so that each mode carries 1W of power. Whereas the mode field profiles of the circularly symmetric fibres are well known, the modal analysis of PCFs is more demanding and requires numerical methods. System (2-3) is then readily solved to obtain the field amplitudes of the coupled modes along the fibre for a given wavelength (Snyder & Love, 2000; Erdogan, 1997 a).

Grating resonances are best visualised by constructing the grating characteristics -- a family of curves  $\Lambda(\lambda)$  for different cladding modes over a range of wavelengths. Resonant wavelengths are then found in intersections of these curves and the line  $\Lambda=L$  representing the beat length equal to the grating period  $L$ . In general case, the grating is not perfectly sinusoidal, and the higher order terms in the Fourier transform of its refractive index must be taken into account. This results in the resonant condition  $\Lambda=L/N$  for the  $N$ th order grating (Kashyap, 1999).

For the gratings with weak index modulation and narrow attenuation bands two-mode description is usually sufficient. These conditions are fulfilled in the majority of practical applications.

### 2.3 Numerical Model of the Photonic Crystal Fibre

The starting point in the fibre grating analysis is the characterisation of the modes supported by the fibre. PCFs studied here have a hexagonal 'holy' photonic crystal as the inner cladding and a solid core produced by omitting the central hole. These fibres have been represented by the model based on the effective refractive indices of the core and the photonic crystal cladding (Russell, 2003). Due to the presence of air holes effective index of the cladding is lower than the index of the core, which keeps the light confined to the core. However, the analogy with the step-index fibres is not complete as there is no clear boundary between the core and the cladding. Due to the complex geometry of PCFs and the high refractive index contrast between the pure silica and air holes, modes of these fibres are most accurately calculated by solving Maxwell's equations by a full-vectorial numerical solver. A comparison of the different numerical methods used to study PCFs can be found in (Uranus & Hoekstra, 2004). A problem in hand imposes additional constraints on the choice of the method. In our case, the analysis of LPG in air and its sensitivity to the refractive index of the surrounding medium, precludes the use of methods that assume infinite photonic crystal, e.g. the super-lattice method. As opposed to the typical problems of nonlinear optics and transmission, which are mainly concerned with the propagation of the core mode, the intrinsic property of LPG to couple the core to the cladding modes requires accurate calculation of the propagation constants and field profiles of many modes in the whole fibre cross section. Here we choose the finite element method which meets both requirements and offers additional benefits of simulating fibres of different geometries and fibres with random variations in hole diameters. The calculations were performed by the commercial software Comsol 3.1 (COMSOL AB).

Eigenmodes and their effective indices were found by simulating the cross section of the fibre with the jacket removed and surrounded by air. The necessary resolution of the mesh in the photonic crystal was achieved by exploiting the fibre symmetry. Criteria for the choice of mesh parameters were convergence and accuracy of the effective refractive index.

### 2.4 Models of Grating Sensitivity

Long period grating response to the change in external parameter is observed as a shift in the resonant wavelength or/and as a change in magnitude or shape of the attenuation bands. In most cases, changes in temperature, strain and the refractive index lower than the index of fibre cladding cause wavelength shift, while bending and changes in refractive index to the values higher than the index of the fibre cladding cause changes in shape and magnitude of attenuation bands. In the former case, the grating sensitivity to parameter  $X$  can be calculated by linearisation of the grating characteristic of the resonant mode around the resonant wavelength and is given by expression

$$\frac{\partial \lambda}{\partial X} = \gamma \left( \frac{\partial \Lambda}{\partial X} \delta n^{eff} + \frac{\partial \delta n^{eff}}{\partial n} \frac{\partial n}{\partial X} \Lambda \right). \quad (5)$$

$$\gamma = \frac{1}{1 - \frac{d \delta n^{eff}}{d \lambda} \Lambda} = \frac{1}{\delta n^{eff}} \frac{d \lambda}{d \Lambda} \quad (6)$$

The generalised sensing parameter  $\gamma$  is defined in (MacDougall et al., 1998; Shu et al., 2002) and accounts for the effects of the material and waveguide dispersion of the fibre,  $\delta n^{eff} = \delta n^{eff}(\lambda(X), n(\lambda(X), X))$ . The rightmost term in (6) shows a direct relation between  $\gamma$  and the slope of the grating characteristic. As the derivatives in the above equations are obtained numerically, this method will be referred to as semi-analytical.

Change in an external parameter can have two major effects on an LPG: change in the grating period and in the refractive index of the fibre. If the index change is incorporated in the model of the PCF and the resonant wavelength found using the new grating period, the approximation made in the linear model is eliminated. Graphic representation of this solution distinguishes contributions of each effect as will be shown in the next Section. This method will be referred to as numerical.

The most important assumptions made in the model are that the index change in the grating is small and that the symmetry of the fibre is preserved. The profile of the grating and the fibre itself are not restricted in any other way. Moreover, constraints imposed by symmetry can be dropped at the expense of the mesh quality and the calculation time. Nonuniform grating can be treated by transfer matrix method that uses CMT to evaluate transmission matrix of each uniform part. Therefore, the suggested numerical model of the wavelength shift based sensitivity applies to a vast majority of LPGs in practical use today.

## 2.5 Reverse Engineering of the LPG from its Spectrum

In this section we consider an actual index profile of the grating in more detail. The general types of perturbation are: (i) change in the refractive index of the waveguide and (ii) changes in the geometry of the fibre such as the change in hole radii, tapering, corrugation, Fig. 1a)-c). Whereas gratings written in step-index fibres usually consist of the change in the refractive index of the photosensitive core, gratings written in PCFs are slightly more complicated. They comprise change in the refractive index across the fibre cross-section and the change in the geometry of the PCF, for example squeezing of holes induced by the strong electric-arc (Morishita & Miyake, 2004). As the waveguiding principle of PCF lifts the requirement for the photosensitive core, all parts of the fibre can be made of the same material (usually silica) which makes them equally sensitive to the writing technique. Moreover, light scattering on the holes impairs precise focusing into the core of the PCF. Structure of the gratings in PCFs has been a subject of several studies, e.g. (Humbert & Malki, 2002; Fotiadi et al., 2007). Here we describe method for nondestructive analysis of the grating profile based on spectral data taken during the grating fabrication. The idea behind the analysis is to establish a connection between the parameters of the induced index profile and the grating property which can be measured in a way that generates enough data to extract these parameters but that does not affect grating performance. The measurement of the dynamics of grating transmission spectrum during the fabrication is recognised as suitable since it is easily recorded and contains signatures of the values of coupling coefficients and detuning for a range of grating lengths.

According to the CMT, grating transmission is a function of the coupling coefficients defined by (4). In its simplest form, which assumes that the detuning from the resonant wavelength is balanced by the dc coupling, the expression for the grating transmission is given by

$$T(z) = \cos^2(\kappa z) \quad (7)$$



Cross coupling coefficient  $\kappa$  depends on the grating index profile and field profiles of the resonant modes. By averaging the index change in the photonic crystal, integral in (4) can be replaced by the sum of contributions of the core (co), photonic crystal (pc) and the outer cladding (cl) of the fibre

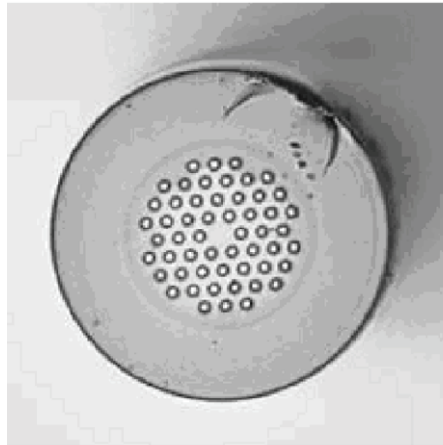
$$\kappa = \frac{\omega \mathcal{E}_0 n}{4} \sum_{j=co,pc,cl} I_j^{co-cl} \Delta n_j \quad (8)$$

where  $I_j^{co-cl}$  is the overlap integral of the normalised core and cladding modes and  $\Delta n_j$  is the overall refractive index change in the  $j$  part of the fibre. The domains of the fibre cross section are defined purely geometrically and not in the relation to the spatial extent of fibre modes. It is assumed that the grating profile consists of the change in hole radius  $\Delta R_h$  and the refractive index of silica  $\Delta n$ . As the change in the size of holes does not significantly affect core nor cladding,  $\Delta n_{co} = \Delta n_{cl} = \Delta n$ . On the other hand,  $\Delta n_{pc}$  is calculated by averaging the contributions of the air and silica to the dielectric constant of the photonic crystal. The best fit of the calculated minimal transmission to the maximum of the attenuation band for different grating lengths gives the parameters  $\Delta R_h$  and  $\Delta n$ . This model reflects the guiding principle of the studied PCF. Nevertheless, it should be noted that the average index of the photonic crystal that features in our model is not equivalent to the effective index of the crystal used in the model of ESM PCF in (Birks et al., 1997), as the latter is based on the propagation constant of the fundamental space-filling mode of the photonic crystal.

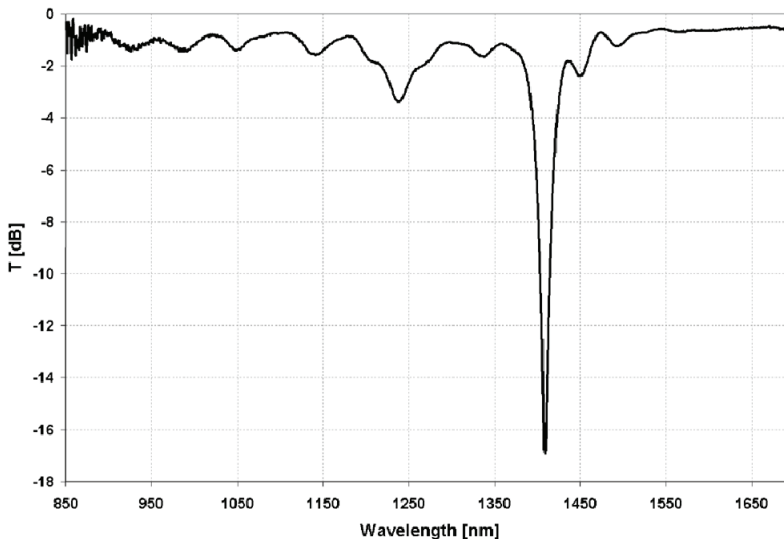
### 3. Example: LPG in PCF fabricated by Electric Arc

#### 3.1 Description of the device

Long period grating in endlessly single mode ESM 1550-01 PCF reported in (Dobb et al., 2004) is studied as an original example of the grating insensitive to temperature and simultaneously sensitive to other external parameters. The fibre was made from pure silica with four rings of hexagonally arranged air holes with the space between adjacent holes being  $8\mu\text{m}$ . The central hole was omitted to form the core, Fig. 3a). The filling factor was 0.46. A series of LPGs with different periods were inscribed by exposing the PCF to the electrical discharge provided by a commercial splicer (Fitel S175 v2000) (Dobb et al., 2006). A detailed inspection of the grating by the phase microscope did not reveal any change in the hole size. The LPG with period  $500\mu\text{m}$  and length  $25.5\text{mm}$  is studied in detail. Its transmission spectrum, shown in Fig. 3b), features two pronounced attenuation bands at  $1402\text{nm}$  and  $1239\text{nm}$ . Increase in the grating period causes a blue shift in the wavelength spectrum, in contrast to LPG behaviour in conventional single mode fibre, but similar to other LPGs in PCFs (Morishita & Miyake, 2004). Since neither the grating spectrum nor the bending sensitivity indicated any birefringence, the original hexagonal symmetry of the fibre was considered unaffected by the electric arc.



a)



b)

Figure 3. a) Cross section of ESM 1550-01 PCF. b) Transmission spectrum of an LPG fabricated in this fibre by electric arc (Dobb et al., 2004)

### 3.2 Grating Spectrum and Resonant Modes

Calculation of the modes of ESM-1550 PCF is facilitated by its hexagonal symmetry. It belongs to the so called  $C_{6v}$  symmetry group, which means that its modes can be divided into eight symmetry classes: non-degenerate classes 1, 2, 7, 8 with the irreducible zone angle of  $\pi/6$  and degenerate classes 3, 4, 5, 6 with the irreducible zone angle of  $\pi/2$ . Four classes in each group are the result of permutations of the two boundary conditions: perfect magnetic

conductor -  $\vec{n} \times \vec{H} = 0$  and perfect electric conductor -  $\vec{n} \times \vec{E} = 0$ , (McIsaac, 1975). The effective index of the core mode was calculated with the accuracy better than  $2 \cdot 10^{-7}$  and the effective indices of cladding modes with the accuracy better than  $10^{-6}$ . Examples of fibre modes and irreducible zones are shown in Fig. 4.

Modal map of the fibre is used to construct the grating characteristic shown in Fig. 5. It confirms the experimental observation that an increase in the grating period causes blue shift in the resonant wavelength. In the given wavelength range such behaviour is characteristic of PCFs and has been explained in (Morishita & Miyake, 2004). Resonant wavelengths of the first order grating are found at intersections of these curves with the line  $\Lambda=L$ , where  $L$  is the grating period. Fig. 4b) shows the intensity profile of the quasi LP mode that has been identified as resonant at 1402nm.

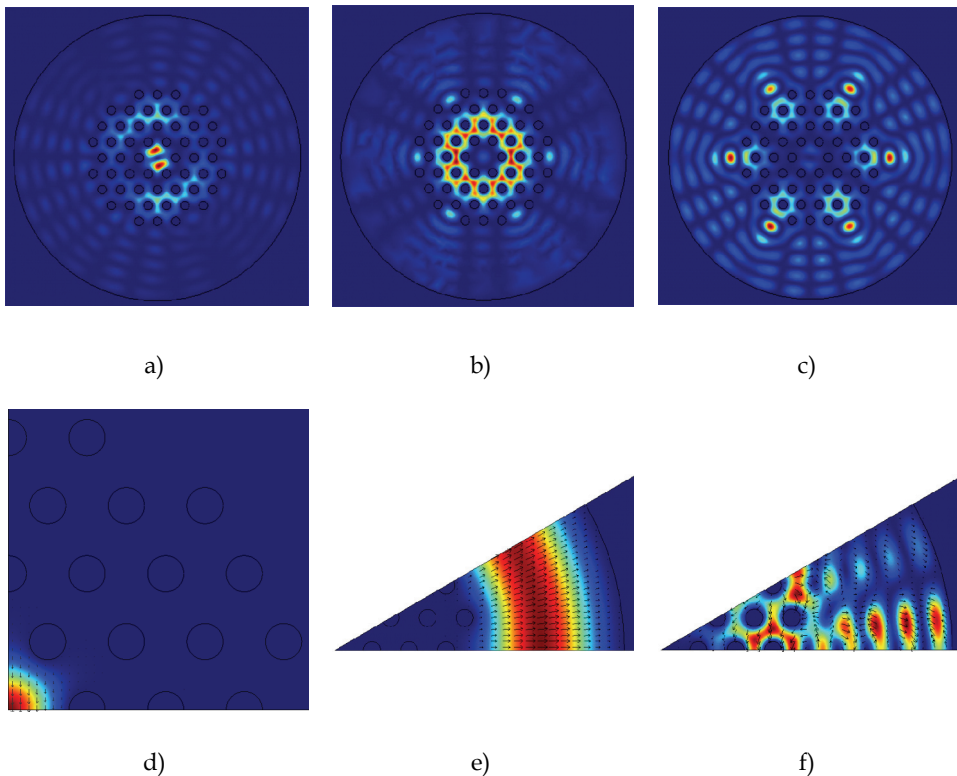


Figure 4. Modes of ESM PCF. a), b), c) - examples of modes guided by different parts of the fibre. d), e), f) illustrate irreducible zones of the fibre. Core mode in d) belongs to a degenerate class while modes in e) and f) belong to non-degenerate classes

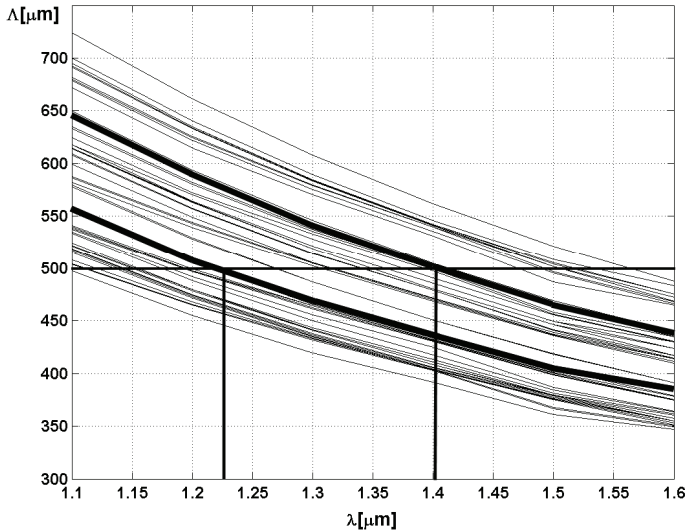


Figure 5. Characteristic of the LPG in ESM 1550-01 PCF. The resonances marked by the vertical lines correspond to the attenuation bands at 1239nm and 1402nm shown in Fig. 3b). Characteristic curves of the resonant modes are emphasized by thick lines

### 3.3 Grating Sensitivity

#### 3.3.1 Sensitivity to Strain

Expression for the sensitivity to strain was derived from (5) by substitution of  $X$  by the linear strain  $\varepsilon \equiv \delta\varepsilon = \Delta\Lambda/\Lambda = \Delta L/L$  and is given by

$$\frac{\partial\lambda}{\partial\varepsilon} = \gamma\lambda\left(1 + \frac{\partial\delta n^{eff}}{\partial n} \frac{\eta_\varepsilon}{\delta n^{eff}}\right) \quad (9)$$

The strain-optic coefficient  $\eta_\varepsilon$  accounts for the change in the refractive index of the fibre due to the applied strain. It was derived from the change in the optical indicatrix for the field polarized perpendicularly to the direction of the applied strain (Hocker, 1979),  $\eta_\varepsilon = -0.5n^3(p_{12} - \mu(p_{12} + p_{11}))$  where  $p_{11} = 0.121$  and  $p_{12} = 0.27$  are elements of the strain-optic tensor (Guenther, 1990) and  $\mu = 0.17$  is the Poisson's coefficient for pure fused silica. The calculated sensitivity to strain was  $-1.57\text{nm}/\text{m}\varepsilon$ .

The numerical solution was based on the change in the refractive index of silica caused by the maximal strain applied in the experiment  $\varepsilon_{\text{max}} = 2\text{m}\varepsilon$ . The beat length of the strained fibre was calculated in the range of 8nm around the resonant wavelength. The new resonant wavelength was found by interpolation of the  $\Lambda$  curves at the points determined by the new grating period  $\Lambda = L(1 + \varepsilon)$ . From Fig. 6 it can be seen that both the contribution from the elongation of the grating and from the strain-optic effect lead to a blue wavelength shift, the former having the major effect.

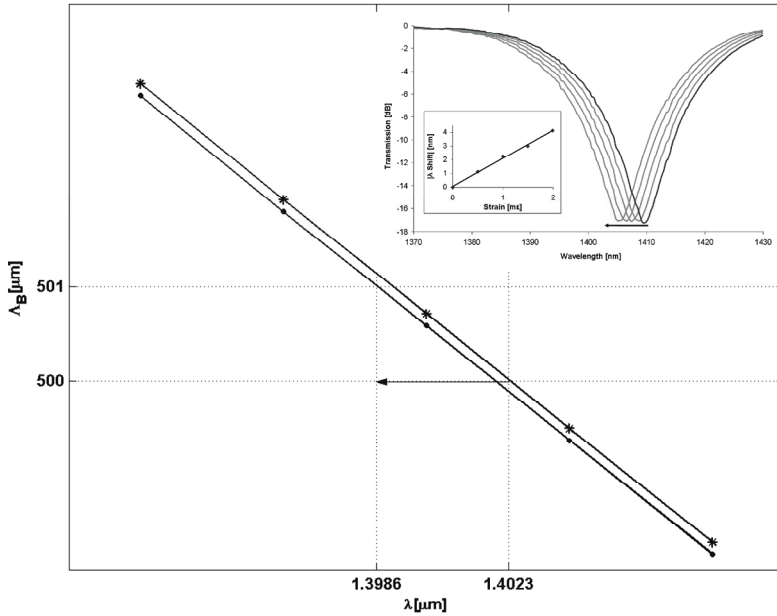


Figure 6. Numerical solution for the shift in the resonant wavelength of the LPG in ESM PCF due to the applied strain. \* - unstrained fibre, • - fibre under strain of 2 mε. Arrow – overall wavelength shift. Inset: Measured sensitivity to strain (Dobb et al., 2004)

The model was validated by comparison to the experimental results. The strain response of the LPG in ESM 1550-01 was linear with the sensitivity of  $-2.08 \pm 0.05$  nm/mε, as shown in Fig. 6. The numerical result for the sensitivity of  $-1.85$  nm/mε differs from the measured value by 11%, which is better than the error of the semi-analytical result of nearly 25%. Along with the experimental error of 2.4%, the discrepancy between the theoretical and experimental results can be attributed to several neglected effects: inhomogeneous distribution of strain in the PCF caused by the presence of air holes, change in the geometry of the fibre profile due to strain, dispersion of the strain-optic coefficients and the neglected average change in the refractive index of the grating, (Petrovic et al, 2007 a).

### 3.3.2 Sensitivity to Temperature

Similarly to strain, the expression for the LPG’s sensitivity to temperature is a specific case of the generic expression given by (5)

$$\frac{\partial \lambda}{\partial T} = \gamma \lambda \left( \alpha + \frac{\partial \delta n^{eff}}{\partial n} \frac{\eta_T}{\delta n^{eff}} \right) \tag{10}$$

in which  $\alpha = \partial \Lambda / \Lambda \partial T = 5 \cdot 10^{-7} \text{ } ^\circ\text{C}^{-1}$  is the thermal expansion coefficient of silica and  $\eta_T = \partial n / \partial T = 7.8 \cdot 10^{-6} \text{ } ^\circ\text{C}^{-1}$  is the thermo-optic coefficient of silica (Hocker, 1979). For the

range of temperatures applied in the experiment (20°C-90°C) the maximal change in the refractive index is  $5 \cdot 10^{-4}$ , hence under the assumption of linear grating response the derivatives already calculated in the previous section could be used. The semi-analytical model gave sensitivity to temperature of  $3.8 \text{ pm}/^\circ\text{C}$ .

The numerical solution was obtained reusing the curves from Fig. 6 and following the steps outlined in the previous section. The calculated change in the grating period of  $-19.23 \text{ nm}$ , Fig. 7, corresponds to the sensitivity of  $4.0 \text{ pm}/^\circ\text{C}$ .

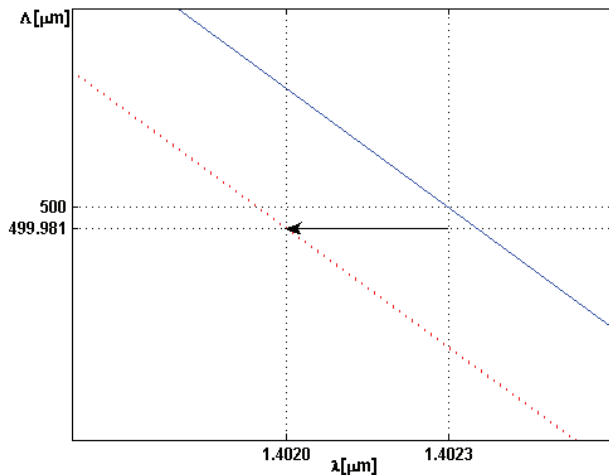


Figure 7. Numerical solution for the sensitivity of the LPG in ESM PCF to temperature. Solid line – grating at the room temperature, dotted line - grating temperature decreased by  $77^\circ\text{C}$ . Note the difference in the wavelength shift here and that in Fig. 6

Waveguide dispersion of the resonant mode is such that the thermo-optic effect and the thermal expansion of the fibre cause wavelength shifts of the opposite signs. Although the thermo-optic effect dominates the effect of linear expansion of the fibre, it is itself small because both core and cladding modes are guided mostly through the silica so that their effective indices undergo almost the same change and lead to the small value of the derivative  $\partial\delta n^{\text{eff}}/\partial n$ . This explains the very low sensitivity of the LPG to temperature reported in (Dobb et al., 2004).

The sign and the order of magnitude of the calculated wavelength shift agree with the experimental result, but the calculated sensitivity overestimates the experimental value  $2 \pm 1 \text{ pm}/^\circ\text{C}$ . This disagreement is partly due to the large error in the linear regression caused by scattering of the experimental data and partly due to the neglect of the average index change in the model of LPG and linearisation over the large temperature span.

### 3.4 Reverse Engineering of the Grating Index Profile

The model explained in Section 2.4 was used to find the impact of the electric arc on the ESM PCF. Experimental result of H. Dobb (inset in Fig. 8) shows no wavelength shift during the grating growth. According to the theory in (Erdogan, 1997 b) this justifies application of Eq. (7) to the grating used in this example. Fit of the numerical results to these

measurements gave an estimate of relative decrease in the hole radius of 0.07% and of change in the refractive index of silica of  $-3 \cdot 10^{-4}$ . The former was confirmed by observation by the phase microscope. The latter can be explained as follows. Decrease in the index of core equals decrease in the index of silica, while the index of cladding decreases less due to the contribution of the air holes to it. Consequently, index difference between the core and the photonic crystal decreases and the confinement of modes weakens causing the increase in overlap of the core and inner cladding modes. This enables coupling between the core and cladding modes necessary for the operation of LPG.

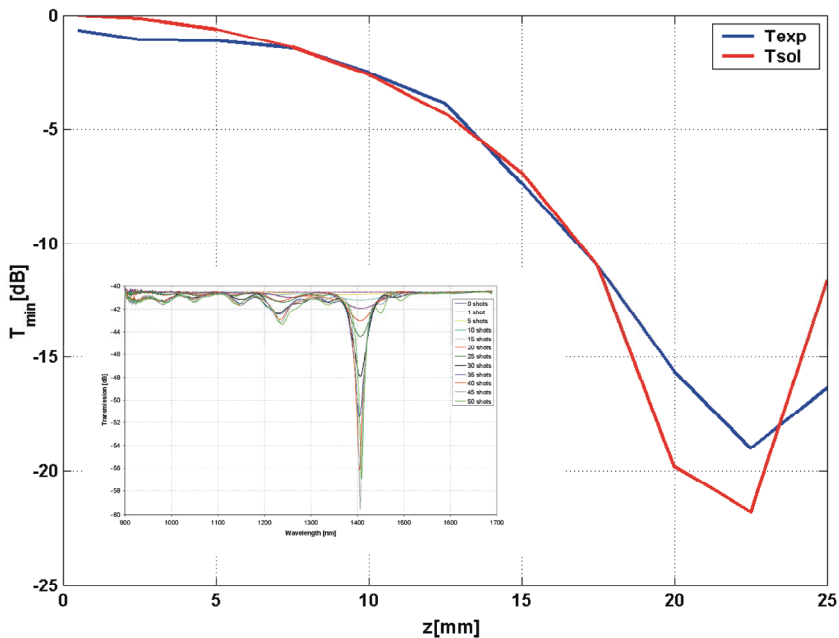


Figure 8. The best fit of the calculated minimal grating transmission (red line) to the experimental result (blue line) vs. grating length. Inset: growth of the LPG spectrum recorded during the grating fabrication by the electric arc

#### 4. Discussion

Without or with minor modifications the described model can be applied to practically any LPG in ESM PCF. Here we assess the generality of the basic model of the grating as well as its further applications in sensing and index profiling.

The calculation of fibre modes and their propagation constants represents the main challenge. Finite element method enables calculation of eigenmodes of fibres with different photonic crystals, fibres with random fluctuations in the hole size that may be introduced during the fabrication process and of asymmetric fibres. Furthermore, the grating characteristic, resonant wavelengths and sensitivity can be reasonably well estimated without knowing the exact grating index profile. The knowledge of the exact grating profile

could be inserted to the model to improve accuracy of these calculations. On the other hand, for the inverse engineering of the grating correct assumption on the induced index change is crucial. If the information on the grating profile is not available, estimate of the index change obtained by averaging explained in Sec. 2.5 can be used in the model of the PCF as a new input condition. As stated above, the geometry of the simulated fibre can be altered easily, hence calculation can be reiterated and the model of grating refined until the match with experiment becomes satisfactory. Incorporation of the problem related physical effects, which are usually neglected at the first instance, can also improve the accuracy of the model. A good example is the sensitivity to strain, the results for which can be refined by taking into consideration the inhomogeneous distribution of strain in the cross section of PCF caused by the presence of the air holes and the dispersion of the strain-optic coefficients.

Implementation of the proposed model is application driven, e.g. for the calculation of the sensitivity based on the wavelength shift the knowledge of the real part of the mode propagation constant is sufficient whereas the calculation of the light power irradiated from the fibre due to the LPG requires knowledge of the complex propagation constant.

Generality of the model is not always desirable as it can lead to ambiguity. Without experimental input, it can be wrongly concluded that all the gratings inscribed in the same fibre with the same period have the same resonant wavelengths. LPGs in PCFs are particularly sensitive to such claims, mainly due to the possible change in the fibre geometry as well as the refractive index which both shift the propagation constants of the fibre. Direct writing, e.g. by femtosecond laser, can easily induce asymmetry in the fibre. If this is ignored, the results will fail to give any information on grating birefringence. Therefore, results obtained from the model should be considered only in conjunction with the information on grating fabrication, measured spectrum and index profile.

## 5. Conclusion

A general numerical model of long period gratings fabricated in photonic crystal fibres has been presented. It has been illustrated by the example of the grating fabricated by an electric arc in ESM PCF. The generality of the model stems from its capability to simulate LPGs in PCFs of different geometries and composition. Model has been applied to calculate sensitivity of the grating to an external parameter and the examples of temperature and strain sensitivity have been given. To facilitate studies of the structure of these LPGs, the tool has been added to the model, which enables reverse calculation of the parameters of an assumed grating index profile from the recorded growth of grating transmission spectrum during the fabrication. Due to the flexibility of the finite element method the actual index profile of the grating can be easily incorporated into the model. This is particularly important in the calculations of grating strength which requires the calculation of the coupling coefficients, hence the resonant mode profiles.

While the model enables straightforward analysis of a variety of gratings and their sensitivity, its implementation depends on the index profiles of the grating and fibre in hand and its refinement depends on the goal of the study. A general refinement strategy would be to replace the model of unperturbed fibre by the average of perturbed and unperturbed index profiles of the fibre along the grating. However, in practice, measuring the index profile usually implies destroying the device. The procedure for nondestructive index profiling suggested here can be used instead. As its accuracy depends on the model of the index change induced during the grating fabrication, which is based on experimental



observation and measurement, the optimal method should close the loop between the experiment and theory, the loop within which they help and benefit most from each other.

## 6. Acknowledgement

Author would like to thank Vladimir Mezentsev for advice on numerical modelling, Helen Dobb, David Webb and Kyriacos Kalli for discussions and sharing their experimental data, and Thomas Allsop for useful comments and the grating spectrum in Fig. 1d).

## 7. References

- Birks, T.A.; Knight, J.C. & St. J. Russell, P. (1997) Endlessly single-mode photonic crystal fiber, *Optics Letters*, Vol. , No 13. 961-963
- Dobb, H.; Kalli, K. & Webb, D. J. (2004). Temperature-insensitive long period grating sensors in photonic crystal fibre. *Electronic Letters*, Vol. 40, 657-658
- Dobb, H.; Kalli, K. & Webb, D. J. (2006). Measured sensitivity of arc-induced long-period grating sensors in photonic crystal fibre, *Optics Communications*, Vol. 260, No. 1, 184-191
- Eggleton, B. J.; Westbrook, P. S.; White, C. A.; Kerbage, C.; Windeler, R. S. & Burdge, G. L. (2000). Cladding-Mode-Resonances in Air-Silica Microstructure Optical Fibres. *Journal of Lightwave Technology*, Vol. 18, No. 8, 1084 -1099
- Erdogan, T. (1997). Cladding-mode resonance in short- and long-period fiber grating filters. *Journal of Optical Society of America A*. Vol. 14, No. 8, 1760-1773 a)
- Erdogan, T. (1997). Fiber grating spectra. *Journal of Lightwave Technology*, Vol. 15, No. 8, 1277 - 1294 b)
- Ferrando, A.; Silvestre, E.; Miret, J. J.; Andres, P. & Andres, M. V. (1999) Full-vector analysis of a realistic photonic crystal fiber, *Optics Letters*, Vol. 24, No. 5 , 276-278
- Fotiadi, A. A.; Brambilla; G., Ernst; T., Slattery S. A. & Nikogosyan, D. (2007) TPA-induced long-period gratings in a photonic crystal fibre: inscription and temperature sensing properties, *Journal of Optical Society of America B*, Vol. 24, No. 7, 1475-1480
- Guenther, R. (1990). *Modern Optics*, John Wiley and Sons, Inc.
- Hocker, G. B. (1979). Fiber-optic sensing of pressure and temperature. *Applied Optics*, Vol. 18, No. 9, 1445-1448
- Humbert, G. & Malki, A. (2002) Characterizations at very high temperature of electric arc-induced long-period fiber gratings, *Optics Communications*, Vol. 208, No. 4-6, 329 - 335
- James, S. W. & Tatam, R. P. (2003) Optical fibre long-period grating sensors: characteristics and application. *Measurement Science and Technology*, Vol. 14, No. 5, 49-61
- Kashyap, R. (1999). *Fiber Bragg Gratings*, Academic Press
- Knight, J.C.; Birks, T.A; Russell, P.St.J; & Atkin, D.M. (1996) All-silica single-mode optical fiber with photonic crystal cladding, *Optics Letters*, Vol. 21, No. 19, 1547-1549
- MacDougall, T. W.; Pilevar, S.; Haggans, C. W. & Jackson, M. A. (1998). Generalized expression for the growth of long period gratings. *IEEE Photonics Technology Letters*, Vol. 10, No. 10, 1449-1451
- McIsaac, P. R. (1975). Symmetry-induced modal characteristics of uniform waveguides. I Summary of results. *IEEE Transactions on Microwave Theory Technology*, MTT-23, 421-429

- Morishita, K. & Miyake, Y. (2004) Fabrication and resonance wavelengths of long-period gratings written in a pure-silica photonic crystal fiber by the glass structure change, *Journal of Lightwave Technology*, Vol. 22, No. 1, 625-630
- Vengsarkar, A. M.; Pedrazzani, J. R.; Judkins, J. B.; Lemaire, P. J.; Bergano, N. S. & Davidson, C.R. (1996) Long-period fibre-grating-based gain equalizers. *Optics Letters*, Vol. 21, No. 5, 336-338
- Othonos, A. & Kalli, K. (1999). *Fiber Bragg Gratings*, Artech House Inc.
- Park, K. N.; Erdogan T. & Lee, K. S. (2006) Cladding mode coupling in long-period gratings formed in photonic crystal fibres. *Optics Communications*, Vol 256, No. 2, 541-545
- Petrovic, J. S.; Mezentsev, V.; Dobb, H.; Kalli, K.; Webb, D. J. & Bennion, I. (2007) Sensitivity of LPGs in PCFs Fabricated by an Electric Arc to Temperature, Strain, and External Refractive Index. *Journal of Lightwave Technology*, Vol. 25, No. 5, 1306-1312 a)
- Petrovic, J. S.; Webb, D. J.; Dobb, H.; Mezentsev, V.; Kalli, K. & Bennion, I. (2006). Nondestructive Index Profiling of Long Period Gratings in Photonic Crystal Fibres. *Optical and Quantum Electronics*, Vol. 38, No. 9-11, 913-920 b)
- Russell, P. (2003). Photonic Crystal Fibres. *Science*, Vol. 299, 358-362
- Shu, X.; Zhang, L. & Bennion, I. (2002). Sensitivity characteristics of long-period fiber gratings. *Journal of Lightwave Technology* Vol. 20, No. 2, 255-266
- Snyder, A.W. & Love, J.D. (2000). *Optical Waveguide Theory*, Kluwer Academic Publishers
- Uranus, H. P. & Hoekstra, H. J. W. M. (2004). Modelling of microstructured waveguides using a finite-element-based vectorial mode solver with transparent boundary conditions, *Optics Express*, Vol. 12, No. 12, 2795-2809
- Vengsarkar, A. M.; Lemaire, P. J.; Judkins, J. B.; Bhatia, V.; Erdogan T. & Sipe, J. E. (1996). Long-period gratings as band-rejection filters. *Journal of Lightwave Technoogy*, Vol. 14, No. 1, 58-65
- Zhu Z. & Brown, T. G. (2002). Full-vectorial finite-difference analysis of microstructured optical fibres. *Optics Express*, Vol. 10, No. 17, 853-864

# A New Methodology for RF MEMS Simulation

Peyrou David, Coccetti Fabio, Achkar Hikmat, Pennec Fabienne,  
Pons Patrick and Plana Robert  
*LAAS-CNRS, Toulouse University  
France*

## 1. Introduction

RF MEMS have demonstrated, during the last ten years, very attractive potential to allow the introduction of “intelligence” in the RF front end architecture (Rebeiz & Muldavin, 2001) through analog signal processing techniques. Nevertheless, those devices with moveable structures still have some issues to be successfully introduced at the industrial level.

The first issue deals with the actuation medium and the corresponding reliability. Today, it is well known that membranes and cantilevers can be actuated through electrostatic, thermal, magnetic and piezoelectric forces. Each of these types of actuators features benefits and drawback and it seems that today electrostatic actuators could offer the best trade-off when issues concerning the very high actuation voltage and reliability issues are solved (Mellé et al., 2005) (Yuan et al., 2006) (Reid & Webster, 2002) (Sprengen et al., 2004). As they are made of moveable and fragile structures (beams, cantilevers...), RF MEMS switches must be encapsulated in order to protect them from hostile environments, to increase their reliability and lifetime.

The second issue comes from the lack of efficient and easy-to-use simulation tools covering the complete MEMS design procedure, from individual MEMS component design to complete system simulation. Finite element analysis (FEA) methods offer high efficiency and are widely used to model and simulate the behaviour of MEMS components.

However, as MEMS are subject to multiple coupled physical phenomena (Figure 1) at process level and play, such as initial stress, mechanical contact, temperature, thermoelastic, electromagnetic effects, thus finite element models may involve large numbers of degrees of freedom so that full simulation can be prohibitively time consuming. As a consequence, designers must simplify models or specify interesting results in order to obtain accurate but fast solution.

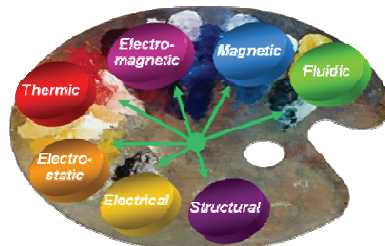


Figure 1. MEMS are multiphysics

In this problematic, we are working on a systematic and robust conception flow. Figure 2 describes the whole conception flow, starting from the conceptual specifications thru mask design and finishing with the complete simulation at system level.

The main challenge concerns the bottom-up conception flow (Figure 2) which needs a special effort in the modeling of the full process of MEMS technology. In fact we need to create a virtual prototype of the device able to take into account the inherent interrelated physical phenomena at process level and play, such as initial stress, mechanical contact, temperature, thermoelastic, electromagnetic effects.

The best way to solve each coupled physics simultaneously (not sequentially) relies on using only one tool. For example, two softwares provided by ANSYS and COMSOL offer multiphysics environment. Even these multiphysics software are great, we cannot hope a well proven and dedicated tool to solve each specifics physics with respect to a reasonable time consuming. So this chapter outlines an original approach based on reverse engineering method used to both interface different Computer-Aided Design (CAD) softwares each other and also advanced characterization software.

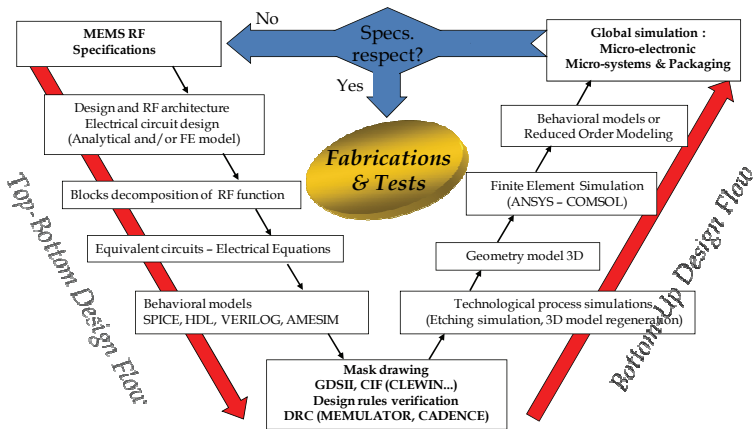


Figure 2. Systematic and robust conception flow

## 2. Reverse Engineering method

The basic idea is really simple, reverse engineering is a method to create a 3D virtual model of an existing physical part for use in 3D CAD software. The reverse engineering process involves measuring an object and then reconstructing it as a 3D model. The physical object can be measured using 3D scanning technologies like optical profilometer or Atomic Force Microscopy (AFM) for example. The measured data alone, usually represented as a point cloud, lacks topological information and is therefore processed and modeled into a more usable format such as a stereolithography format which is an ASCII file used in standard CAD softwares.

Thus, our concept relies on this method to first build the model using the real shape of the device (process level) and then to interface different software each other. The last point needs to create a new 3D virtual model from the deformed shape obtained with the simulations made by the software called 1 as the input of software called 2, so a sequential coupling can be done using different software.

### 3. Applications

#### 3.1 Capacitance simulation

This application shows our reverse engineering method to discover the origin of the mismatch between the theoretical down state capacitance and measurements of an RF-MEMS Capacitive Switch. This numeric approach allows us to understand the roughness effect of the dielectric on the down-state capacitance. The agreement between the modelling and the analytical model is very good and validates this novel numeric step.

For capacitive switches, both dielectric charging and surface roughness (Palasantzas & DeHosson, 2006) will impact the isolation. So, to enhance the down-state capacitance, we focus our work on a methodology to simulate the real capacitance using the measured data of the dielectric surface. The goal of this application is to show how to set up and generate a CAD model obtained by measured data.

##### 3.1.1 Roughness characterization

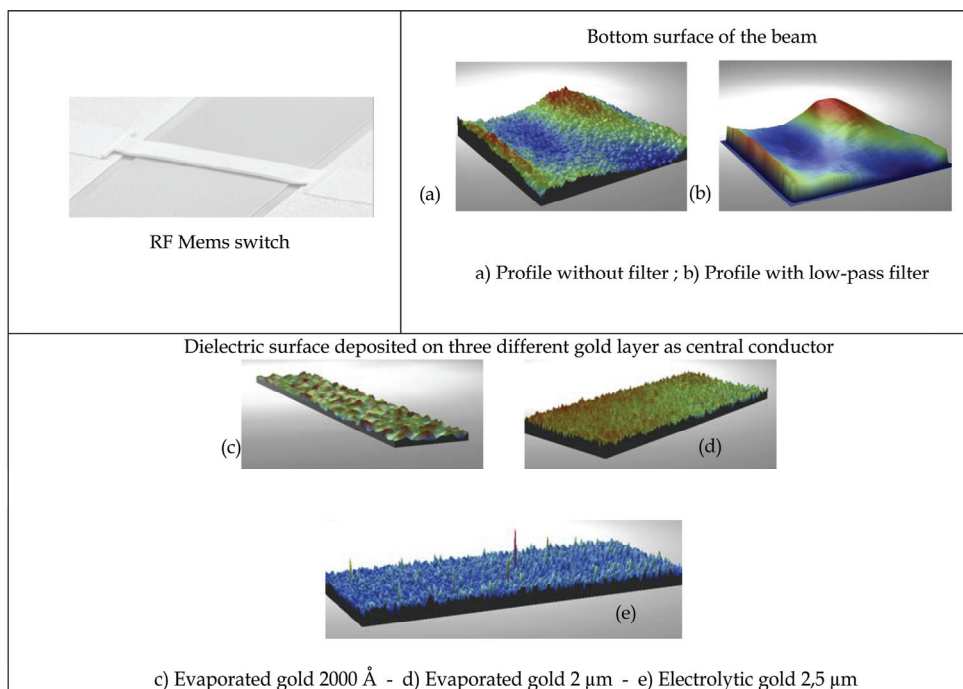


Figure 3. Roughness characterization for RF MEMS switch

Topographical characterization of both the textured dielectric on the central conductor above the beam and the gold surface on the bottom was performed using optical profilometry (Figure 3). This technique, using Wyko NT1000 from Veeco instrumentation, allows to map the surface in 3-D without affecting the surface properties or deforming the substrate. Profilometry data and 3-D rendering of the surface was accomplished using WYKO Vision32 version 2.303 software package.

Many parameters are used to describe surface roughness but we can distinguished two main parameters (see Figure 4):

- $R_a$ , Roughness Average (Absolute value of the surface height averaged over the surface ie high frequency aspect)
- $\lambda_a$ , Average Wavelength (mean spacing between peaks, with a peak defined relative to the mean line ie low frequency aspect)

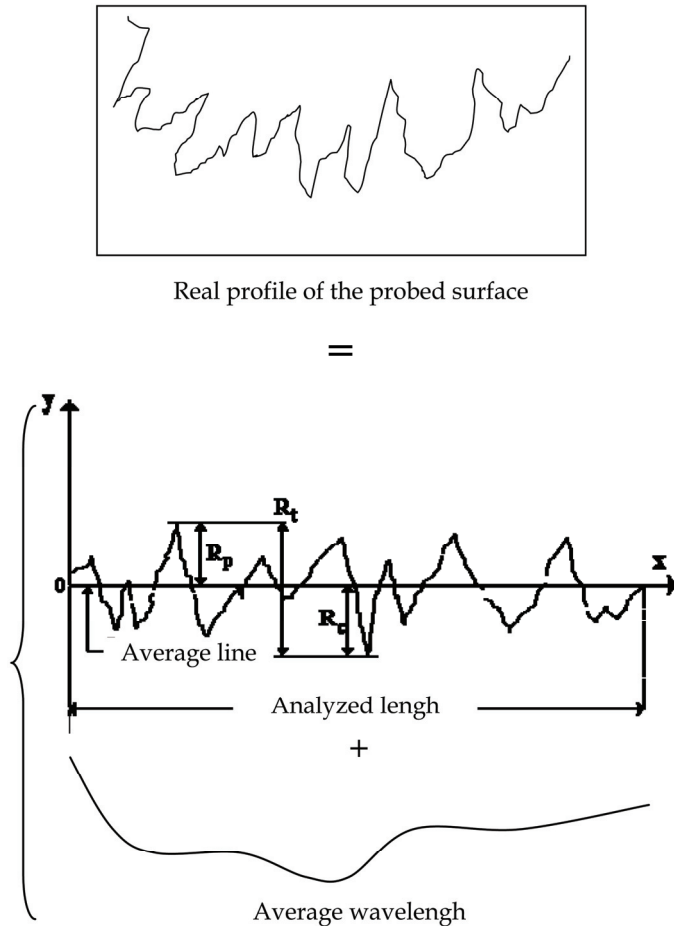


Figure 4. Roughness decomposition

### 3.1.2 Analytic expression of the down state capacitance

We define an analytic model for the down state capacitance of RF MEMS Switch (see Figure 5) which take into account air gap between the beam and the dielectric using low-pass filter (average wavelength) and high-pass filter (average roughness) as it is shown in figure 3.

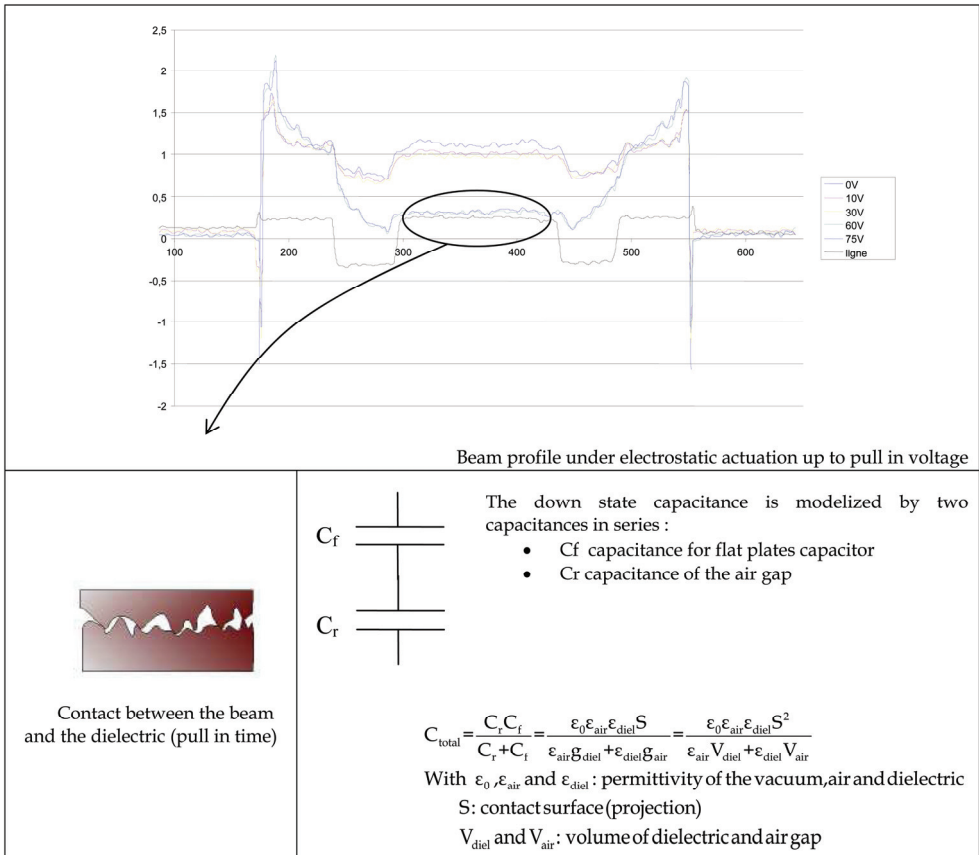


Figure 5. Capacitance model

### 3.1.3 Reverse engineering methodology

We used an optical profilometer (VEECO) to capture three-dimensional (3D) data points of the dielectric surface. Then, using Matlab functions we insert the generated surface as the top surface of a block. For CAD modeling, the segmented data are further transformed into individual surfaces. Several mathematical schemes for representing geometrical shapes are available. We choose to convert the closed surface into stereolithography format because this is an ASCII file used in most standard CAD softwares. Moreover, generated solid model are described by a list of the triangular surfaces which can be easily implemented on Matlab. The last step is to import the generated solid into a CAD software (COMSOL) to make the down-state capacitance analysis.

Figure 6 illustrates the full method and data flow : dielectric roughness is scanned by the optical profilometer (A) to generate an ASCII file (B) representative of 3D coordinates points of the surface. Than solid model (C) and object file (E) as STL, VRML or Comsol geometry can be obtained using Matlab. To enhance the shape, one can use (D) some filters (filter2 for MatLab or a CAD software , CATIA for example).

After this, the model is ready to be imported into a finite element software (F). We used multiphysics software provided by COMSOL, to set up the electrostatic model (materials and boundaries conditions (F) - meshing (G), results and post processing (H)).

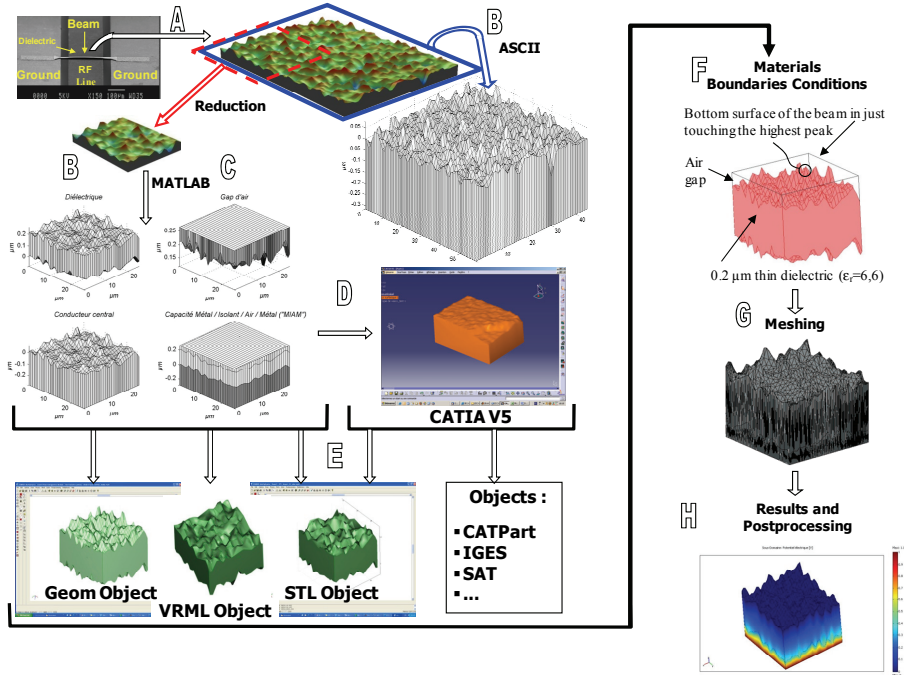


Figure 6. Description of the Reverse Engineering method

### 3.1.4 Results and discussions

Measured capacitances were realized using automatic probe station facility (Karl Suss AP6, see Figure 7) including an optical profilometer (Fogale).

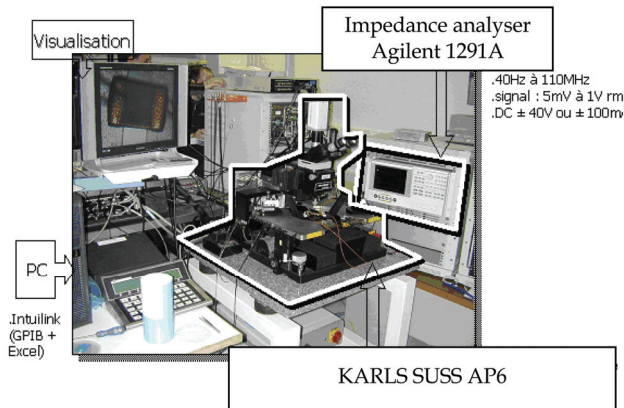


Figure 7. Capacitance bench test



In this section, we present results about measured capacitance at down state with the following dimensions and materials properties:

- Central conductor : Thick electrolytic gold (2.5 μm)
- Dielectric : Thin layer (0.2 μm), permittivity of 6.6
- The surface area related to the flat plate area is 130x80 μm<sup>2</sup> = 1.04e4μm<sup>2</sup>

Table 1 shows measurements realized with the capacitance bench test on five samples, the mean capacitance is about 1,41 pF.

Sample number	Measured capacitance
1	1,60 pF
2	1,35 pF
3	1,36 pF
4	1,29 pF
5	1,46 pF
Mean capacitance	1,41 pF

Table 1. Measured capacitance for five samples

In order to decrease the number of freedom during the finite element analysis, capacitance simulations were performed using a reduced area (647.61 μm<sup>2</sup>) mapped by the optical profilometer. So we assume the roughness fluctuations of the in plane position is correctly estimated by the reduced sample. Thus we modified the simulated capacitance multiplying it by 16 which is the ratio of the real area and the simulated area (1.04e4/647.61=16).

Simulated capacitance is obtained using a multiphysics software (COMSOL 3.2). Table 2 shows the simulated and corrected results obtained from simulation as shown in Figure 8.

Simulated capacitance	Simulated capacitance with area correction (x16)
6,222879e-2 pF	0.999335 pF

Table 2. Simulated capacitance

Equation 1 gives the analytic evaluation of the down state capacitance (expression shown before in Figure 4) uses air gap and dielectric volumes obtained by integration during simulations (see Figure 7) :

$$C_{total} = \frac{\epsilon_0 \epsilon_{air} \epsilon_{diel} S^2}{\epsilon_{air} V_{diel} + \epsilon_{diel} V_{air}} = 0.9571255 \text{ p F} \tag{1}$$

To show the influence of the roughness we calculated the theoretical capacitance (Eq.2) for flat plate capacitor:

$$C_{th} = \frac{\epsilon_0 \epsilon_{diel} S}{g_{air}} = 3.034554 \text{ pF} \tag{2}$$

As shown in table 3, simulated and calculated capacitances are closed within 4.2%. This difference could be explained by the electric field gradient near the peaks that increased locally the capacitance, these effects are not introduced in our analytic model.

Simulated	Calculated	Measured
0.999335 pF	0.9571255 pF	1.41 pF

Table 3. Capacitance results

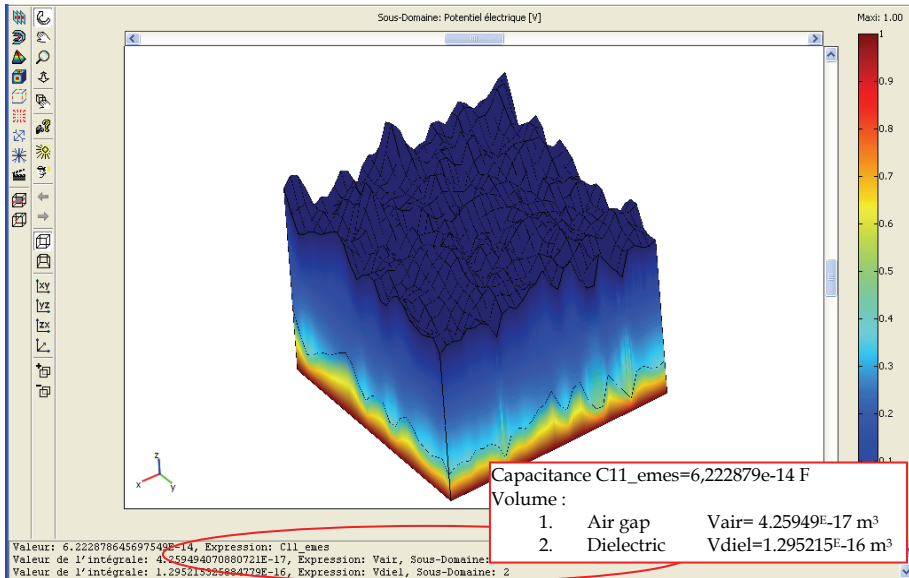


Figure 8. Simulated capacitance (bottom corner: results, Subdomain : Electric field)

But there is an important mismatch, near 30%, between simulated (or calculated) and measured data of down state capacitance. We assume this difference relies on the three following points:

Simulations were done without accounting:

1. for fringing fields (beam length was taken as the central conductor width)
2. for rough surface of the beam
3. for real contact beam versus dielectric at pull in voltage (we assume the beam to be stopped by the highest dielectric peaks, see Figure 9)

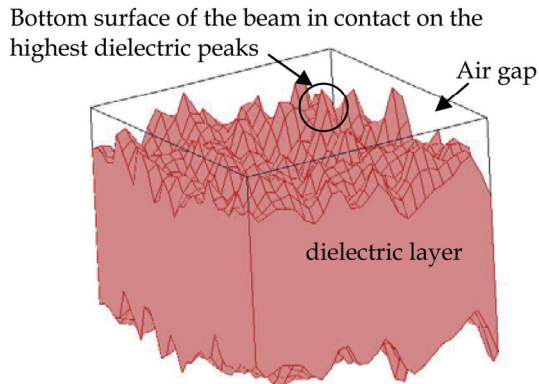


Figure 9. Contact modeling

Simulations show (as predicted) down-state capacitance decrease with the roughness of the dielectric about three time less than the theoretical formulation on flat plate capacitor. We find an accurate analytic model of the down state capacitance which take into account the roughness including an air gap capacitor. Moreover, Mismatches between simulated and measured data are explained and will be studied in further work to improve our model.

### 3.2 Electrical contact resistance simulation

For the DC contact RF MEMS, it has been identified that most of the limitations are related to the quality and the repeatability of the contact that drive the RF performance (insertion losses, isolation, power handling) and the reliability (Rebeiz, 2003). In order to propose new generation of RF MEMS devices, it is important to get a deeper insight on the physic of contact in order to choose appropriate materials, topology and architecture. It has to be furthermore outlined that the insertion of RF MEMS into real architecture will necessitate reduced actuation voltage, dimensions and a better control of the electrical and electromechanical behavior that will give more importance to surface effects.

The testing and development of contact material or contact topology can be addressed with a dedicated experimental set up for monitoring test structures. However, it is difficult to perform the tests under realistic conditions and in particular to duplicate the switch geometry, the contact geometry and the contact force. Moreover, the fabrication process must be optimized and it may take many months to fabricate a set of switches to test a single candidate contact material or contact bump shape.

In order to tackle these issues advanced simulation tools are needed. These tools for finite element analysis allow us to model assembly structures quickly and accurately with a minimal amount of effort. Then, they offer precious guidelines to choose appropriate design parameters and contact material.

In this section, we present an innovative numerical method used to calculate the contact resistance between rough surfaces from real shape of the surfaces that come in contact.

#### 3.2.1 Reverse engineering methodology

So far, surface effects were ignored in the analysis, because of the difficulty to generate a rough surface model and also to simplify the model in order to reduce computation times.

With the increase of computation capabilities, the topography of the surface can be included in finite element simulations. Thus we describe the new methodology that allows the simulation of the DC contact of RF MEMS devices through finite element multi-physics simulation and surface characterization.

A variety of methods to generate rough surfaces have been proposed. But all of these methods deal with a statistical or fractal description of the surface's roughness. The originality of this work relies on a novel approach using a reverse engineering method to generate the real shape of the surface. For this purpose, we used either an optical profilometer (VEECO) or an Atomic Force Microscope (AFM) to capture three-dimensional data points of contact surfaces. Then, using Matlab functions we convert the closed surface from a stereo-lithographic format to an ASCII file compatible with ANSYS Parametric Design Language (APDL). In the final step, the rough surface was obtained by creating key points from the imported file. Since the key points are not co-planar, ANSYS uses Coons patches to generate the surface, and then we used a bottom up solid modeling to create the block volume with the rough surface on the top.

Figure 10 describes the full method developed on ANSYS platform.

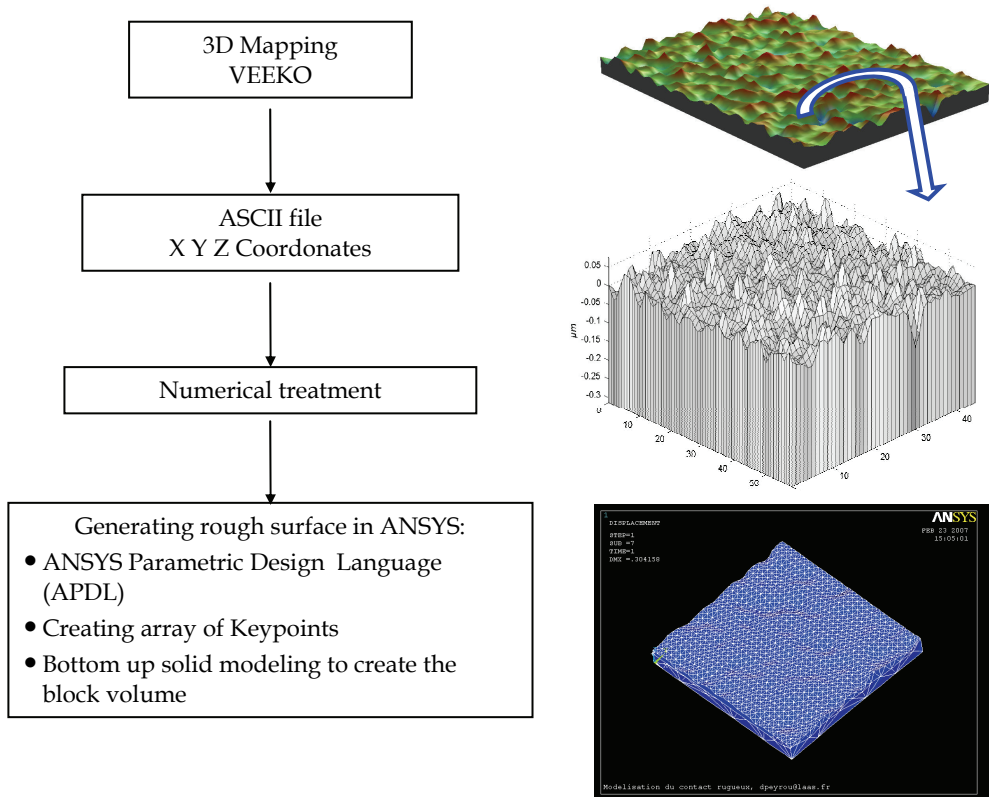


Figure 10. Reverse engineering methodology

### 3.2.2 Model definition and simulation

The model consists of an electroplated gold layer defined as a flexible material (Figure 11) with a Young's modulus and a Poisson's ratio taken respectively to 80GPa and 0.42. Yield stress is also introduced and the material behavior is described by a bilinear stress-strain curve starting at the origin with positive stress and strain values. Since the evaporated/electroplated gold bilayer of the beam is deposited during the fabrication on a photoresist sacrificial layer, the roughness of the bottom membrane (dimple) can be neglected. And so the target surface (indenter) is assumed to be a flat, smooth surface.

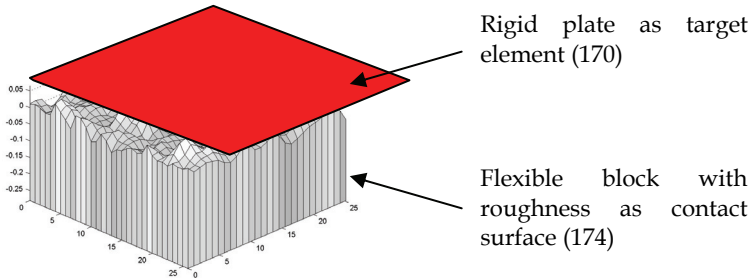


Figure 11. Model definition

To perform the finite element analysis, we choose the combined method based on penalty and lagrangian methods called the Augmented Lagrange method (see Figure 12). That is a penalty method with penetration control :

- The Newton-Raphson iterations start off similar to the pure penalty method.
- Similar to the pure Lagrange multiplier method, the real constant TOLN determines the maximum allowable penetration.
- If the penetration at a given equilibrium iteration exceeds this maximum allowable penetration ( $x_{pene}$ ), the contact stiffness per contact element ( $k_{cont}$ ) is augmented with Lagrange multipliers for contact force ( $\lambda_i$ ). For the contact element's stiffness, the force is:

$$\lambda_{i+1} = \lambda_i + k_{cont} \cdot x_{pene}$$

if the penetration is greater than the maximum allowed value.

This numerical method is used to predict the real contact area as a function of the contact force between rough surfaces starting from real shape of the surfaces that come in contact. Then using analytical expressions it is possible to extract the electrical contact resistance. The novel approach relies on a reverse engineering method to generate the real shape of the surface. The post-processing generates the distribution of the contact pressure on the contact surface. From the pressure distribution and size of each contact spot it is possible then to use an analytical expression (see next section) to extract the electrical contact resistance.

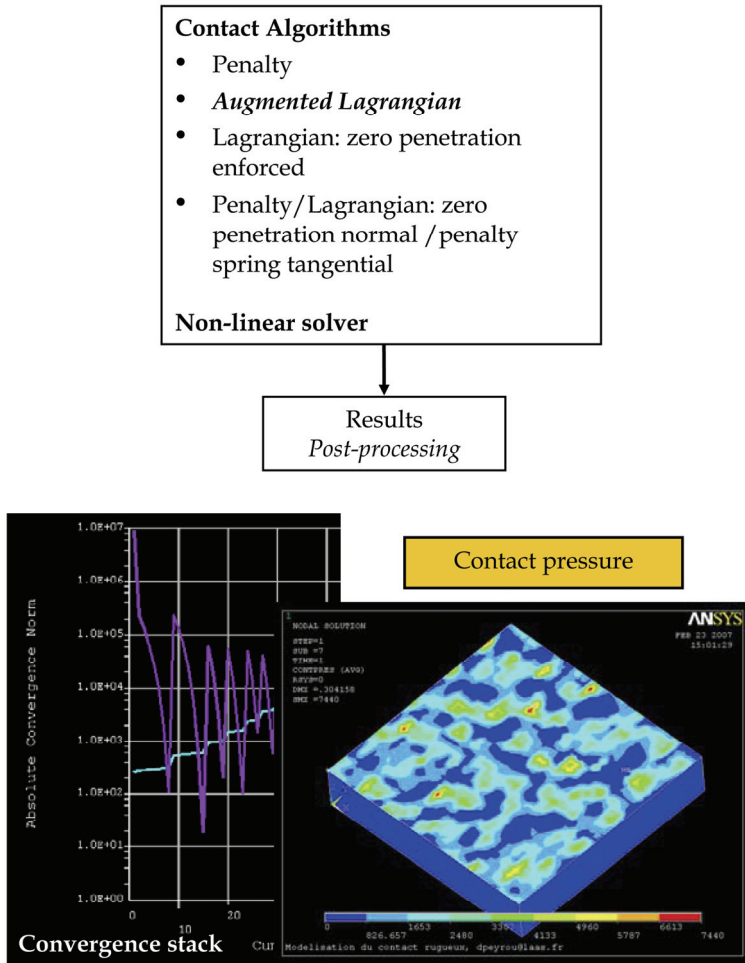


Figure 12. Contact algorithms and post processing in ANSYS

### 3.2.3 Overview of theories for the electrical contact resistance

Several works have already been published about the different theories describing the electrical contact. Thus, this part proposes several ways to estimate the Electrical Contact Resistance (ECR) called  $R_c$ , depending at the same time on the mechanical behaviour, directly governing by the contact area, and on electrical assumptions.

#### Contact resistance models for a single circular contact spot

The way the electrons are transported through electrical connections (ballistic, quasi-ballistic or ohmic transport) between two contact parts of a MEMS switch needs to be determined in order to evaluate the resistance of contact, (Coutu et al., 2006).

### Ohmic contact

Firstly, if considering a single circular spot of contact, "Ohmic contact" means that the contact size  $a$ , that is to say its radius, is at least one order of magnitude higher than the mean free path  $l_e$  of the electrons in the material ( $l_e \ll a$ ). In this case the Ohm's law can be applied everywhere, (Holm, 1999). The measured contact resistance is dominated essentially by a diffuse scattering mechanism, and is given by the Maxwell spreading resistance formula (Eq.3):

$$R_{Maxwell} = \frac{\rho}{2a} \quad (3)$$

### Ballistic contact

This model must be used if the mean free path of the electrons,  $l_e$ , is high compared with the radius of contact. The conduction of the contact spot is then dominated by a semi-classical approximation called Sharvin's resistance (Sharvin, 1965):

$$R_S = \frac{4\rho K}{3\pi a} \quad \text{where} \quad K = \frac{l_e}{a} \quad (4)$$

where  $a$  is the radius of the contact spot.

### Mixed conduction

If the two precedent models are not applicable ( $l_e \sim a$ ), a mixed one has to be used in this middle situation. Wexler (Wexler, 1966) has given a solution of the Boltzmann equation using variational principle to maintain the continuity of the conduction behaviour between the diffusive and the ballistic domain:

$$R_W = R_S + \Gamma(K)R_M \quad \text{where} \quad \Gamma(K) = \frac{2}{\pi} \int_0^\infty e^{-Kx} \text{Sinc}(x) dx \quad (5)$$

with  $\Gamma(K)$  a slowly varying Gamma function. Mikrajuddin et al., 1999, derived a well behaved Gamma function. In conclusion, the only criterion used here to discriminate the models is the radius of the contact area  $a$  compared to the mean free path of the electrons in the material  $l_e$ .

Secondly, it is important to keep in mind that, generally, the current flows is spread over multiple asperities. Three different models with the consideration of interactions between each contact point can be used to find approximate solutions: Holm's, Greenwood's and Boyer's models.

### Contact resistance models for a cluster of circular microcontact

In general, multiple asperities come into contact resulting in multiple contact spots of varying sizes. The effective contact resistance arising from the contact spots depends on the radii of the spots and the distribution of the spots on the contact surface.

### Ballistic contact

This model can be correctly used if the radius of the apparent contact area (that contains all the contact spots) is smaller than the electron mean free path. In this case, the formula of Sharvin's resistance is applied by computing the resistance of a circular area of radius  $a_{eff}$

and of area equal to the total area of all the individual contact spots combined (for  $N$  asperities,  $a_{eff} = N.a$ ).

### Ohmic contact

A lower bound can be obtained on the contact resistance by assuming that contact spots are independent and conduct in parallel. Exact solution when the radii of contact spots are small compared to the separation between the spots. Denoting the contact resistance of a spot  $i$  as  $R_i$ :

$$\frac{1}{R_{lb}} = \sum_i \frac{1}{R_i} \quad (6)$$

Considering the case of  $n$  elementary spots of radius  $a$  regularly spread in a disc of radius  $R$  representing the interface of contact of two metals of equal resistivity  $\rho$ , an improved expression) of the resistance is proposed, (Timsit, 1999), (Holm, 1999) :

$$R_{Holm} = \frac{\rho}{2na} + \frac{\rho}{2R} \quad (7)$$

where the first term represents the resistance of all the spots in parallel, and the second term, the resistance due to the interaction between all the spots.

Greenwood (Greenwood, 1966) derived a formula for the constriction resistance of a set of circular spots. The electrodes communicate via the spots with no interface film between them.

$$R_{GW1} = \frac{\rho}{2\sum a_i} + \frac{\rho}{\pi} \times \frac{\sum \sum_{ij} \frac{a_i a_j}{d_{ij}}}{(\sum a_i)^2} \quad (8)$$

with  $a_i$  the radius of the spot  $i$ ,  $d_{ij}$  the distance between the centers of the spots  $i$  and  $j$ .

If there is no correlation between the size of a given spot and its position, the author presented a formula resulting from an approximation of equation 8 :

$$R_{GW2} = \frac{\rho}{2\sum a_i} + \frac{\rho}{\pi n^2} \times \sum \sum_{ij} \frac{1}{d_{ij}} \quad (9)$$

This formula is exact when the  $n$  spots are all the same size.

In the case where the spots are regularly spread inside a disc of radius  $R$ , Greenwood substitutes the double summation in (Eq. 9) by  $16n^2/3\pi R$ , using the Timoshenko and Goodier's approximation :

$$R_{GW3} = \frac{\rho}{2Na} + \frac{16\rho}{3\pi^2 R} \quad (10)$$

And as  $16/3\pi^2=0.5404$ , the equation 10 is close to the Holm's expression (Eq. 7).



As this expression is still incorrect with  $R=a$  and  $n=1$ , Boyer, Noël and Houzé (Boyer et al., 1990), (Boyer, 2001) introduce a new expression for the constriction resistance which introduce a correction term that will be effective in the limit case of a single contact spot :

$$R_{\text{Boyer}} = \frac{\rho}{2Na} + \frac{\rho}{2R} \left(1 - \frac{1}{\sqrt{N}} \left(N \frac{a^2}{R^2}\right)^{\frac{\sqrt{N}-1}{2}}\right) \quad (11)$$

In conclusion, the radius of the contact area  $a$  and the number of asperities  $N$ , and its comparison with the mean free path of the electrons in the material  $l_e$ , allow us to discriminate an electric contact model in diffusive or ballistic electron transport. Then, for a cluster of microcontact, the possible presence of interaction between different asperities leads to the choice of the more appropriate model.

### Influence of contamination thin films

When a conductive film of surface resistance  $\lambda$  ( $\Omega\text{m}^2$ ) is present between two electrodes communicating through a circular spot of radius  $a$ , a resistance due to the presence of this film  $R_{\text{film}}$  has to be added to the Maxwell resistance  $R_M$ .

$$R_{\text{film}} = \frac{\lambda}{\pi a^2} \quad (12)$$

For  $n$  circular contact spots of radius  $a$ , the resistance  $R_{\text{film}}$  of the interface film is:

$$R_{\text{film}} = \frac{\lambda}{n\pi a_{\text{eff}}^2} \quad (13)$$

### 3.2.3 Results and discussion

In ANSYS post-processing, we can extract the nodes on the contact surface for which the contact pressure is not null. Next, we developed a program allowing the extraction of the real shape and dimensions of each contact spot. From the distribution and size of the contacts spots we can use an analytical expression (based on Wexler's approximation of the integral) to extract the electrical contact resistance (Eq. 12). In fact, for both ohmic constriction and boundary scattering, the contact resistance  $R_c$  for a spot of radius  $a$  is, (Wexler, 1966) and (Coutu, 2006) :

$$R_c = \Gamma \left(\frac{l_e}{a}\right) R_M + R_s = \frac{1+0.83\left(\frac{l_e}{a}\right)}{1+1.33\left(\frac{l_e}{a}\right)} \rho + \frac{4\rho l_e}{3\pi a^2} \quad (14)$$

Where  $l_e$  is the electron mean free path, and  $\rho$  is the electrical resistivity.  $R_M$  is the Maxwell spreading resistance (the resistance due to lattice scattering, diffusive transport), and  $R_S$  is the Sharvin resistance (the additional resistance due to boundary scattering in small constrictions, ballistic transport).

Using this model for a single spot and the Greenwood's model for a cluster of microcontacts (Eq.6), we performed the contact resistance of all single contact spots in parallel and then added the resistance due to their interaction. The graph figure 13 illustrates the evolution of contact resistance as a function of the applied force.

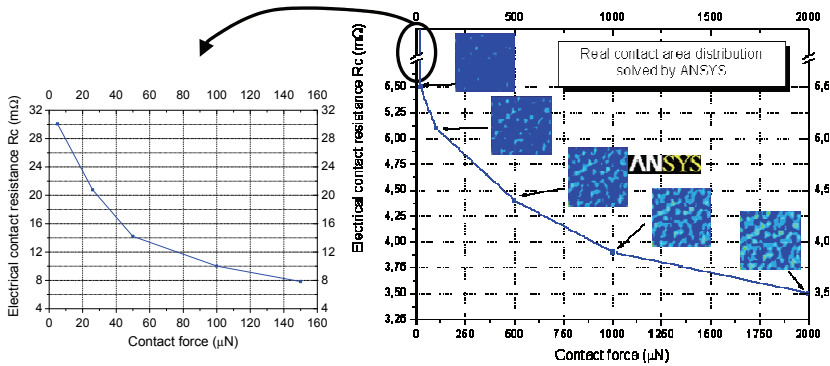


Figure 13. Electrical contact resistance versus contact force

## 4. Application manager for interfacing different CAD

### 4.1 Introduction

To simulate different topologies of deformable micro structures, some multiphysics softwares are under investigation. In order to weigh the software, the criteria are the precision of the results with an acceptable time of calculation to simulate different models with multiple variables. The existence of COMSOL 3.3, at a time linking all the physics and having a good interactive interface seemed to be a good solution. Being incomplete, COMSOL 3.3 needed to be linked to another software to complete its functions and make it more powerful. As a first step, we validated the numerical platform by comparing results of different softwares (Peyrou et al., 2006) and also some analytical solutions (Achkar et al., 2007). The basic advantages and drawbacks of each softwares were considered then we have developed a method to link COMSOL and ANSYS since we think they are complementary. In terms of time of calculation, an interesting result concerning the speed of COMSOL to solve the problem when compared to ANSYS, while keeping the same precision of calculation.

### 4.2 Problem definition

In the domain of structural mechanics, the major difficulty in design relies on, modelling MEMS having high aspect ratio, properly defining the material properties used, and well describing the geometry defined by the technological process.

Generally, in MEMS simulations, we need to combine with the mechanical simulation other physics like Electrostatics, Piezoelectricity... from where comes the need for multi-physics softwares. Multiphysics softwares are now getting more abundant in the research domain specially in the MEMS domain where different physics find their arena to show their interaction and their influence on these systems.

For any application in MEMS, deformable micro structures using different kinds of actuation with repetitive behaviour are to be simulated in order to study their possible functioning. This functioning is based on designing a mechanical structure deformed piezoelectrically (Chen et al., 2004), thermomechanically, or electrostatically, mainly to get into contact with another part, in order to play an electrical function.

To facilitate the task of designers, we need a multiphysics software offering at a time, a well developed solver to reduce the time of calculation and a facility to build parametric models

(parametric geometry and parametric properties), without losing too much accuracy on the results.

Following this need, COMSOL 3.3 appeared as software that is capable to do piezoelectric simulations combined to mechanical structure and contact problems, without forgetting thermal and initial stress effects. The problem appears here, when we need to simulate complicated contact problems and where COMSOL solver fails most of the time.

When talking about contact in COMSOL, it is somehow critical and difficult to converge the simulation specially that we have to vary the contact parameters and it's still not sure to converge. The convergence of the contact model using COMSOL failed; one have then to find a way to link both ANSYS and COMSOL in order to use ANSYS contact models. By exchanging the deformed geometry between them and then running the convenient simulation using the appropriate tool, some simulation problems can be solved.

In this chapter, you will learn how to link the software the most efficient for your application in order to obtain a complete tool to analyse your structures. Both the accuracy of COMSOL in deflection and stress, and the reduced calculation time makes it very useful and specially after completing its contact models with ANSYS contact model.

### 4.3 Description of the method

As already stated, we need to link ANSYS and COMSOL in a way to exchange deformed geometry and treat it in the convenient software. This section describes the full method in order to regenerate geometries starting from the deformation obtained from a mechanical simulation.

A very practical way to run simulations on two different softwares, is to pilot it using Matlab. To achieve our purpose, we created in Matlab some functions which make the piloting and the link between the softwares easier. In what follows, the flow chart shows the key steps of the method by using a simple membrane of  $200 \times 200 \mu\text{m}^2$  subjected to constant pressure and blocked at its corner.

We can begin the cycle from where we want, either from ANSYS or from COMSOL. In the flow chart, we began from COMSOL, with a simple membrane under pressure (Figure 14). This is a typical material characterization test used in MEMS (Xiang & Vlassak, 2004) and (Xiang & Vlassak, 2005).

The geometry is drawn, and then the loads and boundary conditions are applied. A mechanical simulation is run in order to obtain the deformation of the membrane. Considering that a contact analysis is needed after the deformation of the membrane, so we export the deformation of the membrane into a text file. In the text file there will be the displacement of each node of the chosen surface of interest as well as some data that we don't need. Matlab will treat this file to clean unneeded information and to reorganize data in the file. The treated file will be used then to create a cloud of keypoints, by creating it one by one, and then generating surfaces from the keypoints. In ANSYS now, we will mesh the regenerated geometry, we will define the physics that we need to study (in our case it's the contact) and then run a new simulation. The deformation is once again output in a text file, giving the displacement value for each node of the surface of interest. Another treatment and organization of the output data file, before being injected in the function that we created in Matlab which regenerates the surface and export it to COMSOL. The geometry is ready to be used in COMSOL, new objects can be added to it, for example electrode, before going into meshing and then boundary condition, to finish into a new simulation. The loop can turn as much times as we need, passing from software to another, until we attain our goal.

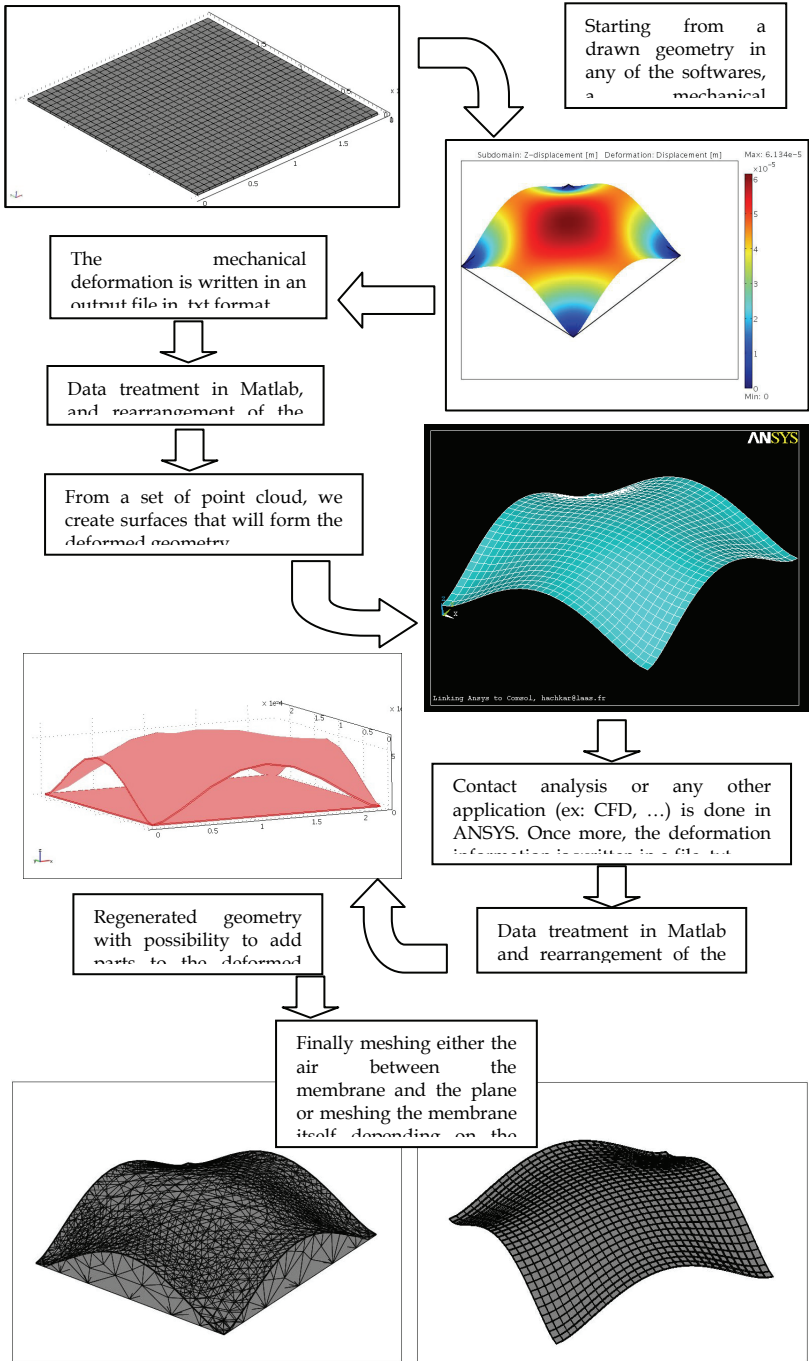


Figure 14. Electrical contact resistance versus contact force

## 8. Acknowledgement

The authors would like to acknowledge the French National Center for Scientific Research (CNRS) and the University of Toulouse, FRANCE. Also, authors are grateful for the teams' support of the Microdevices and Microsystems of Detection (M2D) Department and the Micro and Nanosystems for wireless Communications (MINC) Department at the Laboratory for Analysis and Architecture of Systems (LAAS) of Toulouse, FRANCE.

## 9. References

- Achkar, H.; Pennec, F.; Peyrou, D.; Ahmad, M.AL. Sartor, M.; Plana, R.; Pons, P. (2007). Validation of simulation platform by comparing results and calculation time of different softwares, *Proceeding of EUROSIME 2007*, (April 2007) pp.520-524
- ANSYS : <http://www.ansys.com/>
- Boyer, L.; Noël, S. & Houzé, F. (1990). Constriction resistance of a multispot contact : an improved analytical expression, *36th IEEE Holm Conf. on Electric Contacts Montreal Canada*, (August 1990) pp.134-136
- Boyer, L. (2001). Contact Resistance Calculations: Generalizations of Greenwood's Formula Including Interface Films, *IEEE Trans. Comp. Pack. Tech.*, Vol.24, (March 2001) pp.50-58
- Chen, X; Fox, C H J.; William, S Mc. (2004). Modeling of a tunable capacitor with piezoelectric actuation, *J.Micromech. Microeng*, Vol.14, (2004) pp.102-107
- COMSOL : <http://www.comsol.com/>
- Coutu, R.A.; Reid, J.R.; Cortez, R.; Strawser, R.E.; Kladitis, P.E. (2006) Microswitches with sputtered Au, AuPd, Au-on-AuPt, and AuPtCu alloy electric contacts, *IEEE Trans. On Components and Packaging Technologies*, Vol.29; No.2, (June 2006) pp 341-349
- Greenwood, J. A. (1966). Constriction resistance and the real area of contact, *Brit. J. Appl. Phys.*, Vol.17, (1966) pp. 1621-1632
- Holm, R. (1969). *Electric Contacts: Theory and Applications*, Fourth Edition, Berlin, Springer-Verlag, 2000, ISBN-3540038752
- Mellé, S.; Conto, D.De; Dubuc, D.; Grenier, K., Vendier, O.; Muraro, J.L.; Cazaux, J.L.; Plana, R. (2005) Reliability Modeling of capacitive RF-MEMS, *IEEE Transactions on Microwave Theory and Techniques*, Vol.53, No.11, (November 2005) pp.3482-3488.
- Mikrajuddin, A.; Shi, F.; Kim, H. & Okuyama, K. (1999). Size-dependent electrical constriction resistance for contacts of arbitrary size : from Sharvin to Holm limits, *Proc. Mater. Sci. Sem.*, Vol. 2, (1999) pp. 321-327
- Palasantzas, G. & DeHosson, J.Th.M. (2006) Surface roughness influence on the pull-in voltage of microswitches in presence of thermal and quantum vacuum fluctuations, *Surfaces Sciences*, Vol.600, No.7 (April 2006) pp 1450-1455
- Peyrou, D. & al. (2006). Multiphysics Softwares Benchmark on Ansys / Comsol Applied For RF MEMS Switches Packaging Simulations, *Eurosime 2006*, (April 2006) pp.494-501
- Rebeiz, G.M. & Muldavin, J.B. (2001). *RF MEMS switches and switch circuits*, IEEE Microwave magazine, pp. 59-71
- Rebeiz, G. (2003), *RF MEMS Theory, Design and Technology*, New Jersey: Wiley, ISBN-0471201693.

- Reid, J.R. & Webster, R.T. (2002) Measurements of charging in capacitive microelectromechanical switches, *Electron lett*, Vol.38, No24, (November 2002) pp 1544-1545.
- Sharvin, Y. V. (1965). Sharvin Resistance Formula, *Sov. Phys. JETP*, Vol. 21, (1965) p. 655
- Sprengen, W.M. van; Puers, R.; Mertens, R. & Wolf, I.De (2004) A comprehensive model to predict the charging and reliability of RF MEMS switches, *J.Micromech. Microeng.*, Vol.14, No.4, (January 2004) pp 514-521.
- Timsit, R.S. (1999). Electrical contact resistance: Fundamental principles, *Electrical Contacts: Principles and Applications*, Ed. P.G. Slade, (1999) pp.1-88, Marcel Dekker, New York
- Wexler, G. (1966). The size effect and the nonlocal Boltzmann transport equation in orifice and disk geometry, *Proc. Phys. Soc.*, Vol.89, (1966) pp. 927-941.
- Xiang, Y. & Vlassak, J.J. (2004). The effects of passivation layer and film thickness on the mechanical behavior of freestanding electroplated Cu thin films with constant microstructure, *Mat. Res. Soc. Symp. Proc.*, Vol. 795, (2004)
- Xiang, Y. & Vlassak, J.J. (2005). Bauschinger effect in thin metal films, *Scripta Materialia*, Vol.53, (2005) pp.177-182
- Yuan, X.; Peng, Z.; Wang, J.C.M.; Forehand, D.; Goldsmith, C. (2006) Acceleration of dielectric charging in RF MEMS capacitive switches, *IEEE Transactions on device and materials reliability*, Vol.6, No.4, (December 2006) pp 556-563I

# Active Magnetic Suspension and Bearing

Adam Krzysztof Piłat  
*AGH University of Science and Technology  
Poland*

## 1. Chapter overview

The aim of this chapter is to present investigation, modelling and simulation of Active Magnetic Levitation Systems (AMLS). Active means that the operating mode is fully controlled with desired performance specified by a user defined controller law. Active Magnetic Suspension (AMS) and Active Magnetic Bearing (AMB) are AMLS representatives. These systems can be characterized as the mechatronics devices because they combine a number of technologies: mechanics, electrical engineering, electronics, computer science and control theory. These devices are structurally unstable and the application of a control law is necessary for the stable operation in levitation mode. To levitate an object the appropriate value of electromagnetic force has to be generated by the stabilizing controller. In the AMS the electromagnetic force counteracts the gravity force to obtain object levitation while in the AMB the electromagnetic forces counteract to each other and to gravity. The electromagnetic force is generated by the electromagnet consisting of the stator of a specific design as far as the shape and number coils are concerned. The electromagnets are formed in the C or E shapes typically. One of advanced modelling and designing tasks is to find the optimal shape for the particular solution. At the modelling stage the graphical form of the electromagnet can be represented by a set of graphical primitives. Using Bézier curves it is possible to obtain the parameterised and continuous electromagnet shape which could be optimised under many criteria: maximal force, Eddy current losses, resistive heating, flux saturation, controller quality, required stiffness and damping. All these problems ought to be analysed at the modelling, simulation and experimental investigation stage.

Typically AMLS models are based on ordinary differential equation parameterised by the optimisation of identification results. The nonlinear form of these equations allows to describe almost all phenomena existing in the particular construction and configuration of power actuators, sensors and control system. The experimental investigation is required for better understanding of a problem and for model verification but construction aspects, used materials are still ambiguous, thus it is very difficult to obtain a general model to be used in the future. Better is to say that the knowledge base has been achieved that describes a particular AMLS application. Nowadays control and construction designers are aiming at the ideal system similar to ideal set of springs and dampers working in the whole operating range with programmable stiffness and damping. Thus, at the modelling stage the construction properties and controller design ought to be analysed in a complex form. The controller is designed when the working system was investigated and

modelled. In this case the controller must be fitted accurately for the required application performance.

The author recommends to include the control strategy into the designing phase. AMLS are specific mechatronics devices in which the construction and control laws are strongly coupled. The modern COMSOL Multiphysics (Comsol, 2007) software allows to perform multidisciplinary analysis based on partial (PDE) and ordinary (ODE) differential equations, using material and geometry properties. The controlled magnetic field is studied under the satisfying geometry and current flow constraints. Due to the COMSOL Multiphysics software the interdisciplinary model can be obtained and embedded into MATLAB/Simulink for the closed loop simulation purposes. This feature has never been studied in the literature despite that research and it gives an unexpected possibilities in the AMLS optimal design and control.

## 2. Introduction

The Samuel Earnshaw theorem (Earnshaw, 1842) proves that it is not possible to achieve a static levitation using any combination of fixed magnets and electric charges. The static levitation means the stable suspension of an object against gravity. However, there are a few exceptions around it which violate the assumptions (Braunbeck, 1939), (Jayawant, 1981): quantum mechanics, rotation, diamagnetism, oscillating fields and feedback. This chapter deals with feedback systems. The first recorded system which offered an alternative to the wheel-on-rail was the floating train developed by Girard in 1864 (Sinha, 1987). In 1937 Beams and Holes used an electromagnetic suspension for testing material strength. Their patent related to AMB is dated to 1941. The AMB technology started to operate with digital control technology under work of Habermann (Habermann & Liard, 1979) and Schweitzer (Schweitzer, 1976). The first international symposium on the active magnetic bearing technology was held in 1988 with the founding of the International Society of Magnetic Bearings by Prof. Schweitzer, Prof. Allaire (University of Virginia), and Prof. Okada (Ibaraki University).

Nowadays, worldwide there is a number of research centres and companies focused on the AMS and AMB research. They have their own individual test-rigs and particular experience in this research domain. The results are presented and discussed by researchers and development engineers during the International Symposium on the Magnetic Bearings (ISMB) event that is organized once every two years. Another conference that shares the issue of the magnetic levitation technology is the International Conference on Magnetically Levitated Systems and Linear Drives. The research of the AMS properties and control allows to transfer knowledge and methods to the AMB, which is a part of it. The advances in material, microelectronics, computer science, nonlinear control, modelling and simulation have made the AMLS a more available technology up to now. Nowadays, a detailed analysis and optimisation of all the AMLS components are required to minimize its complexity and high costs.

In recent years a number of machines with Active Magnetic Bearings have been designed in order to eliminate the lubricant medium, vibration, noise and to achieve high velocities and loads. These systems are complicated due to mechanical, electrical and electronic circuits construction. A wide range of analyses is required during the designing procedure - from the construction stage up to the development of the control algorithm architecture. The finite element method can be a tool for the magnetic field analysis. Many scientists working



on magnetic bearings or self bearing motors use this method at the designing stage. The numerical analysis allows to check if the new proposed AMB structure is effective with respect to levitation forces, magnetic field properties and electro-mechanical interactions.

The finite element method was also used to analyse the air gap flux and radial forces in the miniature self bearing motors (Kanabako at al., 2002), (Ohmori at al., 2002). In small-sized systems essential modelling errors are often caused by leakage and nonlinear effects that could be neglected in larger systems. The appropriate AMB construction is a trade-off among many requirements and should be specific for different applications. The development stage of a machine equipped with the AMB demands co-operation of many experts in mechanics, structure of materials, electronics and control. The proper machine construction, optimal AMB structure and dedicated control algorithm allow to achieve a modern industrial unit.

The basis of the AMLS operation is an electromagnetic force generated by the electromagnet (see Fig. 1) that can be calculated using Maxwell's equations.

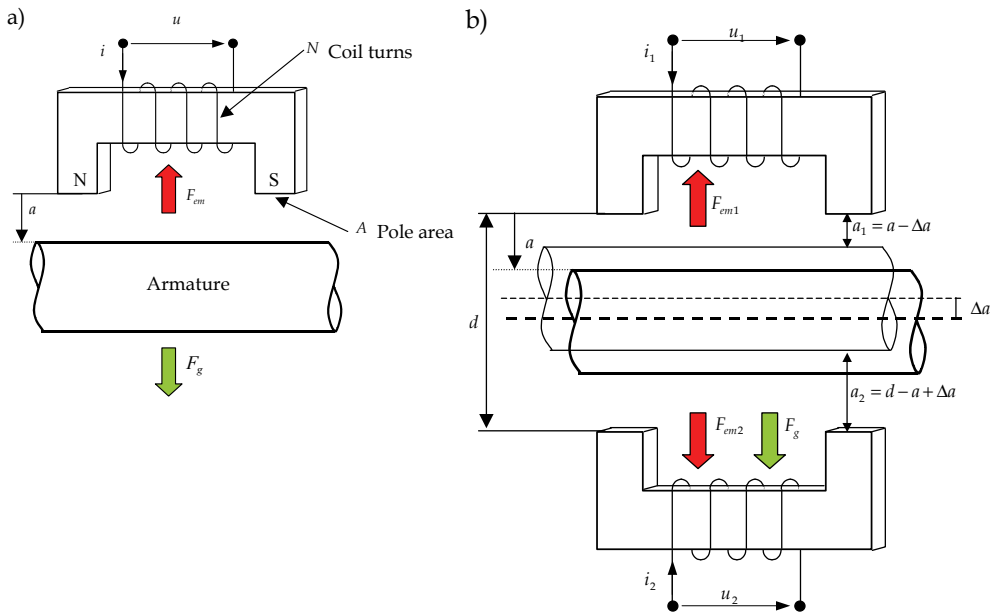


Figure 1. Armature suspension in two configurations: a) single electromagnet, b) two electromagnets

It is a set of equations, describing relationships between the fundamental electromagnetic quantities. These quantities are the electric field intensity  $E$ , the electric displacement or electric flux density  $D$ , the magnetic field intensity  $H$ , the magnetic flux density  $B$ , the current density  $J$ , and the electric charge density  $\rho$ . For general time-varying fields, Maxwell's equations and equation of continuity can be written as differential equations that the finite element method can handle.

$$\begin{aligned}\nabla \times H &= J + \frac{\partial D}{\partial t}, \quad \nabla \times E = -\frac{\partial B}{\partial t} \\ \nabla \cdot D &= \rho, \quad \nabla \cdot B = 0 \\ \nabla \cdot J &= -\frac{\partial \rho}{\partial t}\end{aligned}\tag{1}$$

The electromagnetic force is calculated using magnetic field energy  $W$ :

$$F_{em} = -\frac{\partial W}{\partial a}, \quad W = \frac{1}{2} \int BHdV\tag{2}$$

where  $F_{em}$  is the electromagnetic force,  $a$  is the distance between field source and armature and  $V$  is the air gap volume. Setting the armature at desired distance  $a$  the electromagnetic force can be calculated with respect to the flux density, coil current  $i$ , coil inductance  $L$  and armature distance  $a$ .

$$F_{em}(B) = A \cdot B^2 \mu_0^{-1}, \quad F_{em}(a, i) = -\frac{K i^2}{4 a^2}, \quad F_{em}(a, i) = \frac{1}{2} \frac{dL(a)}{da} i^2\tag{3}$$

where:  $K = \mu_0 N^2 A$  is an electromagnet constant,  $A$  is a pole area,  $\mu_0$  - permeability of vacuum and  $N$  - no of coil turns.

### 3. Principles of active control

As mentioned before the controller is required to obtain the stable levitation with the desired performance of the suspended object. The complex controller has to realize many tasks (Maslen, 1995), (Schweitzer, 1994): coordinate transformation of sensor signals, collection of any other parameters needed by control algorithm, generation of control current (or flux) requests: executing control algorithm, coordinates transformation, biasing of amplifier signals and additionally permit modification of control algorithm, implement diagnostic measurements.

The controller can be realized in the analog or digital form. They serve worse or better to the control goals and both of them have some advantages and disadvantages. The analog controller is based on op-amps, resistors and capacitors and generally performs a linear control strategy. It is an inexpensive and simple solution but has a fixed configuration and a component drift can occur. The digital control technology is based on FPGAs, DSPs and microcontrollers together with A/D and D/A converters. The controller complexity is high but linear and nonlinear control strategies can be easily implemented and modified (Grega & Pilat, 2001). With this technology some additional control, diagnostic and monitoring features can be implemented.

The ferromagnetic suspension system is inherently unstable and thus the active control needs to be incorporated for stable suspension. The basic principle of the AMLS operation is to apply the voltage to an electro-magnet to keep a ferromagnetic armature levitated. The function of a control action is modifying the force-distance characteristics to obtain required

stiffness and damping properties. The control can be realized in the explicit feedback (the external sensor is used to measure the distance or flux) or the implicit feedback (based on changes of the magnet coil inductance owing to the variations in the air gap). Additionally, the coil current is measured to explore identification and multi loop or nonlinear control strategies.

One of electromagnets of the AMLS can be analysed as the single-degree-of-freedom mass-spring-damper system with controllable stiffness and damping. Using the non-contact actuator both parameters are controlled by the formulated control strategy and when choosing the appropriate values of the poles we can obtain the required dynamic behaviour of the closed loop. The controller parameters can be designed to satisfy requirements of the closed loop performance determined by the undamped natural frequency and the damping ratio. Choosing the appropriate values we can control the speed of the system response to the external disturbance. The highest natural angular frequency gives faster system response and the damping mode can be controlled after setting the appropriate value of damping ratio.

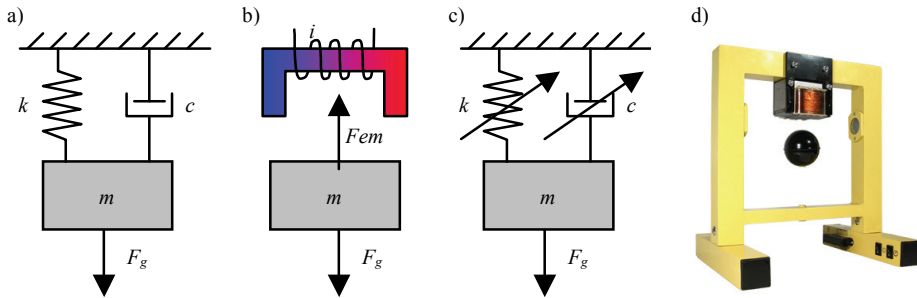


Figure 2. Object suspension: a) a typical mechanical approach - the spring mass-damper system, b) electromagnetic suspension, c) non-contact system equivalent to the controllable stiffness and damping, d) MLS0201 - active suspension at work (Pilát, 2005a)

Mounting the second electromagnet opposite to the first one we can obtain the differential model of the controlled armature (eq. 5). Controlling the damping and stiffness in the course of action both electromagnets ought to be controlled independently or in a differential mode. In this case the gravity factor could be neglected if the electromagnetic forces are much higher than the gravity one. In this case much higher stiffness and damping can be obtained. This kind of configuration is the basic solution in the typical AMBs, where four electromagnets are used. The control law can be applied separately to each of them, to both pairs or in a global case to all of them.

$$m\ddot{a} = F_{em} + F_g \quad (4)$$

$$m\ddot{a} = F_{em2} - F_{em1} + F_g \quad (5)$$

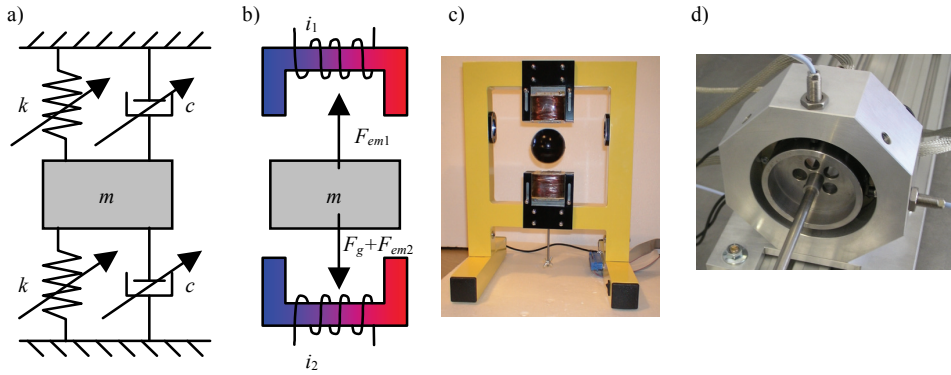


Figure 3. Electromagnet counteraction: a) mechanical representative, b) non-contact system equivalent to the controllable stiffness and damping, b) MLS0202 - laboratory test-rig, c) radial AMB (Piłat 2006)

Another possibility to simplify the AMB construction is to use three poles only (Meeker & Maslen, 2006) or to eliminate one of electromagnets. Three sources of the magnetic field are a necessary minimal number of actuators required for the rotor levitation in the bearing space. A small number of execution units and electronics circuits allow to minimize a bearing size, production costs and energy consumption. The disadvantages of this solution correspond to the slighter stability region and strong nonlinearities. The rotor suspension can be described by equation (6) (Gosiewski 1993, Kozanecka 2000).

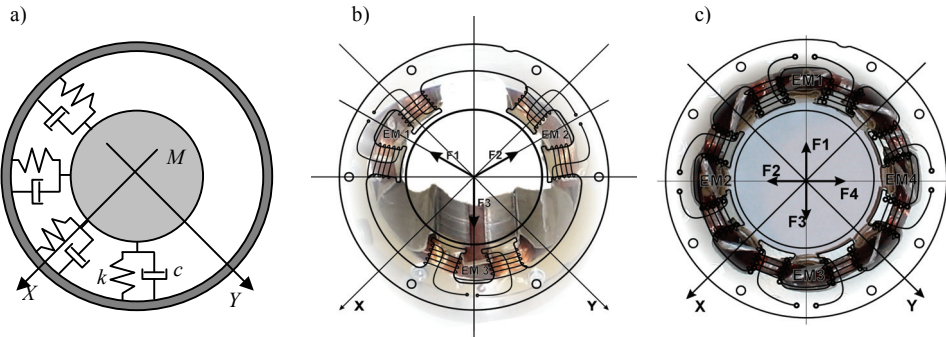


Figure 4. Three and four electromagnet based AMB constructions: a) general model, b and c) author's AMB prototypes

$$M\ddot{q} + C\dot{q} + Kq = F \tag{6}$$

Where  $q$  is a state vector,  $F$  is vector of forces and  $M, C, K$  are mass, damping and stiffness matrices respectively.

The nonlinear and robust control strategies are studied to maximize the performance of the AMLS. The power of automatics and control theory implemented in digital or analogue programmable device (Piłat, 2005a) allows to reconfigure controller configuration while operating.

#### 4. Mechatronics approach

The Active Magnetic Suspension and Active Magnetic Bearings can be categorized as mechatronics systems. Mechatronics is the synergistic combination of precision mechanical engineering, electronic control and systems thinking in the design of products and manufacturing processes. It relates to the design of systems, devices and products aimed at achieving an optimal balance between basic mechanical structure and its overall control.

The new technology devices equipped with electromagnetic actuators require precise design and manufacturing. The AMLS consist of components from a few brands (techniques) mechanics, electrical engineering, electronics informatics and automatics). The typical and mostly used designing path is based on a few steps realized in the serial way: calculation stage, mechanical construction design, sensors, actuators and control units design, integration and application of control strategy. Such a designed and manufactured prototype is identified and tested practically. After collecting the identification results and handling the data the system knowledge base increases and can be used to modify the existing project components and in a project development. Every project modification requires to rebuild a prototype, which could be an expensive task. On the other hand, this knowledge is still limited to the prototyped devices family. The prototyping path could include identical or similar devices.

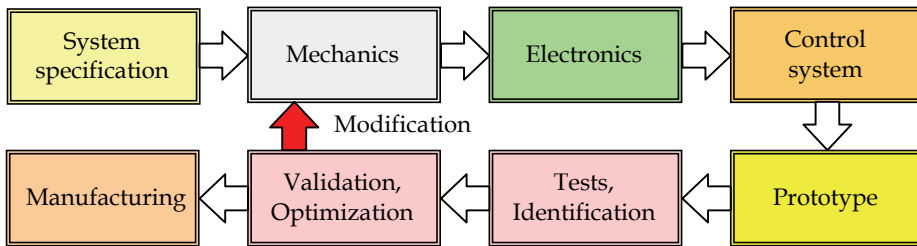


Figure 5. Traditional Design Approach - particular elements are designed separately and then the prototype is mounted and analysed. Each of the prototyping stages is well modelled and simulated, but does it satisfy the perfect prototype operation?

Moreover, the AMLS operation is based on the control strategy that is customized to the system application and it should be done in an optimal way to satisfy the application requirements. Thus, the conventional modelling, simulation and prototyping path is insufficient for levitation systems. So it is necessary to develop a method for modelling and simulation of a complex levitated system. The research being realized with typical and well known CAD/CAM tools, MATLAB/Simulink calculation package and custom hardware has shown that it is desirable to perform complex modelling and simulation of the AMLS. This kind of analysis consists of the actuator unit properties including materials and construction characteristics and complies to physical phenomena related to the system operation. Thus, the virtual prototype of AMLS is proposed. This prototype should be designed in a parallel way with an interdisciplinary analysis feature. The development of such complex model will enable effective and optimal designing of the electromagnetic actuator together with a control strategy.

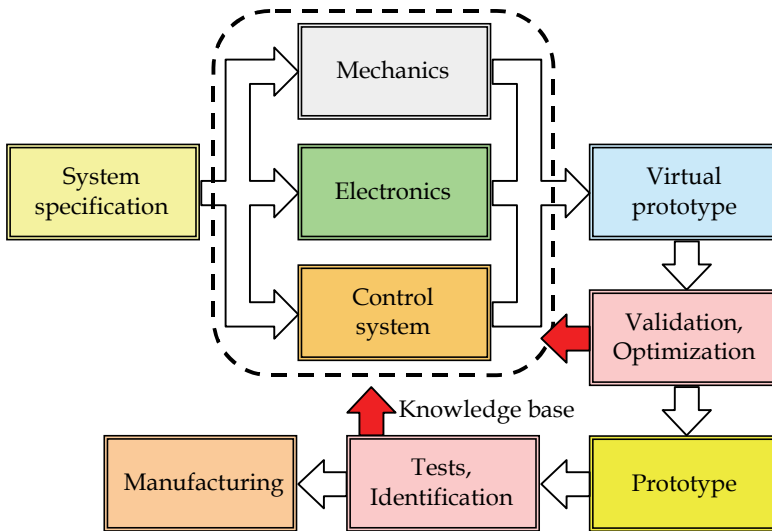


Figure 6. The proposed interdisciplinary Design Approach where virtual prototype is being developed and studied

Nowadays, most of the automatic execution units and mechatronic systems, and particularly actuators for levitated systems are designed and tested in the integrated MATLAB/Simulink package. A set of analytical calculations is performed, where the modelling of systems dynamics is studied using ordinary differential equations. The dynamics is formulated on mathematical models under a set of assumptions that simplifies formulas and dependencies, but can limit the real-system behaviour. To extend traditional modelling and simulation stage an interdisciplinary approach is proposed.

#### 4. Modelling and simulation

In the realized research the analytical approach is being used to solve differential equations and calculate surfaces and volumes. These calculations are supported by numerical computing. The static and dynamic properties of the AMLS are modelled and simulated by ordinary differential equations in MATLAB/Simulink environment, which is nowadays the most popular and advanced engineering and scientific tool. A wide range of toolboxes especially dedicated to control and optimisation problems allows to design and perform specialized analysis of the considered control problem. The proposed control strategies are also implemented and tested in MATLAB/Simulink package. The realized models contain system specifics characterized by its architecture, sampling frequencies, used devices (e.g. A/D and D/A quantization effects), serial and/or parallel data processing. The real-time environment and dedicated boards with user-defined signal processing (Pilat 2002a, Pilat 2006) are used to collect the data for model verification purposes. The investigation of

AMLS is realized with the parallel signal data acquisition that cancels any delays and guarantees causality of component behaviour.

During the design of AMS (Pilat, 2003), (Pilat & Turnau, 2005) and the reconfigurable laboratory test-rig for the AMB (Pilat, 2004b), (Pilat & Grega, 2005c) it has been noted that a complex interdisciplinary analysis is necessary to achieve an almost real model of such systems. The constructed prototype gives a number of information about system static and dynamic properties. Applied sensors allow to identify existing physical phenomena's and their cross couplings. The designed AMLS prototypes have been designed before FEM tools were used at the modelling and simulation stage. The analysis of the existing constructions and collection of identified data build the knowledge base and is used at the FEM modelling and simulation verification stage.

COMSOL Multiphysics (COMSOL, 2007) is a powerful interactive environment for modelling and solving all kinds of scientific and engineering problems based on partial differential equations (PDEs). To solve the PDEs, COMSOL Multiphysics uses the proven finite element method (FEM). The software runs the finite element analysis together with adaptive meshing and error control using a variety of numerical solvers. A user can perform various types of analysis including stationary and time-dependent analysis, linear and nonlinear analysis, eigenfrequency and modal analysis. The user can operate a well designed graphical interface and/or COMSOL Script. Using a script programming method the user can apply data structures and functions to realize non-standard or multidisciplinary modelling. This feature allows to customize designing and analysis procedures. The full interface to MATLAB/Simulink environment allows to realize interdisciplinary analysis, which is very important from the automatic control point of view. When using FEM for AMLS it is important to accurately select mesh properties due to a bigger difference between device sizes and the levitation area (e.g. 50000:1), thus, after shape discretization the quality of the generated mesh should be measured and analysed. This feature is offered by the COMSOL Multiphysics software where the user can set predefined or individual settings for the selected regions and mesh them with required accuracy. Taking into consideration the levitated systems, the modelling of the air gap with the specified accuracy is crucial for electromagnetic force and system dynamics analysis, but strongly increases computational effort.

The electromagnetic force generated by the electromagnet depends on its geometry, coil parameters, coil current and ferromagnetic object distance from its front side. Nowadays, all these parameters play an important role in the efficient and optimal electromagnet design for magnetic suspension and active magnetic bearings applications.

The application of the magnetic field for an attraction of ferromagnetic objects requires proper electromagnet construction design and plays an important role in the control applications.

The magnetic properties of the used materials can be entered and used in the modelling process. The same can be done with coil parameters, current density and distance. Such a prepared model represents an ideal form of a modelled system and ought to be verified.

Since many years the author has been interested in a complex system modelling and simulation. Nowadays it becomes available. The only limits are introduced by a quasi real-time computer operation. For the control research it would be nice to have an adequate model of the real system. The designed set of identification tools allows to model the

dynamics of the AMLS and design control strategy which is verified on the laboratory test-rigs.

The most important problem is to have a realistic model of the AMLS. As mentioned before the AMS and AMB are complex mechatronics systems and they should be designed under consideration of all possible physics phenomena and particularly under the controller supervision. While developing new constructions and control strategies the researcher ought to think in an interdisciplinary way to fulfill the analysis of interaction between all physical fields existing in the levitated system under active control. Three steps in modelling and simulation: geometry modelling, magnetic field analysis and dynamics simulation in an interdisciplinary environment are presented in the consecutive points.

#### **4.1 Modelling actuator geometry**

When analysing the equations (3) one can notice that the electromagnetic force depends on the medium volume existing between the levitating object and electromagnet. The assumption of the parallel armature position to the electromagnet is mostly used when the force is calculated and therefore, the model operates well for small distances and regular shapes. Generally, the levitated object has a different shape e.g. spherical or cylindrical and the electromagnet poles can be located at the circumference. In the most general form the air gap volume and its reluctance ought to be included in the model. As mentioned above the electromagnet and object geometries are important while the magnetic field is formed to interact between each other. The geometry of a particular object is designed with the CAD software support. Most of them is based on geometry primitives – lines and arcs created with the use of the manual drawing procedure and/or Boolean operations.

The first approach to the AMLS interdisciplinary modelling was based on the designed CAD drawings. The exported stator shapes were used at the modelling stage to carry magnetic flux. The COMSOL CAD translation feature allows to save a great deal of time when laying out large or complex models. The designed electromagnet shapes can be imported from DXF files and then used at the magnetic field modelling stage. The second method based on graphical primitives and Boolean operation allows to simply create an electromagnet model corresponding to the standard laminations. The recommended method for creating a virtual prototype in an automatic way is based on the programming approach using the analytical form of polylines including Bézier curves (Piłat, 2007). The obtained form of the AMB components (see Fig. 7) can be easily used at the optimisation stage to find an adequate form of a bearing to a particular application. This modelling tool allows to parameterise the whole AMLS geometry along with rounded corners.

The AMB front and back planes are parallel, thus the 3D form can be extruded from the 2D shape. In this case the modelling process can be performed in the 3D space without extra CAD/CAM software interaction. Moreover, the drawing resolution set in 2D is kept in 3D space. Figure 7c presents a 3D view of the AMB prototype form with a specified depth.



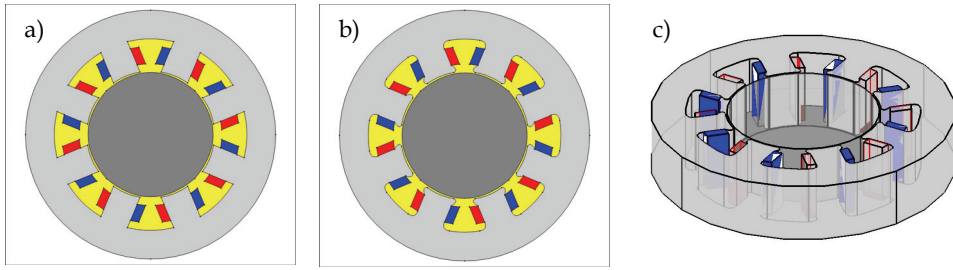


Figure 7. Automatically generated AMB shapes: a) standard form b) smooth form c) 3D model

The same methods can be applied to any electromagnet design and/or electrical drives. The geometry components account for an initial form for the interdisciplinary modelling stage.

#### 4.2 Modelling magnetic field

The results presented in this chapter have been obtained using the magnetostatic mode for analysis purposes. The magnetostatic module is one of the COMSOL software features based on Maxwell's equations.

Four areas can be considered in the analysed example (Fig. 8a):

Two ferromagnetic elements: the stator in three parts and the shaft. The stator core consists of thin laminated electrical steel plates for the purpose of reducing eddy current effects and characterized by a nonlinear function of relative permeability. The shaft is made of iron block.

The air gap that fills the area between the stator, rotor, coils and the shaft is assumed as a paramagnetic region.

Coils made of copper wire wound up on the stator pole shoe. The magnetizing current is required to set up a given magnetic flux in the iron circuit. The number of turns and the current level determine the flux intensity and the electromagnetic force, respectively. The coil along with the pole shoe make an electromagnet called the solenoid actuator.

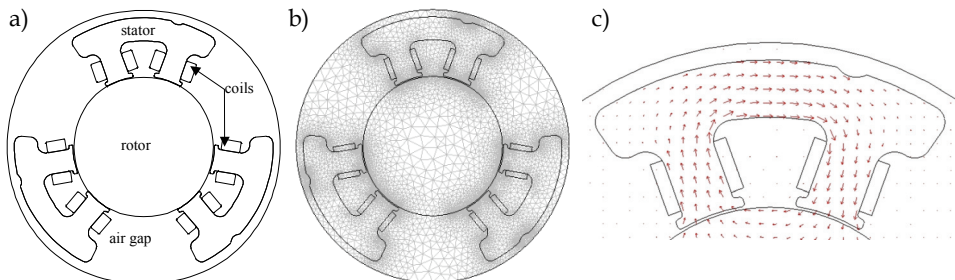


Figure 8. AMB FEM modelling a) subdomains, b) mesh, c) magnetic flux density in the selected stator

The results of the previous research (Piłat, 2004) have been very useful in the three-coil AMB design. The experience in the CAD design and the import advantages of the COMSOL CAD files have been very helpful in the model formulation (Fig. 8a). Coils represented by the rectangular model components have been formulated in the COMSOL Draw Mode to achieve the required quality of the adherent regions. For the precise CAD import it is recommended to select import parameters with respect to the geometric sizes, the appropriate material qualities have been assigned to the selected subdomains. The coil current density has been set using parameters for easy value modification. In this study 2 rotors have been considered: the pipe-type and the solid ones. The next step in the analysis of the bearing construction is the mesh generation (see Fig. 8b). The mesh parameters have been set to achieve the best performance in the most important regions: the interior of the stator and the air gap between the rotor and stator.

For the desired coil parameters: a number of turns, the current value and the coil intersection surface it is possible to calculate the current density. The nonlinear function of electrical steel magnetization (see Fig. 12b) has been used in sequence to obtain realistic results of calculations. The performed analysis of the magnetic flux flow through the magnetic core shows that the areas with the highest flux density are concentrated at the stator edges and coil windings. Smooth edges in the stator construction result in the minimization of the flux concentration. The highest density of the magnetic flux is located in the stator pole shoes at the shortest path of the magnetic flux. The flux direction flow is determined by the coil current direction (Fig. 8c). The analysis of the rotor influence shows that it is possible to modify its construction while the parameters of the magnetic circuit remain the same (Fig. 9).

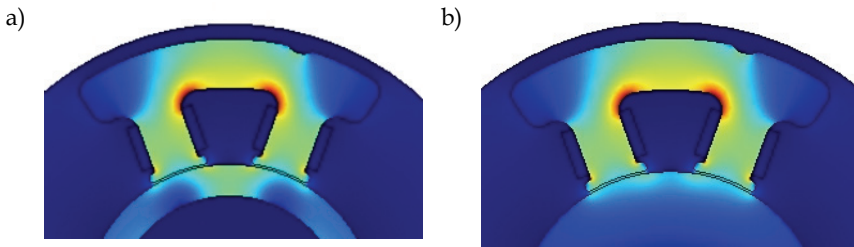


Figure 9. Magnetic flux density in the selected stator with two types of the rotor: a) pipe-type, b) disk-type

The research that follows focuses on the shaft movement influence on the magnetic field in the AMB. Figure 10 presents the potential of the magnetic field while the rotor is located at the bearing centre and moved vertically 300 micrometers up and down with respect to the bearing centre. The potential of the magnetic field is changed due to the rotor motion while the current density remains the same. This fact is obvious but important for the AMB dynamics modelling and the controller synthesis. In case of the rotor movement the air gap width changes under the pole shoes. The air gap change is nonlinear due to the circular shaft shape and the air gap size with respect to the shaft diameter. In case of the three-coil AMB this nonlinear gap change plays an important role in the nonlinear bearing dynamics modelling and the controller synthesis. The magnetic flux change strongly depends on the distance between the shaft and the pole shoe. Thus, when the air gap decreases, the magnetic flux increases, and conversely (Fig. 10).

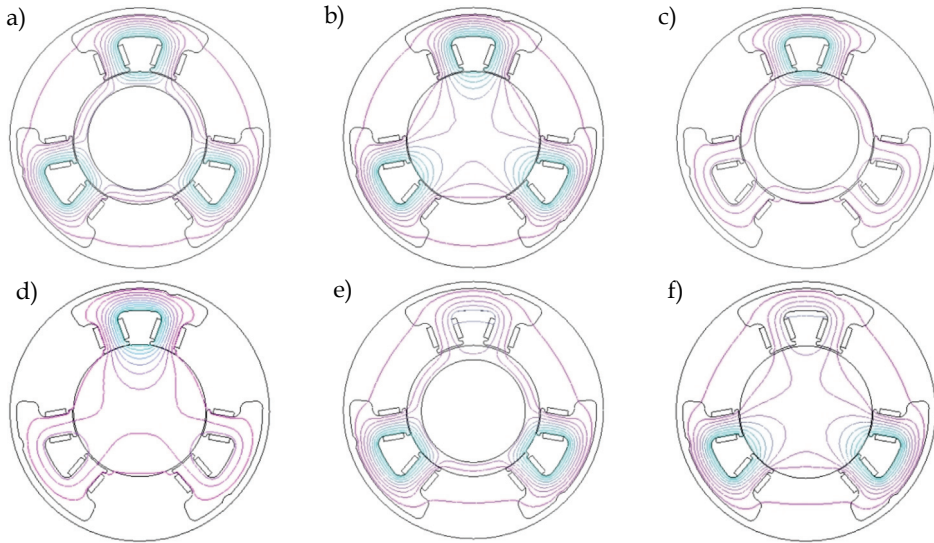


Figure 10. Magnetic potential in the AMB at various rotor configurations

In conventional active magnetic bearings the rotor is stabilized by the control algorithm based on the rotor displacement measurements. High quality eddy currents probes are used to precisely measure the rotor position in the bearing area. The aim of the research that follows is to analyse the flux sensor application. That part of the bearing stator has been specially designed (see Fig. 11a). While using the COMSOL feature that allows to measure field properties at the defined point the magnetic potential was measured at different rotor displacements. For the selected electromagnet three additional points (Left, Sensor, Right) were created for postprocessing purposes (see Fig. 11a). In the course of the application of the selected points the magnetic field potential (Wb/m) has been evaluated.

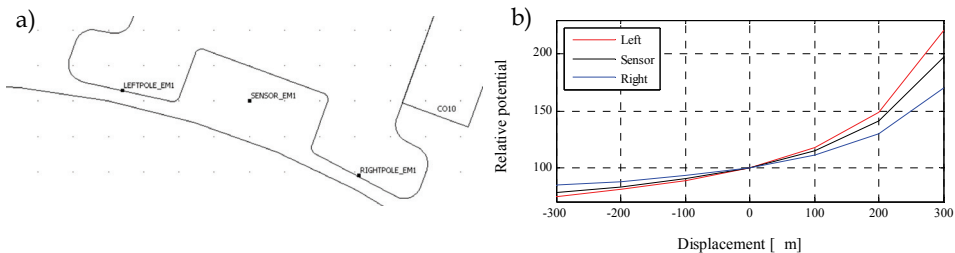


Figure 11. The designed pole for sensing purposes with diagnostic points (Left, Sensor, Right) and simulated relative potential

The magnetic field calculation procedure consists of the following steps: modification of the rotor location at the bearing plane, solution of the problem, data reading form the specified points. This procedure has been executed for the vertical and horizontal rotor movement. The obtained magnetic potential values were related to the value calculated for the central

rotor position (Fig. 11b). This factor shows changes in the magnetic field when the rotor movement occurs.

The vertical movement represents the axial movement regarding the upper stator axis. Positive values correspond to the rotor movement in the upright directions. The horizontal rotor movement is realized in the perpendicular axis and positive values indicate the right side location. This analysis shows that the sensor can be located in the stator pole. Its displacement characteristics are nonlinear and depend on the rotor movement. For the rotor variations up to 10% of the nominal radial air gap the sensor characteristics can be successfully linearized which is favourite for the controller design and operation.

### 4.3 The AMLS interdisciplinary modelling and simulation

The presented magnetostatic approach is one of the modes that are available in COMSOL Multiphysics. Considering the AMLS the dynamics study is the most important condition of modelling and simulation. The formula (4) describing the levitated object dynamics contains the electromagnetic force which ought to be calculated with the accurate configuration of the device. With Maxwell equations this force could be calculated as the surface stress tensor. The following appropriate qualities are set to the AMLS subdomains: copper, air, iron, magnetisation curve for stator steel material (See Fig. 12a). The physical properties of electrical steel are measured (at 50Hz) and specified by manufacturers (see Fig. 12b).

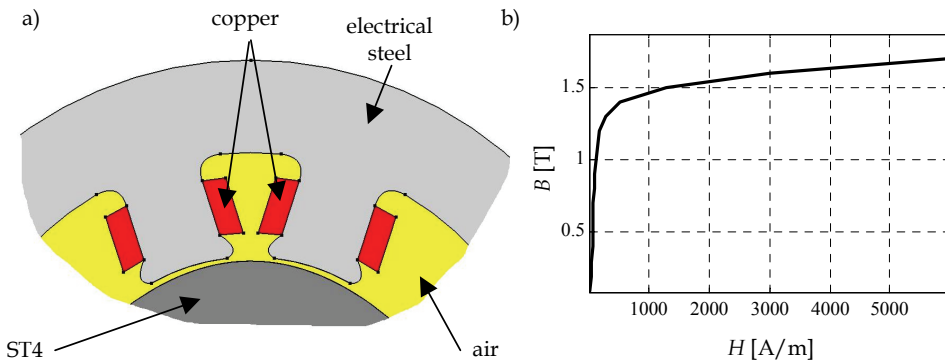


Figure 12. Materials assignment: a) AMB subdomains, b) nonlinear magnetization curve of non oriented steel strip M330-50A. (On courtesy of STALPRODUKT-Bochnia S.A.)

The realistic model of the system is obtained. The appropriate PDE related to the AC/DC perpendicular currents module allows to calculate the electromagnetic field affecting the object. The dynamical movement is described by the ODE equation and the state variables are used to modify the moving mesh status. With this feature the dynamical behaviour of the levitated object can be studied. Moreover, the coil current is controlled from the MATLAB/Simulink where the appropriate controller is implemented. Taking this into account, all existing models and designed controllers can be used in this complex multiphysics modelling and simulation mode. Moreover, the created interdisciplinary model can be extended with additional modes: e.g. heating, fluid. Having a set of PDEs the complex multiphysics model representing the real system can be achieved.

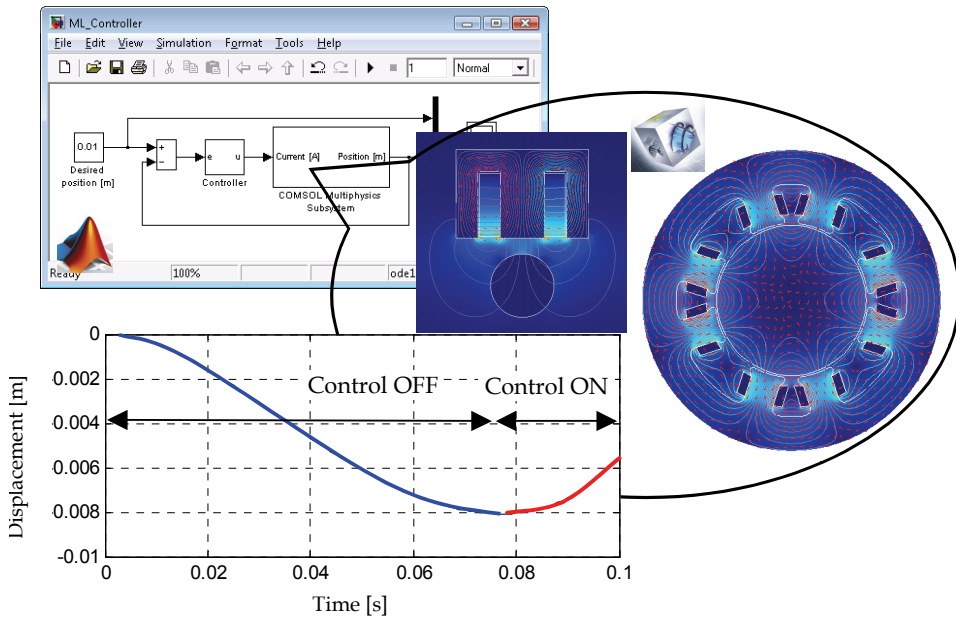


Figure 13. Interdisciplinary dynamics modelling and simulation

With this kind of modelling and simulation the power losses, eddy currents, resistive heating and more and more physical phenomena could be considered. Finally, this modelling and simulation methodology can be used in the rapid prototyping path for the real-time system operation (see Fig. 14).

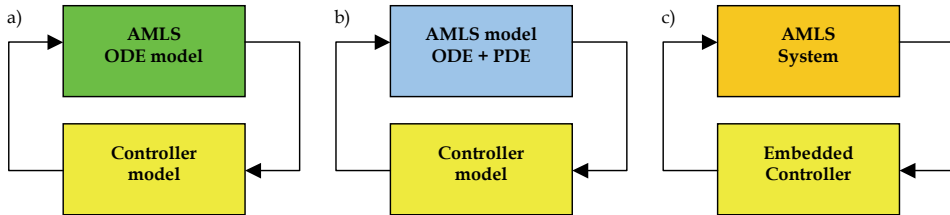


Figure 14. Model based controller design and analysis development path: a) typical, b) proposed, c) implemented

The interactive modelling and simulation are becoming an element in the controller design and development stage. The suggested controller can be validated on the realistic model of the AMLS and then successfully applied to the dedicated hardware.

### 7. Conclusion

One of the advantages of the proposed modelling and simulation methodology is the connection of many disciplines for their co-interaction to perform a multidisciplinary analysis. With the use of graphical modelling and representation of the designed

components along with the Finite Element Method it is possible to obtain a virtual model of the designed system. Moreover, while using time-dependent solvers and simulating the prototype under the controller supervisory the system dynamics can be studied. The obtained virtual prototype contains all elements of a new device. With the detailed analysis and optimisation procedures the virtual prototype could be modified to satisfy all criteria required in the machine operation.

Nowadays, the main disadvantage of this method is the limited performance of existing computers. In this case it is impossible to simulate in the real-time the dynamics of the machine equipped with AMLS (e.g. rotor levitated in Active Magnetic Bearings). The announced development of the COMSOL Multiphysics software and application of grid computing will allow to model and simulate large-scale dynamical problems. The powerful hardware will allow to create a virtual prototype of the designed devices.

It is possible to optimise and reconfigure the AMLS construction having the geometry generated in a programmable way with respect to the required criteria.

The actual and future work will be focused on the AMLS model development to cover all possible physical phenomena, existing interactions, component properties and the controller interaction to be as close as possible to the real working system. The most important question is how to obtain such a model solvable in a real-time for control purposes (model predictive control, model reference control)? These goals could be satisfied with a wide range of identification experiments and application of the proposed methods running on a powerful computer.

Calculations based on the finite element method give a deeper insight into the phenomena of the AMLS. The performed analysis plays an important role in the design procedures of AMLS and helps in the verification of the construction assumptions. It is essential to use appropriate materials for the shaft and stator. The pole shoes arrangement, their sizes and coil parameters strongly influence the electromagnetic force value produced by the electromagnet. As shown above the design procedure of the AMLS is a complex task consisting of a few elements: analysis of the AMLS operating mode parameters, calculation of electromagnetic force, selection of materials and calculation of magnetic field properties to obtain the desired force value, and the choice of the controller architecture. The application of the COMSOL package gives a possibility to establish a connection with the MATLAB/Simulink, with data exchange. This is very useful when the multiphysics analysis is connected with the control algorithm design. The computational effort strongly depends on the mesh density.

Current author's research realized in the framework of the Polish Post-Doc project is focused on 2D and 3D modelling and analysis using the electromagnetic module together with Simulink interactions to examine the static and dynamic AMB behaviour in the real operation environment. Accordingly to the author's knowledge this kind of methodology has never been applied to Active Magnetic Levitation Systems.

## 8. Acknowledgement

Thanks to the Lord for some talents and to my family for love. Special acknowledgment goes to COMSOL A.B. ([www.comsol.com](http://www.comsol.com)) for the recent version of the COMSOL Multiphysics software and COMSOL local distributor in Poland Technika Obliczeniowa ([www.tobl.com.pl](http://www.tobl.com.pl)). You are cordially invited to visit the AGH page related to magnetically levitated systems [www.maglev.agh.edu.pl](http://www.maglev.agh.edu.pl) and my private homepage

home.agh.edu.pl/~ap. Some of presented results have been obtained during the realized research POL-POST DOC II held by Białystok Technical University (www.air.pb.edu.pl).

## 9. References

- Brauer, J. R. (2006). *Magnetic Actuators and Sensors*, John Wiley & Sons, Inc., ISBN: 978-0-471-73169-6, New Jersey.
- Earnshaw, S. (1842). On the nature of the molecular forces which regulate the constitution of the luminiferous ether., *Trans. Camb. Phil. Soc.*, 7, pp 97-112 (1842)
- Braunbeck, W. (1939). Free suspension of bodies in electric and magnetic fields, *Zeitschrift für Physik*, 112, 11, pp. 753-763, (1939)
- Jayawant, B.V. (1981). *Electromagnetic Levitation and Suspension Systems*, Publishers: Edward Arnold, London, 1981
- Banks, J. (ed.) (1998). *Handbook of Simulation, Principles, Methodology, Advances, Applications, and Practice*, John Wiley & Sons, Inc., ISBN 0-471-13403-1, New York
- Comsol 3.3 (2007). *User's Guide and Introduction*, COMSOL AB, Sweden.
- Gosiewski, Z. (1993). *Magnetic bearings for rotary machinery. Theoretical Basis.*(in Polish) Wyższa Szkoła Inżynierska, Koszalin 1993.
- Gosiewski, Z. & Falkowski, K. (2003), *Multifunction magnetic bearings*, (in Polish), Biblioteka Naukowa Instytutu Lotnictwa. Warszawa,
- Grega, W. & Piłat, A. (2001). A Comparison of Nonlinear Controllers for Magnetic Levitation System. *Proc. of 5<sup>th</sup> World Multiconference on Systemics, Cybernetics and Informatics*, July 2001, Orlando-Florida, USA
- Habermann, H. & Liard, G. (1979). Practical Magnetic Bearings, *IEEE Spectrum*, Vol. 16, No. 9, September, 1979
- Hammond, P. & Sykulski J. K. (1994). *Engineering Electromagnetism – Physical Processes and Computation*, Oxford University Press, ISBN 0-19-856289-6, New York.
- Kanebako, H. & Okada, Y. (2002), New Design of Hybrid type Self-Bearing Motor for High-Speed Miniature spindle, *Proc. of The Eighth International Symposium on Magnetic Bearings*, August 2002, Mito, Japan
- Kozanecka, D. (2000). *Digitally controlled magnetic bearing*. (in Polish). Zeszyty Naukowe Politechniki Łódzkiej, Łódź, 2000.
- Maslen, E. (1995). *Magnetic Bearings*. University of Virginia, Department of Mechanical, Aerospace and Nuclear Engineering, Charlottesville, Virginia, 1995.
- Meeker, D.C & Maslen, E. (2006). Analysis and Control of a Three Pole Radial Magnetic Bearing, *Proceedings of 10<sup>th</sup> International Symposium on Active Magnetic Bearings*, August 2006, Martigny, Switzerland
- Noh, M. D. & Maslen, E. H.: Self Sensing Active Magnetic Bearings Based on Parameter Estimation. *IEEE Transactions on Instrumentation and Measurement*, 46(1), 1997 February, pp. 45 ÷ 50.
- Ohmori, K.; Kim, S.; Masuzawa, T. & Okada, Y. (2002). Design of an Axial-type Self Bearing Motor for Small Axial Pump, *Proc. of The Eighth International Symposium on Magnetic Bearings*, pp. 15 ÷ 20, August 2002, Mito, Japan
- Piłat, A. (1999a). *Magnetic levitation – system description*. AGH, Kraków 1999 (in Polish)
- Piłat, A. (1999b). Genetic algorithms applied to optimal PID controller tuning for magnetic levitation system. *Proc. of Computer Methods and Systems*, pp. 271 ÷ 276, October 1999, Kraków, Poland.

- Piłat, A. (2000). Feedback Linearization and LQ Control for Magnetic Levitation System. *6<sup>th</sup> International Conference on Methods and Models in Automation and Robotics*, pp. 407 ÷ 412, August 2000, Międzyzdroje, Poland,.
- Piłat, A. (2001) Time-Optimal Control for Magnetic Levitation System. *7<sup>th</sup> International Conference on Methods and Models in Automation and Robotics*, pp. 873-878, August 2001, Międzyzdroje, Poland,
- Piłat, A. (2002a). *Control of magnetically levitated systems*. Ph.D. Dissertation (in Polish), AGH University of Science and Technology, Kraków, Poland
- Piłat, A. (2002b). Feedback Linearization Control of AMB System. *Proceedings of The Eight International Symposium on Magnetic Bearings*, August 2002, Mito, Japan
- Piłat, A. (2003). Fuzzy logic controller for Active Magnetic Bearing. *Proceedings of Active Noise and Vibration Control Methods*, May 2003, Kraków, Poland
- Piłat, A. (2004). FEMLab software applied to active magnetic bearing analysis, *International Journal of Applied Mathematics and Computer Science*. 2004, vol. 14 no. 4 spec. iss.: Issues in modelling, optimization and control pp. 497 ÷ 501
- Piłat, A. (2005a). Programmable analog hardware for control systems exemplified by magnetic suspension, *Proc. of Computer Methods and Systems*, pp.143-148, November 2005, Kraków, Poland
- Piłat, A. & Turnau A. (2005b). Self-organizing fuzzy controller for magnetic levitation system, *Proc. of Computer Methods and Systems*, pp. 101-106, November 2005, Kraków, Poland
- Piłat, A. & Grega W. (2005c). Reconfigurable test-rig for AMB control, *Proceedings of 7<sup>th</sup> Conference on Active Noise and Vibration Control Methods*, pp. 1-8, June 2005, Wigry, Poland
- Piłat, A. (2006). PD control strategy for 3 coils AMB, *Proceedings of 10<sup>th</sup> International Symposium on Active Magnetic Bearings*, August 2006, Martigny, Switzerland
- Piłat, A. (2007). Automatic generation of Active Magnetic Bearing geometry with COMSOL Multiphysics, *Proc. of Computer Methods and Systems CMS'07*, pp. 147-150, Krakow, November 2007, Krakow, Poland
- Rothwell, E. J. & Cloud, M. J. (2001). *Electromagnetics*, ISBN 0-8493-1397-X, CRC Press, Boca Raton.
- Sinha, P. K. (1984). Design of Magnetically Levitated Vehicle. *IEEE Transactions On Magnetics*, vol. MAG-20, no. 5, September 1984, pp. 1672 ÷ 1674.
- Sinha, P. K. (1987). *Electromagnetic Suspension. Dynamics & Control*. Peter Perginus Ltd., London.
- Silva, Clarence de W., (2000), *Vibration Fundamentals and Practice*, CRC Press 2000.
- Schweitzer, G. (1976). Characteristics of a Magnetic Rotor Bearing for Active Vibration Control, Paper C239/76, *Proc. of First International Conference on Vibrations in Rotating Machinery*, (1976)
- Schweitzer, G.; Traxler, A. & Bleuler, H. (1994). *Magnetlager*. Springer-Verlag.
- Yeadon, W. H. (ed.) & Yeadon A.W., (2001). *Handbook of small electric motors*, McGraw-Hill, ISBN 0-07-072332-X, New York.
- Zienkiewicz, O. C. & Taylor, R. L. (2000). *The Finite Element Method. Vol. 1. The Basis*. 5<sup>th</sup> ed., Butterworth-Heinemann, ISBN 0 7506 5049 4, Oxford



# Modeling and Simulation of Piezoelectric Devices

Dorina Popovici, Florin Constantinescu, Mihai Maricar, Florea Ioan Hantila, Miruna Nitescu and Alexandru Gheorghe  
*Politehnica University of Bucharest  
Romania*

## 1. Introduction

The piezoelectric effect occurs in materials for which an externally applied elastic strain causes a change in electric polarization which produces a charge and a voltage across the material. The converse piezoelectric effect is produced by an externally applied electric field, which changes the electric polarization, which in turn produces an elastic strain.

The most known piezoelectric material is quartz crystal. Many other natural crystalline solids, as Rochelle salt, ammonium dihydrogen phosphate, lithium sulfate, and tourmaline as well as some man-made crystal as gallium orthophosphate, aluminium nitride (AlN), and langasite exhibit piezoelectric properties. A lot of artificial ceramics as barium titanate, lead titanate, lead zirconate titanate (PZT), potassium niobate, lithium niobate, and lithium tantalite have similar properties.

The most known technical application is the piezoelectric transducer. In the last years electromechanical AlN resonators emerged as a very efficient solution for mobile communications filters due to the possibility to be integrated at a relatively low cost together with CMOS circuits in systems on a chip and systems in a package.

In most applications the piezoelectric devices have a linear behaviour. In Section 2 the linear and nonlinear equations of the piezoelectric effect are described, a new iterative procedure for solving the nonlinear equations is given, and some aspects of the Finite Element solution are discussed. An electromechanical field analysis of a displacement transducer is presented in Section 3. Sections 4 and 5 show some recent applications in the mobile communication technology. The field analysis of a bulk acoustic wave (BAW) resonator using 3D linear models is presented in Section 4. Some nonlinear effects in power BAW resonators together with their circuit models are discussed in Section 5.

## 2. Electromechanical field equations of piezoelectric devices

### 2.1 Linear behaviour

In the case of linear behaviour (Cady, 1964; Wilson, 1989), the equations giving the

displacement  $\mathbf{u}$ , the stress  $\bar{\mathbf{t}}$  and the electric potential  $V$  are<sup>1</sup>:

$$\nabla \cdot \bar{\mathbf{t}} - \mathbf{f}_f - \rho \ddot{\mathbf{u}} = \mathbf{f} \quad (1)$$

$$-\nabla \cdot \bar{\boldsymbol{\varepsilon}} \nabla V + \nabla \cdot \mathbf{P}_M = 0 \quad (2)$$

where:

- $\bar{\boldsymbol{\varepsilon}}$  is the dielectric permittivity tensor.
- $\mathbf{f}$  is the external force.

The friction force is:

$$\mathbf{f}_f = \eta \dot{\mathbf{u}} \quad (3)$$

- The stress tensor  $\bar{\mathbf{t}}$  has two components:  $\bar{\mathbf{t}} = \bar{\mathbf{t}}_M + \bar{\mathbf{t}}_E$
- The mechanical stress tensor depends on the strain tensor  $\bar{\mathbf{s}}$ :

$$\bar{\mathbf{t}}_M = \hat{\mathbf{c}}(\nabla_s \mathbf{u}) = \hat{\mathbf{c}} \bar{\mathbf{s}} \quad (4)$$

where  $\hat{\mathbf{c}}$  is the elastic stiffness matrix evaluated for constant electric field intensity,  $\mathbf{E} = -\nabla V$  and  $\nabla_s \mathbf{u} = \frac{1}{2}[(\nabla \mathbf{u}) + (\nabla \mathbf{u})^T]$  (the superscript  $T$  denotes the transpose of the matrix).

- The piezoelectric stress tensor depends on the electric field intensity:

$$\bar{\mathbf{t}}_E = \hat{\mathbf{e}}^T(\nabla V) \quad (5)$$

where  $\hat{\mathbf{e}}$  is the piezoelectric matrix.

- The component of the polarization due to the strain is:

$$\mathbf{P}_M = \hat{\mathbf{e}} \bar{\mathbf{s}} = \hat{\mathbf{e}}(\nabla_s \mathbf{u}) \quad (6)$$

Using (3),(4),(5),(6), equations (1) and (2) become:

$$\nabla \cdot \hat{\mathbf{c}}(\nabla_s \mathbf{u}) + \nabla \cdot \hat{\mathbf{e}}^T(\nabla V) - \eta \dot{\mathbf{u}} - \rho \ddot{\mathbf{u}} = \mathbf{f} \quad (7)$$

$$\nabla \cdot \bar{\boldsymbol{\varepsilon}} \nabla V - \nabla \cdot \hat{\mathbf{e}}(\nabla_s \mathbf{u}) = 0 \quad (8)$$

For equations (2) and (8) we consider the static regime of the electric field. In order to have a unique solution, mechanical and electrical boundary conditions must be added:  $\mathbf{u} = 0$ , for clamped surfaces,  $\mathbf{n} \bar{\mathbf{t}} = 0$ , for free surfaces, a hybrid boundary condition (BC) in the case of a very light movable electrode;  $V =$  imposed for electrodes,  $\mathbf{n} \cdot \mathbf{D} = 0$  for field surfaces or symmetry surfaces, where:

$$\mathbf{D} = -\bar{\boldsymbol{\varepsilon}} \nabla V + \mathbf{P}_M \quad (9)$$

<sup>1</sup> Notations: the boldface letters represent vectors, tensors are represented as  $\bar{\mathbf{t}}$ ,  $\nabla \mathbf{u}$  is a diadic product, while  $\nabla \cdot \mathbf{u}$  is a scalar product and a dot above a variable denotes a time derivative..

The friction forces are neglected for modal analysis. Equations (7) and (8) become:

$$\nabla \cdot \hat{c}(\nabla_s \mathbf{u}) + \nabla \cdot \hat{e}^T(\nabla V) + \omega^2 \rho \mathbf{u} = \mathbf{0} \quad (10)$$

$$\nabla \cdot \varepsilon \nabla V - \nabla \cdot \hat{e}(\nabla_s \mathbf{u}) = 0 \quad (11)$$

The values  $\omega_k$  which allow nontrivial solutions  $\mathbf{u}_k$  of equations (10),(11) give resonance frequencies.

## 2.2 Nonlinear constitutive equations

The nonlinear behaviour can be modelled using the nonlinear constitutive equations:

1. The friction force depends nonlinearly on the velocity (time derivative of displacement):

$$\mathbf{f}_f = F(\dot{\mathbf{u}}) \quad (12)$$

2. The relationship  $\bar{t} - \bar{s}$  is nonlinear. This is possible in the case of large strains (powerful stress). The dielectric may be destroyed and the durability decreases. Hence, this case must be avoided.
3. The relationship  $\mathbf{D}-\mathbf{E}$  is nonlinear:

$$\mathbf{D} = \mathbf{D}(-\nabla V) + \mathbf{P}_M \quad (13)$$

We do not know yet results which present this kind of relationship.

4. The relationships of the piezoelectric effects are nonlinear:

$$\bar{t} = \mathbb{T}(\mathbf{E}) \quad (14)$$

$$\mathbf{P}_M = \mathbb{P}(\bar{s}) \quad (15)$$

If the complementary energy may be defined:

$$\delta \mathcal{U}^* = \sum_{i,j=1}^3 t_{ij} ds_{ij} - \sum_{k=1}^3 P_k dE_k \quad (16)$$

we have:

$$\frac{\partial T_{ij}}{\partial E_k} = -\frac{\partial P_k}{\partial s_{ij}} \quad (17)$$

In the linear case, relationship (17) defines the same matrix  $\hat{e}$  in (5) and (6).

## 2.3 Iterative Procedures for Nonlinear Materials

The usual method taking into account the nonlinearity is Newton-Raphson, which is used in most commercial simulators. This method provides a great convergence speed, but in some cases the convergence is not always achieved.

The nonlinearity of the friction force relationship may be treated using the fixed point Picard-Banach procedure. We replace the relation (12) by:

$$\mathbf{f}_f = \eta \dot{\mathbf{u}} + \mathbf{f}_r \quad (18)$$

where the nonlinearity is contained in:

$$\mathbf{f}_r = F(\dot{\mathbf{u}}) - \eta \dot{\mathbf{u}} = G(\dot{\mathbf{u}}) \quad (19)$$

It may be proved (Hantila et al., 2000) that if the function  $F$  is uniformly monotonic

$$(F(\mathbf{a}) - F(\mathbf{b})) \cdot (\mathbf{a} - \mathbf{b}) \geq \lambda |\mathbf{a} - \mathbf{b}|^2, \quad \lambda > 0, \quad \forall \mathbf{a}, \mathbf{b} \quad (20)$$

and Lipschitzian

$$|F(\mathbf{a}) - F(\mathbf{b})| < A |\mathbf{a} - \mathbf{b}|, \quad \forall \mathbf{a}, \mathbf{b} \quad (21)$$

we can find a value for  $\eta$  so that the function  $G$ , defined by (19) is a contraction i.e.

$$|G(\mathbf{a}) - G(\mathbf{b})| \leq \theta |\mathbf{a} - \mathbf{b}|, \quad \theta < 1, \quad \forall \mathbf{a}, \mathbf{b} \quad (22)$$

We propose the following iterative procedure:

- We choose an arbitrary initial value  $\mathbf{f}_r^{(0)}$ .
- We compute  $\mathbf{u}^{(1)}$  and hence  $\dot{\mathbf{u}}^{(1)}$  solving the system (7) and (8), where the force  $\mathbf{f}$  is replaced by  $\mathbf{f} + \mathbf{f}_r^{(0)}$ .
- We correct the force  $\mathbf{f}_r$  with (19):

$$\mathbf{f}_r^{(1)} = G(\dot{\mathbf{u}}^{(1)}) \quad (23)$$

The steps b) and c) are repeated until the error

$$er^{(n)} = \int_{\Omega} \int_0^t \eta (\Delta \dot{\mathbf{u}}^{(n)})^2 d\tau d\Omega = \|\Delta \dot{\mathbf{u}}^{(n)}\|_{\eta}^2 \quad (24)$$

is small enough, where  $\Delta \dot{\mathbf{u}}^{(n)} = \dot{\mathbf{u}}^{(n)} - \dot{\mathbf{u}}^{(n-1)}$ .

It may be proved that for a given  $\mathbf{f}_r$  equations (7) and (8) have a unique solution  $\mathbf{u}$ , hence  $\dot{\mathbf{u}} = W(\mathbf{f}_r)$  and the function  $W$  is non-expansive:

$$|W(\mathbf{a}) - W(\mathbf{b})| \leq |\mathbf{a} - \mathbf{b}|, \quad \forall \mathbf{a}, \mathbf{b} \quad (25)$$

Therefore, the above procedure gives the Picard-Banach convergent sequence of the contraction  $GW$ , where the function  $G: L^2([0, t] \times \Omega) \rightarrow L^2([0, t] \times \Omega)$  is defined by the local function  $G$ . The procedure has several important advantages: we may evaluate the errors with respect to the exact solution, the overrelaxation may be applied, the system matrix of the numerical form of equations (7), (8) is the same at each iteration.

The most convenient procedure for space discretization of equations (7), (8) is the finite element method (see (Makkonen et al., 2001), for instance). The spectral decomposition is recommended for time discretization.

### 2.4 FEM solution of the coupled electromechanical field problem

In Finite Element Method (FEM), the complete problem domain is discretized. This implies that FEM encounters inherent difficulties in dealing with open boundary field problems, as the problem domain needs to be truncated to keep the size finite. Truncation inevitably introduces an artificial boundary and, consequently, a modelling error resulting from an approximation of the BC on this boundary. Considering acoustic waves, the truncation of the model causes reflections of the wave on the artificial boundaries (see Fig. 1).

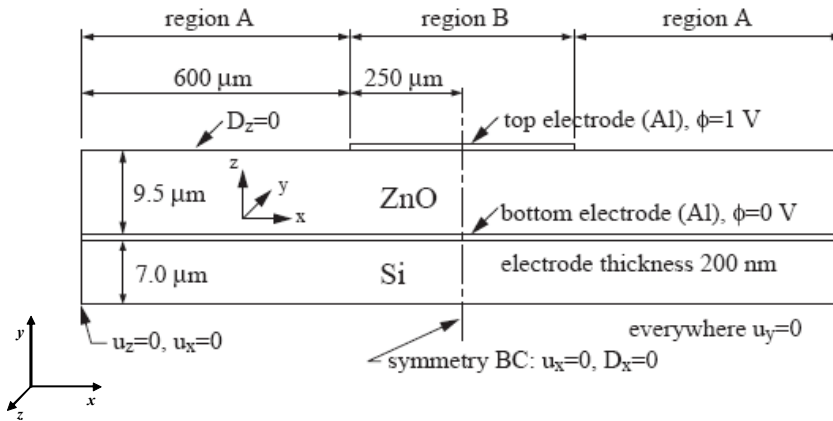


Figure 1. Cross section of a membrane-type composite thin-film BAW resonator showing the boundary conditions imposed in the FEM model

Placing infinite elements along the artificial boundary on the side of the continuum has been suggested as a solution to this problem. The infinite elements strive to implement an ideal absorbing boundary condition, such that a wave incident on the boundary would not reflect back. Instead of infinite elements, one may simply introduce regions at the boundaries of the model where the attenuation of the material increases from zero to a given finite value. Since the increase of the attenuation is gradual, there is no abrupt change in the materials properties which would give rise to reflections of the wave. With a sufficiently high attenuation, the amplitude of the wave entering the region will decay rapidly such that there is no reflection. This solution has the benefit that it can be readily applied without any need for special FEM elements (Makkonen, 2005).

A possible solution is to combine FEM with another method which is used to model the semi-infinite region. An example of such a modelling technique is the FEM/boundary-element-method (BEM) formalism, which is used in the modelling of surface-acoustic wave devices.

The electromechanical constitutive equations for linear material behaviour that FEM softwares solve are:

$$\begin{aligned} \mathbf{T} &= c_E \mathbf{S} - e \mathbf{E} \\ \mathbf{D} &= e^T \mathbf{S} + \epsilon_S \mathbf{E} \end{aligned} \tag{26}$$

where:  $\mathbf{T}$  is the stress vector (referred to as  $\sigma$  elsewhere);  $\mathbf{D}$  is the electric flux density vector;  $\mathbf{S}$  is the strain vector (referred to as  $\epsilon$  elsewhere);  $\mathbf{E}$  is the electric field vector;  $c_E$  is the

elasticity matrix (evaluated at constant electric field);  $e$  is piezoelectric stress matrix, and  $\varepsilon_S$  is the dielectric matrix (evaluated at constant mechanical strain).

The elasticity matrix  $c$  can be given directly in uninverted form  $[c]$  as a general anisotropic symmetric matrix:

$$c_E = \begin{bmatrix} c_{11} & c_{12} & c_{13} & c_{14} & c_{15} & c_{16} \\ & c_{22} & c_{23} & c_{24} & c_{25} & c_{26} \\ & & c_{33} & c_{34} & c_{35} & c_{36} \\ & & & c_{44} & c_{45} & c_{46} \\ \text{symmetric} & & & & c_{55} & c_{56} \\ & & & & & c_{66} \end{bmatrix} \quad (27)$$

The input can also be  $c_D$ , the elasticity matrix (evaluated at constant electric flux density):

$$c_D = c_E + \frac{e^2}{\varepsilon_S} \quad (28)$$

The piezoelectric stress matrix  $e$  relates the electric field vector  $\mathbf{E}$  in the order  $x, y, z$  to the stress vector  $\mathbf{T}$  in the order  $x, y, z, xy, yz, xz$  and has the form:

$$e = \begin{bmatrix} e_{11} & e_{12} & e_{13} \\ e_{21} & e_{22} & e_{23} \\ e_{31} & e_{32} & e_{33} \\ e_{41} & e_{42} & e_{43} \\ e_{51} & e_{52} & e_{53} \\ e_{61} & e_{62} & e_{63} \end{bmatrix} \quad (29)$$

The piezoelectric matrix can also be given as a piezoelectric strain matrix  $d$ . The piezoelectric strain matrix  $d$  can be converted to the piezoelectric stress matrix  $e$  using the elasticity matrix  $c$ :

$$e = c \cdot d \quad (30)$$

The dielectric matrix  $\varepsilon_S$  uses the electrical permittivities and can be described in orthotropic or anisotropic form:

$$\varepsilon_S = \begin{bmatrix} \varepsilon_{11} & 0 & 0 \\ 0 & \varepsilon_{22} & 0 \\ 0 & 0 & \varepsilon_{33} \end{bmatrix} \text{ or } \varepsilon_S = \begin{bmatrix} \varepsilon_{11} & \varepsilon_{12} & \varepsilon_{13} \\ & \varepsilon_{22} & \varepsilon_{23} \\ \text{symmetric} & & \varepsilon_{33} \end{bmatrix} \quad (31)$$

The dielectric matrix can also be given as a dielectric permittivity matrix at constant stress  $\varepsilon_T$ . We can convert the dielectric matrix at constant stress to the dielectric matrix at constant strain:

$$\varepsilon_S = \varepsilon_T - e^T d \quad (32)$$

The finite element discretization is performed by establishing nodal solution variables and element shape functions over an element domain which approximates the solution.

$$u_c = N_u^T \cdot u \quad (33)$$

$$V_c = N_V \cdot V \quad (34)$$

where:  $u_c$  is the displacement within element domain in the  $x, y, z$  directions;  $V_c$  is the electrical potential within element domain;  $N_u$  is the matrix of displacement shape functions;  $N_V$  is the vector of electrical potential shape function;  $u$  is the vector of nodal displacements, and  $V$  is the vector of nodal electrical potential.

Then the strain  $\mathbf{S}$  and electric field  $\mathbf{E}$  are related to the displacements and potentials, respectively, as:

$$\mathbf{S} = B_u \cdot u \quad (35)$$

$$\mathbf{E} = -B_V \cdot V \quad (36)$$

$$B_u = \begin{bmatrix} \frac{\partial}{\partial x} & 0 & 0 & \frac{\partial}{\partial y} & 0 & \frac{\partial}{\partial z} \\ 0 & \frac{\partial}{\partial y} & 0 & \frac{\partial}{\partial x} & \frac{\partial}{\partial z} & 0 \\ 0 & 0 & \frac{\partial}{\partial z} & 0 & \frac{\partial}{\partial y} & \frac{\partial}{\partial x} \end{bmatrix}^T \quad (37)$$

$$B_V = \begin{bmatrix} \frac{\partial}{\partial x} & \frac{\partial}{\partial y} & \frac{\partial}{\partial z} \end{bmatrix}^T \quad (38)$$

After the application of the variational principle and finite element discretization, the coupled finite element matrix equation is:

$$\begin{bmatrix} M & 0 \\ 0 & 0 \end{bmatrix} \begin{bmatrix} \ddot{u} \\ \ddot{V} \end{bmatrix} + \begin{bmatrix} C & 0 \\ 0 & 0 \end{bmatrix} \begin{bmatrix} \dot{u} \\ \dot{V} \end{bmatrix} + \begin{bmatrix} K & K_z \\ K_z^T & K_d \end{bmatrix} \begin{bmatrix} u \\ V \end{bmatrix} = \begin{bmatrix} F \\ L \end{bmatrix} \quad (39)$$

The following equations provide an explanation of the submatrices in (39). Structural mass ( $\rho$  is the mass density):

$$M = \int_{\text{element}} \rho N_u N_u^T dv \quad (40)$$

The damping matrix (C) may be used in harmonic, damped modal and transient analyses as well as substructure generation. In its most general form, it is:

$$M = \alpha M + (\beta + \beta_c) K + \sum_{j=1}^{N_m} \left[ \left( \beta_j^m + \frac{2}{\Omega} \beta_j^s \right) K_j \right] + \sum_{k=1}^{N_s} C_k + C_s \quad (41)$$

where:  $C$  is the structure damping matrix;  $a$  is the mass matrix multiplier;  $M$  is the structure mass matrix;  $\beta$  is the stiffness matrix multiplier;  $\beta_c$  is the variable stiffness matrix multiplier;  $K$  is the structure stiffness matrix;  $N_m$  is the number of materials with  $\beta_j^m$  (stiffness matrix multiplier for material  $j$ ),  $\beta_j^\xi$  (constant (frequency-independent) stiffness matrix coefficient for material  $j$ ,  $\Omega$  - circular excitation frequency) and  $K_j$  the portion of structure stiffness matrix based on material  $j$ ;  $N_e$  is the number of elements with specified damping ( $C_k$  - element damping matrix,  $C_\xi$  - frequency-dependent damping matrix).  
Structural stiffness:

$$K = \int_{\text{element}} B_u^T c B_u dv \quad (42)$$

Dielectric conductivity:

$$K_d = - \int_{\text{element}} B_V^T \epsilon B_V dv \quad (43)$$

Piezoelectric coupling matrix:

$$K_z = - \int_{\text{element}} B_u^T e B_V dv \quad (44)$$

Structural load vector,  $F$ , is a vector of nodal forces, surface forces, and body forces. Electrical load vector,  $L$ , is a vector of nodal, surface, and body charges.

In a FEM mesh, each node point is connected only to a limited number of other nearby located nodes. The benefit of this local connectivity is that the FEM matrices (system matrices) which describe the complete modelled system have a band structure. The relevant system matrices are the electromechanical stiffness matrix  $K$  and mass matrix  $M$ . In each node point of the FEM mesh, at least four field variables are considered (i.e., the three components of displacement and the electric potential). The values of the fields at a node point are the unknowns or degrees of freedom (DOFs) which are finally computed from the FEM equations.

In the modal analysis, the eigenproblem resulting from the FEM formulation is solved for the frequencies of the vibration modes (eigenfrequencies) and for their mode shapes (eigenvectors).

FEM software can also solve the field problem, where the response of the structure to time harmonic loading is computed. In harmonic analysis, the damping can be taken into account, since a solver for complex-valued linear systems of equations can be included into the FEM software.

Starting from coupled electroelastic equations (Ostergaard & Pawlak, 1986) four types of solutions are possible:

- Static Analysis (inertial and damping effects are ignored except static acceleration effects such as gravity; displacements and/or electric potentials are obtained).
- Mode-Frequency Analysis (mode shapes and natural frequencies may be obtained).
- Harmonic Analysis (the investigation of a piezoelectric structure under the influence of harmonic forces, currents, displacements, and/or voltages; system response characteristics to harmonic loads are obtained).



- Transient Analysis (the investigation of a piezoelectric structure under the influence of time-dependent forces, currents, displacements, and/or voltages; transient response of the system is computed).

### 3. Field analysis of a displacement transducer

The FEM analysis of a cantilever beam deformation producing electrical voltages through a direct piezoelectric effect is described in the following (Dorina Popovici et al., 2006).

#### 3.1 Geometry of the model

To simulate the structure we have chosen a multiphysics problem: plane stress and piezo plane stress. The geometry used is presented in figure below:

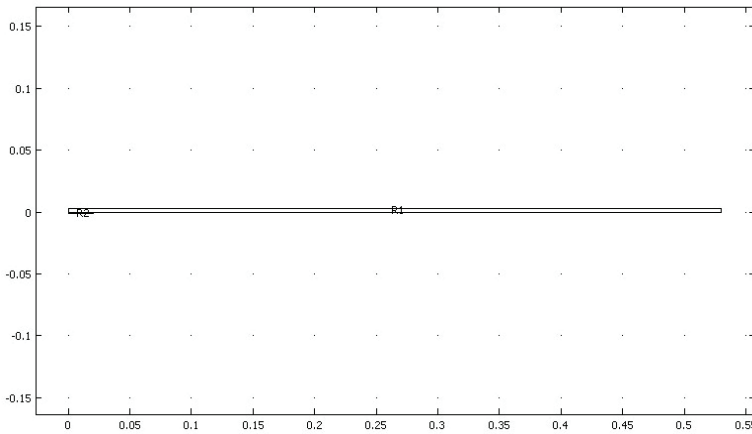


Figure 2. The geometry of the problem

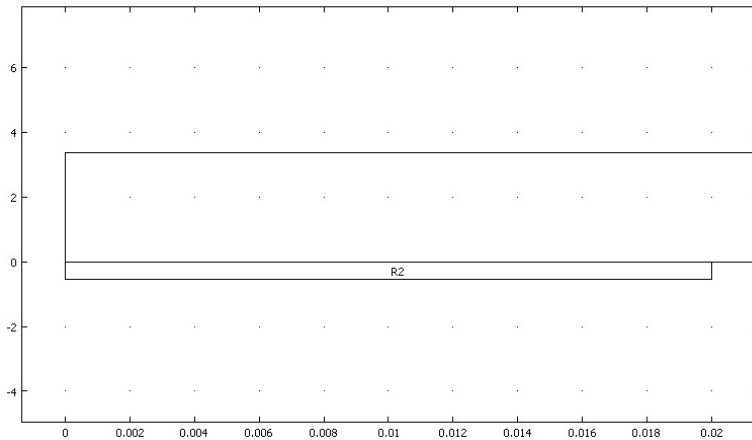


Figure 3. Zoom in the PZT cell section

The domain R1 is an isotropic structural steel beam with a length of 550 mm, width of 50 mm and thickness of 5 mm. This material is defined in Library 1 of (COMSOL, 2005). The domain R2 is the PZT 5H cell which has a length of 20 mm, width of 50 mm and thickness of 0,5 mm.

For the structural steel we used the following material constants  $E = 2 \cdot 10^5$  [MPa], Poisson's ratio  $\nu = 0.33$  and density  $\rho = 7850$  kg/m<sup>3</sup>.

The PZT - 5H properties are those listed in (COMSOL, 2005):  $c_E$  ( $c_{11}=c_{22}=126$ ,  $c_{12}=80.5$ ,  $c_{13}=c_{23}=126$ ,  $c_{33}=117$ ,  $c_{44}=23.3$ ,  $c_{55}=c_{66}=23$ , all in GPa),  $e$  ( $e_{51}=e_{42}=17$ ,  $e_{13}=e_{23}=17$ ,  $e_{33}=23.3$ , [C/m<sup>2</sup>]),  $\epsilon_S$  ( $\epsilon_{11}=\epsilon_{22}=1704$ ,  $\epsilon_{33}=1433$ , relative values).

The boundary conditions resulted from the working conditions. For the mechanical part of the problem a constraint of zero displacement on the left side of the beam and the PZT cell has been considered. The load was applied on the right end of the beam only on the y direction.

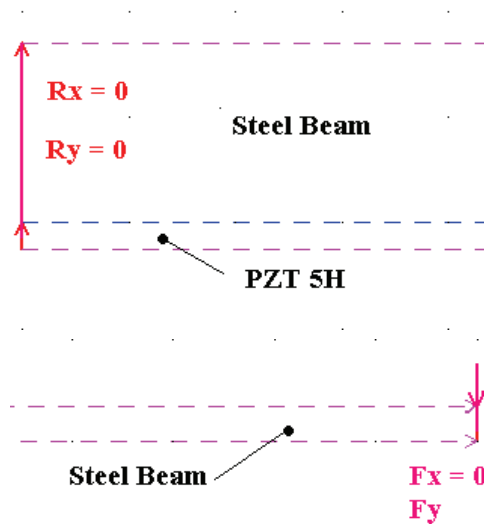


Figure 4. The mechanical boundary conditions

We set the horizontal bottom surface of the PZT cell to ground and a zero charge/symmetry condition was considered on the top surface.

The meshed model contains 3516 triangular elements.

### 3.2 Results

Three basic analysis types available in the Structural Mechanics Module have been considered:

- Static
- Eigenfrequency
- Transient.

At first, a static analysis has been made, where a uniform distributed load has been applied at the right end of the beam. This force has only a vertical component  $f_y = 10000$

N/m. The stationary direct linear solver UMFPACK has been used. In Fig. 5, 6, 7 are represented the displacements along the y axis, the maximum displacement at the end of the beam, and the local voltage along the PZT cell.

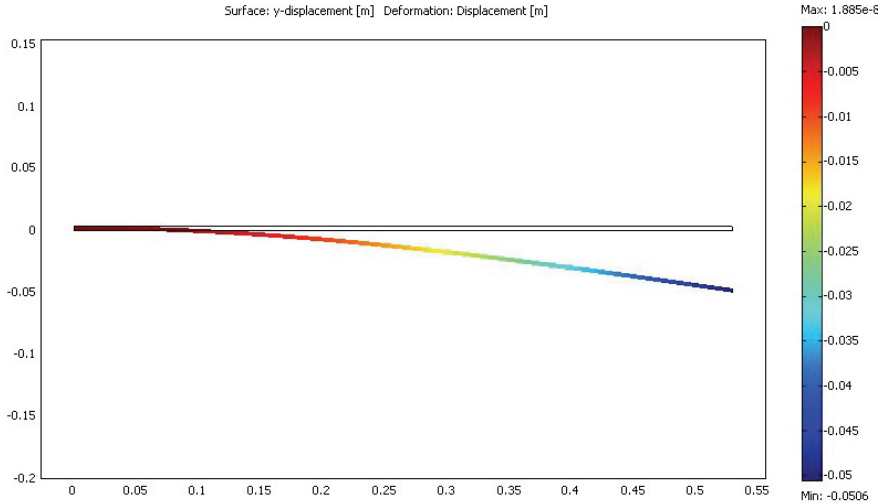


Figure 5. Displacement of the beam on the y axis for  $f_y = 10000$  [N/m]

The maximum stress calculated with Von Mises criteria has been determined in the left side of the beam (in the vicinity of the clamping side) and was equal to 294 [MPa] and the minimum value in the right side of the beam 0,168 [MPa].

The voltage response of the PZT cell at different loads ( $f_y \in \{500, 1000, 2500, 5000, 7500, 10000\}$  [N/m]) has a linear variation as we can see in Fig. 8. For the same loads we determined the displacement on y axis of the right side of the beam (Fig. 9) and the maximum stress values (Fig. 10) which has the same linear variation.

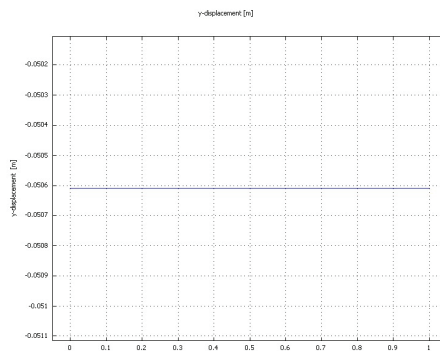


Figure 6. y -displacement of the right end of the beam vs. relative position on z

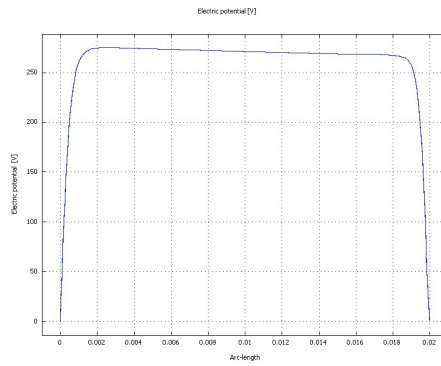


Figure 7. Local voltage vs. longitudinal position along PZT cell

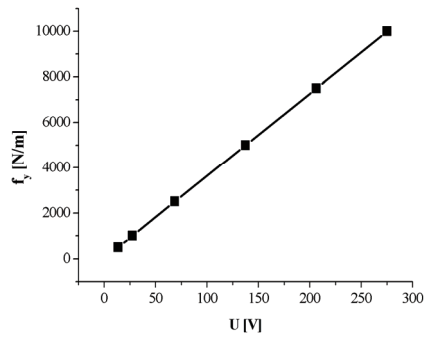


Figure 8. The linear dependence  $F(U)$

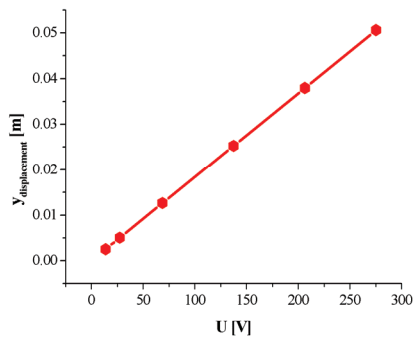


Figure 9. Displacement of the right end of the beam

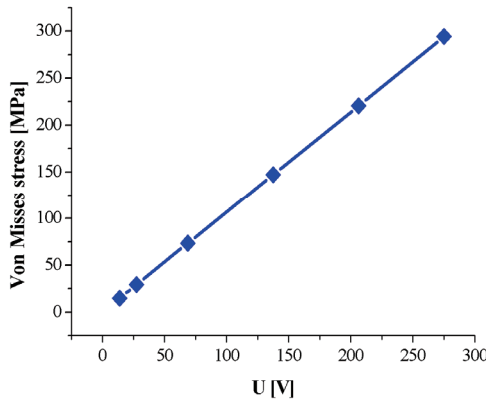


Figure 10. The maximum stress values

The simulation results used to draw figures 8 to 10 are given in Table 1.

$f_y$ [N/m]	Von Misses stress [MPa]	$y_{\text{displacement}}$ [mm]	U [V]
500	14.71	2.53	13.75
1000	29.42	5.06	27.51
2500	73.55	12.65	68.77
5000	147.1	25.30	137.55
7500	220.6	37.95	206.33
10000	294.2	50.61	275.10

Table 1. Values determined in static analysis

An eigenfrequency analysis finds the eigenfrequencies and modes of deformation of the analyzed structure. The eigenfrequencies  $f$  in the structural mechanics field are related to the eigenvalues  $\lambda$  returned by the solvers through:

$$f = \frac{\sqrt{\lambda}}{2\pi}$$

The purpose of the eigenfrequency analysis is to find the six lowest eigenfrequencies and their corresponding shape modes. This model uses the same material, load and constraints as the static analysis. A direct system solver Umfpack was used and the results are presented below:

$f_1$	$f_2$	$f_3$	$f_4$	$f_5$	$f_6$
9.98 Hz	64.48 Hz	174.73 Hz	341.91 Hz	564.31 Hz	841.75 Hz

Table 2. The first six eigenfrequencies of the model

A transient analysis giving the displacements and velocities as functions of time was used. In this case, loads and boundary conditions are functions of time. The purpose of this analysis was to find the transient response to a harmonic load with the same amplitude as the static load during the first two periods. The excitation frequency has been taken 50 Hz,

which is between the first and second eigenfrequency found in the eigenfrequencies analysis.

A harmonic load  $f_x = 0$  and  $f_y = 10000 \sin(100 \pi t)$  [N/m] has been used. Damping is very important in transient analysis but difficult to model. The Structural Mechanics Module supports Rayleigh damping, specifying damping parameters proportional to the mass ( $\alpha_{dM}$ ) and stiffness ( $\beta_{dK}$ ) in the following way:

$$C = \alpha_{dM} M + \beta_{dK} K$$

where  $C$  is the damping matrix,  $M$  is the mass matrix, and  $K$  is the stiffness matrix. The structure has a constant damping ratio of 0.1. Two frequencies near the excitation frequency (20Hz and 60 Hz) have been considered to calculate the damping parameters, according to the FEMLAB code (COMSOL, 2005):  $\alpha_{dM} = 18.849$  1/s and  $\beta_{dK} = 3.979 \cdot 10^{-4}$  s.

The computation used a solver with the time interval  $[0; 0.08]$ [s] within a step of 0.001, a relative tolerance of 0.05 and an absolute tolerance of  $10^{-9}$ .

The following waveforms for the displacement on the x and y axes are represented in Fig.11 and 12.

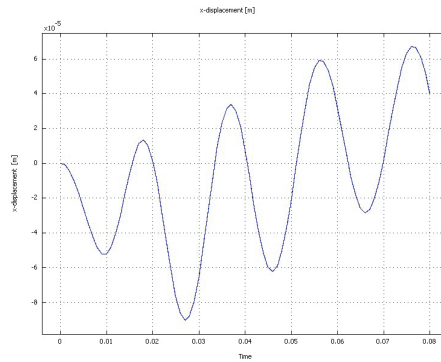


Figure 11. The x displacement of the right end of the beam

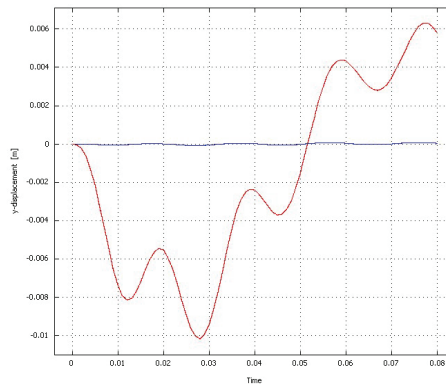


Figure 12. The x displacement (—) and the y displacement (—) of the right end of the beam  
 The voltage output computed on the PZT crystal has a sinusoidal figure with a maximum value of 182.072 [V] and a minimum value of -150.962 V.

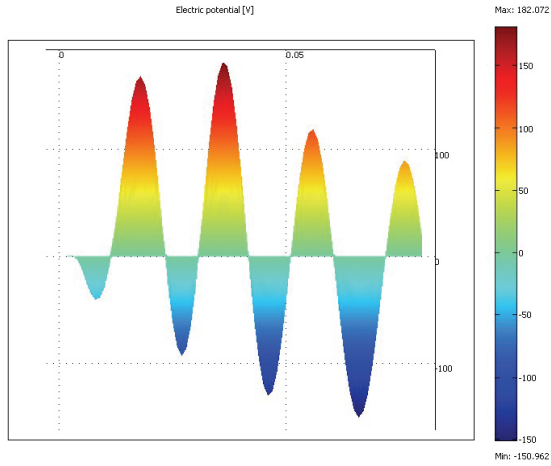


Figure 13. The PZT crystal voltage vs. time

For a more accurate solution the time interval has been increased from 0.08 to 0.2 [s] ; in this case, the total displacement and the equivalent voltage response are represented in Fig.14 and 15.

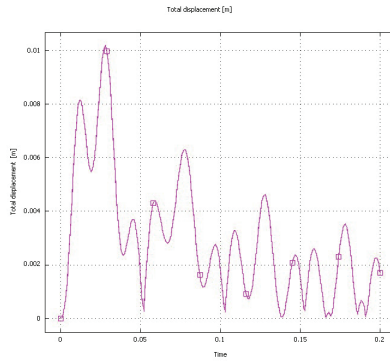


Figure 14. The total displacement of the right side of the beam

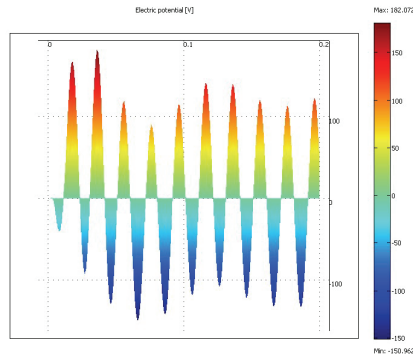


Figure 15. The PZT crystal voltage

#### 4. Field analysis of a BAW resonator

We assume that the cause for material deterioration is the high level of the local stress in resonator layers. It follows that the regions in which material deteriorates correspond to the regions of maximum local stress.

To compute the local stress FEM analysis of a 3D electromechanical field problem must be done. In order to do this, material parameters of various resonator layers must be known. A part of them haven't been measured directly for the case in point, being taken from literature. To verify the parameter values, a model taking into account only longitudinal wave propagation (on z axis) has been analyzed, the results being reported in paragraph 4.1. Further on, a 3D model of a quarter of a resonator is analyzed in paragraph 4.2.

For piezoelectric analysis (ANSYS, 2005) performs the so called "strong coupling analysis" meaning that the whole equation system of the coupled field problem is used.

##### 4.1 Numerical simulation of longitudinal wave propagation in a BAW resonator structure

Mat. No.	Material	Density $\rho$ [kg/m <sup>3</sup> ]	Longitudinal velocity [m/s]	$c_{33}$ [GPa]	$\epsilon_{33}$ [pF/m]	$e_{33}$ [C/m <sup>2</sup> ]
1	Mo	10000	6600	435.6		
3	SiOC	1500	2400	10.14		
4	SiN	2700	9300	233.523		
5	Si	2330	8400	164.4		
6	AlN	3300	11000	399.3	82.6	1.5

Table 3. Material properties used for analytical model simulations

Block No.	Mat. No.	Material
1	4	SiN
3	1	Mo
4	6	AlN
5	1	Mo
6	3	SiOC
7	4	SiN
8	3	SiOC
9	4	SiN
10	3	SiOC
11	5	Si substrate

Table 4. List of materials used to fabricate the device



Additional material properties:

AlN  $c_{11}=345$  GPa,  $c_{12}=125$  GPa,  $c_{13}=120$  GPa,  $c_{22}= 345$  GPa,  $c_{23}= 120$  GPa,  $c_{33}= 372.06$  GPa,  $c_{44}= 118$  GPa,  $c_{55}= 110$  GPa,  $c_{66}= 110$  GPa (each at constant E field)  $e_{33}= 1.5$  C/m<sup>2</sup>,  $e_{13}= -0.58$  C/m<sup>2</sup>,  $e_{23}=-0.58$  C/m<sup>2</sup>

Si Major Poisson's ratios:  $PRXY=PRYZ=PRXZ=0.26$ , Young's Modulus  $E_x=E_y=E_z= 134.36$  GPa

SiN  $PRXY=PRYZ=PRXZ=0.29$ ,  $E_x=E_y=E_z= 178.20$  GPa

SiOC  $PRXY=PRYZ=PRXZ=0.22$ ,  $E_x=E_y=E_z= 8.88$  GPa

Mo  $PRXY=PRYZ=PRXZ=0.31$ ,  $E_x=E_y=E_z= 314.26$  GPa

The resonator has an area of 22500 μm<sup>2</sup>.

*Other assumptions about the model:*

Mechanical boundary conditions: zero displacement constraints for all directions imposed on the bottom surface of the last block (only for stack configuration 10).

Meshing:

- Only one 3-D 20-node brick element is considered in all transversal sections (the transversal waves of propagation are practically neglected).
- Each layer is meshed longitudinally with a number of 3-D 20-node brick elements, that have the height less than 1/8 of the wavelength, and this number is increased until we reach the stability of the resonance and antiresonance frequency values.

This stable solution is reached in general for elements with heights about 1/(16÷25) of the wavelength.

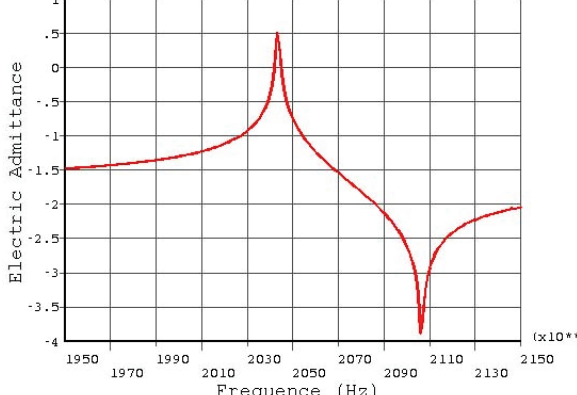
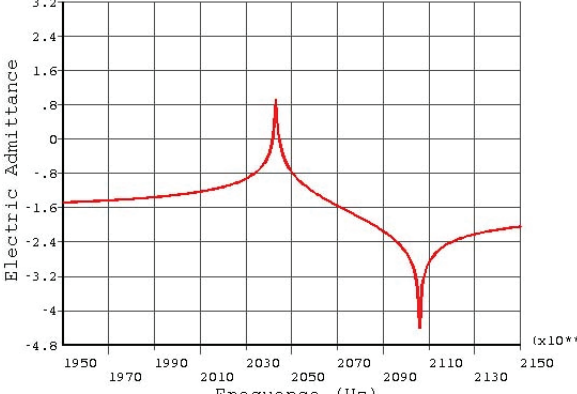
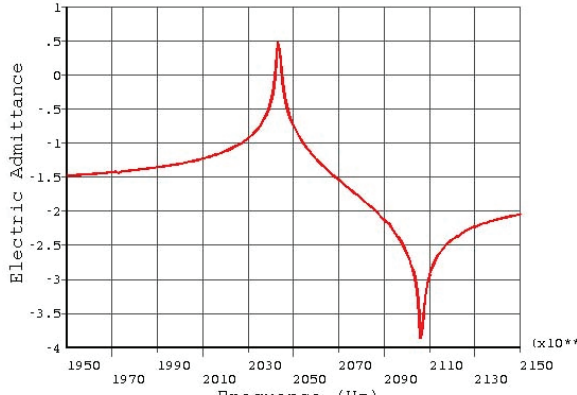
Mechanical losses have been taken into account by using a constant damping ratio of 3×10<sup>-3</sup>.

In this model only longitudinal wave propagation is reproduced. The FEM analysis results have been computed adding layer by layer and are given in the following. The resonance frequencies are compared to those obtained using the Mason multilayer model.

Stack configuration	Resonance frequencies computed with FEM simulation	FEM simulation result
<p><b>Config 1:</b> only AlN 1170 nm</p>	<p><math>F_r = 4.568</math> GHz, <math>F_a = 4.702</math> GHz Mason model: <math display="block">F_a = \frac{1}{2l} \sqrt{\frac{c_{33} + \frac{e_{33}^2}{\rho}}{\rho}} = 4.7009</math> GHz (simple anti-resonance formula for thickness mode)</p>	

<p><b>Config 2:</b>                  Config 1                  + Mo 240 nm                  (atop the AlN layer)</p> <p><math>F_r = 3.093\text{GHz},</math>  <math>F_a = 3.180\text{ GHz}</math></p>	
<p><b>Config 3:</b>                  Config 2                  + Mo 280 nm                  (under the AlN layer)</p> <p><math>F_r = 2.138\text{ GHz},</math>  <math>F_a = 2.208\text{ GHz}</math></p>	
<p><b>Config 4:</b>                  Config 3                  + SiN 200 nm                  (atop the stack)</p> <p><math>F_r = 2.037\text{ GHz},</math>  <math>F_a = 2.103\text{ GHz}</math></p>	

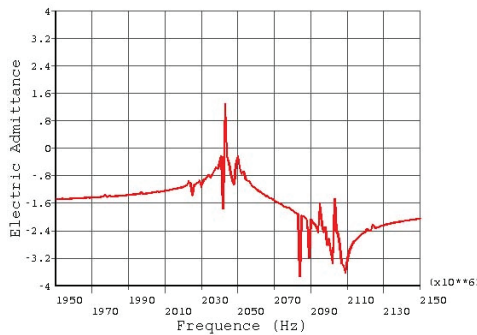
<p><b>Config 5:</b>                  Config 4                  + SiOC 295                  nm (under the                  stack)</p>	<p>2 resonances:  <math>Fr_1 = 1.850</math> GHz,  <math>Fa_1 = 1.895</math> GHz  <math>Fr_2 = 2.408</math>GHz,  <math>Fa_2 = 2.440</math> GHz</p>	
<p><b>Config 6:</b>                  Config 5                  + SiN 1160                  nm (under the                  stack)</p>	<p><math>Fr = 2.043</math> GHz,  <math>Fa = 2.107</math> GHz</p>	
<p><b>Config 7:</b>                  Config 6                  + SiOC 295                  nm (under the                  stack)</p>	<p>2 resonances:  <math>Fr_1 = 2.033</math> GHz,  <math>Fa_1 = 2.090</math> GHz  <math>Fr_2 = 2.185</math> GHz,  <math>Fa_2 = 2.193</math> GHz</p>	

<p><b>Config 8:</b> Config 7 + SiN 1160 nm (under the stack)</p>	<p><math>F_r = 2.042</math> GHz, <math>F_a = 2.106</math> GHz</p>	
<p><b>Config 9:</b> Config 8 + SiOC 295 nm (under the stack)</p>	<p><math>F_r = 2.042</math> GHz, <math>F_a = 2.106</math> GHz</p>	
<p><b>Config 10:</b> Config 9 + Si 725 <math>\mu</math>m (under the stack) = real resonator</p>	<p><math>F_r = 2.042</math> GHz, <math>F_a = 2.106</math> GHz</p>	

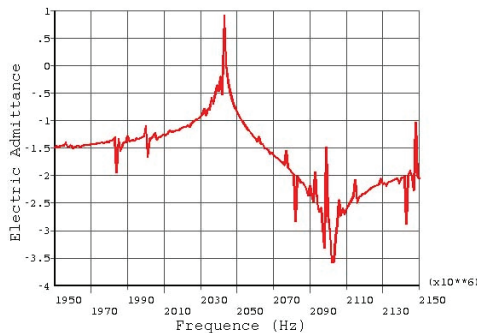
A good agreement between ANSYS numerical results and the analytical Mason multilayer model (Rosenbaum, 1988; Christopoulos, 1995) has been observed.

### 4.2 3D numerical simulation of a BAW resonator structure

Only a quarter of the resonator structure (as is it seen in transversal plane) has been taken into account in order to reduce the computational FEM effort required by 3D FEM simulations of the whole stack (Fig. 16. (a),(b)). Mechanical boundary conditions (zero displacement constraints for transversal directions,  $u_x=0$  or  $u_y=0$ ) and  $dV/dn=0$  boundary condition (for piezoelectric layer) are imposed on the symmetry planes. The mesh discretization for longitudinal directions is the same as in previous chapter. For lateral directions we used a discretization of  $ndiv \times ndiv$  20-node brick elements.



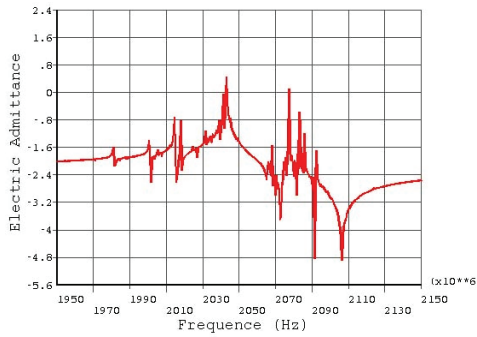
(a) Lateral boundaries are free



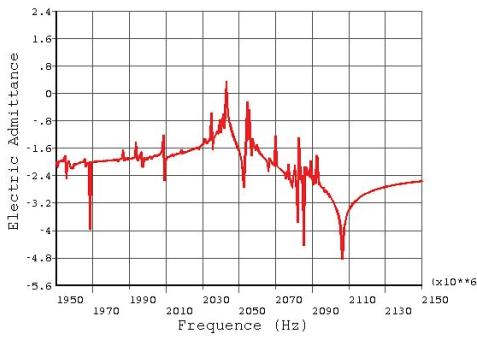
(b) Lateral boundaries have zero displacement constraints for all directions

Figure 16. 3D simulations ( $ndiv = 8$ )

In order to establish a more realistic model for transversal wave propagation we extend all layers by  $ext \mu\text{m}$  in each lateral side (because the abrupt end of the mesh is far from the real structure). For this new volume the mesh is much less dense. The electrodes have the area of  $\frac{1}{4} \times 22500 \mu\text{m}^2$ . Some results obtained using this approach are presented in Fig. 17 and Fig. 18. Obviously, the results taking into account a larger extended part are closer to the real structure.



(a) Lateral boundaries are free



(b) Lateral boundaries have zero displacement constraints for all directions

Figure 17. 3D simulations for lateral extended stack ( $n_{div} = 6$  and 2 divisions for lateral extended side with  $ext=100\mu m$ )

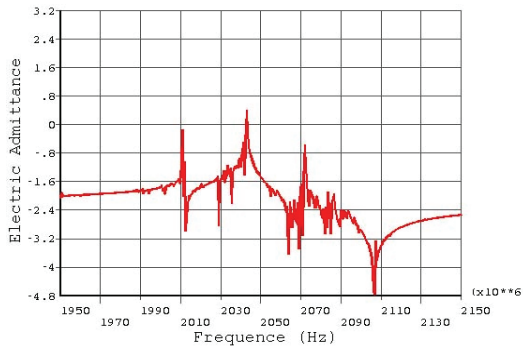


Figure 18. 3D simulations for lateral extended stack ( $n_{div} = 8$  and 4 divisions for lateral extended side with  $ext=200\mu m$ , lateral boundaries have zero displacement constraints for all directions.)

The local stress values are shown in Fig. 19. According to common expectations, the maximum values are obtained for the series resonance frequency.

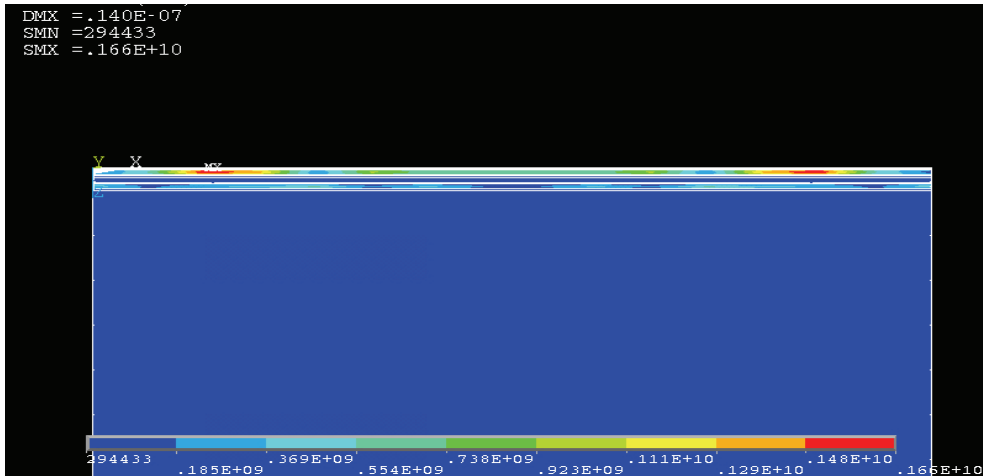


Figure 19. Local stress

*Remarks:*

- The resonance frequencies corresponding to longitudinal propagation are the same for all models.
- The lateral modes are more accentuated and unstable. Some possible causes:
  - Model assumptions which are not satisfied by the real structure
    - a. Thickness uniformity
    - b. Approximate layer lateral dimensions
    - c. Approximate lateral boundary condition (mechanical)
  - Ill- conditioned meshing (in order to save CPU time, a small number of lateral divisions has been considered)
  - Approximate material parameters (not measured)
    - a. Some AlN parameters on transversal directions are taken from literature (where different values are given)
    - b. All layers, except AlN, are considered isotropic (perhaps they are not); the parameters on lateral directions being considered equal to that on the longitudinal direction.

## 5. Circuit models for power BAW resonators and filters

As BAW resonators are used to build filters which are parts of intricate circuits, like the power amplifier and duplexer in the mobile phone, circuit models are very useful in the design at system level. At a relatively low incident power the BAW resonator has a linear behaviour which can be described in a broad frequency range by the Mason model (Wilson, 1989), a circuit which contains lumped and distributed parameter elements. In the vicinity of a resonance frequency pair (as, for example corresponding to the thickness mode) a simpler model, the Butterworth-Van Dyke (BVD) circuit, can be used (Fig. 20).

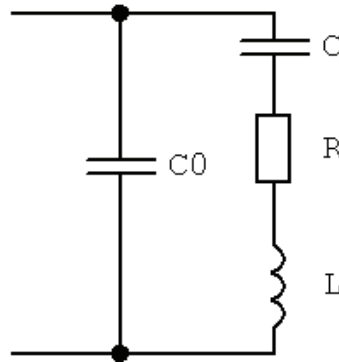


Figure 20. Butterworth-Van Dyke circuit

A high power fed into the BAW resonator produces three nonlinear effects, namely: the amplitude-frequency effect, the intermodulation effect, and the bias-frequency effect (Nosek, 1999; Aigner et al., 2005).

The amplitude-frequency effect is illustrated by the series resonance frequency increase as excitation amplitude increases for a quartz resonator (Fig. 21) (Nosek, 1999). A decrease of the series resonance frequency as the excitation amplitude increases has been observed in the case of an AlN stack crystal filter (Ketcham et al., 1988). The intermodulation effect consists, for example, in measuring some harmonic components of the response to a sinusoidal excitation (Nosek, 1999; Aigner et al., 2005; Ketcham et al., 1988). The shift of the series resonance frequency as a function of bias voltage is the bias-frequency effect (Aigner et al., 2005).

The linear parametric model in Fig. 22, valid for the response on the fundamental frequency, which is able to reproduce this amplitude-frequency effect, is described in (Nosek, 1999). The resistance and the capacitance in the motional branch of the BVD circuit are considered as dependent on the r.m.s. current value  $I$  in this branch:

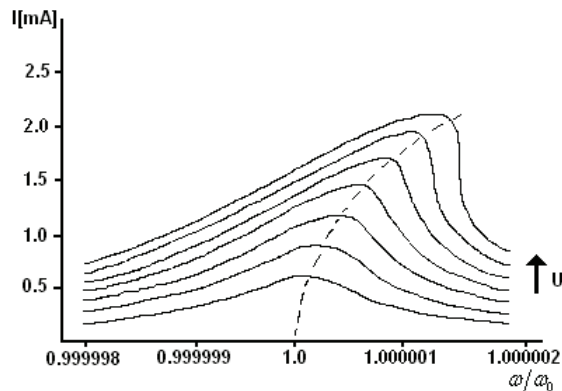


Figure 21. Frequency characteristics of a quartz resonator ( $I$ - resonator current,  $U$ - excitation voltage)



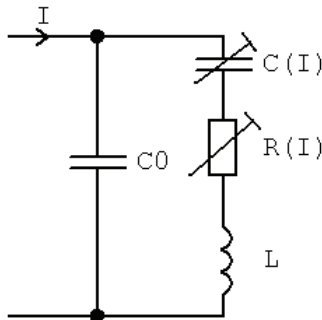


Figure 22. Linear parametric model of a quartz resonator

$$R(I) = R(1 + \beta I^2) \qquad \frac{1}{C(I)} = \frac{1}{C}(1 + \alpha I^2). \qquad (44)$$

This linear parametric model and other similar ones (Constantinescu et al., 2007) can reproduce the amplitude-frequency effect but don't give intermodulation products.

These linear models contain parametric circuit elements whose characteristics depend on a r.m.s. value. This kind of dependence is not allowed in circuit simulators working in the frequency domain as ADS and APLAC (Constantinescu et al., 2007). Moreover, it cannot be used in a circuit simulator working in the time domain as SPICE or SPECTRE (Constantinescu et al., 2007). To overcome this difficulty, iterative AC analyses have been implemented in APLAC and MAPLE (Constantinescu et al., 2007). Even though these methods can lead to correct results in a reasonable amount of time for the analysis of a circuit composed by several resonators, they cannot be used for the analysis of an intricate system like the power amplifier and duplexer in a mobile phone.

Starting from an idea in (Aigner et al., 2005) two new nonlinear circuit models have been developed (Constantinescu et al., 2007). The first model is based on the BVD circuit in which the nonlinear resistor, inductor and capacitor are implemented as nonlinear controlled sources (Fig. 23).

The following parameter values were used for the APLAC implementation of this circuit:

$$C0 = 1.566e-12$$

$$CCVS \ R1 \ 1 \ 2 \ 1 \ b \ [4.695*(CI(0)+0.5*CI(0)^2+0.5*CI(0)^3)] \ R$$

$$CCVS \ L1 \ 2 \ 3 \ 1 \ b \ [3.5e-9*(CI(0)-5e-2*CI(0)^2+1e-2*CI(0)^3)] \ L$$

$$VCCS \ C1 \ 3 \ 5 \ 1 \ 3 \ 5 \ [1.7666e-12*(CV(0)+1e-2*CV(0)^2+1e-4*CV(0)^3)] \ C$$

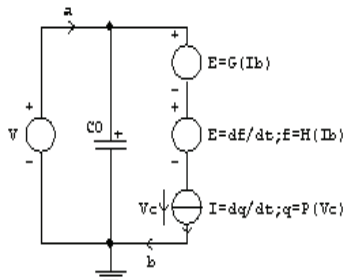


Figure 23. Controlled source implementation of the first nonlinear circuit model

The amplitude-frequency effect of this model is shown in Fig. 24, where the frequency characteristics for the 1V, 3V, and 5V excitation amplitude are given. The decreasing of the series resonance frequency as the excitation amplitude increases may be observed. The second and third harmonic amplitudes obtained with the first model are given in Fig. 25 for three excitation frequencies.

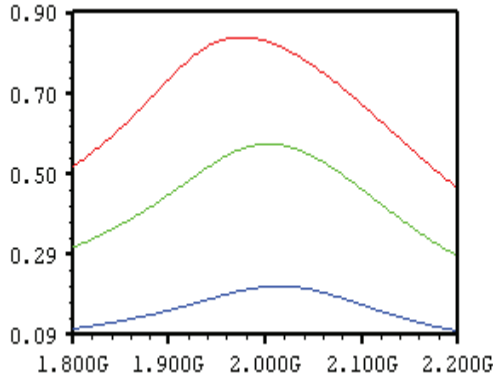


Figure 24.  $I_a$  vs. frequency for the first nonlinear model

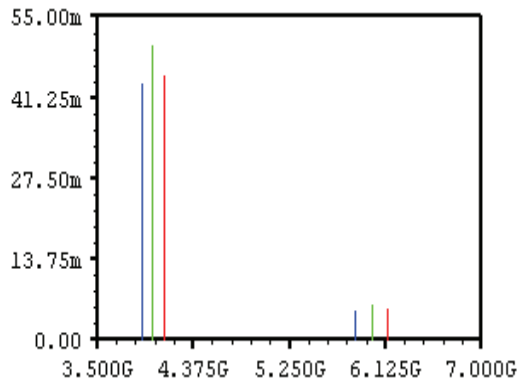


Figure 25. Intermodulation products for  $V=5V$ , first model

Forcing the current value in the motional branch by means of the VCCS, the capacitor has a dominant role in this model, both the resonance frequency shift and the amplitudes of the intermodulation products depending mainly on its nonlinear characteristic. To avoid this disadvantage a second model is proposed (Fig. 26).

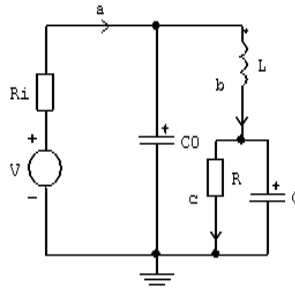


Figure 26. Second nonlinear circuit model

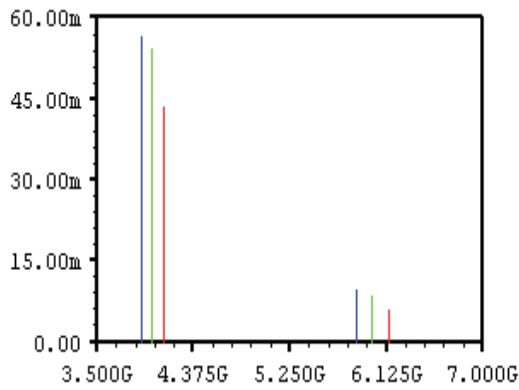


Figure 27. Intermodulation products for V=5V, second model

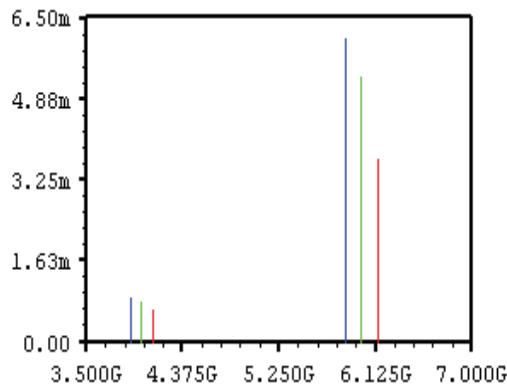


Figure 28. Intermodulation products, second model with modified inductor

The following parameter values were used for the APLAC implementation of this circuit:

$$C0 = 1.566e-12$$

$$CCVS L1 1 2 1 b [3.5e-9*(CI(0)+.1*CI(0)^2+1e-2*CI(0)^3)] L$$

$$CCVS R1 3 5 1 c [430*(CI(0)+2e-2*CI(0)^2+2e-2*CI(0)^3)] R$$

$$VCCS C1 3 GND 1 3 GND [.177e-12*(CV(0)+5e-5*CV(0)^2+5e-5*CV(0)^3)] C$$

This circuit shows an amplitude-frequency effect similar to the first model. Its intermodulation effect is illustrated in Fig. 27.

In order to show the better fitting properties of this second model, let's modify the inductance parameters as:

$$CCVS L1 1 2 1 b [3.5e-9*(CI(0)+\underline{1e-3*CI(0)^2}+\underline{1e-3*CI(0)^3})] L$$

(changed values are underlined). Using this new inductance the amplitude-frequency effect remains the same, while the amplitude of the second harmonic practically vanishes as it is shown in Fig. 28.

The second circuit model allows a better control of both amplitude-frequency effect and intermodulation effect than the first one. This control is obtained by varying the coefficients of the polynomial nonlinearities. In order to validate these models, we considered the measured dependence of the series resonance frequency on the incident power (Constantinescu et al., 2008). A comparison between the simulated and measured data is given in Fig. 29.

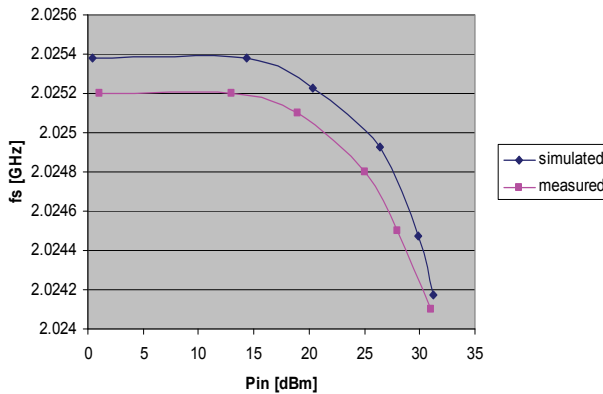


Figure 29. The dependence of the series resonance frequency on the incident power

In order to compare simulation results in time domain (TD) and frequency domain (FD) the two resonator filter in Fig. 30 has been analyzed both with periodic steady state analysis (PSS) and harmonic balance analysis of SPECTRE.

These analyses are implemented in the IC 6.1.0 package of CADENCE. The polynomial nonlinearities are defined by the coefficients  $a_0$ ,  $a_1$ ,  $a_2$ , whose meaning has been shown before. The running options are:

```
SetOption1 options iabstol=1e-13 vabstol=1e-12 digits=8 fund=2.025G harms=4
outputtype=all errpreset= conservative
```

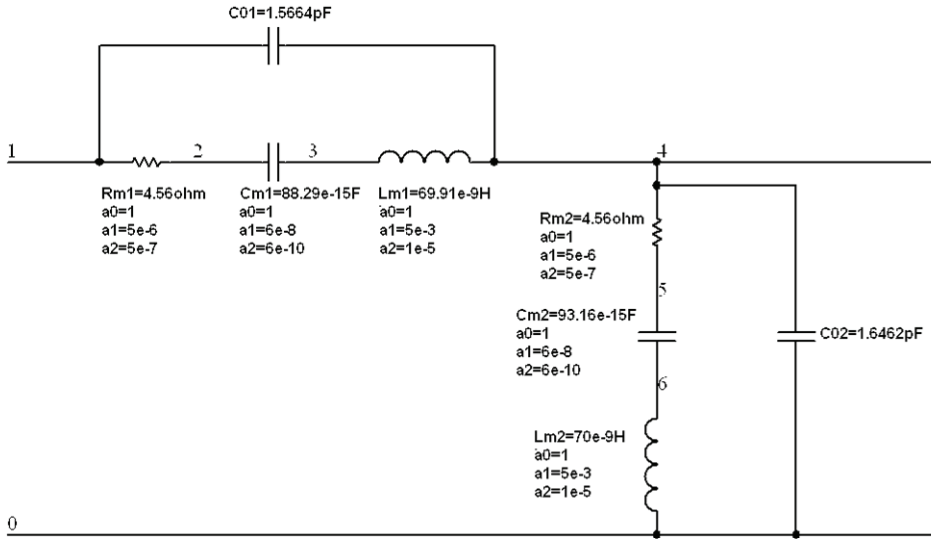


Figure 30. A nonlinear model of a two resonator power BAW filter

The harmonic components of the output signal are given in the following tables, for two values of the parameter “reltol”.

	TD	FD
f component	3.646 V	3.646 V
2f component	239 uV	239 uV
3f component	191.6 nV	118.8 nV

Table 5. Harmonic components of the output signal, reltol=1e-6

	TD	FD
f component	3.646 V	3.646 V
2f component	238.9 uV	239 uV
3f component	115.5 nV	118.8 nV

Table 6. Harmonic components of the output signal, reltol=1e-9

These results show a very good agreement between the TD and FD analyses. Further research will be devoted to filter modeling and simulation taking into account real RF signals (not sinusoidal ones as in the case of the results given before). To this end new nonlinear circuit models can be developed using simple impedance transformations.

### 6. Acknowledgments

The authors acknowledge the financial support of the FP6 project MOBILIS.

## 7. References

- Cady, W. G. (1964). Piezoelectricity. An Introduction to the Theory and Applications of Electromechanical Phenomena in Crystals, *Dover Publ.*, Vols. I and II, , New York.
- Wilson, O. B. (1989). *Introduction to the theory and design of sonar transducers*, Peninsula Publishing, ISBN: 978-0-9321-4622-9, Los Altos, California.
- Hantila, F.I.; Preda, G. & Vasiliu, M. (2000). Polarization Method for Static Fields, *IEEE Transaction on Magnetics*, Vol.36, No.4, Jul 2000, pp. 672-675, ISSN: 0018-9464.
- Makkonen, T.; Holappa, A.; Ella, J. & Salomaa, M. (2001), Finite Element Simulations of Thin-Film Composite BAW Resonators, *IEEE Transactions on Ultrasonics, Ferroelectrics, and Frequency Control*, Vol.48, No.5, Sep 2001, pp. 1241-1257, ISSN: 0885-3010.
- Makkonen, T. (2005). *Numerical Simulations of Microacoustic Resonators and Filters*, Doctoral Dissertation, Helsinki University of Technology, apr. 2005, ISBN 9512276364, pp. 1-75.
- Ostergaard, D. F. & Pawlak, T. P. (1986). Three-Dimensional Finite Elements for Analyzing Piezoelectric Structures, 1986 *IEEE Ultrasonics Symposium*, pp. 639-644.
- Popovici, D.; Păltănea, V.; Păltănea, G. & Jiga, G. (2006). Determination of the stress and strain state in metallic structures using piezoelectrical transducers, *Proceedings of the COMSOL Users Conference*, 2006, Prague.
- \*\*\* (2005). COMSOL 3.2., Structural Mechanics, *Manual*, Comsol, AB, Sweden.
- \*\*\* (2005). ANSYS, Inc., Release 10.0 Documentation for ANSYS, online documentation, documentation CD.
- Rosenbaum, J. F. (1988). Bulk Acoustic Waves Theory and Devices, *Artech House*, Boston.
- Christopoulos, C. (1995). The Transmission-Line Modeling Method: Tlm, *IEEE Computer Society Press*, ISBN: 978-0-7803-1017-9.
- Nosek, J. (1999). Drive level dependence of the resonant frequency in BAW quartz resonator and his modeling, *IEEE Transactions on Ultrasonics, Ferroelectrics, and Frequency Control*, Vol.46, No.4, Jul 1999, pp. 823-829, ISSN: 0885-3010.
- Aigner, R.; Huynh, N.-H.; Handtmann, M. & Markensteiner, S. (2005). Behavior of BAW devices at high power levels, *Proceedings of IEEE IMS-MTT-S 2005*, Long Beach.
- Ketcham, R. S.; Kline, G. R. & Lakin, K. M. (1988). Performance of TFR filters under elevated power conditions, *42-nd Annual Frequency Control Symposium*, pp. 106-111, USA, 1-3 Jun 1988, Baltimore.
- Constantinescu, F.; Nitescu, M. & Gheorghe, A. G. (2007). Circuit Models for Power BAW Resonators - Set-up and Implementation, *Proceedings of AFRICON 2007*, pp. 1-6, ISBN: 978-1-4244-0987-7, Namibia, 26-28 Sept., 2007, Windhoek.
- Constantinescu, F.; Nitescu, M. & Gheorghe, A. G. (2008). New Nonlinear Circuit Models for Power BAW Resonators, *IEEE International Conference on Circuits and Systems for Communications*, Shanghai, China, May 26-28, 2008.

# Multiphysical Modeling of DC and AC Electroosmosis in Micro- and Nanosystems

Michal Příbyl, Dalimil Šnita and Miloš Marek  
*Institute of Chemical Technology, Prague  
Czech Republic*

## 1. Introduction

A large family of microfluidic devices employs the electrokinetic transport of liquids. The integration of mechanical components such as high-pressure pumps or valves is not required in the electrokinetically driven microfluidic chips. Instead of a pressure gradient, a gradient of electric potential is imposed over the microfluidic system. It can be provided by either DC or AC electric field. The DC electroosmotic transport in microchannels has been intensively theoretically and experimentally studied. The origin of the DC electroosmosis arises from the coulombic interaction between an external DC electric field and a mobile electric charge localized at an electrolyte-dielectric interface. The use of the electroosmosis forced by a low amplitude AC electric field is a novel area investigated only for several years. The AC electroosmosis is mostly based on the coulombic interaction between an imposed AC electric field and a mobile electric charge temporally arising at electrolyte-metal electrode interfaces.

The chapter is organized as follows. The origin of the electrokinetic transport and the principle of DC and AC electroosmotic micropumps are shortly described in the first section. The basic features of the AC micropumps are summarized in more detail. The multiphysical model of electro-microfluidic systems based on the Poisson-Nernst-Planck-Navier-Stokes approach and its possible simplifications are briefly described in the second section. The implementation procedure of this multiphysical problem in a CFD software and frequently arising problems are discussed in the next section.

Various electro-microfluidic systems have been investigated in our research group. Here, we present and discuss selected results of the numerical analysis of three particular micro- and nano-fluidic systems: (i) a tubular microfluidic sensor for heterogeneous immunoassay driven by a DC electric field, (ii) a submicron channel/pore interacting with a DC electric field and the surrounding electrolyte, (iii) AC electrokinetic micro- and nano-pumps realized in channels with spatially periodic arrays of co-planar electrodes. The discussed AC pumps rely either on the asymmetric geometry of interdigital electrodes or on an electric field phase shift applied to electrodes (the three phase arrangement).

### 1.1 Origin of Electroosmotic Transport

The electroosmotic transport can be induced by an external electric field in fluidic systems where the electric polarization (charging) of solid surfaces occurs. Some organic

(polystyrene, plexiglass) or inorganic polymers (glass) gain a surface electric charge if immersed in an electrolyte. The fixed charge can arise, e.g., from dissociation of surface chemical groups of either the polymer substrate itself or of adsorbed additives. Counterions are attracted to the charged solid phase via the coulombic force and the electric double layer (EDL) is formed. In the immediate proximity, the counterions are tightly bound to the charged surface and thus become immobile. This thin part of EDL is called the Stern layer. Further away from the solid phase in the diffusive part of EDL, the attraction coulombic force is relatively weak and the counterions remain mobile. The diffusive layer is usually much wider than the Stern layer. The imaginary surface between the diffusive and the Stern layers is called the outer Helmholtz plane - OHP, Fig. 1(A). The electric potential localized on this surface and related to the reference potential value in the bulk solution ( $\Phi_0$ ) is an important characteristic of EDL, so-called zeta-potential ( $\zeta$ ). Let us note that the EDL structure depicted in Fig. 1 represents a typical steady state that is established when: (i) the dielectric or the electrode surface is in a contact with the electrolyte for a long time, (ii) any temperature changes and bulk concentration changes do not occur in space and time, and (iii) the electrolyte does not move. These conditions are often not satisfied in real applications and thus the EDL structure can be more complex. However, the idea of the steady state EDL is good enough for a basic introduction of the problems studied below.

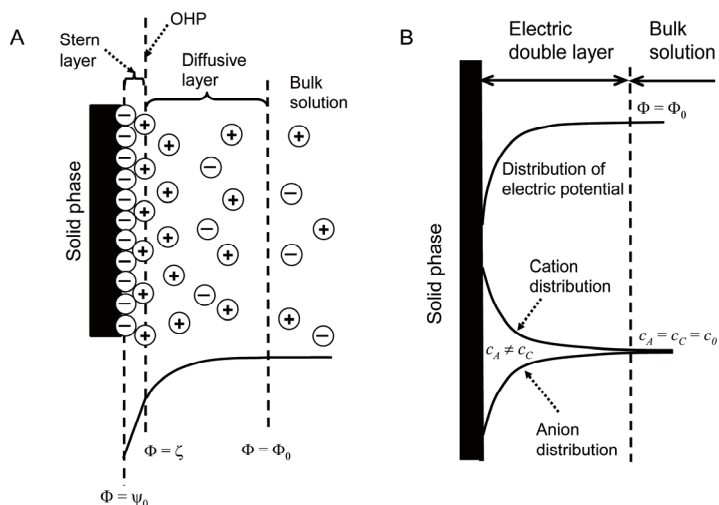


Figure 1. (A) Structure of electric double layer. (B) Properties of electric double layer

For aqueous electrolytes, the EDL width is typically in the range 1 nm - 1 $\mu$ m. The EDL width is approximately equal to the Debye length  $\lambda_D$ . For a symmetric uni-univalent electrolyte, the Debye length can be estimated as

$$\lambda_D = \sqrt{RT\varepsilon/(2c_0F^2)}, \quad (1)$$

where the symbols  $R$ ,  $T$ ,  $c_0$ , and  $F$  denote the molar gas constant, temperature, the electrolyte concentration in the bulk, and Faraday's constant, respectively. The permittivity of the



environment  $\varepsilon$  is equal to the product of the vacuum permittivity  $\varepsilon_0$  and the dielectric constant (relative permittivity) of the environment  $\varepsilon_r$ .

The fixed electric charge on the solid phase is usually negative (depends on the substrate and the electrolyte pH value). Then, the electric potential decreases from the electrolyte bulk to the solid surface. In the same direction, the anion concentration decreases and the cation concentration increases with respect to the bulk concentration. Hence, the electrolyte in the EDL region does not satisfy the electroneutrality condition, i.e., a nonzero concentration of a mobile electric charge exists in EDL, Fig. 1(B).

More information about EDL and electrohydrodynamic phenomena can be found, e.g., in (Probstein, 1994, Squires & Bazant, 2004, Squires & Quake, 2005).

**1.2 DC Pumps**

The most common feature of the DC electroosmotic micropumps is the fact that the systems work either in or close to a hydrodynamic steady state. The principle of these devices is depicted in Fig. 2. If a DC electric field is applied in the direction tangential to the solid surface, the electric body force acts on the clouds of the mobile electric charge in the diffusive part of EDL. The vector of the local body force can be expressed as

$$f_E = qE, \tag{2}$$

where  $q$  and  $E$  are the volume concentration of the mobile electric charge and the vector of the electric field strength, respectively, defined by

$$q \equiv F \sum_i z_i c_i, \quad E \equiv -\nabla\Phi, \tag{3}$$

where the symbols  $z_i$ ,  $c_i$ , and  $\nabla\Phi$  denote the charge number of the  $i^{\text{th}}$  ion, the volume concentration of the  $i^{\text{th}}$  ion, and the gradient of electric potential, respectively.

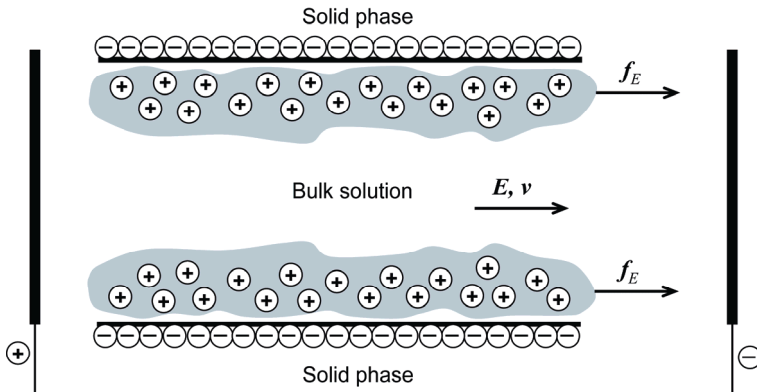


Figure 2. Principle of DC electroosmosis in a microchannel

The mobile electric charge is represented by ionic particles. As the mobile ions are forced to move via the coulombic body force, they act on the ambient liquid by viscous forces. The liquid in EDL starts to flow and induces the movement of the electrolyte body. In the steady state when the distribution of the surface electric charge is homogeneous, the velocity vector has the same direction as the tangential component of electric field strength. The velocity

profile is flat in the electrolyte body where the velocity attains its maximal value, i.e., the slip velocity. In the diffusive part of EDL, the velocity gradually decreases to zero at the outer Helmholtz plane. The slip velocity  $v_t$  tangential to the solid surface can be estimated from the Helmholtz-Smoluchowski equation

$$v_t = -\frac{\varepsilon\zeta}{\eta} E_t, \quad (4)$$

where  $\zeta$ ,  $\eta$ , and  $E_t$  are the zeta-potential, the dynamic viscosity of the electrolyte, and the tangential component of the electric field strength, respectively.

The DC electroosmotic pumps are widely exploited in experimental and commercial microfluidic devices, e.g., see reviews (Becker & Locascio, 2002, Beebe et al., 2002, Bilitewski et al., 2003, Chang & Yang, 2007, Laser & Santiago, 2004). The reaction transport processes in such devices have been also modeled and analyzed, e.g., (Erickson, 2005, He & Huan, 2006, Postler et al., 2008). The DC devices suffer from a serious disadvantage: the potential difference imposed on microdevices usually has to be in the order of kilovolts. It results, e.g., in an undesirable bubble formation or an electrolyte contamination due to faradaic interactions on the source electrodes. This particular problem can be eliminated in the electroosmotic AC pumps.

### 1.3 AC Pumps

Ramos *et al.* was the first to study the effects of a low amplitude AC electric field imposed on co-planar electrodes in a microchannel filled by an electrolyte (Ramos et al., 1998). They observed electrokinetic transport of a new kind above the source electrodes up to frequency 500 kHz. In 2000, Ajdari proposed a design of the AC electrokinetic micropumps based on arrays of asymmetric pairs of co-planar microelectrodes (Ajdari, 2000). It has been expected that the asymmetry of electric field will lead to a net flow of the electrolyte. His predictions were verified by several experimental and theoretical works (Campisi et al., 2005, Garcia-Sanchez et al., 2006, Green et al., 2002, Mpholo et al., 2003, Studer et al., 2004, Zhang et al., 2006). In general, the authors used microelectrodes with characteristic dimensions ranging from micrometers to tens of micrometers. The observed velocity of the net flow typically attained few hundreds of microns per second.

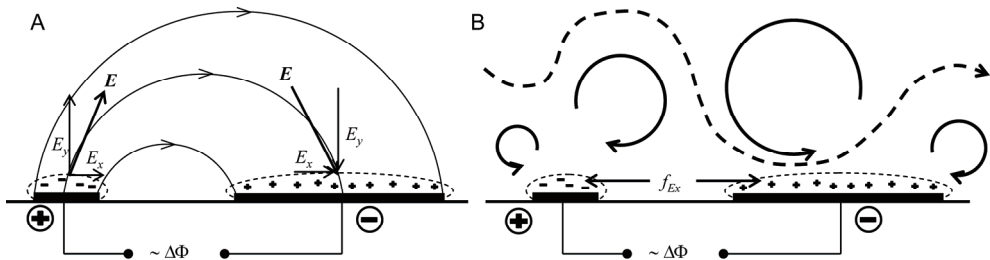


Figure 3. The principle of the AC electroosmotic flow above co-planar electrodes. (A) The electric field acts on the electric charge. (B) Electrostatic volume force induces the eddy formation (solid line) and the net flow (dashed line)

In the most frequent co-planar interdigitated arrangement of the electrodes, the AC electric field has the tangential and the normal components, Fig. 3(A). The normal component

induces electrode polarization via coulombic force (capacitive charging). Then, the tangential component of the electric field forces the accumulated electric charge to move along the electrodes. The highest tangential coulombic force was predicted and observed at the electrode edges (Green et al., 2000). As the electric charge is formed by ions of a nonzero diameter, the moving ionic particles pull the surrounding liquid via viscous forces, Fig. 3(B). The combination of coulombic, pressure and viscous forces in the liquid result in the formation of eddies above the electrodes. This has been experimentally proved by the PIV technique (Garcia-Sanchez et al., 2006, Green et al., 2002).

The velocity of the net flow strongly depends on several parameters: the frequency and the amplitude of the imposed electric field, the concentration of the used electrolyte and the geometric properties of the microfluidic system. The frequency dependence is given by characteristic rates of two transport processes: (i) the rate of the electrode polarization (the formation of the EDL) and (ii) the rate/frequency of an AC electric field. There are three qualitatively different regimes that can arise above the electrodes. For very low AC frequencies, the nonzero tangential coulombic force is restricted only to the electrode edges due to a complete capacitive charging of the electrodes. The force on one side of an electrode equilibrates the force on the other side and thus the net flow goes to zero. If the AC frequency is high, almost no mobile electric charge is formed at the electrode surface because the polarization process is relatively slow compared with the rate of changes of the AC electric field. As the electric field acts on zero electric charge, no net flow is induced. The AC electroosmosis can be observed between these two cases because then both a nonzero tangential component of the electric field and a nonzero mobile electric charge at the electrode surface are formed.

The AC frequencies, for which the nonzero net velocity is expected, can be estimated by means of characteristic time scales of the processes inside microchannels. Let us define the following quantities

$$\tau_{AC} \equiv (2\pi f_{AC})^{-1}, \quad \tau_E \equiv \lambda_D L / D_i, \quad \tau_D \equiv \lambda_D^2 / D_i, \quad (5)$$

where  $\tau_{AC}$  and  $\tau_E$  are the time scales of the AC electric field and the electrode charging, respectively.  $\tau_D$  is the Debye time scale. The symbols  $f_{AC}$ ,  $L$ , and  $D_i$  denote the AC electric field frequency, the electrode-electrode distance (alternatively the longitudinal size of electrodes), and the ionic diffusivity, respectively. There is an important difference in the physical meaning of the Debye scale and the charging scale. While the Debye time is approximately equal to the shortest time necessary for the formation of an electric charge at an electrode surface, the charging time is a typical characteristic time scale of the electrode polarization. The charging time depends on both the EDL dimension and the distance between the electrodes (Squires & Bazant, 2004). It follows from the analysis of resistor-capacitor circuits representing the AC electrokinetic systems. We can write the following condition for the value of the AC period ( $\tau_{AC}$ ) for which the net hydrodynamical effects are expected to be the most intensive

$$\tau_D \leq \tau_{AC} \approx \tau_E. \quad (6)$$

The Debye time gives us a good approximation of the shortest AC period for which the net flow can be observed. The charging time estimates the typical AC period for the maximal net flow velocity.

It has been found that the direction of fluid pumping is also frequency and amplitude dependent (Garcia-Sanchez et al., 2006, Studer et al., 2004). This important phenomenon has not been adequately explained yet. It is assumed that the flow reversal is caused by one or more of the following effects: (i) local salt depletion, (ii) faradaic reactions or (iii) interactions of EDL with the convective transport of ions. The transport processes related to the flow reversal are discussed in paragraph 4 in more detail.

The velocity of the net flow dramatically decreases with an increasing electrolyte concentration (Studer et al., 2004). Green *et al.* showed that the time averaged net velocity decreases with a growing capacitance of the diffuse part of EDL (Green et al., 2002). The capacitance increases with the increasing concentration because the characteristic width of the capacitor, i.e. the Debye length, is proportional to  $c_0^{-0.5}$  according to Eq. (1). The concentration effect on the net velocity can be a limiting factor of the use of the AC electroosmosis for the transportation of biological samples typically diluted in 10 – 100 mM buffers.

There are two possible ways how to compensate the concentration effect: (i) a reduction of the electrode size, (ii) a fabrication of geometrically more complex electrodes. The former way is based on the increase of tangential electric volume force. When the amplitude of an AC field is kept constant and the electrode dimension is reduced in size, the tangential component of the electric field strength increases. The problem is that the fabrication of submicron electrodes is difficult and expensive. The latter possibility has been investigated, e.g., by (Bazant & Ben, 2006, Olesen et al., 2006, Urbanski et al., 2006). Bazant *et al.* predicted that a three-dimensional design of the electrodes (instead of the classical co-planar design) will increase the electrolyte net velocity up to  $\text{mm s}^{-1}$  (Bazant & Ben, 2006). Their theory arises from the fact that the counter-rotating regions of fluid observed above the electrode arrays inhibit the net flow, Fig. 3(B). Hence, the authors have proposed a three-dimensional electrode design where the inhibition should be negligible. It has been experimentally verified that the net velocity can be increased at least by one order of magnitude with respect to the purely co-planar arrangement (Urbanski et al., 2007, Urbanski et al., 2006).

Except of the net flow forced by asymmetric interdigitated microelectrodes, the electrokinetic transport can be induced by a traveling-wave electric potential applied to an array of microelectrodes or by a spatio-temporally modulated surface potential at an insulating microchannel wall (Ejsing et al., 2006, Mortensen et al., 2005, Ramos et al., 2005). A phase shift of an AC electric field has to be provided along microchannel walls. The traveling-wave arrangement also exhibits nonlinear phenomena such as the flow reversals observed at certain AC amplitudes (Ramos et al., 2005).

Different types of microfluidic pumps and mixers based on the AC faradaic electrode polarization have been proposed (Lastochkin et al., 2004). If the amplitude of an AC electric field is higher than the electrochemical limit, the electric charge on electrodes is produced via electrochemical reactions instead of the capacitive charging. The faradaic reactions do not necessarily lead to gas formation. The electrode gas produced in each AC half cycle can dissolve in the electrolyte without nucleating macroscopic bubbles. For the faradaic AC micropumps are typical higher AC frequencies, AC amplitudes and electrolyte concentrations than for the capacitive charging micropumps. The net velocity attains millimeters per second.

The general feature of all types of the AC electrokinetic devices is that the systems do not work in a steady state. After the initial transient, they can attain a stable periodic regime. This aspect of the AC devices substantially increases the demands on numerical analysis of

model equations. From technical point of view, the most interesting velocity characteristic of the flow is the net velocity that can be obtained as the tangential velocity averaged over one period of the stable periodic regime.

No comprehensive numerical study of the AC electrokinetics in microchannels has been reported. There are particularly focused studies mostly relying on the slip approximations (Kim et al., 2007, Loucaides et al., 2007) or the Poisson-Boltzmann equation (Khan & Reppert, 2005, Olesen et al., 2006, Wang & Wu, 2006, Zhang et al., 2006) but parametric studies based on mathematical models containing the full EDL description (the Poisson-Nernst-Planck-Navier-Stokes models) are rare (Mortensen et al., 2005).

One can observe an interesting progress in the area of electroosmotically driven microfluidic devices. Especially the DC devices have found the use in commercial bioanalytical applications. However, there are still a lot of problems to solve. The multiphysical approach to complex analysis of the transport and also the reaction processes in microfluidic chips is often missing. Linear analysis has serious limitations. Hence, robust mathematical models should be developed for a comprehensive analysis and optimization of the produced and the designed microdevices of various complexities.

Below we demonstrate the use of our multiphysical mathematical model to solve selected problems related to the electroosmotically driven microfluidic devices. We focus on: (i) the effects of the electric charge number of antibodies and the surface electric charge on the performance of a bioassay in a tubular microchip, (ii) the analysis of strongly nonlinear dependence of the net flow velocity on AC frequency in the electroosmotic AC pumps, especially the observed flow reversals, (iii) nonlinear electrohydrodynamics and other transport phenomena in a DC single nanopore system with a fixed electric charge.

## 2. Mathematical Model

Nonequilibrium model of spatially distributed micro-electrochemical systems based on the mean field physical principles is formulated and discussed. We have used the following approximation: (i) systems are isothermal, (ii) the relative permittivity, the electrolyte viscosity, the electrolyte density and the ionic diffusivities are constant in each spatial domain represented by a single phase, (iii) the electrolytes are dilute and behave like Newtonian liquids, and (iv) the gravity effects are neglected.

### 2.1 Basic Equations and Boundary Conditions

Under the above mentioned simplifications, the velocity and the pressure fields can be computed from the Navier-Stokes equation and the continuity equation

$$\rho \left( \frac{\partial \mathbf{v}}{\partial t} + \mathbf{v} \cdot \nabla \mathbf{v} \right) = \mathbf{f}_E - \nabla p + \eta \nabla^2 \mathbf{v}, \quad (7)$$

$$\nabla \cdot \mathbf{v} = 0, \quad (8)$$

where  $p$  is pressure and  $\mathbf{v}$  is the velocity vector. According to Eq. (2), the local value of the electric body force  $\mathbf{f}_E$  depends on the distributions of the electric charge and the electric field strength  $E$ . The volume concentration of electric charge can be computed from Eq. (3) if the distributions of all ions are known. The ionic concentrations  $c_i$  are evaluated using the molar balances

$$\frac{\partial c_i}{\partial t} + \mathbf{v} \cdot \nabla c_i = -\nabla \cdot \mathbf{J}_i + r_i, \quad (9)$$

where  $r_i$  is the total source of the  $i^{\text{th}}$  component in all chemical reactions. The symbol  $\mathbf{J}_i$  denotes the sum of the local diffusive and the local electromigration flux intensities of the  $i^{\text{th}}$  ionic component given by the Nernst-Planck equation

$$\mathbf{J}_i = -D_i \nabla c_i + z_i D_i F c_i \mathbf{E} / (RT). \quad (10)$$

The distribution of the electric field strength or electric potential can be computed using the Poisson equation (a constant dielectric constant is considered)

$$\nabla^2 \Phi = -q/\epsilon. \quad (11)$$

The next task, and probably the most difficult one, is to find a consistent set of boundary conditions. There is no general approach how to solve this problem. The boundaries of microfluidic systems can be divided into two main groups: (i) the liquid-solid boundaries and (ii) the open boundaries.

For the former group, we can, for example, use: (i) the nonslip velocity conditions, (ii) the reference pressure at a specified point (in systems with periodic boundary conditions), (iii) the normal flux of ionic components equal to zero (without chemical reactions) or the normal flux of ionic components equal to the rate of the component consumption by a surface chemical reaction (with surface chemical reactions), (iv) a specified value of electric potential (electrode surfaces, polarized dielectric surfaces) or the electric potential gradient equal to zero (electric insulator surfaces) or Gauss's law applied on a boundary (polarized dielectric surfaces, the boundary between two dielectrics).

For the latter case, we can, for example, specify: (i) the velocity profile, (ii) the reference pressure, (iii) fixed values of ionic concentrations or the Danckwerts boundary conditions (continuous flow systems), (iv) a specified value of electric potential (the potential applied on the boundary) or the electric potential gradient equal to zero (electrically insulated boundaries). The periodic boundary conditions can be applied on the open boundaries, e.g., when the system is represented by a periodic element of a microfluidic channel. In such case, it is necessary to specify the reference pressure in a single point of the system.

The used sets of boundary conditions for the microfluidic systems described here can be found in (Postler et al., 2008, Pribyl et al., 2006a, Pribyl et al., 2006b).

The model equations are usually transformed into a dimensionless form. The choice of the scaling factors can differ for different microfluidic systems. Examples of nondimensionalization and scaling factors can be found, e.g., in (Postler et al., 2008, Pribyl et al., 2006a, Squires & Bazant, 2004, Squires & Quake, 2005).

## 2.2 Model Applicability, Possible Simplifications and their Limitations

We can recognize at least two spatial scales characterizing the micro- and nanochannel systems: (i) the Debye layer scale  $\lambda_D$ , (ii) the microchannel/microelectrode scale  $L$ . Depending on the  $L/\lambda_D$  ratio, we can distinguish three different types of such systems: (i) microsystems where  $L \gg \lambda_D$ , (ii) submicrosystems where  $L > \lambda_D$ , and (iii) nanosystems where  $L < \lambda_D$ . For the latter type, the use of the continuum approximation has to be cautious. In systems where the effects of a single molecule can be significant, the described mathematical model is not appropriate. The continuum approximation applied in the other

two types is usually reasonable. Generally, the numerical analysis of the submicrosystems is a somewhat easier than in the analysis of the microsystems because the characteristic spatial scales are not much different. In the microsystems, the ratio of the Debye length and the characteristic width of a microchannel is typically about  $10^{-4}$ . The largest gradients of electric potential, ionic concentrations, velocity and pressure are usually observed in the thin Debye layer. The processes in the Debye layer affect the global behavior of microfluidic systems. Hence, in the numerical analysis of the model equations, this fact leads to substantial discretization problems connected with the increase of the problem dimension and the decrease of the computational speed.

Many simplifications of the model equation were developed. One of them is based on the idea of the slip velocity. In this approach, the processes in the thin Debye layer are neglected and a nonzero tangential velocity given by Eq. (4) is considered on the interface: diffusive part of the Debye layer – the bulk solution. Thus, one of the spatial scales is eliminated. The introduction of the slip velocity also results in a substantial simplification of the model equation. If the Debye layer is an exclusive source of the nonzero mobile electric charge, the local electroneutrality is established everywhere. The right hand side of the Poisson equation is equal to zero, Eq. (11), and the distribution of electric potential is then described by the Laplacian. The electric volume force term in the Navier-Stokes equation, Eq. (7), also vanishes. Finally, the balance equations of the ionic components, Eq. (9), need not be solved. The slip velocity approach is powerful in many practical cases, e.g. (Pribyl et al., 2005); however, there are limitations. The slip velocity approach and the local electroneutrality condition should not be used, e.g., if: (i) the thickness of the Debye layer is comparable with the characteristic dimension of microfluidic channels (Pribyl et al., 2006a), (ii) an ionic component of the electrolyte interacts with a receptor bound on polarized dielectrics (Pribyl et al., 2006a), (iii) very fast chemical interactions take place (Lindner et al., 2002) etc.

Another simplification assumes the Boltzmann distribution of the electric charge at the dielectric surface. It means that the microscopic velocity is low and the EDL is considered to be in the thermal equilibrium. Instead of the Poisson equation, the Poisson-Boltzmann equation (PBE) has to be solved in order to get the electric potential distribution. The PBE written for a symmetric uni-univalent electrolyte is

$$\nabla^2 \Phi = 2c_0 F \sinh\left(\frac{F\Phi}{RT}\right) / \epsilon. \quad (12)$$

If the Boltzmann distribution is assumed, only the concentration of ions in the bulk has to be known. The molar balances of the ionic components are not solved. In some cases, the right hand side of Eq. (12) can be linearized and an exact distribution of electric potential in the EDL can be found. The linearized Eq. (12) describes the distribution with a good precision up to  $\Phi \approx 25$  mV.

The inertial forces are negligible in most microfluidic devices due to small characteristic dimensions. The nonlinear term  $\mathbf{v} \cdot \nabla \mathbf{v}$  in Eq. (7) can be neglected and we can obtain

$$\rho \frac{\partial \mathbf{v}}{\partial t} = \mathbf{f}_E - \nabla p + \eta \nabla^2 \mathbf{v}. \quad (13)$$

Further, the nonstationary term in Eq. (13) can be omitted if: (i) the flow is stationary or (ii) the flow is nonstationary but the order of the magnitude of the nonstationary term is smaller than that of the viscous term.

### 3. Numerical Analysis

Numerical analysis of model equations can be carried out with the help of a commercial or a self-made software. In our research group, we usually employ Comsol Multiphysics software for both the stationary and the nonstationary simulations. The software is based on the finite element method and designed for various multiphysical problems.

Because we mostly analyze the reaction-transport processes in the entire spatial domain including EDL, the critical step of the implementation is a proper domain discretization. The required characteristic dimension of the finite elements at polarized surfaces typically differs from the element size in the rest of the domain of a microsystem by the factor  $10^{-4}$ . It can be only partially resolved by the construction of a nonequidistant mesh of finite elements, e.g., a triangular mesh. While the tangential extent of the EDL is given by the dimensions of a dielectric surface, the normal extent of the EDL is approximately equal to the Debye length. It is almost impossible to construct an isotropic even if a nonequidistant mesh and not to exceed the memory capacity of a modern single CPU computer. Hence, an anisotropic (mapped) mesh of finite elements has to be constructed, e.g. a rectangular mesh. The anisotropic elements have one characteristic dimension much larger than other dimensions. Modern simulation software also enables to simply combine more types of finite element meshes on a single spatial domain.

The systems described below were discretized using anisotropic or combined meshes. The elements with the highest aspect ratio were localized at the surfaces represented by polarized dielectrics or electrodes.

### 4. Results and Discussions

#### 4.1 Microfluidic Biosensor

As the DC electrokinetic transport is often used in various microfluidic applications, we have decided to develop and analyze two types of mathematical models of a microfluidic biosensor. The first one is based on the physical nonslip description mentioned in the paragraph 2.1, the other one exploits the slip approximation (see the paragraph 2.2).

The geometry of the microfluidic biosensor is depicted in Fig. 4. It has been considered that the microsensor is realized in a tubular microfluidic channel. Because the axial symmetry has been assumed, the reaction-transport processes have been described only in the  $r - z$  (radial-axial) coordinates and the model equation were spatially two-dimensional. The system consists of five spatial domains: (I.) the inlet compartment, (II. and IV.) the compartments with charged walls, (III.) the reaction compartment with charged or uncharged walls, (V.) the outlet compartment. The sample solution containing a ligand is introduced in the system via the boundary (1). The solution flows through all the compartments and leaves the system via the boundary (16). The ligand can bind to the receptor that is immobilized on the boundary (9), where the ligand-receptor complex is formed. In principle, the amount of the complex is proportional to the ligand concentration in the sample. We have considered that the sample is introduced in the system for a certain time period; then, an electroosmotically dosed buffer washes out the unbound ligand and the total amount of the formed complex can be detected on the boundary (9). The bioaffinity reaction scheme and the reaction parameters used in our analysis can be found in (Pribyl et al., 2006a).



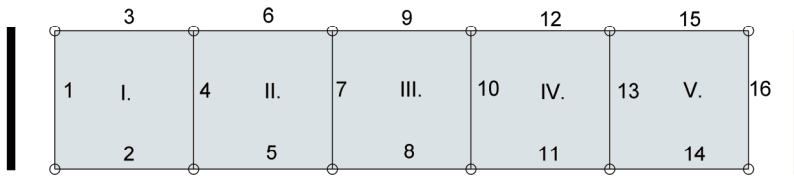


Figure 4. The scheme of the microfluidic sensor geometry. The roman and the arabic letters denote the domain and the boundary indexes, respectively. The width of each domain is equal to  $200\ \mu\text{m}$ . The height is equal to the biosensor radius,  $R_0$ . The thick lines depict the DC source electrodes

The boundaries indexed in Fig. 4 can be sorted into several groups: (1, 16) – the open boundaries (the Danckwerts boundary conditions, the applied potential difference, the reference pressure), (2, 5, 8, 11, 14) – the boundaries representing the symmetry axis (the normal flux of the ionic components, the normal electric field strength and the radial velocity are equal to zero), (3, 15) – the solid uncharged boundaries (the normal flux of components, the normal electric field strength and the velocity vector are equal to zero), (4, 7, 10, 13) – the internal boundaries, (6, 12) – the solid charged boundaries at which electroosmosis is induced (the normal flux of components equal to zero, a nonzero surface electric charge, the velocity vector equal to zero or the tangential velocity equal to the slip velocity), (9) – the reaction boundary (the same as the charged boundaries except that the normal flux of the ligand is equal to the rate of the ligand consumption by a surface chemical reaction).

The detailed mathematical description of both the slip and the nonslip models, their nondimensionalization and the values of the model parameters are given in the electronic supplement of (Pribyl et al., 2006a).

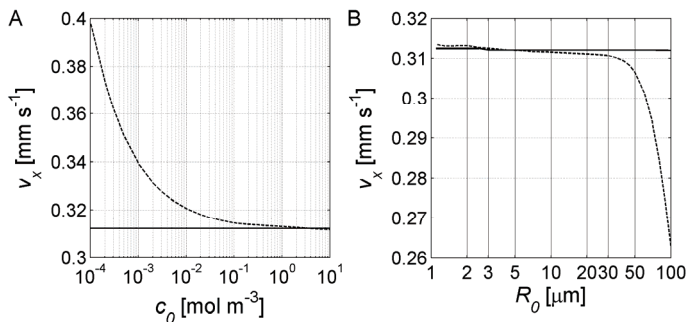


Figure 5. Comparison of the slip and the nonslip modeling; slip (solid line), nonslip (dotted line). (A) Dependence of the net velocity on the electrolyte concentration,  $R_0 = 10\ \mu\text{m}$ . (B) Dependence of the net velocity on the biosensor radius,  $c_0 = 10\ \text{mol m}^{-3}$

Dependence of the electroosmotic net velocity on the electrolyte concentration and the microchannel radius were computed for both models. The plots in Fig. 5. represent only an example of these dependencies found in the parametric space. Hence, the below mentioned discussion is relevant to this particular case and can not be generalized. In the slip model,

the dependence on the electrolyte concentration is constant because the electroosmotic velocity predicted by the Helmholtz-Smoluchowski equation is independent of concentration, Eq. (4), Fig. 5(A). The nonslip model gives almost the same net velocity as the slip model if the electrolyte concentration is higher than  $0.1 \text{ mol m}^{-3}$ . It means that the slip modeling is applicable for the most biochemical applications where buffers with a typical concentration  $10 \text{ mol m}^{-3}$  are used. If the concentration is low, the Debye length at the polarized surfaces expands according to Eq. (1) and the dimension of the EDL becomes comparable with the microchannel radius. Thus the result predicted by the slip model, that neglects the EDL processes, is no longer correct.

One of the important model parameters is the microchannel radius. One can be interested for what characteristic size of the biosensor the slip model is applicable. In this study, Fig. 5(B), the concentration is fixed at the value relevant for many bioapplications,  $c_0 = 10 \text{ mol m}^{-3}$ . The error of the slip modeling is negligible if the microchannel radius is in the range  $1\text{-}30 \text{ }\mu\text{m}$ . When the radius is larger, the error of the slip modeling becomes serious. The error is caused by the increase of the ratio of the radius and the length of the charged compartments. Intuitively, if this ratio increases to infinity, then the dimension of the cloud of the mobile charge will be negligible and the rate of the electroosmotic convection falls to zero. This effect can not be described by the slip approach due to the nonzero slip velocity at boundaries. Further, it is expected that the error of the slip model will be large if the microchannel radius will be very small, i.e., comparable to the Debye length.

The slip model does not describe the coulombic interaction between the ligand molecules and the polarized solid surface. As the biological macromolecules often have a nonzero charge number, the electrostatic interaction can crucially affect the result of a bioassay. The number of the formed ligand-receptor complexes can differ by several orders of magnitude in the parametric plane: surface density of the electric charge versus the ligand charge number, Fig. 6. As expected, if the electric charge fixed on the solid surface has the same sign as the ligand molecule, the total number of the formed complex molecules substantially decreases due to the electrostatic repulsion. Thus the pH value of the electrolyte is a very important parameter because it can tune both the zeta-potential and the ligand charge number.

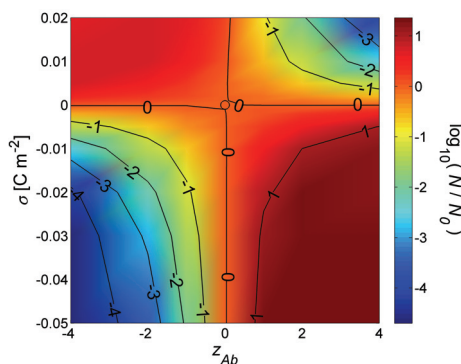


Figure 6. The number of the formed molecules of the ligand-receptor complex in the parametric plane: the surface density of the electric charge  $\sigma$  at the reaction zone versus the ligand charge number  $z_{Ab}$ . The number of molecules is related to the reference state without electrostatic interaction between the ligand and the surface,  $c_0 = 10 \text{ mol m}^{-3}$ ,  $R_0 = 20 \text{ }\mu\text{m}$

### 4.2 Submicron Pore

Submicron channels can be found, for example, in: (i) porous ion exchange membranes, (ii) packed layers, (iii) fluidic systems with extremely thin dosing channels etc. The solid surfaces are often polarized when filled with an electrolyte. The interaction of the polarized surfaces with an external DC electric field can give rise to interesting transport phenomena because the Debye length scale and the geometric scale are comparable. From the practical point of view, the submicrochannel systems interacting with a DC electric field are exploited, e.g., in electro dialyzers.

We have developed a nonequilibrium model of a single submicron pore that is filled with an electrolyte. The pore is in the contact with two surrounding electrolytes – the anolyte and the catholyte. It has been considered that the studied system consists of two phases: (i) the solid dielectric phase and (ii) the liquid electrolyte. The system can be divided into three subdomains: (i) the anolyte compartment (the electrolyte outside of the pore facing the anode), (ii) the pore compartment containing the internal electrolyte and the solid dielectrics, and (iii) the catholyte compartment (the electrolyte outside of the pore facing the cathode).

The geometric domain is spatially two dimensional because we have assumed that the width of the pore is much smaller than the third spatial dimension. Another geometric simplification comes from the axial symmetry. Hence, the transport processes were studied only in one half of the pore.

The schematic side view of the modeled geometry is shown in Fig. 7. We describe the left and the right open boundaries (1, 29) as the interfaces between the well mixed electrode compartments and the stagnant layers. Fixed values of the model variables are considered on the open boundaries (electric potential, pressure and concentrations). The other boundaries can be sorted into three groups: (14, 15, 19) – the electrolyte/solid interfaces with a fixed value of the surface electric charge, (2, 3, 5, 6, 8, 11, 13, 18, 21, 23, 25, 27, 28) – the boundaries representing the plane of the axial symmetry, and (4, 7, 8, 9, 10, 12, 17, 20, 22, 24, 26) – the internal boundaries used for the interfacing of structured and unstructured discretization meshes.

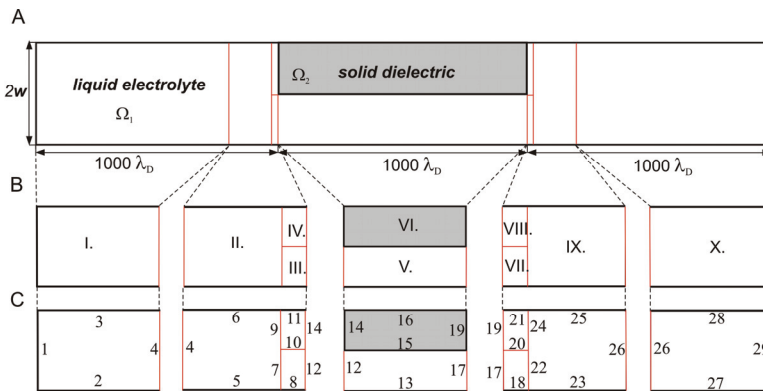


Figure 7. (A) The schematic view of the submicron pore geometry, (B) the domain indexes, (C) the boundary indexes. The symbol  $w$  denotes the half-width of the system that varies in the range of 1-5 Debye length units ( $\lambda_D$ )

As an illustrative example, the effect of the half-width of the system  $w$  on the current-voltage and the velocity-voltage characteristics is shown. The dependencies of the mean electric current density (averaged over the pore width) on the mean electric field strength

for various pore widths are plotted in Fig. 8(A). In the case of the widest pore, the curve (e), the system obeys Ohm's law and behaves like an electroosmotic pump, i.e., the electroosmotic velocity linearly increases with the applied potential difference according to Eq. (4). The situation is different for thinner pores, curves (a), (b) and (c), for which nonlinear current-voltage characteristics are observed. Here, the system behaves like a cation-exchange membrane with the typical nonlinear shape of the current-voltage characteristics. For a low electric field strength, an ohmic (linear) region is observed followed by a plateau, where the limiting current is reached. If the imposed electric field is further increased, the slope again becomes higher; i.e., an over-limiting current is attained. The case (d) represents the width where the system behavior qualitatively changes.

The corresponding velocity-voltage characteristics are plotted in Fig. 8(B). The fluid velocity in the wider pore, curve (e), is linearly proportional to the applied voltage; i.e., the Helmholtz-Smoluchowski approximation remains valid, while for the thinner pores, the curves (a), (b) and (c), the characteristics show nonlinearities. If the system approaches the limiting current, the driving force (the applied potential difference) mainly acts outside the pore in the free electrolyte, which results in a significant drop of the fluid velocity with respect to a wider pore. This decrease is caused by the development of a narrow layer of a very low conductivity in the anolyte compartment. This layer acts like a conductivity plug for the transport of the electrically charged species (Postler et al. , 2008).

Stationary velocity fields for two qualitatively different stationary regimes are plotted in Fig. 9. The velocity fields are represented by streamlines. The fluid flow structure remains almost unaffected over the entire studied range of the applied potential differences. The plug-flow velocity profile typical for the DC electroosmosis is observed within the pore Fig. 9(A). However, it has been found that a very high difference of the electric potential can cause irregularities in the velocity profile and eddies are formed at the pore/anolyte and the pore/catholyte interfaces, Fig. 9(B). The development of the eddies can significantly affect the stirring up of the transported electrolyte. The eddies probably result from the acting of the electrostatic field on the narrow layers of the low conductive electrolyte. More comprehensive information on the submicroporous system can be found in (Postler et al. , 2008).

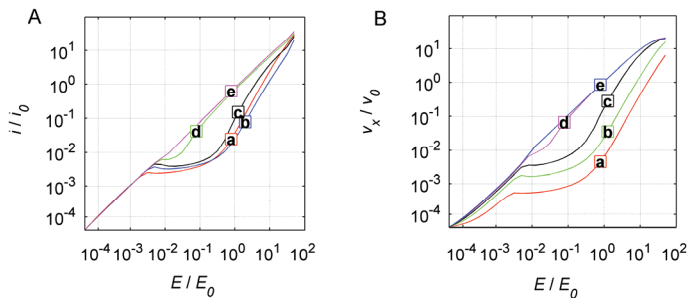


Figure 8. The dependencies of (A) the mean electric current intensity and (B) the mean fluid velocity on the mean electric field strength for several values of pore widths: (a)  $w/\lambda_D = 1$ , (b)  $w/\lambda_D = 2$ , (c)  $w/\lambda_D = 3$ , (d)  $w/\lambda_D = 4$ , and (e)  $w/\lambda_D = 5$ . The length, the electric field strength, the electric current density, and the net velocity are scaled by the characteristic values:  $\lambda_D = 9.63 \times 10^{-9}$  m,  $E_0 = 2.68 \times 10^6$  V m<sup>-1</sup>,  $i_0 = 4.01 \times 10^4$  A m<sup>-2</sup>,  $u_0 = 2.08 \times 10^{-1}$  m s<sup>-1</sup>, respectively. These scaling factors were evaluated for water solution of potassium chloride,  $c_0 = 1$  mol m<sup>-3</sup>

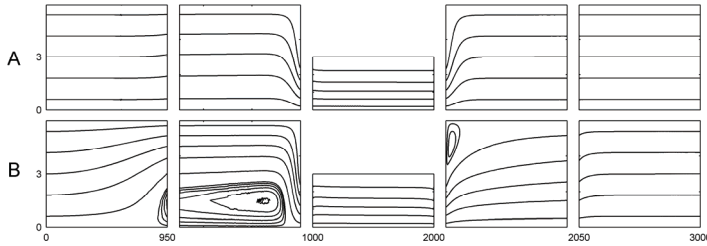


Figure 9. The velocity field, (A)  $E/E_0 = 0.1$ , (B)  $E/E_0 = 50$ . The pore width is  $w/\lambda_D = 3$

### 4.3 AC Micropumps

AC electrokinetic micro- and nano-pumps are frequently realized in microfluidic channels using periodic arrays of co-planar electrodes. The electrode arrays are deposited on a channel wall. Mostly, a pair of asymmetric co-planar electrodes is placed in a single segment of the microchannel. In order to analyze the electroosmotic transport with the use of the nonequilibrium model, we have proposed the geometry of a single segment, Fig. 10.

The single segment has been described in the cartesian coordinates. Spatially two-dimensional segment has been considered. We have assumed that the height of the channel is much smaller than the third spatial dimension of the channel, i.e., the channel profile looks like a flat rectangle. The system consists of five spatial domains: (I. and V.) the inlet/outlet compartments representing the distance between two segments of the AC pump, (II. and IV.) the compartments with the deposited electrodes, (III.) the compartment separating the electrodes. The electrolyte solution is introduced or released from the periodic segment via the open boundaries (1, 16) that are connected by the periodic boundary conditions. The boundaries (2, 3, 6, 8, 9, 12, 14, 15) represent the solid channel walls without any fixed electric charge (the normal flux of components, the surface electric charge, and the velocity vector are equal to zero). The boundaries (5) and (11) denote the electrode surfaces with an applied harmonic (sinusoidal) voltage and the reference electric potential, respectively. The zero velocity field and the zero normal flux of ionic components were considered on the electrodes. The group of the internal boundaries involves segments (4, 7, 10, 13). The reference pressure was specified only at a single point, as the single segment is not open. In this study, the amplitude of the AC electric field was equal to 1 V and the concentration of a symmetric uni-univalent electrolyte was  $0.01 \text{ mol m}^{-3}$ . The mathematical description of the model and the other model parameters are given in (Pribyl et al., 2006b).

In numerical analysis, it was necessary to compute the entire transient from the initial steady state to the stable periodic regime. The initial steady state was chosen as homogeneous in the entire segment, i.e., the zero velocity vector, the reference pressure, the reference electric potential, and the bulk concentration of the ionic components were independent of spatial coordinates. The duration of the transients depends on the AC frequency. The net velocity and the electric volume force were computed as the mean value over a single period of the stable periodic regime.

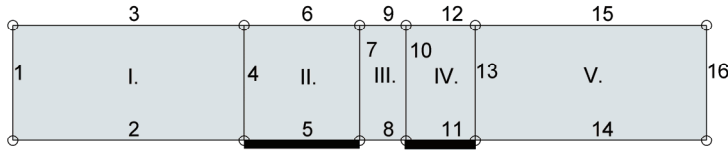


Figure 10. The scheme of a single segment of the AC microfluidic pump. The roman and the arabic letters denote the domain and the boundary indexes, respectively. The widths of the domains are 10  $\mu\text{m}$ , 5  $\mu\text{m}$ , 2  $\mu\text{m}$ , 3  $\mu\text{m}$ , and 10  $\mu\text{m}$ , respectively. The height is 10  $\mu\text{m}$ . The thick lines depict the AC source electrodes

As mentioned in the paragraph 1.3, the net velocity of the AC electroosmotic pumping depends nonlinearly on the AC frequency. Our results also exhibit this nonlinearity, Fig. 11(A). As the AC frequency grows, one can observe two flow reversals. The net velocity is negative in the intervals  $\langle 1 \times 10^{-1}; 3 \times 10^1 \rangle \text{ s}^{-1}$  and  $\langle 4 \times 10^2; 1 \times 10^5 \rangle \text{ s}^{-1}$ . Positive values of the net velocity were found in the frequency interval  $\langle 3 \times 10^1; 4 \times 10^2 \rangle \text{ s}^{-1}$ . The existence of the flow reversals is in a qualitative agreement with the published data (Garcia-Sanchez et al., 2006, Studer et al., 2004). For the given set of parameters, the maximal net velocity attains only few tens of microns per second. However, it can be substantially increased by the optimization of the geometric and the electric field parameters.

If the AC frequency is low, e.g.  $1 \times 10^{-1} \text{ s}^{-1}$ , the system behaves like a condenser, i.e., the current-voltage phase shift is equal to 90 degrees, Fig. 11(B). In such regime, the electrode surfaces are fully polarized and the tangential component of the electric field strength is equal to zero except at the electrode boundaries, which results in the zero net velocity. The maximal velocity in the absolute value is observed for the AC frequency  $2 \times 10^3 \text{ s}^{-1}$ . Almost the same frequency value can be estimated from the theory as the reciprocal charging time  $\tau_E$ , Eq. (5). The phase shift is then about 20 degrees. If the AC frequency is high, e.g.,  $1 \times 10^5 \text{ s}^{-1}$ , the system behaves as a resistor, i.e., the current-voltage phase shift is equal to 0 degrees. The AC period is then approximately equal to the Debye time  $\tau_D$ , Eq. (5). As no mobile electric charge can be formed at the electrode surfaces in such regime, the zero net velocity is observed.

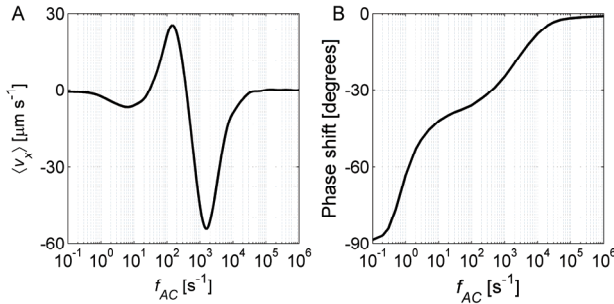


Figure 11. Dependencies of the net velocity (A) and the current-voltage phase shift (B) on the applied AC frequency

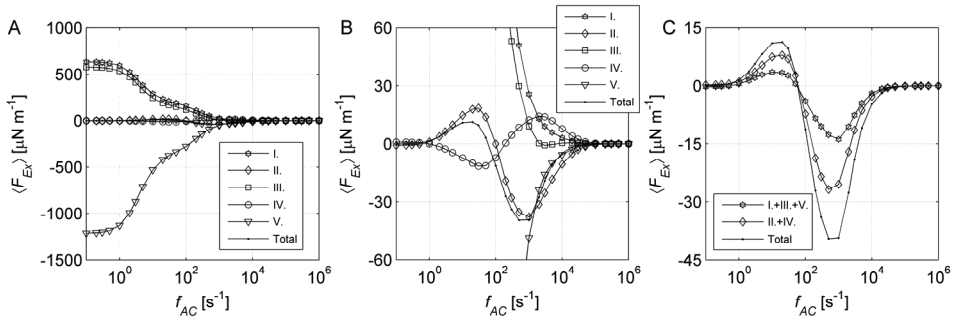


Figure 12. Dependencies of the tangential (longitudinal) component of the electric volume force on the applied AC frequency. (A) The force in each compartment and the total volume force in the entire segment, (B) the same as (A) in detail, (C) the force summed over the nonelectrode compartments, summed over the electrode compartments, and summed over the entire segment

The dependencies in Fig. 11 are strongly nonlinear. It can be helpful to study the dependence of the tangential component of the electric force  $\langle F_{Ex} \rangle$  on the AC frequency, Fig. 12. The force has been evaluated in each segment domain as a surface integral of the tangential component of the electric volume force. The force in the nonelectrode compartments is much higher than in the electrode compartments in the AC frequency interval  $(1 \times 10^{-1}; 1 \times 10^3) \text{ s}^{-1}$ . However, the sum of the electric body force over all nonelectrode compartments is always smaller (in the absolute value) than that summed over the electrode compartments, Fig. 12(C).

If the AC frequency is very low, the force is localized only at the electrode-dielectric interface (the boundary interfaces 2/5, 5/8, 8/11, 11/14, see Fig. 10). Only here, the mobile electric charge and the tangential gradient of electric potential are localized together. As the transport processes are faster than the electric field alternation, the electric force is symmetric with respect to the electrode centers, i.e., the force at the 2/5 and 8/11 interfaces compensate the forces at the 5/8 and 11/14 interfaces, respectively. The phase shift is almost 90 degrees in such a regime, Fig. 11(B).

In the AC frequency range  $(1 \times 10^0; 1 \times 10^4) \text{ s}^{-1}$ , the electric body force above the larger electrode (domain II.) is in the absolute value always higher than above the smaller one (domain IV.), Fig. 12(B). The dependence of the total volume force on the AC frequency has a similar shape as the velocity dependence (compare Figs. 11(A) and 12(C)). However, there are also differences: (i) the force dependence crosses zero value only once, (ii) the electric body force and the net velocity can differ in the sign at some frequencies, and (iii) the main flow reversal at  $f_{AC} = 2 \times 10^{-3} \text{ s}^{-1}$  is not accompanied by an electric body force reversal.

As expected, the dependence of the maximal amount of the electric charge  $Q_M$  on the AC frequency is plotted in Fig. 13(A) as a solid line. This dependence monotonically decreases with the growing frequency. In the same figure, the amount of the mobile electric charge at the time, when the applied voltage is equal to the amplitude, is plotted by the dotted line,  $Q_A$ . For low frequencies, these two quantities are almost the same because the electrode charging process is much faster than the electric field alternation. If the AC frequency is high, the degree of the electrode polarization is low and  $Q_A$  becomes smaller than  $Q_M$ . The

ratio  $Q_A / Q_M$  is not monotonic and has a local minimum at  $f_{AC} = 1 \times 10^1 \text{ s}^{-1}$  and a local maximum at  $f_{AC} = 1 \times 10^2 \text{ s}^{-1}$ , Fig. 13(B).

If one looks on the characteristics, it can be seen that the nonlinear dependence of the net velocity can not be explained only on their bases. It will be necessary to analyze the spatial distributions of: (i) the mobile electric charge at various phases of the AC electric field, (ii) the normal component of the electric field strength, (iii) the velocity and the pressure fields, etc. At this stage, we can only conclude that the observed flow reversals do not rely on the faradaic interactions because those are not considered in our mathematical model.

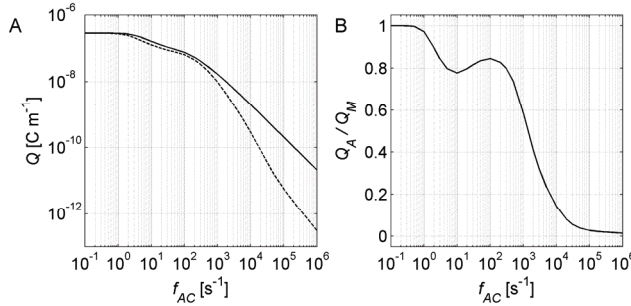


Figure 13. Dependencies of the mobile electric charge in the electrode compartments on the applied AC frequency. (A) The maximal mobile electric charge during an AC period  $Q_M$  (solid line), the mobile electric charge if the voltage is equal to the voltage amplitude  $Q_A$  (dotted line), (B) the  $Q_A / Q_M$  ratio

The use of a phase shift of an AC electric field applied on a field of symmetric coplanar electrodes is an alternative to the asymmetric coplanar design. In this study, we have proposed two different realizations either with the two-phase arrangement, Fig. 14(A), or with the three-phase arrangement, Fig. 14(B). In the two-phase and the three-phase systems, the relative phase shifts  $180^\circ$  and  $120^\circ$  are applied on the adjacent electrodes, respectively. In principle, the same mathematical description as in the system depicted in Fig. 10 has been used. There are only two differences: (i) all electrodes are of the same size and (ii) the axial symmetry is assumed, i.e., the electrodes are deposited on two opposite walls.

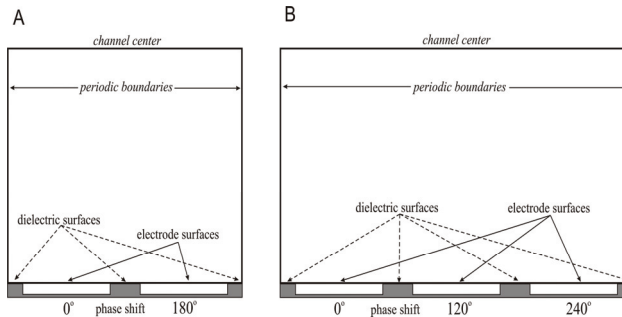


Figure 14. The scheme of a single segment of the AC electroosmotic pump with an imposed phase shift between coplanar electrodes, (A) two-phase arrangement, (B) three-phase arrangement. The dimension of the electrodes, the dimension of the gap between the electrodes and the channel half-width are  $300 \lambda_D$ ,  $50 \lambda_D$ ,  $1000 \lambda_D$ , respectively, ( $\lambda_D = 9.63 \times 10^{-9} \text{ m}$ )



The qualitative comparison of the two-phase and the three-phase realizations is depicted in Fig. 15. For the former realization, the resulting net velocity is equal to zero because the velocity fields with  $90^\circ$  phase shift have the same structure but the flow direction is opposite, Fig. 15 (A). For the latter realization, one can observe a nonzero net velocity in the direction from the right to the left, Fig. 15 (B). If two velocity fields with  $120^\circ$  phase shift are compared, we can see that the velocity field structure is again the same, however, spatially shifted by one electrode distance (in this case to the left). The direction of the flow can be reversed if the order of phases is reversed similarly as in a three-phase electromotor.

## 5. Conclusion

The described Poisson-Nernst-Planck-Navier-Stokes nonequilibrium mathematical model is a powerful tool for analysis of the reaction transport processes in various microfluidic devices, namely, geometrically complex microfluidic structures with polarizable dielectric walls or deposited metal electrodes with an imposed electric potential under the electrochemical limit. The microfluidic structures have to be filled with a liquid electrolyte, no electrochemical interactions have to occur, and the applications have to be performed under isothermal conditions. For example, the proposed mathematical model enables numerical analysis of: (i) chemical and biochemical interactions in homogeneous and heterogeneous arrangement, (ii) the combined diffusion-electromigration-convective transport of ionic and electroneutral components, (iii) the DC electroosmotic convection induced at polarized surfaces, (iv) the AC electroosmotic convection forced at microelectrode arrays, (v) the pressure and the velocity fields etc.

It has been demonstrated that the use of the nonequilibrium model is necessary, e.g., when the characteristic dimension of the microfluidic device is comparable with the thickness of EDL (low concentrated electrolytes, very thin microchannels) or the polarized dielectric walls interact with an ionic reaction components diluted in the electrolyte.

We have shown that a porous structure surrounded by an aqueous electrolyte and affected by an external DC electric field can behave as either a DC micropump or an ionexchange membrane. The behavior depends on the pore diameter, the electrolyte concentration and other parameters. Interesting nonlinear hydrodynamic phenomena such as the eddy formation were observed in our simulations. In the future, our work will deal with the analysis of complex electrohydrodynamic processes in the pores and the surrounding electrolyte in the overlimiting current domain. It can contribute to the overlimiting current theory.

Selected characteristics of the AC electroosmosis forced by the coulombic force in the studied microchannels have been presented. Both asymmetric (interdigitated) and symmetric (traveling wave) arrangements were analyzed by means of the nonequilibrium model. The obtained characteristics are nonlinear and the explanation of the flow reversals remains unclear, except the finding that the flow reversals do not necessarily rely on the electrochemical reactions. However, the model gives us the opportunity to get not only qualitative but also quantitative insights into flow reversals via detailed analysis of spatiotemporal fields of all dependent variables.

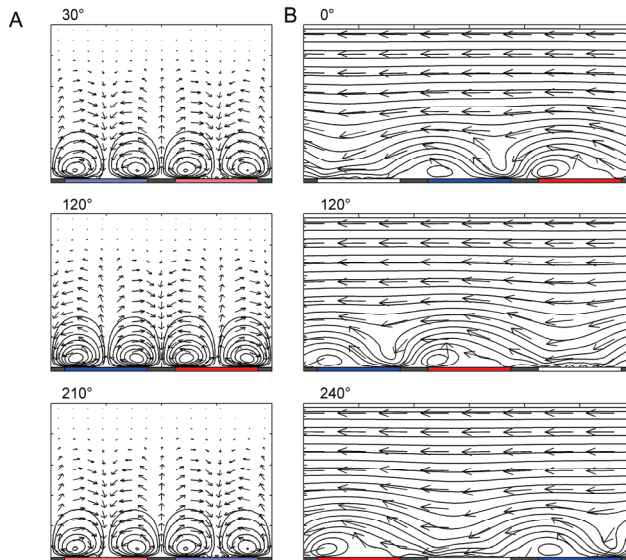


Figure 15. The velocity fields for the two-phase arrangement (A) and for the three-phase arrangement (B) at different times expressed in the phase angles of one period. The period of the AC electric field  $\tau_{AC} = 100 \tau_D$ , Eqs. (5) and (6), and the AC amplitude  $A = 10RT/F$

## 6. Acknowledgement

The authors thank for the support by the grant of the Grant Agency of the Czech Academy of Science KAN208240651 and by the grant of the Ministry of Education, Youth and Sport of the Czech Republic MSM 6046137306.

## 7. References

- Ajdari, A. (2000). Pumping liquids using asymmetric electrode arrays. *Physical Review E*, 61, 1, R45-R48, 1063-651X
- Bazant, M.Z. & Ben, Y.X. (2006). Theoretical prediction of fast 3D AC electro-osmotic pumps. *Lab on a Chip*, 6, 11, 1455-1461, 1473-0197
- Becker, H. & Locascio, L.E. (2002). Polymer microfluidic devices. *Talanta*, 56, 2, 267-287, 0039-9140
- Beebe, D.J.; Mensing, G.A. & Walker, G.M. (2002). Physics and applications of microfluidics in biology. *Annual Review Of Biomedical Engineering*, 4, 261-268, 1523-9829
- Bilitewski, U.; Genrich, M.; Kadow, S. & Mersal, G. (2003). Biochemical analysis with microfluidic systems. *Analytical And Bioanalytical Chemistry*, 377, 3, 556-569, 1618-2642
- Campisi, M.; Accoto, D. & Dario, P. (2005). ac electroosmosis in rectangular microchannels. *Journal of Chemical Physics*, 123, 20, 204724, 0021-9606

- Ejsing, L.; Smistrup, K.; Pedersen, C.M.; Mortensen, N.A. & Bruus, H. (2006). Frequency response in surface-potential driven electrohydrodynamics. *Physical Review E*, 73, 3, 037302, 1539-3755
- Erickson, D. (2005). Towards numerical prototyping of labs-on-chip: modeling for integrated microfluidic devices. *Microfluidics and Nanofluidics*, 1, 4, 301-318, 1613-4982
- Garcia-Sanchez, P.; Ramos, A.; Green, G. & Morgan, H. (2006). Experiments on AC electrokinetic pumping of liquids using arrays of microelectrodes. *Ieee Transactions on Dielectrics and Electrical Insulation*, 13, 3, 670-677, 1070-9878
- Green, N.G.; Ramos, A.; Gonzalez, A.; Morgan, H. & Castellanos, A. (2002). Fluid flow induced by nonuniform ac electric fields in electrolytes on microelectrodes. III. Observation of streamlines and numerical simulation. *Physical Review E*, 66, 2, 026305, 1063-651X
- Green, N.G.; Ramos, A. & Morgan, H. (2000). Ac electrokinetics: a survey of sub-micrometre particle dynamics. *Journal of Physics D-Applied Physics*, 33, 6, 632-641, 0022-3727
- He, X. & Hauan, S. (2006). Microfluidic modeling and design for continuous flow in electrokinetic mixing-reaction channels. *Aiche Journal*, 52, 11, 3842-3851,
- Chang, C.C. & Yang, R.J. (2007). Electrokinetic mixing in microfluidic systems. *Microfluidics and Nanofluidics*, 3, 5, 501-525, 1613-4982
- Khan, T. & Reppert, P.M. (2005). A finite element formulation of frequency-dependent electro-osmosis. *Journal of Colloid and Interface Science*, 290, 2, 574-581, 0021-9797
- Kim, B.J.; Yoon, S.Y.; Sung, H.J. & Smith, C.G. (2007). Simultaneous mixing and pumping using asymmetric microelectrodes. *Journal of Applied Physics*, 102, 7, 074513, 0021-8979
- Laser, D.J. & Santiago, J.G. (2004). A review of micropumps. *Journal Of Micromechanics And Microengineering*, 14, 6, R35-R64, 0960-1317
- Lastochkin, D.; Zhou, R.H.; Wang, P.; Ben, Y.X. & Chang, H.C. (2004). Electrokinetic micropump and micromixer design based on ac faradaic polarization. *Journal of Applied Physics*, 96, 3, 1730-1733, 0021-8979
- Lindner, J.; Snita, D. & Marek, M. (2002). Modelling of ionic systems with a narrow acid base boundary. *Physical Chemistry Chemical Physics*, 4, 8, 1348-1354, 1463-9076
- Loucaides, N.; Ramos, A. & Georghiou, G.E. (2007). Novel systems for configurable AC electroosmotic pumping. *Microfluidics and Nanofluidics*, 3, 6, 709-714, 1613-4982
- Mortensen, N.A.; Olesen, L.H.; Belmon, L. & Bruus, H. (2005). Electrohydrodynamics of binary electrolytes driven by modulated surface potentials. *Physical Review E*, 71, 5, 056306, 1539-3755
- Mpholo, M.; Smith, C.G. & Brown, A.B.D. (2003). Low voltage plug flow pumping using anisotropic electrode arrays. *Sensors and Actuators B-Chemical*, 92, 3, 262-268, 0925-4005
- Olesen, L.H.; Bruus, H. & Ajdari, A. (2006). ac electrokinetic micropumps: The effect of geometrical confinement, Faradaic current injection, and nonlinear surface capacitance. *Physical Review E*, 73, 5, 056313, 1539-3755
- Postler, T.; Slouka, Z.; Svoboda, M.; Pribyl, M. & Snita, D. (2008) Parametrical studies of electroosmotic transport characteristics in submicrometer channels. *Journal of Colloid and Interface Science*, 320, 1, 321-332, 0021-9797

- Pribyl, M.; Knapkova, V.; Snita, D. & Marek, M. (2005). Analysis of reaction-transport phenomena in a microfluidic system for the detection of IgG. *Chemical Papers-Chemické Zvesti*, 59, 6A, 434-440, 0366-6352
- Pribyl, M.; Knapkova, V.; Snita, D. & Marek, M. (2006a). Modeling reaction-transport processes in a microcapillary biosensor for detection of human IgG. *Microelectronic Engineering*, 83, 4-9, 1660-1663, 0167-9317
- Pribyl, M.; Schrott, W.; Shahravan, A. & Snita, D. (2006b). Mathematical modeling of a microchip driven by AC electric field, *Proceedings of 2006 International Symposium on Electrohydrodynamics*, pp. 309-312, CD ROM, ISBN 950-29-0964-X, Universidad de Buenos Aires, Buenos Aires
- Probstein, R.F., *Physicochemical hydrodynamics: An Introduction*. second ed. 1994, New York: Wiley and Sons.
- Ramos, A.; Morgan, H.; Green, N.G. & Castellanos, A. (1998). Ac electrokinetics: a review of forces in microelectrode structures. *Journal of Physics D-Applied Physics*, 31, 18, 2338-2353, 0022-3727
- Ramos, A.; Morgan, H.; Green, N.G.; Gonzalez, A. & Castellanos, A. (2005). Pumping of liquids with traveling-wave electroosmosis. *Journal of Applied Physics*, 97, 8, 084906, 0021-8979
- Squires, T.M. & Bazant, M.Z. (2004). Induced-charge electro-osmosis. *Journal of Fluid Mechanics*, 509, 217-252, 0022-1120
- Squires, T.M. & Quake, S.R. (2005). Microfluidics: Fluid physics at the nanoliter scale. *Reviews of Modern Physics*, 77, 3, 977-1026, 0034-6861
- Studer, V.; Pepin, A.; Chen, Y. & Ajdari, A. (2004). An integrated AC electrokinetic pump in a microfluidic loop for fast and tunable flow control. *Analyst*, 129, 10, 944-949, 0003-2654
- Urbanski, J.P.; Levitan, J.A.; Burch, D.N.; Thorsen, T. & Bazant, M.Z. (2007). The effect of step height on the performance of three-dimensional ac electro-osmotic microfluidic pumps. *Journal of Colloid and Interface Science*, 309, 2, 332-341, 0021-9797
- Urbanski, J.P.; Thorsen, T.; Levitan, J.A. & Bazant, M.Z. (2006). Fast AC electro-osmotic micropumps with nonplanar electrodes. *Applied Physics Letters*, 89, 14, 143508, 0003-6951
- Wang, X.M. & Wu, J.K. (2006). Flow behavior of periodical electroosmosis in microchannel for biochips. *Journal of Colloid and Interface Science*, 293, 2, 483-488, 0021-9797
- Zhang, Y.L.; Wong, T.N.; Yang, C. & Ooi, K.T. (2006). Dynamic aspects of electroosmotic flow. *Microfluidics and Nanofluidics*, 2, 3, 205-214, 1613-4982

# Efficient Simulation of Thermal and Electrical Behaviour of Industrial Cables

Hans-Peter Schmidt  
*University of Applied Sciences Amberg-Weiden  
Germany*

## 1. Introduction

Numerical modelling is applied in industrial applications in various ways. This chapter describes the application of modern simulation packages for distributed parameters combined with standard network type calculations and numerical procedures. In an application driven approach, simulation with distributed parameters is used as input for lumped parameter calculations. Thermal loading and electrical behaviour with regards to signal transmission in plant and process automation is dealt with. The main focus is on efficient modelling which yields sufficient accurate results for the application while covering the relevant range of operating conditions.

The well-known governing equations of electromagnetism and conservation equations for energy, momentum and mass may be solved via FEM and FVM methods to yield appropriate values for lumped parameters. Using these parameters an efficient network type calculation is carried out. Modelling and results for special cables used in power and data transmission are presented. Current carrying capacities for various operating conditions are studied.

## 2. Application

In industrial applications like materials handling, decentralized automation becomes widely applied. Loads like variable speed drives are not radially fed but connected to a power bus. Furthermore, power and data might be transmitted within one single cable. Here the need for thermal and electrical simulations arises.

A model is derived to calculate the ampacity for various operating conditions and Comsol (Comsol 2006) is applied to determine thermal resistances. For the data transmission cable, parameter and crosstalk are determined for multi core cables.

## 3. Thermal behaviour

When a non standard cable is used, the ampacity is to be determined for various laying and operating conditions. This maximum permissible current  $I_z$  for a cable with respect to thermal overload is usually determined for a well-defined operational condition and then related to various actual conditions via equation 1 (IEC 60287, VDE 0299).

$$I_z = I_r \cdot \prod f_i \tag{1}$$

The “rated current”  $I_r$  and the correction factors  $f_i$  are to be determined to cover the relevant range of operational conditions. For optimal utilization actual operational conditions can be modelled in detail and appropriate corrections factors may be deduced.

**3.1 Thermal Modelling**

Joule heating is balanced by conduction, convection and radiation. All of the processes are temperature dependent and lead to a system of non-linear partial differential equations. A complete 3 D solution of the energy, momentum and continuity equation via a SIMPLEC (Patankar, 1980) type simulation (Bauder et. al. 1996, Schmidt 1996, Schmidt 2005) yields temperatures with reasonable accuracies.

Nevertheless this is no practical way to determine the required correction factors. More suitable is the lumped parameter approach. This modelling of heat flow with an electrical network requires appropriate simplifications. However, the resulting non-linear circuit is solved with standard numerical procedures and the maximum permissible current may be determined explicitly. As an example a typical multi-core flat cable is considered which is used for power and data transmission.

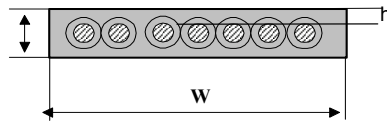


Figure 1. Schematic sketch of a typical flat multi core cable

**3.2 Lumped Parameter Model**

The usual modelling via an equivalent electrical circuit is applied (IEC 60287; Schmidt, 2005; Wutz;1991). Current sources account for temperature dependent Joule heating where cooling is modelled via resistances. The simple model with only one conductor is readily extended to the multi core case. The temperature depended heating is given via  $P_{v,} = I^2 R_{el}(\vartheta)$ . The thermal resistance of the insulation is modelled via  $R_{th\_iso}$ , convection is modelled via  $R_{th\_a}$  and  $R_{th\_s}$  accounts for radiative heat transfer.

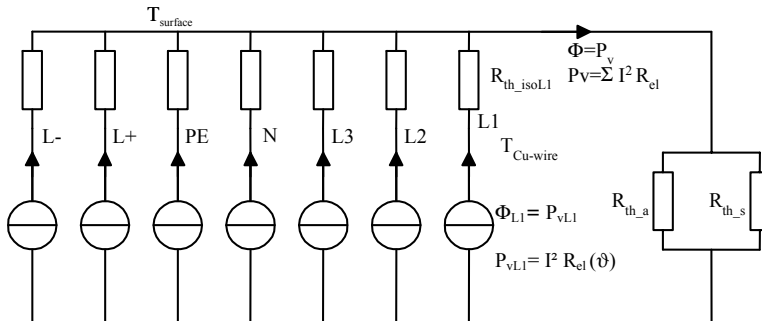


Figure 2. Equivalent circuit with seven conductors and a single surface temperature

With this simple model the surface temperature of the cable is calculated from equation 2, using the effective thermal resistance which covers the heat transfer from the surface of the cable to the ambience.

$$\Delta\vartheta_{Sur} = \Phi \cdot \frac{R_{th\_a} R_{th\_s}}{R_{th\_a} + R_{th\_s}} \quad (2)$$

The total heat flux is given by the summation over the conductors which may be at different temperatures as indicated in equation 3.

$$\Phi_{ges} = \left( \sum_{i=1}^{N_{max}} I_i^2 \cdot R_{el\_i}(\vartheta_{C\_i}) \right) \quad (3)$$

This may be expanded to account for various operational conditions or for a more geometrically detailed model of the surface. Therefore the temperature of the surface may be calculated from a single non-linear equation (xx) if core temperatures  $\vartheta_{C\_i}$  are known.

$$\Delta\vartheta_{Sur} = \left( \sum_{i=1}^{N_{max}} I_i^2 \cdot R_{el\_i}(\vartheta_{C\_i}) \right) \cdot \left( \frac{R_{th\_a}(\vartheta_{Sur}, \vartheta_{amb}) \cdot R_{th\_s}(\vartheta_{Sur}, \vartheta_{amb})}{R_{th\_a}(\vartheta_{Sur}, \vartheta_{amb}) + R_{th\_s}(\vartheta_{Sur}, \vartheta_{amb})} \right) \quad (4)$$

The core and the surface temperature are related by the heat flux and may be substituted as required. Therefore effective thermal resistances may be presented in terms of surface or core temperatures. On the other hand, core temperatures have to be calculated from a set of non-linear equations.

$$\Delta\vartheta_{C\_j} = I_j^2 \cdot R_{el\_i}(\vartheta_{C\_i}) \cdot R_{th\_iso} + \left( \sum_{i=1}^{N_{max}} I_i^2 \cdot R_{el\_i}(\vartheta_{C\_i}) \right) \cdot \left( \frac{R_{th\_a}(\vartheta_{Sur}, \vartheta_{amb}) \cdot R_{th\_s}(\vartheta_{Sur}, \vartheta_{amb})}{R_{th\_a}(\vartheta_{Sur}, \vartheta_{amb}) + R_{th\_s}(\vartheta_{Sur}, \vartheta_{amb})} \right) \quad (5)$$

Since the maximum permissible temperatures of the cores are known equation 5 may be simplified substantially. The electrical resistance of the core is calculated at the maximum permissible temperature. Then the related maximum permissible currents may be calculated. If the cores are loaded with the identical currents then this model leads to a single non linear equation and the maximum current can be given for different number of loaded cores.

$$I = I_1 = I_2 = \dots = I_N$$

$$I = \sqrt{\frac{\Delta\vartheta_{C\_j}}{R_{el}} \cdot \frac{1}{R_{th\_iso} + N \cdot R_{thAmb}(\Delta\vartheta_{C\_j}, T_{amb})}} \quad (6)$$

Maximum permissible currents for various operating conditions can be calculated efficiently. The relevant quantities for the application i.e.  $I_r$  and  $f_i$  ( eq. 1 ) are readily taken from these results.

### 3.3 Determination of Lumped Parameter Values

Assuming a constant temperature at the surface, one can approximate the thermal resistance from conduction. The values are readily found by solving the well-known energy

conservation equation for heat conduction. Both FEM/FVM calculations yield high accuracy for arbitrary geometry and non-linear materials.

$$\nabla \circ \lambda \cdot \nabla \vartheta = -s \quad (7)$$

$s$  denotes the source term i.e. ohmic heating,  $\lambda$  denotes the thermal conductivity. From the solution, i.e. the temperature field, the thermal resistances can be calculated by the ratio of temperatures to applied power. The thermal resistance calculated from this basic relation is in good agreement with an analytical approximation. More complex are convective and radiative heat transfer. The thermal resistance for natural convection may be represented by

$$R_{th\_a} = \frac{1}{aA} \quad (8)$$

The heat transfer coefficient  $a$  may be determined via the boundary layer approach (VDI WärmAtlas 2006)

$$a = \frac{Nu \cdot \lambda}{L} \quad (9)$$

Nusselt number:

$$Nu = \left[ 0,825 + 0,325 Ra^{1/6} \right]^2 \quad (10)$$

Rayleigh number:

$$Ra = Gr \cdot Pr \quad (11)$$

Prandtl number:

$$Pr = \frac{\eta c_p}{\lambda} \quad (12)$$

Grasshof number:

$$Gr = \frac{g \beta \Delta T L L'^2}{\nu^2} \quad (13)$$

$\eta$  viscosity,  $c_p$  thermal capacity,  $\lambda$  thermal conductivity,  $\beta$  compressibility,  $\nu$  viscosity,  $L$  length of surface,  $L'$  effective length

Clearly, the heat transfer coefficient might be taken from detailed SIMPLEC type calculations, but this is not really efficient. So this is only used to check the boundary layer results for uncertainties. These are effective length and the like.

Likewise the thermal resistance for radiation is temperature dependent. The simplest model (Wutz, 1991; Schmidt, 2005) leads to

$$R_{th\_s} = \frac{1}{A \varepsilon \sigma (T + T_u) \cdot (T^2 + T_u^2)} \quad (14)$$

Considering different ambient conditions e.g. cable layings these effective resistances have to be re-determined.



### 3.4 Results of thermal modelling

As an example, the results are given for two different laying conditions. The maximum permissible current for the relevant range of ambient temperatures is shown below.

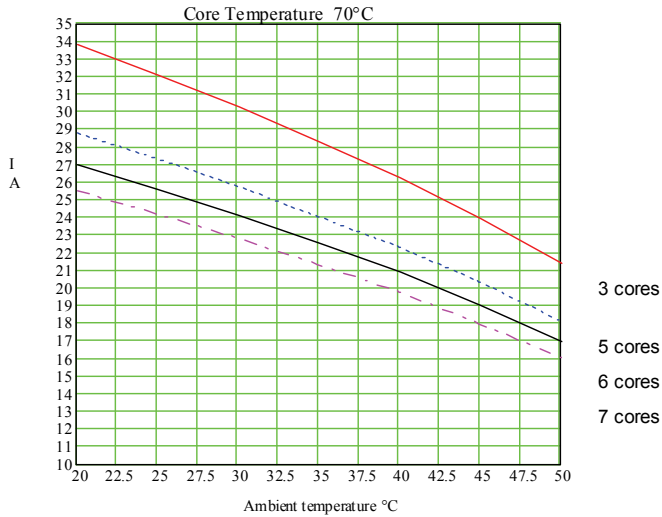


Figure 3. Maximum currents for laying on a concrete wall (70°C conductor temperature)

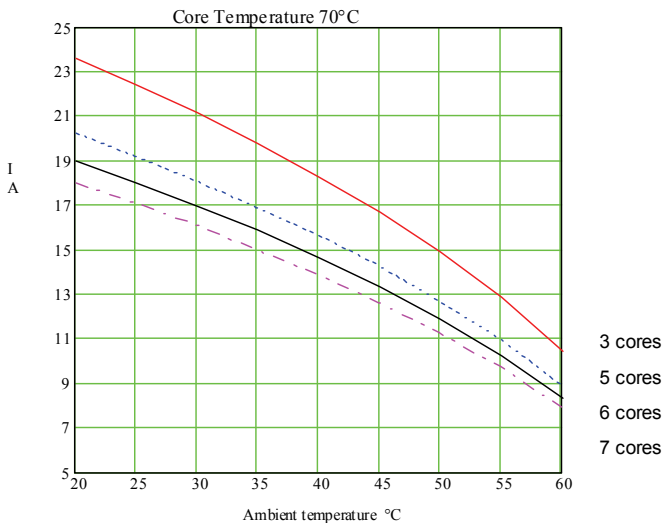


Figure 4. Maximum currents for laying on an insulating wall (70°C conductor temperature)

In figure 3, maximum permissible currents for a standard PVC installation (70°C max) are given for a laying on a concrete wall. In comparison, figure 4 gives these permissible currents when the cable is laid on an insulating wall.

The current carrying capacity (e.g. three cores loaded) is higher than that found in the standards. The standards deal mostly with round cables. Usually this type of cable has air pockets and is not compact. The flat cable considered here has no air pockets whatsoever and conduction to the surface is more effective. Furthermore, the surface area is larger than that considered in standards.

All of the results are in good agreement with measurements by Graf ( Graf 2003). The reduction with temperature is also in very good agreement with derating factors given in standards (IEC 60287 and VDE 0299).

#### 4. Modelling of the Electrical behaviour

In automation, so-called hybrid cables with elaborate screening are commonly used to transmit data and auxiliary power within a single cable. A different approach is investigated here with AS-I (Actor Sensor interface) communication. Usually this communication employs a two-wire flat cable without shielding and piercing contacts. Data are encoded with sin square pulses at 167 kHz.

The feasibility of using standard multi core cables for data and power transmission is investigated. Various cables are investigated and compared to standard cables as given by the specifications.

Firstly, the cable parameters are determined and checked against the standard requirements. Secondly, the coupling between pairs of conductors is detailed to access cross talk from the power transmission to the signal carrying conductors. Again results are checked against measurements.

##### 4.1 Modelling

Depending on cable laying various stray capacitances or inductances may come into play. E.g. cables may be mounted directly on a metal support (aluminium or sheet steel). This may affect stray and total capacitance with regard to the signal. Inductance and losses might increase considerably with steel supports.

Relevant frequencies are smaller than 500 kHz and installations are limited to extensions of approximately 100 m. Thus a quasi static approach may be used.

Lumped parameters are determined by calculations using Comsol (Comsol 2006). These parameters are used in network calculations where coupling and distortions are determined.

##### 4.2 Capacitances

The geometry of the cables are specified and the capacitances are readily calculated when the dielectric properties of the insulation are known. Materials in use vary e.g. from EPDM to PUR partly with PVC core insulation.

The potential distribution is calculated from a standard Laplace equation, since there are no space charges.

$$\nabla \circ \varepsilon \cdot \nabla \Phi = 0 \quad (15)$$

$\Phi$  potential,  $\varepsilon$  dielectric constant

Boundary condition are used to mimic the AS-I conditions. Within the AS-i system there is strictly no grounding. Coupling to the actual ground/earth is via stray capacitances.

Therefore “floating potentials” are used as boundary condition for the conductors. A potential is set at the boundaries of the conductors which are not carrying the signals such that no current flow occurs.

$$\int_{surface} \vec{n} \circ \vec{J} = 0 \quad (16)$$

Energies are calculated from the according fields.

$$W_{el} = \frac{1}{2} \iiint_{Volume} \vec{E} \circ \vec{D} \, dv \quad (17)$$

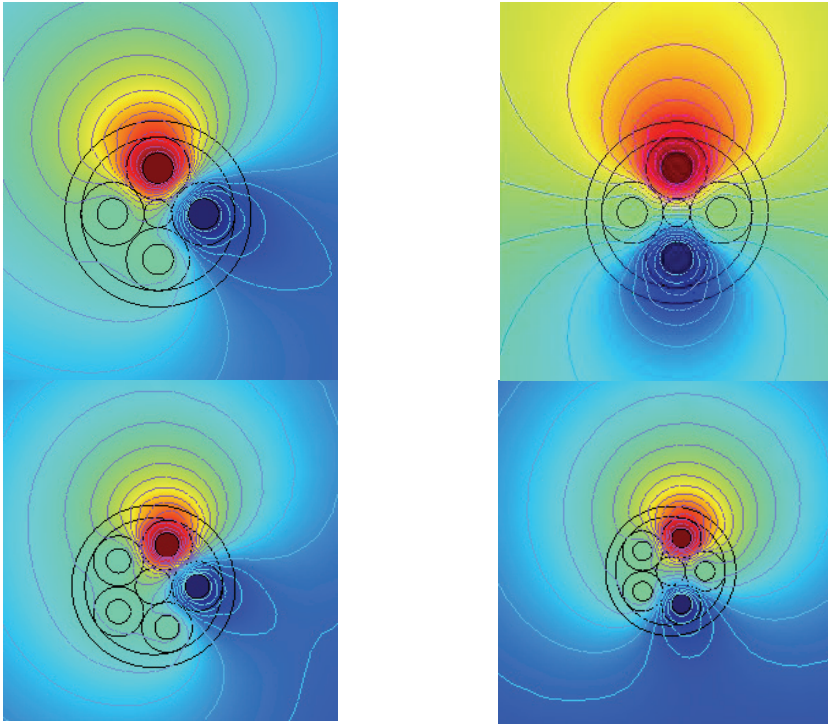


Figure 5. Potential distributions for calculating capacitances using the floating potential approach.

For the two signal carrying conductors there operational capacity is readily taken from that energy and the applied boundary conditions.

$$C = 2 \frac{W_{el}}{(\Phi_2 - \Phi_1)^2} \quad (18)$$

For assessing the coupling the mutual capacitances are to be determined from the capacitance matrix. The capacitance matrix is again computed from electric energy. The coefficients are given by the energies with only conductors  $i$  and  $j$  set to a voltage/ potential of 1 V and all other set to 0V. The capacitance of a conductor to ground is then given via the sum over the according row (Simonyi 1996).

$$C_{ii} = \iiint_{Volume} \vec{E} \circ \vec{D} \, dv \quad \Phi_i = \begin{cases} 1V & i = j \\ 0V & i \neq j \end{cases} \quad (19)$$

$$C_{ij} = \frac{1}{2} \left( \iiint_{Volume} \vec{E} \circ \vec{D} \, dv - (C_{ii} - C_{jj}) \right) \quad \Phi_l = \begin{cases} 0V & l \neq i = j \\ 1V & l = i, j \end{cases}$$

A comparison of the capacitance calculated via the floating potentials and via matrix yields good agreement.

Potential distributions are shown in figure 5 for four and five core cables. The capacitance is deducted from the floating potential approach. Adjacent and distant conductor pairs are compared.

**4.3 Inductances and resistances**

Inductances are calculated from DC flux coupling analogous to the capacitive matrix (Simonyi 1996). The governing equation reads

$$\nabla \times \left( \frac{1}{\mu} \nabla \times \vec{A} \right) = J \cdot \vec{e}_z \quad (20)$$

An iron support structure was assessed for some typical values of the permeability (100-2000). With calculation at 167 kHz skin effect, proximity and eddy currents were studied.

The governing equation becomes

$$(j\omega\sigma - \omega^2 \epsilon) \vec{A} + \nabla \times \left( \frac{1}{\mu} \nabla \times \vec{A} \right) = J \cdot \vec{e}_z \quad (21)$$

Losses and therefore resistance are quite affected by skin and proximity effects. With iron support structures additional losses may contribute remarkably.

**4.4 Lumped parameter modelling**

An equivalent circuit is used where a voltage is applied to a conductor pair and the voltage of the As-I pair is determined using standard network calculation. Tools like PSPICE are applied here. As an example the equivalent circuit for multi core round cables are shown in figure 6.

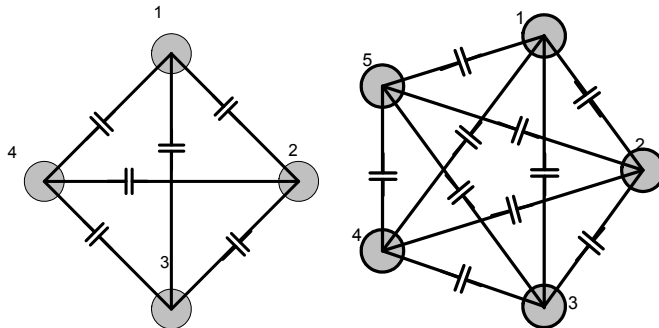


Figure 6. Equivalent circuit of a multi core cable used for capacitive coupling, where capacitance to ground is not shown for clarity

Attenuation and distortion is calculated from equivalent circuits were the cable is modelled by a multitude of the circuits shown in figure 7.

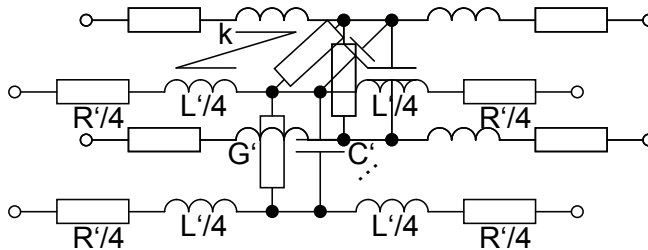


Figure 7. Equivalent circuit for a short piece of a four conductor cable

Other equipment is also modelled with standard equivalent circuits. These include the so called As-I master, the power supply and the slaves. With this modelling different topologies are investigated.

#### 4.5 Results und Discussion

The capacitance matrices are calculated for various cables. Since manufacturers do not necessarily provide actual values of dielectric constants or their tolerances, these values have to be varied. Once adjusted to meet measurements of capacitances, tolerance might be investigated.

The standard requirements for AS-i cables are  $C' < 80 \text{ pF/m}$ ,  $0.4 \text{ } \mu\text{H/m} < L' < 1.3 \text{ } \mu\text{H/m}$ ,  $R' < 90 \text{ m}\Omega/\text{m}$ ;  $G' \leq 5 \text{ } \mu\text{s/m}$ ;  $70 \text{ } \Omega \leq Z \leq 140 \text{ } \Omega$ . These requirements for resistance and capacitances, are usually met by cables with reasonably large cross-sections ( $> 1.5 \text{ mm}^2$ ).

As expected, the parameters of all investigated AS-i standard cables fulfil the requirements. Resulting capacitance of  $40 \text{ pF/m}$  to  $60 \text{ pF/m}$  may increase by 38% if the cable is laid on a metal support. With an iron support ( $\mu_r$  up to 2000) the inductances increase by approx. 15%.

Almost all round cables which have been investigated fulfil the requirements. These include either four or five cores, cross sections of  $1.5 \text{ mm}^2$  up to  $4 \text{ mm}^2$  with various insulations. Inductances were well within the limits, capacitances reached up to  $70 \text{ pF/m}$ . Values of the characteristic impedance  $Z$  were not met for some five core cables. But adjacent pairs of conductors must not be used for AS-i data transmission when a round cable is used. Despite this, a seven core flat cable was found to meet the requirements when two adjacent conductors carry the data signal.

Only differences in capacitive coupling affect data transmission, since data are encoded with differential signals. If a four wire cable would be completely symmetric, there were to be no coupling at all when not using any adjacent conductor pairs. If adjacent cores are used, the amplitude of the capacitive coupled signal reaches 28% of the coupling amplitude. With a five-core cable, this capacitive coupling reaches app. 15% for non adjacent pairs and 23% for adjacent pairs. Coupling inductance reaches approx.  $0.2 \text{ } \mu\text{H/m}$ . Metal support structures have only a weak influence since cores are helically wound along the cable run.

With the flat cable, the outer conductor pair is used for data transmission. The capacitive coupling reaches app. 15% when a metallic support is used and approx. 5% without a metal support. The coupling inductance reaches up to  $0.15 \text{ } \mu\text{H/m}$ . The protective earth, which is

next to the "As-i cores", carries the harmonics from frequency inverters. Due to the relatively high frequency, this may well affect data transmissions. To improve signal integrity the protective earth core may be grounded at several points along the cable run. Also, short circuit current at power frequencies may lead to voltages that exceed safe operating conditions. Surge protection becomes mandatory.

### Experimental results

The line parameters were measured with a precision impedance meter. Coupling was measured with a 10 kVA arbitrary wave form generator. 5 kHz square pulses with amplitudes up to 850 V were applied to check the capacitive coupling. Current pulses at 5 kHz with up to 13 A were used to measure inductive coupling. Results from calculations were in reasonably good agreement with measurement.

The amount of erroneous As-i telegrams was assessed. There was virtually no telegram repetition with the 4 core cable (no adjacent cores). Considerable inductive coupling led to telegram repetition with the flat cable and even more with the 5 core round cables. This is in accordance with the inductances. With increasing amplitudes malfunction of the AS-I data transmission was found. Reasonable agreement was also found for calculated and measured attenuation and signal wave forms.

Further investigations are will carried to simulate the complete data transmission including the translation of the physical signal wave form to actual data.

## 5. References

- Bauder U.-H., Schmidt H.-P., Arcs, sparks and other discharges, *Encyclopedia of Applied Physics*, Editor L. Trigg, American Physical Society VCH Publishers NY
- Comsol (2006) *Electromagnetics Users Guide* Version 3.2, published by Comsol Sweden; Stockholm
- Graf R. (2003) *Optimal Utilization of Power Busses*, *Master Theses* University of Applied Sciences Amberg Weiden
- IEC 60287 (2006) 287-1-1 Calculation of current ratings; Current rating equations. *International standard published* by International Electrotechnical Commission
- 287-2-1 *Thermal resistance* Section 1 Calculation of thermal resistance
- 287-2-2 *Thermal resistance*; A method for calculating reductions factors.
- Patankar, S. (1980) *Heat transfer and fluid flow*, *Hemisphere*, ISBN 0891165223, New York
- Schmidt H.-P. (2005) *Optimal Utilization of Power Buses for Photovoltaic Installations*, *Proceedings Distributed Power Systems*, University Pilsen Pernink
- Schmidt H.-P.(1996), Speckhofer G., Experimental and theoretical investigation of high pressure arcs Part II: The magnetically deflected arc column (3D-modeling), *IEEE Transactions on Plasma Science* Vol. 24, No. 4 Aug. 1996
- Simonyi (1996) *Theoretische Elektrotechnik*, VEB Verlag *Technik*, ISBN 3-341-01155-2, Berlin
- VDI Wärmearbeitsatlas (2006), *VDI-Gesellschaft Verfahrenstechnik und Chemieingenieurwesen* (GVC) Springer, ISBN 3540255036, Berlin
- Wutz (1991), *Wärmeabfuhr in der Elektronik* Vieweg, ISBN 3528063920, Frankfurt.

# Finite Element Simulation of Heat Transfer in Ferrofluid

Tomasz Strek

*Poznan University of Technology, Institute of Applied Mechanics  
Poland*

## 1. Introduction

During the last decades, an extensive research work has been done on the fluids dynamics in the presence of magnetic field (magnetorheological fluids and ferrofluids). The effect of magnetic field on fluids is worth investigating due to its innumerable applications in wide spectrum of fields. The study of interaction of the magnetic field or the electromagnetic field with fluids have been documented e.g. among nuclear fusion, chemical engineering, medicine, high speed noiseless printing and transformer cooling.

Ferrofluids are industrially prepared magnetic fluids which consist of stable colloidal suspensions of small single-domain ferromagnetic particles in suitable carrier liquids. Usually these fluids do not conduct electric current and exhibit a nonlinear paramagnetic behavior.

An external magnetic field imposed on a ferrofluid with varying susceptibility, e.g., due to a temperature gradient, results in a non-uniform magnetic body force, which leads to a form of heat transfer called thermomagnetic convection. This form of heat transfer can be useful when conventional convection heat transfer is inadequate, e.g., in miniature microscale devices or under reduced gravity conditions.

This chapter contains numerical results of computer simulation of heat transfer through a ferrofluid in channel flow under the influence of magnetic dipole, ferrofluid cooling of heat-generating device and heat transfer through a ferrofluid in channel with porous walls.

All considered problems describe two-dimensional time dependent heat transfer through a ferrofluid in channel in response to magnetic force arising from the magnetic field of the magnetic dipole. Numerical results show us the potential of ferrofluid in cooling of heat-generating devices. In last problem we can observe a form of heat transfer called thermomagnetic convection.

In this chapter results of time dependent problems are obtained using standard computational fluid dynamics code COMSOL Multiphysics with modifications to account for the magnetic term (e.g. the Kelvin body force and the thermal power) when needed. COMSOL is a powerful interactive environment for equation-based multiphysics modeling and solving all kinds of scientific and engineering problems based on partial differential equations using the finite element method.

The governing equations for considered problems are derived from conservation of energy, momentum, heat and magnetic induction equation. The resulting equations depend on the properties of ferrofluid and magnetic field. In this chapter magneto-thermo-mechanical

problems are modeled by coupled dimensionless equations. Governed equations cannot generally be determined without a supplementary assumptions.

## 2. Ferrofluids

Ferrofluids (Rosensweig, 1985) are non-conducting fluids and the study of the effect of magnetisation has yielded interesting information. In equilibrium situation the magnetization property is generally determined by the fluid temperature, density and magnetic field intensity and various equations, describing the dependence of static magnetization on these quantities. The simplest relation is the linear equation of state. It can be assumed that the magneto-thermo-mechanical coupling is not only described by a function of temperature, but by an expression involving also the magnetic field strength. This assumption permit us not to consider the ferrofluid far away from the sheet at Curie temperature in order to have no further magnetization. This feature is essential for physical applications because the Curie temperature is very high (e.g. 1043 Kelvin degrees for iron) and such a temperature would be meaningless for applications concerning most of ferrofluids. So instead of having zero magnetization far away from the sheet, due to the increase of fluid temperature up to the Curie temperature this formulation allows us to consider whatever temperature is desired and the magnetisation will be zero due to the absence of the magnetic field sufficiently far away from the sheet.

Moreover, ferrofluids are mostly organic solvent carriers having ferromagnetic oxides, acting as solute. Ferrofluids consist of colloidal suspensions of single domain magnetic nanoparticles. They have promising potential for heat transfer applications, since a ferrofluid flow can be controlled by using an external magnetic field (Ganguly et al., 2004). However, the relationship between an imposed magnetic field, the resulting ferrofluid flow and the temperature distribution is not understood well enough. The literature regarding heat transfer with magnetic fluids is relatively sparse.

An overview of prior research on heat transfer in ferrofluid flows e.g. thermomagnetic free convection, thermomagnetic forced convection and boiling, condensation and multiphase flow are presented in paper (Ganguly et al., 2004). Many researchers are seeking new technologies to improve the operation of existing oil-cooled electromagnetic equipment. One approach suggested in literature is to replace the oil in such devices with oil-based ferrofluids, which can take advantage of the pre-existing leakage magnetic fields to enhance heat transfer processes. In paper (Tangthieng et al., 1999) authors present results of an initial study of the enhancement of heat transfer in ferrofluids in magnetic fields which are steady but variable in space. Finite element simulations of heat transfer to a ferrofluid in the presence of a magnetic field are presented for flow between flat plates and in a box. The natural convection of a magnetic fluid in a partitioned rectangular cavity was considered in paper (Yamaguchi et al., 2002). It was found that the convection state may be largely affected by improving heat transfer characteristic at higher Rayleigh number when a strong magnetic field was imposed. Numerical results of combined natural and magnetic convective heat transfer through a ferrofluid in a cube enclosure were presented in paper (Snyder et al., 2003). The purpose of this work was to validate the theory of magnetoconvection. The magnetoconvection is induced by the presence of magnetic field gradient. The Curie law states that magnetization is inversely proportional to temperature. That is way the cooler ferrofluid flows in the direction of the magnetic field gradient and displaces hotter ferrofluid. This effect is similar to natural convection where cooler, more



dense, material flows towards the source of gravitational force. Results were obtained using standard computational fluid dynamics codes with finite element method.

The effect of magnetic field on the viscosity of ferroconvection in an anisotropic porous medium was studied in paper (Ramanathan & Suresh, 2004). It was found that the presence of anisotropic porous medium destabilizes the system, where as the effect of magnetic field dependent viscosity stabilizes the system. In this paper the investigated fluid was assumed to be incompressible having variable viscosity. Experimentally it has been demonstrated in prior research that the magneto viscosity has got exponential variation, with respect to magnetic field. As a first approximation for small field variation, linear variation of magneto viscosity has been used in paper (Ramanathan & Suresh, 2004).

One of the problems associated with drug administration is the inability to target a specific area of the body. Among the proposed techniques for delivering drugs to specific locations within the human body, magnetic drug targeting (Voltairas et al., 2002, Ritter et al., 2004) surpasses due to its non-invasive character and its high targeting efficiency. Although the method has been proposed almost 30 years ago, the technical problems obstruct possible applications. It was the aim of the paper (Voltairas et al., 2002) to classify the emerging problems and propose satisfactory answers. A general phenomenological theory was developed and a model case was studied, which incorporates all the physical parameters of the problem. A hypothetical magnetic drug targeting system, utilizing high gradient magnetic separation principles, was studied theoretically using FEMLAB simulations in paper (Ritter et al., 2004). This new approach uses a ferromagnetic wire placed at a bifurcation point inside a blood vessel and an externally applied magnetic field, to magnetically guide magnetic drug carrier particles through the circulatory system and then to magnetically retain them at a target site.

### 3. Governing equations

#### 3.1 The magnetic field intensity

In this paper the considered flow is influenced by magnetic dipole. We assumed that the magnetic dipole is located at distance  $|b|$  below the sheet at point  $(a, b)$ . The magnetic dipole gives rise to a magnetic field, sufficiently strong to saturate the fluid. In the magnetostatic case where there are no currents present, Maxwell-Ampere's law reduces to  $\nabla \times \mathbf{H} = \mathbf{0}$ . When this holds, it is also possible to define a magnetic scalar potential by the relation  $\mathbf{H} = -\nabla V_m$  and its scalar potential for the magnetic dipole is given by

$$V_m(\mathbf{x}) = V_m(x_1, x_2) = \frac{\gamma}{2\pi} \frac{x_1 - a}{(x_1 - a)^2 + (x_2 - b)^2} \quad (1)$$

where  $\gamma$  is the magnetic field strength at the source (of the wire) and  $(a, b)$  is the position where the source is located.

#### 3.2. Heat transfer and fluid flow

The governing equations of the fluid flow under the action of the applied magnetic field and gravity field are: the mass conservation equation, the fluid momentum equation and the energy equation for temperature in the frame of Boussinesque approximation.

The mass conservation equation for an incompressible fluid is

$$\nabla \cdot \mathbf{v} = 0. \quad (2)$$

The momentum equation for magnetoconvective flow is modified from typical natural convection equation by addition of a magnetic term

$$\rho_0 \left( \frac{\partial \mathbf{v}}{\partial t} + \mathbf{v} \cdot \nabla \mathbf{v} \right) = -\nabla p + \nabla \cdot \mathbf{S} + \alpha \rho_0 g (T - T_0) \mathbf{k} + (\mathbf{M} \cdot \nabla) \mathbf{B} \quad (3)$$

where  $\rho_0$  is the density,  $\mathbf{v}$  is the velocity vector,  $p$  is the pressure,  $T$  is the temperature of the fluid,  $\mathbf{S}$  is the extra stress tensor,  $\mathbf{k}$  is unit vector of gravity force and  $\alpha$  is the thermal expansion coefficient of the fluid.

The energy equation for an incompressible fluid which obeys the modified Fourier's law is

$$\rho_0 c \left( \frac{\partial T}{\partial t} + \mathbf{v} \cdot \nabla T \right) = k \nabla^2 T + \eta \Phi - \mu_0 T \frac{\partial \mathbf{M}}{\partial T} \cdot ((\mathbf{v} \cdot \nabla) \mathbf{H}) \quad (4)$$

where  $k$  is the thermal conductivity,  $\eta$  is the viscosity and  $\eta \Phi$  is the viscous dissipation

$$\Phi = \left( 2 \left( \left( \frac{\partial v_1}{\partial x} \right)^2 + \left( \frac{\partial v_2}{\partial y} \right)^2 \right) + \left( \frac{\partial v_2}{\partial x} + \frac{\partial v_1}{\partial y} \right)^2 \right). \quad (5)$$

The last term in the energy equation represents the thermal power per unit volume due to the magnetocaloric effects.

### 3.3. The Kelvin body force for magnetoconvective flow

The last term in the momentum equation represents the Kelvin body force per unit volume

$$\mathbf{f} = (\mathbf{M} \cdot \nabla) \mathbf{B}, \quad (6)$$

which is the force that a magnetic fluid experiences in a spatially non-uniform magnetic field. We have established the relationship between the magnetization vector and magnetic field vector

$$\mathbf{M} = \chi_m \mathbf{H}. \quad (7)$$

Using the constitutive relation (relation between magnetic flux density and magnetic field vector) we can write the magnetic induction vector in the form

$$\mathbf{B} = \mu_0 (1 + \chi_m) \mathbf{H}. \quad (8)$$

The variation of the total magnetic susceptibility  $\chi_m$  is treated solely as being dependent on temperature (Ganguly et al., 2004)

$$\chi_m = \chi_m(T) = \frac{\chi_0}{1 + \alpha(T - T_0)}. \quad (9)$$

Finally, the Kelvin body force can be represented by

$$\mathbf{f} = \frac{1}{2} \mu_0 \chi_m (1 + \chi_m) \nabla(\mathbf{H} \cdot \mathbf{H}) + \mu_0 \chi_m \mathbf{H}((\mathbf{H} \cdot \nabla)\chi_m) . \quad (10)$$

Using equations (7)-(8) we can write Eq. (3) and (4) in the form, respectively

$$\begin{aligned} \rho_0 \left( \frac{\partial \mathbf{v}}{\partial t} + \mathbf{v} \cdot \nabla \mathbf{v} \right) = & -\nabla p + \nabla \cdot \mathbf{S} + \alpha \rho_0 g (T - T_0) \mathbf{k} + \\ & + \frac{1}{2} \mu_0 \chi_m (1 + \chi_m) \nabla(\mathbf{H} \cdot \mathbf{H}) + \mu_0 \chi_m \mathbf{H}((\mathbf{H} \cdot \nabla)\chi_m) \end{aligned} \quad (11)$$

and

$$\rho_0 c \left( \frac{\partial T}{\partial t} + \mathbf{v} \cdot \nabla T \right) = k \nabla^2 T + \eta \Phi - \mu_0 T \frac{\partial(\chi_m \mathbf{H})}{\partial T} \cdot ((\mathbf{v} \cdot \nabla)\mathbf{H}) . \quad (12)$$

### 3.4. The Brinkman equations for porous media flow

Fluid and flow problems in porous media have attracted the attention of industrialists, engineers and scientists from varying disciplines, such as chemical, environmental, and mechanical engineering, geothermal physics and food science. There has been a increasing interest in heat and fluid flows through porous media.

The Brinkman equations describe flow in porous media where momentum transport by shear stresses in the fluid is of importance. The model extends Darcy's law to include a term that accounts for the viscous transport, in the momentum balance, and introduces velocities in the spatial directions as dependent variables. The flow field is determined by the solution of the momentum balance equations in combination with the continuity equation

$$\rho_0 \frac{\partial \mathbf{v}_B}{\partial t} = -\nabla p_B + \nabla \cdot \mathbf{S}_B + \frac{\eta}{k_p} \mathbf{v}_B + \mathbf{F} \quad (13)$$

where  $\eta$  is the viscosity,  $k_p$  is the permeability of the porous structure (unit:  $m^2$ ).

The Brinkman equations applications are of great use when modelling combinations of porous media and free flow. The coupling of free media flow with porous media flow is common in the field of chemical engineering. This type of problems arises in filtration and separation and in chemical reaction engineering, for example in the modelling of porous catalysts in monolithic reactors.

Flow in the free channel is described by the Navier-Stokes equations and the mass conservation equation described in previous sections. In the porous domain, flow is described by the Brinkman equations according

$$\rho_0 \frac{\partial \mathbf{v}_B}{\partial t} = -\nabla p_B + \nabla \cdot \mathbf{S}_B + \frac{\eta}{k_p} \mathbf{v}_B \quad (14)$$

and

$$\nabla \cdot \mathbf{v}_B = 0 . \quad (15)$$

### 3.5. The dimensionless equations

For simplicity the preferred work choice is to work in non-dimensional frame of reference. Now some dimensionless variables will be introduced in order to make the system much easier to study (Strek, 2005, Strek & Jopek, 2007). Moreover some of the dimensionless ratios can be replaced with well-known parameters: the Prandtl number  $Pr$ , the Rayleigh number  $Ra$ , the Eckert number  $Ec$ , the Reynolds number  $Re$ , the Darcy number  $Da$  and the magnetic number  $Mn$ , respectively:

$$Pr = \frac{\eta_0}{\rho_0 \kappa}, \quad Ra = \frac{\alpha \rho_0 g h^3 \delta T}{\eta_0 \kappa}, \quad Ec = \frac{v_r^2}{c \delta T} = \frac{\kappa^2}{c \delta T h^2}, \quad Re = \frac{h \rho_0 v_r}{\eta_0} = \frac{\rho_0 \kappa}{\eta_0}, \quad Da = \frac{h^2}{k_p},$$

$$Mn = \frac{\mu_0 H_r^2}{\rho_0 v_r^2} = \frac{\mu_0 H_r^2 h^2}{\rho_0 \kappa^2}. \quad (16)$$

Since now primes will not be written (old variables symbols will be used) but it is important to remember that they are still there. The dimensionless form of Navier-Stokes (11) and thermal diffusion (12) equations are as follows:

$$\frac{\partial \mathbf{v}}{\partial t} + \mathbf{v} \cdot \nabla \mathbf{v} = -\nabla p + Ra Pr \left( T - \frac{T_0}{\delta T} \right) \mathbf{k} + Pr \nabla \cdot \mathbf{S} + Mn \mathbf{f} \quad (17)$$

and

$$\frac{\partial T}{\partial t} + \mathbf{v} \cdot \nabla T = \nabla^2 T + Pr Ec \eta \Phi + Mn Ec T \frac{\partial(\chi_m \mathbf{H})}{\partial T} \cdot ((\mathbf{v} \cdot \nabla) \mathbf{H}) \quad (18)$$

where

$$\mathbf{f} = \frac{1}{2} \chi_m (1 + \chi_m) \nabla H^2 + \chi_m \mathbf{H} ((\mathbf{H} \cdot \nabla) \chi_m) \quad (19)$$

and

$$\chi_m = \chi_m(T(\mathbf{x})) = \frac{\chi_0}{1 + (\alpha \delta T) \left( T(\mathbf{x}) - \frac{T_0}{\delta T} \right)}. \quad (20)$$

Dimensionless Brinkman equations are as follows

$$\frac{\partial \mathbf{v}_B}{\partial t} = -\nabla p_B + Pr \nabla \cdot \mathbf{S}_B + Pr Da \mathbf{v}_B. \quad (21)$$

In the presents of magnetic field Kelvin body force is added

$$\frac{\partial \mathbf{v}_B}{\partial t} = -\nabla p_B + Pr \nabla \cdot \mathbf{S}_B + Pr Da \mathbf{v}_B + Mn \mathbf{f}. \quad (22)$$

## 4. Numerical results

In this section we present numerical simulation results of heat transfer in ferrofluid. The flow takes place in channel and in channel with porous walls. The two-dimensional time

dependent flows are assumed viscous, incompressible and laminar. Above the channel magnetic dipole is located. The fluid is assumed to be electrically nonconducting. It is assumed also that there is no electric field effects. This magneto-thermo-mechanical problem is governed by dimensionless equations (17-22).

**4.1 Heat transfer in ferrofluid in channel**

Considered flow takes place in channel between two parallel flat plates. The length of the channel is  $L$  and distance between plates is  $h$ .

The corresponding boundary conditions for dimensionless variables are assumed:

- For the upper wall: the upper wall temperature is kept at constant temperature  $T_u / \delta T$ . The velocity is 0 (no slip condition).
- For the lower wall: the lower wall temperature is kept at constant temperature  $T_l / \delta T$ . The velocity is 0 (no slip condition).
- For inlet (the left wall): the temperature is varying linearly from  $T_l / \delta T$  to  $T_u / \delta T$  and is given by equation  $T_{in} = \frac{T_u - T_l}{\delta T} y + \frac{T_l}{\delta T}$  where  $\delta T = |T_u - T_l|$ . There is a parabolic laminar flow profile given by equation  $u_{in} = -4 \frac{u_0}{u_r} y(y - 1)$  for  $y \in \langle 0,1 \rangle$  at the inlet end.
- For outlet (the right wall) ( $x=L, 0 \leq y \leq 1$ ): the convective flux is assumed for temperature,  $\mathbf{n} \cdot (-k\nabla T) = 0$ . Pressure outlet is also assumed,  $(-p\mathbf{I} + \mathbf{S})\mathbf{n} = -p_0\mathbf{n}$ , where  $p_0$  is the dimensionless atmospheric pressure.

The following initial conditions for dimensionless variables are assumed: the fluid is motionless, the pressure is zero and the temperature is varying linearly from lower to upper wall.

The time-dependent flow is considered for dimensionless time  $t \in \langle 0,0.5 \rangle$ . The problem is solved with COMSOL code using direct UMFPAK linear system solver. Relative and absolute tolerance used in calculations are 0.05 and 0.005, respectively.

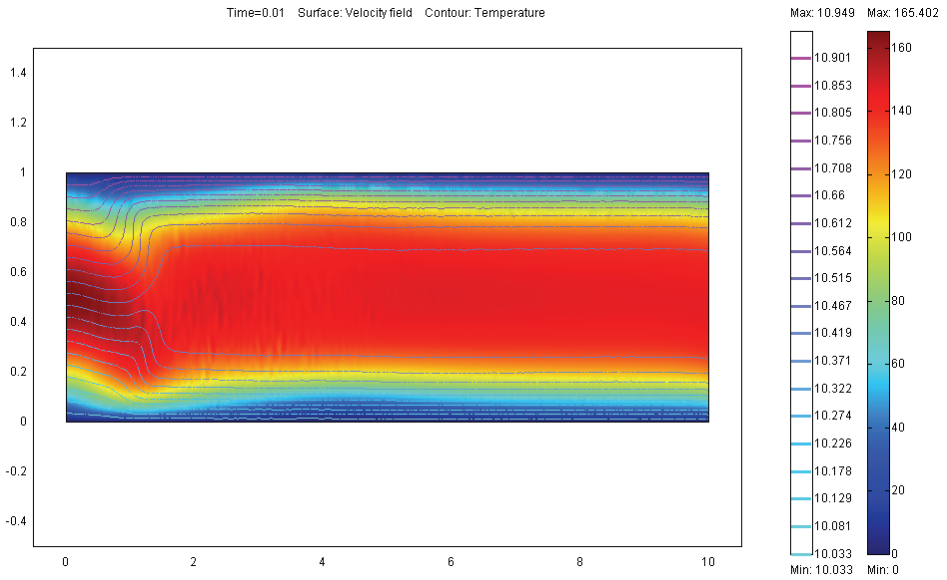
The following values of temperatures are assumed  $T_l = T_0$ ,  $T_u = T_0 + \delta T$  where  $T_0 = 300K$  and  $\delta T = 30K$ .

Quantity	Flow A	Flow B	Flow C
$H_r$	<b>3819.71</b>	<b>5092.95</b>	<b>12732.39</b>
$Mn$	<b>1.6961e+7</b>	<b>3.0154e+7</b>	<b>1.8846e+8</b>
$Pr$	1.4	1.4	1.4
$Ra$	2.5701e+7	2.5701e+7	2.5701e+7
$Ec$	2.1810e-12	2.1810e-12	2.1810e-12
$Re$	0.7142	0.7142	0.7142

Table 1. The quantities for ferrofluid flows A-C

It can be observed that the maximum value of the magnitude of the velocity field of the flow in the channel under the magnetic dipole increases due to the value of the magnetic number.

a



b

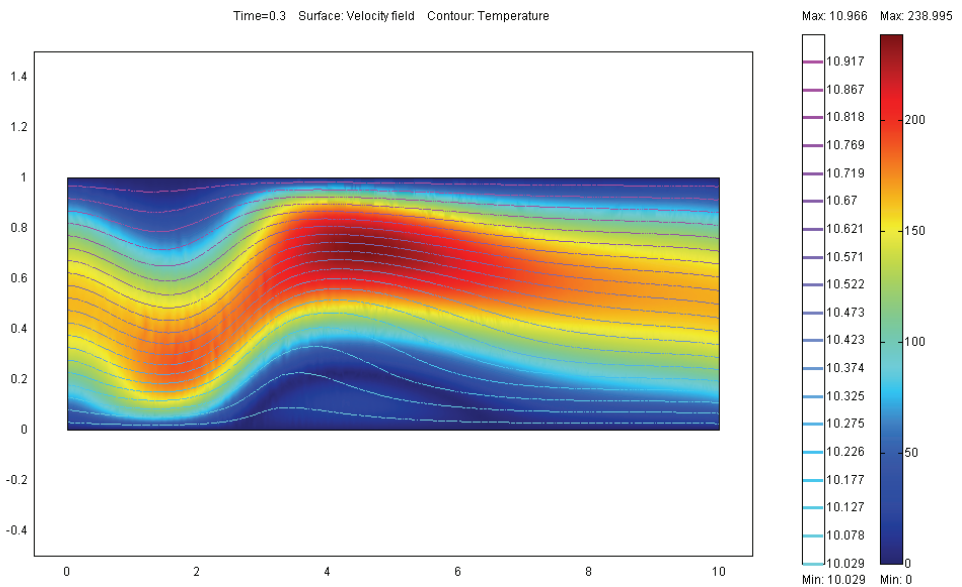
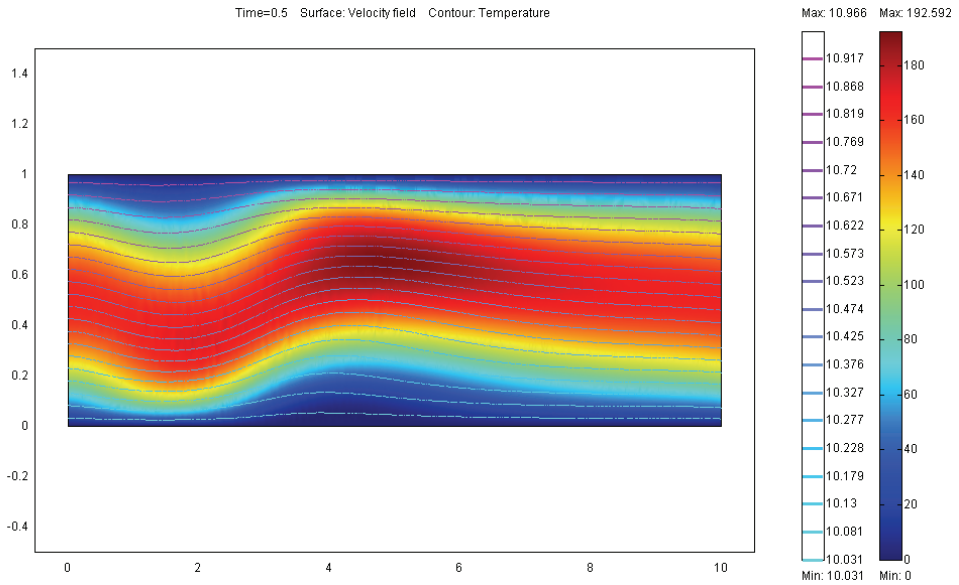


Figure 1. Time evolution of dimensionless velocity field (surface) and temperature contour of flow B for (a)  $t=0.01$  (b)  $t=0.3$

a



b

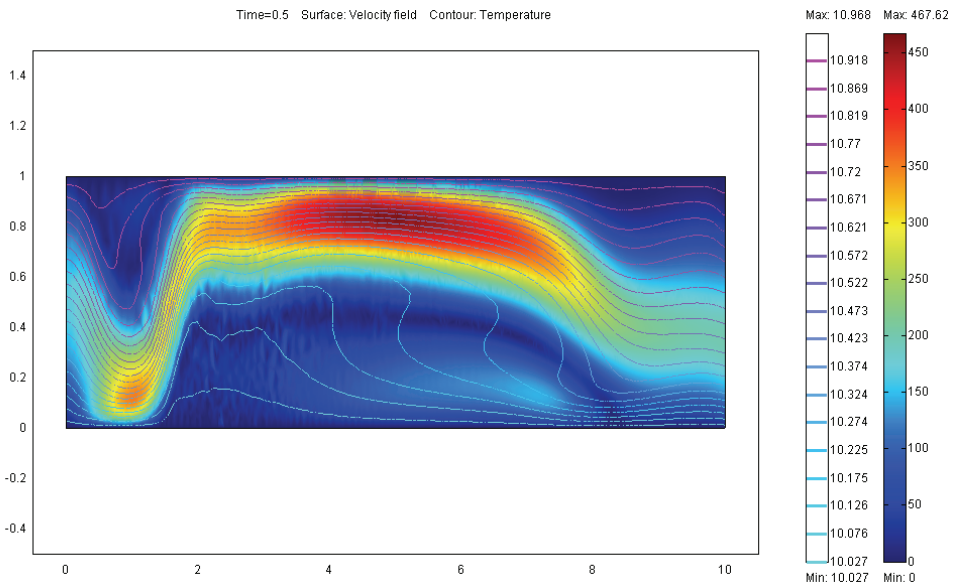


Figure 2. Comparison of dimensionless velocity field (surface) and temperature contour for the different values of magnetic number: (a) flow A (b) flow C

The flow was relatively uninfluenced by the magnetic field until its strength was large enough for the Kelvin body force to overcome the viscous force. It can be observed that the cooler ferrofluid flows in the direction of the magnetic field gradient and displaced hotter ferrofluid (Fig. 1,2). This effect is similar to natural convection where cooler, more dense material flows towards the source of gravitational force. Ferrofluids have promising potential for the heat transfer applications because a ferrofluid flow can be controlled by using an external magnetic field.

## 4.2 Ferroconvection

Flow takes place in channel between two parallel porous domains. The length of the channel is  $L$  and distance between porous domains is  $h$ . The length of porous domains are  $L$  and the height are  $4h/10$ .

The corresponding boundary conditions for dimensionless variables in channel flow are assumed:

- For free-porous structure interface - the upper and the lower wall, free-porous structure interface:  $p = p_B$ . The expression for the pressure at the boundary between the channel and the porous domain states that the pressure is continuous across this interface.
- For inlet (the left wall): the temperature is varying linearly from  $T_l / \delta T$  to  $T_u / \delta T$  and is given by equation  $T_{in} = \frac{T_u - T_l}{\delta T} y + \frac{T_l}{\delta T}$  where  $\delta T = |T_u - T_l|$ . There is a parabolic

laminar flow profile given by equation  $u_{in} = -4 \frac{u_0}{u_r} y(y-1)$  for  $y \in \langle 0,1 \rangle$  at the inlet end.

- For outlet (the right wall): the convective flux is assumed for temperature,  $\mathbf{n} \cdot (-k\nabla T) = 0$ . Pressure outlet is also assumed,  $(-p\mathbf{I} + \mathbf{S})\mathbf{n} = -p_0\mathbf{n}$ , where  $p_0$  is the dimensionless atmospheric pressure.

The corresponding boundary conditions for dimensionless variables in porous domain are assumed:

- For free-porous structure interface:  $\mathbf{v}_B = \mathbf{v}$ . These conditions imply that the components of the velocity vector are continuous over the interface between the free channel and the porous domain.
- For the upper domain walls: the temperature is kept at constant temperature  $T_u / \delta T$ . The velocity is 0 (no slip condition).
- For the lower domain walls: the temperature is kept at constant temperature  $T_l / \delta T$ . The velocity is 0 (no slip condition).

The following initial conditions for dimensionless variables are assumed: the fluid is motionless, the pressure is zero and the temperature is  $T_l / \delta T$ .

The time-dependent flow is considered for dimensionless time  $t \in \langle 0,0.1 \rangle$ . The problem is solved with COMSOL code using direct UMFPACK linear system solver. Relative and absolute tolerance used in calculations are 0.05 and 0.005, respectively.



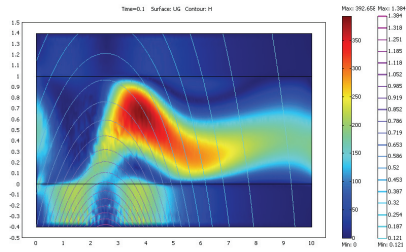
The following values of temperatures are assumed  $T_l = T_0$ ,  $T_u = T_0 + \delta T$  where  $T_0 = 300K$  and  $\delta T = 30K$ . The numerical values of variables and dimensionless numbers are presented in Table 2.

The heat transfer in ferrofluid flowing in channel with porous walls is considered in four different flows with different magnetic susceptibility, inlet velocity or permeability of the porous structure. The most interesting example of flow we can observe in the last considered flow (flow G). In this case the ferroconvection is observe (Figures 3d,4-5). We observe convection rolls created near the centre of magnetic dipole. Each roll is moving from left to right where the magnetic field intensity is getting smaller. The intensity of magnetic field is plotted on each figure presented in this subsection as contour lines.

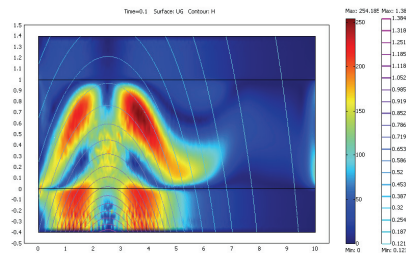
Quantity	Flow D	Flow E	Flow F	Flow G
$H_r$	12732.39	12732.39	12732.39	12732.39
$\chi_0$	<b>0.06</b>	<b>0.06</b>	<b>0.01</b>	<b>0.01</b>
$u_0$	<b>5e-3</b>	<b>5e-4</b>	<b>5e-2</b>	<b>5e-4</b>
$Mn$	1.8846e+8	1.8846e+8	1.8846e+8	1.8846e+8
$Pr$	1.4	1.4	1.4	1.4
$Ra$	2.5701e+7	2.5701e+7	2.5701e+7	2.5701e+7
$Ec$	2.1810e-12	2.1810e-12	2.1810e-12	2.1810e-12
$Re$	0.7142	0.7142	0.7142	0.7142
$Da$	<b>4000</b>	<b>4000</b>	<b>40</b>	<b>40</b>

Table 2. The quantities for the ferrofluid flows D-G

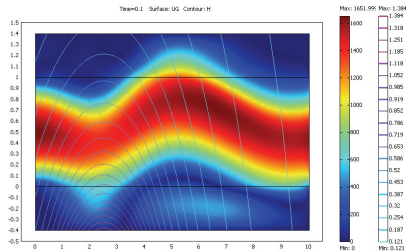
a



b



c



d

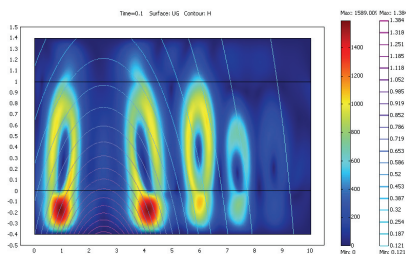
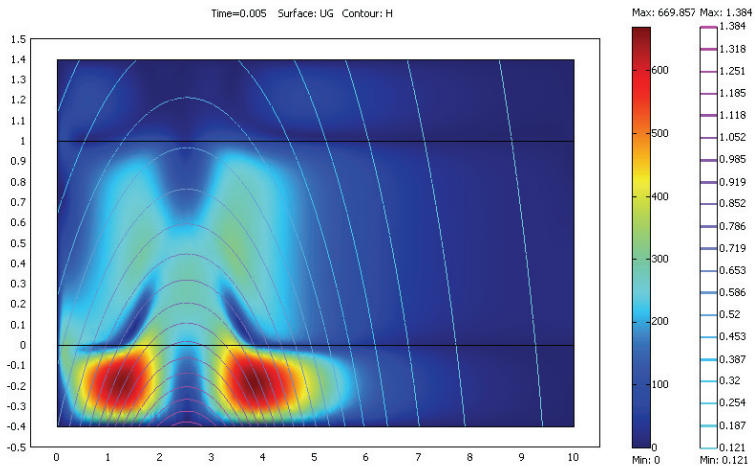


Figure 3. Comparison of dimensionless velocity field for the different flows in channel with porous walls: (a) flow D (b) flow E (c) flow F (d) flow G for time  $t=0.1$

a



b

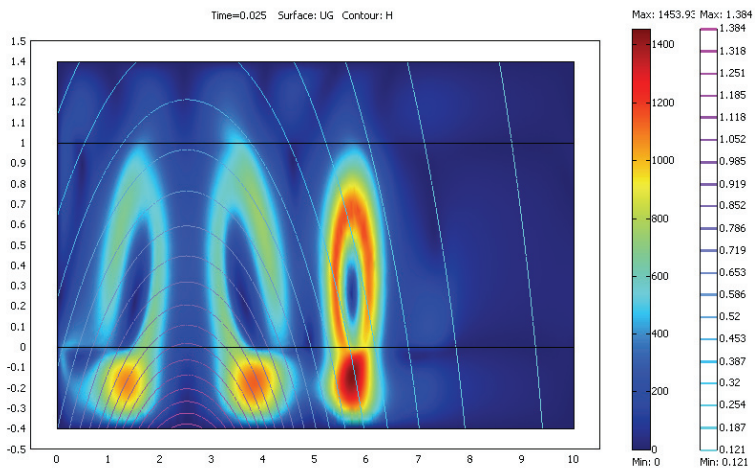
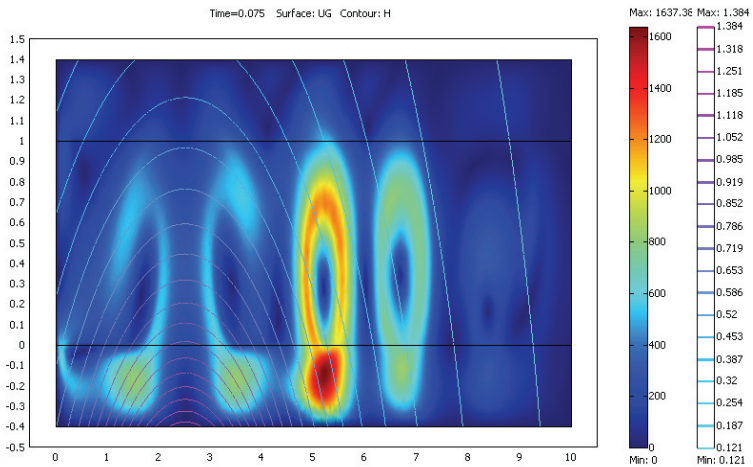


Figure 4. Time evolution of dimensionless velocity field (surface) of flow G for (a)  $t=0.005$  (b)  $t=0.025$

a



b

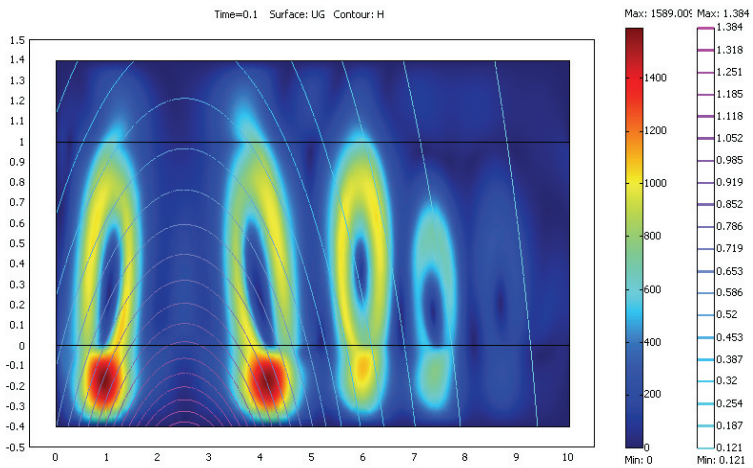


Figure 5. Time evolution of dimensionless velocity field (surface) of flow G for (a)  $t=0.075$  (b)  $t=0.1$

### 4.3 Ferrofluid cooling

This case examines the temperature field in the ferrofluid and in the electronic component with heat source. The ferrofluid transports heat by convection and conduction. Finally, to approximate the electronic component that requires cooling, the model uses a rectangular blocks with a given volume heat source. The electronic components transports thermal energy by pure conduction.

The viscous, two-dimensional, incompressible and laminar ferromagnetic fluid flow is considered in this subsection. Flow takes place in channel between two parallel flat plates. There are rectangular blocks (heat-generating devices) below the upper wall. The length of the channel is  $L = 10$  and distance between plates is  $h = 1$ . Outside the channel the magnetic dipole is located at point  $(a, b)$ .

Good way to describe the convective heat transfer is to model the heat transfer in combination with the fluid-flow field. The results then accurately describe the heat transport and temperature changes. These types of models are somewhat complex but are useful for unusual geometries and complex systems such as circuit-board cooling.

The following boundary conditions for dimensionless variables are assumed:

- For upper wall: The velocity is 0 (no slip condition). Insulation condition for heat transfer by conduction (in solid domain)  $\mathbf{n} \cdot \mathbf{q} = \mathbf{n} \cdot (-k_s \nabla T) = 0$  and for heat transfer by conduction and convection (in fluid domain)  $\mathbf{n} \cdot \mathbf{q} = \mathbf{n} \cdot (-k_f \nabla T + \rho_f c_f T \mathbf{u}) = 0$  specifies where the domain is well insulated.
- For lower wall: The velocity is 0 (no slip condition). Insulation condition for heat transfer by conduction and convection (in fluid domain)  $\mathbf{n} \cdot \mathbf{q} = \mathbf{n} \cdot (-k_f \nabla T + \rho_f c_f T \mathbf{u}) = 0$ .
- For inlet (left wall): The temperature is  $\frac{T_l}{\delta T}$  where  $\delta T = |T_u - T_l|$ . At the inlet boundary there is a parabolic laminar flow profile given by equation  $u_{in} = -4 \frac{u_0}{u_r} y(y-1)$  for  $y \in (0, 1)$ .
- For outlet (right wall): The convective flux is assumed for temperature,  $\mathbf{n} \cdot (-k_s \nabla T) = 0$ . Pressure outlet is also assumed,  $(-p \mathbf{I} + \mathbf{S}) \mathbf{n} = -p_0 \mathbf{n}$ , where  $p_0$  is the dimensionless atmospheric pressure.
- For solid-fluid interface: The velocity is 0 (no slip condition). Continuity equation for heat transfer equation  $\mathbf{n} \cdot (\mathbf{q}_s - \mathbf{q}_f) = 0$  where  $\mathbf{q}_s = -k_s \nabla T$  and  $\mathbf{q}_f = -k_f \nabla T + \rho_f c_f T \mathbf{u}$ .

The following initial conditions for dimensionless variables are assumed: fluid is motionless (velocity is zero), pressure is zero and temperature is  $\frac{T_l}{\delta T}$  for whole domain (with fluid and solid).

Numerical results of solved problem of ferrofluid cooling of heat-generating device in channel flow under the influence of magnetic dipole generated by permanent magnet are presented below. The numerical values of variables and dimensionless numbers are

presented in Table 3 and Table 4. Problem was solved using finite element method with 2373 Lagrange quadratic triangular mesh elements and 15242 degrees of freedom. Time-dependent flow is considered for time  $t \in \langle 0, 0.5 \rangle$ . The problem is solved with finite element method COMSOL code using direct UMFPACK linear system solver. Relative and absolute tolerance used in calculations are 0.05 and 0.005, respectively.

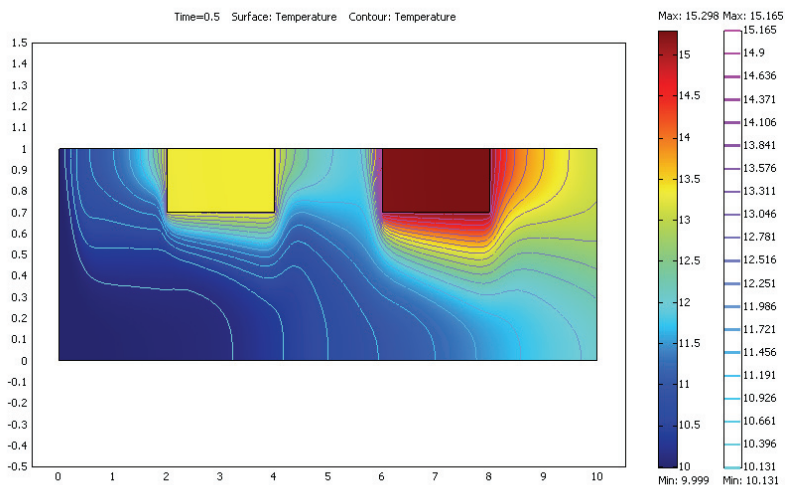
Quantity	Flow H	Flow I	Flow J	Flow K
$a$	<b>2</b>	<b>2</b>	<b>2</b>	<b>2</b>
$b$	<b>-3</b>	<b>-2.5</b>	<b>-2</b>	<b>-1.5</b>
$H_r$	<b>1.768388e+5</b>	<b>2.546479e+5</b>	<b>3.978874e5</b>	<b>7.073553e+5</b>
Pr	560			
$Ra$	200.7938			
$Ec$	1.16324e-13			
$Re$	0.001786			
$Mn$	<b>2.272182e+9</b>	<b>4.711597e+9</b>	<b>1.150292e+10</b>	<b>3.635492e+10</b>
$Qn$	64.019097			
$V_{avg}$ (fluid)	<b>292.980369</b>	<b>309.281869</b>	<b>331.905089</b>	<b>371.38104</b>
$T_{avg}$ (fluid)	<b>101.330192</b>	<b>101.314674</b>	<b>101.096441</b>	<b>100.801837</b>
$T_{dom}$ (channel)	<b>118.521428</b>	<b>118.261882</b>	<b>117.760089</b>	<b>117.17941</b>

Table 3. Quantities of flow H-K

Quantity	Flow L	Flow M	Flow N	Flow O
$\chi_0$	<b>0.5</b>	<b>0.1</b>	<b>0.06</b>	<b>0.04</b>
$H_r$	1.768388e+5			
Pr	560			
$Ra$	200.7938			
$Ec$	1.16324e-13			
$Re$	0.001786			
$Mn$	2.272182e+9			
$Qn$	64.019097			
$V_{avg}$ (fluid)	<b>411.490459</b>	<b>306.564373</b>	<b>292.980369</b>	<b>284.589693</b>
$T_{avg}$ (fluid)	<b>100.741705</b>	<b>101.246393</b>	<b>101.330192</b>	<b>101.453763</b>
$T_{dom}$ (channel)	<b>116.618815</b>	<b>118.171175</b>	<b>118.521428</b>	<b>118.846783</b>

Table 4. Quantities of flow L-O

a



b

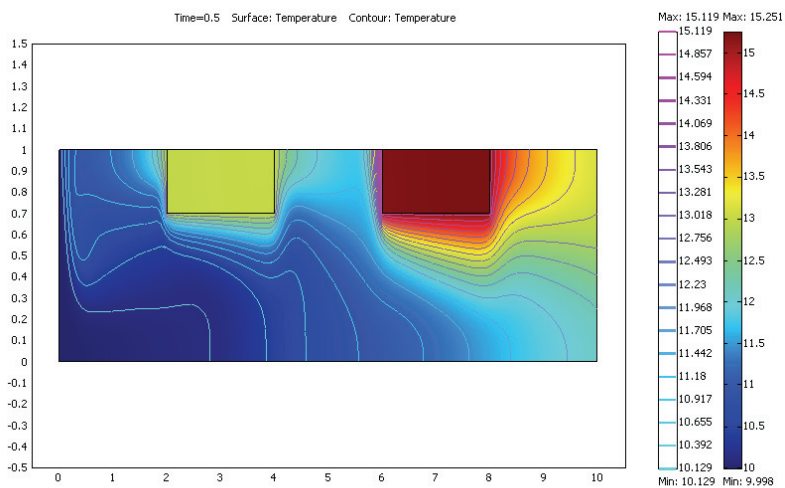
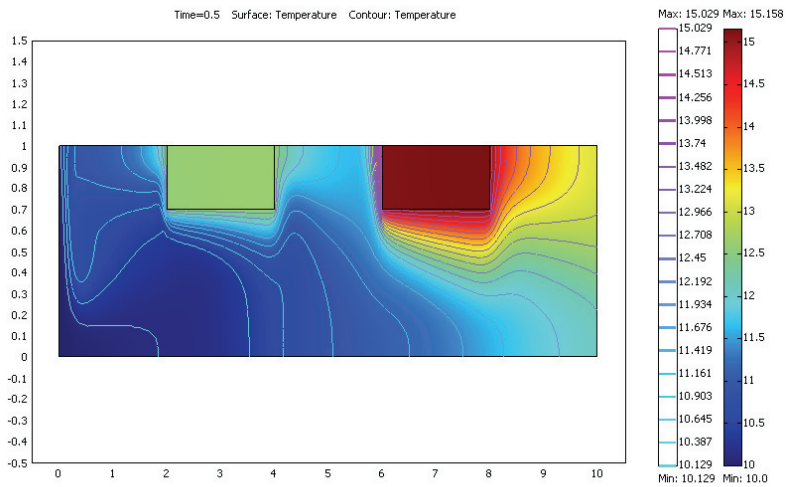


Figure 6. Comparison of temperature in channel and heat generating devices for the different flows in channel: (a) flow H, (b) flow I for time  $t=0.5$

a



b

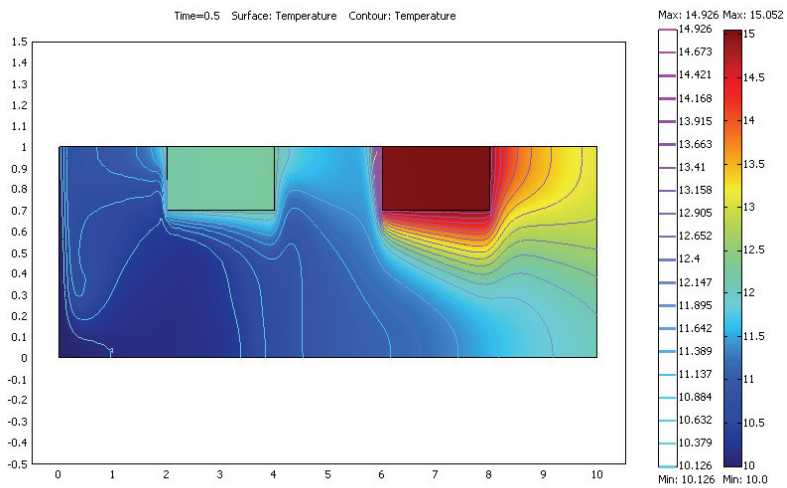
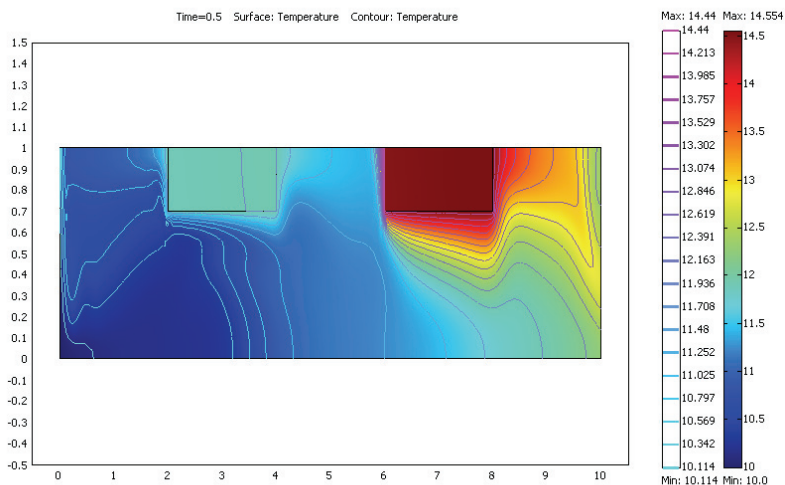


Figure 7. Comparison of temperature in channel and heat generating devices for the different flows in channel: (a) flow J, (b) flow K for time  $t=0.5$



a



b

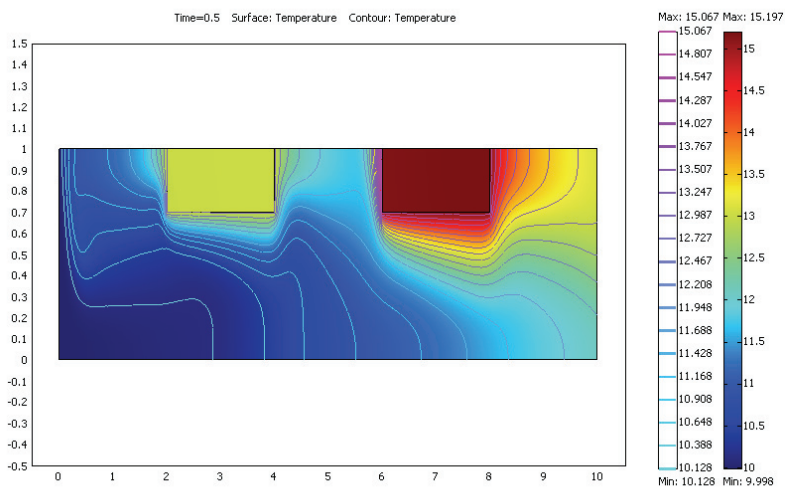
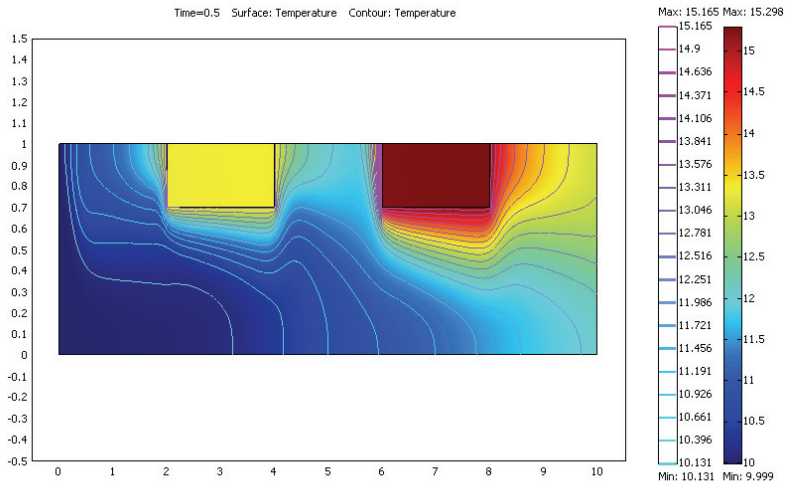


Figure 8. Comparison of temperature in channel and heat generating devices for the different flows in channel: (a) flow L, (b) flow M for time  $t=0.5$

a



b

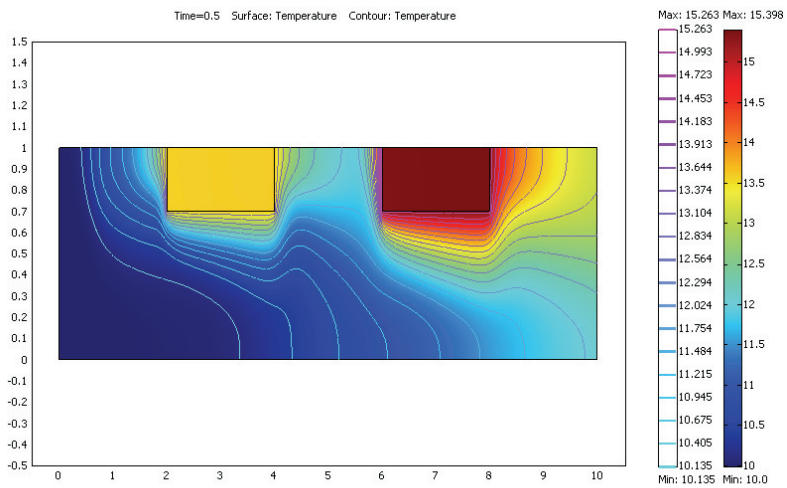


Figure 9. Comparison of temperature in channel and heat generating devices for the different flows in channel: (a) flow N, (b) flow O for time  $t=0.5$

Dimensionless values  $V_{avg}$ ,  $T_{avg}$  and  $T_{dom}$  are calculated using following formulas

$$V_{avg} = \iint_{A_p} |\mathbf{u}| dA_p, \quad (23)$$

$$T_{avg} = \iint_{A_p} T dA_p, \quad (24)$$

$$T_{dom} = \iint_A T dA, \quad (25)$$

where  $A_p$  denotes area of domain with fluid,  $A$  - area of the channel (fluid and solid). In these examples we have  $A_p = 8.8$  and  $A = 10$ .

## 5. Conclusions

We have simulated two-dimensional heat transfer in ferrofluid channel flow under the influence of the magnetic field created by magnetic dipole using computational fluid dynamics code COMSOL based on finite element method. At the left end of rectangular channel there was assumed a parabolic laminar flow profile. The upper plate was kept at constant temperature  $T_u$  and the lower at  $T_l$ .

The flow was relatively uninfluenced by the magnetic field until its strength was large enough for the Kelvin body force to overcome the viscous force. The magnetoconvection was induced by the presence of magnetic field gradient.

We observed that the cooler ferrofluid flows in the direction of the magnetic field gradient and displaced hotter ferrofluid. Ferrofluids have promising potential for heat transfer applications because a ferrofluid flow can be controlled by using an external magnetic field. The Kelvin body force arises from the interaction between the local magnetic field within the ferrofluid and the molecular magnetic moments characterized by the magnetization. An imposed thermal gradient produces a spatial variation in the magnetization through the temperature-dependent magnetic susceptibility for ferrofluids and therefore renders the Kelvin body force non-uniform spatially. This thermal gradient induced inhomogeneous magnetic body force can promote or inhibit convection in a manner similar to the gravitational body force.

A strong magnet placed near the device which produces heat will always attract colder ferrofluid towards it more than warmer ferrofluid thus forcing the heated ferrofluid away, towards the heat sink. This is an efficient cooling method which requires no additional energy input.

## 6. References

- Ganguly R., Sen S., Puri I.K (2004). Heat transfer augmentation using a magnetic fluid under the influence of a line dipole, *Journal of Magnetism and Magnetic Materials*, 271 (2004) pp.63-73.

- Ramanathan A., Suresh G. (2004). Effect of magnetic field dependent viscosity and anisotropy of porous medium on ferroconvection, *International Journal of Engineering Science*, 42, pp.411-425.
- Ritter J.A., Ebner A.D., Daniel K.D, Stewart K.L (2004). Application of high gradient magnetic separation principles to magnetic drug targeting, *Journal of Magnetism and Magnetic Materials*, 280, s.184-201.
- Rosensweig R.E. (1985). *Ferrohydrodynamics*, Cambridge University Press, Cambridge.
- Snyder S.M., Cader T., Finlayson B.A. (2003). Finite element model of magnetoconvection of a ferrofluid, *Journal of Magnetism and Magnetic Materials*, 262, pp.269-279.
- Strek T. (2005). Ferrofluid channel flow under the influence of magnetic dipole, *International Journal of Applied Mechanics and Engineering*, vol. 10, pp. 103-109.
- Strek T., Jopek H. (2007). Computer simulation of heat transfer through a ferrofluid, *Physica Status Solidi (B)*, 244, No. 3, pp. 1027-1037.
- Tangthieng C., Finlayson B.A., Maulbetsch J., Cader T. (1999). Heat transfer enhancement in ferrofluids subjected to steady magnetic fields, *Journal of Magnetism and Magnetic Materials*, 201, pp.252-255.
- Yamaguchi H., Zhang Z., Shuchi S., Shimada K. (2002). Heat transfer characteristic of magnetic fluid in a partitioned rectangular box, *Journal of Magnetism and Magnetic Materials*, 252, pp.203-205.
- Voltairas P.A., Fotiadis D.I., Michalis L.K. (2002). Hydrodynamics of magnetic drug targeting, *Journal of Biomechanics*, 35, pp. 813-821.

# Computational Modelling of Mass Transport in Large Arteries

Nanfeng Sun, Nigel B. Wood and X. Yun Xu  
*Imperial College London  
United Kingdom*

## 1. Introduction

Atherosclerosis is a major cause of mortality and morbidity in the developed and developing countries. The development of atherosclerosis begins in childhood and characteristically shows a focal distribution, with a particular predisposition to occur at sites of branching and curvature. Macromolecular accumulation plays an important role in atherogenesis and focal distribution of atherosclerosis, suggesting that mechanical factors, especially wall shear stress (WSS), are implicated in its development. In the present study, mass transport of macromolecules in large arteries, as well as its relationships with fluid mechanics and localisation of atherosclerosis, was studied.

### 1.1 Preliminaries

Atherosclerosis is a disease of the arterial wall initiated by the accumulation of macromolecules. The arterial wall consists of several layers, with the endothelium being the innermost layer. It is a thin membrane serving as a continuous selective molecular sieve on blood contacting surfaces. The rest of the arterial wall is conventionally divided into three concentric zones: the tunica intima, media and adventitia. The intima consists of a thin subendothelial layer of elastin and collagen fibres. Its thickness varies with arterial geometry, age and disease. Partition between the intima and the media is provided by the internal elastic lamina (IEL). The tunica media forms the major part of the wall, comprising of orderly arranged fibres and smooth muscle cells. The external elastic lamina (EEL) partitions the media and the adventitia. The adventitia consists of collagen and elastic tissues and merges with the surrounding connective tissue.

Atherosclerosis is a disease of large- and medium-size arteries. It is caused by the formation of plaques within the arterial wall. It is believed that the infiltration and entrapment of low-density lipoprotein (LDL) in the arterial wall are involved in the initiation and progression of the disease. Arterial mass transport refers to the movement of blood borne species from flowing blood to and through the arterial wall. It is related to the localisation of atherosclerosis. Considering the arterial wall structure, arterial mass transport can be divided into three parts: mass transport from the bulk blood flow to the endothelium or trans-luminal transport, mass transport across the endothelium or trans-endothelial transport, and mass transport through the arterial wall or transmural transport. These subsystems not only are influenced by various factors such as fluid mechanics and

endothelial cell metabolism but also interact with each other, leading to a complicatedly coupled transport system.

Trans-endothelial transport plays an important role as an intermediary. Whether the transport process is limited by lumen-side transport or by wall-side transport is somehow determined by the efficiency of trans-endothelial transport. If trans-luminal transport is more efficient than trans-endothelial transport, an accumulation of solute molecules would be found on the luminal surface. This phenomenon is called concentration polarisation. It is usually observed in macromolecular transport: macromolecules are forced to the luminal surface by a strong convection driven by the transmural flow, but most of them are retarded to remain on the luminal surface because of the limited capacity of transport pathways. In this case, the transport is described as limited by the endothelium or limited by the wall. On the other hand, if trans-luminal transport is less efficient than trans-endothelial transport, a depletion of solute molecules would be found on the luminal surface. Oxygen transport often shows this characteristic depletion because it is spontaneously consumed by the arterial wall. In this case, the transport is said to be limited by the fluid phase.

Trans-luminal transport is coupled with the bulk blood flow while transmural transport is coupled with the transmural flow. The magnitude of the transmural flow is several orders of magnitude smaller than that of the bulk blood flow. Therefore, the time-scales characterising these two sub-processes are dramatically different. The time-scale for trans-luminal transport is the same as the period of a cardiac cycle or around one second, whereas the time-scale for transmural transport is measured using the time needed by plasma to flow across the wall or  $300 \mu\text{m} / 0.03 \mu\text{m s}^{-1} = 10^{-4} \text{ s}$ <sup>1</sup>. The influence of this remarkable difference is discussed later in the chapter.

## 1.2 Literature Reviews

A powerful way to investigate arterial mass transport is computational modelling, which provides detailed descriptions of local transport features (Ethier, 2002). Early studies as well as recent developments on computational modelling of arterial mass transport are reviewed here.

Early studies (Back, 1975a; b; Friedman and Ehrlich, 1975; Ehrlich and Friedman, 1977) on computational modelling of arterial mass transport focused on trans-luminal transport in two-dimensional geometries. Following these pioneering studies, a number of researchers extended the trans-luminal transport model in various aspects. Ma et al. (1997) studied steady mass transport in a generalised two-dimensional carotid bifurcation. It was found that convection of oxygen was impaired in the carotid bulb, creating a thickened concentration boundary layer. In a series of studies, Perktold and co-workers (Rappitsch and Perktold, 1996a; Rappitsch and Perktold, 1996b; Rappitsch et al., 1997) investigated shear-dependent oxygen and albumin transport in various generic geometries. Results given by both shear-dependent and constant permeability showed reductions in the wall flux at the incipient flow separation points, whereas the shear-dependent permeability led to an even stronger spatial variation in the wall flux. However, in the investigation of albumin

---

<sup>1</sup> This calculation is carried out by assuming the intima-media thickness is  $300 \mu\text{m}$  and transmural velocity is  $3 \times 10^{-8} \text{ m s}^{-1}$ .

transport, the authors did not observe the concentration polarisation phenomenon because the transmural flow was not modelled.

Deng and co-workers (Deng et al., 1993; Deng et al., 1994; Deng et al., 1995) studied concentration polarisation of LDL numerically in two-dimensional T-junction models. Counter-diffusion from the luminal surface to the bulk flow was found to be suppressed in the regions of disturbed flow, leading to higher degrees of concentration polarisation. Wada and Karino (1999) carried out a more systematic investigation by studying the influences of various physical and fluid mechanical factors on LDL concentration polarisation in a straight tube. They found that the degree of concentration polarisation increased with increasing filtration velocity, decreasing flow rate, and decreasing LDL plasma diffusivity. The authors also carried out investigations on LDL trans-luminal transport in a segment of a human right coronary artery (RCA) with multiple bends (Wada and Karino, 2002). LDL concentration was found to be elevated at low WSS locations and increased sharply as the WSS decreased from 1 to 0 Pa. As both the filtration velocity and LDL permeability were assumed to be constant, this indicated that concentration polarisation was dependent on WSS even when the shear-dependent transport pathways were discounted. But this dependence was due to the flow driven convection and removal of LDL particles, which were characterised by WSS distribution to some extent.

Qiu and Tarbell (2000), in their investigation of oxygen transport in a two-dimensional idealised coronary artery, found that the transport was limited by fluid phase at the outer wall of a bend, whereas at the inner wall, fluid phase transport did not limit the wall consumption of oxygen. Kaazempur-Mofrad and Ethier (2001) extended this investigation to an image-based model of a right coronary artery. Based on the observations, it was argued that complex secondary flows in a realistic arterial model can produce substantial local variations in blood-wall mass transfer rates and precise geometries should be acquired to ensure the accuracy of flow and hence concentration predictions.

When modelling the arterial mass transport, it is of great interest to obtain detailed concentration fields in the arterial wall. Due to the enhanced computing power, researchers have been working on more sophisticated mathematical models to include trans-endothelial and transmural transport. Karner and Perktold (2000) and Karner et al. (2001) developed a multi-layered model for macromolecular transport, where the transmural flow was modelled using Darcy's Law and transmural transport was modelled using the volume-averaged convection-diffusion-reaction equation. The intima and the media were treated as transport domains while the endothelium and the IEL were assumed to be membranes where matching conditions were prescribed. To estimate transport properties of different wall layers, the authors employed pore theory. The model was first tested in a straight tube and later applied to a more complex geometry (Prosi et al., 2005). A novel electric analogy approach was used to derive the values of transport parameters because a mismatch in LDL trans-endothelial flux was found by using the parameter values determined by Karner et al. (2001). This zero-dimensional method used experimental data as inputs to seek the transport resistances provided by different layers of the wall.

In a series of studies, Stangeby and Ethier (2002a; b) proposed a fluid-plus-porous-wall method (FPPWM) to couple the transmural flow to the bulk blood flow and LDL transport. To incorporate the inhomogeneous uptake of LDL, a concentration and WSS dependent endothelial permeability was derived based on experimental data.

There exist a number of major problems in computational investigations of arterial mass transport. First of all, due to the complex and coupled dynamics in the mass transport process, slight variations of model parameters may bring about substantial changes in mass transfer patterns. However, most of the existing methods for parameter estimation, including theoretical models exploiting pore theory (Karner and Perktold, 2000; Karner et al., 2001; Ai and Vafai, 2006; Yang and Vafai, 2006) and electric analogy (Prosi et al., 2005), could not produce satisfactory estimations of the parameters. Secondly, the effects of WSS on arterial mass transport need to be further investigated. Although some researchers have studied shear-dependent trans-endothelial transport by employing shear-dependent permeability, the role of WSS in the whole arterial mass transport process needs to be elucidated. Finally, while most of the models assumed steady flow conditions, it is important to incorporate time-dependent trans-luminal and transmural transport, which are characterised by different time-scales, into a model framework. In the present study, these problems were addressed using improved methodologies.

## 2. Mathematical Models

Arterial mass transport is coupled with both the bulk blood flow in the lumen and the transmural flow in the wall. Therefore, fluid dynamic models and solute dynamic models should be included. It is worth noting that, in the context of arterial mass transport, the arterial wall refers to the intima and the media, with the adventitia as the outer boundary (not included in the models). In this study, a fluid-wall model was formulated and numerical procedures used to carry out time-dependent simulations were introduced.

### 2.1 A Fluid-wall mass transport model

The fluid-wall model included fluid dynamics and solute dynamics in the blood lumen and the arterial wall. The computational domains and dividing boundaries for the model are shown in Fig. 1. Navier-Stokes equations were employed to model bulk blood flow in the lumen ( $\Omega_l$ ), whereas Darcy's Law was used to model transmural flow in the arterial wall ( $\Omega_w$ ). As for the modelling of mass balance, the convection-diffusion equation was employed in the lumen ( $\Omega_l$ ), and an additional consumption term was added to form a convection-diffusion-reaction equation for the wall ( $\Omega_w$ ). Furthermore, the Kedem-Katchalsky equations were employed to couple fluid dynamics and mass balance at the endothelium ( $\Gamma_{end}$ ), the interface between the arterial lumen and the arterial wall. Please refer to our earlier study (Sun et al., 2006) for details of the model.

#### *Fluid dynamics*

Blood flow was assumed to be incompressible, laminar, Newtonian and hence described by the Navier-Stokes equations

$$\rho \frac{\partial \mathbf{u}_l}{\partial t} - \mu \nabla^2 \mathbf{u}_l + \rho (\mathbf{u}_l \cdot \nabla) \mathbf{u}_l + \nabla p_l = 0 \quad (1)$$

$$\nabla \mathbf{u}_l = 0 \quad (2)$$

in the fluid domain, where  $\mathbf{u}_l$  is blood velocity in the lumen,  $p_l$  is pressure,  $\mu$  is dynamic viscosity of the blood, and  $\rho$  is density of the blood.



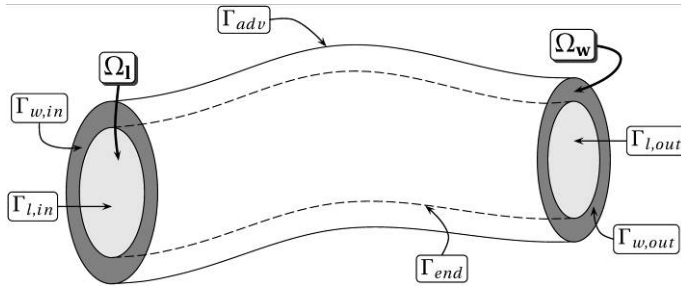


Figure 1. Computational domains and boundaries of the single-layered model.  $\Omega_l$  and  $\Omega_w$  are the lumen domain and the wall domain, respectively;  $\Gamma_{l,in}$  and  $\Gamma_{l,out}$  are the inlet and outlet boundaries of the lumen domain, respectively;  $\Gamma_{w,in}$  and  $\Gamma_{w,out}$  are the side boundaries of the wall domain;  $\Gamma_{end}$  is the endothelial boundary;  $\Gamma_{adv}$  is the outer wall boundary (the external elastic lamina and the adventitia)

The transmural flow in the arterial wall was modelled by Darcy's Law

$$\mathbf{u}_w - \nabla \cdot \left( \frac{\kappa_w}{\mu_p} p_w \right) = 0 \quad (3)$$

$$\nabla \mathbf{u}_w = 0 \quad (4)$$

where  $\mathbf{u}_w$  is the velocity of the transmural flow in the wall,  $p_w$  is pressure in the wall,  $\mu_p$  is viscosity of the blood plasma, and  $\kappa_w$  is the Darcian permeability coefficient of the wall. Therefore, the velocity in the wall is proportional to pressure gradient.

#### Solute dynamics

Mass transfer in the blood lumen was coupled with the blood flow and modelled by the convection-diffusion equation as follows

$$\nabla \cdot (-D_l \nabla c_l + c_l \mathbf{u}_l) = 0 \quad (5)$$

in the fluid domain, where  $c_l$  is the solute concentration in the blood lumen, and  $D_l$  is the solute diffusivity in the lumen.

Mass transfer in the arterial wall was coupled with the transmural flow and modelled by the convection-diffusion-reaction equations as follows

$$\nabla \cdot (-D_w \nabla c_w + K_{lag} c_w \mathbf{u}_w) = r_w c_w \quad (6)$$

where  $c_w$  is the solute concentration in the arterial wall,  $D_w$  is the effective solute diffusivity in the arterial wall,  $K_{lag}$  is the solute lag coefficient,  $r_w$  is the consumption rate constant.

#### Interface coupling

At the fluid-tissue interface (i.e. the endothelium), volume flux and solute flux were defined by the Kedem-Katchalsky equations (Kedem and Katchalsky, 1958) as follows

$$J_{v,end} = L_{p,end} (\Delta p_{end} - \sigma_{d,end} \Delta \pi_{end}) \quad (7)$$

$$J_{s,end} = P_{end} \Delta c_{end} + (1 - \sigma_{f,end}) J_{v,end} \bar{c}_{end} \quad (8)$$

where  $J_{v,end}$  is the volume flux,  $J_{s,end}$  is the solute flux,  $L_{p,end}$  is the hydraulic conductivity of the endothelium,  $\Delta c_{end}$  is the solute concentration difference across the endothelium,  $\Delta p_{end}$  is the pressure drop across the endothelium,  $\Delta \pi_{end}$  is the osmotic pressure difference across the endothelium,  $\sigma_{d,end}$  is the osmotic reflection coefficient of the endothelium,  $\sigma_{f,end}$  is the solvent reflection coefficient of the endothelium,  $P_{end}$  is the solute permeability of the endothelium,  $\bar{c}_{end}$  is the mean interface concentration. In the present study, the osmotic pressure difference  $\Delta \pi_{end}$  was neglected to de-couple the fluid dynamics from solute dynamics.

#### *Boundary conditions*

For the Navier-Stokes equations, a given velocity profile at the inlet of the lumen was prescribed; a zero relative pressure was assigned at the outlet of the lumen; and the outward transmural velocity given by the Kedem-Katchalsky equations was imposed at the endothelium. For Darcy's Law, zero velocity normal to the side boundaries was prescribed; the inward transmural velocity was imposed at the endothelium; and a constant pressure was given at the outer wall boundary. For the convection-diffusion equation in the lumen, a flat concentration profile was prescribed at the inlet; a zero diffusive flux condition was imposed at the outlet; and the outward trans-endothelial flux given by the Kedem-Katchalsky equations was assigned at the endothelium. For the convection-diffusion-reaction equation in the wall, an insulated condition was imposed at the side boundaries; the inward trans-endothelial flux given by the Kedem-Katchalsky equations was assigned at the endothelium; and a constant concentration was prescribed at the outer wall boundary.

## **2.2 Implementation of pulsatile flow simulations**

It is relatively straightforward to carry out steady state simulations, with all the time-dependent terms eliminated in the governing equations. So far, most of the computational studies on arterial mass transport have indeed assumed steady flow which seems to be a reasonable assumption for the long term mass transport process. However, as indicated earlier, arterial mass transport is influenced by two dramatically different time-scales. Thus, although concentration fluctuations in the wall are negligible within one cardiac cycle, the accumulated effect of haemodynamic factors over a longer time span could be significant.

Therefore the effects of pulsatility on long term transport of macromolecules needs to be investigated and the validity of the steady flow assumption needs to be examined. However, it is difficult to carry out transient simulations of macromolecular transport over a long time span using the fluid-wall model with the current computing power. To circumvent the difficulties, lumen-free cyclic (LFC) and lumen-free time-averaged (LFTA) computational procedures were proposed to incorporate into the fluid-wall model.

A couple of assumptions need to be made towards the development of the lumen-free methods. First of all, the highly convection-dominated mass transport in the lumen was omitted and a constant macromolecular concentration was assumed in the arterial lumen. This was also why the computational schemes were termed "lumen-free". Although the luminal convection of macromolecules could induce concentration polarisation, its influence on transmural transport is minor because the rate limiting process is wall-side transport (Caro, 1973; Tarbell, 2003). Secondly, it was assumed that hydraulic conductivity and macromolecular permeability of the endothelium changed simultaneously with WSS. Although this may not be true *in vivo*, our current understanding of the dynamic process limits the formulation of a mathematical model accounting for the dynamic response of transport properties.

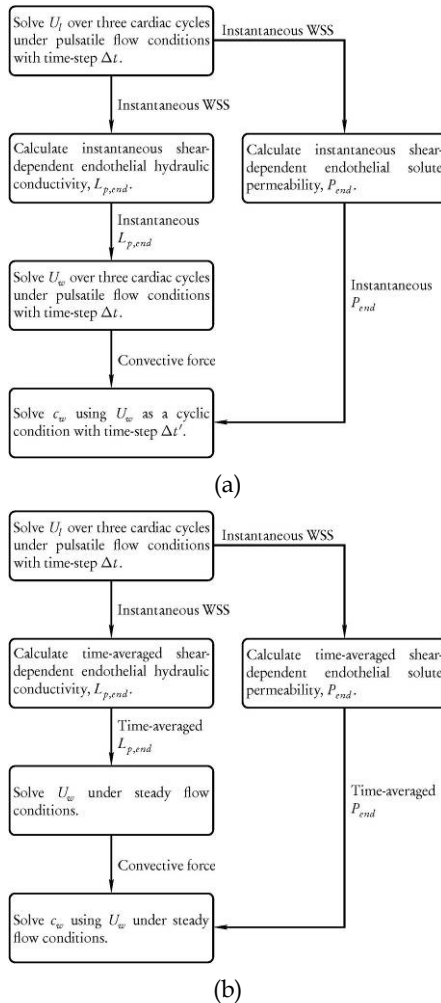


Figure 2. Schematic views of the proposed LFC (a) and LFTA (b) procedures.  $U_l$  represents the dynamics of the bulk blood flow,  $U_w$  the dynamics of the transmural flow, and  $c_w$  the dynamics of macromolecular transport in the arterial wall

A lumen-free cyclic (LFC) procedure was proposed to investigate the accumulated effect of haemodynamics and the influence of flow pulsatility on long term macromolecular transport. Fig. 2(a) shows the schematic view of the LFC procedure. In the LFC procedure, the periodic bulk blood flow is simulated over three cardiac cycles using a time step  $\Delta t$  to determine instantaneous values of WSS. Based on these WSS values, shear-dependent transport properties are calculated. The calculated instantaneous hydraulic conductivity is then employed to simulate the transmural flow over 3 cardiac cycles using the same time steps as in the pulsatile flow simulation. The resulting transmural flow field of the last cycle is then used as a cyclic condition and applied to the simulation of long-term (multi-cycle) macromolecular transport in the arterial wall employing the calculated instantaneous solute

permeability. An appropriate time step,  $\Delta t'$ , is selected through sensitivity test to preserve the characteristics of transmural flow within each cardiac cycle and save computational time. In addition to the LFC procedure, a lumen-free time-averaged (LFTA) procedure was also proposed to simulate the wall-side transport of macromolecules under a steady-state framework with time-averaged endothelial transport properties calculated using the instantaneous WSS from a pulsatile blood flow simulation. As shown in Fig. 2(b), periodic bulk blood flow is simulated over 3 cardiac cycles to determine the instantaneous WSS. On this basis, time-averaged shear-dependent model parameters are obtained and used in transmural momentum and LDL transport simulations. More details about the lumen-free models can be found in one of our earlier studies (Sun et al., 2007b).

### 3. Determination of Model Parameters

In the present study, the momentum transport properties were validated against experimental data reported by Meyer et al. (1996). The same experimental data were also used to determine the macromolecular mass transport properties using an optimisation approach based on one-dimensional simulations. Furthermore, shear-dependent models of endothelial hydraulic conductivity and albumin permeability were derived from experimental data reported by Sill et al. (1995) and Kudo et al. (1998), respectively.

#### 3.1 Momentum transport parameters

The values of fluid phase momentum transport parameters, i.e. blood density and viscosity were well defined in the literature. In the present study, blood density was assumed to be  $1.05 \times 10^3 \text{ kg/m}^3$ , and blood was assumed to be a Newtonian fluid with a constant viscosity  $3.5 \times 10^{-3} \text{ Pa}\cdot\text{s}$ . The tissue phase momentum transport parameters were validated against transmural velocities measured by Meyer et al. (1996). These included plasma viscosity  $\mu_p = 7.2 \times 10^{-4} \text{ Pa}\cdot\text{s}$ , endothelial hydraulic conductivity  $L_{p, \text{end}} = 3 \times 10^{-12} \text{ m}/(\text{Pa}\cdot\text{s})$ , and Darcian permeability of the wall  $\kappa_w = 1 \times 10^{-18} \text{ m}^2$ . These parameter values were mainly taken from Karner et al. (2001) and Prosi et al. (2005).

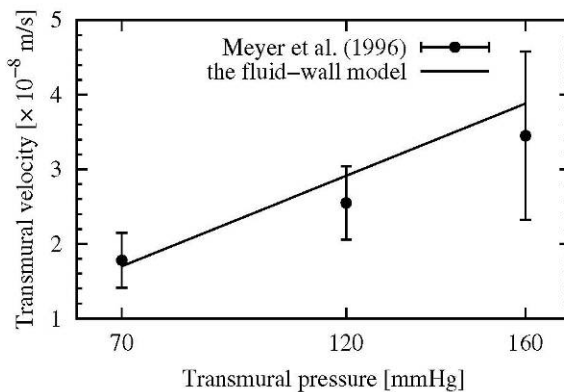


Figure 3. Comparison between the 1-D simulation results and the experimental data for transmural velocity

Employing these parameter values, the transmural velocities given by the one-dimensional fluid-wall model were compared with experimental data in Fig. 3. It is shown that the fluid-wall model was able to predict transmural velocities in a reasonable range with constant momentum transport parameters under different transmural pressures.

### 3.2 Mass transport parameters

Mass transport parameters refer to the model parameters which characterise the transport properties of solutes in the arterial lumen and the wall. The solute transport properties in the arterial lumen were well defined in the literature, whereas the determination of solute transport properties in the arterial wall was usually difficult and needed specially designed methods to exploit the limited experimental observations. In the present study, an optimisation approach which minimised the difference between one-dimensional simulation results and experimental data was developed (Sun et al., 2007a).

In the formulation of the optimisation problem, the mass transport properties were denoted by vector  $\mathbf{x}$ . The simulated concentration distribution samples at predefined locations according to experimental data were denoted by vector  $\mathbf{c}$ . The relationship between  $\mathbf{x}$  and  $\mathbf{c}$  was described by a one-dimensional convection-diffusion-reaction transport model  $\mathbf{c} = f(\mathbf{x})$  with appropriate boundary conditions. The optimisation problem was formulated as follows

$$\begin{aligned} \min \quad & \sum_{j=1}^n W_j (C_j - c_j)^2 \\ \text{s. t.} \quad & c_j = f(x_1, x_2, \dots, x_m), \quad j = 1, 2, \dots, n \\ & lb_k \leq x_k \leq ub_k, \quad k = 1, 2, \dots, m \end{aligned} \quad (9)$$

where  $C_j$  is the experimental value of LDL concentration at  $j$ th sampling point,  $c_j$  is the simulation result of LDL concentration at  $j$ th sampling point,  $W_j$  is the weighting coefficient of the  $j$ th sampling point,  $\mathbf{lb}$  is the vector of lower bounds of  $\mathbf{x}$ ,  $\mathbf{ub}$  is the vector of upper bounds. In this formulation, every sampling point in the experimental data was taken into account and hence the method preserved the concentration distribution in the arterial wall.

To solve this optimisation problem, the weighted accumulated-error was minimised by finding the optimal vector  $\mathbf{x}$  subject to physiological bounds  $\mathbf{lb}$  and  $\mathbf{ub}$ . The minimisation was carried out by implementing a pattern search method. The vector  $\mathbf{x}$  contained the most sensitive parameters, i.e.  $P_{end}$ ,  $D_w$ ,  $K_{lag}$  and  $r_w$ , in the fluid-wall model. It was assumed that the consumption rate constant remained constant under different transmural pressures. In the present study, four sets of these parameters were determined and summarised in Table 1 for albumin transport parameters under transmural pressure of 70 mmHg, and LDL transport parameters under transmural pressures of 70, 120, and 160 mmHg. The one-dimensional simulation results obtained by the fluid-wall model using the optimal parameters were compared with experimental data in Fig. 4 for albumin transport under transmural pressure of 70 mmHg and LDL transport under transmural pressure of 120 mmHg. It is shown that the model with determined parameter values adequately predicted the transmural macromolecular distributions seen in the experimental data.

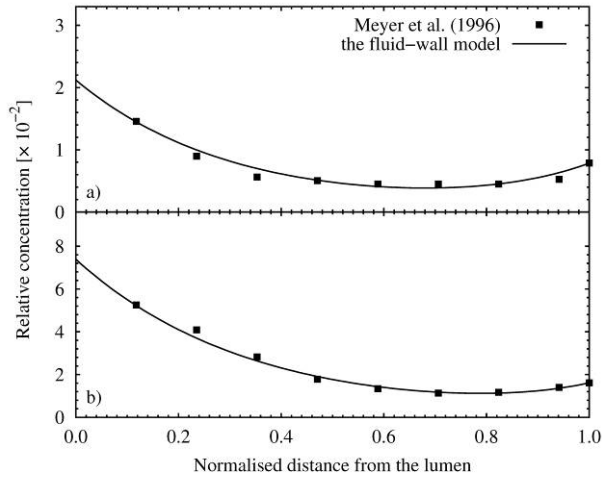


Figure 4. Comparison between 1-D simulation results and the experimental data for (a) transmural albumin concentration under transmembrane pressure of 70 mmHg, and (b) LDL concentration under transmembrane pressures of 120 mmHg

Parameter sets	$D_w$ [ $m^2/s$ ]	$P_{end}$ [ $m/s$ ]	$r_w$ [ $1/s$ ]	$K_{lag}$ [ $n/a$ ]
Albumin, 70 mmHg	$8.16 \times 10^{-11}$	$1.20 \times 10^{-9}$	$-1.04 \times 10^{-3}$	1.58
LDL, 70 mmHg	$1.42 \times 10^{-12}$	$5.21 \times 10^{-10}$	$-6.05 \times 10^{-4}$	0.15
LDL, 120 mmHg	$3.50 \times 10^{-12}$	$4.84 \times 10^{-9}$	$-6.05 \times 10^{-4}$	1.05
LDL, 160mmHg	$1.56 \times 10^{-12}$	$9.38 \times 10^{-9}$	$-6.05 \times 10^{-4}$	0.90

Table 1. Parameters determined by the simulation-based optimisation

### 3.3 Shear-dependent parameters

Trans-endothelial momentum and mass transport is believed to be influenced by biomechanical forces, especially WSS (Caro et al., 1971). A conventional approach to examine the influence of WSS on trans-endothelial transport is to employ analytical models for shear-dependent transport parameters. In the present study, analytical shear-dependent models of endothelial hydraulic conductivity ( $L_{p,end}$ ) and endothelial albumin permeability ( $P_{end,alb}$ ) were constructed from available experimental data. A model for a shear-dependent endothelial LDL permeability ( $P_{end,ldl}$ ) was not formulated and  $P_{end,ldl}$  was assumed to be constant under a given transmembrane pressure due to a lack of suitable data.

The effect of shear stress on hydraulic conductivity ( $L_{p,end}$ ) of bovine aortic endothelium was examined *in vitro* by Sill et al. (1995) under constant shear stress conditions. When exposed to higher shear stresses, the endothelium presented higher hydraulic conductivity. The experimental data were fitted with a logarithmic function to obtain a model of the shear-dependent hydraulic conductivity. The resulting logarithmic function representing the best fit is given by

$$g(|\tau_w|) = 0.4669 \ln(|\tau_w| + 0.015) + 3.327 \quad (10)$$

where  $\tau_w$  is WSS, and  $g$  is the normalised hydraulic conductivity. This fitted curved is compared with experimental data in Fig. 5.

Kudo et al. (1998) reported a dual response of albumin uptake by cultured endothelial cells to shear stress. It was found that the albumin uptake increased with increasing WSS at lower shear stresses ( $< 1$  Pa) and decreased with increasing WSS at higher shear stresses ( $> 2$  Pa). Their data were fitted with a Gaussian function in the present study to construct an analytical model for a shear-dependent endothelial albumin permeability, given by

$$h(|\tau_w|) = 1.0175 \exp\left(\frac{-(|\tau_w| - 0.804)^2}{1.887}\right) + 0.2778 \tag{11}$$

where  $h$  is the normalised endothelial albumin permeability. This fitted curved is compared with experimental data in Fig. 6.

These two models for normalised shear-dependent parameters were scaled to real values employed in the simulations using the base values validated or determined previously.

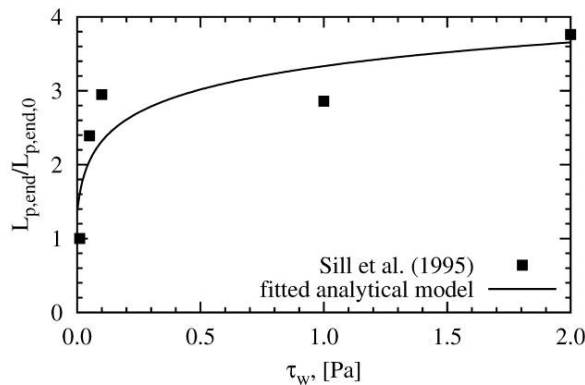


Figure 5. Comparison between experimental data reported by Sill et al. (1995) and the fitted analytical model on shear-dependent endothelial hydraulic conductivity

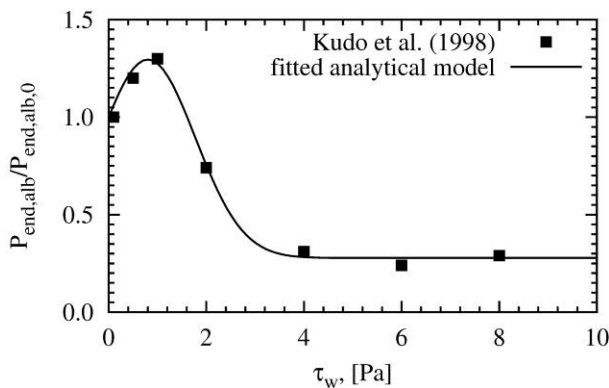


Figure 6. Comparison between experimental data reported by Kudo et al. (1998) and the fitted analytical model on shear-dependent endothelial albumin permeability

### 4. Test cases

In the present study, the fluid-wall model and the lumen-free numerical procedures were tested in an idealised computational geometry.

#### 4.1 Albumin transport in an idealised model of a stenosed coronary artery

Coronary artery disease is the most common type of heart disease in human beings. It happens when the arteries that supply blood to the heart muscles become narrowed due to the formation of multiple plaques. It can eventually lead to a heart attack. Therefore, it is important to study macromolecular transport in coronary arteries. Here albumin transport in an idealised geometry was investigated as a preliminary analysis.

An axisymmetric stenosis with 51% area reduction was adopted. As shown in Fig. 7, the total length (z-axis) of the geometry is  $25D$ , where  $D = 0.004m$  is the diameter of the non-stenosed region of the artery. The length of the stenosis is  $1D$ , leaving  $4D$  upstream and  $20D$  downstream to minimise the effects of boundary conditions.

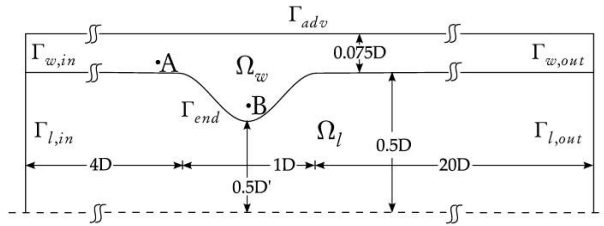


Figure 7. An axisymmetric geometry of a mild stenosed (51% constriction by area) coronary artery for the fluid-wall model. The dashed line is the axis of symmetry. Note the different axial and radial scales

The endothelium geometry at the interface between the lumen and the wall of the axisymmetric stenosis was modelled by the following cosine expression:

$$\frac{r_{end}(z)}{R} = \frac{\alpha_{end}}{D} \cos\left(\frac{2\pi(z - z_1 - z_2)}{z_2 - z_1}\right) + \frac{\beta_{end}}{D} \tag{12}$$

for  $4D < z < 5D$ , where  $r_{end}(z)$  is the position of the endothelium (radius of the lumen) at location  $z$  in the arterial segment,  $R$  is the radius of the non-stenosed region of the artery,  $\alpha_{end} = 0.15D$  and  $\beta_{end} = 0.85D$  are the parameters for lumen constriction,  $z_1 = 4D$  is the start point of the stenosed region, and  $z_2 = 5D$  is the end point of the stenosed region. The wall geometry was defined as  $r = 0.575D$  with a wall thickness of  $0.075D$  at the non-stenosed region and  $0.225D$  at the throat of the stenosis.

The transmural pressure was assumed to be 70 mmHg and the corresponding mass transport parameters were employed. To investigate the effects of shear-dependent transport parameters, both constant and shear-dependent endothelial hydraulic conductivities and albumin permeabilities were used in the simulations. A fully developed parabolic steady velocity profile with mean velocity  $0.24 \text{ m/s}$  was prescribed at the lumen inlet. The resulting Reynolds number was 288 and Peclet number was 10,655,000. The inlet albumin concentration was assumed to have a normalised value of 1. The normalised



albumin concentration at the outer wall boundary was assumed to be 0.00785 based on measurements by Meyer et al. (1996). To implement finite element simulations using a commercial package, Comsol Multiphysics, Version 3.3 (COMSOL AB, Sweden), the computational domain was discretised. The lumen was divided into 19,950 quadrilateral elements with 20,774 nodes and 291,213 quadrilateral elements with 293,820 nodes for solutions of the Navier-stokes equations and the convection-diffusion equation, respectively. The wall domain was divided into 7,890 quadrilateral elements with 8,789 nodes and 49,780 quadrilateral elements with 52,290 nodes for solution of Darcy's Law and the convection-diffusion-reaction equation, respectively. A mesh sensitivity test was carried out in a generic computational geometry to ensure that the meshes used in the present study were able to capture the concentration gradient in the boundary layer.

Variations of WSS magnitude in the axisymmetric geometry is shown in Fig. 8. Imposing shear-dependent endothelial hydraulic conductivity had little effect on the near-wall flow field and WSS, due to the fact that the transmural flow is several orders of magnitude smaller than the bulk flow. The two points where WSS values were zero correspond to the separation point and reattachment point, respectively. The area between these two points was the flow recirculation region.

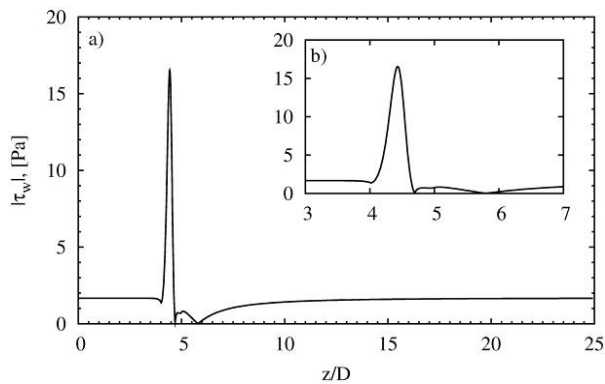


Figure 8. Magnitude of WSS distribution along the entire length of the axisymmetric geometry (a) and in the vicinity of the stenosis (b)

The transmural velocity ( $J_{v,end}$ ) and trans-endothelial albumin flux ( $J_{s,end}$ ) profiles in the immediate vicinity of the stenosis calculated using constant and shear-dependent parameters are compared in Fig. 9. The reduction in transmural velocity at the stenosis in both cases was due to the higher resistance provided by the thickened wall. When shear-dependent parameters were employed, the transmural velocity was much lower in the post-stenotic region and had two minima which corresponded to the separation point and the reattachment point, respectively. This is because the endothelium provides a higher resistance to plasma transport when subject to low WSS. Similarly, due to a higher resistance provided by the thickened wall, reduction in albumin flux can be observed at the stenosis in both cases. In the flow recirculation region, an increase in  $J_{s,end}$  can be found, which was induced by a higher endothelial albumin permeability. The reduced albumin flux at the separation and reattachment points is mainly attributed to the decrease in the convective flux driven by the transmural flow. Also, because the shear-dependent

endothelial albumin permeability was characterised by a dual response, it decreased with decreasing WSS in a low WSS range.

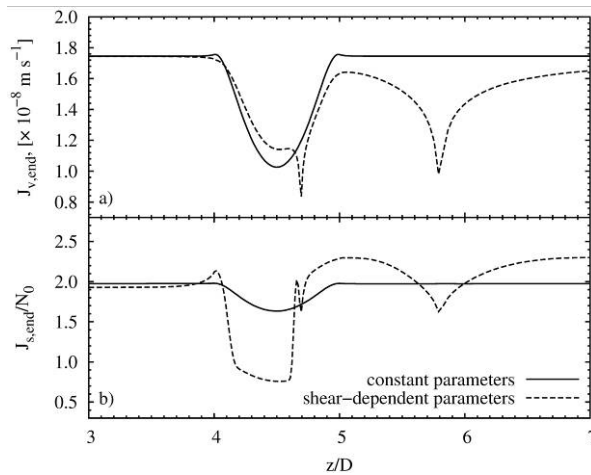


Figure 9. Comparison of transmural velocity (a) and trans-endothelial albumin flux (b) in the vicinity of the stenosis given by simulations employing constant and shear-dependent transport parameters

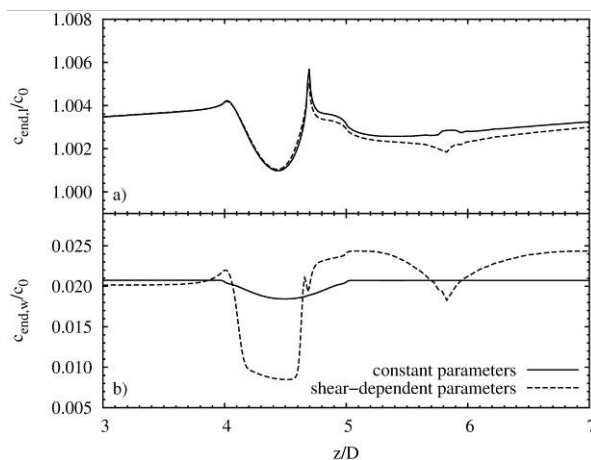


Figure 10. Comparison of endothelial albumin concentration on the lumen side (a) and on the wall side (b) in the vicinity of the stenosis given by simulations employing constant and shear-dependent transport parameters

The endothelial albumin concentration profiles on the lumen and the wall sides for both cases are compared in Fig. 10. It is shown that the effect of shear-dependent transport

parameters on albumin concentration polarisation was minor. However, endothelial albumin concentration on the wall side was significantly different when shear-dependent transport parameters were employed. The distribution pattern of wall side concentration mainly followed that of trans-endothelial albumin flux, showing a lower concentration at the separation point, the reattachment point and the throat of the stenosis but a higher concentration in the recirculation region.

#### 4.2 Transient LDL transport in an idealised model of a stenosed coronary artery

To avoid simulating the bulk blood flow for a prolonged period, the lumen-free cyclic (LFC) and the lumen-free time-averaged (LFTA) computational procedures were developed in the present study. To carry out a preliminary analysis, they were applied to model LDL transport in the same axisymmetric stenosis used previously.

The transmural pressure was assumed to be 120 mmHg and corresponding mass transport parameters were employed. The shear-dependent endothelial hydraulic conductivity was used in the simulations. The effects of pulsatile flow were incorporated by using the LFC and LFTA procedures respectively and their results were compared. For transient flow simulations, a sinusoidal waveform was used to describe the variation of mean axial velocity at the inlet

$$\bar{u}_{in}(t) = U_0 [1 - \cos(\omega t)] \quad (13)$$

where  $U_0 = 0.24 \text{ m/s}$  is the time-averaged mean inlet velocity and  $\omega = 2\pi$  is the angular frequency with a pulse period of one second. Womersley velocity profiles corresponding to the waveform were calculated and applied at the inlet (Womersley, 1955). The resulting mean Reynolds number was 288. The normalised value of LDL concentration in the lumen was assumed to be 1. A convective flux condition was assumed at the outer wall boundary. For the initial condition, zero concentration in the arterial wall was assumed.

To solve the equations, the fluid domain was divided into 85,880 quadrilateral elements with 91,027 nodes for solutions of the Navier-Stokes equations. The wall domain was divided into 46,320 quadrilateral elements with 46,980 nodes for solution of Darcy's Law and the convection-diffusion-reaction equation. The time-steps for pulsatile flow simulation and mass transfer transient simulation were set to be 0.01 s and 0.05 s, respectively.

Cross-sectional profiles of LDL concentration upstream of the stenosis at different time points are shown in Fig. 11(a). It is observed that the concentration profile upstream of the stenosis developed significantly from 5 minutes to 30 minutes, moderately from 30 minutes to 90 minutes, and very little from 90 minutes to 150 minutes. The results suggested that LDL concentration evolved at a higher rate within the first 30 minutes after the perturbation was imposed. The rate of change then decayed before equilibrium was finally reached at approximately 90 minutes. A similar observation can be made at the throat of the stenosis, as shown in Fig. 11(b). However, the average LDL concentration at the throat of the stenosis was significantly lower than that at the upstream. This was due to the fact that the wall was thicker at the throat of the stenosis and provided higher resistance to transmural LDL transport.

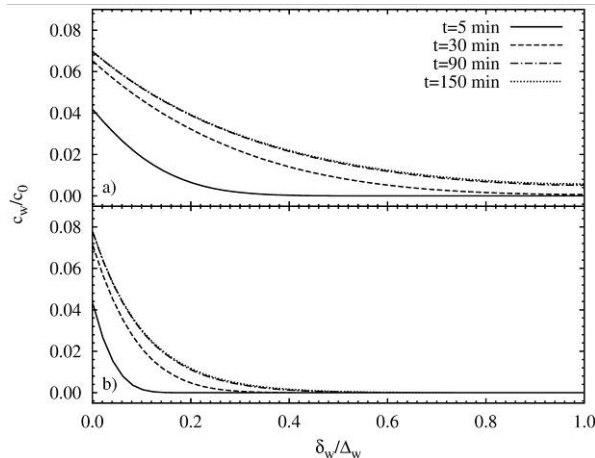


Figure 11. Cross-sectional profiles of LDL concentration in the wall upstream of the stenosis at  $z = 3D$  (a) and at the throat of the stenosis ( $z = 4.5D$ ) (b) at different time points. The distance ( $\delta_w$ ) from the lumen was normalised by the total wall thickness ( $\Delta_w$ )

In Fig. 12, subendothelial LDL concentration profile along the stenosis given by the LFC simulation was compared with those obtained by LFTA and steady flow simulations. It was obvious that the LFTA procedure, which used time-averaged hydraulic conductivity as input data for steady-state LDL transport simulation, produced very similar LDL concentration distribution to the time-dependent LDL transport simulation (LFC procedure). However, the LDL concentration profile obtained under the steady flow assumption was very different. The steady flow simulation predicted a pronounced peak in the post-stenotic region and the maximum concentration of LDL co-localised with the reattachment point. This finding was explained by weaker local convective clearance effects of the transmural flow: when hydraulic conductivity of the endothelium was low and hence transmural velocity was high, LDL particles could not be effectively “flushed” away from the subendothelial layer. A similar explanation can be applied to the wider and less marked peaks predicted by LFC and LFTA simulations. Under pulsatile flow conditions, the flow separation zone in the post-stenotic region expands and contracts during a cardiac cycle, resulting in oscillation of the reattachment point along the luminal surface. Thus, when the calculated instantaneous WSS was used to simulate transmural LDL transport, LDL distribution induced by low WSS was more diffused than under steady flow conditions. Likewise, using the time-averaged transport properties calculated based on instantaneous WSS also diffused the LDL distribution in the post-stenotic region as shown by the LFTA simulation. The good agreement between results from the LFC and LFTA simulations implied that transmural LDL transport responds slowly to changes in WSS arising from pulsatile flow, and the transport of LDL is more likely to be influenced by the time-averaged transport properties (Tarbell, 2003).

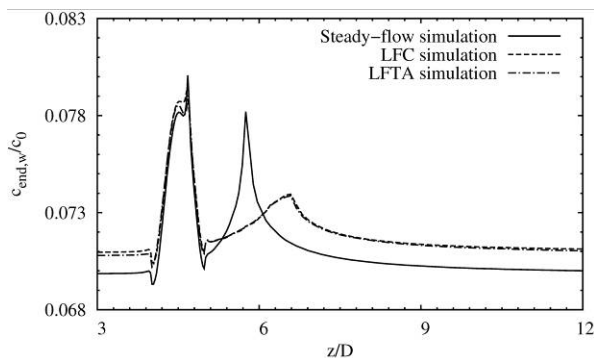


Figure 12. LDL concentration distribution at the endothelium on the wall side given by the steady flow simulation, LFC simulation, and LFTA simulation

This preliminary analysis indicated that the LFTA procedure could be an effective tool to investigate the effect of pulsatile flow on arterial mass transport as it takes into account the transient haemodynamics whilst saving the computational time through an appropriate time-averaging procedure. Furthermore, the results showed that LDL transport reached a quasi steady-state after 2 hours assuming that there was no LDL in the wall initially and a transmural pressure of 120 mmHg. This result can serve as a guideline for future experimental investigations on transmural LDL transport.

## 5. Model Application: Albumin Transport in a human Right Coronary Artery

The right coronary artery (RCA) originates from the aortic root above the right cusp of the aortic valve and supplies the myocardium with oxygen and nutrients. Coronary artery disease (CAD) is a result of formation of atheromatous plaques in the arterial wall. After decades of progression, some plaques may rupture and release thrombogenic materials. The resulting thrombosis can limit blood flow to the heart muscle with morbid or fatal results. Since the early processes of atherogenic progression and plaque formation include the accumulation of macromolecules, mass transport of albumin was investigated, in a human RCA in this study. Specifically, the fluid-wall model was combined with shear-dependent models for endothelial hydraulic conductivity and albumin permeability. The LFTA procedure was used to investigate the influence of pulsatility on macromolecular transport in the image-based patient geometry.

### 5.1 Image-based geometry and computational details

A computer aided design (CAD) model of a human RCA lumen was reconstructed from computed tomographic (CT) scans of a patient. The patient was a 51-year-old male who had a clinically identified stenosis in his RCA. The study complied with Declaration of Helsinki and was approved by the St. Mary's Hospital Research Ethics Committee. The patient gave written, informed consent. Fig. 13 shows the reconstructed lumen geometry of the RCA viewed from the epicardial, medial and pericardial sides. The lumen inlet diameter of the RCA was 3.8 mm. The length of the RCA segment was about 75 mm (around 20 diameters). Two local constrictions can be identified in this geometry: one near the proximal end, the other in the middle of the segment. Since the intima-media thickness cannot be resolved by

CT, it was assumed to be  $300\ \mu\text{m}$  throughout the vessel although it would have been thicker at the stenosis. The wall domain was generated by extruding the luminal surface in the normal direction by the defined wall thickness. To maintain good practice in applying boundary conditions in the flow simulation, straight 5-diameter (5D) extensions were added at the inlet and outlet of the RCA lumen geometry. The end of the inlet extension was designed to be circular so that the corresponding fully-developed velocity profiles could be readily applied.

In steady flow simulations, a parabolic velocity profile was prescribed at the inlet of the lumen. In pulsatile flow simulations, a realistic coronary velocity waveform obtained in a different patient was prescribed (shown in Fig. 14) and the corresponding Womersley velocity profiles were applied. In both cases, the mean inlet velocity was  $0.1613\ \text{m/s}$  and the resulting mean Reynolds number was 184. The transmural pressure was assumed to be  $70\ \text{mmHg}$  and the corresponding transport parameters for albumin were employed.

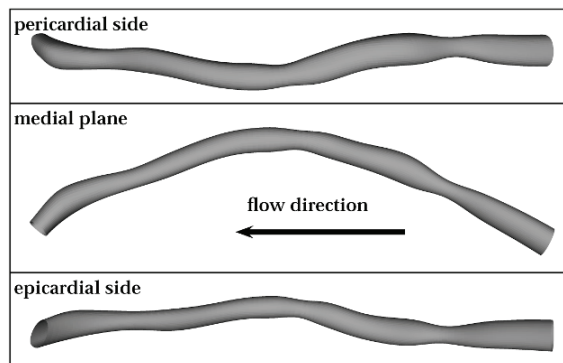


Figure 13. Computational geometry of a human right coronary artery (RCA) reconstructed from CT images

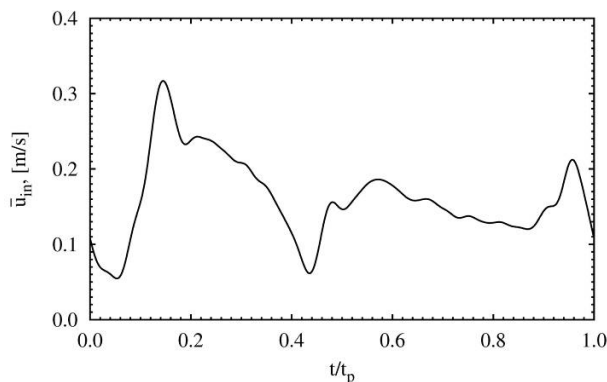


Figure 14. A coronary flow waveform acquired in a patient *via* an endovascular Doppler ultrasound probe

In the patient-specific geometry, Navier-Stokes equations were simulated using a commercial CFD package, ANSYS CFX 10.0 (ANSYS, Inc., USA), while the rest of the model was implemented using Comsol Multiphysics 3.3 (COMSOL AB, Sweden). The fluid domain

was divided into 109,824 hexahedral elements with 116,171 nodes for solutions of the Navier-Stokes equations and 86,112 second order hexahedral elements (excluding inlet and outlet extensions) with 704,965 nodes for solutions of the convection-diffusion equation. The wall domain was divided into 66,240 hexahedral elements with 73,392 nodes for solutions of Darcy's Law and the convection-diffusion-reaction equation. A mesh independence test was carried out in a generic geometry to ensure that the employed computational mesh was able to resolve the mass transfer boundary layer. The implicit time step in the pulsatile flow simulation was chosen as 0.002 s.

## 5.2 Computational results

Contours of WSS magnitude for steady flow and time-averaged WSS (TAWSS) for pulsatile flow are shown on the epicardial and pericardial sides of the RCA in Fig. 15. Low WSS can be identified mainly in three regions in both sets of results: downstream of the stenosis in the proximal part (Region 1), downstream of the second stenosis in the middle of the segment (Region 2), and in the expansion at the distal end of the RCA (Region 3). However, minor differences can be seen between the steady flow results and pulsatile flow results. First of all, the magnitude of steady WSS was lower than that of TAWSS in low shear stress regions. Secondly, the low WSS regions in the steady flow results were slightly smaller than those in the pulsatile flow results. These differences could be attributed to the fact that the flow recirculation regions were contracting and expanding with the reattachment points oscillating along the luminal surface under the pulsatile flow condition.

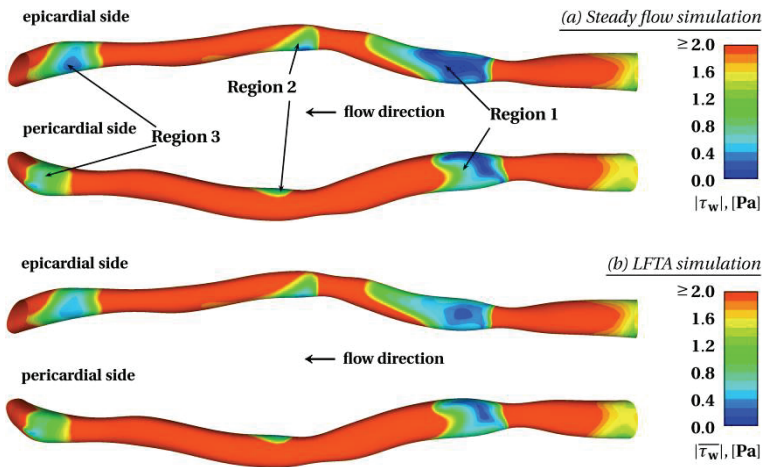


Figure 15. Distribution of WSS magnitude calculated from the steady flow simulation (a) and LFTA simulation (b)

Based on the predicted WSS values, shear-dependent endothelial hydraulic conductivities  $L_{p,end}$  were calculated. Using the computed hydraulic conductivities, transmural flow was simulated. It was found that the predicted transmural velocity was between  $1.0 \times 10^{-8}$  m/s and  $2.0 \times 10^{-8}$  m/s (see Fig. 16); which was consistent with experimental data on filtration velocities (Meyer et al., 1996). It was also observed that WSS has a strong influence on

plasma filtration through the arterial wall: the transmural velocity in the low WSS regions was much lower than that in other locations, indicating that the endothelium contributes significantly to the overall resistance to transmural flow. Furthermore, highly localised minimum transmural velocity was observed in the steady flow results, but not in the pulsatile flow results, because the nonlinearity of the shear-dependent hydraulic conductivity model amplified the difference between the steady and the pulsatile flow cases.

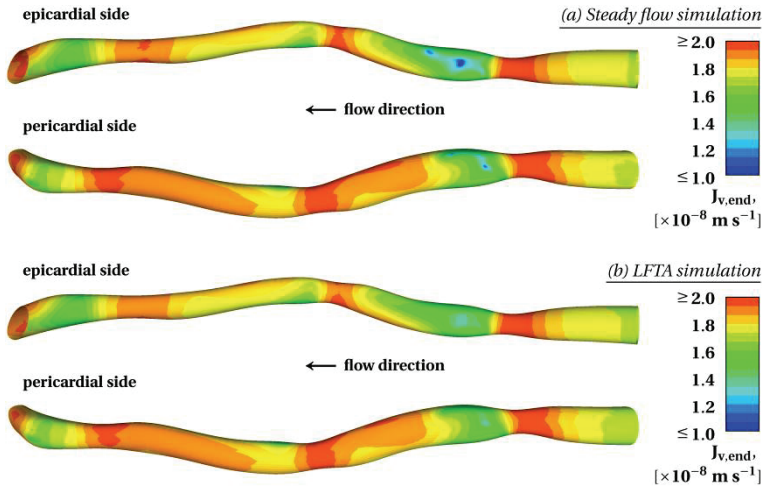


Figure 16. Distribution of transmural velocity calculated from the steady flow simulation (a) and LFTA simulation (b)

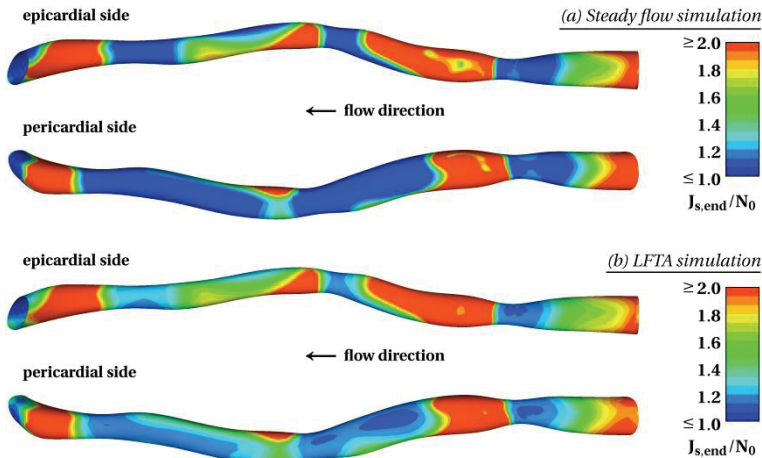


Figure 17. Distribution of trans-endothelial albumin flux calculated from the steady flow simulation (a) and LFTA simulation (b). Flux was normalised by a reference flux  $N_0 = 1 \times 10^{-11} \text{ m/s}$ .



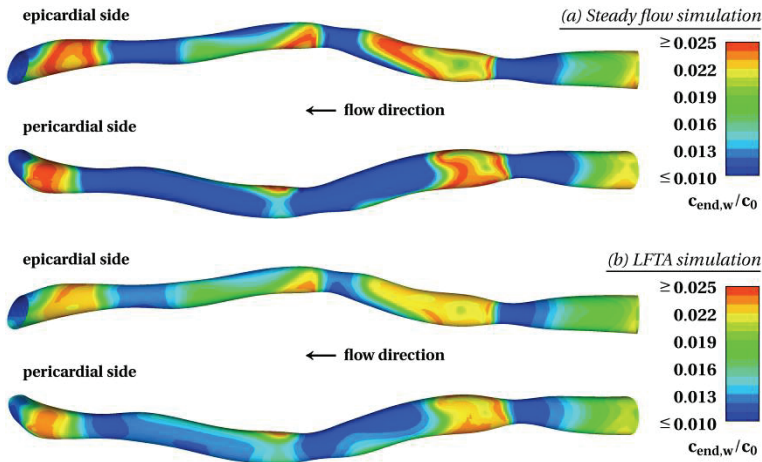


Figure 18. Distribution of sub-endothelial albumin concentration calculated from the steady flow simulation (a) and LFTA simulation (b)

The shear-dependent albumin permeability was calculated using WSS distributions. Trans-endothelial albumin flux computed in the steady flow and the LFTA simulations are compared in Fig. 17. It is found that the flux was significantly higher in the low WSS regions where permeability was generally high. By comparing results from the steady flow and LFTA simulations, obvious differences can be seen especially in the high flux regions, which were considerably larger in the pulsatile flow results. This again illustrated the wider and more diffuse distribution pattern observed in the LFC and LFTA simulations in the preceding section. Sub-endothelial albumin concentrations are shown in Fig. 18. It was found that prominent albumin accumulation in the sub-endothelial layer, which showed up to 100% elevation, co-localised with low WSS. This was caused by the greater flux across the endothelium in the low WSS regions. Furthermore, discrepancies between steady flow and LFTA results were found: the differences in WSS distribution caused by the expansion and contraction of the recirculation regions in the pulsatile flow simulation, after being amplified by the nonlinearity of the shear-dependent models for trans-endothelial transport parameters, led to a wider and more diffuse distribution pattern in both trans-endothelial albumin flux and sub-endothelial albumin concentration.

### 5.3 Discussion

It was shown that the LFTA simulation produced different results from those given by the steady flow simulations. Generally speaking, more diffuse and wider distribution patterns were found with the LFTA simulation in terms of calculated transmural velocity, trans-endothelial flux and sub-endothelial concentration. This was mainly because the dynamic behaviours of the blood flow in pulsatile flow simulations caused different WSS distribution from steady flow simulations and the nonlinearity of the models for shear-dependent transport parameters amplified these differences. Therefore, although it has been suggested that haemodynamic factors only contribute to the average physiological environment for mass transport, these factors might not be accurately represented by steady flow

simulations. It can be speculated that, in more complex geometries where the flow pattern is likely to be more disturbed, differences between steady flow and LFTA results would be even more pronounced. Taking into account the pulsatile flow is vital, especially when nonlinear shear-dependent trans-endothelial transport parameters are employed. It is important to point out that the LFTA procedure implicitly assumed that the endothelium responds instantaneously to changes in WSS. However, the endothelium may take a considerable period of time to adapt to WSS variations *in vivo*. An empirical dynamic model for endothelial adaptation may help relax the assumption but substantial experimental data are needed for the development of such a model.

In summary, the fluid-wall model was used to simulate albumin transport in a patient-specific human RCA and showed that albumin accumulation (up to 100% elevation) occurred in the low WSS regions. It was also found that steady flow simulation could overestimate the magnitude and underestimate the area of accumulation. The association between low WSS and accumulation of macromolecules leading to atherosclerosis may be mediated through effects on transport properties and mass transport and is also influenced by flow pulsatility.

## 6. Conclusion

In the present study, a fluid-wall model was developed to simulate arterial mass transport of macromolecules in atherosclerosis-prone arteries. To incorporate time-dependent transport processes in the arterial wall, two time-averaged numerical procedures were proposed and compared. Model parameters, especially the transport properties of the arterial wall layers, were estimated using a simulation-based optimisation approach. Furthermore, shear-dependent transport properties, such as hydraulic conductivity and permeability were derived from relevant experimental data in the literature to incorporate the shear-dependence of trans-endothelial transport. The mathematical model and corresponding parameters were tested in idealised arterial geometries as preliminary investigations. The model was then applied to a patient-specific case, albumin transport in a human right coronary artery. The main outcomes of this study include the following. 1) The determination of four sets of model parameters, including albumin transport parameters under transmural pressure of 70 mmHg, LDL transport parameters under transmural pressures of 70 mmHg, 120 mmHg, and 160 mmHg. It was shown that the simulation-based optimisation approach led to much better parameter estimations than existing methods. 2) Preliminary model tests showed that the conventional steady flow assumption in the arterial mass transport models may not be adequate, especially when the bulk flow is highly disturbed. The LFTA numerical procedures provided an efficient way to incorporate the effects of flow pulsatility on shear-dependent trans-endothelial transport. Results suggested that the influence of transient haemodynamic conditions on macromolecular transport can be modelled as a time-averaged effect. 3) Albumin accumulation in the subendothelial layer was found to be co-localised with low WSS, implying that the arterial wall exposed to low WSS is atherosclerosis-prone due to a greater lipid accumulation. The accumulation was mainly due to a greater influx in the low WSS regions where the endothelium is more permeable.

A number of limitations existed in the present study, including the use of a vascular scale model, parameter-related limitations, and limitations in the time-averaged numerical procedures.

In the present study, transmural transport was approximated using volume-averaged notations, leading to formulation of a vascular scale model which could only simulate the spatially-averaged phenomenon. For instance, although sub-cellular scale variations in concentration polarisation have been found (Vincent et al., 2007), the present model predicted a smooth luminal distribution of LDL because of the vascular scale formulation.

The present study used available experimental data (Meyer et al., 1996) to determine the model parameters by a simulation-based optimisation approach. In these experiments, the fluid medium was only circulated for 30 minutes. However, it was shown that LDL concentration takes more than 2 hours to reach a quasi steady-state. Therefore, the experimental data that were used to determine the model parameters were somewhat questionable. Nevertheless, they were the most suitable data and were also used in other studies (Prosi et al., 2005; Ai and Vafai, 2006) to determine model parameters.

In the time-averaged numerical procedures, two major assumptions were made. Luminal concentration of macromolecules was assumed to be constant to avoid fully transient mass transport simulation for a prolonged period. In the long term, a better alternative should be developed, especially when the degree of concentration polarisation is predicted to be high.

The endothelial cells *in vitro* take hours to reach a new steady state when a simple step change in WSS is imposed. However, instantaneous response of the endothelium to WSS was assumed here, due to the lack of relevant data and plausible models on how WSS induces changes in endothelial transport properties. This assumption needs to be evaluated further by using a dynamic model for endothelial response to WSS.

The long term goal of computational investigations of arterial mass transport is to develop an experiment-assisted computational modelling framework spanning multiple spatial and time-scales to advance the understanding of arterial hyperlipidemia and its relations to progression and localisation of atherosclerosis. Therefore, the main tasks are to resolve physical and biological phenomena in different spatial- and time-scales. An optimal approach to improve the spatial resolution would be the combination of models in different spatial scales. The sub-cellular scale model has a better capacity to accommodate essential micro-scale physical phenomena that build up the macroscopic situation. When the sub-cellular scale predictions are made, the vascular scale model should be tuned to adapt to the observation and eventually give a broad picture. Efforts should also be made to improve the temporal resolution of the model. As discussed previously, the arterial mass transport processes are characterised by dramatically different time-scales. Therefore, to gain a complete understanding of the disease progression, it is essential to investigate phenomena that occur at different time-scales. That is to say, when looking at lipid accumulation in the arterial wall, one should not ignore haemodynamics in the fluid phase, which determines trans-endothelial transport. The present study attempted to integrate these transport processes into one model framework using time-averaged techniques, but major improvements are still needed. Furthermore, more subject-specific investigations should be carried out in the future to assess the feasibility of using the model predictions to facilitate disease diagnosis and management.

## 7. Acknowledgement

This work was supported by the Leverhulme Trust (F07 058/AA). The authors thank Dr. Andrew Wright, Dr. Andrew Dowsey, and Dr. Ryo Torii for their help on the RCA

geometry data, Dr. Nearchos Hadjiloizou for provision of the coronary waveform, and Prof. Simon Thom and Prof. Alun Hughes for various discussions.

## 8. References

- Ai, L. and Vafai, K. (2006). A coupling model for macromolecule transport in a stenosed arterial wall. *Int. J. Heat. Mass. Tran.* Vol. 49: 1568-1591.
- Back, L. H. (1975a). Theoretical investigation of mass transport to arterial walls in various blood flow regions - I. flow field and lipoprotein transport. *Math. Biosci.* Vol. 27: 231-262.
- Back, L. H. (1975b). Theoretical investigation of mass transport to arterial walls in various blood flow regions - II. oxygen transport and its relationship to lipoprotein accumulation. *Math. Biosci.* Vol. 27: 263-285.
- Caro, C. (1973). Transport of  $^{14}\text{C}$ -4-cholesterol between intra-luminal serum and artery wall in isolated dog common carotid artery. *J. Physiol. (Lond.)* Vol. 233: 37P-38P.
- Caro, C. G., Fitz-Gerald, J. M. and Schroter, R. C. (1971). Atheroma and arterial wall shear observation, correlation and proposal of a shear dependent mass transfer mechanism for atherogenesis. *Proc. R. Soc. London, Ser. B Biol. Sci.* Vol. 177: 109-159.
- Deng, X., King, M. and Guidoin, R. (1993). Localization of Atherosclerosis in Arterial Junctions. Modeling the Release Rate of Low Density Lipoprotein and its Breakdown Products Accumulated in Blood Vessel Walls. *ASAIO J.* Vol. 39: M489-M495.
- Deng, X., King, M. and Guidoin, R. (1995). Localization of Atherosclerosis in Arterial Junctions. Concentration Distribution of Low Density Lipoproteins at the Luminal Surface in Regions of Disturbed Flow. *ASAIO J.* Vol. 41: 58-67.
- Deng, X., Marois, Y., King, M. and Guidoin, R. (1994). Uptake of  $^3\text{H}$ -7-cholesterol along the Arterial Wall at an Area of Stenosis. *ASAIO J.* Vol. 40: 186-191.
- Ehrlich, L. W. and Friedman, M. H. (1977). Steady convective diffusion in a bifurcation. *IEEE Trans. Biomed. Eng.* Vol. 24: 12-18.
- Ethier, C. R. (2002). Computational Modeling of Mass Transfer and Links to Atherosclerosis. *Ann. Biomed. Eng.* Vol. 30: 461-471.
- Friedman, M. H. and Ehrlich, L. W. (1975). Effect of spatial variations in shear on diffusion at the wall of an arterial branch. *Circ. Res.* Vol. 37: 446-454.
- Kaazempur-Mofrad, M. R. and Ethier, C. R. (2001). Mass Transport in an Anatomically Realistic Human Right Coronary Artery. *Ann. Biomed. Eng.* Vol. 29: 121-127.
- Karner, G. and Perktold, K. (2000). Effect of Endothelial Injury and Increased Blood Pressure on Albumin Accumulation in the Arterial Wall: A Numerical Study. *J. Biomech.* Vol. 33: 709-715.
- Karner, G., Perktold, K. and Zehentner, H. P. (2001). Computational Modeling of Macromolecule Transport in the Arterial Wall. *Comput. Methods. Biomed. Engin.* Vol. 4: 491-504.
- Kedem, O. and Katchalsky, A. (1958). Thermodynamic analysis of the permeability of biological membranes to non-electrolytes. *Biochem. Biophys. Acta.* Vol. 27: 229-246.
- Kudo, S., Ikezawa, K., Matsumura, S., Ikeda, M., Oka, K. and Tanishita, K. (1998). Effect of wall shear stress on macromolecule uptake into cultured endothelial cells. *Tran. JSME* Vol. 64: 367-374.

- Ma, P., Li, X. and Ku, D. N. (1997). Convective Mass Transfer at the Carotid Bifurcation. *J. Biomech.* Vol. 30: 565-571.
- Meyer, G., Merval, R. and Tedgui, A. (1996). Effects of Pressure-induced Stretch and Convection on Low-density Lipoprotein and Albumin Uptake in the Rabbit Aortic Wall. *Circ. Res.* Vol. 79: 532-540.
- Prosi, M., Zunino, P., Perktold, K. and Quarteroni, A. (2005). Mathematical and Numerical Models for Transfer of Low-density Lipoproteins through the Arterial Wall: a New Methodology for the Model Set up with Applications to the Study of Disturbed Luminal Flow. *J. Biomech.* Vol. 38: 903-917.
- Qiu, Y. and Tarbell, J. M. (2000). Numerical Simulation of Oxygen Mass Transfer in a Compliant Curved Tube Model of a Coronary Artery. *Ann. Biomed. Eng.* Vol. 28: 26-38.
- Rappitsch, G. and Perktold, K. (1996a). Computer Simulation of Convective Diffusion Processes in Large Arteries. *J. Biomech.* Vol. 29: 207-215.
- Rappitsch, G. and Perktold, K. (1996b). Pulsatile Albumin Transport in Large Arteries: a Numerical Simulation Study. *ASME J. Biomech. Eng.* Vol. 118: 511-519.
- Rappitsch, G., Perktold, K. and Pernkopf, E. (1997). Numerical Modelling of Shear-dependent Mass Transfer in Large Arteries. *Int. J. Numer. Methods Fluids* Vol. 25: 847-857.
- Sill, H. W., Chang, Y. S., Artman, J. R., Frangos, J. A., Hollis, T. M. and Tarbell, J. M. (1995). Shear stress increases hydraulic conductivity of cultured endothelial monolayers. *Am. J. Physiol. Heart Circ. Physiol.* Vol. 268: 535-543.
- Stangeby, D. K. and Ethier, C. R. (2002a). Computational analysis of coupled blood-wall arterial LDL transport. *ASME J. Biomech. Eng.* Vol. 124: 1-8.
- Stangeby, D. K. and Ethier, C. R. (2002b). Coupled computational analysis of arterial LDL transport - effects of hypertension. *Comput. Methods. Biomech. Biomed. Engin.* Vol. 5: 233-241.
- Sun, N., Wood, N. B., Hughes, A. D., Thom, S. A. M. and Xu, X. Y. (2006). Fluid-Wall Modelling of Mass Transfer in an Axisymmetric Stenosis: Effects of Shear-Dependent Transport Properties. *Ann. Biomed. Eng.* Vol. 34: 1119 - 1128.
- Sun, N., Wood, N. B., Hughes, A. D., Thom, S. A. M. and Xu, X. Y. (2007a). Effects of transmural pressure and wall shear stress on LDL accumulation in the arterial wall: a numerical study using a multilayered model. *Am. J. Physiol. Heart Circ. Physiol.* Vol. 292: 3148-3157.
- Sun, N., Wood, N. B., Hughes, A. D., Thom, S. A. M. and Xu, X. Y. (2007b). Influence of Pulsatile Flow on LDL Transport in the Arterial Wall. *Ann. Biomed. Eng.* Vol. 35: 1782-1790.
- Tarbell, J. M. (2003). "Mass Transport in Arteries and the Localization of Atherosclerosis." *Annu. Rev. Biomed. Eng.* Vol. 5: 79-118.
- Vincent, P., Sherwin, S. and Weinberg, P. (2007). Sub-cellular scale variations in low density lipoprotein concentration adjacent to the endothelium. *Fifth Physiological Flow Meeting: Size, Sex and Sight.*
- Wada, S. and Karino, T. (1999). Theoretical Study on Flow-dependent Concentration Polarization of Low Density Lipoproteins at the Luminal Surface of a Straight Artery. *Biorheology* Vol. 36: 207-223.

- Wada, S. and Karino, T. (2002). Theoretical Prediction of Low-Density Lipoproteins Concentration at the Luminal Surface of an Artery with a Multiple Bend. *Ann. Biomed. Eng.* Vol. 30: 778-791.
- Womersley, J. R. (1955). Method for the calculation of velocity, rate of flow and viscous drag in arteries when the pressure gradient is known. *J. Physiol.* Vol. 127: 553-563.
- Yang, N. and Vafai, K. (2006). Modeling of low-density lipoprotein (LDL) transport in the artery-effects of hypertension. *Int. J. Heat. Mass. Tran.* Vol. 49: 850-867.

# Modeling of Surface-bed Reactor for Endothermic and Exothermic Reactions Coupling

Salvatore Vaccaro and Paolo Ciambelli

*Department of Chemical and Food Engineering, University of Salerno  
Italy*

## 1. Introduction

Hydrogen has acquired great importance in the last decade mainly because its combustion with air does not give rise to pollutant emissions in the atmosphere (either toxic or producing greenhouse effect). Therefore, it is seen as the future transportation fuel at least for urban areas (Jamal & Wyszynski (1994); Moore & Raman, (1998); Kruger, et al., 2003; Lerer et al., 2006). A second reason for the growth of its importance is the proposed use as main energy carrier for fuel cells (Rostrup-Nielsen, 2004). However, hydrogen cannot be considered a fuel in the conventional meaning of the term since it is not available in elemental form in concentrations and amounts suitable for human needs. It is, more appropriately, an energy carrier because it can be produced industrially at reasonable costs from fossil fuels or also from water electrolysis but in a very expensive way (Lincoln, 2006). The needs for hydrogen of the chemical industry are, generally, satisfied by the process of catalytic steam reforming of fossil fuels, which produces synthesis gas ( $H_2$  and  $CO$ ) that in turn is used for many important processes including methanol/dimethyl ether (DME) synthesis, ammonia production, olefins oxosynthesis to aldehydes (Marschner et al., 2005), carbonylation, hydrodesulphurization, hydrocracking, etc. (Rostrup-Nielsen, 1995) or as feedstock to the Fischer-Tropsch process for liquid hydrocarbons production (Rostrup-Nielsen et al., 2001; Cao et al., 2005).

Commercial processes for methane steam reforming use tubular reactors packed with supported nickel catalysts. In the conventional reactors, strong endothermic reactions occur at high temperatures for high conversion with fast kinetics. In these conditions the reaction becomes diffusion controlled and, therefore, a suitable catalyst structure design play an important role in obtaining high activity and stability. In addition, because of the endothermicity of the steam reforming process, the rate at which heat is transferred from an outside occurring exothermic reaction to the reactor tubes may become controlling.

In recent years, microchannel reactors have been developed for process intensification and used in exothermic and endothermic reactions for their noticeable temperature control and improved mass transfer (Ehrfeld et al., 2000; Jensen, 2001; Schubert et al., 2001; Lerou & Ng (1996); Holladay et al., 2004). The use of microchannels potentially minimizes the temperature gradient and allows the reaction occurring at a higher average temperature so that the process efficiency is enhanced. A structured metallic support, with high thermal

conductivity, can be used as a substrate of catalysts and integrated for plate-type reactors and microchannel reactor applications. Thin layers of catalyst coating (typically of the order of 10-100 nm) on the metal substrate give much shorter transport distances than that of conventional catalysts (Wang et al., 2005). Beside industrial applications, multifunctional autothermal reactor concepts have been proposed for the thermal coupling of endothermic reactions with auxiliary combustion reactions for an efficient heat-integrated process. These concepts aim to minimizing fuel consumption and waste heat production in stand-alone hydrogen production, which gains increasing interest for innovative power generation systems, e.g., fuel cells (Kolios et al., 2004).

Surface-bed reactors or plate-type reactors and microchannel reactors with microstructured catalysts have been suggested for steam reforming of hydrocarbons or for exothermic reactions (Tronconi & Groppi (2000); Zanfiri & Gavriilidis (2003); Robbins et al., 2003; Kolios et al., 2004; Cao et al., 2005). In developing such reactors, the knowledge of the temperature profile within the reactor is important for designing and optimizing the catalysts structure and the reactor geometry to achieve the best performance. However, temperature measurement within the catalyst structures in such a small dimension devices becomes difficult, either due to insufficient room for a thermocouple or to potential interference with local fluid-dynamics (Cao et al., 2005). Therefore, to evaluate not only the local temperature profiles but the whole reactor performance in terms of conversion and selectivity, accurate descriptive or predictive models are necessary. As a mature technology, methane steam reforming kinetics in a conventional fixed bed reactor has been well described (Bridger, 1980; Rostrup-Nielsen et al., 1988). Pseudo-homogeneous two-dimensional models have been used to simulate operation of the catalytic steam reformers (Xu & Froment (1989a); Kvamsdal et al., 1999). Numerous studies have focused on the kinetics of methane steam reforming (Akers & Camp (1955); Allen et al., 1975; Aparicio, 1997; Luna and Becerra 1997; Craciun et al., 1998; Xu & Froment, 1989b; Hou & Hughes, (2001)), especially on Ni catalysts.

Nevertheless, few modeling attempts of methane steam reforming in surface-bed or plate-type reactors are currently available in the open literature (Avci et al., 2001; Zanfiri & Gavriilidis (2003); Kolios et al., 2004; Cao et al., 2005). They are 2D and all include simplifying assumptions. For instance, Zanfiri & Gavriilidis (2003) adopted a two-dimensional geometry for the gas phase and the solid wall, while the catalyst layers were modeled by one-dimensional approach. The motion field was assumed fully developed laminar flow in both endothermic and exothermic channel. In addition, due to its small thickness, the catalyst layer was considered isothermal in the transverse direction and the pressure drop along the channels was neglected.

In this context, the present work aimed at studying an autothermal, dual catalyst, surface-bed reaction system for hydrogen production from methane for portable devices. Such devices were thought to be employed for the remote production of electric power via endothermic reactions, such as ammonia decomposition or hydrocarbon steam reforming (endothermic reactions), to produce hydrogen for fuel cells. Heat for the endothermic reaction is provided by an exothermic reaction occurring over the other face of the plate where the reforming reaction occurs. The reaction system was mathematically modeled in steady-state both 2D and 3D and model solutions by a FEM software (COMSOL Multiphysics) were carried out.



The purpose of the stationary model discussed here is to predict the methane conversion and temperature distribution within the microstructure in a 2D and 3D geometry. A sensitivity study of the simulation was used to allow the design of the catalyst structure and reactor geometry to reduce the mass/heat transfer limitation in the process and take advantage of the fast kinetics of the methane steam reforming reaction.

## 2. Reacting system

The main chemical reactions occurring in the reactor are:

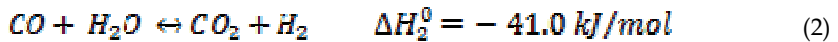
- Methane steam reforming:



For which the reaction rate equation utilized in the calculation is:

$$r_1 = \frac{\frac{k_1}{F_{\text{H}_2}^2} \left( p_{\text{CH}_4} \cdot p_{\text{H}_2\text{O}} - \frac{p_{\text{H}_2}^3 \cdot p_{\text{CO}}}{K_{s,1}} \right)}{\text{Den}^2} \quad \left[ \frac{\text{kmol}}{\text{kg}_{\text{cat}} \cdot \text{h}} \right] \quad (1')$$

- Water gas-shift:



For which the corresponding rate equation is:

$$r_2 = \frac{\frac{k_2}{F_{\text{H}_2}^2} \left( p_{\text{CO}} \cdot p_{\text{H}_2\text{O}} - \frac{p_{\text{H}_2} \cdot p_{\text{CO}_2}}{K_{s,2}} \right)}{\text{Den}^2} \quad \left[ \frac{\text{kmol}}{\text{kg}_{\text{cat}} \cdot \text{h}} \right] \quad (2')$$

where

$$\text{Den} = 1 + K_{\text{CO}} \cdot p_{\text{CO}} + K_{\text{H}_2} \cdot p_{\text{H}_2} + K_{\text{CH}_4} \cdot p_{\text{CH}_4} + \frac{K_{\text{H}_2\text{O}} \cdot p_{\text{H}_2\text{O}}}{F_{\text{H}_2}} \quad (2'')$$

The rate equations (1') and (2') are those derived by Xu & Froment (1989b), for a catalyst containing 15.2% Ni supported on MgO- $\alpha$ -Al<sub>2</sub>O<sub>3</sub>.

- Methane combustion:



For which the corresponding rate equation is:

$$r_2 = k_2 \cdot c_{CH_4} \quad \left[ \frac{\text{kmol}}{\text{m}^2 \cdot \text{s}} \right] \quad (3')$$

The rate equation (3'), suggested in the literature (Zanfir & Gavriilidis (2003)), is valid for a catalyst containing Pt supported on  $\alpha\text{-Al}_2\text{O}_3$

<b>Pre-exponential factors <math>k_{k,0}</math></b>		Activation energy, $E_{ak}$ (kJ/mol)
$k_{1,0}$ (kmol bar <sup>0.5</sup> /(kg <sub>cat</sub> ·s))	$1.1736 \times 10^{12}$	240.1
$k_{2,0}$ (kmol/(kg <sub>cat</sub> ·s·bar))	$1.955 \times 10^6$	67.13
$k_{3,0}$ (s <sup>-1</sup> )	$4.0 \times 10^8$	90.0
<b>Pre-exponential factor <math>K_{i,0}</math></b>		Heat of adsorption, $\Delta H_i$ (kJ/mol)
$K_{CO,0}$ (bar <sup>-1</sup> )	$8.23 \times 10^{-5}$	- 70.65
$K_{CH_4,0}$ (bar <sup>-1</sup> )	$6.65 \times 10^{-4}$	- 38.28
$K_{H_2O,0}$ -	$1.77 \times 10^5$	88.68
$K_{H_2,0}$ (bar <sup>-1</sup> )	$6.12 \times 10^{-9}$	- 82.9
<b>Equilibrium constants</b>		
$K_{e,1} = \exp(-26830/T + 30.114)$ (bar <sup>2</sup> )		
$K_{e,2} = \exp(4400/T - 4.036)$		

Table 2. Kinetic parameters for the reaction rate equations

Partial pressures of gases  $p_i$  in equations (1'), (2') and (2'') were correlated to their own concentrations by the ideal gas law. The values of pre-exponential factors and activation energies used in the Arrhenius expression for the kinetic constants, i.e.  $k_k = k_{k,0} \exp(-E_{ak}/RT)$ , in equations (1'), (2') and (3') are reported in Table 2 with the relevant dimensions. In the same Table the values of the pre-exponential factors and of the heats of adsorption, taken from the literature (Perry & Green, 1997) and used in Van't Hoff expression, i.e.  $K_i = K_{i,0} \exp(-\Delta H_i/RT)$ , for the constants in equation (2'') and the expressions of the equilibrium constants  $K_{e,1}$  and  $K_{e,2}$  in equations (1') and (2') are also shown.

### 3. Reactor model

#### 3.1 Physical description

A 2D scheme of the reactor model is shown in Figure 1 where the various parts are identified by numbers. The system is symmetric with respect to the channel 5 centerline and then the parts 1 and 9, 2 and 8, 3 and 7 and 4 and 6 are identical pairs. With reference to Figure 1, reforming gas goes through the central channel 5 while combustion gas through channels 1 and 9. Parts 3 and 7 represent metallic plates where the structured catalysts layers for combustion (2 and 8) and steam reforming (4 and 6), respectively, lie. It is not very different from modular reactors made of stackable plates suggested in the literature (Xu & Froment (1989a); Loffler et al., 2002). The main difference is that in this case the external boundaries 10 and 11 (in Figure 1) are surfaces with no slip gas velocity while in the recalled case they were symmetry surfaces.

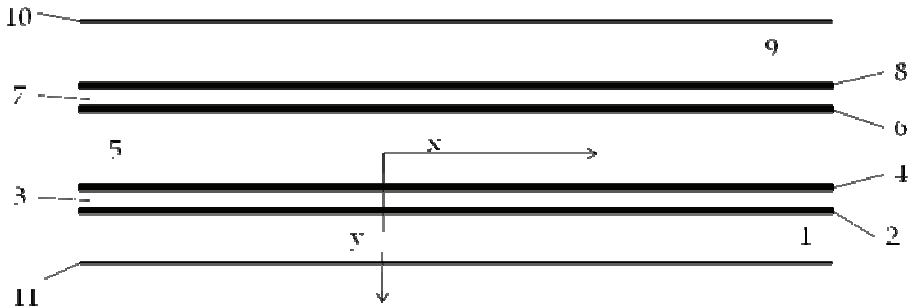


Figure 1. Reactor scheme

With respect to conventional catalytic reactors, where a bed of catalytic solid particles fills the reactor volume and the gas crosses the bed, in the present case the catalytic solid particles are located on the lateral surfaces of the reactor thus forming a surface bed. Actually, in the case in the object the true reactor is the catalyst layers while the homogeneous portions of the reactor (channels) act merely as ducts.

**3.2 Model**

A three-dimensional heterogeneous steady-state model was developed in order to describe velocity, concentration and temperature distributions inside the surface-bed reactor system with structured catalysts. The model consists of the material, energy and momentum balances equations and contains the constitutive equations for physical chemistry properties of the reactants species and the kinetic expressions for the reactions as found from the literature and presented above.

The model assumes that: a) the variations of density due to the change of gas composition and temperature are small so that incompressible Navier-Stokes motion equation applies; b) on the combustion side only the methane total oxidation reaction to H<sub>2</sub>O and CO<sub>2</sub> occurs; c) on the reforming side only the methane steam reforming and the water gas shift reactions occur; d) reactions occur only inside the catalyst layers where, instead, convective momentum is not present; e) conductive heat transfer is the only transport phenomenon occurring inside the metallic plates; f) as suggested in the literature (Hou & Hughes (2001); Zafir. & Gavriilidis (2003)), carbon formation and deposition due to side reactions can be neglected by using an excess of steam, that is a minimum steam/methane molar ratio of 1.7; f) body forces are neglected, the reacting species being gaseous.

The velocity variation in the reactor takes into account the influence of temperature and composition changes so that the global mass balance is satisfied:

$$\iint_0^{z_s} \rho_i u_x dy dz |_{x=0} = \iint_0^{z_s} \rho_i u_x dy dz |_{x=x} \tag{4}$$

Reactor performance were evaluated by the methane conversions, calculated by integrating the local molar flow rates:

$$X_{CH_4}(x) = 1 - \frac{\iint_0^{z_s} C_{CH_4} \cdot u_x dy dz |_{x=x}}{\iint_0^{z_s} C_{CH_4} \cdot u_x dy dz |_{x=0}} \tag{5}$$

According to Figure 1, for each catalyst layer and channel and for the metal sheets the due momentum, energy and mass balances were set together with the proper boundary conditions in the rectangular coordinates (x-y-z) (Cartesian coordinates are indicated in Figure 1 and the z direction is perpendicular with respect to the scheme) with dependent variables: velocity components, pressure, temperature (T) and species concentrations ( $c_i$ ). Equations vectorial formulation are reported in the following so they are valid for both 2D and 3D formulations.

*Combustion channels 1 and 9 and steam reforming channel 5*

#### Momentum balance

$$\rho \vec{v} \cdot \nabla \vec{v} = \nabla(-P\vec{I} + \mu \cdot (\nabla \vec{v} + \nabla(\vec{v})^T)) \quad (6)$$

$$\nabla \cdot \vec{v} = 0 \quad (7)$$

Boundary conditions are:

- specified velocity with normal component at the channel ingress  $\vec{v} \cdot \vec{n} = v_g$
- no slip at the channel boundaries in the y (2D and 3D) and z (3D) directions  $\vec{v} = \mathbf{0}$
- specified pressure at the channel exit  $P = P_0$

With reference to Figure 1 for the momentum balance equations the boundaries of channels 1 and 9 are the external boundaries (10 and 11) of the reactor and the internal boundaries between the channels and the catalyst layers, respectively, while the boundaries of channel 5 are the internal boundaries between the channel and the catalyst layers.

#### Energy balance

$$\nabla \cdot (-k \nabla T) = \rho c_p \vec{v} \cdot \nabla T \quad (8)$$

Boundary conditions are:

- specified temperature at the channel ingress  $T = T_0$
- convective heat flux at the channel exit  $\vec{n} \cdot \nabla(-kT) = 0$
- *Channels 1 and 9*: no heat flux through the channel external boundaries in the y (2D and 3D) and z (3D) directions, i.e.  $\vec{n} \cdot (-k \nabla T + \rho c_p T \vec{v}) = \mathbf{0}$  and thermal continuity  $\vec{n} \cdot (q_1 - q_2) = 0$   $q_l = k_l \nabla T_l + \rho c_{p,l} T_l \vec{v}_l$  at the internal boundaries (l: gas phase and catalyst phase).
- *Channel 5*: thermal continuity  $\vec{n} \cdot (q_1 - q_2) = 0$   $q_l = k_l \nabla T_l + \rho c_{p,l} T_l \vec{v}_l$  at the internal boundaries (l: gas phase and catalyst phase).

#### Mass balances

$$\nabla \cdot (-D_{i,j} \nabla c_i + c_i \vec{v}) = 0 \quad (9)$$

Boundary conditions are:

- specified concentrations at the channel ingress  $c_i = c_{i,0}$
- continuity through the boundary between the gas phase and the catalyst layer, i.e.  $\vec{n} \cdot (N_{i,1} - N_{i,2}) = 0$  where  $N_{i,1} = D_{i,j,1} \nabla c_{i,1} + c_{i,1} \vec{v}$  and  $N_{i,2} = (-D_{eff,i,j,2} \nabla c_{i,2})$
- convective mass flux at the channel exit  $\vec{n} \cdot (-D_{i,j} \nabla c_i) = 0$

where i and j subscript refers to the *ith* and *jth* specie, respectively.

*Catalyst Layers 2 and 8***Energy balance**

$$\nabla \cdot (-k_{cat}^{cc} \nabla T) - r_3 \Delta H_3 \quad (10)$$

Boundary conditions are:

- thermal continuity at the layers boundaries in the y directions (2D and 3D)  
 $\vec{n} \cdot (q_1 - q_2) = 0$   $q_l = k_l \nabla T_l + \rho c_{p,l} T_l \vec{v}_l$  ( $l$ : gas phase and catalyst phase).
- thermal insulation at the layer boundaries in the x (2D and 3D) and z (3D) directions  
 $\vec{n} \cdot (-k \nabla T + \rho c_p T \vec{v}) = 0$

**Mass balances**

$$\nabla \cdot (-D_{eff,i,j} \nabla c_i) = \theta_i r_3 \quad (11)$$

being  $\theta_i$  the stoichiometric coefficient of the  $i$ th specie.

Boundary conditions are:

- continuity through the boundary between the layer and the gas phase  
 $\vec{n} \cdot (N_{i,1} - N_{i,2}) = 0$  where  $N_{i,1} = D_{i,i,1} \nabla c_{i,1} + c_{i,1} \vec{v}$  and  
 $N_{i,2} = (-D_{eff,i,j,2} \nabla c_{i,2}) = 0$  and no mass flow  $\vec{n} \cdot (-D_{eff,i,j} \nabla c_i + c_i \vec{v}) = 0$   
between the layer and the metal sheets in the y (2D and 3D) direction
- no mass flux through the layer boundaries in the x (2D and 3D) and z (3D) directions  
 $\vec{n} \cdot (-D_{eff,i,j} \nabla c_i + c_i \vec{v}) = 0$

*Metal sheets 3 and 7*

**Energy balance**

$$\nabla \cdot (-k_s \nabla T) = 0 \quad (12)$$

Boundary conditions are:

- thermal insulation at the sheet boundaries in the x (2D and 3D) and z (3D) directions  
 $\vec{n} \cdot (-k_s \nabla T) = 0$
- thermal continuity on the sheet boundaries in the y direction (2D and 3D)  
 $\vec{n} \cdot (q_1 - q_2) = 0$   $q_l = k_l \nabla T_l$

*Catalyst Layers 4 and 6*

**Energy balance**

$$\nabla \cdot (-k_{cat}^{sr} \nabla T) = r_1 \Delta H_1 + r_2 \Delta H_2 \quad (13)$$

Boundary conditions are:

- thermal insulation at the layer boundaries in the x (2D and 3D) and z (3D) directions  
 $\vec{n} \cdot (-k_{cat}^{sr} \nabla T) = 0$
- thermal continuity on the layers boundaries in the y direction (2D and 3D)  
 $\vec{n} \cdot (q_1 - q_2) = 0$   $q_l = k_l \nabla T_l$

**Mass balances**

$$\nabla \cdot (-D_{eff,i,j} \nabla c_i) = \theta_{1,i} r_1 + \theta_{2,i} r_2 \quad (14)$$

being  $\theta_{j,i}$  the stoichiometric coefficients of the  $i$  specie in the  $j$  reaction.

Boundary conditions are:

- continuity through the boundary between the layer and the gas phase  

$$\vec{n} \cdot (N_{i,1} - N_{i,2}) = 0 \quad \text{where} \quad N_{i,1} = D_{i,j,1} \nabla c_{i,1} + c_{i,1} \vec{v} \quad \text{and}$$

$$N_{i,2} - (-D_{eff,i,j,2} \nabla c_{i,2}) = 0 \quad \text{and} \quad \text{no} \quad \text{mass} \quad \text{flow}$$

$$\vec{n} \cdot (-D_{eff,i,j} \nabla c_i + c_i \vec{v}) = 0$$
 between the catalyst layer and the metal sheet in the y (2D and 3D) direction
- no mass flux through the layer boundaries in the x (2D and 3D) and z (3D) directions  

$$\vec{n} \cdot (-D_{eff,i,j} \nabla c_i + c_i \vec{v}) = 0$$

In the balances above the gas densities were calculated using the ideal gas law whereas for catalyst density a constant value was assumed. Viscosities and thermal conductivities of the gaseous species refer to the values of the component largely in excess in the specific gas mixtures, that is H<sub>2</sub>O for the steam reforming channel and air for the combustion channels. Their dependence of the temperature was excerpted from experimental values from the literature (Perry & Green (1997)) and included as interpolated functions inside the calculation software. To work out heat capacities, expressions such as:

$$c_p = A + BT + CT^2 \quad (15)$$

were used where A, B and C were evaluated by the regression of an expression (Perry & Green (1997)) such as:

$$c_{p,i} = C1 + C2 \left[ \frac{C_3}{T} \right]^2 + C4 \left[ \frac{C_3}{\cosh \frac{C_3}{T}} \right]^2 \quad (16)$$

The diffusivity coefficients were calculated for a binary mixture between component *i*th and H<sub>2</sub>O (in the reforming channel) or air (in the combustion channels). The effective diffusion coefficient inside the catalyst layer is (Perry & Green (1997)):

$$D_{eff,i,j} = \frac{\varepsilon}{\tau} \left[ \frac{1}{D_{i,j}^k} + \frac{1}{D_{i,j}} \right]^{-1} \quad (17)$$

where  $\varepsilon$  is the catalyst porosity,  $\tau$  the tortuosity,  $D_{i,j}^k$  and  $D_{i,j}$  the Knudsen diffusion coefficient and the molecular diffusion coefficient of the *i*th specie in the *j*th specie, respectively. Molecular diffusion coefficients were evaluated using (Perry & Green (1997)):

$$D_{i,j} = \frac{0.1013 T^{1.75} \left( \frac{1}{M_i} + \frac{1}{M_j} \right)^{0.5}}{\pi \left[ (\sum \varphi_i)^{2/3} + (\sum \varphi_j)^{2/3} \right]^2} \quad (18)$$

where T is the temperature in [K],  $\pi$  the total pressure of the system in [Pa],  $M_i$  and  $M_j$  the molecular weights of *i*th and *j*th species, respectively, and  $\varphi_i$  the atomic diffusion volumes, characteristic for each component (Perry & Green (1997)). Knudsen diffusion coefficients were evaluated using (Perry & Green (1997)):

$$D_{i,j}^k = 97 R_p \sqrt{\frac{T}{M_{i,j}}} \quad (19)$$

where  $R_p$  is the mean pore radius and T the temperature into the catalyst.

### 3.3 Numerical stuff and reference case simulation

The finite element solution algorithm was completed using COMSOL Multiphysics (Comsol, Inc., version 3.3a). Multiphysics modules of incompressible Navier-Stokes, convection-diffusion and conduction-convection were applied, when appropriate, to the three-phase domains. Meshing parameters were different for the 2D and the 3D FEM schemes. In particular, in the case of 2D a mapped mesh scheme was employed with rectangular extra fine meshes and edge vertex distribution as follows: longitudinal edges 100:1; transverse edges 5:1 (metallic plate) and 10:1 (catalyst layers and channels). In the case of 3D predefined mesh sizes, extra coarse with characteristics listed in Table 3, were employed.

Number of degrees of freedom	381162
Number of mesh points	6976
Number of elements	33702
Tetrahedral	33702
Number of boundary elements	12840
Triangular	12840
Number of edge elements	740
Number of vertex elements	24
Minimum element quality	0.158
Element volume ratio	0.015

Table 3. Mesh Statistics

A reference case with given reactor geometric configuration and operating conditions was chosen to carry out a reference case simulation. Other simulations were carried out to explore the influence on the reactor performance of specific geometrical and/or operating parameter changes. The conditions used in the calculations for the reference case are listed in Table 4. Inlet conditions for the reforming side are similar to those used by Xu and Froment (1989b), but for the total pressure close to atmospheric in our case, 29 bar, characteristic of industrial operation, in the kinetics from Xu & Froment. This because, as suggested in the literature (Kolios et al., 2004), small-scale hydrogen production, which is the potential application for such type of reactor is expected to operate at low pressure.

This represents a limit of the present work. However, similar detailed rate equations for the investigated reacting system are not available at ambient pressure in the literature. Data reported in Table 4 show that the inlet reforming reaction mixture has a steam/methane ratio of 3 and contains trace amounts of CO<sub>2</sub>, H<sub>2</sub> and CO. On the methane combustion side, the air-methane mixture has a 40% air excess with respect to stoichiometric. The inlet temperature of both streams is 800 K that is close to that typical of industrial steam reforming. The inlet methane mass flow rate in the reforming channel is fixed at 1.67 cm<sup>3</sup>/s at STP, while the inlet methane mass flow rate in the combustion channel is obtained from an overall heat balance. The data for reforming catalyst used in the calculations are typical for such a reaction and similar to that used by Xu & Froment (1989a) for a catalyst containing 15.2% Ni supported on MgO- $\alpha$ Al<sub>2</sub>O<sub>3</sub>.

Gas phase	Reforming channel	Combustion channels
Inlet conditions		
co-current flow		
compositions, vol. %		
H <sub>2</sub> O	66.66	
CH <sub>4</sub> :	33.33	7.50
CO <sub>2</sub>	1 10 <sup>-3</sup>	
CO	1 10 <sup>-3</sup>	
O <sub>2</sub>		19.43
N <sub>2</sub>		73.07
H <sub>2</sub>	1 10 <sup>-3</sup>	
temperature	800 K	800 K
CH <sub>4</sub> mass flow rate, cm <sup>3</sup> /s (STP)	1.67	0.417
pressure	101 kPa (channel outlet)	101 kPa (channel outlet)
channel width, m	2 10 <sup>-3</sup>	1 10 <sup>-3</sup>
channel height, m		1.0 10 <sup>-2</sup>
average velocity, m/s	0.97	0.87
channel length, m		5 10 <sup>-2</sup>
<b>Catalyst layers</b>		
thickness ( $\delta_c$ ), $\mu\text{m}$		200
Average pore radius, nm		15
porosity		0.5
tortuosity		4
<b>Metal plates</b>		
Thickness, m		5 10 <sup>-4</sup>
material		aluchrom
Thermal conductivity, w/(m K)		Temperature dependent

Table 4. Data used for reference case calculations

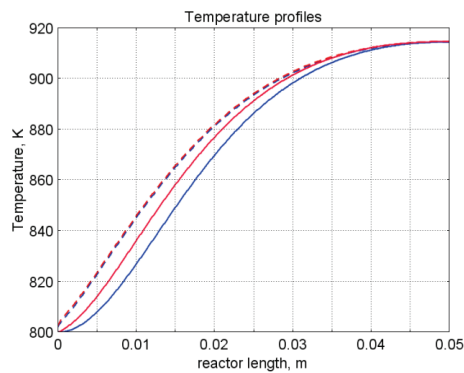


Figure 2. Temperature space profiles along the reactor: centerline of the reforming channel (solid blue), centerline of the combustion channel (solid red), centerline of the reforming catalyst (dashed blue) and centerline of the combustion catalyst (dashed red)



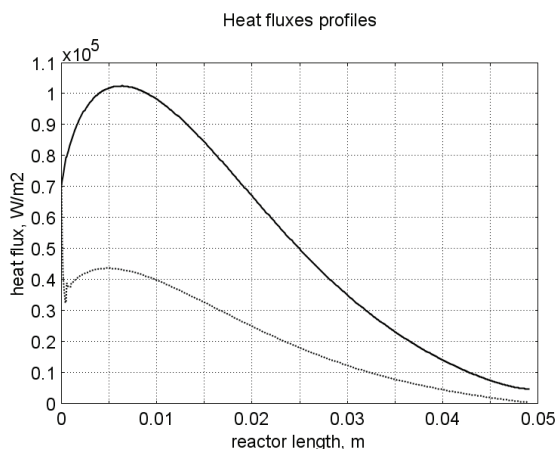


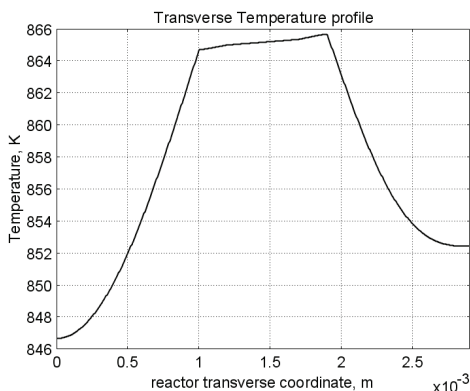
Figure 3. Axial profiles of heat flux in the y direction adjacent to the reforming catalyst: in the metallic plate (solid line), in the reforming channel (dotted line)

The catalyst layer density is assumed to be  $2300 \text{ kg/m}^3$ . For both type of catalyst layers an average pore radius of  $15 \text{ nm}$ , together with a porosity of  $0.5$  and a tortuosity factor of  $4$  are considered. These values are typical for both combustion and reforming catalysts (De Deken et al., 1982; Xu & Froment, 1989 b; Groppi et al., 1995).

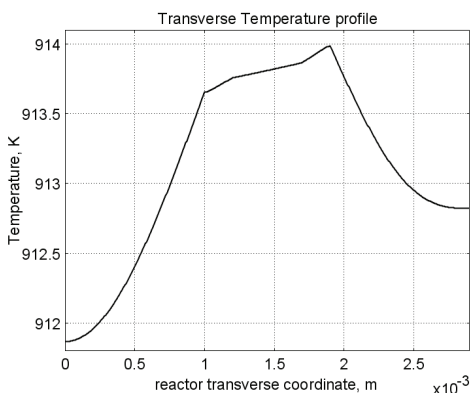
## 4. Results

### 4.1 Thermal behaviour

Given the symmetry of the reactor, for both 3D and 2D simulations only half of the reactor was simulated by substituting the proper boundary conditions (symmetry) in place of the lacking half. Results in simulations performed with the 2D model, under the reference case conditions, are shown in Figures 2-7. The first aspect to consider is the thermal coupling of steam reforming with catalytic combustion in terms of evolution of both exothermic and endothermic conversion. Figure 2 shows the temperature longitudinal profiles on the centerlines of the combustion and the reforming channels, and in the combustion and reforming catalysts. The profiles are very close each other and they increase from the inlet value of  $800$  to  $914 \text{ K}$  at the reactor outlet. Therefore, the catalytic combustion provides the necessary heat flux to heat up both reaction mixtures and to simultaneously drive the endothermic process. A methane conversion at the reactor outlet of  $0.89$  for combustion and  $0.74$  for reforming are achieved. Figure 3 shows the axial profiles of the absolute values of the heat fluxes in the y direction at the boundaries of the reforming catalyst. One profile (solid line) is the heat flux from the metallic plate towards the reforming catalyst, the other the heat flux from the reforming catalyst to the gas mixture in the reforming channel. The two profiles present similar shapes with a maximum at  $7 \text{ mm}$  and  $5 \text{ mm}$  from the reactor entrance (distances within which the profiles are increasing). The difference between the profiles represents the heat absorbed by the reforming reaction system (eq.s (1) and (2)). The maxima heat fluxes generated and consumed reach values of the order of  $10^5 \text{ W/m}^2$  i.e.  $10 \text{ W/cm}^2$  that, considering the very small temperature gradients (Figure 2), is a very high value with respect to that attainable in industrial practice.



a)



b)

Figure 4. Reactor temperature transverse profiles: a) at 1.5 cm from the reactor entrance; b) at 1.0 cm from the reactor outlet. From 0 to 1: reforming channel. From 1 to 1.2: reforming catalyst. From 1.2 to 1.7: metallic plate. From 1.7 to 1.9: combustion catalyst. From 1.9 to 2.4: combustion channel

A further aspect to be examined is the magnitude of the transverse temperature gradients. From Figure 2 it is already evident that the four profiles are very close each other. However, the transverse temperature gradients can be better analyzed from Figure 4 where the transverse temperature profiles at 1.5 cm (Figure 4a) from the reactor entrance and at 0.5 cm (Figure 4b) from the reactor outlet are shown. In particular, Figure 4a, which pertains to the distance from the reactor inlet where the highest transverse temperature gradients develop, evidences that the maximum temperature difference between reforming and combustion catalyst is 0.7 K while the maximum difference between the reforming and combustion channels is less than 10 K although that inside the reforming channel is almost 20 K. Much lower differences can be observed close to the reactor outlet. Specifically, Figure 4b shows that the maximum temperature difference between reforming and combustion catalyst is 0.1 K, that between the reforming and combustion channels is less than 1 K and that inside the reforming channel is almost 2 K. As a result, the high thermal conductivity of the metallic

wall makes possible an efficient heat transfer at a temperature difference of the order of tenths of K. With reference to Figure 4, it must be remarked that the value 0 of the transverse coordinate represents the centre of the reactor and the centre of the reforming channel. Therefore, at that point there is not a physical boundary, the heat flux and the momentum flux are both zero and the x component of the gas velocity is maximum. On the contrary, the value  $2.9 \cdot 10^{-3}$  m of the transverse coordinate represents a solid wall that is the external boundary of the reactor and the boundary of the combustion channel. This means that the heat flux is zero, both components of the gas velocity are zero and the momentum flux is not zero. This is one of the reasons because for the same distance in the transverse direction (y) the gas phase temperature difference in the reforming channel results always larger than that in the combustion channel (Figures 2, 4a and 4b).

#### 4.2 Mass transfer and chemical reactions

The concentration on the centerline of the reforming channel of the various species involved in the reactions occurring within the reforming catalyst are shown in Figure 5. This yields an overall picture of the reactor performance. The hydrogen concentration steadily increases from the initial value to about  $9 \text{ mol/m}^3$  resulting the most abundant component in the exit gas mixture. The ratio between the hydrogen concentration and CO concentration is very high (about 9).

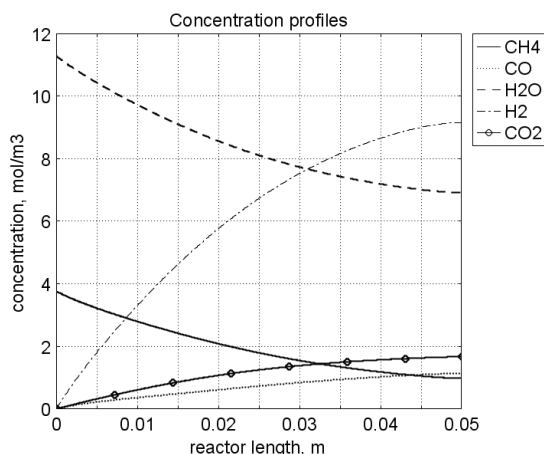
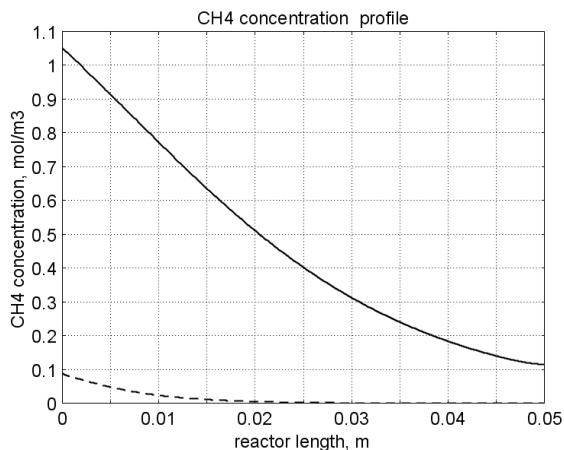


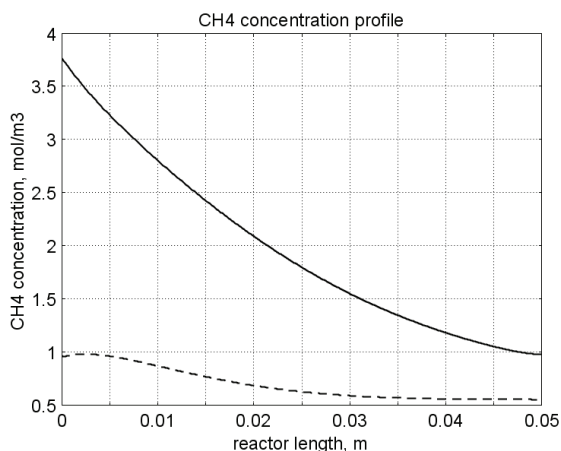
Figure 5. Axial profiles of species concentrations on the centerline of the reforming channel

One important aspect to determine is the effect of interphase mass transport resistance. Figure 6a shows the methane concentration axial profiles on the centerlines of the combustion channels and of the combustion catalyst while Figure 6b shows the correspondent profiles for the reforming section of the reactor. From these Figures the differences between the channel and the catalyst profiles in each section yield a measure of the resistance to the interphase transport. As expected, in the combustion section the axial methane concentration profiles both in the channel and in the catalyst show an exponentially decreasing trend, which reflects the relatively simple kinetics of the reaction. In contrast, a more complex trend is shown by the axial methane concentration profile in the catalyst because of the non linearity of the kinetics and the simultaneous occurrence of two

reactions (eq.s (1) and (2)). Another aspect to examine is the size of the concentration gradients in the transverse direction. These can be appreciated from Figure 7 where the transverse methane concentration profiles at 1.5 cm from the reactor inlet and at 0.5 cm from the reactor outlet are shown. In particular, the first profile, which pertains to the distance from the reactor inlet where the highest transverse temperature gradients develops, evidences that the gradients inside the reforming and the combustion channels are negligible with respect to the gradients in the catalyst phase. The order of magnitude of these latter range from  $10^5$  mol/m<sup>4</sup> close to the reactor inlet to  $10^4$  mol/m<sup>4</sup> in the remaining part of the reforming catalyst and in all the combustion catalyst too.



a)



b)

Figure 6. Axial methane concentration profiles along the reactor: (a) solid line combustion channel, dashed line combustion catalyst; (b) solid line reforming channel, dashed line reforming catalyst

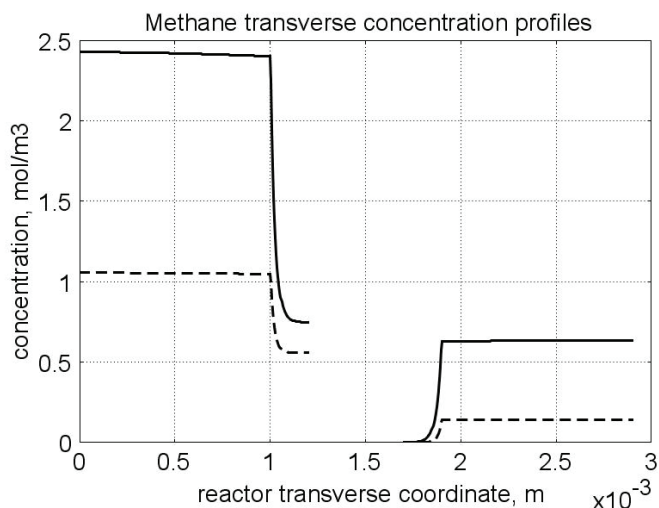


Figure 7. Methane concentration transverse profiles at 1.5 cm from the reactor entrance (solid line) and at 1.0 cm from the reactor outlet (dashed line). From 0 to 1: reforming channel. From 1 to 1.2: reforming catalyst. From 1.2 to 1.7: metallic plate. From 1.7 to 1.9: combustion catalyst. From 1.9 to 2.4: combustion channel

#### 4.3 Methane concentration in the combustion channel

A basic requirement of the system in the object, which is thought to be used for energy feeding of portable electric devices, should be the complete reliability with respect to possible uncontrolled rises in temperature or even to a possible explosion hazard. In this view, the coordination between exothermic and endothermic reaction rates appears fundamental. However, even in the case such a coordination occurs, the possible progress of the combustion reaction in the homogeneous phase may represent an hazard. In addition, if the concentration of the reacting mixture entering the combustion channel is within the flammability limits and the temperature becomes high enough, it could ignite before the reactor inlet. Therefore, for safety purposes the occurrence of the exothermic reaction, here represented by the methane combustion, in the homogeneous phase should be avoided. A possible way to make the system of hydrogen generation intrinsically safe is to feed the combustion mixture at a methane concentration below the LEL (lower explosivity limit). Considering that at STP the LEL of methane in air is about 5 vol%, that the autoignition temperature for air/methane mixtures is around 900 K, the estimated LEL of methane in air at such a temperature should be about 3 vol% (Crowl & Louvar (2002)). Therefore, a safe operating concentration should be about 3 vol%. To this purpose in this work, beside those carried out under the conditions considered in the reference case, other simulations were effected for which, for a given methane mass flow rate, its concentration at the combustion channel inlet was kept below 3 vol%. In this way, the system is intrinsically safe, because the reacting mixture cannot ignite spontaneously. In addition, the simulation becomes more realistic the contribution to the methane combustion of the homogeneous phase being really absent, as implicitly hypothesized in this work.

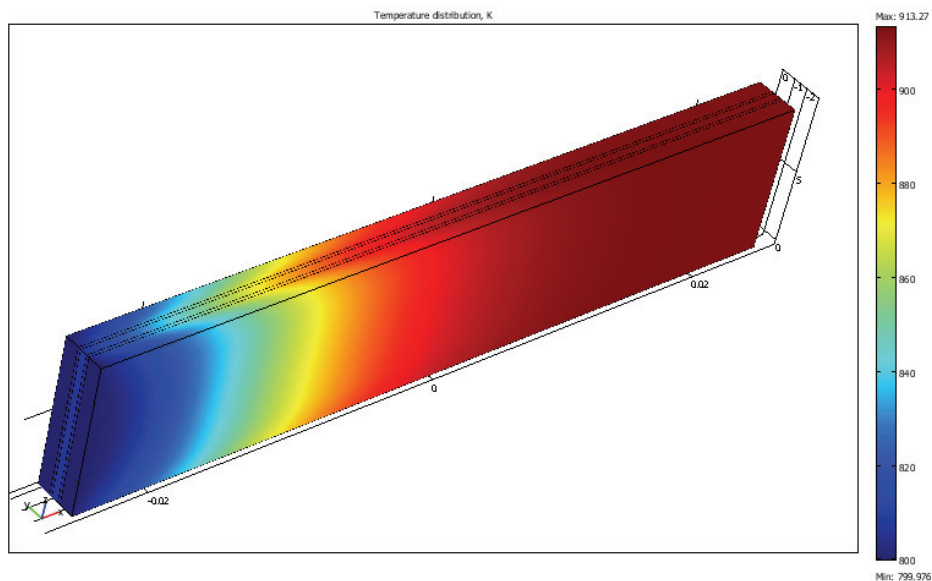


Figure 8. Temperature distribution over the boundaries of the 3D reactor

The comparison of results of runs performed under these conditions with those effected under the conditions of the reference case are reported in the following when analyzing the influence of various parameters on the reactor performance. These simulations are labeled in the paper as **n-expl.** in contrast to the others that are recalled as **expl.**

#### 4.4 Comparison between 2D and 3D results

For given operating conditions some simulations were carried out in both 2D and 3D geometry. In principle, a plane 2D geometry represents a slice of the reactor where the  $z$  dimension is greatly prevalent with respect to the  $y$  dimension. Actually, the model reactor has not such characteristics, the length in the  $z$  dimension being 10 mm, that is only 5 times the reforming channel width. This means that the boundary effects due to the presence of the boundary walls in the  $z$  direction may have a significant influence on the velocity, temperature and species concentration profiles that certainly influence the overall reactor performance. Figures 8 shows the temperature distribution over the boundaries of the 3D reactor obtained under operating conditions of the reference case. From this Figure the effect of the boundaries along the  $z$  direction appears evident.

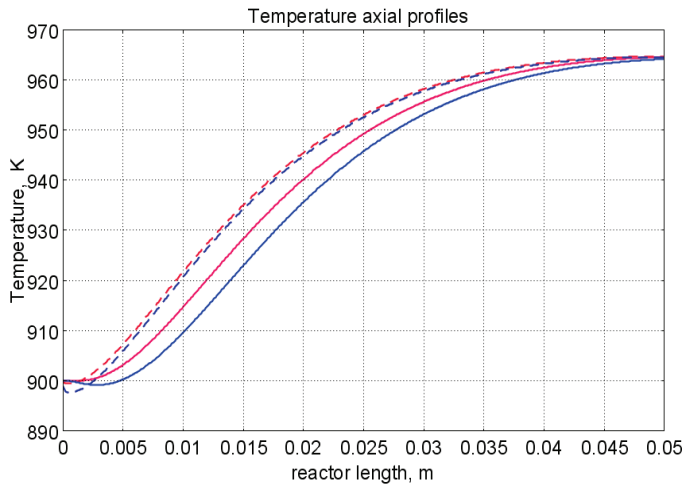


Figure 9. Temperature space profiles along the reactor calculated with the 2D model. (for the legend see caption to Figure 2)

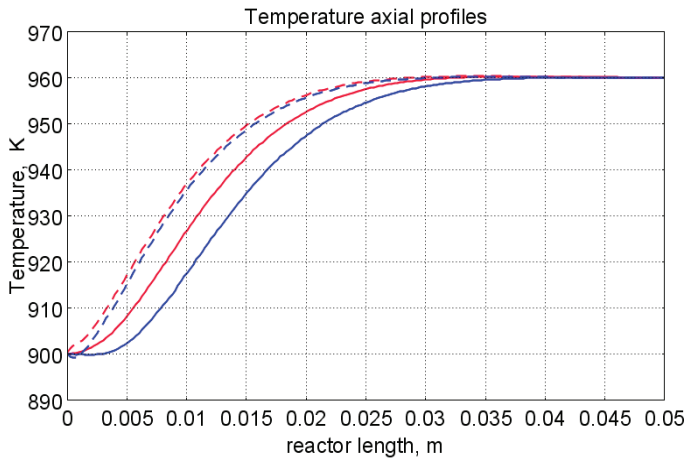


Figure 10. Temperature space profiles along the reactor calculated with the 3D model. (for the legend see caption to Figure 2)

Figures 9 and 10 show the reactor temperature longitudinal profiles on the centerlines of the combustion and the reforming channels, and on the centerline of the combustion and reforming catalysts in the case of 2D and 3D geometry models, respectively. Both were calculated under the same operating conditions, i.e.: same inlet mass flow rates and compositions of the reference case (expl.) but inlet temperature of 900 K. In the case of the

3D simulation (Figure 10) the temperature profiles are those lying over a xy plane intersecting the reactor in the middle of its height along z. The two sets of profiles appear quite similar: the temperatures in the combustion section (catalyst and channel) are always slightly higher than the corresponding ones in the reforming section. However, a closer inspection reveals some significant differences. In the 2D case the temperature, after an initial slow growth, increases steadily from 900 K at the reactor inlet up to 965 K at the reactor outlet while in the other case it grows faster, reaches 960 K at 60% of the reactor length and remains constant up to the outlet. Another difference is represented by the larger transverse temperature gradients of the 3D case with respect to 2D. In the 2D case they are comparable with those observed in Figure 2 for the reference case while in the 3D case they are almost double. This is true for all combinations, i.e. catalyst-catalyst, catalyst-channel and channel-channel. On the whole, the 3D case shows a faster progress of the reactions with consequent need for faster heat transfer. These differences in the thermal behaviour between 2D and 3D simulations persist when the comparison is extended to other operating conditions and, in addition, they reflect the better overall performance of the 3D reactor with respect to the 2D, as can be seen by the following discussion.

The quantitative comparison between the 2D and 3D simulations was made with respect to the main results, i.e. the methane conversion in both the combustion and the steam reforming channels, as obtained from equation 5. Further, beside the methane conversions, other parameters are employed, i.e. a) the gas hourly space velocities GHSV in the combustion and steam reforming sides of the reactor, calculated as ratio between gas flow rates at the reactor inlet temperature and volume of catalyst; b) the maximum temperature reached in the reactor; c) the mean gas residence time,  $t_{rm}$ , in both the combustion and the reforming channel, calculated as ratio between the gas flow rates at the reactor inlet temperature and the volume of the channel; and d) the hydrogen yield,  $\varphi_{H_2}$ , evaluated as ratio between the amounts of methane reacted and hydrogen produced. GHSV and  $t_{rm}$  were useful to allow the comparison of simulations carried out by changing the catalyst volume or the channel width, as discussed later. Results of simulations carried out with the 2D and 3D models under various operating conditions are reported in Table 5. Those referring to the operating conditions of the reference case are listed in the first two rows of such a Table. The other operating conditions are: i) same inlet temperature of the reference case but different methane concentration in the combustion channel (3rd and 4th rows of Table 5) and ii) different inlet temperatures for the two conditions above (5th-8th rows of Table 5). Focusing the comparison on the results of the simulations in 2D and 3D with the same operating conditions, it appears that, in general, the methane conversions at the reactor outlet calculated with the 2D geometry in both the combustion and reforming channels are lower than the correspondent in 3D geometry but in one case ( $X_{ch4-sr}$  3<sup>rd</sup> and 4<sup>th</sup> rows of the Table). This finding reflects the differences in the thermal behaviour discussed above. In any case, such conversions differ by less than 10% but in the last two rows of the Table where the differences are larger. It is worth noting, however, that even in this case the values of the conversions are congruent with the overall results of the simulation. For instance, the lower value of  $X_{ch4-co}$  in the 2D with respect to the correspondent in 3D results in a lower value of  $X_{ch4-sr}$  and in a lower maximum temperature reached in the reactor.



Geometry		$T_{inr}$ K	$X_{ch4-co}$	$X_{ch4-sr}$	$T_{max}$ , K	$T_{rm-co}$ , ms	$T_{rm-sr}$ , ms	$GHSV_{co}$ , h <sup>-1</sup>	$GHSV_{sr}$ , h <sup>-1</sup>	$\phi_{H2}$
2D	expl	800	0.89	0.74	914	0.057	0.026	314840	702884	3.29
3D	expl	800	0.96	0.77	914	0.057	0.026	314840	702884	3.33
2D	n-expl	800	0.36	0.45	827	0.020	0.026	900588	702884	3.44
3D	n-expl	800	0.40	0.41	828	0.020	0.026	900588	702884	3.56
2D	expl	900	0.95	0.90	965	0.051	0.023	354194	790745	3.05
3D	expl	900	0.99	0.93	960	0.051	0.023	354194	790745	3.00
2D	n-expl	900	0.49	0.69	900	0.018	0.023	1013162	790745	3.22
3D	n-expl	900	0.68	0.79	920	0.018	0.023	1013162	790745	3.18

Table 5. Comparison of 2D and 3D results obtained under the same operating conditions

For what concerns the hydrogen yield, focusing again the comparison on the results of the simulations in 2D and 3D at the same operating conditions, data show that  $\phi_{H2}$ 's obtained with the 2D geometry model are lower than that in 3D model but in one case (7<sup>th</sup> and 8<sup>th</sup> row of Table 5). It is worth noting that  $\phi_{H2}=3$  would be the stoichiometric value if reaction (1) were the only occurring in the reforming catalyst so that the amount exceeding 3 is due to the contribution of reaction (2).

Data in Table 5 also shows the influence on the reactor performance of temperature and inlet methane concentration in the combustion channel. In the case of inlet temperature of 900 K and methane concentration within the explosivity limits (case referring to results in Figures 9 and 10) the methane conversion is practically 1 (3D model) for the combustion reaction and very high for the reforming reactions. However, under these conditions the hydrogen yield is the lowest. In contrast, when the highest hydrogen yield is reached the lowest methane conversion is achieved. Similar considerations can be done for the other results in the Table so that a general trend can be drawn from such results. The higher the maximum temperature reached in the reactor the higher the methane conversions and the lower the hydrogen yield.

#### 4.5 Influence of the channels width

The reactor thermal behaviour and performance was studied for different channels width,  $W_c$ , at constant inlet flow rates of the reaction mixtures. Runs were also carried out by keeping constant the mean inlet velocities of reaction mixtures. The variation range for the combustion channels width,  $W_{c-co}$ , was 1-1,5 mm and for the reforming channel width,  $W_{c-sr}$ , 2-3 mm. All other parameters were kept at their reference case values. Keeping constant the inlet mass flow rates and altering the channel width results in modifying the inlet velocities in the reactor and consequently the mean residence time ( $t_{rm}$ ) of the gases in the channels but the GHSV's do not change. The results in terms of methane conversions in the combustion and reforming channels are reported in Table 6 for the reference cases (3<sup>rd</sup> and 4<sup>th</sup> row in Table) and for cases where the methane concentration in the combustion channels were below the LEL (1<sup>st</sup> and 2<sup>nd</sup> row). At constant mass flow rates the influence of the channel width or, better, of  $t_{rm}$ , appears negligible under n-expl. conditions with a slight

prevalence of the reactor with narrower channels, and weak under expl. conditions with, in contrast, better performance for the reactor with wider channels. Therefore, it is not possible to draw conclusions.

$W_{c-sr}$ mm		$T_{inr}$ K	$X_{ch4-co}$	$X_{ch4-sr}$	$T_{max}$ K	$t_{rm-co}$ ms	$t_{rm-sr}$ ms	$GHSV_{co}$ $h^{-1}$	$GHSV_{sr}$ $h^{-1}$	
2	n-expl	800	0.36	0.45	827	0.020	0.026	900588	702884	
3	n-expl	800	0.34	0.44	819	0.030	0.038	900588	702884	
2	expl	800	0.89	0.74	914	0.057	0.026	314840	702884	
3	expl	800	0.92	0.81	940	0.086	0.038	314840	702884	
$V_{cost}^{-3}$	3	n-expl	800	0.22	0.33	800	0.020	0.026	1350882	1054327

Table 6. Comparison between reactor performance as a function of channel width

Unlike the previous case, where inlet flow rates were kept constant, an increase in channel width keeping the mean gas velocity and the value of  $t_{rm}$  constants affects significantly the outlet conversions. In this case the amount of reactants flowing through the reactor per unit catalyst volume and, then, GHSV increases (compare 1<sup>st</sup> and 5<sup>th</sup> rows in Table 5).

Increasing channel widths from their reference case value ( $W_{c-sr} = 2$  mm and  $W_{c-co} = 1$ ) at constant gas inlet velocity leads to methane conversion reduction because: a) the catalyst amount becomes insufficient for the amount of reactants fed in the reactor and b) the external mass transfer resistances play a stronger role. The overall reaction heat fluxes remain the same as channel width increases, leaving a similar amount of sensible heat to be used for heating up larger amounts of reactants. This results in lower temperatures along the reactor.

#### 4.6 Influence of catalyst thickness

The influence of catalyst thickness,  $\delta_c$ , on the reactor behaviour was studied by keeping constant the reactants mass flow rates. The reactor operation was simulated for three values of catalyst thickness, i.e. 200, 100, and 50  $\mu m$  while keeping all the other parameters at their reference case values but for what concerns the inlet methane concentration in the combustion channel that was at non explosive level. This with respect to the reference case corresponds to decreasing GHSV of factors 2 and 4, respectively. Changes in the catalyst thickness influence considerably both thermal behaviour and outlet conversions.

As above the comparison is made through the methane conversions achieved in the two cases both in the steam reforming and in the combustion channels. The results are reported in Table 7. It is evident that the loss of performance due to a decrease of 50% of  $\delta_c$  from 200 to 100  $\mu m$  is almost negligible. This is mainly due to the conservative parameters used for defining the catalyst layer characteristics (i.e. mean pore radius and tortuosity) that results in a very impervious path for diffusing gases. However, when  $\delta_c$  is further decreased, methane conversion both in the combustion and in the reforming section significantly decrease. The hydrogen yield does not change too much within the limits of the three cases analyzed.

$\delta_c, \mu\text{m}$		$T_{in}, \text{K}$	$X_{\text{CH}_4-\text{co}}$	$X_{\text{CH}_4-\text{sr}}$	$T_{max}, \text{K}$	$t_{\text{rm-co}}, \text{ms}$	$t_{\text{rm-sr}}, \text{ms}$	$\text{GHSV}_{\text{co}}, \text{h}^{-1}$	$\text{GHSV}_{\text{sr}}, \text{h}^{-1}$	$\phi_{\text{H}_2}$
200	n-expl	800	0.36	0.45	827	0.020	0.026	900588	702884	3.44
100	n-expl	800	0.35	0.45	827	0.020	0.026	1801176	1405768	3.44
50	n-expl	800	0.27	0.38	800	0.020	0.026	3602352	2811536	3.42

Table 7. Comparison between reactor performance as a function of catalyst thickness

## 5. Discussion

As seen in the previous section (4), there are several operating parameters that influence the performances of the system. They are typical of reacting systems and can be summarized as GHSV's,  $t_{\text{mr}}$ 's and inlet gas temperatures. The particularity of the present case is the simultaneous occurrence of two coupled reactions, one exothermic and the other endothermic, in which the extent of the second depends on the extent (heat produced) of the first and the effectiveness of the heat transferred. In addition, the coupling of the two reactions does not exclude to have for each set of values of the mentioned parameters pertaining to one reaction several sets of parameters for the other reaction. This makes the system quite complex and difficult to analyze. However, some general considerations can be drawn.

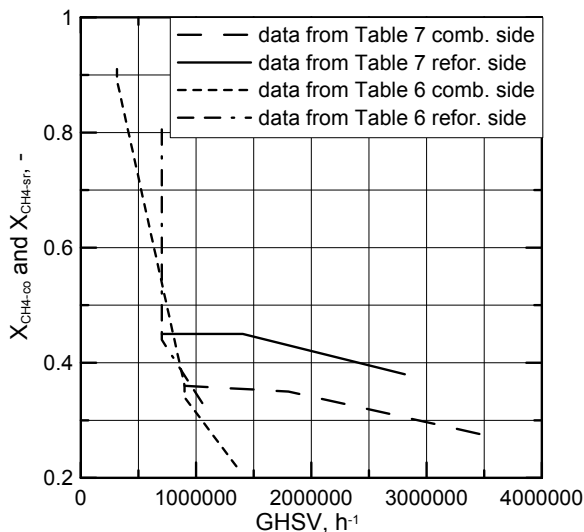


Figure 11. Methane conversions in the combustion and reforming sides of the reactor as a function of GHSV for various operating conditions available in Table 6 and 7

The first is that, as expected, GHSV plays a key role in determining the reactor performances although this is supported by only a part of the data. For instance data in Table 7, pertaining to simulations of the influence of such a parameter, carried out by changing GHSV in the same way for both sections of the reacting system, shows a clear effect of GHSV: the reactor

performance decreases as GHSV increases on both sides of the reactor. Such an influence does not appear strong, the conversion change being about 20% against GHSV variations of a factor 4 (Figure 11). The influence of GHSV is more evident from data in Table 6, pertaining to simulations of the influence of  $t_{mr}$ . In fact, also in this case a clear trend appears and the influence, even though in the same direction of the previous case, appears much stronger since with respect to a GHSV change of about 20%, the methane conversion varies by a factor 4 (Figure 11). Such a strong influence is due to the combined effect of  $t_{mr}$  especially on the combustion side of the reactor (cfr. Table 6). Instead, for data in Table 5 pertaining to simulations of the reliability of 2D and 3D models and the effect of gas inlet temperature, it is not possible to highlight a clear influence.

The comparison between the results obtained with the 2D and 3D models under the same operating conditions have evidenced differences in the performance of the reactor not large but significant. When we move from 2D to 3D models, such differences result in an increase from 5 to 20% of both  $X_{ch4-co}$  and  $X_{ch4-sr}$ , which reflects a different thermal behavior of the reacting system and influence also the hydrogen yield. It is worth noting that the computation time required in the two cases is very different. Specifically, using an HP xw8400 workstation equipped with 2 Xeon processors and 4 GB of RAM a 2D simulation takes on the average about 20 minutes with respect to 50-60 hours necessary in the 3D case.

It is impossible by now to establish which is the more correct or the more reliable. In particular, it should be assessed if 2D simulations are suitable for purpose of reactor design and experimental data interpretation. The answer should come from the comparison of the results of such simulations with experimental data obtained with a real reactor geometrically comparable, operated under conditions as much as similar to those fixed for the simulations. This represents argument for coming work of the authors.

Further interesting aspects to be studied are the simulation of unsteady-state conditions and, specifically, of the system start-up and of the system response to small changes in the gas feeding flow rates and temperatures.

## 6. Conclusions

Methane steam reforming coupled with methane catalytic combustion by means of indirect heat transfer in a surface-bed catalytic reactor was studied by 2D and 3D models. The reactor consists of a central reforming channel and two lateral combustion channels. A reference case for what concerns operating conditions and reactor geometry was chosen and its simulation was carried out. Changes of reactor performance as consequence of operating parameters and reactor geometry variations were analyzed with respect to the reference case.

The simulation showed that suitable amount of fuel and adequate catalyst activity in the combustion channel can provide enough heat to simultaneously heat up the reaction mixture and drive the endothermic process. The proximity between the heat source and the heat sink increases the efficiency of heat transfer resulting in transverse temperature gradients do not exceeding, generally, 0.7 K across the metallic wall and 20 K across the gas in the channel. Decrease of transverse temperature differences and intraphase mass transfer resistances have the global effect of reducing the reactor dimension and the catalyst amount. The influence of channels width, and catalyst layer thickness on reactor behaviour was also studied. At constant inlet flow rates, changes of channel width in the range 1-2 mm do not introduce significant differences in the reactor performance. Rather small differences in the

catalyst axial temperature profiles and outlet methane conversions are observed. In contrast, altering the channel width at constant inlet velocities has strong influence. Larger channel width results in lower conversion and smoother axial temperature profiles. Intraphase resistances are present even for catalyst thickness of micrometers for both reforming and combustion processes. Increasing GHSV, that is the inlet flow rate/catalyst volume ratio, leads to lower outlet conversions. Due to different effect of catalyst layer thickness on reforming and combustion channels, there are significant changes in the reactor temperature profile. Results indicate that steam reforming of methane in a surface-bed reactor is feasible provided that mass flow rates, channels width, catalyst loadings and thickness are properly designed.

## 7. Notation

$c_p$	specific heat, J/(mol K)
$c$	concentration, mol/m <sup>3</sup>
$D_{\text{eff}}$	effective diffusion coefficient, m <sup>2</sup> /s
$D$	molecular diffusion coefficient, m <sup>2</sup> /s
GHSV	gas hourly space velocity, h <sup>-1</sup>
$k$	thermal conductivity, W/(m K) or reaction rate constant
$K_e$	equilibrium constant
$M$	molecular weight, kg/mol
LEL	lower explosivity limit, vol %
$\vec{n}$	unit vector perpendicular to the flux surface
$N$	molar flux at the boundary, mol/(m <sup>2</sup> s)
$p$	partial pressure, bar
$P$	total pressure, bar
$q$	thermal flux at the boundary, J/(m <sup>2</sup> s)
$r$	reaction rate, various dimensions (see eq.s 1', 2' and 3')
$R_p$	catalyst pore radius, nm
STP	standard temperature and pressure (298 K and 101 10 <sup>3</sup> Pa)
$t$	time, s
$T$	temperature, K
$t_s$	transverse surface
$u_x$	Velocity component on the x coordinate
$\vec{v}$	velocity vector
$v$	normal component of velocity at the channel ingress
$x$	axial coordinate, m
$X$	conversion
$y$	transverse coordinate, m
$W_c$	distance between the reactor plates, m
$z$	vertical coordinate, m
<i>Greek letters</i>	
$\Delta H_r^0$	heat of reaction at reference state conditions, KJ/mol
$\delta_c$	catalyst thickness, $\mu\text{m}$
$\varepsilon$	catalyst porosity
$\varphi$	atomic diffusion volume or chemical reaction yield

$\theta$	stoichiometric coefficient
$\rho$	density, kg/m <sup>3</sup>
$\tau$	catalyst tortuosity

#### Subscripts and superscripts

cat	catalyst
co	combustion
CH <sub>4</sub>	methane
H <sub>2</sub>	hydrogen
in	inlet
i	chemical species
j	channel
k	reaction
l	phase
rm	mean residence
s	metal sheet
sr	steam reforming
0	channel ingress
1	reforming reaction
2	water gas shift reaction
3	combustion reaction

## 8. Acknowledgements

The authors gratefully acknowledge the financial support of MIUR under grant PRIN n° 2006094333004.

## 9. References

- Akers, W.W. & Camp, D.P. (1955) Kinetics of the methane–steam reaction. *A.I.Ch.E. Journal*, Vol. 1, 471–475. ISSN:0001-1541.
- Allen, D.W., Gerhard, E.R. & Likins Jr., M.R. (1975) Kinetics of the Methane–Steam Reaction. *Ind. Eng. Chem. Proc. Des. Dev.*, Vol. 14, No. 3, 256–259, ISSN:0196-4305.
- Aparicio, L., (1997) Transient Isotopic Studies and Microkinetic Modeling of Methane Reforming over Nickel Catalysts. *Journal of Catal.*, Vol. 165, No. 2, 262–274 ISSN: 0021-9517.
- Avci, A.K., Trimm, D.L. & İlsen Önsan, Z. (2001) Heterogeneous reactor modeling for simulation of catalytic oxidation and steam reforming of methane. *Chem. Eng. Sci.*, Vol. 56, No 2, 641–649 ISSN:0009-2509
- Bridger, G.W. (1980) The steam reforming of hydrocarbons. *Catalysis*, Vol. 3, 39–69, ISSN:0140-0568.
- Cao, C., Wang, Y. & Rozmiarek R.T. (2005) Heterogeneous reactor model for steam reforming of methane in a microchannel reactor with microstructured catalysts. *Catal. Today*, Vol. 110, No 1–2, 92–97, ISSN: 0920-5861.
- Craciun, R., Shereck, B. & Gorte, R.J. (1998) Kinetic studies of methane steam reforming on ceria-supported Pd. *Catal. Lett.*, Vol. 51, No. 3–4, 149–153, ISSN: 1011-372x.

- Crowl, D.A. & Louvar, J.F. (2002) *Chemical Process Safety: fundamentals with applications* 2<sup>nd</sup> ed., Prentice Hall PTR, Upper Saddle River, NJ, USA. ISBN: 0-13-018176-5
- De Deken, J. C., Devos, E. F., & Froment, G. F. (1982). Steam reforming of natural gas. Intrinsic kinetics, diffusional influences and reactor design. ACS Symposium Series, 196, 181-197, ISSN:0097-6156
- Ehrfeld, W. & Hessel, V., Lowe, H. (2000) *Microreactor*, Wiley-VCH Verlag GmbH, D-69469, ISBN Weinheim, Germany.
- Gosiewski, K. (2001) Simulations of non-stationary reactors for catalytic conversion of methane to synthesis gas. *Chem. Eng. Sci.*, Vol. 56, No 4, 1501-1510 ISSN
- Groppi, G., Belloli, A., Tronconi, E., Forzatti, P. (1995). A comparison of lumped and distributed models of monolith catalytic combustors. *Chem. Eng. Sci.*, Vol. 50, No. 17, 2705-2715. ISSN:0009-2509
- Holladay, J.D., Wang, Y. & Jones, E. (2004) Review of Developments in Portable Hydrogen Production Using Microreactor Technology. *Chem. Rev.*, Vol. 104, No 10, 4767-4790 ISSN: 0009-2665.
- Hou, K. & Hughes, R. (2001) The kinetics of methane steam reforming over a Ni/ $\alpha$ -Al<sub>2</sub>O<sub>3</sub> catalyst. *Chem. Eng. Journal*, Vol. 82, No. 1-3, 311-328 ISSN: 1385-8947
- Jamal, Y. & Wyszynski, M. L. (1994). On-board generation of hydrogen-rich gaseous fuels: a review. *Int. J. of Hydrogen Energy*, Vol. 19, No. 7, 557-572, ISSN: 0360-3199.
- Jensen, K.F. (2001) Microreaction engineering : is small better?. *Chem. Eng. Sci.*, Vol. 56, No 2, 293-303. ISSN:0009-2509
- Kolios, G., Gritsch, A., Gloickler, B. & Sorescu G. (2004) Novel Reactor Concepts for Thermally Efficient Methane Steam Reforming: Modeling and Simulation. *Ind. Eng. Chem. Res.*, Vol. 43, No 16, 4796-4808, ISSN:0888-5885
- Kruger, P., Blakeley, J. & Leaver, J. (2003) Potential in New Zealand for use of hydrogen as a transportation fuel. *Int. J. of Hydrogen Energy*, Vol. 28, No. 8, 795-802, ISSN: 0360-3199.
- Kvamdsdal, H.M., Svendsen, H.F., Hertzberg, T. & Olsvik, O. (1999) Dynamic simulation and optimization of a catalytic steam reformer. *Chem. Eng. Sci.*, Vol. 54, No. 13-14, 2697-2706. ISSN:0009-2509
- Lerer, M., Duic, N., Alves, L.M. & Carvalho, M.G. (2006) H<sub>2</sub> RES, energy planning tool for increasing the penetration of renewable energy sources in island energy supply. In: *New and Renewable Technologies for Sustainable Development*. M.G. Carvalho and N.H. Afgan (Ed. s), 15-30, World Scientific, ISBN: 10 981-270-505-8, Singapore.
- Lerou, J.J. & Ng, K.M. (1996) Chemical reaction engineering: A multiscale approach to a multiobjective task. *Chem. Eng. Sci.*, Vol. 51, No 10, 1595-1614 ISSN:0009-2509.
- Lincoln, S.F. (2006) *Challenged Earth*, ch.7, Imperial College Press, ISBN: 1-86094-526-0, London
- Loffler, D. G., Faz, C. F., Sokolovskii, V. & Iglesia, E. (2002) Catalytic separator plate reactor and method of catalytic reforming of fuel to Hydrogen. PCT Int. Appl., WO 02/28769 A2.
- Luna, C. & Becerra, A.M. (1997) Kinetics of methane steam reforming on a Ni on alumina-titania catalyst. *React. Kinet. Catal. Lett.*, Vol. 61, No. 2, 369-374, ISSN: 0133-1736.
- Marschner, F., Renner, H.J. & Boll, W. (2005) Electronic Encyclopedia, Release 2005, 7<sup>th</sup> ed. in: *Ullmann's Encyclopedia of Industrial Chemistry*, M. Bohnet, et al. (Eds.), Vol. a12, John Wiley & Sons, ISBN-13: 978-3-527-30385-4

- Moore, R. B. & Raman, V. (1998) Hydrogen infrastructure for fuel cell transportation. *Int. J. of Hydrogen Energy*, Vol. 23, No 7, 617-620, ISSN: 0360-3199..
- Perry, R.H. & Green, D.W., (1999) *Perry's Chemical Engineers' Handbook* (7th Ed.), McGraw-Hill. ISBN: 0-07-049841-5
- Robbins, F. A., Zhu, H. & Jackson, G.S. (2003) Transient modeling of combined catalytic combustion/CH<sub>4</sub> steam reforming. *Catal. Today*, Vol. 83, No 1-4, 141-156, ISSN: 0920-5861.
- Rostrup-Nielsen, J.R., Christiansen, L.J. & BakHansen, J.H. (1988) Activity of steam reforming catalysts: Role and assessment. *Appl. Catal.*, Vol. 43, No 2, 287-303, ISSN:0166-9834.
- Rostrup-Nielsen, J.R. (1995) Innovation and the catalytic process industry - the science and challenge. *Chem. Eng. Sci.*, Vol. 50, No 24, 4061-4071, ISSN:0009-2509
- Rostrup-Nielsen, J.R., Dybkjaer, I. & Coulthard, G.R.G. (2001) Topical Conf. Proc. AIChE Spring National Meeting, Houston, TX, April, Paper No. 1.
- Rostrup-Nielsen, J.R. (2004) Fuels and Energy for the Future: The Role of Catalysis. *Catal. Rev. - Science and Engineering*, Vol. 46, No. 3-4, 247-270, ISSN:0161-4940.
- Schubert, K., Brandner, J., Fichtner, M., Linder, G., Schyhulla, U. & Wenka, A. (2001) Microstructure devices for applications in thermal and chemical process engineering. *Microscale Thermophys Eng.*, Vol 5, No 1, 17-39, ISSN:1089-3954.
- Tronconi, E. & Groppi, G. (2000) A study on the thermal behavior of structured plate-type catalysts with metallic supports for gas/solid exothermic reactions. *Chem. Eng. Sci.* Vol.: 55, Issue: 24, December, 6021-6036, ISSN:0009-2509
- Wang, Y., Johnson, B.R., Cao, C., Chin, Y., Rozmiarek, R.T., Gao, Y., Tonkovich, A.L. (2005) Engineered catalysts for microchannel reactor applications, In: *Microreactor Technology and Process Intensification*, Y. Wang, J. Holladay (Eds.), 65-73, ACS Symposium Series, Vol. 914, ISBN-13: 9780841239234
- Xu, J. & Froment, G.F. (1989a) Methane steam reforming II. Diffusional limitations and reactor simulation. *A.I.Ch.E. Journal*, Vol. 35, No. 1, 97-103 ISSN:0001-1541.
- Xu, J. & Froment, G.F. (1989b) Methane steam reforming, methanation and water-gas shift. I. Intrinsic kinetics. *A.I.Ch.E. Journal*, Vol. 35, No. 1, 88-96, ISSN:0001-1541.
- Zanfir, M. & Gavriilidis, A. (2003) Catalytic Combustion Assisted Methane Steam Reforming. *Chem. Eng. Sci.*, Vol. 58, No 17, 3947- 3960, ISSN:0009-2509



# Multiscale Heat, Air and Moisture Modelling and Simulation

A.W.M. van Schijndel  
*Eindhoven University of Technology*  
*Netherlands*

## 1. Introduction

### 1.1 Background

It is widely accepted that simulation can have a major impact on the design and evaluation of building and systems performances. Also, the modelling and simulation of whole building heat, air and moisture (further-on called HAM) responses in relation to human comfort, energy and durability are relevant. IEA Annex 41 (2005) focuses on a holistic approach of HAM transfer between the outside, the enclosure, the indoor air and the heating, ventilation and air-conditioning (HVAC) systems. Therefore integrated HAM models capable of covering all these issues are sought-after. There is no single simulation tool that covers all of the issues (Augenbroe (2002)). One option is the external coupling of tools (Hensen et al. (2004); Djunaedy (2005)). Recent developments in general modelling and simulation tools give rise to another option: the use of a single computational environment. Important requirements for such a simulation environment are:

- a) A lot of existing HAM models are based on Ordinary Differential Equations (ODEs) or Partial Differential Equations (PDEs). Therefore it should be relative easy to implement and couple such models in the simulation environment.
- b) The modelling and simulation results should be reproducible and accessible. This means that the relation between mathematical model and numerical model should be clear and people in the scientific community should have access to models
- c) For practical use, a whole building model, capable of simulation the building response, should also be present.

MatLab (including toolboxes) (2008) has become the standard tool for scientific computations. The aim of this chapter is to investigate whether the MatLab simulation environment, including SimuLink & Comsol, is capable of meeting all requirements.

### 1.2 HAM models

Over the past years hundreds of tools are developed (Crawley et al. (2005)). The aim of this Section is not to obtain an exhaustive list of HAM models, but to obtain a representative group of HAM models that will be used in the next Section for identifying common HAM related modelling problems. The work in this chapter is related to: (1) Annex 41 (2005), (2) building energy programs, (3) modelling and simulation techniques; (4) Matlab/SimuLink related tools. For each of the four items, a summary of involved HAM models is presented

now. First, in 2005, 14 different tools were used in an Annex 41 common exercise (2005) about simulating the dynamic interaction between the indoor climate of a room and the HAM response of the enclosure. All tools model the indoor air and the enclosure. Six HAM models are stand-alone simulation tools and have promising capabilities for simulating HVAC systems: Bsim (2008), IBPT (2008), IDA-ICE (2008), TRNSYS (2008), EnergyPlus (2008), and HAMLab (2008). The latter is presented in this chapter. Second, the energy related software tools at the Energy Tools website U.S. Department of Energy U.S (2008) has been used for several comparison studies. A recent overview is provided by Crawley et al. (2005). Furthermore, Schwab et al. (2004) used the same website for a study on programs that might simulate whole building HAM transfer. The criteria were based on: moisture storage in building materials, calculate indoor climate, moisture exchange in HVAC system, access to source code. Three tools met all criteria: Bsim (2008), TRNSYS (2008) and EnergyPlus (2008). These tools are already mentioned. Third, Gough (1999) reviews tools with the focus on new techniques for building and HVAC system modelling. In this study four simulation techniques were investigated. Proved techniques related with HAM modelling are the equation-based method techniques such as Neutral Model Format and IDA solver, which are included in IDA-ICE (2008) and TRNSYS (2008). The other mentioned techniques of Gough (1999) are simulation environments with limited HAM modelling capabilities for building simulation. Fourth, Riederer (2005) provides a recent overview of Matlab/SimuLink based tools for building and HVAC simulation. The tools who are most related with the work in this chapter are discussed now. SIMBAD (2008) provides HVAC models and related utilities to perform dynamic simulation of HVAC plants and controllers. The toolbox focuses on thermal processes with limited capabilities for moisture transport simulation. In addition to this work, this chapter presents how models that include moisture transport, can be simulated in SimuLink. The International Building Physics Toolbox (IBPT) (2008) is constructed for the thermal system analysis in building physics. The tool capabilities also include 1D HAM transport in building constructions and multi-zonal HAM calculations. (Sasic Kalagasidis (2004)). All models including the 1D HAM transport in building constructions are implemented using the standard block library of SimuLink. The developers notice the possibility to couple to other codes / procedures for 2D and 3D HAM calculations. In addition to this work, this chapter shows how this can be done using Comsol.

### 1.3 Common modelling problems

All HAM tools mentioned in previous Sections, face at least one limitation that cannot be solved by the tool itself. Either a problem occurs at the integration of HVAC systems models into whole building models, or a problem occurs at the integration of 2D and 3D geometry based models (for example airflow and HAM response of constructions) into whole building models. The first problem, a time scale problem, is caused by the difference in time constants between HVAC components and controllers (order of seconds) and building response (order of hours). This can cause inaccurate results and long simulation duration times (Gouda et al. (2003) and Felsman et al. (2002)). The second problem, a lumped/distributed parameters problem, is caused by the lack of lumped parameter tools to include internal 2D, 3D finite element method (FEM) capabilities (Sahlin et al. (2004)).

**1.4 Objectives and outline of this chapter**

The key question is whether a single simulation environment is suitable for solving both the above-mentioned multi physics modelling problems concerning different time scales and lumped/distributed parameters. Our method was, first to develop, implement and validate the following modelling facilities into the simulation environment SimuLink:

1. a whole building (global) modelling facility, for the simulation of the indoor climate and energy amounts;
2. an ordinary differential equation (ODE) solving facility, for the accurate simulation of HVAC systems and controllers;
3. a partial differential equation (PDE) solving facility, for the simulation of 2D/3D HAM responses of building constructions and 2D internal/external airflow.

The second step was to evaluate our results with regard to the key question.

The outline of this chapter is as follows. Sections 2 through 4 present the integration of models into SimuLink, including validation results, concerning respectively: a whole building model (Section 2), ODE based models of HVAC and primary systems (Section 3) and PDE based models of: indoor airflow, HAM transport in constructions and external airflow/driving rain (Section 4). Finally, in Section 5, the results are discussed. At the appendix, technical details of the implementation of the models are given. This additional information provides the relation between mathematical model and code. Furthermore, it can be used as a guideline for the development of new HAM models.

**2. Whole building model**

Our whole building model originates from the thermal indoor climate model (ELAN) which was already published in 1987 (de Wit et al. (1988)). Separately a model for simulating the indoor air humidity (AHUM) was developed. In 1992 the two models were combined (WAVO) and programmed in the MATLAB environment (van Schijndel & de Wit (1999)). Since that time, the model has constantly been improved using newest techniques provided by recent MATLAB versions. Currently, the hourly-based model is named HAMBBase, which is capable to simulate the indoor temperature, the indoor air humidity and energy use for heating and cooling of a multi-zone building. The physics of this model is extensively described by de Wit (2006). The main modeling considerations are summarized below. The HAMBBase model uses an integrated sphere approach. It reduces the radiant temperatures to only one node. This has the advantage that also complicated geometries can easily be modeled. In figure 1, the thermal network is shown.

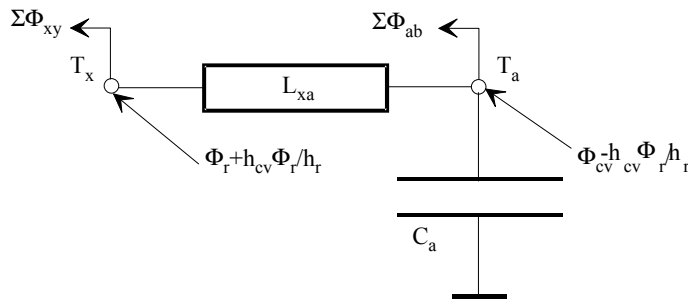


Figure 1. The room model as a thermal network

$T_a$  is the air temperature and  $T_x$  is a combination of air and radiant temperature.  $T_x$  is needed to calculate transmission heat losses with a combined surface coefficient.  $h_r$  and  $h_{cv}$  are the surface weighted mean surface heat transfer coefficients for convection and radiation.  $\Phi_r$  and  $\Phi_{cv}$  are respectively the radiant and convective part of the total heat input consisting of heating or cooling, casual gains and solar gains<sup>1</sup>.

For each heat source a convection factor can be given. For air heating the factor is 1 and for radiators 0.5. The factor for solar radiation depends on the window system and the amount of radiation falling on furniture.  $C_a$  is the heat capacity of the air.  $L_{xa}$  is a coupling coefficient (Wit et al. 1988):

$$L_{xa} = A_t h_{cv} \left( 1 + \frac{h_{cv}}{h_r} \right) \tag{1}$$

$\sum \Phi_{ab}$  is the heat loss by air entering the zone with an air temperature  $T_b$ .  $A_t$  is the total area. In case of ventilation  $T_b$  is the outdoor air temperature.  $\sum \Phi_{xy}$  is transmission heat loss through the envelope part y. For external envelope parts  $T_y$  is the sol-air temperature for the particular construction including the effect of atmospheric radiation.

The admittance for a particular frequency can be represented by a network of a thermal resistance ( $1/L_x$ ) and capacitance ( $C_x$ ) because the phase shift of  $Y_x$  can never be larger than  $\pi/2$ . To cover the relevant set of frequencies (period 1 to 24 hours) two parallel branches of such a network are used giving the correct admittance's for cyclic variations with a period of 24 hours and of 1 hour. This means that the heat flow  $\Phi_{xx}(tot)$  is modeled with a second order differential equation. For air from outside the room with temperature  $T_b$  a loss coefficient  $L_v$  is introduced. The model is summarized in figure 2

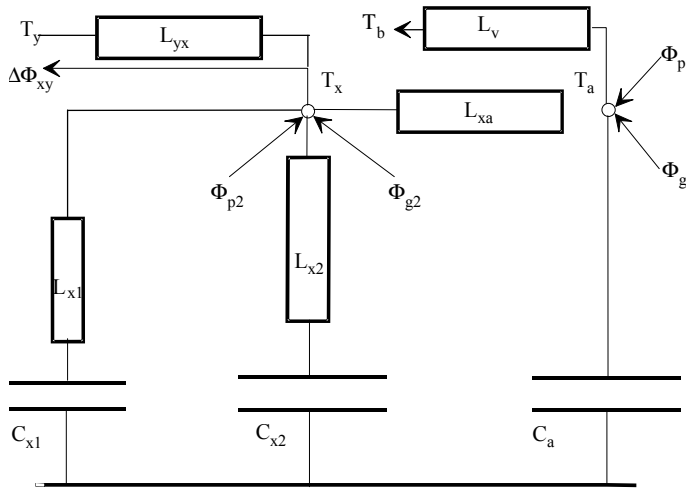


Figure 2. The thermal model for one zone

In a similar way a model for the air humidity is made. Only vapour transport is modeled, the hygroscopic curve is linearized between RH 20% and 80%. The vapour permeability is

<sup>1</sup> Please note that the model presented in figure 1 is a result of a delta-star transformation.

assumed to be constant. The main differences are: a) there is only one room node (the vapour pressure) and b) the moisture storage in walls and furniture, carpets etc is dependent on the relative humidity and temperature.

## 2.1 Integration and the time scale problem

It is obvious that the hourly based approach of HAMBase is not accurate enough if we want to integrate building systems with its relative small time scales (order seconds). Our major recent improvement is the development of a so called hybrid model that consists of both a continuous part with a variable time step as well as a discrete part with a time step of one hour. We adapted our HAMBase model by splitting the energy and vapor flows into two parts. First, a discrete part was developed for modelling the transmittance through walls. Second, a continuous part was developed for the rest (admittance, ventilation, sources, etc.). We implemented this approach by using so-called S-Functions for SIMULINK (see also the Appendix). This new model, named HAMBASE\_S to avoid confusion, is able to simulate complicated HVAC installations and controls simultaneously with the building. We summarize the main advantages:

- The dynamics of the building systems where small time scales play an important role (for example on/off switching) are accurately simulated.
- The model becomes time efficient as the discrete part uses 1-hour time steps. A yearly based simulation takes less than 3 minutes on a Pentium 3.4 GHz, 2GB computer.
- The moisture (vapor) transport model of HAMBase is also included. With this feature, the (de-) humidification of HVAC systems can also be simulated.

## 2.2 Verification

### 2.2.1 Standard test (thermal)

The Bestest (ASHRAE, (2001)) is a structured approach to evaluate the performance of building performance simulation tools. The evaluation is performed by comparing results of the tested tool relative to results by reference tools. The procedure requires simulating a number of predefined and hierarchal ordered cases. Firstly, a set of qualification cases have to be modelled and simulated. If the tool passes all qualification cases the tool is considered to perform Bestest compliant. In case of compliance failure the procedure suggests considering diagnostic cases to isolate its cause. Diagnostic cases are directly associated with the qualification cases (Judkoff and Neymark 1995). The first qualification case, case 600 (see figure 3) was used for the performance comparison.

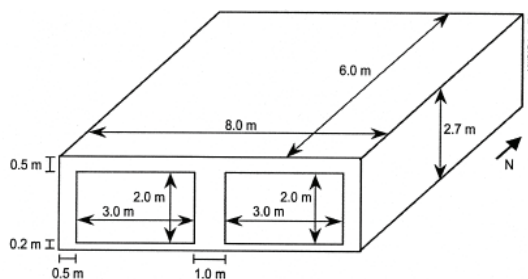


Figure 3. Bestest Case Geometry

The thermal part of HAMBase has been subjected to a standard method of test (Bestest ASHRAE, (2001)) with satisfactory results. For further details, see Table 1.

<i>CASE</i>	<i>NR. SIMULATION OF</i>	<i>MODEL RESULT</i>	<i>MIN.TEST</i>	<i>MAX. TEST</i>
600ff	mean indoor temperature [°C]	25.1	24.2	25.9
600ff	min. indoor temperature [°C]	-17.9	-18.8	-15.6
600ff	max. indoor temperature [°C]	64.0	64.9	69.5
900ff	mean indoor temperature [°C]	25.1	24.5	25.9
900ff	min. indoor temperature [°C]	-5.1	-6.4	-1.6
900ff	max. indoor temperature [°C]	43.5	41.8	44.8
600	annual sensible heating [MWh]	4.9	4.3	5.7
600	annual sensible cooling [MWh]	6.5	6.1	8.0
600	peak heating [kW]	4.0	3.4	4.4
600	peak sensible cooling [kW]	5.9	6.0	6.6
900	annual sensible heating [MWh]	1.7	1.2	2.0
900	annual sensible cooling [MWh]	2.6	2.1	3.4
900	peak heating [kW]	3.5	2.9	3.9

Table 1. Comparison of the room model with some cases of the standard test

### 2.2.2 Parameter sensitivity test (thermal)

The Bestest case 600 is used to study uncertainties by Hopfe et al. (2007). Uncertainties have been assigned to 48 input parameters describing the physical properties of the case and its operation. The input parameters used are exactly the same for three tools, IESVE, VA114

and HAMBase. The model parameters are normally distributed using a fixed standard deviation of 5% for all variables. A standard deviation of 5% does not represent a realistic parameter uncertainty but defines a common base for the tool performance comparison. For each input parameter 200 samples were generated by latin hypercube sampling. The prototypes were deployed to generate simulation input files from the sample matrix and run the simulations. Figure 4 shows the parameter sensitivities for the annual sensible heating (case 600) produced by the four tools.

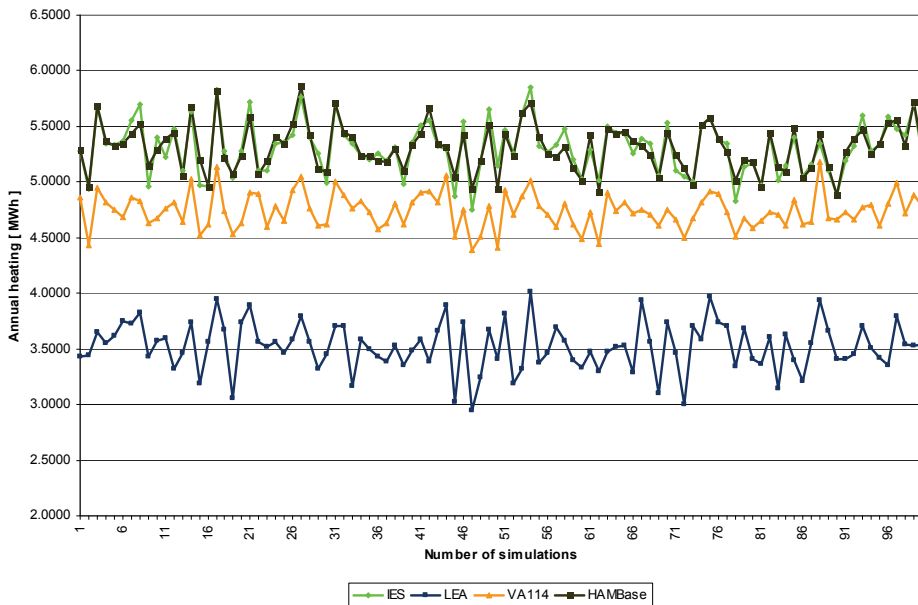


Figure 4. Parameter sensitivity test for four building energy simulation tools

Figure 4 shows a very good agreement between the IESVE and HAMBase tools. This is remarkable because both tools have quite different modeling approaches. We may conclude both modeling approaches give similar results for the considered case studies.

### 2.2.3 Annex 41 test (hygric)

The hygric parts of both HAMBase and HAMBase\_S have been subjected to a new benchmark case developed by the IEA Annex 41 (2005). The geometry is identical to the Bestest (ASHRAE standard (2001)). Further test conditions are as follows: (1) there is only one 1D construction type with linear properties; (2) the exposure is completely isothermal; (3) the outside relative humidity (RH) is 30%; (4) there are no windows; (5) the internal gains equal 500g/hour; (6) the ventilation rate is 0.5 ach. Bednar & Hagentoft (2005) provide the analytical solution of this benchmark. Figure 5 and 6 show the results of the two benchmarks representing moisture buffering by air alone and by combined air and the construction.

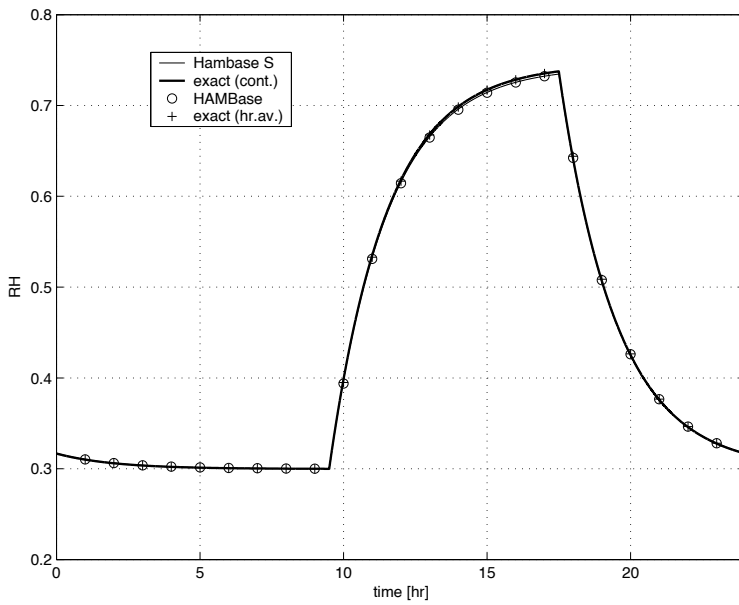


Figure 5. Simulated RH of the indoor climate with only moisture buffering by air

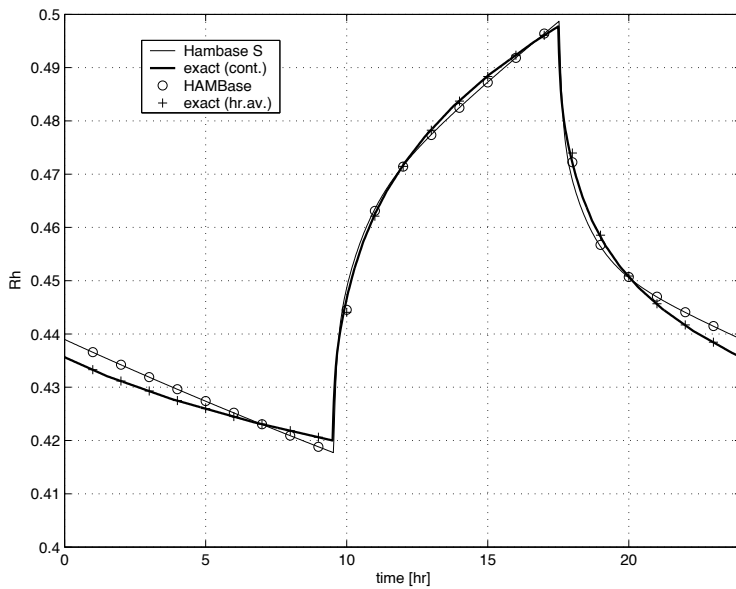


Figure 6. Simulated RH of the indoor climate with moisture buffering by air and the construction



Both figures provide four results: the hourly and continuous analytical solution of Bednar & Hagentoft (2005), the hourly based HAMBase solution and the continuous HAMBase\_S solution. The results show a good agreement between all solutions.

### 2.3 Validation

The intention of the following study, developed within the Annex 41, was to retrieve an experimental based and well defined benchmark for evaluating the involved HAM models. The experiment comprehends two real and almost identical rooms, which are located at the outdoor testing site of the Fraunhofer-Institute of building physics in Holzkirchen. During the winter of 2005-2006, tests were carried out. The walls and the ceiling of the test room were fully covered with aluminum foil. In the reference room 50 m<sup>2</sup> of the walls was not covered with aluminum providing more buffering capacity of the walls compared to the test room. The air temperature in both rooms was kept between 19.8 and 20.2 °C. The next results are presented: the measured and simulated RH in the reference room (figure 7) and heating power to the reference room (figure 8).

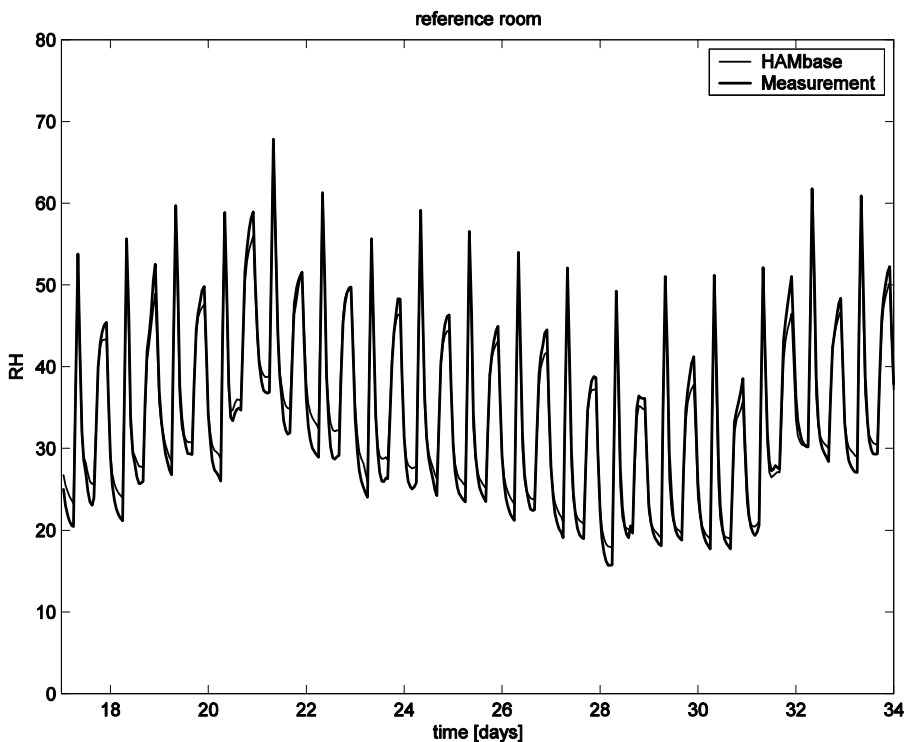


Figure 7. The measured and simulated RH in the reference room

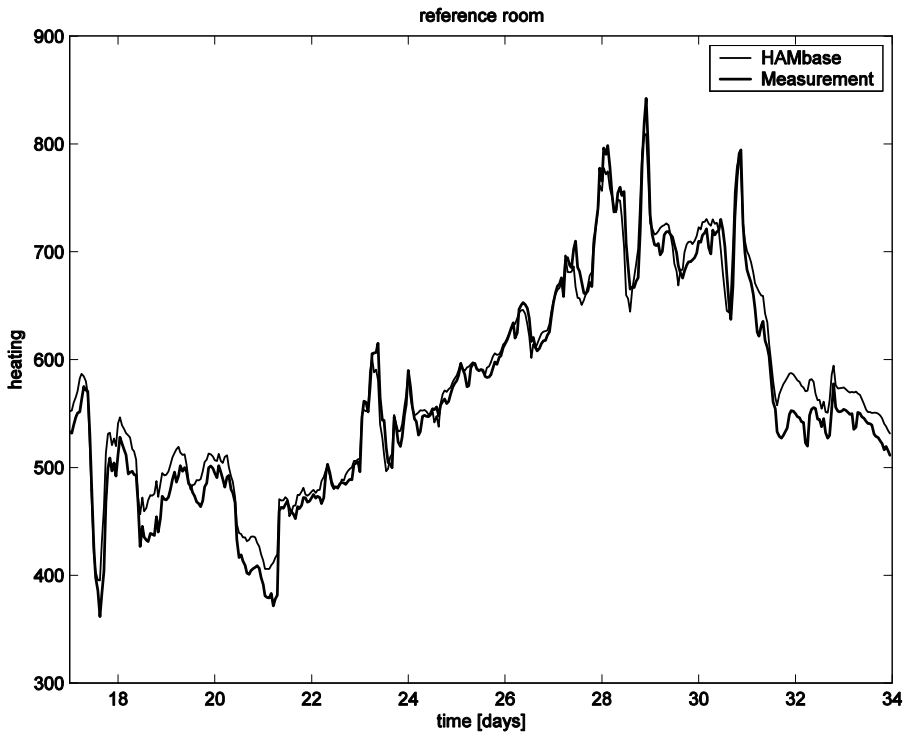


Figure 8. The measured and simulated heating power in the reference room

The results of the test room are similar to the reference room and are therefore left out. The results from figure 7 and 8 show a good agreement between measured and simulated results.

We may conclude that our approach of discrete/continuous modelling provide accurate results within acceptable simulation duration times and thus providing us a good solution to the mentioned time scale problem.

### 3. ODE based modelling

Often, mathematical models of HVAC and primary systems and controllers can be expressed as a system of Ordinary Differential Equations (ODEs). In this Section we present the integration of ODE based models into SimuLink and thus providing a coupling between building and systems.

#### 3.1 Integration

A complete case study on how to integrate a model described by a system of ODEs into SimuLink is now exemplarily shown for a heat pump model. We start with a mathematical model of the heat pump, based on first principles, in the form of ODEs:

$$\left[ \begin{array}{l} \text{COP} = k \cdot \frac{0.5 \cdot T_{\text{cin}} + 0.5 \cdot T_{\text{cout}} + 273.15}{(0.5 \cdot T_{\text{cin}} + 0.5 \cdot T_{\text{cout}}) - (0.5 \cdot T_{\text{vin}} + 0.5 \cdot T_{\text{vout}})} \\ C_c \frac{dT_{\text{cout}}}{dt} = F_{\text{cin}} \cdot c_w \cdot (T_{\text{cin}} - T_{\text{cout}}) + \text{COP} \cdot E_{\text{hp}} \\ C_v \frac{dT_{\text{vout}}}{dt} = F_{\text{vin}} \cdot c_w \cdot (T_{\text{vin}} - T_{\text{vout}}) - (\text{COP} - 1) \cdot E_{\text{hp}} \end{array} \right. \quad (2)$$

Where  $T$  is temperature [ $^{\circ}\text{C}$ ], COP Coefficient of Performance [-],  $k$  heat pump efficiency [-],  $c_w$  specific heat capacity of water [ $\text{J}/\text{kgK}$ ],  $C$  heat capacity of the water and pipes in the heat pump [ $\text{J}/\text{K}$ ],  $t$  time[s],  $F$  mass flow [ $\text{kg}/\text{s}$ ],  $E_{\text{hp}}$  heat pump electric power supply [ $\text{W}$ ]. Subscript  $c$  means water at the condenser,  $v$  water at the evaporator, in, incoming, out, outgoing.

The second step is to define the input-output definition of the model. The final step is to implement the mathematical model into a S-Function, a programmatic description of a dynamic system. The technical details of the last two steps are presented in the Appendix.

The importance of these details is that the relation between mathematical model and implemented model is clear and it is very useful for developers who want to create their own ODE based models. It should be mentioned that the time scale problem seems less relevant in case of ODE based models because there are special designed solvers for this case. So-called stiff solvers can handle such a problem accurately and time efficient. On the other hand, simulating controllers for example (rapid) on/off switching can generate small time steps during simulation. Although accurate results are obtained in this case, it could still lead to relative long simulation duration times.

### 3.2 Validation

At a test site of the Eindhoven University, a configuration with a heat pump, an energy roof and a thermal energy storage has been investigated with a focus on the convective heat recovery from ambient air. Also one of the goals of this project was to evaluate the modelling approach of previous Section applied to respectively a heat pump, an energy roof and a thermal energy storage. From this work, published in van Schijndel & de Wit (2003c), we show the validation results of the heat pump which are presented in figure 9.

In this figure the measured and simulated water temperatures of the outgoing flows at the condenser and evaporator are compared and show a good agreement. The other components: energy roof and thermal energy storage were validated with similar results. We may conclude that the presented ODE based modelling approach provide accurate results. In general it is expected that systems modeled as a system of ODEs can be relative easy and accurately simulated using the presented modelling approach.

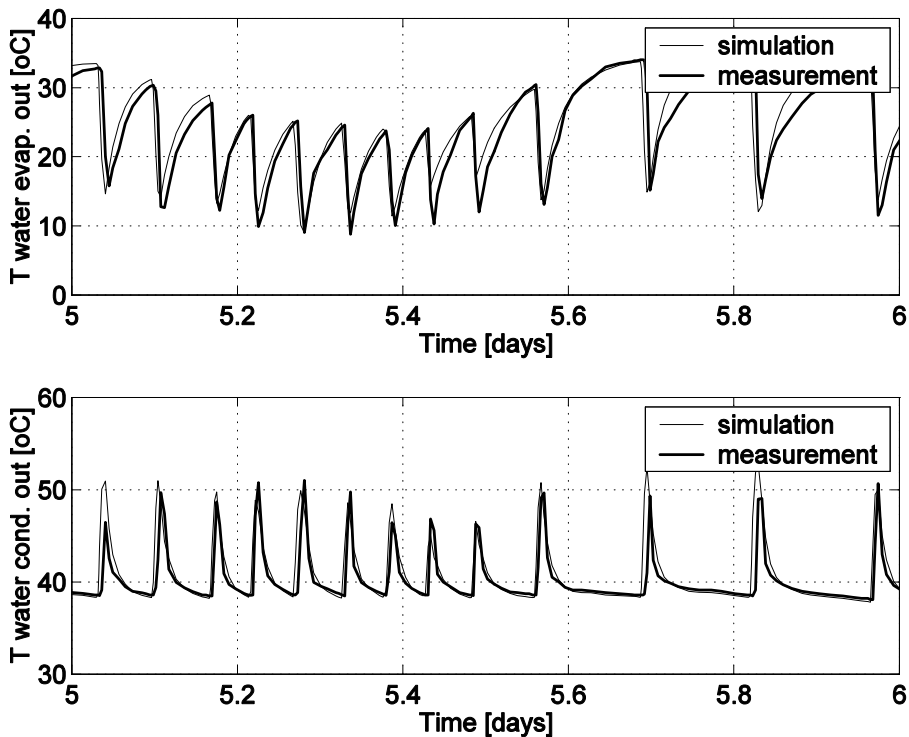


Figure 9. The measured and simulated water temperature of the evaporator (top) and condenser (bottom)

#### 4. PDE based modelling

HAM responses of building constructions and internal/external airflow can be modeled and simulated with Comsol (formerly FemLab) (2008). This is an environment for modelling scientific and engineering applications based on partial differential equations (PDEs). Comsol [Comsol 2006] is a toolbox which solves systems of coupled PDEs (up to 32 independent variables). The specified PDEs may be non-linear and time dependent and act on a 1D, 2D or 3D geometry. The PDEs and boundary values can be represented by two forms. The coefficient form is as follows<sup>2</sup>

$$d_a \frac{\partial u}{\partial t} - \nabla \cdot (c \nabla u + \alpha u - \gamma) + \beta \nabla u + a u = f \quad \text{in } \Omega \quad (3a)$$

$$\underline{n} \cdot (c \nabla u + \alpha u - \gamma) + q u = g - \lambda \quad \text{on } \partial \Omega \quad (3b)$$

<sup>2</sup>\* The symbols provided by the Comsol modeling guides are also used here.

$$hu = r \qquad \qquad \qquad \text{on } \partial\Omega \qquad (3c)$$

The first equation (3.1a) is satisfied inside the domain  $\Omega$  and the second (3.1b) (generalized Neumann boundary) and third (3.1c) (Dirichlet boundary) equations are both satisfied on the boundary of the domain  $\delta\Omega$ .  $n$  is the outward unit normal and is calculated internally.  $\lambda$  is an unknown vector-valued function called the Lagrange multiplier. This multiplier is also calculated internally and will only be used in the case of mixed boundary conditions. The coefficients  $d_a$ ,  $c$ ,  $\alpha$ ,  $\beta$ ,  $\gamma$ ,  $a$ ,  $f$ ,  $g$ ,  $q$  and  $r$  are scalars, vectors, matrices or tensors. Their components can be functions of the space, time and the solution  $u$ . For a stationary system in coefficient form  $d_a = 0$ . Often  $c$  is called the diffusion coefficient,  $\alpha$  and  $\beta$  are convection coefficients,  $a$  is the absorption coefficient and  $\gamma$  and  $f$  are source terms.

The second form of the PDEs and boundary conditions is the general form:

$$d_a \frac{\partial u}{\partial t} + \nabla \cdot \Gamma = F \qquad \text{in } \Omega \qquad (4a)$$

$$-\underline{n} \cdot \Gamma = G + \lambda \qquad \text{on } \partial\Omega \qquad (4b)$$

$$R = 0 \qquad \text{on } \partial\Omega \qquad (4c)$$

The coefficients  $\Gamma$  and  $F$  can be functions of space, time, the solution  $u$  and its gradient. The components of  $G$  and  $R$  can be functions of space, time, and the solution  $u$ .

Given the geometry, an initial finite element mesh is automatically generated by triangulation of the domain. The mesh is used for discretisation of the PDE problem and can be modified to improve accuracy. The geometry, PDEs and boundary conditions are defined by a set of fields similarly to the structure in the language C. A graphical user interface is used to simplify the input of these data. For solving purposes Comsol contains specific solvers (like static, dynamic, linear, non-linear solvers) for specific PDE problems.

#### 4.1 HAM models and validation

In (Comsol 2006) examples are already present which show the accuracy and reliability of Comsol. However there are no validations for typical building physics problems. Specific for validating building physics simulations in Comsol, this Section deals with two (very different) time dependent non-linear problems. Each problem is solved and compared with measured data.

##### 4.1.1 1D Moisture transport in a porous material

The water absorption in an initially dry brick cylinder (length 24-mm) is studied. All sides except the bottom are sealed. This side is submerged in water at  $t=0$  sec. The PDE and boundary conditions for this problem are:

$$\begin{aligned}
 \frac{\partial \theta}{\partial t} &= \nabla \cdot (D(\theta) \nabla \theta) && \text{on } 0 < x < 0.024, \\
 \theta &= 0.27 && \text{on } x = 0, \\
 \frac{\partial \theta}{\partial x} &= 0 && \text{on } x = 0.024
 \end{aligned}
 \tag{5}$$

The coefficient form (3) is used. The results of measured water absorption of several brick materials based on (Brocken 1998) are shown in figure 10, left hand side. The moisture profiles are shown versus lambda (lambda is defined by the position divided by the square root of the time). For each material the diffusivity as a function of the moisture content is given [Brocken 1998] and used to simulate the corresponding profiles.

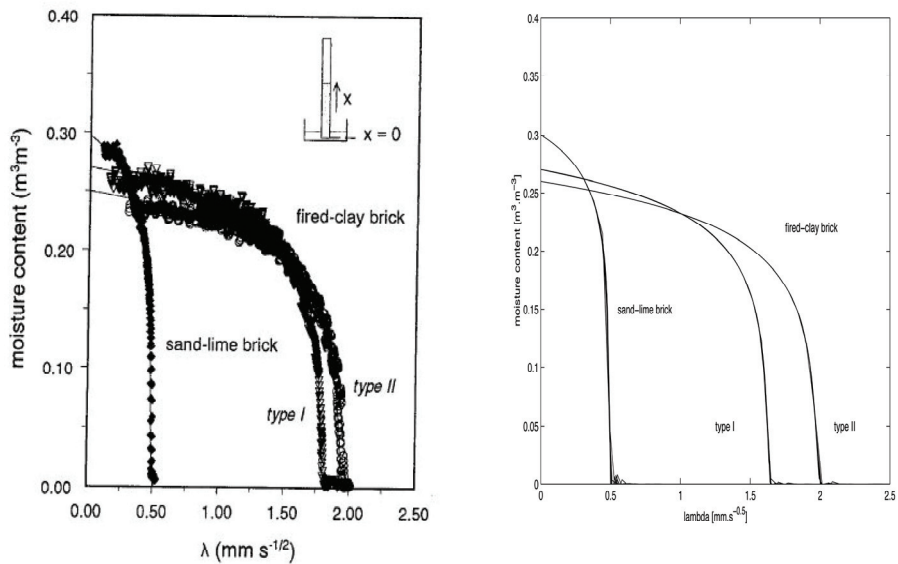


Figure 10. Measured and simulated moisture content profiles versus lambda of the 1D moisture transport problem. Left hand side: Measured moisture contents, Right hand side: Simulated moisture contents

The simulation results in figure 10, right hand side, are compared with the measured profiles<sup>3</sup>.

<sup>3</sup> Such a comparison is used to gain confidence in the model and simulation tool.

**4.1.2 2D Airflow in a room**

This example from Sinha (2000) deals with the velocity and temperature distribution in a room heated by a warm air stream. In figure 11 the geometry and boundary conditions are presented.

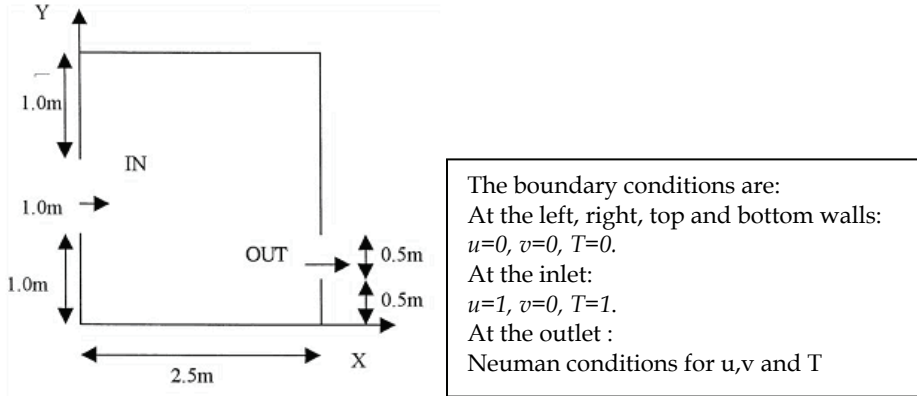


Figure 11. The geometry and boundary conditions for the 2D-airflow problem  
 The problem is modelled by 2D incompressible flow using the Boussinesq approximation with constant properties for the Reynolds and Grasshof numbers.  
 U-momentum equation

$$\frac{\partial u}{\partial t} = -\frac{\partial(uu)}{\partial x} - \frac{\partial(vu)}{\partial y} - \frac{\partial p}{\partial x} + \frac{1}{Re} \nabla^2 u$$

V-momentum equation

$$\frac{\partial v}{\partial t} = -\frac{\partial(uv)}{\partial x} - \frac{\partial(vv)}{\partial y} - \frac{\partial p}{\partial y} + \frac{1}{Re} \nabla^2 v + \frac{Gr}{Re^2} T$$

Continuty equation

(6)

$$\frac{\partial u}{\partial x} + \frac{\partial v}{\partial y} = 0$$

Energy equation

$$\frac{\partial T}{\partial t} = -\frac{\partial(uT)}{\partial x} - \frac{\partial(vT)}{\partial y} + \frac{1}{Re Pr} \nabla^2 T$$

The general form (4a-c) is used for this type of non-linear problem. In (Sinha 2000) the problem is solved and validated with measurements for several combinations of Re and Gr. In figure 12 these results are presented.

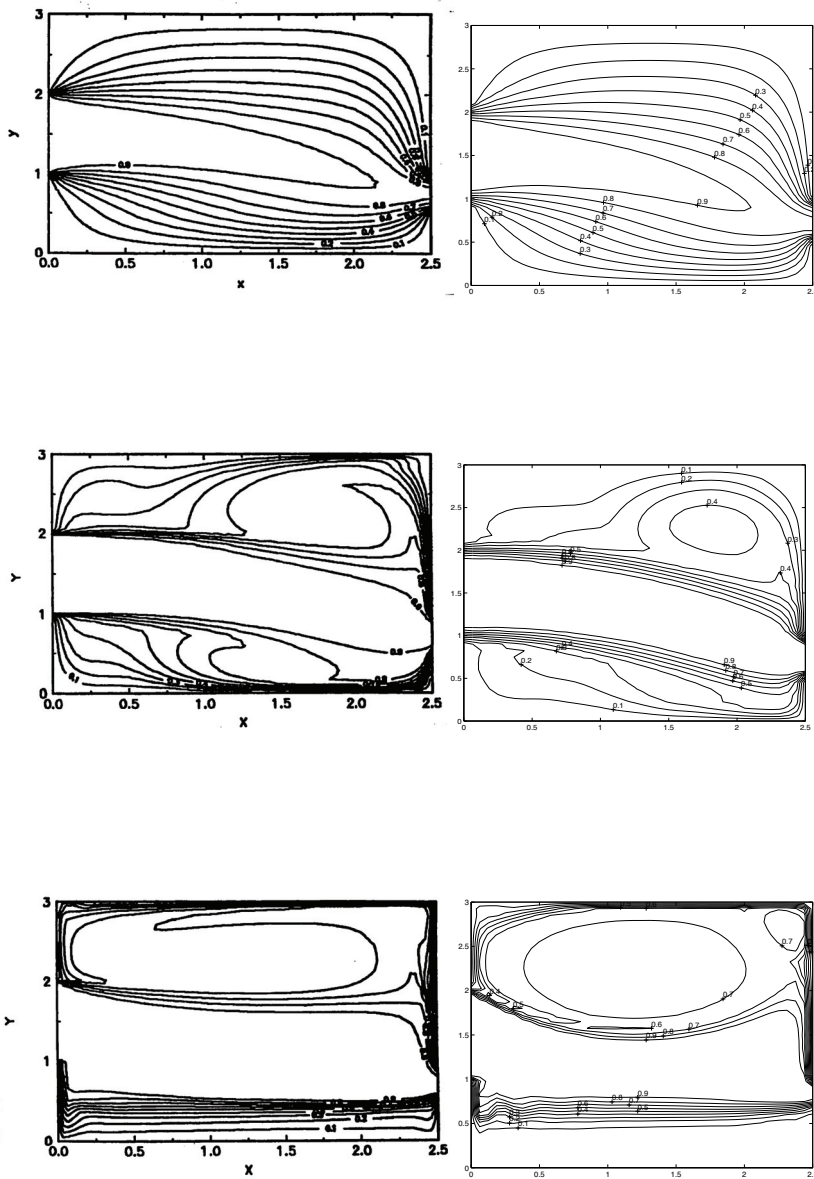


Figure 12. Dimensionless temperature contours comparison of the validated simulation results of [Sinha 2000] (left hand side) with the Comsol results (right hand side) for the 2D-airflow problem



The left-hand side shows the results obtained by (Sinha 2000) and the right side show the corresponding Comsol results. The verification results are satisfactory.

**4.1.3 2D wind surrounding a building and driving rain**

In addition to the above mentioned models, a new developed model concerning driving rain is presented now. The model is verified by another benchmark case of the mentioned IEA Annex 41 (2005), on boundary conditions. The benchmark covers for several building geometries: (a) Simulated wind velocity profiles around buildings; (b) Simulated raindrop trajectories; (c) Simulated wind-driving-rain coefficients on the building facades.

The solution of (a) is obtained by using the standard k-epsilon turbulence model of Comsol. Figure 13 shows the simulated wind profile around the lower building.

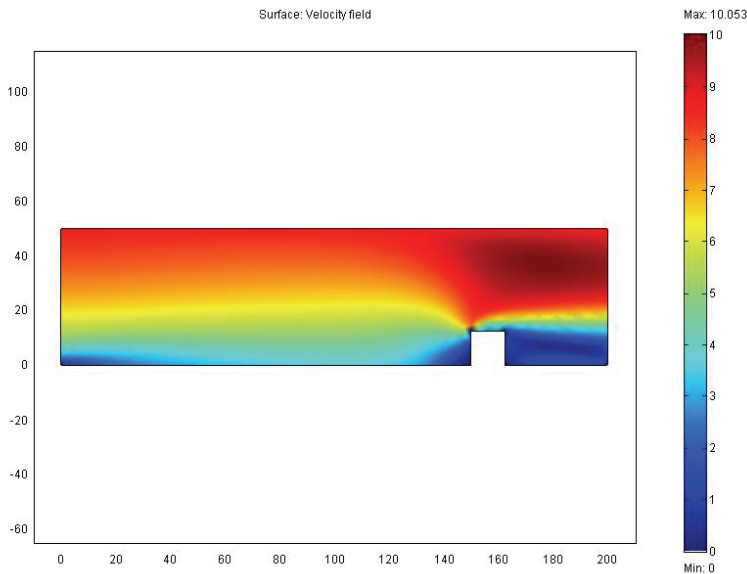


Figure 13. The wind velocity profile: absolute value of the velocity [m/s] for each coordinate x, y [m]

The solution of (b) is obtained from the equation of motion of a raindrop (Gunn & Kinzer (1949)), moving in a wind-flow field characterized by a velocity vector v:

$$g + f(Cd, Re) \cdot (v - \frac{dr}{dt}) = \frac{d^2r}{dt^2} \tag{7}$$

where g is gravity, f is a function dependent on Re (Reynolds number) and Cd (drag coefficient), v is wind velocity, t is time and r is the position of raindrop. Equation 2 is solved with the ODE solver of MatLab providing raindrop trajectories. The result for the low building benchmark case is shown in figure 14.

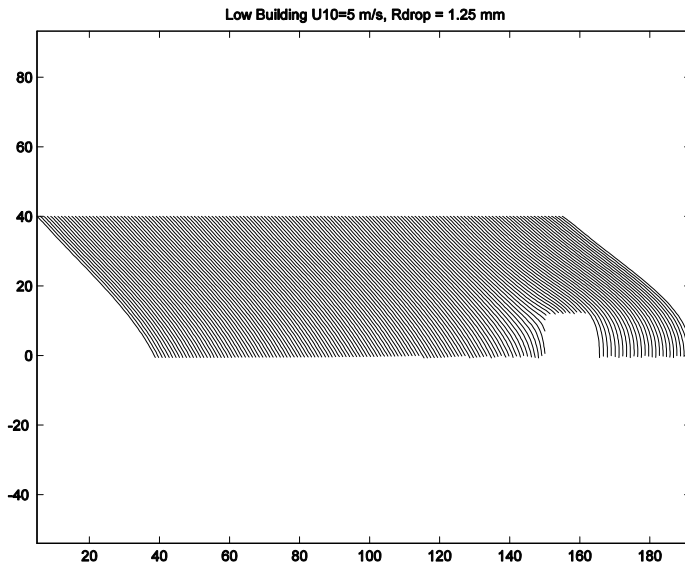


Figure 14. The raindrop trajectories

The solution of (c) is obtained from the locations of raindrops hitting the building façade. The preliminary results are in good agreement with the results obtained by a reference solution. This is shown in figure 15.

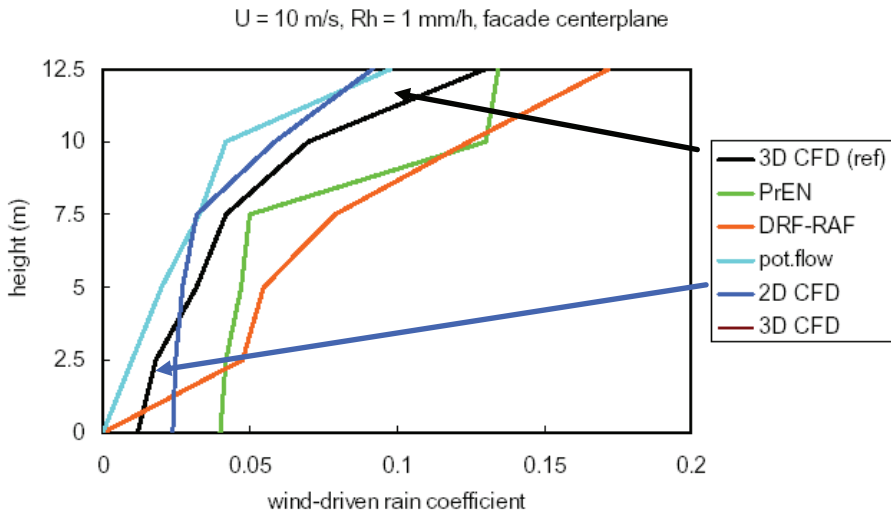


Figure 15. Wind-driven rain coefficient at the centre of the building (reference solution: 3D CFD, our solution: 2D CFD)

#### 4.1.4 Full 3D HAM modeling study

This Section demonstrates the integration of a 3D HAM model of a roof/wall construction into a whole building model. The geometry of the building is identical to one in [ASHRAE 2001]. HAMBase SimuLink is used as whole building model. Figure 16 shows the input/output structure of the integrated model.

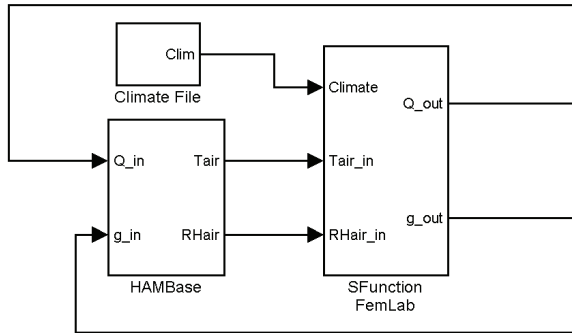


Figure 16. Input/output structure of the SimuLink model

The output (air temperature and RH) of this model and climate data are used as input for the Comsol model of a 3D roof/wall construction. The output of the Comsol model (heat and moisture flow) is connected to the input of the building model. The Comsol model is similar to the model presented in Section 3.4. Figure 17 and 18 demonstrate the 3D temperature and vapour distributions at a specific time.

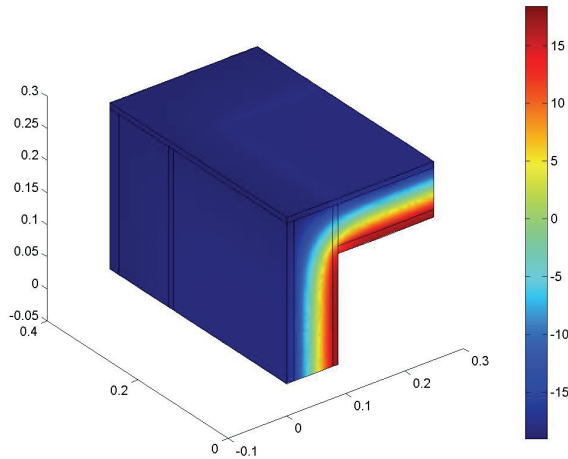


Figure 17. The temperature distribution: temperature [°C] for each coordinate x, y, z [m]

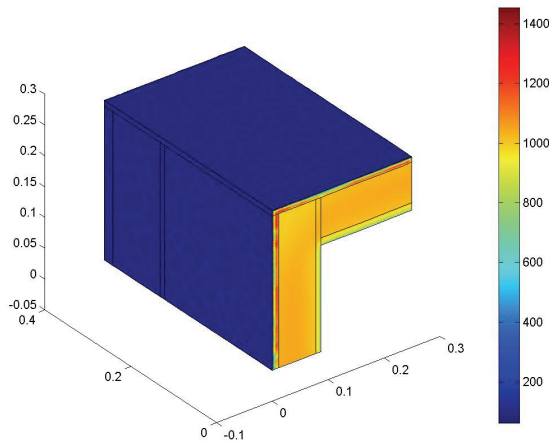


Figure 18. The vapour pressure distribution: vapour pressure [Pa] for each coordinate  $x, y, z$  [m]

The integrated model is capable of simulating the indoor climate and construction details within reasonable simulation time: 1 year simulation, takes about 12 hours of computation time (Pentium 4, 500MB)

#### 4.1.5 Discussion on reliability

The test cases in this Section show that Comsol is very reliable even for a highly non-linear problem such as convective airflow. Furthermore, for all the simulation results presented in this chapter, the default mesh generation and solver are used. So good results can be obtained without a deep understanding of the gridding and solving techniques. The simulation times (based on processor Pentium 3, 500 MHz) ranged from fast (order ~seconds) for linear problems such as the 2D thermal bridge example, medium (order ~minutes) for non linear problems in the coefficient form such as the 1D moisture transport example to high (order ~hours) for highly non linear problems in the general form such as the airflow problem.

#### 4.2 Integration and the lumped/distributed parameter problem

A second new development concerns the integration of a distributed parameter model and lumped parameter model in SimuLink. In this case study, the 2D airflow model of van Schijndel is implemented using the discrete part of an S-function. After each time step (in this case 1 sec) the solution is exported. Dependent on the controller, different boundary values can be applied. Furthermore, the airflow at the inlet is now controlled by an on/off controller with hysteresis (Relay) of SimuLink. The sensor temperature (lumped parameter) is calculated as mean of a several air temperature nodes (distributed parameter). If the temperature of the sensor above 20.5 °C the air temperature at the inlet is 17 °C if the air temperature is below 19.5 °C the inlet temperature is 22 °C. Initially the inlet temperature is 18 °C. Figure 19 gives an overview of the results.

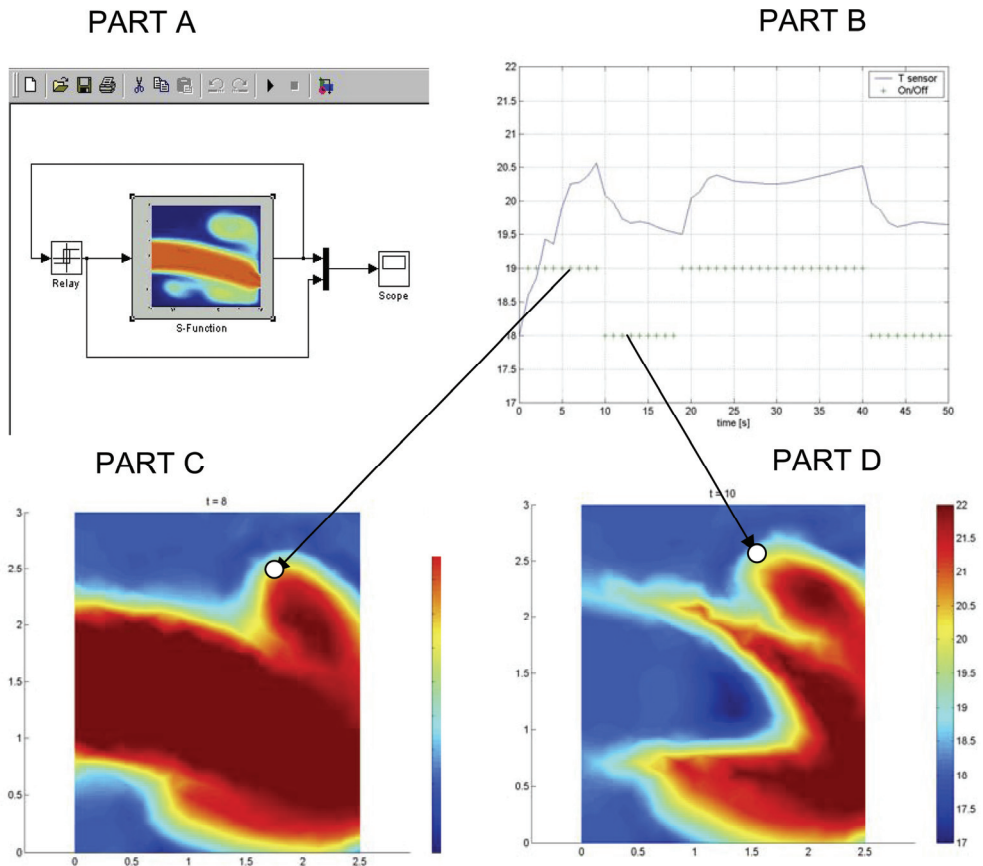


Figure19. Part A, The SimuLink model including the S-function of the Comsol model and controller (Relay), Part B, the temperature of the sensor (-) and the output of the on/off controller (+) versus time, Part C, the air temperature distribution at 8 sec. (hot air is blown in) and Part D, the air temperature distribution at 10 sec. (cold air is blown in) (o = sensor position)

Again the technical details are provided at the Appendix. From figure 19, it is clear that the controller has a great impact on the indoor airflow dynamics and temperature distribution. Many researchers perhaps overlook this phenomenon because most of the time, quasi steady airflow is assumed. This also shows the need of integrated models as presented here. Furthermore, we compared the amount of computational time used for solving the airflow problem to the rest of processes including calculation of the lumped parameter and the on/off controller. It turned out (as expected) that in this case most of the time (>98%) was consumed for solving exclusively the airflow problem.

## 5. Conclusion

It is concluded that the presented simulation environment Matlab/SimuLink/Comsol is capable of solving a large range of integrated HAM problems. Furthermore, it seems promising in accurately solving modelling problems that are caused by the presence of different time scales and/or lumped/distributed parameters. However, there are some limitations: (1) some specific solvers such as time-dependent k-epsilon turbulence solvers are not available yet. This means that, for example, time dependent 3D airflow around buildings cannot be integrated without external coupling; (2) Although it is possible to construct a full 3D integrated HAM model of the indoor air and all constructions in the simulation environment, the simulation duration time would probably be far too long to be of any practical use; (3) The modelling of radiation is not included in this research. The main benefits of our modelling approach are: (1) it takes advantage of the facilities of the well maintained Matlab/SimuLink and Comsol simulation environment such as the state-of-art ODE/PDE solvers, controllers library, graphical capabilities etc; (2) all presented models in this chapter are public domain; (3) although not explicitly shown in this chapter, compared to other HAM models, it is relative easy to integrate new models that are based on ODEs and/or PDEs. (4) the simulation facilitates open source modelling and if desired, models can be compiled into stand-alone (web) applications.

## 6. References & tools

- Augenbroe, G. (2002). Trends in building simulation, *Building and Environment* 37, pp.891-902
- ASHRAE (2001). Standard method of test for the evaluation of building energy analysis computer programs, *standard 140-2001*.
- Bednar, T. & C.E. Hagentoft. (2005). Analytical solution for moisture buffering effect; Validation exercises for simulation tools. *Nordic Symposium on Building Physics, Reykjavik 13-15 June 2005* pp. 625-632
- Brocken, H., 1998, Moisture transport in brick masonry, Ph.D. thesis, Eindhoven University of Technology
- Clarke J.A. (2001). Domain integration in building simulation, *Building and Environment* 33, pp. 303-308
- Crawley, D.B., Hand, J.W. Kummert, M. & Griffith B. (2005). Contrasting the capabilities of building performance simulation programs, *9<sup>TH</sup> IBPSA Conf. Montreal* pp 231- 238
- Djunaedy, E. (2005) External coupling between building energy simulation and computational fluid dynamics. *PhD thesis*, Technische Universiteit Eindhoven
- Felsmann C., Knabe G., Werdin H. (2002). Simulation of domestic heating systems by integration of TRNSYS in a MATLAB/SIMULINK model, *Proc. 6<sup>TH</sup> Int. Conference System Simulation in Buildings Liege, December 16-18*
- Gouda M.M., Underwood C.P., Danaher S. (2003). Modelling the robustness properties of HVAC plant under feedback control, *Building Serv. Eng. Res. Techn.* 24,4 pp. 271-280
- Gough M.A. (1999). A review of new techniques in building energy and environmental modelling, No. BREA-42. Garston, Watford, UK: Building Research Establishment.
- Gunn, R. & G.D. Kinzer (1949). The terminal velocity of fall for water droplets in stagnant air. *Journal of Meteorology* 6 pp. 243-248

- Hagentoft C.E. and 13 other authors. (2002). HAMSTAD - Final Report,, *Report R-02:8*, Chalmers Univ. of Tech., Sweden
- Hensen, E. Djunaedy, M. Radosevic, A. Yahiaoui. (2004), Building performance simulation for better design: some issues and solutions, *21TH PLEA Conference Eindhoven*, pp.1185-1190
- Christina Hopfe, Christian Struck1, Petr Kotek, Jos van Schijndel1, Jan Hensen and Wim Plokker (2007) uncertainty analysis for building performance simulation; a comparison of four tools *Proceedings: Building Simulation 2007*
- IEA Annex 41 (2005). <http://www.ecbcs.org/annexes/annex41.htm>
- Judkoff, R. and Neymark, J. (1995). International energy agency building energy simulation test (BESTEST) and diagnostic method, National Renewable Energy Laboratory, Golden, CO.
- Kunzel H.M., (1996). IEA Annex 24 HAMTIE, *Final Report - Task 1*
- Rieder P. (2005) MatLab/SimuLink for building and HVAC simulation - state of art. *9TH Int. IBPSA Conference Montreal 2005*, pp1019-1026
- Sasic Kalagasidis, (2004) HAM-Tools; An Integrated Simulation Tool for Heat, Air and Moisture Transfer Analyses in Building Physics, *PhD thesis*, Chalmers Univ. of Techn.
- Sahlin P. Eriksson L., Grozman P., Johnson H., Shapovalov A. Vuolle M.( 2004). Whole-building simulation with symbolic DAE equations and general purpose solvers. *Building and Environment 39*, pp. 949-958.
- Schellen, H.L. (2002), Heating Monumental Churches, Indoor Climate and Preservation of Cultural heritage; *PhD thesis*, Eindhoven University of Technology.
- Schijndel, A.W.M. van & Wit, M.H. de, (1999), A building physics toolbox in MatLab, *7TH Symposium on Building Physics in the Nordic Countries Goteborg*, pp81-88
- Schijndel A.W.M. van (2003a). Modeling and solving building physics problems with FemLab, *Building and Environment 38*, pp 319-327
- Schijndel A.W.M. van, Schellen, H.L., Neilen D. (2003b). Optimal setpoint operation of the climate control of a monumental church, *2ND international conf. on research in building physics, Leuven*, Sept. 14-18 2003, pp. 777-784
- Schijndel A.W.M. van, Wit M.H. de (2003c). Advanced simulation of building systems and control with SimuLink, *8TH IBPSA Conference Eindhoven*. pp. 1185-1192
- Schijndel, A.W.M. van (2003d). Integrated building physics simulations with FemLab/SimuLink /Matlab, *8TH Int. IBPSA Conference, Eindhoven*, pp. 1177-1184
- Schijndel A.W.M. van 2004. Advanced use of HAMLab on CE1, Annex 41 *preliminary chapter TUE Oct 2004 Chapter A41-T1-NL-04-5*, available in 2008.
- Schijndel A.W.M. van, Schellen H.L. (2005). Application of an integrated indoor climate & HVAC model for the indoor climate design of a museum, submitted for the *7TH symposium on building physics in the Nordic Countries*, 13-15 June 2005, Iceland
- Schijndel A.W.M. van (2007), Integrated Heat Air and Moisture Modeling and Simulation, *PhD thesis*, Eindhoven University of Technology, ISBN: 90-6814-604-1, 200 pages
- Schwab M. and Simonson C.J. 2004. Review of building energy simulation tools that include moisture storage in building materials and HVAC systems, Annex 41 *preliminary chapter A41-T2-C-04-6*, available in 2008.
- Sinha S.L. 2000. Numerical simulation of two-dimensional room air flow with and without buoyancy, *Energy and Buildings 32* pp121-129

- U.S. Department of Energy, 2008 <http://www.eere.energy.gov/>
- Wit M.H. de ,H.H. Driessen 1988, ELAN A Computer Model for Building Energy Design. *Building and Environment, Vol.23,4*, pp. 285-289
- Wit, M.H. de, 2006, HAMBBase, Heat, Air and Moisture Model for Building and Systems Evaluation, *Bouwstenen 100*, ISBN 90-6814-601-7 Eindhoven University of Technology
- BSIM 2008. <http://www.bsim.dk/>
- COMSOL 2008. <http://www.comsol.com/>
- Energyplus 2008. <http://www.eere.energy.gov/>
- Fluent 2008. <http://www.fluent.com/>
- HAMLab 2008. <http://sts.bwk.tue.nl/hamlab/>
- IES VE 2008 <http://www.iesve.com>
- IBPT 2008. <http://www.ibpt.org/http://www.iesve.com>
- IDA ICE 2008. <http://www.equa.se/ice/intro.html>
- Matlab 2008. <http://www.mathworks.com/>
- SIMBAD 2008. <http://software.cstb.fr/>
- TRNSYS 2008. <http://sel.me.wisc.edu/trnsys/>
- VABI 2008 <http://www.vabi.nl/>

## 7. Appendix

In the appendix, technical details of the implementation of the models are given. This additional information provides the relation between mathematical model and code needed to reproduce our results. A complete example how to model a system of ODEs with an S-function of SimuLink is shown for the heat pump model. The first step is to define the input-output definition of the model. This is presented in Table 2.

Name	Input (u) / Output (y)	Description
$T_{vin}$	u(1)	Incoming water temperature at the evaporator [°C]
$F_{vin}$	u(2)	Incoming mass flow at the evaporator [kg/s]
$T_{cin}$	u(3)	Incoming water temperature at the condenser [°C]
$F_{cin}$	u(4)	Incoming mass flow at the condenser [kg/s]
Ehp	u(5)	Power of electrical supply [W]
k	u(6)	efficiency [-]
$T_{vout}$	y(1)	Outgoing water temperature at the evaporator [°C]
$T_{cout}$	y(2)	Outgoing water temperature at the condenser [°C]
COP	y(3)	Coefficient Of Performance [-]

Table 2. The input-output definition of the heat pump model

The second step is to formulate a mathematical model by a system of ODEs. This is done using (1). The third step is to implement the mathematical model into a S-function, a programmatic description of a dynamic system. Details about this subject can be found in MatLab 2008. Figure 20 shows the corresponding SimuLink model. Figure 21 provides the complete program code.



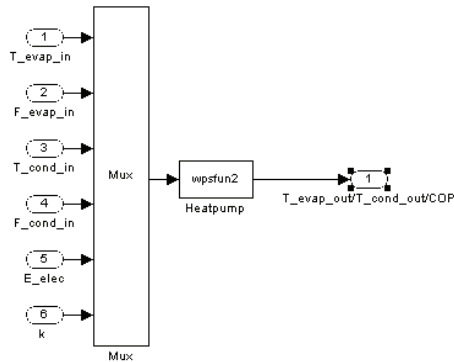


Figure 20. The input-output structure in SimuLink

```

function [sys,x0,str,ts] = wpsfun2(t,x,u,flag)
    %WPSFUN2 Heat pump
    %u(1)=Tvin [oC], u(2)=Fvin [kg/s], u(3)=Tcin [oC],
    %u(4)=Fcin [kg/s], u(5)=Ehp [W], u(6)=k [-]
    %y(1)=Tvout [oC] (=x(1)), y(2)=Tcout [oC] (=x(2))
    %y(3)=COP
    switch flag ... end
function [sys,x0,str,ts]=mdlInitializeSizes
    sizes.NumContStates = 2; % Number of Cont. states
    sizes.NumDiscStates = 0; % Number of Disc. states
    sizes.NumOutputs = 3; % Number of Outputs
    sizes.NumInputs = 6; % Number of Inputs
    x0 = [10; 10]; % Initial values
function sys=mdlDerivatives(t,x,u)
    Tvm=(u(1)+x(1))/2;
    Tcm=(u(3)+x(2))/2;
    COP=u(6)*(273.15+Tcm)/(Tcm-Tvm);
    Cc=200000;Cv=200000;cv=4200;cc=4200;
    xdot(1)=(1/Cv)*(u(2)*cv*(u(1)-x(1))-(COP-1)*u(5));
    xdot(2)=(1/Cc)*(u(4)*cc*(u(3)-x(2))+COP*u(5));
    sys = [xdot(1); xdot(2)];
function sys=mdlOutputs(t,x,u)
    Tvm=(u(1)+x(1))/2; Tcm=(u(3)+x(2))/2;
    COP=u(6)*(273.15+Tcm)/(Tcm-Tvm);
    sys = [x(1); x(2); COP];

```

Figure 21. The contents of the S-Function for the heat pump model

The main part of program code (with comments) to integrate an airflow model into SimuLink using a S-functions is provided in figure 22.

```

function [sys,x0,str,ts] = dsfun(t,x,u,flag)
% t: time; x = state vector ; u = input vector;
% flag = control parameter by SimuLink
global OutT Outsol
% specify variable 'fem': the Comsol model geomtry, mesh,
% PDE coefficients and boundary conditions
switch flag,
    case 0,
        [sys,x0,str,ts] = mdlInitializeSizes(fem,tstap,u0);% Initialization %
    case 2,
        sys = mdlUpdate(t,x,u,fem,tstap); %update discrete part
    case 3,
        sys = mdlOutputs(t,x,u,fem,tstap); %produce output
    case 9,
        sys = []; %terminate
    end %end dsfunc
function [sys,x0,str,ts] = mdlInitializeSizes(fem,tstap,u0)
global OutT Outsol
% calculated the next values needed for SimuLink
% calculated initial values for time OutT(1) and
% initial values for solution Outsol(1)
% x0 are all values of the temperature on the mesh
OutT(1)=0;
Outsol(1)=x0;
function sys = mdlUpdate(t,x,u,fem,tstap)
global OutT Outsol
if u(1)>0.5 % if dimensionless Temperature of sensor > 0.5 then
    fem.bnd.r={    {'-u1'; '-u2';0 ;'0-u4'} ... %boundary value cold air
else
    fem.bnd.r={    {'-u1'; '-u2';0 ;'1-u4'} ... % bounadry value hot air
end
tjtd=[t; t+tstap/2; t+tstap]; %calculate simulatetime for Comsol model
fem.sol=femtime(fem,'atol',{1,1,Inf,1}),'ode','fldae',...
    'sd','on','report','on','tlist',tjtd,'init',x); %simulate airflow
OutT=[OutT (t+tstap)]; % update time
Outsol=[Outsol fem.sol.u(:,ntjtd)]; % update solution
function sys = mdlOutputs(t,x,u,fem,tstap)
global OutT Outsol
Points=[69 84 101 167 188 211 259 261]; % location of sensor in mesh
sys=mean(x(Points)); % output

```

Figure 22. Example of the implementation of a Comsol model in the discrete section of a S-function of SimuLink

# Numerical Simulation of Turbulent Air Flows in Aseptic Clean Rooms

Eleonora Bottani, Roberto Rizzo and Giuseppe Vignali  
*Department of Industrial Engineering, University of Parma  
 Italy*

## 1. Introduction

Sterile air condition is an increasingly important requirement, as several manufacturing processes, such as food production, preparation of aseptic products for the pharmaceutical industry, manufacturing of microelectronics components, compact discs and photographic films, need optimal air cleaning.

Aseptic clean rooms were developed to satisfy the above requirement. According to Wirtanen et al. (2002), a clean room can be defined as “a room in which the concentration of airborne particles is controlled, and which is constructed and used in a manner to minimize the introduction, generation, and retention of particles inside the room, and in which other relevant parameters, e.g. temperature, humidity, and pressure, are controlled as necessary”. The objective of clean room technology in various clean room classes in the food and beverage industry is to ensure the control of contaminants in sensitive processes. Use of this technology should be considered in processes where microbial inactivation, e.g. through thermal sterilization or deep freezing, is not feasible. If critical process risks are identified due to exposure of the product to airborne microbes during processing or if severe sedimentation of airborne microbes can occur on critical process surfaces, clean room technology can be used to solve the problems (Schicht, 1999; Whyte, 2001). In an aseptic clean room, the air flow, properly filtered, is flushed from the top of the chamber to special grids placed at the bottom of the structure. Then, it is recirculated by an air filtering unit; here, part of the air flow is ejected and replaced by external air that will undergo filtration. A main requirement of clean rooms is that they are maintained at a pressure higher than the external one, to prevent pollutants air flow from the environment.

Currently accepted standards describing clean rooms are developed by the Federal Standard (Federal Standard 209 E, 1992) and adopted by ISO (2006); such standards suggest an international classification of clean rooms, based on thirteen possible classes depending on the maximum allowed number of pollutant particles in the room. Eq.1 provides an empirical relation between the aseptic class  $M$  and the diameter of the pollutant particles  $d$  [mm] in the room:

$$\text{Particles/m}^3 = 10 M (0.5/d)^{2.2} \quad (1)$$

When designing an aseptic room, special care should be taken to ensure a well distributed flow of relatively dry, high-efficiency particulate air (HEPA) filtered air along walls,

windows and ceiling. Due to its characteristics, the aseptic room can involve laminar unidirectional or turbulent non-unidirectional air flows. In both cases, air flow within the clean room area is an important factor in the precise control of air over the container into which food products are assembled (Wirtanen et al., 2002).

Previous studies have examined several aspects of the air flow in the clean room, such as the influence of air velocity on contamination control as a function of room characteristics (e.g. Ogawa, 2000) or factors affecting airflow in clean rooms (e.g. Fitzpatrick, 1994). Moreover, in the last decade, many research works proposed numerical models to predict the clean room air flow (Divelbiss & Winter, 1995; Cheng et al., 1999; Chen et al., 2007). Thanks to the increasing performance of PC, the numerical analysis of the flow behavior inside indoor environments became more detailed and refined. In particular, several commercial CFD packages allow analyzing 3-dimensional fields using several solver methods (Norton & Sun, 2006).

In this chapter, we focus on developing a simulation model to reproduce and analyze the flow of sterile air within an aseptic clean room in the case of a non-unidirectional fluid flow. The analyzed clean room is used in aseptic beverage bottling, to perform sterilization of bags containing High Density Poly-Ethylene (HDPE) caps, by flushing hydrogen peroxide vapor. Hence, the analysis carried out aims at developing a tool that can be usefully exploited to improve the sterilization ability of the aseptic clean rooms at the design phase, with a particular focus on optimizing sterile air circulation inside the room.

This chapter is organized as follows. In the next section, we provide some theoretical fundamentals about turbulent flow modeling. To adequately reproduce the turbulent air flows in the aseptic room and to ensure correspondence with real aseptic plants, in developing the simulation tool two possible turbulence models are considered, namely the  $k-\epsilon$  (Launder & Spalding, 1974) and the  $k-\omega$  (Wilcox, 1988) models, which are detailed in that section. Then, the model developed and the settings are presented. In section 4, we provide validation of the model based on experimental data and analyze the turbulent flow behavior. In the conclusion section a brief discussion about the two turbulence models adopted and future research directions are presented.

## 2. Turbulent flow modeling

### 2.1 Introduction

A turbulent flow is a chaotic process, which is difficult to describe in details. For this purpose, Reynolds (1883) introduced a decomposition of the flow parameters, considering average values and their fluctuation, this latter resulting from turbulence. Based on this approach, a generic parameter  $\varphi$  can be quantified starting from its average value  $\Phi$  measured during a defined time interval  $\Delta t$ , and its fluctuating part, i.e.:

$$\varphi = \varphi'(t) + \Phi \quad (2)$$

Both components of  $\varphi$  can be obtained from averaging equations, usually referred to as "Reynolds Averaging Navier-Stokes" (RANS) equations, resulting from the integration in time of the parameter examined. The integration time  $T$  ("averaging time") should be carefully chosen, to be sufficiently larger than the turbulent time interval, but at the same time small enough so as relevant information about the fluctuation of the fluid in time is not missed.

Following eq.2, the instantaneous velocity of a point  $u_i(\bar{x},t)$  can be written as the sum of an average value  $\bar{u}_i(\bar{x})$  and a variable one  $u_i'(\bar{x},t)$ , according to the following formula:

$$u_i(\bar{x},t) = \bar{u}_i(\bar{x}) + u_i'(\bar{x},t) \tag{3}$$

where  $\bar{u}_i(\bar{x})$ , in turn, is defined as:

$$\bar{u}_i(\bar{x}) = \frac{1}{T} \int_t^{t+T} u_i(\bar{x},t) dt \tag{4}$$

being  $T$  the averaging time. Some of the properties of the above formulae are described in the following equations:

$$\overline{\bar{u}_i(\bar{x})} = \frac{1}{T} \int_t^{t+T} \bar{u}_i(\bar{x}) dt = \bar{u}_i(\bar{x}) \tag{5}$$

$$\overline{u_i'(\bar{x},t)} = 0 \tag{6}$$

Hence, the average of the  $\bar{u}_i(\bar{x})$  parameter equals the average of the velocity  $u_i(\bar{x},t)$ , and the average value of the fluctuating component  $u_i'(\bar{x},t)$  is null.

Applying the averaging approach to the mass equation, the following formula is derived:

$$0 = \frac{\partial \bar{\rho}}{\partial t} + \frac{\partial \bar{\rho} \bar{u}_i}{\partial x_i} + \frac{\partial \bar{\rho}' u_i'}{\partial x_i} \tag{7}$$

From eq.7, it can be seen that a new parameter  $\bar{\rho}' u_i'$  should be added in the computation. To derive the fluctuations in density, in the case of compressible fluids, the approach proposed by Favre (1969), suggests computing the weighted average of velocity, being weight the fluid density. Eq.8 summarises the computation:

$$\tilde{u}_i(\bar{x}) = \frac{1}{\bar{\rho}} \int \rho(\bar{x},t) u_i(\bar{x},t) dt \tag{8}$$

where  $\bar{\rho}$  [kg/m<sup>3</sup>] is the average value of density computed according to Reynolds (1883). Moreover, the velocity  $u_i(\bar{x},t)$  can be rewritten as:

$$u_i(\bar{x},t) = \tilde{u}_i(\bar{x}) + u_i''(\bar{x},t) \tag{9}$$

Combining the above formula with eq.7, the following expressions are derived:

$$\frac{\partial \bar{\rho}}{\partial t} + \frac{\partial \bar{\rho} \cdot \tilde{u}_i}{\partial x_i} = 0 \tag{10}$$

$$\frac{\partial(\bar{\rho} \cdot \tilde{u}_i)}{\partial t} + \frac{\partial(\bar{\rho} \cdot \tilde{u}_i \cdot \tilde{u}_j)}{\partial x_j} = - \frac{\partial \bar{p}}{\partial x_i} + \frac{\partial(\mu \cdot \nabla \tilde{u}_i)}{\partial x_j} - \frac{\partial(\bar{\rho} \cdot u_i'' \cdot u_j'')}{\partial x_j} + S_{M_i} \tag{11}$$

The above equations can be solved applying the average values defined by Favre (1969), except the  $\bar{\rho} \cdot u_i'' \cdot u_j''$  parameter, known as Reynolds "stress", which should be defined

starting from the boundary conditions of the case examined. In the case of turbulent flows, in particular, all terms should be modelled to derive a solution describing the average values of the fluid motion. To this extent, several turbulence models were proposed, whose applicability depends on the level of detail required and on the value of the Reynolds number.

Turbulence models grounds on the assumption that, under high Reynolds number, the fluid energy substantially increases, and could not be dissipated during flow; hence, the fluid experiences a macroscopic destabilization, which leads to vortices formation and to energy transfer from larger to smaller vortices. Under this flow regime, the system can be described by the energy transfer between vortices, which is measured by means of the dissipation  $\varepsilon$  [ $\text{m}^2/\text{s}^3$ ] and by the turbulent kinetic energy  $k$  [ $\text{J}/\text{kg}$ ]. The formal definition of  $\varepsilon$  is provided by the following equation:

$$\varepsilon = \frac{u'^2}{L} \quad (12)$$

being  $L$  [m] the length measurement scale and  $u'$  [ $\text{m}/\text{s}^2$ ] the fluctuation of the velocity in time. The Reynolds number referred to the measurement scale of the above system is defined as:

$$R_{eL} = \frac{u'L}{\nu} \quad (13)$$

being  $\nu$  [ $\text{m}^2/\text{s}$ ] the kinematic viscosity of the fluid. During energy transfer, the Reynolds number  $R_{eL}$  significantly decreases, reaching values close to one, this latter corresponding to the situation where inertia and viscous forces are almost balanced. The Kolmogorov scale  $\eta_k$  (Kolmogorov, 1941) was introduced to identify microscopic turbulent flows that occur in this latter case; the scale is defined as:

$$\eta_k = \left( \frac{\nu^3}{\varepsilon} \right)^{\frac{3}{4}} \quad (14)$$

and corresponds to a unitary Reynolds number, according to the following computation:

$$R_{e\eta k} = \frac{\varepsilon^{\frac{1}{3}} \eta_k^{\frac{4}{3}}}{\nu} = 1 \quad (15)$$

The ratio between macroscopic and microscopic flows can be expressed as:

$$\frac{L}{\eta_k} = R_{eL}^{\frac{3}{4}} \quad (16)$$

## 2.2 Two-equation turbulence models

In most practical cases, eq.11 is solved applying turbulence models grounded on the Boussinesq assumption (Rajagopal et al., 1996), stating that Reynolds "stress" can be expressed as per the following formula:

$$-\overline{\rho u_i u_j} = \mu_t \left( \frac{\partial u_i}{\partial x_j} + \frac{\partial u_j}{\partial x_i} \right) - \frac{2}{3} \left( \rho k + \mu_t \frac{\partial u_i}{\partial x_i} \right) \delta_{ij} \quad (17)$$

Eq.17 describes the Reynolds “stress” based on a fluctuating value, which is related to the average value by introducing the turbulent viscosity  $\mu_t$  [kg/m<sup>2</sup>/s].

Two-equation models are all grounded on the equation describing the transport of kinetic energy  $k$ , and on an additional formula, describing a further system characteristic. In this chapter, we focus on models describing either the dissipation  $\varepsilon$  or the specific dissipation rate  $\omega$  [1/s]. Such models have emerged from the literature as the most widely adopted in similar studies (Kuznik et al., 2007).

### The standard $k$ - $\varepsilon$ model

The  $k$ - $\varepsilon$  model (Launder & Spalding, 1974) is one of the most widely adopted approaches for turbulent flow simulation under commercial software packages. In this model, the turbulent viscosity  $\mu_t$  is computed according to the following formula:

$$\mu_t = \rho C_\mu \frac{k^2}{\varepsilon} \quad (18)$$

where the kinetic energy  $k$  and the dissipation  $\varepsilon$  are derived from the resolution of the following set of equations:

$$\frac{\partial}{\partial x_j} (\rho u_j k) = \frac{\partial}{\partial x_j} \left[ \frac{\mu_{eff}}{\sigma_k} \frac{\partial k}{\partial x_j} \right] + \mu_t \left( \frac{\partial u_i}{\partial x_j} + \frac{\partial u_j}{\partial x_i} \right) \left( \frac{\partial u_i}{\partial x_j} \right) - \rho \varepsilon \quad (19)$$

$$\frac{\partial}{\partial x_j} (\rho u_j \varepsilon) = \frac{\partial}{\partial x_j} \left[ \frac{\mu_{eff}}{\sigma_\varepsilon} \frac{\partial \varepsilon}{\partial x_j} \right] + C_{\varepsilon 1} \frac{\varepsilon}{k} \mu_t \left( \frac{\partial u_i}{\partial x_j} + \frac{\partial u_j}{\partial x_i} \right) \left( \frac{\partial u_i}{\partial x_j} \right) - \rho C_{\varepsilon 2} \frac{\varepsilon^2}{k} \quad (20)$$

$$\mu_{eff} = \mu + \mu_t \quad (21)$$

being  $\mu$  the molecular viscosity,  $\mu_t$  the turbulent viscosity of the fluid. The  $C_i$  and the  $\sigma_i$  parameters are set to the following values:  $\sigma_k=0.9$ ;  $\sigma_\varepsilon=1.30$ ;  $C_{\varepsilon 1}=1.44$ ;  $C_{\varepsilon 2}=1.92$ ;  $C_\mu=0.09$  (Cheng et al., 1999).

### The standard $k$ - $\omega$ model

The  $k$ - $\omega$  model (Wilcox, 1988) differs from the previous one in that it takes into account the specific dissipation rate  $\omega$  instead of the dissipation  $\varepsilon$ . The dissipation rate is defined as a function of the dissipation  $\varepsilon$  as:

$$\omega = \frac{\varepsilon}{k\beta^*} \quad (22)$$

According to Wilcox (1988), the computation of  $\omega$  instead of  $\varepsilon$  allows the model to better reproduce the fluid behavior close to the system boundaries. Eqs.23-25 are exploited in the model to derive the  $k$  and  $\omega$  parameters:

$$\frac{\partial k}{\partial t} + u_j \frac{\partial k}{\partial x_j} = \tau_{ij}^R \frac{\partial \bar{u}_i}{\partial x_j} - \beta^* k \omega + \frac{\partial}{\partial x_j} \left[ (\mu + \sigma \mu_t) \frac{\partial k}{\partial x_j} \right] \quad (23)$$

$$\frac{\partial \omega}{\partial t} + u_j \frac{\partial \omega}{\partial x_j} = \alpha \frac{\omega}{k} \tau_{ij}^R \frac{\partial \bar{u}_i}{\partial x_j} - \beta \omega^2 + \frac{\partial}{\partial x_j} \left[ (\mu + \sigma \mu_t) \frac{\partial \omega}{\partial x_j} \right] \quad (24)$$

$$\mu_t = \frac{k}{\omega} \quad (25)$$

$\tau_{ij}^R$  in eqs.23-24 indicates the components of the Reynolds stress tensor.  $\alpha$ ,  $\beta$ ,  $\beta_0$ ,  $\sigma$ ,  $\chi_{\omega r}$ ,  $\chi_{k r}$ ,  $f_{\beta}$  are empirical coefficients whose values are set by the software used for numerical simulations (Comsol Inc., 2005; Wilcox, 1998).

### 3. Model development

The simulation tool to reproduce the flow of sterile air inside the clean room is based on a Finite Element Method (FEM) numerical model, developed under COMSOL Multiphysics release 3.3 (Comsol Inc.) commercial package. Specifically, the RANS formulation of Navier-Stokes equations (eqs.10-11), implemented in the "Chemical Engineering Module" of COMSOL Multiphysics, is adopted to describe the fluid motion. The simulation model was run on a 2.4 GHz Pentium IV PC, with 2Gb RAM memory, under Windows XP professional platform.

The volume of the clean room examined is 2.786x2.786x1.5 m<sup>3</sup>. The air flow is flushed in the room from four filters, whose size is 0.61x0.61 m<sup>2</sup>, sited at the top of the chamber. As many exit grids are located on the chamber walls. These latter are partially covered, to ensure that the air flow does not immediately exit the chamber. Figure 1 shows a picture of the chamber geometry developed under COMSOL Multiphysics.

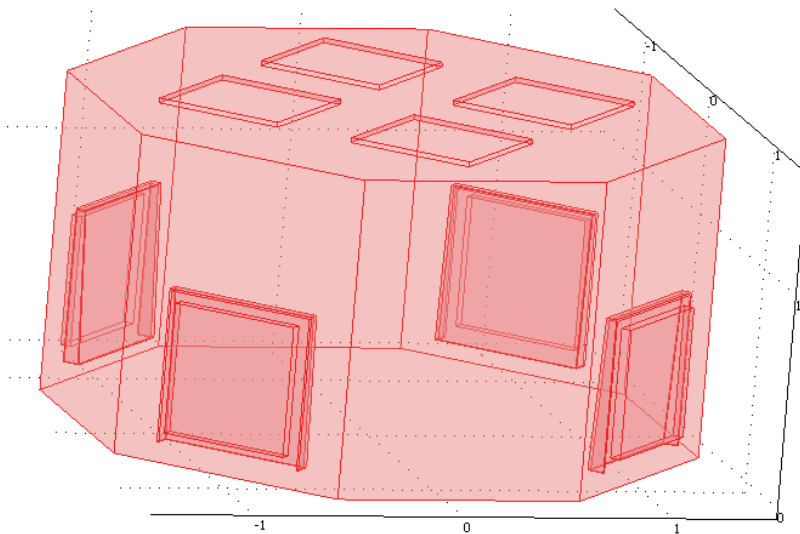


Figure 1. Domain of the model developed

The mesh used to solve the flow equations for the aseptic room consists of 7,555 elements, yielding approximately 66,817 degrees of freedom.



To reduce memory consumption, the GRMES (Generalised Minimum RESidual) indirect iterative solver has been adopted to solve the air flow equations in the aseptic room. Steady state nonlinear analysis and time-dependent iterative solver were exploited to solve the equations of the model.

### 3.1 $k$ - $\varepsilon$ boundary settings

#### Inlet surfaces

Boundary settings of the  $k$ - $\varepsilon$  model were defined as follows. For inlet surfaces, a uniform velocity distribution was assumed, whose value  $U$  was set to  $-0.542$  m/s along the  $z$ -axis (i.e. on the vertical direction). This value, corresponding to the typical velocity of an operating clean room, was derived from the air flow entering the chamber, accounting for  $2,900$  m<sup>3</sup>/h and the surface of the entering grid.  $k$  and  $\varepsilon$  values for the grid surface were set to the following values:

$$k = 1.5 \cdot (UI_T)^2 \quad (26)$$

$$\varepsilon = C_\mu^{0.75} \cdot k^{1.5} / L_T \quad (27)$$

being  $U$  the flow velocity [m/s] and  $I_T=0.054$  and  $L_T=0.07$  the turbulence intensity and length scales, respectively. Numerical values for  $I_T$  and  $L_T$  were derived from the software user's guide (Comsol Inc., 2005).

#### Outlet surfaces

For outlet surfaces, we set the atmospheric pressure as boundary condition. Moreover, the following conditions were set for the  $k$  and  $\varepsilon$  values:

$$\mathbf{n} \cdot \nabla k = 0 \quad (28)$$

$$\mathbf{n} \cdot \nabla \varepsilon = 0 \quad (29)$$

#### Wall surfaces

In the case of turbulent flows in a confined space, numerical results significantly depend on the model settings for surfaces close to the system walls. Those surfaces, in fact, are more likely to be affected by vortices or turbulence formation, resulting in a rapid fluctuation of the model parameters. In this regard, two procedures can be followed to set the model parameters for the system walls. A first approach suggests modifying the model settings so that the flow parameters can be easily computed; in particular, as the model parameters can rapidly change, the number of cells used for the computation should be sufficiently increased, if compared with other points of the domain, to capture those fluctuations. This may correspondingly increase the computational time.

In this study, we follow the "wall function" approach, which suggests keeping the turbulence model unchanged even for surfaces close to the system wall; as a result, the effect of viscous flows is neglected in the computation. Hence, the model setting requires the first mesh nodes to be located at a sufficient distance from the wall, so as for intermediate points the logarithmic wall function can be used for the computation of velocity.

Accordingly, the logarithmic wall function was applied as boundary condition for the room walls; as a result, the normal component of the velocity is set to zero, i.e.:

$$\mathbf{n} \cdot \mathbf{U} = 0 \quad (30)$$

To take into account the tangential component of the velocity  $U_T$ , a friction force at the room wall is introduced, which is defined by the following set of equations:

$$\tau_w = \frac{\rho C_\mu^{1/4} k^{1/2}}{\frac{1}{\kappa} \ln(y^+) + C} U_T \quad (31)$$

$$y^+ = \frac{\delta_w \rho C_\mu^{1/4} k^{1/2}}{\eta} \quad (32)$$

being  $\delta_w$  [m] the distance from the wall and  $C$  a parameter describing the surface roughness. The numerical values of those parameters were set to the mesh size (corresponding to the default setting of COMSOL) and to 5.5, respectively.  $\kappa$  is the von Karman constant ( $\kappa \approx 0.418$ ). For the remaining parameters, the logarithmic wall function involves the following boundary conditions:

$$\mathbf{n} \cdot \nabla k = 0 \quad (33)$$

$$\varepsilon = \frac{C_\mu^{3/4} k^{3/2}}{\kappa \delta_w} \quad (34)$$

### 3.2 $k$ - $\omega$ settings

#### Inlet surfaces

The settings of the  $k$ - $\omega$  model were defined following a similar procedure. More precisely, as per the previous model, for inlet boundaries a uniform velocity distribution was assumed, with the same numerical value  $U$  of -0.542 m/s along the  $z$ -axis.

$k$  and  $\omega$  values for the inlet surfaces were defined based on the following equations:

$$k = 1.5 \cdot (U I_T)^2 \quad (35)$$

$$\omega = \frac{C_\mu^{-0.25} \cdot k^{0.5}}{L_T} \quad (36)$$

where the  $I_T$  and  $L_T$  parameters were set to the same values of the  $k$ - $\varepsilon$  model (Comsol Inc., 2005).

#### Outlet surfaces

As per the previous model, for outlet surfaces, we set the atmospheric pressure as boundary condition. Moreover, the following condition was set for the  $k$  and  $\omega$  values:

$$\mathbf{n} \cdot \nabla k = 0 \quad (37)$$

$$\mathbf{n} \cdot \nabla \omega = 0 \quad (38)$$

#### Wall surfaces

As per the previous model, the logarithmic wall function was exploited to examine the fluid flow for wall surfaces. Accordingly, the same conditions described in eqs.30 and 33 were

defined in the model. In this case, however, the  $\omega$  parameter is defined instead of  $\varepsilon$ . The following equation is adopted to this extent:

$$\omega = \frac{C_{\mu}^{-0.25} k^{0.5}}{\kappa \delta_w} \tag{39}$$

## 4. Results and discussion

### 4.1 Data collection

To validate the simulation tool developed, an appropriate experimental campaign has been performed to derive data that could be compared with simulation outcomes provided by the model developed. To collect data, a prototypical aseptic clean room was exploited, available at the production line of an Italian company, manufacturing aseptic bottling plants.

Experimental data collected refer to fluid velocity in 4 locations of the aseptic room, namely:

- (i) the middle zone of the clean room (location A);
- (ii) a point close to the outlet ducts (location B);
- (iii) a point at a defined distance from the outlet ducts (location C); and
- (iv) the middle of the clean room along the z-axis (location D).

To collect the experimental data, the aseptic room was stopped and the sterilizing solution was removed from the chamber, to ensure that the conditions of data collection were as similar as possible to those reproduced by the turbulence model. The measurements of fluid velocity in the areas described above were performed both with a hot-wire anemometer and plate anemometer, both provided by the company. The plate anemometer was especially used when it was necessary to only derive one component of the fluid velocity. In the following, we detail the experimental measurements performed for the above described locations.

#### Location A

The hot-wire anemometer was initially placed at  $(x; y; z)=(0; 0.375; 0.325)$ , and moved along the  $y$ -axis up to the room center, following the path shown in Figure 2.

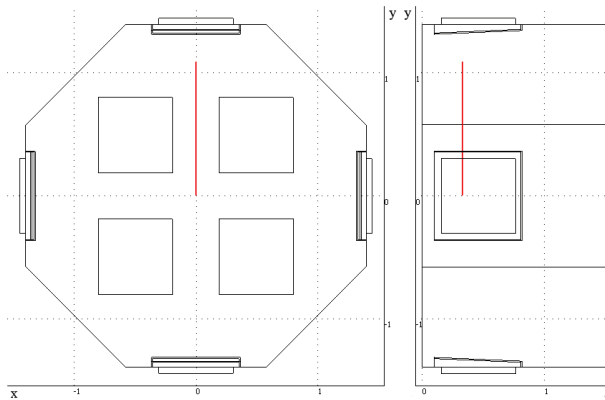


Figure 2. Location A

**Location B**

The hot-wire anemometer was located close to the outlet grids, as shown by the red line in Figure 3. Data were collected at five different points, whose coordinates are  $(x; y; z)=(x_n; 1.363; 0.095)$ , with  $x_1=-0.335$ ;  $x_2=-0.1775$ ;  $x_3=0$ ;  $x_4=0.1775$ ;  $x_5=0.335$ .

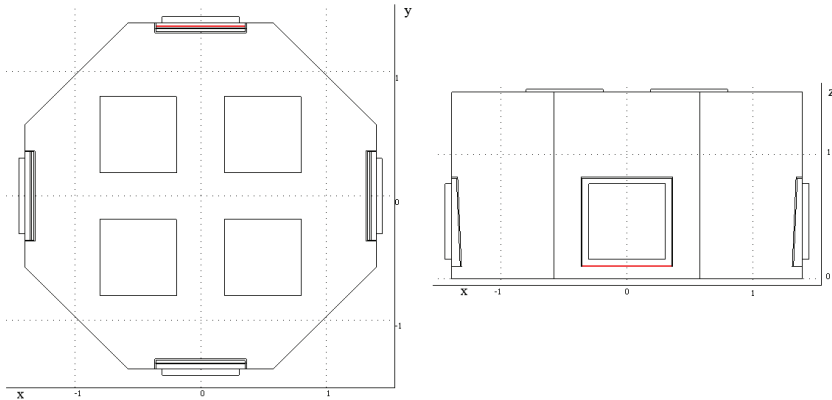


Figure 3. Location B

**Location C**

The plate anemometer was located 0.237 m far from the outlet grid, at 0.055 m height from the chamber floor, as shown in Figure 4. Data were collected at five different points, whose coordinated are  $(x; y; z)=(x_n; 1.086; 0.055)$ , with  $x_1=-0.335$ ;  $x_2=-0.1775$ ;  $x_3=0$ ;  $x_4=0.1775$ ;  $x_5=0.335$ .

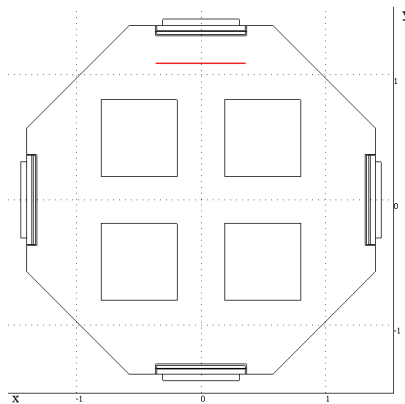


Figure 4. Location C

**Location D**

As shown in Figure 5, the plate anemometer was located in the middle of one of the inlet grids, at point  $(x; y; z)=(0.495; 0.495; z_n)$ . Several values of height from the chamber floor were considered, namely  $z_1=0.225$ ;  $z_2=0.55$ ;  $z_3=0.875$ ;  $z_4=1.2$ ;  $z_5=1.345$ .

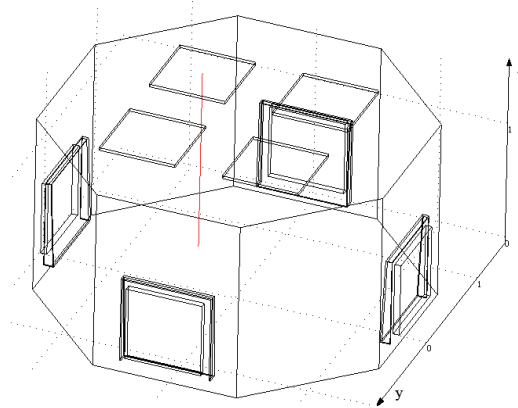


Figure 5. Location D

**4.2 Model validation**

Figure 6 shows the results of the  $k-\epsilon$  model, in terms of both stationary analysis and transitory one, this latter representing the initial 2.8 s of the numerical simulation. By comparing those outcomes, it can be observed that, under transitory conditions, the flow velocity reaches stabilization in time, and assumes values very similar to outcomes of the stationary analysis. Based on this consideration, the results of the stationary analyses were assumed as reference to compare the simulation outcomes with the experimental data.

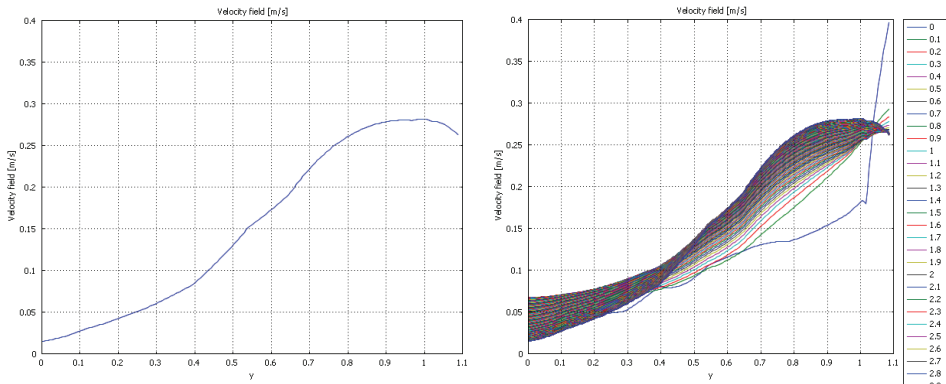


Figure 6. Comparison between transitory and stationary conditions – location A

Detailed results of the numerical models are proposed in Table 1 for both the  $k-\epsilon$  and  $k-\omega$  models, together with experimental data collected in the locations examined.

Subsequent Figure 7-Figure 10 graphically illustrate the comparison between numerical outcomes and experimental data collected.

	Measurement point [m]	Velocity values [m/s]		
Location A	(x;y;z)=(0;y;0.325)	Experimental	Numerical $k-\epsilon$	Numerical $k-\omega$
	y=0	0.02	0.015	0.21
	y=0.375	0.05	0.077	0.227
	y=0.612	0.15	0.18	0.252
	y=0.849	0.25	0.27	0.285
	y=1.086	0.31	0.27	0.282
Location B	(x;y;z)=(x;1.363;0.095)	Experimental	Numerical $k-\epsilon$	Numerical $k-\omega$
	x=-0.335	4.64	5.41	7.01
	x=-0.1775	3.95	4.7	4.52
	x=0	4.17	3.93	2.65
	x=0.1775	4.35	4.36	4.25
	x=0.335	4.68	6.09	6.55
Location C	(x;y;z)=(x;1.086;0.055)	Experimental	Numerical $k-\epsilon$	Numerical $k-\omega$
	x=-0.335	0.46	0.61	0.697
	x=-0.1775	0.51	0.76	0.643
	x=0	0.56	0.79	0.59
	x=0.1775	0.57	0.76	0.613
	x=0.335	0.49	0.56	0.687
Location D	(x;y;z)=(-0.495;0.495;z)	Experimental	Numerical $k-\epsilon$	Numerical $k-\omega$
	z=0.225	0.34	0.15	0.26
	z=0.55	0.4	0.322	0.282
	z=0.875	0.41	0.451	0.31
	z=1.2	0.48	0.534	0.31
	z=1.345	0.53	0.537	0.475

Table 1. Comparison between experimental and simulated results

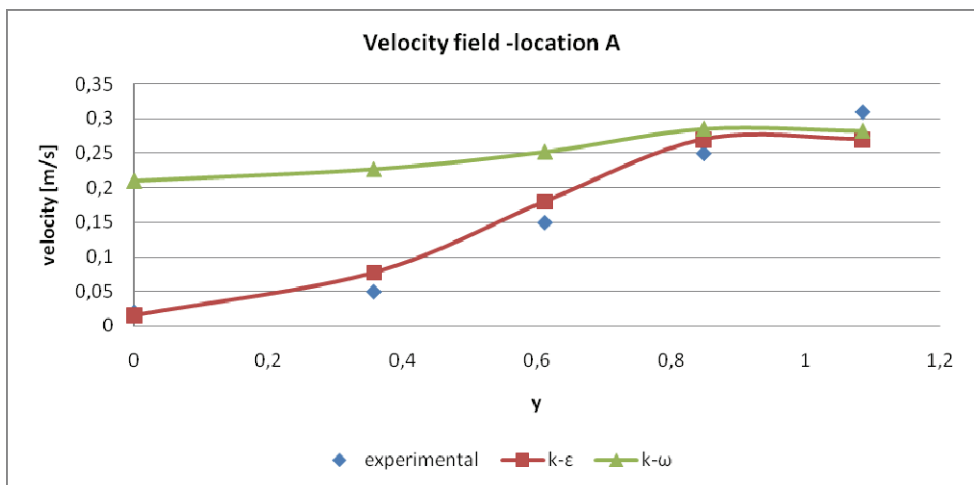


Figure 7. Comparison between experimental and numerical results – location A

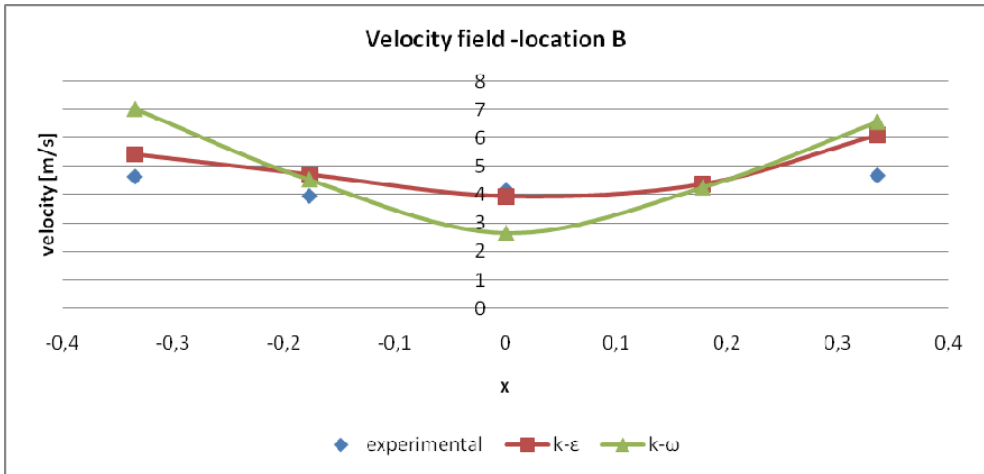


Figure 8. Comparison between experimental and numerical results – location B

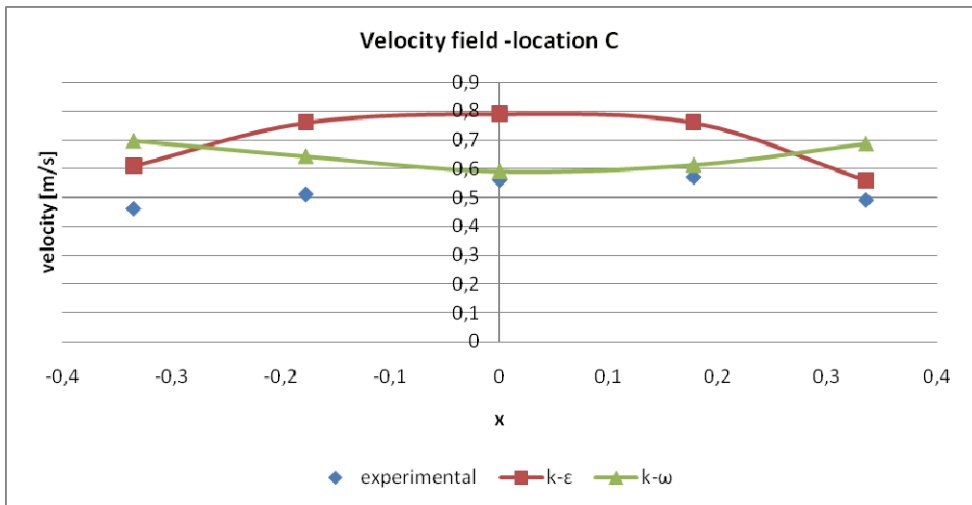


Figure 9. Comparison between experimental and numerical results – location C

The comparison between experimental data and simulation outcomes shows that the  $k-\epsilon$  turbulence model is in general able to accurately reproduce the velocity profile observed during experimental measurements. In particular, as can be seen from Figure 7 and Figure 8, location A, corresponding to the central area of the clean room, and location B, corresponding to the outlet grids, show the highest correspondence between experimental and simulated values. In both cases, the simulation outcomes allow correctly reproducing the experimental velocity profile. Conversely, the  $k-\omega$  model tends to overestimate the air velocity measured at location A, except for  $y$  values greater than about 1 m. Similar considerations can be drawn for location B, where the velocity profile resulting from the  $k-\omega$  does not precisely reproduce the experimental data.

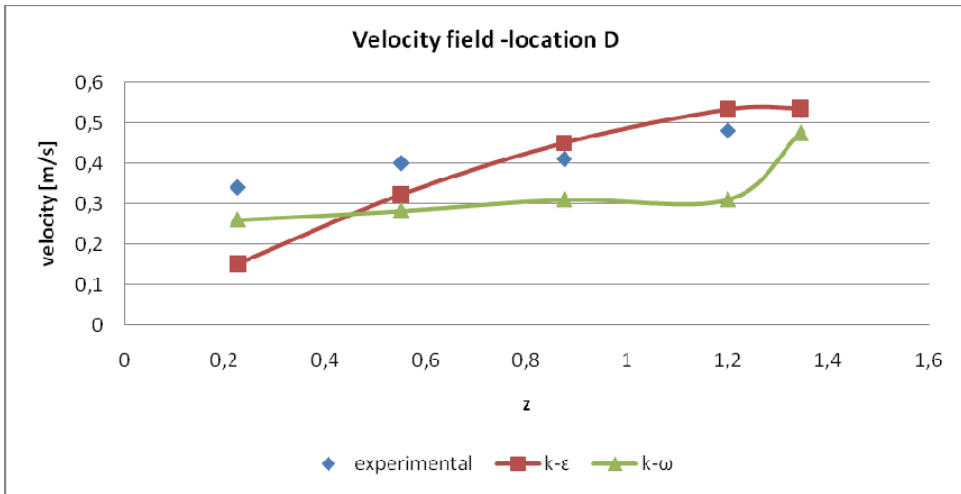


Figure 10. Comparison between experimental and numerical results – location D

Results for location C (see Figure 9) show that the numerical  $k-\epsilon$  model slightly overestimates (approx 0.2 m/s) the air velocity in proximity of the outlet grids. This result could be explained considering possible disturbances during the experimental measurements, due to the presence of one or more employees measuring the flow velocity. In addition, due to the presence of the plate, the anemometer used for those measurements does not enable to measure the flow velocity in a precise point, but rather in a zone perpendicular to the plate. This may affect the capability of correctly identifying the height along the  $z$ -axis to be assumed as reference to assess the correctness of the simulation results. Conversely, results of the  $k-\omega$  model are able to accurately predict the fluid flow only for  $0.1775 < x < 0$ ; for the remaining points, numerical outcomes seem to suggest a trend of flow velocity significantly different from experimental values.

Finally, numerical results for location D (see Figure 10) show that the  $k-\epsilon$  model is able to accurately reproduce the air flow in the middle of the clean room only for  $z$  values higher than 0.875 m. For lower values, the model seems to slightly underestimate the resulting flow. As per the location C, such a difference could be expected, as the same measurement instrument has been used to derive the fluid flow in location D, resulting in difficult identification of the  $z$  value to be assumed as reference to assess the the correctness of the simulation outcomes. Conversely, the  $k-\omega$  model seems to better reproduce the velocity profile, although numerical values always underestimate the experimental values.

### 4.3 Flow analyses

Once the simulation model was developed, the subsequent analyses were focused on examining the fluid flow inside the aseptic clean room, in terms of fluid velocity and pressure, and turbulent kinetic energy. On the basis of the results detailed in the previous section, the  $k-\epsilon$  model was exploited to this extent.

Figure 11 shows the simulation results in terms of the velocity field at the centre of the clean room ( $x=0$ ). As can be seen from the figure, the velocity inside the room can range from approx 0.036 m/s to 5 m/s. Velocity values from 3 to 5 m/s, however, are achieved only at



the outlet grids, while the flow velocity inside the clean room is always lower than 1 m/s. This does not necessarily involve laminar flow, as Ljungqvist & Reinmuller, (1997), point out that turbulent flows occur in aseptic clean room even at low speed (0.2 m/s).

On the other hand, low velocity could involve poor air recirculation and not well distributed flow of air in central zone of the chamber, which is a main requirement of clean rooms technology.

Moreover, streamlines in Figure 11 indicate flow recirculation at the top left and right of the chamber. This suggests that the air flow does not immediately exit the clean room, allowing the chamber to be maintained at a pressure higher than the external, and thus preventing pollutants entrance from the environment. Such conclusion is supported by the simulated pressure values resulting inside the clean room; they are detailed in Figure 12 (a) for  $x=0$ . As can be seen from the figure, the chamber is maintained at approx  $1.014 \cdot 10^5$  Pa pressure, which is higher to the external one.

Finally, the turbulent kinetic energy  $k$  was examined to assess whether the chamber considered experiences significant turbulence. Figure 12 (b) shows that simulated values of turbulent kinetic energy for the aseptic room examined ranges from  $9.37 \cdot 10^{-3}$  to  $9.335$  J/kg. In particular, highest values are achieved at the centre of the outlet grids, while the body of the chamber highlights kinetic energy values lower than 1 J/kg. This suggests that the aseptic room examined experiences limited turbulence, which is mainly located at the outlet grids.

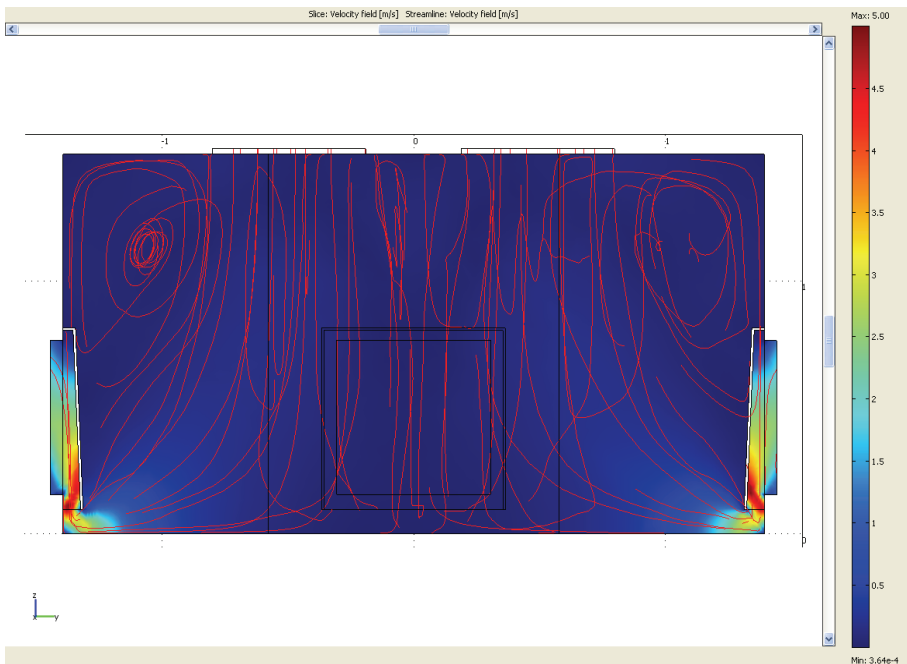


Figure 11. Simulated velocity field of the aseptic clean room at  $x=0$  ( $k-\epsilon$  model)

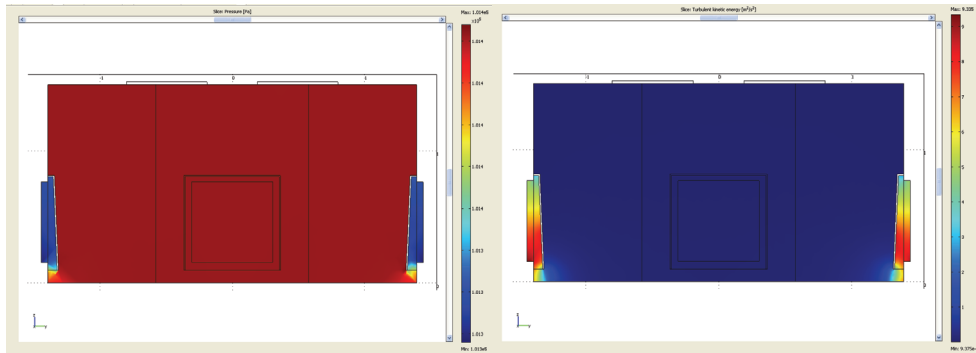


Figure 12. Simulated pressure values (a) and turbulent kinetic energy (b) of the aseptic clean room at  $x=0$  ( $k-\varepsilon$  model)

## 5. Conclusions

Contamination control has become a key factor in assuring product reliability in many high technology industries, and strictly depends on the capability to precisely control the turbulent flows of sterile air inside the container into which products are assembled.

To help manufacturers to tackle this issue at the design phase, in this work a simulation model has been developed to reproduce and analyze the flow of sterile air within a clean room for aseptic beverage bottling.

Two turbulence models were considered in developing the simulation tool, namely the  $k-\varepsilon$  and the  $k-\omega$ , whose results were validated by comparing them to experimental measurements. The models used exploit different approaches to the turbulence problem, which result in different performance in predicting the fluid flow. Specifically, the  $k-\varepsilon$  model is in general able to accurately reproduce the velocity profile observed during experimental measurements; this is particularly the case of the central area of the clean room (i.e. location A) and the outlet grid (i.e. location B). Conversely, the  $k-\omega$  model seems to provide better estimations of fluid velocity when considering locations close to the chamber floor (i.e. location C), while some limitations of the model emerge when simulating the centre of the clean room (e.g. locations A and D), where the fluid reaches the free flow conditions.

On the basis of the results of the validation, as well as subsequent analyses performed, we can conclude that the  $k-\varepsilon$  model developed can be usefully exploited to predict the fluid flow in real aseptic rooms, and, in particular, to design room size and equipments to improve air circulation. We thus believe that aseptic plant manufacturers could substantially benefit from our model as a possible tool to improve the performance of aseptic rooms.

Some of the limitations of the study should be mentioned. As a first point, both models adopted grounds on the Boussinesq hypothesis, which greatly simplifies the computation of Reynolds stress, thus speeding up the computation time. Moreover, such models are generally robust, and provide reliable results. However, the simplification used in the formulation of transport equations could affect the accuracy of the results provided. In particular, the Boussinesq hypothesis provides a definition of the turbulent viscosity as a scalar quantity, which implicitly suggests viscosity to be an isotropic value. Such an assumption is rarely satisfied, except for simple systems, which could not be the case of the aseptic clean room examined. Moreover, an additional source of error of two-equation

models has to be found in the assumption of direct proportion between kinetic energy  $k$  and dissipation rate  $\varepsilon$ . Such assumption can be considered as satisfied only for high Reynolds numbers. From the simulation point of view, a main limitation of the work is the number of elements used in the mesh. To improve the model accuracy, this should be increased, either by adopting segregated solvers or by increasing the computational capacity of the system.

Starting from this study, future research can be directed at:

- (i) exploiting the model developed to design possible improvements for the aseptic clean room, with the ultimate aim of improving the circulation of sterile air along walls, windows and ceiling of the room;
- (ii) exploiting the model to define the hydrogen peroxide flow inside the clean room, with the aim to derive the fluid distribution in the room and to examine the corresponding sterilization performance;
- (iii) applying different turbulence models to the simulation tool developed, such as the RNG and realizable  $k$ - $\varepsilon$  models or the  $k$ - $\omega$  SST model (Kuznik, et al., 2007), with the aim to improve the simulation results and to better predict the fluid flow in the aseptic clean room.

## 6. References

- Chen S.C., Tsai C.J., Li S.N., Shih H.Y. (2007). Dispersion of gas pollutant in a fan-filter-unit (FFU) cleanroom. *Building and Environment*, 42, 1902-1912
- Cheng M., Liu G.R., Lam K.Y., Cai W.J., Lee E. L. (1999). Approaches for improving airflow uniformity in unidirectional flow cleanrooms. *Building and Environment*, 34, 275-284
- Comsol Inc., (2005), *User's Guide*, Comsol Multiphysics 3.2a, Sweden
- Divelbiss J., Winter B. (1995). Isolator evaluation using computer modelling. Part 2: hydrogen peroxide sterilization with two diluents fluids. *Pharmaceutical Engineering*, 15(3), 84-96
- Favre, A. (1969). Statistical equations of turbulent gases. In Lavrentev, M.A., (Ed.), *Problems of Hydrodynamics and Continuum Mechanics*. Society for Industrial and Applied Mathematics, 0-898-71039-1, Philadelphia
- Federal Standard 209E, (2002), *Airborne Particulate Cleanliness Classes in Cleanrooms and Clean Zones*. Institute of Environmental Sciences, Illinois. Available at <http://www.set3.com/papers/209e.pdf>
- Fitzpatrick, B.W.F. (1994). Contamination control in the food industry . assembly of food components in clean rooms. *Swiss Food*, 16, 7-8
- ISO 14644-8:2006 Cleanrooms and associated controlled environments. Classification of airborne molecular contamination.
- Kolmogorov, A.N. (1941). The local structure of turbulence in incompressible viscous fluid for very large Reynold's numbers. *C. R. Dokl. Acad. Sci. URSS*, 30, 301-305
- Kuznik F., Rusaouen G., Brau J. (2007). Experimental and numerical study of a full scale ventilated enclosure: Comparison of four two equations closure turbulence models. *Building and Environment*, 42, 1043-1053
- Launder B.E., Spalding D.B. (1974). The numerical computation of turbulent flow. *Computer Methods in Applied Mechanics and Engineering*, 3, 269-289
- Ljungqvist B., Reinmuller B. (1997). *Clean room design/minimizing contamination through proper design*. Interpharm Press, 1-574-91032-9, Buffalo Grove

- Norton T., Sun D.W. (2006). Computational fluid dynamics (CFD) – an effective and efficient design and analysis tool for the food industry: A review. *Trends in Food Science & Technology*, 17(11), 600-620
- Ogawa, M. (2000). Contamination control in HVAC systems for aseptic processing area. Part I: Case study of the airflow velocity in a unidirectional airflow workstation with computational fluid dynamics. *PDA Journal of Pharmaceutical Science and Technology*, 54, 27-31
- Rajagopal K.R., Ruzicka M., Srinivasa A.R. (1996). On the Obserbeck–Boussinesq approximation. *Mathematical Models & Methods in Applied Sciences* 6, 1157–1167
- Reynolds, O. (1883). An experimental investigation of the circumstances which determine whether the motion of water shall be direct or sinuous, and of the law of resistance in parallel channels. *Philosophical Transactions of the Royal Society*, 174, 935-982
- Schicht, H.H. (1999). Cleanroom technology and its benefits to the food and beverage industry. *New Food*, 1, 18-23
- Whyte, W. (2001). *Cleanroom technology, Fundamentals of design, testing and operation*. John Wiley & Sons Ltd., 0-471-86842-6, Chichester
- Wilcox, D.C. (1988). Re-assessment of the scale-determining equation for advanced turbulence models. *AIAA Journal*, 26, 1414-1421
- Wilcox, D.C. (1998). *Turbulence Modeling for CFD*. DCW Industries Inc., 1-928729-10-X, USA
- Wirtanen, G., Miettinen, H., Pahkala, S., Enbom, S. & Vanne, L. (2002). *Clean air solutions in food processing*. Available at [www.vtt.fi/inf/pdf/publications/2002/P482.pdf](http://www.vtt.fi/inf/pdf/publications/2002/P482.pdf)

# Elastic Modulus FEM Modelling of the Layered Woven Composite Material

Pavla Vozkova

*Technical University of Liberec, Faculty of Textile Engineering  
Czech Republic*

## 1. Introduction

Composites are top materials used for special applications. In place of traditional material, e.g. steel, the composites lower its weight much more than the traditional material. It is based on low weight of a composite itself, on specific properties of the components and on creation possibility of composite with a specific use. The combination of the materials provides specific properties of a final composite, e.g. chemical resistance, electric and thermo-insulate properties.

The basis of a fibre reinforcing is the fact that fibres have got strength and stiffness much higher than polymer matrix. Fibres are deformed less than matrix during tensile load applied from outer power. Adhesion between components allows to distributing tension from matrix to each of all fibres.

Nowadays it is the denoted composites using, which makes possible to satisfy high requirements for special mechanical applications. Effective development is practicable only when an innovation and a construction of new composite products are set in the production - market will be developed, economical aspects will be taken into account, productivity and quality will be watched carefully, safety and ecology will be raised. Material evolution, construction principles, non-destructive testing, modelling and prediction have to be innovating and develop for materials, technology and complex system of composite materials.

The testing without a plastic deformation is not only a detection of present defects but by scanning of mechanical vibrations it is also possible to evaluate elastic constants. An alternative method for determining properties of future composite construction is a calculation with commercial software which allows corrections of equations and defining of special coefficients. The finite element method is in a use and is proved by wide science population.

The composite modelling is also an important part of the research. A visualisation of structure inside composite is necessary for an evaluation of composite properties. The structure modelling in multi-scale supports calculation in finite element method effectively.

Nowadays composites are top in the aircraft industry, automotive industry and water craft construction. Building of chemical and energetic machines and construction of manufacturing machines used composites more and more in these days.

This chapter targets the study of elastic properties of carbon/carbon composites with woven

reinforcement prepared by the prepreg technology. A simulation is based on the multi-scale modelling as a structure defining. Comsol Multiphysics™ is a tool for a finite element modelling and it is possible to solve partial differential equations. An experimental measurement is compared with a simulation for a validation of results. A non-destructive testing of resonant frequencies based on an excitation of mechanical frequencies is used for an evaluation of elastic modules in the experiment. The Hooke's law is valid during the experimental work.

### 1.1 Textile reinforced composites

Composite consists of two or more structural components. Their cooperation in the system evokes synergy - it means that properties of the end product are better than sum of component's properties only. Non-continuous components are fibres which carry the load. Continuous component is matrix and it fills surrounding around fibres. Fibres have to be the firm and high modulus. The most important property of matrix is a good adhesion to the fibre surface (Agarwal & Broutman, 1987).

Fibres and matrix are prepared from various kinds of materials according to the application. Carbon for fibres and also for matrix is a top application for the space industry. Material has got a high tenacity, fracture toughness, high-temperature resistance, good thermal, chemical and electrical conductivity and it is easy to influence the anisotropy. Some problems with degradation in oxygen atmosphere can occur there (Savage, 1993), (Berthelot, 1999).

Composites with textile reinforcement have got good resistance against to progression of cracks. Fabric is a bidirectional layer which gives good tensile properties in warp and weft directions. The structure modelling of carbon/carbon composites is a complex problem. Here there is a irregularly crimped textile reinforcement with various inherent defects (pores, bubbles and cracks) which has risen during pyrolysis process of polymer precursor in carbon matrix. Different shrinkage during cooling plays its role too (Savage, 1993), (Fitzer & Manocha, 1998). It is difficult to include all aspects of this complex structure to one model. The idealisation is based on geometric models as the bricks or sinusoidal curve of woven reinforcement (Bogdanowich & Pastore, 1996), (Lomov, 2007). But results are different from experiments (Lomov et al., 2001). The description of woven interlace is very hard to study nowadays. Carbon/carbon composite with a plain weave reinforcement structure was studied by image analysis at the Technical University of Liberec. The porosity was included from 20% - 25% in the structure (Tomkova, 2006). On the image a multi-scale geometric model of the composite structure applied in following properties simulation analysis was based (Vozkova, 2007).

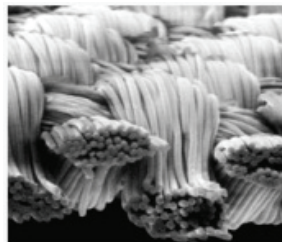


Figure 1. Plain weave of infinite fibre bundle as a possible reinforcement (Kuhn, 2007)

## 2. Composite modelling based on geometric models with finite elements

A complex structure of the composite has to be adapted for computing. Some levels of a structure idealisation are used from simple brick models and weave idealisation to complex multi-scales. The finite element method is then used for calculation among others (Discrete Fourier transformation and different algorithms) (D'Amato, 2001), (Reddy, 2006). The finite element method is a numerical tool for a simulation process of stress, strain, heat flow and more for physical model. A continuous area is discretized to the countable number of units. It is possible to apply the simulation for a long-term testing and for a detection of critically loaded area (Hokr, 2006). Tested area is covered with the net of triangles or quadrangles that cover surface without overlapping. Loadings in the sample body are transferred to the equivalent loadings in the net structure. Each element is taken as an independent area with some boundary conditions (Reddy, 2006).

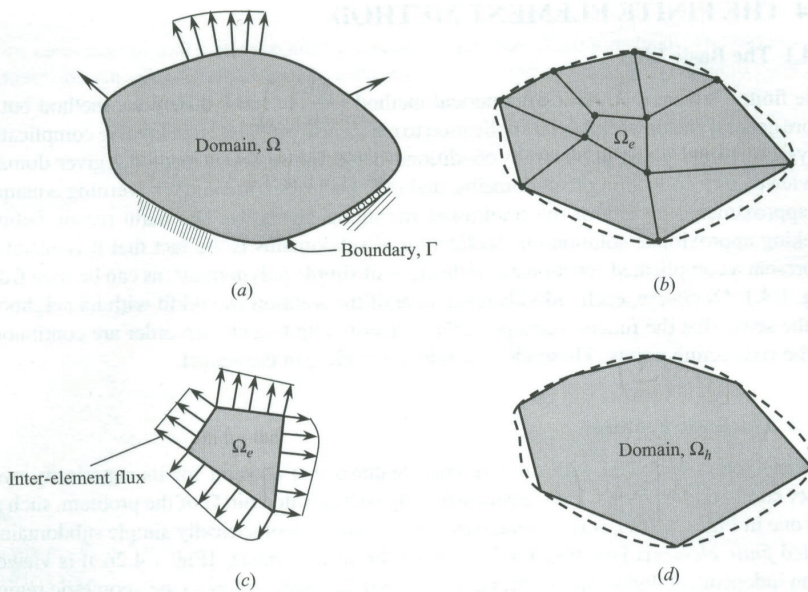


Figure 2. Representation of a two-dimensional domain by a collection of triangles and quadrangles (Reddy, 2006)

(a) geometrical complex domain, (b) collection of geometrically simple subdomains, (c) finite element as an independent subdomain, (d) assembled relations from all elements

Subchapters contain description of model characterisation, original work from other authors about multi-scale modelling and introduction of two-dimension model for simulation use.

### 2.1 Basics of the geometric models

The volume element of a structure exists as a representative of the mechanical response for the whole composite body as an assumption. The representative volume element (RVE) is based on the type of reinforcement and on the scale. Fibres and matrix are always included in the representative volume element. A stiffness and compliance tensor describes the

representative volume element with a mean stress and a mean strain in the volume element of the material (Berthelot, 1999).

One dimension reinforced composites, e.g. reinforced with parallel fibres which should be defined by an iso-strain model (Fig. 3.). For the model in multi-component system in loading strain of all components it is the same but there is no stress. The stiffness tensor  $C_s$  for system with  $n$  components is

$$C_s = \sum_{i=1}^n k_i C_i \tag{1}$$

where  $C_i$  is the stiffness tensor of  $i$  component and  $k_i$  is the volume ratio of this component. Model of iso-stress (Fig. 4.) has got the same stress for all components as an assumption but there is no strain. The compliance tensor  $S_s$  for this model should be

$$S_s = \sum_{i=1}^n k_i S_i \tag{2}$$

The compliance tensor is inverse for the stiffness tensor. Both models are on the highest and on the lowest limits for elastic properties of the composites. Both models are also applied straight to the laminate with longitudinal infinite fibres (Bogdanowich & Pastore, 1996).

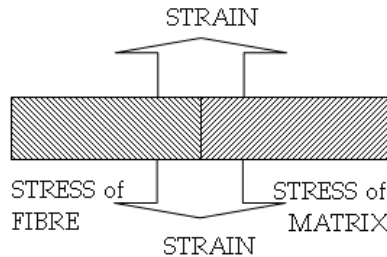


Figure 3. Model iso-strain (Tomkova, 2005)

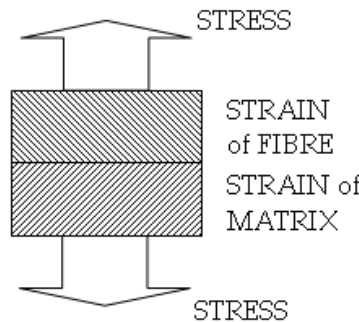


Figure 4. Model iso-stress (Tomkova, 2005)

Non-homogenous material is replaced by homogenous for the Hooke's law in mechanics of continuum. Basically is valid that the stress  $\sigma_{ij}$  and the strain  $\varepsilon_{ij}$  from each component with volume ratio are sums for total stress and strain according to



$$\begin{aligned} [\sigma_{ij}] &= \sum_n V_n [\sigma_{ij}^n] \\ [\varepsilon_{ij}] &= \sum_n V_n [\varepsilon_{ij}^n] \end{aligned} \quad (3)$$

where  $V_n$  is the volume ratio of each component. From the tensors stress  $\sigma_{ij}$  and the strain  $\varepsilon_{ij}$  it is possible to count array of stiffness  $C_{ijkl}$

$$[\sigma_{ij}] = [C_{ijkl}] [\varepsilon_{kl}] \quad (4)$$

Modules of elasticity are defined in this array. Inverse to stiffness array is compliance array with coefficients of deformation. Both arrays are tensors of the fourth grade (Miravete, 2000), (Vinson & Chou, 1975). Matrix material is presumed isotropic and homogenous with a structure close to vitreous carbon (Marvalova, 2000). Elastic constants are not changed during rotation around axes. Pores properties are also isotropic and do not accept gas compression (Berthelot, 1999). Reinforcement is a homogenous and transversely isotropic material. In one axis direction the properties are the same in all cases. The cross to the fibre axis is plane (Berthelot, 1999), (Stříž, 2002).

Composite from laminas is an orthotropic material with three axes of symmetry, i.e. warp, weft and cross to fabric. Stiffness array is than

$$\begin{bmatrix} \sigma_1 \\ \sigma_2 \\ \sigma_3 \\ \sigma_4 \\ \sigma_5 \\ \sigma_6 \end{bmatrix} = \begin{bmatrix} c_{11} & c_{12} & c_{13} & 0 & 0 & 0 \\ c_{12} & c_{22} & c_{23} & 0 & 0 & 0 \\ c_{13} & c_{23} & c_{33} & 0 & 0 & 0 \\ 0 & 0 & 0 & c_{44} & 0 & 0 \\ 0 & 0 & 0 & 0 & c_{55} & 0 \\ 0 & 0 & 0 & 0 & 0 & c_{66} \end{bmatrix} \begin{bmatrix} \varepsilon_1 \\ \varepsilon_2 \\ \varepsilon_3 \\ \varepsilon_4 \\ \varepsilon_5 \\ \varepsilon_6 \end{bmatrix} \quad (5)$$

and the compliance array is

$$\begin{bmatrix} \varepsilon_1 \\ \varepsilon_2 \\ \varepsilon_3 \\ \varepsilon_4 \\ \varepsilon_5 \\ \varepsilon_6 \end{bmatrix} = \begin{bmatrix} s_{11} & s_{12} & s_{13} & 0 & 0 & 0 \\ s_{12} & s_{22} & s_{23} & 0 & 0 & 0 \\ s_{13} & s_{23} & s_{33} & 0 & 0 & 0 \\ 0 & 0 & 0 & s_{44} & 0 & 0 \\ 0 & 0 & 0 & 0 & s_{55} & 0 \\ 0 & 0 & 0 & 0 & 0 & s_{66} \end{bmatrix} \begin{bmatrix} \sigma_1 \\ \sigma_2 \\ \sigma_3 \\ \sigma_4 \\ \sigma_5 \\ \sigma_6 \end{bmatrix} \quad (6)$$

Nine independent constants are necessary to find (Berthelot, 1999).

The compliance tensor could be found also as a relation between Young's modules, shear modules and Poisson's ratio from simplification of plain tensile test in warp direction, plain tensile test in weft direction and plain shear test from (Berthelot, 1999), (Laš, 2004) as

$$S = \begin{bmatrix} \frac{1}{E_1} & -\frac{\mu_{12}}{E_1} & -\frac{\mu_{13}}{E_1} & 0 & 0 & 0 \\ -\frac{\mu_{12}}{E_1} & \frac{1}{E_2} & -\frac{\mu_{23}}{E_2} & 0 & 0 & 0 \\ -\frac{\mu_{13}}{E_1} & -\frac{\mu_{23}}{E_2} & \frac{1}{E_3} & 0 & 0 & 0 \\ 0 & 0 & 0 & \frac{1}{G_{23}} & 0 & 0 \\ 0 & 0 & 0 & 0 & \frac{1}{G_{13}} & 0 \\ 0 & 0 & 0 & 0 & 0 & \frac{1}{G_{12}} \end{bmatrix} \quad (7)$$

Loading in on axis direction has to be transferred to the symmetry axis in defined angle  $\delta$  (Berthelot, 1999). Loading is than transferred to the main directions. Longitudinal modulus could be defined as

$$\frac{1}{E_x} = S_{11} \cos^4 \delta + S_{22} \sin^4 \delta + (2S_{12} + S_{66}) \cos^2 \delta \sin^2 \delta \quad (8)$$

and with inclusion constants from compliance tensor

$$\frac{1}{E_x} = \frac{1}{E_L} \cos^4 \delta + \frac{1}{E_T} \sin^4 \delta + \left( \frac{1}{G_{LT}} - \frac{2\mu_{LT}}{E_L} \right) \cos^2 \delta \sin^2 \delta \quad (9)$$

Shear modulus has got simple presumption

$$G_{xy} = \frac{1}{S_{66}} \quad \text{so} \quad \frac{1}{G_{xy}} = 2 \left( \frac{2}{E_L} + \frac{2}{E_T} - \frac{1}{G_{LT}} + \frac{4\mu_{LT}}{E_L} \right) \cos^2 \delta \sin^2 \delta + \frac{1}{G_{LT}} (\sin^4 \delta + \cos^4 \delta). \quad (10)$$

## 2.2 Complex geometric models

The multi-scale modelling allows decomposition of complex heterogeneous structure to the partial levels from the simplest composition to the composition of whole sample body. They are substituted from the lowest level properties to higher and also highered up to the higher studied composite structure. The accuracy of the simulation is better because specifications and properties from each scale are combined during processing. On Fig. 7. is parting to the scales (Berthelot, 1999), (Lomov et al., 2007).

Interesting research for complex geometry of the textile reinforced composites made the team of prof. Lomov from Belgium. They introduced the set of programs of a structure geometry composition, modelling of complex geometry, meshing of nets and properties calculation. On Fig. 8. is simple diagram of their work (Lomov et al., 2001), (Lomov et al., 2007). Each program is specialized for some operation and together it is possible to compute properties of some composite.

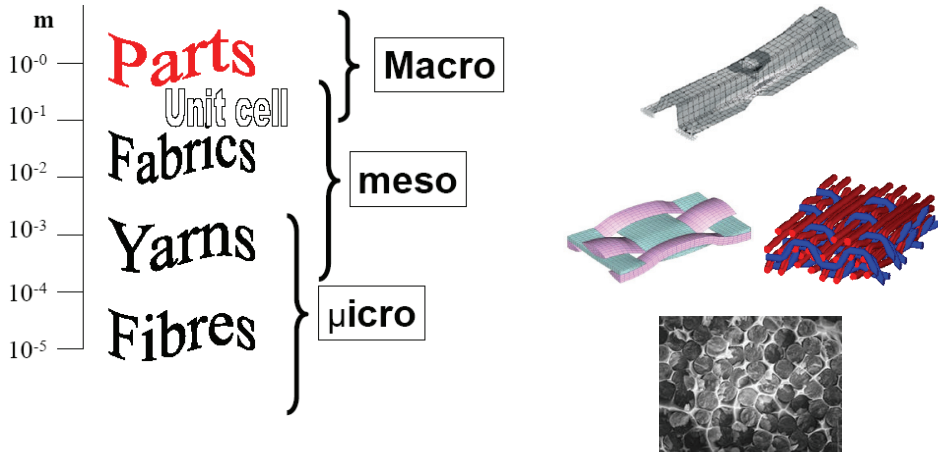


Figure 7. Scale distribution of sample geometry (Lomov et al., 2007)

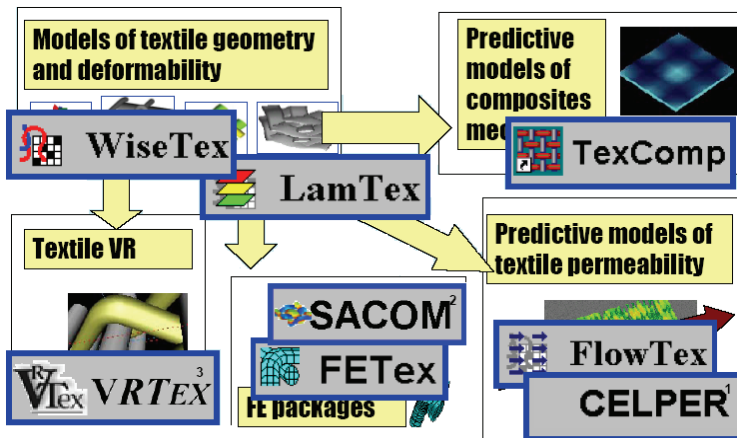


Figure 8. System for composite simulation (Lomov, 2007)

Many authors are following Lomov's team and their outputs. Mechanical or thermal properties are counted from these programs for the textile reinforced composites, tensile tests, bending, plain shear, etc. A similar way was found by the team of prof. Sejnoha from the Czech Republic. The multi-scale modelling is applied on textile composites but also on the more mechanical objects, e.g. bridges (Šejnoha, 2007), (Skoček et al., 2005).

### 2.3 Multi-scale modelling for simulation

A consideration about the structure of composites could be done from Fig. 9. A simulation in this chapter presents the two-dimensional model of lengthwise and crosswise fibre bundles surrounded with matrix. Defects are mentioned here, too. It is necessary to include defects in the bundles, between laminas and voids raised during pyrolysis and layering. Whole structure is a combination of geometry formations.

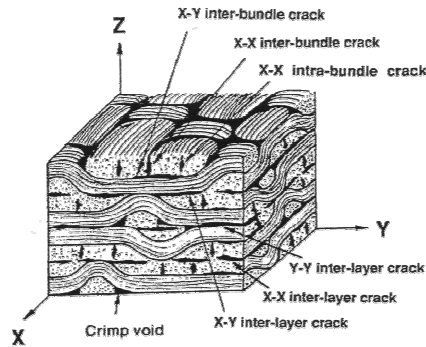


Figure 9. Model of structure for composite with textile reinforcement (Tomkova, 2006)

The lowest scale of tested structure in a microstructure with fibres and matrix, q.v. fibre bundle on Fig. 10. Properties and geometry are not changed during testing for fibres and matrix too. Fibres are circular. Structure is random with volume ratio around 60% (Tomkova, 2006), (Šejnoha, 2007).

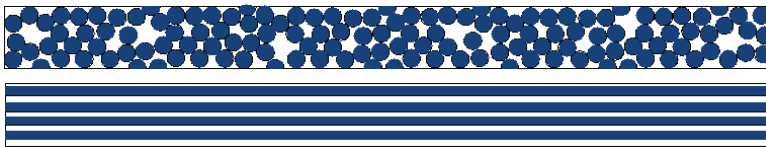


Figure 10. Lengthwise and crosswise section of the fibre bundle (blue- fibres, white - matrix)

Pores have risen during the production process in the fibre bundle. Fig. 11. shows microstructure scale of whole bundle with pores inside the structure. Pores are filled with the air, if they are open. Closed pores contain pyrolytic gas but for simulation air was filled (Tomkova, 2006), (Šejnoha, 2007).

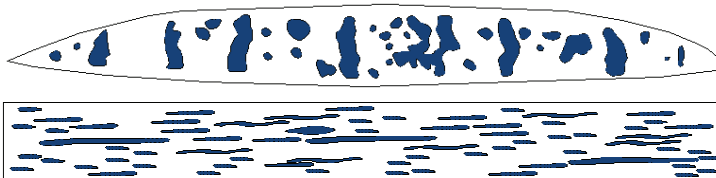


Figure 11. Lengthwise and crosswise section of the fibre bundle with pores (blue- pores, white - carbon part of fibres and matrix)

Next scale level is a Unit cell as a meso-scale structure. Repeating of Unit cell forms whole plain weave fabric. On Fig. 12. there are three Unit cells. The first is a simple Unit cell for plain weave. Two others are obtained from complete observation of microphotographs of real composite structure. These three Unit cells form lamina (Fig. 13.). (Tomkova, 2006) demonstrates that pores and cracks in the structure of Unit cell are necessary for precise computation. Defects rise in structure during fabrication as a lamina sliding and bridging of cross bundles (Tomkova, 2006), (Šejnoha, 2007).

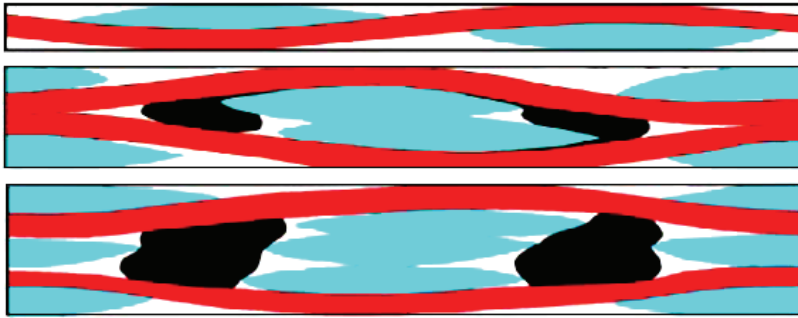


Figure 12 Structural Unit cell 1,2,3 (Tomkova, 2006) (blue – crosswise fibre bundles, red – lengthwise fibre bundles, black – voids, white – matrix)

Laminae model whole composite structure on Fig. 14. In the simulation lamina and composite structure are idealized as a bricks with identical properties in each brick counted from lower scale (unit cell → lamina bricks → composite bricks) (Tomkova, 2006), (Šejnoha, 2007). Table 1. shows sizes of all defined structure elements from multi-scale model.



Figure 13. Structural model of Lamina (Tomkova, 2006) (blue – crosswise fibre bundles, red – lengthwise fibre bundles, black – voids, white – matrix)



Figure 14. Whole composite structure (Tomkova, 2006) (blue – crosswise fibre bundles, red – lengthwise fibre bundles, black – voids, white – matrix)

Scale and type of the tested sample	length [m]	high [m]
<b>Crosswise bundle section</b>	$2,2 \cdot 10^{-4}$	$1,8 \cdot 10^{-5}$
<b>Lengthwise bundle section</b>	$2,2 \cdot 10^{-4}$	$1,8 \cdot 10^{-5}$
<b>Crosswise bundle with defects</b>	$1,8 \cdot 10^{-3}$	$1,8 \cdot 10^{-4}$
<b>Lengthwise bundle section with defects</b>	$1,8 \cdot 10^{-3}$	$1,8 \cdot 10^{-4}$
<b>Structure unit cell 1</b>	$4,5 \cdot 10^{-3}$	$0,3 \cdot 10^{-3}$
<b>Structure unit cell 2</b>	$4,5 \cdot 10^{-3}$	$0,5 \cdot 10^{-3}$
<b>Structure unit cell 3</b>	$4,5 \cdot 10^{-3}$	$0,7 \cdot 10^{-3}$
<b>Lamina 1</b>	0,0315	$0,3 \cdot 10^{-3}$
<b>Lamina 2</b>	0,0315	$0,5 \cdot 10^{-3}$
<b>Lamina 3</b>	0,0315	$0,7 \cdot 10^{-3}$
<b>Whole composite structure</b>	0,0315	$1,5 \cdot 10^{-3}$

Table 1. Size of structure elements of multi-scale model for simulation

### 3. Direct testing of composites

Destructive and non-destructive testing and its brief description are included below. An experimental and also a simulation work are based on oscillation of composite samples. Movement equations are presented here also with special experiment premises.

#### 3.1 Destructive testing

The tensile testing is time and money consuming but it is widely used specially for explicit results. It includes the tensile testing to rupture, bending, pressure, cycle testing, dynamic and high loaded testing of fibres, as well as whole composites. Tested samples have to be prepared precisely before testing and special handling is also necessary (Bogdanovich & Pastore, 1996), (Ivanov et al., 2007).

#### 3.2 Non-destructive testing

The non-destructive testing is a treatment on the sample without a rise of non-reversible deformation. These tests were used for safety at first. The testing is repeatable and cheaper because a sample is not destructed. Special signal impacts the sample and response of material is detected. Detection of defects is widely used in non-destructive tests. Optical and visualisation methods scan surface of the sample with optical microscopes, magnifying glass or glasses on the unit cell level or lamination where a component boundary is clearly visible. Magnification is possible with scanning electron microscopes etc. (Introduction to NDT, 2002), (Diedericks, 2002). The penetrate method also detects volume characteristics of composite surface. It is necessary to use a penetrate liquid which is in the contact with surface, so a clear medium and nonporous structure is important (NDT encyclopedia, 2007). The magnetic inspection is possible only for ferromagnetic materials, demagnetisation ending and clear medium (Introduction to NDT, 2002).

The radiography is used for inspection through a material structure. Neutron, roentgen and gamma radiography are spread. The principle is an application of short weave lengths. An intensity of trans-illumination is detected. Places with lower density and with defects transmit more radiation than surroundings. A danger from an irradiation is the biggest problem of this method (Introduction to NDT, 2002), (La Plante et al., 2005).

An ultrasound is widely used for a defect detection, a thickness determination, a monitoring of degradation and abrasion, an impregnation ratio, a delaminating, a density, a porosity and a size of crystals. It is called a contact measurement. Weaves go through a sample and come back from the next end or from the defect. It is possible to vibrate with very thin samples (La Plante et al., 2005), (NDT encyclopedia, 2007).

A mechanical response of material is detected from various methods. The proof experimental method for obtaining mechanical properties is an evaluation of eigen-frequencies of vibration going through a composite plate. Lagrange's, Euler-Bernoulli's, Rayleigh's and Timoshenko's theories are relevant (Černý, 2000). The Lagrange's theory is valid for the longitudinal oscillation. Theory Euler-Bernoulli is basic for the transversal oscillation and Rayleigh with Timoshenko made corrections of it (Brepta et al., 1994). In (Puchegger, 2003) is valid only for isotropic material. Sample is hanged on two carbon fibre loops. These loops are connected with a piezo-electric sensor. In the sample a bending oscillation and a transversal vibration is detected. The longitudinal oscillation is used for testing of elastic properties of plane wings in (Cheby & Hwu, 2006). Sample is clamped on

one side and free end which is on the second side. A sensor is on the free end. A longitudinal mechanical vibration is detected. The method used here is based on the analysis of longitudinal oscillation and on transversal Timoshenko's oscillation for orthotropic material (Černý, 2000). It was tested at the Department of Structure and Mechanics of Rocks of Science Academy of the Czech Republic. Deeper description follows.

### 3.3 Longitudinal vibrations theory

A thin axially symmetry beam is an assumption. Basically, cross-sections of the beam are planar during deformation and a stress is uniformly distributed in the cross-section. Only uniaxial loading is mentioned there. Transversal movements absorb neglectable amount of energy. See Fig. 15. (Brepta et al., 1994), (Brepta, 1997).

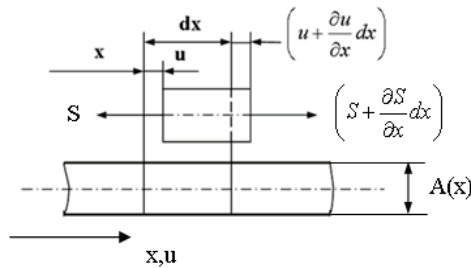


Figure 15. Deformation of thin beam evoked by longitudinal wave (Brepta et al., 1994)

The Hooke's law is valid for stress influences to the beam element for uniaxial load

$$\sigma = E\varepsilon = E \frac{\partial u}{\partial x} \quad (12)$$

where  $E$  is the longitudinal tensile modulus,  $\partial u / \partial x$  is the elongation same as  $\varepsilon$ . The motion equation is than

$$A(x) \frac{\partial^2 u}{\partial t^2} = \frac{E}{\rho} \frac{\partial}{\partial x} \left[ A(x) \frac{\partial u}{\partial x} \right] \quad (13)$$

where  $A$  is the cross-section area,  $\rho$  is the density,  $\sigma$  is the stress,  $u$  is the movement in the  $x$  direction,  $E$  is the Young's modulus. The phase velocity of wave is defined as

$$c_0^2 = \frac{E}{\rho} \quad (14)$$

and the relation has to be valid

$$\frac{\partial u}{\partial x} \pm \frac{1}{c_0} \frac{\partial u}{\partial t} = konst \quad (15)$$

The general integral of wave equation is

$$u(x, t) = f(c_0 t + x) + g(c_0 t - x) \quad (16)$$

A solution is based on two waves going in the opposite directions. Relation between element velocity  $v$ , density  $\rho$ , wave velocity  $c$  and stress  $\sigma$  is

$$\sigma = \rho c_0 v = E \frac{v}{c_0} \quad (17)$$

The initial conditions for free end beam for free oscillation is that stress is at zero.

$$E \left( \frac{\partial u}{\partial x} \right)_{x=0} = 0 \quad (18)$$

is valid when end of the beam is on the zero of coordinates and phase is not changed (Brepta et al., 1994), (Brepta, 1997).

### 3.4 Transversal vibrations theory

The Euler-Bernoulli's theory based on an assumption that cross-sections of the beam stays planar and a deflection is made only in the cross to  $x$  axis. The deflection is flat and very small anyway. Movements in  $x$  direction are neglected. Loading in element  $dx$  is shown on Fig. 16 (Brepta et al., 1994)

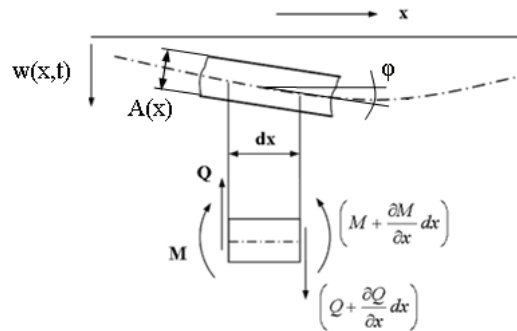


Figure 16. Loading on the element during trans oscillation (Brepta et al., 1994)

Motion equation is

$$\rho A(x) dx \frac{\partial^2 w}{\partial t^2} = \frac{\partial Q}{\partial x} dx \quad (19)$$

and deflection curve for flat curves is

$$M = -EI(x) \frac{1}{R} = -EI \frac{\partial^2 w}{\partial x^2} \quad (20)$$

where  $EI$  is the flexural rigidity,  $R$  is the radius of curvature,  $w$  is the deflection. Timoshenko made corrections to basic theory. Here is neglected crimp of the cross-section. Gradient angle of the deflection curve is a sum of turn angle  $\psi$  (affected by bending) and angle change  $\beta$  (shear affected by displacement)



$$\frac{\partial w}{\partial x} = \psi + \beta \quad (21)$$

Bending moment is

$$M = -EI \frac{\partial \psi}{\partial x} \quad (22)$$

where quotient is the curvature of deflection curve.

Motion equation for movement of element is

$$A\rho \frac{\partial^2 w}{\partial t^2} dx = \frac{\partial Q}{\partial x} \quad (23)$$

where  $Q$  is moving force. Equation for element turning is

$$\rho I \frac{\partial^2 \psi}{\partial t^2} dx = Q dx - \frac{\partial M}{\partial x} dx \quad (24)$$

Movement equation for deflection  $w(x,t)$  is at the end

$$c_0^2 k^2 \frac{\partial^4 w}{\partial x^4} + \frac{\partial^2 w}{\partial t^2} - k^2 \left( 1 + \frac{E}{G\alpha} \right) \frac{\partial^2 w}{\partial x^2 \partial t^2} + \frac{1}{\alpha} \frac{k^2}{c_2^2} \frac{\partial^4 w}{\partial t^4} = 0 \quad (25)$$

where  $c_2$  is the velocity of shear waves in continuum defined  $c_2^2 = G/\rho$  and it is valid  $E/G = 2(1 + \mu)$ ,  $\mu$  is the Poisson's ratio and  $\alpha$  is the coefficient of cross-section shape. Theory gives good results for thin beams (Brepta et al., 1994), (Brepta, 1997).

### 3.5 Resonant frequency method description

An application of the method of resonant frequencies was developed at the Department of Structure and Mechanics of Rocks of Science Academy of the Czech Republic (Černý, 2000). Than Lengthwise tensile modulus and Poisson ratio of orthotropic plate is possible to determine from resonant frequency spectrum of the longitudinal mechanical oscillation. Shear modulus is determined from a resonant spectrum of a transversal oscillation. The big advantage is accuracy of this method. The experiment is fast and absolutely non-destructive (Žaloudková, 2006).

The experiment is measured on the sensor for resonant frequency Erudite CNS Electronics Ltd., London, UK. On the exciting electrode there is brought an alternating voltage. Voltage is harmonically running with amplitude 400 V and exciting 10 Hz - 100 kHz. Electrostatic load effects grounded conductive sample. Than electrostatic load excites mechanical oscillation. The electric current goes through the sample in the alternating voltage. So signal of a mechanic oscillation is detected on the same principle as an exciting (Černý, 2000), (Žaloudková, 2006).

It is important that axes of sample orthotropy (warp and weft of the plain weave) are positioned in the same direction as an oscillating propagation during testing. A sample has to be prepared for it. If this is not correct, propagation would be applied as a general longitudinal and transversal oscillation and explicit resonant spectrum could not be found (Černý, 2000).

## 4. Experiment

In the experiment there is a description of the results obtained from the simulation in Comsol Multiphysics™. A deeper discussion is presented for longitudinal vibrations. The experiment is compared with a simulation and it is visualized in polar diagram for the in-plane treatment in the plain weave reinforcement.

The tested composite is eight layered laminate from carbon fibre in plain weave surrounded with carbon matrix. Matrix was prepared from phenolic resin Umaform LE with high-temperature treatment. Matrix has got good size stability, thermo stability, chemical resistance and low shrinkage. Bundle is made from 6000 parallel infinite high strength carbon fibres Toray®. Porosity is 20 - 25%. Important input properties are in Table 2.

Component	Density [kg.m <sup>-3</sup> ]	Young's modulus [MPa]	Poisson's ratio [-]
Fibres Toray 800 HB	1810	294 000	0,24
Matrix	1400	89	0,30
Voids - air	1,3	0,0	0,0

Table 2. Values of important input mechanical properties

### 4.1 Simulation results

The Structural Mechanical Module was used for computation in Comsol Multiphysics™ 3.2. The Eigenfrequency Analysis was set as application compatible with experiment. The structure is defined at first. The properties of components, the boundaries and the external impact are defined in Physics. The help constants and equations could be defined in Options. After meshing and solving the result graphs are shown in Postprocessing.

The results for all modules are shown in Table 3. Dividing of stress and strain gives us these values as critical elastic properties. The longitudinal modulus is very different for lengthwise and crosswise bundle. The difference is smaller for bundles with defects but it is still high. The unit cell is combined from various components so the difference is minimal between unit cells. Value is in the range from previous lower scales. The laminas and the whole composites modules are at same units as unit cells. The synergy effect increases modules slowly from the unit cell to the whole composite.

The result response is defined for the first eigenfrequency of sample with free ends. One node point is detected in the middle of sample. The free ends oscillate across along the lengthwise axis. The colour scale in the figure goes from minimal dark blue through middle green to the maximal dark red for value of output property in every case. Following figures have got some geometry adaptation for better resolution and predicative possibility. Full models were described in subchapter 2.3.

The longitudinal stress of crosswise bundle is concentrated in the matrix where fibres and matrix are in the contact vertically (Fig. 17.). The lowest longitudinal stress is in the fibres in the contact with each other and matrix between them but from the scale it is clear that this stress is opposite than in matrix. The fibres are loaded with pressure. Mean stress is in the middle of the fibres. The longitudinal strain of crosswise bundle (Fig. 18.) is in the fibres and in the matrix near fibres. The pressure is in the matrix too where fibres are close together in the horizontal position. The longitudinal stress of lengthwise bundle is maximal in the matrix (Fig. 19.). The lengthwise fibres are minimal loaded in the middle but maximal at the

ends. The longitudinal strain of lengthwise bundle (Fig. 20.) has got a maximum at the ends. The lowest strain is in the middle (in the node point of the eigenfrequency).

Scale and type of the tested sample	Longitudinal modulus [MPa] $E_x = \sigma_x / \varepsilon_x$	Transversal modulus [MPa] $E_y = \sigma_y / \varepsilon_y$	Shear modulus [MPa] $G_{xy} = \sigma_{xy} / \varepsilon_{xy}$
Crosswise bundle	252,8	52,9	103,2
Lengthwise bundle	160289,0	97,9	61570,8
Crosswise bundle with defects	189,6	129,0	38,6
Lengthwise bundle with defects	130663,1	623,0	40005,0
Unit cell 1	54813,2	408,2	9530,1
Unit cell 2	62374,9	716,8	9267,2
Unit cell 3	53259,2	949,7	8491,5
Lamina 1	54807,5	534,8	6859,4
Lamina 2	62384,7	626,3	7607,7
Lamina 3	53245,4	554,1	6684,2
Whole composite	<b>86264,1</b>	<b>617,2</b>	<b>7340,0</b>

Table 3. Results from the simulation in Comsol Multiphysics

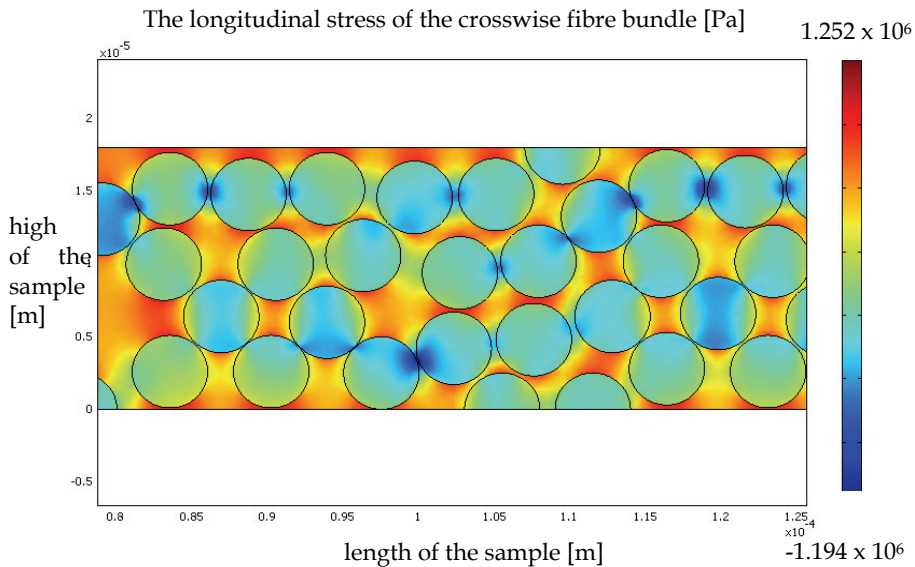


Figure 17. Longitudinal stress of the crosswise fibre bundle

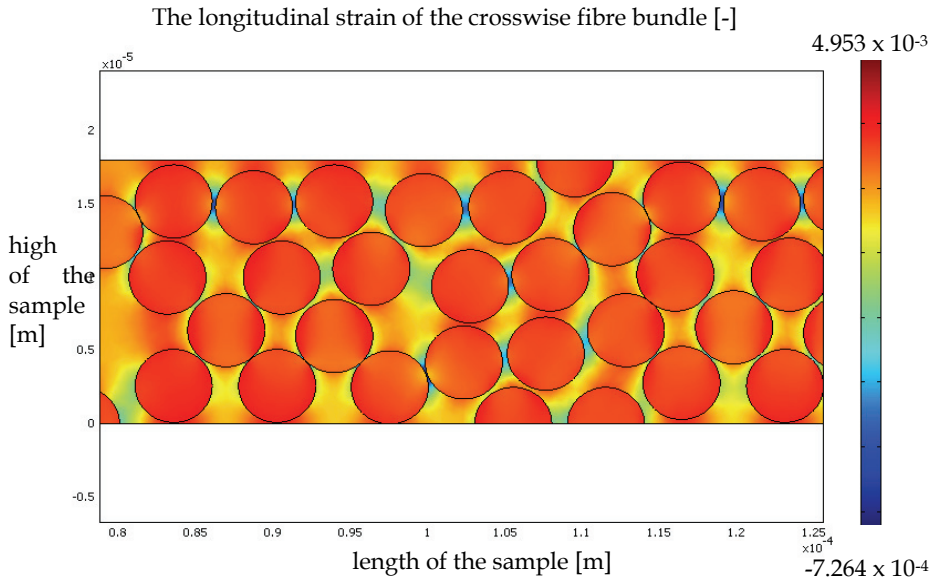


Figure 18. Longitudinal strain of the crosswise fibre bundle

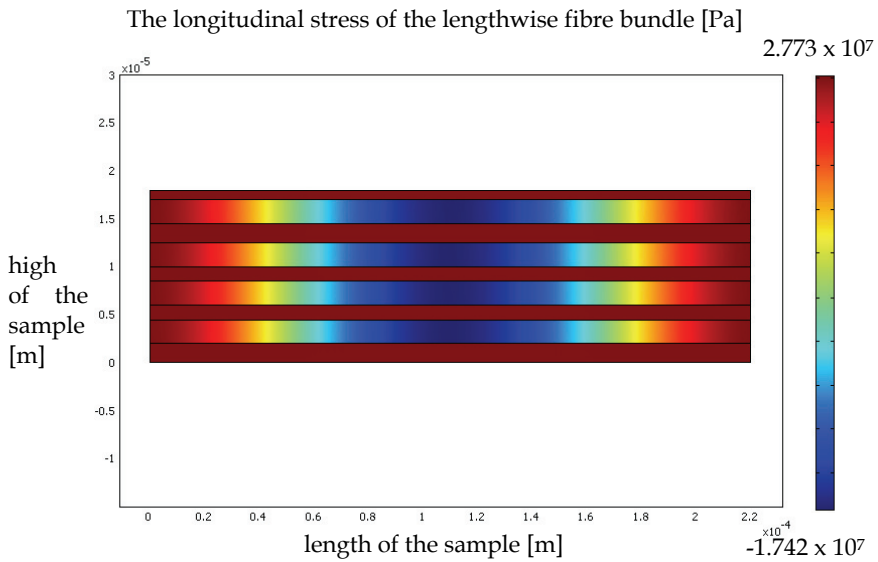


Figure 19. Longitudinal stress of the lengthwise fibre bundle

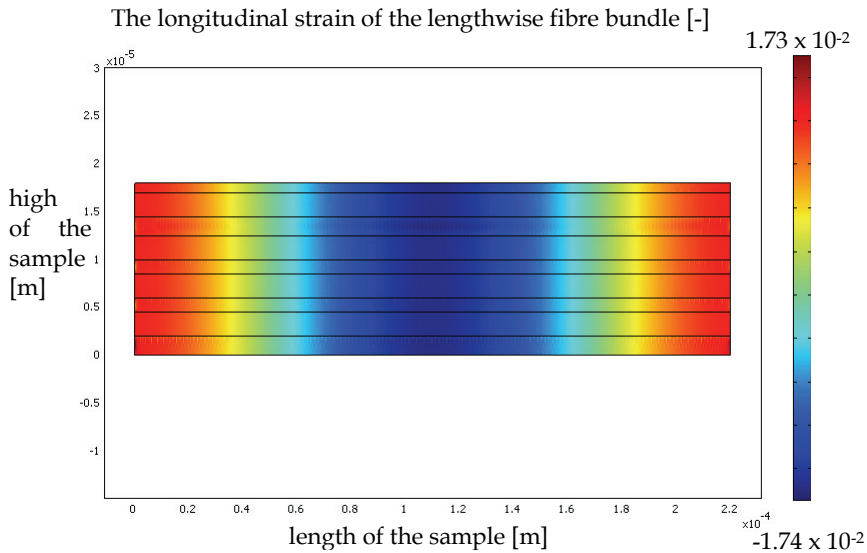


Figure 20. Longitudinal strain of the lengthwise fibre bundle

The crosswise bundle with defects has got the highest longitudinal stress in the carbon part near defects horizontal curvature (Fig. 21.). The longitudinal strain is maximal in the pores in the transversal curvature of the defects (Fig. 22.). A minimum is everywhere else. The concentration of the stress and of the strain is highly affected by the occurrence of the defects in the carbon part. The same results are shown on the Fig. 23. and Fig. 24. for the lengthwise bundle with the defects. The critical longitudinal stress is located in the carbon part and longitudinal strain is concentrated in the pores. A conclusion could be set that the carbon part carries stress and the pores localize strain.

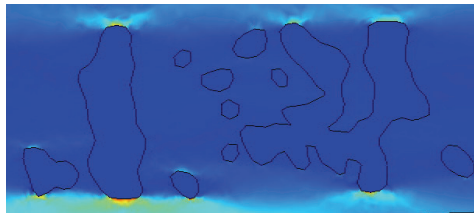


Figure 21. Longitudinal stress - crosswise bundle with defects

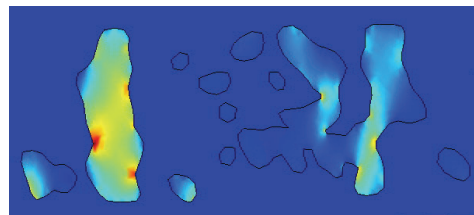


Figure 22. Longitudinal strain - crosswise bundle with defects

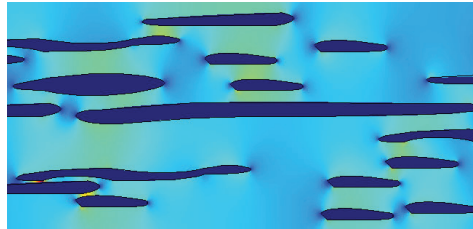


Figure 23. Longitudinal stress - lengthwise bundle with defects

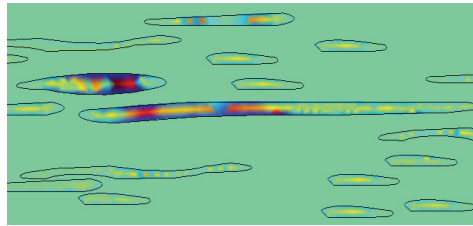


Figure 24. Longitudinal strain - lengthwise bundle with defects

The longitudinal stress for the Structural unit cell 1 (Fig. 25.) is occurred mostly in the lengthwise bundle of the reinforcement in the middle of the sample where the node point is. Minimal stress is elsewhere. The longitudinal strain in the same Structural unit cell 1 is located in the all components in the node at maximum (Fig. 26.). Stress is located in the lengthwise bundle but strain is in all material.

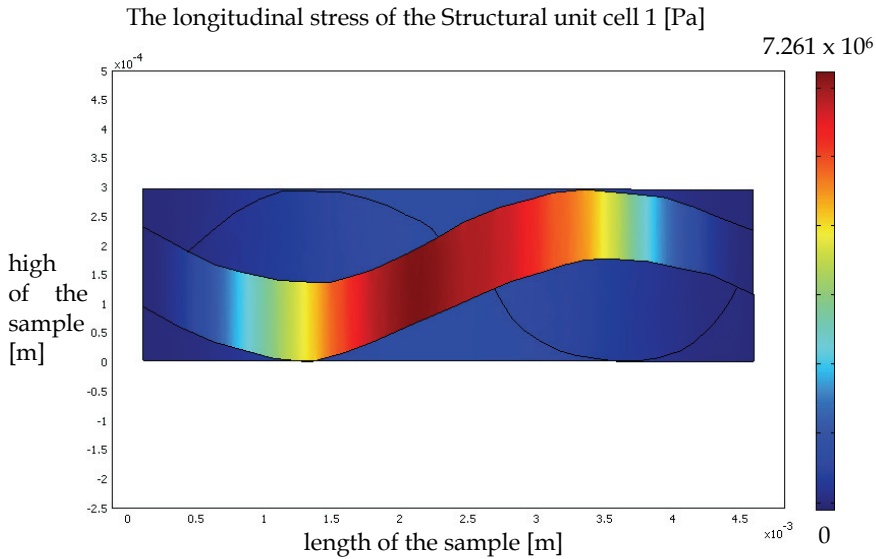


Figure 25. Longitudinal stress of the Structural unit cell 1

Structural unit cell 2 has got the critical value of the longitudinal stress also in the lengthwise bundles (Fig. 27.). The critical loading is transferred to the side because crosswise bundles slide during processing. On the other hand the strain is maximal in the defects (Fig. 28.). The longitudinal strain in Structural unit cell 3 is also localised in the pores (Fig. 30.). The Structural unit cell 3 has got more balanced loading for the stress properties than others. The longitudinal stress is high here but not really critical. The stress is located mostly in the lengthwise bundles in the Structural unit cells as general. The strain is the highest in all materials where defects are not but where defects were occurred strain is concentrated in the pores.

Laminas 1, 2, 3 have got the highest stress and strain in the node point and in the surrounded area. The lamina is combined from bricks with the same parameters so these results are expected.

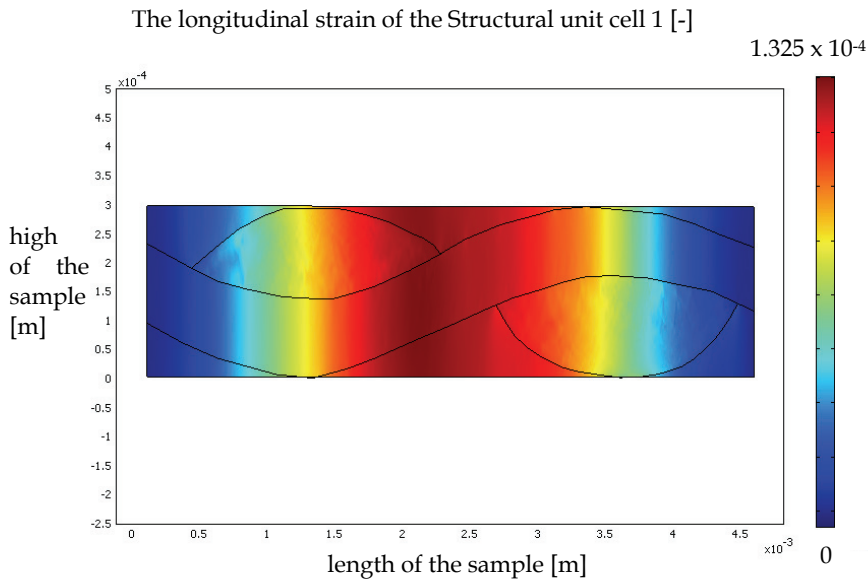


Figure 26. Longitudinal strain of the Structural unit cell 1

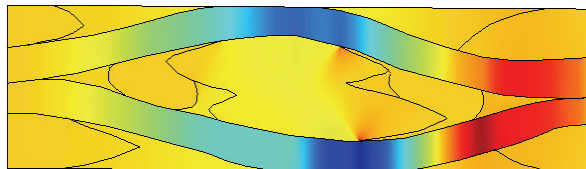


Figure 27. Longitudinal stress of the Structural unit cell 2

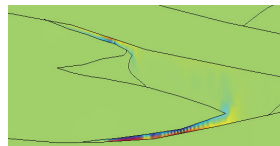


Figure 28. Longitudinal strain of the Structural unit cell 2

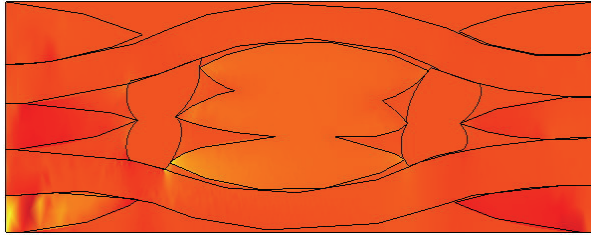


Figure 29. Longitudinal stress of the Structural unit cell 3

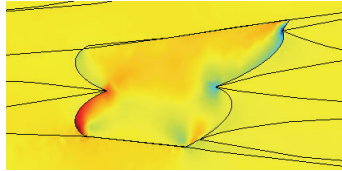


Figure 30. Longitudinal strain of the Structural unit cell 3

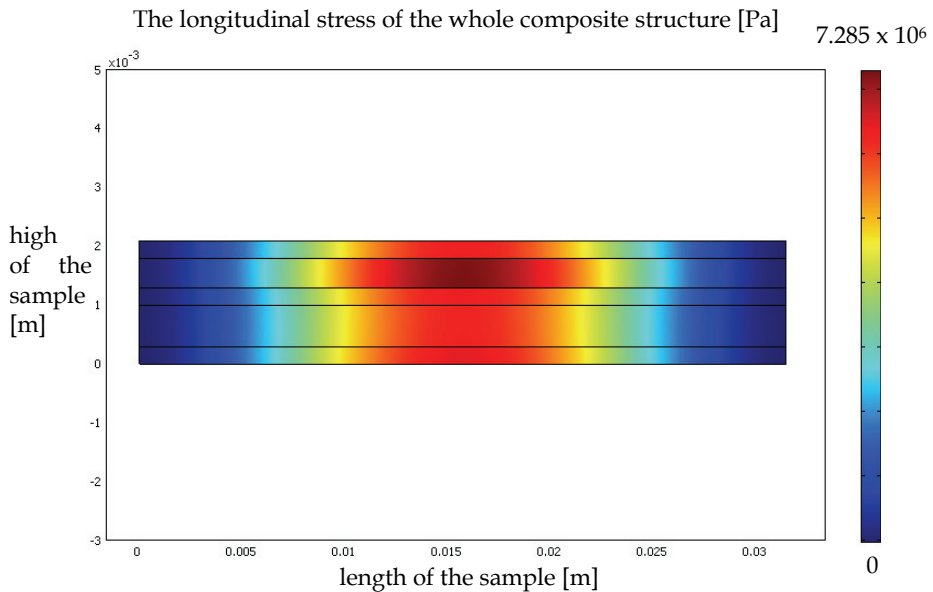


Figure 31. Longitudinal stress of the whole composite structure

The whole composite combined from laminas has got longitudinal stress the highest in the middle of the sample similarly like single lamina (Fig. 31.). The higher impact goes farther for lamina which it has got higher longitudinal stress from the previous single testing. The



longitudinal strain for composite is also maximal in the middle (Fig. 32). But impact is the same no matter which lamina it is.

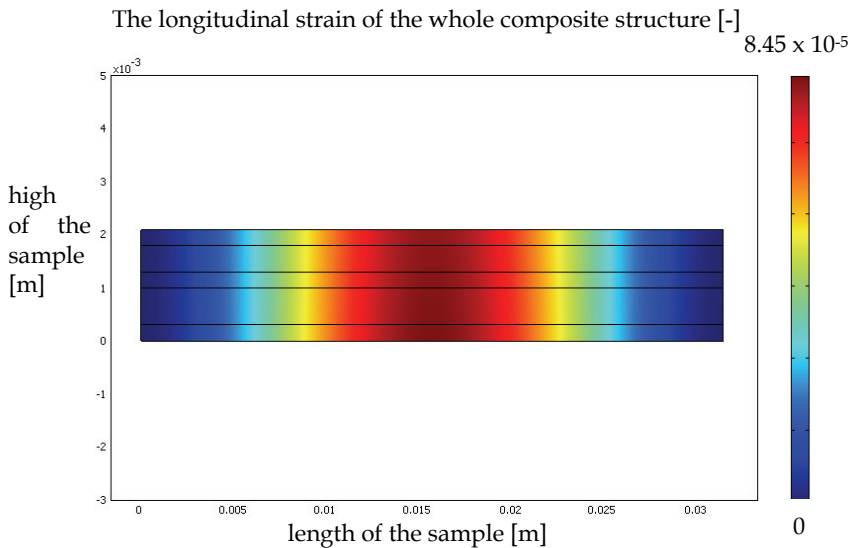


Figure 32. Longitudinal strain of the whole composite structure

#### 4.2 Simulation and experimental comparison

The experiment was measured at Department of Structure and Mechanics of Rocks of Science Academy of the Czech Republic. Composite with the same properties as simulation model was prepared in directions of the warp, the weft and in the  $\pm 45^\circ$  angle from the warp. The results are used for the in-plane discussion between simulation and experimental data on the following figures. All is completed with computed axial impact from equations in subchapter 2.1. The warp longitudinal modulus and shear modulus from simulation and experiment were input for equations completed with various angle  $\delta$  in-plane of reinforcing fabric.

Table 4. shows results from experiment and simulation. The longitudinal modulus from simulation agrees with the experimental longitudinal modulus good. The simulation is a bit lower but it is still near to the hundreds of GPa. The shear modules are nearly the same for experiment and simulation.

The longitudinal modulus from simulation is a smaller than experimental only in the warp and weft direction, see Fig. 33. Longitudinal modulus in from the computation is nearly the same in  $45^\circ$  from the warp direction. Calculation is in  $45^\circ$  angle from the warp is same not only for experiment and simulation, but validity of equation is confirmed with comparison of measured experimental longitudinal modulus in  $45^\circ$  which is also the same. Loading transformation in equation agree for all longitudinal modules.

	Longitudinal modulus [MPa] $E_x = \sigma_x / \epsilon_x$	Transversal modulus [MPa] $E_y = \sigma_y / \epsilon_y$	Shear modulus [MPa] $G_{xy} = \sigma_{xy} / \epsilon_{xy}$
Whole composite structure from simulation	86264	617	7340
Composite from experiment - warp direction	103000	-	7630
Composite from experiment - 45° to the warp direction	25000	-	54000
Composite from experiment - weft direction	108000	-	7550
Composite from experiment - -45° to the warp direction	24000	-	50000

Table 4. Simulation and experimental elastic modules

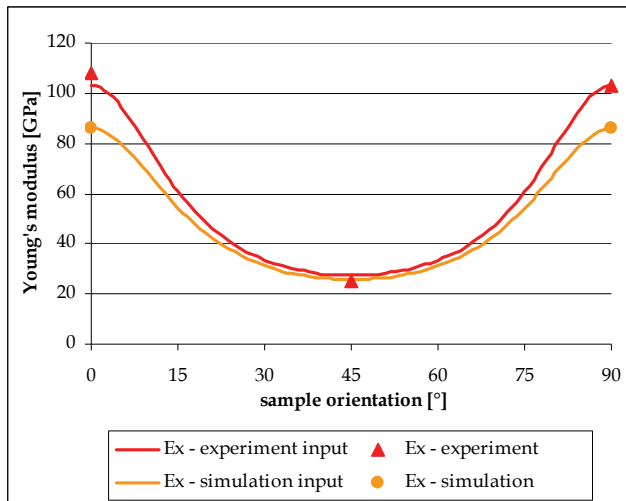


Figure 33. Longitudinal modulus from experiment and simulation

The shear modulus is the same in warp and weft direction for both compared cases, see Fig. 34. The shear modulus are different in the 45° from the warp. The experimental measured shear modulus is the highest. The computed shear modulus from experiment is in the middle. The computed shear modulus from simulation is the lowest. The equation prediction is not completely the same as an experiment but results are good anyway. The shear modulus from computation gives relevant data as a critical value with margin.

On Fig. 35. is a visualisation of whole in-plane loading of longitudinal and transversal modules. The previous discussion is still valid. More, the longitudinal modulus goes in different trend than the shear modulus for both, experiment and simulation.

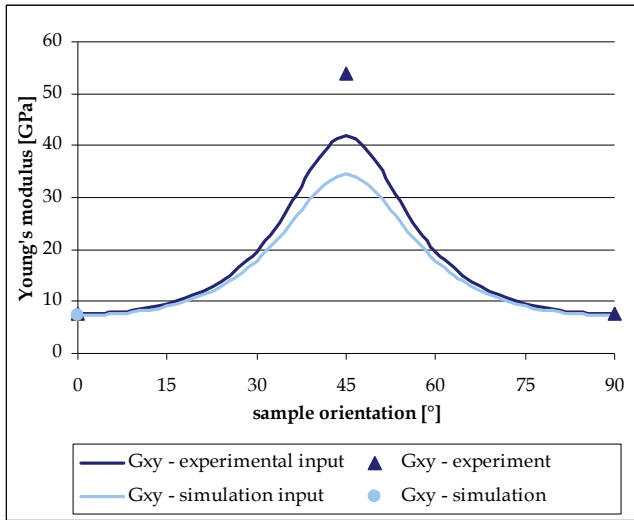


Figure 34. Shear modulus from experiment and simulation

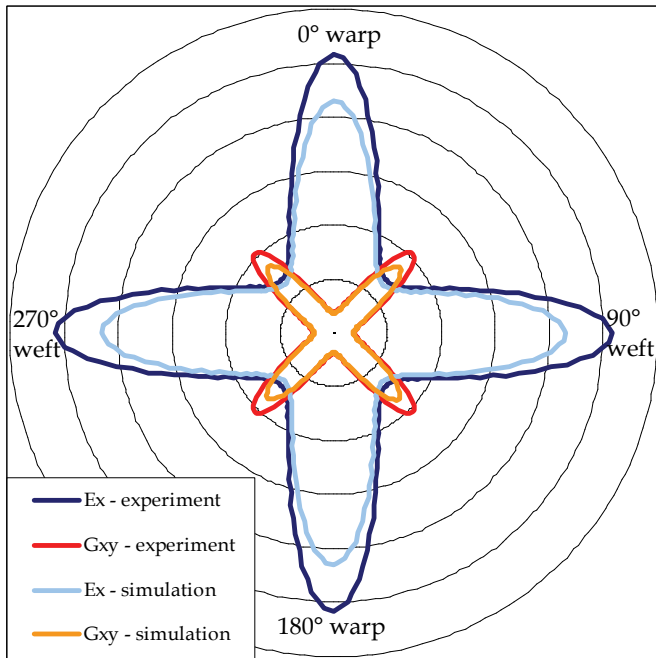


Figure 35. In-plane comparison of experiment and simulation

## 7. Conclusion

The conclusion from the previous pages follows as estimation between the experiment and the simulation of elastic properties of the carbon/carbon composite with the plain weave reinforcement. The non-destructive testing is widely used for evaluation of the composites. The brittle carbon/carbon composite is necessary to be tested with the non-destructive methods because critical loading is not occurred with plastic deformation. Simulations with the finite element method are fast and precise same as a resonant oscillation experiment. Both methods were compared here. Experiment was tested at Department of Structure and Mechanics of Rocks of Science Academy of the Czech Republic and was used as a special comparing property for the multi-scale simulation. The commercial software Comsol Multiphysics™ was used for calculation with proper determination of the material properties.

The simulation and experiment correlate well for longitudinal modulus of the whole composite in all directions in the in-plane of the reinforcement. The shear modules embody also good agreement between the simulation and the experimental values. Longitudinal modulus go opposite way than the shear modulus in both cases. The theory agrees well for it. Where warp and weft reinforce composite greatly, shear is not possible to expand. Sliding between warp and weft bundles results the higher shear modulus in the 45° angle from the warp direction.

The most influencing factor for the elastic properties is an amount of the lengthwise bundles for the longitudinal modulus. The position of the crosswise bundles with the matrix properties influences the shear modulus. The transversal modulus is mostly affected by the presence of the defects. Defects work upon all others modulus anyway.

Presented study affords two-dimensional multi-scale model with the good match for the testing of the real composites. The simulation was adapted well for the real composite. Combination of the multi-scale and the finite element simulation provide highly relevant data of the elastic modulus which is confirmed by the used experiment.

Eigenfrequency helps to evaluate properties in longitudinal and also in the transversal directions for material with an orthotropic properties. More directions are offered to the evaluation and not only isotropic structure is possible to be used. It is an advantage of the experiment. The disadvantage it is possible testing of a thin sample body only. Some more advanced sample preparing should be done in the future for making thin plates in different directions of the composite especially for the direction transversely to the reinforcement.

The simulation with the multi-scale modelling is necessary to evaluate precise input values for the lowest scale. Here it is not problem with the fibre testing. Many methods are used and suitable. The matrix properties are more complicated to obtain. Testing of the matrix alone is a problem still and it should be solved soon.

Previous non-destructive testing is possible to use for any material with the similar structure and the same prepreg technology. If geometry models on the Structural unit cell scale are adapted, different technology should be evaluated with the same procedure too.

Both methods presented here, the experiment of resonant oscillations and the finite element simulation, are good instrument together for the testing of the elastic properties and preparing of the new composites with varied structure or material properties.

## 8. References

- Agarwal, B.D.; Broutman, L.J. (1987). *Fibre composites*. (Czech translation), SNTL, DT 531.8:677.499.004.12, Prague, CR
- Berthelot, J.-M. (1999). *Composite Materials. Mechanical Behavior and Structural Analysis*. Springer-Verlag, ISBN 0-387-98426-7, New York, USA
- Bogdanovich, A.E.; Pastore, C.M. (1996). *Mechanics of textile laminated composites*. Chapman and Hall, ISBN 0 412 61150 3, London, UK
- Brepta, R. (1997). *Stress waves and beat effect in linear elastic and viscoelastic environment*. Lenam, s.r.o. Liberec, ISBN 80-7083-228-2, Liberec, CR
- Brepta, R.; Půst, L.; Turek, F. (1994). *Oscillation mechanics*. (In Czech), Technical guide 71, Sobotáles, ISBN 80-901684-8-5, Prague, CR
- Cheby, S.H.; Hwu, CH. (2006). On-line measurement of material properties for composite wing structures. *Composites Science and Technology*, Volume 66, Issues 7-8, page numbers (1001-1009)
- Composite authors (2002). Introduction to Nondestructive Testing. Interent pages of organisation: The Collaboration for NDT Education. <http://www.ndt-ed.org/GeneralResources/IntroToNDT/GenIntroNDT.htm>
- Composite authors (2007). *NDT Applications and Limitations*, NDT Encyclopedia of nondestructive testing, NDT net. <http://www.ndt.net/news/files/4556.php>
- Černý, M. (2000). *Evaluation of elastic constants of orthotropy material in state of beams and tubes*. Dissertation thesis, CTU, Prague, CR
- D'Amato, E. (2001) Finite Element Modeling of Textile Composites. *Composite Structures*, Elsevier, No. 54, page numbers (467-475)
- Diederichs, R. (2007). Internet pages about NDT, Available from Wikipedia NDT Encyclopedia. <http://www.ndt.net/ndtaz/ndtaz.php>
- Fitzer, E.; Manocha, L.M. (1998). *Carbon reinforcement and Carbon-Carbon Composites*. Springer-Verlag, ISBN 3-540-62933-5 Berlin, Germany
- Hokr, M. (2006). *Application of computer modelling*. (In Czech), Study material, Technical University of Liberec, Liberec, CR
- Ivanov, S.; Ivanov, D.; Lomov, S.; Verpoest, I. (2007) Modelling of mechanical behaviour of textile glass-polypropylene composite. *CD Proceedings of BEM-FEM Conference*, St.Petersburg, Russia, 09/2007, Catholic University of Leuven, Leuven
- Kühn Gb.R. (2007) *Mesoscopic resolution of plain-weave*. Internet pages: Fraunhofer Institute for High-Speed Dynamics, Ernst-Mach-Institut (EMI), Freiburg, Germany, <http://www.emi.fraunhofer.de/EN/ResearchFieldsAndContacts/ProjectExample s/WovenFabrics.asp>
- LaPlante, G.; et al. (2005). Detection of water ingress in composite sandwich structures: a magnetic resonance approach, *NDT and E International*, Volume 38, Issue 6, page numbers (501-507)
- Laš, V. (2004). *Mechanics of composite materials*. West Bohemia University of Plzeň, ISBN 80-7043-273-X, Plzeň, CR
- Lomov, S.V.; et al. (2001). Textile composites: modelling strategies. *Composites Part A: applied science and manufacturing*, Elsevier Science Ltd., page numbers (1379-1394)
- Lomov, S.V. (2007). *Virtual textile composites software WiseTex: Integration with micro-mechanical, permeability and structural analysis*. Catholic University of Leuven, Leuven, Belgium, 2007

- Lomov, S.V.; et al. (2007). Meso-FE modelling of textile composites: road map, data flow and algorithms. *CD Proceedings of International conference ICCM-15*, Kyoto, Japan
- Marvalová, B. (2000). *Determination of effective mechanical properties of plain weave reinforcement composites*. (In Czech), Inaugural dissertation, TU v Liberci, Liberec, CR
- Miravete, A. (2000). *3-D textile reinforcements in composite materials*. Book of contributors. Woodhead Publishing Ltd Cambridge England and CRC Press, ISBN 1-85573-376-5, Cambridge, UK
- Puchegger, S. et al. (2003) Experimental validation of the shear correction factor. Letter to editor, *Journal of Sound and Vibration*. No. 261, page numbers (177-184)
- Reddy, J.N. (2006). *An Introduction to the Finite Element Method*. Third Edition, Mc Graw-Hill Higher Education, ISBN 0-07-246685-5, New York, USA
- Savage, G. (1993). *Carbon-Carbon Composites*. Chapman and Hall, ISBN 0-080-43716-6, London, UK
- Skoček, J.; Zeman, J.; Šejnoha, M. (2005). On determination of periodic unit cell for plain weave fabric composites: Geometrical modelling of real world materials. *Engineering Mechanics*, CTU, Prague, CR
- Stříž, B. (2002). *Textile Mechanics II. Application of continuum mechanics*. Technical University of Liberec, Liberec, CR
- Šejnoha M. (2007). *Homogenisation of heterogeneous materials - similarity between textile reinforcement and historical masonry constructions*. Lecture for Centre of quality and reliability of manufacturing, Technical University of Liberec, Liberec, CR
- Tomková, B. (2005). *Blending rules*. 10. lecture for lesson Composite with textile reinforcement, Study material, Technical University of Liberec, Liberec, CR
- Tomková, B. (2006). *Modelling of Thermophysical Properties of Woven Composites*. Dissertation thesis, Technical University of Liberec, Liberec, CR
- Vinson, J.R.; Chou T.W. (1975). *Composite materials and their use in the structure*. Applied science publishers Ltd., London, UK
- Vozková, P. (2007). Elastic Properties of Woven Composites. *CD Proceedings of the Conference 15th Annual International Conference on Composites/Nano Engineering*, Haikou, Hainan Island, China, 08/2007, University of New Orleans, New Orleans
- Žaloudková, M. (2006). *Porosity determination of C/C composites with image analysis and correlation with mechanical properties*. (In Czech), Dissertation thesis, Technical University of Liberec, Liberec, CR

# Two-Dimensional PEM Fuel Cells Modeling using COMSOL Multiphysics

Zhongying Shi and Xia Wang  
*Oakland University*  
USA

## 1. Introduction

A fuel cell has been considered as an efficient and clean alternative power source for automobile industry since the energy crisis forced people to find a substitution for fossil fuels. A proton exchange membrane fuel cell, also known as polymer electrolyte membrane fuel cell (PEMFC), becomes a prime candidate for applications in vehicles because of its following features: the PEMFC operates at a relative low temperature (less than 90°C); the PEMFC can start quickly; the PEMFC has a higher current density due to thin membrane electrodes assembly (MEA) compared to other types of fuel cells; and there are no corrosive fluid hazards since there is no liquid electrolyte present in the PEMFC.

Nevertheless, the wide application of a PEMFC is limited due to high capital cost, fuel availability, and durability etc. The difficulty of maintaining suitable thermal management and water management also affects the fuel cell performance significantly. For example, too much water produced on the cathode side will fill the pores of gas diffusion layers (GDLs), and therefore block the diffusion of reactants to reach the catalyst layer. Too little water on the anode side will dry up the membrane so that protons cannot migrate through it. Both cases result in a decrease in the cell output power.

Experimental research and numerical simulation have been used in fuel cell design in order to improve the performance of fuel cells. Experimental data is useful to validate the models. The computational models are efficient in predicting the cell performance under a variety of design parameters. Fuel cell models can be classified into 1D, 2D and 3D according to dimensions. The accuracy of 1D model (Springer et al., 1991), (Gurau et al., 2000) is sacrificed due to some assumptions made in order to simplify the problem to 1D. A 3D model simulates the reactant gas flow in the directions along the flow channel and perpendicular to the flow channel simultaneously, which results in more accurate results but requires longer computational time and larger computing capacity facility (Haralldsson & Wipke et al., 2004) (Berning et al., 2002). A 2D fuel cell model (Siegel et al., 2003) (Biyikoglu, 2005) (Hwang, 2006) combines the benefits of 1D and 3D models and gains its popularity in PEM fuel cell modeling due to its higher computational efficiency compared to 3D models and better simulation accuracy compared to 1D models.

A two-dimensional mathematical model of a PEM fuel cell can be conducted in two different modes: parallel or perpendicular to the gas flow direction in the gas channel

while the other modelling dimension is across the membrane in both cases. Models conducted in the first mode (parallel to the gas flow direction) consider the influence of fluid behavior in the channel; while in the second mode (perpendicular to the gas flow direction), the interdigitated flow pattern can be easily investigated. The goal of the present work is to develop 2-D isothermal PEM fuel cell models in two different modes to investigate the performance of fuel cells such as the mass concentration and velocity distribution of reactants, the polarization curve, the output power density, etc. The results from two modes are then compared to each other.

The organization of this paper is as follows: in section 2, the single-phase two-dimensional PEM fuel cell models are developed and the models are solved using the commercial software package COMSOL Multiphysics. The main results obtained from the present work are discussed in section 3. In section 4, the main conclusions derived from the present work are summarized.

## 2. Model

Fig. 1 schematically shows a 3D single PEMFC and its various components including the membrane, flow channels, gas diffusion layers and catalyst layers on both anode and cathode sides. To conduct a 2 D simulation, there are two options to choose the modeling geometry: one is in x-y plane as shown in Fig. 2(a), and the other is in x-z plane as shown in Fig. 2(b). Both geometries will be studied in this paper.

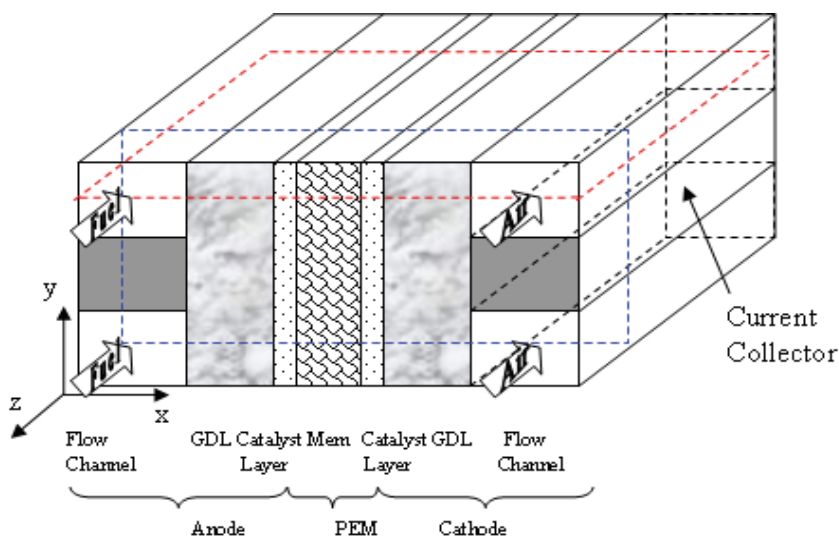


Figure 1. Three dimensional diagram of a PEMFC and its various components



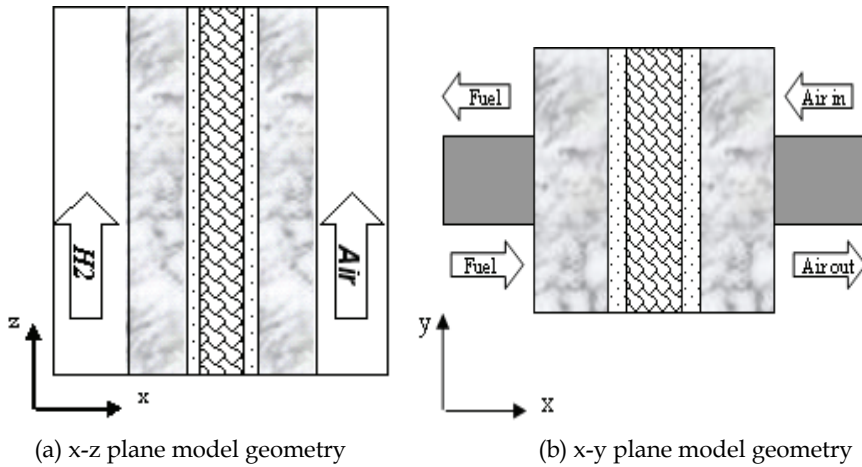


Figure 2. Two-dimensional PEM fuel cell modelling geometry

## 2.1 Assumptions

The present model is established based on the following assumptions:

1. Flow is laminar everywhere due to small gas pressure gradient and low Reynolds number.
2. Reactant gases behave as the ideal gas mixture.
3. The electrodes and membrane are made of homogeneous materials.
4. The temperature distribution across the cell is uniform.
5. Water exists only in the gas phase in the fuel cell.
6. The polymer electrolyte membrane is impermeable to reactant gases.
7. Protons can only transport through the electrolyte, and electrons through the solid phase.
8. Three species including oxygen, water and nitrogen are considered on the cathode side while only hydrogen and water are considered on the anode side.
9. The fuel cell is operating at the steady state.

## 2.2 Governing equations

### 2.2.1 Flow channels

Based on the model assumptions, the reactant gas flow in the gas channel is governed by the continuity equation to insure the mass conservation and the steady state incompressible Navier-Stokes equation to describe the momentum conservation of Newtonian fluids.

N-S Equation:

$$\rho(u \cdot \nabla)u = \nabla \cdot [-PI + \mu(\nabla u + (\nabla u)^T)] \quad (1)$$

Continuity Equation:

$$\nabla \cdot u = 0 \quad (2)$$

where  $u$  is velocity vector, m/s;  $P$ , pressure, Pa;  $\rho$ , mixture density, kg/m<sup>3</sup>;  $\mu$ , dynamic viscosity, kg/(m s).

The multi-component diffusion and convection in flow channels are described by the Maxwell-Stefan equation. It solves for the fluxes in terms of mass fraction. The general form of the Maxwell-Stefan equation is shown below:

Maxwell-Stefan Equation:

$$\frac{\partial}{\partial t} \rho a_i + \nabla \cdot [-\rho a_i \sum_{j=1}^N D_{ij} \left\{ \frac{M}{M_j} (\nabla \omega_j + \omega_j \frac{\nabla M}{M}) + (x_j - \omega_j) \frac{\nabla P}{P} \right\} + a_j \rho u] = R_i \quad (3)$$

where  $D_{ij}$  is the diffusion coefficient, m<sup>2</sup>/s;  $R_i$ , the reaction rate and is zero in the flow channel, kg/(m<sup>3</sup>.s);  $x$ , the mole fraction;  $\omega$ , the mass fraction;  $M$ , the molecular mass, kg/mol. The density of mixture gas  $\rho$  is a function of mixture components and is described by the following equation:

$$\rho = \left( \sum_i x_i M_i \right) P / (RT) \quad (4)$$

where  $x_i$  is the mole fraction;  $R$ , the universal gas constant, 8.314 J/(mol.K);  $T$ , the cell temperature, K. The subscript  $i$  (or  $j$ ) represents each species of hydrogen and water on the anode side, and oxygen, water, nitrogen on the cathode side.

On the cathode side, the transport equations are solved for two species since the third species can always be obtained from the mass balance equation given as following:

$$w_{N_2} = 1 - w_{O_2} - w_{H_2O} \quad (5)$$

On the anode side, the hydrogen transport equation is solved first, and then the mass fraction of water can be obtained by:

$$w_{H_2O} = 1 - w_{H_2} \quad (6)$$

### 2.2.2 Gas diffusion layers and catalyst layers

Since gas diffusion layers (GDL) and catalyst layers are porous media, the velocity distribution is therefore formulated by Darcy's law and mass conservation equation.

Darcy's Law:

$$u = -\frac{\kappa}{\mu} \nabla p \quad (7)$$

where  $\kappa$  is the permeability, m<sup>2</sup>; and  $\mu$  the dynamic viscosity, Pa.s;

Continuity equation:

$$\nabla \cdot (\rho u) = S \quad (8)$$

where  $S$  is the source term,  $\text{kg}/(\text{m}^3\cdot\text{s})$ . The continuity equation for the gas flow mixture describes the sum of all the involved gas species at each side. The source term,  $S$ , accounts for the total consumption and production during the electrochemical reactions.

In the catalytic layer, the reaction rate  $R_i$  corresponding to each species is given as:

$$R_{H_2} = -\frac{j_a}{2F} M_{H_2} \quad (9)$$

$$R_{O_2} = -\frac{|j_c|}{4F} M_{O_2} \quad (10)$$

$$R_{H_2O} = \frac{|j_c|}{2F} M_{H_2O} \quad (11)$$

### 2.2.3 Current transport

The continuity of current in a conducting material is described by

$$\nabla \cdot i = 0 \quad (12)$$

In a PEM fuel cell, the conducting materials are porous electrodes and membrane. The current is therefore split into two parts: the ionic current and the electronic current. Protons travel through the ionic conductor (the membrane) to form an ionic current denoted by  $i_e$ , while electrons can only be transferred through the solid matrix of electrodes which results in an electronic current denoted by  $i_s$ . The continuity equation of current then becomes:

$$\nabla \cdot i = \nabla \cdot i_s + \nabla \cdot i_e = 0 \quad (13)$$

In the catalyst layer, where a chemical reaction occurs on a three-phase boundary, electrons are either transferred from the solid matrix to electrolyte or vice versa. This two-way transfer of electrons between solid matrix and electrolyte makes the transfer current density, denoted by  $j$ , a source term in one phase, and a sink term in the other phase. The potential equations for both solid and electrolyte phases are obtained by applying Ohmic's law to Eq. (13).

Electron transport

$$\nabla \cdot (-\sigma_s \nabla \phi_s) = S_s \quad (14)$$

Proton transport

$$\nabla \cdot (-\sigma_e \nabla \phi_e) = S_e \quad (15)$$

Where  $\phi$  is the phase potential, V;  $\sigma$ , the effective electric conductivity,  $\text{s}/\text{m}$ ;  $S$  the current source term,  $\text{A}/\text{m}^3$ ; the subscript  $s$  denotes the property of a solid phase and  $e$  denotes that of an electrolyte phase. The source terms in the electron and proton transport equations, i.e., Eq. (14-15), result from the electrochemical reaction occurring in the catalyst layers of anode and cathode sides.

Anode Catalyst layer:

$$S_e = j_a \quad ; \quad S_s = -j_a \quad (16)$$

Cathode Catalyst layer:

$$S_e = j_c \quad ; \quad S_s = -j_c \quad (17)$$

where  $j_a$  and  $j_c$  are the transfer current density corresponding to the electrochemical reaction at the anode and cathode catalyst layers, which is formulated by the agglomerate model. In the catalyst layers, the agglomerate is formed by the dispersed catalyst, and this zone is filled with electrolyte. Oxygen is dissolved into the electrolyte and reaches the catalyst site. The agglomerate model describes the transfer current density as following (Broka, 1995):

Anode:

$$j_a = -\frac{6(1-\varepsilon)FD_H^{agg}}{(R^{agg})^2} (c_H^{agg} - c_H^{ref} \exp(-\frac{2F}{RT}\eta)) \cdot (1 - \sqrt{\frac{j_{o,a}s}{aFc_H^{ref}D_H^{agg}} R^{agg}} \coth \sqrt{\frac{j_{o,a}s}{aFc_H^{ref}D_H^{agg}} R^{agg}}) \quad (18)$$

Cathode:

$$j_c = R \frac{12(1-\varepsilon)FD_O^{agg}}{(R^{agg})^2} c_O^{agg} \cdot (1 - \sqrt{\frac{j_{o,c}s(R^{agg})^2}{4Fc_O^{ref}D_O^{agg}} \exp(-\frac{0.5F}{RT}\eta)}) \cdot \coth \sqrt{\frac{j_{o,c}s(R^{agg})^2}{4Fc_O^{ref}D_O^{agg}} \exp(-\frac{0.5F}{RT}\eta)} \quad (19)$$

where  $c^{agg}$  is the gas concentration at the surface of the agglomerates, mol/m<sup>3</sup>;  $c^{ref}$  the dissolved gas concentration at a reference state, mol/m<sup>3</sup>; F, the Faraday constant, coulomb/mol;  $D^{agg}$  the diffusion coefficient, m<sup>2</sup>/s of the dissolved gas inside the agglomerate;  $R^{agg}$  the agglomerate radius, m;  $j_0$  the exchange current density, A/m<sup>2</sup>;  $s$  the specific surface area, m<sup>2</sup>/m<sup>3</sup>;  $\eta$  the electrochemical overpotential, V, which is expressed by the potential difference between solid matrix and electrolyte and is defined as:  
Anode side:

$$\eta = \phi_s - \phi_e \quad (20)$$

Cathode side:

$$\eta = \phi_s - \phi_e - U_{OC} \quad (21)$$

where the open-circuit potential  $U_{oc}$  is given by

$$U_{OC} = 1.23 - 0.9 \times 10^{-3} (T - 298) \quad (22)$$

The dissolved gas concentration at the surface of the agglomerates is corresponding to the molar fraction in the gas phase through Henry's Law:

$$c^{agg} = \frac{c_{gas}P}{H} \quad (23)$$

where H is the Henry's constant, Pa.m<sup>3</sup>/mol.

### 2.3 Numerical procedure

COMSOL Multiphysics, a commercial solver based on the finite element technique, is used to solve the governing equations. The stationary nonlinear solver is used since the source terms of the current conservation equation make the problem non-linear. Furthermore, the convergence behavior of this non-linear solver is highly sensitive to the initial estimation of the solution. To accelerate the convergence, the following procedures are adopted: the Conductive Media DC module is firstly solved based on the initial setting; secondly, Darcy's Law and Incompressible Navier-Stokes modules are solved together using the results from the previous calculation as initial conditions. After the previous two modules converge, all the coupled equations including Maxwell-Stefan Diffusion and Convection module are solved simultaneously until the convergence is obtained as shown in Fig. 3.

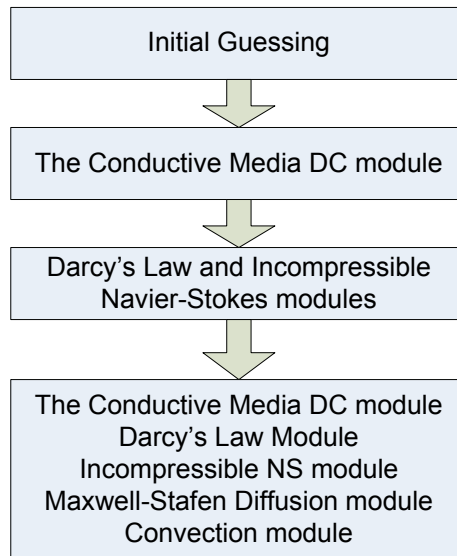


Figure 3. Solving procedure in COMSOL Multiphysics

### 3. Results and discussion

Using the aforementioned procedures, the X-Z geometry as described in Fig. 2a and the X-Y geometry in Fig. 2b are simulated separately. The X-Z mode represents the PEM fuel cell with straight or serpentine channels on the bipolar plates while the X-Y mode represents those with interdigitated channels. The material properties used in the model are selected

from Meng and Wang, 2005. The parameters describing the electrochemical reaction are based on the agglomerate model from (Broka, 1995).

Figure 4 shows the polarization curve obtained from the X-Z model. Figure 5 shows the profile of oxygen mass fraction on the cathode side for the cell operating voltages of 0.8 volt and 0.3 volt. The reactant gas concentration decreases along the flow direction and across the membrane direction due to the consumption of fuel in the electrochemical reaction at the catalyst layer. A higher fuel concentration gradient is found at 0.3 volt (the left figure in Fig.5), which is due to the faster consumption of fuel when the cell is working at low output voltage but high current density.

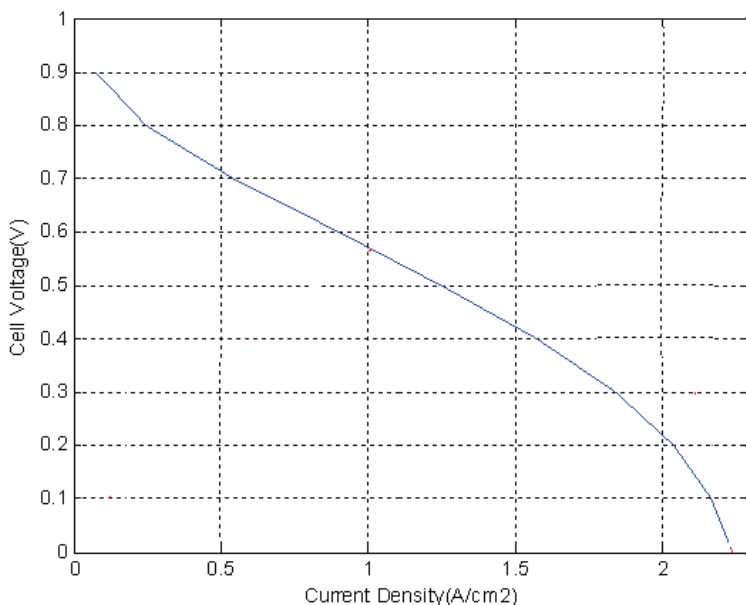


Figure 4. Polarization curves: the X-Z model

Figure 6 shows the polarization curve of X-Y model. Figure 7 shows the concentration profile of oxygen of X-Y model. The flow channel is not included in this model; however, this model can provide more detailed descriptions of fuel cell performance across the membrane direction. The oxygen mass fraction decreases from the inlet to outlet, and it decreases faster at the low voltage and high current density conditions, which is again due to the faster fuel consumption in chemical reactions since that the consumption rate is proportional to the cell operating current density.

Fig. 8 and Fig. 9 show the distribution of solid phase and electrolyte phase potentials across the membrane obtained from the X-Z and X-Y models, respectively. The potential distribution displays a similar behaviour for two different models. An obvious potential drop is found within the membrane due to the low proton conductivity of membrane. The ohmic losses, however, are very small on both anode and cathode electrodes. A high overpotential is found on the cathode side due to the slow kinetic reaction of oxygen reduction.

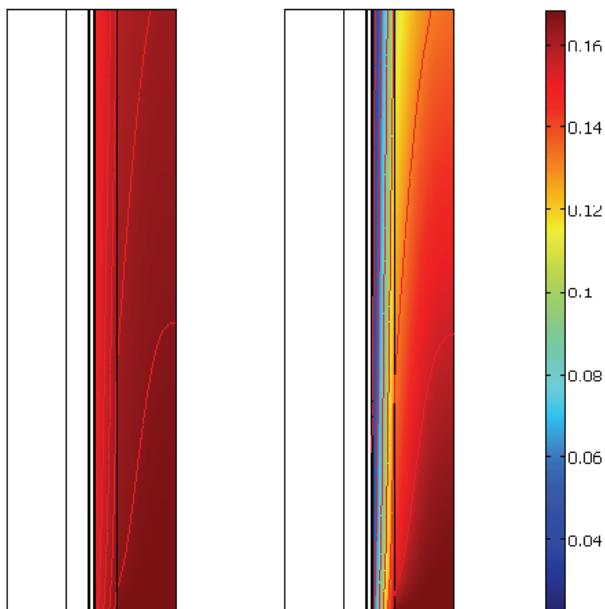


Figure 5. Oxygen mass fraction distribution in the X-Z mode (Left:  $V_{cell}=0.8\text{ V}$ , Right:  $V_{cell}=0.3\text{ V}$ )

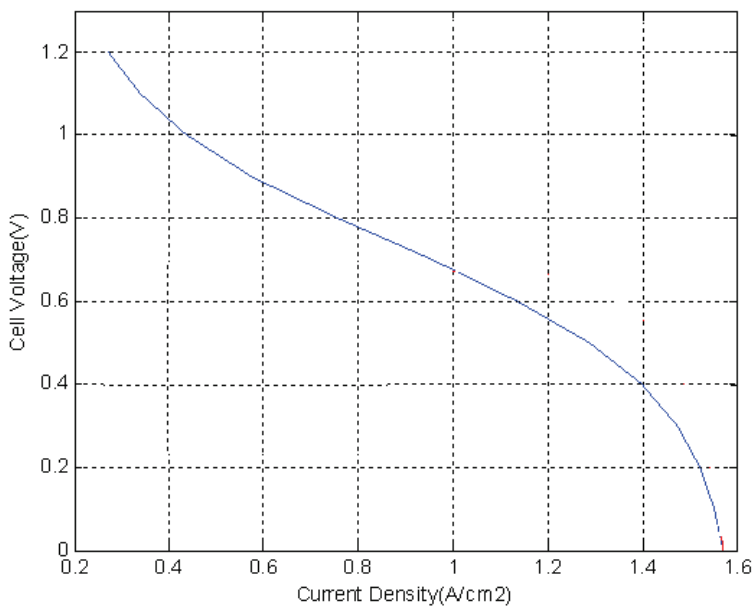


Figure 6. Polarization curves: the X-Y mode

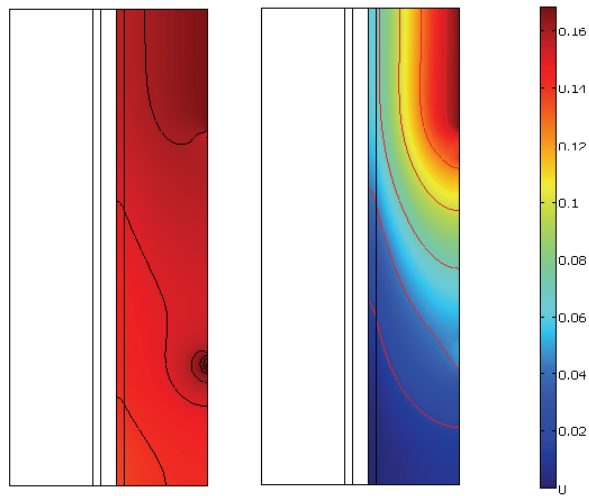


Figure 7. Oxygen mass fraction distribution in the X-Y mode (Left:  $V_{cell}=0.8$  V, Right:  $V_{cell}=0.3$  V)

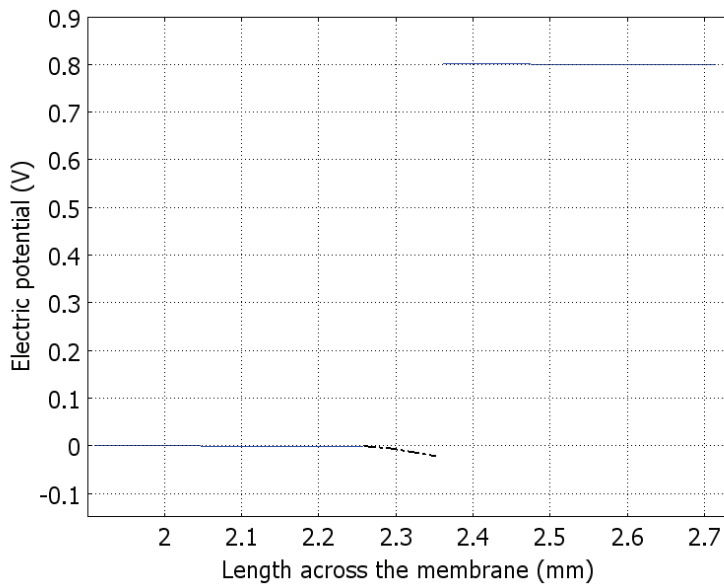


Figure 8. Electrical potential distribution in the electrodes and membrane profiles: the X-Z model (Solid line: solid phase potential, Dashed line: electrolyte phase potential)



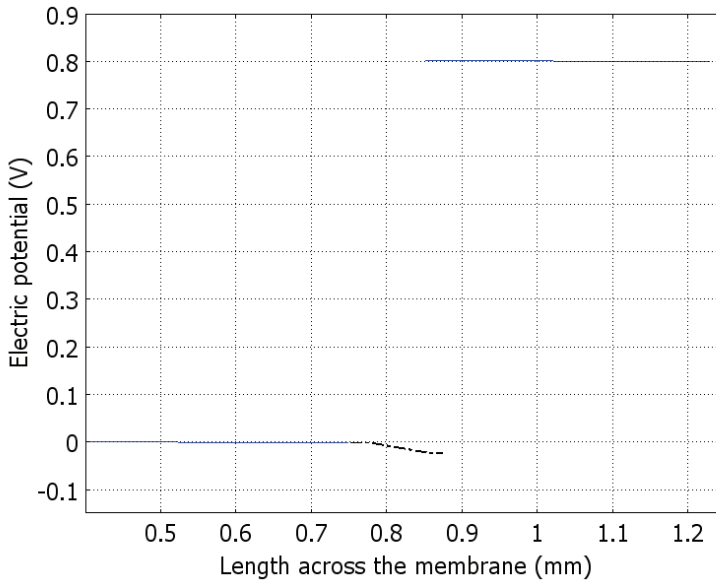


Figure 9. Electrical potential distribution in the electrodes and membrane profiles: the X-Y model (Solid line: solid phase potential, Dashed line: electrolyte phase potential)

#### 4. Conclusions

Two-dimensional, single-phase and isothermal models of PEM fuel cells were developed in two different modes. These models are solved using commercial software package, COMSOL Multiphysics, based on finite element techniques. The models are able to investigate the transport phenomena and electrical potential distribution in the various PEM fuel cell components including the gas channels, gas diffusion layers, catalyst layers and membrane.

The polarization curves were presented. The X-Z model was used to study the fuel cell with straight channels or serpentine channels design. The X-Y model is suitable for the fuel cell with interdigitated flow patterns. Both X-Z and X-Y model show the fuel mass fraction decrease faster when the cell is working at low voltage and high current density region. In both X-Y and X-Z models, the potential distribution indicated a major potential drop occurring across the membrane, and a higher overpotential was found on the cathode catalyst layer. These two modes of models can be combined together to describe the overall behavior of PEM fuel cells in all directions.

#### 5. References

- Berning T., Lu D.M. & Djilali N. (2002). Three-dimensional computational analysis of transport phenomena in a PEM fuel cell, *Journal of Power Sources*, 106, 284-294
- Biyikoglu A. (2005), Review of proton exchange membrane fuel cell models, *International Journal of Hydrogen Energy*, 30, 1181-1212

- Broka K. (1995), Characterization of the Components of the Proton Exchange Membrane Fuel Cell, Technical licentiate Thesis, Royal Institute of Technology, Stockholm, Sweden.
- Gurau V., Barbir F. & Liu H. (2000), An Analytical Solution of a Half-Cell Model for PEM Fuel Cell, *Journal of The Electrochemical Society*, 147, 2468-2477
- Haraldsson K. & Wipke K. (2004), Evaluating PEM fuel cell system models, *Journal of Power Sources*, 126, 88-97
- Hwang J.J. (2006). Thermal-Electrochemical Modeling of a Proton Exchange Membrane Fuel Cell, *Journal the Electrochemical Society*, 153, A216-A224
- Meng H. & Wang C.Y. (2005), Model of Two-Phase Flow and Flooding Dynamics in Polymer Electrolyte Fuel Cells, *Journal of the Electrochemical Society*, 152, A1733-A1741
- Siegel N.P., Ellis M.W., Nelson D.J. & Spakovsky von M.R. (2003). Single domain PEMFC model based on agglomerate catalyst geometry, *Journal of Power Sources*, 115, 81-89
- Springer T.E., Zawodzinske T.A. & Gatteadold S. (1991). Polymer Electrolyte Fuel Cell Model, *Journal of Electrochem. Soc.*, 138, 2334-2342